ISSN 1304-7191
E-ISSN 1304-7205

sigma

Journal of Engineering and Natural Sciences

Mühendislik ve Fen Bilimleri Dergisi

Volume 43
Number 6
Year 2025

YTU PRESS

www.sigma.yildiz.edu.tr

E-ISSN 1304-7205

Sigma
Journal of Engineering and Natural Sciences
Mühendislik ve Fen Bilimleri Dergisi

Volume 43 Number 6 Year 2025 - December

EDITOR-IN-CHIEF

Ahmet Selim DALKILIÇ
Department of Mechanical Engineering, Yıldız Technical University, İstanbul, Turkey

ASSOCIATE EDITORS

İhsan KAYA
Department of Industrial Engineering, Yıldız Technical University, İstanbul, Turkey

Nergis ARSU
Department of Chemistry, Yıldız Technical University, İstanbul, Turkey

SECTION EDITORS

Ali ERDOĞMUŞ
Department of Chemistry, Yıldız Technical University, İstanbul, Turkey

Alper YILMAZ
Department of Bioengineering, Yıldız Technical University, İstanbul, Turkey

Azmi Seyhun KIPÇAK
Department of Chemical Engineering, Yıldız Technical University, İstanbul, Turkey

Banu MANSUROĞLU
Department of Moleculer Biology and Genetics, Yıldız Technical University, İstanbul, Turkey

Emel AKYOL
Department of Chemical Engineering, Yıldız Technical University, İstanbul, Turkey

Eyüp DEBİK
Department of Enviromental Engineering, Yıldız Technical University, İstanbul, Turkey

Fatih AKYOL
Department of Metallurgical and Materials Engineering, Yıldız Technical University, İstanbul, Turkey

Gülhayat GÖLBAŞI ŞİMŞEK
Department of Statistics, Yıldız Technical University, İstanbul, Turkey

Hakan YILMAZER
Department of Metallurgy and Malterials Engineering, Yıldız Technical University, İstanbul, Turkey

Hasan KÖTEN
Department of Mechanical Engineering, İstanbul Medeniyet University, İstanbul, Turkey

Hayriye SUNDU PAMUK
Department of Physics, Kocaeli University, Kocaeli, Turkey

Mesut AKGÜN
Department of Chemical Engineering, Yıldız Technical University, İstanbul, Turkey

Metin TÜLÜ
Department of Chemistry, Yıldız Technical University, İstanbul, Turkey

Muhammet Kasım ŞENER
Department of Chemistry, Yıldız Technical University, İstanbul, Turkey

Müslüm ARICI
Department of Mechanical Engineering, Kocaeli University, Kocaeli, Turkey

Nader JAVANI
Department of Mechanical Engineering, Yıldız Technical University, İstanbul, Turkey

Osman Nuri UÇAN
Department of Electrical and Electronics Engineering, Altınbaş University, İstanbul, Turkey

Ömer Said TOKER
Department of Food Engineering, Yıldız Technical University, İstanbul, Turkey

E-ISSN 1304-7205

Sigma
Journal of Engineering and Natural Sciences
Mühendislik ve Fen Bilimleri Dergisi

Volume 43 Number 6 Year 2025 - December

Necmiye Özlem ÜNVERDİ
Department of Electronics and Communication Engineering, Yıldız Technical University, İstanbul, Turkey
Selçuk ÇEBİ
Department of Industrial Engineering, Yıldız Technical University, İstanbul, Turkey
Sevil YÜCEL
Department of Bioengineering, Yıldız Technical University, İstanbul, Turkey
Vildan ÇETKİN
Department of Mathematics, Kocaeli University, Kocaeli, Turkey
Yasemin BUDAMA KILINÇ
Department of Bioengineering, Yıldız Technical University, İstanbul, Turkey

REGIONAL EDITORS

Abdelraheem Mahmoud ALY
South Valley University, Egypt
Abdullahi YUSUF
Federal University Dutse, Nigeria;
Biruni University Istanbul, Turkey
Adem KILICMAN
Department of Mathematics, University Putra, Malaysia
Amin SHAHSAVAR
Kermanshah University of Technology, Iran
Chandramohan V.P.
National Institute of Technology Warangal, India
Gobinath RAVINDAN
SR University, India
Hijaz AHMAD
University of Engineering and Technology Peshawar, Khyber Pakhtunkhwa, Pakistan
Md. Sabir HOSSAIN
Chittagong University of Engineering and Technology, Bangladesh
Mohammad Reza SAFAEI
Department of Civil and Enviromental Engineering, Florida International University, USA
Mostafa Safdari SHADLOO
Insa of Rouen, France
Muthu Poosan MOOPANAR
Department of Mathematics, National Institute of Technology, Warangal, India
Oscar CASTILLO
Tijuana Institute of Technology, Mathematics Division, Mexico
Pravin KATARE
Marathwada Mitra Mandal's College of Engineering, India
Ravindar KUMAR
Lovely Professional University, India
Sania QURESHI
Department of Basic Sciences and Related Studies, Mehran University of Engineering and Technology, Pakistan
Siamak HOSEINZADEH
Department of Planning, Design, and Technology of Architecture, University of Roma, Italy
Shengda ZENG
School of Mathematics and Statistics, Yulin Normal University, Yulin, China;
Faculty of Mathematics and Computer Science, Jagiellonian University in Krakow, Krakow, Poland
Taha M. RABABAH
Department of Nutrition and Food Technology, Jordan University of Science and Technology, Jordan

E-ISSN 1304-7205

Sigma Journal of Engineering and Natural Sciences
Mühendislik ve Fen Bilimleri Dergisi

Volume 43 Number 6 Year 2025 - December

ADVISORY EDITORS

Bestami ÖZKAYA
Department of Civil Engineering, Yıldız Technical University, İstanbul, Turkey

Cengiz KAHRAMAN
Department of Industrial Engineering, İstanbul Technical University, İstanbul, Turkey

Erol TUTUMLUER
Department of Civil Engineering, University of Illinois Urbana-CHampaign, USA

Hari Mohan SRIVASTAVA
Department of Mathematics and Statistics, University of Victoria, Canada

Mohsen SHEIKHOLESLAMI
Babol Noshirvani University of Technology, Iran

Melike Elif BİLDİRİCİ
Department of Economics, Yıldız Technical University, İstanbul, Turkey

Somchai WONGWISES
Department of Mechanical Engineering, King Mongkut's University of Technology, Thonburi, Thailand

Umut Rıfat TUZKAYA
Department of Industrial Engineering, Yıldız Technical University, İstanbul, Turkey

Zekai ŞEN
İstanbul Medipol University, İstanbul, Turkey

Zeynep IŞIK
Department Civil Engineering, Yıldız Technical University, İstanbul, Turkey

SECRETARY

Senol BİLGİN
Yıldız Technical University, İstanbul, Turkey

Abstracting and Indexing:
- Directory of Open Access Journals (DOAJ)
- EBSCO Host Online Research Databases
- Emerging Sources Citation Index (ESCI)
- Scopus
- MIAR
- Scilit
- OUCI
- Research4Life
- Ideal Online

Journal Description: The journal is supported by Yıldız Technical University officially, and is a blind peer-reviewed free open-access journal, published bimontly (February-April-June-August-October-December).

Owner: Yıldız Technical University

Editor-in-Chief: Ahmet Selim Dalkiliç

Language of Publication: English

Frequency: Bimontly (6 issues per year)

Publication Type: Online e-version

Publisher: Kare Publishing

E-ISSN 1304-7205

Sigma
Journal of Engineering and Natural Sciences
Mühendislik ve Fen Bilimleri Dergisi

Volume 43 Number 6 Year 2025 - December

CONTENTS

Research Articles

1897 **To the 90th anniversary of professor Telman A. Aliev**
Naila MUSAEVA, Ana MAMMADOVA

1905 **Determination of factors affecting greenhouse gases emitted to the atmosphere in eurostat countries with multiple linear regression model**
Ömer Faruk KIZIL, Özge KURAN

1915 **Optimizing textual sentiment recognition through LASSO-based feature selection and ensemble voting technique**
NISHA, Rakesh KUMAR

1930 **Numerical investigation of the mathematical model including the possibility of reinfection in infectious diseases**
Mehmet KOCABIYIK

1943 **Biosynthesis of silver nanoparticles using aerial parts of *Cardaria draba* L.: Phytochemical analysis, characterization, evaluation of antibacterial, cytotoxic on human colon cancer cell line properties and enzyme inhibitory potentials**
Özlem BAKIR BOĞA, Esabi BAŞARAN KURBANOĞLU

1957 **Separation of cations by capillary electrophoresis: The effects of temperature and voltage**
Ahmet DURSUN, Cahit DEMETGÜL

1967 **Trigonometric based B-spline method for singularly perturbed sobolev problems with initial layers**
Shegaye Lema CHERU, Gemechis File DURESSA, Tariku Birabasa MEKONNEN

1982 **Productivity improvement in manufacturing of furniture using quality function deployment approach**
Dhananjay APTE, Prafulla HATTE, Vishal PRADHAN

E-ISSN 1304-7205

Sigma
Journal of Engineering and Natural Sciences
Mühendislik ve Fen Bilimleri Dergisi

Volume 43 Number 6 Year 2025 - December

1995 **In *vitro* degradation studies of polylactide/ polyethylene glycol electrospun fiber blends**
Oluwashina Philips GBENEBOR, Abimbola Patricia POPOOLA

2006 **Ultrasonic waveguide sensor design using bend reflectors for elastic moduli and temperature measurement**
Anubhav SRIVASTAVA, Arun VALABHOJU, Abhishek KUMAR, Suresh PERIYANNAN

2017 **Statistical modeling of alkali pretreatment for degradation of saccharum**
Muhammad IRFAN, Misbah GHAZANFAR, Hafiz Abdullah SHAKIR, Muhammad KHAN, Marcelo FRANCO

2031 **The role of artificial intelligence in rooting local architecture**
Israa Mohammad A. AL-SAFFAR, Osamah Abdulmunem AL-TAMEEMI, Fawzia Irhayyim AL-ASSADI

2050 **A study on copolymers of styrene with a methacrylamide containing benzofuran side group: Their monomer reactivity ratios, thermal stabilities, thermal degradation kinetics**
Esra BARIM, Pınar DEMIR, Mustafa DEĞIRMENCI, Cumhur KIRILMIŞ

2066 **Effect of pier-collar system on flow characteristics of composite hydraulic structure**
Rafi Mohammed QASIM, Khalid AL-ASADI, Ihsan Abdulkareem ABDULHUSSEIN, Qusay Abdulrazzaq MAATOOQ

2084 **Effect of reinforcements in aluminium 5052-magnesium AZ31 explosive cladding**
S. SARAVANAN

2094 **Aczel alsina aggregation operators of (M,N,Q)-spherical hesitant fuzzy sets and their applications in multi-attribute decision-making**
Şerif ÖZLÜ

2108 **A model to protect disaster recovery centers from cyber threats with multi-layered network security architecture**
Aykut YILMAZ, Ali GÜNEŞ

2127 **Heat generation from 32650 cylindrical cell battery pack at various load and speed conditions**
Shashank GAWADE, Virendra BHOJWANI, Pradeep PATIL, M. ZUBAIRUDDIN

E-ISSN 1304-7205

sigma
Journal of Engineering and Natural Sciences
Mühendislik ve Fen Bilimleri Dergisi

Volume 43 Number 6 Year 2025 - December

2140 **Strategic load scheduling in smart home: Leveraging IOT and optimization algorithms for energy cost reduction**
Ganesh SHIRSAT, Aniruddha MUKHERJEE, Ankit Kumar SHARMA

2152 **Treatability of landfill leachate pre-treated with a two-stage biological treatment process to the level of receiving environment standards by using the fenton process**
Uğur KURT, Ömer APAYDIN, Yaşar AVŞAR, Mustafa Talha GÖNÜLLÜ

2164 **Male lifestyle habits and in vitro fertilization outcomes: The effects of alcohol and smoking on sperm characteristics and pregnancy rates**
Tamara AL-BARQ, Manal GHANNAM, Bilgen KAYMAKAMZADE, Evren HINCAL, Muhammad FARMAN

2174 **Evaluation of health care systems using supervised and unsupervised machine learning approaches**
Canan BULUT, Tuğba SÖNAL, Dilek KOLCA, Fatih TARLAK

2186 **Cosine Kumaraswamy family of distributions: Properties and applications to real-world datasets**
Ibrahim ALI, Alhaji Modu ISA, Sule Omeiza BASHIRU, Arum Kingsley CHINEDU

2198 **Enhancing battery safety and performance through advanced cooling solutions for electric vehicles**
Madhavi NERKAR, Govind Rai GOYAL, Aniruddha MUKHERJEE, Bhanu Pratap SONI

2213 **Static and dynamic slope stability analyses based on finite elements method: The example of Birecik Slopes**
Ferit TAYLAN, Ali SARIIŞIK, Mustafa ULUKAVAK, Songül CAN

2234 **Simulation of engine oil driven second grade ternary hybrid nanofluid flow subject to thomson and troian slip velocity addressing the thermo-convection effect**
Tusar Kanti DAS, Mintu SAUD, Nayanto HAJONG, Bidyut KALITA

2248 **Experimental and microstructural investigation of geopolymer concrete**
Swapnil D. KURHADE, Subhash V. PATANKAR

E-ISSN 1304-7205

Journal of Engineering and Natural Sciences
Mühendislik ve Fen Bilimleri Dergisi

Volume 43 Number 6 Year 2025 - December

2263 **Double-sided bandpass frequency selective surface design for C band WLAN radome applications2262**
Burak Can KIŞLA, Bilge ŞENEL

2272 **Comparative study of fermatean fuzzy soft sets with normalized distances and its application in diagnose infectious diseases**
Saika SHEWALI, Borah Manash JYOTI, Mahanta Dimpal JYOTI

2279 **Centralized controller-based on optimal power flow (OPF) algorithm for power management in microgrid systems**
Abumuslim KHUJAEV, Abbas UĞURENVER

Sigma J Eng Nat Sci, Vol. 43, No. 6, pp. 1897–1904, December, 2025

Sigma Journal of Engineering and Natural Sciences
Web page info: https://sigma.yildiz.edu.tr
DOI: 10.14744/sigma.2025.00000

Research Article

To the 90th anniversary of professor Telman A. Aliev

Naila MUSAEVA[1,2], Ana MAMMADOVA[1,2]

[1]*The Azerbaijan University of Architecture and Construction, Baku, AZ1073, Azerbaijan*
[2]*Institute of Control Systems, Baku, AZ1141, Azerbaijan*

ARTICLE INFO

Article history
Received: 09 July 2025
Accepted: 21 July 2025

Keywords:
Noise Characteristics; Noise Technologies; Signal Processing

ABSTRACT

The article briefly describes scientific and pedagogical achievements of Professor Telman Abbas Aliev, Doctor of Technical Sciences, and highlights the key historic events of his life and academic career, his bibliography: books, articles and conference papers.
T.A. Aliev has shown that the traditional conditions of "absence of correlation between the useful signal and the noise" in the analysis of noisy signals at the beginning of emergency state of objects are not fulfilled. To ensure accident-free operation of control objects, it is necessary to create a technology for analyzing noisy signals in the presence of correlation between the useful signal and the noise, which occurs at the beginning of accidents. T.A. Aliev has proposed technologies that allow to ensure accident-free operation of control objects to a significantly larger extent. To validate the effectiveness of these results, experimental studies were conducted for many years at compressor stations, oil fields, drilling rigs, offshore platforms, in transportation, medicine, construction and seismology. These results have been outlined in numerous articles and in three monographs published by Springer.

Cite this article as: Musaeva N, Mammadova A. To the 90th anniversary of professor Telman A. Aliev. Sigma J Eng Nat Sci 2025;43(6):1897–1904.

INTRODUCTION

On May 2, 2025, the outstanding computer scientist, Advisor to the Azerbaijan National Academy of Sciences and Head of the Information Technologies and Systems Department of Azerbaijan University of Architecture and Construction, DSc in Engineering, Professor, Academician Telman A. Aliev celebrated his 90th birthday. The article gives a brief summary of scientific and pedagogical achievements of T.A. Aliev.

Biography

Telman Abbas Aliev was born on May 2, 1935, in Goranboy, Azerbaijan. He attended the Delimamedli village secondary school in Goranboy from 1943 to 1950, and the Azizbekov village secondary school from 1950 to 1953 (Fig. 1). After graduating the M. Azizbekov Azerbaijan Industrial Institute (1953 to 1958), he started working at the Computing Centre, first as a technician, later as engineer and chief engineer until starting postgraduate studies in 1962 (Fig. 2) and (Fig. 3).

*Corresponding author.
*E-mail address: musanaila@gmail.com

This paper was recommended for publication in revised form by Editor-in-Chief Ahmet Selim Dalkilic

Published by Yıldız Technical University Press, İstanbul, Turkey
© Author. This is an open access article under the CC BY-NC license (http://creativecommons.org/licenses/by-nc/4.0/).



Figure 1. Baku. 1st year. 1953.



Figure 2. Work experience internship after completing the 3rd year. Leningrad. 1956.

Telman Aliev founded and, until 1976, headed the Laboratory of Electronic Computing Machines, which was established in Azerbaijan between 1958 and 1960 and played a crucial role in developing computer science in the country (Fig. 4.). He sat on the Board of the Computer Science and Computer Engineering Society, as well as on the computer science, computer engineering and cybernetics expert council of the USSR. Telman Aliev has authored



Figure 3. Working on diploma in Lviv. 1957.



Figure 4. BESM-2 mainframe computer.

Amirov A., Aliev T., Gasimov E. 1960

several key works at the intersection of computer science, cybernetics, and physics.

In 1966, Telman Aliev successfully defended his Candidate's dissertation, which was overseen by Prof. V.V. Solodovnikov at Bauman Moscow State Technical University (Fig. 5). He went on to complete his DSc dissertation in 1977. He was elected a Corresponding Member of the Azerbaijan National Academy of Sciences (ANAS) in 1983 and a Full Member of ANAS in 2001.

Telman Aliev became Deputy Director at the Institute of Cybernetics in 1982, honorary head of department of the AzUAC in 1984. The title of Professor was awarded to Telman Aliev in 1985. He held the position of the Director of the Institute of Control Systems (formerly the Institute of Cybernetics) from 1988 to 2020.

From 1993 to 1998, he chaired the Expert Council of the Higher Attestation Commission under the President of



Figure 5. At International Symposium in Veliky Novgorod. Prof. V.V.Solodovnikov, Prof. T.A. Aliev, Prof. L.T. Kuzin.



Figure 7. Prof. T.A. Aliev

Azerbaijan, became a UNESCO computer science expert in 1994.

From 1997 to 2001, Prof. Aliev served as the Academician Secretary of the Division of Physical, Mathematical and Technical Sciences (PMTS) of ANAS. He was on the Presidium of the Higher Attestation Commission from 2008 to 2015.

More recently, Prof. Aliev has led the introduction of a new RNM system at 500 facilities of the Bibiheybat NGDU. This system enables remote diagnosis and management of downhole oil extraction equipment, effectively doubling their profitability (Fig. 6).

Since 2013, Telman Aliev is on the editorial board of the Russian (Moscow) *Mekhatronika, Avtomatika, Upravlenie* journal and the Ukrainian (Kyiv) *Problems of Control and Informatics* journal.

In 1991, T.A. Aliev was awarded the Keldysh Medal for his achievements in scientific and scientific-public work, in 2004 the Shohrat Order. He was awarded the title of Honorary Scientist of the Republic of Azerbaijan in 2009, the Nasreddin Tusi Prize of the ANAS in 2015, and the Academician Azad Mirzajanzade International Silver Medal in 2018. He chaired the dissertation council of the Institute of Control Systems. In 2024, Prof. Aliev received the "100th Anniversary of Heydar Aliev (1923-2023)" jubilee medal (Fig. 7).

Telman Aliev has authored 594 publications, including many in journals indexed by the Web of Science (WoS), and 3 monographs at Springer. The most recent of them, *Noise Control of the Beginning and Development Dynamics of Accidents* (2019, 201 p.), was included in the "Springer Link Engineering" e-book collection by Springer Publishing House in 2019 and was published as part of it. In this



Figure 6. Implementation of the oil well monitoring system based on Noise technology at the "Shirvan Oil" oil field.

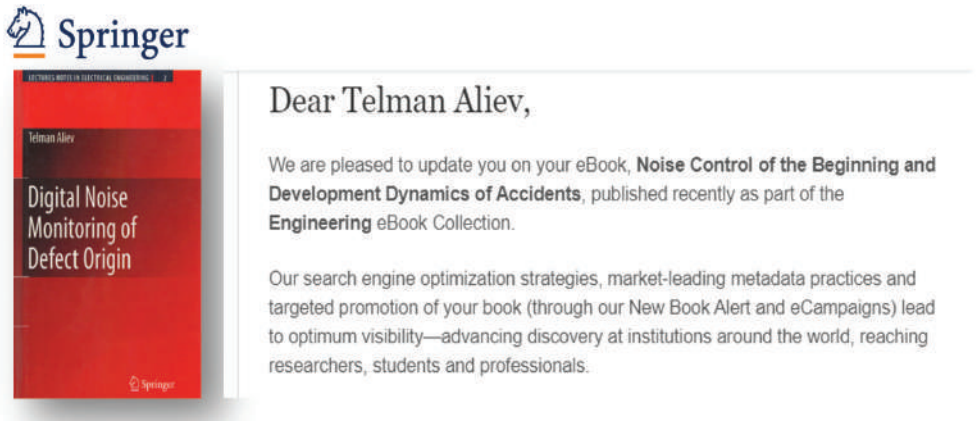


Figure 8. Letter from Springer Publishing House.

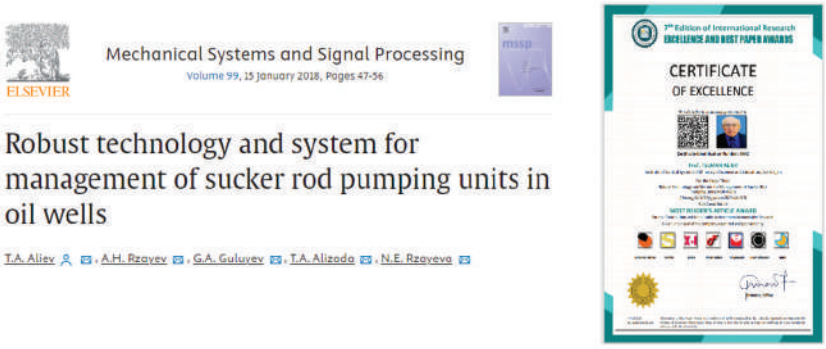


Figure 9. Telman Aliyev's article and certificate in the "most read article".

regard, a letter was addressed to Academician Telman Aliev by Springer Publishing House (Fig. 8).

On July 4, 2023, Telman Aliyev's article published in the international journal "Mechanical Systems and Signal Processing" was awarded a certificate in the "Most Read Article" nomination in the "International Achievements in Research and Best Article" category (Fig. 9).

Telman Aliev was academic advisor of 37 PhD and 13 DSc candidates. He is the author of 35 monographs, 462 research papers and 132 patents.

Out of 35 monographs 3 were published by Springer, 11 by Lambert Academic Publishing in Germany and other publishers, 7 of them were published in Moscow.

Of these 462 papers, 193 were published in prestigious English-language journals, 102 in national journals, 91 at international conferences and 76 in the proceedings of national conferences.

It should also be noted that out of 132 patents 67 are international patents and 65 are inventor's certificates issued in the USSR.

He is married, has a son and a daughter.

MAIN SCIENTIFIC RESULTS

At present, the number of unexpected accidents depends largely on the qualification of personnel (master). Based on accumulated experience and information received from control systems, the latter intuitively establishes the current condition of the object and the onset of possible accidents. However, sometimes their reaction is delayed and accidents with enormous damage occur. In these facilities, the controlled parameters $g(t)$ are noisy signals, $g(t) = X(t) + \varepsilon(t)$, which, on the recommendation of Prof. N. Wiener, are filtrated from the accompanying noise $\varepsilon(t)$. This was justified by zero correlation between useful signal $X(t)$ and noise $\varepsilon(t)$: $R_{X\varepsilon}(t) = 0$. However, in real life, in real objects, when various faults preceding accidents occur, the noise $\varepsilon_2(t)$ emerges, which is correlated with the useful signal $X(t)$. In this case, the correlation $R_{X\varepsilon}(t) \neq 0$ emerges between the total noise $\varepsilon(t) = \varepsilon_1(t) + \varepsilon_2(t)$ and the useful signal $X(t)$, and the conditions of "no correlation" are violated and a part of the spectrum of the useful signal $X(t)$ overlaps with the spectrum of the noise $\varepsilon(t)$ and during filtering the results are "distorted". For this reason, the information about the onset of the accident is reflected in the measuring devices

of "control" systems with a delay. Because of this, in rare cases catastrophic accidents occur on railroad transport, in aviation, at power plants, on drilling rigs, on oil wells, on offshore platforms and communications, etc.

Unfortunately, under the influence of the great authority of Prof. Norbert Wiener and other authoritative scientists, the conditions of "zero correlation between the useful signal $X(t)$ and the noise $\varepsilon(t)$" are still widely used in the analysis of noisy signals. To improve the safety of operation of control objects, using the authoritative international organizations, as well as recognized scientists, it is necessary to accelerate the solution of the problem by creating a technology of signal analysis in the presence of correlation between $X(t)$ and $\varepsilon(t)$, that occurs at the beginning of accidents.

Springer has published a monograph by Prof. Telman Aliev on this problem.

He carried out work to monitor the onset of the latent period of earthquake preparation in order to verify the applicability of signal analysis technology in the case of correlation between the useful signal and the noise.

It is well known that many different systems have been created and are used to control the beginning of seismic processes. Thanks to this, as a result of their operation, both in individual seismically active regions and throughout the world, very important information about seismic processes in the relevant countries and regions is formed.

Over time, in any seismically active region, the accumulated information is used to assess seismic hazard, for example, when planning further development of the region. However, currently, the existing seismic station equipment does not allow obtaining information about the onset of the earthquake preparation process (EPP) in advance. Our experiments have demonstrated the possibility of using the proposed technologies of noise analysis for monitoring and generating information about the onset of earthquake preparation. The results obtained have been experimentally confirmed over a long period of time. It has been established that when seismic signals are filtered in traditional seismic stations, informative attributes that arise during the onset of the earthquake preparation process are lost. It has been established that the beginning of earthquake preparation is reliably detected by using the estimates of the variance of the noise and the cross-correlation function between the useful signal and the noise of seismic-acoustic signals. Several hours later, similar estimates of seismic signals are used to repeatedly detect the continuation of the earthquake preparation process.

In order to test the practical application of the proposed technologies, a network of stations was built, which use the shafts of suspended oil wells (at depths of 38 m, 55 m, 110 m, 200 m, 300 m, 1430 m, 1800 m, 3145 m, 4000 m, and 4900 m) as inverted antennas. It has been established that in traditional technologies, when filtering out noise of seismic signals, informative attributes that arise at the beginning of the earthquake preparation process are lost. It has also been established that the onset of earthquake preparation is consistently detected, using the aforementioned estimates. It has also been established that, over a period of time, it is possible to repeatedly record the continuation of the EPP using the same characteristics of the noise of seismic signals. Based on these technologies, a hybrid intelligent system has been proposed, using which seismologists can determine the approximate time of the onset of expected earthquakes, using combinations of the results obtained.

It has also been established that by analyzing unfiltered seismic signals using these technologies, commonly used standard seismic stations can detect the onset of the EPP 0.5-1 hour before it begins. This will allow seismologists to use standard modern seismic stations to issue warnings of expected seismic hazards.

CONCLUSION

Attached are the results of experimental work carried out between 2010 and 2025 on a network of stations that use mothballed oil wells as communication channels to obtain seismic and seismic-acoustic data from the earth's deep strata.

His monographs [1-13] and works [14-66] include the results of experimental studies conducted over many years at compressor stations, oil fields, drilling rigs, offshore platforms, in transportation, medicine, construction, and seismology.

AUTHORSHIP CONTRIBUTIONS

Authors equally contributed to this work.

DATA AVAILABILITY STATEMENT

The authors confirm that the data that supports the findings of this study are available within the article. Raw data that support the finding of this study are available from the corresponding author, upon reasonable request.

CONFLICT OF INTEREST

The author declared no potential conflicts of interest with respect to the research, authorship, and/or publication of this article.

ETHICS

There are no ethical issues with the publication of this manuscript.

STATEMENT ON THE USE OF ARTIFICIAL INTELLIGENCE

Artificial intelligence was not used in the preparation of the article.

REFERENCES

[1] Aliyev TA. Robust technology with analysis of interference in signal processing. New York: Kluver Academic Plenum Publishers; 2003. p. 199.

[2] Aliyev TA. Digital noise monitoring of defect origin. London: Springer-Verlag; 2007. p. 235

[3] Aliyev TA. Noise technologies for minimization of damage caused by earthquakes. Lambert Academic Publishing; 2012. p. 220.

[4] Aliyev TA. Interference technologies for minimizing damage from earthquakes. Lambert Academic Publishing; 2012. p. 216.

[5] Aliyev TA, Rzayeva NE, Alizada TA. Noise control of heart by means of a mobile phone. Lambert Academic Publishing; 2012. 156 p.

[6] Aliyev TA, Aliyev E. Distributed noise-monitoring systems for seismic stability faults. Lambert Academic Publishing; 2014. 380 p.

[7] Aliyev TA, Aliyev E. Distributed noise monitoring systems for seismic vulnerability assessment. Palmarium Academic Publishing; 2014. 408 c.

[8] Aliyev TA. Noise monitoring of accidents. Technologies for robust noise monitoring to identify the hidden period of transition of objects to an emergency state. Palmarium Academic Publishing; 2016. 384 c.

[9] Aliyev TA. Noise monitoring of accidents. Theories, technologies and systems of identification of the latent period of objects' transition into an emergency state. Saarbrücken: Scholar's Press, Omni Scriptum GmbH & Co KG; 2016. 360 p.

[10] Aliev TA. Intelligent seismic-acoustic system for identifying the area of the focus of an expected earthquake. In: Zouaghi T, editor. Earthquakes: tectonics, hazard and risk mitigation. London: Intech; 2017. p. 293–315. [CrossRef]

[11] Aliyev TA. Noise control of the beginning and development dynamics of accidents. Springer; 2019. p. 201. [CrossRef]

[12] Aliyev TA. Noise technology and control systems. Baku; 2022. 226 p.

[13] Aliev TA, Guluyev GA, Rzayev AH, Pashayev FH. Technologies and system for signaling the beginning of accidents on drilling rigs based on the wattmeter charts of their electric motors. In: Oil and gas wells – recent advances in drilling and completion technologies; 2023. [CrossRef]

[14] Aliev TA, Rzayev AH, Guluyev GA, Alizada TA, Rzayeva NE. Robust technology and system for management of sucker rod pumping units in oil wells. Mech Syst Signal Process 2018;99:47–56. [CrossRef]

[15] Aliev TA, Alizada TA, Rzayeva NE. Noise technologies and systems for monitoring the beginning of the latent period of accidents on fixed platforms. Mech Syst Signal Process 2017;87:111–123. [CrossRef]

[16] Aliev TA, Guluyev GA, Pashayev FH, Sadygov AB. Noise monitoring technology for objects in transition to the emergency state. Mech Syst Signal Process 2012;27:755–762. [CrossRef]

[17] Aliev TA, Rzayeva NE, Sattarova UE. Robust correlation technology for online monitoring of changes in the state of the heart by means of laptops and smartphones. Biomed Signal Process Control 2017;31:44–51. [CrossRef]

[18] Aliev T, Guluyev G, Pashayev F, Sattarova U, Rzayeva N. Intelligent seismic-acoustic system for identifying the location of the areas of an expected earthquake. J Geosci Environ Prot 2016;4:147–162. [CrossRef]

[19] Aliev TA, Abbasov AM, Guluyev GA, Pashaev FH, Sattarova UE. System of robust noise monitoring of anomalous seismic processes. Soil Dyn Earthq Eng 2013;53:11–25. [CrossRef]

[20] Aliev TA, Musaeva NF, Guluyev GA, Sattarova UE, Rzaeva NE. System of monitoring of period of hidden transition of compressor station to emergency state. J Automat Inf Sci 2011;43:66–81. [CrossRef]

[21] Aliev TA, Musaeva NF, Nusratov OQ, Rzayev AG, Sattarova UE. Models for indicating the period of failure of industrial objects. In: Zadeh L, Abbasov A, Abbasov A, Yager R, et al, editors. Recent developments and new direction in soft-computing foundations and applications. Studies in fuzziness and soft computing. Cham: Springer; 2016. p. 389–405. [CrossRef]

[22] Aliev TA, Abbasov AM, Aliev ER, Guliev GA. Digital technology and systems for generating and analyzing information from deep strata of the earth for the purpose of interference monitoring of the technical state of major structures. Autom Control Comput Sci 2007;41:59–67. [CrossRef]

[23] Aliev TA, Aliev ER. Multichannel telemetric system for seismo-acoustic signal interference monitoring of earthquakes. Autom Control Comput Sci 2008;42:223–228. [CrossRef]

[24] Aliev TA, Musayeva NF, Sattarova UE. Noise technologies for operating the system for monitoring of the beginning of violation of seismic stability of construction objects. In: Zadeh L, Abbasov A, Yager R, et al, editors. Recent developments and new directions in soft computing. Studies in fuzziness and soft computing. Cham: Springer; 2014. p. 211–232. [CrossRef]

[25] Aliev TA, Musaeva NF, Sattarova UE. The technology of forming the normalized correlation matrices of the matrix equations of multidimensional stochastic objects. J Automat Inf Sci 2013;45:1–15. [CrossRef]

[26] Aliev TA, Alizade AA, Etirmishli GD, Guluev GA, Pashaev FG, Rzaev AG. Intelligent seismoacoustic system for monitoring the beginning of anomalous seismic process. Seismic Instrum 2011;47:15–23. [CrossRef]

[27] Aliev TA, Abbasov AM, Mamedova GG, Guluev GA, Pashaev FG. Technologies for noise monitoring of abnormal seismic processes. Seismic Instrum 2013;49:64–80. [CrossRef]
[28] Aliev TA. Robust technology for systems analysis of seismic signals. Autom Control Comput Sci 2000;34:17–26.
[29] Aliev TA, Abbasov AM. Digital technology and a system of interference monitoring of the technical state of physical structures and warnings of anomalous seismic processes. Autom Control Comput Sci 2005;39:1–7.
[30] Aliev TA. A robust system for checking marine oil deposit seismic stability. Autom Control Comput Sci 2001;35:1–7.
[31] Aliev TA. Algorithms and methodology for analysis of interference as an information-carrying medium. Autom Control Comput Sci 2002;36:1–10.
[32] Aliev TA. Theoretical foundations of interference analysis of noisy signals. Autom Control Comput Sci 2004;38:18–27. [CrossRef]
[33] Aliev TA. Theoretical fundamentals of interference analysis and failure prediction. Cybern Syst Anal 2008;44:482–492. [CrossRef]
[34] Aliev T, Aliev E. Technology of noise analysis and monitoring of defect origin. Appl Comput Math 2007;6:246–252.
[35] Aliev TA, Guluyev GA. Information system for diagnostics and interference prediction of failures at compressor stations. Autom Control Comput Sci 2003;37:28–33.
[36] Aliev TA. Theory of interference analysis. Autom Control Comput Sci 2002;36:29–39.
[37] Aliev TA. Theory and technology of interference-enabled prediction of system breakdowns. Autom Control Comput Sci 2003;37:15–22.
[38] Aliev TA. Algorithms for improving functional robustness of diagnostic systems. Autom Control Comput Sci 2000;34:43–50.
[39] Aliev TA, Rzaeva NE. Techniques for determining robust estimates of correlation functions for random noisy signals. Meas Tech 2017;60:343–349. [CrossRef]
[40] Aliev TA, Guluev GA, Pashayev FH, Sadiqov AB. Algorithms for determining the coefficient of correlation and cross-correlation function between a useful signal and noise of noisy technological parameters. Cybern Syst Anal 2011;47:481–489. [CrossRef]
[41] Aliev TA. Robust methodology for improving the conditionedness of correlation matrices. Autom Control Comput Sci 2001;35:8–20.
[42] Aliev TA, Guluyev GA, Rzayev AH, Pashayev FH. Correlation indicators of microchanges in technical states of control objects. Cybern Syst Anal 2009;45:655–662. [CrossRef]
[43] Aliev TA, Aliev ER, Mastalieva DI, Rzaeva UE. Adaptive technology of the sampling of noise-corrupted signals. Autom Control Comput Sci 2008;42:20–25. [CrossRef]
[44] Aliev TA, Musaeva NF, Sattarova UE. Robust technologies for calculating normalized correlation functions. Cybern Syst Anal 2010;46:153–166. [CrossRef]
[45] Aliev TA, Musaeva NF, Sattarova UE. Technology of calculating robust normalized correlation matrices. Cybern Syst Anal 2011;47:152–165. [CrossRef]
[46] Aliev TA, Amirov ZA. Algorithm to choose the regularization parameters for statistical identification. Autom Remote Control 1998;59:859–866.
[47] Aliev TA, Musaeva NF. Algorithm for reducing errors in estimation of a correlation function of a noisy signal. Optoelectron Instrum Data Process 1995;4:100–106.
[48] Aliev TA, Musaeva NF. An algorithm for eliminating microerrors of noise in the solution of statistical dynamics problems. Autom Remote Control 1998;59:679–688.
[49] Aliev TA, Ali-Zade TA. Robust algorithms for spectral analysis of the technological parameters of industrial plants. Autom Control Comput Sci 1999;33:38–44.
[50] Aliev TA, Guliev QA, Rzaev AH, Pashaev FH, Abbasov AM. Position-binary and spectral indicators of microchanges in the technical states of control objects. Autom Control Comput Sci 2009;43:156–165. [CrossRef]
[51] Aliev TA. A robust technology for improving correlation and spectral characteristic estimators, correlation matrix conditioning, and identification adequacy. Autom Control Comput Sci 2001;35:10–19.
[52] Aliev TA, Alizadeh TA. Robust technology for calculation of the coefficients of the Fourier series of random signals. Autom Control Comput Sci 2000;34:18–26.
[53] Aliyev TA, Musayeva NF. Statistical identification with error balancing. J Comput Syst Sci Int 1996;34:119–124.
[54] Aliev TA, Musaeva NF. Algorithms for determining a dispersion and errors caused by random signal interferences. Optoelectron Instrum Data Process 1997;3:74–86.
[55] Aliev TA, Musaeva NF. Algorithms for improving adequacy of statistical identification. J Comput Syst Sci Int 1997;36:363–369.
[56] Aliev TA, Nusratov OK. Position-width-pulse analysis and sampling of random signals. Autom Control Comput Sci 1998;32:44–48.
[57] Aliev TA, Nusratov OK. Pulse-width and position method of diagnostics of cyclic processes. J Comput Syst Sci Int 1998;37:126–131.

[58] Aliev TA, Mamedova UM. Positional binary methodology for extraction of interference from noisy signals. Autom Control Comput Sci 2003;37:12–19.
[59] Aliev T, Babayev T, Alizada T, Rzayeva N. Control of the beginning of accidents in railroad operation safety systems in seismically active regions using the noise technology. Transport Probl Int Sci J 2019;14:155–162. [CrossRef]
[60] Aliev T, Babayev T, Alizada T, Rzayeva N. Noise control of the beginning and development dynamics of faults in the running gear of the rolling stock. Transport Probl Int Sci J 2020;15:83–91. [CrossRef]
[61] Aliev T, Babayev T, Alizada T, Rzayeva N, Alibayli E, Ahmedov H. Intelligent system of noise control of the technical condition of railroad tracks. Transport Probl Int Sci J 2021;16:65–73. [CrossRef]
[62] Aliev T, Musaeva N, Babayev T, Mammadova A, Alibayli E. Technologies and intelligent systems for adaptive vibration control in rail transport. Transport Probl Int Sci J 2022;17:31–38. [CrossRef]
[63] Aliev T, Babayev T, Musaeva N, Gadimov R, Mammadova A. An intelligent system for identifying track hauls requiring out-of-turn control of the railroad bed. Mekhatronika Avtomatizatsiya Upravlenie 2024;25:223–230. [CrossRef]
[64] Aliev TA, Mammadova AI. Principle of construction of analog-to-digital converters with adaptive determination of sampling interval of analyzed signals. Mekhatronika Avtomatizatsiya Upravlenie 2024;25:401–406. [CrossRef]
[65] Aliev T, Musaeva N, Rzayeva N, Mammadova A. Technologies and systems for monitoring the onset of accidents at strategic construction. In: ITTA Conference; 2024 Apr 23–25; Baku. Cham: Springer; 2024. p. 42–51. [CrossRef]
[66] Aliev TA, Mammadova AI. Technology of adaptive control of the beginning of the latent period of accident of objects. Mekhatronika Avtomatizatsiya Upravlenie 2025;26:77–83. [CrossRef]

Sigma Journal of Engineering and Natural Sciences
Web page info: https://sigma.yildiz.edu.tr
DOI: 10.14744/sigma.2025.1925

Research Article

Determination of factors affecting greenhouse gases emitted to the atmosphere in eurostat countries with multiple linear regression model

Ömer Faruk KIZIL[1,*], Özge KURAN[2]

[1]*Department of Statistics, Graduate School of Natural and Applied Science, Dicle University, Diyarbakır, 21280, Türkiye*
[2]*Department of Statistics, Faculty of Science, Dicle University, Diyarbakır, 21280, Türkiye*

ARTICLE INFO

Article history
Received: 16 April 2024
Revised: 26 June 2024
Accepted: 17 October 2024

Keywords:
Atmosphere; Emissions; Greenhouse Gases; Industrial Sectors; Multiple Linear Regression

ABSTRACT

Greenhouse gases (water vapor (H_2O), carbon dioxide (CO_2), nitrous oxide (N_2O), methane (CH_4), ozone (O_3) and numerous other harmful gases), also known as both natural and anthropogenic gaseous components of the atmosphere, increase the planet's temperature by absorbing solar radiation and trapping this energy in the atmosphere rather than reflecting it back to the Earth. Therefore, identifying the factors that influence greenhouse gases is crucial for combating climate change, protecting human health and ensuring environmental sustainability. This study aims to investigate the effect of "agriculture, forestry and fishing (AFF); manufacture of food products, beverages and tobacco products (FBT); manufacture of paper and paper products (PPP); manufacture of chemicals and chemical products (CCP); water supply, sewerage, waste management and remediation activities (WSR); transportation and storage (TS)" industrial sectors on greenhouse gases emitted into the atmosphere in 17 Eurostat countries between 2010 and 2021 using a multiple linear regression model. The results of this research show that the AFF, FBT, CCP, WSR and TS have a strong effect on greenhouse gas emissions (GHGEs), as indicated by their Pearson correlation values close to 1, while the PPP variable has a lesser effect with a value of o.650, which is less close to 1. With the coefficient of determination R^2 value of 0.924, which very close to 1, the model effectively explains the variation in GHGEs, confirming the significant influence of these variables. Additionally, according to mean of GHGEs, France records the highest values in GHGE, AFF, FBT, PPP, CCP, WSR, and TS, while Cyprus, Slovenia, and Iceland show the lowest values. The findings are expected to provide important insights for environmental policymakers and sustainability researchers.

Cite this article as: Kızıl ÖF, Kuran Ö. Determination of factors affecting greenhouse gases emitted to the atmosphere in eurostat countries with multiple linear regression model. Sigma J Eng Nat Sci 2025;43(6):1905–1914.

***Corresponding author.**
*E-mail address: mrfrkkzl@gmail.com

This paper was recommended for publication in revised form by Editor-in-Chief Ahmet Selim Dalkilic

Published by Yıldız Technical University Press, İstanbul, Turkey
© Author. This is an open access article under the CC BY-NC license (http://creativecommons.org/licenses/by-nc/4.0/).

INTRODUCTION

The globe is under the sway of escalating production requirements, leaving environmental imprints. On the flip side, this dynamic engenders environmental degradation linked to the generation of greenhouse gas emissions (GHGE), depletion of the protective ozone layer, the onset of global warming, climate change, and environmental sustainability. These factors have far-reaching effects on humanity, including health.

Industrial expansion throughout the 19th and 20th centuries intensified the emission of greenhouse gases and other atmospheric pollutants, which in turn accelerated the onset of global warming. In recent decades, global warming has become a critical global issue, largely driven by the continuous rise in GHGE and its associated climatic disruptions [1].

Greenhouse gases comprise several environmentally harmful constituents, such as water vapor (H_2O), carbon dioxide (CO_2), nitrous oxide (N_2O), methane (CH_4), ozone (O_3), and many other trace gases. The Earth stays within a livable temperature range by keeping a balance between the warmth it receives from the sun and the heat it releases back into space. This balance exists because of the greenhouse effect [2], which holds part of the sun's heat and keeps the planet from becoming too cold. But when greenhouse gases rise above normal levels, more heat gets trapped than the Earth can release, disturbing this balance [3]. Over time, the planet warms faster than it can cool, bringing higher average temperatures, longer and more frequent heat waves, and serious risks to human health. Rising warmth also encourages more pollen in the air, which can worsen breathing problems and increase heat-related illnesses. Higher temperatures also promote greater pollen production, worsening respiratory conditions and increasing the risk of heat-related illnesses and deaths. In addition, prolonged drought conditions have intensified the frequency and severity of wildfires, resulting in greater risks of burns and other heat-related injuries. These changes clearly demonstrate that climate change has negative short- and long-term impacts on human health [4]. Furthermore, high greenhouse gas concentrations weaken the adaptive capacity and overall health resilience of societies, as reflected in the disease burden measured in disabilityadjusted life years (DALYs) [5].

Assessing the determinants of GHGEs holds significant value for advancing environmental sustainability. The relationship between GHGE and environmental sustainability is a critical aspect of the ongoing discourse on global environmental challenges. The planet has undergone significant alterations in its climate, prompting international organizations and governments to initiate policy measures in the battle against climate change [6]. While the scientific community universally recognizes climate change as a subject of research, regrettably, not every nation views climate change and the imperative to diminish GHGEs as political priorities [7]. Environmental factors, whether anthropogenic or natural in origin, exert a substantial influence on GHGEs levels. This influence becomes evident through the release of pollutants into the atmosphere, primarily resulting from the combustion of fossil fuels such as diesel and gasoline in densely populated urban areas, which intensifies the greenhouse effect. Beyond transportation, considerable emissions also arise from agriculture, forestry, and fisheries, as well as from the production of food and beverages, tobacco, paper products, and a wide range of chemical goods. Furthermore, emissions are associated with water supply, sewerage, waste management, remediation activities, as well as transportation and storage [8-12]. The influence of different sectors on GHGEs can be outlined as follows.

1. **Agriculture, forestry and fishing:** This industry is a big source of CH_4 emissions, mostly because of how livestock is cared for and how manure is thrown away. Using fertilizers and different ways to care for the soil can also make N_2O. Also, cutting down trees to make room for farming makes the warming effect worse by raising CO_2 levels in the air.
2. **Manufacture of food, beverages and tobacco products:** This sector contributes to GHGEs primarily through intensive energy use in processing, packaging, and refrigeration. Additional emissions arise from the combustion of fossil fuels for heat and electricity generation, as well as from waste management and transportation activities associated with production and distribution.
3. **Manufacture of paper and paper products:** Since wood raw materials are used in this sector, it may contribute to C_{O2} emissions. There may also be energy-related GHGEs due to energy-intensive production processes.
4. **Manufacture of chemicals and chemical products:** Chemical production processes may cause GHGEs. Chemical plants, in particular, can release greenhouse gases such as N_2O and other chemical emissions into the atmosphere.
5. **Water supply, sewerage, waste management and remediation activities:** This sector can cause CH_4 emissions during sewage and waste management. It can also produce energy-related greenhouse gases during energy use and operation of facilities.
6. **Transport and storage activities:** Transportation is a sector where CO_2 emissions are especially high due to the use of fossil fuels. The transportation sector is a major source of greenhouse gases into the atmosphere.

There are studies in the literature that use multiple linear regression models to determine the factors affecting greenhouse gases [13-20]. Based on this, the aim of this study is to examine the effect of "agriculture, forestry and fishing (AFF); manufacture of food products, beverages and tobacco products (FBT); manufacture of paper and paper products (PPP); manufacture of chemicals and chemical products (CCP); water supply, sewerage, waste

management and remediation activities (WSR); transportation and storage (TS)" industrial sectors on greenhouse gases emitted into the atmosphere in 17 Eurostat countries between 2010 and 2021 using a multiple linear regression model. Up to this point, the connections between these explanatory factors and GHGEs have not been looked at in the 17 Eurostat countries. This study employs a country-specific comparative methodology, introducing an innovative model to analyze these correlations.

This research provides a significant contribution through its detailed assessment of several industrial sectors in the European context. Based on previous studies, it provides a more detailed and holistic view of how different sectors contributed to GHGEs across the 17 Eurostat countries between 2010 and 2021. Whereas much of the existing literature has tended to analyze either single sectors or broad aggregates, this study extends the discussion by examining cross-sectoral linkages and the cumulative effects of industrial activities on total emissions. Adopting this multi-sectoral perspective provides a more holistic understanding of the emissions structure and deepens our understanding of the complex dynamics underlying cross-sector interactions.

To determine the strength of each explanatory variable's influence on the GHGEs, it is benefited from a multiple linear regression model. For this goal, in Section 2, greenhouse gas dataset and the multiple linear regression model that will be investigated in the analysis of this data are handled. The findings and the interpretation of the results are discussed in Section 3 and finally, concluding remarks are given in Section 4.

GREENHOUSE GAS DATASET AND MODELLING

Greenhouse gas dataset consists of "greenhouse gases (CH_4 in CO_2 equivalent, HFC in CO_2 equivalent, PFC in CO_2 equivalent, SF_6 in CO_2 equivalent, NF_3 in CO_2 equivalent (in tonne)); AFF; FBT; PPP; CCP; WSR; TS" variables belonging to Belgium, Bulgaria Hungary, Netherlands, Austria, Poland, Portugal Slovenia, Finland, Norway, Switzerland, France, Spain, Iceland, Greece, Cyprus, Latvia countries between 2010-2021 years [21].

Regression analysis involves utilizing features extracted from a dataset as independent variables in a regression model to estimate the dependent variable, which assumes a continuous value. This predictive outcome is achieved by understanding the association between the independent (input, explanatory) variable x and the dependent (output) variable y.

A basic form of regression analysis is the simple regression analysis, where a sole feature is employed to anticipate the value of the dependent variable. The equation for the linear regression model is articulated as follows:

$$y = \beta_0 + \beta_1 x + \varepsilon$$

where y represents the dependent variable, x is the independent variable, β_i signifies the parameters to be estimated for $i = 0, 1$ and ε denotes the error term.

Linear regression analysis involves establishing the relationship between independent variables and the dependent variable by fitting a linear or non-linear curve to the data. For an accurate curve fitting, a measure of goodness-of-fit must be defined to discern the curve that provides a superior fit compared to others. In the context of simple linear regression, the objective is to determine the slope and intercept values of the line that minimize the goodness-of-fit measure.

In the multiple linear regression model

$$y = \beta_0 + \beta_i x_i + \varepsilon$$

where x_i denotes the independent variables for $i = 0, 1, ..., n$.

The most basic assumption of the multiple linear regression model is that the dependent variable has a normal distribution. This situation is checked with Kolmogorov-Smirnov and Shapiro-Wilk tests. If p>0.05, this means that the distribution has a normal distribution. For regression coefficients estimates, the least squares method (LSM) are used. The regression analysis is done using IBM SPSS Statistics 21.

In the context of the multiple linear regression model,

1. The null hypothesis H_0 asserts that all regression coefficients are equal to zero, denoted as $H_0 = \beta_0 = \beta_1 = \beta_2 = \ldots = \beta_n$. Conversely, the alternative hypothesis H_1 suggests that at least one β_i coefficient is different from zero. The overall significance of the multiple linear regression model is assessed using an F-test and the empirical significance level (the so-called p-value). If p-value<0.05 is satisfied, H_0 is rejected and so, H_1 is accepted.
2. For the individual significance testing of regression parameters, t-tests are employed. The information given in number 1 regarding the p value is also valid here.

The coefficient of determination R^2 represents the percentage of the dependent variable explained by the independent variables included in the model. The coefficient of determination, ranging from 0 to 1, elucidates the proportion of variability in the GHGEs variable explicated by the estimated model. A heightened determination coefficient signifies a greater extent of the model's ability to clarify the variability observed in the dependent variable.

RESULTS AND DISCUSSION

During the period from 2010 to 2021, the analysis of industrial sector variables such as "AFF (x_1); FBT (x_2); PPP (x_3); CCP (x_4); WSR (x_5); TS (x_6)" allows for the investigation of their impacts on GHGEs (y). This analysis enables the application of a country-specific comparative approach to identify the determinants influencing the distribution of greenhouse gases across the 17 Eurostat nations. This approach allows us to explore the presence of correlations

between the considered categories, a prerequisite for establishing a cause-and-effect relationship among them. Utilizing this method, we could construct model resulting in an empirical model represented by a regression equation, which is articulated as follows:

$$y = \beta_0 + \beta_1 x_1 + \beta_2 x_2 + \beta_3 x_3 + \beta_4 x_4 + \beta_5 x_5 + \beta_6 x_6 + \varepsilon.$$

The results of the normality tests for GHGEs based on country data are presented in Table 1. Upon close examination of Table 1, it is observed that the p values for the normality tests across all countries exceed the threshold of 0.05. This indicates that the assumption of normality is satisfied for the dataset. As a result, it is appropriate to proceed with the application of the multiple linear regression model to analyze the relationships between the variables in the study.

In Table 2, the Pearson correlation coefficients are reported for the independent variables, which include AFF, FBT, CCP, WSR and TS, and the dependent variable, which is GHGEs. When Table 2 is investigated, it is seen that Pearson correlation coefficients close to 1 and then, it is said that independent variables have a strong relationship with the dependent variable.

Among AFF, FBT, CCP, WSR, and TS demonstrate a notably strong influence on GHGEs, underscoring their predictive importance. But, conversely, the PPP variable shows a relatively weaker impact on GHGEs. While PPP still contributes to variations in emission levels, its influence appears modest relative to the other explanatory factors included in the analysis. This situation can also be seen through Figure 1.

In Figure 1, country-based scatter plot matrix of GHGEs, AFF, FBT, PPP, CCP, WSR and TS variables is given. Upon examining the scatter matrix graph presented in Figure 1, it is evident that a strong positive linear relationship exists between all independent variables and the GHGEs dependent variable, with the exception of the PPP variable. In contrast, the relationship between the PPP independent variable and the GHGEs dependent variable appears to be weakly positive and not particularly linear.

The results for the model summary, ANOVA, and the coefficients of the multiple linear regression analysis are presented in Tables 3, 4, and 5, respectively. When we examine Table 3, we observe that the independent variables included in the regression model explain the variation in the dependent variable, GHGEs, to a considerable extent. This is evident from R^2, which is very close to 1. This high score signifies that about 92.4% of the variation in GHGEs is accounted for by the independent variables in the model. This indicates that the model effectively predicts GHGEs, with the chosen variables providing significant explanatory power for the observed emission patterns. Furthermore, the magnitude of the R^2 value highlights the reliability of the model in explaining the relationships between GHGEs and their predictor variables, confirming that the model used in this study has a clearly defined and statistically robust framework.

An analysis of Table 4 reveals that the explanatory variables, taken together, have a statistically significant impact on GHGEs. The p-value obtained from the F-test is much smaller than the conventional significance threshold of 0.05, indicating that the overall regression model is

Table 1. Tests of normality for country-based GHGEs

Country	Kolmogorov-Smirnov	Shapiro-Wilk	Country	Kolmogorov-Smirnov	Shapiro-Wilk
	Sig.	Sig.		Sig.	Sig.
Austria	0.200	0.640	Latvia	0.200	0.997
Belgium	0.141	0.177	Netherland	0.061	0.028
Bulgaria	0.200	0.870	Norway	0.082	0.494
Cyprus	0.200	0.448	Poland	0.200	0.555
Finland	0.200	0.615	Portugal	0.065	0.093
France	0.200	0.868	Slovenia	0.200	0.604
Greece	0.200	0.733	Spain	0.176	0.182
Hungary	0.200	0.313	Switzerland	0.066	0.090
Iceland	0.162	0.082			

Table 2. Pearson correlation coefficient values

		AFF	FBT	PPP	CCP	WSR	TS
GHGEs	Pearson correlation	0.954	0.934	0.650	0.871	0.920	0.801

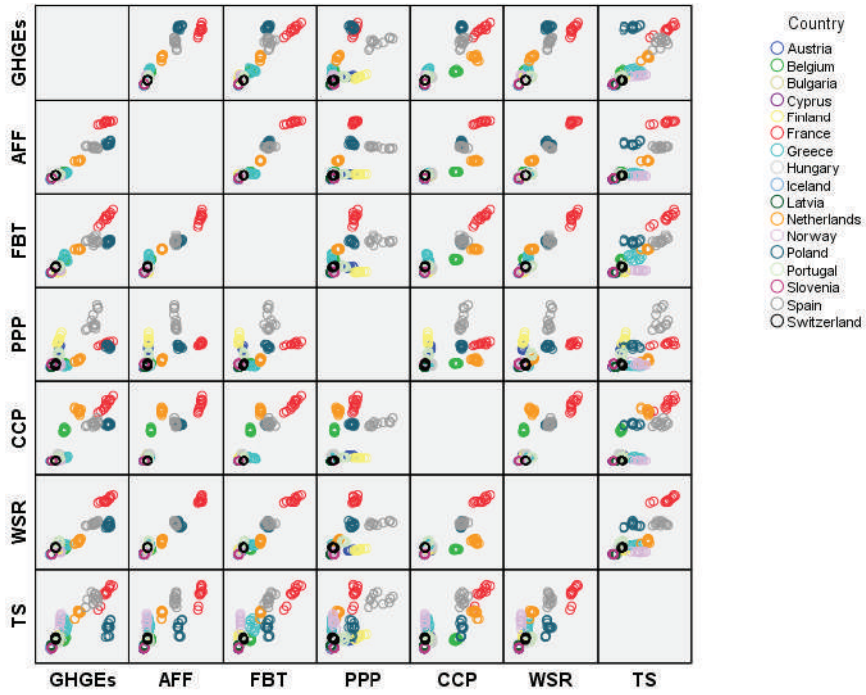


Figure 1. Country-based scatter plot matrix of GHGEs, AFF, FBT, PPP, CCP, WSR and TS variables.

statistically sound and meaningful. This finding implies that the independent variables, when assessed collectively, play a substantial role in explaining the observed variation in the dependent variable, rather than this variation being due to random factors. In other words, the model effectively captures consistent and meaningful relationships between the explanatory variables and GHGEs. Since the p-value lies well below the 0.05 significance level, we can confidently reject the null hypothesis that "the independent variables do not influence the dependent variable," reinforcing the evidence that the explanatory variables jointly contribute to the model's explanatory power.

The statistical data obtained support that the multiple linear regression model has a strong predictive power and show that the relationships between the independent variables and GHGEs are not random but statistically significant.

To assess the individual contribution of each independent variable to the overall model, Table 5 must be carefully examined.

Table 3. Model summary[b]

Model	R	R square	Adjusted R square	Std. error of the estimate
1	0.961[a]	0.924	0.921	30954154.25937

a. Predictors: (Constant), TS, PPP, CCP, WSR, FBT, AFF

b. Dependent Variable: GHGEs

Table 4. ANOVA[a]

Model		Sum of squares	Df	Mean Square	F	Sig.
1	Regression	2.287E+18	6	3.812E+17	397.891	0.000[b]
	Residual	1.888E+17	197	9.582E+14		
	Total	2.476E+18	203			

a. Dependent Variable: GHGEs

b. Predictors: (Constant), TS, PPP, CCP, WSR, FBT, AFF

Table 5. Coefficients[a]

Model		Unstandardized coefficients		Standardized coefficients	t	Sig.	95.0% Confidence ınterval for B	
		B	Std. error	Beta			Lower bound	Upper bound
1	(Constant)	19989595.20	3385050.94		5.905	0.000	13314007.204	26665183.210
	AFF	4.018	0.594	0.846	6.763	0.000	2.847	5.190
	FBT	10.086	4.892	0.253	2.062	0.041	0.438	19.734
	PPP	10.036	2.306	0.127	4.352	0.000	5.489	14.584
	CCP	1.282	0.843	0.085	1.521	0.130	-0.380	2.943
	WSR	-4.647	2.023	-0.268	-2.297	0.023	-8.636	-0.658
	TS	-0.321	0.376	-0.036	-0.855	0.394	-1.063	0.420

a. Dependent Variable: GHGEs

Table 5 presents the statistical significance of each independent variable in predicting GHGEs. Their p-values of CCP and TS, 0.130 and 0.394 respectively, exceed the standard significance threshold of 0.05. Given these values, it can be inferred that CCP and TS contribute little to the model's explanatory power and have a limited effect on predicting GHGEs.

Table 5 also presents the parameter estimates for the model using LSM. The estimates for the intercept and the coefficients of the independent variables are given as follows: $\hat{\beta}_0$ =19989595,207, $\hat{\beta}_1$ = 4,018, $\hat{\beta}_2$ = 10,086, $\hat{\beta}_3$ = 10,036, $\hat{\beta}_4$ = 1,282, $\hat{\beta}_5$ = -4,647, $\hat{\beta}_6$ = -0,321. These coefficients indicate the extent to which each independent variable is believed to influence GHGEs, assuming the other factors remain constant. In addition, the 95% confidence intervals calculated for each estimate show that the true population parameters are likely to fall within these ranges with 95% confidence. This information helps assess the direction and magnitude of each effect, as well as the precision of the resulting estimates.

Given that the CCP and TS variables were found to be statistically insignificant, it seemed logical to assess whether removing them from the model would improve the model. For this purpose, the regression analysis was re-estimated after removing these two variables from the model. The results showed that removing CCP and TS did not significantly affect the R^2 value.

This analysis shows that the model could still explain changes in GHGEs even after these variables were taken out. Therefore, excluding the CCP and TS variables did not lead to any changes in the model. Although these variables were statistically insignificant, they did not improve the overall performance of the model. This result demonstrates that the existing definition is both robust and appropriate for elucidating the relationship between the independent variables and GHGEs. And then, the original model was retained in its entirety without further adjustments.

Figure 2 presents the country-based mean values for GHGEs, along with the independent variables AFF, FBT, PPP, CCP, WSR, and TS.

An analysis of the mean values for GHGEs reveals that France and Finland have the highest averages, suggesting that these countries are the leading contributors to total emissions. In contrast, Cyprus, Slovenia, and Iceland exhibit the lowest average values. A similar trend is observed for the AFF variable, with France consistently ranking highest, while Cyprus, Slovenia, and Iceland are at the lower end of the spectrum.

In the context of FBT, France maintains the highest average, while the smaller economies of Cyprus, Slovenia, and Iceland routinely report the lowest figures. In terms of PPP, Spain has the highest average, whereas Switzerland and Iceland demonstrate the lowest values. In terms of CCP, France once again records the highest average, while Cyprus, Slovenia, and Iceland show the lowest results.

In the context of WSR, France consistently shows the highest average, while Cyprus, Slovenia, and Iceland show the lowest. In terms of TS, the findings show that France and Finland exhibit the highest averages, while Cyprus, Slovenia, and Iceland consistently appear at the lower end of the spectrum.

The findings collectively demonstrate that France is a prominent emitter across several sectors, while Cyprus, Slovenia, and Iceland contribute relatively little amounts to overall GHGEs, highlighting structural and economic disparities across these nations.

Figure 3 illustrates the mean values of GHGEs at the country-level throughout the study period, providing a visual representation of the variations in emission levels among nations. An analysis of these trends indicates that France consistently exhibits the greatest values for both GHGEs and the corresponding independent variables — AFF, FBT, PPP, CCP, WSR, and TS. This pattern suggests that France has consistently been a leading contributor to both GHGEs and the associated economic sectors during the observed years.

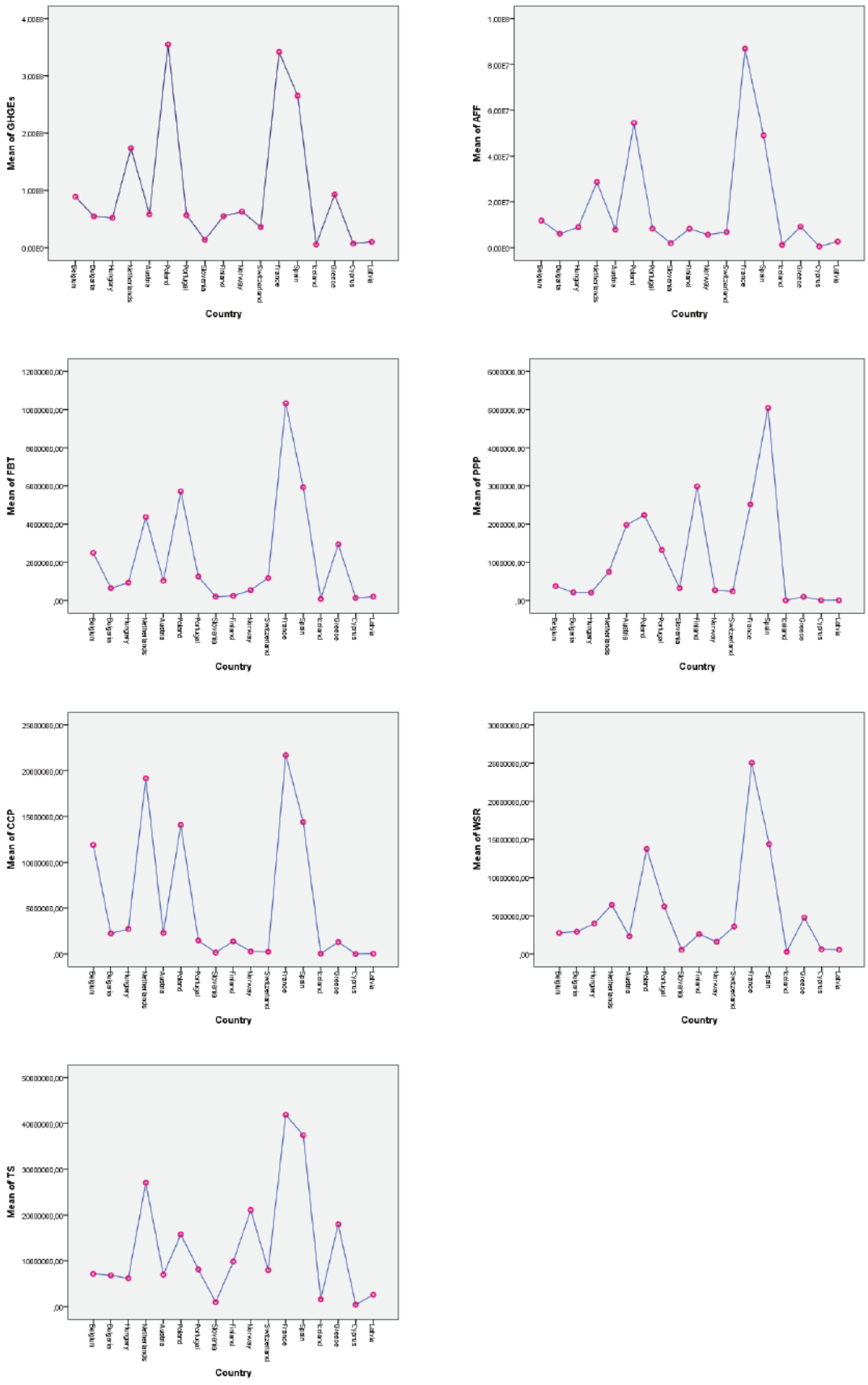


Figure 2. Country-based mean of GHGEs, AFF, FBT, PPP, CCP, WSR and TS graphics.

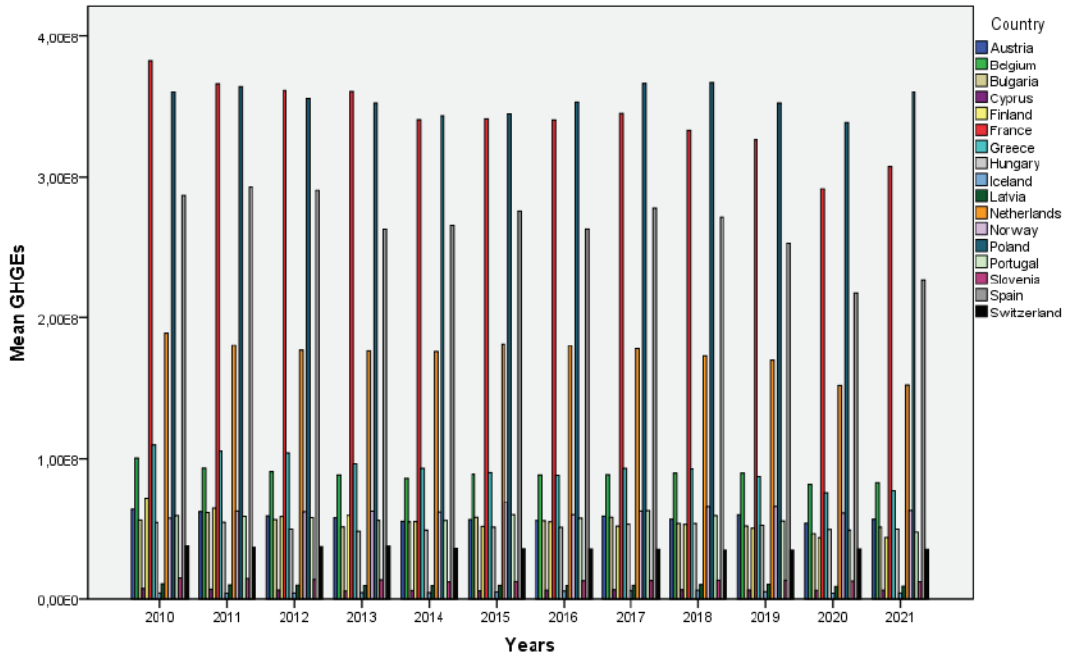


Figure 3. Average GHGEs by country and year graphic.

Conversely, Cyprus, Slovenia, and Iceland consistently demonstrate the lowest values across the same set of criteria. Their total contribution to GHGEs and associated economic sectors seems rather minor, positioning them at the bottom end of the distribution throughout the investigated timeframe. This pattern persists consistently over time, with minimal fluctuation in their respective contributions to emissions and sectoral activity. The analysis of Figure 3 leads to the conclusion that the general distribution of GHGE values, along with the independent variables, remains fairly consistent year after year. France stays at the top because it has the greatest average values for most variables. Cyprus, Slovenia, and Iceland, on the other hand, always have the lowest average values. Importantly, these relative positions have not changed much or at all over time. This suggests that the differences in GHGEs and related economic activity in these countries have stayed mostly the same during the study period.

CONCLUSION

This study explores the effects of several industrial sectors—AFF, FBT, PPP, CCP, WSR, and TS—on overall atmospheric greenhouse gases emissions. The analysis relies on data from 17 Eurostat countries spanning 2010–2021 and applies multiple linear regression to assess the connection between sectoral activities and total emission levels.

The results show that some core sectors, particularly AFF, FBT, CCP, WSR, and TS, exert a significant influence on total greenhouse gases emissions. High Pearson correlation coefficients approaching one confirm a strong and positive link between activity within these sectors and overall emission levels. In practical terms, increased production or economic intensity in these industries is closely associated with higher greenhouse gas outputs. This highlights their decisive role in shaping national emission structures. By contrast, the PPP sector displays a relatively weaker association with total greenhouse gases emissions, with a correlation coefficient of 0.650. Although PPP contributes to emissions, its effect appears less pronounced compared with the other independent variables, implying a more modest role in driving greenhouse gases emissions among the analyzed countries.

The strength of the regression model is reflected in its coefficient of determination (R^2) of 0.924, suggesting that approximately 92.4% of the variation in total emissions is explained by the selected independent variables. This high explanatory power demonstrates how strongly sectors such as AFF, FBT, CCP, WSR, and TS influence emission outcomes across the dataset.

Significant differences across countries are also evident in both average emission levels and sectoral contributions. France exhibits the highest mean values for total greenhouse gases emissions as well as for sectoral components—AFF, FBT, PPP, CCP, WSR, and TS—making it the leading emitter within the group. In contrast, Cyprus, Slovenia, and Iceland record the lowest averages for these same variables and contribute less to overall emissions.

Over time, these cross-country patterns remain fairly stable. Only minor fluctuations occur in the relative ranking of nations or the influence of particular sectors on emissions. This consistency suggests that the structural forces

shaping greenhouse gases emissions have changed little between 2010 and 2021. Such persistence points to the continued importance of these industries in defining the emission profiles of the studied countries.

The findings provide valuable guidance for policymakers, sustainability experts, and environmental stakeholders aiming to reduce greenhouse gas emissions. They emphasize the importance of targeted, sector-based approaches focused on industries with the greatest impact. Since AFF, FBT, CCP, WSR, and TS have substantial effects on emissions, prioritizing mitigation within these sectors should form the basis of effective environmental strategy. The model's strong explanatory value ($R^2 = 0.924$) reinforces the urgency of focused action directed at high-emission sources. Without timely, sector-specific intervention, achieving global mitigation targets will be extremely difficult.

A stronger grasp of how industrial activities contribute to greenhouse gas emissions makes it possible to build policies that support growth without sacrificing environmental goals. Many European economies still depend on energy-intensive industries for jobs and income, yet this reliance also exposes them to higher emission levels. Cutting emissions therefore requires more than new technologies; it calls for structural shifts in the way economies are organized. Decision-makers should focus on strategies that promote cleaner production methods, diversify energy sources, and strengthen circular-economy practices that separate economic expansion from environmental harm.

For these actions to be successful, cooperation among all levels of government is necessary. Local, regional, and national authorities each have their own duties in planning, supervision, and enforcement. Institutions should be equipped with stronger administrative capacity, greater transparency, and closer collaboration between public and private sectors. Working together across different fields can spark new ideas and practical solutions. In addition, financial measures such as carbon pricing, specific subsidies, or environmentally focused tax adjustments can encourage industries to adopt more sustainable methods and reduce their environmental footprint.

Attention must also turn to the human side of the transition. Shifting to low-carbon production should be fair and inclusive, supported by retraining programs that help workers adapt to new roles. By linking environmental, economic, and social goals in this way, governments can make progress on climate targets while protecting economic stability and maintaining public confidence.

Concentrating on the most influential sources of emissions allows governments to develop more effective and efficient reduction policies. Recognizing the key factors behind greenhouse gases emissions is essential for sound policy design. Determining which sectors and activities—such as energy generation, industrial processes, or agriculture—contribute most enables decision-makers to implement well-targeted strategies for emission reduction, improving the overall success of climate initiatives.

Recognizing the primary drivers of emissions also aids in setting clear priorities for resource allocation. Focusing financial and human capacity on sectors with the highest reduction potential ensures a more meaningful environmental impact.

In addition, identifying emission determinants supports technological innovation and progress. When policymakers and researchers understand the principal challenges more clearly, they can better develop and promote cleaner technologies and sustainable solutions. For instance, measures that boost energy efficiency or accelerate the shift toward renewable sources can advance the transition to greener production systems.

This understanding forms a reliable basis for putting environmental policies into practice and checking how well they work. Policymakers can benefit from regularly examining emission records and seeing whether current actions are producing the desired results. Ongoing observation makes it easier to notice problems early and make the necessary changes before existing programs lose their effectiveness. Keeping this process active allows policies to adapt to new environmental and economic conditions, helping climate strategies stay strong and effective over time.

Looking beyond national borders, understanding what drives emissions also builds stronger cooperation between countries. When governments compare their results and share what has worked for them, it creates opportunities for open discussion and learning from one another. This kind of collaboration leads to coordinated global efforts rather than fragmented actions, making progress toward emission reduction far more realistic.

Identifying the main factors behind greenhouse gas emissions lays the groundwork for designing and improving environmental policies. This understanding also drives practical innovation and strengthens collaboration among countries. When policy choices rely on real data and shared experience rather than assumptions, actions to reduce emissions become clearer, more efficient, and better aligned with long-term sustainability and global confidence.

AUTHORSHIP CONTRIBUTIONS

Authors equally contributed to this work.

DATA AVAILABILITY STATEMENT

The authors confirm that the data that supports the findings of this study are available within the article. Raw data that support the finding of this study are available from the corresponding author, upon reasonable request.

CONFLICT OF INTEREST

The author declared no potential conflicts of interest with respect to the research, authorship, and/or publication of this article.

ETHICS

There are no ethical issues with the publication of this manuscript.

STATEMENT ON THE USE OF ARTIFICIAL INTELLIGENCE

Artificial intelligence was not used in the preparation of the article.

REFERENCES

[1] Jones P, Wynn M, Hillier D, Comfort D. The sustainable development goals and information and communication technologies. Indones J Sustain Account Manag 2017;1:11–15. [CrossRef]

[2] Arrhenius S, Holden ES. On the influence of carbonic acid in the air upon the temperature of the earth. Publ Astron Soc Pac 1897;9:14–24. [CrossRef]

[3] Kweku DW, Bismark O, Maxwell A, Desmond KA, Danso KB, Oti-Mensah EA, et al. Greenhouse effect: greenhouse gases and their impact on global warming. J Sci Res Rep 2018;17:1–9. [CrossRef]

[4] McMichael AJ, Woodruff RE, Hales S. Climate change and human health: present and future risks. Lancet 2006;367:859–869. [CrossRef]

[5] Eckelman D, Gregory M, Samuel A. An empirical examination of the environmental Kuznets curve hypothesis for carbon dioxide emissions in Ghana: an ARDL approach. Environ Socio-Econ Stud 2020;4:1–12. [CrossRef]

[6] Kamieniecki S, Kraft M. The Oxford handbook of U.S. environmental policy. Oxford (UK): Oxford University Press; 2012.

[7] Milanes-Montero P, Esteban Perez-Calderon E, Dias AI. Greenhouse gas emission allowances: financial reporting transparency. J Bus Manag 2022;62:1–19. [CrossRef]

[8] Philippe FX, Nicks B. Review on greenhouse gas emissions from pig houses: production of carbon dioxide, methane and nitrous oxide by animals and manure. Agric Ecosyst Environ 2015;199:10–25. [CrossRef]

[9] Prado-Lorenzo JM, Rodríguez-Domínguez L, Gallego-Álvarez I, García-Sánchez IM. Factors influencing the disclosure of greenhouse gas emissions in companies worldwide. Manag Decis 2009;47:1133–1157. [CrossRef]

[10] Psaraftis HN. Market-based measures for greenhouse gas emissions from ships: a review. WMU J Marit Aff 2012;11:211–232. [CrossRef]

[11] Ranson M, Stavins RN. Linkage of greenhouse gas emissions trading systems: learning from experience. Clim Policy 2016;16:284–300. [CrossRef]

[12] Voigt C, Lamprecht RE, Marushchak ME, Lind SE, Novakovskiy A, Aurela M, et al. Warming of subarctic tundra increases emissions of all three important greenhouse gases–carbon dioxide, methane, and nitrous oxide. Glob Change Biol 2017;23:3121–3138. [CrossRef]

[13] Kolasa-Wiecek A. Stepwise multiple regression method of greenhouse gas emission modeling in the energy sector in Poland. J Environ Sci 2015;30:47–54. [CrossRef]

[14] Neves FD, Resende AD, Filho PR, Santos BR. Analysis of the profile of the greenhouse gas emissions in Brazil. J Sustain Dev 2023;16:135–153. [CrossRef]

[15] Filipiak BZ, Wyszkowska D. Determinants of reducing greenhouse gas emissions in European Union countries. Energies 2022;15:9561. [CrossRef]

[16] Ahmad K, Irshad Younas Z, Manzoor W, Safdar N. Greenhouse gas emissions and corporate social responsibility in USA: a comprehensive study using dynamic panel model. Heliyon 2023;9:e13979. [CrossRef]

[17] Georgina A. Greenhouse gas emissions and health outcomes in Nigeria. Afr J Econ Sustain Dev 2023;6:72–88. [CrossRef]

[18] Hosseini S, Saifoddin A, Shirmohammadi R, Aslani A. Forecasting of CO_2 emissions in Iran based on time series and regression analysis. Energy Rep 2019;5:619–631. [CrossRef]

[19] Güler E, Yerel Kandemir S. Estimation of CO_2 emissions by OECD countries using linear and cubic regression analyzes. Eur J Sci Technol 2022;134:175–180.

[20] Ünal C, Özel G. Investigation of the effects of Ankara meteorological parameters on air pollution by regression analysis. J Quant Sci 2023;5:135–150. [CrossRef]

[21] Eurostat. Air emissions accounts by NACE Rev. 2 activity. 2023. Available at: https://ec.europa.eu/eurostat/databrowser/view/env_ac_ainah_r2__custom_7965996/default/table?lang=en Accessed on Nov 05, 2025.

Sigma Journal of Engineering and Natural Sciences
Web page info: https://sigma.yildiz.edu.tr
DOI: 10.14744/sigma.2025.00136

Research Article

Optimizing textual sentiment recognition through LASSO-based feature selection and ensemble voting technique

NISHA[1,*], Rakesh KUMAR[1]

[1]*Department of Computer Science & Applications, Kurukshetra University, Haryana, 136119, India*

ARTICLE INFO

Article history
Received: 10 September 2024
Revised: 04 November 2024
Accepted: 14 January 2025

Keywords:
Grid Search; LASSO; Multidomain Textual Sentiment Recognition; Preprocessing; Random Forest; Soft Voting; SVM

ABSTRACT

The nuances of opinion mining across varied datasets demands robust, generic models that can efficiently handle varied emotions in a text. This work handles the stated problem by proposing a novel ensemble-based model aimed at boosting both accuracy and interpretability in sentiment analysis tasks, which is crucial for applications such as customer feedback analysis, public opinion monitoring, and review systems. This article utilizes ensemble soft voting that uses Support Vector Machine and Naive Bayes as base classifiers, leveraging state-of-art feature selection approaches such as grid search optimized LASSO and Chi-square. The rationale of using these strategies due to their proven capacity of dealing high dimensional textual data with reducing the variability.The proposed method was independently evaluated using three publicly available datasets: Sentiment140, US Airlines, and Internet Movie Database, achieving accuracies of 81.75%, 93.25%, and 93.2% respectively. The results depict the proposed model adaptability with both balanced and imbalanced datasets and its strength to identify meaningful features, affirming consistent performance throughout. This work innovation is in fusing ensemble method with grid search-optimized LASSO for selecting the features, surpassing current individual and ensemble models. This work pave the groundwork for future progress, encompassing the extension to larger datasets and the integration of multiple emotion.

Cite this article as: Nisha, Kumar R. Optimizing textual sentiment recognition through LASSO-basedfeatureselectionandensemblevotingtechnique.SigmaJEngNatSci2025;43(6):1915–1929.

INTRODUCTION

Sentiment is the English word but originally rooted from the French word "santement, sentiment", which means "to express" or "to convey feelings". An integral part of language in human communication is sentiment [1]. When faced with a challenging scenario, our emotions often guide us to make important judgments. Artificial Intelligence systems need to consider human emotions. There are three domains where it has a major impact: decision-making, pattern recognition, and Human Computer Interaction (HCI). From the past decade, research on emotion has been flourishing exponentially. Far reaching availability of electronic devices, people largely engaged in spectrum of online activities nowadays such as social media, shopping, video games, online education, and related fields. The COVID-19 epidemic has significantly increased the frequency of these actions, which in turn has boosted their popularity

*Corresponding author.
*E-mail address: nisha.jrf.dcsa@kuk.ac.in

This paper was recommended for publication in revised form by Editor-in-Chief Ahmet Selim Dalkilic

Published by Yıldız Technical University Press, İstanbul, Turkey
© Author. This is an open access article under the CC BY-NC license (http://creativecommons.org/licenses/by-nc/4.0/).

and acceptability [2]. Existing literature demonstrated that Machine learning (ML) and Deep learning (DL) techniques are highly feasible to build the similar system, but have substantial limitations such as more computational power is required to build DL model for emotion detection, at the same time ML classifiers can be less precise [3,4], [5]. Further the nature of data could be balanced or imbalanced adding further complexity in detecting emotions. There may be an imbalance in the data if one emotion is underrepresented in Textual Sentiment Classification (TSC) results compared to others. This disparity arises from a variety of causes, including gender and age differences, cultural backgrounds, linguistic diversity, challenges in correctly categorizing, the individual's inherent emotional distribution, data collection constraints, and other related issues [6]. Data preparation is the first stage in preparing the text for further processing. Due to the absence of a defined data model, the unstructured text is unfit for further processing. Therefore, certain data preparation or preprocessing techniques are required to reduce text size, eliminate noise, and find relevant patterns [7]. When dealing with textual data, it is necessary to employ text representations which transformed unstructured text into structured vectors, enabling ML models to analyzed them effeciently. BoW (Bag of Words), TF-IDF (Term Frequency–Inverse Document Frequency), Term Class Relevance (TCR), and phrase representation are commonly employed feature extraction techniques for textual data [8]. The aim of feature selection phase is to feed the classifier with a minimal relevant feature by eliminating noise and redunandant features and thus improving model's performance [9]. Significant scientific endeavors have been devoted to this field in previous years. Nevertheless, the problem of managing a huge feature set from multiple domains continues to provide significant challenges. LASSO (Least Absolute Shrinkage and Selection Operator) and Ridge are regularization techniques but have inbuilt feature reduction capability. This research tackles this difficulty by utilizing a LASSO technique using a grid search. TSC has several use cases: including customer feedback analysis, social media monitoring [4], brand monitoring, product and service reviews, market research [3], political analysis, tourism [10], financial analysis, healthcare [11], government intelligence, E-learning, education, and most recent use case is scientometric analysis where the goal is to examine the writers' feelings as they relate to citations in scientific papers [12]. This research proposes a method for understanding textual sentiment using ensemble ML voting classifier. The reason for this is that ML models are simpler and more direct compared to DL models. The effects of different text representation and preprocessing techniques on English text with stemming and lemmatization, to preprocessing, and to regularization approaches such as LASSO and Ridge with inherent feature selection are explored in this work to check their efficacy in detecting sentiments. Here, the proposed Ensemble Soft Voting Classifier leverages the computational power of three distinct base classifiers, including Support Vector Machines (SVM), Random Forest (RF), Naive Bayes (NB). This work introduces a grid search optimized feature selection strategy to tackle the short textual dataset with diverse domains. The high-dimensionality of the multidomain textual data results into the wide spectrum of vocabulary, thus demands a strong feature selection method. Employing Grid Search-based CV(Cross-Validation) feature selection using LASSO, this study handles multicollinearity problem in textual datasets by reducing dimensionality and feeding relevant features for a model.

The main contributions of this work are detailed below:

- We introduced a novel grid search optimized LASSO feature selection in conjuction with ensemble soft voting which is capable of handling high dimensional imbalanced textual data.
- The proposed framework is grouping of five unified steps: data preprocessing, feature extraction and selection, training a model, and thus evaluation. The use of multivariate feature selection LASSO in compare to univariate Chi-square making the system more robust and accurate.
- Proposed model leverages the ensemble soft voting for final prediction which constitute three heterogeneous base classifiers: SVM, RF, and NB. Grid search optimization is employed to automatically choose hyperparameters of these ML model.
- The proposed work is independently evaluated on publicly available three textual datasets, such as Sentiment140, US Airlines, and IMDB (Internet Movie Database) aiming to enhance the task of sentiment analysis (SA).
- The experimental evaluation reveals that our proposed ensemble framework in conjuction with LASSO feature selection approach attains better classification accuracies than without feature selection.

The subsequent sections of the paper are organized in the following manner: Section 2, presents the literature survey, which offers a comprehensive summary of the current research in the field. In Section 3, the suggested design is delineated, providing a comprehensive account of the features incorporated and the classifiers under consideration. The outcomes of conducted experiments are detailed and evaluated in Section 4 of this study, which also contains the experimental data. In the concluding section of this paper Section 5, summarize the main results and conduct an in-depth evaluation of the possible conclusions that may be taken from this study.

Literature Survey

ML algorithms have recently made significant improvements, which led to their widespread use cases in multiple fields. Previous studies shown that ML can robustly determine the toughness of Mode-I rock fractures using metaheuristic optimization algorithms [13], as well as optimize the compression of respiratory signals and predict

financial system profits using DL models [14,15]. These instances demonstrate how ML may be tailored to address intricate, industry-specific challenges. Taking advantage of this adaptability, we utilize ensemble techniques to tackle natural language processing (NLP) and classification-specific problems in SA of textual data. Using ML [16–18] and DL [19–22] for textual data classification and analysis, has become an important application area in the field of NLP. There have been a lot of research looking into different ways to make sentiment detection systems better and faster. The methods, datasets, and results of these works are summarized in Table 1, which offers a comparative overview of important contributions to SA. In recent years, academics have made significant advancements in the field of TSC by developing, refining, and comparing various feature extraction and selection methodologies, classification algorithms, and databases. Significant contributions have been made by researchers in the fields of ensemble learning [23–25] and feature selection [16,17,24]. However, there is a dearth of research undertaken on multidomain projects incorporating different domains with large datasets.

Table 1. Literature review summary

Reference	Dataset	Feature selection /extraction	Classifier	Drawbacks
[16]	Sentiment140 Movie review	POS	NB ME	Only 1000 tweets via random selection were utilized in the experiments. Despite using less no of instances; the model is not precise.
[17]	Rotten Tomatoes	N-gram TF-IDF	SVM NB ME	Potential difficulty in analyzing short Twitter comments.
[18]	IMDB	TF-IDF	SVM	The suggested hybrid feature selection technique does not exhibit enhanced classification performance on specific datasets, perhaps because of the limited availability of high-quality training data.
[19]	SST-1 Restaurant reviews	POS	CNN	There are potential complexities in integrating DL and rule-based methods which possibly affect the scalability and interpretability of the model.
[20]	US-airline, US-presidential election, IMDB, Car reviews	Word2vec Glove BERT	CBRNN	A too complex model with high computational power.
[21]	IMDB	---	Hybrid CBRNN	The scaling of the model to larger datasets or real-world applications may necessitate additional computational and resource resources, which are not taken into consideration.
[22]	Sentiment140 IMDB	Word2Vec BERT	LSTM Bi-GRU	Complex ensemble framework and adaptability issues due to constant legth preprocessing.
[23]	Twitter data	TF-IDF	Ensemble (LR-SGD)	A small single-domain dataset is used and the accuracy achieved is only 79%.
[24]	Tourism reviews	Rule based	Ensemble SVM, NB, & RF	The challenge of efficiently extracting valuable information from voluminous and noisy user-generated data.
[25]	Movie E-commerce	Uni-gram Bi-gram	SVM NB Bagging	The study focused on the Turkish language and a few examples, allowing for potential generalizability to other languages or cultures.
[26]	IMDB, Amazon movie	Word2vec	Hybrid CNN-LSTM	CNNs contain a multitude of convolutional layers to capture long-term dependencies making the model complex. Only one domain is captured during modeling.

Table 1. Literature review summary

Reference	Dataset	Feature selection /extraction	Classifier	Drawbacks
[27]	Twitter US Airline	TF-IDF	KNN, RF, MNB ANN, LSTM, Bi-LSTM	A single-domain dataset is used. Extensive hyperparameter tuning is required
[28]	IMDB SST2 MR	---	Bi-LSTM	While the study highlights the potential of simpler architectures, it lacks a comprehensive exploration of interpretability and robustness across diverse datasets, and a lack of robustness in handling imbalanced datasets.
[29]	IMDB Twitter US Airline SMS Spam Collection	TF-IDF BOW	LSTM	The efficacy of the model could be significantly enhanced through the incorporation of a variety of hyperparameter tuning with the base model, as its current accuracy fails to meet anticipated levels.
[30]	Sentiment140	---	BERT	This research was limited to a singular investigation into the effect of word elongation on sentiment classification, and encountered difficulties in assembling the dataset.
[31]	IMDB Twitter US Airline Sentiment140	GloVe	BERT LSTM	The reliance on GloVe pre-trained word embedding for data augmentation may limit the model's adaptability to domains with specialized vocabularies or dialects.
[32]	IMDB Twitter US Airline Sentiment140	GloVe	RoBERTa BiLSTM GRU	A possible limitation of this research pertains to the computational requirements and complexity associated with the execution and enhancement of the ensemble hybrid DL model.
[33]	Twitter dataset	Word2vec	CLAS (CNN-LSTM-Attention-SVM)	DL models used in this research need substantial computational resources for both training and inference processes, hence imposing limitations on their accessibility and scalability, particularly in contexts with limited resources.

PROPOSED METHODOLOGY

The processing unit is a critical element in TSC systems as it is tasked with extracting essential information from the incoming text. Subsequently, a ML classifier is used to determine the primary text sentence's expressed subjectivity. Figure 1 depicts the proposed methodology used in this work which makes the use of base classifiers as SVM and NB coupled with LASSO as feature selection. This section gives a synopsis of the classification methods used to build the proposed model, as well as the datasets used, feature extraction and selection, and model development.

Datasets

The proposed system's effectiveness and scalability are evaluated on various datasets, including three cutting-edge ones, with both positive and negative evaluations conducted, excluding neutral ones. The datasets for US airlines reviews [34], IMDB review, and Sentiment 140 [35] were obtained from Kaggle, IMDB review, and Twitter API. The US Airlines dataset, which contains 11,517 tweets about six US airlines, has an inherent imbalanced distribution. The IMDB review dataset, which contains 50,000 reviews, has a well-balanced distribution with 25,000 favorable and 25,000 unfavorable evaluations. The Sentiment140 dataset, which contains 160,000 tweets, has an imbalanced distribution with a mean word count below 115 words. The distribution of original samples from the datasets as shown in Figure 2.

Data Preprocessing

The aim of this phase is preprocessing the disorganized social media reviews for further classification. It goes over a lot of different methods, such as Normalization which involves a series of simultaneous activities, such as converting text to lowercase, removing URLs, and eliminating punctuation, hashtags, and whitespace, to improve the preparation process uniformity. Tokenization is the process of breaking down large text fragments into smaller tokens, dividing them into smaller units for efficient data analysis. We used Wordnet tokenizer for this study. Stemming and lemmatization, both destined to do same work. Stemming removes prefixes, suffixes, and definite articles from words,

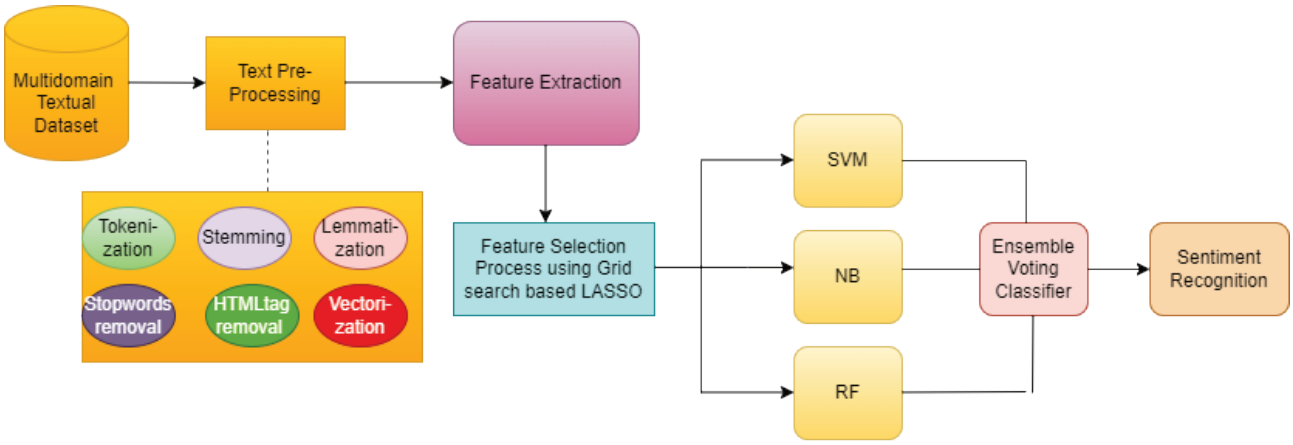


Figure 1. Architecture of the proposed ensemble model.

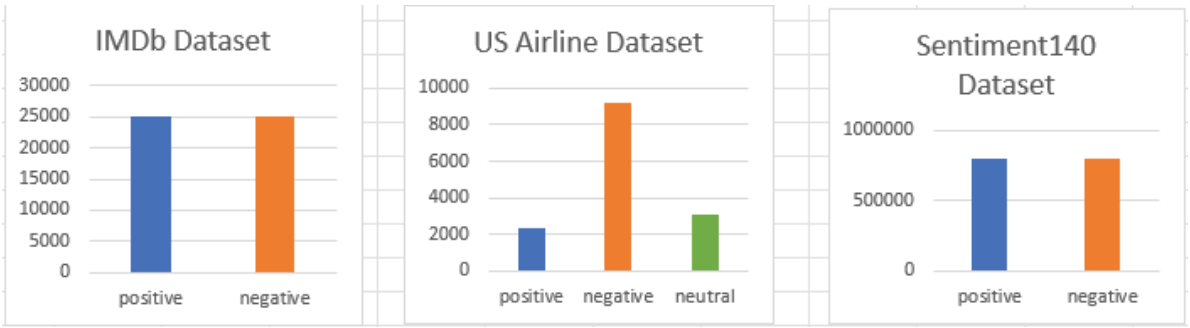


Figure 2. The distribution of samples from the datasets.

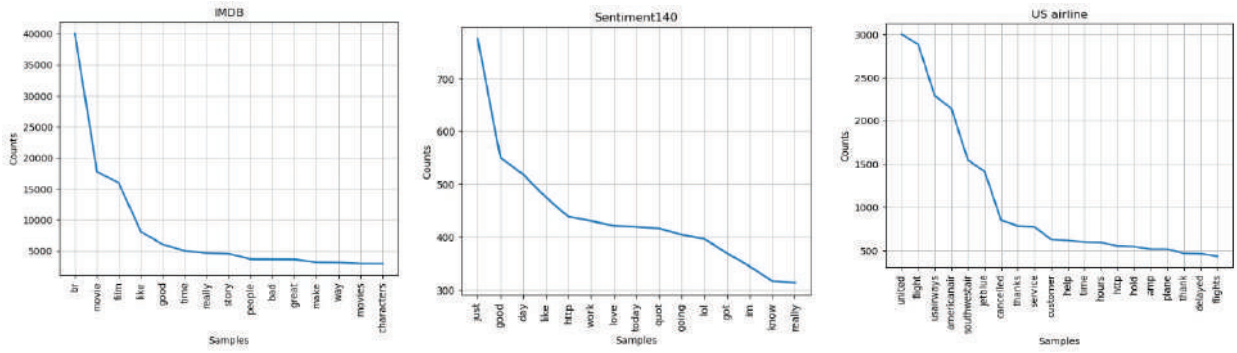


Figure 3. Top 15 most common words after removal of stop words for IMDB, Sentiment140, and US airline dataset.

using hybrid, mild, and root stemming procedures, while lemmatization merges words into a single word, eliminating termination through morphological examination. The conducted experiment utilized lemmatization due to its perceived more meaningful linguistic representations, despite the minimal impact of stemming or lemmatization on accuracy. Stop words, such as "at" "is" and "the" are common in any language but not relevant to SA process. The distribution of the top 15 words in corresponding datasets after removing stop words are depicted in Figure 3.

Figure 4 represent before and after preprocessing results on few reviews of sentiment140 dataset which include removal of hastags, punctuations symbols and others which doesn't add on subjectivity of text. Natural Language Toolkit (NLTK) and Scikit-learn stop words used here to enhance text preparation and reduce noise.

Feature Extraction

Words are too complex for ML techniques to comprehend, therefore feature extraction turns them into vectors

	text	target	cleaned_tweets_w/o_Stopwords	cleaned_tweets_with_SW
0	@ home studying for maths wooot ! im so going to fail this shit	-1	home studying for math wooot i am so going to fail this shit	home studying math wooot going fail shit
1	Pickin up @misstinayao waitin on @sadittysash 2 hurry up...I odeeee missed dem Table talk 2nite...LOL bout to be fat...	-1	pickin up waitin on hurry up i odeeee missed dem table talk nite lol bout to be fat	pickin waitin hurry odeeee missed dem table talk nite lol bout fat
2	@ProudGamerTweet I rather average 32370	-1	i rather average	average
3	@officialnjonas Good luck with that	1	good luck with that	good luck
4	this song's middle change just doesn't want to be born..... arghhhh!!	-1	this song is middle change just doe not want to be born arghhhh	song middle change want born arghhhh
5	im starting my many hours of work now	-1	i am starting my many hour of work now	starting hour work
6	Thunderstorms yesterday, more on the way. Looks like I won't be online much again today. HAPPY FATHER'S DAY	-1	thunderstorm yesterday more on the way look like i will not be online much again today happy father s day	thunderstorm yesterday way look like online today happy father day
7	@cloecouturier Yes, I do have a few .. 4 Girls ... You son is 23 ... all grown up now .. happens fast!!	1	yes i do have a few girl you son is all grown up now happens fast	yes girl son grown happens fast
8	Last free travel at AP-1 http://yfrog.com/0uvu5j	-1	last free travel at ap	free travel
9	TF2 has updated but its way to late to play. looks like I'll be spying and sniping my heart out tomorrow	1	tf ha updated but it way to late to play look like i will be spying and sniping my heart out tomorrow	updated way late play look like spying sniping heart tomorrow
10	@PreternaReviews yeah, but, dude, that's the key here. I'm a CHICK. Chicks wear pink. Especially the ultra cool rocker chicks	1	yeah but dude that is the key here i am a chick chick wear pink especially the ultra cool rocker chick	yeah dude key chick chick wear pink especially ultra cool rocker chick

Figure 4. An illustration showcasing the results of before and after data transformation (Sentiment140 dataset).

in space. After comparing TF-IDF and BoW approaches, TF-IDF was selected because of its better performance. It improves the importance of important terms by quantifying the rank of each term in a document, taking term frequency and overall corpus frequency into account. The following equation illustrates the process of calculating TF-IDF using IDF.

$$TF = \frac{total\ number\ of\ time\ a\ term\ present\ in\ the\ document}{total\ terms\ in\ the\ document} \quad (1)$$

$$IDF\ (t, D) = log\left(\frac{|D|}{|\{d\ \in D; t\ \in d\}|}\right) \quad (2)$$

$$TF - IDF(t, d, D) = tf(t, d) * IDF(t, D) \quad (3)$$

Here *'t'* denotes the term in the document *'d'* and *'D'* represents the full corpora of the document.

Feature Selection

Finding useful features in pre-processed text input is the goal of feature selection, a method that improves the performance of ML models. Thus, selecting the essential features making model more transparent, maintain overfitting and results into much better computional efficient. We experminted with three feature selection methods here: Chi-square, LASSO- feature selection method which proven to be better accuracy than filter and reduced computional overhead than wrapper method. It is done by adding a regularizer term which create sparsity to less important feature thus refines the model's foreseeability and transparency [37]. When it comes to feature selection in SA with textual data, LASSO works incredibly well since it automatically removes redundant features, resulting in a model that is easier to understand. LASSO helps concentrate on the most relevant words or phrases by reducing the coefficients of less important features to zero by incorporating an L1 penalty into the model. This improves model generalizability and lessens overfitting, both of which are essential for managing big and frequently noisy text input in SA tasks. This work assesses the efficacy of LASSO on balanced and imbalanced textual datasets, despite the fact that its use in feature selection for textual datasets has received less attention. By punishing big regression coefficients and deleting extraneous characteristics from the model, the multivariate approach LASSO performs exceptionally well on high-dimensional datasets such as text. Accordingly, we used grid search-based cross-validation to determine the ideal regularization value, which allowed us to accomplish our goal in both balanced and imbalanced datasets. Excluding certain words or keywords is a common way to do this with textual data. Applying LASSO to textual data that has been processed using TF-IDF produces effective results, as shown in Equation 4.

$$minimize\left(\frac{1}{2n}\sum_{i=1}^{n}\left(yi - \sum_{j=1}^{p}\beta j\ xij\right)^2 + \alpha\sum_{j=1}^{p}|\beta j|)\right) \quad (4)$$

The Equation above represents the objective function of LASSO which build upon two components. First is loss function which calulate mean squared error (MSE) between the predicted (yi) and actual values ($\sum_{j=1}^{p}\beta j\ xij$) and also shows how well the model fits the data. The second is Regularization Term ($\alpha\sum_{j=1}^{p}|\beta j|$) which applies a penalty that is directly proportionate to the total of the absolute values of the coefficients ($|\beta j|$), facilitates sparsity by reducing

some coefficients to zero, hence executing feature selection. The other variables used in Lasso equation are explained below:

- n represents the number of text documents in your dataset.
- p signifies the number of unique words extracted from the text documents, which serve as feature space.
- xij signifies the presence or frequency of the j-th word or term in the i-th text document.
- yi signifies the output variable pertinent with the i-th text document.
- βj represents the coefficient linked with the j-th word or term, signifying its importance in projecting the target variable yi.
- α is the regularization parameter that controls the strength of the regularization (penalty term) and model fit (MSE term). Higher values of α result in more coefficients (βj) being shrunk towards zero, effectively removing less important words or terms from the model.

A balanced relationship between sparsity (the simplicity of the model) and predictive performance is guaranteed by an ideal α, for this reason the ideal regularization strength is found by methodically here by exploring several values of α in Grid Search CV. Less important feature coefficients are reduced to zero by the regularization process in LASSO, which imposes a penalty on their magnitude. To encourage sparsity through the removal of irrelevant features and simplify the model for improved interpretability, features with lower correlation with the target variable are penalized more severely. By keeping one feature from a set of correlated variables and rejecting the others, LASSO efficiently handles multicollinearity and improves the model's efficiency and resilience. By improving generalization, decreasing overfitting, and concentrating on the most important features, regularization greatly boosts model performance. This is especially important when dealing with high-dimensional datasets, such as textual SA, because the model can easily get overwhelmed by irrelevant information. To avoid underfitting due to over-regularization and overfitting from under-regularization, it is necessary to properly tune the regularization parameter (α). Another benefit of regularization is that it makes the model faster and easier to understand by lowering the number of features which is very helpful in case of high dimensional textual features.

SENTIMENT CLASSIFIER

SVM Classifier

The most widely used algorithm for SA provides high precision for extensive datasets [38]. The SVM strategy use hyperplanes to assess data and establish decision boundaries in this technique. SVM are a form of deterministic supervised learning method commonly employed for classification purposes. The fundamental SVM is to identify the hyperplane that may effectively split the data into multiple groups. SVM aims to identify the hyperplane that has the maximum possible margin.

Naïve Bayes

NB is a Bayesian classification method using Baye's theorem to determine the probability of a label from a set of features. To classify texts based on presence/absence features, Bernoulli NB (BNB) variant of NB is employed here, which excels at representing features as binary or Boolean [39].

Random Forest Classifier

RF is as an ensemble classifier, meaning it combines the predictions of multiple DTs to get its final prediction as shown in Figure 5. The model uses decision trees (DT) trained on various datasets, with the final output determined by majority vote. It exhibits high resilience, stability, and reduced overfitting. The ideal split is determined by selecting features and building DT.

Ensemble Voting Classifier

Ensemble model works on "wisdom of crowds" that capitalizes the power of multiple base classifiers, aiming to build more accurate and robust predictive model. The potency of ensemble method relies on the accuracy of their constituent participating classifiers, necessitating that these classifiers perform better than the top-performing individual classifier. The investigation involves examining the top six classifiers to construct a customized ensemble technique known as the voting classification model. Included in the consideration are SVM, RF, BNB, SVM-Chi-square, SVM-LASSO, RF-Chi-square, RF-LASSO, BNB-Chi-square, and BNB-LASSO. However, the Ridge feature selection method displayed inadequate performance and is therefore not

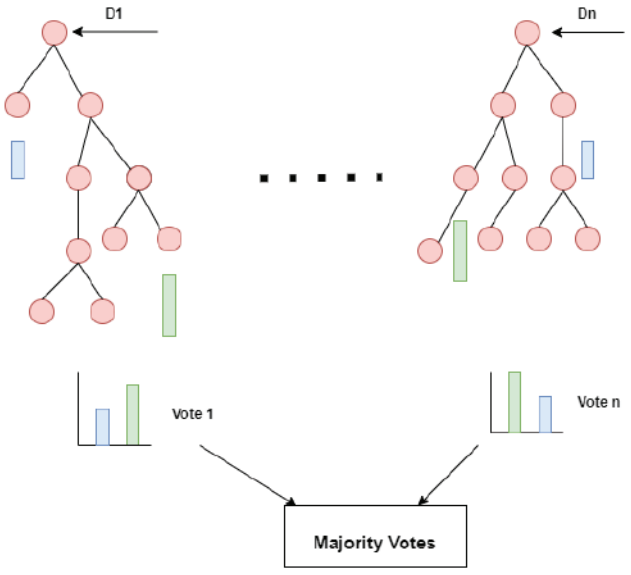


Figure 5. Random Forest classification procedure with n= tree count.

being considered for the final classifier selection. Soft voting has been used in this work indicating that the predicted class labels are determined based on the argmax of the sums of predicted probabilities, suitable for combining probabilities from multiple classifiers. Since in this work, a soft voting classifier is used, the probabilities from each base classifier are combined, and the class with the highest combined probability is chosen as the final prediction. Subsequently, the voting strategy achieved the best accuracy in sentiment prediction out of all the approaches examined by aggregating the classifier's outputs using an average weighting methodology. Here's the corrected equation:

$$P(voting_{soft}) = argmax\,(\sum_{i=1}^{n} w_i P_i(class))$$

In this equation:

- $P(voting)$ represents the probability of the voting classifier.
- wi represents the weight allocated to the ith base classifier.
- Pi (class) represents the probability predicted by the ith base classifier for a particular class.
- n represents the total number of base classifiers.

In the soft voting process, the final class prediction is determined by computing the weighted average of the predicted probability for each base model. Its performance on binary classification is enhanced by this ensemble strategy. However, ensemble model can be computationally expensive sometime, but in this work the main aim is to improve the performance like accuracy and F1 measure. So, the capacity of this technology to assess text content in a balanced and sophisticated way makes it unbeatable by complex sentiment patterns.

The ensemble voting classifier's procedure

1. Gather the data using a suitable group of features.
2. Dataset is splitted into two parts: one for training and one for testing. Eight to two is the ratio that was noted.
3. Individually train SVM, RF and BNB classifiers using a designated training set with or without feature selection methods. Chi, LASSO, and Ridge were used in this study.
4. All classifiers should be utilized to make predictions for the labels of the testing set.
5. Utilize the soft voting procedure to merge the predictions of classifiers. SVM and BNB with LASSO and Chi-square as these two are giving promising result in this work.
6. After the optimization of the ensemble classifier, it gains the ability to make predictions on novel and unobserved data.

EXPERIMENTAL SETUP

The model described in this study was implemented using the following modeling environments: The browser-based interface of Jupyter Notebook an open-source application was utilized to provide freedom for act equally in local and cloud contexts. Google Colaboratory, a Google Research tool, was used for model implementation using Python version 3.7.13, along with various libraries like NumPy, Pandas, Scikit-learn, and Matplotlib. The proposed model was developed and evaluated in a thorough and flexible environment made possible by the combination of various technologies. Additionally, three ML algorithms—SVM, RF, and BNB that are widely used in text categorization were included in the study for a more thorough evaluation. These three methods made use of the BoW and TF-IDF vectorization approaches to extract characteristics from the text input. The ML algorithms are then fed the characteristics or vectors specified earlier. Token density determines how many features each vectorization approach produces for a certain review or text. For these ML algorithms, the TF-IDF method outperformed the BoW method in terms of accuracy. Therefore, evaluation of proposed framework is done with only TF-IDF technique outputs.

RESULTS AND DISCUSSION

The selection of three separate datasets was based on their individual qualities and how well they fit the research goals. Because it does not impose any particular domain restrictions, the sentiment140 dataset was selected for its generalizability. Abbreviations and emojis abound in this dataset which include short messages, usually no more than 100 words long. On the other hand, the IMDB dataset was

Table 2. Specification of the sentiment140, IMDB, and twitter US airline datasets

Sentiment140 IMDB Twitter US Airline			
Input length	150	500	200
Mean word count	90	231	110
Standard deviation	35	170	40
Vocabulary size (before removing stop words)	45977	158898	23032
Vocabulary size (after removing stop words)	29821	45977	13235
Train-test ratio	80:20		
No of classes	2	2	2

incorporated because of its association with the film industry; it contains far more extensive communications, with an average length of about 500 words. The last reason the US airlines dataset was chosen is because of the imbalance in sentiment distribution and the fact that the text review durations are all over the place. The overall specification of discussed datasets is presented in Table 2 below.

The construction of model is both complicated and exciting by virtue of the eclectic mix of datasets. This study primarily aims to create a model that can successfully analyze and comprehend various types of data inputs. The goal is to build a strong model that works well with a variety of inputs by taking use of the unique features of each dataset. The fundamental objective of this study is to establish a model that is highly effective in dealing with the complicated issues presented by the specific datasets that have been chosen. Thus, improved the text cleaning process in the initial step of preprocessing by eliminating a larger variety of frequently used words from both libraries using a combined set of stop words from scikit-learn and NLTK. When you compare the sizes of these words as shown in Table 2, its highly observable how stop words affect the complexity and richness of dataset's language. This comes especially handy when dealing with English text data, which can include many words that are regularly used yet don't really tell us anything.

The feature set in this study typically has many dimensions, noisy, and may contain irrelevant or redundant information due to the nature of textual features. So, there is dire need of allowing only relevant features feed into the model. In this work, filter-based feature selection method, specifically $\chi 2$ known for their potency in processing categorical features is used. These methods are applied both independently and in conjunction with ML classifiers, including SVM, RF, BNB, and proposed ensemble voting classifier to examine their effect on feature relevance and model outcome. This study introduces LASSO a feature selection methodology integrated with an ensemble voting classifier, a regularization technique used which has been rarely studied in case of text SA, that is specifically tailored for a dataset consisting of different domains. Additionally, Grid Search CV is used to identify the optimal hyperparameters for LASSO regularization and other methods. Furthermore, experiments are run with different values of n in the $\chi 2$ method, in order to choose a value that give promisable accuracy. Experimental outcomes with datasets demonstrate that LASSO which is multivariate analysis consistently outperforms the $\chi 2$ which is univariate approach when integrated with the proposed voting classifier. We explored various train-test ratios in this study, but finally concluded that 80:20 ratio yielding the most promising outcomes managing bias-variance tradeoff. In addition, precise hyperparameter tuning was done to refine model performance however, for brevity, only the most accomplished configuration for this study is presented in Table 3.

The experiment was limited to unigram and bigram approaches, and random sampling was used to ensure equal representation of classes. Potential data augmentation

Table 3. Chosen hyperparameter by grid search CV

Model	Chosen Hyperparameter by grid search CV
LASSO	LASSO_model_best_alpha {'alpha': 0.0001}
Chi-sq	K=2000
RF	Random state = 42, estimators =100
SVC	Kernel ='linear', C=1
BNB	Alpha =2.0

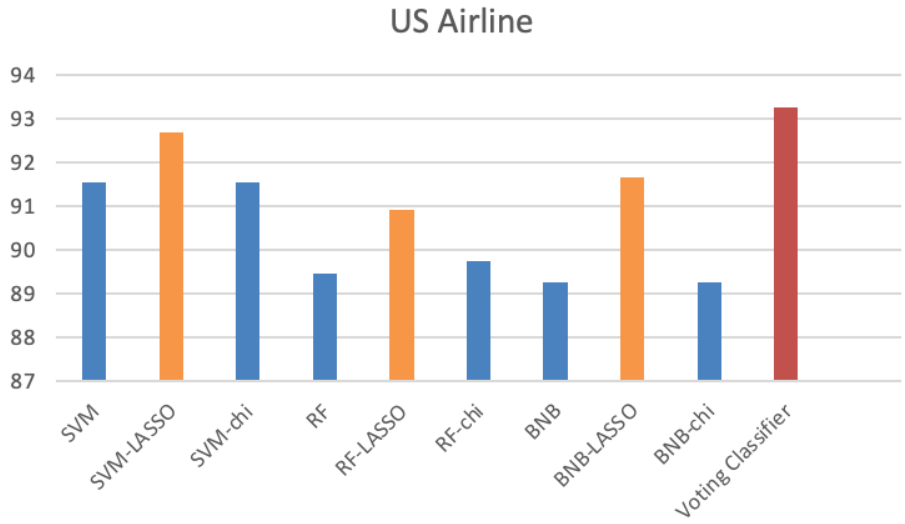


Figure 6. Performance of SVM, RF, BNB, and ensemble voting classifiers on the US Airline dataset using LASSO.



Figure 7. Performance of SVM, RF, BNB, and ensemble voting classifiers on the Sentiment140 dataset using LASSO.

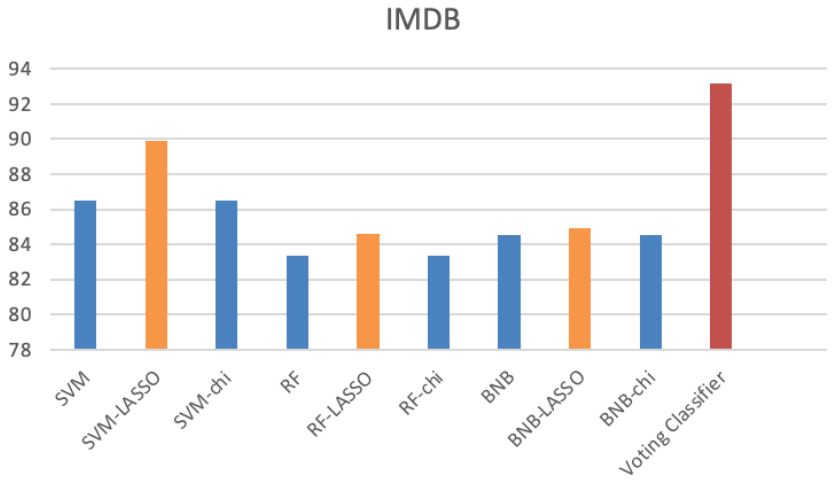


Figure 8. Performance of SVM, RF, BNB, and ensemble voting classifiers on the IMDB dataset using LASSO.

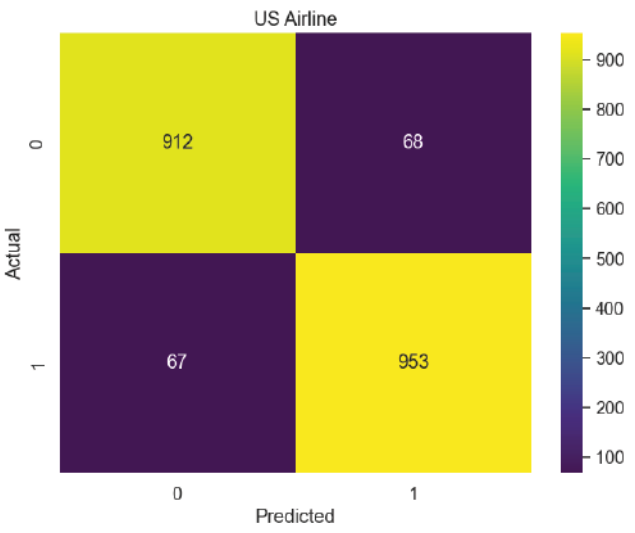


Figure 9. Error matrix of ensemble voting classifier for US Airline using Grid Search based LASSO filtering.

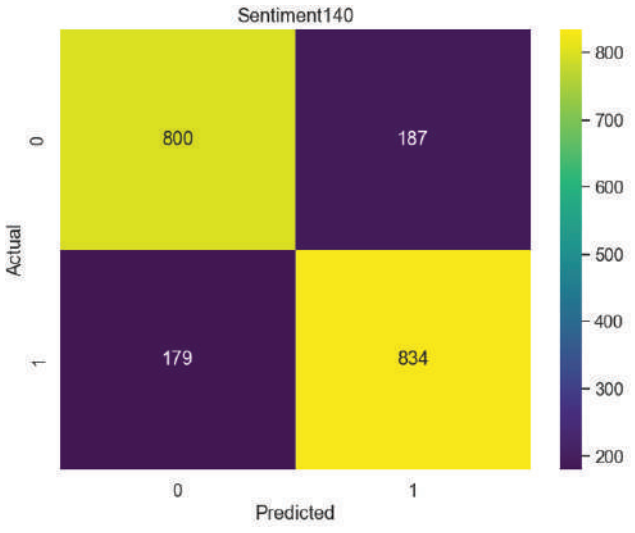


Figure 10. Error matrix of ensemble voting classifier for Sentiment140 using Grid Search based LASSO filtering.

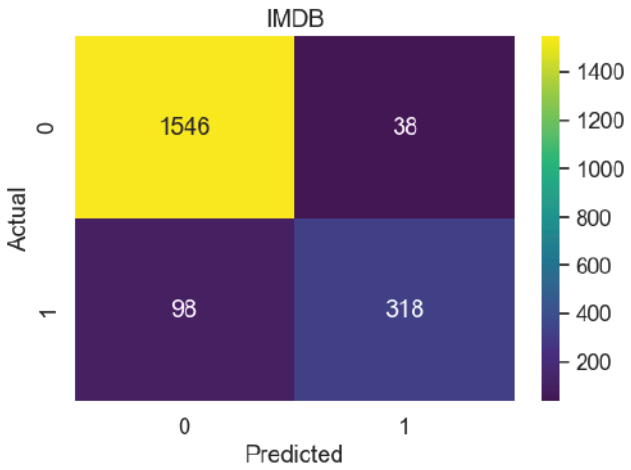


Figure 11. Error matrix of ensemble voting classifier for IMDB using Grid Search based LASSO filtering.

techniques could address class imbalances. Figure 6, 7, and 8 show the variation in classifier accuracy across datasets which shows that our suggested ensemble voting classifier continuously beats all existing classifiers by fusing powerful base classifiers like SVM and BNB with efficient feature selection algorithms like LASSO and Chi-square (Fig. 9-11).

Accuracy, Precision, Recall, and the F-measure (for imbalanced dataset) were some of the performance indicators used to analyze the model's efficacy during this review since. The results for different datasets utilizing the ensemble voting classifier and LASSO are shown in Tables 4, 5, and 6.

Tables 7, 8, and 9 show that our method yields better classification accuracy with least complexity than the work done in previous literature. In comparison to the US Airlines dataset (0.839) and the Sentiment140 dataset (0.800), the IMDB dataset has an MCC of 0.634.

Figure 12, 13, and 14 show the box plots across various metrics for each dataset. For Sentiment140 dataset, box plot shows many outliers indicating that the model's performance varies significantly throughout the dataset which could be due to linguistic features of dataset as it contains very short text with emoticons and varying customer's sentiments on different topics.

The suggested ensemble-voting SA framework shows strong transferability to many domains. Its success on all

Table 4. Precision of all three datasets

Dataset	SVM	RF	BNB	SVM-Chi-square	SVM-LASSO	RF-Chi-square	RF-LASSO	BNB-Chi-square	BNB-LASSO	Voting
IMDB	88.1	84.03	84.01	87.4	88.7	84.03	85.6	85.3	85.8	93.0
Sentiment-140	74.7	74.4	73.3	74.0	74.7	75.0	73.0	73.0	72.0	81.7
US airline	91.9	88.4	85.1	92.1	91.7	88.3	87.4	82.8	87.2	92.8

Table 5. Recall of all three datasets

Dataset	SVM	RF	BNB	SVM-Chi-square	SVM-LASSO	RF-Chi-square	RF-LASSO	BNB-Chi-square	BNB-LASSO	Voting
IMDB	88.4	84.2	84.0	87.4	87.8	84.2	85.0	84.2	85.7	93.0
Sentiment-140	74.6	74.4	73.0	74	75.0	75.0	73.30	73.0	72.0	81.8
US airline	81.6	79.5	87.9	84.4	84.8	78.9	81.3	88.1	87.5	93.2

Table 6. F-1 Score of all three datasets

Dataset	SVM	RF	BNB	SVM-Chi-square	SVM-LASSO	RF-Chi-square	RF-LASSO	BNB-Chi-square	BNB-LASSO	Voting
IMDB	87.6	84.3	84.0	87.4	87.6	84.5	85.0	84.3	85.7	93.0
Sentiment-140	74.6	74.3	72.9	74.0	75.0	75.0	73.0	73.0	72.0	81.7
US airline	85.5	82.8	86.4	87.5	86.9	82.4	83.9	85.0	87.4	93.1

Table 7. Comparison of model complexity and performance on the IMDB dataset

Sr. no	Source & publication year	Feature extraction	Feature filtering	Classifiers	Algorithm complexity	Classification accuracy
[18]	Naïfs & Awang, 2021	TF-IDF	Hybrid SVM+RFE	SVM	O (M×N) M is size of data; N is no of features.	83.16%
[20]	Kokab et al, 2022	Word2vec, Glove	---	CNN, LSTM, CBRNN	O(P∗F∗T) P stands for the parameter count. F represents the computational complexity of the forward pass through the network, T represents the training time required to train the model on a given dataset.	93%
[22]	Subba & Kumari, 2022	GloVe, Word2vec, Bert	---	Ensemble LSTM, GRU	O ((P1+P2+p3) ∗ (F1+F2+ F3) ∗ T) Here, P combines all parameters from Word2Vec, GloVe, BERT, and LSTM/GRU models; F combines their respective forward pass complexities; and T reflects the overall training time, influenced by data size and training epochs.	92%
[26]	Rehman et al., 2019	Word2vec	---	CNN + LSTM	O (M × K) + O (M × H2) M is size of input sequence, H is no of input unit, K is kernel size.	91.78%
--	Proposed work	TF-IDF	LASSO	Ensemble (SVM, BNB, RF)	O(P*Q) + T*log(n) P is size of data, Q is count of features, T is count of trees and n is total samples count in dataset.	93.20%

Table 8. Comparison of model complexity and performance on the US airlines dataset

Sr. no	Source & Publication Year	Feature extraction	Feature filtering	Classifiers	Algorithm Complexity	Classification Accuracy
[29]	Bataineh & Kaur, 2021	Keras embedding	---	CSA-LSTM	O (P * F * T)	92.25%
[31]	Tan et al, 2022	GloVe	---	RoBERTa-LSTM	$O(L*N^{2*}d) + O(N*d*h)$ N is the sequence length, d is the input dimension h is the hidden size of the LSTM.	85.89%
[32]	Tan et al, 2022	GloVe	---	Ensembling of RoBERTa with LSTM, BiLSTM, GRU	$O(L*N^{2}*d) + O(N*d*h_{LSTM}) + O(2*N*d*h_{BiLSTM}) + O(N*d*h_{GRU})$	91.77%
--	Proposed work	TF-IDF	LASSO	Ensemble Voting (SVM, RF BNB)	O(P*Q) + T*log(n) P is size of data, Q is count of features, T is count of trees and n is total samples count in dataset.	93.25%

Table 9. Comparison of model complexity and performance on the sentiment140 dataset

Sr. no	Source & Publication Year	Feature extraction	Feature filtering	Classifiers	Algorithm Complexity	Classification Accuracy
[40]	Singla et al, 2022	Word2vec	---	BERT	O(M*2)∗ d Here M is input sequence length; d is dimensionality of the model.	81.03%
--	Proposed work	TF-IDF	LASSO	Ensemble Voting (SVM, RF BNB)	O(P*Q) + T*log(n) P is size of data, Q is count of features, T is count of trees and n is total samples count in dataset.	81.75%

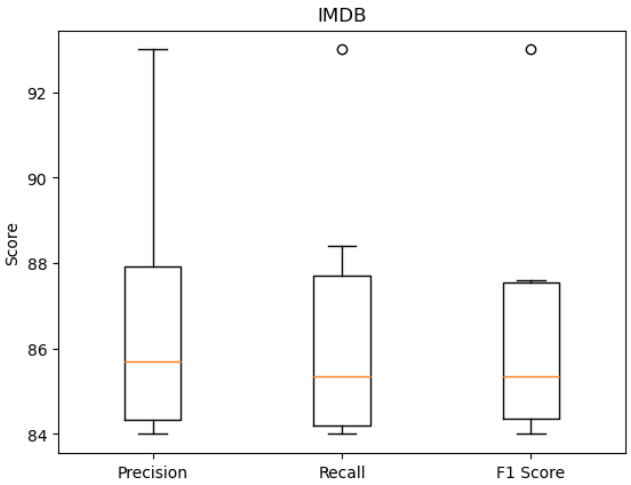


Figure 12. Visualization of metrics across IMDB using whisker plot.

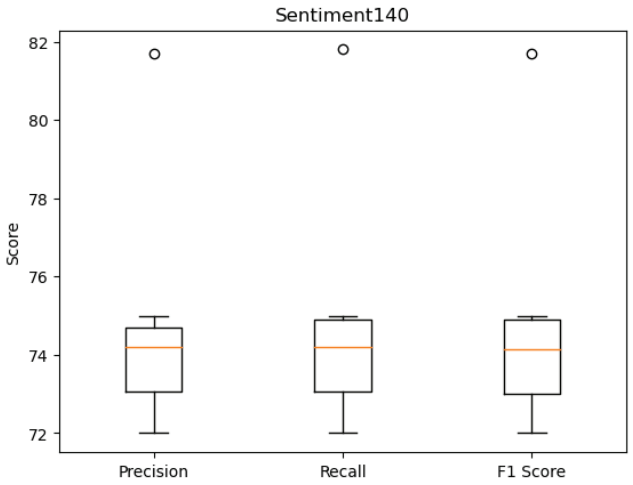


Figure 14. Visualization of metrics across sentiment140 using whisker plot.

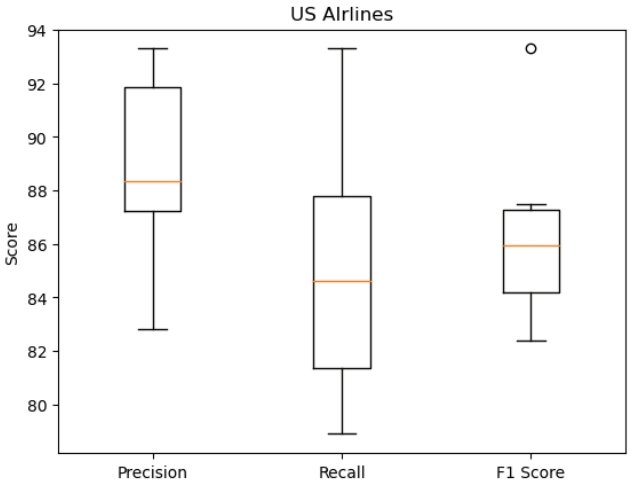


Figure 13. Visualization of metrics across US Airlines using whisker plot.

three datasets depicts that it might be useful to analyze trends, public opinion monitoring, and wide-scale consumer input in fields like social media, entertainment, and travel. Although the proposed model's result proven better detection of sentiments, but there are still some limitations of this study. In high-dimensional text data, nuanced predictors may be useful, but LASSO has tendency to enforce sparsity by zeroing out less important features, can lead to their permanent removal and additionally ensemble model can be complex and computationally heavy, especially when balancing base classifiers share. Sometimes, this extra complexity makes things harder to understand and makes real-time analysis less efficient.

CONCLUSION

Using LASSO, an inherent feature selection method based on multivariate analysis, this work aims to detect textual data polarity. To generalize the effectiveness of proposed ensemble voting classifier, model is test on dataset with different domain and different length of input text like short in sentiment140 and long for Internet Movie Database and also with balanced and imbalanced in case of US airline dataset. Results showing satisfactory accuracy as compared to DL models which are more complex and black

box in nature. It must be emphasized that Grid Search-based LASSO is a noteworthy feature selection method. For the Sentiment140, Internet Movie Database, and US airlines dataset, the ensemble voting model with Grid Search-based LASSO achieves an accuracy of 81.75%, 93.20%, and 93.25% respectively. A proposed voting classifier which is an ensemble model based on soft voting was built in this study using the Grid Search-based multivariate feature selection method LASSO in conjunction with the classifiers SVM, RF, and BNB. In our forthcoming research, we intend to assess the efficacy of the model in several tasks, including the identification of distinct emotions (e.g., sadness, happiness) and the analysis of emotions based on certain aspects. Furthermore, we will also look into data imbalances and tweets that include non-textual elements such as emojis. In addition, methods for pre-trained text embedding will be utilized to construct sophisticated emotion model. To handle class imbalance by dynamically prioritizing cases from underrepresented emotions, future study could investigate the possibility of using ensemble classifiers from adaptive weighted neural networks for real-time text emotion identification.

AUTHORSHIP CONTRIBUTIONS

Authors equally contributed to this work.

DATA AVAILABILITY STATEMENT

The authors confirm that the data that supports the findings of this study are available within the article. Raw data that support the finding of this study are available from the corresponding author, upon reasonable request.

CONFLICT OF INTEREST

The author declared no potential conflicts of interest with respect to the research, authorship, and/or publication of this article.

ETHICS

There are no ethical issues with the publication of this manuscript.

STATEMENT ON THE USE OF ARTIFICIAL INTELLIGENCE

Artificial intelligence was not used in the preparation of the article.

REFERENCES

[1] Ligthart A, Catal C, Tekinerdogan B. Systematic reviews in sentiment analysis: a tertiary study. Artif Intell Rev 2021;54:1–57. [CrossRef]

[2] Krakovsky M. Artificial (emotional) intelligence. Commun ACM 2018;61:18–19. [CrossRef]

[3] Wankhade M, Rao ACS, Kulkarni C. A survey on sentiment analysis methods, applications, and challenges. Artif Intell Rev 2022;55:5731–5780. [CrossRef]

[4] Kumar R. Twitter sentiment analysis for polarity detection: a survey. In: 2023 5th International Conference on Advances in Computing, Communication Control and Networking (ICAC3N). IEEE; 2023. p. 559–564. [CrossRef]

[5] Altınel Girgin AB, Gümüşçekiççi G, Birdemir N. Turkish sentiment analysis: a comprehensive review. Sigma J Eng Nat Sci 2024;42:1292–1314.

[6] Ren R, Wu DD, Liu T. Forecasting stock market movement direction using sentiment analysis and support vector machine. IEEE Syst J 2018;13:760–770. [CrossRef]

[7] Alhaj YA, Xiang J, Zhao D, Al-Qaness MA, Abd Elaziz M, Dahou A. A study of the effects of stemming strategies on Arabic document classification. IEEE Access 2019;7:32664–32671. [CrossRef]

[8] Ravi K, Ravi V. A survey on opinion mining and sentiment analysis: tasks, approaches and applications. Knowl Based Syst 2015;89:14–46. [CrossRef]

[9] Rasool A, Tao R, Kamyab M, Hayat S. GAWA – a feature selection method for hybrid sentiment classification. IEEE Access 2020;8:191850–191861. [CrossRef]

[10] Ye Q, Zhang Z, Law R. Sentiment classification of online reviews to travel destinations by supervised machine learning approaches. Expert Syst Appl 2009;36:6527–6535. [CrossRef]

[11] Korkontzelos I, Nikfarjam A, Shardlow M, Sarker A, Ananiadou S, Gonzalez GH. Analysis of the effect of sentiment analysis on extracting adverse drug reactions from tweets and forum posts. J Biomed Inform 2016;62:148–158. [CrossRef]

[12] Shaik T, Tao X, Dann C, Xie H, Li Y, Galligan L. Sentiment analysis and opinion mining on educational data: a survey. Nat Lang Process J 2023;2:100003. [CrossRef]

[13] Mahmoodzadeh A, Nejati HR, Mohammadi M, Ibrahim HH, Khishe M, Rashidi S, et al. Prediction of Mode-I rock fracture toughness using support vector regression with metaheuristic optimization algorithms. Eng Fract Mech 2022;264:108334. [CrossRef]

[14] Mosavi MR, Aghababaie M, Naseri MJ, Khishe M. Compression of respiratory signals using linear predictive coding method based on optimized algorithm of humpback whales to transfer by sonobouy. Iran J Mar Technol 2020;7:1–13.

[15] Tang W, Yang S, Khishe M. Profit prediction optimization using financial accounting information system by optimized DLSTM. Heliyon 2023;9:e19431. [CrossRef]

[16] Appel O, Chiclana F, Carter J, Fujita H. A hybrid approach to the sentiment analysis problem at the sentence level. Knowl Based Syst 2016;108:110–124. [CrossRef]

[17] Tiwari P, Mishra BK, Kumar S, Kumar V. Implementation of n-gram methodology for rotten tomatoes review dataset sentiment analysis. In: Cognitive analytics: concepts, methodologies, tools, and applications. IGI Global; 2020. p. 689–701. [CrossRef]

[18] Nafis NSM, Awang S. An enhanced hybrid feature selection technique using TF-IDF and SVM-RFE for sentiment classification. IEEE Access 2021;9:52177–52192. [CrossRef]

[19] Ray P, Chakrabarti A. A mixed approach of deep learning method and rule-based method to improve aspect level sentiment analysis. Appl Comput Inform 2022;18:163–178. [CrossRef]

[20] Kokab ST, Asghar S, Naz S. Transformer-based deep learning models for the sentiment analysis of social media data. Array 2022;14:100157. [CrossRef]

[21] Soubraylu S, Rajalakshmi R. Hybrid convolutional bidirectional recurrent neural network based sentiment analysis on movie reviews. Comput Intell 2021;37:735–757. [CrossRef]

[22] Subba B, Kumari S. A heterogeneous stacking ensemble based sentiment analysis framework using multiple word embeddings. Comput Intell 2022;38:530–559. [CrossRef]

[23] Yousaf A, Umer M, Sadiq S, Ullah S, Mirjalili S, Rupapara V, et al. Emotion recognition by textual tweets classification using voting classifier (LR-SGD). IEEE Access 2020;9:6286–6295. [CrossRef]

[24] Saraswathi N, Rooba TS, Chakaravarthi S. Improving the accuracy of sentiment analysis using a linguistic rule-based feature selection method in tourism reviews. Meas Sens 2023;29:100888. [CrossRef]

[25] Catal C, Nangir M. A sentiment classification model based on multiple classifiers. Appl Soft Comput 2017;50:135–141. [CrossRef]

[26] Rehman AU, Malik AK, Raza B, Ali W. A hybrid CNN-LSTM model for improving accuracy of movie reviews sentiment analysis. Multimed Tools Appl 2019;78:26597–26613. [CrossRef]

[27] Gouthami S, Hegde NP. Feature selection based sentiment analysis on US airline twitter data. Delta 2023;955;723:544.

[28] Hameed Z, Garcia-Zapirain B. Sentiment classification using a single-layered BiLSTM model. IEEE Access 2020;8:73992–74001. [CrossRef]

[29] Al Bataineh A, Kaur D. Immunocomputing-based approach for optimizing the topologies of LSTM networks. IEEE Access 2021;9:78993–79004. [CrossRef]

[30] Rafae A, Erritali M, Roche M. Fusion of BERT embeddings and elongation-driven features. Multimed Tools Appl 2024;83:80773–80797. [CrossRef]

[31] Tan KL, Lee CP, Anbananthen KSM, Lim KM. RoBERTa-LSTM: A hybrid model for sentiment analysis with transformer and recurrent neural network. IEEE Access 2022;10:21517–21525. [CrossRef]

[32] Tan KL, Lee CP, Lim KM, Anbananthen KSM. Sentiment analysis with ensemble hybrid deep learning model. IEEE Access 2022;10:103694–103704. [CrossRef]

[33] Baqach A, Battou A. CLAS: A new deep learning approach for sentiment analysis from Twitter data. Multimed Tools Appl 2023;82:47457–47475. [CrossRef]

[34] Wan Y, Gao Q. An ensemble sentiment classification system of Twitter data for airline services analysis. In: 2015 IEEE International Conference on Data Mining Workshop (ICDMW). IEEE; 2015. p. 1318–1325. [CrossRef]

[35] Nisha, Kumar R. Comparison between feature extraction algorithms for sentiment recognition from text. In: International Conference on Intelligent Systems Design and Applications. Springer; 2023. p. 301–310. [CrossRef]

[36] Ahmad SR, Bakar AA, Yaakub MR. A review of feature selection techniques in sentiment analysis. Intell Data Anal 2019;23:159–189. [CrossRef]

[37] Tan M, Tsang IW, Wang L. Matching pursuit LASSO part I: Sparse recovery over big dictionary. IEEE Trans Signal Process 2014;63:727–741. [CrossRef]

[38] Cervantes J, Garcia-Lamont F, Rodríguez-Mazahua L, Lopez A. A comprehensive survey on support vector machine classification: Applications, challenges and trends. Neurocomputing 2020;408:189–215. [CrossRef]

[39] Badik ŞT, Akar M. Machine learning classification models for the patients who have heart failure. Sigma J Eng Nat Sci 2024;42:235–244. [CrossRef]

[40] Singla C, Al-Wesabi FN, Pathania YS, Alfurhood BS, Hilal AM, Rizwanullah M, et al. An optimized deep learning model for emotion classification in tweets. Comput Mater Contin 2022;70:6365–6380. [CrossRef]

Sigma Journal of Engineering and Natural Sciences
Web page info: https://sigma.yildiz.edu.tr
DOI: 10.14744/sigma.2025.1926

Research Article

Numerical investigation of the mathematical model including the possibility of reinfection in infectious diseases

Mehmet KOCABIYIK[1,*]

[1]*Department of Mathematics, Burdur Mehmet Akif Ersoy University, Burdur, 15200, Türkiye*

ARTICLE INFO

Article history
Received: 24 July 2024
Revised: 09 September 2024
Accepted: 06 November 2024

Keywords:
Discretization; Infectious Diseases; Numerical Analysis; Stability

ABSTRACT

This study examines the challenges of reinfection in infectious disease modeling, emphasizing the risk that previously infected individuals may lose temporary immunity and become susceptible again. Accurate modeling of reinfection dynamics is vital for understanding disease spread and assessing intervention strategies. To address this, an adapted Susceptible, Infected, Treated, Recovered, Susceptible model is being developed. The adapted model differs from traditional models by incorporating distributed order differential equations, as opposed to standard ordinary or fractional models, which allows for a more flexible representation of disease dynamics. In addition, the adapted version also includes the possibility of reinfection. This improves the ability to interpret the situation of individuals who have re-infected. This approach improves both the interpretability and the computational efficiency of the model. The equilibrium points of the modified system are derived, and stability analyses are performed. The nonstandard finite difference method is used to eliminate instabilities. Numerical simulations are performed to evaluate the performance of the model. The data here is taken from sources derived from real world scenarios. Comparisons are then made based on this data. The results show that the improved model fits experimental data and previous studies quite well, giving a faster and more accurate picture of how diseases change over time. The models showed that adding reinfection can significantly change the expected paths of outbreaks and the effects of interventions. The novelty of this work lies in the incorporation of reinfection dynamics into a distributed order framework, hence augmenting the model's practical applicability compared to previous conventional models. This advance provides faster and more accurate insights into the behaviour of infectious diseases and represents a significant step forward in the field.

Cite this article as: Kocabıyık M. Numerical investigation of the mathematical model including the possibility of reinfection in infectious diseases. Sigma J Eng Nat Sci 2025;43(6):1930–1942.

INTRODUCTION

Mathematical modeling of infectious diseases has received significant attention in recent years. These models are necessary for figuring out how diseases spread, how well public health measures work, and when outbreaks may happen in the future. The convergence of infectious disease

***Corresponding author.**
*E-mail address: mkocabiyik@mehmetakif.edu.tr

This paper was recommended for publication in revised form by Editor-in-Chief Ahmet Selim Dalkilic

Published by Yıldız Technical University Press, İstanbul, Turkey
© Author. This is an open access article under the CC BY-NC license (http://creativecommons.org/licenses/by-nc/4.0/).

epidemiology and mathematical modeling establishes a comprehensive framework for examining the dissemination and regulation of infectious illnesses.

Mathematical models are important tools in epidemiology because they give us information that we can't get from real-world data alone. For example, models can show how different ways of stopping disease spread, such vaccination or social separation, would work. They can also be used to figure out important epidemiological numbers, including the basic reproduction number [1].

The field of infectious disease modeling has evolved significantly. This evolution has been greatly affected by improvements in computer power and the availability of data. For example, agent-based models show how people in a population interact with each other, showing the differences in behavior and contact patterns [2]. These models have been extremely useful in studying illnesses with complex transmission dynamics, such as influenza and HIV. Network-based models are likewise becoming more common. These make it evident how people are grouped together in space and time. This strategy helps us learn more about how diseases spread across various contact networks, such as schools, workplaces, and homes [3].

These models use real-world data about how people interact with each other to make disease transmission more realistic. Then, they help make focused treatments easier to plan. Recent research has shown how important mathematical models are for dealing with public health emergencies. During the COVID-19 pandemic, for instance, models were used to anticipate how the virus would spread, help make policy decisions, and make sure that healthcare resources were used in the best way possible [4]. These models have enabled governments and health organizations to act quickly and effectively. Consequently, the epidemic's impact has diminished.

Mathematical modeling of infectious illnesses is still a field that is always changing and growing. Novel problems are coming up, such as novel germs and the growing complexity of global health systems. Consequently, the use of models in directing public health interventions is growing progressively essential. It is vital to continuously improving modeling methods in order to overcome these difficulties. Innovations are more likely to improve health outcomes around the world when they are coupled with work from other fields.

A major focus in this area is the development and refinement of epidemic models such as SIR (Susceptible-Infectious-Recovered), SEIR (Susceptible-Exposed-Infectious-Recovered), and STIR (Susceptible-Treated-Infectious-Recovered). Kermack and McKendrick [5] were the first to come up with the SIR model. Researchers that have worked on these models since then have looked into how different types of immunity, latency periods, and transient immunity affect the spread of disease. Differential equations and other mathematical methods have been used to explain how quickly each portion of the model changes. This gives us useful knowledge about how public health measures might work and how infectious illnesses usually act in communities. This continuous research is essential for formulating more effective strategies to manage and prevent the dissemination of infectious illnesses [6].

Çilli et al. employed SI and SIS models to forecast the dissemination of epidemic diseases, including TB, malaria, HIV/AIDS, CCHF, and measles across various nations. Their research demonstrates that these models accurately predict the exact number of infected individuals, showing notable precision and responsiveness to real data trends [7]. Uçar et al. focus on obtaining numerical approximate solutions for the nonlinear modified Burgers' equation (MBE) using modified cubic B-spline differential quadrature methods. The results show that this approach is an effective numerical scheme for solving the MBE, supported by a stability analysis [8].

Karakoç et al. present a finite element scheme for numerically solving the Gilson-Pickering equation using septic B-spline functions. They perform a Von-Neumann stability analysis and demonstrate the reliability of their method by examining the behaviour of single solitons, with the results illustrated by tables and graphs showing the effectiveness of the method [9]. Özgür and Demir explain a mathematical framework to investigate the stability of a neural field model involving two neuron populations with small delays. The primary aim of this analysis is to provide a unifying framework that illustrates the effects of small delays in the context of the Routh-Hurwitz criterion [10].

Elsonbaty et al. present a discrete fractional SITRS (Susceptible, Infectious, Treated, Recovered, Susceptible) model to simulate the COVID-19 pandemic. This study includes the potential for reinfection due to the loss of temporary immunity. They also talked about the wrong idea that the infection rates are the same for people who are normally susceptible and those who are more likely to get sick. Because of what they did, they were able to fit their models to the experimental data [11].

In this study, the SITRS model is investigated using distributed order differential equations. This adjustment makes it possible to better show how the disease changes over time by showing how the rates of infection and recovery fluctuate. The model may take into consideration how complicated and diverse the development of a disease is by using distributed order differential equations. So, it is a more realistic and flexible way to model how infectious diseases like COVID-19 spread and how to stop them.

There is a substantial amount of literature in this field. Some of the studies conducted in this area can be summarised as follows. Ayoub et al. found that the test-negative design was highly effective in predicting the protective efficacy of prior COVID-19 infection against reinfection, as shown by %97.0 and %85.5 protection estimates against Alpha and Beta variants, respectively, in Qatar. The method remains robust to potential misclassification and changing infection levels in the population [12].

Shah and colleagues developed a three-compartment model to examine the reinfection of viral infections, including COVID-19. The model includes a hybrid fractal-fractional equation system that includes key theoretical aspects such as stability analysis and sensitivity of the basic reproduction number. Lagrange interpolation polynomials were used to run numerical simulations that tested the model by comparing real data to simulated data [13].

Schuh et al. propose a mathematical model that encapsulates both the acute and chronic dynamics of post-acute SARS-CoV-2 infection. The model also looks at reinfection situations using attributes that are distinct to each variety. This gives us information that can be used in both clinical and public health settings [14]. Salman and Mohd employed a reaction-diffusion system to simulate the transmission dynamics of COVID-19, incorporating both SEIRS-type kinetics and the spatial distribution of individuals. The research assessed the effects of reinfection, spatial dissemination, and control strategies utilizing optimal control theory and numerical simulations. Thus, the effectiveness of vaccination and treatment in preventing future outbreaks was highlighted. [15].

The literature review shows that the reinfection situation is important in infectious diseases. However, it is noteworthy that the studies focus on a single equation type in the light of these studies. This type of equation is usually an ordinary or fractional differential equation. In other words, expressing the solutions in a single style is quite important even in the numerical analysis section, but it also reveals the necessity of using ordinary and fractional type equation systems in some models. For this reason, this study was planned considering the deficiency in this section of the literature. By adapting the equation system used to distributed order differential equations, comments can be made about both ordinary and fractional order differential equations. This is because distributed order differential equations involve the analysis of other types of equations due to the function they contain.

Although the first contact of infectious diseases is important, reinfection is more important. This is because if the immune system encounters the disease twice, it can have a vital effect. It is therefore essential to be able to interpret the reinfection situation quickly and accurately in different situations or conditions and to develop the ability to act accordingly. The aim of our study is to link the dynamics to a single equation system and to determine numerical simulations under different equation systems or conditions by changing several functions.

In similar studies or models addressing reinfection dynamics, it is observed that different equation systems are developed for each unique effect of the disease, which can lead to delays in interpreting results. These delays can result in wasted time and, ultimately, deaths due to the lack of available resources. The first barrier that distributed order differential equations aim to overcome is precisely this issue. By employing a density function, the equations are designed to adapt to various external influences without needing to change the system itself. In the current model, which incorporates reinfected individuals, this approach has been tested for the first time, and the comparison of results has demonstrated its suitability.

Distributed order differential equations were introduced and developed by Caputo [16]. They include a system of differential equations that integrates Caputo, Riemann-Liouville, and Grünwald-Letnikov fractional derivatives. The most important feature is the density function it contains. This function allows the system to be transformed into either an ordinary or a fractional differential equation. This ability allows a better understanding of different systems of equations and the behaviour of the system under different external influences. Numerous studies have applied distributed order differential equations to diverse areas, including the modeling of dielectric induction and diffusion [17], numerical solutions [18,19], reaction diffusion equations [20], and the SVIR model analysis [21,22].

The numerical analysis in this study is performed using the Nonstandard Finite Difference (NSFD) method. This approach helps get rid of instabilities by letting you choose the denominator function. Introduced by Mickens, the NSFD method has been shown to be applicable to various differential equation systems [23,24], with further details available in relevant literature [25-30].

Computational advances have made it possible to achieve faster results while minimizing errors. This model's modern method is better at getting rid of instability than other methods, which makes it easier to spot associated developments. As a result, the temporal gaps that could cause problems in systems have been cut down, making forecasts more reliable and accurate.

This work is new since it uses distributed order differential equations to create a new version of the SITRS model. This advancement facilitates a more thorough and precise representation of disease dynamics, including the complexities of re-infection and the variability of immunity.

This study significantly impacts infectious disease modeling by the application of modern mathematical methodologies. The better model makes it easier to forecast how diseases will spread. It also makes public health programs work better. It also highlights its relevance and specificity in advancing our understanding of infectious diseases. The results address gaps in current research. That is, it highlights the importance of developing epidemiological models to improve public health outcomes.

There are five sections to this study. The second section provides the necessary background for the reformulation and discretization of the system. The third section presents the discretization of the adapted distributed order system. The fourth section carries out a numerical investigation using equilibrium points under different conditions. The fifth section presents the results and discussion.

DEFINITIONS AND FUNDAMENTALS

Caputo's development of distributed order differential equations represents a significant advance in the field of fractional calculus [16]. This method builds on classical fractional differential equations by letting differential equations be spread out over an interval. Distributed order differential equations are mathematical equations that use several fractional derivatives instead of whole values. This makes it easier to model complicated systems, including how infectious illnesses spread. These explanations are meant to help people understand the ideas better and how they apply to actual life. In this situation, it also has a density function. A density function is a math tool that shows how a certain amount is spread out throughout a population or area. In infectious disease models, it shows how people with different traits (such immunity or susceptibility) are distributed out over the community, which helps us understand how diseases spread in more detail. This flexibility makes it possible to simulate complicated systems more accurately, because distinct processes may change at different speeds.

One advantage of Caputo's distributed order differential equations is that they can handle real-world circumstances better. Applications span a wide range of fields, including physics, engineering, and biology. These equations provide a more detailed understanding of processes related to memory and hereditary influences.

Definition 2.1: The Caputo derivative of order α for a function $f(t)$ is defined as:

$$D^{\alpha} f(t) = \frac{1}{\Gamma(n-\alpha)} \int_{\alpha}^{t} \frac{f^{(n)}(\tau)}{(t-\tau)^{\alpha-n+1}} d\tau, \qquad (1)$$

where, $n \in \mathbb{N}^{+}$, $n - 1 < \alpha \leq n$, Γ is the Gamma function and $f(n)$ is the n - th derivative of $f(t)$ [31]. The Caputo derivative, denoted as $D^{\alpha}f(t)$, is commonly used in fractional calculus to describe processes that involve memory or non-local behavior.

Definition 2.2: The Riemann-Liouville fractional derivative of order α for a function $f(t)$ is defined as:

$$D^{\alpha} f(t) = \frac{1}{\Gamma(n-\alpha)} \frac{d^{n}}{dt^{n}} \int_{\alpha}^{t} \frac{f(\tau)}{(t-\tau)^{\alpha-n+1}} d\tau, \qquad (2)$$

where, $n \in \mathbb{N}^{+}$, $n - 1 < \alpha \leq n$, Γ is the Gamma function [31]. The Riemann-Liouville derivative, denoted as $D^{\alpha}f(t)$, is a conventional technique in fractional calculus, mostly utilized to model systems with memory; nonetheless, it encounters difficulties in handling beginning conditions due to its requirement for non-integer initial values.

Definition 2.3: The Grünwald-Letnikov fractional derivative is defined as:

$$D^{\alpha} f(t) = \lim_{h \to 0} \frac{1}{h^{\alpha}} \sum_{k=0}^{\alpha} (-1)^{k} \binom{\alpha}{k} f(t - kh), \qquad (3)$$

where h is a small step size and $\binom{\alpha}{k}$ is the generalized binomial coefficient [31]. The Grünwald-Letnikov derivative, denoted as $D^{\alpha}f(t)$, provides a discrete approximation of fractional derivatives, making it useful for numerical implementations and simulations of systems with fractional dynamics.

Definition 2.4: The Distributed order derivative of a function $f(t)$ can be expressed as:

$$D_{t}^{k(\alpha)}(f(t), k(\alpha), \alpha) = \int_{0}^{1} k(\alpha)\, D^{\alpha} f(t)\, d\alpha, \qquad (4)$$

where $k(\alpha)$ is a density function that defines the distribution of the orders, $D^{\alpha}f(t)$ is a fractional derivative of order α. The distributed order derivative, $D^{k(\alpha)}(f(t), k(\alpha), \alpha)$, introduces a more generalized concept. Instead of applying a single fractional order, it incorporates a range of fractional derivatives, weighted by a function $k(\alpha)$, and integrates over all possible orders. This allows the model to capture a broader spectrum of dynamic behaviors without needing to adjust the system for different conditions. $D^{\alpha}f(t)$ fractional derivative it can be chosen as Caputo, Riemann-Liouville or Grünwald-Letnikov fractional derivative [16,32].

In distributed order differential equations, the Caputo derivative is better, especially for situations with beginning conditions. It makes it easier to understand how to deal with these situationsCaputo employs integer order derivatives to characterize initial conditions, distinguishing it from the Riemann-Liouville derivative. These are more familiar and make more sense in a physical way. This makes it easier to add real-world beginning data to the model. Caputo's technique makes sure that beginning conditions fit together naturally in dispersed order systems with more than one fractional order. This avoids complications in interpretation. As a result, it is more suitable for applications like infectious disease dynamics, where initial states are critical for accurate simulations.

The NSFD method represents a significant innovation in the numerical analysis for differential equations [23]. This method was developed to overcome the stability problems found in traditional finite difference approaches. The approach uses carefully chosen denominator functions to make the numbers more stable. The main advantage of the NSFD method is its ability to increase the stability and accuracy in numerical solutions of differential equations. This benefit is especially helpful when working with difficult issues or equations that oscillate quickly. It can be used in many fields of science and engineering, including as fluid dynamics, reaction-diffusion systems, and epidemiological modeling. It makes it easier to solve complex dynamic systems. People often utilize numerical approaches like Runge-Kutta, Adams, and Theta to study how populations interact with each other. But the magnitude of the time step has a big effect on how accurate and stable they are. In contrast, the NSFD method guarantees positive discrete solutions for positive initial conditions. On the other hand, the structured NSFD scheme may introduce a slight delay in travelling wave propagation when large step sizes are used [33,34].

Definition 2.5: The general form of a nonstandard finite difference scheme for a differential equation $\frac{dy}{dt} = f(y,t)$ can be written as:

$$\frac{y_{n+1}-y_n}{\varphi(h)} = f(y_n, t_n), \tag{5}$$

where y_n is the approximation of $y(t)$ at the discrete time step t_n and h is the time step size. $\varphi(h)$ is designed to fit the behavior of a continuous system. It is usually a function chosen to ensure that certain properties are preserved. In the literature it is referred to as the denominator function [23].

THE DISCRETIZATION OF ADAPTED ENDEMIC MODEL

In this section, we present a new SITRS model that includes two groups of susceptible individuals $S_1(t)$ and $S_2(t)$, an infected individual $I(t)$, a treatment individual $T(t)$, and a recovered individual $R(t)$. The improved model builds on the traditional SITR model by allowing for the possibility that recovered individuals may lose temporary immunity and become re-susceptible to the virus. In addition, the original model assumes that infection rates are the same for both the general susceptible population and for elderly or seriously ill individuals. This model does not have this limitation [11]. In addition, the system is transformed into a distributed order model with different arrangement. The updated SITRS model is presented below:

$$\begin{aligned}
D_t^{k(\alpha)}S_1 &= G - b\,I(t)S_1(t) - dS_1(t) + lR(t),\\
D_t^{k(\alpha)}S_2 &= G - b\,I(t)S_2(t) - dS_2(t) + lR(t),\\
D_t^{k(\alpha)}I &= (-\tau - d + c)I(t) + bI(t)\big(S_1(t) + S_2(t)\big) - T(t),\\
D_t^{k(\alpha)}T &= \gamma I(t) - wT(t),\\
D_t^{k(\alpha)}R &= \tau I(t) - (d + l)\,R(t).
\end{aligned} \tag{6}$$

In this definition, the $D^{\alpha}f(t)$ derivative is chosen as a Caputo type fractional derivative. The reason for this selection is to choose the most suitable fractional derivative that can be used with the initial data we have.

The parameters in this system are given in Table 1, where G is the natural growth rate of susceptible individuals; b is the infection rate of contact between susceptible and infected individuals; l is the rate of loss of immunity of recovered individuals; d is the mortality rate; c is the rate of dry cough, cold and fever of infected individuals; γ is the cure rate of infected individuals; τ is the recovery rate of treated individuals; and w is the treatment control parameter of treated individuals. The constants listed in Table 1, are derived from empirical studies where these parameters have been measured and analyzed in real world settings. These values have been chosen from existing literature that explicitly deals with these variables to make sure that the comparisons are correct and useful. By basing these constants on real-world data, we make the model stronger and more believable, which makes it more like how diseases really work. If the defined discretization is applied to the system of equations, the discrete state of the system becomes as follows:

$$\begin{aligned}
\sum_{j=1}^{A}\frac{k(\alpha_j)}{A}\sum_{i=0}^{n+1}u_i^{\alpha_j}S_{n+1-i}^1 &= G - b\,I_nS_{n+1}^1 - dS_{n+1}^1 + lR_n,\\
\sum_{j=1}^{A}\frac{k(\alpha_j)}{A}\sum_{i=0}^{n+1}u_i^{\alpha_j}S_{n+1-i}^2 &= G - b\,I_nS_{n+1}^2 - dS_{n+1}^2 + lR_n,\\
\sum_{j=1}^{A}\frac{k(\alpha_j)}{A}\sum_{i=0}^{n+1}u_i^{\alpha_j}I_{n+1-i} &= (-\tau - d + c)I_{n+1} + bI_{n+1}(S_n^1 + S_n^2) - T_n,\\
\sum_{j=1}^{A}\frac{k(\alpha_j)}{A}\sum_{i=0}^{n+1}u_i^{\alpha_j}T_{n+1-i} &= \gamma I_n - wT_{n+1},\\
\sum_{j=1}^{A}\frac{k(\alpha_j)}{A}\sum_{i=0}^{n+1}u_i^{\alpha_j}R_{n+1-i} &= \tau I_n - (d + l)R_{n+1},
\end{aligned} \tag{7}$$

where $v,\ j = 1,2,3,4,5,\ 0 < \alpha_j < 1,\ u_0^{\alpha_j} = (\varphi_v(h))^{-\alpha_j}$, and denominator functions are chosen as:

$$\begin{gathered}
\varphi_1(h) = \frac{1 - e^{dh}}{d},\ \varphi_2(h) = \frac{1 - e^{dh}}{d},\ \varphi_3(h) = \frac{1 - e^{(\tau + d - c)h}}{\tau + d - c},\\
\varphi_4(h) = \frac{1 - e^{wh}}{w},\ \varphi_5(h) = \frac{1 - e^{(d+l)h}}{d+l}.
\end{gathered} \tag{8}$$

By expanding the terms on the left and rearranging the system of equations,

$$\begin{aligned}
\sum_{j=1}^{A}\frac{k(\alpha_j)}{A}\left(u_0^{\alpha_j}S_{n+1}^1 + \sum_{i=1}^{n+1}u_i^{\alpha_j}S_{n+1-i}^1\right) &= G - b\,I_nS_{n+1}^1 - dS_{n+1}^1 + lR_n,\\
\sum_{j=1}^{A}\frac{k(\alpha_j)}{A}\left(u_0^{\alpha_j}S_{n+1}^2 + \sum_{i=1}^{n+1}u_i^{\alpha_j}S_{n+1-i}^2\right) &= G - b\,I_nS_{n+1}^2 - dS_{n+1}^2 + lR_n,\\
\sum_{j=1}^{A}\frac{k(\alpha_j)}{A}\left(u_0^{\alpha_j}I_{n+1} + \sum_{i=1}^{n+1}u_i^{\alpha_j}I_{n+1-i}\right) &= (-\tau - d + c)I_{n+1} + bI_{n+1}(S_n^1 + S_n^2) - T_n,\\
\sum_{j=1}^{A}\frac{k(\alpha_j)}{A}\left(u_0^{\alpha_j}T_{n+1} + \sum_{i=1}^{n+1}u_i^{\alpha_j}T_{n+1-i}\right) &= \gamma I_n - wT_{n+1},\\
\sum_{j=1}^{A}\frac{k(\alpha_j)}{A}\left(u_0^{\alpha_j}R_{n+1} + \sum_{i=1}^{n+1}u_i^{\alpha_j}R_{n+1-i}\right) &= \tau I_n - (d + l)R_{n+1}.
\end{aligned} \tag{9}$$

Table 1. Description of the constants for the distributed order model

Symbol	Description	Symbol	Description
G	*Natural grow rate*	*c*	*Dry cough, cold and fever rate*
b	*Infection rate*	*γ*	*Treatment rate*
l	*Loss of temporary immunity rate*	*w*	*Treatment control parameter*
d	*Death rate*	*τ*	*Recovering rate*

Hence

$$\begin{aligned}
&\sum_{j=1}^{A}\frac{k(\alpha_j)}{A}\varphi_1(h)^{-\alpha_j}S_{n+1}^1+\sum_{j=1}^{A}\frac{k(\alpha_j)}{A}\sum_{i=1}^{n+1}u_i^{\alpha_j}S_{n+1-i}^1=G-b\,I_nS_{n+1}^1-dS_{n+1}^1+lR_n,\\
&\sum_{j=1}^{A}\frac{k(\alpha_j)}{A}\varphi_2(h)^{-\alpha_j}S_{n+1}^2+\sum_{j=1}^{A}\frac{k(\alpha_j)}{A}\sum_{i=1}^{n+1}u_i^{\alpha_j}S_{n+1-i}^2=G-b\,I_nS_{n+1}^2-dS_{n+1}^2+lR_n,\\
&\sum_{j=1}^{A}\frac{k(\alpha_j)}{A}\varphi_3(h)^{-\alpha_j}I_{n+1}+\sum_{j=1}^{A}\frac{k(\alpha_j)}{A}\sum_{i=1}^{n+1}u_i^{\alpha_j}I_{n+1-i}=(-\tau-d+c)I_{n+1}+bI_{n+1}(S_n^1+S_n^2)-T_n,\\
&\sum_{j=1}^{A}\frac{k(\alpha_j)}{A}\varphi_4(h)^{-\alpha_j}T_{n+1}+\sum_{j=1}^{A}\frac{k(\alpha_j)}{A}\sum_{i=1}^{n+1}u_i^{\alpha_j}T_{n+1-i}=\gamma I_n-wT_{n+1},\\
&\sum_{j=1}^{A}\frac{k(\alpha_j)}{A}\varphi_5(h)^{-\alpha_j}R_{n+1}+\sum_{j=1}^{A}\frac{k(\alpha_j)}{A}\sum_{i=1}^{n+1}u_i^{\alpha_j}R_{n+1-i}=\tau I_n-(d+l)R_{n+1}.
\end{aligned}\tag{10}$$

The last expressions can be simplified as follows

$$\begin{aligned}
&S_{n+1}^1\left(\sum_{j=1}^{A}\frac{k(\alpha_j)}{A}\varphi_1(h)^{-\alpha_j}+b\,I_n+d\right)=G+l\,R_n-\sum_{j=1}^{A}\frac{k(\alpha_j)}{A}\sum_{i=1}^{n+1}u_i^{\alpha_j}S_{n+1-i}^1,\\
&S_{n+1}^2\left(\sum_{j=1}^{A}\frac{k(\alpha_j)}{A}\varphi_2(h)^{-\alpha_j}+b\,I_n+d\right)=G+l\,R_n-\sum_{j=1}^{A}\frac{k(\alpha_j)}{A}\sum_{i=1}^{n+1}u_i^{\alpha_j}S_{n+1-i}^2,\\
&I_{n+1}\left(\sum_{j=1}^{A}\frac{k(\alpha_j)}{A}\varphi_3(h)^{-\alpha_j}+\tau+d-c-b(S_n^1+S_n^2)\right)=-T_n-\sum_{j=1}^{A}\frac{k(\alpha_j)}{A}\sum_{i=1}^{n+1}u_i^{\alpha_j}I_{n+1-i},\\
&T_{n+1}\left(\sum_{j=1}^{A}\frac{k(\alpha_j)}{A}\varphi_4(h)^{-\alpha_j}+w\right)=\gamma I_n-\sum_{j=1}^{A}\frac{k(\alpha_j)}{A}\sum_{i=1}^{n+1}u_i^{\alpha_j}T_{n+1-i},\\
&R_{n+1}\left(\sum_{j=1}^{A}\frac{k(\alpha_j)}{A}\varphi_5(h)^{-\alpha_j}+d+l\right)=\tau I_n-\sum_{j=1}^{A}\frac{k(\alpha_j)}{A}\sum_{i=1}^{n+1}u_i^{\alpha_j}R_{n+1-i}.
\end{aligned}\tag{11}$$

with $\sum_{j=1}^{A}\frac{k(\alpha_j)}{A}\varphi_i(h)^{-\alpha_j}=K_i, for\ i,j=1,2,3,4,5$, and finally

$$\begin{aligned}
S_{n+1}^1&=\frac{G+l\,R_n-\sum_{j=1}^{A}\frac{k(\alpha_j)}{A}\sum_{i=1}^{n+1}u_i^{\alpha_j}S_{n+1-i}^1}{K_1+b\,I_n+d},\\
S_{n+1}^2&=\frac{G+l\,R_n-\sum_{j=1}^{A}\frac{k(\alpha_j)}{A}\sum_{i=1}^{n+1}u_i^{\alpha_j}S_{n+1-i}^2}{K_2+b\,I_n+d},\\
I_{n+1}&=\frac{-T_n-\sum_{j=1}^{A}\frac{k(\alpha_j)}{A}\sum_{i=1}^{n+1}u_i^{\alpha_j}I_{n+1-i}}{K_3+\tau+d-c\ -b(S_n^1+S_n^2)},\\
T_{n+1}&=\frac{\gamma I_n-\sum_{j=1}^{A}\frac{k(\alpha_j)}{A}\sum_{i=1}^{n+1}u_i^{\alpha_j}T_{n+1-i}}{K_4+w},\\
R_{n+1}&=\frac{\tau I_n-\sum_{j=1}^{A}\frac{k(\alpha_j)}{A}\sum_{i=1}^{n+1}u_i^{\alpha_j}R_{n+1-i}}{K_5+d+l}.
\end{aligned}\tag{12}$$

Thus, the final state of the discretized system is found as Equation 12.

NUMERICAL INVESTIGATION OF DISCRETIZED SYSTEM

In this section, equilibrium point analysis and numerical simulations have been performed. Constant values are important for analysis and simulations. The values have been chosen as shown in Table 2 and evaluations are made accordingly [11].

Equilibrium point analysis is very important for this model since it helps us understand how the system will behave throughout time. We can find out if these points are stable by finding and studying equilibrium points. This tells us if the disease will stay the same, get worse, or die out in a certain group of people. This method allows researchers and public health officials to predict what might happen if an infectious disease emerges and identify the best ways to stop it. For example, an unstable balance point indicates that a small change, such as an increase in infection rates, could cause infections to return. A stable point means the disease is likely to remain under control.

The equilibrium points chosen for this model are meant to show how things work in the actual world, especially during epidemics of infectious diseases like COVID-19. One of the equilibrium points, for instance, would be when the population reaches herd immunity, which is important for figuring out what has to happen to stop the virus from spreading.

The identified equilibrium points can also help identify constraints for intervention strategies. If the study indicates that a particular region has a low incidence of infection, this information can help public health officials establish regulations to maintain low transmission levels. By comparing equilibrium points with existing data from COVID-19 outbreaks, such as hospitalization rates and infection trends, we can improve our understanding of the mechanisms of the disease. This interpretation strengthens the theoretical framework of the model and highlights its practical importance in addressing public health challenges.

Firstly, finding the equilibrium point is a crucial requirement in discretized systems. This requires the solution of Equation 13.

Table 2. Initial conditions and the constants' values for equilibrium point analysis

Initial Conditions	Values	Parameter Conditions 1	Values	Parameter Conditions 2	Values
$S_1(0)$	0.65	G	0.3	G	0.3
$S_2(0)$	0.15	b	0.35	b	0.3
I(0)	0.75	l	0.3	l	0.3
T(0)	0.35	d	0.25	d	0.2
R(0)	0.1	c	0.01	c	0.01
		γ	0.2	γ	0.03
		w	0.1	w	0.1
		τ	0.1	τ	0.15

$$S_n^1 = \frac{G + l\,R_n - \sum_{j=1}^{A} \frac{k(\alpha_j)}{A} \sum_{i=1}^{n+1} u_i^{\alpha_j} S_n^1}{K_1 + b\,I_n + d},$$

$$S_n^2 = \frac{G + l\,R_n - \sum_{j=1}^{A} \frac{k(\alpha_j)}{A} \sum_{i=1}^{n+1} u_i^{\alpha_j} S_n^2}{K_2 + b\,I_n + d},$$

$$I_n = \frac{-T_n - \sum_{j=1}^{A} \frac{k(\alpha_j)}{A} \sum_{i=1}^{n+1} u_i^{\alpha_j} I_n}{K_3 + \tau + d - c - b(S_n^1 + S_n^2)}, \quad (13)$$

$$T_n = \frac{\gamma I_n - \sum_{j=1}^{A} \frac{k(\alpha_j)}{A} \sum_{i=1}^{n+1} u_i^{\alpha_j} T_n}{K_4 + w},$$

$$R_n = \frac{\tau I_n - \sum_{j=1}^{A} \frac{k(\alpha_j)}{A} \sum_{i=1}^{n+1} u_i^{\alpha_j} R_n}{K_5 + d + l}.$$

If the system expressed by Equation 13 is solved using the Maple software package, the equilibrium points can be determined. However, due to the lengthy calculations required for the second equilibrium point, it is expressed later using parameters.

$$Eq_1 = \left(\frac{G}{K_1 + d + \sum_{j=1}^{A} \frac{k(\alpha_j)}{A} \sum_{i=1}^{n+1} u_i^{\alpha_j}}, \frac{G}{K_2 + d + \sum_{j=1}^{A} \frac{k(\alpha_j)}{A} \sum_{i=1}^{n+1} u_i^{\alpha_j}}, 0,0,0 \right) \quad (14)$$

$$Eq_2 = (eq_{21}, eq_{22}, eq_{23}, eq_{24}, eq_{25}) \quad (15)$$

Another requirement for the analysis of equilibrium points is the Jacobian matrix. Therefore, the Jacobian matrix corresponding to the discretized Equation 12 is determined as follows:

$$J = \begin{pmatrix} s_{11} & 0 & s_{13} & 0 & s_{15} \\ 0 & s_{22} & s_{23} & 0 & s_{25} \\ s_{31} & s_{32} & s_{33} & s_{34} & 0 \\ 0 & 0 & s_{43} & s_{44} & 0 \\ 0 & 0 & s_{53} & 0 & s_{55} \end{pmatrix}$$

$$s_{11} = \frac{-\sum_{j=1}^{A} \frac{k(\alpha_j)}{A} \sum_{i=1}^{n+1} u_i^{\alpha_j}}{K_1 + b\,I_n + d}, s_{13} = \frac{-b\,(G + l\,R_n - \sum_{j=1}^{A} \frac{k(\alpha_j)}{A} \sum_{i=1}^{n+1} u_i^{\alpha_j} S_n^1)}{(K_1 + b\,I_n + d)^2},$$

$$s_{15} = \frac{l\,R_n}{K_1 + b\,I_n + d}, s_{22} = \frac{-\sum_{j=1}^{A} \frac{k(\alpha_j)}{A} \sum_{i=1}^{n+1} u_i^{\alpha_j}}{K_2 + b\,I_n + d},$$

$$s_{23} = \frac{-b\,(G + l\,R_n - \sum_{j=1}^{A} \frac{k(\alpha_j)}{A} \sum_{i=1}^{n+1} u_i^{\alpha_j} S_n^2)}{(K_2 + b\,I_n + d)^2}, s_{25} = \frac{l}{K_2 + b\,I_n + d},$$

$$s_{31} = \frac{b\,(-T_n - \sum_{j=1}^{A} \frac{k(\alpha_j)}{A} \sum_{i=1}^{n+1} u_i^{\alpha_j} I_n)}{(K_3 + \tau + d - c - b(S_n^1 + S_n^2))^2}, s_{32} = \frac{b\,(-T_n - \sum_{j=1}^{A} \frac{k(\alpha_j)}{A} \sum_{i=1}^{n+1} u_i^{\alpha_j} I_n)}{(K_3 + \tau + d - c - b(S_n^1 + S_n^2))^2},$$

$$s_{33} = \frac{-\sum_{j=1}^{A} \frac{k(\alpha_j)}{A} \sum_{i=1}^{n+1} u_i^{\alpha_j}}{K_3 + \tau + d - c - b(S_n^1 + S_n^2)}, s_{34} = \frac{-1}{K_3 + \tau + d - c - b(S_n^1 + S_n^2)},$$

$$s_{43} = \frac{\gamma I_n}{K_4 + w}, s_{44} = \frac{-\sum_{j=1}^{A} \frac{k(\alpha_j)}{A} \sum_{i=1}^{n+1} u_i^{\alpha_j}}{K_4 + w}, s_{53} = \frac{\tau}{K_5 + d + l},$$

$$s_{55} = \frac{-\sum_{j=1}^{A} \frac{k(\alpha_j)}{A} \sum_{i=1}^{n+1} u_i^{\alpha_j}}{K_5 + d + l}.$$

In order to perform a stability analysis using the Jacobian matrix and eigenvalues, it is necessary to use some criteria. The following definition is given.

Definition 4.1: According to the Matignon criterion, let J denote the Jacobian matrix obtained by the classical method, and let λ represent the set of eigenvalues of this Jacobian matrix. The equilibrium point is considered to be locally asymptotically stable if the following condition is satisfied [35]:

$$\left|arg(\lambda(J))\right| > \frac{\alpha\pi}{2}.$$

The choice of the Matignon criterion for stability analysis is particularly suitable for this model due to the inclusion of density functions in distributed order differential equations, which exhibit fractional-order behavior. This criterion effectively addresses the complexities associated with fractional derivatives, enhancing the understanding of stability.

The Matignon criterion is crucial for determining the stability of fractional differential equations. This makes it easier to see how stable solutions are over time, even while fractional derivatives don't behave like they should. On the other hand, the Matignon criterion can handle the problems that come up in fractional systems, where memory effects are quite important.

This method is very important for making sure that systems with distributed order behavior work correctly. By looking at stability areas, it helps researchers uncover important things that determine how well a system works. Employing the Matignon criterion, researchers can ascertain the long-term outcomes and the stability of various equilibrium points. This ultimately leads to enhanced strategies for disease management and treatment.

Analysis of stability for the first initial condition

According to the first initial conditions, the equilibrium points E_1 and E_2 are as follows:

$$E_1 = (0.2383316093, 0.2383316093, 0, 0, 0),$$
$$E_2 = (3.821405429, 3.821405429, -6.053820498, -1.091269786, 0.3887500955),$$

where $k(\alpha) = \Gamma(2 - \alpha)$. Substituting the first equilibrium point into the Jacobian matrix yields the following characteristic equation:

$$P(\lambda) = (0.008008005674 + \lambda)^2\,(0.0009463035997 + 0.1465278380\,\lambda + 0.2360336746\,\lambda^2 + \lambda^3)$$

After solving the characteristic equations, it is evident that

$$\lambda_1 = -0.008008005674, \lambda_2 = -0.008008005674,$$
$$\lambda_3 = -0.006463069302, \lambda_4 = -0.008570149079 + 0.3825488356i, \lambda_5 = -0.008570149079 - 0.3825488356i.$$

If the Matignon criterion is checked with the eigenvalues, the result is $|\arg(\lambda_g)| = \pi > \alpha\pi/2$, *for* $g = 1,2,3$, with the order satisfying $0 < \alpha < 2$ On the other hand, $|\arg(\lambda_4)| = |\arg(\lambda_5)| = 0.32158245\pi > \alpha\pi/2$ is satisfying $\alpha < 0.64316490$.

Our conclusion is the equilibrium point is E_1 locally asymptotically stable if the order satisfies the condition $0 < \alpha < 0.64316490$. Equilibrium point E_1 represents the disease-free equilibrium, which is significant because it indicates a state where the disease does not persist in the population. It is important to understand how stable is E_1, since it can help us figure out if therapies are working to stop the spread of the disease. If the eigenvalues meet the stability criterion for E_1, it means that the disease can be gotten rid of in some situations. So, looking at this equilibrium point not only shows how important it is to the model, but it also shows how useful it is for public health initiatives that want to manage disease.

Similarly, by substituting the second equilibrium point into the Jacobian matrix gives the characteristic equation:

$$P(\lambda)=\lambda^5 + 0.1680779743\,\lambda^4 + 37.44603747\,\lambda^3 + 1.926168284\,\lambda^2 - 0.2164013283\,\lambda - 0.002077367950$$

After solving the characteristic equations, it can be seen that

$$\lambda_1 = -0.05830984123 + 6.119020776\text{i},$$
$$\lambda_2 = -0.05830984123 - 6.119020776i,$$
$$\lambda_3 = -0.009004270986,\ \lambda_4 = -0.1025395746,$$
$$\lambda_5 = 0.06008555375.$$

If the Matignon criterion is checked on the basis of the eigenvalues obtained $|\arg(\lambda_3)| = |\arg(\lambda_4)| = \pi > \alpha\pi/2$, with the order satisfying $0 < \alpha < 2$, and $|\arg(\lambda_1)| = |\arg(\lambda_2)| = 0.3204179\ \pi > \alpha\pi/2$ is satisfying $\alpha < 6408358$. On the other hand, since it is $|\arg(\lambda_5)| = 0 < \alpha\pi/2$, it was seen that the second eigenvalue does not satisfy Matignon criterion. So, our conclusion is that E_2 is not locally asymptotically stable under these conditions.

Stability analysis for the second condition

The equilibrium point E_2 according to the second condition is

$$E_2 = (2.292233390, 2.292233390, -3.756823905, -0.1015815158, -0.3738128142)$$

The characteristic equation is obtained by substituting the second equilibrium point under the second set of conditions:

$$P(\lambda) = \lambda^5 + 0.003221828833\,\lambda^4 + 0.00005278835547\,\lambda^3 + 0.8488407333\,10^{-7}\lambda^2 + 0.4624925316\,10^{-10}\,\lambda + 0.8237844801\,10^{-14}$$

After solution of characteristic equations, it is seen that

$$\lambda_1 = -0.0007656339572 + 0.006977097614i,$$
$$\lambda_2 = -0.0007656339572 - 0.006977097614\text{i},$$
$$\lambda_3 = -0.0004046569892,\ \lambda_4 = -0.0006299162648,$$
$$\lambda_5 = -0.0006559876645.$$

Using the eigenvalues obtained to check the Matignon criterion, $|\arg(\lambda_3)| = |\arg(\lambda_4)| = |\arg(\lambda_5)| = \pi > \alpha\pi/2$, with the order satisfying $0 < \alpha < 2$. On the other hand, $|\arg(\lambda_1)| = |\arg(\lambda_2)| = 0.3291035\ \pi > \alpha\pi/2$ is satisfying $\alpha < 0.6582070$. E_2 is locally asymptotically stable if the order satisfies the condition $0 < \alpha < 0.6582070$.

An examination of the numerical simulations after the equilibrium point analysis has the following results.

Figure 1 shows that with the density function chosen according to condition 1, the results are quite consistent with the literature. At the same time, it has been observed that there is an approach to the equilibrium point with this shape. When examining the literature studies in this area, it has been shown through simulation that the equilibrium point of the ordinary order differential equation can be reached by selecting the equilibrium point [11,36].

Figure 2 examines the behaviour of susceptible and treated individuals in time-varying situations. As can be seen here, the dynamic analysis of the system can be interpreted quickly by changing the density function. In other words, the aim of the study is achieved. It can sometimes take a long time to understand the effects of external influences on infectious diseases. Writing the density function based on these external effects can minimize this effect. Looking more closely at Figure 2, the rate of increase of susceptible and treated individuals can be expressed as a function of time and external effects. In this way it has been seen that the density function can be more effective in determining the dynamics by choosing the threshold value of α.

Figure 3 shows that the system works under changing conditions and analysis can be made according to the equilibrium points. Here it is shown that changing external effects can be slower in reaching the equilibrium point. It is not necessary to set up another system of equations for this, it is shown that only the change in the equilibrium point is sufficient.

Figure 4 shows the effect of changing the density function for sensitive individuals. It has been found that the analysis is faster if the external effects are defined within the density function. As can be seen in the figure, it has been observed that the variability increases with the change. In other words, it has been shown that when the re-infection rate increases, the effect of the disease can be observed again with this system of equations.

In Figure 5, the variability between infected, treated and recovered individuals is obtained by selecting the density function. By changing the density function, for example, the number of individuals recovering over time can be determined. However, this system of equations can also be used to determine the acceleration or deceleration of the increase in newly infected individuals, as shown in the other simulation in the figure. The same dynamics can be determined for infected and treated individuals. The simulations in this section were carried out using the MATLAB package programme.

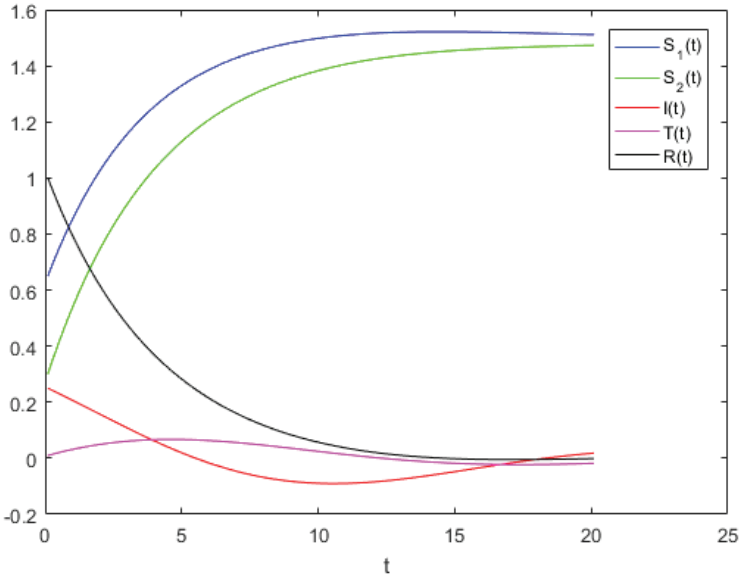


Figure 1. Time series of population variables in the SITRS model with conditions 1 for $k(\alpha) = \Gamma(\alpha - 0.5)$.

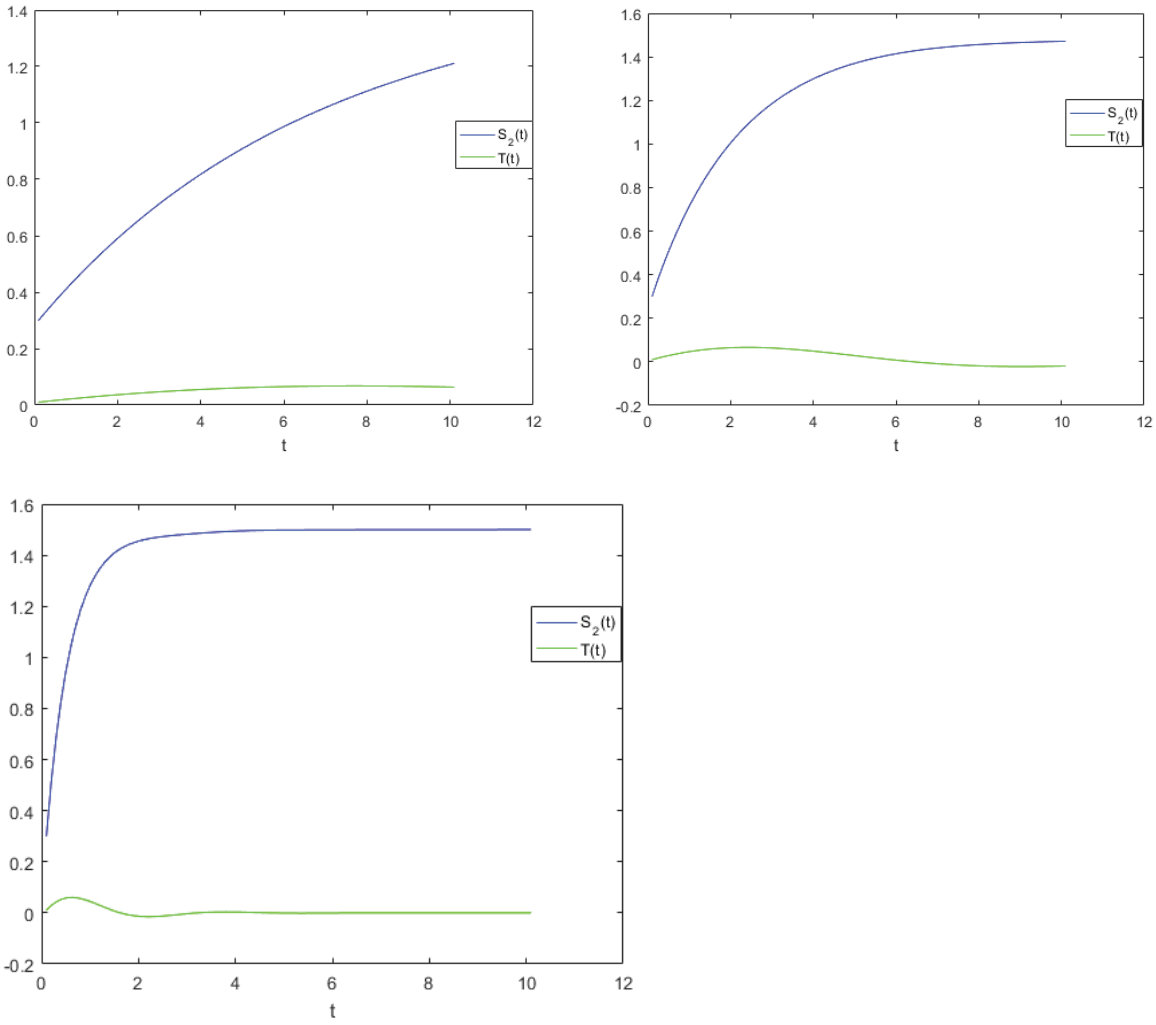


Figure 2. Estimation of Susceptible and Treatment individuals in infectious diseases using the proposed distributed SITRS model (Conditions 1 for $k_1(\alpha) = \Gamma(\alpha - 0.7)$, $k_2(\alpha) = \Gamma(\alpha + 0.7)$ and $k_3(\alpha) = \Gamma(2\alpha + 0.3)$).

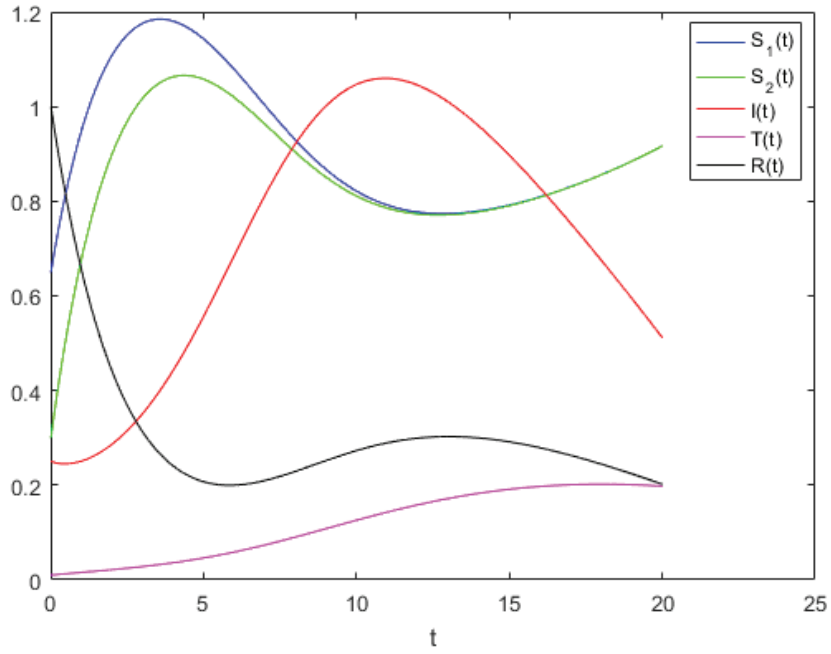


Figure 3. Time series of population variables in the SITRS model with conditions 2 for $k(\alpha) = \Gamma(\alpha - 0.1)$.

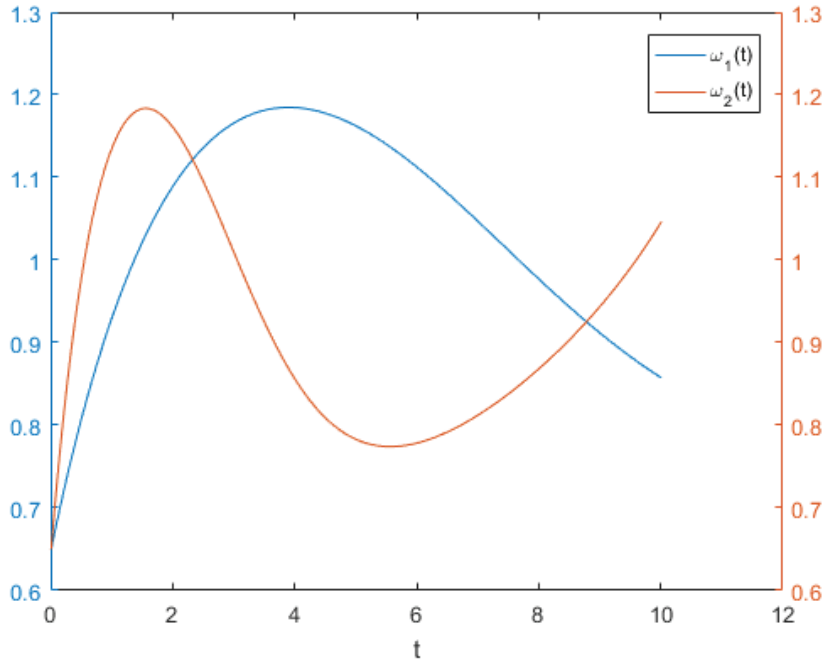


Figure 4. Prediction of behavior of susceptible individuals with varying density function [Conditions 2 for $w_1(\alpha) = \Gamma(\alpha - 0.2)$ and $w_2(\alpha) = \Gamma(\alpha - 0.8)$] .

As stated in our paper, the ability to interpret the behavior of the system largely depends on the variation in the density function. From the figures, it is clear that changes in the infection rare and recovery rates are appropriately reflected in our model equations. Moreover, the use of distributed-order modeling is precisely intended to account for such variations. In other words, changes in these factors can be accommodated through adjustments to the density function, which is dependent on the conditions. This approach allows us to select the density function based on these rates and avoid unnecessary time loss.

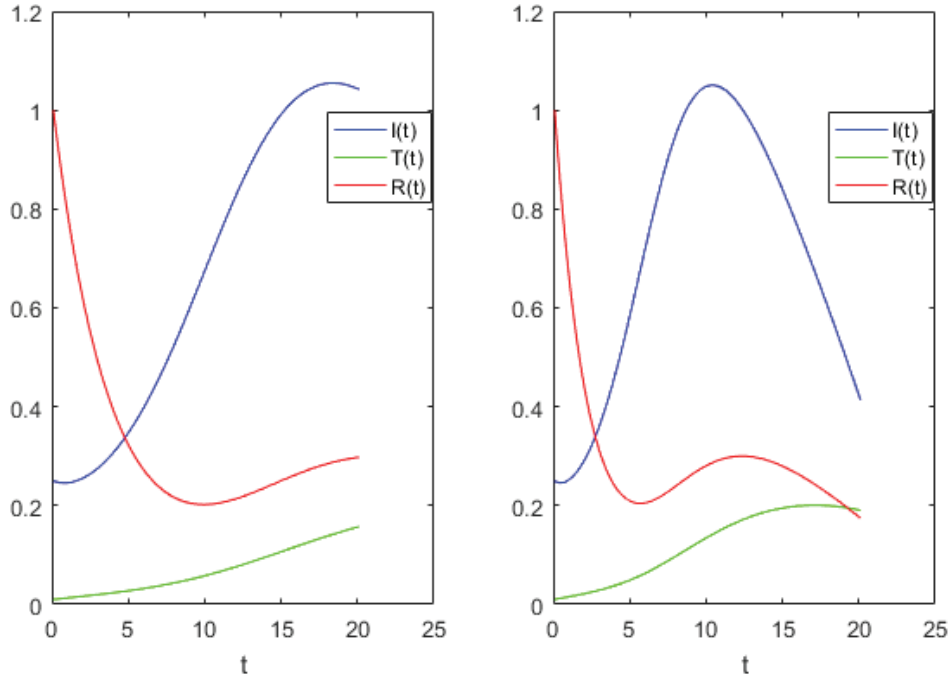


Figure 5. Numerical analysis of Infected, Treatment and Recovered individuals with conditions 2 for $k_1(\alpha) = \Gamma(\alpha - 0.5)$ and $k_2(\alpha) = \Gamma(\alpha)$.

For comparison with clinical data, the study by Elsonbaty et. al. [11] was considered. Data from this study and from COVID-NET were compared with our findings [37]. The data in question were collected in 14 US states and represent a population of approximately 32 million people living in these states. Firstly, the comparisons showed that the rate of increase of infection in the given area was similar to Figure 1. Therefore, the modified SITRS model was found to be an appropriate model. Again, when the same data were examined, it was found that the graph shown in Figure 4 best predicted the first or second wave phase of the disease. Finally, it was found that the rate of increase of infected individuals in Figure 5, expressed under the wave, was again consistent with the COVID-NET data [11,37].

CONCLUSION

In this study, the mathematical Susceptible, Infected, Treated, Recovered, Susceptible model, which is crucial for determining the dynamics of endemic models, was examined. The modified version of the model is described using distributed order differential equations. This approach allows for greater flexibility in the interpretation of different types of equation systems through the use of density functions. Equilibrium points, which are critical for the analysis of the disease, have been examined. Stability analyses of the equilibrium points were carried out and the results were found to be consistent with the data. This shows that distributed order equations are suitable for such systems. The results are compared with sources using real world data. The results are highly consistent, indicating the potential for more rapid and effective monitoring of infectious disease dynamics. Future work will focus on improving density functions and analyzing their impact across multiple scenarios, including changing population dynamics and intervention strategies. This article fills a research gap by examining the use of distributed order differential equations in public health models. It demonstrates the importance of having rapid methods for preventing and managing diseases. Our goal is to use these equations more frequently to facilitate modeling of infectious diseases and other basic science domains. This will enable us to create frameworks that are more robust and versatile.

AUTHORSHIP CONTRIBUTIONS

Authors equally contributed to this work.

DATA AVAILABILITY STATEMENT

The authors confirm that the data that supports the findings of this study are available within the article. Raw data that support the finding of this study are available from the corresponding author, upon reasonable request.

CONFLICT OF INTEREST

The author declared no potential conflicts of interest with respect to the research, authorship, and/or publication of this article.

ETHICS

There are no ethical issues with the publication of this manuscript.

STATEMENT ON THE USE OF ARTIFICIAL INTELLIGENCE

Artificial intelligence was not used in the preparation of the article.

REFERENCES

[1] Anderson RM, May RM. Infectious diseases of humans: dynamics and control. Oxford: Oxford University Press; 1991. [CrossRef]

[2] Keeling MJ, Eames KT. Networks and epidemic models. J R Soc Interface 2005;2:295–307. [CrossRef]

[3] House T, Keeling MJ. Household structure and infectious disease transmission. Epidemiol Infect 2009;137:654–661. [CrossRef]

[4] Ferguson NM, Laydon D, Nedjati-Gilani G, Imai N, Ainslie K, Baguelin M, et al. Impact of non-pharmaceutical interventions (NPIs) to reduce COVID-19 mortality and healthcare demand. Imperial College COVID-19 Response Team 2020;20:77482.

[5] Kermack WO, McKendrick AG. A contribution to the mathematical theory of epidemics. Proc R Soc Lond A 1927;115:700–721. [CrossRef]

[6] Brauer F. Mathematical epidemiology: past, present, and future. Infect Dis Model 2017;2:113–127. [CrossRef]

[7] Çilli A, Ergen K, Akat E. Some mathematical models and applications used in epidemics. Sigma J Eng Nat Sci 2019;37:17–23.

[8] Uçar Y, Yağmurlu M, Başhan A. Numerical solutions and stability analysis of modified Burgers equation via modified cubic B-spline differential quadrature methods. Sigma J Eng Nat Sci 2019;37:129–142.

[9] Karakoç SBG, Bhowmik SK, Omrani K, Sucu DY. A numerical treatment for the Gilson-Pickering equation using collocation method with error estimation. Sigma J Eng Nat Sci 2023;41:875–884. [CrossRef]

[10] Özgür B, Demir A. The stability analysis of a neural field model with small delay. Sigma J Eng Nat Sci 2024;42:900–904. [CrossRef]

[11] Elsonbaty AMR, Sabir Z, Ramaswamy R, Adel W. Dynamical analysis of a novel discrete fractional SITRS model for COVID-19. Fractals 2021;29:2140035. [CrossRef]

[12] Ayoub HH, Tomy M, Chemaitelly H, Altarawneh HN, Coyle P, Tang P, et al. Estimating protection afforded by prior infection in preventing reinfection: applying the test-negative study design. Am J Epidemiol 2024;193:883–897. [CrossRef]

[13] Shah K, Sarwar M, Abdeljawad T. A comprehensive mathematical analysis of fractal-fractional order nonlinear re-infection model. Alexandria Eng J 2024;103:353–365. [CrossRef]

[14] Schuh L, Markov PV, Veliov VM, Stilianakis NI. A mathematical model for the within-host (re) infection dynamics of SARS-CoV-2. Math Biosci 2024;371:109178. [CrossRef]

[15] Salman A, Mohd MH. Sustainable COVID-19 control measures: a mathematical modelling study. J Sustain Sci Manag 2024;19:25–35. [CrossRef]

[16] Caputo M. Mean fractional-order-derivatives differential equations and filters. Ann Univ Ferrara Sci Mat 1995;41:73–83. [CrossRef]

[17] Caputo M. Distributed order differential equations modelling dielectric induction and diffusion. Fract Calc Appl Anal 2001;4:421–442.

[18] Diethelm K, Ford NJ. Numerical analysis for distributed-order differential equations. J Comput Appl Math 2009;225:96–104. [CrossRef]

[19] Katsikadelis JT. Numerical solution of distributed order fractional differential equations. J Comput Phys 2014;259:11–22. [CrossRef]

[20] Morgado ML, Rebelo M. Numerical approximation of distributed order reaction-diffusion equations. J Comput Appl Math 2015;275:216–227. [CrossRef]

[21] Kocabıyık M, Ongun MY, Çetinkaya İT. Numerical analysis of distributed order SVIR model by nonstandard finite difference method. J BAUN Inst Sci Technol 2021;23:577–591. [CrossRef]

[22] Kocabiyik M, Ongun MY. Construction a distributed order smoking model and its nonstandard finite difference discretization. AIMS Math 2022;7:4636–4654. [CrossRef]

[23] Mickens RE. Nonstandard finite difference models of differential equations. Singapore: World Scientific; 1994. [CrossRef]

[24] Mickens RE. Nonstandard finite difference schemes for differential equations. J Differ Equ Appl 2002;8:823–847. [CrossRef]

[25] Ongun MY, Arslan D, Garrappa R. Nonstandard finite difference schemes for a fractional-order Brusselator system. Adv Differ Equ 2013;2013:1–13. [CrossRef]

[26] Çetinkaya İT, Kocabıyık M, Ongun MY. Stability analysis of discretized model of glucose–insulin homeostasis. Celal Bayar Univ J Sci 2021;17:369–377. [CrossRef]

[27] Kocabıyık M. Nonstandard discretization and stability analysis of a novel type malaria-Ross model. J Inst Sci Technol 2022;12:1023–1033. [CrossRef]

[28] Melkamu B, Mebrate B. A fractional model for the dynamics of smoking tobacco using Caputo–Fabrizio derivative. J Appl Math 2022;2022:2009910. [CrossRef]

[29] Çetinkaya İT. An application of nonstandard finite difference method to a model describing diabetes mellitus and its complications. J New Theory 2023;45:105–119. [CrossRef]

[30] Öztürk Z, Bilgil H, Sorgun S. A new application of fractional glucose-insulin model and numerical solutions. Sigma J Eng Nat Sci 2024;42:407–413. [CrossRef]

[31] Podlubny I. Fractional differential equations: an introduction to fractional derivatives, fractional differential equations, to methods of their solution and some of their applications. San Diego: Academic Press; 1999.

[32] Ding W, Patnaik S, Sidhardh S, Semperlotti F. Applications of distributed-order fractional operators: a review. Entropy 2021;23:110. [CrossRef]

[33] Liu L, Clemence DP, Mickens RE. A nonstandard finite difference scheme for contaminant transport with kinetic Langmuir sorption. Numer Methods Partial Differ Equ 2011;27:767–785. [CrossRef]

[34] Kocabiyik M, Ongun MY. Distributed order hantavirus model and its nonstandard discretizations and stability analysis. Math Methods Appl Sci 2024;1–17. [CrossRef]

[35] Matignon D. Stability results for fractional differential equations with applications to control processing. In: Computational engineering in systems applications. 1996;2:963–968.

[36] Widayati R, Muntoha RH, Ma'rifah U, Yulianti N. Analisa kestabilan bebas penyakit model SITRS pada penyebaran DIARE. Diophantine J Math Its Appl 2024;3:52–63. [CrossRef]

[37] Centers for Disease Control and Prevention. COVID-NET interactive database. Available at: https://www.cdc.gov/covid/php/covid-net/index.html Accessed on Nov 05, 2025.

Sigma Journal of Engineering and Natural Sciences
Web page info: https://sigma.yildiz.edu.tr
DOI: 10.14744/sigma.2025.00092

Research Article

Biosynthesis of silver nanoparticles using aerial parts of *Cardaria draba* L.: Phytochemical analysis, characterization, evaluation of antibacterial, cytotoxic on human colon cancer cell line properties and enzyme inhibitory potentials

Özlem BAKIR BOĞA[1,*], Esabi BAŞARAN KURBANOĞLU[1]

[1]*Department of Biology, Faculty of Science, Ataturk University, Erzurum, 25240, Türkiye*

ARTICLE INFO

Article history
Received: 20 December 2024
Revised: 21 March 2025
Accepted: 11 May 2025

Keywords:
Cardaria Draba L.; Colorectal Adenocarcinoma Cancer; Enzyme İnhibition; Green Synthesis; Silver Nanoparticles

ABSTRACT

Green nanoparticle synthesis using plant methods has garnered considerable interest from scientific groups because of its benefits, including being environmentally benign and time-efficient. *Cardaria draba* L., aqueous extract was used in this work to create silver nanoparticles in an environmentally friendly manner. SEM, EDX, XRD, UV-VIS, and FT-IR were all employed in the characterization investigations. Silver nanoparticles were measured to have a mean particle size of 41 nm. It was observed that silver nanoparticles' absorbance increased at 460 nm in the UV-Vis spectrum. Using EDX analysis, it was discovered that 78.11% of the scanned region contained Ag. GC-MS analysis revealed that the allyl isothiocyanate compound was responsible for 74.07 percent of the total weight of the plant extract. In the LC-MS/MS results of *Cardaria draba*, vitexin is the phenolic compound found in the highest amount with 8561.6281 ng/mL. Its antibacterial properties have been investigated on various microorganisms that cause infection, which suggests it may offer alternative solutions for treating infectious diseases. The MTT technique was used to assess the cytotoxic effects of silver nanoparticles on human colon cancer cell lines. In the human colon cancer cell line, studies have shown that the administration of silver nanoparticles increased cell death. It was determined that silver nanoparticles synthesized from *C.draba* have high inhibitory effects on the enzymes urease (44.64%) and collagenase (35.55%). This study did not show any LOX enzyme inhibition activity. It has been revealed that these enzyme potential are of interest as a research area in the pharmaceutical and cosmetic industries.

Cite this article as: Bakir Boğa Ö, Başaran Kurbanoğlu E. Biosynthesis of silver nanoparticles using aerial parts of *Cardaria draba* L.: Phytochemical analysis, characterization, evaluation of antibacterial, cytotoxic on human colon cancer cell line properties and enzyme inhibitory potentials. Sigma J Eng Nat Sci 2025;43(6):1943–1956.

***Corresponding author.**
*E-mail address: ozlembakir@atauni.edu.tr

This paper was recommended for publication in revised form by Editor-in-Chief Ahmet Selim Dalkilic

Published by Yıldız Technical University Press, İstanbul, Turkey
© Author. This is an open access article under the CC BY-NC license (http://creativecommons.org/licenses/by-nc/4.0/).

INTRODUCTION

The field of nanotechnology is the most dynamic research area in material sciences, and the synthesis of nanoparticles is increasing significantly worldwide. Nanotechnology is a field in which nanomaterials are produced using particles in the <100 nm size range . As a result of the research and discoveries, AgNPs (silver nanoparticles) have garnered interest due to their chemical, physical, and biological properties and their widespread use in both industrial and health fields [1]. In addition, the synthesis of metal nanoparticles, such as AgNPs, which exhibit antioxidant and antimicrobial activities has gained importance in biochemical applications [2]. Recently, many studies have proven that plants can act as effective precursors for metal nanoparticle synthesis. These studies have enabled people to realize new production models in an environmentally friendly way despite the pollution they experience in modern times [3]. The green synthesis method has become quite popular in recent years [4]. In the green synthesis method, biological resources such as plants, bacteria, fungi, and algae, among others, are used as reducing agents to form nanoparticles. Thus, high costs and waste generation are prevented by using materials that are suitable for large-scale commercial production, non-toxic, highly stable, environmentally friendly, and inexpensive. Since the plants involved in green synthesis form compounds containing functional groups such as phenolics and flavonoids, the nanoparticles formed by the reduction of these compounds have antioxidant, antibacterial and catalytic properties [5]. Thus, metal oxide nanoparticles produced via green synthesis are applied in many areas such as the enzyme industry, drug delivery systems, and biomedical and pharmaceutical applications [6, 7, 8].

Cardaria draba (Brassicaceae), known as watercress, is an annual herbaceous plant. Animal feed and treatment: the aboveground parts are fed to animals. The leaves are crushed and applied externally to wounds on the heads of animals infected with anthrax; these leaves are changed several times a day, and it is said that this method heals the wound. The aboveground parts are used as food [9, 10, 11], animal feed [12], a pain reliever [11], a sedative, a wound healer [13], a diuretic, and to remove kidney stones [14]. Although *C. draba* prefers alkaline conditions, it can be found in different soil types with adequate moisture, growing in a wide variety of habitats such as shady open spaces, meadows, fields, croplands, grasslands, and roadsides [15]. *C. draba* has been used against various ailments in the past [16]. The aerial parts of *C. draba* contain alkaloids, saponins, flavonoids, terpenoids, tannins, triterpenoids, and leukoanthocyanins. The essential oil contains o-xylene, p-xylene, nonane, styrene, hexane-3,3,4-trimethyl, octane-2,6-dimethyl, heptane, 3-methyl-2-ethyl, decane, and nonan-4-methyl; it is also registered to have nonane-2-methyl, benzene-1-ethyl-2-methyl, cyclohexene-2-methylpropyl, mesitylene, dodecane, limonene, benzenacetaldehyde, tetradecane, and 5-(methylthio)-pentane compounds. While Kaempferol, quercetin and isorhamnetin are the most abundant compounds in the ethanolic extract of the leaves, the most abundant compounds in the ethanolic extract of the seeds are ellagic acid, sinapic acid, p-coumaric acid and caffeic acid [17, 18]. it is also used against kidney stones due to its expectorant and diuretic effects. *C. draba* seeds and leaves have expectorant and laxative effects [19]. It has been used as a carminative and has antiscorbutic activity [20]. In the past, *C. draba,* as one of the existing traditional medicines, has been used against a wide variety of ailments. For example, it has been used in anti-inflammatory, anticancer, antimicrobial, antioxidant, hypoglycemic, and other areas.

The selection of *C. draba* was made for a number of reasons. The antibacterial properties of medicinal plants are one of their beneficial aspects, and examining these properties is crucial for understanding their potential applications. Many bacteria have developed resistance to antibiotics as a result of the increased usage of antibiotics. Therefore, the search for novel sources of antibacterials is crucial. Using medicinal herbs is a top priority for this reason. Furthermore, compared to medicines, their potent antibacterial chemicals provide less risk to the user. Medicinal herbs have long been regarded as chemical alternatives because of their affordability, ease of use, low toxicity, and fewer adverse effects. Medicinal plants have made many contributions to the literature in the search for antibacterial sources and in the field of nanotechnology. Silver nanoparticles made with *C.origanifolium* extract were found to have antimicrobial properties that were superior to those of synthetic antimicrobial medications by inhibiting the growth of *Pseudomonas aeruginosa* bacteria, and *Candida albicans* pathogenic fungus [21]. Silver nanoparticles (AgNP) synthesized using extract of *Amygdalus spinosissima* were studied for their antibacterial, antioxidant, anticancer, and apoptotic properties. It was shown that AgNPs exhibited strong antibacterial activity against Gram-negative bacteria [22]. *Cardaria draba (L.)* was collected in July 2023 at approximately 2000 meters altitude and 39°54′0″N 41°15′0″E coordinates in Erzurum (Turkey), and silver nanoparticles were obtained from the aboveground parts. In our study, AgNPs were synthesized biologically using the aboveground parts of the *C. draba* plant. Characterization was performed with UV-Vis, XRD, FT-IR and SEM analyses. In addition to examining the antibacterial activities of AgNPs, enzyme inhibition on some enzymes of medical importance was examined. The cytotoxicity of the human colon cancer cell line (DLD-1) was investigated.

MATERIALS AND METHODS

Preparation of *Cardaria draba* L. Extract and Synthesis of Silver Nanoparticles

The aboveground parts of the plant were collected, washed thoroughly with pure water twice, dried, and ground thoroughly in a porcelain mortar. Thirty grams

of ground plant parts were mixed in 100 mL of deionized water, with a magnetic stirrer for 30 minutes. Then, it was heated in a water bath at 60°C for 10 minutes. After cooling to room temperature, it was centrifuged at 3500 rpm for 10 minutes and filtered through filter paper to obtain the plant extract [23]. Synthesis of silver nanoparticles was carried out similarly to the working procedures of Manosalva et al (2019) [24]. To obtain silver nanoparticles, 20 mL of plant extract was added dropwise to 100 mL of 1 mmol (0.170 g) AgNO3 solution using a dropping funnel. The reaction continued for 2 hours at 50°C in a magnetic stirrer. The light yellow plant extract turned brown with the addition of silver nitrate solution. This brown colloidal solution was centrifuged at 10,000 rpm for 15 minutes to precipitate AgNPs. The AgNPs precipitated by centrifugation were washed several times with deionized water and then dried.

Characterization of Silver Nanoparticles

Ultra violet (UV-VIS) spectral analysis

Whether pure Ag+ ions were reduced was determined by UV-Vis spectral analysis. UV-vis spectra of biosynthesized AgNPs were determined in the wavelength range of 300-700 nm using a spectrophotometer (Agilent CARY 60 UV-visible spectrophotometer).

Scanning electron microscopy (SEM) analysis

It was characterized by scanning electron microscopy (SEM) (Tescan Maıa3 XMU) to determine morphology and the particle size.

X-ray diffraction (X-RD) analysis

The morphology of the crystal structure of AgNPs was analyzed by XRD (RIGAKU ULTIMA IV XRD) in the range of 3° to 79° for 2θ. The crystal size of AgNPs was calculated by using the Debye-Scherrer equation ($D=K\lambda/\beta \cos\theta$).

Fourier transform infra red spectroscopy (FT-IR) analysis

FT-IR (Perkin Elmer Spectrum 100 FTIR) spectroscopy analysis was performed to determine the functional groups present in the plant extract, as well as those playing a role in the reduction, in the range of 4000-400 cm-1 at the end of the reaction.

GC/MS (Gas chromotography/mass spectrometry) analysis

GC/MS analysis was performed according to Basar et al. (2024) [25].

Phenolic Component Analysis OF *C. draba* Extract by LC-MS/MS Method

LC-MS/MS analysis of the phenolic compound was performed using an Agilent 6460 Triple Quadrupole model (Agilent Technologies, Wilmington, DE, USA). The column temperature was fixed at 40 °C. The elution gradient was formed from mobile phase A (water, 0.1% Formic acid) and mobile phase B (acetonitrile with 0.1% formic acid). The mobile phase gradient was programmed as follows: 98% A (v/v) from 0 to 4.0 min, 98–80% A (v/v) from 4.0–7.0 min, 80–10% A (v/v) from 7.0–14.0 min, 10% A (v/v) from 14.0–15.0 min, 10–98% A (v/v) from 15.0–17.0 min. The total run time was 17 min, and the column equilibration time between each run was 4 min [26].

Antibacterial Activity

Antibacterial activity was determined by working on Gram negative (*Escherichia coli* ATCC 25922, *P. aeruginosa* ATCC 27853, *A. baumannii* ATCC 17978) and Gram positive (*Bacillus cereus* DSSM 4312, *S. aureus* ATCC 25923, *E. faecalis* ATCC 29212) bacteria. The disk diffusion method was used to determine antibacterial activity (NCCLS 1997). Nutrient broth liquid medium, which was inoculated with each microorganism using loop inoculation, was incubated for 12-16 hours at 37 °C. 100 µl sample of the test microorganisms, prepared from an overnight culture, was taken and spread on nutrient agar solid medium. Then, 10 µl of different concentrations of all extracts were taken and absorbed onto sterile paper disks, which were placed in petri dishes, and the spread was made. Inhibition zone diameters were measured after 24 hours, of incubation at 37 °C for bacteria. The same procedure was repeated for positive (Chloramphenicol) and negative controls (ethanol and water). Each test was performed in three replicates at different times [27].

Enzyme Inhibition

Antiurease and anticollagenase enzyme inhibition were performed according to Bakır and Kurbanoglu (2022) [28]. Lipoxygenase (LOX) enzyme inhibition was performed according to Bakır et al. (2022) [29].

RESULTS AND DISCUSSION

SEM Analysis

Figure 1 illustrates the scanning electron microscopy (SEM) images of silver nanoparticles (AgNPs) produced via the green synthesis process using *C. draba*. It is evident from the SEM images that the particles exhibit a range of sizes. Silver nanoparticles were discovered to have spherical shapes with an average diameter of 41 nm. From the SEM images, it can be observed that the silver nanoparticles are larger than expected as a result of a series of reactions triggered by the evaporation of the solvent due to the aggregation of the nanoparticles during sample preparation. This may have caused the differences in particle size [30]. The size of the particles was found to be 30-70 nm in the SEM study of AgNPs generated from *Vitis vinifera* (grape) fruit [31]. According to studies by Shah et al. (2018) on *Daphne mucronata* and Santhoshkumar et al. (2017) on *Gnidia glauca*, a species in the Thymelaeaceae family, silver nanoparticles have a spherical shape [32, 33]. The size and surface charge of the synthesized particles have an important effect on the interaction with the cells. Accordingly, when establishing the optimal conditions, the criteria exhibiting the smallest values for these parameters in the synthesized nanoparticles were selected.

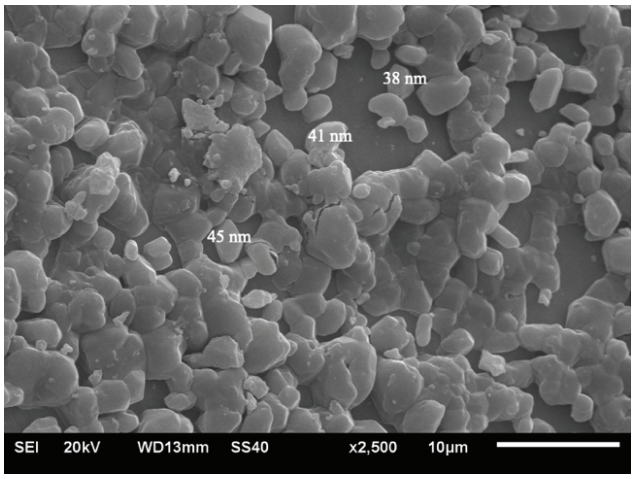
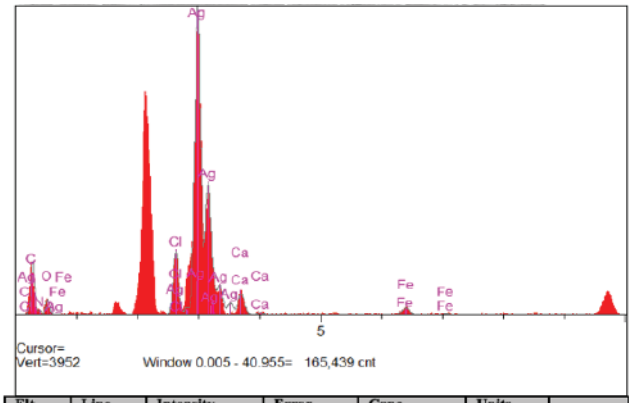


Figure 1. Images of SEM analyze of synthesized silver nanoparticles.



Elt.	Line	Intensity (c/s)	Error 2-sig	Conc	Units	
C	Ka	138.68	4.299	8.800	wt.%	
N	Ka	10.83	1.853	4.901	wt.%	
O	Ka	38.24	2.899	1.737	wt.%	
Cl	Ka	163.52	5.938	3.053	wt.%	
Ca	Ka	71.72	4.579	2.008	wt.%	
Fe	Ka	34.75	3.456	1.381	wt.%	
Ag	La	1,123.31	11.466	78.119	wt.%	
				100.000	wt.%	Total

Figure 2. EDX result of nanoparticles.

EDX Analysis

As illustrated in Figure 2, the elemental composition of the AgNPs produced at room temperature was determined to be 78.11 % Ag, 8.8 % C, 4.9 % N, 3.05 % Cl, 2.00 % Ca and 1.38 % Fe . The strong peaks of the formed AgNPs in an optical absorption band at 3 eV indicate the presence of silver within the particles. It indicates that AgNPs are dense. At the same time, it was determined that some elements other than silver also formed weak peaks. In another study, it was reported that nanoparticles obtained from *Salvia officinalis* (Sage) plant contained 60.97% silver [34]. AgNPs synthesized from *Murraya koenigii* (Curry) plant were found as 60% Ag, 19% C, 12% O, and 6% Cl [35]. Also, the EDX spectrum shows the presence of Cl, N, O, K, and C atoms in different percentages. Weak signals such as chlorine, carbon, and oxygen in the EDX profile are caused by phytochemicals found on the surface of the nanoparticles. Bacteria have the genetic ability to transmit and acquire drug resistance to therapeutic drugs. Resistant bacteria pose a challenge in the treatment of various well-known infections and require new substances with antimicrobial properties. The composition of the remaining substances in EDX and their effects on antimicrobial purposes may have implications.

FT-IR Analysis

FT-IR analyses show that AgNPs are surrounded by biomolecules, reducing the potential for metal nanoparticles to come together and form clusters, and increasing their stability in the solution environment. The peaks in the FT-IR spectrum of *C. draba* plant extract indicate the presence of 3675.83 -OH and -NH (polyphenols and amine) groups. The peaks at 2988.26 and 2901.60 cm^{-1} indicate the presence of –CH and -CH2 aliphatic groups, and the peaks at 1056.84 and 1028.01 cm^{-1} indicate the presence of -C-O groups, namely terpenoids, flavones, and carbohydrate structures (Fig. 3). It has been reported that FT-IR peaks in plant extract support the presence of antioxidant flavonoids and phenolic acids, and the presence of phenolics in the extract may be responsible for the reduction of metal ions and the formation of nanocomposites [36]. It was observed that AgNPs showed absorption peaks at 3675.72, 2988.77, 1513.93, 1393.93, 1230.26, 1141.96, 1066.27 cm^{-1} (Fig. 3). The first peak is seen as a band around 3675 cm^{-1}. The peak observed in this region generally represents -OH (hydroxyl) groups. It shows that the AgNPs sample contains various organic functional groups and compounds. The presence of hydroxyl (-OH) and carbonyl (C=O) groups, in particular, suggests that there are water molecules, alcohol, a phenol, or aldehyde, or ketone, or other related compounds on the surface of the sample. The peak located around 1513 cm^{-1} represents the stretching vibrations of carbonyl (C=O) and C=C double-bonded groups. Carbonyl groups can be found in aldehyde, ketone, or amide groups and the peak in this wavenumber region suggests the presence of such functional groups in the sample [37]. A comparison of the extract and nanoparticle peaks in FTIR analysis, conducted using Cornelian cherry fruit for the synthesis of AgNP, revealed that the 3159 cm-1 O-H, 1717 cm-1 C=O, 1224 cm-1 C-OO groups were the primary contributors to Ag reduction [37]. According to the FTIR analysis results, the -OH group at 3332 cm-1, the -C≡N group at 2145 cm-1, and the -C=O group at 1635 cm-1 participate in the synthesis process of nanoparticles [38]. FT-IR analysis shows that AgNPs have a complex chemical structure; organic and inorganic components are present on their surface. May have a suitable profile for use in potential biomedical and chemical applications.

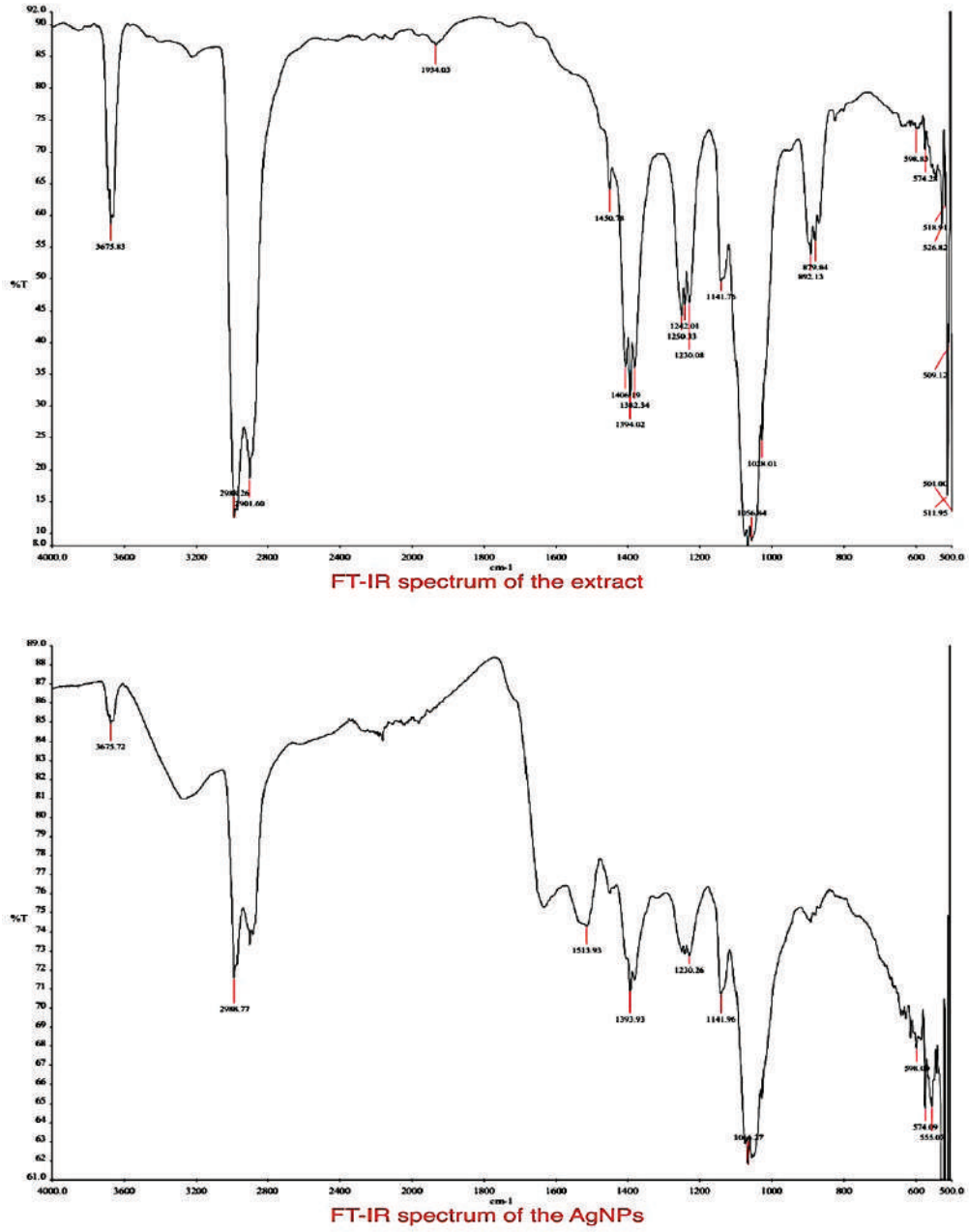


Figure 3. FT-IR result of extract and AgNPs.

XRD Analysis

Peaks from the (111), (200), (220), and (311) crystal structures were seen as a result of the resulting difraction patterns. These peaks corresponded to the angle values of 2θ=38.38°, 44.61°, 64.97°, and 78.09°, for metallic silver (JCPDS 04-0783) (Fig. 4). These findings led to the understanding that, in this context, a face-centered cubic structure contained metallic silver. Furthermore, the metals from the factory were identified as contaminants based on the difraction patterns. Using the Scherrer equation and the XRD data, the particle sizes of AgNPs were determined in this section of the study. The particle size of AgNP is 18.51 nm according to the Debye-Scherrer equation. According to Agarwal et al. (2018), who synthesized AgNPs from *Cymbopogon citratus*, the aforementioned peaks correspond to those of silver [39]. It was found that in *Nigellla sativa* plant, there were diffraction bands of (111), (200), (220) and (311) with 2Θ values around 38.35º, 44.50º, 64.76º and 77.80º [40]. The sharpness of the peaks reveals that the synthesized nanoparticles have a high crystalline structure. In addition, the absence of peaks belonging to any other phase in the graph supports the high purity of the synthesized nanoparticles.

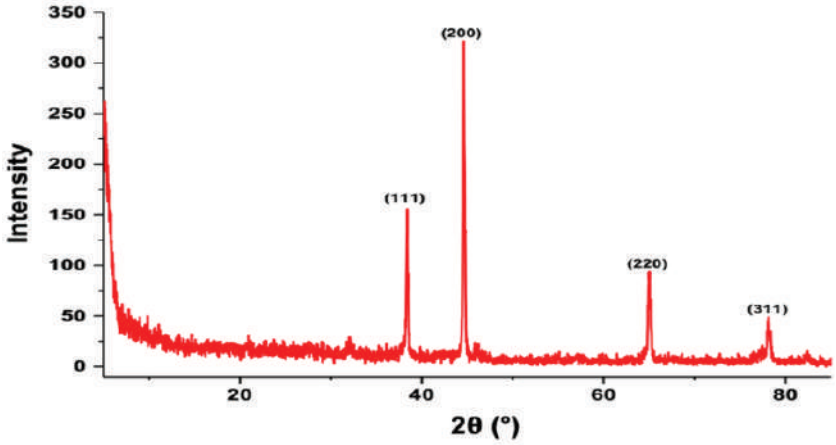


Figure 4. XRD result of nanoparticles.

UV-Visible Spectral Analysis

UV-Vis spectra of AgNPs synthesized from *C. draba* plants were taken. As seen in Figure 5, absorbance values are in the range of 400 to 500 nm. According to previous studies, the absorbance ranges of AgNPs generally occur at 400-500 nm. It has been reported that the transformation from a light yellow to brown colloidal solution during the reaction allows the qualitative detection of AgNPs. The color change is due to the plasmon resonances (SPR) on their surfaces and indicates an increase in the concentration of AgNPs over time. When literature findings are evaluated, they show that the synthesis was carried out successfully in the research.

This analysis confirmed the literature indicating that silver nanoparticles typically exhibit maximum absorption values at approximately 400 nm wavelength. AgNPs were synthesized with extracts obtained from *Rubus ellipticus*, and it was determined that the maximum absorbance value was obtained around 430 nm [41]. AgNPs were synthesized using *Punica granatum* extract. The maximum UV-vis absorbance value of the plant extract was determined to be 367 nm. The maximum UV-vis absorbance value of AgNPs was determined as 462 nm [42]. The greatest absorbance peak was observed in the range of 420–450 nm when AgNPs were produced from the *Salvia limbata* (sage) plant [43]. This finding substantiates the hypothesis that when exposed to the bioactive elements of the plant extract, the silver ion undergoes a transformation into silver nanoparticles [44].

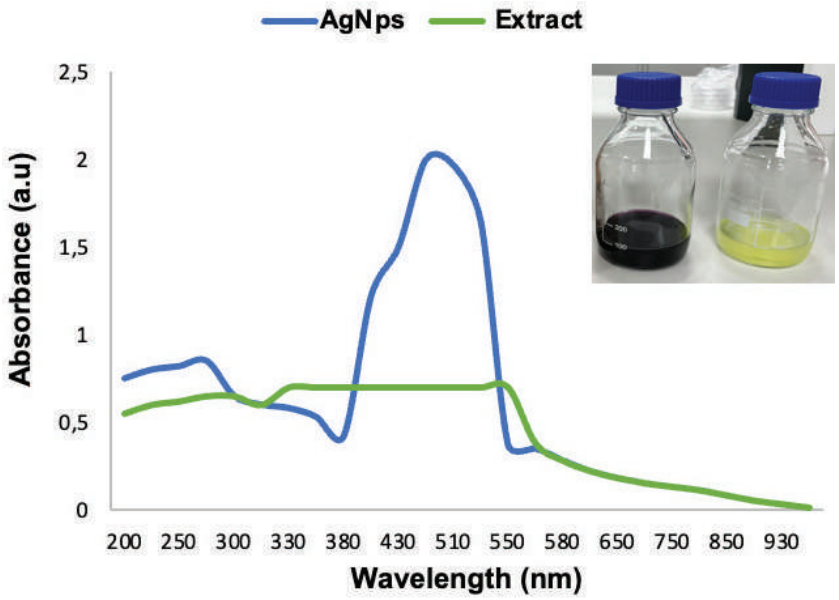


Figure 5. UV-Vis result of AgNPs and extract.

Gas Chromatography–Mass Spectrometry (GC/MS) Results

Gas chromatography-mass spectrometry (GC-MS) was used to analyze the essential oils obtained from the aerial part of the *C. draba* plant. The analysis revealed that the allyl isothiocyanate compound was responsible for 74.07 percent of the total weight of the plant extract. After the allyl isothiocyanate compound, thiocyanic acid, 2-propenyl ester compound, comprising 8.45 percent of the weight, constituted a significant part of the plant extract . Other components in the extract were less than 2 percent of the total extract weight (Table 1). Chemical analysis of *C. draba* flower, leaf, stem, and root sections gathered from Iran revealed that 6-10, 14-Trimethyl-2-pentadecanone (16.4%) and 3-butenyl isothiocyanate (26.4%) were the most prevalent components [45]. Chemical analysis of *C. draba* aerial organs and leaves obtained from France revealed that 6,10,14-trimethyl-2-pentadecanone (20.61%) and (E)-phytol (11.38%) were the most significant components [46]. *C. draba* roots, stems, leaves, flowers, and fruits gathered from Tunisia were examined for their primary fragrance volatiles, which included hexadecanoic acid (34.6%), 6-methyl-5-hepten-2-one (18.3%), decanal (15.0%), 6,10,14-trimethyl-2-pentadecanone (13.2%), and n-pentacosane (13%) [47].

Liquid Chromatography–Mass Spectrometry (LC-MS/MS) Results

In the LC-MS/MS results of the *C. draba*, Vitexin compound is the phenolic compound found in the highest amount with 8561.6281 ng/mL. Luteolin is the second most abundant phenolic compound after Vitexin. Rosmarinic acid, which has a large amount of reactive functional groups, was found at a concentration of 1.0837 ng/mL. Further data on other reactive phenolic compounds can be reviewed in Table 2. Since the focus was on the most abundant compounds in the plant extract, seven compounds are included in Table 2.

Antibacterial Activity

In the study, the paper disc method was used to examine the antibacterial activity of *Cardaria draba* extract and AgNPs biologically generated from *Cardaria draba* extract. The antibacterial impact of the extract on both Gram-positive and Gram-negative bacteria, including *B. subtilis, S. aureus*, and *E. faecalis was investigated* The antimicrobial activity tests yielded an inhibitory zone of 18–30 mm generated by chloramphenicol antibiotic discs in Petri dishes, which served as positive controls. The aqueous extract of *Cardaria draba* demonstrated a significant bactericidal effect on both Gram-negative and Gram-positive bacteria, with zones of inhibition ranging from 6 mm to 9 mm. The most effective antibacterial dose against *P. aeruginosa* was 9 (Fig. 6). For *S. aureus* ATCC 25923 and *E. faecalis* ATCC 29212, AgNPs showed an inhibitory zone for the bacteria *E. coli* ATCC 25922, *P. aeruginosa* ATCC 27853, *B. subtilis* DSMZ 1971, and *S. enteritidis* ATCC 13075 (Table 3).

When the antibacterial activity of silver nanoparticles synthesized from *Trema orientalis* (L.) was examined, it was found that silver nanoparticles formed a 9 mm zone at a concentration of 25 μg/mL, for *S. aureus* [48]. The antibacterial activity of silver nanoparticles synthesized using Ferula gummosa essential oil against Gram-positive and Gram-negative bacteria was shown with inhibition zones of 10 mm and 8 mm in diameter for *E. coli* and *S. aureus*, respectively [49]. In the antibacterial activity of silver nanoparticles made from *Mirabilis jalapa* leaf extract, *Staphylococcus aureus* showed a 10 ± 1.58 mm inhibition zone, *Pseudomonas aeruginosa* showed a 6 ± 1.15 mm inhibition zone, and Staphylococcus aureus AgNPs showed a 10 ± 1.58 mm inhibition zone [50]. Inhibition was observed in

Table 1. Biologically active chemical compounds of *Cardaria draba* aqueous extract

Name of compounds (molecular formula)	Retention time, min	%
Allyl Isothiocyanate	13.999	74.07
Thiocyanic acid, 2-propenyl ester	16.915	8.45
Silane, ethenylethoxydimethyl-	35.281	2.77
Benzaldehyde (CAS)	19.049	1.45
Isobutyl isothiocyanate	12.498	1.33
Alpha-Terpineol	24.519	1.20
Ethanone, 1-(1,3a,4,5,6,7-hexahydro-4-hydroxy-3,8-dimethyl-5-azulenyl)-	32.412	0.66
Cyclobutanol (CAS)	0.019	0.59
Propanoic acid, 2-methyl-, 3-hydroxy-2,4,4-trimethylpentyl ester	29.104	0.54
Benzeneethanol (CAS)	30.157	0.49
2,2,4-Trimethyl-1,3-pentanediol diisobutyrate	29.413	0.47
Cycloheptasiloxane, tetradecamethyl-	19.569	0.45
trans-.beta.-Ionone	30.768	0.43

Table 2. Most abundant phenolic compounds in quantitative analysis results

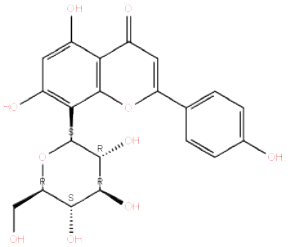
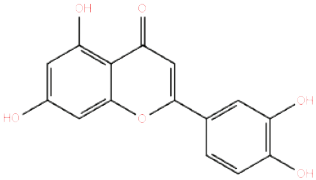
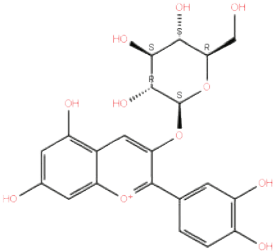
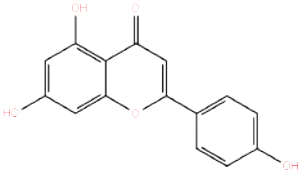
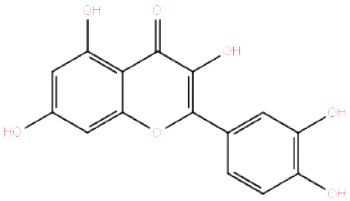
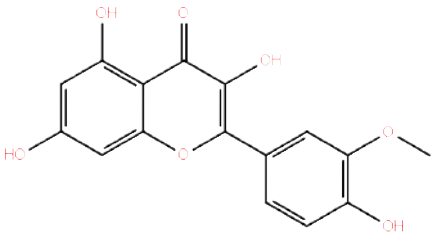
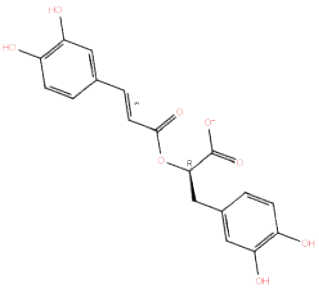
Molecule name	Structure	Final cons. (ng/mL)
Vitexin		8561.6281
Luteolin		569.0751
Cyanidin-3-o-glucoside		446.8699
Apigenin		108.6049
Quercetin		60.4772
Isorhamnetin		58.1453
Rosmarinic Acid		1.0837

Table 3. Zone diameters (in mm) and mean ± SE values of AgNPs' effects against bacterial strains, as determined by the disk diffusion method, are given in the table

Bacterial isolates	AgNPs (mm)	Chloramphenicol
B. cereus (ATCC 11778)	6.6±1.23	17 mm
S. aureus (ATCC 25923)	8.3±0.3	18 mm
E. faecalis (ATCC 29212)	5±0.5	17 mm
P. aeruginosa (ATCC 27853)	6.8±0.0	18 mm
E. coli (ATCC 25922)	7±0.0	17 mm
A. baumannii (ATCC 17978)	5.6±0.3	18 mm

the antibacterial effect of silver nanoparticles formed with the aqueous extract of *Aquilegia pubiflora* against *E. coli* (10.9 ± 0.29), *B. subtilis* (10.2 ± 0.31), *Klebsiella pneumoniae* (9.8 ± 0.33), *S. epidermidis* (9.3 ± 0.37), and *P. aeruginosa* (9.1 ± 0.34) [51]. The antibacterial impact of *C. draba* may be linked to the presence of phenolic chemicals, which have demonstrated antimicrobial action. The antibacterial activity of Brassicaceae members against clinical bacterial isolates was examined by Panghal [52]. The generally higher antibacterial activity of AgNPs may be due to the large surface area of nanoparticles, which provides better contact with microorganisms. According to the literature, the precise mechanism of AgNPs remains unclear. AgNPs have antibacterial properties because they create pits in bacterial cell walls [53].

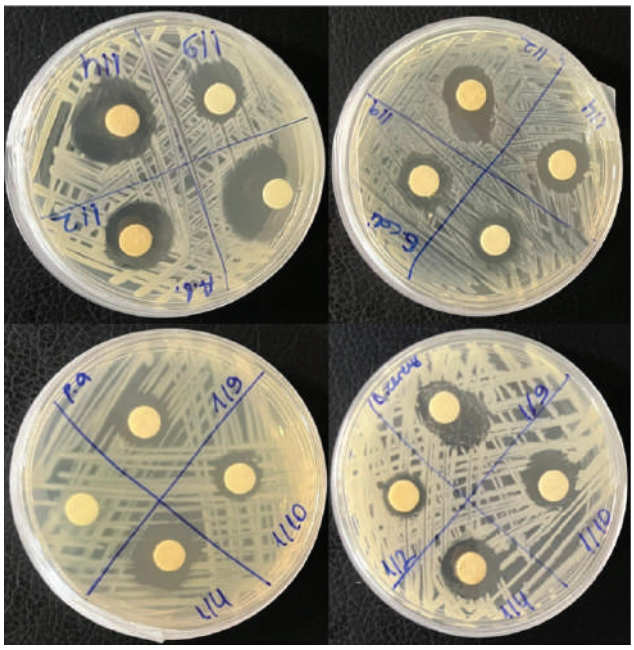


Figure 6. a) Zone diameters of AgNPs against Gram-negative bacteria, b) Zone diameters of AgNPs against Gram-positive bacteria.

Enzyme Inhibition

To observe the inhibitory effects of *C.draba* extract and AgNPs synthesized from it, tests were performed on three different enzymes: urease, collagenase, and lipoxygenase. Percentage inhibition and IC_{50} values were determined.

Effect on Urease

The urease inhibition test demonstrated significant inhibitory effects of *C. draba* extract and AgNPs. C. draba extract showed 34.44% (IC_{50}: 2.60± 1.32 µg/mL) inhibition at 2 µg/mL concentration. AgNPs showed 44.64% (IC_{50}: 2.23± 1.65 µg/mL) inhibition at the same concentration. AgNPs produced with *C. draba* extract showed strong inhibitory activity against urease. Thiourea, when used as a positive control, showed strong inhibition of 57.77% (Table 4). Ovais et al. evaluated the capacity of the green synthesis of AgNPs to inhibit urease enzyme activity using *Olax nana* Wall. ex *Benth.* AgNPs showed significant inhibitory activity with a urease inhibition of 39.23 ± 0.42% at a concentration of 0.2 mg/mL [54]. In the study conducted by Kaya et al., when *Thymbra spicata* L subsp. *spicata* L was tested at a concentration of 100 µg/mL, urease enzyme inhibition was observed, reducing its activity by 34.62±2.33%, [55]. AgNPs and AuNPs were synthesized with *Crataegus oxyacantha* extract. Among the synthesized nanoparticles, AgNPs showed inhibitory activity with an IC_{50} value of 1.38 ± 0.3 µM. The –NH, –OH, and C=O groups of the stabilizing phytochemicals, which interact with Ni in the urease enzyme, may be the cause of the notable urease inhibitory actions of NPs [56].

Effect on Collagenase

Collagenase inhibition test showed significant inhibitory effects of *C. draba* extract and AgNPs. *C. draba* extract showed 12.59% inhibition at a 2 µg/mL concentration. AgNPs showed 35.55% inhibition at the same concentration. AgNPs produced with *C. draba* extract showed strong inhibitory activity against collagenase. EGCG (Epigallocatechin gallate), used as a positive control, showed 48.14% inhibition (Table 4). In the study by Kaya et al., *Thymbra spicata* L. subsp. *spicata* L. was determined to exhibit a low collagenase enzyme inhibitory activity (10.57±0.30%) [57]. Radwan et al.[58] stated that

the nanoparticles they obtained inhibited the collagenase enzyme by an average of 75%. AgNPs obtained from *F. vesiculosus* have been shown to have stronger anti-collagenase activity than *F. vesiculosus* extract. Terpenoids and flavonoids, two naturally occurring antioxidants, work in concert to block the collagenase enzyme [59]. It may be claimed that various plant extracts are the source of bioactive compounds that can block the activity of the same enzymes, which is consistent with the findings of Andrade et al. (2021) [60] and Gomes et al. (2022) [61].

Effect on Lipoxygenase (LOX)

The lipoxygenase inhibition test showed significant inhibitory effects of *C. draba* extract and AgNPs. *C . draba* extract showed 27.40% inhibition at 2 µg/mL concentration. AgNPs showed 38.88% inhibition at the same concentration. AgNPs produced with *C .draba* extract showed strong inhibitory activity against lipoxygenase. Nordihydroguaiaretic acid (NDGA), used as a positive control, showed strong inhibition of 54.44% (Table 4). This study did not show any LOX enzyme inhibition activity. This study highlights the possible variation in enzyme inhibitory activity based on elements including the plant's particular composition, the plant material's place of origin, and the experimental setup.

Cytotoxicity Analysis

The cytotoxicity of AgNPs was investigated. Figure 7 illustrates the cell viability rates for the DLD-1 colorectal adenocarcinoma cell line when AgNPs was administered at varying concentrations (2500, 1250, 625, and 312.5 ppm). The lowest concentration of AgNPs applied in the study, when compared to the control group, was 312.5 ppm. The remaining applied concentrations were observed to exert a diminished cytotoxic effect. The lowest concentration in the AgNPs, that was found to be less cytotoxic than the control group, was determined to be 312.5 ppm. Furthermore, concentrations of 625 and 1250 ppm were demonstrated to be less cytotoxic than the specified threshold value. The human body's digestive system is capable of transporting nanoparticles into the bloodstream, where they can subsequently be delivered the liver, brain, and other organs. Nanoparticles have the potential to deliver therapeutic medications to the brain and other organs [62]. The decrease

Table 4. Enzyme inhibitory activity of extracts and AgNPs from *C. draba*

Enzyme	Tested samples	Concentrations	% inhibition	IC50
Urease	*C. draba*	2 µg/mL	34.44	2.60± 1.32 µg/mL
	AgNPs	2 µg/mL	44.64	2.23± 1.65 µg/mL
	Thiourea	2 µM	57.77	21.98 ± 1.01 µM
Collagenase	*C. draba*	2 µg/mL	12.59	2.14 ± 1.09 µM
	AgNPs	2 µg/mL	35.55	2.29 0.88 µg/mL
	EGCG (Epigallocatechin gallate)	2 µM	48.14	13.76± 0.64 µg/mL
Lipoxygenase (LOX)	*C. draba*	2 µg/mL	27.40	2.1 ± 0.88 µg/mL
	AgNPs	2 µg/mL	38.88	4.66 ± 0.00 µg/mL
	Nordihydroguaiaretic acid (NDGA)	2 µM	54.44	1.55 ± 0.64 µM

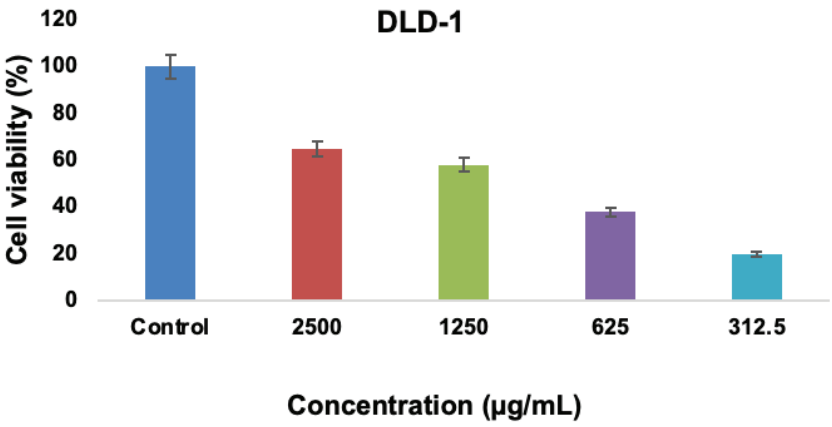


Figure 7. The effect of AgNPs on colorectal adenocarcinoma cell line DLD-1.

in cell viability rate compared to the administered dose indicates that AgNPs exert a cytotoxic effect on the DLD-1 cell line. Sivri et al. (2023) investigated the effects of ZnO nanoparticles using *Laurus nobilis* leaf extract in DLD-1 and L929 cell lines. They found that the nanoparticles were only effective in the DLD-1 cell line and stated that they have the potential to be used in biomedical applications due to their antibacterial and anticancer activities [63]. Pillai et al. (2022) investigated the toxicity of iron oxide NPs in DLD-1 human colon cancer cells and normal L929 (fibroblast) cells. They showed significant cytotoxicity in DLD-1 cancer cell lines [64]. Bidian et al. (2023) showed that gold and silver nanoparticles obtained from *Cornus mas* fruit extract both protected normal cells and induced the death of DLD-1 tumor cells, particularly through apoptosis [65]. El-Bahr et al. (2021) investigated the healing effects of iron oxide nanoparticles prepared from *Petroselinum crispum* leaf extract in anemic rats and showed that they can be used as an effective treatment [66].

CONCLUSION

In this study, AgNPs were produced using a straightforward, inexpensive, rapid, and environmentally friendly biosynthetic approach, employing fresh *C. draba* as the source material. The antibacterial properties of the substance have been investigated in relation to various infectious microorganisms. It has been observed that the nanoparticles obtained from these plants have an inhibitory effect on the nosocomial infection agents *E. coli, Staphylococcus aureus, Acinetobacter baumannii, Pseudomonas aeruginosa,* and *Enterobacter* species, which have multiple antibiotic resistance. We think that AgNPs may provide an alternative solution in the treatment of infectious diseases due to their broad-spectrum antibacterial activity, supported by optimization studies. The MTT method was employed for the determination of anticancer activity using a colorectal adenocarcinoma cell line. Test results revealed significant cytotoxicity. In addition to its antibacterial and anticancer effects, it is a good source of molecules effective against urease and collagenase. It is also suggested that the plant samples used may serve as efficacious biological agents when all the data are taken into account, and they can be developed and used in the treatment of various diseases.

AUTHORSHIP CONTRIBUTIONS

Authors equally contributed to this work.

DATA AVAILABILITY STATEMENT

The authors confirm that the data that supports the findings of this study are available within the article. Raw data that support the finding of this study are available from the corresponding author, upon reasonable request.

CONFLICT OF INTEREST

The author declared no potential conflicts of interest with respect to the research, authorship, and/or publication of this article.

ETHICS

There are no ethical issues with the publication of this manuscript.

STATEMENT ON THE USE OF ARTIFICIAL INTELLIGENCE

Artificial intelligence was not used in the preparation of the article.

REFERENCES

[1] Zayed MF, Mahfoze RA, El-Kousy SM, Al-Ashkar E. In-vitro antioxidant and antimicrobial activities of metal nanoparticles biosynthesized using optimized Pimpinella anisum extract. Colloids Surf A Physicochem Eng Asp 2020;585:124167. [CrossRef]

[2] Chahar HS, Corsello T, Kudlicki AS, Komaravelli N, Casola A. Respiratory syncytial virus infection changes cargo composition of exosome released from airway epithelial cells. Sci Rep 2018;8:1–18. [CrossRef]

[3] Hussain I, Singh NB, Singh A, Singh H, Singh SC. Green synthesis of nanoparticles and its potential application. Biotechnol Lett 2016;38:545–560. [CrossRef]

[4] Geraldes AN, da Silva AA, Leal J, Estrada-Villegas GM, Lincopan N, Katti KV, et al. Green nanotechnology from plant extracts: synthesis and characterization of gold nanoparticles. Adv Nanoparticles 2016;5:176–185. [CrossRef]

[5] Shahidi F, Ho C. Phenolics in foods and natural health products: An overview. ACS Symp Ser 2005. [CrossRef]

[6] Vijayakumar S, Malaikozhundan B, Shanthi S, Vaseeharan B, Thajuddin N. Control of biofilm forming clinically important bacteria by green synthesized ZnO nanoparticles and its ecotoxicity on Ceriodaphnia cornuta. Microb Pathog 2017;107:88–97. [CrossRef]

[7] Kanakalakshmi A, Janaki V, Shanthi K, Kamala-Kannan S. Biosynthesis of Cr (III) nanoparticles from electroplating wastewater using chromium-resistant *Bacillus subtilis* and its cytotoxicity and antibacterial activity. Artif Cells Nanomed Biotechnol 2017;45:1304–1309. [CrossRef]

[8] Şahin M, Gübbük İH. Synthesis of antioxidant silver nanoparticles, characterization and catalysis Applications. Int J Adv Eng Pure Sci 2019;31:75–83. [CrossRef] [Turkish]

[9] Doğan Y, Başlar S, Mert HH, Ay G. The use of wild edible plants in Western and Central Anatolia (Turkey). Econ Bot 2004;58:684–690. [CrossRef]
[10] Şimşek I, Aytekin F, Yeşilada E, Yıldırımlı Ş. An ethnobotanical survey of the Beypazarı, Ayaş and Güdül district towns of Ankara Province (Turkey). Econ Bot 2004;58:705–720. [CrossRef]
[11] Akgül A. Midyat (Mardin) civarında etnobotanik. Yüksek Lisans Tezi, Ege Üniversitesi, Fen Bilimleri Enstitüsü, Biyoloji Anabilim Dalı, İzmir; 2008.
[12] Ertuğ F. An ethnobotanical study in Central Anatolia (Turkey). Econ Bot 2000;54:155–182. [CrossRef]
[13] Mart S. Bahçe ve Hasanbeyli (Osmaniye) halkının kullandığı doğal bitkilerin etnobotanik yönden araştırılması. Yüksek Lisans Tezi, Çukurova Üniversitesi Fen Bilimleri Enstitüsü, Biyoloji Anabilim Dalı, Adana; 2006.
[14] Erol MK, Tuzlacı E. Turkish folk medicinal plants. Part II: Eğirdir (Isparta). Fitoterapia 1999;70:593–610. [CrossRef]
[15] Radonić I, Blažević J, Mastelić M, Zekić M, Skočibušić A, Maravić, Phytochemical analysis and antimicrobial activity of *Cardaria draba* (L.) Desv. volatiles. Chem Biodivers 2011;8:1170–1181. [CrossRef]
[16] Naser EH, Khthr MFA, Abed SA. Phytochemistry and therapeutic uses of *Cardaria draba* L. Plant Arch 2019;19:118–125.
[17] Tuzlacı E, Erol MK. Turkish folk medicinal plants. Part II: Eğirdir (Isparta). Fitoterapia 1999;70:593–610. [CrossRef]
[18] Desv L, Bayan Y. Chemical composition and antifungal activity of the plant extracts of Turkey *Cardaria draba*. Egypt J Biol Pest Control 2016;26:579–581
[19] Al-Khafaji NMS, Al-Marzoqi AH, Hussein HJ. Influence of the crude phenolic, alkaloid and terpenoid compounds extracts of *Cardaria draba* (Lepidium draba L.) on human pathogenic bacteria. Eur J Botany Plant Sci Phytol 2016;3:15–19.
[20] Sharifi-Rad J, Hoseini-Alfatemi M, Sharifi-Rad JAT, Silva JD, Rokni M, Sharifi-Rad M. Evaluation of biological activity and phenolic compounds of *Cardaria draba* (L.) extracts. J Biol Today's World 2015;4:180–189. [CrossRef]
[21] Aktepe N, Baran A, Atalar MN, Baran MF, Keskin C, Taşkin A, Yavuz Ö, Demirtaş İ, Oğuz E, Jahan I. Analysis of bioactive compounds using LC–ESI–MS/MS, cytotoxic, antimicrobial effects, and enzyme activities from *Cyclotrichium origanifolium*. Chem Biol Drug Des 2023;101:740–748. [CrossRef]
[22] Farahani AF, Hamdi SMM, Mirzaee A. GC/MS analysis and phyto-synthesis of silver nanoparticles using *Amygdalus spinosissima* extract: Antibacterial, antioxidant effects, anticancer and apoptotic effects. Avicenna J Med Biotechnol 2022;14:223. [CrossRef]
[23] Antony JJ, Nivedheetha M, Siva D, Pradeepha G, Kokilavani P, Kalaiselvi S, Sankarganesh A, Balasundaram A, Masilamani V, Achiraman S. Antimicrobial activity of *Leucas aspera* engineered silver nanoparticles against *Aeromonas hydrophila* in infected *Catla catla*. Colloids Surf B Biointerfaces 2013;109:20–24. [CrossRef]
[24] Manosalva N, Tortella G, Diez MC, Schalchli H, Seabra AB, Durán N. Green synthesis of silver nanoparticles: effect of synthesis reaction parameters on antimicrobial activity. World J Microbiol Biotechnol 2019;35:88. [CrossRef]
[25] Başar Y, Yenigün S, Gül F, Özen T, Demirtaş İ, Alma MH, Temel S. Phytochemical profiling, molecular docking and ADMET prediction of crude extract of *Atriplex nitens* Schkuhr for the screening of antioxidant and urease inhibitory. Int J Chem Technol 2024;8:62–71. [CrossRef]
[26] Seraglio SKT, Valese AC, Daguer H, Bergamo G, Azevedo MS, Gonzaga LV, Costa ACO. Development and validation of a LC–ESI–MS/MS method for the determination of phenolic compounds in honeydew honeys with the diluted-and-shoot approach. Food Res Int 2016;87:60–67. [CrossRef]
[27] Hudzicki J. Kirby-Bauer disk diffusion susceptibility test protocol. Am Soc Microbiol 2009;15:55–63.
[28] Bakır Ö, Kurbanoğlu EB. Investigation of antioxidant activity and antiurease, anticollagenase enzyme inhibition profile of oleaster seeds. Int J Life Sci Biotechnol 2022;5:213–224. [CrossRef]
[29] Bakır Ö, Güller P, Kurbanoğlu EB. Synthesis, characterization, antibacterial, antioxidant activity, and lipoxygenase enzyme inhibition profile of silver nanoparticles (AgNPs) by green synthesis from *Seseli resinosum* Freyn & Sint. Int J Plant-Based Pharm 2022;2:182–189. [CrossRef]
[30] Ramirez-Acosta CM, Cifuentes J, Cruz JC, Reyes LH. Patchy core/shell, magnetite/silver nanoparticles via green and facile synthesis, routes to assure biocompatibility. Nanomaterials 2020;10:9. [CrossRef]
[31] Hashim N, Paramasivam M, Tan JS, Kernain D, Hussin MH, Brosse N, Gambier F, Raja PB. Green mode synthesis of silver nanoparticles using *Vitis vinifera*'s tannin and screening its antimicrobial activity/apoptotic potential versus cancer cells. Mater Today Commun 2020;25:101511. [CrossRef]
[32] Shah A, Lutfullah G, Ahmad K, Khalil AT, Maaza M. *Daphne mucronata*-mediated phytosynthesis of silver nanoparticles and their novel biological applications, compatibility and toxicity studies. Green Chem Lett Rev 2018;11:318–333. [CrossRef]
[33] Santhoshkumar J, Rajeshkumar S, Venkat Kumar S. Phyto-assisted synthesis, characterization and applications of gold nanoparticles – A review. Biochem Biophys Rep 2017;11:46–57. [CrossRef]

[34] Okaiyeto K, Hoppe H, Okoh AI. Plant-based synthesis of silver nanoparticles using aqueous leaf extract of *Salvia officinalis*: characterization and its antiplasmodial activity. J Cluster Sci 2021;32:101–109. [CrossRef]

[35] Qais FA, Shafiq A, Khan HM, Husain FM, Khan RA, Alenazi B, Alsalme A, Ahmad I. Antibacterial effect of silver nanoparticles synthesized using *Murraya koenigii* (L.) against multidrug-resistant pathogens. Bioinorg Chem Appl 2019;1:11. [CrossRef]

[36] Atarod M, Nasrollahzadeh M, Sajadi SM. Euphorbia heterophylla leaf extract mediated green synthesis of Ag/TiO2 nanocomposite and investigation of its excellent catalytic activity for reduction of variety of dyes in water. J Colloid Interface Sci 2016;462:272–279. [CrossRef]

[37] Keskin M. Waste corn silk for eco-friendly silver nanoparticles: Green synthesis, characterization and determination of enzyme inhibition properties. J Serb Chem Soc 2025;90:369–382. [CrossRef]

[38] Aktepe N, Erbay N, Baran A, Baran M, Keskin C. Synthesis, characterization, and evaluation of the antimicrobial activities of silver nanoparticles from *Cyclotrichium origanifolium* L. Int J Agric Environ Food Sci 2022;6:426–434. [CrossRef]

[39] Filip GA, Moldovan B, Baldea I, Olteanu D, Suharoschi R, Decea N, Cismaru CM, Gal E, Cenariu M, Clichici S, David L. UV-light mediated green synthesis of silver and gold nanoparticles using Cornelian cherry fruit extract and their comparative effects in experimental inflammation. J Photochem Photobiol B Biol 2019;191:26–37. [CrossRef]

[40] Agarwal UP, Ralph SA, Reiner RS, Hunt CG. Production of high lignin-containing and lignin-free cellulose nanocrystals from wood. Cellulose 2018;25:5791–5805. [CrossRef]

[41] Karakaya Y, Janbazi H, Wlokas I, Levish A, Winterer M, Kasper T. Experimental and numerical study on the influence of equivalence ratio on key intermediates and silica nanoparticles in flame synthesis. Proc Combust Inst 2021;38:1375–1383. [CrossRef]

[42] Habib A, Bibi Y, Qayyum I, Farooq M. Hierarchical plant extracts in silver nanoparticles preparation: Minuscular survey to achieve enhanced bioactivities. Heliyon 2024;10:e24303. [CrossRef]

[43] Sahoo B, Panigrahi LL, Das RP, Pradhan AK, Arakha M. Biogenic Synthesis of Silver Nanoparticle from *Punica granatum* L. and Evaluation of Its Antioxidant, Antimicrobial and Anti-biofilm Activity. J Inorg Organomet Polym Mater 2022;32:4250–4259. [CrossRef]

[44] Nematollahi F. Silver nanoparticles green synthesis using aqueous extract of *Salvia limbata* CA Mey. Int J Biosci 2015;6:30–35. [CrossRef]

[45] Khane Y, Benouis K, Albukhaty S, Sulaiman GM. Green synthesis of silver nanoparticles using aqueous *Citrus limon* zest extract: Characterization and evaluation of their antioxidant and antimicrobial properties. Nanomaterials 2022;12:2013. [CrossRef]

[46] Eghbali S, Taleghani A, Moghimi R, Farhadi F, Hajizadeh M, Sarayan MS. Exploring the phytochemical and biological activity of *Cardaria draba*: Insights into Volatile and Nonvolatile Compounds. 2024;8:1170–1181. [CrossRef]

[47] Younes K, Merghache S, Djabou N, Selles C, Muselli A, Tabti B, et al. Chemical Composition and Free Radical Scavenging Activity of Essential Oils and Extracts of Algerian *Cardaria draba* (L.) Desv. J Essent Oil-Bear Plants 2015;18:1448–1458. [CrossRef]

[48] Saadellaoui W, Kahlaoui1 S, Hcini K, Haddada A, Sleimi N, Roberta. Profiles of the headspace volatile organic and essential oil compounds from the Tunisian *Cardaria draba* (L.) Desv. and Its leaf and stem epidermal micromorphology. Phyton-Int J Exp Bot 2024;93:725–744. [CrossRef]

[49] Das R, Kumar P, Singh AK, Agrawal S, Albukhaty S, Bhattacharya I, Al-aqbi ZT. Green synthesis of silver nanoparticles using *Trema Orientalis* (L.) extract and evaluation of their antibacterial activity. Green Chem Lett Rev 2025;18:2444679. [CrossRef]

[50] Valinezhad N, Talebi AF, Alamdari S. Biosynthesize, physicochemical characterization and biological investigations of chitosan-Ferula gummosa essential oil (CS-FEO) nanocomposite. Int J Biol Macromol 2023;241:124503. [CrossRef]

[51] Rauf S, Hameed H, Tariq M, Afareen A, Gulfaraz S, AlKubaisi NA, et al. Phytochemical-mediated synthesis and characterization of silver nanoparticles using *Mirabilis jalapa* leaf extract and their antibacterial. Microsc Res Tech 2025;88:1–11. [CrossRef]

[52] Jan H, Zaman G, Usman H, Ansir R, Drouet S, Gigliolo-Guivarc'h N, Abbasi BH. Biogenically proficient synthesis and characterization of silver nanoparticles (Ag-NPs) employing aqueous extract of *Aquilegia pubiflora* along with their in vitro antimicrobial, anti-cancer and other biological applications. J Mater Res Technol 2021;15:950–968. [CrossRef]

[53] Panghal M, Kaushal V, Yadav JP. In vitro antimicrobial activity of ten medicinal plants against clinical isolates of oral cancer cases. Ann Clin Microbiol Antimicrob 2011;10:21. [CrossRef]

[54] Kim SH, Lee HS, Ryu DS, Choi SJ, Lee DS. Antibacterial activity of silver-nanoparticles against *Staphylococcus aureus* and *Escherichia coli*. Microbiol Biotechnol Lett 2011;39:77–85.

[55] Ovais M, Khalil AT, Raza A, Islam NU, Ayaz M, Saravanan M, Ali M, Ahmad I, Shahid M, Shinwari ZK. Multifunctional theranostic applications of biocompatible green-synthesized colloidal nanoparticles. Appl Microbiol Biotechnol 2018;102:4393–4408. [CrossRef]

[56] Kaya EC, Akdeniz M, Ugurlu P, Yigitkan S, Toksoy MO, Firat M, Ertas A. Nanoparticle formation capacity and acaricidal effect (*Hyalomma marginatum*) of essential oil of *Thymbra spicata* L. subsp. spicata L. J Essent Oil-Bear Plants 2025;1-19.

[57] Ali S, Bacha M, Shah MR, Shah W, Kubra K, Khan A, et al. Green synthesis of silver and gold nanoparticles using *Crataegus oxyacantha* extract and their urease inhibitory activities. Biotechnol Appl Biochem 2021;68:992–1002. [CrossRef]

[58] Radwan RA, El-Sherif YA, Salama MM. A novel biochemical study of anti-ageing potential of *Eucalyptus camaldulensis* bark waste standardized extract and silver nanoparticles. Colloids Surf B Biointerfaces 2020;191:111004. [CrossRef]

[59] Savitri ES, Rahmawaty AE, Minarno EB. Antioxidant, anti-collagenase, and antibacterial activities of *Fucus vesiculosus* silver nanoparticles. Narra J 2024;4:e882. [CrossRef]

[60] Andrade JM, Domínguez-Martín EM, Nicolai M, Faustino C, Rodrigues LM, Rijo P. Screening the dermatological potential of *plectranthus* species components: Antioxidant and inhibitory capacities over elastase, collagenase and tyrosinase. J Enzyme Inhib Med Chem 2021;36:258–270. [CrossRef]

[61] da Costa Gomes A, Figueiredo CCM, Granero FO, Junior JLB, Ximenes VF, Silva LP, da Silva RMG. Antioxidant and antiglycation activities and inhibitory action of *Passiflora cincinnata* on collagenase, elastase and tyrosinase: in vitro and in silico study. Biocatal Agric Biotechnol 2022;44:102464. [CrossRef]

[62] Abudayyak M, Guzel E, Özhan G. Nickel oxide nanoparticles are highly toxic to SH-SY5Y neuronal cells. Neurochem Int 2017;108:7–14. [CrossRef]

[63] Sivri FM, Önem E, Akkoç S, Çırrık C, Ezer A. Biosynthesis of ZnO nanoparticles using *Laurus nobilis* leaf extract and investigation of antiproliferative and antibacterial activity potential. Int J Secondary Metabolite 2023;10:414–424. [CrossRef]

[64] Pillai RR, Sreelekshmi PB, Meera AP, Thomas S. Biosynthesized iron oxide nanoparticles: Cytotoxic evaluation against human colorectal cancer cell lines. Mater Today Proc 2022;50:187–195. [CrossRef]

[65] Bidian C, Filip GA, David L, Moldovan B, Olteanu D, Clichici S, Baldea I. Green synthesized gold and silver nanoparticles increased oxidative stress and induced cell death in colorectal adenocarcinoma cells. Nanomaterials 2023;13:1251. [CrossRef]

[66] El-Bahr SM, Elbakery AM, El-Gazzar N, Amin AA, Al-Sultan S, Alfattah MA, Hamouda AF. Biosynthesized iron oxide nanoparticles from *Petroselinum crispum* leaf extract mitigate lead-acetate-induced anemia in male albino rats: hematological, biochemical and histopathological features. Toxics 2021;9:123. [CrossRef]

Sigma J Eng Nat Sci, Vol. 43, No. 6, pp. 1957–1966, December, 2025

Sigma Journal of Engineering and Natural Sciences
Web page info: https://sigma.yildiz.edu.tr
DOI: 10.14744/sigma.2025.1927

Research Article

Separation of cations by capillary electrophoresis: The effects of temperature and voltage

Ahmet DURSUN[1,*], Cahit DEMETGÜL[2]

[1]*Department of Food Engineering, Faculty of Agriculture, Hatay Mustafa Kemal University, Hatay, 31034, Türkiye*
[2]*Department of Chemistry, Faculty of Art and Science, Hatay Mustafa Kemal University, Hatay, 31034, Türkiye*

ARTICLE INFO

Article history
Received: 01 October 2024
Revised: 19 November 2024
Accepted: 30 January 2025

Keywords:
Plate Number; Resolution; Sodium; Tailing Factor

ABSTRACT

Cation analysis plays a crucial role in various industries, including food, agriculture, and environmental monitoring. This study explored capillary electrophoresis for the separation of ammonium, potassium, sodium, calcium, magnesium cations, focusing on the effects of temperature (20-30°C) and voltage (20-30 kV) on peak and separation parameters: migration time, plate number, response factor, tailing factor, resolution, and selectivity. The shortest migration times for cations (from ammonium to magnesium) were observed at 30°C-30 kV (from 4.27 to 7.11 min), while the longest times (from 7.45-12.9 min) occurred at 20°C-20 kV. The temperature significantly interacted with voltage on the migration of cations ($p<0.05$). The highest plate number was observed for magnesium (36800), followed by calcium (32031), potassium (14712), ammonium (6927), and sodium (5060). Temperature increases significantly ($p<0.05$) improved sodium's plate number (from 2560 to 5060) but reduced it for other cations. Both temperature and voltage significantly ($p<0.05$) enhanced peak symmetry for sodium, as indicated by increase in its tailing factor (from 0.54 to 0.58 and from 0.54 to 0.57, respectively). Furthermore, the temperature and voltage showed a significant ($p<0.05$) interaction on the tailing factors of ammonium and potassium. Resolution between sodium and calcium was suboptimal (<1) at 20°C-30 kV but reached to 2.19 at 30°C-30 kV. These findings demonstrate that higher temperature and voltage conditions enhance separation efficiency, particularly for sodium, by improving plate number, peak symmetry, and resolution. This study presents a comprehensive quantitative comparison and offers specific capillary electrophoresis conditions to facilitate further research and method validation for cation analyses.

Cite this article as: Dursun A, Demetgül C. Separation of cations by capillary electrophoresis: The effects of temperature and voltage. Sigma J Eng Nat Sci 2025;43(6):1957–1966.

INTRODUCTION

The cations of sodium, potassium, calcium and magnesium are essential minerals that play crucial roles in human health. High intake of sodium is linked to hypertension while low levels of calcium can affect the bones [1]. The most common reduction of sodium is by substituting with potassium, hence providing health benefits such as blood pressure

***Corresponding author.**
*E-mail address: adursun@mku.edu.tr

This paper was recommended for publication in revised form by Editor-in-Chief Ahmet Selim Dalkilic

Published by Yıldız Technical University Press, İstanbul, Turkey
© Author. This is an open access article under the CC BY-NC license (http://creativecommons.org/licenses/by-nc/4.0/).

reduction, decreased cardiovascular disease, and kidney injury [2]. Calcium is essential in the maintenance of bone health and cellular functions, while magnesium is essential in enzyme activity and energy metabolism. Ammonium is a cation derived from ammonia (NH_3), a common compound in soil and water. It plays a crucial role in the nitrogen cycle and is available to plants for nutrition [3]. In water, the cations also play an important role in taste, hardness, and its suitability for drinking, agriculture and industrial applications [4]. Similarly, in many countries around the world, including Türkiye, labelling regulations require very explicit reporting on mineral cation content in foodstuffs and beverages; these further applications the need for appropriate and reliable analytical techniques [5]. Sodium adsorption ratio (SAR) calculated from the relative concentration of sodium to calcium and magnesium is widely used to assess the suitability of water for agricultural irrigation since it provides an indication of the potential impact of sodium on the structure and permeability of the soil [6]. Sodium and potassium are essential in formulating intravenous fluids and medications to ensure isotonicity. Calcium and magnesium are widely used in pharmaceutical industries as supplements to address deficiencies and as antacids acid, respectively [7]. The knowledge of the behavior and concentration of the cations present in foodstuffs, determination of water quality, industrial processing, and monitoring would be significant in applications. The precision of cation analysis, hence, is principle in ensuring product quality and consumer health, apart from being an inevitable tool in the enforcement of regulatory requirements.

The most common techniques followed for the determination of cations in such natural samples are atomic absorption spectroscopy (AAS), flame photometry, and ion chromatography [8, 9, 10]. AAS generally offers lower detection limits and can analyze a wider range of elements than flame photometry. While flame photometry is easier to operate, making it preferred choice for analysis of major cations [11]. Ion chromatography (IC) also separates cations based on their interaction with a stationary phase and a mobile phase [8]. While these methods are effective, they are costly, require extensive maintenance, and may need larger sample volumes. Therefore, an alternative simple method which can determine the cations in natural samples has been tried to be obtained by capillary electrophoresis (CE). CE is a powerful analytical technique widely used for the separation of ions with many advantages compared to other analytical techniques. CE has even produced higher separation efficiency compared to AAS and IC [12, 13] in testing of water samples while consuming lower sample volumes [8, 14, 15]. However, gaps remain regarding the effects of temperature and voltage on peak and separation parameters during the analysis of capillary electrophoresis. The effects of temperature and voltage in CE can be related to two phenomena: joule heating and electroosmotic flow (EOF). Although, voltage increases the EOF and accelerates the migration, applying excessive voltage may negatively affect both the resolution of analytes and the efficiency of the capillary due to the heating effect [16, 17]. An increase in temperature lowers the viscosity of the buffer, which in turn increases the EOF and ion mobility, causing the analyte to migrate faster. However, an excessively high temperature can clearly accelerate EOF, leading to a loss of resolution and selectivity [18, 19]. Knox and McCormack [20] stated that Joule heating in capillaries increases molecular diffusion resulting in a smaller than expected rise in the plate number, causing peak broadening, and decreasing in separation efficiency. Besides, Joule heating decreases resolution owing to the increased thermal diffusion which makes the sample broaden with the consequence of reducing separation efficiency [21]. A low resolution between the Mg^{2+} and Ca^{2+} cations had been observed in works dealing with the analysis of cations by CE, with applied voltages of 15 kV and 20 kV [15, 22]. The application of a voltage of 30 kV resulted in low resolution for the Na^+ and Mg^{2+} cations [23]. Despite its potential, the interactive effects of temperature and voltage on the peak and separation characteristics of cations are not well known for multi-cation analysis.

In this study, it was aims to determine the temperature (20-30°C) and voltage (20-30 kV) that can improve migration time, plate number, peak symmetry, resolution, and selectivity in cation analysis by CE. By addressing these operational conditions, the findings are expected to improve the applicability of CE in industries where precise cation analysis is critical for quality control, and regulatory compliance.

MATERIALS AND METHODS

Standards

The cation standard test sample containing 100 ppm each of ammonium (NH_4^+), potassium (K^+), sodium (Na^+), calcium (Ca^{2+}), and magnesium (Mg^{2+}) was used (5064-8205, Agilent Technologies, Santa Clara, CA, USA). Buffer solution (5064-8203, Agilent Technologies) was filtered using 0.22 μm syringe filter and degassed for 5 min using an ultrasonic bath (621.06.003, ISOLAB GmbH, Germany) prior to runs. The pH values were 2.8 for the cation standard and 3.2 for the buffer, respectively. The water used to CE analysis was purified by passage through an Ultra-Pure Milli-Q plus water system from Millipore (Millipore, Milford, MA, USA). A standard NaOH solution (1 N, 5062-8576, Agilent Technologies) was used for conditioning the capillary.

Instrumentation

Separation of cations was carried out using a capillary electrophoresis system (Agilent G7100) coupled with a real-time UV-Visible diode-array detector (190 to 600 nm) and interfaced with ChemStation software (Agilent Technologies, Santa Clara, CA, USA). The separation capillary used was a standard bare fused silica with 80.5 cm

total length and an internal diameter of 50 µm (G1600-62211, Agilent Technologies). The distance from the point of injection to the deuterium lamp on-column detection was 72 cm.

Procedures

The cation standard sample was diluted to 25 ppm with MilliQ water and filtered using a 0.22 µm PTFE syringe filter. Separation of cations by CE was performed according to the procedure described by Varden and Bou-Abdallah [24]. Prior to use, the capillary was conditioned with 0.1 M NaOH for 10 min, ultra-pure water for 10 min, and running buffer for 15 min as recommended by the manufacturer. Between each run the capillary was purged with buffer for 5 min. The buffer was replaced after every change in operation conditions. The cations were separated under constant voltage (positive polarity) and temperature of the capillary were as follows: 20 kV and 20°C, 20 kV and 30°C, 30 kV and 20°C, 30 kV and 30°C, respectively. These ranges were chosen to evaluate their effects on the resolution and migration of cations. The voltage directly affects the electrophoretic migration of analytes; higher voltage generally leads to faster migration and/or shorter analysis times, but with a potential decrease in resolution. Similarly, the temperature of the capillary affects the buffer viscosity and ion mobility; higher temperature generally reduces viscosity and increases ion separation. Also, the parameters were determined by previous studies [14, 22-25], ensuring compatibility with the CE system.

Samples were injected by electro-migration at 5 kV for 5 s. The detector was set at UV signal of 280 nm (bandwidth 20 nm), with an indirect reference signal of 214 nm (bandwidth 10 nm), a response time of 2.0 s, and a sampling rate of 2.5 Hz. Total run time was 15 minute. Each sample was run at least three times. At the end of each day's analyses, the capillary was washed with purified water for 15 min and then flushed with air for 3 min.

Peak and Separation Characteristics

Migration time (Mt) refers to the amount of time it takes for an analyte to migrate from the point of injection to the detector. The plate number (N), also known as the number of theoretical plates, was calculated using the following formula:

$$N = 5.54\left(\frac{Mt}{W_{1/2}}\right)^2 \qquad \text{(Eq. 2.1)}$$

Where:

Mt is the migration time.

$W_{1/2}$ is the width of the peak at half-height.

The response factor (Rf) is calculated as the ratio of the peak area to its corresponding known concentration (25 ppm). Tailing factor (Tf) was calculated at 5% of the peak height using the following formula:

$$Tf = \frac{W_{0.05}}{2f} \qquad \text{(Eq. 2.2)}$$

Where:

$W_{0.05}$ is the width of the peak.

f is the distance from the peak apex to the leading edge of the peak.

Selectivity (a) is defined as the ratio of the effective electrophoretic mobilities of two analytes. It is calculated as the ratio of the migration times for two adjacent peaks [26]. Resolution (Rs) was calculated using the following formula:

$$Rs = \frac{2\left(M_{t2} - M_{t1}\right)}{W_{b1} + W_{b2}} \qquad \text{(Eq. 2.3)}$$

Where:

Mt_1 and Mt_2 are the migration times of the first and second peaks, respectively.

W_{b1} and W_{b2} are the baseline widths of the first and second peaks, respectively.

Statistical Analysis

Peak and separation characteristics were subjected to a (2x2)x3 factorial analysis of variance with fixed factors of 2 voltage levels (20 kV and 30 kV) and 2 temperature levels (20°C and 30°C) in a completely randomized design. The general linear model is as follows:

$$Y_{ijk} = \mu + \alpha_i + \beta_j + (\alpha\beta)_{ij} + e_{ijk}$$

Where:

Y_{ijk}, recorded the value of separation parameters

µ, mean of the population

α_i, the effect of ith voltage group i= 1-2

β_j, the effect of jth temperature group j= 1-2

$\alpha\beta_{ij}$, the effect of relationship between voltage and temperature

e_{ijk}, error term

The parameters of migration time and tailing factor for which the interaction between temperature and voltage was found to be significant, it was illustrated using an interaction plot. Differences between the mean values were analyzed using one-way ANOVA and Duncan's multiple comparison test. All statistical analyses and interaction plots were performed using the SPSS package program (Version 22, IBM Statistics, USA).

RESULTS AND DISCUSSION

Peak Characteristics

The electropherogram of cations separated by CE under different temperature and voltage conditions was shown in Fig. 1. The effect of temperature and voltage applied to the separation of cations on migration time of cations was

shown in Fig. 2. Ammonium was the first migrated cation, followed by K^+, Na^+, Ca^{2+} and Mg^{2+}. The longest and the shortest migration times of cations were at 20°C-20 kV (from 7.45 to 12.9) and 30°C-30 kV (from 4.27 to 7.11) conditions, respectively (Fig. 1 and 2). This can also be attributed to the lower viscosity of the buffer at higher temperatures, which enhances the electroosmotic flow (EOF) and the mobility of cations [14, 19].

The shorter migration times have been previously reported for the same cations separated by CE [15, 27]. However, Opekar and Tuma [28] reported higher migration times for cations than those observed in the present study. It was also reported that cations in drinking water [29] and milk [30] migrated in less than 5 minutes at 25 kV and 20 kV, respectively. These differences could be attributed to the column and/or buffer used in the separation of cations by CE. Rizelio et al. [15] separated cations in honey using a 48.5 cm length capillary under 15 kV applied voltage within 1.5 minutes.

As shown in Figure 2, the temperature interacted with voltage to affect the migration time of all cations ($P<0.05$). This finding is consistent with the statement of Rathore [19], who reported that the degree of Mt shortening with increasing temperature is greater at higher voltages. It can also be stated that the increase in voltage also shortens the Mt even more as the temperature increases (Fig. 2). As expected, voltage increased the EOF of cations, while temperature reduced the time cations spent in the capillary column. The EOF refers to the bulk flow of the electrolyte solution in the capillary, which is driven by the applied electric field [21]. Increasing the voltage increases the electric field strength, which generally leads to faster migration times for cations. Higher temperatures can increase the kinetic energy of the ions, which may enhance their mobility. Similarly, Cheng et al. [31] reported that the migration times of cations decreases as the voltage increased from 18 kV to 30 kV.

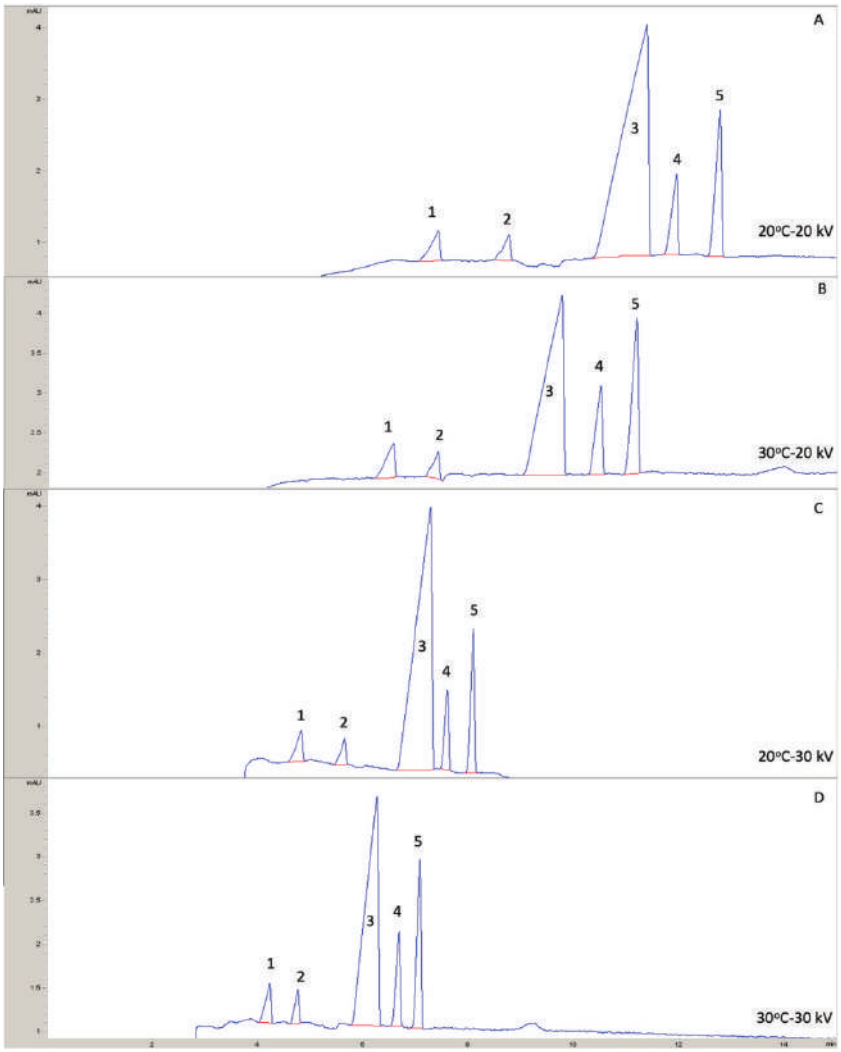


Figure 1. Electropherogram of cations (1: NH_4^+, 2: K^+, 3: Na^+, 4: Ca^{2+}, 5: Mg^{2+}) separated by capillary electrophoresis under 20°C-20 kV (A), 30°C-20 kV (B), 20°C-30 kV (C), and 30°C-30 kV (D).

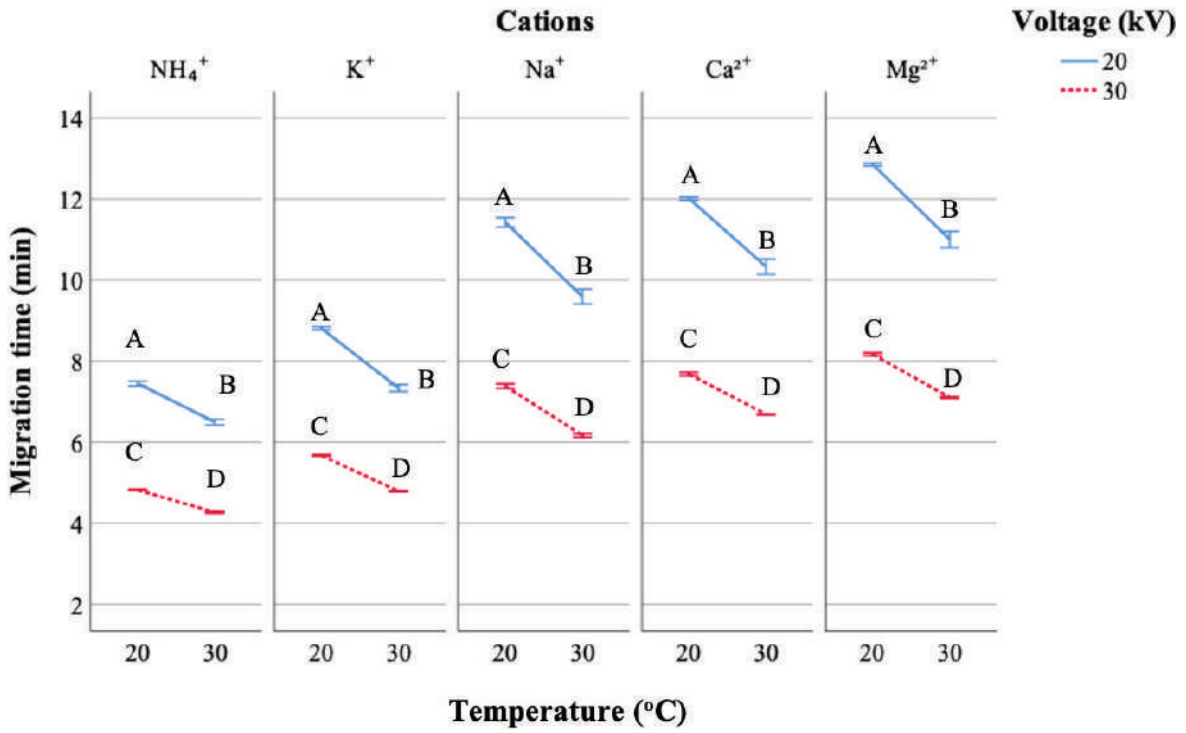


Figure 2. The effect of interaction between temperature and voltage on the migration time of cations. Error bars indicate standard errors (n=3). [A-C] Different capital letters indicate significant differences between samples ($p<0.05$).

The plate number of cations separated by CE under different temperature and voltage were given in Table 1. The plate number (N), also referred to as the number of theoretical plates, serves as a key parameter for assessing efficiency of the chromatographic separation [32]. The highest N value was observed for Mg^{2+} (36800), followed by Ca^{2+} (32031), K^+ (14712), NH_4^+ (6927), and Na^+ (5060). Opekar and Tuma [28] observed a similar ranking for cations ($Mg^{2+}>Ca^{2+}>K^+>NH_4^+$) with respect to plate number. The plate numbers of K^+, Ca^{2+} and Mg^{2+} cations separated by CE at 25 kV and 25°C were determined as 5500, 37000 and 42000, respectively [33]. Shi and Fritz [34] stated that the plate number of cation peaks depends on the concentration injected to CE and determined the N value of 100 ppm Zn^{2+} to be lower than 100000. As shown in Table 1, temperature had a significant ($p<0.05$) effect on the plate number of all cations. An increase in temperature significantly ($p<0.05$) increased the N value for Na^+ (from 2560 to 5060), while it significantly ($p<0.05$) decreased the N values for the other cations (Table 1). The plate numbers for Ca^{2+} and Mg^{2+} were higher when analyzed at 20 kV compared to 30 kV at both temperatures (Table 1). This can be attributed to the 'Joule heating' as a result of high voltage, as reported by Copper [16]. This could be attributed to increase in temperature reduced the viscosity of the buffer, thereby enhancing the mobility and separation of Na^+ more significantly than the others. As regard to other cations, factors such as increased diffusion or thermal broadening may have counteracted the advantages of reduced viscosity [19, 20].

Table 1. Plate number of cations separated by capillary electrophoresis under varying temperatures and voltages

Cations	Factors of temperature (T) and voltage (V)				Significance		
	20°C-20 kV	20°C-30 kV	30°C-20 kV	30°C-30 kV	T	V	TxV
NH_4^+	9337±1313	7688±631	6807±1148	7046±626	*	ns	ns
K^+	19719±1572	17610±964	15118±2348	14305±1484	**	ns	ns
Na^+	3063±1815	2077±351	3995±1025	6124±2735	*	ns	ns
Ca^{2+}	45957±2247	44255±1469	33491±1461	30570±633	***	*	ns
Mg^{2+}	57452±136	51770±880	39075±1791	34525±233	***	***	ns

The data were expressed as mean±standard deviation (n=3). *p<0.05, **p<0.01, ***p<0.001, ns: not significant (p>0.05)

The response factor of cations separated by CE under different temperature and voltage were given in Table 2. A higher response factor indicates that the detector generates a stronger response for each unit of the standard analyte [35]. The response factor of Na^+ was 5 to 24 times higher than those of the other cations (Table 2). Lee and Lin [36] also reported that Na^+ has a higher peak height than other cations separated by capillary electrophoresis at 25°C and 25 kV. Therefore, Na^+ can be determined with better sensitivity by capillary electrophoresis compared to other cations. This also means that analytes with higher response factors naturally exhibit higher calibration slopes. Fung and Lau [14] also determined a higher calibration slope for Na^+ among the 13 cations analyzed by CE. Since K^+ has the lowest response factor among the cations (Table 2), its detection limit is expected to be higher than those of the others, which is consistent with the findings of Suarez-Luque et al. [37] and Abe et al. [33].

Among the cations, the response factor for Na^+ was the only one to decrease significantly (P<0.05) with increasing temperature, regardless of whether the voltage was 20 kV or 30 kV (Table 2). With respect to voltage, no significant difference was observed in the response factors, except for Na^+ (Table 2). This situation may be due to changes in the plate number of Na^+ peak. The plate number of the Na^+ peak was highest at 30°C with 30 kV applied, whereas other cations exhibited the lowest plate numbers under the same conditions. In this context, it appears that the response factor may be negatively affected by the plate number of peak. When the plate number is low, it indicates broader peaks, which can lead to a lower response factor. As plate number is a measure of column efficiency, a higher plate number indicates better separation, reducing peak overlap and improving resolution [38].

The effect of temperature and voltage applied for the separation of cations on tailing factor of cations was shown in Fig. 3. Tailing factor (Tf) of a chromatographic peak is calculated to assess the shape of the peak, particularly how symmetrical it is. An ideal chromatographic peak is characterized as a 'Gaussian peak'. For the perfect peak symmetry, the tailing factor (Tf) should be '1'. As the Tf value deviates negatively from '1', the peak's fronting increases, while positive deviations indicate increased tailing [35, 39]. All analyzed cations showed fronting with Tf values less than '1'. It is difficult to find peak tailing factor data for cations analyzed by CE in the literature. The cation with the highest fronting was Na^+, which exhibited the lowest Tf value (Fig 3). The temperature and voltage interacted to influence the Tf of NH_4^+ and K^+, which migrate faster in the capillary than the other cations (Fig 1). This can be attributed to the smaller size and higher electrophoretic mobilities of NH_4^+ and K^+ ions, as well as the fact that temperature and voltage accelerate these cations more than the others [20]. As shown in Fig. 3, the tendency for temperature to increase Tf value depends on the applied voltage. The temperature increased Tf significantly only when a voltage of 30 kV was applied to separate the NH_4^+, K^+ cations. Thus, applying 30 kV instead of 20 kV for cation separation increased the Tf value, resulting in more symmetrical peaks. Also, the significant interaction between temperature and voltage means that their combined effect was greater than the sum of their individual effects on peak symmetry of NH_4^+, K^+ cations. This highlights the need to optimize both parameters simultaneously to maximize separation efficiency and peak quality. In applications where precise quantification is required, such as in quality control or environmental monitoring, symmetric peaks ensure accurate analysis.

This could be attributed to the higher voltage application increasing the number of plates. Changes in the tailing factor were consistent with the plate number. In fact, a statistically significant positive correlation (r=0.654, p<0.001) has been identified between the plate number of peaks and the tailing factor. Dyson [38] also noted that tailing negatively affects the plate number by causing peak broadening, thereby reducing separation efficiency.

Separation Characteristics

The separation characteristics of selectivity and resolution determined in cations were shown in Table 3 and Table 4, respectively. As stated by Dursun and Güler [35], selectivity (α), also known as the separation factor or relative retention, is used to describe the ability to distinguish between two analytes based on their electrophoretic mobilities. Since selectivity is defined as the ratio of migration

Table 2. Response factor of cations separated by capillary electrophoresis under varying temperatures and voltages

Cations	Factors of Temperature (T) and Voltage (V)				Significance		
	20°C-20 kV	20°C-30 kV	30°C-20 kV	30°C-30 kV	T	V	TxV
NH_4^+	0.20±0.02	0.13±0.01	0.21±0.04	0.13±0.00	ns	***	ns
K^+	0.14±0.01	0.10±0.01	0.13±0.02	0.08±0.01	ns	***	ns
Na^+	4.34±2.52	3.59±0.74	1.95±0.25	0.94±0.64	*	ns	ns
Ca^{2+}	0.36±0.02	0.23±0.01	0.36±0.01	0.22±0.01	ns	***	ns
Mg^{2+}	0.62±0.03	0.40±0.00	0.63±0.00	0.40±0.01	ns	***	ns

The data were expressed as mean±standard deviation (n=3). *P<0.05, ***P<0.001, ns: not significant (P>0.05)

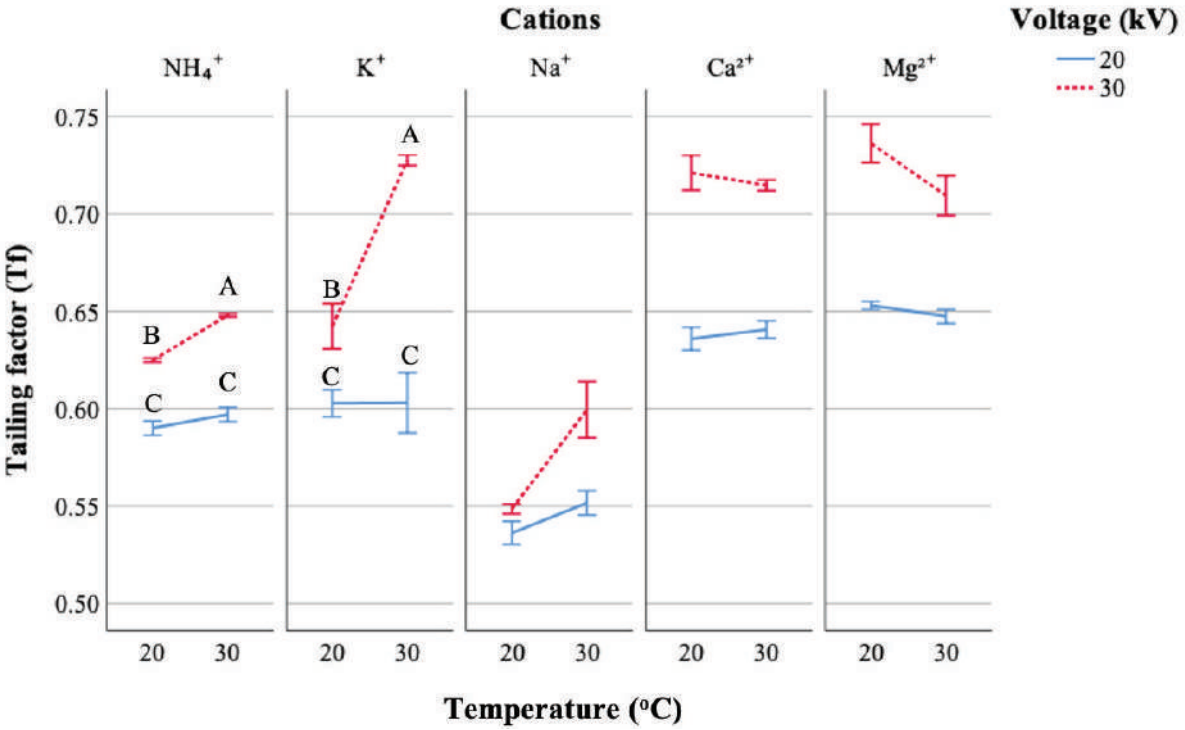


Figure 3. The effect of interaction between temperature and voltage on the tailing factor of cations. Error bars indicate standard errors (n=3). [A-C] Different capital letters indicate significant differences between samples ($p<0.05$).

times for two adjacent peaks, the smallest possible value is '1' [26]. The α values of cations were found higher than '1' (Table 3).

The α values alone may not be sufficient for evaluating the separation, as they are calculated solely from migration times. Resolution, being a function of the retention factor, separation factor, and theoretical plate number, serves as a good indicator of how well chromatographic peaks are separated [35]. An increase in temperature has been found to enhances the resolution of K^+-Na^+ and Na^+-Ca^{2+} (from 4.40 to 5.45 and from 0.94 to 1.98, respectively) but decrease the resolution of NH_4^+-K^+ and Ca^{2+}-Mg^{2+} (from 4.59 to 2.94 and from 3.59 to 2.86). The better resolution of Na^+ from the preceding K^+ and following Ca^{2+} cations (Table 4), particularly at higher temperatures, was consistent with the increased plate number (Table 1) and tailing factor (Fig. 3). There was no significant difference in the resolution of Na^+-Ca^{2+} separated under 20 kV and 30 kV (Table 4). With the increase in voltage from 20 kV to 30 kV, the resolution of NH_4^+-K^+ (from 3.93 to 3.60) and Ca^{2+}-Mg^{2+} (from 3.41 to 3.04) decreased significantly ($p<0.01$).

While an Rs value of '1' is acceptable, an Rs value exceeding '1.5' signifies better separation, with consecutive peaks fully separated from each other [26, 40]. As shown in Table 4, good resolution was obtained except for Na^+-Ca^{2+} separated at 20°C both at 20 kV (1.13) and 30 kV (0.74). Better resolution was determined for Ca^{2+}- Mg^{2+} and NH_4^+-K^+ compared to cations separated at 20 kV with a 50 cm capillary [22] and 30 kV with a 55 cm capillary [23]. This is most likely due to the longer capillary (80.5 cm total length)

Table 3. Selectivity of cations separated by capillary electrophoresis under varying temperatures and voltages

Cations	Parameters of Temperature (T) and Voltage (V)				Significance		
	20°C-20 kV	20°C-30 kV	30°C-20 kV	30°C-30 kV	T	V	TxV
NH_4^+- K^+	1.18±0.01	1.18±0.00	1.13±0.00	1.12±0.00	***	ns	ns
K^+- Na^+	1.30±0.03	1.30±0.01	1.31±0.02	1.29±0.02	ns	ns	ns
Na^+- Ca^{2+}	1.05±0.02	1.04±0.00	1.08±0.00	1.08±0.01	***	ns	ns
Ca^{2+}- Mg^{2+}	1.07±0.00	1.06±0.00	1.07±0.00	1.06±0.00	ns	**	ns

The data were expressed as mean±standard deviation (n=3). **p<0.01, ***p<0.001, ns: not significant (p>0.05)

Table 4. Resolution of cations separated by capillary electrophoresis under varying temperatures and voltages

Cations	Parameters of Temperature (T) and Voltage (V)				Significance		
	20°C-20 kV	20°C-30 kV	30°C-20 kV	30°C-30 kV	T	V	TxV
NH_4^+- K^+	4.82±0.17	4.35±0.06	3.03±0.27	2.85±0.09	***	**	ns
K^+- Na^+	4.64±0.69	4.17±0.14	5.27±0.11	5.64±0.74	**	ns	ns
Na^+- Ca^{2+}	1.13±0.59	0.74±0.13	1.76±0.21	2.19±0.72	**	ns	ns
Ca^{2+}- Mg^{2+}	3.83±0.16	3.35±0.07	2.99±0.04	2.73±0.07	***	***	ns

The data were expressed as mean±standard deviation (n=3). **p<0.01, ***p<0.001, ns: not significant (p>0.05).

used in the present study. It was observed that Na^+ and Ca^{2+} had Rs values above '1.5' when analyzed at 30°C. This was compatible with the increased number of theoretical plates for the Na^+ peak as temperature increased (Table 1). The Rs values determined for NH_4^+ (1.57), K^+ (5.64), and Na^+ (5.23) were reported by Neaga et al. [41].

CONCLUSION

To our knowledge, this is the first report on the peak and separation characteristics of cations including analysis by capillary electrophoresis at varying temperatures and voltages. The findings demonstrate that an increase in both temperature and voltage significantly reduced the migration times of cations. The efficiency of separation varied among the cations, with magnesium exhibiting the highest plate number. Especially at 30°C, the increase in the plate number of the sodium peak resulted in better separation from the preceding potassium and following calcium peaks, thus enhancing resolution. The interaction between temperature and voltage resulted in a better symmetry for the ammonium and potassium peaks, emphasizing the importance of optimizing both parameters to obtain better results in terms of efficiency. The selectivity and resolution of cations analyzed, particularly at 30°C, indicated better separation ability. Overall, these findings provide valuable insights for improving analytical methods in capillary electrophoresis, potentially enhancing selectivity of cation separation.

Our findings provide a robust method for detecting cations, which can significantly enhance routine quality control practices in the food, agricultural, chemical and medicinal industries. In conclusion, the operating at 30°C with a higher voltage in the separation of cations by capillary electrophoresis could be recommended, especially as it increases the plate number and improves peak symmetry for sodium, thereby enhancing the resolution and providing a shorter analysis time.

AUTHORSHIP CONTRIBUTIONS

Authors equally contributed to this work.

DATA AVAILABILITY STATEMENT

The authors confirm that the data that supports the findings of this study are available within the article. Raw data that support the finding of this study are available from the corresponding author, upon reasonable request.

CONFLICT OF INTEREST

The author declared no potential conflicts of interest with respect to the research, authorship, and/or publication of this article.

ETHICS

There are no ethical issues with the publication of this manuscript.

STATEMENT ON THE USE OF ARTIFICIAL INTELLIGENCE

Artificial intelligence was not used in the preparation of the article.

REFERENCES

[1] National Research Council (US) Division on Earth, Life Studies, Commission on Life Sciences, Committee on Diet. Diet and health: implications for reducing chronic disease risk. Washington (DC): National Academies Press (US); 1989.

[2] Cepanec K, Vugrinec S, Cvetković T, Ranilović J. Potassium chloride-based salt substitutes: a critical review with a focus on the patent literature. Compr Rev Food Sci Food Saf 2017;16:881–894. [CrossRef]

[3] Shilpha J, Song J, Jeong BR. Ammonium phytotoxicity and tolerance: an insight into ammonium nutrition to improve crop productivity. Agronomy 2023;13:1487. [CrossRef]

[4] Atikul Islam M, Zahid A, Rahman MM, Rahman MS, Islam MJ, Akter Y, Shammi M, Bodrud-Doza M, Roy B. Investigation of groundwater quality and its suitability for drinking and agricultural use in the south central part of the coastal region in Bangladesh. Expo Health 2017;9:27–41. [CrossRef]

[5] Tarım ve Hayvancılık Bakanlığı. Türk Gıda Kodeksi Gıda Etiketleme ve Tüketicileri Bilgilendirme Yönetmeliği. Resmi Gazete 2017;29960.
[6] Suarez DL, Wood JD, Lesch SM. Effect of SAR on water infiltration under a sequential rain–irrigation management system. Agric Water Manag 2006;86:150–164. [CrossRef]
[7] Murray M. The pill book guide to natural medicines: vitamins, minerals, nutritional supplements, herbs, and other natural products. New York: Bantam; 2008.
[8] Padarauskas A, Olsauskaite V, Paliulionyte V. Simultaneous determination of inorganic anions and cations in waters by capillary electrophoresis. J Chromatogr A 1998;829:359–365. [CrossRef]
[9] Evans EH, Dawson JB, Fisher A, Price WJ, Smith CM, Tyson JF. Advances in atomic emission, absorption and fluorescence spectrometry and related techniques. J Anal At Spectrom 2002;17:622–651. [CrossRef]
[10] Cıftcı H, Er Calıskan C, Erdogan Cakar A, Olcucu A, Ramadan MS. Determination of mineral and trace elements in some medicinal plants by spectroscopic method. Sigma J Eng Nat Sci 2020;38:2133–2144.
[11] Farrukh MA. Atomic absorption spectroscopy. Norderstedt: BoD–Books on Demand; 2012.
[12] Rahmi D, Zhu YB, Fujimori E, Umemura T, Haraguchi H. Multielement determination of trace metals in seawater by ICP-MS with aid of downsized chelating resin-packed mini column for preconcentration. Talanta 2007;72:600–606. [CrossRef]
[13] Kuban P, Karlberg B. Simultaneous determination of small cations and anions by capillary electrophoresis. Anal Chem 1998;70:360–365. [CrossRef]
[14] Fung YS, Lau KM. Separation and determination of cations in beverage products by capillary zone electrophoresis. J Chromatogr A 2006;118:144–150. [CrossRef]
[15] Rizelio VM, Gonzaga LV, Borges GDSC, Maltez HF, Costa ACO, Fett R. Fast determination of cations in honey by capillary electrophoresis: a possible method for geographic origin discrimination. Talanta 2012;99:450–456. [CrossRef]
[16] Cooper CL. Capillary electrophoresis: part I. theoretical and experimental background. J Chem Educ 1998;75:343–347. [CrossRef]
[17] Cao J, Hong FJ, Cheng P. Numerical study of radial temperature gradient effect on separation efficiency in capillary electrophoresis. Int Commun Heat Mass Transf 2007;34:1048–1055. [CrossRef]
[18] Kuhr WG. Separation of small organic molecules. In: Camilleri P, editor. Capillary electrophoresis: theory and practice. Boca Raton (FL): CRC Press; 1993. p. 1–35.
[19] Rathore AS. Joule heating and determination of temperature in capillary electrophoresis and capillary electrochromatography columns. J Chromatogr A 2004;1037:431–443. [CrossRef]
[20] Knox JH, McCromack KA. Temperature effects in capillary electrophoresis. 1: internal capillary temperature and effect upon performance. Chromatographia 1994;38:207–214. [CrossRef]
[21] Burgi DS, Salomon K, Chien RL. Methods for calculating the internal temperature of capillary columns during capillary electrophoresis. J Liq Chromatogr 1991;14:847–867. [CrossRef]
[22] Salimi-Moosavi H, Cassidy RM. Control of separation selectivity and electroosmotic flow in nonaqueous capillary electrophoretic separations of alkali and alkaline earth metal ions. J Chromatogr A 1996;749:279–286. [CrossRef]
[23] Bachmann K, Boden J, Haumann I. Indirect fluorimetric detection of alkali and alkaline earth metal ions in capillary zone electrophoresis with cerium (III) as carrier. J Chromatogr A 1992;626:259–265. [CrossRef]
[24] Varden L, Bou-Abdallah F. Detection and separation of inorganic cations in natural, potable, and wastewater samples using capillary zone electrophoresis with indirect UV detection. Am J Anal Chem 2017;8:81–94. [CrossRef]
[25] Ali I, Aboul-Enein HY. Determination of metal ions in water, soil, and sediment by capillary electrophoresis. Anal Lett 2002;35:2053–2076. [CrossRef]
[26] Snow NH. How chemistry determines separations: influence of selectivity on resolution. LCGC North Am 2023;41:99–102. [CrossRef]
[27] Mayrhofer K, Zemann AJ, Schnell E, Bonn GK. Capillary electrophoresis and contactless conductivity detection of ions in narrow inner diameter capillaries. Anal Chem 1999;71:3828–3833. [CrossRef]
[28] Opekar F, Tuma P. Dual-channel capillary electrophoresis for simultaneous determination of cations and anions. J Chromatogr A 2016;1446:158–163. [CrossRef]
[29] Saad B, Pok FW, Sujari ANA, Saleh MI. Analysis of anions and cations in drinking water samples by capillary ion analysis. Food Chem 1998;61:249–254. [CrossRef]
[30] Schmitt M, Saulnier F, Malhautier L, Linden G. Effect of temperature on the salt balance of milk studied by capillary ion electrophoresis. J Chromatogr 1993;640:419–424. [CrossRef]
[31] Cheng K, Zhao Z, Garrick R, Nordmeyer FR, Lee ML, Lamb JD. Separation of metal cations by electrophoresis in a positively charged coated capillary. J Chromatogr A 1995;706:517–526. [CrossRef]
[32] Muzikar J, van de Goor T, Kenndler E. The principal cause for lower plate numbers in capillary zone electrophoresis with most organic solvents. Anal Chem 2002;74:434–439. [CrossRef]
[33] Abe S, Jun-Ichiro M, Maeda M, Arakawa H. Simultaneous determination of inorganic cations and anions in medical electrolytes by capillary electrophoresis. Anal Lett 2006;39:317–326. [CrossRef]

[34] Shi Y, Fritz JS. New electrolyte systems for the determination of metal cations by capillary zone electrophoresis. J Chromatogr A 1994;671:429–435. [CrossRef]

[35] Dursun A, Güler Z. Elution conditions for effective separation on an aged sulfonated polystyrene–divinylbenzene column of organic acids from meat. Food Anal Methods 2023;16:699–708. [CrossRef]

[36] Lee YH, Lin TI. Determination of metal cations by capillary electrophoresis: effect of background carrier and complexing agents. J Chromatogr A 1994;675:227–236. [CrossRef]

[37] Suarez-Luque S, Mato IM, Huidobro JF, Simal-Lozano J. Determination of major metal cations in milk by capillary zone electrophoresis. Int Dairy J 2007;17:896–901. [CrossRef]

[38] Dyson N. Peak distortion, data sampling errors, and the integrator in the measurement of very narrow chromatographic peaks. J Chromatogr A 1999;842:321–340. [CrossRef]

[39] Haidar Ahmad IA. Necessary analytical skills and knowledge for identifying, understanding, and performing HPLC troubleshooting. Chromatographia 2017;80:705–730. [CrossRef]

[40] Ghanjaoui ME, Mandil A, Ait Sidi Mou A, Slimani R. High performance liquid chromatography quality control. Int J Adv Chem 2020;8:160–169. [CrossRef]

[41] Neaga IO, Iacob BC, Bodoki E. The analysis of small ions with physiological implications using capillary electrophoresis with contactless conductivity detection. J Liq Chromatogr Relat Technol 2014;37:2072–2090. [CrossRef]

Sigma J Eng Nat Sci, Vol. 43, No. 6, pp. 1967–1981, December, 2025

Sigma Journal of Engineering and Natural Sciences
Web page info: https://sigma.yildiz.edu.tr
DOI: 10.14744/sigma.2025.1928

Research Article

Trigonometric based B-spline method for singularly perturbed sobolev problems with initial layers

Shegaye Lema CHERU[1,*], Gemechis File DURESSA[2], Tariku Birabasa MEKONNEN[1]

[1]*Department of Mathematics, Wallaga University, Nekemte, 395, Ethiopia*

[2]*Department of Mathematics, Jimma University, Jimma, 378, Ethiopia*

ARTICLE INFO

Article history
Received: 22 May 2024
Revised: 18 July 2024
Accepted: 24 September 2024

Keywords:
Pseudo-Parabolic (Sobolev) Problem; Parameter-Uniform Convergence; Singular Perturbation Problems; Trigonometric Cubic B-Spline

ABSTRACT

In this work, we investigate and numerically approximate an initial-boundary value problem governed by Sobolev type differential equation exhibiting an initial layer. The problem is approached through a finite difference framework specifically designed to remain unaffected by the presence of a small perturbation parameter, ensuring robustness and stability. A novel hybrid numerical strategy is constructed by employing a non-polynomial trigonometric cubic B-spline (TCBS) collocation technique for the spatial discretization on a uniform partition, while time advancement is carried out through an implicit Euler procedure defined over a Shishkin mesh to effectively capture sharp solution gradients. The developed scheme guarantees parameter-uniform convergence, and its theoretical stability and error properties are rigorously analyzed. A set of numerical simulations is performed to validate the effectiveness of the method, demonstrating its high accuracy, consistency, and suitability for handling singularly perturbed pseudo-parabolic problems with initial layer.

Cite this article as: Cheru SL, Duressa GF, Mekonnen TB. Trigonometric based B-spline method for singularly perturbed sobolev problems with initial layers. Sigma J Eng Nat Sci 2025;43(6):1967–1981.

INTRODUCTION

This section focuses on a class of singularly perturbed pseudo-parabolic equations defined in the domain $\Omega \cup [0,T]$, where $\Omega = (0,1)$ and, $Q = \Omega \times (0,T]$.

$$\begin{cases} \ell w: \equiv \varepsilon \ell_1 \left[\dfrac{\partial w}{\partial t}\right] - \dfrac{\partial}{\partial x}\left[a(x,t)\dfrac{\partial w}{\partial x}\right] + b(x,t)\dfrac{\partial w}{\partial x} \\ \qquad + c(x,t)w = \aleph(x,t),\ (x,t) \in Q, \\ w(x,0) = \varphi(x), x \in \Omega, \\ w(0,t) = w(l,t) = 0, t \in (0,T], \end{cases} \tag{1}$$

where

$$\ell_1\left[\frac{\partial w}{\partial t}\right] = -\frac{\partial^3 w}{\partial t \partial x^2} + \frac{\partial w}{\partial t}.$$

Here ε denotes small perturbation parameter, while coefficient function, source term, and initial conditions are assumed to be smooth functions that fulfill specific regularity requirements, which will be detailed later.

Sobolev equations represent a distinctive category of partial differential equations (PDEs) in which the

*Corresponding author.
*E-mail address: shegaye04@gmail.com

This paper was recommended for publication in revised form by Editor-in-Chief Ahmet Selim Dalkilic

Published by Yıldız Technical University Press, İstanbul, Turkey
© Author. This is an open access article under the CC BY-NC license (http://creativecommons.org/licenses/by-nc/4.0/).

highest-order spatial derivative is coupled with time derivative, leading to a hybrid mathematical structure that blends features of parabolic and hyperbolic equations. Such equations model a wide range of physical phenomena, thermodynamics [1], appearing in mathematical physics and fluid Dynamics [1-3], shear in second order fluids [4], astro-physics [5, 6], filtration theory [7], and propagation of long waves of small amplitude [8]. Some existence and uniqueness results of equation (1) can be found in [6,9-11]. In 1950 Sergi Sobolev started researching pseudo-parabolic equations. A significant part of the recent advances in Sobolev-type problems has been driven by the shift from classical parabolic equations to pseudo-parabolic formulations. Building upon these advancements, researchers in [11, 12] utilized advanced higher-order difference schemes to investigate delay pseudo-parabolic equations. A three-layer finite difference scheme was proposed for pseudo-parabolic equations incorporating a time-delay within the second-order derivative term [13]. Furthermore, higher-order discretization techniques were developed for one-dimensional delay pseudo-parabolic problems [14]. In addition, Zhang [15] introduced linearized compact finite difference methods to address nonlinear Sobolev-type equations involving delay terms.

The aforementioned investigations primarily address the regular (non-singular) settings. In contrast, Eq. (1) is characterized by the inclusion of mixed derivatives involving both temporal and spatial variables in its highest-order terms, an intrinsic and defining attribute of Sobolev (pseudo-parabolic) equations. Despite their significance in modeling diverse physical processes, the literature addressing problems of this type remains relatively scarce, with only a limited number of studies available [2-5,16-19], with presence of ε which makes it singularly perturbed in nature. In [5], the author examined Sobolev problems with one spatial dimension using a finite difference method (FDM) to handle boundary layers efficiently. In a related development, [17] introduced a parameter-uniform approach for initial boundary value problems (IBVPs) utilizing a standard S-mesh in the time direction. It is widely recognized that classical discretization techniques fail to maintain accuracy when the perturbation parameter takes on small values. Hence, it becomes essential to design robust and efficient numerical methods for such problems, ensuring that the accuracy of the evaluated solution remains uniform and does not deteriorate as.

The numerical estimate of singularly perturbed problems (SPPs) is inherently intricate, primarily due to the emergence of sharply localized boundary-layer phenomena within their exact solutions. The presence of small perturbation parameters causes rapid variations in narrow regions, giving rise to boundary or interior layers. As a result, conventional numerical methods often fail to capture these sharp gradients accurately and typically do not converge uniformly when the perturbation parameter becomes sufficiently small. To overcome these difficulties, specially designed parameter-robust schemes and layer-adapted meshes, such as Shishkin or Bakhvalov meshes, are widely employed to ensure stability and uniform convergence across all ranges of the perturbation parameter [20-23].

Several researchers [2-5, 16-19] have developed numerical techniques for addressing singularly perturbed Sobolev problems (SPSPs), both with and without time delays. Nonetheless, these studies have predominantly centered on approaches grounded in interpolating quadrature rules involving specific weight and basis functions. Insofar as the existing literature reveals, no further investigations have extended beyond this framework. In this study, we propose a novel computational framework that utilizes TCBS collocation technique for spatial discretization on a uniform mesh, in combination with an implicit Euler scheme functional on S-mesh for the temporal derivative.

B-spline functions have evolved into powerful and versatile analytical instruments for the numerical resolution of PDEs [19, 21-22]. Among these, TCBS collocation technique has garnered considerable scholarly interest, being effectively employed for the accurate numerical treatment of various classes of PDEs [24-26]. Unlike conventional FDM, spline-based approaches possess the inherent capability to approximate the solution with high precision at any location within the computational domain, thereby significantly enhancing spatial accuracy. Furthermore, when compared with classical polynomial B-spline formulations, the TCBS method has demonstrated superior performance, delivering more precise numerical approximations for both linear and nonlinear IBVPs. This enhanced accuracy arises from the trigonometric structure of the basis functions, which allows for better representation of oscillatory and boundary-layer behaviors often present in SPPs [25-26].

In this work, we develop a numerical method tailored for SPSPs characterized by the presence of initial layers. The key objectives are to evaluate the computational efficiency of the proposed approach, validate its accuracy, and analyze how perturbation parameters influence the formation and behavior of boundary-layer structures in the solutions. The original problem is first transformed into a more tractable formulation, after which the temporal derivative is discretized using the implicit Euler method on S-mesh. The resulting system of ordinary differential equations is subsequently solved through a TCBS collocation technique applied on a uniform spatial mesh.

PRELIMINARY FRAMEWORK AND ANALYTICAL SOLUTION

Eq. (1) is subsequently transformed into the following equivalent representation:

$$\begin{cases} \ell u := \varepsilon \dfrac{\partial w}{\partial t} - \varepsilon \dfrac{\partial^3 w}{\partial t \partial x^2} + a(x,t)\dfrac{\partial^2 w}{\partial x^2} + d(x,t)\dfrac{\partial w}{\partial x} \\ \qquad + c(x,t)w = \aleph(x,t), (x,t) \in Q, \\ w(x,0) = \varphi(x), x \in \Omega, \\ w(0,t) = w(1,t) = 0, \end{cases} \tag{2}$$

where $d(x,t) = b(x,t) - \dfrac{\partial a(x,t)}{\partial x}$ and $a(x,t)$ is a continuous functions and $\dfrac{\partial a(x,t)}{\partial x} \in C^2(\Omega)$. Eq. (2) is renowned by the presence of a mixed temporal-spatial derivative in which a small perturbation parameter ε appears in both the highest order term and the temporal derivative component, thereby delineating the specific class of SPSPs addressed in this study. The functions $(a, d, c, \aleph)(x,t)$ and $\varphi(x)$ are sufficiently smooth and satisfy the required regularity conditions, such that $a(x,t) \geq \alpha > 0$. At this stage, Eq. (2) is reformulated in an operator representation, expressed as follows:

$$\ell w = \varepsilon \frac{\partial w}{\partial t} - \varepsilon \frac{\partial^3 w}{\partial t \partial x^2} + a(x,t)\frac{\partial^2 w}{\partial x^2} + d(x,t)\frac{\partial w}{\partial x} + c(x,t)w. \tag{3}$$

The operator presented in Eq. (3) adheres to the subsequent principle of maximum.

Lemma 1. Let $\Phi(x,t) \in C^0(\overline{Q}) \cap C^2(Q)$, $\ell\Phi(x,t) \geq 0$ satisfies in $Q, \Phi(x,t) \geq 0$ on Ω. Then $\Phi(x,t) \geq 0, \forall (x,t) \in \overline{Q}$.

Proof. Let $(v^*, \xi^*) \in \overline{Q}$ such that $\Phi(v^*, \xi^*) = min_{(x,t)\in\overline{Q}} \Phi(x,t)$ and assume that $\Phi(v^*, \xi^*) < 0$. Now, from assumption, we have $(v^*, \xi^*) \neq \overline{Q}$ for $(v^*, \xi^*) \in Q$. As it attains minimum at (v^*, ξ^*), we have $\Phi_x = \Phi_t = \Phi_{tx} = 0$ and $\Phi_{xx} \geq 0$ at (v^*, ξ^*). Now, we have

$$\begin{aligned} \ell\Phi(x,t) &= \underbrace{\varepsilon\Phi_t(v^*,\xi^*) - \varepsilon\Phi_{txx}(v^*,\xi^*)}_{=0} - a(v^*,\xi^*)\Phi_{xx}(v^*,\xi^*) \\ &\quad + \underbrace{\tilde{b}(v^*,\xi^*)\Phi_x(v^*,\xi^*)}_{=0} + c(v^*,\xi^*)\Phi(v^*,\xi^*), \\ &=\leq a(v^*,\xi^*)\Phi_{xx}(v^*,\xi^*) + c(v^*,\xi^*)\Phi(v^*,\xi^*), \\ &< 0, \text{ since } a(v^*,\xi^*) \geq \alpha > 0, \end{aligned}$$

which is a contradiction as $\ell\Phi(x,t) \geq 0$. Hence, $\Phi(x,t) \geq 0, \forall (x,t) \in \overline{Q}$ [19]. Lemma 2 immediately guarantees the uniqueness of the solution to the problem.

Remark 2.1. (**Friedrichs inequality**)-For a domain G with a Lipschitz boundary, there exist constants c_1, c_2 dependent on G but independent of a functions in D, such that:

$$\int_G w^2 dx \leq c_1 \sum_{k=1}^{N} \int_G \left(\frac{\partial w}{\partial x_k}\right) dx + c_2 \int_\Gamma w^2(s) ds, \tag{4}$$

holds $\forall w \in D$. For N = 1, if $D \in C^1(0, l)$, the Friedrichs inequality is expressed as follows

$$\int_0^1 w^2 dx \leq c_1 \int_0^l (w')^2 (x) dx + c_2 w^2(0),$$

$$\int_0^1 w^2 dx \leq c_1 \int_0^l (w')^2 (x) dx + c_2 w^2(l),$$

$$\int_0^1 w^2 dx \leq c_1 \int_0^l (w')^2 (x) dx + c_2 \left[w^2(0) + w^2(l)\right].$$

If a function in D satisfy additional conditions, such that $w(0) = 0$ or $w(l) = 0$, special cases of the previously derived estimates are obtained. Specifically, if $D_1 \subseteq D$ with $w(0) = 0 = w(l)$, the estimates takes the form:

$$\int_0^l w^2 dx \leq c_1 \int_0^l (w')^2 (x) dx, \quad w \in D_1. \tag{5}$$

By selecting one of the estimates for c_1, we derive the following inequality:

$$\int_0^1 w^2 dx \leq c_1 \frac{(l-0)}{\pi^2} \int_0^l (w')^2 (x) dx, \tag{6}$$

which is valid for for all $w \in D_1$, that is for all $w \in D$ which satisfies the above condition.

Remark 2.2. At the critical points (0,0) and (l,0), the functions $\varphi(x)$ and $\aleph(x,t)$ gratify the subsequent compatibility requirements:

$$\varphi(0) = \varphi(l) = 0 \tag{7}$$

and

$$\begin{cases} -\dfrac{\partial}{\partial x}\left(a(0,0)\dfrac{d\varphi(0)}{dx}\right) + b(0,0)\dfrac{d\varphi(0)}{dx} + c\varphi(0) = \aleph(0,0), \\ -\dfrac{\partial}{\partial x}\left(a(l,0)\dfrac{d\varphi(l)}{dx}\right) + b(l,0)\dfrac{d\varphi(l)}{dx} + c\varphi(l) = \aleph(l,0). \end{cases} \tag{8}$$

Lemma 2. Let $\dfrac{\partial a}{\partial x}, \dfrac{\partial b}{\partial x}, c, \aleph \in C^2(\overline{\Omega})$ and

$$\alpha + \pi^{-2} l^2 \zeta_0 > 0, \text{ where } \zeta_0 = \min_{\overline{Q}} \left(c - \frac{1}{2}\frac{\partial b}{\partial x}\right). \tag{9}$$

Accordingly, the solution of Eq. (1) satisfies the ensuing estimations as established in [13, 16-17].

$$\left|\frac{\partial^{k+z}w}{\partial t^k \partial x^z}\right| \le C\varepsilon^{-k},\ (x,t)\in\overline{Q},\quad k=0,1;\ \ z=0,1,2. \tag{10}$$

Proof. Multiply both sides of Eq. (1) by $w(x,t)$. In this case, we obtain

$$\left(\ell w, w\right)_0 = \left(\aleph, w\right)_0. \tag{11}$$

Expanding Eq. (11) through the inner product yields:

$$\left(-\varepsilon\frac{\partial^3 w}{\partial t\partial x^2}, w\right)_0 + \left(\varepsilon\frac{\partial w}{\partial t}, w\right)_0 - \left(\frac{\partial}{\partial x}\left(a\frac{\partial w}{\partial t}\right), w\right)_0 + \left(b\frac{\partial w}{\partial x}, w\right)_0 + \left(cw, w\right)_0 = \left(\aleph, w\right)_0.$$

We now employ the technique of energy-based inequalities, achieved by performing a scalar multiplication with $w(x,t)$ wherein

$\left(w,v\right) = \int_0^l wv\,dx,\ \|w\|_0^2 = \left(w,w\right)_0$. Here

$$\left(-\varepsilon\frac{\partial^3 w}{\partial t\partial x^2}, w\right)_0 = -\varepsilon\int_0^l \frac{\partial^3 w}{\partial t\partial x^2} w\,dx = \frac{\varepsilon}{2}\frac{\partial}{\partial t}\left\|\frac{\partial w}{\partial x}\right\|_0^2,$$

$$\left(\varepsilon\frac{\partial w}{\partial t}, w\right)_0 = \int_0^l \varepsilon\frac{\partial w}{\partial t} w\,dx = \frac{1}{2}\int_0^l \left(w^2\right)_t dx = \frac{\varepsilon}{2}\frac{\partial}{\partial t}\int_0^l w^2 dx = \frac{\varepsilon}{2}\frac{\partial}{\partial t}\|w\|_0^2,$$

$$\left(\left(aw_x\right)_x, w\right)_0 = \int_0^l \left(aw_x\right)_x w\,dx = \left[aw_x w\right]_0^l - \alpha\int_0^l w_x^2 dx = -\alpha\left\|\frac{\partial w}{\partial x}\right\|_0^2,$$

since $a(x,t)\ge\alpha>0$,

$$\left(bw_x, w\right)_0 = \int_0^l bw_x w\,dx = \int_0^l b\left(w^2\right)_x dx = \left(w^2 b\right)_0^l - \frac{1}{2}\frac{\partial b}{\partial x}\int_0^l w^2 dx$$

$$= -\frac{1}{2}\frac{\partial b}{\partial x}\|w\|_0^2,$$

$$\left(cw, w\right)_0 = \int_0^l cw^2 dx = c\|w\|_0^2,\ \text{ since }\ c\in C^2\left(\overline{\Omega}\right),$$

$$\left|\left(\aleph, w\right)\right| \le \|w\|_0\|\aleph\|_0.$$

Upon inserting this expression into Eq. (1) and performing subsequent algebraic manipulations, we obtain:

$$\frac{\varepsilon}{2}\frac{d}{dt}\left(\left\|\frac{\partial w}{\partial x}\right\|_0^2 + \|w\|_0^2\right) \le -\alpha\left\|\frac{\partial w}{\partial x}\right\|_0^2 + \frac{1}{2}\frac{\partial b}{\partial x}\|w\|_0^2 - c\|w\|_0^2 + \|w\|_0\|\aleph\|_0,$$

$$\varepsilon\frac{d}{dt}\left(\left\|\frac{\partial w}{\partial x}\right\|_0^2 + \|w\|_0^2\right) \le -2\alpha\left\|\frac{\partial w}{\partial x}\right\|_0^2 + \frac{\partial b}{\partial x}\|w\|_0^2 - 2c\|w\|_0^2 + 2\|w\|_0\|\aleph\|_0,$$

$$\le -2\alpha\left\|\frac{\partial w}{\partial x}\right\|_0^2 - 2\left(c - \frac{1}{2}\frac{\partial b}{\partial x}\right)\|w\|_0^2 + 2\|w\|_0\|\aleph\|_0,$$

$$\le -2\alpha\left\|\frac{\partial w}{\partial x}\right\|_0^2 - 2\xi_0\|w\|_0^2 + 2\|w\|_0\|\aleph\|_0,$$

$$= -2\alpha\left\|\frac{\partial w}{\partial x}\right\|_0^2 - 2\xi_0\|w\|_0^2 + \Re(t),$$

where $\Re(t) = 2\|w\|_0\|\aleph\|_0$. Now, we have two cases:

1. If $\alpha\le\xi_0$, then

$$\varepsilon\chi'(t) \le -2\alpha\chi(t) + \Re(t), \tag{12}$$

where $\chi(t) = \left\|\frac{\partial w}{\partial x}\right\|_0^2 + \|w\|_0^2$.

2. Given $\alpha\le\xi_0$, and $0<\vartheta<1$, employing the embedding inequality in Eq. (6) leads to the following result:

$$\alpha\left\|\frac{\partial w}{\partial x}\right\|_0^2 + \xi_0\|w\|_0^2 = \alpha(1-\vartheta)\left\|\frac{\partial w}{\partial x}\right\|_0^2 + \alpha\vartheta\left\|\frac{\partial w}{\partial x}\right\|_0^2 + \xi_0\|w\|_0^2,$$

$$\ge \alpha(1-\vartheta)\left\|\frac{\partial w}{\partial x}\right\|_0^2 + \left(\alpha\vartheta\frac{\pi^2}{l^2} + \xi_0\right)\|w\|_0^2,$$

choosing ϑ from equality $\alpha(1-\vartheta) = \alpha\vartheta\frac{\pi^2}{l^2}$ and considering Eq. (9), we obtain

$$\vartheta = \frac{1-\alpha^{-1}\xi_0}{1+\pi^2 l^{-2}};\ \ 1-\vartheta = \frac{\pi^2 l^{-2}+\alpha^{-1}\xi_0}{1+\pi^2 l^{-2}}.$$

By inserting these expressions into the preceding equation, we arrive at:

$$\varepsilon\chi'(t) \le -2\frac{\alpha\pi^2 l^{-2}+\xi_0}{1+\pi^2 l^{-2}}\chi(t) + \Re(t). \tag{13}$$

Hence, combining the results of Eqs. (12) and (13) yields:

$$\varepsilon\chi'(t) \le -2c_0\chi(t) + \Re(t),$$
$$\text{where } c_0 = \begin{cases} \alpha & \text{if } \alpha\le\xi_0 \ \text{ for case 1,} \\ \dfrac{\alpha\pi^2 l^{-2}+\xi_0}{1+\pi^2 l^{-2}} & \text{if } \alpha>\xi_0 \ \text{ for case 2.} \end{cases} \tag{14}$$

Furthermore, for $\Re(t)$ expression, by using $\left|\left(w,v\right)\right| \le \mu\|w\|^2 + \frac{1}{4\mu}\|v\|^2$ inequality, we obtain

$$2\|w\|_0\|\aleph\|_0 \le 2c_0\|w\|_0^2 + \frac{1}{2c_0}\|\aleph\|_0^2 \Rightarrow 2\|w\|_0\|\aleph\|_0 \le c_0\|w\|_0^2 + \frac{1}{c_0}\|\aleph\|_0^2,$$

where $c_0 = 2c_0$ is a constant. Now, substituting this values in place of $\Re(t)$, we have

$$\varepsilon\chi'(t) \le -2c_0\chi(t) + c_0\|w\|_0^2 + \frac{1}{c_0}\|\aleph\|_0^2 \le -c_0\chi(t) + c_0^{-1}\|\aleph\|_0^2.$$

Since $-c_0\left\|\frac{\partial w}{\partial x}\right\|_0^2$ is a constant and omitting from the expression, we get

$$\varepsilon\chi'(t) \le -c_0\chi(t) + c_0^{-1}\|\aleph\|_0^2. \tag{15}$$

From Eq. (15) and Gronwalls's inequality, the integrating factor is $I.F = e^{\int(p(x))dx}$, where $p(x)$ depends on x. After some manipulation, we obtain:

$$\frac{d\chi(t)}{dt}e^{\frac{c_0}{\varepsilon}t} \le -\frac{c_0}{\varepsilon}\chi(t)e^{\frac{c_0}{\varepsilon}t} + \frac{c_0^{-1}}{\varepsilon}\|\aleph\|_0^2 e^{\frac{c_0}{\varepsilon}t}, \text{ multiply by I.F}$$

$$\Rightarrow \frac{d}{dt}\left(\chi(t)e^{\frac{c_0}{\varepsilon}t}\right) \le \frac{c_0^{-1}}{\varepsilon}\|\aleph\|_0^2 e^{\frac{c_0}{\varepsilon}t},$$

integrating both sides with respect to t

$$\Rightarrow \chi(t)e^{\frac{c_0}{\varepsilon}t} \le \frac{c_0^{-1}}{\varepsilon}\int_0^t \|\aleph(\tau)\|_0^2 e^{-\frac{c_0}{\varepsilon}(t-\tau)}d\tau + \chi(0),$$

$$\Rightarrow \chi(t) = \chi_0 e^{-\frac{c_0}{\varepsilon}t} + c_0^{-2}\max_{0\le\tau\le t}\|\aleph(\tau)\|_0^2\left(1-e^{-\frac{c_0 t}{\varepsilon}}\right),$$

where $\chi_0 = \|\varphi\|_1^2$

Thus, from the above, we get

$$\left\|\frac{\partial w}{\partial x}\right\|_0^2 + \|w\|_0^2 \le \chi_0 e^{-\frac{c_0 t}{\varepsilon}} + c_0^{-2}\max_{0\le\tau\le t}\|\aleph(\tau)\|_0^2,$$

$$\text{since } \max\left(1-e^{-\frac{c_0 t}{\varepsilon}}\right) = 1.$$

Next, by embedding inequality and Poincare inequality, $\frac{l}{4}\left\|\frac{\partial w}{\partial x}\right\|_0^2 \ge \left\|\frac{\partial w}{\partial x}\right\|_{\infty,\Omega}^2$, we get

$$\|w\|_{\infty,\Omega}^2 \le \frac{l}{4}\chi_0 e^{-\frac{c_0 t}{\varepsilon}} + \frac{l}{4}c_0^{-2}\max_{0\le\tau\le t}\|\aleph(\tau)\|_0^2 \Rightarrow |w(x,t)|$$

$$\le \frac{\sqrt{l}}{2}\left(\chi_0^{1/2}e^{-\frac{c_0 t}{\varepsilon}} + c_0^{-1}\max_{0\le\tau\le t}\|\aleph(\tau)\|_0\right),$$

which proves Eq. (10) for $z = k = 0$. Again multiply Eq. (1) by $\frac{\partial^2 w}{\partial x^2}$, we obtain

$$\varepsilon\left(\frac{\partial w}{\partial t}, \frac{\partial^2 w}{\partial x^2}\right)_0 - \varepsilon\left(\frac{\partial^3 w}{\partial t\partial x^2}, \frac{\partial^2 w}{\partial x^2}\right)_0 - \left(\frac{\partial}{\partial x}\left(a\frac{\partial w}{\partial x}\right), \frac{\partial^2 w}{\partial x^2}\right)_0$$

$$+\left(b\frac{\partial w}{\partial x}, \frac{\partial^2 w}{\partial x^2}\right)_0 + \left(cw, \frac{\partial^2 w}{\partial x^2}\right)_0 = \left(\aleph, \frac{\partial^2 w}{\partial x^2}\right)_0 \Rightarrow \left(\ell u, \frac{\partial^2 w}{\partial x^2}\right)_0$$

$$= \left(\aleph, \frac{\partial^2 w}{\partial x^2}\right)_0.$$

Analogous to the earlier scenarios, following appropriate algebraic manipulations and reorganization, we obtain:

$$\left\|\frac{\partial^2 w}{\partial x^2}\right\|_0^2 \le C, \tag{16}$$

Given that $\varphi'' \in L_2(\Omega)$ and by using the boundedness of $\|w\|_0$ and $\left\|\frac{\partial w}{\partial x}\right\|_0$. The estimate Eq. (16), in turn $\left\|\frac{\partial w}{\partial x}\right\|_{\infty,\Omega} \le C\left\|\frac{\partial^2 w}{\partial x^2}\right\|_0$ gives Eq. (10) for $k = 0, z = 1$. Once more, by utilizing the given identity, $\left(\ell w, \frac{\partial^3 w}{\partial x^2\partial t}\right)_0 = \left(\aleph, \frac{\partial^3 w}{\partial x^2\partial t}\right)_0$, we obtain

$$\left\|\frac{\partial^3 w}{\partial t\partial x^2}\right\|_0^2 + \left\|\frac{\partial^2 w}{\partial t\partial x^2}\right\|_0^2 \le \frac{C}{\varepsilon^2}\left(\|w\|_0^2 + \left\|\frac{\partial w}{\partial x}\right\|_0^2 + \left\|\frac{\partial^2 w}{\partial x^2}\right\|_0^2 + \|\aleph\|_0^2\right),$$

which leads to Eq. (10) for $k = 1, z = 0,1$ by using just proved estimates for $\left\|\frac{\partial^z w}{\partial x^z}\right\|_0^2, (z = 0,1,2)$.

In conclusion, expressing Eq. (1) in the following form yields:

$$\varepsilon\frac{\partial^3 w}{\partial x^2\partial t} + a(x,t)\frac{\partial^2 w}{\partial x^2} = \Gamma(x,t),$$

with

$$\Gamma(x,t) = \varepsilon\frac{\partial w}{\partial t} - \frac{\partial a}{\partial x}\frac{\partial w}{\partial x} + b\frac{\partial w}{\partial x} + cw - \aleph, \text{ and } |\Gamma(x,t)| \le C,$$

The estimates Eq. (10) then follows immediately for $k = 0,1$, $z = 2$.

Lemma 3. Assume $\frac{\partial a}{\partial t}, \frac{\partial^2 a}{\partial t\partial x}, \frac{\partial b}{\partial t}, \frac{\partial c}{\partial t}, \frac{\partial\aleph}{\partial t} \in C(\overline{\Omega})$ and assumptions of Lemma 2 are valid. Then the estimate:

$$\left\|\frac{\partial^{l+z}w}{\partial t\partial x^z}\right\| \le C\left\{1 + \frac{1}{\varepsilon}e^{-\frac{\alpha_0 t}{\varepsilon}}\right\}, \ t \in [0,T], \ z = 0,1,2, \tag{17}$$

holds where $\alpha_0 = c_0/2$ and c_0 is given by Eq. (14).

Proof. The argument is presented in [16-17, 19].

NUMERICAL METHOD IMPLEMENTATION

Mesh Generation and Discretization

The domain Q is partitioned using mesh points $\Lambda = \Lambda_N \times \Lambda_M$, where $\Lambda_N = \{x_i = ih : i = 1(1)N - 1, h = l/N\}$ and $\Lambda_M = \{0 = t_1 < t_2 < \cdots < t_M = T, \tau_j = t_j - t_{j-1}\}$. The temporal mesh Λ_M is chosen as a piecewise-uniform grid. A fitted piecewise-uniform S-mesh is introduced on $[0,T]$ to resolve the initial layer at $t = 0$. The interval is split into $[0,\sigma]$ and $[\sigma,T]$,

each divided into $M/2$ equal parts, with the transition point σ defined as in .

$$\sigma = min\left\{\frac{T}{2}, \alpha_0^{-1}\varepsilon \ln(M)\right\}, \tag{18}$$

where α_0 is constant, $\alpha_0 = c_0/2$ and c_0 is given in Eq. (14). Since $\sigma \ll T$, the mesh is refined over $[0,\sigma]$ and coarser over $[\sigma,T]$. Let τ_1 and τ_2 denote the step sizes these respective subintervals. Now, $\tau_1 = 2\sigma M^{-1}$, $\tau_2 = 2(T-\sigma)M^{-1}$, $\tau_1 \le TM^{-1}, TM^{-1} \le \tau_2 < 2TM^{-1}, \tau_2 + \tau_2 = 2TM^{-1}$, so we get

$$\overline{\Lambda}_M = t_j = \begin{cases} j\tau_1, & \text{if } j = 0(1)M/2, \\ \sigma + (j - M/2)\tau_2, & \text{if } j = M/2(1)M. \end{cases} \tag{19}$$

It is assumed that $\sigma = \alpha_0^{-1}\varepsilon \ln(M)$; otherwise N grows exponentially relative to ε.

Semi-Discretization in Time

The time domain is discretized on an S-mesh with step size τ_j, while x is kept continuous, yielding the following ODE system.

$$\begin{aligned} &-\left(\varepsilon + \tau_j a^{j+1}(x)\right)\left(w_{xx}(x)\right)^{j+1} + d^{j+1}(x)\left(w_x(x)\right)^{j+1} \\ &+\left(\varepsilon + \tau_j c^{j+1}(x)\right)w^{j+1}(x) \\ &+\varepsilon\left(w_{xx}(x)\right)^j - \varepsilon w^j(x) = g(x,t_{j+1}), \\ &w(x,0) = w^0(x) = \varphi(x),\ x\in\overline{\Omega}, \\ &w^{j+1}(0) = w^{j+1}(l) = 0,\ 0 \le j \le M,\ t\in(0,T], \end{aligned} \tag{20}$$

At the $(j+1)th$ time step, Eq. (20) takes the form:

$$\begin{cases} \ell_\varepsilon^M w^{j+1}(x) = -\left(\varepsilon + \tau_j a^{j+1}(x)\right)\left(w_{xx}(x)\right)^{j+1} + d^{j+1}(x)\left(w_x(x)\right)^{j+1} \\ \qquad +\left(\varepsilon + \tau_j c^{j+1}(x)\right)w^{j+1}(x) = g(x,t_{j+1}), \\ \qquad w(x,0) = w^0(x) = \varphi(x),\ x\in\overline{\Omega}, \\ \qquad w^{j+1}(0) = w^{j+1}(l) = 0,\ 0 \le j \le M,\ t\in(0,T], \end{cases} \tag{21}$$

where, $g(x,t_{j+1}) = -\varepsilon\left(w_{xx}(x)\right)^j + \varepsilon w^j(x) + \tau_j \aleph^{j+1}(x)$.

Lemma 3.1. (Semi-Discrete Version of Maximum Principle.) Let $\Phi^{j+1}(x)$ be sufficiently smooth on $\overline{\Lambda}$. If $\Phi^{j+1}(0) \ge 0$, $\Phi^{j+1}(1) \ge 0$ and $\ell_\varepsilon^M \Phi^{j+1}(x) \ge 0, x\in\Lambda$, then $\Phi^{j+1}(x) \ge 0,\ \forall x\in\overline{\Lambda}$.

Proof. Let σ^* is such that $\Phi_{j+1}(\sigma^*) = \min_{x\in\overline{\Omega}} \Phi_{j+1}(0) < 0$. We know that $\sigma^* \notin \{0,1\} \Rightarrow \sigma^* \in (0,1)$. Using extrema values, $\frac{d}{dx}\Phi_{j+1}(\sigma^*) = 0$ and $\frac{d^2\Phi_{j+1}(\sigma^*)}{dx^2} \ge 0$. Then we have

$$\begin{aligned} \ell_\varepsilon^M \Phi^{j+1}(\sigma^*) &= -\left(\varepsilon + \tau_j a^{j+1}(\sigma^*)\right)\left(\Phi_{xx}\right)^{j+1}(\sigma^*) \\ &\quad + d^{j+1}(\sigma^*)\left(\Phi_x\right)^{j+1}(\sigma^*) \\ &\quad + \left(\varepsilon + \tau_j c^{j+1}(\sigma^*)\right)\Phi^{j+1}(\sigma^*), \\ &\le \left(\varepsilon + \tau_j c^{j+1}(\sigma^*)\right)\Phi^{j+1}(\sigma^*), \\ &\le 0,\ as\ \left(\varepsilon + \tau_j c^{j+1}(x)\right) > 0, \end{aligned}$$

given that $\ell_\varepsilon^M \Phi^{j+1}(\sigma^*) < 0$ which is a contradiction to $\ell_\varepsilon^M \Phi^{j+1}(\sigma^*) \ge 0,\ \forall x\in\overline{\Omega}$. Therefore, $\Phi^{j+1}(x) \ge 0, \forall x\in\overline{\Omega}$. Thus, ℓ_ε^M satisfies the semi-discretized form of the maximum principle.

Time Semi-Discretization: Error Analysis

Let $w^{j+1}(x)$ reprent the semi-discrete approximation of the exact solution $w(x,t_{j+1})$ of Eq. (4) at time level τ_j. Then, applying the implict Euler method, the semi-discrete scheme for Eq. (2.1) can be expressed as:

$$\begin{cases} \Upsilon^0(x) = \varphi_0(x),\ x\in\overline{\Omega}, \\ \ell_\in^M \Upsilon^{j+1}(x) = g(x,t_{j+1}), \\ \Upsilon^{j+1}(0) = 0 = \Upsilon^{j+1}(l), 0 \le j \le M, t\in(0,T], \end{cases} \tag{22}$$

where

$$\begin{aligned} \ell_\in^M \Upsilon^{j+1}(x) &= -\left(\in + \tau_j a^{j+1}(x)\right)\left(w_{xx}(x)\right)^{j+1} \\ &\quad + d^{j+1}(x)\left(w_x(x)\right)^{j+1} \\ &\quad + \left(\in + \tau_j c^{j+1}(x)\right)w^{j+1}(x) \end{aligned}$$

and $g(x,t_{j+1}) = -\varepsilon\left(w_{xx}(x)\right)^j + \varepsilon w^j(x) + \tau_j \aleph^{j+1}(x)$.

Definition 3.1. [6, 12, 25, 27, 28] A FDM is stable for $\|.\|$, if there exists positive constants L1 and L2, independent from τ_j, such that when τ_j approaches τ_1 and τ_2, we have

$$\left\|w^j\right\| \le L_1\left\|w^0\right\| + L_2\|\aleph\|.$$

Here, w^0 represents the initial condition, while $\aleph$ denotes the source term.

Lemma 3.2. [22, 27, 28] Let the function $\Upsilon \in C^0\left(\overline{\Lambda}\right) \cap C^2(\Lambda)$. Then we have

$$\|\Upsilon\| \le \|\Upsilon\|_{\partial\Omega} + \left\|\ell_\varepsilon^M \Upsilon^{j+1}(x)\right\|_{\overline{\Lambda}}.$$

Lemma (3.2) ensures that Eq. (22) admits unique solution $\Upsilon^{j+1}(x)$ at time level τ_j. Moreover, by Lemma (3.2), this solution $\Upsilon^{j+1}(x)$ remains uniformly bounded with respect to ε. Define $\Xi^{j+1}(x) = \Upsilon(x,t_{j+1}) - \overline{\Upsilon}(x,t_{j+1})$, as the local

error of Eq. (22) at t_{j+1}, where $\overline{\Upsilon}\left(x,t_{j+1}\right)$ solves the corresponding auxiliary BVP:

$$\begin{cases} \ell_{\varepsilon}^{M}\overline{\Upsilon}^{j+1}\left(x\right)=g\left(x,t_{j+1}\right), \\ \overline{\Upsilon}^{j+1}\left(0\right)=0=\overline{\Upsilon}^{j+1}\left(1\right), \quad 0\le j\le M. \end{cases} \tag{23}$$

Lemma 3.3. (Local Truncation Error(LTE)): The local error $\Xi^{j+1}\left(x\right)$ obeys the following bound:

$$\left\|\Xi^{j+1}\left(x\right)\right\|\le C\left(\Delta t\right)^{2}, \text{ where } \Delta t=M^{-1}\ln\left(M\right). \tag{24}$$

Proof. Depending on the magnitude of σ, there arise two conditions:

1. If $j=0(1)\dfrac{M}{2}$, $t_j=j\tau_1$ and $\tau_1=\dfrac{2\sigma}{M}$, then we have

$$\begin{aligned} \tau_j&=t_j-t_{j-1}=j\tau_1-\left(j-1\right)\tau_1\Rightarrow \\ t_j&=\tau_1=\frac{2\alpha_0^{-1}\varepsilon\ln(M)}{M} \\ &\le KM^{-1}\ln(M), K=2\alpha_0^{-1}\varepsilon \end{aligned}$$

Evaluating at t_{j+1} with $\tau_j=\Delta t=KM^{-1}\ln(M)$ and applying Taylor expansion to Eqs. (19) and (22), we get

$$\begin{cases} \ell_{\varepsilon}^{M}\Xi^{j+1}(x)=K_1\left(M^{-1}\ln(M)\right)^{2},\ K_1=K^2,\ x\in\Omega, \\ \Xi^{j+1}\left(0\right)=0=\Xi^{j+1}\left(l\right),\ j=0(1)M/2. \end{cases} \tag{25}$$

2. If $j=\dfrac{M}{2}+1,...,M$, $t_j=\sigma+\left(j-\dfrac{M}{2}\right)\tau_2$ and $\tau_2=\dfrac{2\left(1-\sigma\right)}{M}$.

Now

$$\begin{aligned} \tau_j=t_j-t_{j-1}&=\sigma+\left(j-M/2\right)\tau_2-\left(\sigma+\left(\left(j-1\right)-M/2\right)\tau_2\right), \\ &=\sigma+\left(j-M/2\right)\tau_2-\sigma-j\tau_2+\tau_2+M/2\tau_2, \\ &=\tau_2=2\frac{1-\alpha_0^{-1}\varepsilon\ln(M)}{M}, \\ &\le K_4M^{-1}, \text{ since } 2\alpha_0^{-1}\varepsilon\ln(M)\le 2M^{-1}. \end{aligned}$$

Considering the estimate at $t_{j+1}=\Delta t_2=K_4M^{-1}$ and applying Taylor series expansion to Eqs. (22) and (19), we get:

$$\begin{cases} \ell_{\varepsilon}^{N,M}\Xi^{j+1}\left(x\right)=K_5\left(M^{-1}\right)^{2},\ K_5=K_4^2,\ x\in\Omega, \\ \Xi^{j+1}\left(0\right)=0=\Xi^{j+1}\left(l\right),\ j=(M/2)+1(1)M. \end{cases} \tag{26}$$

Applying Lemma (3.2) to $\Xi^{j+1}\left(x\right)$ yields estimates for both regions. The total LTE is expressed as the sum of the finer-and coarse-mesh contributions, i.e.,

$$\begin{aligned} \left\|\Xi^{j+1}\left(x\right)\right\|&=K_1\left(M^{-1}\ln(M)\right)^{2}+K_5\left(M^{-1}\right)^{2}, \\ &=C\left(M^{-1}\ln(M)\right)^{2},\ C=K_1+K_5\left(M^{-1}\right)^{2}. \end{aligned} \tag{27}$$

Lemma 3.4. (Global Error). The global error $\Sigma^{j}\left(x\right)$ is bounded at t_j as follows:

$$\sup_{(j+1)\Delta t\le T}\le K_*\left(\Delta t\right),\ \Delta t=M^{-1}\ln(M). \tag{28}$$

Proof. Let $\left\|\Sigma^{j}\left(x\right)\right\|=\Upsilon(x,t_{j+1})-\overline{\Upsilon}(x,t_{j+1})$. By applying Eq. (27) togher with Lemma (3.3), we obtain the global error at $(j+1)th$ time step.

$$\begin{aligned} \left\|\Sigma^{j}\left(x\right)\right\|_{\infty}&=\left|\sum_{l=1}^{j}\Xi_l\right|,\ j\le T/\Delta t,\ \Delta t=K\left(M^{-1}\ln(M)\right)^{2}, \\ &\le\left\|\Xi_1\right\|_{\infty}+\left\|\Xi_2\right\|_{\infty}+...+\left\|\Xi_j\right\|_{\infty}, \\ &\le C_1j\left(\Delta t\right)^{2},\quad \text{using } Eq.(3.10) \\ &\le C_1\left(jM^{-1}\ln(M)\right)\left(M^{-1}\ln(M)\right), \\ &\le C_1T\left(M^{-1}\ln(M)\right), \text{ as } j\left(M^{-1}\ln(M)\right)\le T, \\ &\le C_4\left(M^{-1}\ln(M)\right),\quad C_4=C_3T. \end{aligned}$$

Spatial Semi-Discretization

The TCBS method is employed to approximate the solution of Eq. (21) and its spatial derivatives using linear spline expansions.

Cubic Trigonometric B-Spline Techniques

The domain Λ divided into N equal intervals, the approximate solution at $(j+1)th$ is expressed as:

$$W\left(x,t\right)=\sum_{i=-1}^{N+1}\delta_i\left(t\right)CTB_i\left(x\right), \tag{29}$$

where $\delta_i(t)$ are determined to approximate $W(x,t)$ to exact solution $W_e(x,t)$ at (x_i, t_j), and $CTB_i(x)$ represent the TCBS basis functions , which is given as[29-30]

$$CTB_i\left(x\right)=\frac{1}{\vartheta}\begin{cases} \sin^3\left(\xi_1\right), & \text{if } \left[x_{i-2},x_{i-1}\right] \\ \sin\left(\xi_1\right)\left[\sin\left(\xi_1\right)\sin\left(\xi_2\right)+\sin\left(\xi_3\right)\sin\left(\xi_4\right)\right] & \\ \quad+\sin^2\left(\xi_4\right)\sin\left(\xi_5\right), & \text{if } \left[x_{i-1},x_i\right], \\ \sin\left(\xi_5\right)\left[\sin\left(\xi_4\right)\sin\left(\xi_3\right)+\sin\left(\xi_5\right)\sin\left(\xi_6\right)\right] & \\ \quad+\sin\left(\xi_1\right)\sin^2\left(\xi_3\right), & \text{if } \left[x_i,x_{i+1}\right] \\ \sin^3\left(\xi_5\right), & \text{if } \left[x_{i+1},x_{i+2}\right] \\ 0, & \text{otherwise,} \end{cases} \tag{30}$$

where, $\vartheta=\sin\left(\xi\right)\sin\left(2\xi\right)\sin\left(3\xi\right)$, $\xi=\dfrac{h}{2}$, $\xi_1=\dfrac{x-x_{i-2}}{2}$, $\xi_2=\dfrac{x_i-x}{2}$, $\xi_3=\dfrac{x_{i+1}-x}{2}$, $\xi_4=\dfrac{x-x_{i-1}}{2}$, $\xi_5=\dfrac{x_{i+2}-x}{2}$ and $\xi_6=\dfrac{x-x_i}{2}$. Consider the iterative relation provided in Eq. (31).

Table 1. The values of $CTB_i(x)$, $CTB_i'(x)$ and $CTB_i''(x)$ at the nodal points obtained using Eq. (30)

	x_{i-2}	x_{i-1}	x_i	x_{i+1}	x_{i+2}
$CTB_i(x)$	0	μ_1	μ_2	μ_1	0
$CTB_i'(x)$	0	μ_3	0	μ_4	0
$CTB_i''(x)$	0	μ_5	μ_6	μ_5	0

$$CTB_i^k(x) = \frac{\sin\left(\frac{x-x_i}{2}\right)}{\sin\left(\frac{x_{i+k-1}-x_i}{2}\right)} CTB_i^{k-1}(x) + \frac{\sin\left(\frac{x_{i+k}-x}{2}\right)}{\sin\left(\frac{x_{i+k}-x_{i+1}}{2}\right)} CTB_i^{k-1}(x), \quad k = 2,\ldots. \tag{31}$$

This iterative formula defines TCBS, beginning with first order case. Table 1 display $CTB_i(x)$ and its derivative values at the mesh points.

Table 1 lists the entries as:

$$\mu_1 = \sin^2(\zeta)\csc(2\zeta)\csc(3\zeta),\ \mu_2 = \frac{2}{1+2\cos(2\zeta)},$$
$$\mu_3 = -\frac{3}{4}\csc(3\zeta),\ \mu_4 = \frac{3}{4}\csc(3\zeta),$$
$$\mu_5 = \frac{3(1+3\cos(2\zeta))\csc^2(\zeta)}{16(2\cos(\zeta)+\cos)(3\zeta)},\ \mu_6 = \frac{-3\cot^2(3\zeta)}{2+4\cos(2\zeta)},$$

where $\zeta = \frac{h}{2}$.

The approximation W_i^j at (x_i, t_j) over sub-interval $[x_i, x_{i+1}]$ is given as:

$$W_i^j = \sum_{i=-1}^{N+1} \delta_i^{j+1} CTB_i(x). \tag{32}$$

Owing to the local support of B-splines, only $CTB_{i-1}(x)$, $CTB_i(x)$ and $CTB_{i+1}(x)$ are non-zero on the given interval. Using Eqs. (30) and (32), the nodal values and derivatives of W_i^j are expressed through the time parameters δ_i^{j+1} as follows:

$$\begin{cases} W_i^{j+1} = \mu_1\delta_{i-1}^{j+1} + \mu_2\delta_i^{j+1} + \mu_1\delta_{i+1}^{j+1}, \\ (W_x)_i^{j+1} = \mu_3\delta_{i-1}^{j+1} + \mu_4\delta_{i+1}^{j+1}, \\ (W_{xx})_i^{j+1} = \mu_5\delta_{i-1}^{j+1} + \mu_6\delta_i^{j+1} + \mu_5\delta_{i+1}^{j+1}. \end{cases} \tag{33}$$

The approximate solution at the mesh boundaries is obtained from Eq. (32) combined with the boundary conditions in (2.1) as follows:

$$\begin{cases} W(x_0, t_{j+1}) = \mu_1\delta_{-1}^{j+1} + \mu_2\delta_0^{j+1} + \mu_1\delta_1^{j+1} = 0, \\ W(x_N, t_{j+1}) = \mu_1\delta_{N-1}^{j+1} + \mu_2\delta_N^{j+1} + \mu_1\delta_{N+1}^{j+1} = 0. \end{cases} \tag{34}$$

Once δ_i is computed and $CTB_i(x)$ with its derivatives are substituted into Eq. (21), we obtain $N + 1$ equations with $N + 3$ unknowns.

$$\ell_\varepsilon^{N,M} W = r_i^- \delta_{i-1}^{j+1} + r_i^c \delta_i^{j+1} + r_i^+ \delta_{i+1}^{j+1} = E_i^- \delta_{i-1}^j + E_i^c \delta_i^j + E_i^+ \delta_{i+1}^j + F_i, \quad \text{for } i = 0,1,\ldots,N, \tag{35}$$

where, the coefficients take the following form

$$\begin{cases} r_i^- = \varepsilon(\mu_1 - \mu_5) - \tau_j\mu_5 a_i^{j+1} + \tau_j\mu_3 a_i^{j+1} + \tau_j\mu_1 c_i^{j+1}, \\ r_i^c = \varepsilon(\mu_2 - \mu_6) - \tau_j\mu_6 a_i^{j+1} + \tau_j\mu_2 c_i^{j+1}, \\ r_i^+ = \varepsilon(\mu_1 - \mu_5) - \tau_j\mu_5 a_i^{j+1} + \tau_j\mu_3 d_i^{j+1} + \tau_j\mu_1 c_i^{j+1}, \\ E_i^- = \varepsilon(\mu_1 - \mu_5),\ E_i^c = \varepsilon(\mu_2 - \mu_6), \\ E_i^+ = \varepsilon(\mu_1 - \mu_5),\ F_i = \tau_j \aleph_i^{j+1}. \end{cases} \tag{36}$$

Treatement of boundary conditions

To eliminate δ_{-1} and δ_{N+1} from Eq. (35), we apply boundary conditions given in Eq. (34). Now, for $i = 0$, Eq. (35) is reduced to

$$\left(r_0^c - r_0^- \frac{\mu_2}{\mu_1}\right)\delta_0^{j+1} + \left(r_0^+ - r_0^-\right)\delta_1^{j+1} = \left(E_0^c - E_0^- \frac{\mu_2}{\mu_1}\right)\delta_0^j + \left(E_0^+ - E_0^-\right)\delta_1^j + F_0. \tag{37}$$

Eq. (35) simplified to the form for $i = N$

$$\left(r_N^- - r_N^+\right)\delta_{N-1}^{j+1} + \left(r_N^c - r_N^+ \frac{\mu_2}{\mu_1}\right)\delta_N^{j+1} = \left(E_N^- - E_N^+\right)\delta_{N-1}^j + \left(E_N^c - E_N^+ \frac{\mu_2}{\mu_1}\right)\delta_N^j + F_N. \tag{38}$$

Now, Eqs. (35)- (38) lead to $(N + 3) \times (N + 3)$ system with $(N + 3)$ unkowns $\delta_{-1}, \delta_0, \ldots, \delta_N, \delta_{N+1}$. Excluding the unkowns δ_{-1} and δ_{N+1} from Eq. (37) and Eq. (38) for $i = 0$ and $i = N$, then Eq. (35) becomes $(N + 1) \times (N + 1)$.

equations with $(N + 1)$ unknowns $\delta_0, ..., \delta_{N-1}, \delta_N$ in matrix form as

$$A\delta_i^{j+1} = B\delta_i^j + F, \quad i = 1,2,...,N-1. \tag{39}$$

The elements of the tridiagonal matrices $A = \omega_{ij}$ and $B = \psi_{ij}$ are defined as follows:

$$A = \begin{bmatrix} p_1 & p_2 & 0 & 0 & \dots & 0 & 0 & 0 \\ r_1^- & r_1^c & r_1^+ & 0 & \cdots & 0 & 0 & 0 \\ 0 & r_2^- & r_2^c & r_2^+ & \cdots & 0 & 0 & 0 \\ \vdots & \vdots & \vdots & \ddots & \ddots & \vdots & \vdots & \vdots \\ 0 & 0 & 0 & 0 & \cdots & r_{N-1}^- & r_N^c & r_{N+1}^+ \\ 0 & 0 & 0 & 0 & \cdots & 0 & p_3 & p_4 \end{bmatrix},$$

$$B = \begin{bmatrix} p_5 & p_6 & 0 & 0 & \dots & 0 & 0 & 0 \\ E_1^- & E_1^c & E_1^+ & 0 & \cdots & 0 & 0 & 0 \\ 0 & E_2^- & E_2^c & E_2^+ & \cdots & 0 & 0 & 0 \\ \vdots & \vdots & \vdots & \ddots & \ddots & \vdots & \vdots & \vdots \\ 0 & 0 & 0 & 0 & \cdots & E_{N-1}^- & E_N^c & E_{N+1}^+ \\ 0 & 0 & 0 & 0 & \cdots & 0 & p_7 & p_8 \end{bmatrix}.$$

The entries of the given matrix are

$$p_1 = \left(r_0^c - r_0^- \frac{\mu_2}{\mu_1}\right),\ p_2 = \left(r_0^+ - r_0^-\right),$$

$$p_3 = \left(r_N^- - r_N^+\right),\ p_4 = \left(r_N^c - r_N^+ \frac{\mu_2}{\mu_1}\right),$$

$$p_5 = \left(E_0^c - E_0^- \frac{\mu_2}{\mu_1}\right),\ p_6 = \left(E_0^+ - E_0^-\right),$$

$$p_7 = \left(E_N^- - E_N^+\right), p_8 = \left(E_N^c - E_N^+ \frac{\mu_2}{\mu_1}\right).$$

The vectors δ^{j+1} and F are defined as:

$$\delta_i^{j+1} = \left(\delta_{-1}^{j+1}, \delta_0^{j+1}, \delta_N^{j+1}, \delta_{N+1}^{j+1}\right)^T \text{ and } F = \tau_j\left(\aleph_0^{j+1}, \aleph_1^{j+1}, ..., \aleph_N^{j+1}, \aleph_{N+1}^{j+1}\right)^T.$$

Rearranging Eq. (39) gives

$$A\overline{\mathrm{X}} = \mathrm{H}, \text{ where } \overline{\mathrm{X}} = \delta^{j+1}, \text{ and } \mathrm{H} = B\delta_i^j + F. \tag{40}$$

The initial vector $\left(\delta_{-1}^0, ..., \delta_{N+1}^0\right)$ is determined by solving the corresponding interpolation for Eq. (35).

$$\begin{cases} \left(\dfrac{\partial W^0}{\partial x}\right)_0 = \left(\dfrac{\partial \varphi^0}{\partial x}\right)_0, & i = 0, \\ W^0\left(x_i\right) = \varphi^0\left(x_i\right), & i = 0(1)N, \\ \left(\dfrac{\partial W^0}{\partial x}\right)_l = \left(\dfrac{\partial \varphi^0}{\partial x}\right)_l, & i = N, \end{cases} \tag{41}$$

where $W^0\left(x\right) = \sum_{i=-1}^{N+1} \delta_i^0 CTB_i\left(x\right)$. Eq. (41), formulated for the initial conditions, consists of $N + 1$ equations and $N + 3$ unknowns. To solve the system, δ_{-1}^0 and δ_{N+1}^0 must be eliminated. After simplications, we obtain:

$$\begin{cases} \mu_2\,\delta_0^0 + \left(\mu_1 - \dfrac{\mu_1\mu_4}{\mu_3}\right)\delta_1^0 = \varphi(0) - \dfrac{\mu_1}{\mu_3}\varphi'(0), \\ \mu_1\,\delta_{i-1}^0 + \mu_2\,\delta_i^0 + \mu_1\,\delta_{i+1}^0 = \varphi\left(x_i\right), \quad i = 1(N-1), \\ \left(\mu_1 - \dfrac{\mu_1\mu_4}{\mu_3}\right)\delta_{N-1}^0 + \mu_2\,\delta_N^0 = \varphi\left(x_N\right) - \dfrac{\mu_1}{\mu_3}\varphi'\left(x_N\right). \end{cases} \tag{42}$$

Now, Eq. (42) gives $(N + 1) \times (N + 1)$ system of equations. This system is easily solved for δ_0^0 using matrix inversion algorithm and provides the initial values for Eq. (39).

Stability Analysis

This section applies Von-Neumann stability analysis [8] to examine the scheme's stability. At knots with $\aleph(x,t) = 0$, substituting $W(x,t)$ and its derivatives into Eq. (35) yields the following difference equation in δ_i:

$$r_i^-\delta_{i-1}^{j+1} + r_i^c\delta_i^{j+1} + r_i^+\delta_{i+1}^{j+1} = E_i^-\delta_{i-1}^j + E_i^c\delta_i^j + E_i^+\delta_{i+1}^j, \tag{43}$$

where r_i^-, r_i^c, r_i^+ and E_i^-, E_i^c, E_i^+ are given in Eq. (36). Substituting trial solution

$$\delta_n^l = \zeta^l e^{in\eta h}, \tag{44}$$

where η is the wave number, l is the time level, ζ^l the Fourier coefficient, h the spatial step, $i = \sqrt{-1}$ the imaginary unit, and η the node index, into Eq. (43) gives:

$$\begin{aligned} &r_i^-\zeta^{l+1}e^{i(n-1)\eta h} + r_i^c\zeta^{l+1}e^{i(n)\eta h} + r_i^+\zeta^{l+1}e^{i(n+1)\eta h} = \\ &E_i^-\zeta^l e^{i(n-1)\eta h} + E_i^c\zeta^l e^{in\eta h} + E_i^+\zeta^l e^{i(n+1)\eta h}. \end{aligned} \tag{45}$$

Dividing Eq. (45) by $e^{in\varphi}$, where $\varphi = \eta h$ and rearranging to obtain

$$\frac{\zeta^{l+1}}{\zeta^l} = \Pi = \frac{E_i^c + E_i^-e^{-i\varphi} + E_i^+e^{i\varphi}}{r_i^c + r_i^-e^{-i\varphi} + r_i^+e^{i\varphi}}, \tag{46}$$

where Π is intensification factor. The error plenty should not intensify, so it is $|\Pi| \le 1$. Eq. (46) is reformulated by using Euler relation $e^{\pm i\varphi} = \cos(\varphi) \pm i\sin(\varphi)$,

$$\Pi = \frac{E_i^c + \left(E_i^- + E_i^+\right)\cos(\varphi) + i\left(E_i^+ + E_i^-\right)\sin(\varphi)}{r_i^c + \left(r_i^- + r_i^+\right)\cos(\varphi) + i\left(r_i^+ + r_i^-\right)\sin(\varphi)}. \tag{47}$$

From, Eq. (47), we obtain

$$\Pi = \frac{X_1 + iY_1}{X_2 + iY_2}. \tag{48}$$

By applying basic arithmetic manipulations to the complex numbers, Eq. (48) can be expressed in the following form:

$$\Pi = \frac{X_1X_2 + Y_1Y_2}{X_2^2 + Y_2^2} + i\frac{Y_1X_2 - X_1Y_2}{X_2^2 + Y_2^2}, \tag{49}$$

where

$$\begin{cases} X_1 = E_i^c + \left(E_i^- + E_i^+\right)\cos(\varphi),\ Y_1 = \left(E_i^+ + E_i^-\right)\sin(\varphi), \\ X_2 = r_i^c + \left(r_i^- + r_i^+\right)\cos(\varphi), \quad Y_2 = \left(r_i^+ + r_i^-\right)\sin(\varphi). \end{cases}$$

Since Π is a complex number, stability condition $|\Pi| \le 1$ yields the relation

$$|\Pi| = \sqrt{\left(\frac{X_1X_2 + Y_1Y_2}{X_2^2 + Y_2^2}\right)^2 + \left(\frac{Y_1X_2 - X_1Y_2}{X_2^2 + Y_2^2}\right)^2} \le 1. \tag{50}$$

By inserting $X_i, Y_i\ (i = 1,2)$ into Eq. (50) and since $\varphi = \eta h, 0 \le \varphi \le \pi$, the equation needs verification only at extreme values. Setting $\varphi = \pi$, gives:

$$\left(\frac{E_i^- - E_i^c + E_i^+}{r_i^- - r_i^c + r_i^+}\right)^2 \le 1. \tag{51}$$

The inequality in Eq. (51) can be expressed equivalently as:

$$-1 \le \frac{E_i^- - E_i^c + E_i^+}{r_i^- - r_i^c + r_i^+} \le 1. \tag{52}$$

Substitution of these values of parameters r_i^-, r_i^c, r_i^+ and E_i^-, E_i^c, E_i^+ yields the relation

$$-1 \le \frac{\varepsilon\left(2\mu_1 - \mu_2\right) + \varepsilon\left(\mu_6 - 2\mu_5\right)}{\Xi_1\left(2\mu_1 - \mu_2\right) + \Xi_2\left(\mu_6 - 2\mu_5\right) + \Xi_3} \le 1 \Rightarrow |\Pi| \le 1, \tag{53}$$

where $\Xi_1 = \varepsilon + \tau_j c_i^{j+1}$, $\Xi_2 = \varepsilon + \tau_j a_i^{j+1}$ and $\Xi_3 = 2\mu_3\tau_j d_i^{j+1}$. The inequalities in Eq. (53) hold universally, guaranteeing a non-vanishing denominator. Since the eigenvalue modulus does not exceed unity, the scheme with $\aleph(x,t) = 0$ is unconditionally stable, as shown in Eq. (4.12). This stability extends to the general case $\aleph(x,t)$ by Duhamel's principle [25], which asserts that stability for $P_{k,h}V = \aleph$ follows from stability for $P_{k,h}V = 0$. Consequently, no constraints are imposed on the spatial grid or temporal step size, though their selection should enhance the scheme's accuracy [8].

Analysis of Convergence

Lemma 5.1. [8, 30] The TCBS: $CTB_{-1},...,CTB_{N+1}$ given in Eq. (32) gratify the inequality:

$$\sum_{i=-1}^{N+1}\left|CTB_i(x)\right| \le 6, \quad 0 \le x \le 1. \tag{50}$$

Proof. As $\left|\sum_{i=-1}^{N+1} CTB_i(x)\right| \le \sum_{i=-1}^{N+1}\left|CTB_i(x)\right|$, at $x = x_i$, right side of Eq. (50)

$$\begin{aligned}\sum_{i=-1}^{N+1}\left|CTB_i(x)\right| &= \left|CTB_{i-2}(x)\right| + \left|CTB_{i-1}(x)\right| \\ &\quad + \left|CTB_i(x)\right| + \left|CTB_{i+1}(x)\right|, \\ &= |\mu_2| + |\mu_1| + |\mu_1| + |\mu_2| \le 6.\end{aligned}$$

Thus, for all $x \in [0,1]$, we have

$$\begin{aligned}\sum_{i=-1}^{N+1}\left|CTB_i(x)\right| &= \left|CTB_{i-1}(x)\right| + \left|CTB_i(x)\right| \\ &\quad + \left|CTB_{i+1}(x)\right| \le 6.\end{aligned}$$

Lemma 5.2. The approximation $CTB(x)$ from Eq. (32) is uniformly bounded, that is $\left|CTB(x)\right| \le C$, $\forall x \in \overline{\Omega}$.

Proof. For the proof, we refer the reader to [8, 26, 29].

Let $\overline{w}(x)$, be the exact solution of BVPs Eq. (35)-(38), and also $W(x) = \sum_{i=-1}^{N+1}\delta_i CTB_i(x)$ be the TCBS approximation to the exact solution. Due to the round of errors[24, 29], let $\overline{W}(x) = \sum_{i=-1}^{N+1}\overline{\delta}_i CTB_i(x)$ is the computed CTBS approximation to $\overline{w}(x)$, where $\overline{\delta}_i = \left(\overline{\delta}_0, \overline{\delta}_1, ..., \overline{\delta}_N\right)^T$. To estimate , we must estimate the errors $\|\overline{w}(x) - \overline{W}(x)\|$ and $\|\overline{W}(x) - W(x)\|$ respectively. Following Eq. (40) for $\overline{W}(x)$, we obtain

$$\overline{\overline{A}}\,\overline{\overline{X}} = \overline{H}, \tag{51}$$

where $\overline{\overline{X}} = \left(\overline{\delta}_0, \overline{\delta}_1, ..., \overline{\delta}_N\right)^T$. Eqs. (40) and (51) together lead to:

$$A\left(\overline{X} - \overline{\overline{X}}\right) = H - \overline{H}. \tag{52}$$

Prior to continuing, the subsequent theorem is required:

Theorem 5.3. Suppose that $\Gamma(x) \in C^4[0,l]$ and $\{0 = x_0, ..., x_N = 1\}$ be partition of [0,*l*]. If $R(x)$ be the unique TCBS approximation for $\Gamma(x)$ at the knots $x_0, ..., x_{N-1}, x_N$, then

$$\begin{aligned}&\left\|R(x) - \Gamma(x)\right\| \le \mathrm{O}(h^3), \\ &\left\|R^{(k)}(x) - \Gamma^{(k)}(x)\right\| \le \mathrm{O}(h^2), \quad k = 1,2, \\ &\left\|R^{(k)}(x) - \Gamma^{(k)}(x)\right\| \le \mathrm{O}(h), \quad k = 3.\end{aligned}$$

Proof. Refer to [8, 25, 29] and the references cited therein.

Referring to Eq. (21) and Theorem 5.3, we obtain the bound on $\left\|H - \overline{H}\right\|$ as follows:

$$\left|H-\overline{H}\right| = \left|\alpha_1 u_j^{"} - \beta_1 u_j^{'} - \gamma_1 u_j - \alpha_1 \left(\overline{u}\right)_j^{"} - \beta_1 \left(\overline{u}\right)_j^{'} - \gamma_1 \overline{u}_j\right|,$$
$$\leq |\alpha_1|\left|u_j^{"} - \left(\overline{u}\right)_j^{"}\right| + |\beta_1|\left|u_j^{'} - \left(\overline{u}\right)_j^{'}\right| + |\gamma_1|\left|u_j - \overline{u}_j\right|,$$

where $\alpha_1 = -\left(\varepsilon + \tau_j a_i^{j+1}\right)$, $\beta_2 = d_i^{j+1}$ and $\gamma_1 = \left(\varepsilon + \tau_j c_i^{j+1}\right)$. Then using Theorem 5.3,

$$\left\|H-\overline{H}\right\| \leq |\alpha_1| O\left(h^2\right) + |\beta_1| O\left(h^2\right) + |\gamma_1| O\left(h^3\right),$$
$$\leq \Theta h^2, \quad \text{where } \Theta = |\alpha_1| + |\beta_1| + |\gamma_1| O(h). \tag{53}$$

Substituting Eq. (53) into Eq. (52) yields

$$A\left(\overline{X} - \overline{\overline{X}}\right) = H - \overline{H} \Rightarrow \left\|\overline{X} - \overline{\overline{X}}\right\| \leq \left\|A^{-1}\right\| \left\|H - \overline{H}\right\| \leq \Theta h^2 \left\|A^{-1}\right\|. \tag{54}$$

Based on the given properties, TCBS basis functions vanish outside the interval $[x_{i-2}, x_{i+2}]$ while within this range, $CTB_i(x)$ assumes non-zero values at the mesh points. Likewise, their first and second derivatives exhibit similar behavior at these points. Consequently, the resulting matrix ||A|| takes the form of a tridiagonal band matrix characterized by dominant principal diagonal elements and non-zero off-diagonal entries. Therefore, A^{-1} remains bounded, and the matrix A is non-singular. Hence, we get:

$$\left\|\overline{X} - \overline{\overline{X}}\right\| \leq \Theta_1 h^2, \quad \text{where } \Theta_1 = \Theta\left\|A^{-1}\right\|. \tag{55}$$

From $W(x) - \overline{W} = \sum_{i=-1}^{N+1}\left(\delta_i - \overline{\delta}_i\right) CTB_i\left(x\right)$, and Lemma (50), we get

$$\left\|\overline{W}\left(x\right) - W\left(x\right)\right\| \leq \overline{\Theta} h^2, \text{ where } \overline{\Theta} = 6\Theta_1. \tag{56}$$

Theorem 5.4. Let $\bar{w}$(x) be the exact solution of Eqs. (35)-(38) and let $W(x)$ be the TCBS collocation approximation, then

$$\left\|\bar{w}\left(x\right) - W\left(x\right)\right\| = O\left(h^2\right).$$

Proof. From Theorem 5.3, Eq. (56) and triangle inequalities, we have

$$\left\|\bar{w}\left(x\right) - W\left(x\right)\right\| = \left\|\bar{w}\left(x\right) - \overline{W}\left(x\right) + \overline{W}\left(x\right) - W(x)\right\|,$$
$$\leq \left\|\bar{w}\left(x\right) - \overline{W}\left(x\right)\right\| + \left\|\overline{W}\left(x\right) - W\left(x\right)\right\|, \tag{57}$$
$$\leq O\left(h^3\right) + \overline{\Theta}\left(h^2\right) \leq O\left(h^2\right).$$

The convergent theorem below follows directly from Lemma (3.3-3.4) and Theorem 5.4.

Theorem 5.5. Let $\bar{w}$(x) denote the exact solution to Eq. (1) and $W(x,t)$ its numerical approximation. Then, it follows that:

$$\left\|\overline{w}(x)\left(x_i, t_{j+1}\right) - W\left(x_i, t_{j+1}\right)\right\| \leq C\left(M^{-1}\ln\left(M\right) + N^{-2}\right), \tag{58}$$
$$0 \leq i \leq N, 0 \leq j \leq M.$$

RESULTS AND DISCUSSION

A representative numerical example is provided to illustrate the accuracy and performance of the proposed method. The absolute errors are computed using the double-mesh approach, and the maximum pointwise error corresponding to each value of ε is obtained through:

$$E_\varepsilon^{N,M} = \max_{0\leq i,j\leq N,M}\left|W^{N,M}\left(x_i, t_j\right) - W^{2N,2M}\left(x_{2i}, t_{2j}\right)\right|, \tag{59}$$

where $W^{N,M}\left(x_i, t_j\right)$ is numerical solution at N, M mesh points whereas $W^{2N,2M}\left(x_{2i}, t_{2j}\right)$ denote the numerical solution at $2N$, $2M$ mesh points.

Example 6.1. Let us analyze the following illustrative problem from [16]:

$$\begin{cases} -\varepsilon\dfrac{\partial^3 w}{\partial t \partial x^2} + \varepsilon\dfrac{\partial w}{\partial t} - \dfrac{\partial}{\partial x}\left(\left(e^{-t} + \dfrac{1}{2}x^2 + 4\right)\dfrac{\partial w}{\partial x}\right) + \left(x^3 - t^2\right)\dfrac{\partial w}{\partial x} + \\ \qquad \left(e^{-t} + x^2\right)u = e^{-t}\sin\left(\pi x\left(1-x\right)\right), \\ w\left(x,0\right) = \sin\left(\pi x\right),\ x \in \overline{\Omega}_x, \\ w\left(0,t\right) = w(1,t) = 0,\ t \in (0,1]. \end{cases}$$

We can write Example (6.1) as, $d(x,t) = b(x,t) - \dfrac{\partial a}{\partial x} = \left(x^3 - x - t^2\right)$.

$$\begin{cases} \varepsilon\dfrac{\partial w}{\partial t} - \varepsilon\dfrac{\partial^3 w}{\partial t \partial x^2} - \left(e^{-t} + \dfrac{1}{2}x^2 + 4\right)\dfrac{\partial^2 w}{\partial x^2} \\ + \left(x^3 - x - t^2\right)\dfrac{\partial w}{\partial x} + \left(e^{-t} + x^2\right)w \\ = e^{-t}\sin\left(\pi x\left(1-x\right)\right), \\ w\left(x,0\right) = \sin\left(\pi x\right),\ x \in \overline{\Omega}_x, \\ w\left(0,t\right) = w(1,t) = 0,\ t \in (0,1]. \end{cases}$$

The parameter α_0 = 1.999 in Eq. (29) is chosen based on the boundedness of the solution, Lemma 2.2, and Definition 3.1.

The results are displayed through Tables and Figures. Tables (2), (3), and (4) list the computed maximum pointwise errors. Analysis of these tables demonstrates that the proposed method attains ε^- uniform convergence, with the maximum pointwise error consistently decreasing as the mesh sizes (N, M) increase for each value of ε.

Table 2. Maximum pointwise errors at discrete points with $N = M$ for various ε.

ϵ	$N = M = 8$	$N = M = 16$	$N = M = 32$	$N = M = 64$	$N = M = 12$	$N = M = 256$
10^{-2}	4.679e – 04	1.183e – 04	3.460e – 05	8.025e – 06	1.825 – 06	6.488 – 07
10^{-4}	4.658e – 04	1.186e – 04	3.586e – 05	7.718e – 06	1.840 – 06	7.559 – 07
10^{-6}	4.658e – 04	1.186e – 04	3.587e – 05	7.715e – 06	1.840 – 06	7.577 – 07
10^{-8}	4.658e – 04	1.186e – 04	3.587e – 05	7.715e – 06	1.840 – 06	7.578 – 07
10^{-10}	4.658e – 04	1.186e – 04	3.587e – 05	7.715e – 06	1.840 – 06	7.578 – 07
	⋮	⋮	⋮	⋮	⋮	⋮
10^{-20}	**4.658e – 04**	**1.186e – 04**	**3.587e – 05**	**7.715e – 06**	**1.840 – 06**	**7.578 – 07**
10^{-22}	**4.658e – 04**	**1.186e – 04**	**3.587e – 05**	**7.715e – 06**	**1.840 – 06**	**7.578 – 07**
$E_{\epsilon}^{N,M}$	**4.679e – 04**	**1.186e – 04**	**3.587e – 05**	**8.025e – 06**	**1.840 – 06**	**7.578 – 07**

Table 3. Pointwise maximum errors for different values of ε, N and M.

ϵ ↓	$N = 16$ $M = 8$	$N = 32$ $M = 16$	$N = 64$ $M = 32$	$N = 128$ $M = 64$	$N = 256$ $M = 128$
10^{-2}	1.184e – 04	3.519e – 05	7.867e – 06	1.832e – 06	6.488e – 07
10^{-4}	1.186e – 04	3.586e – 05	7.716e – 06	1.840e – 06	7.559e – 07
10^{-6}	1.186e – 04	3.587e – 05	7.715e – 06	1.840e – 06	7.577e – 07
10^{-8}	1.186e – 04	3.587e – 05	7.715e – 06	1.840e – 06	7.578e – 07
10^{-10}	1.186e – 04	3.587e – 05	7.715e – 06	1.840e – 06	7.578e – 07
	⋮	⋮	⋮	⋮	⋮
10^{-20}	1.186e – 04	3.587e – 05	7.715e – 06	1.840e – 06	7.578e – 07
10^{-22}	1.186e – 04	3.587e – 05	7.715e – 06	1.840e – 06	7.578e – 07
$E_{\varepsilon}^{N,M}$	1.186e – 04	3.587e – 05	7.867e – 06	1.840e – 06	7.578e – 07

Table 4. Calculated $E_{\varepsilon}^{N,M}$ for a range of ε values and varying N and M.

ϵ ↓	$M = 10$ $N = 16$	$M = 20$ $N = 32$	$M = 40$ $N = 64$	$M = 80$ $N = 128$	$M = 160$ $N = 256$
10^{-2}	3.014e – 04	7.647e – 05	1.875e – 05	5.154e – 06	1.345e – 07
10^{-4}	3.031e – 04	7.742e – 05	1.894e – 05	5.607e – 06	1.216e – 07
10^{-6}	3.031e – 04	7.743e – 05	1.895e – 05	5.615e – 06	1.215e – 07
10^{-8}	3.031e – 04	7.743e – 05	1.895e – 05	5.615e – 06	1.215e – 07
10^{-10}	3.031e – 04	7.743e – 05	1.895e – 05	5.615e – 06	1.215e – 07
	⋮	⋮	⋮	⋮	⋮
10^{-20}	3.031e – 04	7.743e – 05	1.895e – 05	5.615e – 06	1.215e – 07
10^{-22}	3.031e – 04	7.743e – 05	1.895e – 05	5.615e – 06	1.215e – 07
$E_{\varepsilon}^{N,M}$	3.031e – 04	7.743e – 05	1.895e – 05	5.615e – 06	1345e – 07

Figure 1 shows the numerical solution profile for $N = M = 128$ and $\varepsilon = 10^{-2}$ highlighting the presence of an initial layer near $t = 0$. Figure 2 illustrates the solution for $N = M = 128$ and $\varepsilon = 10^{-8}$, clearly demonstrating that as $\varepsilon \to 0$, the solution develops steep gradients, with the surface plot becoming increasingly dense around the boundary layer region. where the boundary layer forms. This dense clustering of the solution profile reflects the strong influence of the perturbation parameter and highlights the effectiveness of the numerical scheme in capturing the layer behaviour. Figure 3 displays the numerical solution profile obtained with $N = M = 256$, $\varepsilon = 10^{-8}$ using mesh plot. The figure reveals the

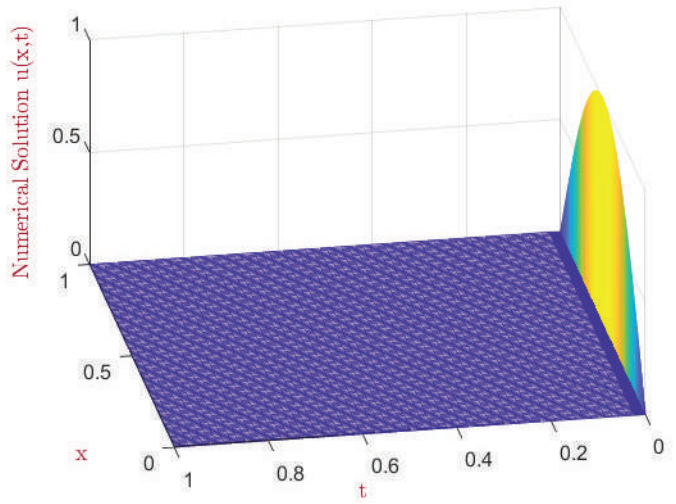


Figure 1. Mesh plot of the numerical solution profiles for $N = M = 128$, $\varepsilon = 10^{-2}$.

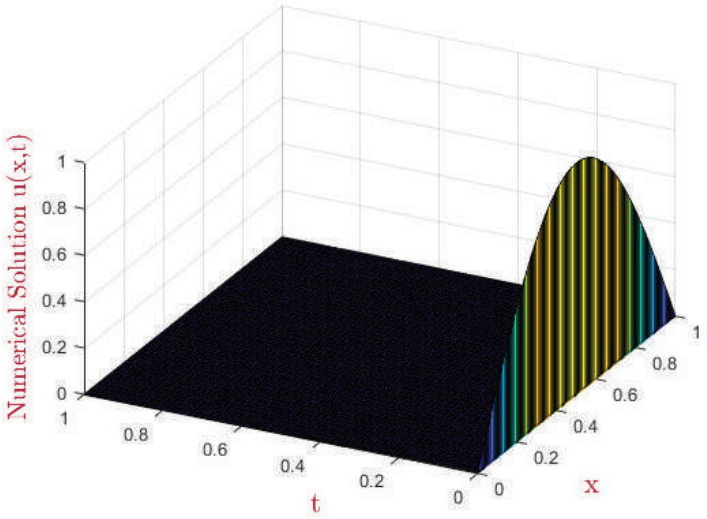


Figure 2. Surface plot illustrating the numerical solution for $N = M = 128$, $\varepsilon = 10^{-8}$.

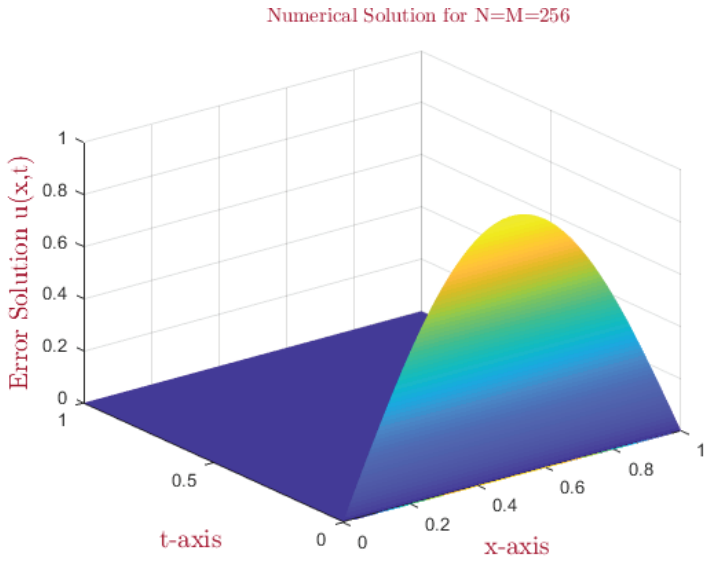


Figure 3. Numerical solution profiles corresponding to $N = M = 256$, $\varepsilon = 10^{-8}$.

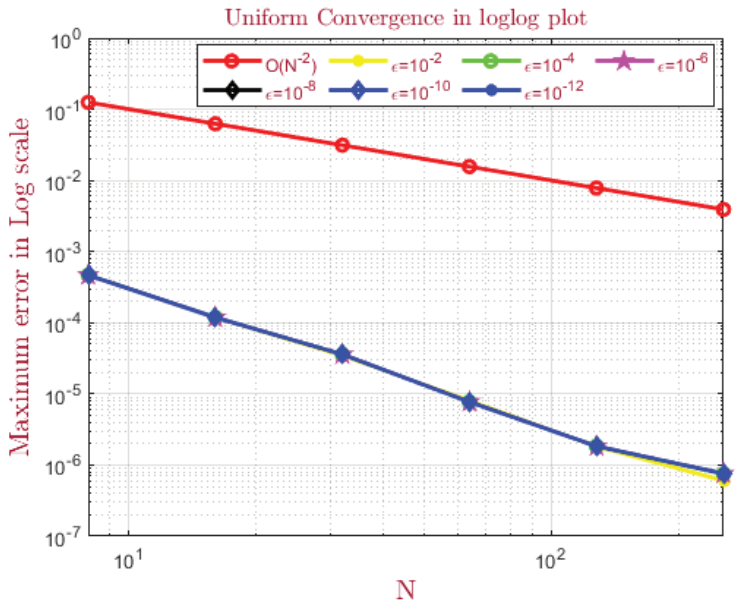


Figure 4. Log-log representation of the maximum point-wise error corresponding to Table 2.

presence of a pronounced intitial layer concentrated near $t = 0$, demonstrating the steep variation of the solution in the nearly region. In Figure 3, the log-log plot appears as a straight line, demonstrating the relationship between the numerical solution and the spatial variable. This linearity on the logarithmic scale indicates that although the error remains constant, the solution exhibits a power-law dependence on the spatial variable.

CONCLUSION

This study examines a numerical scheme designed for a class of SPSPs of one-dimensional IBVPs involving an initial jump. To obtain solutions that remain stable regardless of the perturbation parameter, a specialized difference scheme is introduced. The spatial derivatives are approximated using a uniform mesh combined with a TCBS based non-polynomial basis, while the temporal derivatives are treated with an Implicit Euler method on a Shishkin mesh. This combined approach effectively addresses the difficulties caused by the small perturbation parameter, particularly the formation of initial boundary layers. Compared to other cubic splines, the TCBS approach yields more accurate results. It encourages us to select this approach for the issue under consideration. From the analysis, it is demonstrated that the current scheme is convergent, independent of the perturbation parameter and mesh parameters. We look at a model example, and the computed results show that the proposed numerical method produces more accurate solutions for different values of ε, N and M. Our goal is to expand the current approach to include higher order SPSPs in upcoming work.

ACKNOWLEDGEMENT

The authors sincerely thank the anonymous reviewers for their insightful feedback, which greatly improved this manuscript. This work received no external funding or financial support.

AUTHORSHIP CONTRIBUTIONS

Authors equally contributed to this work.

DATA AVAILABILITY STATEMENT

The authors confirm that the data that supports the findings of this study are available within the article. Raw data that support the finding of this study are available from the corresponding author, upon reasonable request.

CONFLICT OF INTEREST

The author declared no potential conflicts of interest with respect to the research, authorship, and/or publication of this article.

ETHICS

There are no ethical issues with the publication of this manuscript.

STATEMENT ON THE USE OF ARTIFICIAL INTELLIGENCE

Artificial intelligence was not used in the preparation of the article.

REFERENCES

[1] Khompysh K, Shakir AG. An inverse source problem for a nonlinear pseudoparabolic equation with p-Laplacian diffusion and damping term. Quaest Math 2023;46:1889–1914. [CrossRef]

[2] Amiraliyev GM, Mamedov YD. Difference schemes on the uniform mesh for singularly perturbed pseudo-parabolic equations. Turk J Math 1995;19:207–222.

[3] Chiyaneh AB, Duru H. On adaptive mesh for the initial boundary value singularly perturbed delay Sobolev problems. Numer Methods Partial Differ Equ 2020;36:228–248. [CrossRef]

[4] Chiyaneh AB, Durus H. Uniform difference method for singularly pertubated delay Sobolev problems. Quaest Math 2020;43:1713–1736. [CrossRef]

[5] Duru H. Difference schemes for the singularly perturbed Sobolev periodic boundary problem. Appl Math Comput 2004;149:187–201. [CrossRef]

[6] Sobolev SL. Selected works of SL Sobolev. Volume I: Equations of Mathematical Physics, Computational Mathematics, and Cubature Formulas. London, Berlin, New York: Springer Nature; 2006.

[7] Mohapatra J, Shakti D. Numerical treatment for the solution of singularly perturbed pseudo-parabolic problem on an equidistributed grid. Nonlinear Eng 2020;9:169–174. [CrossRef]

[8] Zahra W. Trigonometric B-spline collocation method for solving PHI-four and Allen–Cahn equations. Mediterr J Math 2017;14:122. [CrossRef]

[9] Ewing RE. Numerical solution of Sobolev partial differential equations. SIAM J Numer Anal 1975;12:345–363. [CrossRef]

[10] Gu H. Characteristic finite element methods for nonlinear Sobolev equations. Appl Math Comput 1999;102:51–62. [CrossRef]

[11] Amiraliyev GM, Amiraliyeva IG. Difference schemes for the singularly perturbed Sobolev equations. In: Proc Int Conf Differ Equ Spec Funct Appl 2007. p. 23–40. [CrossRef]

[12] Amirali I. Analysis of higher order difference method for a pseudo-parabolic equation with delay. Miskolc Math Notes 2019;20:755–766. [CrossRef]

[13] Amirali I, Amiraliyev GM. Three layer difference method for linear pseudo-parabolic equation with delay. J Comput Appl Math 2022;401:113786. [CrossRef]

[14] Amiraliyev GM, Cimen E, Amirali I, Cakir M. High-order finite difference technique for delay pseudo-parabolic equations. J Comput Appl Math 2017;321:1–7. [CrossRef]

[15] Zhang C, Tan Z. Linearized compact difference methods combined with Richardson extrapolation for nonlinear delay Sobolev equations. Commun Nonlinear Sci Numer Simul 2020;91:105461. [CrossRef]

[16] Amiraliyev GM, Duru H, Amiraliyeva IG. A parameter-uniform numerical method for a Sobolev problem with initial layer. Numer Algorithms 2007;44:185–203. [CrossRef]

[17] Gunes B, Duru H. A second-order difference scheme for the singularly perturbed Sobolev problems with third type boundary conditions on Bakhvalov mesh. J Differ Equ Appl 2022;28:385–405. [CrossRef]

[18] Gunes B, Duru H. A computational method for the singularly perturbed delay pseudo-parabolic differential equations on adaptive mesh. Int J Comput Math 2023;100:1667–1682. [CrossRef]

[19] Cheru SL, Duressa GF, Mekonnen TB. Adaptive mesh extended cubic B-spline method for singularly perturbed delay Sobolev problems. Tamkang J Math 2025;56:165–185. [CrossRef]

[20] Clavero C, Jorge JC, Lisbona F. Uniformly convergent schemes for singular perturbation problems combining alternating directions and exponential fitting techniques. Appl Adv Comput Methods Bound Inter Layers 1993:33–52.

[21] Daba IT, Duressa GF. Extended cubic B-spline collocation method for singularly perturbed parabolic differential-difference equation arising in computational neuroscience. Int J Numer Methods Biomed Eng 2021;37:e3418. [CrossRef]

[22] Gelu FW, Duressa GF. A uniformly convergent collocation method for singularly perturbed delay parabolic reaction-diffusion problem. Abstr Appl Anal 2021;2021:8835595. [CrossRef]

[23] Cheru SL, Duressa GF, Mekonnen TB. Robust numerical approach for singularly perturbed parabolic problems with discontinuous convection coefficients and source terms. Comput Methods Differ Equ 2025;30:e03064. [CrossRef]

[24] Hall CA. On error bounds for spline interpolation. J Approx Theory 1968;1:209–218. [CrossRef]

[25] Nikolis A, Seimenis I. Solving dynamical systems with cubic trigonometric splines. Appl Math E-Notes 2005;5:116–123.

[26] Strikwerda JC. Finite difference schemes and partial differential equations. Philadelphia: Soc Ind Appl Math; 2004. [CrossRef]

[27] Gao F, Cui J, Zhao G. Weak Galerkin finite element methods for Sobolev equation. J Comput Appl Math 2017;317:188–202. [CrossRef]

[28] Nikan O, Avazzadeh Z. A localisation technique based on radial basis function partition of unity for solving Sobolev equation arising in fluid dynamics. Appl Math Comput 2021;401:126063. [CrossRef]

[29] Rektorys K. Variational methods in mathematics, science and engineering. Dordrecht: Springer Sci Bus Media; 2012.

[30] Singh S, Kumar D, Deswal K. Trigonometric B-spline based ε-uniform scheme for singularly perturbed problems with Robin boundary conditions. J Differ Equ Appl 2022;28:924–945. [CrossRef]

Sigma Journal of Engineering and Natural Sciences
Web page info: https://sigma.yildiz.edu.tr
DOI: 10.14744/sigma.2025.00139

Research Article

Productivity improvement in manufacturing of furniture using quality function deployment approach

Dhananjay APTE[1], Prafulla HATTE[2,*], Vishal PRADHAN[3]

[1]Symbiosis International (Deemed University), Pune, 412115, India
[2]MIT Academy of Engineering, Pune, 412105, India
[3]Vijay Patil School of Management, Nerul, Navi Mumbai, 400706, India

ARTICLE INFO

Article history
Received: 27 September 2024
Revised: 19 November 2024
Accepted: 30 December 2024

Keywords:
Quality Function Deployment, Benchmarking, Productivity, Voice of the Customer, Furniture Manufacturing

ABSTRACT

Micro, Small, and Medium Enterprises often face challenges in balancing customer demands, design attributes, production parameters, and productivity. Research has been done on matrix diagrams, correlations, tabularization techniques, and quality deployments, but none of them have linked productivity to design qualities and customer needs. This study aims to evaluate productivity and the related monetary savings by applying a Lean management tool- Quality Function Deployment. Furthermore, strapping focuses on the 'Voice of the Customer' of furniture products' profile. The focal objective has been to identify specific process improvements related to design features and assess the impact of these enhancements on overall productivity. By integrating design quality with operational improvements, the study seeks to demonstrate the savings through increased productivity.

During the use of 'Quality Function Deployment', non-value-adding elements in the furniture manufacturing process were eliminated. The implementation of Lean Six Sigma methodology further enhanced the overall quality management strategy. Data analysis and subsequent execution led to a substantial 21.16% increase in productivity, translating to annual cost savings of INR 55,200. The significance of design qualities (named as Technical Requirements), was assessed using Quality Function Deployment, providing a foundation for developing an optimized furniture production process. The integrated application of Lean Six Sigma and Quality Function Deployment has demonstrated the potential to reduce processing times, boost productivity, and increase profitability without compromising customer satisfaction. The approach emphasized the importance of collaborative Lean management, maintaining a well-organized workplace, improving process efficiency, and eliminating non-value-adding activities. In essence, this study uniquely contributes to operational optimization by focusing on the relationship between Technical Requirements and the Voice of the Customer in furniture manufacturing processes. This approach can be widely applied to various manufacturing industries.

Cite this article as: Apte D, Hatte P, Pradhan V. Productivity improvement in manufacturing of furniture using quality function deployment approach. Sigma J Eng Nat Sci 2025;43(6):1982–1994.

***Corresponding author.**
*E-mail address: prhatte@mitaoe.ac.in

This paper was recommended for publication in revised form by Editor-in-Chief Ahmet Selim Dalkilic

Published by Yıldız Technical University Press, İstanbul, Turkey
© Author. This is an open access article under the CC BY-NC license (http://creativecommons.org/licenses/by-nc/4.0/).

INTRODUCTION

Productivity enhancement is a persistent challenge in various industries. Quality Function Deployment (QFD) is a valuable tool for data collection and analysis, facilitating the translation of customer needs into engineering design characteristics. By integrating marketing, design, engineering, and other relevant functions, QFD optimizes product development.

The furniture industry, characterized by intense competition and rapidly changing consumer preferences, is compelled to continually improve productivity. To effectively address customer needs and incorporate them into product attributes, QFD could offer a valuable tool [1-3].

The study describes a procedure for prioritization of 'Technical Requirements' (TRs) that best fulfil the customer voice, benchmarking the competitor level to fulfil the customers' needs, and improving the manufacturing processes and resources through opinion polls, a rating matrix, along with a Six Sigma approach. More specifically, it is the DMAIC (Define- Measure- Analyze- Improve- Control) approach. The findings of this study are valuable to operations excellence practitioners across various manufacturing sectors, enabling them to enhance productivity and profitability. The overall flow of the study is shown in Figure 1.

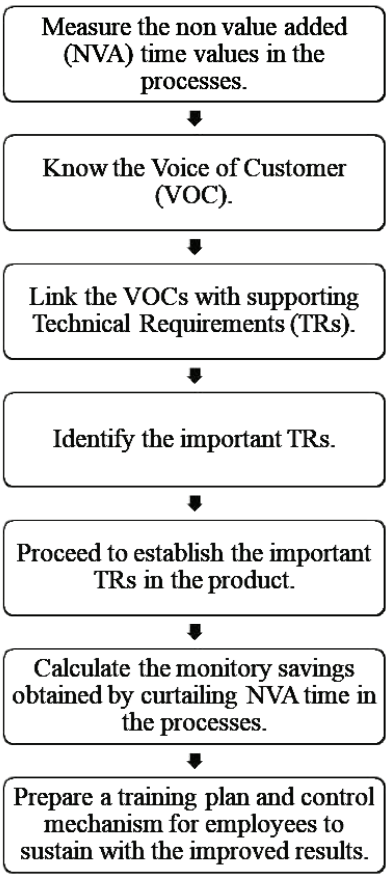


Figure 1. Chart of steps in the study.

Literature Review

A literature review on comprehending the existing usage of QFD, its conjunction with other concepts and methodologies, and the relevant gaps is made in the first phase. Out of the several research material reviews, only a handful of the most relevant cases to our study are chosen. Below are the takeaways-

According to a poll conducted by an organization with sixty participants, there is a significant correlation between customer happiness and QFD, covering several strategic aspects and viewpoints. QFD can work in tandem with other Lean techniques to get a comprehensive productivity result. This can be illustrated by utilizing an innovative approach to problem-solving (called TRIZ), in conjunction with QFD [2,3]. An Ethiopian company that manufactures leather shoes used 'Failure Mode Effect Analysis' (FMEA) in conjunction with QFD to assess collaborative design features. FMEA is a preventive risk analysis and hence possesses the capability to reduce external breakdown costs, leveraging improvement in productivity [4].

An integrated model for capturing engineering students' needs from the viewpoints of educational institution facilities and infrastructure was developed using a Seroquel model (service quality) in conjunction with QFD, which has accounted for probable risks in the usage of traditional educational methods [5].

These studies aimed to understand the use of QFD, which had assumed a diversified segment of products that has helped to create a basic theoretical framework for this research work.

The diversity in the references, particularly in terms of case studies or papers on similar QFD applications in other industries, has been made, which could provide a more robust foundation for the QFD implementation. A summary is made in Table 1 below

The intention of the above reviews was to judge the scalability of QFD in product profiles other than furniture. It was required to comprehend whether there could be any possibility to use QFD as a general approach for the fulfillment of the aim of this research. While casting the use of QFD for furniture, it was beneficial to develop a know-how of its apt application. Below are the takeaways-

Table 1. Other studies

Product segment	Author(s)
Internet banking services	[6]
Supply chain digitization	[7]
Cell phone closed-loop supply chain optimization	[8]
Service expectations of low-cost airlines	[9]
Autonomous electric car	[10]
Renewable Energy for different vehicles	[11]
Smart home products	[12]

As a general practice, the correlations between VOCs and TRs are described by the three correlation values, 9,3, and 1 [6,7]. The 9 and 1 values are retained in this study. However, another value could be in the middle of this (i.e., 5). A value of 4 is taken for the safer side. A prioritization between VOCs and TRs was noted for exercising the roof part of QFD. A weighted sum technique is feasible for the elements that are not of the same nature. QFD could consider customer priorities in the ranking based on the customer perspectives. A fuzzy-based logic can be suitably used for service industries. However, for the product industry, it has a different consideration [8,9]. A Kano model approach that divides the customer requirements as basic, intermediate, and delighter, helps to identify the customer priorities scale. It can be associated with QFD to derive both the benefits [10,11].

An integration of TRIZ (an English meaning is 'Theory of Inventive Problem Solving') with QFD is feasible. The concept of assembling identical or similar parts to perform parallel operations was executed while devising the process enhancements in furniture manufacture. A sustainable user experience theme was established while inviting the ranking of wood selection for the coffee table [12].

Noted with the framework aspects from the above literature studies, it was further aimed to know the use of QFD typically for furniture products, specifically to learn how design enhancements are performed or how manufacturing excellences are accounted for. Information was collected from a partial literature review of the past ten years' relevant research publications, specifically to know the customers' expectations, fulfillment trends, scope, and limitations. Table 2 describes this.

The use of the Lean Six Sigma methodology and its operational excellence approach, with respect to Indian work culture, has also been exercised in the research. Few of the process enhancements were derived from the fundamental Lean lacunas like workmanship and discipline, which proved a time saving of 66.5% in a panel cutting workshop through industrial engineering interventions. In today's competitive landscape, maintaining a strong commitment to both internal and external customers is crucial. Effective mechanisms must be in place to capture and address their evolving needs [20,21].

Various literature references have provided a critical evaluation of the application and applicability of QFD as well as Lean operations along with the related design process. It has revealed the importance of QFD with respect to design and development and expressed implicitly the need for further investigation to employ productivity. QFD mix, or gathering the Voice of the Customer and using the associated qualities in the product or services, has been in use in crafting the design; however, linking the outcome to productivity needs to be exercised [1].

While previous research has utilized QFD to capture and analyze the Voice of the Customer (VOC), it has often neglected the optimization of batch manufacturing processes by eliminating non-value-added activities (NVAs). While these studies emphasize the product development quotient, the manufacturing quotient falls outside their scope.

The existing literature highlights a gap in the application of QFD to bridge the link between design and operational excellence for improved productivity. This research study addresses this gap through applied research focused on the furniture industry. Specifically, the study aims to frame a QFD approach for common furniture items such as chairs, sofas, and dining tables, to enhance productivity.

RESEARCH PARTNER

This research study was conducted in collaboration with Prabha Furniture (Hereafter called Prabha), a Pune-based furniture firm that experiences significant process waste (MUDA). Prabha's flagship product line includes coffee tables, outfeed tables, indoor sofas, and indoor chairs. This study focuses on these products, drawing conclusions

Table 2. Product details and gain

Furniture type	Gain of the review	Paper Number
Household furniture.	Obtained a product functional design attribute, those common to the furniture.	[13]
Prototype plywood wardrobe.	The extent of satisfaction level owing to the new prototype among the TRs. The level increment from 2.71 to 4.08 points has been noted.	[14]
Computer workstation.	The aspects of increased customer satisfaction from the furniture's value perspective.	[15]
Wood frame furniture.	Insights applied to outdoor wooden furniture design in campus space.	[16]
Drafting table for Engineering students.	Product design quality attributes- weight and odor.	[17]
Children's rocking chair.	Utilization of QFD, TRIZ, and FEM towards improvement of design efficiency. Principle of separation in TRIZ.	[18]
Smart dining table.	Smarter design aspects for general customers- Ease of cleaning.	[19]

Table 3. Process MUDAs and equivalent INR conversion

Year	Process MUDA time (in hours)	Equivalent conversion (in INR)
2019	739	55,425.00
2020	877	70,160.00
2021	775	69,750.00
2022	816	77,520.00
2023	776	77,600.00
Average number of hours per year	**797(Rounded value)**	

based on data collected between 2019 and 2023. A pilot study conducted at Prabha revealed that manufacturing processes have been plagued by MUDA for several years, resulting in an annual loss of 797 clock hours. This loss equates to the potential production of 106 additional chairs, representing a missed profit opportunity of INR 1,69,600. Given the high demand for chairs within Prabha's core product range, it was selected as the baseline product for this analysis. Prabha's willingness to participate in this research aligns with the study's objective of exploring the Voice of the Customer (VOC) and Technical Attributes to enhance productivity.

Problem Statement

The furniture manufacturing processes were found to be inefficient, exceeding the standard cycle time and resulting in substantial financial losses. To address these inefficiencies, the researchers, along with Prabha employees (called 'team'), proposed a comprehensive approach that integrates Quality Function Deployment (QFD) with Lean Six Sigma methodologies. This integrated approach aims to optimize processes, reduce waste, and ultimately increase production capacity.

Objectives of the Research

The research study had the following primary objectives.

1. To generate the TRs with respect to the VOCs in the canvas of benchmarking outcomes in furniture craft.
2. To formulate the strategies in the process organization of selected processes, based on TRs.
3. To demonstrate the savings by elevating productivity.

Measurement of the Data

The second phase of the DMAIC (Define-Measure-Analyze-Improve-Control) process involved the study of past records of non-value-added time in processes (Process MUDA). The team converted it into monetary value using the operator rates provided by Prabha's costing executive.

The rates were:

Year 2019: INR 75.00 per hour, Year 2020: INR 80.00 per hour, Year 2021: INR 90.00 per hour, Year 2022: INR 95.00 per hour, Year 2023: INR 100.00 per hour. The process MUDA was observed in the range between 739 and 877 hours from the year 2019 to 2023. This is shown in Table 3.

Also, a comprehensive mapping of the furniture manufacturing processes was performed for the current year. A significant discrepancy was observed between the standard and actual process times for certain operations. To address this issue, a detailed analysis of thirteen processes from four flagship products was undertaken. These processes were selected based on a time value criterion, focusing on operations with a time gap exceeding 20% between the standard and actual times.

The process MUDA was observed consistently for a set of similar processes. The monetary loss due to the MUDA process was being ignored by Prabha. Table 4 describes the data for one of the batches out of past 6 batches observations. The batch having the lowest total actual time (i.e.860 minutes) has been considered here.

Analysis

The data collected during the measurement phase revealed significant opportunities to reduce non-value-added (NVA) activities and improve productivity without compromising customer satisfaction. To understand customer needs and expectations (VOCs- Voice of Customers), survey reports from Prabha were analyzed. Additionally, a brainstorming session with the team and furniture experts from Prabha was conducted to identify key technical requirements (TRs).

VOCs were derived from customer concerns, considering factors like gender and occupation (male and female, business professionals and individuals). A check sheet was distributed to 70 exhibition visitors, and a weighted average of their responses was calculated, assigning a 60:40 weight ratio to female and male respondents, respectively. Input was also gathered from furniture designers and shop front-end sellers associated with Prabha. To finalize the VOCs, several criteria were considered, including product quality, customer satisfaction, and operational efficiency. A screening process was applied to identify the eight most significant VOCs. These VOCs were prioritized using a five-point Likert scale, with 1 representing the lowest priority and 5 representing the highest priority, as shown in Table 5.

In the case of various VOCs, strength was the essential one. This accommodates impact or a larger load. This is an essential feature for executive-class customers. The parameters- type of wood, balance, hardness, and porosity are related

Table 4. Processes with time values

Sr. No.	Product	Process	Time (minutes)	
			Standard time	Actual time
1	Coffee table	Gluing the top and shelf	32	46
2	Coffee table	Cutting the table legs	43	66
3	Indoor chair	Tapering the legs and armrest	72	96
4	Coffee table	Adding stretchers to table legs	62	78
5	Outfeed table	Attaching legs to the frames	38	52
6	Indoor chair	Cutting parts and assembling seat	58	79
7	Indoor chair	Cutting chair body to legs	52	83
8	Indoor chair	Joining the legs and armrest	8	17
9	Indoor sofa	Attaching sofa sides to the base	14	25
10	Indoor chair	Attaching cleats for chair slats	76	93
11	Indoor sofa	Attaching sofa sides to the base	3	12
12	Indoor sofa	Building sofa base	74	97
13	Indoor sofa	Assembling the sofa	84	116
Total			**616**	**860**

Table 5. VOCs with their priorities

VOCs	VOC Priority
Strength	5
Easy to move	3
Light weight	4
Suitable size and shape	3
Polish odor	5
Low maintenance	4
Resale value	3
Ease of cleaning	4

Priority Legend: 1. Extreme low, 2. Low, 3. Medium, 4. High, 5. Extreme high

to this. The ease of movement of a furniture product and its weight correspond to the type of wood and porosity grade. A size and shape generate an aesthetic appearance, which relates to gravitational balance. Polish type plays an important role in terms of its odor, while maintenance and cleaning ease correspond to the type of wood and corrosion resistance.

Technical Requirements (TRS)

TRs are key parameters, essentially needed in the product, which address VOCs. TRs, generated through brainstorming, were used subsequently in QFD. The nine TRs were:

1. Type of wood, 2. C.G. and balance, 3. Polish Grade 4. Porosity Grade, 5. Surface hardness, 6. Corrosion resistance (for metal hardware), 7. Smell level of polish, 8. Cost fluctuation index, 9. Coefficient of friction

Analyze VOCs and Link them with TRS

A Quality Function Deployment (QFD) matrix framework was employed to analyze the relationships between VOCs and TRs. VOCs were prioritized, and correlations between pairs of VOCs and TRs were assessed. Some relationships were evaluated based on prior experience, while others were visualized and analyzed using scatter plots and regression analysis in Minitab software. The Pearson Correlation Coefficient, calculated using Minitab, was used to quantify the strength of these relationships. For instance, a correlation coefficient of 0.9 was observed between polish and polish odor grade, while a correlation of -0.9 was found between porosity grade and strength grade. An absolute value of 0.9 was used in the QFD calculations. Scatter plots, as depicted in Figures 2 and 3, were used to visualize these correlations with historical data.

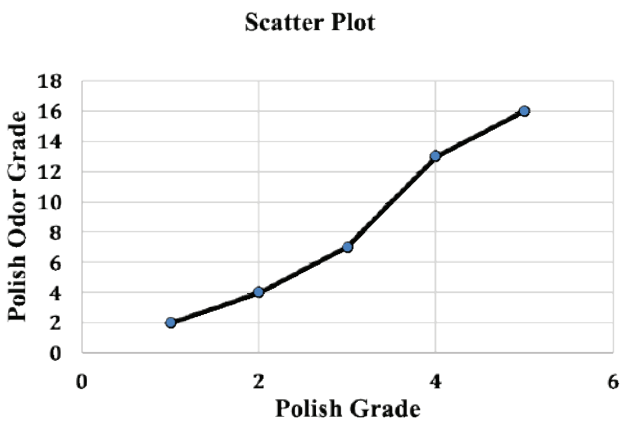


Figure 2. Scatter plot- polish grade, polish odor grade.

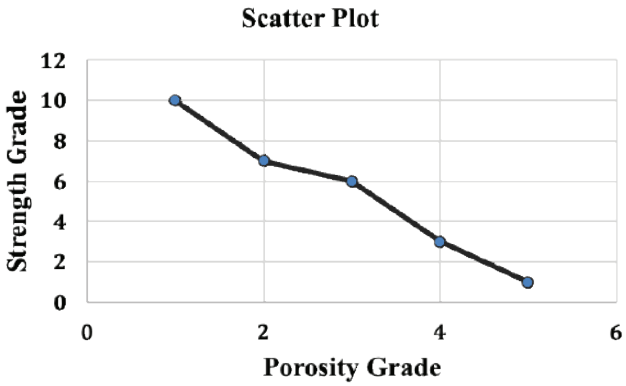


Figure 3. Scatter plot- porosity grade, strength grade.

Benchmarking

Based on quality functions, a decision was taken to benchmark Prabha Furniture's current performance with competitors' performance. Among the various competitors, Mitta Furniture, which possesses the biggest market share in the given product category, was selected as an ethical performance benchmarking partner.

The team takes the support of benchmarking consultants. They do the comparison with other brand products. A discussion was made with respect of VOCs- Strength, Easy to move, etc. A common understanding of VOCs was established during the benchmarking discussions. Benchmarking revealed the extent of customers' requirements met by Prabha and Mitta Furniture in coffee tables and sofas (a common product in attributes, category, and value). The numbers '1' through '5' were listed in the competitor rating. A rating value of '1' was assigned to weak performance, while '5' was assigned to superior performance. A scale of 1 to 5 was introduced in the QFD matrix, with a legend of a triangular symbol and a square symbol, against the 1 to 5 number scale. A triangular symbol was considered for Prabha, while the square symbol was for Mitta Furniture.

Preparing QFD

QFD was performed to enhance an organization's ability to communicate, document, analyze, and prioritize the TRs. QFD translates customer needs into engineering design characteristics through the integration of marketing, design, engineering, manufacturing, and other relevant functions of the organization.

The QFD discipline provides both a framework and a structured process to enhance an organization's ability to communicate, document, analyze, and prioritize [20]. QFD was performed through a graphical technique called House of Quality (HOQ) that involves a left window for describing customer needs (VOCs), a right window for giving competitor analysis, a central part for displaying correlations, a ceiling for describing the TRs, and the roof for describing the interrelations.

QFD's central part contains the correlation values between each pair of VOCs and TRs. The team indicated the correlations by symbols, with **, *, and O, with the consideration of correlation (code) values 9, 4, and 1, respectively. The values selected encompass three discrete stage numbers on a scale of 1 to 10. Importance rating was calculated by summing the product of the correlation-coded value with the customer priority value. (e.g. Importance rating for- Type of wood = (5 x 9) + (3 x 4) + (4 x 9) + (3 x 0) + (5 x 1) + (4 x 9) + (3 x 9) + (4 x 1) = 165). Customer priority values were considered on a scale ranging from 1 to 5, in the consideration of lowest to highest, respectively.

The triangular-shaped roof part, shown at the top level of QFD in Figure 4, indicates interrelations among the TRs. The same sign convention- **, *, and O and their respective values- 9,4, and 1 were applied here [22]. The interrelation between the two TRs is known by tracing a triangular path on the roof. For example, the type of wood and porosity grade have a strong interrelation 9, as indicated by a filled circle. A QFD generated by the team is shown in Figure 4.

Interpretations From QFD

- Type of wood, Porosity grade, and Surface hardness have the highest importance rating. Extending the action on these TRs fulfills VOC to the largest extent.
- Roof of QFD indicates a strong interrelation among- Type of wood, Porosity grade, and Surface hardness. Hence, we can conclude that working only on the Type of wood shall cover the other two TRs- Porosity grade, and Surface hardness.
- The right-hand window indicates competitor ratings. A most prior VOC- 'strength' (having priority level 5) is rated 3 with Prabha. It has a rating value of 5 with Mitta furniture. Strength can be increased by adopting the attributes observed with Mitta Furniture products. The respective TR- i.e. Type of wood can be suitably worked out to achieve this.

Selection of the Type of Wood

An opinion survey was conducted to choose the type of wood for the products, specifically the coffee table, outfeed table, indoor chair, and indoor sofa. Expert opinions were solicited from five respondents possessing expertise in furniture production procedures. Respondents were requested to choose the type of wood based on four critical attributes: Strength, weight, maintenance cost, and resale value [23].

The QFD analysis has discovered pertinent technical requirements (TRs) and voice of the customer (VOCs). The selection of these four traits was predicated on this. The rationale for selecting the qualities was to encompass the merging of TRs and VOCs. It was surface hardness correlated with strength, and porosity grade associated with weight. These traits, along with the additional two, maintenance cost and resale value, indicate the type of wood.

The opinion poll was taken independently for each furniture product. The 'Modal value' (Majority option) of

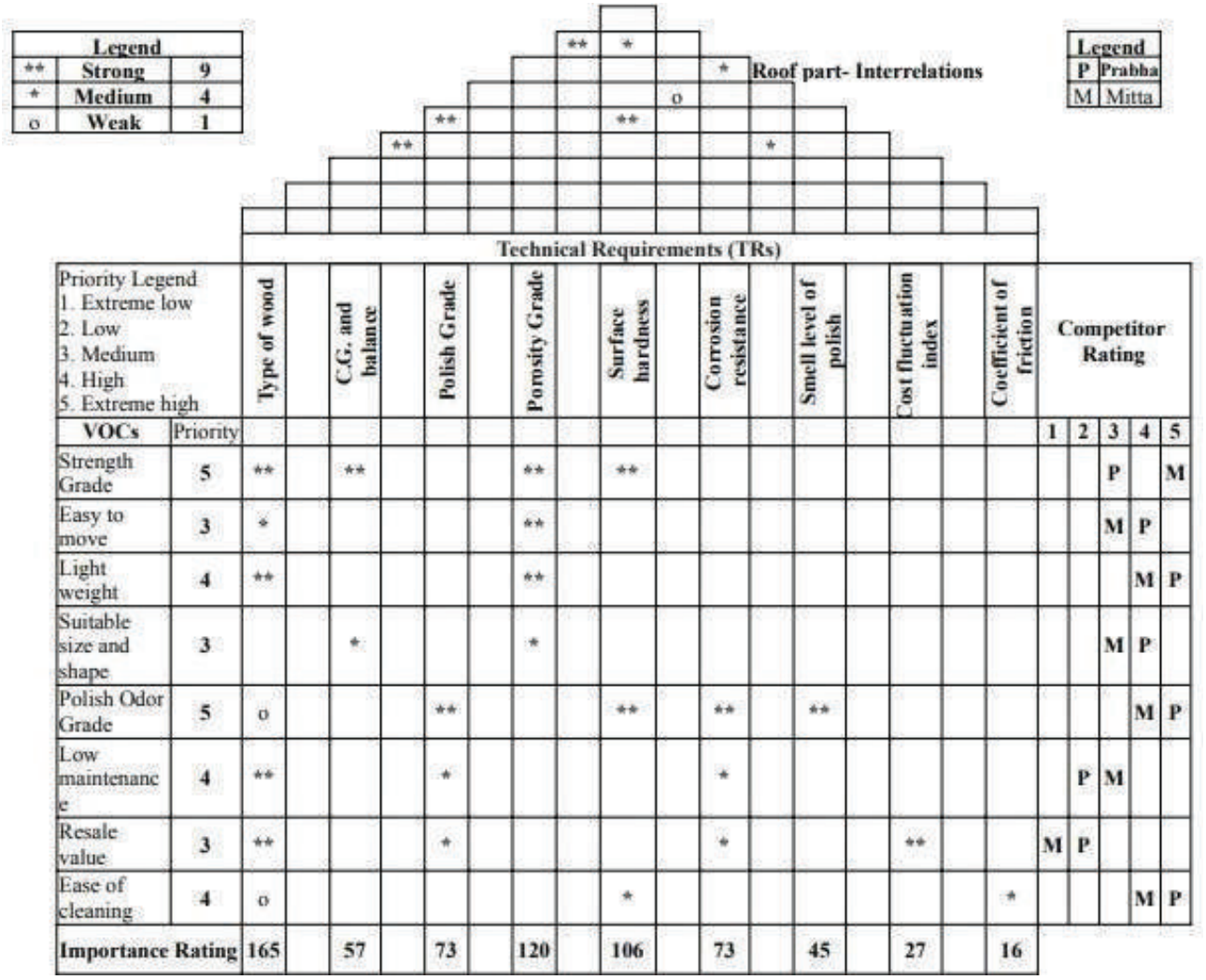


Figure 4. QFD with VOCs and TRs.

the opinion count was considered as the wood selection criterion for a particular attribute. Finally, the decision was made to select the wood for furniture through a peer discussion and an opinion poll (Tables 6 and 7).

According to the modal value of the opinion poll shown in the table, mahogany wood was chosen to be used in the furniture as it had the largest preference (3 times out of 4 times). A due focus was given on Strength, Maintenance cost, and Resale value, while 'Weight' was considered secondary for the selection. (This preference was made following the VOC priority)

The peer team decided Mahogany wood from the available wood options for the coffee table. The decision was taken by the peer team based on various parameters as shown in Table 8. A similar approach was followed for selecting wood for other products- an outfeed table (plywood), an indoor chair, and an indoor sofa (cedar wood). The opinion poll selection matrix is shown in Table 8 and Table 9.

Table 6. Options for the type of wood

Product	Options
Coffee table	Mahogany, Oak, Ash and Maple wood
Outfeed table	Plywood, Fiberboard, Particleboard, Medium Density Fiberboard
Indoor chair and Indoor sofa	Cedarwood, Pinewood

Table 7. Opinion poll of 5 respondents for coffee table

	Attributes			
Respondent	**Surface hardness (Strength)**	**(Porosity grade) Weight**	**Maintenance cost**	**Resale value**
1	Mahogany wood	Ash wood	Mahogany wood	Mahogany wood
2	Mahogany wood	Ash wood	Mahogany wood	Mahogany wood
3	Oak wood	Maple wood	Ash wood	Mahogany wood
4	Mahogany wood	Ash wood	Mahogany wood	Mahogany wood
5	Mahogany wood	Ash wood	Mahogany wood	Mahogany wood
Modal value	**Mahogany wood**	**Ash Wood**	**Mahogany wood**	**Mahogany wood**

Table 8. Opinion poll for the out feed table

Respondent	**Surface hardness (strength)**	**(Porosity grade) weight**	**Maintenance cost**	**Resale value**
1	Plywood	Particle board	Plywood	Plywood
2	Plywood	Particle board	Fiberwood	Plywood
3	Plywood	Plywood	Medium Density Fiberboard	Plywood
4	Plywood	Plywood	Plywood	Plywood
5	Fiberboard	Plywood	Plywood	Plywood
Majority	**Plywood**	**Plywood**	**Plywood**	**Plywood**

Table 9. Opinion poll for indoor chair and indoor sofa

Respondent	**Surface hardness (strength)**	**(Porosity grade) weight**	**Maintenance cost**	**Resale value**
1	Cedar wood	Pine wood	Cedar wood	Cedar wood
2	Pine wood	Pine wood	Pine wood	Cedar wood
3	Cedar wood	Cedar wood	Pine wood	Cedar wood
4	Cedar wood	Cedar wood	Pine wood	Cedar wood
5	Cedar wood	Cedar wood	Cedar wood	Pine wood
Majority	**Cedar wood**	**Cedar wood**	**Pine wood**	**Cedar wood**

Improve Phase

Following the analysis and determination of the wood choices, the team concentrated on enhancing the processes. The manufacturing characteristics, including workmanship capabilities, tool types, surface finish production, and cutting ability, were closely aligned with the critical technical requirements. Workplace organization, utilizing the Lean methodology 5S, was implemented, and MUDAs were addressed following the principles of Poka Yoke, Kaizen, and Kanban.

Improvement in Coffee Table

To devise the actions, a macro process chart was prepared for the coffee table that contained the processes: 1. Gluing the top and shelf, 2. Cutting the table legs, 3. Making sides, 4. Adding stretchers to table legs, 5. Preparing table top, 6. Dry fitting and 7. Finishing and assembling the table. A study of the macro process chart revealed a few options to curtail the processing time with respect to the tapering jig of the coffee table. Four significant options were chosen from brainstorming, and four respondents rated the options. The rating matrix was prepared as given in Table 10.

A rating score of 4 means the solution will effectively solve the problem. A score of 1 means the solution is irrelevant and does not solve the problem. Option 4 (Making a new tapering jig) was the best as the total rating score was the highest, i.e.14

The suggested option was followed, and the respective SOP (Standard Operating Procedure) was created to incorporate sustenance. An SOP for making a new Tapering Jig was formed as below- Step 1: Cut a piece of plywood, Step 2: Attach support on it, Step 3: Add

Table 10. Rating matrix

Options		Team members				Total Rating score
		1	2	3	4	
1	Outsourcing the tapering jig	4	1	1	3	9
2	Purchasing a new tapering jig	1	2	2	1	6
3	Sharing the same tapering jig	3	3	3	2	11
4	Making a new tapering jig	2	4	4	4	14

Table 11. Hurdles and MUDAs

Processes description	Hurdles in processes	MUDA Type
Cutting parts and assembling the Seat	Difficulty in preparing back assembly	Motion
Cutting and tapering the legs and armrest	Tapering jig settings	Overprocessing and waiting
Joining the legs and armrest	Usage of bandsaw involving more steps to perform shaping	Overprocessing
Shaping the DIY		
Attaching cleats for DIY slats	The discrepancies observed in assembly and finishing process.	Rework
Applying finish to DIY		
Connecting chair body to legs	Extra movement of the product and the operator during assembly.	Processing

registration blocks to make repeatable tapers and cut, Step 4: Apply a piece of tape to the jig, Step 5: Apply a piece of tape to the block, Step 6: Apply glue on the piece of tape of block, Step 7: Press the glued block on the piece of tape of jig.

Improvement in Indoor Chairs and Other Products

To identify process MUDAs in the manufacturing process of chairs, the team did a brainstorming activity and investigated various hurdles concerning MUDAs, presented below in Table 11.

To understand the flow and sequence of the assembly process, a flow chart was prepared as shown in Figure 5.

The flow chart and the hurdles brainstorming were an informational and logical background for the team to implement certain actions, which fulfilled the VOCs and aligned with the TRs. Certain action elements for the outfeed table and indoor sofa were extracted from the benchmarking activity and are stated in the same table.

From the reference of these exercises, various improvement actions were taken, and a time study was conducted before and after the action was taken. Table 11 shows time elements, implemented actions for 13 key processes, and cost savings after the improvements. Cost saving was calculated by considering a labor rate of Rs.100 per hour. Table 12 below describes the data for one of the batches out of the 6 batches observed. The batch having the highest total actual time (i.e.678 minutes) has been considered here.

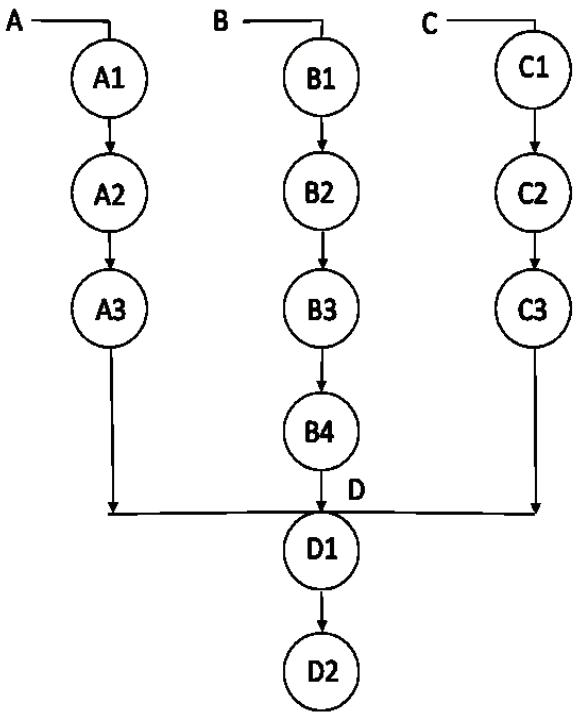


Figure 5. Flow chart of the chair process

A: Seat and seat sides: A1: Cutting, A2: Drilling, A3: Securing

B: Back uprights: B1: Cutting, B2: Cutting, B3: Laying, B4: Cutting

C: Back top rail and back bottom rail: C1: Cutting, C2: Drilling, C3: Clamping and, securing,

D: Back and seat: D1: Securing, D2: Clamping

Table 12. Processes with time values after the improvement

Product	Processes	Actions performed	Time (minutes)			Time saved (minutes)	Cost saved (INR)
			Ideal time	Actual time			
				Before improvement	After improvement		
Coffee table	Gluing the top and shelf	Use of alignment aids	32	46	38	8	13
Coffee table	Cutting the table legs	Tapering jig settings	43	66	47	19	32
Indoor chair	Tapering the legs, armrest		72	96	78	18	30
Coffee table	Adding stretchers to table legs	Drilling hole offset	62	78	65	13	22
Outfeed table	Attaching legs to the frames	Improved attachment	38	52	39	13	22
Indoor chair	Cutting parts and assembling seat	Assembly modification	58	79	65	14	23
Indoor chair	Cutting chair body to legs		52	83	59	24	40
Indoor chair	Joining the legs and armrest	Band saw cutting	8	17	10	7	12
Indoor sofa	Attaching sofa sides to base		14	25	15	10	17
Indoor chair	Attaching cleats for chair slats	Assembly and finishing to retain polish grade	76	93	78	15	25
Indoor sofa	Attaching sofa sides to base	Use of anti-corrosive dowel joineries	3	12	5	7	12
Indoor sofa	Building sofa base	Assembly enhancements	74	97	83	14	23
Indoor sofa	Assembling the sofa		84	116	96	20	33
Total			**616**	**860**	**678**	**182**	**304**

Control

Six Sigma DMAIC methodology emphasizes sustaining the improvements to avoid rework. Currently, internal and external audits are being performed with Prabha. Internal audit is conducted every day at the start of the shift by the Management Representative (MR) for 5S, while external audit is conducted monthly by an appointed consultant. The audit involves an assessment of 5S implementation, catering to a comprehensive background checklist that tries to demonstrate the application of various Lean principles concerning 5S.

RESULTS AND DISCUSSION

This research has integrated Voice of Customer (VOC) with thirteen essential processes through mediating Technical Requirements (TRs). Unlike traditional Lean approaches that often focus solely on bottleneck processes, this study considered both the Voice of Customer and Technical Requirements to identify improvement opportunities. By incorporating customer needs into the productivity enhancement process, Prabha adopted a more competitive stance, aligning with customers' requirements while simultaneously increasing production. The research resulted in improved productivity and reduced processing time. The productivity enhancement was calculated by subtracting the post-implementation duration (678 minutes) from the pre-implementation duration (860 minutes).

A one-sample t-test was conducted using Minitab software at a 5% significance level to determine the statistical significance of the reduction in process time. The new time value of 678 minutes was compared to a hypothesized value of 860 minutes for a sample size of 6, with a standard deviation of 45.8 minutes. The resulting p-value was significantly less than 0.05, indicating a statistically significant reduction in time. A sample size of 6 repetitions was deemed sufficient to capture process and operator variability within the specific context of Prabha's operations. However, it is important to note that sample size and standard deviation may vary across different organizations. The reduction of 182 minutes from the original 860 minutes represents a

Table 13. Consolidated result sheet of a bifurcation of the total time saved

Product	Yearly orders	Time saved per unit (minutes)
Coffee table	192	40
Outfeed table	96	13
Indoor chair	216	78
Indoor sofa	144	51
Total		**182**

Table 14. Time and cost savings

Product	Yearly orders (a)	Time saved per unit (minutes) (b)	Total time saved in a year (minutes) (a x b)
Coffee table	192	40	7680
Outfeed table	96	13	1248
Indoor chair	216	78	16848
Indoor sofa	144	51	7344
Total		**182**	**33120**
			(i.e. 552 hours)

21.16% decrease in process time, leading to a corresponding 21.16% increase in productivity. This change has been proven to be a significant change, as validated through a t-test. Many studies have been made that demonstrated the benefits of using the Lean or Six Sigma approach, the one referred to previously in the literature review, stating a 66.5% saving in a panel cutting process [21]. However, by incorporating QFD, the time saving in the processes has been a unique example, hence beyond comparison. Under conventional situations, i.e., by employing a Lean practice, several studies have reported a significant productivity boost; however, the use of QFD via VOC for productivity improvement has been reported beneficial.

The integrated application of Quality Function Deployment (QFD) and Lean methodologies proved effective in significantly enhancing furniture productivity. The results are summarized in Table 13.

Lean and Six Sigma tools and techniques can be effectively employed to achieve operational excellence in furniture manufacturing. This case study demonstrates the successful application of a collaborative Lean Six Sigma Define-Measure-Analyze-Improve-Control (DMAIC) approach to optimize workplace organization, improve process efficiency, and eliminate non-value-added activities - MUDAs. The research resulted in significant cost savings, as detailed in Table 14.

Cost saving per year (INR) = 552 hours x INR 100 per hour = INR 55,200.00

The average labor and other resources rate is INR 100 per hour, assumed here.

Hence, we can conclude through this real-time data evidence that the use of Quality Function Deployment (QFD) towards enhancements in productivity and the subsequent benefits in cost savings is significant.

CONCLUSION

This study is beneficial to Micro, Small and Medium Enterprises (MSMEs) to investigate appropriate design parameters and link them to their process aspects. Many Micro, Small, and Medium Enterprises (MSMEs) have major concerns about their productivity and face challenges to achieve this rationally. The use of Quality Function Deployment (QFD) towards productivity has been demonstrated in this study and shall stand as a useful reference for Managers of Micro, Small, and Medium Enterprises (MSMEs) as well as for their consultants. This study shall help researchers to further investigate the use of additional Lean tools to integrate in Quality Function Deployment (QFD). Referring to the concepts of this study, functions other than manufacturing can be validated with Quality Function Deployment (QFD). A correlation with the customer satisfaction index and productivity can also be studied by employing QFD. The study correlates design parameters with manufacturing aspects, the one observed in the manufacturing category. This study may possess limitations to account for the situations in service industries.

ACKNOWLEDGEMENTS

We are grateful to Mr. Mahendra Deshmukh, the owner of Prabha Furniture, for allowing us to do this research study, and to Mr. Pratik Mule for his invaluable help in data collection and relevant support.

AUTHORSHIP CONTRIBUTIONS

Authors equally contributed to this work.

DATA AVAILABILITY STATEMENT

The authors confirm that the data that supports the findings of this study are available within the article. Raw data that support the finding of this study are available from the corresponding author, upon reasonable request.

CONFLICT OF INTEREST

The author declared no potential conflicts of interest with respect to the research, authorship, and/or publication of this article.

ETHICS

There are no ethical issues with the publication of this manuscript.

STATEMENT ON THE USE OF ARTIFICIAL INTELLIGENCE

Artificial intelligence was not used in the preparation of the article.

REFERENCES

[1] Lalvand N, Owlia MS. Integrating customer clustering and QFD to improve and develop services: a case study. Int J Bus Innov Res 2024;35:219–237. [CrossRef]

[2] Bahia TH, Idan AR, Athab KR. The effect of quality function deployment (QFD) in enhancing customer satisfaction. Int J Prof Bus Rev 2023;8:18. [CrossRef]

[3] Yang W, Cao G, Peng Q, Sun Y. Effective radical innovations using integrated QFD and TRIZ. Comput Ind Eng 2021;162:107716. [CrossRef]

[4] Reda H, Dvivedi A. Decision-making on the selection of lean tools using fuzzy QFD and FMEA approach in the manufacturing industry. Expert Syst Appl 2022;192:116416. [CrossRef]

[5] Zeynep OC, Sezer ED. An integrated approach to identify engineering student requirements. Sigma J Eng Nat Sci 2022;40:568–576.

[6] Adiandari A, Winata H, Fitriandari M, Hariguna T. Improving the quality of Internet banking services: an implementation of the quality function deployment (QFD) concept. Manag Sci Lett 2020;10:1121–1128. [CrossRef]

[7] Deepu TS, Ravi V. An integrated ANP–QFD approach for prioritization of customer and design requirements for digitalization in an electronic supply chain. Benchmarking Int J 2020;28:1213–1246. [CrossRef]

[8] Allehashemi T, Amin SH, Zolfaghari S. A proposed multi-objective model for cellphone closed-loop supply chain optimization based on fuzzy QFD. Expert Syst Appl 2022;210:118577. [CrossRef]

[9] Pandey MM. Evaluating the strategic design parameters of airports in Thailand to meet service expectations of low-cost airlines using the fuzzy-based QFD method. J Air Transp Manag 2020;82:101738. [CrossRef]

[10] Rampal A, Mehra A, Singh R, Yadav A, Nath K, Chauhan AS. Kano and QFD analyses for autonomous electric cars: design for enhancing customer contentment. Mater Today Proc 2022;62:1481–1488. [CrossRef]

[11] Frizziero LE, Donnici G, Francia DA, Caligiana G, Gaddoni A. Stylistic design engineering (SDE) for an innovative green vehicle following QFD and TRIZ applications. Int J Mech Prod Eng Res Dev 2019;9:805–827. [CrossRef]

[12] Li Y, Ghazilla RA, Abdul-Rashid SH. QFD-based research on sustainable user experience optimization design of smart home products for the elderly: a case study of smart refrigerators. Int J Environ Res Public Health 2022;19:13742. [CrossRef]

[13] Erdil A. Evaluation product development, product design for the furniture–wood industry via quality function deployment and Pareto analysis. Sigma J Eng Nat Sci 2020;11:203–217.

[14] Homkhiew C, Ratanawilai T, Pochana K. Application of a quality function deployment technique to design and develop furniture products. Songklanakarin J Sci Technol 2012;34:663–668.

[15] Annappa CM, Panditrao KS. Integration of quality function deployment and value engineering in the furniture manufacturing industry for improvement of computer workstations. Int J Innov Technol Explor Eng 2013;2:45–52.

[16] Ouyang C, Wu KY. A DFA-based wood frame furniture design using quality function deployment: a case study in school open spaces. In: International Conference on Chemical, Material and Food Engineering. Atlantis Press; 2015. p. 517–520. [CrossRef]

[17] Koleini Mamaghani N, Barzin E. Application of quality function deployment (QFD) to improve product design quality in school furniture. Iran Univ Sci Technol 2019;29:277–287.

[18] Xin YI, Jia-ming LI, Zhuo-qiang LI, Qing-wen WA. Research on the innovative design of children's rocking chair based on the integration of QFD/TRIZ/FEM. China For Prod Ind 2021;58:.

[19] Zhang BY, Ma MY, Chang XQ, Zhao YF, Chen Y. Smart dining table design through the implementation of QFD approach. In: 8th International Conference on Control, Automation and Robotics (ICCAR). IEEE; 2022. p. 40–44. [CrossRef]

[20] Fargnoli M, Haber N. A QFD-based approach for the development of smart product–service systems. Eng Rep 2023;:e12665. [CrossRef]
[21] Dizdar EN, Ozen R. Work study applications in the wooden furniture industry for the production productivity. Technol J 2001;4:1–9.
[22] Fonseca L, Fernandes J, Delgado C. QFD as a tool to improve negotiation process, product quality, and market success in an automotive industry battery components supplier. Procedia Manuf 2020;51:1403–1409. [CrossRef]
[23] Lee IJ. Applying virtual reality for learning woodworking in the vocational training of batch wood furniture production. Interact Learn Environ 2023;31:1448–1466. [CrossRef]

Sigma Journal of Engineering and Natural Sciences
Web page info: https://sigma.yildiz.edu.tr
DOI: 10.14744/sigma.2025.1929

Research Article

In *vitro* degradation studies of polylactide/ polyethylene glycol electrospun fiber blends

Oluwashina Philips GBENEBOR[1,*], Abimbola Patricia POPOOLA[1]

[1]*Department of Chemical, Metallurgical and Materials Engineering, Tshwane University of Technology, Pretoria, 0001, South Africa*

ARTICLE INFO

Article history
Received: 28 February 2024
Revised: 12 June 2024
Accepted: 25 October 2024

Keywords:
Electrospun Fiber; Fiber Blends; Fiber Diameter; Polylactide; Polyethylene Glycol

ABSTRACT

Biomaterials such as polylactide play a crucial role in tissue engineering by accelerating the structural and functional rejuvenation of damaged tissues. Polylactide is however, hydrophobic and this has limited its use in soft tissue engineering as it prevents cell adhesion and proliferation. Tensile strength and strain at break of polylactide need to gradually degrade during wound healing to enhance cell adhesion. Polyethylene glycol has been used to improve the hydrophilicity of polylactide but In *Vitro* studies involving strength and ductility degradation of electrospun polylactide/ polyethylene glycol fibers under physiological conditions have not been investigated. Pellets of both polymers were dissolved in di-chloromethane in different polylactide/ polyethylene glycol rations of 80/20 and 60/40 (% wt. / wt.); the solution was electrospun into fiber mats. The samples were immersed in phosphate buffered saline/solution maintained at pH7.4 and 37°C for 8 weeks. Fourier Transform Infrared Spectroscopy informs that shifts in functional group wavenumbers with formation of additional peaks on 1906 and 2067 cm^{-1} in the electrospun fibers indicate degradation. There is an increase in average fiber diameter ranging from 1.07 to 13.04 µm, where addition of 40 wt. % polyethylene glycol possesses the greatest magnitude. Weight loss result shows that polymer blends degrade faster than neat polylactide. Within 8 weeks, tensile strength of neat polylactide fiber degrades from 0.28 to 0.08 MPa while that for polylactide/ polyethylene glycol (80/20) fiber occurs from 0.31 to 0.08 MPa; degradation of polylactide/ polyethylene glycol (60/40) is evident as its tensile strength reduces from 0.27 MPa before immersion to 0.04 MPa after 8 weeks of immersion. Ductility reduction of 94 % occurs with polylactide blended with 40 wt. % polyethylene glycol after 8 weeks while 70 and 50 % are lost for polylactide/ polyethylene glycol (80/20) and neat polylactide respectively. The performances of these fiber blends (in comparison with neat Polylactide fiber) inform that they can be good for wound dressing.

Cite this article as: Gbenebor OP, Popoola AP. In *vitro* degradation studies of polylactide/ polyethylene glycol electrospun fiber blends. Sigma J Eng Nat Sci 2025;43(6):1995–2005.

***Corresponding author.**
*E-mail address: philipsogbenebor@gmail.com

This paper was recommended for publication in revised form by Editor-in-Chief Ahmet Selim Dalkilic

Published by Yıldız Technical University Press, İstanbul, Turkey
© Author. This is an open access article under the CC BY-NC license (http://creativecommons.org/licenses/by-nc/4.0/).

INTRODUCTION

Biomaterials are very important in tissue engineering because they provide biophysical and biochemical stimuli to guide cells for tissue formation. These materials have been confirmed to also hasten the structural and functional rejuvenation of damage tissues [1-2]. Metals/alloys, ceramics and polymers with their composites (a combination of two or more of these different class of materials) have been used over the years for human body tissues. To aid biomaterials' cellular interactions and regulate their functional behaviours (such as mechanical strength), a three-dimensional (3D) porous structural support needs to be provided. A polymeric material that has been proven to be useful for this device is polylactide / polylactic acid (PLA). The material is taking the lead in the emerging biopolymer market owing to its most attractive manufacturing cost, structure and availability. This biopolymer has been in existence for several decades and it can be sourced from corn [3]. Poor hydrophilicity however, has been a major challenge that has limited its use in tissue applications [4]. Scaffolds made of PLA for instance, have been proven to exhibit unfavourable cell adhesion due to its poor hydrophilicity [5] and this hinders effective wound healing. To improve PLA's hydrophilic tendencies, polyethylene glycol (PEG) can be blended with PLA to form PLA/PEG composite. Polyethylene glycol is a hydrophilic oligomer or polymer synthesized from ethylene oxide which is made up of repeating units of –($O\text{-}CH_2\text{-}CH_2$)-. The ability to attach a variety of reactive functional groups to the terminal sites of PEG polymers has greatly expanded their advantages in tissue engineering applications such as drug delivery and wound healing [6]. Fiber mats/scaffolds of PLA/PEG blend can be processed via electrospinning under the application of electrostatic forces. This often occurs at room temperature where interface of the polymer solution is exposed to an electrical force. This culminates in the ejection of a charged linear spray of solution. While the solvent evaporates, the polymer gathers on a collector (usually aluminum plate or foil) as practiced in earlier studies [7].

Scaffolds for small diameter vascular grafts have been produced by electrospinning blended solutions of polyurethane (PU) and PEG [8]. Addition of equal volumes of N,N dimethylformamide (DMF) to tetrahydrofuran (THF) was used in dissolving PU at a concentration of 10% w/v for 12 h. Varying mass of PEG was added to the PU solution to achieve PU/PEG blend ratios of 90/10, 80/20, 70/30, 60/40 and 50/50 prior to electrospinning. The PU/PEG scaffolds possessed high porosity with improved hydrophylicity which heightened as more contents of PEG were added to PU. Polyethylene glycol provided a plasticizing and hardening effect on PU. Mechanical properties of PU/PEG scaffolds were observed to be similar to human and pig arteries. The researchers concluded that blending 20 and 30 wt. % contents of PEG to PU would produce more promising effects in vascular tissue engineering as they improved cell proliferation and attachments. Electrospinning parameters such as melt solution temperature, applied voltage, collector type, and nozzle collector distance were observed on blending varying contents (wt. %) of PEG with PLA [9]. Granules of PLA was first dissolved in Irganox 1010 after which PEG granules were added to produce PLA/PEG blended melts in ratios 95/5, 90/10, 80/20 and 70/30 wt./wt. At a fixed nozzle-collector distance of 10 cm, applied electrospinning voltage was varied between 20-40 kV; spinning temperature ranged between 170-230 ^oC. At fixed values of spinning voltage and temperature, nozzle-collector distance was varied at 4, 10 and 14 cm. Blending 20 and 30 wt. % PEG with PLA produced the finest fiber even at low spinning temperature and electrostatic forces. Reduced nozzle-collector distance culminated in bending instabilities of scaffolds. Investigation of Kruse et al. [10] was aimed at processing and characterizing electrospun yarns. Different blends of PLA/PGA were dissolved in chloroform solutions and poured in a 5 ml syringe, electrospun at the rate of 2.5 ml/h while a distance of 23 cm was maintained between the nozzle tip and the collector. Formation of beads in the spun fibers was attributed to the reduced viscosity of PLA/PEG solution caused by addition of more PEG. Tensile strength of the polymer blend was noted to increase with increasing content of PEG. Results of cytocompatibility test of polymer blends with endothelial cells showed that the electrospun fibers were cytocompatible. To hasten healing in slow or non-healing wounds, platelet-rich growth factor (PRGF, derived from umbilical cold blood) with gelatin fibers were electrospun with poly-L-lactide (PLLA) to form a three layered scaffold [11]. The PLLA nanofiber was made the outer layer while gelatin/PRGF) was made the inner layer. In *vitro* study showed that healing efficacy of PRGF could be achieved (up to 3-5 days) when made to be released from scaffold. Their research maintained that PRGF would not display healing attributes when used alone but until when released from the electrospun fibers. Nanofibers comprising poly (γ-glutamic acid) (γ-PGA) as the core and PLA as the shell material have been produced via coaxial electrospinning [12] for wound healing. The core-shell membrane possessed favourable hydrophobic properties (contact angle at 90°) which enhanced the maintenance of its morphology during degradation. In *vitro* studies showed that the scaffolds displayed good biocompatibility and supported cell proliferations. Hajikhani et al. [13] employed coaxial electrospinning method to fabricate PLA- polyethylene oxide/ Polyvinylpyrrolidone (PLA-PEO/PVP) complex nanofibers which contained collagen and cefazolin as a wound dressing material. Cefazoline, which served as an antimicrobial agent and core was encased in PLA (shell); collagen was included in the nanofiber shell to quicken healing process while PVP- a super-hydrophilic polymer elevated the release of collagen. Results showed that the scaffold fended off the growth of microorganisms such as Escherichia coli, Staphylococcus aureus, and Pseudomonas aeruginosa. Lopresti et al. [14] focussed on the chemical, antimicrobial

and physical features of electrospun PLA membranes loaded with carvacrol (CRV) and a commercial nisin formulation (Nis) antimicrobial agents. Mechanical characterization showed that the CRV acted as a plasticizer on PLA while Nis made the membranes brittle as their thermal properties remained unaltered. Carvacrol hindered fiber slipping under tension and elevated its elastic properties by 508 %; Nis on the other hand, also contributed positively to membranes' elastic modulus by 100 % as it acted as solid filler. Nisin formulation made the membranes which was initially hydrophobic, hydrophilic. Nanofibers of PLA have been altered on blending with poly(ethylene glycol)-poly(propyl glycol)-poly(ethylene glycol) (PEG/PPG/PEG) copolymers [15]. The copolymer possessed good water stability within 2 months and this enhanced the water retaining capacity of PLA nanofiber. Increasing the content of PEG/PPG/PEG reduced the porosity of electrospun membrane. These features made the researchers conclude that the hybrid polymer fiber would be good for biomedical applications. Polylactide sourced from polysaccharides of -*Bletilla striata* and *Rosmarini*c acid were electrospun by Zhong et al. [16]. In addition to the polymer fiber's ability to encourage cell proliferation, its tensile properties were characterized with the maximum flexibility. The role of PEG in the enhancement of biological and structural modifications of PLA and chitosan membranes has been studied [17]. A hybrid of the three electrospun polymers showed a moderate rate of degradation, reduced hydrophobicity compared to unblended PEG fiber.

These studies have shown that PLA and PEG are both fit for human tissues (most especially as drug carriers) and a successful strategy for increasing hydrophilicity of PLA is by blending with PEG. Few works however, have been investigated on how this electrospun polymer fiber blend behaves when exposed to buffered solution under physiological conditions. Tensile strength and strain at break of electrospun fibers play key role in their ability to serve as potential sites for cell adhesion during wound healing; these properties need to gradually reduce (with time) for this to be achieved. The strength and ductility degradation of electrospun PLA/PEG fibers in PBS has not been studied. This research thus focuses on the degradation studies of electrospun fibers comprising blends of hydrophobic PLA and hydrophilic PEG in a water-based salt solution at pH 7.4 and 37°C.

MATERIALS AND METHODS

Electrospinning of PLA and PLA/PEG Blended Solutions

Corn starch-sourced polylactide with average molecular weight of 250,000 g/mol was obtained from NATUREWORKS while PEG 6000 was purchased from LOBA CHEMIE PVT. LTD.A total of 4 g pellets (PLA with PEG) was dissolved in 20 ml of 95 % purity dichloromethane (DCM) and mixed on a magnetic stirrer at room temperature until a complete dissolution and homogenous viscous liquid was obtained. The polymer solution (electrospinning solution) was fed into a spinneret (60 ml syringe was used) at room temperature and connected to a voltage source (20 kV). The spinneret was positioned vertically downward towards a stationary aluminum foil fiber collector (20 cm x 20 cm) kept 40 mm away from the tip of a 1.4 mm needle diameter fixed at the end of its (spinneret) orifice. The schematic diagram for the PLA/PEG fiber blend spinning from solution is shown in Figure 1. To arrive at the desired content (wt. %) of each combining polymer (PLA and PEG), the mixing ratios considered are displayed in Table 1.

Preparation of Phosphate Buffered Saline/Solution (Pbs)

This solution is widely used in the manufacturing of cell culture owing to its non-toxic nature (to living cells). As a result of this, it is often used for In *Vitro* studies [18-19]. Dibasic sodium phosphate, Na_2HPO_4 (9.47g) was dissolved in 1 L distilled water. A second reagent, mono basic potassium hydrogen phosphate, KH_2PO_4 (9.08g) was dissolved in 1 L distilled water. The mixture of the two solutions was achieved by adding 161 ml Na_2HPO_4 solution with 39 ml KH_2PO_4 solution and maintained at pH 7.4 and 37 °C.

Degradation Test

Electrospun fibers were fully soaked in PBS (maintained at pH 7.4 and 37 °C) for 8 weeks. At the end of each week, each fiber was weighed, oven dried at 50 °C for 12 h and characterized.

CHARACTERIZATIONS

Functional Groups Determination

Polymer functional groups were determined via Fourier Transform Infrared spectroscopy (FTIR) technique with the use of a PerkinElmer UATR Two spectrometer. Measurement was taken for each polymer in transmittance

Table 1. PLA/PEG blend formulations

S/N	PLA (g)	PEG (g)	PLA/PEG Ratio (wt. %)	Total mass (g)
1	4	0	100	4
2	3.2	0.8	80/20	4
3	2.4	1.6	60/40	4

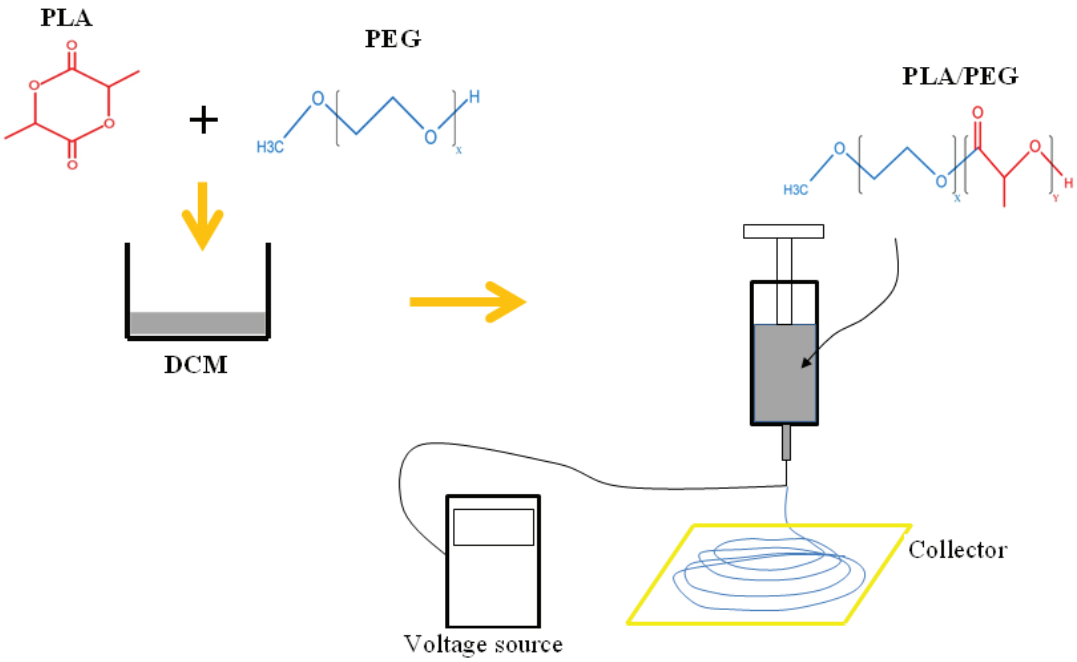


Figure 1. Schematic diagram for PLA/PEG fiber blend spinning from solution.

mode between 500–4000 cm^{-1}. To avoid shifts in baseline, normalisation of spectra were done using OriginLab software.

Scanning Electron Microscope (SEM)

A VEGA 3 TESCAN model variable-pressure scanning electron microscope was used to observe the morphological features of electrospun polymer fibers. Each electrospun fiber was placed on a circular disc lined with carbon and coated with Au for 5 min for electric conduction. Average fiber diameters and pore sizes of samples were determined with the use of Image J software.

Tensile Test

The tensile test of electrospun fibers was determined using the Instron 3369M Tensometer Each fiber was fixed and held firmly at both ends by the gauge as load was applied until the fiber finally failed. This test was done three times for each fiber and the average results were taken. The device recorded maximum stress and final length attained by each fibre prior to fracture; this provided information on the tensile strength (UTS) and ductility of the fibers. Ductility was calculated using equation (1):

$$Ductility\ (\%) = (Extension/Initial\ fibre\ length) \times 100 \quad (1)$$

Extension is the difference between the final and initial fibre length.

Weight Loss

After each period of immersion, each electrospun fiber was oven dried at 50 °C for 12 h. The percentage weight loss was used as a measure of degradation. This was calculated using equation (2):

$$W\% = \frac{W_o - W_f}{W_o} \times 100 \quad (2)$$

Where W_o and W_f are the initial and final dry weights of the fiber.

RESULTS AND DISCUSSION

Polymer Functional Groups

The FTIR spectrum of PEG electrospun fiber is shown in Figure 2a. The OH functional group is found on 3454 cm^{-1}while C-H stretching is represented by 2861 cm^{-1} [20]. Spectra on wavenumbers 1466 and 1334 cm^{-1} are attributed to C-H bending. Deformations of C-H and O-H groups are located on 1243, 1215, 1104 and 937 cm^{-1} [21-22]. Carbonyl group (C=O) stretching of neat electrospun PLA fiber (Fig. 2a) is found on 1724 cm^{-1} and this is ascribed to the vibration of amorphous carbonyl present in the structure; wavenumbers 1459 and 1362 cm^{-1} represent asymmetric and symmetric modes of CH_3 respectively. At 1048 and 1187 cm^{-1}, the bands representing the asymmetric C-O absorption modes exist. In addition, asymmetric and symmetric vibrations also exist on 2993 and 2937 cm^{-1} respectively. Spectra of PLA identified in this study are comparable to the investigations of Singla et al. [23] and Leonés et al. [24]. The FTIR spectra of the blended electrospun fibers (Fig. 2b and c) show that there is a proper mix between the two combining material (PEG and PLA) as PEG functional groups (CH bending) is found at 1449 cm^{-1} and 1359 cm^{-1}.

It is also observed that there exists some similarities in the functional groups between PLA and PEG and this may be responsible for a homogenous mixture each solution blend presented prior to spinning. Degradation of neat PLA fiber after 8 weeks is exemplified by shift in peak at every wavenumber (Fig. 2a). Although each spectrum looks similar, there lie additional peaks at 1906 and 2067 cm^{-1} on the degraded PLA which also indicates that reaction took place during immersion. Reduction/increase in spectra peak intensities have been used to describe degradation of PLA [25,26]. There also exists wavenumber shifts in fiber blends (Fig. 2b and c) with reduced intensities; for instance, the C=O group existing on 1745 cm^{-1} in 80PLA/20PEG shifts to 1738 cm-^{1} (Fig. 2b). The disappearance of C-H functional group at 2866 cm^{-1} in both blends after the 8th week of immersion may imply PEG dissolution. In addition to peak shifts and reduced intensities, degradation of PLA can also be justified by the existence of new peaks at 1906 and 2067 cm^{-1} as exhibited by PLA spectrum after immersion, (Fig. 2a)

Morphological Investigation

Figure 3a-b shows the morphologies of electrospun neat PLA before and after 8 weeks of immersion in PBS. Both structures display cylindrical fibers with few bead formations (indicated in Figure 3) which must have occurred as a result of clogging of PLA solution on the aluminum collector. This is less after 8 weeks soaking (Figure 3b) which implies possible degradation of some PLA beads in PBS. In addition, fiber average diameter of neat PLA increases from 1.07 to 1.35 μm after immersion, which indicates diffusion of PBS solution into PLA's structure. This has also led to an increase in average pore size from 34.3 to 37.4μm. Researchers have reported that there is a linear relationship between fiber diameter and pore size [27]. They concluded that pore size of electrospun fiber mats will increase with the increase in fiber diameter. Moisture (in the air) condensation on the fiber surface was suggested to be a likely mechanism for pores formation on electrospun fiber mats [28].

Increase in average pore size and fiber diameter is observed when 80 wt. % PLA is blended with 20 wt. % PEG (Figure 4a). Before immersion, average pore size of 39.5 μm is calculated while the average fiber diameter is observed to be 2.04 μm. The increase in average fiber diameter is an indication of homogenous mixture between the two polymers during blending. Pores formation is a key feature needed by scaffolds for cell attachments in tissue engineering. It can therefore be said that addition of PEG has helped improve this in PLA. Comparing this to neat PLA fiber (Figure 3b), 7.39 and 45.9 μm are measured for average fiber diameter and pores size respectively. Absorption of PBS is effectively manifested by PEG which may make PLA lose its strength after 8 weeks immersion. Creation of more pores may also be responsible for this, including its weight loss as will be observed in Figure 6.

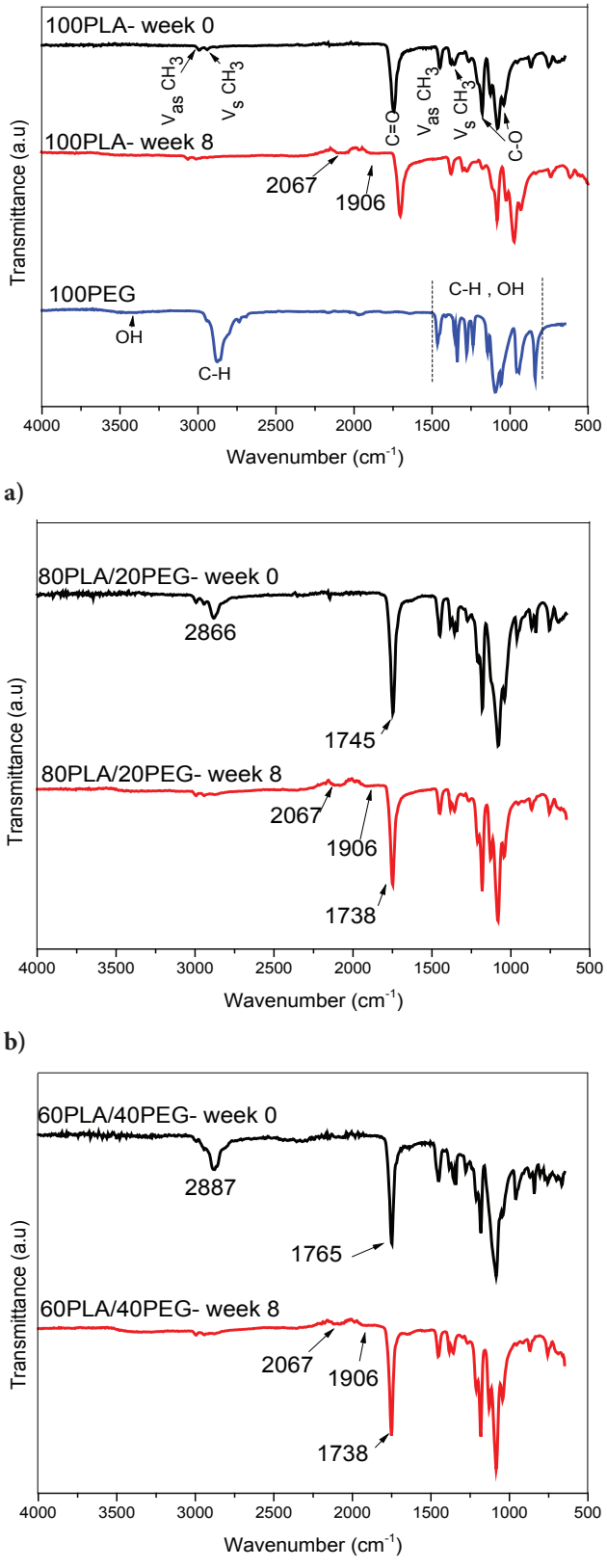


Figure 2. FTIR spectra of (a) 100PLA fiber before(week 0) and after 8 weeks of immersion; 100PEG fiber (b) 80PLA/20PEG fiber (c) 60PLA/40PEG fiber before (week 0) and after 8 weeks of immersion.

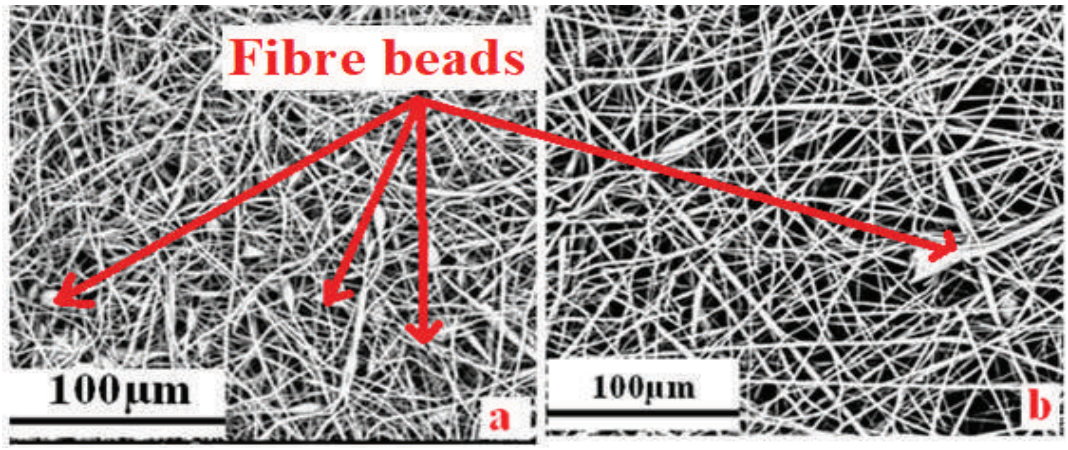


Figure 3. SEM of neat PLA fiber (a) before immersion (b) after 8 weeks immersion in PBS.

A further increase in average fiber diameter of 2.99 µm is measured for 60PLA/40PEG electrospun fiber blend before degradation test (Fig. 5a). After 8 weeks of immersion; the average fiber diameter is raised to 13.04 µm, which is the maximum for all fiber mats processed in this study (Figure 5b). Fiber diameter is uniform (with smooth surface) for the electrospun blend before and after degradation study in PBS. This is an indication that the presence of PEG is instrumental to the formation of a porous structure. Highly porous 3D structures with large surface to volume ratios have been reported to play a key role in antibacterial surfaces [29], scaffolds [30], and wound dressing applications. This makes the production of a porous structure a necessity in biomedical engineering. Degradation of each material is exemplified by increase in fiber diameter after immersion in PBS. This proposition agrees with the findings of Dias et al. [31], who ascribed the diameter increase of their processed electrospun PLA mats after immersion in PBS to hydrolytic degradation. Swelling of PLA/PCL membranes after immersion in distilled water as a result of improved hydrophilicity was characterized by fiber diameter increase [32]. According to the researchers, the diameter increase (as a result of swelling) facilitated cell adhesion and proliferation. A hydrophilic polymer enables solution penetrates through its matrix, which in turn hastens its degradation [33-34]. Asides promoting cell proliferation, enhanced hydrophilicity can culminate in protein adhesion on to the surface of PLA [35], which boosts immunogenicity [36].

Weight Loss in PBS

Figure 6 shows the degradation profiles of LA and PLA/PEG fiber blends in PBS at 37 °C for 8 weeks. The Figure explains that addition of PEG to PLA increases the weight of electrospun PLA/PEG fibers. There is a gradual depreciation in each fiber's weight up to the final time of soaking. This implies that there is a chemical reaction between each polymer and PBS, which leads to loss of weight after drying. Electrospun PLA displays a constant

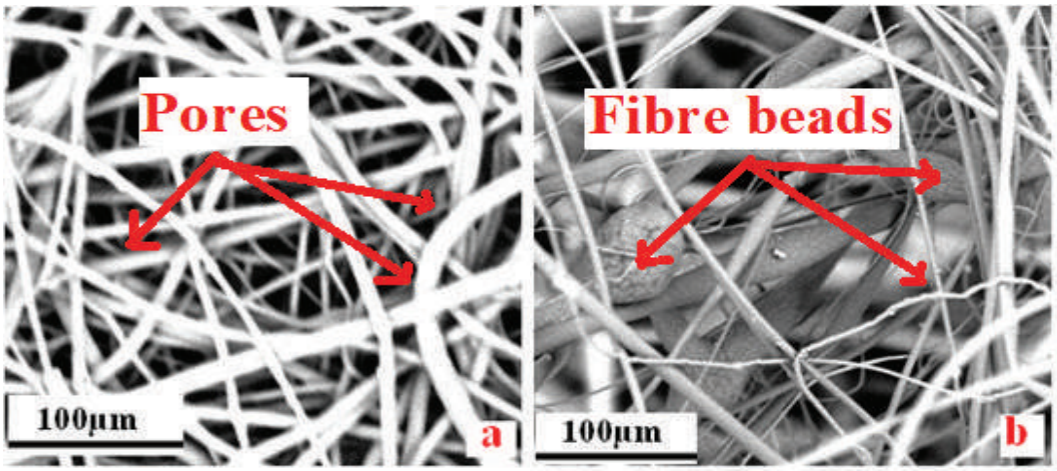


Figure 4. SEM of 80PLA/20PEG fiber: (a) before immersion (b) after 8 weeks immersion in PBS.

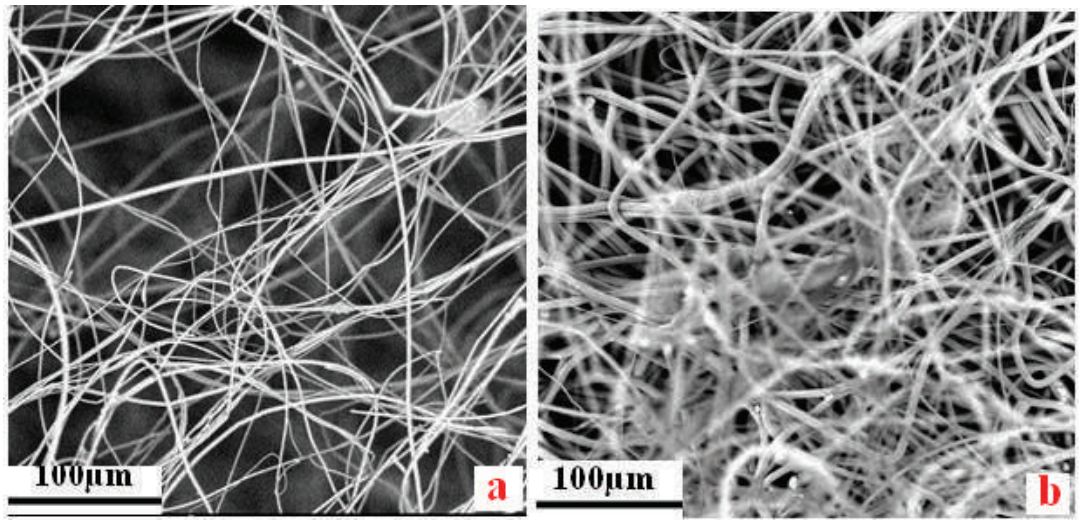


Figure 5. SEM of 60PLA/40PEG fiber: (a) before immersion (b) after 8 weeks immersion in PBS.

weight loss of 0.93 g for 4 weeks after which a gradual loss of weight is recorded for the next 4 weeks. Unlike PLA, blends of 80PLA/20PEG and 60PLA/40 PEG degradation with respect to dry weight loss become obvious after the third week of immersion. This shows that addition of PEG hastens the degradation of PLA. Hydrolytic degradation (surface erosion) of PLA fibres, according to Vaid et al. [37] is fast when the aqueous solution is basic. Reduction in surface changes and fiber characteristics becomes very little as solution pH reduces from 7.4 to 2; this is typical of bulk erosion which is exemplified by a slower degradation. Density functional theory (DFT) calculations employed by the authors affirms that electron withdrawing groups develop positive center at the carbon in carbonyl (C=O) functional group, that ends up creating a nucleophilic attack site by OH^-. Molecular dynamics (MD) simulations also supports the increase in PLA fibre degradation rates in solutions with higher pH values. Degradability and properties of PLA is significantly influenced by hydrolysis while non-catalytic hydrolysis of the polymer entails ester bond cleavage on exposure to water [38]. The researchers confirmed that depending on temperature, highly crystalline PLA exhibits a slower hydrolysis rate compared to amorphous and partially crystalline ones. Vaid et al. [37] however reported that crystallinity of PLA fiber is enhanced by fibre spinning. The hydrolytic degradation produces shorter chains with acid and alcohol terminal groups. The hydrophobic feature of PLA is evident in its degradation profile as its measured dry weight after each week of immersion looks comparable; there is no much difference between the final dry weight (after the eight week) and the dry weight of un immersed electrospun PLA fiber. Plots of 80PLA/20PEG and 60PLA/40 PEG show a much steep profile, indicating fast degradation rate. The physicochemical properties of PLA has been modified by addition of hydrophilic PEG hence, the blends can be useful for tissue engineering applications. Results obtained in this study agree with the works of Hendrick and Frey [4] whose research was aimed at improving the surface hydrophilicity of PLA by addition of PEG homo polymer and PLA-b-PEG co-polymers. Hydrophilicity of PLA was found to be enhanced on addition of PEG homo polymer and PLA-b-PEG co-polymers. Greater increase in water wettability was noticed with PLA-b-PEG co-polymers than PEG homopolymers. Medicated PEG/PLA nanofibrous membranes have been used as a carrier of an antibiotic drug, tetracycline hydrochloride, TCH [39]. The medicated PEG-PLA nanofibers exhibited mechanical barriers which aided the delivery of antibiotics in a sustainable way.

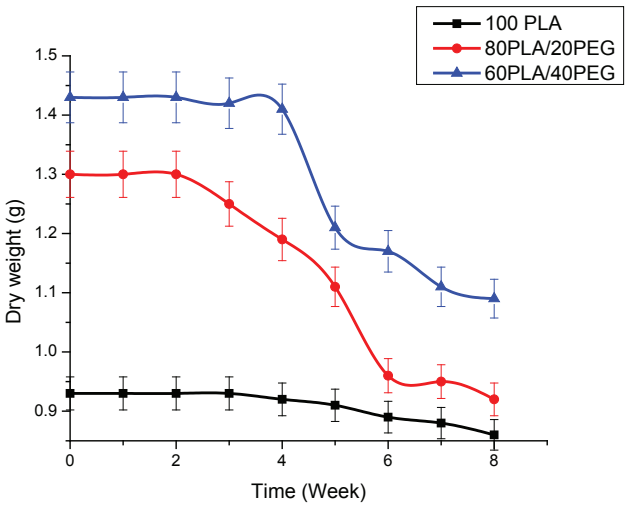


Figure 6. Dry weight loss of PLA and PLA/PEG electrospun fiber blends with time.

Tensile Properties

The maximum strengths of electrospun fibers attained prior to fracture is shown in Figure 7 Prior to immersion, it is observed that 80PLA/20PEG fiber has the greatest magnitude of UTS (0.31 MPa) which is approximately 11% increase from neat PLA fiber (0.27 MPa). An increase in UTS (0.29 MPa) is also noticed when 60 wt. % PLA is blended with 40 wt. % PEG; here, the UTS increase is minimal (approximately 4%). This implies that further additions of PEG to PLA may lead to reduction in UTS. Investigation of Kruse et al. [10] was aimed at processing and characterizing electrospun yarns. Tensile strength of the polymer blend was noted to increase with increasing content of PEG; this was attributed to the reduced viscosity of PLA/ PEG solution caused by addition of more PEG. Toncheva et al. [40] produced PLA/PEG electrospun fibers in two ways for mechanical, thermal and biological properties comparisons. The first method was to physically blend PEG to PLA while chemically grafting PEG on PLA entailed the second processing technique. Physical blending and chemical grafting techniques did not modify the wettability of PLA but provided a plasticizing effect, which was more evident in the PLA/PEG blended mats. This was attributed to more of PEG mobility possessed in the blend. The plasticizing effect of PEG used in this study could be responsible for the strength of electrospun PLA fiber; when this effect is much, it may lower the strength. After the first week of immersion, UTS of electrospun polymer fiber blends become lower than neat PLA. This shows that PEG can improve strength of PLA and also, aid its degradation (provided the content of PEG is controlled). Materials such as these can be useful for soft tissues, where considerable gradual depreciation of strength is required for effective healing.

Effect of the PEG on the ductility of PLA is shown in Figure 8. Ductility of electrospun PLA/ PEG blends are higher than neat PLA which is calculated to be1.18% before immersion in PBS. Addition of PEG has thus improved the elastic properties of PLA. Firoozian et all. [41] reported that the ductility of a composite will reduce if its elastic property is dominated by the matrix. Suradi, et al [42] further proved the position that reduced ductility will happen if the volume fraction of the matrix, which is more elastic of the two, reduces. Result from this study reveals that PEG is more ductile than PLA. Blending 60 wt. % PLA with 40 wt. % PEG displays the highest magnitude of ductility before (1.8 %) and at the end of each immersion period. In a bid to evaluate the lifespan of compression-moulded PLA as a structural implant in the human body, Woo and Wee [43] devised a model where its degradation was made to accelerate in PBS at 50, 60 and 70 °C. Degradation was evaluated in terms of its tensile properties (such as tensile strength and strain at break), which was discovered to reduce as time of exposure (in PBS) lapsed. At 50 °C, noticeable decay in the tensile properties commenced after 28 days while this occurred from the 6th and 2nd day at 60 and 70 °C respectively. In this study, it can be inferred that diffusion of fluid

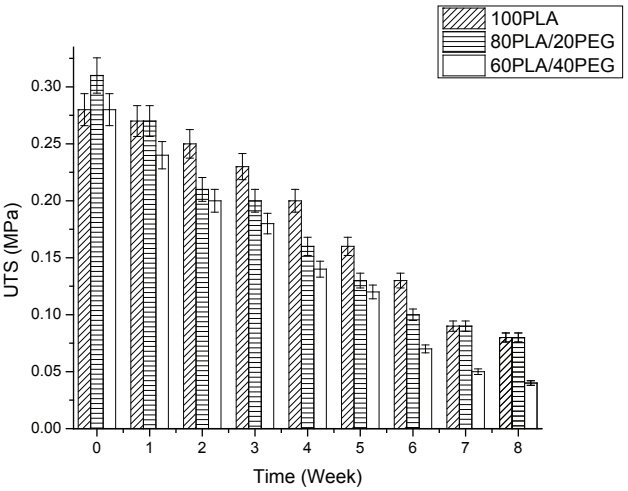


Figure 7. UTS of PLA and PLA/PEG blends with immersion time.

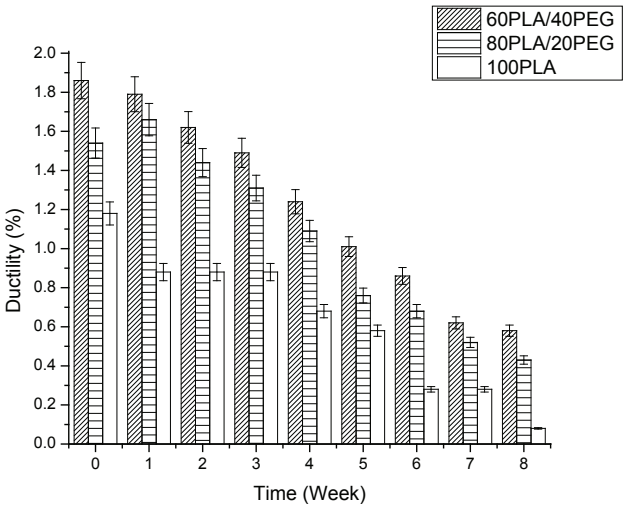


Figure 8. Ductility of PLA and PLA/PEG blends with immersion time.

(PBS) into fibre's structure as evidenced by its swelling, must have culminated in ester bond cleavage as earlier reported by [38]; this could also be responsible for its ductility loss.

CONCLUSION

In this study, the degradation of electrospun polylactide and polylactide/ polyethylene glycol fiber blends in phosphate buffered saline/solution at 37 °C and pH 7.4 have been studied. Results from Fourier Transform Infrared Spectroscopy justify that 100 % miscibility exists between polylactide and polyethylene. Degradation is exemplified by shifts in functional group wavenumbers. Formation of additional peaks on 1906 and 2067 cm^{-1} also depicts

degradation, including the disappearance of C-H functional group at 2866 cm $^{-1}$ in the fiber blends. Presence of polyethylene glycol is responsible for increase in average fiber diameter and this also widens after 8 weeks of immersion in phosphate buffered saline/solution. Before and after immersion, average fiber diameter increase of 1.07-1.35 μm, 2.04-7.39 μm and 2.99-13.04 μm are measured for neat polylactide, polylactide/ polyethylene glycol (80/20) and (60/40) electrospun fibers respectively. This implies that each fiber expands/swells as it absorbs the solution; Electrospun polylactide fiber maintains a constant dry weight loss for 4 weeks after which a gradual loss is recorded for the remaining 4 weeks. On the other hand, it takes 3 weeks for polylactide/ polyethylene glycol (80/20) and (60/40) electrospun fiber blends to start exhibiting considerable weight loss. After 8 weeks, polylactide/ polyethylene glycol (60/40) fiber loses 23 % of its weight while (80/20) variant loses 30 %; final weight of neat polylactide reduces by 5.3 %. This shows that addition of Polyethylene glycol hastens the degradation of Polylactide. Blending polylactide with polyethylene glycol (40 wt. %) displays the highest magnitude of ductility loss at the end of each immersion period; The electrospun fiber blends can be a good wound dresser as they possess the potential to effectively absorb fluids that are often secreted by wounds prior to complete healing; they can also be used as scaffolds for tissue regeneration. The improved tensile strength and ductility degradation of fibers (compared to neat polylactide fiber) will make them suitable for temporary structural supporting devices for soft tissues. To allow proper healing, these fiber blends will gradually lose their mechanical strengths in a faster way compared to unblended polylactide. Evaluation of degradation products and In *Vivo* studies will be conducted on the electrospun fibers in our future work.

AUTHOR CONTRIBUTIONS

Gbenebor O.P.: Conceptualization, investigation, methodology, data analysis, writing an original draft, and reviewing; **Popoola A.P.I.**: Investigation, methodology, editing and funding acquisition. Authors have read and agreed to the published version of the manuscript.

DATA AVAILABILITY STATEMENT

The authors confirm that the data that supports the findings of this study are available within the article. Raw data that support the finding of this study are available from the corresponding author, upon reasonable request.

CONFLICT OF INTEREST

The author declared no potential conflicts of interest with respect to the research, authorship, and/or publication of this article.

ETHICS

There are no ethical issues with the publication of this manuscript.

STATEMENT ON THE USE OF ARTIFICIAL INTELLIGENCE

Artificial intelligence was not used in the preparation of the article.

REFERENCES

[1] Farshidfar N, Iravani S, Varma RS. Alginate-based biomaterials in tissue engineering and regenerative medicine. Mar Drugs 2023;21:189:1–17. [CrossRef]

[2] Huang X, Lou Y, Duan Y, Liu H, Tian J, Shen Y, Wei X. Biomaterial scaffolds in maxillofacial bone tissue engineering: A review of recent advances. Bioact Mater 2024;33:129–156. [CrossRef]

[3] Fouly A, Assaifan AK, Alnaser IA, Hussein OA, Abdo HS. Evaluating the mechanical and tribological properties of 3D printed polylactic-acid (PLA) green-composite for artificial implant: Hip joint case study. Polym 2022;14:1–19. [CrossRef]

[4] Hendrick E, Frey M. Increasing surface hydrophilicity in poly(lactic acid) electrospun fibers by addition of PLA-b-PEG co-polymers. JEFF 2014;9:153–164. [CrossRef]

[5] Saini R, Arora M, Kumar MNV. Poly(lactic acid) blends in biomedical applications. Adv Drug Deliv Rev 2016;107:47–59. [CrossRef]

[6] Mendes JF, Fontes ML, Barbosa TV, Paschoalin RT, Mattoso LHC. Membranes composed of poly(lactic acid)/poly(ethylene glycol) and Ora-pro-nóbis (Pereskia aculeata Miller) extract for dressing applications. Int J Biol Macromol 2024;286:1–15. [CrossRef]

[7] Gbenebor OP, Odili CC, Obasa VD, Ochulor EF, Kusoro SO, Udogu-Obia OC, Adeosun SO. Morphological, mechanical and thermal characteristics of PLA/Cocos nucifera L husk and PLA/Zea mays chaff lignin fibre mats composites. NIJTD 2023;20:1–9. [CrossRef]

[8] Wang H, Feng Y, Fang Z, Yuan W, Khan M. Co-electrospun blends of PU and PEG as potential biocompatible scaffolds for small-diameter vascular tissue engineering. Mater Sci Eng C 2012;32:2306–2315. [CrossRef]

[9] Nazari T, Garmabi H. The effects of processing parameters on the morphology of PLA/PEG melt electrospun fibers. Polym Int 2017;67:178–188. [CrossRef]

[10] Kruse M, Greuel M, Kreimendahl F, Schneiders T, Bauer B, Gries T, Jockenhoevel S. Electro-spun PLA-PEG-yarns for tissue engineering applications. BMT 2018;:1–13. [CrossRef]

[11] Piran M, Shir M, Zomorrod MS, Esmaeili E, Zomorrod MS, Shiran NV, Mahboud H, Daneshpazhouh H, Dehghani N, Hosseinzadeh S. Electrospun triple-layered PLLA/gelatin/PRGF/PLLA scaffold induces fibroblast migration. Cell Biochem 2018;:1–13. [CrossRef]

[12] Fanga Y, Zhub X, Wangb N, Zhangc X, Yangb D, Niea J, Maa G. Biodegradable core-shell electrospun nanofibers based on PLA and γ-PGA for wound healing. Eur Polym J 2019;116:30–37. [CrossRef]

[13] Hajikhani M, Djomeh ZE, Askar G. Fabrication and characterization of mucoadhesive bioplastic patch via coaxial polylactic acid (PLA) based electrospun nanofibers with antimicrobial and wound healing application. Int J Biol Macromol 2021;172:143–153. [CrossRef]

[14] Lopresti F, Botta L, La Carrubba W, Attinasi G, Settanni L, Garofalo G, Gaglio R. Physical and antibacterial properties of PLA electrospun mats loaded with carvacrol and nisin. Express Polym Lett 2022;16:1083–1098. [CrossRef]

[15] Aijaz MO, Yang SB, Karim MR, Othman MHD, Alnaser IA. Preparation and characterization of poly(lactic acid)/poly(ethylene glycol)-poly(propyl glycol)-poly(ethylene glycol) blended nanofiber membranes for fog collection. Membr 2023;13:1–15. [CrossRef]

[16] Zhong G, Qiu M, Zhang J, Jiang F, Yue X, Huang C, Zhao S, Zeng R, Zhang C, Qu Y. Fabrication and characterization of PVA@PLA electrospinning nanofibers embedded with Bletilla striata polysaccharide and rosmarinic acid to promote wound healing. Int J Biol Macromol 2023;234:1–13. [CrossRef]

[17] Samokhin Y, Varava Y, Diedkova K, Yanko I, Husak Y, Pragłowska JR, Pogorielova O, Janus L, Pogorielov M, Korniienko V. Fabrication and characterization of electrospun chitosan/polylactic acid (CH/PLA) nanofiber scaffolds for biomedical application. J Funct Biomater 2023;14:1–17. [CrossRef]

[18] Loh ZW, Zaid MHM, Kechik MMA, Fen YW, Amin KM, Cheong WM. New formulation calcium-based 45S5 bioactive glass: In vitro assessment in PBS solution for potential dental applications. JMR&T 2023;24:3815–3825. [CrossRef]

[19] Guidotti G, Soccio M, Gazzano M, Bloise N, Bruni G, Aluigi A, et al. Biocompatible PBS-based copolymer for soft tissue engineering: Introduction of disulfide bonds as winning tool to tune the final properties. Polym Degrad Stab 2020;182:1–11. [CrossRef]

[20] Sahu M, Reddy VRM, Kim B, Patro B, Park C, Kim WK, et al. Fabrication of Cu_2ZnSnS_4 light absorber using a cost-effective mechanochemical method for photovoltaic applications. Mater 2022;15:1–16. [CrossRef]

[21] Shameli K, Bin Ahmad M, Jazayer SD, Sedaghat SS, Shabanzadeh P, Jahangirian H, et al. Synthesis and characterization of polyethylene glycol mediated silver nanoparticles by the green method. Int J Mol Sci 2012;13:6639–6650. [CrossRef]

[22] Nasirian D, Salahshoori I, Sadeghi M, Rashidi N, Hassanzadeganroudsari M. Investigation of the gas permeability properties from polysulfone/polyethylene glycol composite membrane. Polym Bull 2019;77:5529–5552. [CrossRef]

[23] Singla P, Mehta R, Berek D, Upadhyay SN. Microwave assisted synthesis of poly(lactic acid) and its characterization using size exclusion chromatography. J Macromol Sci Part A Pure Appl Chem 2012;49:963–970. [CrossRef]

[24] Leonés A, Peponi L, Lieblich M, Benavente R, Fiori S. In vitro degradation of plasticized PLA electrospun fiber mats: Morphological, thermal and crystalline evolution. Polym 2020;12:1–18. [CrossRef]

[25] Lero A, Ribeiro S, Grossiord C, Alves A, Vestberg RH, Salles V, et al. FTIR microscopy contribution for comprehension of degradation mechanisms in PLA-based implantable medical device. J Mater Sci Mater Med 2017;87:1–13. [CrossRef]

[26] Suárez L, Ortega Z, Romero F, Paz R, Marrero MD. Influence of giant reed fibers on mechanical, thermal, and disintegration behavior of rotomolded PLA and PE composites. J Environ Polym Degrad 2022;30:4848–4862. [CrossRef]

[27] Kovacina JP, Wise SG, Li Z, Maitz PKM, Young CJ, Wang Y, et al. Tailoring the porosity and pore size of electrospun synthetic human elastin scaffolds for dermal tissue engineering. Biomater 2011;32:6729–6736. [CrossRef]

[28] Megelski S, Stephens JS, Chase DB, Rabolt JF. Micro- and nanostructured surface morphology on electrospun polymer fibers. Macromol 2002;35:8456–8466. [CrossRef]

[29] Su X, Zhai Y, Jia C, Xu Z, Luo D, Pan Z, et al. Improved antibacterial properties of polylactic acid-based nanofibers loaded with ZnO–Ag nanoparticles through pore engineering. ACS Appl Mater Interfaces 2023;5:42920–42929. [CrossRef]

[30] Chen Y, Dong X, Shafiq M, Myles G, Radacsi N, Mo X. Recent advancements on three-dimensional electrospun nanofiber scaffolds for tissue engineering. Adv Fiber Mater 2022;4:959–986. [CrossRef]

[31] Dias J, Ribeiro C, Sencadas V, Botelho G, Ribelles JLG, Mendez SL. Influence of fiber diameter and crystallinity on the stability of electrospun poly (L-lactic acid) membranes to hydrolytic degradation. Polym Test 2012;31:770–776. [CrossRef]

[32] Herrero MH, Torres SA, Fernández MLG, Feltrer GV, Hernández JC, Lluch AV, et al. Influence of chemistry and fiber diameter of electrospun PLA, PCL and their blend membranes, intended as cell supports, on their biological behavior. Polym Test 2021;103:1–11. [CrossRef]

[33] Shi J, Zhang J, Zhang Y, Zhang L, Yang YB, Mano O, You J. Crystallinity dependence of PLLA hydrophilic modification during alkali hydrolysis. Polym 2023;15:1–11. [CrossRef]

[34] Scaffaro R, Maio A, Gulino EF. Hydrolytic degradation of PLA/Posidonia oceanica green composites: A simple model based on starting morpho-chemical properties. Compos Sci Technol 2021;203:1–11. [CrossRef]

[35] Schroepfer M, Junghans F, Voigt D, Meyer M, Breier A, Tanzil GS, et al. Gas-phase fluorination on PLA improves cell adhesion and spreading. ACS Omega 2020;5:5498–5507. [CrossRef]

[36] Sakhabeev RG, Polyakov DS, Sinitsyna ES, Vlakh VAK, Bagaeva IO, Vlakh EGK, et al. Features of the humoral immune response when using protein immobilized on the surface of nano- and microparticles based on poly(lactic acid). J Evol Biochem Physiol 2024;60:466–475. [CrossRef]

[37] Vaid R, Yildirim E, Pasquinelli MA, King MW. Hydrolytic degradation of polylactic acid fibers as a function of pH and exposure time. Mol 2021;26:1–17. [CrossRef]

[38] Limsukon W, Rubino M, Rabnawaz M, Lim LT, Auras R. Hydrolytic degradation of poly (lactic acid): Unraveling correlations between temperature and the three phase structures. Polym Degrad Stab 2023;27:1–10. [CrossRef]

[39] Xu X, Zhong W, Zhou S, Trajtman A, Alfa M. Electrospun PEG–PLA nanofibrous membrane for sustained release of hydrophilic antibiotic. J Appl Polym Sci 2010;118:588–595. [CrossRef]

[40] Toncheva A, Mincheva R, Kancheva M, Manolova N, Rashkov I, Dubois P, et al. Antibacterial PLA/PEG electrospun fibers: Comparative study between grafting and blending PEG. Eur Polym J 2016;83:223–233. [CrossRef]

[41] Firoozian P, Hazizan MA, Khalil HPSA. Prediction of mechanical properties of mica-filled epoxy composite using various mechanical models. J Reinf Plast Comp 2010;29:2368–7268. [CrossRef]

[42] Suradi SS, Yunus RM, Beg MDH. Oil palm bio-fibre-reinforced polypropylene composites: Effects of alkali fibre treatment and coupling agents. J Compos Mater 2010;45:1853–1861. [CrossRef]

[43] Woo SH, Wee JW. Characterization of accelerated hydrolysis degradation of poly(lactic acid) in phosphate buffered saline solution. Polym Degrad Stab 2024;223:1–15. [CrossRef]

Sigma Journal of Engineering and Natural Sciences
Web page info: https://sigma.yildiz.edu.tr
DOI: 10.14744/sigma.2025.1930

Research Article

Ultrasonic waveguide sensor design using bend reflectors for elastic moduli and temperature measurement

Anubhav SRIVASTAVA[1,*], Arun VALABHOJU[1], Abhishek KUMAR[1], Suresh PERIYANNAN[1,*]

[1]*Department of Mechanical Engineering, National Institute of Technology, Warangal, 506004, India*

ARTICLE INFO

Article history
Received: 08 May 2024
Revised: 21 August 2024
Accepted: 17 October 2024

Keywords:
Elastic Moduli; Sensors; Temperature; Time of Flight; Ultrasonic Strip Waveguide

ABSTRACT

This research presents an ultrasonic strip waveguide sensor with various reflector embodiments, including rectangular notches, single, and multiple bends. The ultrasonic waveguide sensor concept is a non-destructive and non-invasive method to measure material properties in elevated temperatures, where conventional techniques often fail. This ultrasonic sensor technique measures the surrounding temperature of the waveguide and its temperature-dependent elastic moduli using the symmetric (S_0) wave mode. Initially, we performed the Finite Element Method (FEM) simulations using Abaqus CAE software to find a better ultrasonic reflector configuration and its dimension based on the ultrasonic waveguide (S_0 mode) signal behavior. The simulation uses a rectangular strip waveguide (stainless steel) with a thickness of 0.5 mm, a width of 3 mm, and a length of 1000 mm. The S_0 mode was excited using a Hanning pulse tone burst signal at one end of the waveguide. Then, FEM studies revealed that the reconfigurable bend reflector (radius 3 mm) is better than rectangular reflector configurations for designing the ultrasonic sensor to obtain better reference reflection. Then, ultrasonic-guided wave experiments were conducted at different temperatures using the same dimension of the stainless-steel strip as a waveguide using the pulse-echo approach with an ultrasonic shear transducer at one end of the waveguide. We considered the ultrasonic parameter time of flight difference to calibrate the sensor based on the surrounding temperature. Also, temperature-dependent elastic moduli were measured, resulting in a maximum measurement error of 3% compared to literature data. The developed novel waveguide technique comprising non-destructive method can easily measure the elastic moduli compared to conventional destructive type testing methods, specimens are reusable, monitoring the components in service, and simple and cost-effective technique for monitoring various industrial components like power plants, oil, and Petro-chemical industries.

Cite this article as: Srivastava A, Valabhoju A, Kumar A, Periyannan S. Ultrasonic waveguide sensor design using bend reflectors for elastic moduli and temperature measurement. Sigma J Eng Nat Sci 2025;43(6):2006–2016.

***Corresponding author.**
*E-mail address: as22mem4r03@student.nitw.ac.in, sureshp@nitw.ac.in

This paper was recommended for publication in revised form by Editor-in-Chief Ahmet Selim Dalkilic

Published by Yıldız Technical University Press, İstanbul, Turkey
© Author. This is an open access article under the CC BY-NC license (http://creativecommons.org/licenses/by-nc/4.0/).

INTRODUCTION

Ultrasonic testing is a well-known nondestructive testing (NDT) technique that utilizes high-frequency sound waves. In ultrasonic testing, the ultrasonic waveguide technique can be used for various applications, such as measurements of the temperature of the surrounding medium, liquid level, rheological properties of fluids, and material properties. In hostile environments, conventional sensors like thermocouples, RTDs, etc., show accuracy problems, whereas ultrasonic sensors can work efficiently. Significant work has been done on ultrasonic sensors in the past few years. Balasubramanium et al. classified the ultrasonic waveguide sensing technique into two broad categories, the forward problem and inverse problem, implying its applications in process industries [1]. Periyannan et al. [2] reported a novel ultrasonic technique for determining elastic moduli (E) using cylindrical waveguides at different temperatures. Bao et al. [3] developed a new sonic resonance method to measure Young's modulus (E) and shear modulus (G) of rail steel at elevated temperatures. They used a laser vibrometer to observe the flexural and torsional resonance frequency at elevated temperatures and used it to measure E and G, respectively. N. Raja et al. demonstrated using a stainless-steel (SS) rod-like waveguide for distributed skin temperature measurement in solid pipes and water. They used bend-notch and notch-notch combinations as sensor regions co-located with the K-type thermocouples for calibration. [4]. Periyannan et al. reported a robust technique for multi-level temperature measurements using six Chromel waveguides of diameter 1.12 mm with varying lengths attached to a single shear transducer for transmitting and receiving the ultrasonic signals. The difference in time in flight and readings from co-located K-type thermocouples were used to calibrate the sensor [5]. Liao et al. have extended the ultrasonic dry-coupled waveguide technique in structural health monitoring (SHM) of critical mechanical components in high-temperature environments [6].

Zhou et al. [7] proposed a high-accuracy ultrasonic temperature estimation technique. They employed maximum length sequence (MLS) modulation on a continuous wave to effectively suppress the effects of echoes. The temperature of distilled water was successfully measured with an error of $\pm 0.04^{o}$C. Periyannan et al. [8] developed a novel technique to measure the temperatures at multiple locations using multiple waveguides with a single bend and a single waveguide with multiple bends. Sahu et al. [9] reported the use of an ultrasound-guided wave technique for mapping the surface temperature of Aluminum plates. A metal strip with rectangular notches was placed in the slots of two Aluminum plates. Shear horizontal (SH_0) wave mode was excited in the waveguide with the help of an ultrasonic shear transducer attached at one end of the waveguide. The waveguide sensor was calibrated using reference temperatures obtained from the data of co-located RTDs. Szelek et al. [10] presented a new evaluation method for temperature-dependent ultrasonic longitudinal and shear velocity measurements. The results obtained from these ultrasonic velocities were further used to determine elastic and shear moduli E and G, respectively. Liang et al. [11] reported a sapphire ultrasonic temperature sensor for monitoring the temperature of an aircraft engine. Periyannan and Balasubramaniam reported a novel technique for the measurement of temperature and temperature-dependent elastic moduli (E(T) and G(T)) using straight and L-bend waveguides with L (0, 1) and T (0, 1) wave modes generated using pulse-echo mode through longitudinal and shear wave transducers, respectively. [12]. Dhayalan et al. developed a novel non-invasive ultrasonic waveguide sensor for liquid level measurement. [13]. Periyannan et al. reported a novel re-configurable ultrasonic temperature sensing technique using a helical spring-like waveguide with multiple notches as reflector embodiments [14].

Nishanth et al. [15] introduced an ultrasonic waveguide technique for distributed temperature measurement on a solid surface. A stainless-steel bent rod waveguide of 1 mm diameter with axisymmetric notches in the bent horizontal region acts as the sensor. Changes in the time of flight of the waves, reflected from the bend and notches, were estimated and used for calibration with the results of K-type thermocouples co-located in the sensor region. Wong et al. [16] presented a precise method for measuring temperatures up to 200°C using ultrasonic waves. Wang et al. [17] proposed a novel U-shaped waveguide sensor for viscosity measurement using a pitch-catch method to excite and receive an SH_0 wave. Kumar et al. [18] demonstrated an ultrasonic waveguide sensor for fluid level sensing using a U-shaped and helical waveguide. They also reported minute-level sensing using flexural wave mode [19, 20]. Balasubramaniam and Periyannan developed an ultrasonic waveguide technique to measure the surrounding media's chemical and physical properties [21, 22]. Signal processing is a significant step in the development of an accurate sensing device; extensive studies of various signal behaviors and analytical solutions are discussed in the literature and used in signal processing in various sensors' sensing applications [23-35]. Uses of NDT techniques are not limited to only metallic materials. Gezer et al. used NDT methods to detect defects in a wooden structure [36]. And Kabay et al. utilized the NDT technique to estimate the core compressive strength of concrete.[37].

Earlier research on ultrasonic waveguide sensors predominantly focused on cylindrical waveguides**,** emphasizing line contact with the transducer surface. Due to line contact, it may not effectively transmit the ultrasonic energy in the waveguide [2, 8, 14, 21, 22]. However, strip waveguides offer enhanced surface contact with the transducer for transmitting the ultrasonic energy effectively in the waveguide due to surface contact. The early works reported ultrasonic reflector dimension (bend radius = 3d (d - wire diameter)) and their empirical constant A=2.5 for E measurements of the cylindrical specimens using L(0, 1) wave mode [38, 39]. However, these are not reported for

strip waveguides in the case of strip specimens' E measurements. The wave propagation behavior may differ in strip specimens (rectangular cross-section) compared to cylindrical specimens due to different geometry/boundaries. Hence, this work reported that E measurements of the strip specimens, ultrasonic reflector dimension (bend radius = 6t (t - strip thickness)), and their empirical constant (A=2) were found using S_0 wave mode. In engineering applications, plenty of metal/alloy strips or bars are generally used.

Furthermore, there is a lack of research on using strip waveguides for Young's modulus (E) estimation as a function of temperature. Hence, this study uses the novel concept to investigate the potential of strip waveguides for temperature-dependent elastic moduli (Ei) measurements [21, 22]. Further, it can act as an ultrasonic temperature sensor too [40, 41].

FINITE ELEMENT METHOD SIMULATIONS

Finite element method (FEM) simulations for the waveguide with different reflector embodiments were conducted using Abaqus software. The material properties and FEM parameters used in the simulation, as shown in Table 1. Initially, wave propagation characteristics in the waveguide were studied using the Disperse calculator/software based on waveguide thickness (0.5 mm). The non-dispersive guided wave propagation velocity and its corresponding frequencies were identified (Fig.1a) [42].

Then, the S_0 wave mode in the waveguide was observed to be non-dispersive in the 200-500 kHz frequency range and then, followed a well-known concept to verify the operating frequency and non-dispersive group velocity using a FEM study and its parameters (2D FFT Vs wave number) [9, 39, 41]. The S_0 wave mode (red line) was ensured to pass through a 200-360 kHz frequency spectrum region. This study was conducted in the frequency bandwidth of 250-350 kHz within the non-dispersive region. We obtained a 2D FFT plot (Fig. 1b) based on received signals from FEM simulations, and these simulations were compared with a dispersion plot.

Table 1. Material properties of SS304 and FEM parameters used in the simulation

Material properties	FEM parameters
Material – SS304	Solver – Abaqus CAE
Density – 7960 kg/m^3	Module – Dynamic, explicit
Young's modulus – 195 GPa	Time increment (t) – 1e^{-8}
Poisson's ratio – 0.27	Element type – C3D8R
	Element size – 0.25 mm
	Frequency (f) – 0.250 MHz
	No. of cycles (n) – 3

Waveguide Sensor Design with Destructive and Non-destructive Type Reflectors

Different reflector embodiments like rectangular notch, single bend, and multiple bends were introduced in the strip waveguides using the Abaqus CAE software, as shown in Figure 2**,** with respective dimensions. Ultrasonic waves were reflected from these reflector embodiments while propagating through the waveguide. The waveguide sensor was designed with a single rectangular notch (made through waveguide thickness) by removing the material to create an ultrasonic (destructive type) reflector, as shown in Figure 2b. The destructive type reflector is useful in case the waveguide material is brittle. The depth of the rectangular notch used was through-thickness (0.5 mm) based on earlier reported literature [4, 21, 22]. The bend configurations (single bend and multiple bends) were preferred over the rectangular notch to make a non-destructive type reflector in the waveguide, as shown in Figure 2c and d. Bend reflectors were more suitable, easy to make, and re-configurable while designing the waveguide sensor using ductile materials. The bend acts as a better reference signal reflector for making an ultrasonic temperature sensor without a temperature gradient, as reported by Periyannan [8]. While using a notch reflector, the waveguide sensors couldn't be

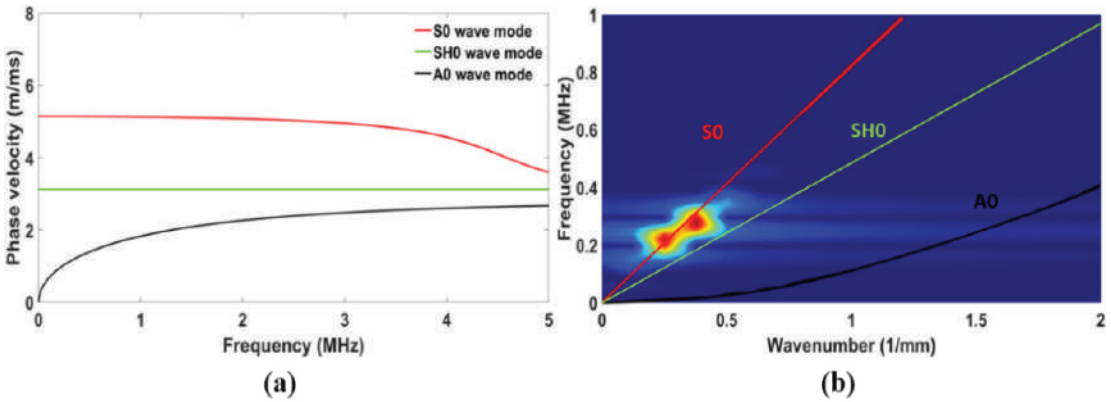


Figure 1. (a) Frequency vs. Phase velocity plot from Dispersion calculator (b) 2D FFT plot.

re-configured, as we wouldn't obtain the waveguide's original geometry. Single-bend waveguides could be useful for single-location measurements, and multiple-bend waveguides could be useful for multi-location measurements. The strength of the ultrasonic reflected signals from the bend reflector could be tuned/varied based on requirements by varying the bend radii. Hence, studies were carried out to determine suitable bend radii for designing the waveguide with distributed bend reflectors, as shown in Table 2, through case A to case D, by varying the radii from 4.5 mm to 10.5 mm for bends.

Stress wave propagation FEM simulations with S_0 wave mode were performed using Abaqus CAE software. A 3-cycle 250 kHz Hanning pulse signal (input excitation) was applied at one end of the waveguide in the FEM simulations, as shown in Eqn. (1). The A-scan (wave propagation time vs. displacement amplitude) plots for all the waveguides (Fig. 2b-d) were obtained, as shown in Figure 3 a-c. The bend reflectors' dimensions were optimized by studying the ultrasonic wave reflections (analyzed using the Hilbert transform tool, Fig. 4) at different bend radii of strip waveguide (Fig. 2 d) using the FEM approach in four Cases (A-D), as shown in Table 2, based on early reported work by Periyannan [8]. Nearly uniform amplitude reflections were obtained from each bend reflector for Case C, as shown in the Hilbert Transform in Figure 4. However, a uniform reflected signal strength was appropriate for making multiple bent sensors [8]. Hence, Case C was found to be a more suitable bend reflector configuration based on results obtained using the FEM approach, as shown in Figure 3c. Then, studies were carried out for the single-bend reflector in the waveguide while varying bend radii from 3 mm to 12 mm, as shown in Figure 3b. Then, it was observed that as the radius decreased, the amplitude of the reflected signal increased, nearly equal to the end reflection for a 3 mm radius. Hence, a 3 mm bend radius was found to be more suitable. Similarly, it was observed that the amplitude of the reference reflected signal increased from the rectangular notch reflector (destructive type) while increasing the width of the notch from 0.3 mm to 1 mm, as shown in Figure 3a. Here, the strength of the reflected signals from the notch and waveguide end was nearly the same when the width of the notch was 1mm.

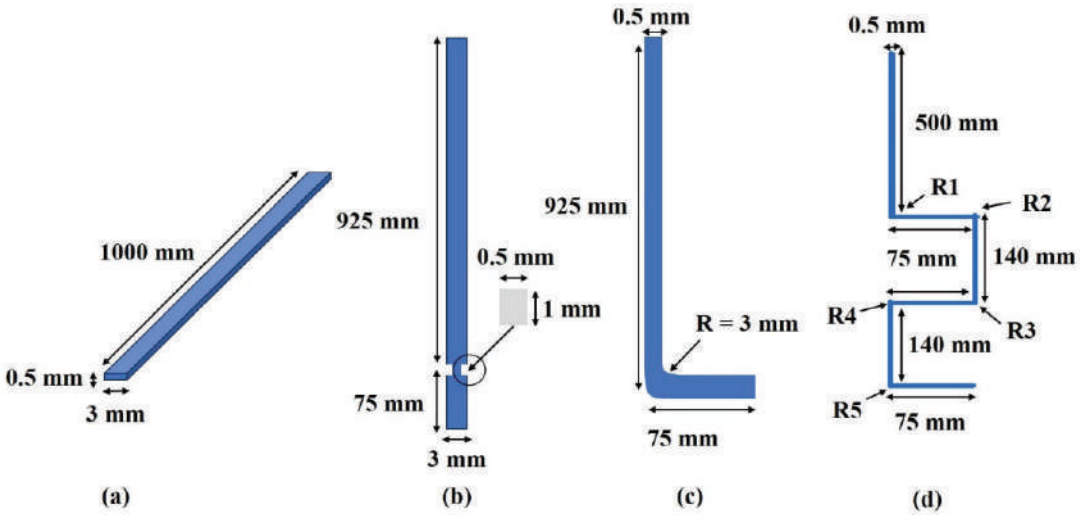


Figure 2. Waveguides with (a) no reflector, (b) rectangular notches through the thickness, (c) single bend, and (d) multiple bends.

Table 2. Bend radii in different cases

Cases	R1	R2	R3	R4	R5
Case A	1.5w	1.75w	2.0w	2.25w	2.5w
Case B	2.5w	2.25w	2.0w	1.75w	1.5w
Case C	3.0w	2.75w	2.5w	2.25w	2.0w
Case D	3.5w	3.25w	3.0w	2.75w	2.5w

All dimensions in mm. Note: width of the waveguide (w) = 3 mm.

$$H = [1 - cos\left(\frac{2\pi ft}{n}\right)].cos(2\pi ft) \quad (1)$$

Different ultrasonic reflectors (Fig. 2) were studied using the FEM approach to find a suitable ultrasonic reflector. It was observed that bend embodiments (non-destructive reflectors) were appropriate ultrasonic reflectors due to their reconfigurability and ability to tune the reflector's signal strength based on our requirements, as shown in Figure 3b and c. However, a single-bend reflector was initially preferred when designing the ultrasonic sensor to measure the waveguide materials' temperature and elastic moduli.

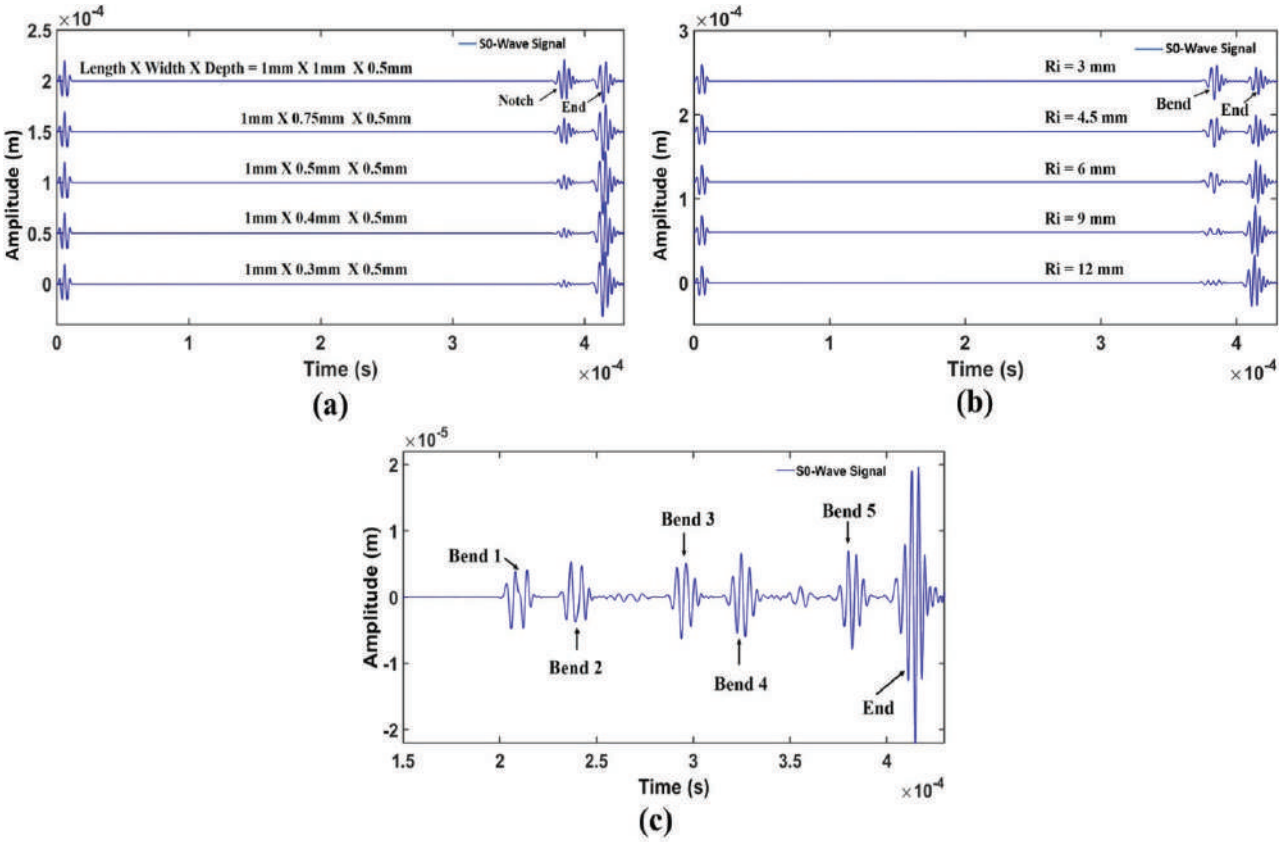


Figure 3. A-Scans of S_0 wave for a waveguide with (a) rectangular notch (b) single bend, and (c) multiple bends.

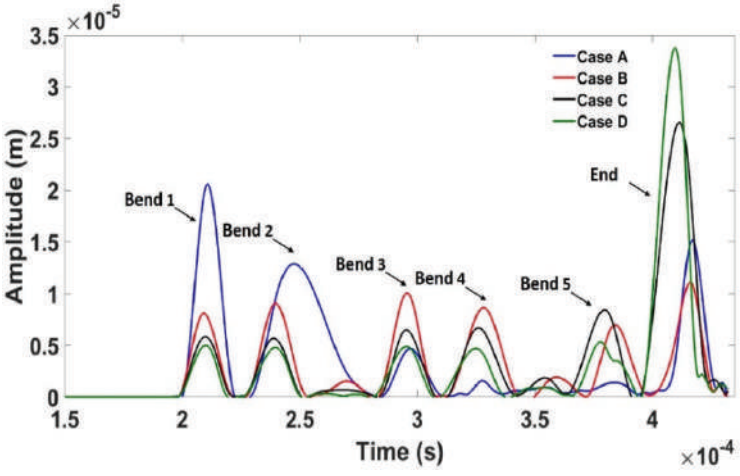


Figure 4. Hilbert transforms different cases to determine suitable bend radii.

EXPERIMENTAL METHODOLOGY

At elevated temperatures, the properties of metals/alloys show significant variation. Periyannan et al. reported the variation of elastic moduli at elevated temperatures of various metals/alloys [2]. Using cylindrical waveguides, they estimated the temperature-dependent Young's and Shear modulus of Inconel-690, Copper, Aluminum, Kanthal, etc. Simmons and Van Echo had well-documented elastic moduli of various types of stainless steel [40]. This research work was intended to develop an ultrasonic strip waveguide sensor that could be utilized to estimate temperature-dependent Young's modulus. Here, a rectangular cross-section (strip) waveguide was used, which provides better surface contact with the transducer surface than cylindrical waveguides. FEM simulation studies on various reflector embodiments suggested that bend reflectors with appropriate bend radii were more suitable based on the reflected signal's amplitudes of A-scan plots, as shown in Figure 3 and Figure 4. The strip waveguide (with bend) approach was followed for estimating the temperature and temperature-dependent Young's modulus of waveguide material. An SS304 strip waveguide with an L-bend (which acts as a sensor region) was used for experiments. The straight portion of the waveguide was 925 mm, and the bend portion was 75 mm long. The technique is illustrated in Figure 5 through a schematic diagram of the experimental setup, where we can see the strip waveguide coupled to the shear transducer (Olympus, V151, 500 kHz, 1-inch diameter, USA) at an angle of 0° to excite the S_0 wave mode and the shear transducer further connected to a personal computer and analog to digital converter as well as to record the data using Pico-Scope. Using silicone grease couplant at one end of the waveguide avoids air gaps between the transducer and the waveguide. We used a pulse-echo approach to transmit and receive S_0 wave mode in the waveguide using JSR Ultrasonic DPR 300 and Pico Scope 3000 series, respectively. During the experiments, control parameters were input voltage 475 V, gain 36 dB, bandpass filter 0-7.5 MHz, pulse-echo frequency 250 kHz, and 100 MHz sampling rate.

The waveguide was exposed inside the temperature-controlled furnace with the L-bend as a measurement point. A thermocouple was co-located with the sensor region to record temperature data at uniform intervals. The transducer was fixed outside the furnace to avoid damage due to high temperature. A bend radius of 3 mm was found to be better for a single-bend sensor design (L-bend) from the FEM simulation study using different bend radii, as shown in Figure 6a. Rose documented the ultrasonic S_0 wave propagation in waveguides [38]. And S_0 velocity was ensured under the non-dispersive region with the help of the Dispersion calculator [42]. Experiments were carried out at room temperature with different bend radii. The results of the simulation studies and experiments were in good agreement, as depicted in the A-scan signals (Fig. 6a-b). Here, the ultrasonic reflection was reduced from the bend while the bend radius was increased, and simultaneously, the end reflection was increased. If the bend radius decreased, then ultrasonic reflection from the bend was increased, and end reflection was decreased, which can be observed from FEM studies and experimental studies, as shown in Figure 6c-d, and finally, observed that a bend radius of 3 mm to 4.2 mm was appropriate to make an optimum bent reflector. Air was the surrounding medium in the furnace, whose physical properties were known a priori. The ultrasonic parameter's difference in time of flight (δToF) was used to calibrate the sensor. We evaluated the δToF by a peak tracking algorithm on reflected signals obtained from the bend and end of the waveguide at different temperatures, as reported by Periyannan [2].

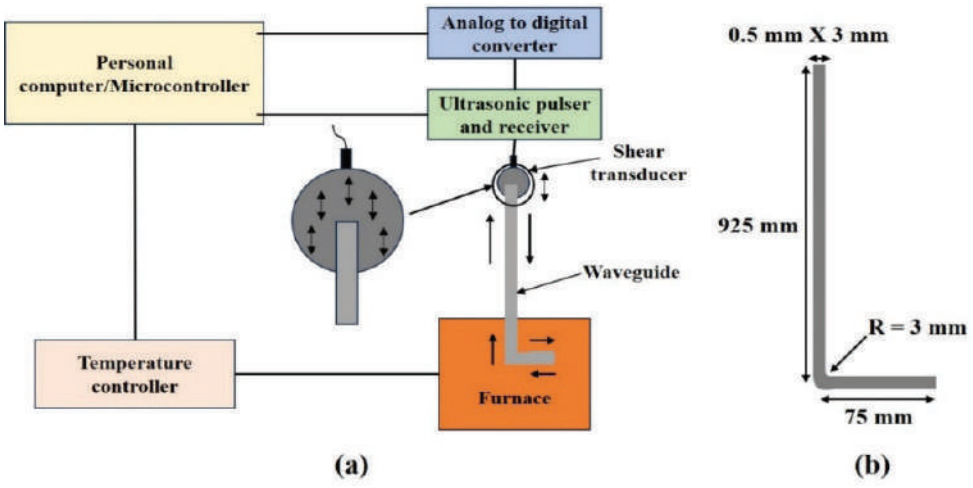


Figure 5. (a) Schematic diagram of the experimental setup, (b) bent waveguide.

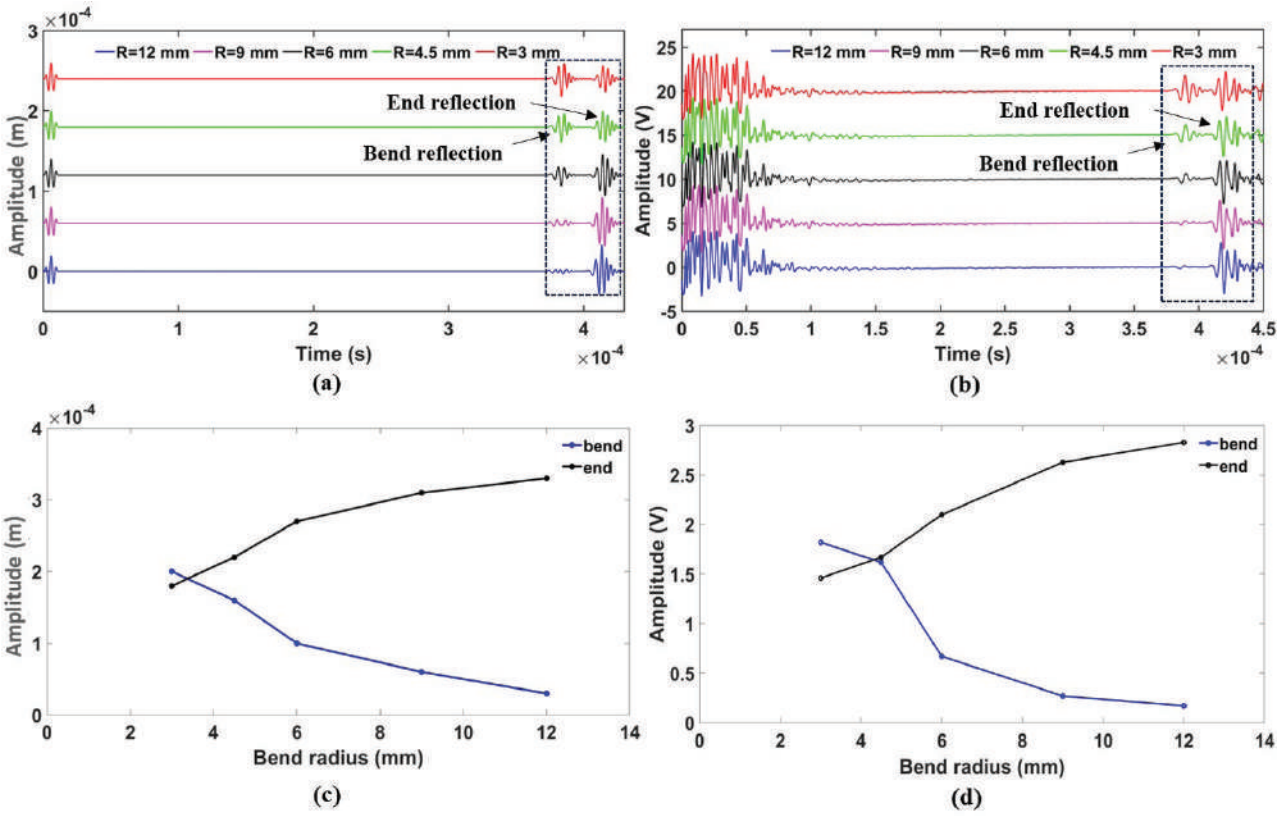


Figure 6. (a) Simulation A-scans, (b) experimental A-scans, (c) simulation amplitude decay with bend radii, and (d) experimental amplitude decay with bend radii.

RESULTS AND DISCUSSION

Experiments were performed in a range of temperatures from 30 °C to 630 °C using a furnace. At an interval of every 10 °C, A-scan signals were obtained at different temperatures due to S_0 wave mode reflection from the bend and end of the waveguide. A clear time/phase shift was observed in A-scan plots due to the changing behaviors of ultrasonic waves at different surrounding temperatures and thermal expansion of waveguide material, as shown in Figure 7, reflected signals shifting towards the right with the increase in temperature from 30°C to 600°C. A peak tracking algorithm was employed to estimate δToF using equations (2) and (3).

$$ToF_o = (ToF_e - ToF_b) \quad (2)$$

$$\delta ToF_i = [(ToF_{ei} - ToF_{bi}) - (ToF_e - ToF_b)] \quad (3)$$

Where, $ToF_{e,b}$ – Time of flight from end (e) and bend (b) at room temperature

$ToF_{ei,bi}$ – Time of flight from the end (e) and bend (b) at the instantaneous temperature

ToF_o – Difference in time of flight from the end and bend at room temperature

δToF_i – Difference in time of flight at instantaneous temperature.

A thermocouple was co-located near the bend region to collect the temperature data throughout the experiment. The ultrasonic sensor was calibrated using the δToF and thermocouple data at various time instants. The co-located thermocouple and waveguide sensor's δToF measurements were used to calibrate the sensor for surrounding temperature measurement. We conducted multiple experiments, and the data from all three experiments were in close agreement, ensuring repeatability evident from the calibration curves of all three experiments, as shown in Figure 8 (a).

Periyannan measured Young's modulus (E) of cylindrical waveguide materials based on L (0,1) wave mode at various temperatures and reported the empirical constant "A=2.5" suitable for cylindrical waveguides. [2]. In this work, the Ei of a strip waveguide was measured using equation (4) based on the S_0 wave mode. The empirical constant fund A =2 for the strip-like waveguide material while comparing (Ei vs Ti) with the literature.

$$Ei = \left(\frac{Eo}{1 + A\left(\frac{\delta ToFi}{ToF}\right)} \right) \quad (4)$$

Here, *Ei* - Young's modulus at instantaneous temperature
Eo - Young's modulus at room temperature (195 GPa).

The sensor was calibrated based on temperature-dependent E measurement using ToF and δToF data in equation (3). The calibration curve is shown in Figure 8b.

Equation (5) denotes the calibration equation for temperature sensing, where "y" denotes temperature and "x" denotes δToF. Equation (6) denotes the calibration equation for temperature-dependent Young's modulus estimation for the waveguide material (SS304) using an ultrasonic strip waveguide sensor, where "y" denotes Young's modulus and "x" denotes temperature. The error was calculated using equation (7). *Ei* computed using equation (4) was compared to the *Ei* given in literature data [40].

$$y = -12.92x^2 + 185.02x + 42.18 \quad (5)$$

$$y = -2.00e^{-5}x^2 - 0.061x + 197.10 \quad (6)$$

$$\%\ Error = \frac{|Ultrasonic\ sensor\ data - Literature\ data|}{Literature\ data}\ X\ 100 \quad (7)$$

Table 3 shows the % error in measuring Ei at various temperatures using a strip waveguide sensor compared to the literature data from ASTM [40]. The results were compared to the recent technique and available ASTM literature [2, 40]. The maximum error observed using a strip waveguide was 3 %, whereas the maximum error for the cylindrical waveguide sensor was 6.2 % [2]. Strip waveguide

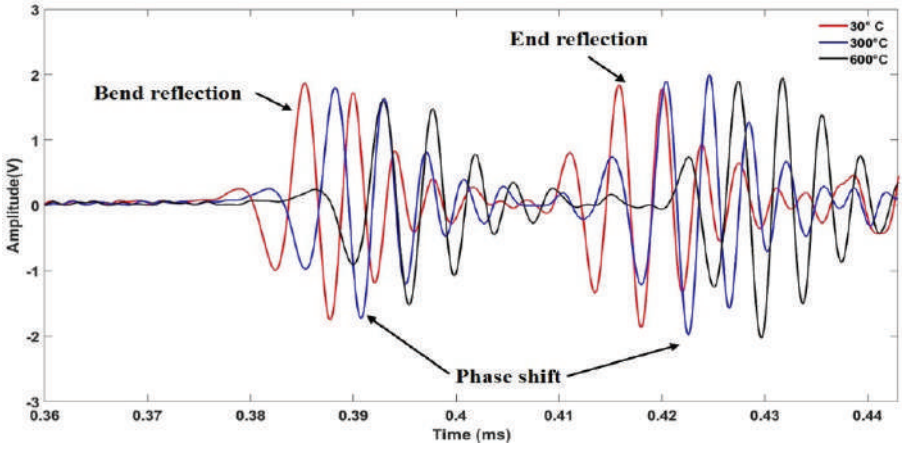


Figure 7. Phase and time shifted A-scan signals at 30°C, 300°C, and 600°C.

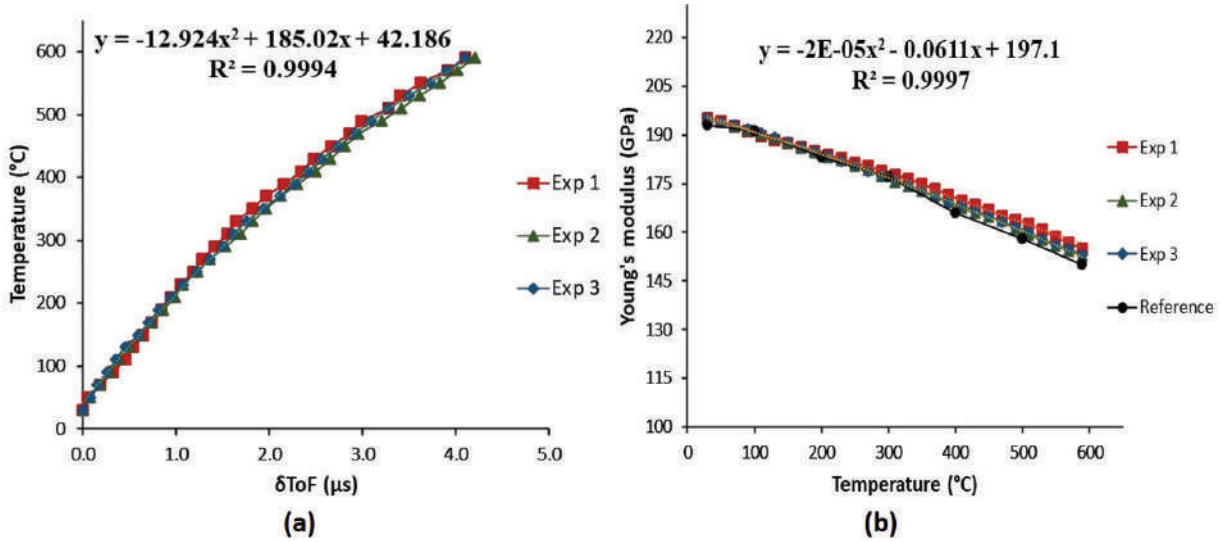


Figure 8. Calibration curves (a) δToF vs. Temperature, and (b) Temperature vs. Young's modulus.

Table 3. Error in the measurement of Ei calculated using strip waveguide sensor and cylindrical waveguide sensor

Temperature (°C)	Literature data Ei (GPa)	Ultrasonic strip waveguide sensor data Ei (GPa)	% Error for strip waveguide sensor	Ultrasonic cylindrical waveguide sensor data Ei (GPa)	% Error for cylindrical waveguide sensor
30	193	195	1.0	205	6.2
100	191	190.94	0.03	197.4	3.3
200	183	184.12	0.65	186.2	1.7
300	177	176.9	0.05	175.8	0.6
400	166	169	2.0	168	1.2
500	156	161.2	3.0	159.3	2.1
600	150	152.8	1.86	147	2.0

sensors' lower and upper error limits were 0.03 % and 3 %, respectively. Also, the observed error difference in both techniques may be due to experimental settings, the type of material/compositions, the initial E_0 values, and their geometries [43].

Since bend reflectors are non-destructive, material removal (notches) is not required to make ultrasonic reflectors. Hence, the waveguide is not permanently damaged but is reconfigurable and reusable. The intensity of the reflected signals can be tuned by varying the bend radius for sensor design. Especially using long waveguides with more bends for distributed temperature sensing. The effect of temperature gradient can be negligible in the horizontal bend region, which can be a better sensor [8].

CONCLUSION

We developed an ultrasonic strip waveguide sensor based on a symmetric wave mode to measure the elastic modulus and the surrounding medium temperature. The notch and bent reflectors were studied using the SS304 strip waveguide using the finite element method approach. The different bend radii were simulated using the finite element method approach to obtain a suitable bend radius and were compared to experimental studies. The bend radius of 3 mm was more appropriate, corresponding to the waveguide thickness for obtaining better signal reflection from the bend reflector. A thermocouple was placed in the bend region to monitor the temperature data at various intervals. We calibrated the sensor based on thermocouple data and the flight time difference. Then, the ultrasonic sensor's difference in time of flight and time of flight data were used to measure the temperature-dependent elastic modulus of the waveguide material at different temperatures. An empirical equation was obtained for the sensor by measuring the temperature-dependent elastic modulus at various temperatures. The measured Ei was compared to the available literature data and recent techniques; it was found to be in good agreement, and the error was ≤ 3 %. Multiple experiments were conducted to develop the ultrasonic temperature sensor and the E measurement as a function of temperature. The empirical constant "A=2" was found for strip waveguide material, and it was appropriate for evaluating the measure of the temperature-dependent elastic modulus of the material. Also, the sensor's repeatability was observed from multiple trials.

The ultrasonic sensors are more suitable in highly flammable or hazardous regions, such as furnaces for steel and glass melting industries. The stiffness of high-temperature materials/metals can be measured using this ultrasonic strip waveguide sensor concept for high-temperature industrial applications. A waveguide with multiple bend reflectors can also measure the hot chamber's distributed temperature. The further scope of ultrasonic waveguide sensors using bend reflectors includes optimizing bend designs and exploring advanced materials to enhance sensor performance at high temperatures. Multiple thermocouple measurements can be done using a single wire (any solid/elastic medium) acting as a waveguide with the distributed sensors: a simple concept and cost-effective technique for measuring multiple parameters simultaneously. Also, the ultrasonic sensor has no junction that can fail. This sensor concept can be extended to real-time monitoring systems for structural health, temperature sensing in power plants and oil industry pipelines, and non-destructive testing for monitoring various industrial components. Efforts toward commercialization and scalability will make this technology more accessible and impactful across diverse fields in industrial applications.

AUTHORSHIP CONTRIBUTIONS

Authors equally contributed to this work.

DATA AVAILABILITY STATEMENT

The authors confirm that the data that supports the findings of this study are available within the article. Raw data that support the finding of this study are available from the corresponding author, upon reasonable request.

CONFLICT OF INTEREST

The author declared no potential conflicts of interest with respect to the research, authorship, and/or publication of this article.

ETHICS

There are no ethical issues with the publication of this manuscript.

STATEMENT ON THE USE OF ARTIFICIAL INTELLIGENCE

Artificial intelligence was not used in the preparation of the article.

REFERENCES

[1] Balasubramaniam K, Raja N, Periyannan S. Ultrasonic waveguide sensors for measurements in process industries. In: IEEE Sensors. New Delhi, India: IEEE; 2018. p. 1-4. [CrossRef]

[2] Periyannan S, Balasubramaniam K. Moduli determination at different temperatures by an ultrasonic waveguide method. Exp Mech. 2016;56:1257-1270. [CrossRef]

[3] Bao Y, Zhang H, Ahmadi M, Karim MA, Felix WH. Measurements of Young's and shear moduli of rail steel at elevated temperatures. Ultrasonics 2014;54:867-873. [CrossRef]

[4] Raja N, Balasubramaniam K, Periyannan S. Ultrasonic waveguide-based multi-level temperature sensor for confined space measurements. IEEE Sens J 2018;18:5699-5706. [CrossRef]

[5] Periyannan S, Balasubramaniam K. Multi-level temperature measurements using ultrasonic waveguides. Meas 2015;61:185-191. [CrossRef]

[6] Liao Z, Zhang X, Liu T, Jia J, Tu ST. Characteristics of high-temperature equipment monitoring using dry-coupled ultrasonic waveguide transducers. Ultrasonics 2020;108:106236. [CrossRef]

[7] Zhou C, Wang Y, Qiao C, Zhao S, Huang Z. High-accuracy ultrasonic temperature measurement based on MLS-modulated continuous wave. Meas 2016;88:1-8. [CrossRef]

[8] Periyannan S, Rajagopal P, Balasubramaniam K. Ultrasonic bent waveguides approach for distributed temperature measurement. Ultrasonics 2017;74:211-220. [CrossRef]

[9] Sahu GP, Raja N, Balasubramaniam K. Surface temperature mapping of a metal plate using ultrasound-guided wave technique. ASME J Nondestruct Eval 2021;4:041009. [CrossRef]

[10] Szelek J, Mackiewicz S, Gutkiewicz P. Ultrasonic measurement of the temperature dependence of elastic moduli in light alloys. Insight Nondestruct Test Cond Monit 2010;52:380-385. [CrossRef]

[11] Liang H, Yang F, Yang L, Liu Z, Wang G, Wei Y, Xue H. Research and implementation of a 1800°C sapphire ultrasonic thermometer. J Sens 2017;2017:9710763. [CrossRef]

[12] Periyannan S, Balasubramaniam K. Temperature gradients and materials properties measurements using ultrasonic guided waves. In: 11th European Conference on Non-Destructive Testing (ECNDT 2014). Prague, Czech Republic: ECNDT; 2014. p. 1-8.

[13] Dhayalan R, Saravanan S, Manivannan S, Rao BPC. Development of ultrasonic waveguide sensor for liquid level measurement in loop system. Electron Lett 2020;56:1120-1122. [CrossRef]

[14] Periyannan S, Rajagopal P, Balasubramaniam K. Re-configurable multi-level temperature sensing by ultrasonic "spring-like" helical waveguide. J Appl Phys 2016;119:1-8. [CrossRef]

[15] Nishanth R, Lingadurai K, Periyannan S, Balasubramaniam K. Ultrasonic waveguide-based distributed temperature measurement on a solid surface. Insight Nondestruct Test Cond Monit 2017;59:358-363. [CrossRef]

[16] Wong TY, Tang Y, Zou F, Su Z. An ultra-high accuracy temperature measurement method using acoustic waveguide. IEEE Sens J 2021;21:2618-2626.

[17] Wang G, Wang Q, Li F. A U-shape shear horizontal waveguide sensor for online monitoring of liquid viscosity. Sens Actuators A Phys 2018;284:35-41. [CrossRef]

[18] Kumar A, Periyannan S. Enhancing the ultrasonic waveguide sensor's fluid level sensitivity using through-transmission and pulse-echo techniques simultaneously. Rev Sci Instrum 2023;94:1-10. [CrossRef]

[19] Kumar A, Periyannan S. Helical waveguide sensor for fluid level sensing using L(0,1), T(0,1) and F(1,1) wave modes simultaneously. IEEE Sens J. Forthcoming. Manuscript Number: Sensors-61676-2023.

[20] Kumar A, Periyannan S. Experimental study of ultrasonic wave propagation in a long waveguide sensor for fluid-level sensing. Russ J Nondestruct Test 2024;60:132-143. [CrossRef]

[21] Balasubramaniam K, Periyannan S. Ultrasonic waveguide technique for distribute sensing and measurements of physical and chemical properties of surrounding media. US Patent 11,022,502. 2021.

[22] Balasubramaniam K, Periyannan S. Waveguide technique for the simultaneous measurement of temperature-dependent properties of materials. US Patent 10,794,870 B2. 2020.

[23] Jena BB, Mishra LN, Paikray SK, Misra UK. Approximation of signals by general matrix summability with effects of Gibbs phenomenon. Bol Soc Parana Mat 2020;38:141-158. [CrossRef]

[24] Mishra A, Padhy BP, Mishra LN, Misra U. On degree of approximation of signals in the generalized Zygmund class by using (E, r)(N, qn) mean. Kragujevac J Math 2023;47:131-141. [CrossRef]
[25] Bhat IA, Mishra LN. A comparative study of discretization techniques for augmented Urysohn type nonlinear functional Volterra integral equations and their convergence analysis. Appl Math Comput 2024;470:128555. [CrossRef]
[26] Bhat IA, Mishra LN, Mishra VN, Tunç C, Tunç O. Precision and efficiency of an interpolation approach to weakly singular integral equations. Int J Numer Methods Heat Fluid Flow 2024;34:1479-1499. [CrossRef]
[27] Karanjgaokar V, Rahatgaonkar S, Rathour L, Mishra LN, Mishra VN. Approximation of periodic functions by wavelet Fourier series. Int J Anal Appl 2024;22:61. [CrossRef]
[28] Paul SK, Mishra LN, Mishra VN, Baleanu D. Analysis of mixed type nonlinear Volterra-Fredholm integral equations involving the Erdélyi-Kober fractional operator. J King Saud Univ Sci 2023;35:102949. [CrossRef]
[29] Sharma MK, Bhargava AK, Kumar S, Rathour L, Mishra LN, Pandey S. A fermatean fuzzy ranking function in optimization of intuitionistic fuzzy transportation problems. Adv Math Models Appl 2022;7:191-204.
[30] Sharma MK, Dhiman N, Kumar S, Rathour L, Mishra VN. Neutrosophic Monte Carlo simulation approach for decision making in medical diagnostic process under uncertain environment. Int J Neutrosophic Sci 2023;22:8-16. [CrossRef]
[31] Rathour L, Singh V, Yadav H, Sharma MK, Mishra VN. A dual hesitant fuzzy set theoretic approach in fuzzy reliability analysis of a fuzzy system. Inf Sci Lett 2024;13:433-440. [CrossRef]
[32] Sharma MK, Chaudhary S, Rathour L, Mishra VN. Modified genetic algorithm with novel crossover and mutation operator in travelling salesman problem. Sigma J Eng Nat Sci 2024;42:1876-1883. [CrossRef]
[33] Negero NT, Duressa GF, Rathour L, Mishra VN. A novel fitted numerical scheme for singularly perturbed delay parabolic problems with two small parameters. Partial Differ Equ Appl Math 2023;8:100546. [CrossRef]
[34] Hogeme MS, Woldaregay MM, Rathour L, Mishra VN. A stable numerical method for singularly perturbed Fredholm integro-differential equation using exponentially fitted difference method. J Comput Appl Math 2024;441:115709. [CrossRef]
[35] Younus A, Dastgeer Z, Rathour L, Mishra LN, Mishra VN, Pandey S. Distinguishability criteria of conformable hybrid linear systems. Nonlinear Eng 2022;11:420-427. [CrossRef]
[36] Gezer ED, Selçuk BA. Determination of damage and defects in historical wooden structures using nondestructive test devices. Sigma J Eng Nat Sci 2020;11:127-134.
[37] Kabay N, Aköz F. Investigation of factors affecting core compressive strength and non-destructive testing of concrete. Sigma J Eng Nat Sci 2020;38:171-182.
[38] Rose JL. Ultrasonic waves in solid media. Cambridge, UK: Cambridge University Press; 1999.
[39] Periyannan S, Balasubramaniam K. Simultaneous moduli measurement of elastic materials at elevated temperatures using an ultrasonic waveguide method. Rev Sci Instrum 2015;86:1-8. [CrossRef]
[40] Simmons JH, Van Echo D. Report on elevated-temperature of stainless-steel properties. ASTM Data Ser Publ DS-5-S1. 1967.
[41] Raja N, Balasubramaniam K, Periyannan S. Ultrasonic waveguide based level measurement using flexural mode F(1,1) in addition to the fundamental modes. Rev Sci Instrum 2019;90:1-10. [CrossRef]
[42] Huber A. Dispersion calculator. Ultrasonics 2018.
[43] Smith M. ABAQUS/Standard user's manual (Version 6.9). Dassault Systèmes Simulia Corp; 2009.

Sigma Journal of Engineering and Natural Sciences
Web page info: https://sigma.yildiz.edu.tr
DOI: 10.14744/sigma.2025.1931

Research Article

Statistical modeling of alkali pretreatment for degradation of saccharum

Muhammad IRFAN[1,*], Misbah GHAZANFAR[1], Hafiz Abdullah SHAKIR[2], Muhammad KHAN[2], Marcelo FRANCO[3]

[1]Department of Biotechnology, University of Sargodha, Sargodha, 40162, Pakistan
[2]Department of Zoology, University of the Punjab, Lahore, 54590, Pakistan
[3]Department of Exact Science, State University of Santa Cruz, Ilheus, 95064, Brazil

ARTICLE INFO

Article history
Received: 24 March 2024
Revised: 18 July 2024
Accepted: 25 October 2024

Keywords:
Base; Kans Grass, Pretreatment, Total Phenol; Total Sugar

ABSTRACT

Saccharum spontaneum (Kans grass) is consistent grass of South Asian descent. It is a source of cheap, renewable and common sugars that microorganisms can easily use to substantive and cost-effective compounds. The objective of the present study was to establish better conditions for Kan's grass pretreatment using the response surface methodology. In the present study, chemical (NaOH) and thermochemical (NaOH followed by steam) pretreatment of the Kans grass was performed. Three independent variables with three different levels, such as: the concentration of NaOH (0.6, 0.8, 1 % w/v), substrate loading (5, 10, 15 %), and time of reaction (4, 6, 8 hours) were employed for the liberation of total sugars (mg/ml), and total phenol content (mg/ml). In the pretreatment with alkaline steam, the substrate was immersed in an alkaline solution for 4, 6, and 8 hours, followed by autoclaving at 121 °C for 2 hours and at 15 psi. The maximum total sugar value released was 115.58 mg/ml in chemical pretreatment when the optimal conditions were 1 % NaOH concentration, 10 % loading of the substrate, and 4 hours of reaction time. The maximum total phenol value released was 65.25 mg/ml in thermochemical pretreatment when the optimal conditions were 1 % NaOH concentration, 10 % loading of the substrate, and 4 hours of reaction time. Statistical analysis of regression model equations and coefficient of determination (R^2) tested model significance. Higher F value supports the model's significance. This study provides a novel approach to optimizing the pretreatment of *Saccharum spontaneum* for enhanced sugar and phenol extraction, positioning it as a viable feedstock for biofuel production and other sustainable applications.

Cite this article as: Irfan M, Ghazanfar M, Shakir HA, Khan M, Franco M. Statistical modeling of alkali pretreatment for degradation of saccharum. Sigma J Eng Nat Sci 2025;43(6):2017–2030.

INTRODUCTION

Limited supply and the growing demand for fuel have led to the exploration of alternative bioenergy sources. Among the alternative bioenergy sources, lignocellulose has been recognized as a major source of biofuels [1-3]. There should be short-term potential substitutes for fossil fuels as they are rapidly depleted. Among biofuels, cellulose-ethanol can be manufactured on an industrial scale

*Corresponding author.
*E-mail address: irfan.biotechnologist@gmail.com, irfan.ashraf@uos.edu.pk

This paper was recommended for publication in revised form by Editor-in-Chief Ahmet Selim Dalkilic

Published by Yıldız Technical University Press, İstanbul, Turkey
© Author. This is an open access article under the CC BY-NC license (http://creativecommons.org/licenses/by-nc/4.0/).

and is also compatible with current automobiles and supply systems [4]. In this scenario, the wild plant *Saccharum spontaneum* could be a better choice for fuel ethanol manufacture. Lignocellulose sources are among the greatest upcoming raw materials for ethanol manufacture.

S. spontaneum is a common weed growing in a vast amount of available non-agricultural land next to roads, canals, and banks. It is a tall perennial grass that spreads in many tropical nations' naturally deserted and pastoral areas. Despite having many possible uses and functions, this species must still be appreciated and utilized. In Hindi, it is referred to as "Kans" and in English as "Wild cane" [5]. Cellulose, hemicellulose, and lignin are the main components of lignocellulose [6]. Lignocellulosic raw materials show elastic resistance to enzymes, so an appropriate pretreatment is required to help contact the plant polysaccharides with the enzymes. Specifically, the pretreatment results typically include a reduction of lignin content, an increase in surface area, and a drop in crystallinity of biomass; all results improved the enzyme rate of hydrolysis and gain [7-9]. Physical treatments are designed to maximize the available surface area of the lignocellulose components by dropping their mechanical consistency and disrupting their basic dimensions. Chemical pretreatment is the most common technique for removing lignin and hemicellulose from lignocellulose compounds and distributing lignocellulose components of lignocellulosic fibers. Chemical pretreatment involves acid and base pretreatment. Steam explosion (steam cracking and explosive decompression) is one of the best physicochemical techniques frequently used for the pretreatment of lignocellulose components. Also, microorganisms or enzymes are functional to pretreat lignocellulosic components. Certain microbes rejected for a selective preparation to prevent hemicellulose and lignin are white, brown, and soft rot fungi [10].

Response surface methodology (RSM) is a precise and arithmetic exploration that is beneficial for demonstrating and investigating issues with the response of concern being affected by numerous variables. RSM is abundantly used to optimize various steps in enzyme hydrolysis and biotechnological processes. RSM's primary objective is to examine response variation by adjusting the factors to get an ideal answer. In contrast to conventional experiment designs, RSM lessens both the number of experiments and the interacting effects of the variables being researched. As a result, there is a corresponding decrease in material use [11-13]. Box-Behnken design (BBD) was selected because of three variables and three levels. Three Box-Behnken designs were used to improve delignification conditions in subsequent enzymatic hydrolysis and obtain a new polynomial of the equation, and three days were used to build feedback plans. Box-Behnken-suggestions are test methods of reaction surfaces, with relationships being examined in a much more descriptive variable and whether there is more than one variable [14].

The main objective of this study was to find the optimum conditions for saccharification of a novel feedstock, Kans grass, to release maximum cellulosic contents. The purpose was to enhance chemical and thermochemical pretreatment by BBD of RSM to increase the total phenol and total sugar content released from Kans grass so that this study could help in utilizing this novel substrate in different industries, especially biofuel industry for renewable energy, in agriculture for organic fertilizers and animal feed, and biochemistry for the development of bioplastics and other bio-based chemicals. These applications promote sustainability and resource efficiency while reducing reliance on fossil fuels.

MATERIALS AND METHODS

Substrate Processing

Kans grass was taken from Sargodha, Pakistan. The substrate was washed, dried, and milled into powder for further processing [15].

Pretreatment

Two pretreatments, chemical and thermochemical pretreatment using NaOH in 13 different experimental runs, were optimized through the Box-Behnken design. Pretreatment experiments were performed in 500 ml Erlenmeyer flasks. BBD was used to explore the synchronized effect of NaOH concentration, biomass used, and reaction time on aggregate phenol and aggregate sugar amount. There were three different ranks for every variable: -1, 0, and 1 (shown in Table 1).

The pretreatment of Kans grass was performed as described in an earlier report [16]. In base pretreatment, 100 mL solutions at various concentrations (0.6, 0.8, 1% w/v) of NaOH were used to pretreat 5, 10, and 15 g chopped substrate and soaked at room temperature for various time

Table 1. Box–Behnken design codes and levels of the variables

Independent variables	Symbols	Coded and actual values		
		-1	0	+1
NaOH concentration (%)	X_1	0.6	0.8	1
Substrate concentration (%)	X_2	5	10	15
Time (h)	X_3	4	6	8

intervals (4, 6, and 8 h). After completion of the pretreatment, all the samples were filtered and cleaned with distilled water till they acquired a neutral condition. Then, they were dried up at a temperature of 70°C for one day and kept in small-sized storage bags at 25°C. The filtrates of all experimental runs were kept in a freezer to analyze phenol and sugar contents.

In thermochemical pretreatment, the whole above procedure was followed by autoclaving at 121 121˚C and 15 psi after the completion of their residence time. The autoclaved samples were filtered, and residues were cleaned with distilled H_2O 5 to 6 times to neutralize them. The filtrate of every pretreated material was kept in the fridge, and residues were dried up at 70 70˚C for further study.

Experimental Design

The investigations were performed on a BBD (Box-Behnken design) with a quadratic model employed to find the combined result of three self-determining variables: concentration of NaOH, biomass loading, and reaction time. The 13 experimental runs were optimized to study the effects of three variables in the experimental reactions because of unnecessary features. The following Equation can be used to calculate the coded and actual values of independent variables:

$$x_i = \frac{X_i - X_0}{\Delta X_i} \quad (1)$$

Here, x_i is the unit less assessment of an autonomous variable, X_i is the actual value of an autonomous variable, X_0 represents the central point value X_i, and ΔX_i indicates the phase variation [17,18]. A second degree polynomial equation was used for the experimental figures using the statistical software Minitab v. 17.0 to calculate the response of the dependent variable and predict the optimal conditions. The second-degree polynomial was stated as:

$$Y=\beta_0 + \beta_1 X_I + \beta_2 X_2 + \beta_3 X_3 + \beta_{11} X_1^2 + \beta_{22} X_2 + \beta_{33} X_3^2 + \beta_{12} X_1 X_2 + \beta_{13} X_1 X_3 + \beta_{23} X_2 X_3 \quad (2)$$

In equation (2), Y is the predicted response, X_1, X_2, and X_3 are independent variables, β_0 is the offset term, β_1, β_2, and β_3 are linear effects, and β_{11}, β_{22}, and β_{13} are interaction terms.

The substrate was filtered through muslin cloth, cleaned with water, dried at 60 60°C for 6 hours, and kept in slider storage bags after the pretreatment time was completed. The material was analyzed to calculate the total sugar and total phenol.

Total Phenol Estimation

As described by the method of Carralero [19], Total phenolic compounds of pretreated biomass were calculated. Samples were diluted, and each run was executed triplicate. In test tubes, 0.5ml of the sample was taken, then 2.5ml of Folin's reagent solution (1:10 solution of Folin's reagent in water) and 2 ml of 7.5% Na_2CO_3 solution were added. The reaction mixture was stayed at room temperature for 2 hours. The optical density of the solution was taken at 765 nm using a spectrophotometer. Vanillin was taken as standard.

Total Sugar Estimation

As described by Dubois [20], the total sugar content of the pretreated substrate was measured. In a test tube, 0.5 ml of filtrate and 0.5 ml of fresh 5% phenol solution were added and tenderly mixed. After that, 2.5 ml of Conc. Sulphuric acid was added gently, which changed the solution color to dark brown. The test tubes were kept at a temperature of 25 °C for 30 minutes, and then absorbance was measured using a spectrophotometer at a wavelength of 490nm. Glucose was taken as standard. The whole methodology is described in Figure No. 1.

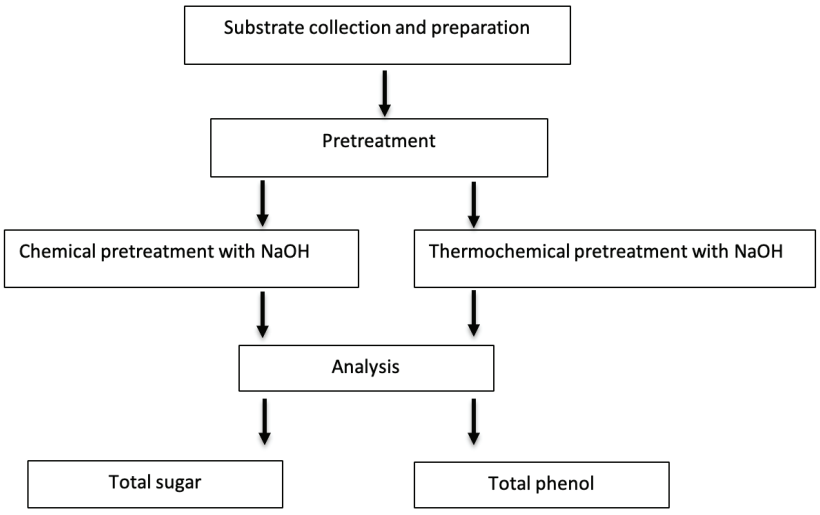


Figure 1. Flow diagram of the methodology used.

RESULTS AND DISCUSSION

Pretreatment experimentation with or without steam for the different concentrations of sodium hydroxide (0.6, 0.8, 1%) time of reaction (4, 6, and 8 h) at a loading of biomass (5, 10, and 15 %) were monitored. With the help of hydrogen bonds, carbohydrate units are strongly attached to lignin while some are covalent bonds. The basic purpose of pretreatment/hydrolysis processes is delignification to break down cellulosic and hemicellulosic biomass into lignin and degradation of the carbohydrates to form simple sugars. Lignin is made up of phenolic compounds, and it is the cause of hardness. The aim of the present investigation was to find out the influence of concentration of base, loading of biomass, and time of exposure on the discharge of phenolic compounds. RSM with median complex as the statistical model was used to increase the formation of phenolic compounds in the hydrolysate optimization process. In run no. 8, the highest total phenolic compounds (62.52 mg/ml) was produced in NaOH pretreatment, when NaOH concentration was 0.6%, time 8h, and substrate loading was 10g (Table 2). While in run no. 4, the highest total phenolic compounds (65.24 mg/ml) was observed in base steam pretreatment when 10g of the substrate and 1% NaOH were used for a reaction time of 4 hours.

The total amount of phenol and total sugar manufactured was calculated using experimental evidence. Total phenolic compounds and total sugar produced using NaOH pretreatments ranged from 10.94 mg/ml to 62.52 mg/ml and 38.39 mg/ml to 115.5 mg/ml, respectively. By using NaOH steam pretreatment, the amount of total phenolic compounds and total sugar produced fluctuated from 16.34 mg/ml to 65.24 mg/ml and 27.89 mg/ml to 93.24mg/ml, respectively. In base and base steam pretreatment, run no. 8 (62.52mg/ml), and Run no. 4 (65.24 mg/ml) produced the maximum phenol content, respectively. By the pretreatment without and with steam, the maximum total sugar contents produced are 115.58mg/ml and 93.24 mg/ml, respectively.

Chemical Pretreatment

In chemical (NaOH) pretreatment, overall total phenol content fluctuated between 10.94 mg/ml for run no. 10 (0.6% Sodium Hydroxide Concentration, 10% w/v substrate used, 4h reaction interval) to 65.24 mg/ml for run no.8 (0.6% NaOH concentration, 10% w/v substrate used, 8 h reaction interval) by BBD experimental set up. Polynomial equations of second order that symbolize association among phenol content and three autonomous variables of base pretreatment are produced by the demonstration of RSM on data obtained through experiments.

$$\text{Total Phenolic compounds (mg/ml)} = 59.4 - 86.9\,X + 5.52X_2 - 14.81\,X_3 + 67.0\,X_1^2 - 0.1564\,X_2^2 + 1.288\,X_3^2 - 1.759X_1X_2 - 0.00\,X_1X_3 - 0.1413\,X_2X_3 \quad (3)$$

$$\text{Total Sugar (mg/ml)} = -32.3 - 58\,X_1 + 5.85X_2 + 13.5\,X_3 + 81.0\,X_1^2 + 0.142\,X_2^2 - 0.039\,X_3^2 - 3.12\,X_1X_2 - 6.67\,X_1X_3 - 0.830\,X_2X_3 \quad (4)$$

The total phenolic content released in response to NaOH pretreatment was evaluated by applying F-Test for the ANOVA, the arithmetical results fit into the polynomial regression equation of second order. The response surface regression of phenolic compounds for chemical (NaOH) pretreatment of *S. spontaneum* (kans grass) is shown in table no. 4. From the F value of the model, which was 9.58

Table 2. Actual and predicted values of total Phenol and total sugar released from base pretreated kans grass using BBD

Run No.	X1	X2	X3	Total Phenol (mg/ml)			Total Sugar (mg/ml)		
				Observed	Predicted	Residual	Observed	Predicted	Residual
1	0.8	10	6	32.89432	32.89432	-0.0000	69.5912	69.5912	0.0000
2	1.0	10	8	56.41936	48.03029	8.3891	79.464	93.8238	-14.3598
3	1.0	15	6	40.22680	38.55917	1.6676	96.5608	93.8024	2.7584
4	1.0	10	4	45.42064	53.14775	-7.7271	115.584	113.1610	2.4231
5	1.0	5	6	20.87720	23.20679	-2.3296	101.8584	92.6801	9.1783
6	0.6	15	6	19.40052	17.07093	2.3296	44.9952	54.1736	-9.1784
7	0.8	5	4	17.10912	7.05242	10.0567	45.8724	57.4738	-11.6014
8	0.6	10	8	62.52976	54.80265	7.7271	38.3904	40.8134	-2.4230
9	0.8	15	8	19.55328	29.60998	-10.0567	47.3172	35.7158	11.6014
10	0.6	10	4	10.94780	19.33687	-8.3891	91.4352	77.0754	14.3599
11	0.6	5	6	15.98888	17.65651	-1.6676	40.4544	43.2129	-2.7585
12	0.8	5	8	37.62988	43.68936	-6.0595	59.598	54.4165	5.1815
13	0.8	15	4	41.95808	35.89860	6.0595	83.076	88.2575	-5.1815

and a probability value of 0.011, indicated that the model was highly significant. The factor of linear term X_3 was highly significant than X_2 and X_1 by having a p-value of 0.04, which is less than 0.05. Since all other square terms are significant. So, X_1X_2 is significant with a p-value of 0.087. For this model, R^2 coefficient of determination was 94.52%, such a high value of R^2, and fitness of the model with the experimental data was displayed by adjusted R^2 (84.65%). This model was established to calculate the number of phenolic compounds produced by the chemical pretreatment using NaOH. After base pretreatment, the regression equation of second order for the discharge of phenolic compounds was used to construct contour plots and surface plots (Fig No. 5-7).

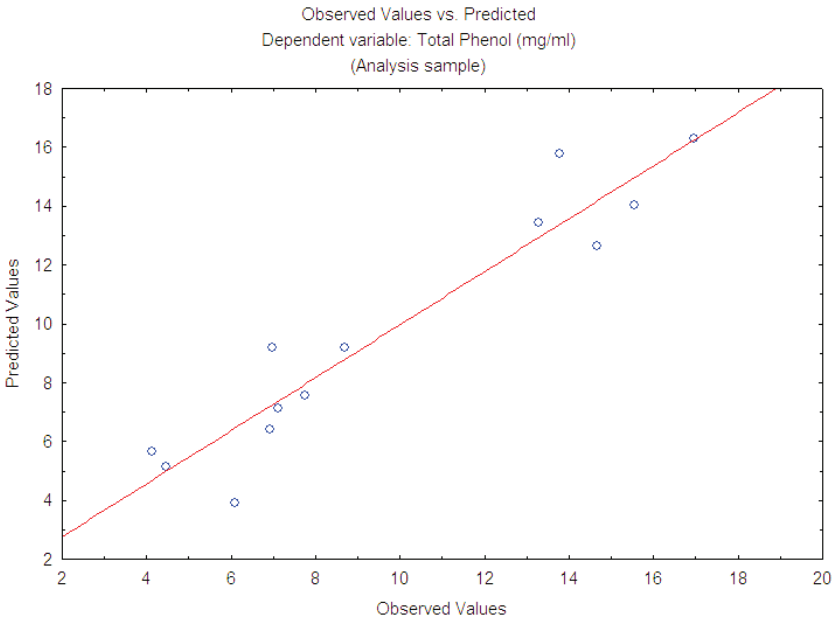


Figure 2. Graph between observed values and predicted values of Total Phenol for chemical (base NaOH) pretreatment of Kans grass.

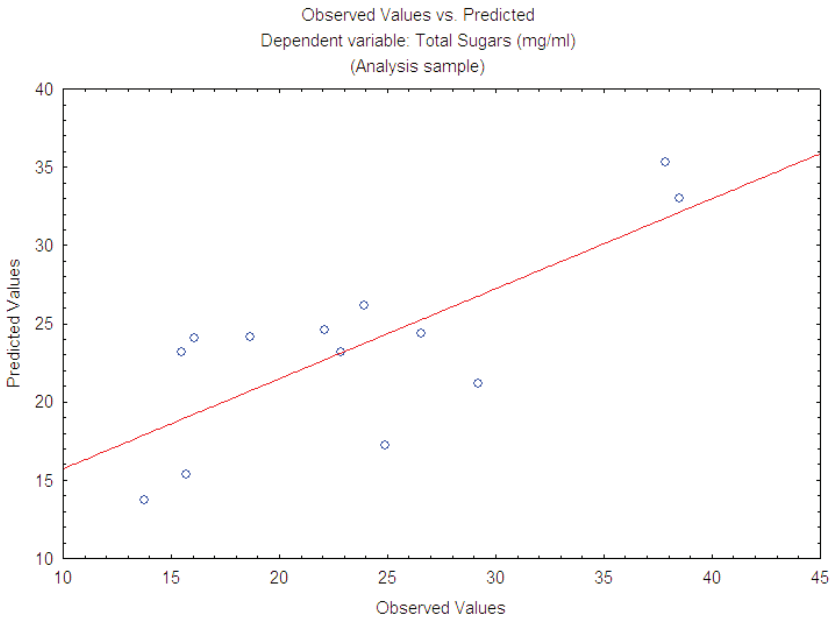


Figure 3. Graph between observed values and predicted values of Total Sugar for chemical (NaOH) pretreatment of Kans grass.

Figure 2 shows a plot between experimental results and predicted values using quadratic model equations for total phenol content after chemical pretreatment of substrate Kans grass. Results showed a strong correlation between actual and predicted values. Figure 3 shows a plot between experimental results and predicted values using quadratic model equations for total sugar content after chemical pretreatment of substrate Kans grass. Results showed a strong correlation between actual and predicted values. Model significance was tested by analysis of variance (ANOVA) of regression model equations and coefficient determination $R^{2,}$ as shown in Table 4. Higher R^2 values 77.64 and 94.52 indicate that the model explained the reaction very well. The higher values of Adj. R^2 37.40 and 84.65 also support the model's significance.

F-value statistically evaluated the significance of terms in polynomial functions at P 0.001, 0.01, and 0.05. The models have F values of 9.58 and 1.93 and probability values of 0.011 and 0.243 for chemical (NaOH) substrate pretreatment for total Phenol and total sugar analysis, respectively.

Table 4. Analysis of variance of total phenol & total sugar after NaOH treatment

Total Phenol (mg/ml)	Sources	DF	Adj SS	Adj MS	F value	P value
	Model	9	237.91	26.35	9.58	0.01
	Linear	3	24.90	8.30	3.02	0.13
	X_1	1	2.24	2.24	0.82	0.40
	X_2	1	3.88	3.88	1.41	0.28
	X_3	1	18.77	18.77	6.82	0.04
	Square	3	191.92	63.97	23.26	0.00
	X_1 2	1	26.50	26.50	9.63	0.02
	X_2 2	1	56.41	56.41	20.51	0.00
	X_3 ^{2}	1	98.02	98.02	36.63	0.00
	2 Way interaction	3	20.36	6.78	2.47	0.17
	X_1*X_2	1	12.37	12.37	4.50	0.08
	X_1*X_3	1	0.00	0.00	0.00	1.00
	X_2*X_3	1	7.98	7.98	2.90	0.14
	Error	5	13.75	2.75		
	Lack of fit	3	13.42	4.47	26.84	0.03
	Pure error	2	0.33	0.16		
	Total	14	250.94			
Total Sugar (mg/ml)	**Sources**	**DF**	**Adj SS**	**Adj MS**	**F value**	**P value**
	Model	9	729.71	81.07	1.93	0.24
	Linear	3	306.39	102.13	2.43	0.18
	X_1	1	0.09	0.09	0.00	0.96
	X_2	1	294.08	294.08	7.00	0.04
	X_3	1	12.22	12.22	0.29	0.61
	Square	3	80.51	26.83	0.64	0.62
	X_1 2	1	38.74	38.74	0.92	0.38
	X_2 2	1	46.27	46.27	1.10	0.34
	X_3 2	1	0.09	0.09	0.00	0.96
	2 way interaction	3	342.79	114.26	2.72	0.15
	X_1*X_2	1	38.87	38.87	0.93	0.38
	X_1*X_3	1	28.43	28.43	0.68	0.44
	X_2*X_3	1	275.49	275.49	6.56	0.05
	Error	5	210.11	42.02		
	Lack of fit	3	114.68	38.22	0.80	0.59
	Pure error	2	95.43	47.71		
	Total	14	939.82			

Table 5. Coded coefficients for total phenol and total sugar after NaOH treatment

	Term	Effect	Coef	SE Coef	T-Value	p
Total Phenol	Constant		7.281	0.958	7.60	0.001
	X_1	1.060	0.530	0.586	0.90	0.407
	X_2	1.394	0.697	0.586	1.19	0.288
	X_3	-3.064	-1.532	0.586	-2.61	0.048
	X_1* X_1	5.358	2.679	0.863	3.10	0.027
	X_2* X_2	-7.818	-3.909	0.863	-4.53	0.006
	X_3* X_3	10.305	5.152	0.863	5.97	0.002
	X_1* X_2	-3.518	-1.759	0.829	-2.12	0.087
	X_1* X_3	-0.000	-0.000	0.829	-0.00	1.000
	X_2* X_3	-2.826	-1.413	0.829	-1.70	0.149
Total Sugar	Constant		18.68	3.74	4.99	0.004
	X_1	0.21	0.11	2.29	0.05	0.964
	X_2	12.13	6.06	2.29	2.65	0.046
	X_3	-2.47	-1.24	2.29	-0.54	0.613
	X_1* X_1	6.48	3.24	3.37	0.96	0.381
	X_2* X_2	7.08	3.54	3.37	1.05	0.342
	X_3* X_3	-0.32	-0.16	3.37	-0.05	0.965
	X_1* X_2	-6.24	-3.12	3.24	-0.96	0.380
	X_1* X_3	-5.33	-2.67	3.24	-0.82	0.448
	X_2* X_3	-16.60	-8.30	3.24	-2.56	0.051

The model's values 9.58, and 1.93 and their respective p values 0.011 and 0.243, F>P>0.001 shows the model's accuracy (Table No.4). A p value of less than 0.05 shows the significance of the model. Model terms X_1, X_2, X_3 and quadratic term interactions X_1X_2, X_2X_3, X_1X_3, X_1^2, X_2^2, X_3^2 were also found significant. Higher R^2 values of 77.64 and 94.52 and the adjusted R^2 values of 37.40 and 84.65 indicate that actual results are by the model's predicted values.

The range of total sugar values was from 38.39 mg/ml to 115.58 mg/ml. Minimum and maximum values are respectively yielded by run no. 8 (0.6% NaOH, 10% loading of substrate, 8 hours time of reaction) and run no. 4, 1% Sodium Hydroxide, 10% loading of substrate, 4 hours time of reaction) as shown in Table No.3. Given polynomial equations of second order are produced by the demonstration of RSM based on experimental data that symbolize association among concentration of sugar and 3 autonomous variables of chemical pretreatment. *S. spontaneum* is a novel substrate with an unlimited potential for ethanol production [21]. Kans grass biomass Cell wall has 68%, 43.78%, and 24.22% dry matter of carbohydrate, cellulose, and hemicellulose fractions, respectively, showing the production cost of fuel ethanol [22]. For the maximum release of the phenol content, the optimal conditions for the base pretreatment recorded were 0.6% NaOH, 10% load of the biomass substrate, and 8h reaction or pretreatment time. A maximum discharge of sugar was observed when 1% NaOH, 10% load, and substrate 4 hours reaction time were used. Total phenol and total sugars liberated at this stage were 62.52 mg/ml and 115.58 mg/ml, respectively. The adjoining analysis demonstrated that raw Kans grass comprised 38.5% celluloses, 18.5% hemicelluloses, and 15% lignin compounds. Raw biomass pretreatment is essential for releasing the highest sugar content in successive scarification and decreasing lignin content. The highest value of cellulosic components and delignification of 60.6% and 51.5%, correspondingly, was attained at a concentration of 2.5% NaOH with a reaction time of 24 hours. Increasing the reaction time up to 48 hours led to a decline in cellulosic components. The earlier study revealed that the highest cellulosic components and delignification were attained after 24 h of reaction time, and a decline was detected at 48 hours of reaction time [23].

The results of ANOVA for overall sugar released after chemical (NaOH) pretreatment are displayed in Table No.8. The model's f and p-value, which were 1.93 and 0.24, respectively, illustrate that the model is insignificant. All this shows that the X_1 factor is more significant than X_2 and X_3 by having 0.04 p-values. Except for X_2X_3 with a p-value of 0.05, which is significant, all other square and interaction terms are insignificant. For this model, R^2 and adjusted R^2 values were 77.64% and 37.40% respectively. The model was well accomplished in chemical pretreatment for clarifying a 77.64% deviation in response to the overall sugar content of the studied variables. After the pretreatment by

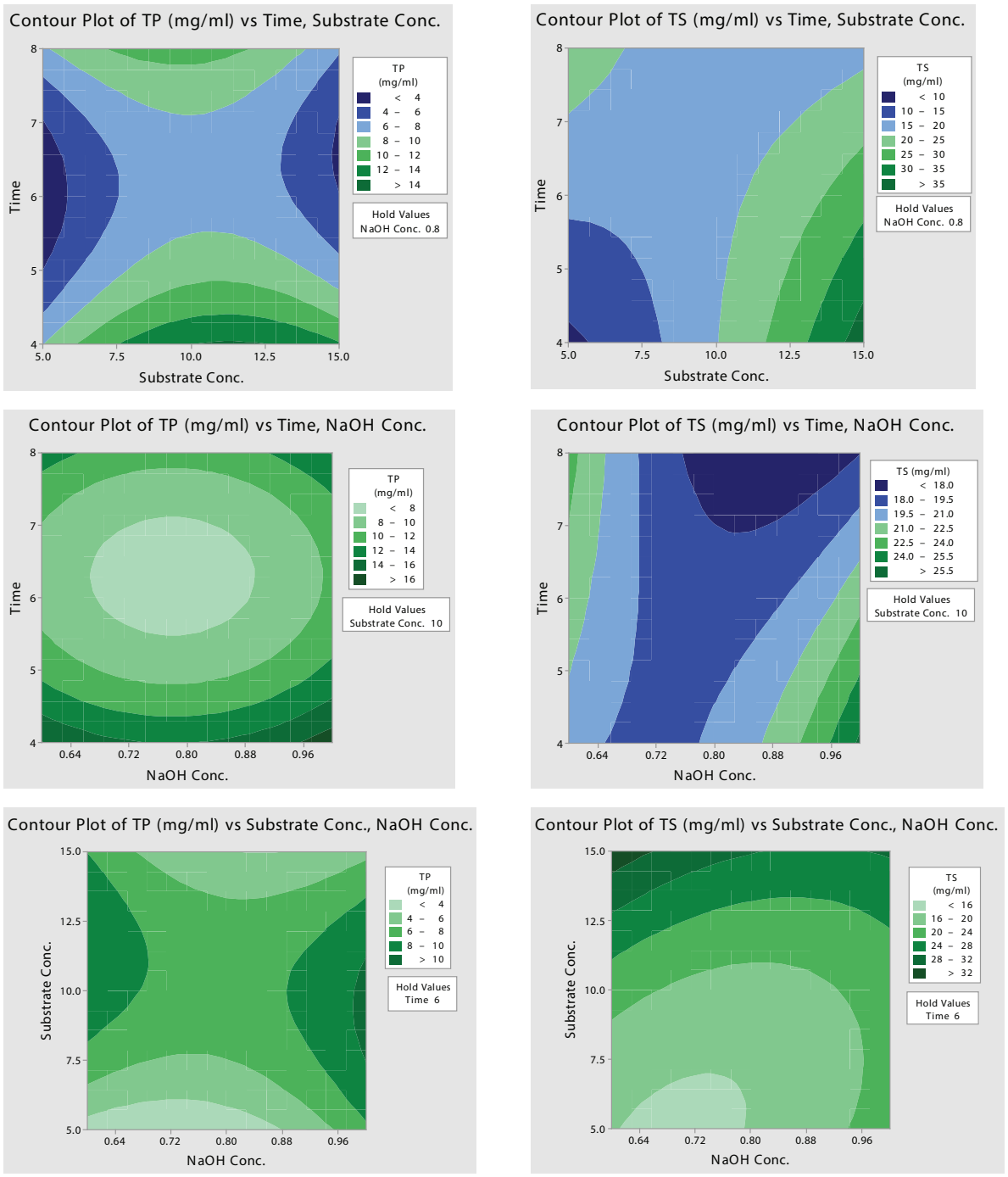


Figure 4. Contour surface plot between substrate concentration, time interval, and NaOH concentration (0.8 %) for chemical (NaOH) pretreatment.

NaOH (base), the second-order regression equation was used to construct 2D contour plots and surface plots to release overall sugar, as shown in Figure 4.

Thermochemical Pretreatment

The predicted and experimental results for base steam pretreatment of kans grass are shown in Table No.6. The observed phenol values ranged from 16.34mg/ml to 65.24 mg/ml. Minimum and maximum phenol content was observed in run no. 6 (0.6% NaOH, 15% biomass, 6h reaction time) and run no. 4 (1% NaOH, 10% loading of substrate, 4h time of reaction). The given below polynomial equation of 2nd order symbolizes the association among overall Phenol and three autonomous variables of thermochemical pretreatment, which are constructed by demonstration of RSM on data obtained through experiments.

$$\text{Total Phenolic contents} = -106 + 270\,X_1 + 6.54\,X_2 + 2.1\,X_3 - 53\,X_1^2 - 0.086\,X_2^2 + 2.90\,X_3^2 + 1.31\,X_1X_2 - 37.9X_1X_3 - 0.782\,X_2X_3 \quad (5)$$

$$\text{Total Sugar} = 337 - 525\,X_1 + 8.6\,X_2 - 40.4\,X_3 + 335\,X_1^2 - 0.228\,X_2^2 + 4.84\,X_3^2 + 5.25\,X_1X_2 - 14.2\,X_1X_3 - 0.986\,X_2X_3 \quad (6)$$

Conclusions drawn using analysis of variance (ANOVA) for thermochemical pretreatment are displayed in Table 8. The f-value of 1.49 and a P-value of 0.34 for total Phenol demonstrate that the model was insignificant. As all the linear terms and quadrates are insignificant, so the X_1X_3 term was more significant than other interactions by having a p-value of 0.07. To display a model using the investigational information, the determination coefficient (R^2) was 72.78%, and the value of R^2 and R^2 adjusted was 23.79%.

Figure No. 5 represents a plot between experimental results and predicted values using quadratic model equations for total phenol content after thermochemical pretreatment of substrate Kans grass. Results showed a strong correlation between actual and predicted values. Figure No. 6 showed a plot between experimental results and predicted values using quadratic model equations for total sugar content after thermochemical pretreatment of substrate Kans grass. Results showed a strong correlation between actual

Table 6. Actual and predicted values of total Phenol and total sugar released by thermochemical (NaOH steam) pretreatment of Kans grass using BBD

Run No.	X_1	X_2	X_3	Total Phenol (mg/ml)			Total Sugar (mg/ml)		
				Observed	Predicted	Residual	Observed	Predicted	Residual
1	0.8	10	6	33.324	33.324	0.000	44.634	44.634	0.000
2	1.0	10	8	42.316	42.976	-0.659	65.291	68.325	-3.034
3	1.0	15	6	65.088	63.571	1.516	93.241	83.240	10.000
4	1.0	10	4	65.247	66.024	-0.777	89.182	88.937	0.244
5	1.0	5	6	35.381	35.460	-0.078	85.57	92.780	-7.210
6	0.6	15	6	16.349	16.270	0.078	71.552	64.341	7.210
7	0.8	5	4	30.784	29.928	0.856	46.827	39.861	6.966
8	0.6	10	8	30.638	29.860	0.777	50.224	50.468	-0.244
9	0.8	15	8	21.412	22.268	-0.856	39.766	46.732	-6.966
10	0.6	10	4	32.105	31.445	0.659	36.051	33.016	3.034
11	0.6	5	6	33.549	35.066	-1.516	27.898	37.899	-10.000
12	0.8	5	8	22.172	21.433	0.7386	49.983	39.738	10.244
13	0.8	15	4	37.670	38.408	-0.738	39.525	49.770	-10.244

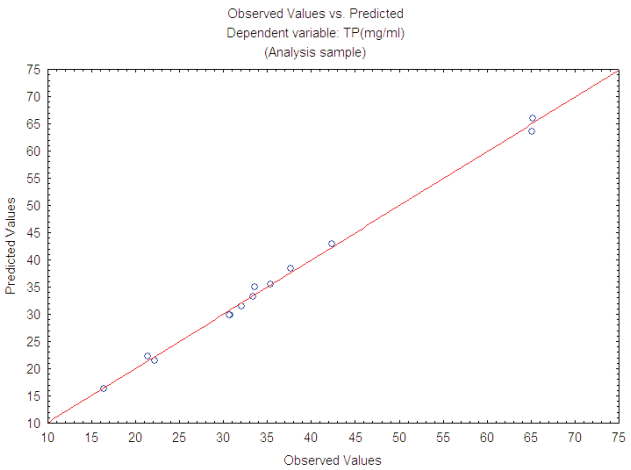


Figure 5. Graph between observed values and predicted values of Total Phenol for thermochemical (NaOH followed by steam) pretreatment of Kans grass.

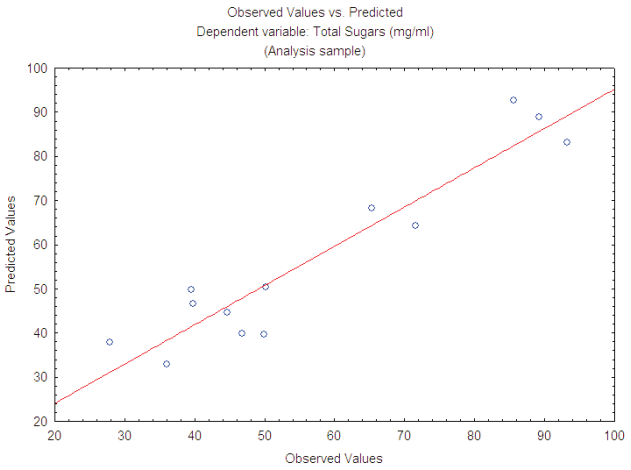


Figure 6. Graph between observed values and predicted values of Total Sugar for thermochemical (NaOH followed by steam) pretreatment of Kans grass.

and predicted values. Model significance was tested by analysis of variance (ANOVA) of regression model equations and coefficient determination R^2. Higher R^2 values, 73.98 and 99.65, indicate that the model explained the reaction very well. The higher values of Adj. R^2 27.16 and 99.01 also support the model's significance.

F-value statistically evaluated the significance of terms in polynomial functions at P 0.001, 0.01, and 0.05. The models have F values of 157.36 and 1.75 and probability values of 0.000 and 0.273 for thermochemical (NaOH followed by steam) substrate pretreatment for total Phenol and total sugar analysis, respectively. The model's values, 157.36, 1.75, and their respective p values 0.000 and 0.273, F>P>0.000, shows the model's accuracy (Table no. 6). Small P value shows the significance of the model. Model terms X_1, X_2, X_3 and quadratic term interactions X_1X_2, X_2X_3, X_1X_3, X_1^2, X_2^2, X_3^2 were also found significant. Higher R^2 values of 73.98 and 99.65

Table 7. Analysis of Variance (ANOVA) of Total Phenol and Total Sugar released after thermochemical (NaOH steam) pretreatment

Total Phenol (mg/ml)	Sources	DF	Adj SS	Adj MS	F value	P value
	Model	9	2620.50	291.17	157.36	0.000
	Linear	3	1484.22	494.74	267.38	0.000
	X_1	1	1137.41	1137.41	614.70	0.000
	X_2	1	43.39	43.39	23.45	0.005
	X_3	1	303.42	303.42	163.98	0.000
	Square	3	456.43	152.14	82.22	0.000
	X_1 2	1	327.44	327.44	176.96	0.000
	X_2 2	1	97.92	97.92	52.92	0.001
	X_3 2	1	0.10	0.10	0.05	0.825
	2 Way interaction	3	679.85	226.62	122.47	0.000
	X_1*X_2	1	550.07	550.07	297.28	0.000
	X_1*X_3	1	115.17	115.17	62.24	0.001
	X_2*X_3	1	14.61	14.61	7.90	0.038
	Error	5	9.25	1.85		0.000
	Lack of fit	3	9.25	3.08		0.000
	Pure error	2	0.00	0.00		0.000
	Total	14	2629.75			0.000
Total Sugar (mg/ml)	**Sources**	**DF**	**Adj SS**	**Adj MS**	**F value**	**P value**
	Model	9	4399.4	488.8	1.58	0.320
	Linear	3	1621.8	540.6	1.75	0.273
	X_1	1	151.9	151.9	0.49	0.515
	X_2	1	1063.0	1063.0	3.44	0.123
	X_3	1	406.9	406.9	1.32	0.303
	Square	3	2149.1	716.4	2.32	0.193
	X_1 2	1	662.9	662.9	2.14	0.203
	X_2 2	1	119.5	119.5	0.39	0.562
	X_3 2	1	1381.6	1381.6	4.47	0.088
	2 way interaction	3	628.5	209.5	0.68	0.602
	X_1*X_2	1	110.4	110.4	0.36	0.576
	X_1*X_3	1	129.3	129.3	0.42	0.547
	X_2*X_3	1	388.9	388.9	1.26	0.313
	Error	5	1547.0	309.4		
	Lack of fit	3	1281.5	427.2	3.22	0.246
	Pure error	2	265.5	132.7		
	Total	14	5946.3			

Table 8. Coded coefficients for total Phenol and total sugar released after NaOH steam treatment

Total Phenol	Term	Effect	Coef	SE Coef	T-Value	P-Value	VIF
	Constant		33.325	0.785	42.43	0.000	
	X_1	23.848	11.924	0.481	24.79	0.000	1.00
	X_2	4.658	2.329	0. 481	4.84	0.005	1.00
	X_3	-12.317	-6.159	0. 481	-12.81	0.000	1.00
	X_1.* X_1	18.834	9.417	0.708	13.30	0.000	1.01
	X_2* X_2	-10.300	-5.150	0.708	-7.27	0.001	1.01
	X_3* X_3	-0.330	-0.165	0.708	-0.23	0.825	1.01
	X_1* X_2	23.454	11.727	0.680	17.24	0.000	1.00
	X_1* X_3	-10.732	-5.366	0.680	-7.89	0.001	1.00
	X_2.* X_3	-3.823	-1.911	0.680	-2.81	0.000	1.00
Total Sugar	**Constant**		**40.80**	**10.22**	**4.02**	**0.010**	
	X_1	-8.71	-4.36	6.22	-0.70	0.515	1.00
	X_2	23.05	11.53	6.22	1.85	0.123	1.00
	X_3	-14.26	-7.13	6.22	-1.15	0.303	1.00
	X_1.* X_1	26.80	13.40	9.15	1.46	0.203	1.01
	X_2* X_2	-11.38	-5-69	9.15	-0.62	0.562	1.01
	X_3* X_3	38.69	19.34	9.15	2.11	0.088	1.01
	X_1* X_2	10.50	5.25	8.79	0.60	0.576	1.00
	X_1* X_3	-11.37	-5.68	8.79	-0.65	0.547	1.00
	X_2.* X_3	-19-72	-9.86	8.79	-1.12	0.313	1.00

and the adjusted R^2 values of 27.16 and 99.01 indicate that actual results are by the predicted values of the model.

According to BBD in table no.6, for NaOH steam pretreatment, total sugar ranged from 27.89 mg/ml at run no. 11 (0.6% Sodium Hydroxide concentration, 5% loading of substrate, 6h time of reaction) to 93.24 mg/ml at run no. 3 (1% Sodium Hydroxide concentration, 15% substrate used, 6h time of reaction). Given polynomial equations of second order are produced by the demonstration of RSM based on experimental data that symbolize association among sugar concentration and 3 autonomous variables of thermochemical pretreatment. The results of ANOVA for overall sugar released after thermochemical pretreatment are displayed in Table 7. The model's f and p-values, which were 1.93 and 0.24, respectively, illustrate that the model is insignificant. All this shows that the X_1 factor is more significant than X_2 and X_3 by having 0.04 p-values. Except for X_2X_3 with a p-value of 0.05, which is significant, all other square and interaction terms are insignificant. For this model, R^2 and adjusted R^2 values were 77.64% and 37.40% respectively. The model was well accomplished in chemical pretreatment for clarifying a 77.64% deviation in response to the overall sugar content of the studied variables. After the pretreatment by NaOH steam, the second-order regression equation was used to construct contour plots for the release of overall sugar, as shown in Figure No. 7. Silverstein [24] described that the highest delignification of 65.63% was attained in 2% NaOH pretreatment for 90 minutes at a temperature of 121°C and pressure of 15 psi. Nadeem also described the results of attaining the highest delignification at a steaming time of 60 minutes [25]. Another study showed that 43% elimination of lignin was attained with 3.5% NaOH at 90°C for 90 minutes of reaction time [26].

In NaOH steam pretreatment, when minimum and maximum phenol content was obtained, the range of overall phenol produced was from 16.34 mg/ml to 65.24 mg/ml. Run no. 6 (0.6% NaOH), 15% substrate, 6 h time of reaction) and run no. 4 (1% NaOH), 10% substrate, 4h time of reaction) respectively. For base steam pretreatment, the range of total sugar was from 27.89 mg/ml in run no.11 (0.6 % NaOH), 5% loading of the substrate, 6h time of reaction) to 93.24 mg/ml at run no. 3 (1% NaOH, 15% biomass loading, 6h reaction time). To test NaOH concentration, reaction time, and temperature, response surface methodology was used by Chittibabu [27], who stated that the production of reducing sugar was improved by increasing the temperature and concentration of base. Maximum reducing sugar content was obtained when the base used was 1 %, the temperature was 110°C, and the time of reaction was 6 h. There was a decline in reducing sugar content over time because of sugar breakdown. These outcomes related to current work in which the highest delignification was perceived at an extreme concentration of base that is 1%, and steam also

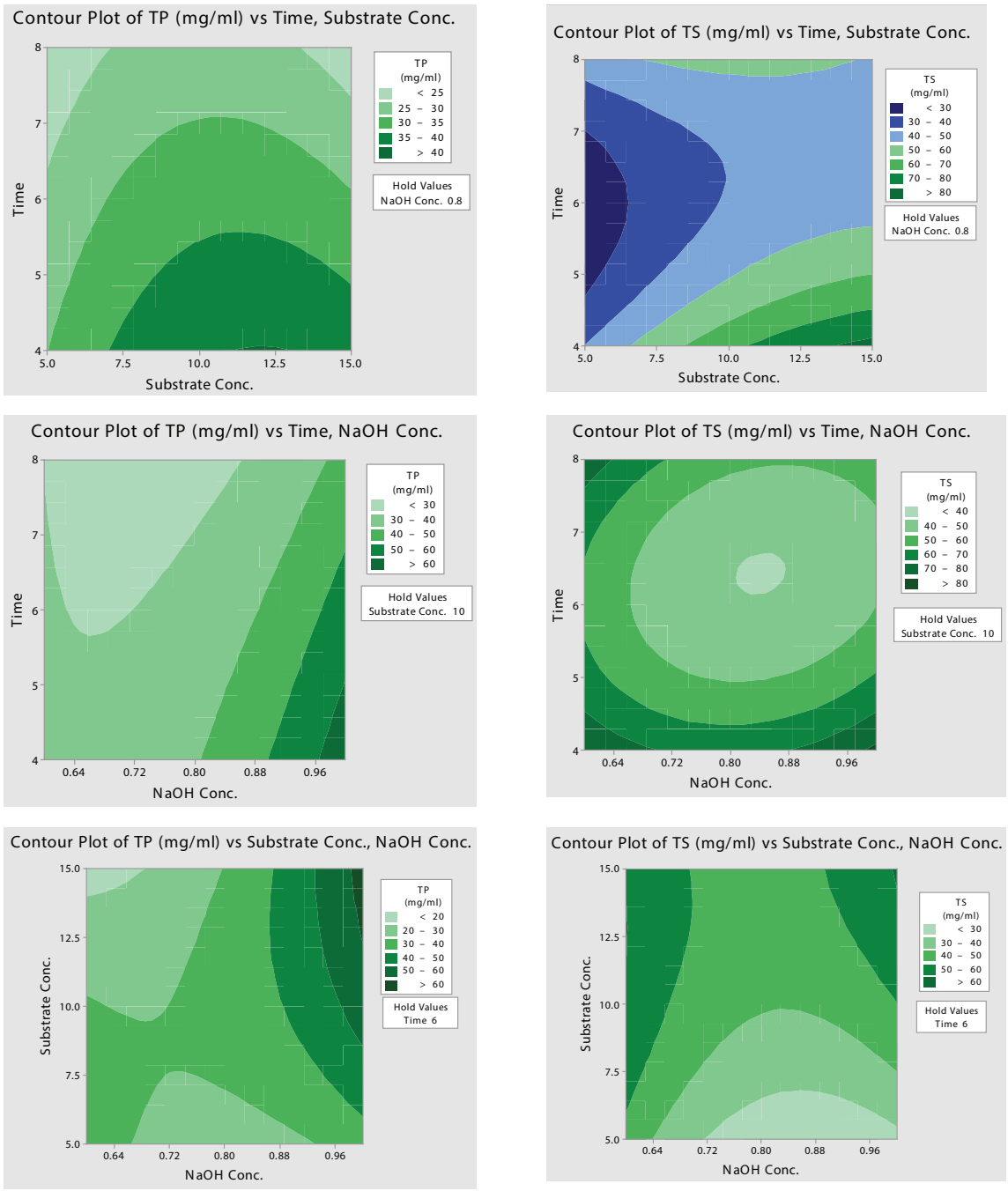


Figure 7. Contour plot between substrate concentration, time interval, and NaOH concentration (0.8 %) for the thermo-chemically pretreated substrate.

enhanced the delignification process as a consequence of elevated temperature.

ACKNOWLEDGEMENTS

Department of Biotechnology, Univrsity of Sargodha is higly acknowledged for providing support to conduct this research.

AUTHORSHIP CONTRIBUTIONS

Authors equally contributed to this work.

DATA AVAILABILITY STATEMENT

The authors confirm that the data that supports the findings of this study are available within the article. Raw

data that support the finding of this study are available from the corresponding author, upon reasonable request.

CONFLICT OF INTEREST

The author declared no potential conflicts of interest with respect to the research, authorship, and/or publication of this article.

ETHICS

There are no ethical issues with the publication of this manuscript.

STATEMENT ON THE USE OF ARTIFICIAL INTELLIGENCE

Artificial intelligence was not used in the preparation of the article.

REFERENCES

[1] Oliva JM, Manzanares P, Ballesteros I, Negro MJ, Gonzalez A, Ballesteros M. Application of Fenton's reaction to steam explosion prehydrolysates from poplar biomass. In: Twenty-sixth symposium on biotechnology for fuels and chemicals. Totowa (NJ): Humana Press; 2005. p. 887–899. [CrossRef]

[2] Sassner P, Mårtensson CG, Galbe M, Zacchi G. Steam pretreatment of H_2SO_4-impregnated Salix for the production of bioethanol. Biores Technol 2008;99:137–145. [CrossRef]

[3] González-Gloria KD, Tomás-Pejó E, Amaya-Delgado L, Rodríguez-Jasso RM, Loredo-Treviño A, Singh A, et al. Biochemical and biorefinery platform for second-generation bioethanol: fermentative strategies and microorganisms. Fermentation 2024;10:361. [CrossRef]

[4] Soni SK, Sharma A, Soni R. Microbial enzyme systems in the production of second generation bioethanol. Sustainability 2023;15:3590. [CrossRef]

[5] Pandey VC, Bajpai O, Pandey DN, Singh N. Saccharum spontaneum: an underutilized tall grass for revegetation and restoration programs. Genet Resour Crop Evol 2015;62:443–450. [CrossRef]

[6] Potumarthi R, Baadhe RR, Bhattacharya S. Fermentable sugars from lignocellulosic biomass: technical challenges. In: Biofuel technology. Berlin: Springer; 2013. p. 3–27.

[7] Chang VS, Nagwani M, Kim CH, Holtzapple MT. Oxidative lime pretreatment of high-lignin biomass. Appl Biochem Biotechnol 2001;94:1–28. [CrossRef]

[8] Kim JS, Lee YY, Kim TH. A review on alkaline pretreatment technology for bioconversion of lignocellulosic biomass. Biores Technol 2016;199:42–48. [CrossRef]

[9] Srivastava N, Singh P, Srivastava M, Lal B, Singh R, Ahmad I, et al. A review on the scope and challenges of Saccharum spontaneum waste in the context of lignocellulosic biomass for sustainable bioenergy applications. Renew Sustain Energy Rev 2024;199:114477. [CrossRef]

[10] Sánchez C. Lignocellulosic residues: biodegradation and bioconversion by fungi. Biotechnol Adv 2009;27:185–194. [CrossRef]

[11] Theydan SK, Ahmed MJ. Optimization of preparation conditions for activated carbons from date stones using response surface methodology. Powder Technol 2012;224:101–108. [CrossRef]

[12] Zheng Y, Zhao J, Xu F, Li Y. Pretreatment of lignocellulosic biomass for enhanced biogas production. Prog Energy Combust Sci 2014;42:35–53. [CrossRef]

[13] Nasseri S, Yaqubov A, Alemi A, Nuriev A. Optimization of copper and zinc ions removal from aqueous solution by modified nano-bentonite using response surface methodology. J Ultrafine Grained Nanostruct Mater 2020;53:78–90.

[14] Hamelinck CN, Faaij APC, Den Uil H, Boerrigter H. Production of FT transportation fuels from biomass: process analysis and optimisation, and development potential. Energy 2004;29:1743–1771. [CrossRef]

[15] Ghazanfar M, Nadeem M, Shakir HA, Khan M, Ahmad I, Franco M, et al. Valorization of Bombax ceiba waste into bioethanol production through separate hydrolysis and fermentation and simultaneous saccharification and fermentation. Fermentation 2022;8:386. [CrossRef]

[16] Ghazanfar M, Irfan M, Nadeem M. Statistical modeling and optimization of pretreatment of Bombax ceiba with KOH through Box-Behnken design of response surface methodology. Energy Sources A 2018;40:1114–1124. [CrossRef]

[17] Jabasingh SA, Nachiyar CV. Utilization of pretreated bagasse for the sustainable bioproduction of cellulase by Aspergillus nidulans MTCC344 using response surface methodology. Ind Crops Prod 2011;34:1564–1571. [CrossRef]

[18] Muhammad N, Man Z, Bustam MA, Mutalib MA, Wilfred CD, Rafiq S. Dissolution and delignification of bamboo biomass using amino acid-based ionic liquid. Appl Biochem Biotechnol 2011;165:998–1009. [CrossRef]

[19] Carralero V, Mena ML, Gonzalez-Cortes A, Yanez-Sedeno P, Pingarrón JM. Development of a high analytical performance-tyrosinase biosensor based on a composite graphite–Teflon electrode modified with gold nanoparticles. Biosens Bioelectron 2006;22:730–736. [CrossRef]

[20] DuBois M, Gilles KA, Hamilton JK, Rebers PT, Smith F. Colorimetric method for determination of sugars and related substances. Anal Chem 1956;28:350–356. [CrossRef]

[21] Osborne CP, Freckleton RP. Ecological selection pressures for C4 photosynthesis in the grasses. Proc Biol Sci 2009;276:1753-1760. [CrossRef]

[22] Singh LK, Chaudhary G, Majumder CB, Ghosh S. Explore the perennial Kans grass (Saccharum spontaneum) biomass for releasing reducing sugars and its optimization. Der Chemica Sinica 2011;2:154–163.

[23] Asghar U, Irfan M, Iram M, Huma Z, Nelofer R, Nadeem M, et al. Effect of alkaline pretreatment on delignification of wheat straw. Nat Prod Res 2015;29:125–131. [CrossRef]

[24] Silverstein RA, Chen Y, Sharma-Shivappa RR, Boyette MD, Osborne J. A comparison of chemical pretreatment methods for improving saccharification of cotton stalks. Biores Technol 2007;98:3000–3011. [CrossRef]

[25] Nadeem M, Ashgar U, Abbas S, Ullah S, Syed Q. Alkaline pretreatment: a potential tool to explore kallar grass (Leptochloa fusca) as a substrate for bio-fuel production. Middle East J Sci Res 2013;18:1133–1139.

[26] Uzunlu N, Hoşgün EZ, Bozan B. Optimization of alkaline pretreatment for enzymatic saccharification of poppy stalks. BioResources 2014;9:2824–2834. [CrossRef]

[27] Chittibabu S, Saseetharan MK, Rajendran K, Santhanamuthu M. Optimization of alkali pretreatment and enzymatic hydrolysis of banana pseudostem for ethanol production by RSM. In: 2012 International Conference on Advances in Engineering, Science and Management (ICAESM). IEEE; 2012. p. 90–94.

Sigma Journal of Engineering and Natural Sciences
Web page info: https://sigma.yildiz.edu.tr
DOI: 10.14744/sigma.2025.1932

Research Article

The role of artificial intelligence in rooting local architecture

Israa Mohammad A. AL-SAFFAR[1], Osamah Abdulmunem AL-TAMEEMI[2], Fawzia Irhayyim AL-ASSADI[2]

[1]*Department of Construction and Projects, University of Baghdad, Baghdad, 10071, Iraq*
[2]*Department of Architecture, University of Baghdad, Baghdad, 10071, Iraq*

ARTICLE INFO

Article history
Received: 03 July 2024
Revised: 14 August 2024
Accepted: 25 October 2024

Keywords:
Artificial Intelligence (AI); Local Architecture; Morphology; Rooting; Traditional Building

ABSTRACT

This paper investigates the application of artificial intelligence in modeling the morphologies of architectural designs, primarily looking at traditional Iraqi architecture of the 1960s and 1970s. The research employs morphological clues based on buildings still standing to compare AI-created models to those traditionally conceived by architects. It assesses morphological characteristics in both AI-generated and human-designed architectures during the stated times using the Jaccard similarity approach. Accordingly, the problem was identified, with a lack of knowledge represented by the role of artificial intelligence in shaping Iraqi architecture preserving local architectural roots, and achieving a balance between technological innovation and authentic architectural identity. Based on that problem, the aim is determined is to provide knowledge represented by the role of artificial intelligence in shaping Iraqi architecture preserving local architectural roots, and achieving a balance between technological innovation and authentic architectural identity. The results indicated that the two had a strong similarity, demonstrating well that AI may be able to successfully emulate traditional architectural forms and materials with good effect.

In particular, it is focused on the ways AI can be employed to preserve and improve the local architectural identity, recognizing that while AI has an immense potential to mimic and maintain cultural heritage within architecture, its scope may well be limited by geographical and cultural specifics. Such limitations make it clear that findings cannot possibly find wide applicability for other regions or architectural styles. The research, however, suggests that a broader extent of the research coverage will overcome such limitations and may even provide wider applicability and insights.

The scores are highly significant, with most AI models scoring higher than 0.5 on the Jaccard index, representing adequate morphological conformity to conventional designs. This therefore implies that AI can greatly aid in preserving local architectural features while bringing efficiency and creativity to the design process. It is therefore hugely important for the future practice of architecture and educational curricula; this is evidence that AI may likely play a critical role in filling the gap between traditional architectural values and modern technological advancements.

Cite this article as: Al-Saffar IMA, Al-Tameemi OA, Al-Assadi FI. The role of artificial intelligence in rooting local architecture. Sigma J Eng Nat Sci 2025;43(6):2031–2049.

***Corresponding author.**
*E-mail address: osamah.al-tameemi@coeng.uobaghdad.edu.iq

This paper was recommended for publication in revised form by Editor-in-Chief Ahmet Selim Dalkilic

Published by Yıldız Technical University Press, İstanbul, Turkey
© Author. This is an open access article under the CC BY-NC license (http://creativecommons.org/licenses/by-nc/4.0/).

INTRODUCTION

The introduction of Artificial Intelligence (AI) is one of the advancements in artificial intelligence, and it introduces a new dimension into the field of architecture, mainly in the optimization of designs through generative design. Roéfero, Sharma, and others pointed out a few works have been done to foster creativity in architecture through Artificial Intelligence (AI) implementation, where the main contributions are in the aspects of generative adversarial networks on image generation and machine learning algorithms for structural analysis. [1]. Yet, research is wanting concerning the application of AI technologies to preservations and reinforcements of local identities in architecture, especially in culturally significant regions. The body of work that exists is more centered on the innovative and streamlining possibilities of AI for existing, contemporary architectural practice; very little attention has been paid to critical needs in the area of cultural conservation in architecture. It is this gap that the current study fills by looking at ways in which AI could be used to anchor local architecture in history and cultural context. The case in point here is Iraq, wherein architectural heritage continues to be one of those important components of cultural identity. [2,3]. This is seen from the instance of Iraqi architecture dating back to the 1960s and 1970s. While qualitatively assessing the similarity between traditional Iraqi architectural forms and examining AI-generated designs via the Jaccard similarity index, the current research is unique in marrying review with comparison [4]. Ertunç and Rathour et al. pointed out that it is hoped that this combined approach will not only break new ground in terms of understanding AI in architecture but also lead to some practical tools for heritage architectural preservation in a globalizing world. Ertunç and Rathour et al. pointed out that it is regarding the current research within the AI and cultural conservation discourse, the paper relates closely to the specific topics of interest in the journal about innovative methodologies and their application in the conservation of cultural heritage. The conclusions bear a special significance for architects, urban planners, and cultural heritage professionals trying to integrate modern technologies with traditional design principles [5,6].

Novelty in this research is dual: first, the use of AI-generated architectural forms reflecting traditional Iraqi ones and materials; second, the use of the quantitative method, the Jaccard similarity index, to compare these AI-generated designs against historical examples. It is novel in the way that it preserves architectural heritage and also very critical in the general discourse on the role played by AI in the conservation of culture. The need for this research is underscored by the latent threat of cultural homogenization in architecture that is driven by designs dominated by globalization, erasing local identities. Architecture and AI can advance in preserving and improving the forms of traditional architecture through this research. Its practical implications will be important for architects, policymakers, and cultural heritage professionals, giving them a new tool with which to balance innovation and the preservation of cultural identity.

MATERIALS AND METHODS

This paper is based on:

A. The main question in the study is: How is artificial intelligence applied to rooting local architecture? To achieve an answer, this study employs mixed methods, first, a descriptive qualitative method was employed, then a quantitative method that relied on using the Jaccard similarity method to compare the results., to the effect of the artificial intelligence technique in rooting the local architecture. It provides a new theoretical horizon for a better understanding and serves as essential to the knowledge of the application of this technique in architecture. Therefore, the investigation is an attempt to initiate an effective link between the design process and architectural principles to develop an approach that draws inspiration from the local elements and is applied in contemporary architectural productions through artificial intelligence to root local architecture
B. The current study will focus on the literature review books, academic journals, conference papers on artificial intelligence and architecture, and morphological aspects within Iraqi architecture. This study employs mixed methods, first, a descriptive qualitative method was employed, then a quantitative method that relied on using the Jaccard similarity method to compare the results [7].
C. Practical application by applying theoretical framework indicators extracted from local buildings dating back to the contemporary period, limited to the 1960s and 1970s of the twentieth century, and applied in two different prompts with artificial intelligence sites, and Comparison in application between local architectural elements and AI-generated elements.
D. Discussion of previous literature and drawing out the research problem:

Past literature generally highlights the significant impact that AI has had on modern architectural practices globally, thereby presenting a considerable opportunity to integrate it with traditional architecture linked with local cultures.

However, most such studies tend to give a general overview of concepts; hence, the emergence of overlapping ideas, and the development of partial aspects in AI applications in architecture without going into the depth of cultural and local dimensions. In fact, the absence of this holistic analysis leads to a gap in understanding how AI can be used effectively to improve the local architectural identity, especially that of historical contexts. Critical analysis of the related literature shows a deficiency regarding the depth of insight about AI's capabilities; most research lacks the emphasis that this technology deserves in the preservation

and promotion of local architectural heritage. Some, for instance, might focus on innovations within their technical dimensions but rarely extend to the way such technologies coexist with and further support conventional architectural forms, such as the specific ones found during the 1960s and 1970s in Iraq. The literature also shows incomplete strategies for balancing technological developments regarding preserving authentic architectural identity.

This research tries to fill these gaps through a critical approach that puts into one piece how AI can shape and develop local architecture in Iraq, considering its historical significance and its modern adaptation. A review of the related literature indicates that while various aspects of AI in architecture have been addressed, focused research on the role of AI in maintaining architectural continuity remains scarce, with a mad rush toward embracing innovation. This work, therefore, aims to find its place within this gap by exploring the causal and logical relationships between AI and the evolution of Iraqi architecture with a view to furnishing a solid bedrock of material upon which new contributions within this subject area will be established.

Artificial Intelligence and Architecture

Until recently, the conventional definition of AI was that it sought to do what human minds can achieve, but that concept is clearly out of date. Del Campo & Leach pointed out that AI is already capable of outperforming humans in a variety of ways [8].

In the same context, Mishra and Mohammed defined artificial intelligence. defines AI as a field of study in computer science. It entails creating computer programs to perform things that would otherwise require human intelligence. AI algorithms can be used to solve problems in learning, perception, problem solving, language understanding, and/or logical reasoning [9,10].

Kaplan and Haenlein define AI as "a system's ability to interpret external data correctly, to learn from such data, and to use those learnings to achieve specific goals and tasks through flexible adaptation" [11].

As Bartnek et al. mention "AI is the study of [intelligent] agents that receive precepts from the environment and take action. Each such agent is implemented by a function that maps percepts to actions, and we cover different ways to represent these functions, such as production systems, reactive agents, logical planners, neural networks, and decision-theoretic systems" [12].

As AI advances in capability, today's architect is presented with a variety of potential sources of intelligence to deploy in the service of the craft;

1) own talents, skills, and experience (as certified, for example, by their professional registration) ;
2) an array of hard-coded computer programs that achieve specific ends (such as energy analysis or structural engineering);
3) machine learning systems (which may learn from data derived from their design projects, or even sensors within finished buildings and provide insight);4) ultimately the speculative prospect of cognitive systems that can reason within context (only seen in science fiction today) [13,14].

Borglund explains that in the fields of architecture and engineering, artificial intelligence and machine learning play a crucial role through a concept known as generative design. This technique primarily focuses on identifying optimal design solutions, diverging from traditional design simulation that relies heavily on extensive, result-oriented data. The generative design takes this simulation process to a higher level, as it does not respond to well-defined questions on functionality, changes, mechanism, or whatever. It provides suggestions in a continuous process that learns and improves through each cycle using set inputs subject to defined constraints and objectives. In this method, the designer changes from an inquirer to a demander. Researchers in design thinking also view generative design tools as creative enablers. They support the ability to explore many alternatives in the early design process to develop creative potential through divergent thinking, an essence of creativity [15]. Figure 1. shows the flowchart of AI and its relation with architecture**.**

Artificial Intelligence Hallucinates Images

Machine vision, also known as image recognition, is a notable achievement in the realm of machine learning. A more advanced development is the ability to 'hallucinate' images, a concept realized in 2015 by Google engineer Alexander Mordvintsev. Merizio et al stated that discovered how to reverse the function of neural networks from merely recognizing to generating images. This innovation led to the creation of Deep Dream, a computer vision program

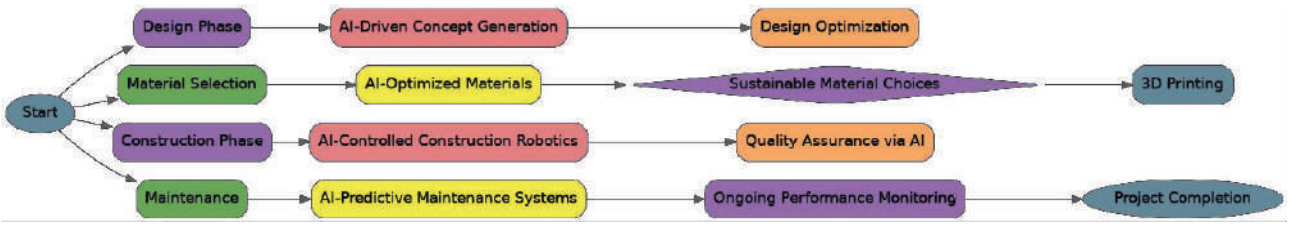


Figure 1. Flowcharts showing the integration of AI in architectural processes. Source: Authors.

that garnered significant attention in artistic communities for its unique, dream-like images. [16]. In the same context, del Campo & Leach pointed out that paved the way for style transfer techniques, such as overlaying zebra stripes onto a horse or interpreting images through neural networks trained on specific art styles, like Van Gogh's paintings. However, the landmark advancement in image generation came in 2014 with the invention of generative adversarial networks (GANs) by computer scientist Ian Good Fellow. GANs operate through the interaction of two neural networks: one generates images (the generator), while the other (the discriminator) evaluates these images against a training dataset. This process resembles an art forger attempting to deceive an art critic with a counterfeit work. The discriminator rejects images until they match the quality of the dataset. Once adequately trained, the discriminator can be removed, allowing the generator to autonomously produce convincing images [8].

Artificial Intelligence Affects Architectural Morphology

Artificial intelligence is also revolutionizing architecture with new and innovative ways of designing and making. One way through which AI impacts architecture is through the morphology of the buildings. AI algorithms can generate designs that are optimized for function. Designs for energy efficiency and design for stability can result in artificial structures that, though within the language of the systems that they represent, have never been seen before in the annals of architectural history. Similarly, designs that are similar to the branching of trees or the logic of water courses will impact the morphology of the building envelope. In a similar vein, AI processes information to make design decisions. These lead the archittes to make sound decisions about the shape and functional schemata of a building [17]. Kumar & Bernstein mention that AI tools, on the other hand, differ from these automatic tools in the way that they process and come up with their output without the direct intervention of the designer [13,18].

Maltret and Zoller suggest that architectural morphologies can be equated to a cosmos—a well-structured composition of elements. The elements are generic, recognizable objects that can produce definite objects by their genealogy. Their system of knowledge is divided into:

- Physical objects and Architectural elements.
- Relationships that link the elements, and in the actual, the elements are differentiated by:
- Characteristics, such as morphologic attributes, architectonical features, or positional characteristics.
- Their parts, and graphical representations.

The two principal inter-object associations as Maltret & Zoller say are filiation with its specialization, and composition relationships managing associations of objects according to a set of rules [19]. From Ismael and Roberts, it is understood that AI has to deliver this wave of change, to revolutionize architectural design and its construction. But Artificial Intelligence (AI) cannot match the human brain for creativity and adaptability. Nevertheless, AI could be used to further improve efficiency at work and must be engaged to extend the design limits [20,21].

Maltret describes what must be perceived as root level attributes for architectural objects:

- A 3D morphology, which in essence is a geometrical primitive from the modeler, which is exemplified by a 3D geometrical volume, or a combination of volumes, each of them defined by their own attributes and performances.
- A 2D morphology, which is the planar projection of the 3D form.
- A typology, which when not specified defaults to 'Notype›.
- An owner, which represents a composition relationship.
- A list of elements, which again is a composition relationship, and when not specified defaults to an empty set.
- The size: for instance, height, width, and length [19].

The following Figure 2 shows some of IA potentialities in the design process.

Rooting Morphology Aspects In Architecture

Based on the Oxford dictionary the word root is defined as 'establish deeply and firmly', or 'have as an origin or cause' [22].

In a broad definition of rooting the term "root architecture" is used in the biological field referring to distinct aspects of the shape and the spatial configuration of the root systems [23,24].

In architecture, rooting refers to the way a building is anchored or rooted to the earth. According to a Quizlet article, architecture can be rooted in the earth's rich resources, allowing buildings to act as a "natural symbolism". The site is the place where a building rests, with its submission to gravity, its raw materials, and centrality in outer space. The way a building is rooted in the earth can have a significant

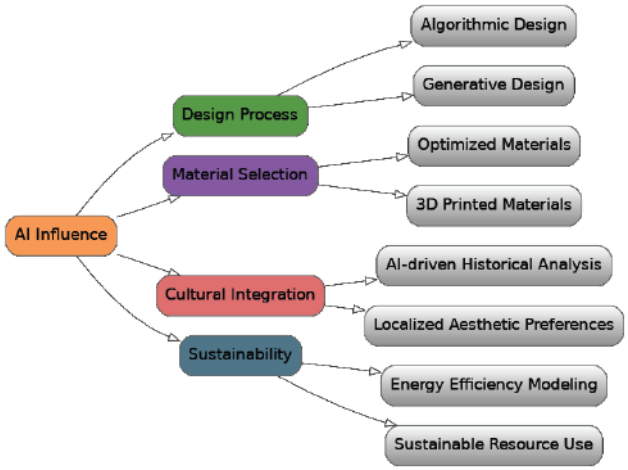


Figure 2. Conceptual models depicting the influence of Artificial Intelligence (AI) on local architectural styles.. Source: Authors

impact on its design and function. For example, Deckker discusses buildings that are rooted more firmly to the earth and may be more stable and better able to withstand natural disasters such as earthquakes [25].

Attributing Research or Examples from Other Regions: The previous application of artificial intelligence in Japanese architecture has been done using similar methodologies as described in this paper. These are examples that restate the fact Artificial Intelligence (AI) might well be a universal tool for cultural identity in architecture.

Rooting Morphology of Local Iraqi Architecture

Contemporary Iraqi architecture dates back to the beginning of the twentieth century, at the end of Ottoman rule and the beginning of the British occupation, with the coronation of King Faisal I as King of Iraq in 1921 (the establishment of the Iraqi state). Al-Assadi et al. state that Iraqi architecture has gone through many stages, numerous political events, and economic, social, and other changes. With the existence of these variables and events, it is noted that new architectural styles entered the local arena, accompanied by the emergence of clear architectural trends or styles that could generally be classified accordingly [26]:

The first stage: Represents the period of the twenties and thirties.

The second stage: Represents the period of the forties and fifties.

The third stage: Represents the sixties and seventies.

The fourth stage: Represents the eighties and nineties, when Iraqi architecture began to deviate from its path that was drawn in the previous period because of multiple wars and economic blockades that led to the isolation of Iraq from the world during that period. Only the first three phases will be investigated for their importance in determining the course of contemporary Iraqi architecture [27].

The first stage: Was characterized by the quality of the buildings constructed during this period, including the dominance of the British classic style, with the use of brick as a basic construction material within the architectural formations of a classic character. Since these architects designed in India with the British Army, the most prominent influences on the orientations and ideas of these architects were:

- Prevailing architectural trends in Britain (conservative classicism).
- Local traditional architecture of Iraq and neighboring Arab countries.

Among the most prominent buildings executed during that period is the General Ports Directorate building in Basra 1927 designed by Wilson and the Al-Zuhur Palace 1932, as in Figure 3. Shows examples of Iraqi architecture during that period.

The second stage: The most significant characteristic of the architecture in this period is represented in its artistic language that approached the propositions of what is known as "modern architecture". The architecture of this phase widely employed modern construction methods and materials.

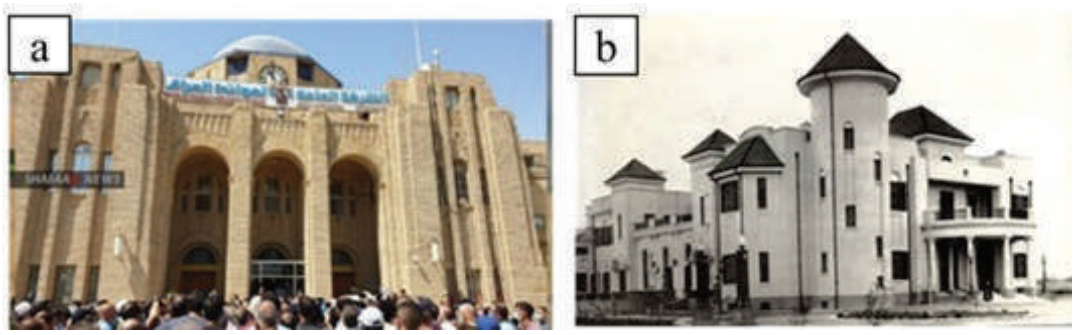


Figure 3. (a) Al-Zuhur Palace building. (b) General Ports Directorate building, [28] with permission from Shafaq News.



Figure 4. (a) Damarchi building. Source: Authors. (b) Sofair building. Source: Authors.

In the same context, Al-Sultani pointed out that: Distinguishably Baghdad skyline began to change through the emergence of multi-story buildings, such as the administrative building of the Sofer Building in Al-Rashid Street in 1946, designed by (Medhat Ali Mazloum, followed by the construction of the Damerchi Building, which was implemented by Niazi Fatou in 1948 and consisted of six floors [29]., as in Figure 4.

The third stage: Marked the beginning of the heritage-oriented stage (the sixties), it witnessed a trend towards the concept of architectural heritage and adhered to it, later in the seventies it expanded and prevailed. It was for the works of Muhammad Makiya and his trends that were reflected in the buildings of the Caliphs Mosque 1964, Al-Rafidain Bank 1968, and the Endowments Library. He used the heritage vocabulary and adapted it to coexist with contemporary ideas at the time. Thus, it was the beginning of an architectural movement that adhered to the local identity and led to the prominent outcome of creating an Iraqi school. As for the most important features of this approach as Al-Assadi & Al-Dewachi also searched is [30]:

This trend affected buildings' shapes and the use of heritage elements and details such as arches, shanasheel, inner courtyards, and others. The return to the use of bricks again in many buildings of this stage in addition to the presence of concrete materials, as in the projects of (Rifaat Aljaderji). Figure 5 shows the use of these elements in buildings of that period.

Nasir & Khudhair explained the existence of human scale in buildings and the use of simple heights and brick details in this period, in addition to the attempt to achieve traditional local character, with the presence of tall buildings at this stage such as communication centers and some ministries and administrative buildings, but the material and the details that were used in facades mitigate the massiveness and height of its construction (Nassir & Khudhaeir, 2010).

Iraqi architects adapted modern architecture in a local style through the use of treatments, details, and building materials such as lifting buildings on columns or using screens in the facades, as in Al-Founoun Institute by Saeed Ali Madhloum, and Al-Mustansiriya University by Qahtan Awni that was distinguished by Iraqi modernity through the employment of heritage in a contemporary style, as the designer resorted to using the brick screen with inscriptions from Iraqi heritage, hanged on concrete structure.

Scientific artistic dissertations tendencies appeared in Iraq towards the attraction of what was new in the field of environment. This concept was limited to the microbiological perspective on the local Baghdadi heritage environment or the folklore forms as metaphorical units, as in the exploitation of the folklore form of the Iraqi carpets in the facade of the University of Al-Mustansiriya or (the use of artistic elements in the design). Table 1.

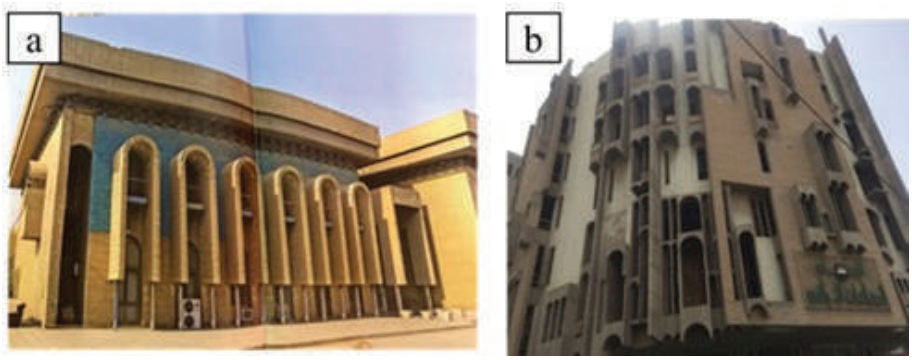


Figure 5. (a) Scientific complex building [31] with permission from the author. (b) Industrial union building. Source: Authors.

Table 1. The most important phases and the characteristics of architectural production within those stages. Source: Authors

Phase	Morphological level	Materialistic level	Scale level	Examples
First	British classical architecture and some features of local traditional architecture	The use of brick material, limited as the main finishing material	Characterized by proportionality and exclusivity	- Al-Zuhur Palace building. - General Ports Directorate building.
Second	Modern architecture and global style	Iron and concrete	Enormity in scale both horizontally and vertically	- Damarchi building - Sofair building
Third	Orientation towards traditional forms	Back to bricks	Human scale	- Scientific complex building - Industrial union building - Al-Mustansiriya University

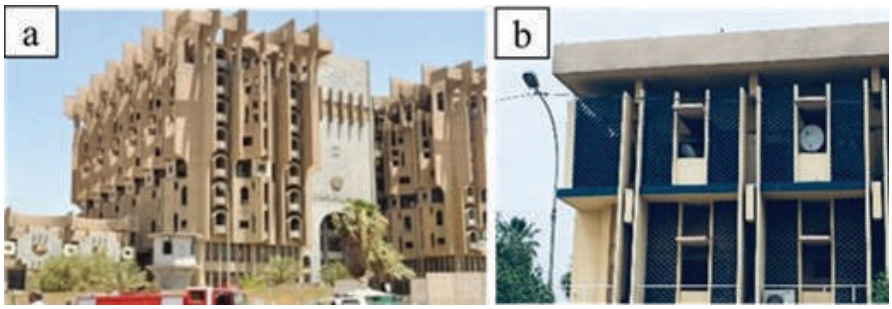


Figure 6. Use of bricks and concrete**.** (a) Ministry of Industry (Bricks). Source: Authors. (b) Awqaf Library (Concrete). Source: Authors.

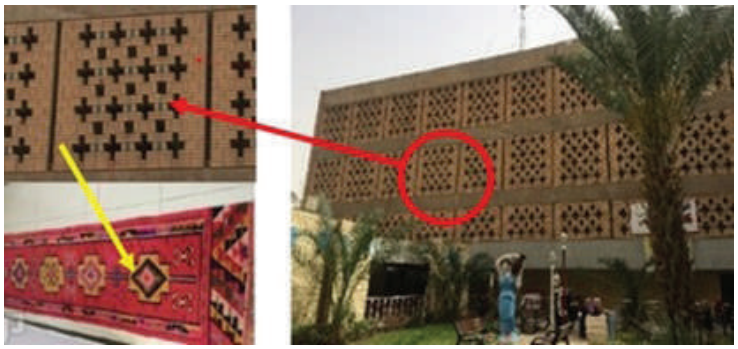


Figure 7. Use of folkloric forms. a & b Source: Authors.



Figure 8. Use of ceramic (greenish blue). (a) Liquefied water building. Source: Authors. (b) Scientific Complex [31]. with permission from the author.

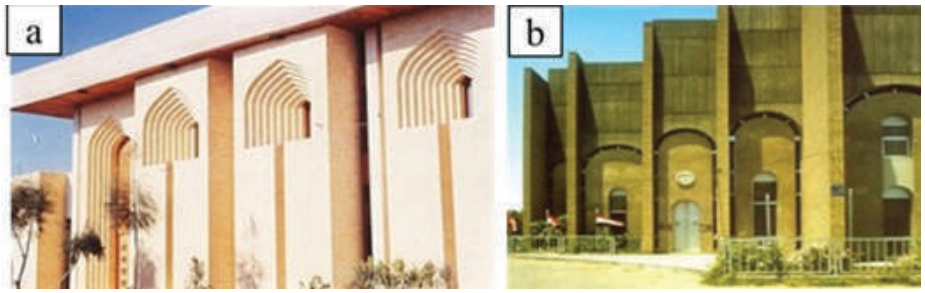


Figure 9. Use of arches. (a) Al-Rafidain Bank/Kufa [35], reproduced with permission from the author (b) Al-Rafidain Bank/Baghdad. [36], reproduced with permission from the page owner.

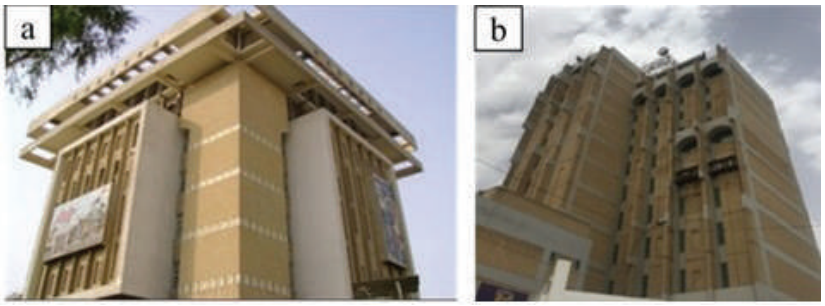


Figure 10. Use of local material (bricks). (a) Real estate Bank. Source: Authors. (b) Al-Sinak call center. Source: Authors.



Figure 11. Use of Abbasid arch in College of Education building. (a) Real Abbasid arch. Source: Authors. (b) Abstract arc to triangle. Source: Authors.

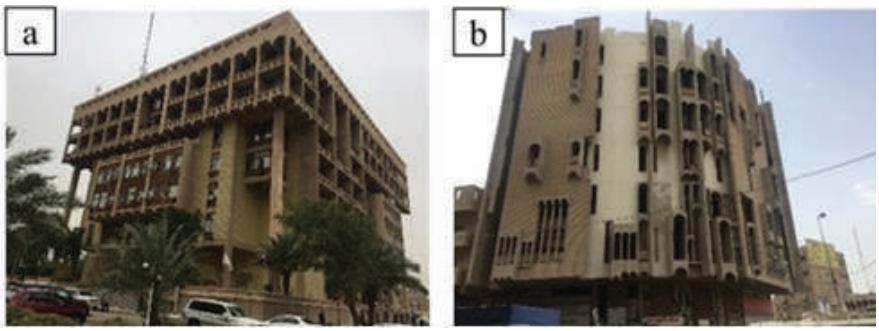


Figure 12. Use of shanasheel. (a) Liquefied water building. Source: Authors. (b) Industries union building. Source: Authors.

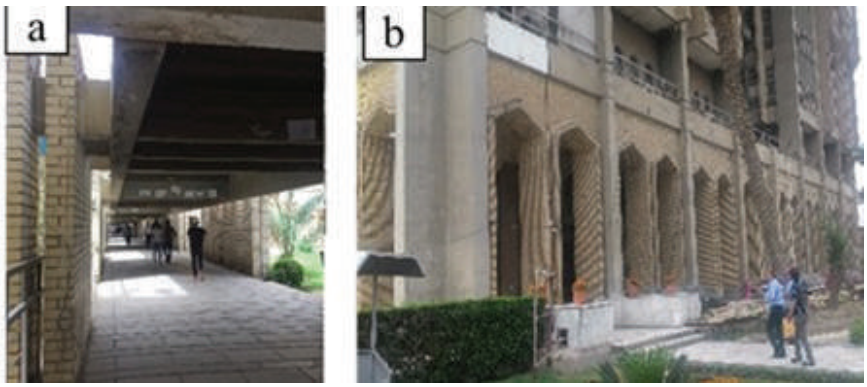


Figure 13. Use of portico. (a) Al-Mustansiriya University. Source: Authors. (b) Baghdad Municipality Building. Source: Authors.

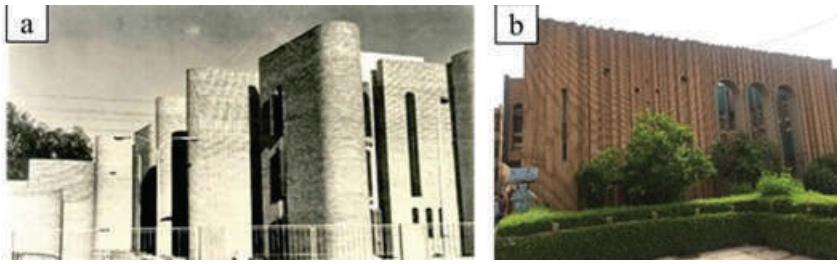


Figure 14. Use of Mesopotamian forms. (a) Semicircular towers. [37] reproduced with permission from Al Mada newspaper. (b)The system of fluting and protrusions. Source: Authors.



Figure 15. Use of (hat) on top of buildings. (a) Ministry of Interior, [38] (used for academic purposes only). (b) Baghdad Municipality Building. Source: Authors.

Characteristics of the Formal Structure of Iraqi Architecture

Al-Saffar suggests that the Local Iraqi architectural features came as a result of circumstances and interactions that include many factors and variables, both physical and non-physical, and what was left of this architecture is a fraction of these overlaps, eventually some features and characteristics can be extracted to compare Iraqi architecture with other civilizations, namely [32]:

- The characteristic of the human dimension.
- Harmony with the content.
- Emphasis on the principle of enclosed space (inner courtyard), whether it is solo or within a group.
- Use of local material (bricks).
- Utilization of stylistic details such as (arch, portico, the system of fluting and protrusions, brick screens, semicircular towers, shanasheel...etc.)

On this basis, the research concludes that as Al-Tameemi shows, the most important stage that characterized contemporary Iraqi architecture in terms of production is the third stage (the sixties and seventies), which stemmed from the beginnings of the emergence of an Iraqi architectural school. This stage can be considered as the distinction of the "heritage" concept on the intellectual scene to a wide extent, coinciding with the emergence of the post-modernism trend, which calls for returning to the past and history and for inspiration [33].

This period witnessed a widespread interest in "heritage" and the means to reflect it in architectural production, architectural experiments emerged to embody inspiration from the materialistic aspect and its presence through traditional heritage elements, while other experiments considered that the issue of inspiration from heritage means reviving the spiritual and historical aspects. Despite the evolution of the heritage notion at this stage, modernist thought was still represented as a contemporary conception that must be followed, but with a heritage vision related to the place, that is, attempts to create a global, regionalized architecture. With this trend, reflections of the architectural concept of heritage began to appear through attempts to draw inspiration from some heritage details such as (arches, and decoration, in addition to the use of brick material and the inner courtyard...etc.) [34], as in Figures 6-15. Shows the most important architectural achievements at that period.

Based on that, the research concludes the most significant indicators of the theoretical framework of Iraqi architecture for the third stage (the sixties and seventies), Table 2. Also, Figure 16 shows the most important elements that give Iraqi architecture its identity.

Regarding the experimental data obtained from models of contemporary Iraqi architecture, the research believes that the benefits will be derived from applying advanced data analysis techniques by using machine learning algorithms able to process small datasets and others. It is possible to use cross-validation techniques or bootstrapping to obtain optimization of the predictive capacity of the available data, even though it was limited.", as well as "The

Table 2. The most significant indicators of the theoretical framework of Iraqi architecture for the third stage (the sixties and seventies) Source: Authors

Third stage	Form level	Material level	Scale level	Detail level
The sixties and seventies	Orientation towards traditional forms	Focusing on the material (brick) as well as concrete and iron	Human scale	Abbasid quadrilateral arch The abstract arc of the triangular shape Using brick material as: Brick decoration Brick screens Use of shanasheel (explicit or abstract form) Using ceramic material in the facades and the details Use of the inner courtyard Using the porticos The cubic or rectangular shape of the building block Use a concrete crown or hat at the top of the building Focus on the design of the corner of the building (smashing, grading, or deletion) The use of concrete and bricks in the details of the facades (in arches, shanasheel, etc.) Use of Mesopotamian details such as: System of fluting and protrusions. Use of square or semicircular towers.

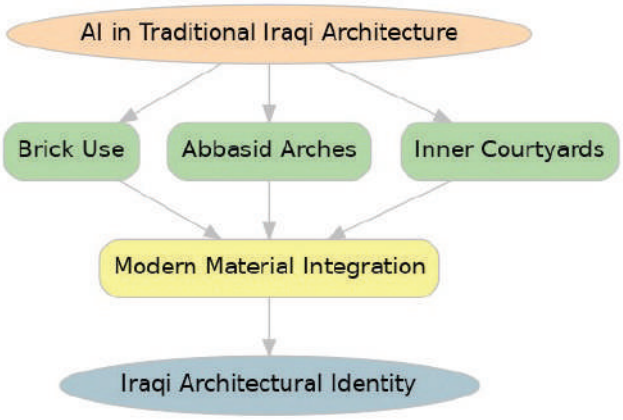


Figure 16. the elements that give Iraqi architecture its identity. Source: Authors.

collection and analysis of larger datasets should be pursued for the improvement of accuracy and generalization of AI-based predictions in local architecture. The approach will lead to a more solid foundation for the application of AI in this field and an improved level of the reliability of architectural practice."

Research Methodology

This study employs a method, first, a descriptive qualitative method was employed to investigate the similarity of the morphological representation of the indicators that can be found in local Iraqi architecture and the AI-generated examples [39]. Then a quantitative method relied on using the Jaccard similarity method to compare the results. Every variable with the value 1 which is considered positive represents the visual morphological representation of the indicator, and the value 0 represents the negative i.e. the absence of the visual depiction of the indicator [40]. It then adopted a numerical scale by calculating the Jaccard coefficient index ratio of the size of the intersection between each AI model and the Iraqi local architecture indicators to obtain a solid base to be able to draw a clear conclusion. The researcher carried out this task and has set the following rules to consider the results as an acceptable or unacceptable role AI towards rooting local Iraqi architecture:

1. The Jaccard coefficient index under 0.5 is considered an unacceptable result.
2. The Jaccard coefficient index of 0.5 and above is considered an acceptable result.

The Jaccard variables are 0 (refers to negative) and 1 (refers to positive). When calculating the Jaccard coefficient index the highest possible result will reach the value 1, and the lowest possible value is 0, therefore it is only reasonable considering the value 0.5 as the cutoff between 0 and 1.

Practical application

The application was carried out by using a set of keywords extracted by the indicators derived from the theoretical framework from Table 2, which represents the morphological aspects expressing the local aspect of Iraqi

architecture, it was applied in two different prompts and used in several artificial intelligence sites to obtain the following results. Table 3.

The models were developed using AI online sites represented by Gencraft AI image generator, lexica AI image generator, and LimeWire. blue willow AI image generator

Models A, B, and C have the same prompt but each one of them was generated using a different Artificial Intelligence (AI) site, and the same process was applied to the models D, E, and F.

Keywords: contemporary, traditional styles, 1960s and 1970s architecture, brick screens, concrete, iron elements, central four-arch Abbasid arch, ceramic facades, inner courtyards, semi-circular towers, Mesopotamian-inspired recesses, square towers, traditional and modern fusion, Iraq's architectural identity.

Prompt: Create a contemporary architectural design inspired by Iraqi traditional styles from the 1960s and 1970s. Incorporate brick, concrete, and iron elements along with the central four-arch Abbasid arch, ceramic facades, inner courtyards, and semi-circular towers. Integrate modern materials while preserving the essence of Mesopotamian-inspired recesses, projections, and square towers. Emphasize traditional and modern fusion, reflecting Iraq's architectural identity with a fresh perspective. Figure 17-19. show contemporary architectural design inspired by traditional Iraqi styles from the 60s and 70s using artificial intelligence**.**

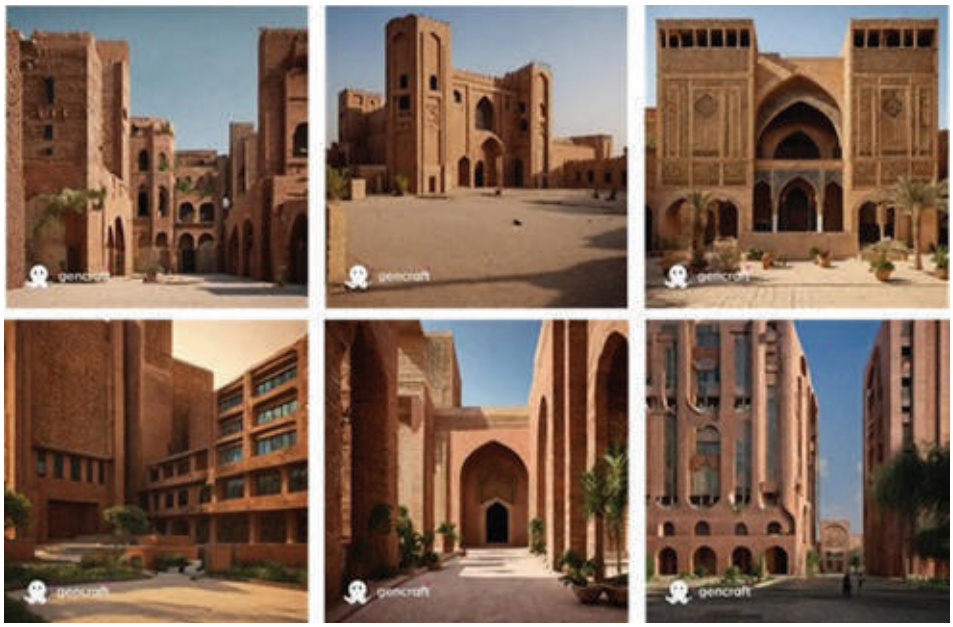


Figure 17. Artificial Intelligence (AI) simulation model A (predicted). Source: Created by the authors using Gencraft AI image generator.



Figure 18. Artificial Intelligence (AI) simulation model B (predicted) Source: Created by the authors using lexica Ai image generator.



Figure 19. AI simulation model C (predicted) Source: Created by the authors using LimeWire. bluewillow Ai image generator.

Table 3. Jaccard similarity for AI models A, B, and C. Source: Authors

Indicators		Iraqi Architecture (Actual)	AI simulation model A (predicted)	AI simulation model B (predicted)	AI simulation model C (predicted)
Orientation toward traditional forms		1	1	1	1
Focusing on material (brick)		1	1	0	1
Focusing on concrete material and iron.		1	0	1	1
Human scale		1	1	1	1
Morphological Details	Abbasid quadrilateral arch	1	1	1	1
	The abstract arc of the triangular shape	1	0	0	0
	Use of shanasheel (explicit or abstract form)	1	0	0	1
	Using ceramic material in the facades and the details	1	0	0	0
	Use of the inner courtyard	1	0	1	1
	Using the porticos	1	0	0	0
	The cubic or rectangular shape of the building block	1	1	1	1
	Use a concrete crown or hat at the top of the building	1	0	0	0
	Focus on the design of the corner of the building (smashing, grading, or deletion)	1	1	1	0
	The use of concrete and bricks in the details of the facades (in arches, shanasheel, etc.)	1	1	0	1
	Use of Mesopotamian system of fluting and protrusions.	1	0	0	0
	Use of Mesopotamian square or semicircular towers.	1	1	1	1

Table 4. Jaccard values for AI models A, B and C. Source: Authors

		AI simulation model A		AI simulation model B		AI simulation model C	
		negative	**positive**	**negative**	**positive**	**negative**	**positive**
actual	negative	0	0	0	0	0	0
	positive	8	8	8	8	6	10

Jaccard Similarity for model A

$$\frac{\text{Overlapping positives}}{\text{total positives}} = \frac{8}{16} = 0.5$$

Jaccard Similarity for model B

$$\frac{\text{Overlapping positives}}{\text{total positives}} = \frac{8}{16} = 0.5$$

Jaccard Similarity for Model C

$$\frac{\text{Overlapping positives}}{\text{total positives}} = \frac{10}{16} = 0.625$$

Below is another example of AI-generating pictures. Models (D, E, F). And Jaccard Similarity for Artificial Intelligence Table 5,6.

Keywords: contemporary, traditional styles, 1960s and 1970s architecture, brick screens, concrete, iron elements, ceramic facades, semi-circular towers, Mesopotamian-inspired recesses, square towers, traditional and modern fusion, Iraq's architectural identity.

Prompt: a contemporary architectural design inspired by Iraqi traditional styles from the 1960s and 1970s. brick screens, concrete, and iron elements, ceramic facades, and semi-circular towers. Integrate modern materials while preserving the essence of Mesopotamian-inspired recesses, projections, and square towers. Emphasize traditional and modern fusion, reflecting Iraq's architectural identity. Get inspiration from Mustansiriya University building design, the Iraqi Industrial Union building, Mohammed Makkiya's work, and modern style. Figures 20-22. these elements are embodied in them using artificial intelligence.



Figure 20. Artificial Intelligence (AI) simulation model D (predicted) Source: Created by the authors using Gencraft AI image generator.



Figure 21. Artificial Intelligence (AI) simulation model E (predicted) Source: Created by the authors using lexica Ai image generator.



Figure 22. Artificial Intelligence (AI) simulation model F (predicted) Source: Created by the authors using LimeWire. bluewillow Ai image generator.

Jaccard Similarity for Model D

$$\frac{\text{Overlapping positives}}{\text{total positives}} = \frac{8}{16} = 0.5$$

Jaccard Similarity for Model E

$$\frac{\text{Overlapping positives}}{\text{total positives}} = \frac{2}{16} = 0.125$$

Jaccard Similarity for Model F

$$\frac{\text{Overlapping positives}}{\text{total positives}} = \frac{11}{16} = 0.6875$$

The following diagram illustrates the practical results for models (A,B,C). (Fig. 23).

RESULTS AND DISCUSSION

This study, conducted in 2024, aimed to understand the role of artificial intelligence in rooting local Iraqi architecture by analyzing the extent to which AI can reproduce the morphological elements of traditional Iraqi architecture. The study employed a mixed-methods approach, beginning with qualitative descriptive analysis to compare the morphological forms found in Iraqi architecture with those

Table 5. Jaccard similarity for AI models D, E and F. Source: Authors

Indicators		Iraqi Architecture (Actual)	AI simulation model D (predicted)	AI simulation model E (predicted)	AI simulation model F (predicted)
Orientation towards traditional forms		1	1	0	1
Focusing on material (brick)		1	1	0	1
Focusing on concrete material and iron.		1	0	1	1
Human scale		1	0	0	1
Morphological Details	Abbasid quadrilateral arch	1	0	0	1
	The abstract arc of the triangular shape	1	0	0	0
	Use of shanasheel (explicit or abstract form)	1	0	0	0
	Using ceramic material in the facades and the details	1	0	0	0
	Use of the inner courtyard	1	0	0	1
	Using the porticos	1	1	0	1
	The cubic or rectangular shape of the building block	1	1	1	1
	Use a concrete crown or hat at the top of the building	1	0	0	0
	Focus on the design of the corner of the building (smashing, grading, or deletion)	1	1	0	0
	The use of concrete and bricks in the details of the facades (in arches, shanasheel, etc.)	1	1	0	1
	Use of Mesopotamian system of fluting and protrusions.	1	1	0	1
	Use of Mesopotamian square or semicircular towers.	1	1	0	1

Table 6. Jaccard values for AI models D, E and F. Source: Authors

		AI simulation model D		AI simulation model E		AI simulation model F	
		negative	positive	negative	positive	negative	positive
actual	negative	0	0	0	0	0	0
	positive	8	8	14	2	5	11

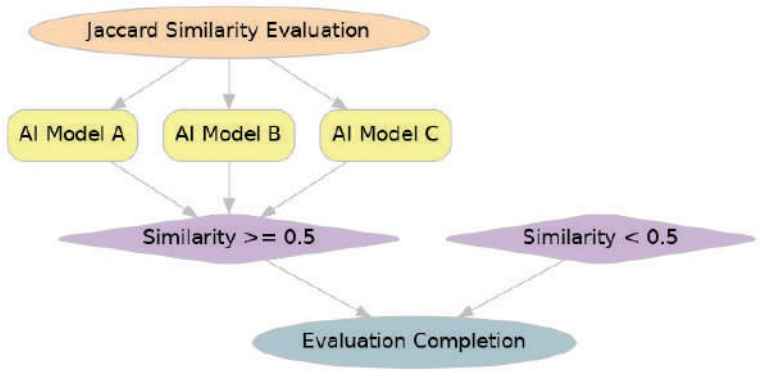


Figure 23. Shows illustrate the practical results. Source: Authors.

Table 7. The final results for all AI models. Source: Authors

	AI simulation model A	AI simulation model B	AI simulation model C	AI simulation model D	AI simulation model E	AI simulation model F
Jaccard coefficient index	0.5	0.5	0.625	0.5	0.125	0.6875

generated by AI, followed by the use of the Jaccard method to measure similarity between them. The results showed that AI is capable of accurately representing some visual aspects of local architecture, though it cannot sometimes fully grasp the cultural and historical depth of architectural elements. The study concluded that AI can be an effective tool in enhancing and developing local architecture if properly guided, with careful consideration of the cultural and historical context in which it operates. Based on that and the comparison between local architectural elements and those generated by AI as shown in Table 7, the following conclusions can be drawn:

Two different AI prompts were applied in the study in order to generate six different models of architecture. The models were in turn evaluated according to their morphological similarity with local Iraqi architecture from the 1960s and 1970s with the Jaccard similarity index. The AI -based models have been compared against a set of morphological indicators directed to be derived from traditional Iraqi architectural elements: the use of bricks, concrete, iron elements, Abbasid quadrilateral arches, inner courtyards, and Mesopotamian-inspired forms. The overall result was that five out of the six models—that is, A, B, C, D, and F—returned Jaccard similarity indices of 0.5 and above, which denotes high morphological similarity with local Iraqi architecture of the studied period. More specifically, Model A scored an index of 0.5, Model B also 0.5, Model C 0.625, Model D 0.5, while Model F was the best with an index of 0.6875. These indices are high and signal that AI can be used in reproduction of such important architectural elements and styles to capture the traditional forms, materials, and design principles that are usually attributed to any given culture. On the other hand, the Jaccard index of morphological resemblance was very low, at 0.125, suggesting that the morphological match and adequacy to represent the architecture of local Iraq is very poor. In this particular model, the major critical tectonic details that denote traditional styles from the 1960s and 1970s were not reflected. The indication is that AI-generated designs can go a long way to ensure that local architectural identity is preserved and anchored by making true imitations of traditional structures and including them in contemporary forms. It also has the implication that it necessitates human intervention during the design process to ensure that such cultural and emotional nuances are captured sufficiently, which AI can miss. This duality approach is a way of embodying efficiency and innovation in AI while structuring the rich cultural heritage and emotional significance of traditional architecture. The research concludes that while AI is bound to revolutionize architectural design, a human touch tends to make authenticity and profound depth of cultural expressions in architecture indispensable. Table 7. represents the final results for all AI models. In other words, this result has practical application in that AI can be used as a powerful tool in developing architectural designs that are efficient and, at the same time, aesthetically pleasing, with traditional aspects and cultural identity. These technologies may be applied in an architectural restoration project or in designing a new building to align with local characteristics, thereby increasing the acceptance of the local community towards these buildings. Table 7.

Thus, five models out of six displayed an acceptable similarity approach towards generating close morphological results of Iraqi architecture.

Expanding the Application of the Results: While the study will be geared toward applying AI to traditional Iraqi local architecture, these results can, to a practical extent, be general in their findings. These principles put in place in this study to evaluate the similarity between traditional Iraqi architecture and AI models can be used in other completely different situations. For example, architectural designing in other parts of the world can use AI. One such part of the world is South Asia or North Africa, where the basis for traditional architecture is based on some unique features that can easily be integrated into modern designs through AI.

RESULTS AND DISCUSSION

As a result, the morphological resemblance of AI-generated architectural forms can be similar to the traditional Iraqi architecture forms of the 1960s and 1970s. Five out of the six models returned Jaccard similarity indices of 0.5 or more. This means that AI can duplicate the form of traditional architecture and materials with a cultural heritage element in a faithful manner. These findings agree with some of the previous works in the literature in which the use of AI has been studied in the context of architecture, especially generative design. For instance, [15] outlined that AI can be used for obtaining design solutions optimized through generative design processes not limited by conventional architectural norms. Along the same lines, the work of Kaplan and [11]underscored the idea that AI can interpret and learn from data so that it can come up with designs in consideration of specific goals and contexts. Still, different from these studies which lean more toward

innovation and optimization, this research takes a special focus on the aspect of keeping or maintaining local identity in architecture and filling in the gap that has resulted from previous works.

Additionally, the findings of the study provide further insights by showing that AI can not only innovate but also succeed in the re-creation of traditional forms with a high degree of accuracy. This is quite contrary to the fears expressed by [20], who feared AI was likely to miss out on some of the nuances within cultural and emotional dimensions of traditional architecture. The results of the current research demonstrate that AI can indeed replicate the known models of traditional architectural forms, but human intervention is very much needed to give real meaning to those cultural and emotional factors. In comparison to previous studies, the present research was conducted using a novel quantitative measure based on the Jaccard similarity index in judging the level of similarity of AI-generated designs to traditional architectural forms. This methodological innovation opens a new tool for researchers and practitioners who seek to balance innovation with cultural conservation in architecture. In this manner, the results of this study contribute not only to the ongoing debate on the role of AI in architecture but also provide practical implications for its application in heritage preservation. That said, a high degree of morphological similarity obtained by AI models underscores the potential for embedding AI in culturally sensitive design processes, provided they are carried out under the guidance of a sophisticated understanding of local architectural traditions.

Loss of the human touch: Although AI can replicate and improve traditional designs such as the Abbasid quadrilateral arch, it may lack the human and emotional touch that gives local architecture its unique character.

Potential neglect of aesthetic and cultural aspects: AI tends to focus on functional and structural efficiency, as in the design of shanashil and the materials used in facades, which may lead to neglect of aesthetic and cultural aspects that are essential to local architecture.

Functional improvement versus tradition: In the case of courtyards and arcades, AI can improve elements such as airflow and sunlight, but it may overlook the social and cultural dimensions that make these elements an integral part of the urban fabric.

Balancing authenticity and efficiency: While AI can enhance the thermal and structural efficiency of a building form, such as a cubic or rectangular one, it may conflict with architectural traditions that carry cultural and historical symbolism.

Accurately reproducing historical details: AI can accurately reproduce fine architectural details such as Mesopotamian architectural elements, but without being able to fully capture the historical and cultural context.

In short, the research demonstrates that AI has great potential to improve the efficiency and functional performance of architectural elements, but may require additional human intervention to ensure that the cultural and aesthetic identity of local architecture is preserved.

CONCLUSION

- **Management of the Ability of AI to Reproduce and Enhance Classical Randomness of Iraqi Architecture:** AI has been shown to have the capability to reproduce and enhance classic architecture of the 1960s and 1970s in Iraq and this has been well shown in this study. The application of AI to preserve cultural heritage has been made strong and properly methodological the first time, and this seals a massive gap in the state-of-the-art. The Jaccard similarity indexes in the models generated by AI are high, which means that AI can play a significant role in protecting local architectural identity. Nevertheless, this research is also suggestive of the fact that, despite the fact that the AI offers potent means of architectural innovation, on the other hand, it should also be supervised by humans to ensure proper capturing of cultural and historical specifics. This extends to Iraq and develops a model which can be utilized in other cultural settings where architectural heritage conservation is an issue.
- **High Fidelity of AI-Generated Architectural Prototypes:** This research has shown that an AI model could produce architectural prototypes that have high fidelity to the form of the original Iraqi architecture that was created in the 60s and 70s. The A, B, C, D, and F AI generated models share morphological features with human designs of that time period and may be the cause of the Jaccard Similarity Index reaching up to 0.5. These parallels justify the fact that AI can integrate indigenous architectural features in contemporary designs and, at the same time, recreate the traditional forms, materials, and design principles. The notable architectural elements that the models have been allowed to take are the use of concrete, brick, elements of iron and heritage ones such as palisades, Abbasid quadrilateral arches and Mesopotamian shapes. Such integration can attest to the fact that AI can be used to aid in maintaining cultural identity in architectural activities, which is evidenced, through incorporation of traditional elements of architecture into present-day design tools.
- **The Significance of Human Control in the Architectural Design Processes with AI Support:** The role of human control in architectural design processes with the assistance of AI is hard to overestimate, and its significance in terms of preserving cultural and emotional nuances in the blueprinting process is difficult to overestimate.
- **Greater International Operational Value:** The results of the research include a source of reference in other cultural backgrounds where architectural heritage conservation is of significance. The AI used in this research indicates that local features can be improved in designs to assist in saving the cultural identities in the context of

global transformations. This is especially relevant to the modern discussion of the global cultural sustainability, where AI is regarded as the means of assisting the preservation of cultural heritage as well as introducing modern architecture practice.

- **AI as a Tool to Enhance Architectural Efficiency and Preserve Cultural Heritage:** Further findings of this research affirm that AI can support architectural design through the integration of traditional architectural elements with modern designs through simulation. It adds another feather in the hat—increased work efficiency in design and, furthermore, more sustainability in cultural heritages and local architectural identity. AI technologies keep on coming with new improvements and embedding themselves within the mainstream procedures for design. However, this research insists on human intervention because designs must encompass the cultural and emotional aspects linked with the people who live near or use such buildings.
- **Future Research Directions on AI in Architectural Design:** This research contributes a preliminary understanding of the incorporation of AI into architectural practices for improving the design process with retained local architectural legacies. Further research has to focus on developing refined AI algorithms that could incorporate cultural and emotional aspects, ensuring holistic approaches to architectural design that are respectful and retentive of local identities. These developments would help to promote more holistic and culturally sensitive applications of AI in architecture.

AUTHORSHIP CONTRIBUTIONS

Authors equally contributed to this work.

DATA AVAILABILITY STATEMENT

The authors confirm that the data that supports the findings of this study are available within the article. Raw data that support the finding of this study are available from the corresponding author, upon reasonable request.

CONFLICT OF INTEREST

The author declared no potential conflicts of interest with respect to the research, authorship, and/or publication of this article.

ETHICS

There are no ethical issues with the publication of this manuscript.

STATEMENT ON THE USE OF ARTIFICIAL INTELLIGENCE

Artificial intelligence was not used in the preparation of the article.

REFERENCES

[1] Roéfero LGP, Chavarette FR, Outa R, Merizio IF, Moro TC, Mishra VN. Optimal linear control applied to a non-ideal capsule system with uncertain parameters. J Appl Math Inform 2022;40:351–370.

[2] Sharma MK, Bhargava AK, Kumar S, Rathour L, Mishra LN, Pandey S. A fermatean fuzzy ranking function in optimization of intuitionistic fuzzy transportation problems. Adv Math Model Appl 2022;7:191–204.

[3] Sharma MK, Dhiman N, Kumar S, Rathour L, Mishra VN. Neutrosophic monte carlo simulation approach for decision making in medical diagnostic process under uncertain environment. Int J Neutrosophic Sci 2023;22:8–16. [CrossRef]

[4] Sharma MK, Chaudhary S, Rathour L, Mishra VN. Modified genetic algorithm with novel crossover and mutation operator in travelling salesman problem. Sigma J Eng Nat Sci 2024;42:1876–1883. [CrossRef]

[5] Ertunç HM. A combined decision algorithm for diagnosing bearing faults using artificial intelligent techniques. Sigma J Eng Nat Sci 2018;36:1235–1253.

[6] Rathour L, Singh V, Yadav H, Sharma MK, Mishra VN. A dual hesitant fuzzy set theoretic approach in fuzzy reliability analysis of a fuzzy system. Inf Sci Lett 2024;13:433–440. [CrossRef]

[7] Gaffar A, Joshi AB, Kumar D, Mishra VN. Image encryption using nonlinear feedback shift register and modified RC4A algorithm. J Appl Math Informatics 2021;39:859–882.

[8] del Campo M, Leach N. Machine hallucinations: Architecture and artificial intelligence. Chichester: John Wiley & Sons; 2022.

[9] Alzubaidy DM, Al-Tameemi OA. Evaluating the perception of virtual reality in historical sites. In: BIO Web Conf. Les Ulis: EDP Sciences; 2024. p. 82. [CrossRef]

[10] Mishra LN, Raiz M, Mishra VN. Tauberian theorems for weighted means of double sequences in intuitionistic fuzzy normed spaces. arXiv preprint arXiv:2103.15585. 2021.

[11] Haenlein M, Kaplan A. A brief history of artificial intelligence: On the past, present, and future of artificial intelligence. Calif Manage Rev 2019;61:5–14. [CrossRef]

[12] Bartneck C, Lütge C, Wagner A, Welsh S. An introduction to ethics in robotics and AI. Cham: Springer Nature; 2021. [CrossRef]

[13] Bernstein P. Machine learning: Architecture in the age of artificial intelligence. London: RIBA Publishing; 2022. [CrossRef]

[14] Kumar D, Joshi AB, Singh S, Mishra VN. Digital color-image encryption scheme based on elliptic curve cryptography ElGamal encryption and 3D Lorenz map. In: AIP Conf Proc. Melville: AIP Publishing; 2021. [CrossRef]

[15] Borglund C. Artificial intelligence in architecture and its impact on design creativity: A study on how artificial intelligence affect creativity in the design process. KTH Royal Institute of Technology; 2022.
[16] Merizio IF, Chavarette FR, Moro TC, Outa R, Mishra VN. Machine learning applied in the detection of faults in pipes by acoustic means. J Inst Eng Ser C 2021;102:975–980. [CrossRef]
[17] Dreith B. How AI software will change architecture and design. Available at: https://www.dezeen.com/2022/11/16/ai-design-architecture-product/ Accessed on Nov 07, 2025.
[18] Kumar D, Joshi AB, Mishra VN. Optical and digital double color-image encryption algorithm using 3D chaotic map and 2D-multiple parameter fractional discrete cosine transform. Results Opt 2020;1:100031.
[19] Maltret JL, Zoller J. Simulation of architectural and urban morphology. In: OEEPE Workshop on 3D-city models. Hanover: Citeseer; 1996.
[20] Ismail Agha D. The impact of artificial intelligence on the future of architecture and architects: The revolution of artificial intelligence. International Conference on Planning, Architecture and Civil Engineering At: Rajshahi University of Engineering & Technology, Rajshahi, Bangladesh 2019.
[21] Outa R, Chavarette FR, Gonçalves AC, da Silva SL, Mishra VN, Panosso AR, et al. Reliability analysis using experimental statistical methods and AIS: Application in continuous flow tubes of gaseous medium. Acta Sci Technol 2021;43:e55825. [CrossRef]
[22] Oxford Languages. Oxford Languages and Google. Available at: https://languages.oup.com/google-dictionary-tr/ Accessed on Nov 07, 2025.
[23] Lynch J. Root architecture and plant productivity. Plant Physiol 1995;109:7.
[24] Outa R, Chavarette FR, Mishra VN, Gonçalves AC, Garcia A, da Silva Pinto S, et al. Analysis and prognosis of failures in intelligent hybrid systems using bioengineering: Gear coupling. J Eng Exact Sci 2022;8:13601–1373. [CrossRef]
[25] Deckker T. Architecture and the humanities. arq Archit Res Q 2014;18:47–54. [CrossRef]
[26] Al-Assadi FI, Najah FT, Al-Saffar IMA. Alienation in contemporary Iraqi architecture: The questions of space–time communication and style. J Int Soc Stud Vernacular Settle 2022;9:387–407.
[27] Al-Assadi FI. Bio-metaphor in Iraqi architecture: Date palm as model. J Eng Res 2022;10:15–31. [CrossRef]
[28] Shafaq. Available at: https://shafaq.com/ar//مجتمع صور - مئات - الموظفين - يحتجون - بتظاهرتين - في - البصرة Accessed on Nov 07, 2025
[29] Al-Sultani K. The architecture of modernity in Baghdad: Years of foundation. Amman (JO): Dar Al-Adeeb Press; 2014.
[30] Al-Assadi FI, Al-Dewachi MH. The role of brick in determining features of Iraqi architecture. In: IOP Conf Ser Mater Sci Eng 2020;88:12018. [CrossRef]
[31] Al-Chalabi MR. Iraqi architecture encyclopedia. 1st ed. Baghdad: Ma'na Publishing & Translation; 2022.
[32] Al-Saffar M. Globalization and its impact on the urban system. Iraqi J Archit Eng 2010;21:277–292.
[33] Al-Tameemi OA, Abdul-Qader S. Constructive truth and creativity in contemporary Iraqi architecture. IOP Conf Ser Mater Sci Eng 2020;745:12120. [CrossRef]
[34] Al-Tameemi OA, Toma TA. Automation in architecture and its effect on the regeneration of traditional buildings: Al-Shawi House as a case study. IOP Conf Ser Mater Sci Eng 2020;881: 012027. [CrossRef]
[35] Manifest05. Rafidain bank in Kufa. 2020. Available at: https://www.tumblr.com/manifest05/148439817089/rafidain-bank-in-kufa-iraq-by-mohamed-makiya Accessed on Nov 07, 2025.
[36] Old Iraq. Old Iraq. 2017. Available at: https://www.facebook.com/oldiraq/posts/مصرف-الرافدين-فرع-المنصور-واتحاد-الصناعات-العراقي-ونصب-الجندي-المجهول-من-تصميم-ر/644816512379784/?locale=ar_AR Accessed on Nov 07, 2025.
[37] Almadapaper. Tobacco restriction building. 2014. Available at: https://almadapaper.net/102098/ Accessed on Nov 07, 2025.
[38] Iraqi News Agency. Ministry of interior. 2020. Available at: https://www.ina.iq/116903--.html Accessed on Nov 07, 2025.
[39] Ayub M, Ghazanfar MA, Khan T, Saleem A. An effective model for Jaccard coefficient to increase the performance of collaborative filtering. Arab J Sci Eng 2020;45:9997–10017. [CrossRef]
[40] Gupta AK, Sardana N. Significance of clustering coefficient over Jaccard index. In: 2015 8th Int Conf Contemp Comput (IC3). Piscataway (NJ): IEEE; 2015. p. 463–466. [CrossRef]

Sigma Journal of Engineering and Natural Sciences
Web page info: https://sigma.yildiz.edu.tr
DOI: 10.14744/sigma.2025.1913

Research Article

A study on copolymers of styrene with a methacrylamide containing benzofuran side group: Their monomer reactivity ratios, thermal stabilities, thermal degradation kinetics

Esra BARIM[1,*], Pınar DEMIR[2], Mustafa DEĞIRMENCI[3], Cumhur KIRILMIŞ[4]

[1]*Vocational School of Tunceli, Munzur University, Tunceli, 62000, Türkiye*
[2]*EOSB Higher Vocational School, Firat University, Elazig, 23119, Türkiye*
[3]*Department of Chemistry, Harran University, Sanliurfa, 63190, Türkiye*
[4]*Department of Chemistry, Adiyaman University, Adiyaman, 02040, Türkiye*

ARTICLE INFO

Article history
Received: 08 May 2024
Revised: 21 August 2024
Accepted: 17 October 2024

Keywords:
Benzofuran; Copolymerization; Free Radical Polymerization; Methacrylamide; Monomer Reactivity Ratio; Thermal Properties

ABSTRACT

The aim of this study was to determine the monomer reactivity ratios, thermal properties and thermal degradation behavior of new P(N-[2-(4-brombenzoyl)-benzofuran-3-yl]-2-methacrylamide-co-styrene) polymers synthesized at different compositions. For this purpose, novel copolymers of N-[2-(4-brombenzoyl)-benzofuran-3-yl]-2-methacrylamide (NBBM) monomer with styrene (St) monomer were prepared using free radical polymerization method. The ^{1}H-NMR spectra was used to calculate the compositions of the copolymers. The reactivity ratios of monomers were calculated in line with the universal copolymerization equation using Kelen-Tüdös and Finemann-Ross linearization methods, and found to be r_1:0,62 r_2:1,09 and r_1:0,61, r_2:1,07 respectively (where r_1 is reactivity ratio of NBBM). DSC, TGA and DTG were used to study the thermal behaviors of the copolymers. The Tg value of P(NBMM) was found to be 211 °C and the Tg values of the studied copolymers were determined to increase from 144 °C to 184 °C with increasing concentration of NBMM units. Thermal data showed that the maximum degradation temperatures increased from 349 °C to 391 °C as the St units increased in the copolymer system. The activation energy (Ea) values of P(NBBM) and the studied copolymer were determined from the TGA curves obtained at different heating rates and the Flynn-Wall-Qzawa, Kissinger, Tang isoconversional methods were used. Solid state reaction mechanisms were also calculated by being used the Van Krevelen method, a non-isoconversion model. The Ea values obtained with isoconversion models for P(NBBM) and copolymer were found very close to the values obtained from non-isoconversion models. Moreover, the R3 mechanism was proposed for the homopolymer and copolymer.

Cite this article as: Barim E, Demir P, Değirmenci M, Kırılmış C. A study on copolymers of styrene with a methacrylamide containing benzofuran side group: Their monomer reactivity ratios, thermal stabilities, thermal degradation kinetics. Sigma J Eng Nat Sci 2025;43(6):2050–2065.

***Corresponding author.**
*E-mail address: esrabarim@munzur.edu.tr

This paper was recommended for publication in revised form by Editor-in-Chief Ahmet Selim Dalkilic

Published by Yıldız Technical University Press, İstanbul, Turkey
© Author. This is an open access article under the CC BY-NC license (http://creativecommons.org/licenses/by-nc/4.0/).

INTRODUCTION

Polymers containing functional groups with different properties have been used in various applications as functional materials. In this regard, polymethacrylates with benzofuran ring in the side group have gained more and more interest lately. One of the most frequently used methods to produce materials with desired properties using monomers containing these functional groups is copolymerization. Functional methacrylate copolymers have many biomedical applications in industry. Drug delivery systems, dental and knee prosthesis, biosensors are some of these areas of applications. Studies have aimed to improving properties such as biocompatibility, bioactivity and long-lasting durability in their areas of use [1-4]. Benzofuran and its derivatives have been investigated for their biological activities [5-8], optical properties [9, 10], thermal properties [11] and these studies are still ongoing. For example, one study reported that 2-acetyl benzofurans can be used for anti-cancer treatment [12]. In another study, anticancer, antibacterial and antioxidant properties of some benzofuran modified compounds were investigated. As a result of the study, it was reported that these compounds showing antiproliferative effect are promising [13]. Some researchers who have studied the effect of benzofurane structures containing bromine for a long time against cancer have found that these structures exhibit quite important effects against leukemia [14]. For these reasons, the synthesis of methacrylamides containing benzofuran groups and further investigation of such polymers will lead to promising results. But when synthesizing a copolymer, it is important to have information about the reactivity ratios of the monomer of the copolymer to be synthesized [15-17]. These reactivity ratio values provide an insight into the design and composition of the product.. As a result, copolymer composition is critical for some applications [18, 19]. In this context, the knowledge of monomer reactivity ratios in methacrylate copolymers containing benzofuran structure synthesized in our study and having many properties enables the use of these copolymers in various application areas. For example, this use could be the production of disposable materials such as gloves, vials and pipettes made from styrene-based polymers containing benzofuran in their structure. In order to determine monomer reactivity ratios, which is such important information, linear and nonlinear mathematical methods as well as some experimental kinetic data are frequently preferred [20-23].

One of the important properties of polymers is their thermal behavior. The fundamental thermal data are significant in terms of the use of polymer materials. The change in mass of a polymer as a function of time and temperature is determined by thermogravimetric analysis [24]. From this analysis it is possible to obtain information about the thermal stability of a polymer, the degree of thermal degradation reaction and the activation energy of thermal degradation [11]. These properties change drastically according to the groups found in the structure of the material [25]. The change in the thermal stability of methacrylate polymers due to the addition of side groups, especially heterocyclic groups, has attracted the interest of researchers [26]. The thermal behavior of some methacrylate copolymers containing benzofuran has also been studied and reported to exhibit high thermal stability. For example, Demirelli et al. examined methacrylate polymers with different benzofuran concentration and reported that thermal stability increased with increasing benzofuran units in the structure. In addition, they reported that the composites of these structures made with graphite oxide have semiconducting properties at all temperatures studied [27].

Styrene is one of the most important monomers for copolymers and composites, which are used today in an increasingly wide range of applications. Therefore, polystyrene is found in many commonly used products. Polystyrene is used in the medical field, especially in the production of implants and devices [28, 29]. It is also widely used in disposable materials such as gloves and vials. Polystyrene is also preferred in the production of laboratory equipment such as petri dishes, pipettes and sterilization trays [30, 31]. In addition to its low cost and thermal stability, its durability, lightness, and ease of processing make polystyrene a suitable candidate for these uses. Due to the recent increasing demand for single-use medical materials, the need for such medical polymers continues to increase significantly. In many studies in the literature, poly(styrene-block-isobutylene-block-styrene) block copolymers have been frequently used for biomedical applications due to their processability, biocompatibility and stability. [32,33]. In addition, the thermal stability, biological, optical and electrical properties of new polymers containing styrene units in their structure have been frequently studied in the literature [34-38].

The benzofuran ring is a fundamental structure found in many medically important compounds. But a vast majority of studies on benzofurans are aimed at synthesising new benzofuran derivatives with small molecular weight by various organic synthesis reactions and investigating their biological properties. When the literatures are examined, studies on the synthesis and properties of benzofuran containing polymers are quite limited [27, 39-41]. Due to the properties mentioned above, P(NBMM-co-St) copolymers can be used in various manufacturing and medical fields, especially in biomedical applications. Therefore, in our study, the monomer reactivity ratios of P(NBMM-co-St) copolymers with functional and characteristic properties to be used for the desired purpose were determined. At the same time, the thermal behaviors of these polymers, which reveal their properties such as processability and resistance to high temperatures, were investigated and their thermal degradation kinetics were studied.

EXPERIMENTAL PROCEDURES

Materials and Characterization

The monomer namely, N-[2-(4-brombenzoyl)-benzofuran-3-yl]-2-methacrylamide (NBBM) was synthesized through a method from the literature [42]. Methanol, ethanol, triethylamine, acetone and methacryloyl chloride (Sigma-Aldrich) were commercial products with analytical grade and were used as received. The comonomer styrene (Sigma-Aldrich) was cleaned up from inhibitor first by being washed with aq. NaOH (5%). Later, it was dried over MgSO4. Azobisisobutyronitrile (AIBN) (Merck) was purified by recrystallisation using the chloroform-methanol mixture.

A Perkin Elmer Spectrum FT-IR spectrometer was used for the FT-IR measurements. A 600 MHz Avance III HD 600 NMR spectrometer with $CDCl_3$ as the solvent was used for the NMR measurements. The molecular weights (Mn and Mw) of the polymers were determined using an Agilent 1100 series gel permeation chromatograph equipped with an RI detector and calibrated to poly(methyl methacrylate) standards. Thermal data were obtained using a Perkin Elmer DSC-8000 instrument at a heating rate of 20 °C min^{-1} in an N_2 atmosphere and a Perkin Elmer SII 7300 model TGA/DTA device at a heating rate of 10 oC min-1 in an N2 atmosphere.

Synthesis of NBBM-ST Copolymers

Conventional free radical polymerization method was applied for the synthesis of copolymers. The typical example for synthesizing copolymers here is as the following. The N-[2-(4-brombenzoyl)-benzofuran-3-yl]-2-methacrylamide was placed in a polymerization tube with a commercial monomer styrene (St) at certain ratios by mole. The monomers were dissolved in the 1,4-Dioxane: tetrahydrofuran (3:2) solvent which is 3 times the total weight taken for polymerization. As initiator, AIBN in the ratio of 1% by weight of the total amount of monomers was added. The tube was flushed with nitrogen gas for 10 minutes in order to remove the air from the polymerization tube and was then allowed to polymerize in an oil bath at a temperature of 70 °C. The polymerization reaction was stopped

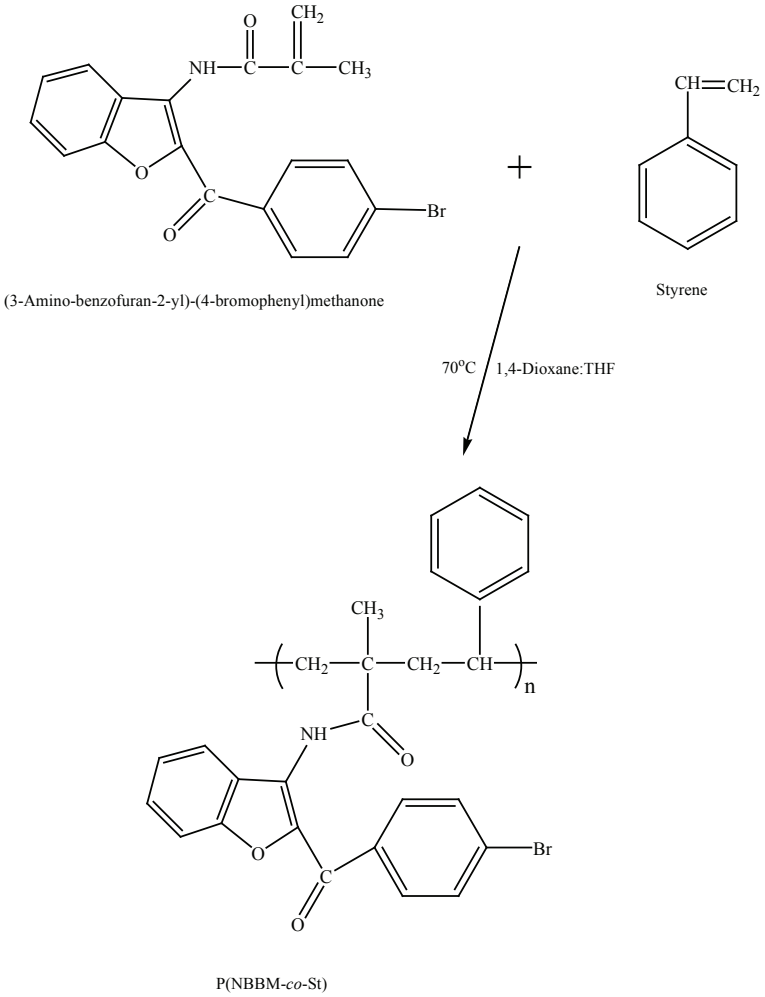


Figure 1. Synthesis of P(NBBM-co-St) copolymers.

after 12 hours. The mixture was precipitated dropwise in ethyl alcohol, filtered and dried under vacuum at 40 °C for 24 hours. The solid product (polymer) was then dissolved in dichloromethane, precipitated again in ethyl alcohol and dried. This purification process was repeated 3 times. Using NBBM and St monomers, a series of copolymers composed of five different compositions by mole was also synthesized by this method. Figure 1 shows the scheme for copolymer synthesis.

RESULTS AND DISCUSSION

Characterization of Copolymers

The copolymerization of the NBBM monomer with styrene has been carried out using the free radical polymerization method. The percentage compositions of NBBM and St copolymers were experimentally calculated from ^{1}H-NMR spectra and NBBM: St mole ratios are found as; Co-1: 18/82, Co-2: 30/70, Co-3: 43/47, Co-4: 59/41, Co-5: 73/27, respectively. FT-IR and ^{1}H-NMR measurements were used to identify the structures of the copolymers. Figure 2 shows the FT-IR spectra of the copolymers. The peaks related to amide carbonyl (NHC═O) at 1700 cm^{-1}, ketone carbonyl (C═O) [43] at 1612 cm^{-1} and mono-substituted benzene derived from St monomer at 700 cm^{-1} have been clearly seen from the FT-IR spectra of copolymers. Additionally, the direct proportional variation of the relative intensity of the peak at 700 cm^{-1}, depending on the molar ratio of the St monomer used in the copolymers, demonstrates clearly the effectuation of the synthesis of the copolymers at different monomer ratios.

In the ^{1}H-NMR spectra of NBBM-St copolymers (Fig. 3), the disappearance of the signals of monomeric vinylic protons at 5.68-6.17 ppm demonstrates clearly the completion of copolymerization reaction. In addition, the presence of aromatic protons of the styrene monomer with the other aromatic protons in the structure at 6.23-8.40 ppm, aliphatic protons at 0.43-2.61 ppm and *NH* proton at 10.58 ppm in the spectrum supported the expected copolymer structures. Both FT-IR and ^{1}H-NMR results were found to agree with the predicted chemical structure of the copolymers [41, 43].

Determination of the Monomer Reactivity Ratios

The ^{1}H-NMR spectra were used to calculate the percentage compositions of the NBBM-St copolymers. The NH protons at 10.58 ppm in the PNBBM units and the aromatic protons at 6.23-8.40 ppm in the NBBM-St units were taken as a basis for the calculation of composition percentages (Table 1).

Copolymer compositions were calculated from the following Equations.

$$C = \frac{Integral\ values\ of\ NH\ protons}{Integral\ values\ of\ aromatic\ CH\ protons} = \frac{m_1}{5m_2 + 8m_1} \quad (1)$$

If it is to simplify;

$$C = \frac{5C}{1 - 3C} \quad (2)$$

Where m_1 and m_2 are the mole fractions of NBBM and St, respectively in the copolymer. Since the total mole fraction is always equal to 1, m_2=1-m_1 if m_1+m_2=1. The calculation method of the copolymer compositions for the Co-1 polymer sample is as follows.

$$\frac{m_1}{5(1 - m_1) + 8m_1} = \frac{31.00}{31.47} \quad (3)$$

It is calculated as % m_1 = 0.18 and % m_2 = 1 - m_1 = 0.82

For the other samples, compositions were determined by similar calculations using the peak heights obtained

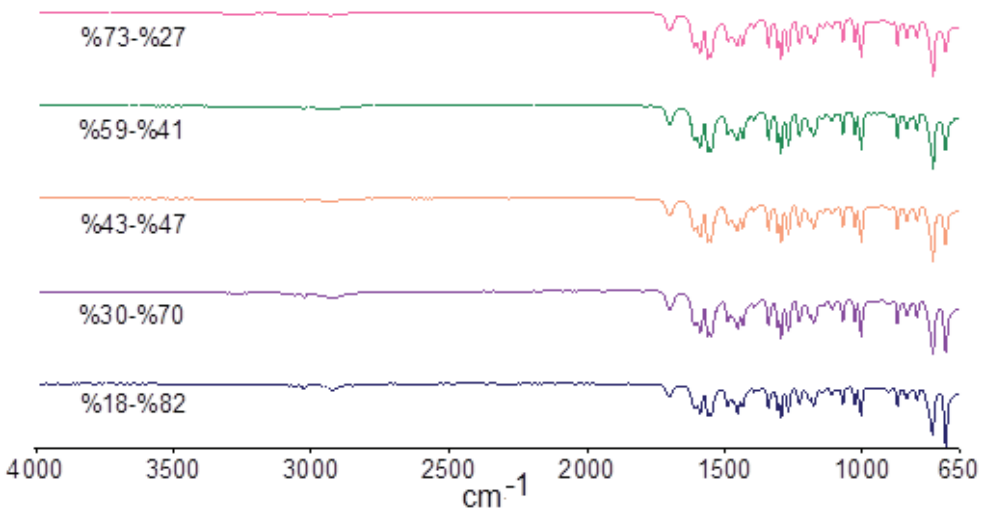


Figure 2. FT-IR spectra of P(NBBM-co-St) copolymers.

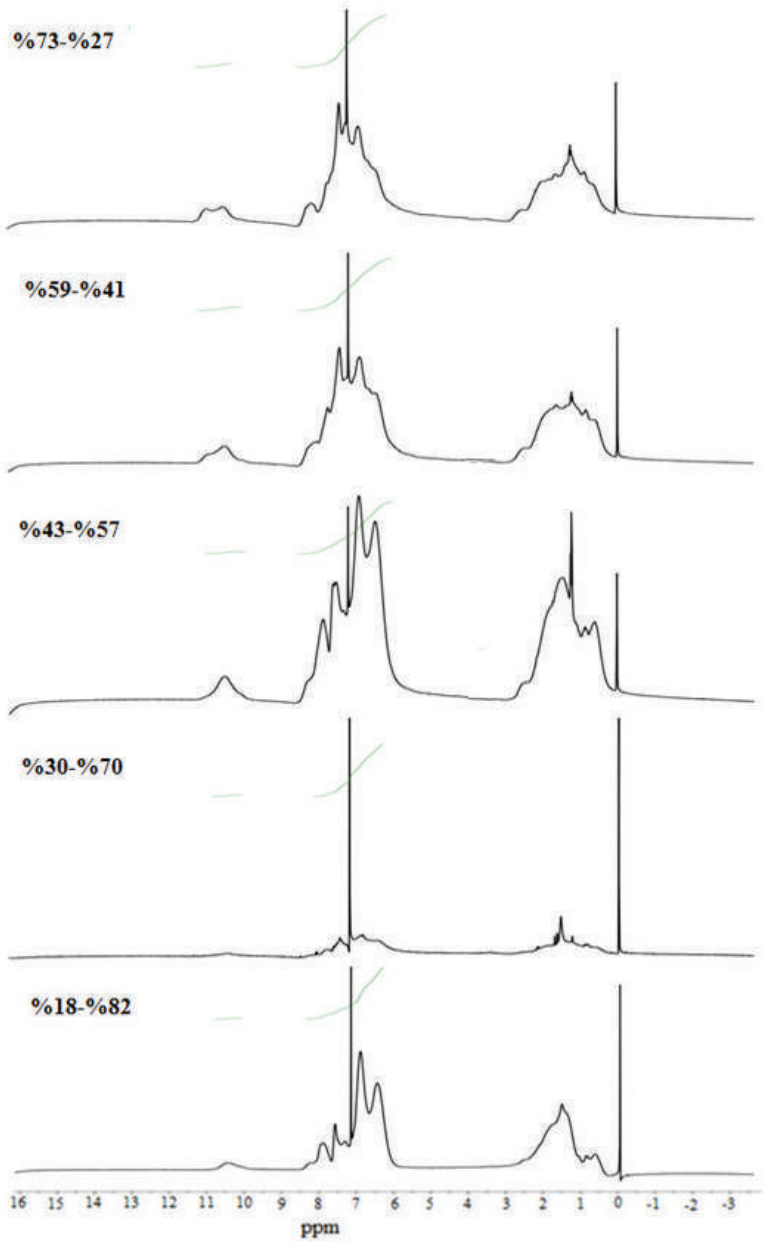


Figure 3. ^{1}H-NMR spectra of P(NBBM-co-St) copolymers.

Table 1. Monomer compositions in feed and in the copolymer

Sample	Feed composition (mole fraction)					Copolymer composition (mole fraction)	
	NBBM (M_1)	St (M_2)	Conversion (%)	*I*Ara	*I*NHb	NBBM (m_1)	St (m_2)
Co-1	0.20	0.80	11	31.47	1.00	0.18	0.82
Co-2	0.35	0.65	9	19.66	1.00	0.30	0.70
Co-3	0.50	0.50	13	14.60	1.00	0.43	0.57
Co-4	0.65	0.35	10	11.52	1.00	0.59	0.41
Co-5	0.80	0.20	15	9.83	1.00	0.73	0.27

[a]Integral values of aromatic C*H* protons
[b]Integral values of N*H* protons

through the ^{1}H-NMR spectra. The copolymer conversions were calculated gravimetrically [44].

The parameters r_1 and r_2, known as monomer reactivity ratios, represent the reactivity ratio of NBBM and St, respectively. Both the feed composition and the reactivity ratio of the monomers affect the composition of the copolymers. Therefore, knowing these ratios is important for synthesizing copolymers with desired properties.

To estimate the monomer reactivity ratios of the synthesized copolymers were used the Kelen Tüdös (K-T) [45] and Fineman-Ross (F-R) [46] Equations 4-5. The Notations in the equations were described in Table 2.

$$(Kelen-Tüdos\ equation)\ \eta = \left(r_1 + \frac{r_2}{\propto}\right)\xi - \frac{r_2}{\propto} \quad (4)$$

$$(\text{Fineman} - \text{Ross equation})\ G = r_1 \text{H} - r_2 \quad (5)$$

Graphs of η versus ξ and G versus H were plotted for Kelen-Tüdös and Finemann-Ross methods, respectively (Fig. 4,5). From the straight line slope and intercept, monomer reactivity ratios of NBBM and St were determined and presented in Table 2.

When the calculated r_1 and r_2 values are examined; the r_1 value of NBBM is smaller than the r_2 value of St monomer, indicating that the NBMM monomer has a lower reactivity than the St monomer and the polymer chain has a higher tendency to add St monomer. That is, there are more St monomers and fewer NBBM monomers in the copolymer chain. The reason of this can probably be interpreted as that the NBBM monomer with large-volume groups have sterically difficulty in adding its own monomer and so tends to add the other monomer, styrene.

Gel Permeation Chromatography (GPC)

The GPC chromatograms of NBBM-St copolymers are monodispers (Fig. 6). The average molecular weights (Mn and Mw) and polydispersities (PI) of the copolymers, given in Table 3, were determined from the GPC measurements. It is known that *PI* value for natural polymers is 1, and this value is close to 1 for living and controlled polymers. The copolymers we synthesized were synthetic and their *PI* values ranged from 1.51 to 1.26 in GPC measurements.

Thermal Properties

The glass transition temperatures of the NBBM-St copolymers have been determined from the DSC curves

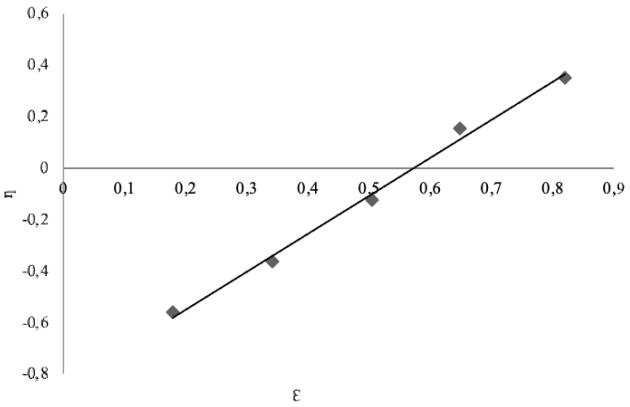


Figure 4. Kelen-Tüdös (K-T) plot for P(NBBM-co-St).

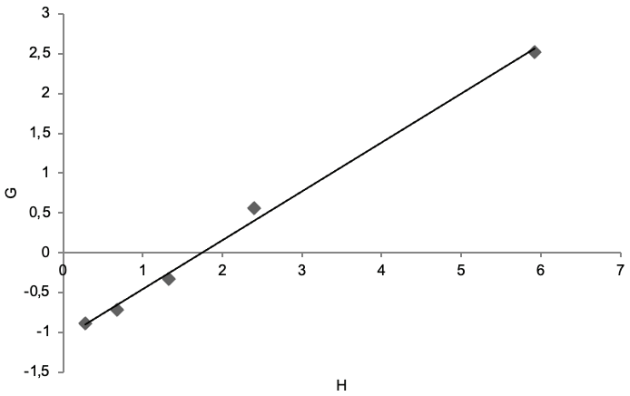


Figure 5. Finemann-Ross (F-R) plot for P(NBBM-co-St).

Table 2. K-T and F-R parameters for P(NBBM-co-St)

Sample	M_1	M_2	m_1	m_2	$F=M_1/M_2$	$f=m_1/m_2$	$G= F(f-1)/f$	$H= F^2/f$	$\eta = \frac{G}{(\alpha + H)}$	$\xi = \frac{H}{(\alpha + H)}$
Co-1	20	80	18	82	0.25	0.219	-0.888	0.284	-0.561	0.179
Co-2	35	65	30	70	0.539	0.428	-0.717	0.676	-0.363	0.342
Co-3	50	50	43	57	1	0.754	-0.325	1.325	-0.124	0.505
Co-4	65	35	59	41	1.858	1.439	0.566	2.396	0.153	0.648
Co-5	80	20	73	27	4	2.703	2.520	5.917	0.349	0.820

$\alpha=\sqrt{Hmax.Hmin}=0.817$
M_1; Mole fraction of NBBM in the feed
M_2; Mole fraction of St in the feed
m_1; Mole fraction of NBBM in the copolymer
m_2; Mole fraction of St in the copolymer

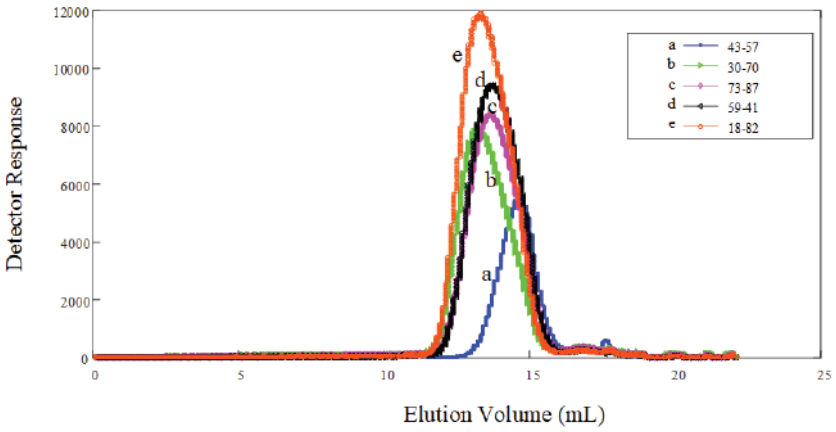


Figure 6. GPC curves of synthesized copolymers.

Table 3. Molecular weights and polydispersity index values of copolymers

Sample	Mn	Mw	HI
Co-1	8 677	13 144	1.51
Co-2	8 396	12 594	1.49
Co-3	6 695	9 979	1.49
Co-4	6 695	9 618	1.47
Co-5	6 515	4 852	1.26

(Fig. 7). The curves were recorded by heating the samples to 300 °C in a nitrogen atmosphere at a heating rate of 20 °C/min. Table 4 shows the glass transition temperatures (Tg) for the NBBM-St copolymers. The Tg value of styrene homopolymer is 105 °C [47] and that of P(NBBM) is 211 °C. The Tg values of the copolymers have been found in the range of the Tg values of the homopolymers. According to these results, an increase in Tg values from 144 °C to 184 °C was observed as the molar fraction of NBBM monomer in the copolymer increased. The cyclic benzofuran structure

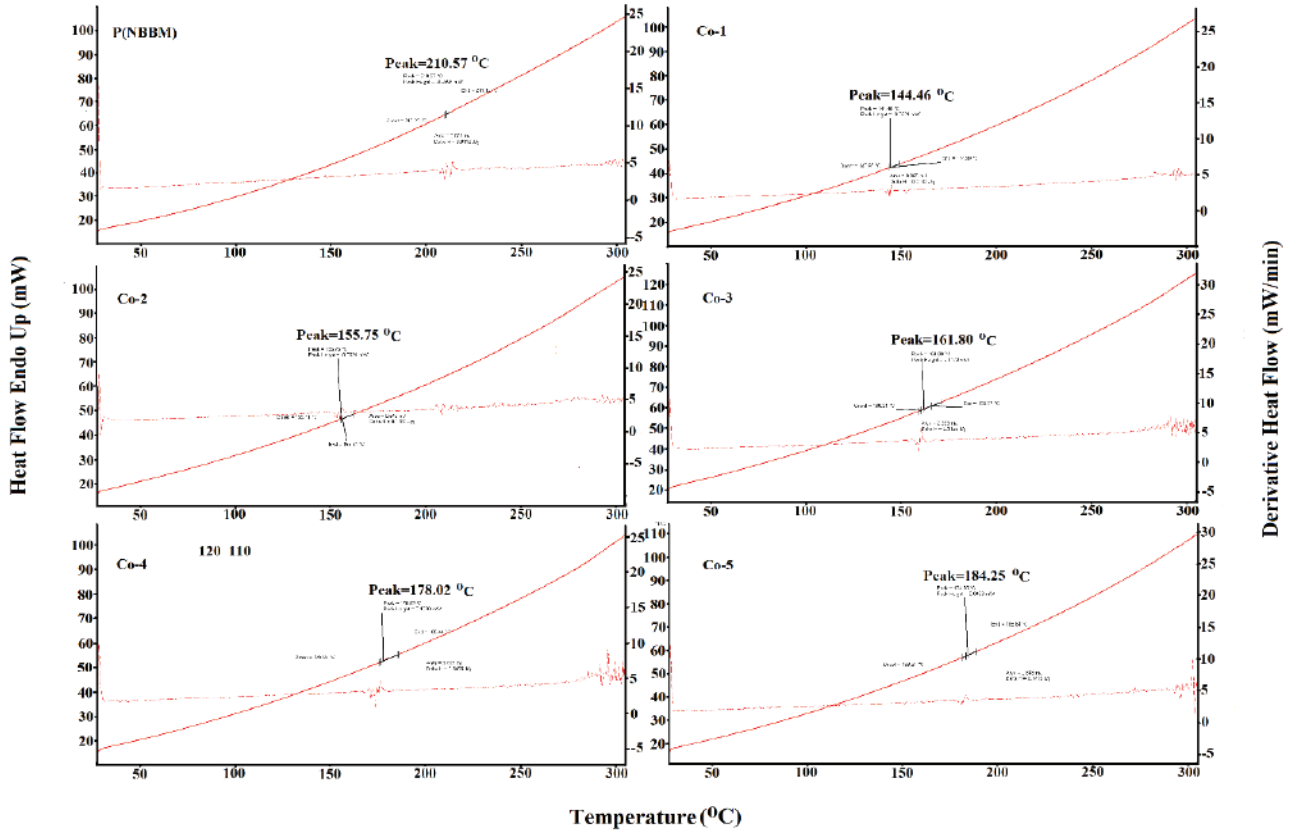


Figure 7. DSC curves of P(NBBM) and its copolymers.

resulting from the NBBM units in the polymer chain gives rigidity to the polymer chain. This restricts the mobility and flexibility of the chain, leading to an increase in the Tg value [47].

Table 4. Tg values of P(NBBM) and its copolymers

Sample	NBMM / St (mol)	Tg (°C)
P(St)	0 / 100	105
Co-1	18 / 82	144
Co-2	30 / 70	156
Co-3	43 / 57	162
Co-4	59 / 41	178
Co-5	73 / 27	184
P(NBBM)	100 / 0	211

The TGA curves of NBBM-St copolymers in a nitrogen atmosphere were recorded from room temperature up to 500 °C at a heating rate of 10 °C/min (Fig. 8). The mass losses of these curves at different temperatures are given in Table 5. When the TGA curves of the copolymers are examined, it was seen that the most heat-resistant polymer is polystyrene P(St), and the least heat-resistant polymer is the P(NBBM). The temperature at which 50% weight loss occurs in polymeric materials can be taken as a measure to determine the thermal stability of materials [48]. While these temperatures were determined as 423 °C for P(St) and 377 °C for P(NBBM), these values were found between their homopolymers for the copolymers studied. The thermal stability of copolymers with St units in their structure was seen to be higher than that of P(NBBM). This is due to the fact that P(St) is more

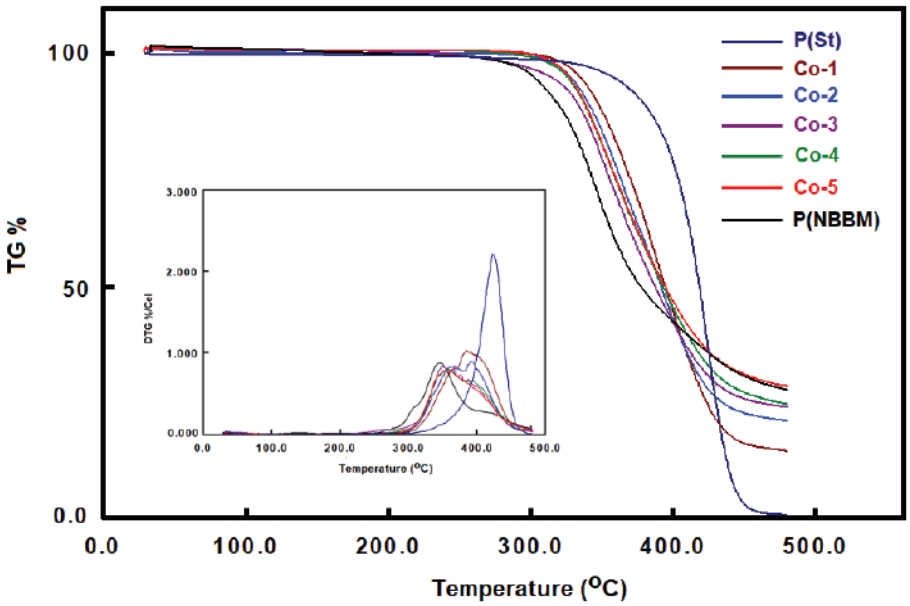


Figure 8. TGA and DTG curves of P(NBBM) and its copolymers.

Table 5. Decomposition temperatures of the copolymers at various compositions

Sample	m_1 [a]	$T_{int.}$ [b] (°C)	T_{max} [c] (°C)	%10 [d]	%30 [d]	%50 [d]	%70 [d]	%90 [d]
PNBBM	1.00	279	347	318	347	377	453	-
PSt	1.00	323	423	378	406	419	428	440
Co-1	0.18	301	385	347	374	394	416	-
Co-2	0.30	305	391	340	367	392	420	-
Co-3	0.43	308	349	332	360	388	427	-
Co-4	0.59	310	357	337	364	393	434	-
Co-5	0.73	293	355	338	364	395	458	-

[a] m_1 Weight fraction of NBBM in the copolymer
[b]: Initial decomposition temperature
[c] Temperature corresponding to maximal mass loss
[d] Temperatures at which the weight loss was respectively 10%, 30%, 50%, 70% and 90%

thermally stable. The initial degradation temperatures ($T_{int.}$) of P(St), P(NBBM) homopolymers were 323 °C and 279 °C, respectively, and $T_{int.}$ values of P(NBBM-co-St) copolymer systems were observed in the range of these two values. The maximum degradation temperatures (Tmax) of the polymer were obtained from derivative of mass loss (DTG) curves were given in Figure 8. Thermal decomposition of both homopolymers and copolymers were occurred in one step. Considering the data obtained from the TGA curves of the copolymers, St units in the copolymer systems studied compared to P(NBBM) caused an increase in Tmax. values.

Thermal Decomposition Kinetics

Thermogravimetric analysis (TGA) is based on mass loss measurement by heating the sample in an environment with inert gas flow at a constant heating rate. This method has an important role in elucidating the mechanism of physical and chemical events that occur during the degradation of polymers under the influence of heat. The rate of an isothermal decomposition reaction in the solid state can be described by the following equation:

$$\frac{d\alpha}{dT} = \frac{A}{\beta} e^{-\frac{E}{RT}} f(\alpha) \quad (6)$$

In equation 6*;* α is the degree of conversion, T is the absolute temperature in Kelvin (K), A is the preliminary exponential factor (min^{-1}), E is the activation energy, (kj mol^{-1}), R is the gas constant, (8.314 $Jmol^{-1}K^{-1}$) and $f(\alpha)$ is a function that depends on the reaction mechanism.

The solid state reaction mechanism in non-isothermal TG experiments was determined from equation 7, which was obtained by rearranging by integrating both sides. In this equation, $g(\alpha)$ is the integral function of the transformation, αp is the degree of transformation at the peak temperature, and Tp depends on the peak temperature. The differential expression of g(a) for different solid state mechanisms is shown in Table 6 [49-51].

$$g(\alpha) = \int_0^{\alpha p} \frac{d\alpha}{f(\alpha)} = \frac{A}{\beta} \int_0^{Tp} e^{-E/RT} \mathrm{dT} \quad (7)$$

In this study, thermal stability and activation energy measurements of decomposition have been performed at different heating rates (10, 15, 20 and 25 °C min^{-1}) between room temperature and 500 °C under a nitrogen atmosphere. Kissinger [52], Flynn-Wall-Ozawa (FWO) [53, 54], Tang [55] methods were chosen, which are integral and isoconversional techniques that do not require any mechanism for activation energy calculation. In addition, calculations were made with the non-isoconversial method, the Van Krevelen method [56], and the type of degradation mechanism was determined. In the calculations carried out by these methods, the decomposition rate (α), temperature (T), and heating rate (β) do not change depending on the reaction model. The proposed reaction model remains the same throughout the reaction. The following are the final equations of the methods for calculating the activation energy:

$$\text{KISSINGER}: \ln\left(\frac{\beta}{Tmax2}\right) = \{ln\frac{AR}{E} + ln[\text{n}(1\text{-}\alpha\ \text{max})\text{n-}1]\} - \frac{E}{RTmax} \quad (8)$$

$$\text{FWO}: \log(\beta) = \log[\frac{AE}{g(\alpha)R}] - 2.315 - \frac{0.457E}{RT} \quad (9)$$

Table 6. Algebraic Expressions for g(α) for the most frequently used mechanisms of solid-state processes

Symbol	g(α)	Solid-state processes
Sigmoidal curves		
A2	$[-\ln(1-\alpha)]^{1/2}$	Nucleation and growth (Avrami eq. (1))
A3	$[-\ln(1-\alpha)]^{1/3}$	Nucleation and growth (Avrami eq. (2))
A4	$[-\ln(1-\alpha)]^{1/4}$	Nucleation and growth (Avrami eq. (3))
Deceleration curves		
R1	α	Phase boundary controlled reaction (One-dimensional movement)
R2	$[1-(1-\alpha)^{1/2}]$	Phase boundary controlled reaction (contraction area)
R3	$[1-(1-\alpha)^{1/3}]$	Phase boundary controlled reaction (contraction volume)
D1	α^2	One-dimensional diffusion
D2	$(1-\alpha)\ln(1-\alpha)+\alpha$	Two-dimensional diffusion
D3	$[1-(1-\alpha)^{1/3}]^2$	Three-dimensional diffusion (Jander equation)
D4	$(1-2/3\alpha)(1-\alpha)^{2/3}$	Three-dimensional diffusion (Ginstling-Brounshtein equation)
F1	$-\ln(1-\alpha)$	Random nucleation with one nucleus on the individual particle
F2	$1/(1-\alpha)$	Random nucleation with two nuclei on the individual particle
F3	$1/(1-\alpha)^2$	Random nucleation with three nuclei on the individual particle

$$\text{TANG: } \ln\left(\frac{\beta}{T1.894661}\right) = \ln\left(\frac{AE}{Rg(\alpha)}\right) + 3.635041 - 1.894661\ln E - \frac{1.001450E}{RT} \quad (10)$$

$$\text{VAN KREVELEN: } \log g(\alpha) = \log \beta + \left(\frac{E}{RTr} + 1\right) + \log T \quad (11)$$

Where; R gas constant, A pre-exponential factor, g(α) differential conversion function, α degradation ratio (α=(-wi-wt)/(wi-wf)), E activation energy.

To evaluate the thermal degradation kinetics of the studied copolymer systems, the copolymer containing 30% NBMM and 70% styrene (Co-2) was chosen as a reference copolymer. The activation energy for P(NBBM) and copolymer (Co-2) was calculated from the slope of the ln(β/T^2max) versus 1000/Tmax plot according to the Kissinger method. The activation energy of P(NBBM) and Co-2 for this method were calculated as 146.66 and 158.52 kj mol^{-1}, respectively (Fig. 8a,b).

The activation energy was calculated from the 1000/T plot against log β at different % conversions using the Flynn-Wall-Ozawa method (Fig. 10a,b) and the results (Ea values) are given in Table 7. Using this method, the average activation energies for P(NBBM) and Co-2 were calculated as 150.7 and 160.89 kj mol^{-1}, respectively.

With the Tang method, activation energies were calculated by using Equation 10 and drawing $\ln(\beta/T^{1.894661})$ and 1/T graphs (Fig. 11a,b) for different conversion percentages, and the results are given in Table 8. With this method, the average activation energy of P(NBBM) and Co-2 were calculated as 142.33 and 151.326 kj mol^{-1}, respectively. The activation energy values obtained by Tang are very close to those calculated by the other two methods. In many studies, the activation energy of polystyrene has been reported as approximately 200 kj mol^{-1} [57, 58]. Activation energy values are higher for copolymers than for homopolymers. In other words, the added styrene units increased the activation energy. There are studies in the literature confirming this result.

These methods, which are in use by some authors for the control of models of the degradation mechanism, have also been used in our study [51, 59].

Using the Van Krevelen Equation (11), the activation energy for each g(α) function listed in Table 8 was obtained from a constant heating rate in the range log[$g(\alpha)$/T2] - log$T$.

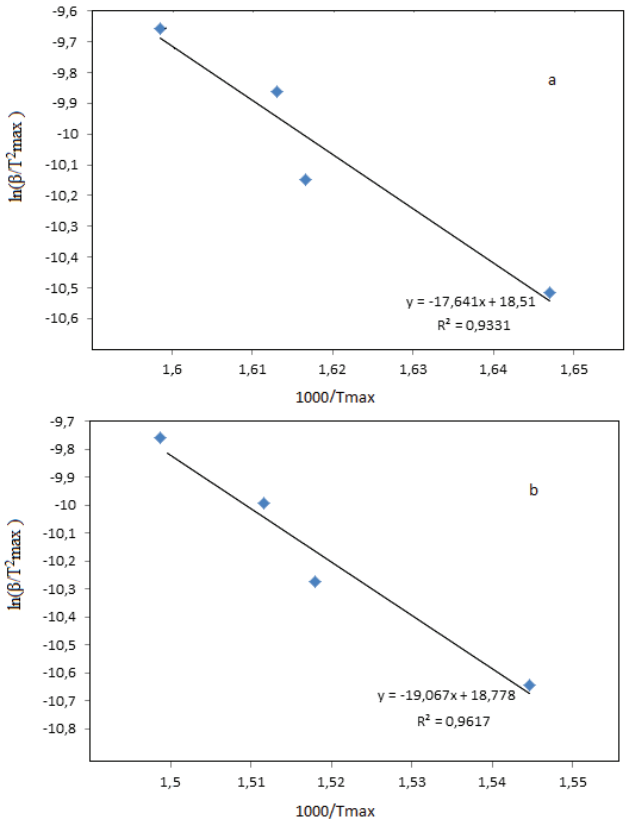


Figure 9. Kissinger method applied to the experimental data at different heating rates (a:P(NBBM), b: P(NBBM-co-St)).

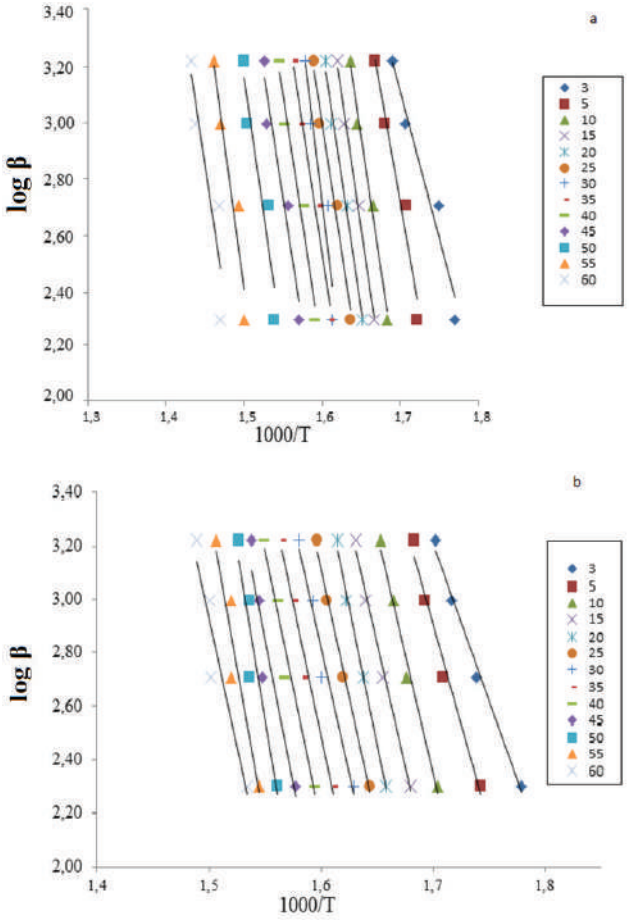


Figure 10. Flynn–Wall–Ozawa method applied to the experimental data (3–60%),(a:P(NBBM), b: P(NBBM-co-St)).

Table 7. Activation energy (Ea) values obtained with the Flynn– Wall–Ozawa method for P(NBBM) and P(NBBM-co-St)

	P(NBBM)		P(NBBM-co-St)	
α (%)	E (kj mol^{-1})	R2	E (kj mol^{-1})	R2
3	86,374	0,9511	96,73339	0,9905
5	130,8707	0,9599	124,2943	0,9811
10	156,378	0,9857	150,5167	0,9858
15	155,9041	0,993	153,2686	0,9933
20	153,0691	0,9851	174,4194	0,9932
25	153,9337	0,9756	157,2261	0,9915
30	185,9177	0,9127	155,5799	0,9747
35	152,1462	0,97	166,2052	0,975
40	152,7781	0,9603	169,431	0,9663
45	149,6271	0,9406	178,2688	0,8887
50	158,5729	0,8941	210,1447	0,8924
55	171,4014	0,9202	196,1356	0,9138
60	152,2543	0,8303	159,3461	0,887
AVERAGE	150,7		160,89	

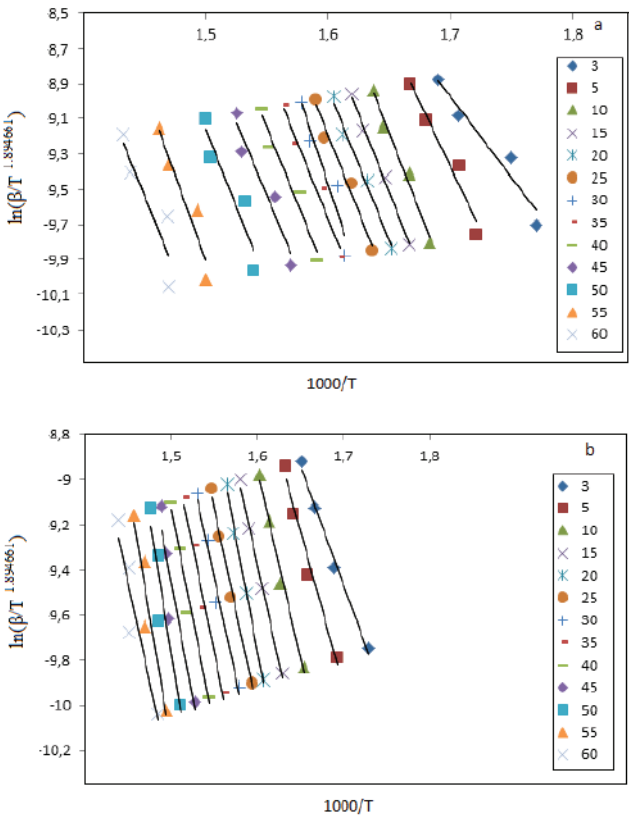


Figure 11. Tang method applied to the experimental data (3–60%),(a:P(NBBM), b: P(NBBM-co-St)).

The activation energies and the correlation between 3% and 60% conversion at different heating rates (10, 15, 20 and 25 °C/min) are shown in Tables 9 and 10. The activation energy values obtained are compatible with those computed by the Kissinger method. From these tables it can be seen that the P(NBBM) at an optimum heating rate of 10 °C/min occurs with the R3 mechanism (Ea: 143.29 kj mol^{-1} (phase boundary controlled reaction (contraction volume)). These values are close to the values obtained from FWO (150.7 kj mol^{-1}) and Kissinger (146.66 kj mol^{-1}) which are methods that do not depend on the mechanism. In addition to the calculation made for the Co-2 for termodegaraditon mechanism of copolymer, at an optimum heating rate of 10 °C/minute takes place with the R3 mechanism (Ea: 151.46 kj mol^{-1}). These values are close to the values obtained from FWO (160.89 kj mol^{-1}) and Kissinger (158.52 kj mol^{-1}) which are methods that do not depend on the mechanism. However, the strong correlation (0.976) is the correlation that corresponds to 10 °C/min for Co-2 at the preferred site with the value obtained by the Van Krevelen method.

CONCLUSION

Copolymer systems were successfully synthesized by free radical polymerization using N-[2-(4-brombenzoyl)-benzofuran-3-yl]-2-methacrylamide and styrene monomers in five different ratios. The structures of the copolymers were characterized by FT-IR and ^{1}H-NMR spectroscopic methods and found to be in accordance with the expected structure. Experimentally, the percentage compositions of P(N-[2-(4-brombenzoyl)-benzofuran-3-yl]-2-methacrylamide-co-Styrene) copolymers were calculated through ^{1}H-NMR spectra. The glass transition temperatures of the copolymers were determined from DSC curves. The glass transition temperature of P(NBMM) is 211 °C, which is a high temperature. It was observed that the glass transition

Table 8. Activation energy (Ea) values obtained with the Tang method for P(NBBM) and P(NBBM-co-St)

	P(NBBM)		P(NBBM-co-St)	
α (%)	Ea (kJ mol^{-1})	R2	Ea (kJ mol^{-1})	R2
3	97,141	0,9885	97,141	0,9885
5	121,3995926	0,9534	114,6583993	0,9534
10	146,6707654	0,9279	140,6435409	0,9279
15	146,106232	0,9389	143,250357	0,9389
20	143,1839413	0,9497	164,2543212	0,9497
25	143,9560238	0,9613	146,977938	0,9613
30	175,7857467	0,9677	145,2428279	0,9677
35	142,0133646	0,9748	155,7365081	0,9748
40	142,5280863	0,9804	158,8663478	0,9804
45	139,2405093	0,983	167,59171	0,983
50	147,9824754	0,9809	199,3218094	0,9809
55	160,5350422	0,9792	185,2001718	0,9792
60	141,1914704	0,9794	148,3643657	0,9794
AVERAGE	142,133		151,326	

Table 9. Activation energy (Ea) values obtained for P(NBBM) with the Van Krevelen method for several solid-state processes at heating rates of 10, 15, 20 and 25 °C min^{-1}

Symbol	10 (°C min^{-1})		15 (°C min^{-1})		20 (°C min^{-1})		25 (°C min^{-1})	
	Ea (kJ mol^{-1})	R2	Ea (kJ mol^{-1})	R2	Ea (kJ mol^{-1})	R2	Ea (kJ mol^{-1})	R2
A2	75,57	0,9381	78,89	0,9442	78,87	0,9199	80,99	0,906
A3	50,41	0,9381	52,61	0,9442	52,58	0,9199	53,99	0,906
A4	37,81	0,9381	39,45	0,9441	39,43	0,9199	40,49	0,906
R1	128,62	0,9106	134,36	0,9183	133,68	0,8866	137,04	0,8704
R2	139,47	0,9251	145,61	0,932	145,22	0,904	149,00	0,8889
R3	143,29	0,9296	149,58	0,9363	149,28	0,9095	153,21	08948
D1	257,26	0,9106	268,71	0,9183	267,37	0,8866	274,1	0,8704
D2	271,14	0,92	283,13	0,9272	282,14	0,8979	289,39	0,8824
D3	286,58	0,9296	299,16	0,8948	298,58	0,96095	306,53	0,8948
D4	59,93	0,9623	62,21	0,9582	63,78	0,9822	66,08	0,9848
F1	151,24	0,9381	157,83	0,9442	157,75	0,9199	161,98	0,9606
F2	48,96	0,9588	50,80	0,9541	52,14	0,9801	54,08	0,9839
F3	97,93	0,9588	101,62	0,9541	104,29	0,94801	108,11	0,9839

temperature increased from 144 °C to 184 °C depending on the increase in the molar ratio of N-[2-(4-brombenzoyl)-benzofuran-3-yl]-2-methacrylamide in the copolymer. This increase in the glass transition temperatures was due to the decrease in the free volume caused by the rather large benzofuran ring in the N-[2-(4-brombenzoyl)-benzofuran-3-yl]-2-methacrylamide monomer. When the TGA curves were examined, it was determined that the thermal stabilities of the copolymers of NBBM with St were higher than the thermal stability of P(NBBM). It is clear that the increase in the thermal stability of the copolymers is due to the styrene units in the polymer chain. Because polystyrene was found to have the highest thermal stability among the polymers studied. While the maximum degradation temperature of Poly(N-[2-(4-brombenzoyl)-benzofuran-3-yl]-2-methacrylamide) was 347 °C, the maximum degradation temperature of Polystyrene was 423 °C. A similar situation was seen in the maximum decomposition temperatures. It was determined that the maximum decomposition temperatures increased in copolymers with St units compared

Table 10. Activation energy (Ea) values obtained for P(NBBM-co-St) with the Van Krevelen method for several solid-state processes at heating rates of 10, 15, 20 and 25 °C min^{-1}

Symbol	10 (°C min^{-1})		15 (°C min^{-1})		20 (°C min^{-1})		25 (°C min^{-1})	
	Ea (kJ mol^{-1})	R2	Ea (kJ mol^{-1})	R2	Ea (kJ mol^{-1})	R2	Ea (kJ mol^{-1})	R2
A2	79,79	0,9815	81,14	0,9684	89,12	0,9721	88,63	0,9647
A3	53,12	0,9815	54,11	0,9684	59,41	0,9721	59,09	0,9647
A4	39,82	0,9815	40,58	0,9680	44,56	0,9721	44,31	0,9647
R1	136,43	0,9626	138,41	0,9647	152,121	0,9505	151,09	0,9406
R2	147,55	0,973	149,9	0,9575	164,66	0,9621	163,66	0,9536
R3	151,46	0,976	153,94	0,9614	168,08	0,9656	169,08	0,9575
D1	272,86	0,9626	276,82	0,9447	304,23	0,9502	302,20	0,9407
D2	286,13	0,9695	291,55	0,9531	320,33	0,958	318,31	0,9492
D3	302,93	0,976	307,89	0,9614	338,16	0,9656	336,17	0,9575
D4	61,35	0,9494	63,45	0,9664	69,28	0,9593	69,37	0,9652
F1	159,59	0,9815	162,34	0,9684	178,25	0,9721	177,35	0,9647
F2	50	0,9397	51,70	0,9577	56,426	0,9499	56,52	0,9563
F3	100,01	0,9397	103,4	0,9577	112,85	0,9499	113,04	0,9563

to P(NBBM). The reactivity values for the P(N-[2-(4-brombenzoyl)-benzofuran-3-yl]-2-methacrylamide-co-Styrene) system are calculated for Kelen-Tüdõs as; r1:0.62, r2: 1.09 and for Finemann-Ross as; r1:0.61, r2: 1.07. r2 value of styrene monomer being larger than r1 value of N-[2-(4-brombenzoyl)-benzofuran-3-yl]-2-methacrylamide monomer means that both monomers prefer styrene radicals. This indicates that there is a tendency towards random copolymerization where the styrene units in the copolymer are more [60, 61]. For the activation energy calculation, the well-known equivalent Kissinger, Flynn-Wall-Ozawa, Tang and Van Krevelen integral techniques were selected. In many studies, the activation energy of polystyrene has been reported to be approximately 200 kj mol^{-1} [57, 58]. The presence of styrene units in the copolymer structure synthesized in the study caused an increase in activation energy values compared to the homopolymer. This increase is an expected result when similar studies are examined in the literature. Calculation results for the analysis of the thermodegradation mechanism showed that the copolymer follows the slowdown (R3) type solid state thermodegradation mechanism. The R3 mechanism calculated by Van Krevelen is compatible with the results obtained by Kissinger and Flynn-Wall-Ozawa methods at heating rates of 10 and 15 °C min^{-1}.

ACKNOWLEDGEMENTS

We would like to thank Harran University Scientific Research Project Unit (HÜBAK) for the financial support in carrying out this study with the project number HÜBAK-13098.

AUTHORSHIP CONTRIBUTIONS

Authors equally contributed to this work.

DATA AVAILABILITY STATEMENT

The authors confirm that the data that supports the findings of this study are available within the article. Raw data that support the finding of this study are available from the corresponding author, upon reasonable request.

CONFLICT OF INTEREST

The author declared no potential conflicts of interest with respect to the research, authorship, and/or publication of this article.

ETHICS

There are no ethical issues with the publication of this manuscript.

STATEMENT ON THE USE OF ARTIFICIAL INTELLIGENCE

Artificial intelligence was not used in the preparation of the article.

REFERENCES

[1] Çankaya N. Synthesis, spectroscopic and thermal characterization of new oxo methacrylate-containing polymers. Sigma J Eng Nat Sci 2020;38:1133–1141.

[2] Çankaya N. Synthesis, characterization and thermal properties of new oxoethyl acrylate containing polymer. Sigma J Eng Nat Sci 2020;38:281–288.
[3] Hosseini S, Shahrousvand M, Mohammadi-Rovshandeh J, Jahanbakhshi M, Javadi A, Soleimani M, et al. Fabrication of pH-responsive amphiphilic poly(vinyl alcohol–methyl methacrylate) copolymer nanoparticles for application in cancer drug delivery systems. Iran J Med Sci 2024;48:99–111. [CrossRef]
[4] Kim J, Baek KJ, Yu S, Yang HS, Khaliq NU, Choi WI, et al. Ferrocene-based acrylate copolymer multilayers with efficient antifouling and electrochemical redox properties. Electrochim Acta 2023;463:142824. [CrossRef]
[5] Basawaraj R, Yadav B, Sangapure SS. Synthesis of some 1H-pyrazolines bearing benzofuran as biologically active agents. Indian J Heterocycl Chem 2001;11:31–34.
[6] Romagnoli R, Baraldi PG, Sarkar T, Cara CL, Lopez OC, Carrion MD, et al. Synthesis and biological evaluation of 2-aroyl-4-phenyl-5-hydroxybenzofurans as a new class of antitubulin agents. Med Chem 2008;4:558–564. [CrossRef]
[7] Xie YS, Kumar D, Bodduri VV, Tarani PS, Zhao BX, Miao JY, et al. Microwave-assisted parallel synthesis of benzofuran-2-carboxamide derivatives bearing anti-inflammatory, analgesic and antipyretic agents. Tetrahedron Lett 2014;55:2796–2800. [CrossRef]
[8] Miao Y, Hu Y, Yang J, Liu T, Sun J, Wang X. Natural source, bioactivity and synthesis of benzofuran derivatives. RSC Adv 2019;9:27510–27540. [CrossRef]
[9] Oter O, Ertekin K, Kirilmis C, Koca M, Ahmedzade M. Characterization of a newly synthesized fluorescent benzofuran derivative and usage as a selective fiber optic sensor for Fe(III). Sens Actuators B Chem 2007;122:450–456. [CrossRef]
[10] Jöhnck M, Müller L, Neyer A, Hofstraat JW. Copolymers of halogenated acrylates and methacrylates for the application in optical telecommunication: optical properties, thermal analysis and determination of unsaturation by quantitative FT-Raman and FT-IR spectroscopy. Eur Polym J 2000;36:1251–1264. [CrossRef]
[11] Koca M, Kurt A, Kirilmis C, Aydogdu Y. Synthesis, characterization, and thermal degradation of novel poly(2-(5-bromobenzofuran-2-yl)-2-oxoethyl methacrylate). Polym Eng Sci 2012;52:323–330. [CrossRef]
[12] Li Q, Jian XE, Chen ZR, Chen L, Huo XS, Li ZH, et al. Synthesis and biological evaluation of benzofuran-based 3,4,5-trimethoxybenzamide derivatives as novel tubulin polymerization inhibitors. Bioorg Chem 2020;102:104076. [CrossRef]
[13] Maluleka MM, Segodi RS, Mphahlele MJ, Mbazima VG, Elhenawy AA, Monchusi BA. Synthesis, structural characterization, and quantum chemical study of the 7-acetyl-5-nitrobenzofurans as anticancer agents with antioxidant properties. J Mol Struct 2024;1311:138398. [CrossRef]
[14] Napiórkowska M, Kumaravel P, Amboo Mahentheran M, Kiernozek-Kalińska E, Grosicka-Maciąg E. New derivatives of 1-(3-methyl-1-benzofuran-2-yl)ethan-1-one: synthesis and preliminary studies of biological activity. Int J Mol Sci 2024;25:1999. [CrossRef]
[15] Wang G, Guo S, Xu W, Chen D, Song C, Ma Y, et al. Synthesis and properties of vinyl ether and acrylonitrile copolymers. Macromol Chem Phys 2024;2400022. [CrossRef]
[16] Rosales-Guzmán M, Pérez-Camacho O, Torres-Lubián R, Harrisson S, Schubert US, Guerrero-Sánchez C, Saldívar-Guerra E. Kinetic and copolymer composition investigations of the free radical copolymerization of 1-octene with glycidyl methacrylate. Macromol Chem Phys 2018;219:1800084. [CrossRef]
[17] Jeemol PA, Mathew S, Nair CPR. Copolymerization of nadic anhydride with styrene: reactivity ratios. Polym Adv Technol 2021;32:1888–1894. [CrossRef]
[18] Gody G, Zetterlund PB, Perrier S, Harrisson S. The limits of precision monomer placement in chain growth polymerization. Nat Commun 2016;7:10514. [CrossRef]
[19] Zhang J, Farias-Mancilla B, Destarac M, Schubert US, Keddie DJ, Guerrero-Sanchez C, et al. Asymmetric copolymers: synthesis, properties, and applications of gradient and other partially segregated copolymers. Macromol Rapid Commun 2018;39:1800357. [CrossRef]
[20] Rosales-Guzmán M, Pérez-Camacho O, Torres-Lubián R, Harrisson S, Schubert US, Guerrero-Sánchez C, et al. Kinetic and copolymer composition investigations of the free radical copolymerization of 1-octene with glycidyl methacrylate. Macromol Chem Phys 2018;219:1800084. [CrossRef]
[21] Harrisson S, Ercole F, Muir BW. Living spontaneous gradient copolymers of acrylic acid and styrene: one-pot synthesis of pH-responsive amphiphiles. Polym Chem 2010;1:326–332. [CrossRef]
[22] Guerrero-Sanchez C, Harrisson S, Keddie DJ. High-throughput method for RAFT kinetic investigations and estimation of reactivity ratios in copolymerization systems. Macromol Symp 2013;325:38–46. [CrossRef]
[23] Erol I, Hossoz MO, Gurler Z. Synthesis and characterization of new methacrylate copolymers having pendant chloroacetophenon; monomer reactivity ratio, thermal degradation kinetics and biological activity. Polym Bull 2022;79:1–26. [CrossRef]
[24] Coskun M, Barim G, Temüz MM, Demirelli K. A study on thermal stabilities of poly(2-methacrylamidopyridine)–poly(methyl methacrylate) blends. Polym Plast Technol 2005;44:677–686. [CrossRef]

[25] Uhl FM, Levchik GF, Levchik SV, Dick C, Liggat JJ, Snape CE, et al. The thermal stability of cross-linked polymers: methyl methacrylate with divinylbenzene and styrene with dimethacrylates. Polym Degrad Stab 2001;71:317–325. [CrossRef]

[26] Perwin A, Mazumdar N. Synthesis of O-acyl salicylaldehyde derivatives and copolymerization of bis-(2-formylphenyl)fumarate with methyl methacrylate. J Mol Struct 2024;1304:137690. [CrossRef]

[27] Demirelli K, Barım E, Tuncer H, Barım G, Abubakar AM. Synthesis and characterization of N-(2-acetylbenzofuran-3-yl)methacrylamide and ethyl methacrylate copolymer/graphite oxide composites and study of their kinetic and electrical properties. Polym Bull 2022;79:4721–4743. [CrossRef]

[28] Shrivastava NK, Singh D, Verma SK, Singh AP, Srivastava A. Toxicology assessment of polymeric material for implants. In: Assessment of Polymeric Materials for Biomedical Applications. Roca Batun, FL: CRC Press; 2023. p.33–54. [CrossRef]

[29] Oliveira MJ, Caetano S, Dalot A, Sabino F, Calmeiro TR, Fortunato E, et al. Simple polystyrene microfluidic device for sensitive and accurate SERS-based detection of infection by malaria parasites. Analyst 2023;148:4053–4063. [CrossRef]

[30] Cunha I, Torres O, Fidalgo-Pereira R, Henriques B, Özcan M, Souza JC. Contamination of resin-matrix composites on chairside handling using latex or nitrile gloves: an in vitro study. Biomed Mater Devices 2024;2:1065–1077. [CrossRef]

[31] Freeland B, McCarthy E, Balakrishnan R, Fahy S, Boland A, Rochfort KD, et al. Review of polylactic acid as a replacement material for single-use laboratory components. Materials 2022;15:2989. [CrossRef]

[32] Shen N, Liu S, Kasbe P, Khabaz F, Kennedy JP, Xu W. Macromolecular engineering and additive manufacturing of poly(styrene-b-isobutylene-b-styrene). ACS Appl Polym Mater 2021;3:4554–4562. [CrossRef]

[33] Zhu Y, Chen M, Wu Y, Liu R, Ding W, Zhang H, et al. Modification of poly(styrene-b-isobutylene-b-styrene) using hyaluronic acid via surface graft polymerization and cytotoxicity investigation. J Appl Polym Sci 2024;141:e55638. [CrossRef]

[34] Kenawy ER, El-Khalafy SH, Abosharaf HA, El-nshar EM, Ghazy AR, Azaam MM. Synthesis, characterization, and anticancer potency of branched poly(p-hydroxy styrene) Schiff-bases. Macromol Biosci 2023;23:2300090. [CrossRef]

[35] Khanppnavar B, Choo JP, Hagedoorn PL, Smolentsev G, Štefanić S, Kumaran S, et al. Structural basis of the Meinwald rearrangement catalysed by styrene oxide isomerase. Nat Chem 2024;16:1496–1504. [CrossRef]

[36] Zaharescu T, Borbath T, Borbath I, Simion E, Mirea R. Thermal stability of styrene block copolymers for nuclear applications. Radiat Phys Chem 2024;223:111828. [CrossRef]

[37] Adıguzel CA, Korkmaz B, Cakar F, Cankurtaran O, Senkal BF. Thermodynamic studies on tert-amine modified polystyrene based polymer/solvent systems by inverse gas chromatography method. Sigma J Eng Nat Sci 2021;39:414–421.

[38] Haladu SA, Elsayed KA, Ercan İ, Ercan F, Kayed TS, Demirci T, et al. Investigation on structural, optical, thermal, and dielectric properties of cellulose propionate/styrene-maleic anhydride copolymer/molybdenum nanocomposite prepared by pulsed laser ablation. J Mol Struct 2024;1310:138262. [CrossRef]

[39] Erol I, Sen O, Cifci C, Gurler Z. New methacrylate copolymers based on the benzofurane ring: synthesis, characterization, monomer reactivity ratios and biological activity. J Macromol Sci Part A Pure Appl Chem 2010;47:1032–1041. [CrossRef]

[40] Erol I. Synthesis and characterization of a new methacrylate polymer with side chain benzofurane and cyclobutane ring: thermal properties and antimicrobial activity. High Perform Polym 2009;21:411–423. [CrossRef]

[41] Barim E, Akman F. Study on vibrational spectroscopy, molecular property, UV-VIS, HOMO-LUMO energies and MEP analysis of N-[2-(4-bromobenzoyl)-benzofuran-3-yl]-acrylamide monomer by DFT method. Pigm Resin Technol 2022;51:69–79. [CrossRef]

[42] Barim E, Değirmenci M. Studies on methacrylamide polymers having pendant benzofurane moieties: synthesis, characterization, monomer reactivity ratios and thermal properties. ADYU J Sci 2016;6:13–30. [CrossRef]

[43] Ilter Z, Şenkal BF, Yakuphanoglu F, Ahmedzade M. Synthesis and characterization of a new photosensitive benzofuran chalcone methacrylamide monomer. J Polym Eng 2008;28:535–552. [CrossRef]

[44] Nanjundan S, Unnithan CS, Selvamalar CJ, Penlidis A. Homopolymer of 4-benzoylphenyl methacrylate and its copolymers with glycidyl methacrylate: synthesis, characterization, monomer reactivity ratios and application as adhesives. React Funct Polym 2005;62:11–24. [CrossRef]

[45] Kelen T, Tudos F. Analysis of the linear methods for determining copolymerization reactivity ratios. I. A new improved linear graphic method. J Macromol Sci 1975;9:1–27. [CrossRef]

[46] Fineman M, Ross SD. Linear method for determining monomer reactivity ratios in copolymerization. J Polym Sci 1950;5:259–262. [CrossRef]

[47] Koroglu AM, Erol I, Korcan E, Konuk M. Synthesis and characterization of novel methacrylate monomers having pendant oxime esters and their copolymerization with styrene. J Macromol Sci Pure Appl Chem 2007;44:817–830. [CrossRef]

[48] Coşkun M, Barim G, Demirelli K. Thermal stabilities of poly(n-acryloyl-n'-methylpiperazine), its

blends with poly(methyl methacrylate), and poly(n-acryloyl-n'-methylpiperazine-co-methyl methacrylate). J Macromol Sci A 2006;43:83–93. [CrossRef]

[49] Mondal S, Martin D. Hydrolytic degradation of segmented polyurethane copolymers for biomedical applications. Polym Degrad Stab 2012;97:1553–1561. [CrossRef]

[50] Hatakeyama T, Quinn FX. Thermal analysis: fundamentals and applications to polymer science. New York: John Wiley & Sons; 1994.

[51] Criado JM, Malek J, Ortega A. Applicability of the master plots in kinetic analysis of non-isothermal data. Thermochim Acta 1989;147:377–385. [CrossRef]

[52] Kissinger HE. Reaction kinetics in differential thermal analysis. Anal Chem 1957;29:1702–1706. [CrossRef]

[53] Ozawa T. A new method of quantitative differential thermal analysis. Bull Chem Soc Jpn 1966;39:2071–2085. [CrossRef]

[54] Koga N. Ozawa's kinetic method for analyzing thermoanalytical curves: history and theoretical fundamentals. J Therm Anal Calorim 2013;113:1527–1541. [CrossRef]

[55] Saha T, Bhowmick AK, Oda T, Miyauchi T, Fujii N. Degradation of polyacrylic elastomers: theoretical and experimental studies. Polym Degrad Stab 2016;134:60–75. [CrossRef]

[56] Tang W, Liu Y, Zhang CH, Wang C. New approximate formula for Arrhenius temperature integral. Thermochim Acta 2003;40:839–843. [CrossRef]

[57] Van Krevelen DW, Van Heerden C, Huntjons FJ. Physicochemical aspects of the pyrolysis of coal and related organic compounds. Fuel 1951;30:253–259.

[58] Senocak A, Alkan C, Karadag A. Thermal decomposition and a kinetic study of poly(para-substituted styrene)s. Am J Anal Chem 2016;7:246–253. [CrossRef]

[59] Marcilla A, Beltran M. Kinetic study of the thermal decomposition of polystyrene and polyethylene-vinyl acetate graft copolymers by thermogravimetric analysis. Polym Degrad Stab 1995;50:117–124. [CrossRef]

[60] Jimenez A, Berenguer V, Lopez J, Sanchez A. Thermal degradation study of poly(vinyl chloride): kinetic analysis of thermogravimetric data. J Appl Polym Sci 1993;50:1565–1573. [CrossRef]

[61] Pazhanisamy P, Reddy BSR. Copolymers of N-cyclohexylacrylamide and n-butyl acrylate: synthesis, characterization, monomer reactivity ratios and mean sequence length. Express Polym Lett 2007;1:391–396. [CrossRef]

[62] Basha KA, Balakrishnan T, Urzua M, Leiva A, Alegría L, Gargallo L, et al. Copolymers of phenoxyethyl methacrylate with glycidyl methacrylate: synthesis, characterization and reactivity ratios. Int J Polym Mater 2008;57:216–227. [CrossRef]

Sigma Journal of Engineering and Natural Sciences
Web page info: https://sigma.yildiz.edu.tr
DOI: 10.14744/sigma.2025.1911

Research Article

Effect of pier-collar system on flow characteristics of composite hydraulic structure

Rafi Mohammed QASIM[1], Khalid AL-ASADI[2], Ihsan Abdulkareem ABDULHUSSEIN[1,*], Qusay Abdulrazzaq MAATOOQ[1]

[1]Southern Technical University, Basrah Engineering Technical College, Basrah, 15425650, Iraq
[2]Department of Civil and Architectural Engineering and Mechanics, University of Arizona, 85721, USA

ARTICLE INFO

Article history
Received: 15 May 2024
Revised: 18 July 2024
Accepted: 17 October 2024

Keywords:
Collar; Composite Hydraulic Structure; Flume; Gate; Pier; Weir

ABSTRACT

The weir-gate compound structure hydraulic characteristics and the hydraulic behavior of the pier mounted by a collar at the base are investigated experimentally. This investigation refers to the fluid-structure interference and, on the other hand, represent the interference among two different structures installed inside the channel. So both structures have a direct influence on the flow features between them. The main target of this work, reveal how the pier-collar system share in raise water depth and how share in change the hydraulic features of weir-gate. The study adopted different weir shapes with an ellipse gate, as well as different sizes of the pier and the collar, to perform the experiments. From the experiments, it was found that the pier size, collar size, and weir shape produced a nonlinear water surface profile at the composite hydraulic structure downstream region. The drag force, static force, and moment that are grown at the pier base are more influenced by the alteration in flow velocity and flow depth that occurs owing to the presence of the pier and the collar. More specifically, the change in the flow velocity and the flow depth due to the presence of the pier and the collar will be reflected directly in the obtained values of the Froude number and Reynolds number. Overall, the collar has a moderate effect on the hydraulic characteristics as compared with the pier. The result shows a discharge coefficient has a direct proportional with actual discharge. The quantitative result which appears from this study the downstream water depth and actual flow rate obey and satisfy confident level equal to and greater than 95%.

Cite this article as: Qasim RM, Al-Asadi K, Abdulhussein IA, Maatooq QA. Effect of pier-collar system on flow characteristics of composite hydraulic structure. Sigma J Eng Nat Sci 2025;43(6):2066–2083.

INTRODUCTION

The weir-gate hydraulic structure is characterized by an absolutely necessary quality that gives attention to managing the water flow either by the use of an open or artificial channel, which can not make any clash in the channel hydraulic characteristics with any hydraulic structure, which is found in the channel. In addition,

***Corresponding author.**
*E-mail address: drengihssan@stu.edu.iq

This paper was recommended for publication in revised form by Editor-in-Chief Ahmet Selim Dalkilic

Published by Yıldız Technical University Press, İstanbul, Turkey
© Author. This is an open access article under the CC BY-NC license (http://creativecommons.org/licenses/by-nc/4.0/).

the structure of weir-gate is used in gauging the control and trying to change any direction flow without showing any condition of not having enough deficit. To tackle this issue, the existence of the weir-gate structure in a channel alone has been dealt with by several studies, whereas little work has been done on the effect of the difficulty experienced on the structure of weir-gate or the interplay between the structure of weir-gate and other structures. These studies are outlined as follows: Qasim et al. [1] performed many experiments on checking the hydraulic patterns of the compound hydraulic structure in order to compare between the state of free flow, that prevailed with no appearance of any obstacle at the downstream of the composite structure, and the state of submerged flow, which is found as a result of existing the obstacle at the downstream of the composite structure. Besides, it is noted that this investigation briefly concentrated on the geometric and hydraulic variables. Abdulhussein et al. [2] tested the composite discharge structure activity owing to the finding of the prevailing longitudinal obstacle. Their study dealt with two parts: the first was based on the experimental work, whereas the second discussed the statistical analysis and the results arrived at from the experiment work done in the first part. Here, the effect of cross-sectional area of the obstacle has been taken into consideration. In this study, the obstacle length is taken into consideration. Referring to this aspect, the longitudinal obstacle shows that there is a significant effect on the hydraulic quantities that are typical for the structure of composite discharge. Also, Abdulhussein et al. [3] executed an experimental work to tackle the interaction found among the hydraulic variables, which showed that there is a strong central influence on the discharge structure work and the obstacles dimensions, which is found at the downstream of the discharge flow. In addition to this, the optimal dimensions of the obstacle have been measured by employing optimization analysis. Referring to Qasim et al.'s studies were done in [4-6], the alteration of the flow properties and the patterns obtained owing to the interaction found among the combined hydraulic structure and the emerging obstacle were taken into consideration. Abdulhussein et al. [7] arrived at a general equation that was taken from the experimental work done to expect the flow rate that passes through the discharge structure. This equation has been derived from the free-flow case. To get reliable data, different shapes of gates and weirs have been adopted. Qasim et al. [8], in an experimental study, examined the effect of the discharge structure's inclination angle on its hydraulic use. In this respect, the inclination angle values are also examined, and several hydraulic factors affecting the discharge structure are studied too. Abdulhussein et al. [9] examined how the weir crest thickness is influenced by the composite hydraulic structure. Qasim et al. [10] gave an evaluation of the main and secondary factors that created influence on the way about the response of the composite hydraulic structure, which shows that there is a contraction between the discharge coefficient, and hydraulic and geometrical factors. Qasim et al. [11] experimentally checked the bed flume contraction's effect on the discharge coefficient for the combined hydraulic structure, as well as they made a comparison between the obtained results or values and the values of the discharge coefficient in relation to the bed with no contraction. Qasim et al. [12-14] made an experiment to examine how the hydraulic structure responds to the combined hydraulic structure. They also focused on investigating the hydraulic and geometrical variables; it tried to find out the difference between these variables. To maintain this type of investigation, the different shapes of weirs and gates featured by the regular and irregular sections are also depended. Qasim et al. [15] studied experimentally the impact of the bed flume discordance on the weir-gate structure. Several variables are adopted in this study, considering different configurations of bed flume discordance. Gharehbaghi et al. [16] used three different models to predict the streamlined weir discharge coefficient; these models are gene expression program methods, intelligent optimization models, and machine learning methods. Based on the scatter plot and statistical metrics, the gene expression program has estimated the value of the discharge coefficient with high accuracy and performance. Li et al. [17] estimated the discharge coefficient of the side semi-circular weir by three optimization algorithms and a support vector machine. It has been shown that the genetic algorithm and support vector machine give accuracy of prediction. Iqbal and Ghani [18] predicted the flow rate capacity of piano key weirs relied on different geometrical variables. Artificial neural networks have been employed to obtain the flow rate. In addition to testing the activity of artificial neural networks, support vector analysis, nonlinear regression, and adaptive neuro-fuzzy interference systems are applied to check the performance of artificial neural networks. Kartal and Emiroglu [19] studied experimentally the flow features of the side weir-gate structure. 650 tests are carried out to estimate the flow features of the weir gate under subcritical flow. Nouri and Hemmati [20] dealt with the discharge coefficient of the weir-gate structure. The Flow-3D numerical model, artificial intelligence models, and regression equation are adopted to compute the discharge coefficient. In order to explore the influence of the pier's existence on the hydraulic characteristics of the composite hydraulic structure, a series of experimental runs are made in the laboratory. Here, the pier is mounted by a collar. The work gives a noticeable realization about the impact of geometrical variables of any obstacle like a pier-collar system on the hydraulic variables of weir-gate structure depending on the different variables. These variables are built based on different pier size, collar size, collar thickness, weir shape, gate dimension, and different downstream distance. Moreover, the effect of downstream water raises on the drag force that has been developed

on the pier and collar is investigated, and the variation in hydrostatic pressure around the pier-collar system is estimated. The unique contribution of the study is based on giving a good vision about the obstacle's existence (in this paper, a pier mounted by a collar is adopted), which led to a rise in water level downstream of the weir gate. It also gives a vision about the variation in the flow velocity owing to the existence of the obstacle, which in turn has a direct effect on the momentum alteration. Therefore, we deal with the subject in order to summarize the contribution on the hydraulic features of weir-gate structures, which are broadly used in water structure work.

FLUID MECHANICS CONCEPTT

The total actual discharge that passes the composite weir-gate hydraulic structure can be determined from:

$$Q_{act} = C_d \cdot (Q_{w,theo} + Q_{g,theo}) \quad (1)$$

where Q_{act}, is the total actual discharge through the composite structure (m^3/sec); $Q_{w,theo}$ and $Q_{g,theo}$ are the theoretical discharges through the weir and gate structures, respectively (m^3/sec); C_d is coefficient of discharge for the composite structure (dimensionless).

Different compound weir-gate shapes were used in this study as indicated below.

Triangular weir – Ellipse gate

Theoretical discharges that pass the triangular weir and ellipse gate can be calculated using equations (2) and (3), respectively [21].

$$Q_{w,theo} = \frac{8}{15}\sqrt{2g}\ \tan\frac{\emptyset}{2}\ h_u^{5/2} \quad (2)$$

$$Q_{g,theo} = \sqrt{2gH}\,A_g \quad (3)$$

According to eq. (1), the total actual discharge that passes through the composite triangular weir-ellipse gate hydraulic structure is:

$$Q_{act} = C_d \left[\frac{8}{15}\sqrt{2g}\ \tan\frac{\emptyset}{2}\ h_u^{5/2} + \sqrt{2gH}\,A_g\right] \quad (4)$$

Rectangular weir – Ellipse gate

Theoretical discharge that passes rectangular weir can be calculated using equations (5) [21].

$$Q_{w,theo} = \frac{2}{3}\sqrt{2g}\ b\ h_u^{3/2} \quad (5)$$

According to eq. (1), the total actual discharge that passes through the composite rectangular weir-ellipse gate hydraulic structure is:

$$Q_{act} = C_d \left[\frac{2}{3}\sqrt{2g}\ b\ h_u^{3/2} + \sqrt{2gH}\,A_g\right] \quad (6)$$

Parabolic weir – Ellipse gates

Theoretical discharge that passes parabolic weir can be calculated using equations (7) [22].

$$Q_{w,theo} = \frac{\pi}{2}\sqrt{f\,g}\cdot h_u^2 \quad (7)$$

According to eq. (1), the total actual discharge that passes through the composite parabolic weir-ellipse gate hydraulic structure is:

$$Q_{act} = C_d \left[\frac{\pi}{2}\sqrt{f\,g}\cdot h_u^2 + \sqrt{2\,g\,H}\ A_g\right] \quad (8)$$

For free flow condition

$$H = d + y + h_u \quad (9)$$

For submerged flow condition

$$H = d + y + h_u - h_d \quad (10)$$

where g is the gravitational acceleration; ϕ is weir angle; H and h_d refer to flow depths at the upstream and downstream of the weir-gate structure, respectively; h_u represents flow depth above weir crest; A_g is gate cross sectional area; y is vertical distance between weir and gate; d is gate opening height; f is focal distance; b is rectangular weir width.

The Reynolds number (R_n) and Froude number (F_r) are calculated by using the following equations (18 and 19) [23]:

$$R_n = \frac{Vh}{\nu} \quad (11)$$

$$F_r = \frac{V}{\sqrt{gh}} \quad (12)$$

Where V is flow velocity, h is flow depth, and ν is the kinematic viscosity of water.

The drag force (F_D) exerted by the pier or collar is calculated using the following equation (19).

$$F_D = \frac{1}{2}\rho\, C_D V^2 Ap \quad (13)$$

where ρ is water density, Ap is a pier or collar projected area, and C_D is drag coefficient.

The C_D value for a cylindrical collar is equal to 1.2 (19), whereas the C_D value for a cylindrical pier can be calculated using the following equation, Cheng, [24] :

$$C_D = 11\,R_n^{-0.75} + 0.9\left[1-\exp\left(-\frac{1000}{R_n}\right)\right] + 1.2\left[1-\exp\left(-\left(\frac{R_n}{4500}\right)^{0.7}\right)\right] \quad (14)$$

Equation (15) was used to calculate the hydrostatic force (F_p) resulting from the hydrostatic pressure surrounding the pier:

$$F_P = \frac{1}{2}\,\rho\, g\, h^2 D_p \quad (15)$$

where D_p is pier diameter.

EXPERIMENTAL SETUP

Several experimental tests have been executed in a rectangular glass flume at the hydraulics laboratory of Basrah Technical Engineering College. The flume is 200 cm long, 7.5cm wide (B), and 15cm deep with a horizontal bed. The flow rate (discharge) through the flume was controlled by a control valve installed at the flume inlet. The depth of the water is determined by a scale fixed to the flume wall, while the volume method is utilized to measure the total actual discharge. The hydraulic structures of different shapes (Fig. 1) were installed at a distance of 80 cm from the beginning of the flume. The hydraulic structures' models were made from a wood sheet 5 mm thick and beveled along all the edges at 45^0 with sharp edges of thickness 1mm, Qasim et al. [12]. Table 1 shows the selected dimensions of the composite hydraulic structures' models. Cylindrical piers of different ($D_{p)}$ values (1cm, 2cm, 3cm, 4cm, and 5cm) mounted by collars of different diameter (D_r) values (4cm, 5cm, and 6cm) and different depth (te) values (0.5cm and 1cm) were installed at the flume and placed at a distance of 40cm downstream of the composite structure. (Fig. 2). Piers and collars models were made from wood material.

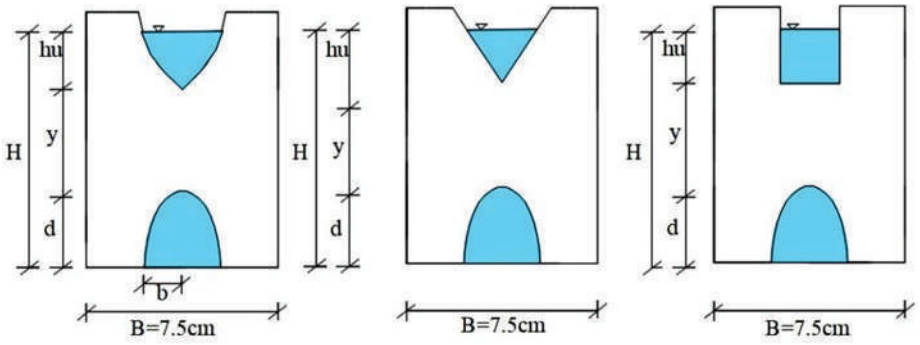


Figure 1. Shapes and dimensions of composite hydraulic structures.

Table 1. Tested model shapes and dimensions

Model	hu (cm)	y (cm)	d (cm)	H (cm)	b (cm)	Aw (cm^2)	Ag (cm^2)	Weir shape	Gate shape
1	3	4.5	2.5	10	1.25	6.93	4.9087	Rectangular	Ellipse
2	2	4.5	2.5	9	1.25	4.62	4.9087		
3	1	4.5	2.5	8	1.25	2.31	4.9087		
4	3	4.0	3.0	10	1.50	6.93	7.0686		
5	2	4.0	3.0	9	1.50	4.62	7.0686		
6	1	4.0	3.0	8	1.50	2.31	7.0686		
7	3	4.5	2.5	10	1.25	6.92	4.9087	Parabolic	Ellipse
8	2	4.5	2.5	9	1.25	3.77	4.9087		
9	1	4.5	2.5	8	1.25	1.34	4.9087		
10	3	4.0	3.0	10	1.50	6.92	7.0686		
11	2	4.0	3.0	9	1.50	3.77	7.0686		
12	1	4.0	3.0	8	1.50	1.34	7.0686		
13	4	3.5	2.5	10	1.25	6.92	4.9087	Triangular	Ellipse
14	3	3.5	2.5	9	1.25	3.89	4.9087		
15	2	3.5	2.5	8	1.25	1.73	4.9087		
16	1	3.5	2.5	7	1.25	0.43	4.9087		
17	4	3.0	3.0	10	1.50	6.92	7.0686		
18	3	3.0	3.0	9	1.50	3.89	7.0686		
19	2	3.0	3.0	8	1.50	1.73	7.0686		
20	1	3.0	3.0	7	1.50	0.43	7.0686		

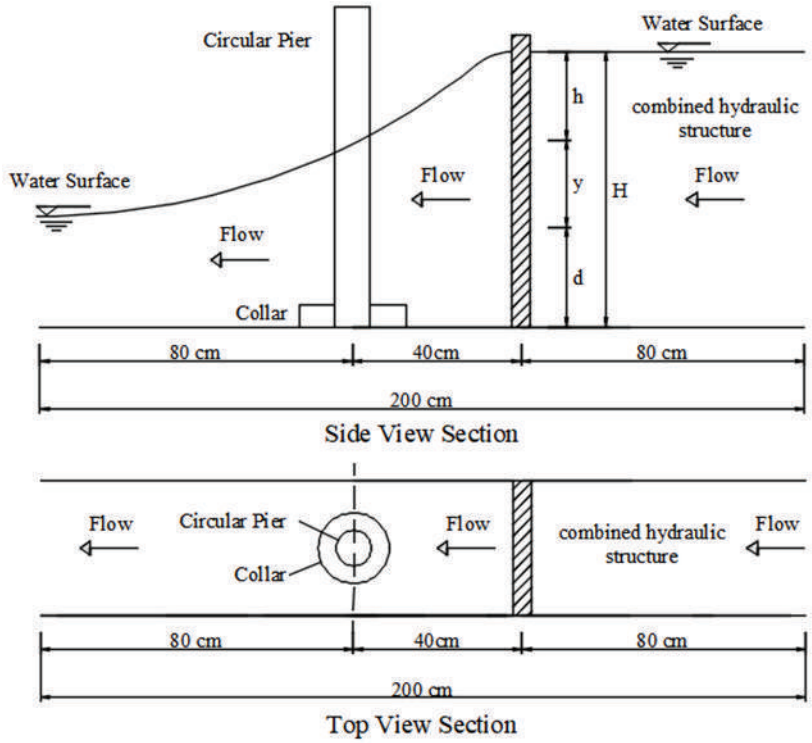


Figure 2. Whole components of hydraulic regime.

An Uncertainty in the Measured Amount

Reliability is the need of every scientific product. The failure of an engineered product is a fixed characteristic or is related to its production. Engineering systems play an important role in making or inventing better reliable products. Uncertainty is the most useful function for analyzing prediction age and reliability. This function can provide the probability of successful operation of the product for up to a certain time without a single failure. Every time, it is not possible to measure the various parameters of the system exactly due to the uncertainty or ambiguity present in their limits. In cases of lack of precision, it is reasonable to use fuzzy parameters rather than exact parameters (values) [25-27]. It is very common for error in parameters to be due to machine error, experimentation, or personal decision. Theories and concepts of uncertainty have been developed and worked on by several researchers, such as; Chandola et al., Sharma et al, Negero et al., Hogeme et al., and Younus et al. [28-32].

Uncertainty is a positive parameter that describes the range of values associated with a measure (the measured quantity). The following equation can be used to express the potential inaccuracies that may arise when measuring a quantity:

$$u_x = \sqrt{S_x^2 + b_x^2} \tag{16}$$

where S_x accounts for the random errors, while the term b_x represents the systematic errors, and u_x is termed the standard uncertainty in x. The sample standard deviation can be used to get the S_x value:

$$S_x = \left\{\frac{1}{N-1}\sum_{i=1}^{N}(x_i - \bar{x})^2\right\}^{1/2} \tag{17}$$

The following equation is used to estimate the uncertainty of a mean value ($U_{\bar{x}}$), which is calculated from a series of N measurements obtained with the same instrument:

$$U_{\bar{x}} = \sqrt{S_{\bar{x}}^2 + b_{\bar{x}}^2} \tag{18}$$

where $S_{\bar{x}}$ is the standard uncertainty of the mean, which is equal to ($=S_x/\sqrt{N}$) while the variable $b_{\bar{x}}$ is the standard deviation linked to systematic errors. It turns out that $b_{\bar{x}} = b_x$.

The standard uncertainty can be multiplied by a coverage factor (k) to determine the extended uncertainty. For example, uncertainty in x can be solved using the following equation:

$$U_{\bar{x}} = k.u_{\bar{x}} = k.\sqrt{S_{\bar{x}}^2 + b_{\bar{x}}^2} \quad (P\%) \tag{19}$$

The k value depends on numerous factors, such as the number of data points and level of confidence P. A P value of 0.95 and 0.99 can be obtained by adjusting the k factor value to equal 2 and 2.6, respectively [33-34].

The uncertainty of a variable indicates what interval the measurement's actual value is most likely to fall inside. The following formats are feasible for the uncertainty interval:

Uncertainty interval=middle value±uncertainty (*P*%) (20)

We want to estimate the uncertainty interval for a population's mean (μ). The uncertainty interval for the true mean value is defined as:

$$\mu = \bar{x} \pm U_{\bar{x}} \quad (P\,\%) \tag{21}$$

MATERIALS AND METHODS

The method used to do this study consists of three parts; these parts are experimental work, hydraulic analysis, and statistical analysis. The experimental works include the following activities: preparing the channel, pump operation to feed the required water quantity, monitoring the water depth over the weir, and finally measuring the flow rate and the flow depth. The hydraulic analysis includes giving a suitable clarification for the relation between hydraulic variables and geometrical variables or relation among the hydraulic variables and the statistical analysis based on analysis of the results of the measured flow rate and the downstream water depth by uncertainty analysis to achieve the required confidence.

RESULTS AND DISCUSSION

As indicated earlier, the main purpose of this study is to investigate the effect of the pier-collar system on the hydraulic characteristics of the composite weir-gate structure. All experimental runs conducted in this study show submerged flow conditions (eq. 10) where the h_d values are greater than the gate height.

Figure 3 shows the variation of the h_d values along the flume reach downstream of the rectangular weir-ellipse gate structure with a pier-collar system of different D_p values, D_r values, and te values of 5cm and 0.5cm, respectively. It can be seen from this figure that the h_d profile is almost nonlinear for all pier diameters, and the h_d values at the upstream region of the pier-collar system are higher than those at the downstream region of the system. This is because of the existence of the pier, which acts as an obstacle to the flowing water.

In Figure 4, the h_d values were sketched along the flume reach downstream of the rectangular weir-ellipse gate structure with a pier-collar system of D_p value 3cm, different D_r values, and te value 0.5cm. It is obvious from this figure that the D_r values have a great effect on the h_d values at the upstream region of the pier-collar system, whereas this effect becomes less noticeable at the downstream region of the system, where there is a slight change in the h_d values. At every section along the upstream region of the pier-collar system, the h_d values increase with increasing D_r values.

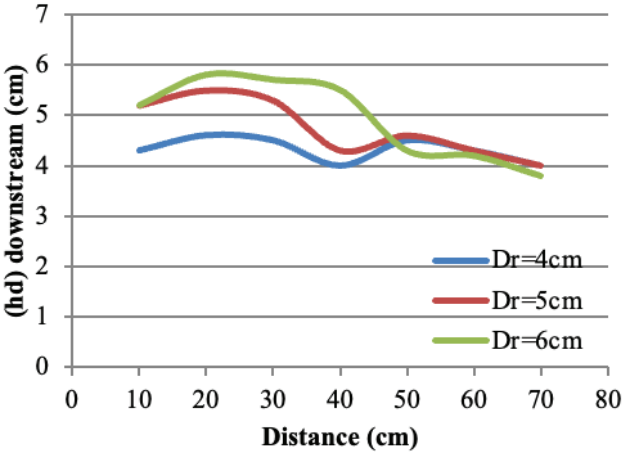


Figure 4. The variation of h_d values along the downstream distance of the rectangular weir-ellipse gate structure for different D_r values (D_p= 3cm, te= 0.5cm).

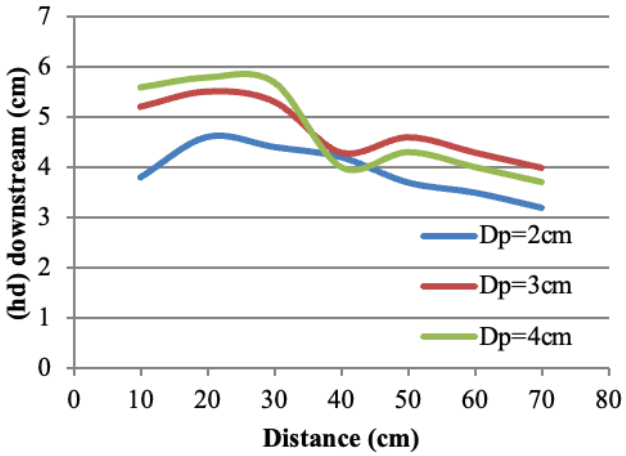


Figure 3. The variation of h_d values along the downstream distance of the rectangular weir-ellipse gate structure for different D_p values and D_r= 5cm and te= 0.5cm.

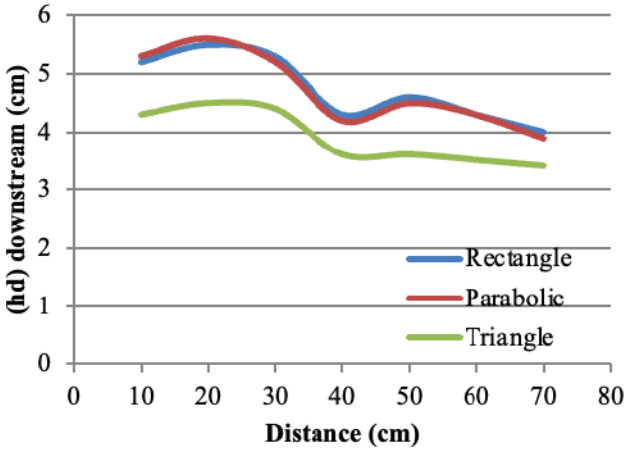


Figure 5. The variation of h_d values along the downstream distance of the composite structure of different weir shapes (D_p= 3cm, D_r=5cm, te= 0.5cm).

This means that the collar also works as an obstacle, and its effect increases with increasing diameter.

Figure 5 shows the variation of the h_d values along the flume reach downstream of the composite hydraulic structure of different weir shapes with pier-collar systems of D_p, D_r, and te equal to 3cm, 5cm, and 0.5cm, respectively. The variations of the h_d values for the hydraulic structures of rectangular and parabolic weirs are approximately the same, and their values are greater than those for the hydraulic structures of triangular weirs. For clarification, the actual discharge through the triangular weir is the smallest one compared with the other weir shapes for the same water depth over the weir crest, and this status will be reflected directly on the water depth downstream.

The variation of the Q_{act} values against the D_p values is shown in Figure 6, considering hydraulic structures of different weir shapes with pier-collar systems of D_r and te equal to 5cm and 0.5cm, respectively. It can be seen from the figure that the Q_{act} values decrease with increasing D_p values. Increasing the D_p values leads to the confinement of a large quantity of the flowing water in the upstream region of the pier-collar system, which in turn causes a decrease in the Q_{act} values. The variations of the Q_{act} values for the hydraulic structure of a triangular weir are less than those for the hydraulic structures of the other weir shapes.

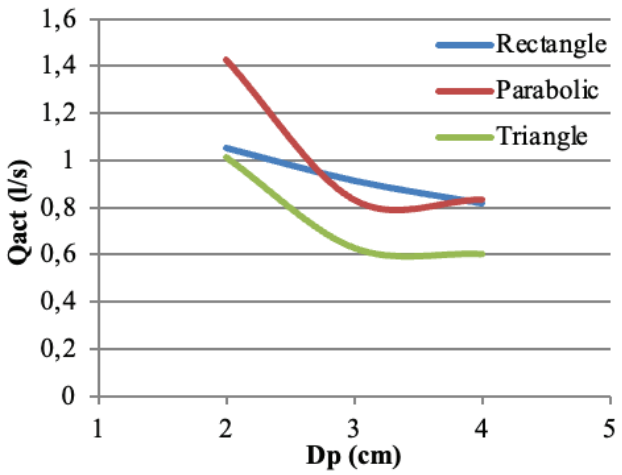


Figure 6. Q_{act} versus D_p for composite structures of different weir shapes (D_r=5 cm, te=0.5 cm).

Figure 7 shows the relationship between the h_d and D_p values for the same arrangement of the composite structures and pier-collar system indicated in Figure 6. In general, as the D_p value increases, the confinement to the flow increases, which in turn causes a reduction in flow velocity and an increase in the water depth value (h_d). This situation is clearly shown for the composite structure of the rectangular weir, whereas it is only slightly shown for the composite structures of the other weir shapes.

The influence of the D_p values on the change of momentum at the pier-collar system for the same arrangement of the composite structures and pier-collar system indicated in Figure 6 was presented in Figure 8. It is obvious from the figure that the change in momentum value increases with an increase in the D_p value. The change in momentum is described by a difference between the drag and static forces, where the former are exerted by the pier-collar system whereas the latter are produced by the static pressure. When the pier diameter increases, this leads to an increase in the projection area of the pier; therefore, the drag force and static force will increase simultaneously, taking into consideration that both forces depend on the projection area of the pier, so as a result, the moment will increase directly. Also, the drag force, which is produced and developed by the collar, has a direct effect on the value of the moment change.

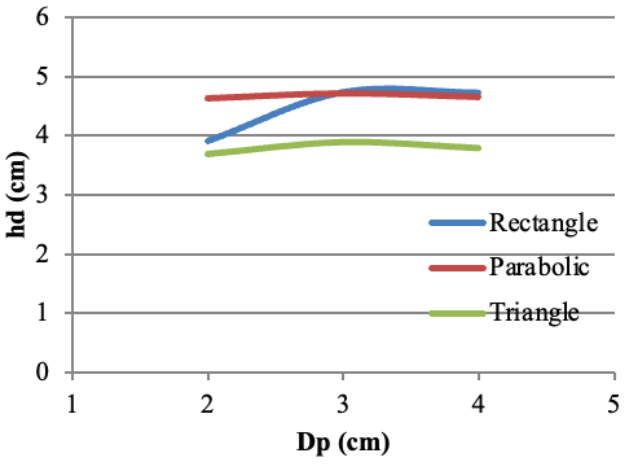


Figure 7. h_d versus D_p for composite structures of different weir shapes (D_r=5 cm, te=0.5 cm).

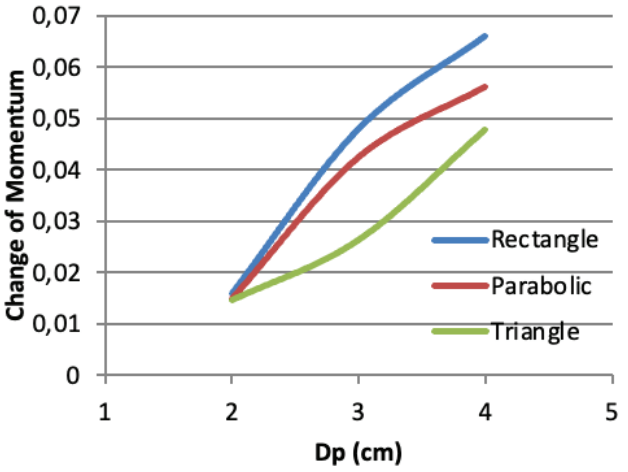


Figure 8. Variation of change of momentum with D_p value for composite structures of different weir shapes (D_r=5 cm, te=0.5 cm).

Figure 9 illustrates the variation of downstream Froude number (Fr_{down}) and R_n values at the downstream region of the composite structure with dimensionless values of the pier diameter (D_p/B) for a composite structure of a rectangular weir with a pier-collar system of D_r and te values equal to 5cm and 0.5cm, respectively. The Fr_{down} and R_n values were determined based on an average value of h_d (h_{davg}). As the (D_p/B) value increased, the values of Fr_{down} and R_n decreased monotonically, as shown in Figure 9. As indicated in Figures 6 and 7, the Q_{act} and h_d values decreased with increasing D_p values. Therefore, with increasing in h_d values, the Fr down value decreased due to the inverse relationship between Fr and water depth (eq. 12). Also with a decrease in Qact value, R_n decreased due to the direct proportionality between R_n and water flow rate (eq. 11).

Figure 10 illustrates the variations of Fr_{down} and R_n values at the downstream region of the composite structure with dimensionless values of the collar diameter (D_r/B) for the composite structure of a rectangular weir with a pier-collar system of D_p and te values equal to 2cm and 0.5cm, respectively. As shown in the figure, as the (D_r/B) increases, both the Froude number and the Reynolds number increase.

As indicated in Figure 4, the h_d value increased with increasing D_r values. Therefore, with increasing in h_d values, the Fr down value decreased due to the inverse relationship between Fr and water depth (eq. 12). The diameter of the collar is very small as compared with the water depth, so the collar diameter has a minor effect on the result of the Froude number and Reynolds number. Here, the results remain affected by the water depth for the Froude number and the flow velocity for the Reynolds number. Any variation in the result will be attributed to the interaction between overflow velocity and underflow velocity.

Figure 11 illustrates the variation of Fr_{down} and R_n values at the downstream region of the composite structure with dimensionless values of the collar depth (te/B) for a composite structure of a rectangular weir with a pier-collar system of D_p and D_r values equal to 2cm and 5cm, respectively. The value of the Fr_{down} decreased monotonically with increasing (te/B) values, whereas the R_n values increased and then decreased with increasing (te/B) values (Fig. 11). Increasing the te value provides additional confinement to the flow, which causes an increase in water depth and then a decrease in the Fr_{down} value (eq. 12). Also, the figure shows a dramatic relationship between the Reynolds number and (te/B); this happens due to the alteration in the flow velocity behavior and the change in the water depth around the pier, which is mounted with a collar.

Figure 12 shows the variation of the Q_{act} value with the C_d value for composite structures of different weir shapes

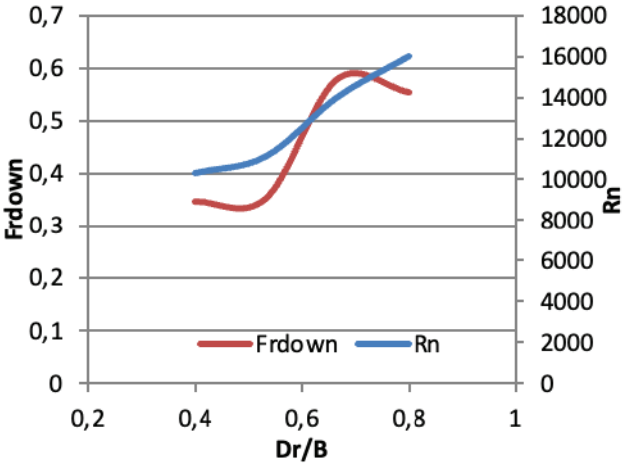


Figure 10. Variation of Fr_{down} and R_n with dimensionless value of D_r for composite structure of rectangular weir (D_p=2 cm, te=0.5 cm).

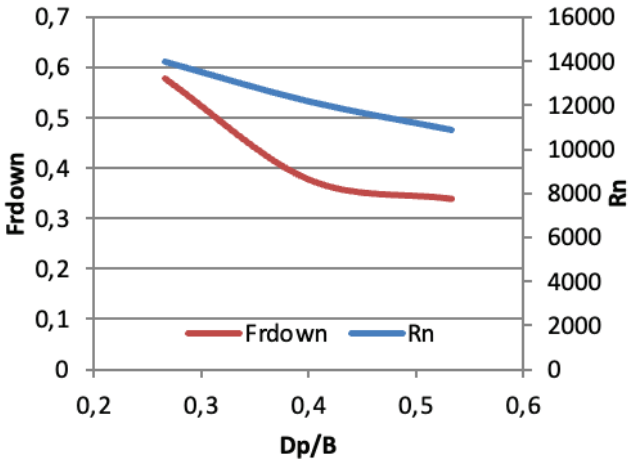


Figure 9. Variation of Fr_{down} and R_n with dimensionless value of D_p for composite structure of rectangular weir (D_r=5 cm, te=0.5 cm).

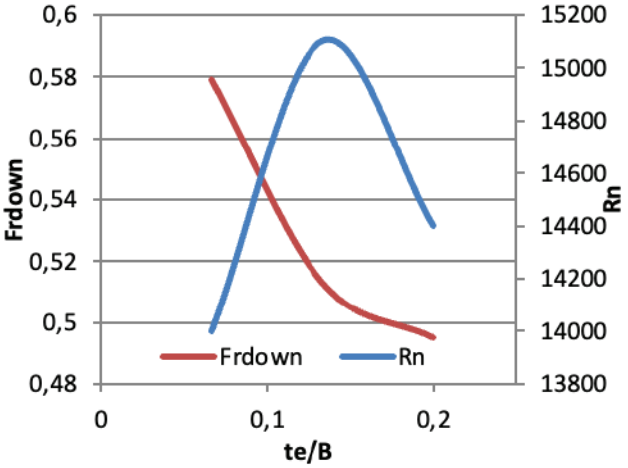


Figure 11. Variation of Fr_{down} and R_n with dimensionless value of te for composite structure of rectangular weir (D_p=2 cm, D_r=5 cm).

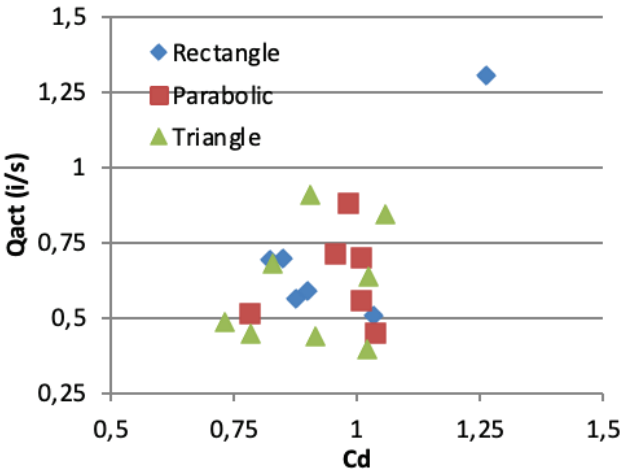


Figure 12. Variation of Q_{act} with C_d for composite structures of different weir shapes (D_p=3 cm, D_r=4 cm, te=1cm).

with pier-collar systems of the D_p, D_r, and te values equal to 3 cm, 4 cm, and 1 cm, respectively. It is obvious from the figure that the Q_{act} value increases with an increase in the C_d value, and this is due to the direct proportionality between them.

Figure 13 illustrates the variation of the variable (H_{new}) and the upstream Froude number (Fr_{up}) for the same arrangement of the composite structures and pier-collar system indicated in Figure 12. The figure shows that the value of Fr_{up} increases with increasing H_{new} values for all shapes of the composite structures, and this is due to the direct proportionality between Froude number and flow depth.

Figures 14 (a), (b), (c), (d), and (e) show the variations of the average value of $h_{d\ average}$ with pier C_D, F_D (pier), F_D (collar), and F_p at the upstream and downstream regions of the pier for composite structures of different weir shapes

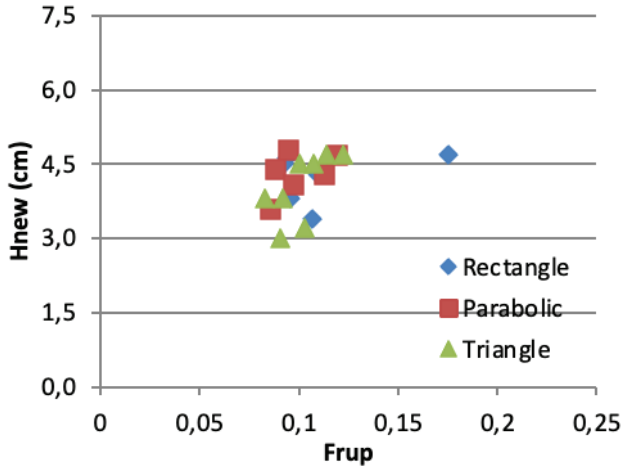


Figure 13. Variation of H_{new} with Fr_{up} for composite structures of different weir shapes (D_p=3 cm, D_r=4 cm, te=1cm).

with pier-collar systems of the D_p, D_r, and te values equal to 4cm, 5cm, and 1cm, respectively. It is clear from the above figures that any increase in the $h_{d\ average}$ will be reflected directly in the mentioned values. In general, the water depth has a direct effect on the drag force value (eq. 13) and on the R_n value, which dominates the value of C_D (eq. 14). In addition, the $h_{d\ average}$ value has a direct impact on the calculated values of the static force due to the direct proportionality between them (eq. 15).

The relationship of the Q_{act} and D_P values for the composite hydraulic structure of a rectangular weir-ellipse gate with a collar of different D_r values and te value of 0.5cm is shown in Table 2. For a constant D_p value, the Q_{act} value increases with an increase in the D_r value. Also, for a constant D_r value, the Q_{act} value fluctuates with an increase in the D_p value due to the interaction between weir discharge and gate discharge.

The relationship between the F_{rdown} and D_P values for the same arrangement indicated in Table 2 is shown in Table 3. For a constant D_p or D_r value, the Q_{act} value increases with an increase in the D_r or D_p value, respectively.

The relationship between the h_d and D_P values for the same arrangement indicated in Table 2 is shown in Table 4. For a constant D_p value, the h_d value increases with an increase in the D_r value, except for the case when D_p = 2 cm, where the h_d values decrease and then increase when the D_r values change from 4cm to 5cm and from 5cm to 6cm, respectively. Also, for a constant h_d value, the Q_{act} value fluctuates with an increase in the D_p value due to the weir flow velocity and gate flow velocity.

The relationship between the change in momentum and D_P values for the same arrangement indicated in Table 2 is shown in Table 5. The variation in the change of momentum values was clearly shown, and it depends mainly on the size of the pier and collar and also on the interference between weir and gate flow velocities, respectively.

The relationship of the Q_{act} and D_P values for the composite hydraulic structure of a rectangular weir-ellipse gate with a collar of different te values and D_r value of 5cm is shown in Table 6. For constant D_p value, the Q_{act} value is fluctuated with increasing in the te value due to the interaction between weir discharge and gate discharge. For a constant te value, the Q_{act} value decreases with increasing in the D_p value except for the case when te = 1.5 cm, where the Q_{act} values have increased and then decreased when the

Table 2. Q_{act} versus D_p for rectangular weir-ellipse gate composite structure with different D_r values (te=0.5cm)

D_p (cm)	Q_{act} (l/sec)		
	D_r=4cm	D_r=5cm	D_r=6cm
2	0.829	1.052	1.201
3	0.831	0.914	1.424
4		0.818	0.**783**

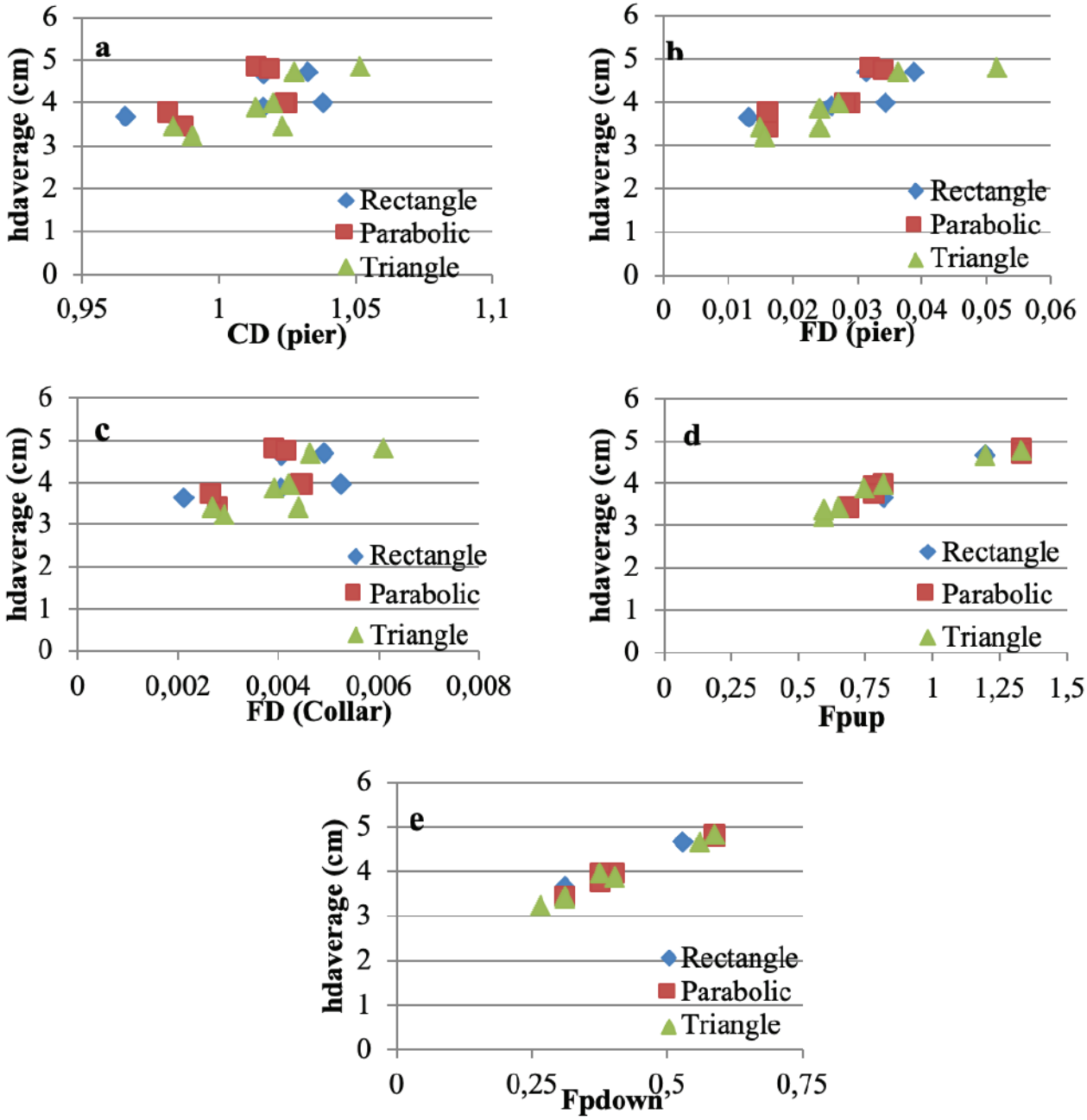


Figure 14. Variations of the $h_{daverage}$ with; (a) C_D(pier) , (b) F_D(pier), (c) F_D(collar) , (d) F_{Pup} , and (e) F_{Pdown} for composite structures of different weir shapes (D_p=4 cm, D_r=5 cm, te=1cm).

Table 3. F_{rdown} versus D_p for rectangular weir-ellipse gate composite structure with different D_r values (te=0.5cm)

D_p (cm)	F_{rdown}		
	D_r=4cm	D_r=5cm	D_r=6cm
2	0.353	0.579	0.554
3	0.395	0.377	0.554
4		0.338	0.365

Table 4. h_d versus D_p for rectangular weir-ellipse gate composite structure with different D_r values (te=0.5cm)

D_p (cm)	h_d (cm)		
	D_r=4cm	D_r=5cm	D_r=6cm
2	4.64	3.19	4.40
3	4.31	4.74	4.93
4		4.73	4.37

Table 5. Change of momentum versus D_p for rectangular weir-ellipse gate composite structure with different D_r values (te=0.5cm)

D_p (cm)	Change of momentum (N)		
	D_r=4cm	D_r=5cm	D_r=6cm
2	0.0369	0.016	0.0428
3	0.0256	0.049	0.0172
4		0.0664	0.0638

Table 6. Q_{act} versus D_p for rectangular weir-ellipse gate composite structure with different te values (D_r=5cm)

D_p (cm)	Q_{act} (l/sec)		
	te=0.5cm	te=1cm	te=1.5cm
2	1.053	1.129	1.079
3	0.914	0.937	1.163
4	0.817	0.703	0.824

Table 7. Fr versus D_p for rectangular weir-ellipse gate composite structure with different te values (D_r=5cm)

D_p (cm)	F_{rdown}		
	te=0.5cm	te=1cm	te=1.5cm
2	0.579	0.320	0.306
3	0.377	0.297	0.304
4	0.338	0.246	0.281

Table 8. h_d versus D_p for rectangular weir-ellipse gate composite structure with different te values (D_r=5cm)

D_p (cm)	h_d (cm)		
	te=0.5cm	te=1cm	te=1.5cm
2	3.91	4.44	4.41
3	4.74	4.71	4.59
4	4.73	4.69	4.56

Table 9. Change of momentum versus D_p for rectangular weir-ellipse gate composite structure with different te values (D_r=5cm)

D_p	Change of Momentum (N)		
(cm)	te=0.5cm	te=1cm	te=1.5cm
2	0.016	0.0217	0.037
3	0.048	0.066	0.026
4	0.066	0.058	0.051

D_p values have changed from 2cm to 3cm and from 3cm to 4cm, respectively.

The relationship between the F_{rdown} and D_p values for the same arrangement indicated in Table 6 is shown in Table 7. For a constant D_p value, the F_{rdown} value fluctuates with an increase in the te value. For constant te the Fr value decreases with an increase in the D_p value.

The relationship between the h_d and D_p values for the same arrangement indicated in Table 6 is shown in Table 8. For a constant D_p or te value, the h_d value fluctuates with an increase in the te or D_p value, respectively. These fluctuations in the h_d values were attributed to the interaction between weir flow velocity and gate flow velocity.

The relationship between the change in momentum and D_p values for the same arrangement indicated in Table 6 is shown in Table 9. The variation in the change of momentum values was clearly shown, and it depends mainly on the size of the pier and collar and also on the interference between weir and gate flow velocities, respectively.

To examine the impact of pier-collar systems on the weir-gate structure, it has been considered how these systems affect the primary hydraulic and geometrical variables that control the hydraulic function of the weir-gate structure. These variables include the water depth of the weir, the vertical distance between the weir and the gate, and the water depth of the gate. Figure (15) displays the variation in the weir water depth with the Froude number for the hydraulic regime for the case, te=1cm, y=4cm, d=3cm, D_p=4cm, and D_r=6cm for three different shapes of weir (rectangular, triangular, and parabolic), based on the alteration in the pier drag force, collar drag force, and hydrostatic pressure at the upstream and downstream faces of the pier. It has been inferred from the figure that rectangular and parabolic weirs respectively, with an increase in the water depth above the weir crest, the Froude number increases directly.

Here, the Froude number depends on the downstream flow velocity and downstream water depth, the downstream water depth relies on the hu, y, and d. If the summation of both values of hu and d is checked, it is found that the summation is always greater than y. Therefore, when the downstream water depth (hu+d) becomes greater than y, the Froude number must decrease directly owing to the inverse proportional between them despite of rise in hu values. Still the interference between weir flow velocity and gate flow velocity will share directly in the increases in Froude number values, owing to the direct proportionality between flow velocity and Froude number. Here, y confine the water depth behind the weir-gate structure. Furthermore, for any curve in the figure, the upstream and downstream hydrostatic pressure increase directly owing to the hydrostatic pressure being directly proportional to the water depth near the pier. Therefore, the rise in water depth leads to a rise in hydrostatic pressure, while the drag force has a linear trend because the water depth rise has a minor impact on the drag force as compared with flow velocity. For a triangular weir,

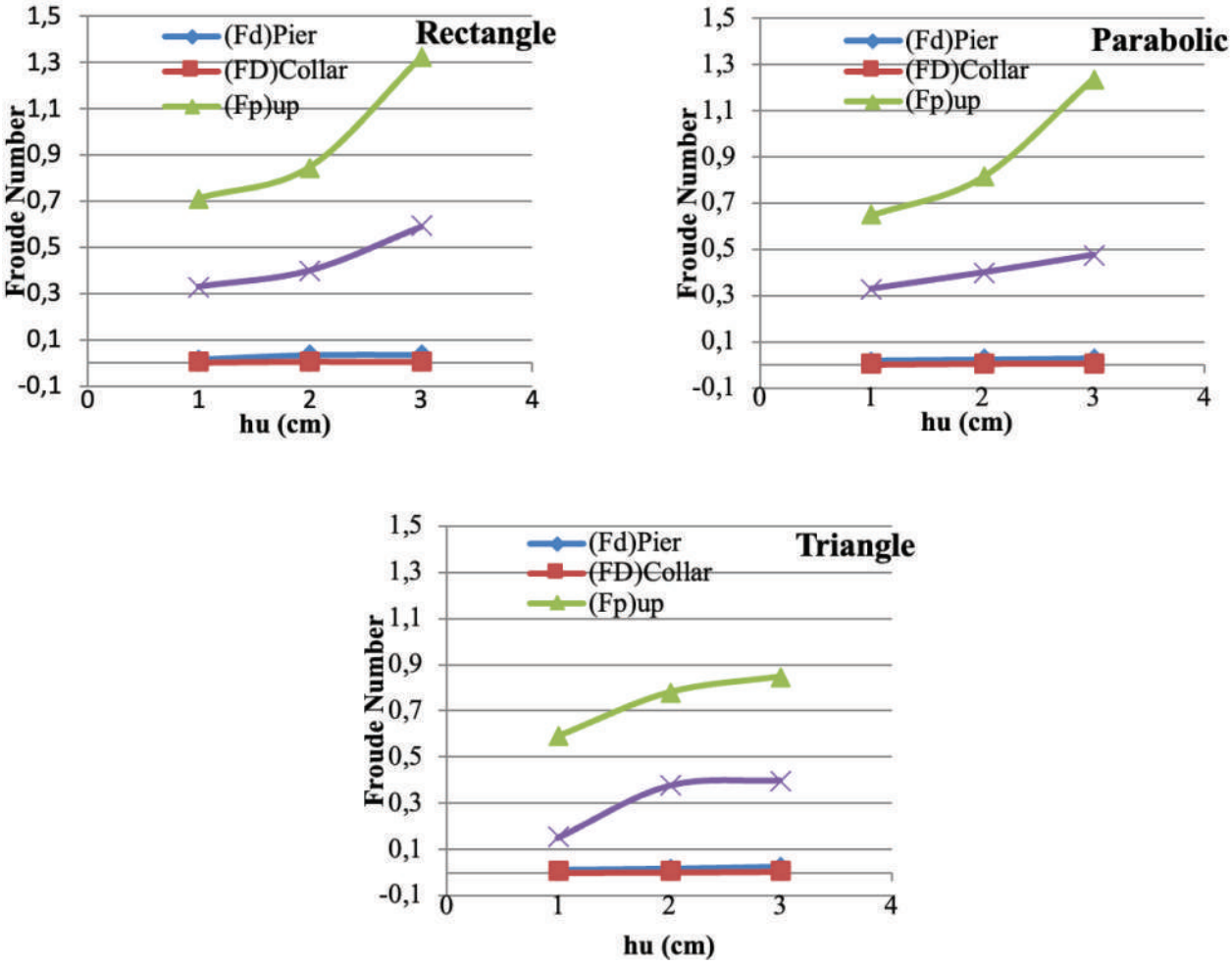


Figure 15. Variation of hu with Froude Number of hydraulic regime for the case, te=1cm, y=4cm, d=3cm, D_p=4cm, and D_r=6cm

there are slightly changes in the relationship trend between water depth over the weir and Froude number, and this occurs owing to the interaction between the weir and gate flow velocity.

The alteration in the Froude number with the water depth above the rectangular weir crest is plotted in Figure 16, considering the variation in the drag force of pier and collar, respectively, for different values of (y). Also, the variation in the (y) values leads to a variation in the values of (d). Two different values are adopted for (y), and these values are y = 4 cm and y = 4.5 cm. It is clear from the figure that with an increase in the water depth above the weir crest, the pier drag force and collar drag force increase sharply. Here, the increase in the hu values leads to an increase in the project area of the pier which has direct contact with water. As the projection area increases the drag force will be increase due to the direct proportionality between drag force and projection area. Also, the alteration in the Froude number with the water depth above the rectangular weir crest is plotted in Figure 16, considering the variation in the upstream and downstream hydrostatic pressure, respectively, for different values of (y). Also, the variation in the (y) values leads to a variation in (d) values. Two different values are adopted for (y) and these values are y = 4cm and y = 4.5cm. It is clear from the figure that with an increase in water depth above the weir crest, the Froude number increases directly. Here, the Froude number depends on the downstream flow velocity and downstream water depth, the downstream water depth relies on the hu, y, and d. It is found that the summation of both values of hu and d is always greater than y. Therefore, when the downstream water depth (hu+d) becomes greater than y, the Froude number must decrease directly owing to the inverse proportionality between them despite the rise in hu values, but the interference between weir flow velocity and gate flow velocity will share directly in the increase of Froude number values, owing to the direct proportionality between flow velocity and the Froude number. Here, y confine the water depth behind the weir-gate structure.

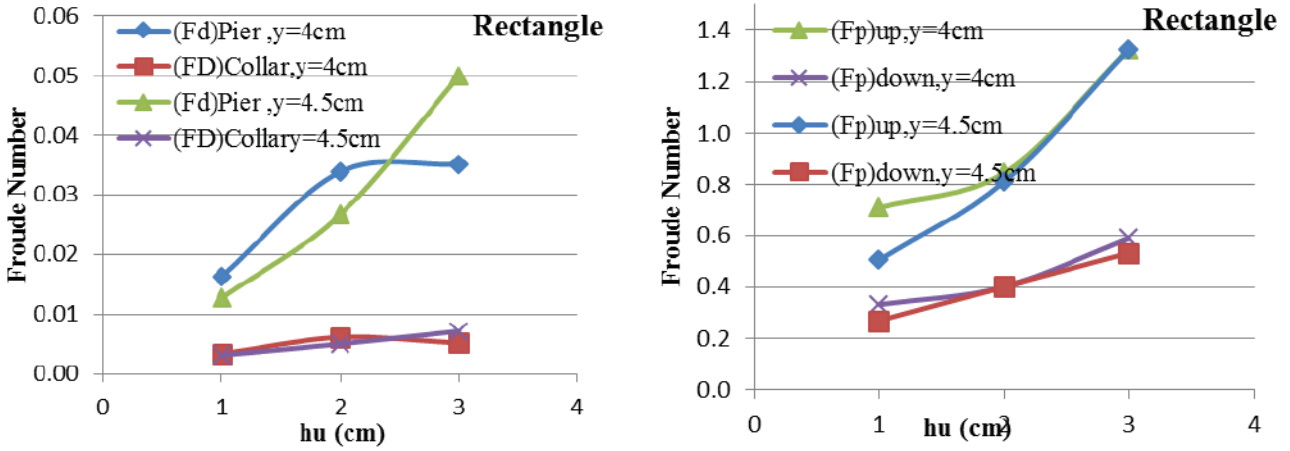


Figure 16. Variation of Froude Number with y and d for the case, te=1cm, H=9cm, Dp=4cm, and D_r=6cm.

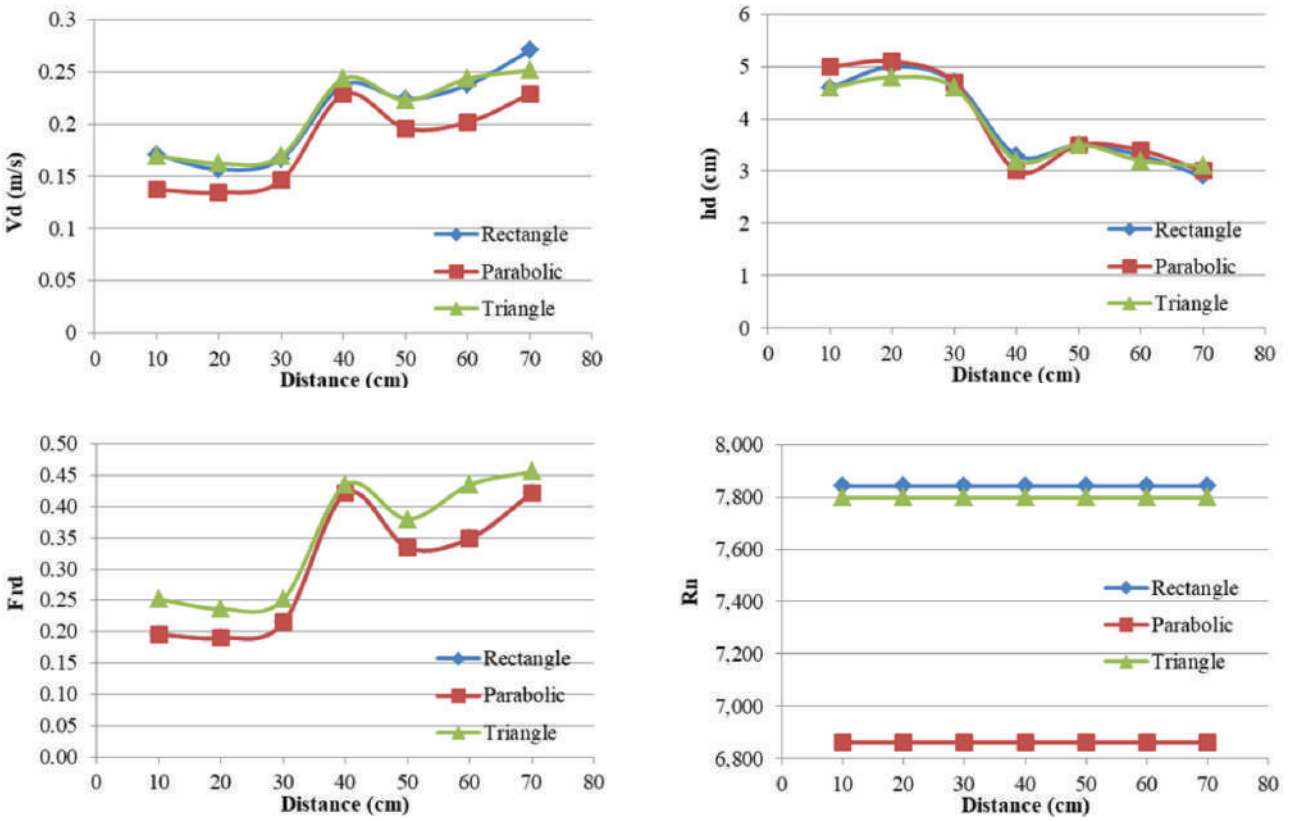


Figure 17. The Profile of downstream velocity, water depth, Froude Number, and Reynold's Number for the case te=1cm, y=4cm, d=3cm, D_p=4cm, and D_r=6cm.

To show the hydraulic patterns due to the interaction between the pier-collar system and the weir-gate structure the alteration in flow velocity, flow depth, Froude numbers, and Reynolds numbers with distance has been plotted respectively using three different weir shapes (rectangular, triangular, and parabolic). Commonly, both Froude number and Reynold's number depend on the flow velocity and flow depth. Figure 17 shows subcritical and turbulent open channel flow. The Froude number profile is similar to the velocity profile owing to the direct proportion between them. Any variation in hydraulic trend will be attributed to flow depth, which is inversely proportional to the Froude

number, and the overlapping between over weir flow and under gate flow will be shared in the flow velocity variation, which will be reflected directly on the Froude number or Reynolds number. The trend in relation between Reynolds numbers and distance is described as linear, regardless of the weir shapes.

QUANTIFYING STATE VARIABLE UNCERTAINTY INTERVALS

The best data available must be utilized to estimate the systematic and random errors. Equation (17) is employed to compute the random error S_x. Then, $(=S_x/\sqrt{N})$ is the standard uncertainty of the mean $S_{\bar{x}}$. Systematic uncertainty estimates cannot be obtained typically from measurements or statistical processes. The elemental error sources that impact each measurement are the first thing to take into account when estimating the systematic uncertainty for a particular variable.

Table 10 shows the potential sources of the two variables (actual discharge and average downstream water depth) that will be assessed in this experiment.

Table 10. Elemental systematic uncertainty details

Source	Systematic uncertainty	
	Actual discharge (l/s)	Downstream water depth (cm)
Conceptual	0.073	0.212
Calibration	0.012	0.100
Calibration	0.006	0.200

The evaluation of systematic uncertainty is based on potential sources of inaccuracy. Conceptual errors are a major source of errors in the composite structure computation experiment. This form of inaccuracy occurs when the measured values at certain sites diverge from the mean value. Table 11 shows the actual discharge values, averaged over three tries, as well as the percentage variance between the values and their average. Table 12 also displays the downstream water depth readings for various locations, the average of these values, and the percentage difference between the average and these values. The absolute average

Table 11. Selected values of actual discharge and differences

Q1 (1)	Q2 (2)	Q3 (3)	Qact (4)	D1= $[\frac{(1)-(4)}{(4)}]$	D2= $[\frac{(2)-(4)}{(4)}]$	D3= $[\frac{(3)-(4)}{(4)}]$
0.6067	0.5946	0.5325	0.5760	0.053	0.032	-0.076
0.5606	0.5653	0.4693	0.5278	0.062	0.071	-0.111
0.6385	0.5693	0.5412	0.5802	0.100	-0.019	-0.067
0.5869	0.5988	0.5948	0.5935	-0.011	0.009	0.002
0.6610	0.6063	0.5553	0.6045	0.094	0.003	-0.081
0.6397	0.6742	0.5357	0.6106	0.048	0.104	-0.123
0.6116	0.5581	0.5556	0.5740	0.066	-0.028	-0.032
0.5784	0.5291	0.4835	0.5275	0.097	0.003	-0.083
0.6106	0.5357	0.6572	0.5969	0.023	-0.102	0.101

Table 12. Selected of average downstream water depth and differences

hd1	hd2	hd3	hd4	hd5	hd6	hd7	hdavg	D1	D2	D3	D4	D5	D6	D7
4.2	4.5	3.8	3.7	3.2	3.0	2.6	3.57	0.176	0.26	0.064	0.036	-0.104	-0.16	-0.272
4.4	4.6	4.3	3.8	4.0	3.7	3.5	4.04	0.088	0.138	0.064	-0.060	-0.011	-0.085	-0.134
4.3	4.5	4.3	3.7	3.7	3.7	3.5	3.96	0.087	0.137	0.087	-0.065	-0.065	-0.065	-0.116
4.5	5.0	4.8	4.2	4.3	4.0	3.8	4.37	0.029	0.144	0.098	-0.039	-0.016	-0.085	-0.131
5.3	5.5	5.3	4.0	4.5	4.0	3.8	4.63	0.145	0.188	0.145	-0.136	-0.028	-0.136	-0.179
4.4	4.5	4.5	3.5	3.5	3.5	3.3	3.89	0.132	0.158	0.158	-0.099	-0.099	-0.099	-0.151
4.0	4.0	3.8	3.2	3.2	3.0	2.8	3.43	0.167	0.167	0.108	-0.067	-0.067	-0.125	-0.183
5.3	5.5	5.5	4.2	4.5	4.2	4.0	4.74	0.117	0.160	0.160	-0.114	-0.051	-0.114	-0.157
4.5	4.4	4.2	3.0	3.3	3.0	2.6	3.57	0.260	0.232	0.176	-0.160	-0.076	-0.160	-0.272

percentage difference of actual discharge and downstream water depth was calculated to be 0.229 and 0.106, respectively. Based on these values, the conceptual uncertainty value is considered to be 12% of the mean value of actual discharge and 5.3% of the mean value of average downstream water depth (about half the absolute average percentage variance). Thus, it can be computed by multiplying the percentage difference by the arithmetic mean of the actual discharge and the downstream depth of the water, respectively. It was found that these values were (0.12*0.609=0.073 l/s) and (0.053*4.013=0.212 cm).

The scalar readability was given a value of (0.1 cm), and the flow ripple in downstream was given a value of (0.2 cm), in relation to the uncertainty coming from the calibration and its connection to the downstream depth of the water. Also, in terms of calibration uncertainty and related to real discharge, the values (0.012 l/s) and (0.006 l/s) were assigned to errors caused by time estimation and other invisible errors, respectively. Table 13 shows the statistics of

Table 13. Statistics and uncertainty parameters of the state variables

Variable	Mean	*Sx*	$S_{\bar{x}}$	$b_{\bar{x}}$	*ux*	$U_{\bar{x}}$	Min.	Max.
Q_{act} (l/s)	0.609	0.168	0.0108	0.0913	0.0919	0.2391	0.3698	0.8481
hd_{avg} (cm)	4.013	0.506	0.0327	0.5127	0.5137	1.0270	2.986	5.0410

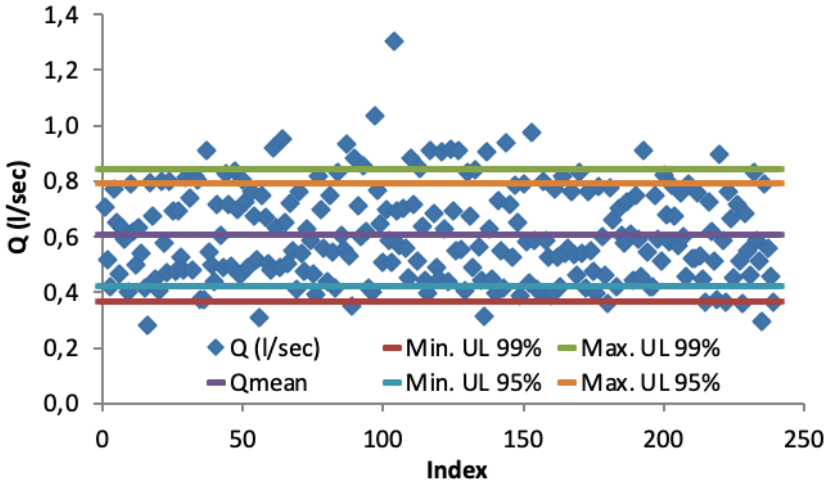


Figure 18. The actual discharge and its mean and uncertainty interval.

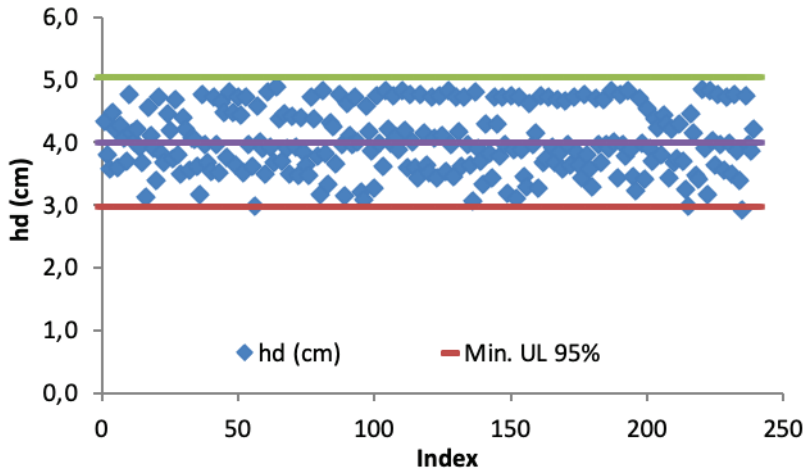


Figure 19. The downstream water depth and its mean and uncertainty interval.

the actual outflow and downstream water depth, as well as the components of uncertainty.

Figures 18 and 19 show plots of the data from Table 13. These graphs depict the mean as a solid line, the 99% and 95% uncertainty intervals for the true mean of the data for actual discharge, and the 95% uncertainty interval for downstream water depth. The uncertainty intervals cover 75% and 88% of the actual discharge values for 95% and 99% uncertainty intervals, respectively, and 100% of downstream water depth data for the 95% uncertainty interval. In this case, the greater variance of the actual discharge compared to the downstream water depth indicates that the experimental data for the actual discharge is more scattered or volatile. Coverage of 100% of the data for the downstream water depth within the uncertainty interval with a confidence level of 95% means that the data is less dispersed relative to the uncertainty interval. Coverage of 75% and 88% for the actual discharge with confidence levels of 95% and 99% reflects a significant increase in dispersion, which requires expanding the range of uncertainty to cover larger proportions of data.

CONCLUSION

The presence of a structure like a pier in the downstream region of the composite hydraulic structure will create a variation in the hydraulic characteristics and the response of the composite hydraulic structure. In addition to the alteration in the flow pattern along the reach of the flume, we can conclude the following vital points:

1. The average downstream water depth has a major impact on the calculated values of the developed moment, drag force, drag coefficient, and static force.
2. The alteration in the flow velocity has a direct impact on the values of the Froude number and Reynolds number.
3. The change in the flow of water depth due to the existence of the pier has a major effect on the values of the Froude number and Reynolds number.
4. The water flow velocity has a major impact on the calculated values of the developed moment, drag force, drag coefficient, and static force.
5. The collar structure has a moderate influence on the hydraulic characteristics of the composite hydraulic structure as compared with the presence of the pier structure.
6. The size of the pier and the collar have a noticeable impact on the values of the Froude number and the Reynolds number.
7. Pier diameter has a dramatic influence on the calculated values of actual discharge, downstream flow velocity, downstream water depth, and moment, which developed at the base of the pier.
8. The water surface profile downstream of the composite hydraulic structure can be described as nonlinear regardless of the pier diameter, collar diameter, and weir shape.
9. Weir shape plays a vital role in dominating the flow pattern between the pier and the composite hydraulic structure.
10. The error margins for actual discharge and downstream water depth are predicted to be 88% and 100% of the values, respectively. Furthermore, the best conclusion is that the downstream water depth is more consistent and dependable in its estimates than the actual discharge, which has a higher variance.

The novelty of the work has been concentrated on how the pier-collar system alter the hydrodynamic behavior and pattern at the downstream of combined structure, also the study deals with the hydraulic variables which has significant impact on the operation of combined structure owing to the pier-collar system, on the other hand the study contains investigation the effect of hydrodynamic response of pier-collar system.

The study limitations relied on several hydraulic and geometrical parameters. For hydraulic parameters, the dominant features are open channel flow regime patterns (flow type), water surface width, water depth before or after placing the weir-gate structure, flow velocity distribution downstream of the weir-gate before and after placing the structure, and flow losses. Geometrical parameters that share in the variation of the open channel or flume regime are pier size, collar size, and vertical distance between the weir and gate. Moreover, the naturality impact of the flume bed has a noticeable effect on flow pattern; in this study, the bed is considered rigid. Therefore, many experiments are done according to information available about the hydraulic features of the prototype channel to avoid any conflict among hydraulic parameters during the weir-gate hydraulic structure's serviceability life.

The implications of the study relied on the hydraulic interaction between flow at downstream of weir-gate structure with flow around pier mounted by collar, therefore to avoid this problem it should be maintained minimum water level or flow rate during hazard conditions like drying season.

It is recommended that before placing the weir-gate structure upstream of the pier in an open channel, many experiments must be done in the laboratory considering many variables that dominate the weir-gate hydraulic response, like weir water head, weir width, gate width, gate water depth, upstream weir-gate water depth, water surface width at upstream and downstream of weir-gate, the horizontal distance between weir-gate and pier, downstream water depth, pier size, and the location of the open channel inlet and outlet concerning both weir-gate and pier. After that, the obtained results were analyzed hydraulically and statistically in order to decide and choose a suitable case.

NOTATION

The following symbols are used in this paper:

H	*Upstream water level*

y	*Distance between top of gate and bottom of weir*
d	*Depth of gate*
b	*width of weir and gate*
B	*Total width of flume and/or composite structure*
h_d	*Downstream water depth*
A_g	*Area of gate*
A_w	*Area of weir*
$Q_{act.}$	*Measured discharge*
$Qw_{theo.}$	*Theoretical discharge through weir*
$Qg_{theo.}$	*Theoretical discharge through gate*
g	*Gravitational acceleration*
$ø$	*Weir angle*
f	*Focal distance*
hu	*Flow depth above weir crest*
Rn	*Reynold's number*
Fr	*Froude number*
V	*Flow velocity*
ρ	*Water density*
F_D	*Drag force*
Ap	*Pier or Collar projected area*
C_D	*Drag Coefficient*
Fp	*Hydrostatic force*
Dp	*Pier diameter*
C_d	*Discharge Coefficient*
H_{nwe}	*Difference between upstream and downstream water depth*
$hd_{average}$	*Average downstream water depth*
S_x	*Random errors*
b_x	*Systematic errors*
u_x	*The standard uncertainty .*
$U_{\bar{x}}$	*The expanded uncertainty*
N	*Number of measurements*
$\bar{x}$	*Mean Value*
$S_{\bar{x}}$	*The standard uncertainty of the mean*
$b_{\bar{x}}$	*The standard deviation associated with systematic errors*
k	*Coverage factor*

AUTHORSHIP CONTRIBUTIONS

Authors equally contributed to this work.

DATA AVAILABILITY STATEMENT

The authors confirm that the data that supports the findings of this study are available within the article. Raw data that support the finding of this study are available from the corresponding author, upon reasonable request.

CONFLICT OF INTEREST

The author declared no potential conflicts of interest with respect to the research, authorship, and/or publication of this article.

ETHICS

There are no ethical issues with the publication of this manuscript.

STATEMENT ON THE USE OF ARTIFICIAL INTELLIGENCE

Artificial intelligence was not used in the preparation of the article.

REFERENCES

[1] Qasim RM, Abdulhussein IA, Mohammed AA, Maatooq QA. Evaluation of the hydraulic behavior of the composite hydraulic structure considering a bed flume with special obstacle. INCAS Bull 2022;14:61–74. [CrossRef]

[2] Abdulhussein IA, Qasim RM, Mohammed AA, Maatooq QA. Flow-composite hydraulic structure-longitudinal obstacle interaction. Int J Geomate 2022;23:40–49. [CrossRef]

[3] Abdulhussein IA, Qasim RM, Maatooq QA. Hydraulic interaction between composite structure and block obstacle. Int J Tech Phys Probl Eng 2022;14:65–73.

[4] Qasim RM, Abdulhussein IA, Mohammed AA, Maatooq QA. The effect of the obstacle on the hydraulic response of the composite hydraulic structure. INCAS Bull 2020;12:159–172. [CrossRef]

[5] Qasim RM, Abdulhussein IA, AL-Asadi K. The effect of barrier on the hydraulic response of composite weir-gate structure. Arch Civ Eng 2020;66:98-118.

[6] Qasim RM, Mohammed AA, Abdulhussein IA, Maatooq QA. Experimental investigation of multi obstacles impact on weir-gate discharge structure. Int J Mechatron Appl Mech 2021;9:76–84.

[7] Abdulhussein IA, Qasim RM, Hameed MA. Determination of the general formula to estimate the discharge quantity of composite structure for free flow. Instrum Meas Metrol 2022;21:13–20. [CrossRef]

[8] Qasim RM, Abdulhussein IA, AL-Asadi K. Experimental study of composite inclined weir–gate hydraulic structure. WSEAS Trans Fluid Mech 2020;15:54–61. [CrossRef]

[9] Abdulhussein IA, Qasim RM, Al-Asadi K, Maatooq QA. The influence of weir crest on the hydraulic characteristics of a composite structure. Test Eng Manag 2020;83:24731–24743.

[10] Qasim RM, Mohammed AA, Abdulhussein IA. Review: weir–gate composite irrigation structure. Int J Eng Tech 2019;5:1–9.

[11] Qasim RM, Abdulhussein IA, Maatooq QA. Effect of bed flume contraction on discharge coefficient of composite weir-gate structure. Int J Sci Eng Investig 2019;8:40–45.

[12] Qasim RM, Abdulhussein IA, Hameed MA, Maatooq QA. Experimental study of coupled parabolic weir over flow and gate under flow rate. J Inf Eng Appl 2018;8:34–42.
[13] Qasim RM, Abdulhussein IA, Hameed MA, Maatooq QA. Experimental study of hydraulic response for combined weir-gate flow of composite shape. Civ Environ Res 2018;10:6–14.
[14] Qasim RM, Abdulhussein IA, Hameed MA. Analysis of flow over weir and under ellipse gate. Innov Syst Des Eng 2018;9:1–9.
[15] Qasim RM, Mohammed AA, Abdulhussein IA. An investigating of the impact of bed flume discordance on the weir-gate hydraulic structure. HighTech Innov J 2022;3:341-355. [CrossRef]
[16] Gharehbaghi A, Ghasemlounia R, Afaridegan E, Haghiabi A, Mandala V, Azamathulla HM, Parsaie A. A comparison of artificial intelligence approaches in predicting discharge coefficient of streamlined weirs. J Hydroinform 2023;25:1513. [CrossRef]
[17] Li S, Shen G, Parsaie A, Li G, Cao D. Discharge modeling and characteristic analysis of semi-circular side weir based on the soft computing method. J Hydroinform 2024;26:175-188. [CrossRef]
[18] Iqbal M, Ghani U. Prediction of the discharge capacity of piano key weirs using artificial neural networks. J Hydroinform 2024;26:175-188. [CrossRef]
[19] Kartal V, Emiroglu ME. Experimental analysis of combined side weir-gate located on a straight channel. Flow Meas Instrum 2022;88:102250. [CrossRef]
[20] Nouri M, Hemmati M. Discharge coefficient in the combined weir-gate structure. Flow Meas Instrum 2020;75:101780. [CrossRef]
[21] Streeter VL, Wylie EB. Fluid Mechanics. 1st SI Metric ed. New York: McGraw-Hill; 1983.
[22] Bos MG. Discharge Measurement Structures. 3rd ed. Int Inst Land Reclam Improv. The Netherlands: Wageningen; 1989.
[23] Fox RW, McDonald AT. Introduction to Fluid Mechanics. 4th SI ed. New York: John Wiley and Sons; 1994.
[24] Cheng NS. Calculation of drag coefficient for arrays of emergent circular cylinders with pseudo fluid model. J Hydraul Eng 2013;139:602–611. [CrossRef]
[25] Sharma MK, Sadhna AK, Bhargava, Kumar S, Rathour L, Mishra LN, Pandey S. A Fermatean fuzzy ranking function in optimization of intuitionistic fuzzy transportation problems. Adv Math Models Appl 2022;7:191–204.
[26] Sharma MK, Dhiman N, Kumar S, Rathour L, Mishra VN. Neutrosophic Monte Carlo simulation approach for decision making in medical diagnostic process under uncertain environment. Int J Neutrosophic Sci 2023;22:8–16. [CrossRef]
[27] Rathour L, Singh V, Yadav H, Sharma MK, Mishra VN. A dual hesitant fuzzy set theoretic approach in fuzzy reliability analysis of a fuzzy system. Inf Sci Lett 2024;13:433–440. [CrossRef]
[28] Chandola A, Pandey RM, Agarwal R, Rathour L, Mishra VN. On some properties and applications of the generalized m-parameter Mittag-Leffler function. Adv Math Models Appl 2022;7:130–145.
[29] Sharma MK, Chaudhary S, Rathour L, Mishra VN. Modified genetic algorithm with novel crossover and mutation operator in travelling salesman problem. Sigma J Eng Nat Sci 2024;42:1876-1883. [CrossRef]
[30] Negero NT, Duressa GF, Rathour L, Mishra VN. A novel fitted numerical scheme for singularly perturbed delay parabolic problems with two small parameters. Partial Differ Equ Appl Math 2023;8:1–8. [CrossRef]
[31] Hogeme MS, Woldaregay MM, Rathour L, Mishra VN. A stable numerical method for singularly perturbed Fredholm integro differential equation using exponentially fitted difference method. J Comput Appl Math 2024;441:115709. [CrossRef]
[32] Younus A, Dastgeer Z, Rathour L, Mishra LN, Mishra VN, Pandey S. Distinguishability criteria of conformable hybrid linear systems. Nonlinear Eng 2022;11:420–427. [CrossRef]
[33] Coleman HW, Steele WG. Experimentation, validation, and uncertainty analysis for engineers. 3rd ed. New York: Wiley; 2009. [CrossRef]
[34] JCGM 100: Evaluation of measurement data—Guide to the expression of uncertainty in measurement. GUM 1995 with minor corrections. Int Bureau of Weights and Measures (BIPM), Serres, France, 2008.

Sigma Journal of Engineering and Natural Sciences
Web page info: https://sigma.yildiz.edu.tr
DOI: 10.14744/sigma.2025.1912

Research Article

Effect of reinforcements in aluminium 5052-magnesium AZ31 explosive cladding

S. SARAVANAN[1]

[1]Department of Mechanical Engineering, Annamalai University, Annamalainagar, Tamilnadu, 608002, India

ARTICLE INFO

Article history
Received: 18 April 2024
Revised: 03 August 2024
Accepted: 13 October 2024

Keywords:
Aluminium 5052; Explosive Cladding; Magnesium AZ31; Microstructure. Silicon Carbide; Strength; Wire-Mesh

ABSTRACT

Aerospace, automobile, and marine industries prefer aluminium-magnesium weld joints for the fabrication of lightweight, corrosion-resistant structures. However, at elevated temperatures, they suffer from reduced strength and display potential for cracking. Hence, in this study, a innovative approach of combining explosive energy and reinforcement materials to improve the strength, thermal stability, ductility, and performance of the aluminium 5052-magnesium AZ31 clads, through explosive cladding is attempted. The interface micrograph of the conventional clad (no reinforcement) shows the continual presence of molten intermetallic layer. The layer formation is inhibited by introducing a stainless steel wire-mesh between the mating alloys, which reduces the velocity of the aluminium sheet owing to the enhanced friction. Similarly, the addition of silicon carbide particles along with the wire-mesh evades the straight impact of mating alloys and thereby suppresses the formation of reaction compounds. With respect to mechanical strength, the clad having both wire-mesh and silicon carbide reinforcement attains the maximum hardness (285 Hv), ram tensile (302 MPa), and shear strength (175 MPa), followed by wire-mesh-reinforced clad (hardness-245 Hv, tensile strength-254 MPa, shear strength-146 MPa), and conventional clad (hardness -98 Hv, tensile strength-102 MPa, shear strength-59 MPa).

Cite this article as: Saravanan S. Effect of reinforcements in aluminium 5052-magnesium AZ31 explosive cladding. Sigma J Eng Nat Sci 2025;43(6):2084–2093.

INTRODUCTION

Magnesium alloys are promising candidates in automobile, and aircraft manufacturing due to their lower density, higher strength, good machining ability, and high damping capacity [1]. In addition, magnesium alloys are eco-friendly in nature [2]. However, detrimental qualities, such as strong chemical vulnerability, low resistance to corrosion, poor room temperature ductility, and wear resistance, limit their industrial applications [3]. To counter this, magnesium is welded with other alloys, such as aluminium, in order to utilize the beneficial characteristics of both [4]. Aluminium alloys are preferred due to their better strength-to-weight ratio, greater resistance to corrosion, better plastic deformation capacity, and higher ductility [5]. The aluminium-magnesium weld joints are used to construct light weight corrosion resistant components in ship building, aircraft and automotive components. Earlier researchers

*Corresponding author.
*E-mail address: ssvcdm@gmail.com

This paper was recommended for publication in revised form by Editor-in-Chief Ahmet Selim Dalkilic

Published by Yıldız Technical University Press, İstanbul, Turkey
© Author. This is an open access article under the CC BY-NC license (http://creativecommons.org/licenses/by-nc/4.0/).

employed various welding techniques to join aluminium and magnesium and are recapitulated below.

In an earlier study, Wang et al. attempted Al-Mg laser welding and reported the presence of γ-$Mg_{17}Al_{12}$ and β-Mg_2Al_3 compounds, which affected the strength adversely [6]. To mitigate the intermetallic compound formation, Meng et al. successfully employed a titanium interlayer between Al and Mg alloys in the laser-arc hybrid lap welding [7]. Likewise, a similar result was obtained by Kumar and Wu, who performed friction stir welding with a nickel interlayer [8]. Varmazyar and Khodaei, on the other hand, used a copper interlayer in diffusion bonding of Al-Mg alloys at various strain conditions (0, 30, and 60%) and holding durations. They concluded that the interlayer reduces the hardness and shear strength [9]. In order to attain higher strength and a defect-free Al 1050–AZ31 alloy magnetic pulse weld, Zhu et al. optimized the process parameters, such as discharge energy and standoff distance [10]. In this context, Jian et al. analyzed the fatigue crack behavior in Al-Mg metal inert-gas welding. They concluded that the stress, bubble formation, orientation of the grain, and coarse grain formation dictated the crack growth [11]. Meanwhile, Liang et al., while friction welding Al-Mg alloys, determined the correlation between constitutional liquation and microstructure [12]. Based on the literature, the main challenge in Al-Mg welding is the development of deleterious reaction compounds and crack formation, which impacts the weld strength negatively. To counter this, explosive cladding provides a feasible solution due to its rapidity and ability to clad larger areas.

With respect to Al-Mg explosive cladding, the metallurgical, mechanical, and corrosion properties of AZ31-Al 5005 clad were studied by Acarer et al. [13]. Meanwhile, Chen et al. concluded that the process parameters, such as explosive mass and standoff distance, are directly proportional to the clad strength [14]. Similarly, Ghaderi et al. [15] developed a welding window and correlated the microstructure and strength characteristics with its positioning [16]. In this context, Paul et al. attempted explosive cladding of eleven Al-Mg foil layers and reported cracks and poor formability due to inadequate energy [17]. In a different attempt, Zeng et al. conducted their explosive cladding trials in a helium atmosphere and obtained superior mechanical properties [15]. Numerical simulation of Al-Mg explosive cladding was separately attempted by Feng et al. [18] and Kumar et al. [1] to determine the temperature and pressure created during the process. In a recent study, Su et al. observed delamination due to impact in Al-Mg explosive cladding [19]. The novelty of this study lies in the innovative use of wire-mesh and silicon carbide reinforcements in the explosive cladding of aluminium-magnesium alloys. By integrating these reinforcements, the study aims to enhance the microstructural refinement and mechanical properties of the clad. The combination of explosive energy and reinforced materials creates a unique interfacial bonding mechanism that improves strength, hardness, and corrosion resistance. This approach offers a new pathway for producing high-performance clad materials with tailored properties, suitable for applications in industries like aerospace, automotive, and defence where lightweight yet strong materials are crucial.

MATERIALS AND METHODS

Al 5052 sheets (chemical composition wt. %: Si-0.25, Mg-2.9, Cr-0.25, Cu-0.1, Mn-0.1, Zn-0.1, Fe-0.4, Al-Bal.) and AZ 31B plates (chemical composition wt. %: Al-2.8, Zn-1.75, Si-0.1, Mn-0.2, Cu-0.05, Mg-Bal.), purchased from Parshwamani Metals, Mumbai, India, were employed as flyer and base plate, respectively. The dimensions of the flyer and base plate are 110 mm x 80 mm (length x breadth), with thicknesses of 2 mm and 6 mm, respectively.

Three explosive cladding experiments, viz., Al-Mg, Al-Mg with stainless steel wire-mesh (purchased from Sysco Piping Solutions Inc., Mumbai, India), and Al-Mg with stainless steel wire-mesh (mesh size of 0.704 mm) and SiC (purchased from Parshwamani Metals, Mumbai, India: 100-120 μm size), were performed at a uniform loading ratio, R (ratio of the mass of the explosive and flyer plate) of 0.8 and 5 mm standoff distance, SD (between flyer and base plates). The parameters were chosen based on preliminary experimental trials. The energy source was the SUN 90 chemical explosive (manufactured by M/s. Vetrivel Explosives Private Limited) having a density of 1.15 g/cm^3 and a detonation velocity of 4200 m/s and was mounted on a 2 mm thick cardboard buffer plate. The reinforcements, viz., stainless steel wire-mesh (chemical composition wt. %: C-0.085, Cr-18, Mn-2, Mo-3, Ni-14, Si-1, S-0.03, Fe-Bal.) of dimension (110 x 80 mm x 0.3 mm) and SiC (micrograph shown in Fig.1) having 1% by weight of flyer plate, are dispersed, separately and together, on the base plate and were cladded by parallel explosive cladding (Fig. 1). Further increase in SiC reinforcements resulted in agglomeration resulting in increased brittleness.

Prior to cladding, the participant alloys and stainless steel wire-mesh (Fig. 2a) were annealed for one hour, followed by furnace cooling (Wire-mesh-900^{0}C, Al-400^{0}C, AZ31B-425^{0}C) to homogenize the metallurgical structure. To ensure good quality, the roughness of the mating surfaces is maintained below 1 μm. Based on the experimental parameters of the welding window, an analytical estimation to determine the nature of the explosive clad interface is determined. The welding window comprises lower and upper boundaries, which are calculated by equations 1 and 2, respectively [20, 21].

$$\beta = 1.14\sqrt{\frac{H_V}{\rho V_C^2}} \quad (1)$$

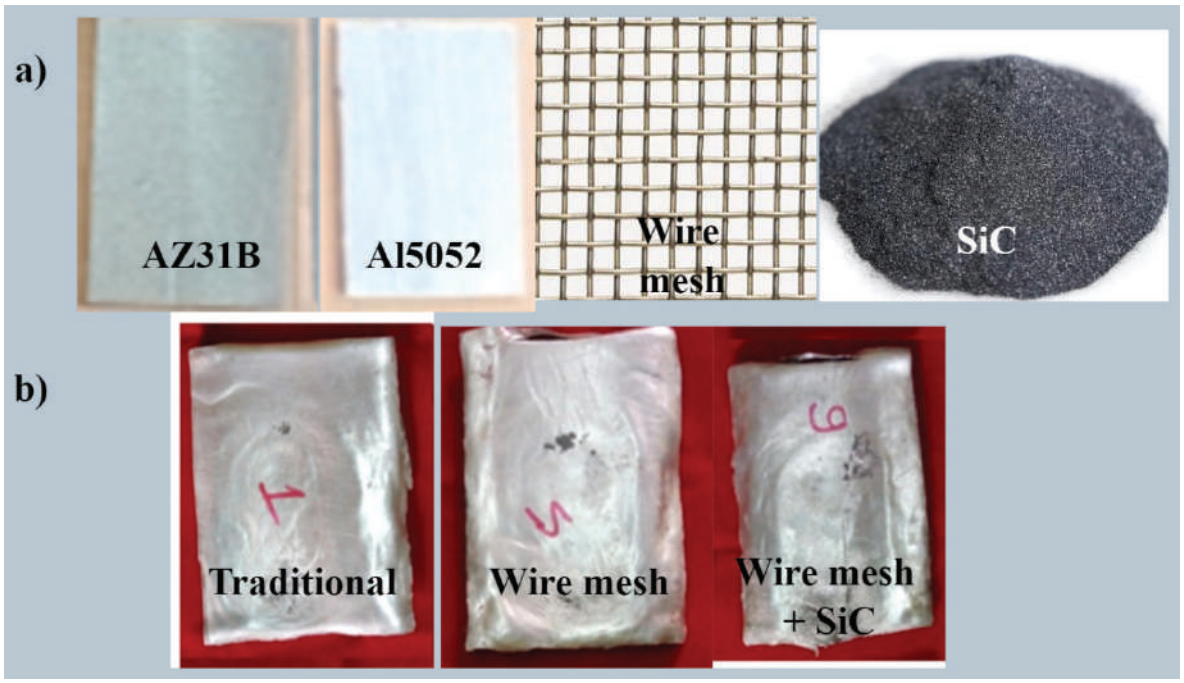


Figure 2. (a) Participant alloys and inclusions (b) explosive clads.

$$\sin\frac{\beta}{2} = \frac{k_3}{\left(t^{0.25}.V_C^{\ 1.25}\right)} \quad (2)$$

Where $k_3 = C_f/2$, $C_f = \sqrt{K/\rho}$, $K = E/3(1-2\nu)$,

The flyer plate moves towards the base plate obliquely at angle β, which is calculated by [22]

$$\beta = 2\sin^{-1}\frac{V_p}{2V_d} \quad (3)$$

Where the flyer plate velocity, V_p is determined by [23]

$$V_p = V_d\,\frac{0.612R}{(2+R)} \quad (4)$$

The experimental conditions attempted in the study are shown as green triangle, which falls inside the boundaries of the welding window (Fig. 3). The photographs of the resulting explosive clads are shown in Figure 2b.

After cladding, the specimens were subjected to standard metallographic procedures and etched for 30 seconds. A VERSAMET optical microscope and a JOEL

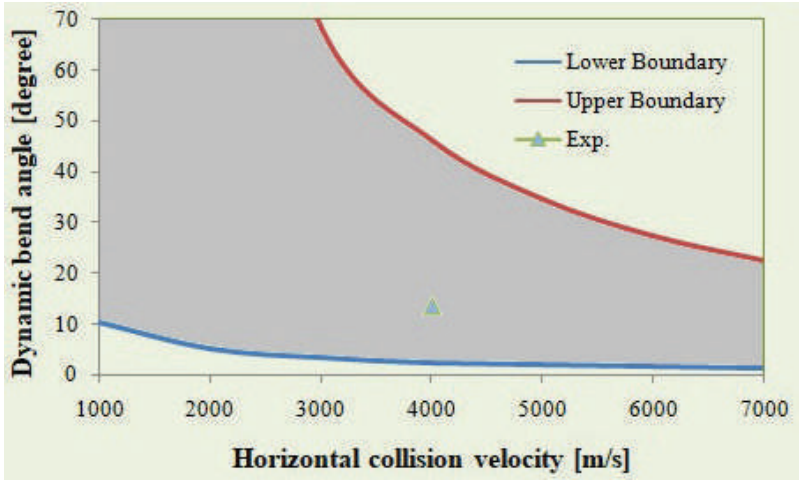


Figure 3. Welding window for Al 5052-AZ 31B explosive cladding.

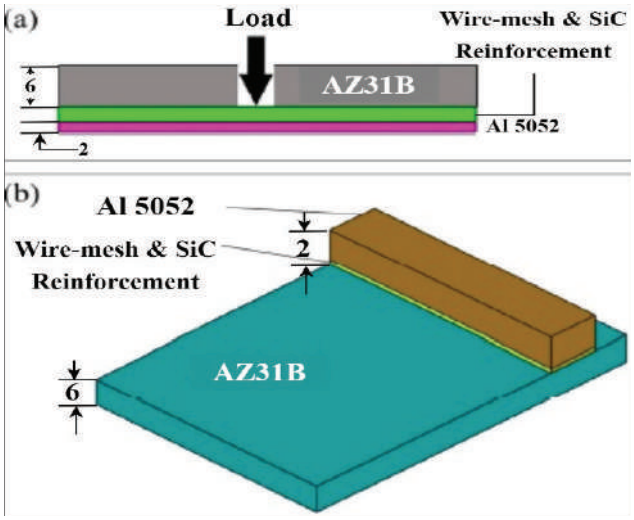


Figure 4. (a) Ram tensile test (b) Shear test.

(JSM-6610LV) scanning electron microscope equipped with EDS were utilized to analyze the microstructures. The constituents of various phases in the interface were identified with a CuK-equipped XRD (Philips X'PERT MPD diffractometer). The phases present in the sample are identified by comparing the observed diffraction peaks with standard reference card numbers. A ZWICK micro-hardness tester with an indenter load of 50g for 10s determines the Vickers hardness across the interface. Ram tensile (Fig. 4 a: MIL-J-24445A) and shear (Fig. 4b: ASTM B 898) tests were performed using 0.2 mm/min and 0.5 mm/min tensile and shear loads, respectively.

RESULTS AND DISCUSSION

Micrograph of the Conventional Al 5052-AZ31B Explosive Clad

The dissimilar explosive clad interface micrograph reveals an undulating nature along with an incessant molten layer (Fig. 5a). The molten layer, weak and fragile regions, is formed due to the utilization of whole kinetic energy (ΔKE) at the interface (0.79 MJ/m^2) followed by rapid cooling. The kinetic energy utilization is analytically determined by [24],

$$\Delta KE = \frac{m_f m_b V_p^2}{2(m_f + m_b)} \quad (5)$$

The effective utilization of kinetic energy promotes a wavy interface; otherwise, a molten layer is formed, as seen in Fig. 5a, if the additional kinetic energy is utilized. Somasundaram et al., while cladding titanium-steel, also observed a streak of molten layer at a higher kinetic energy environment, consistent with the present study [25]. The presence of a molten layer holds a negative impact on the strength characteristics, detailed in sections 3.3 and 3.4.

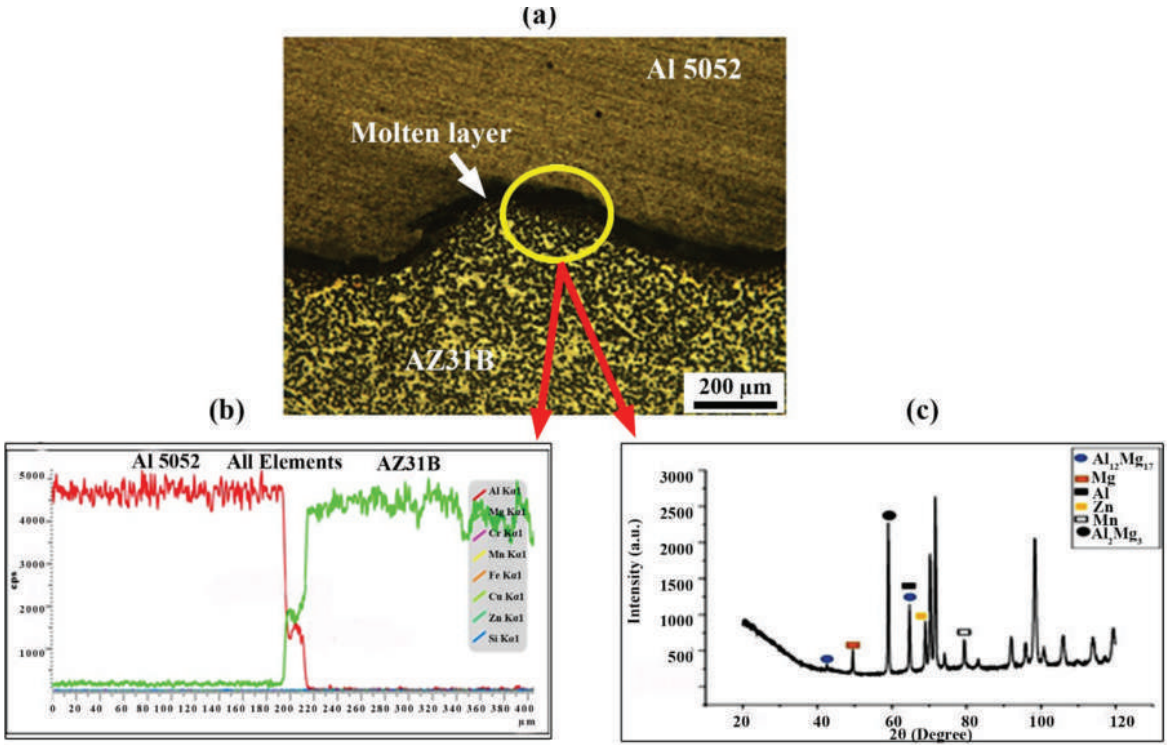


Figure 5. (a) Al 5052-AZ 31B micrograph (b) EDS (c) XRD.

The interface region (depicted by a circle in Fig. 5b) subjected to the EDS examination confirmed higher atomic percentages of aluminium and magnesium, along with a very lower concentration of Cr, Mn, Fe, Cu, and Si elements. Further analysis by the XRD (Fig. 5c) substantiates the existence of $Al_{12}Mg_{17}$ and Al_2Mg_3 compounds (card number: 00-025-1207) at the interface. To counter the intermetallic compound formation, reinforcements are introduced between the mating alloys, and the results are presented below.

Effect of Reinforcements on the Interface Micrograph

The variation in dissimilar clad micrographs, with and without reinforcements for the same parametric conditions, is noteworthy and obvious. The continuous presence of molten layer found in Al 5052-AZ 31B cladding (Fig. 5) is absent in the clads having reinforcements (Fig. 6, 7). The SiC is visible as a black strip, while the stainless steel wire-mesh is seen as white oval dots.

The insertion of a stainless steel wire-mesh transforms the molten layer prevailed in Al 5052-AZ 31B explosive clad into a defect free clad (Fig. 6 a,b). The dynamic collision of aluminium sheet with the wire-mesh instead of magnesium plate, promotes this transformation. The surface variations on the wire-mesh enhance the friction, and reduce the flyer plate velocity (V_p). In addition, the weight of the base plate, m_b (Eq. 5) increases as well. As a consequence, ΔKE improves to 0.81 MJ/m^2, and hinders the interfacial molten layer. The XRD (Fig. 6 c) analysis displays taller Fe, Mg, and Al peaks and a smaller Fe_3Al peak (card number: 03-065-1477). The marginal presence of reaction compounds at the interface is consistent with Gulenc et al [26].

The usage of both stainless steel wire-mesh and SiC particles, as reinforcements, on the base plate further increases the weight of the base plate (m_b), and hence ΔKE (Eq. 5) increases to 0.83 MJ/m^2. The increased ΔKE deforms the SiC particles further, forcing them to trap inside the openings in stainless steel wire-mesh, visible as a thin black strip (Figs. 7 a and b). This band formation at the interface by the SiC particles is consistent with earlier researchers [27, 28].

In addition, the primary chemical relationship between wire-mesh and SiC is quite weak [29]. Subsequently, an intermetallic free clad emerges between the flyer and base plates. The superior thermal conductivity, K of SiC (350 W/mK), accelerates the solidification and prevents the formation of a molten layer as well. The XRD spectrum confirms the existence of Fe, Al, and SiC elements at the interface and the nonexistence of element diffusion across the alloys (Fig. 7c). Since the SiC streak prevents the direct contact, the intermetallic compounds formed in the Al-Mg clad without reinforcements are eliminated. Further, the higher

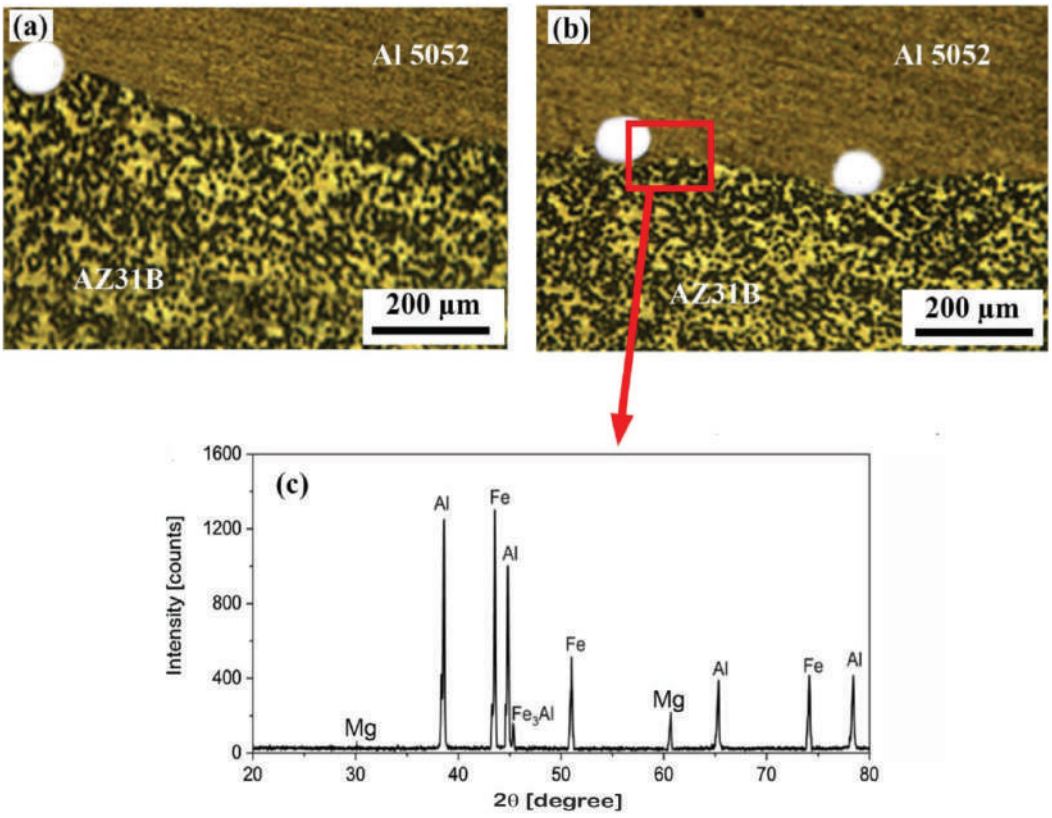


Figure 6. (a,b) Al 5052-WM-AZ 31B explosive clad micrograph (c) XRD.

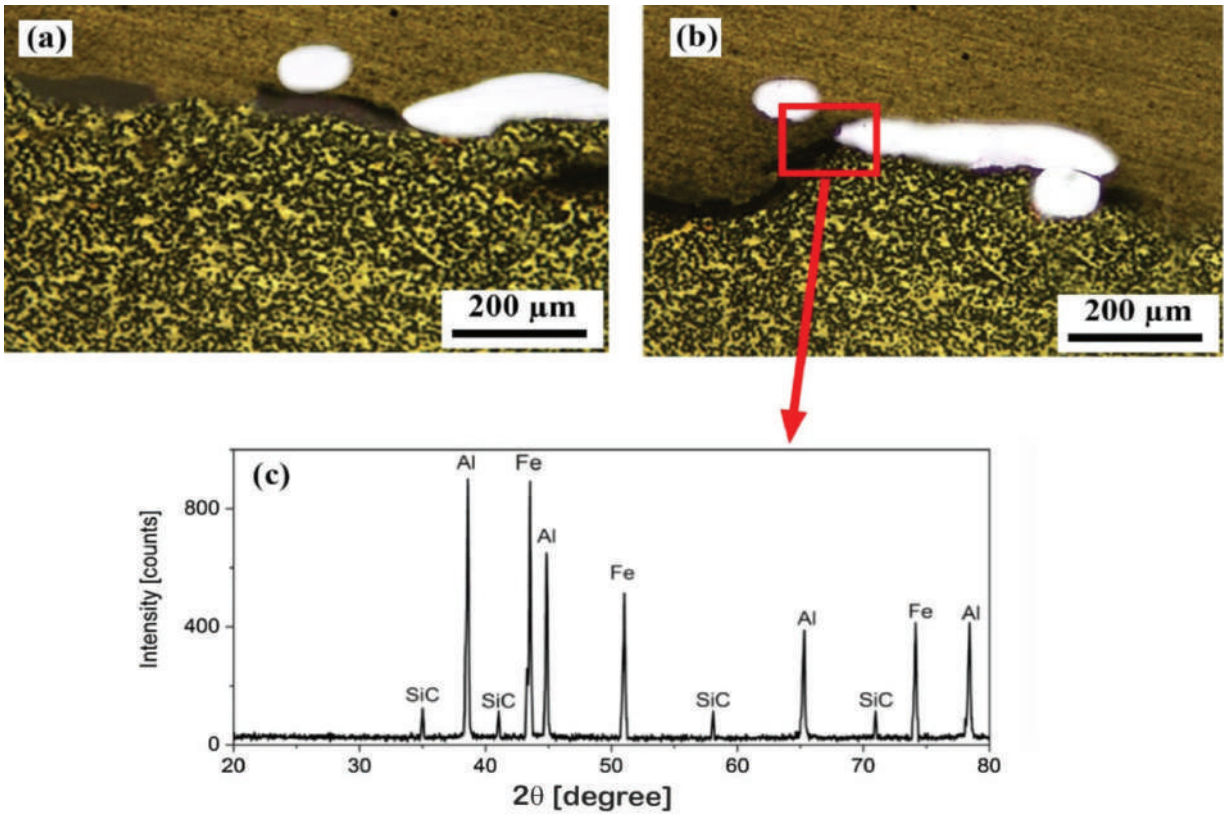


Figure 7. (a,b) Al 5052--AZ 31B explosive clad microstructure with wire-mesh and SiC reinforcements (c) XRD.

strength of these reinforcements improves the strength of the dissimilar clads, detailed in the next section.

Hardness

The average of two hardness measurements across the dissimilar reinforced explosive clad is higher than the clad having no reinforcements (Fig. 8). Further, the highest hardness is observed at the interfaces in all three experiments. The augment is attributed to the sudden impact and the existence of reinforcements. In addition, the rapid nature of the process restricts the interface to experiencing the increase in temperature. As a result, the impact of annealing is mitigated, and hence the hardness of the interface increases.

The interface of the stainless steel wire-mesh and SiC reinforced clad (Fig. 8c: 285 H_v) achieves the highest hardness as both reinforcements have great adhesion to the participating alloys. The existence of wire-mesh and the absence of SiC reduce the interface hardness by 16% to result in a hardness of 245 H_v (Fig. 8 b). The hardness of the Al 5052-WM-AZ 31B interfaces devoid of wire-mesh attains 120H_v, which is higher than the Al-Mg explosive clads (Fig. 8 a: 98Hv). However, the lower interface hardness is higher than the base alloys (Al -68 H_v and Mg -76 H_v), consistent with Inao et al [30]. Further, it is noted that the increase is not evident at locations 200 µm distant from the interface owing to the negligible plastic deformation, as reported by Chen et al. [31].

Ram Tensile and Shear Strengths

Figure 9 illustrate the ram tensile and shear strengths of the parent alloys and the dissimilar explosive clads attempted (stress-strain curves are given in Fig. 10). The use of reinforcements enhanced the ram tensile and shear strengths of the clads, and the maximum is obtained when both wire-mesh and SiC are reinforced (ram tensile-302 MPa, shear strengths-175 MPa). This is due to the cohesiveness of reinforcements and the absence of intermetallic compounds.

The Al 5052-AZ 31B explosive clad reinforced with a wire-mesh attains an 18% lower strength (ram tensile-254 MPa and shear-146 MPa). The reduction in strength is due to the absence of SiC particles. However, the obtained values are higher than the conventional Al 5052-AZ 31B explosive clad (102 MPa and 59 MPa) and base alloys. The reports of earlier researchers who attempted dissimilar cladding are consistent with this behaviour [32, 33].

The fractograph of Al 5052-AZ 31B explosive clad obtained from the ram tensile test (Fig. 11a) reveals a ductile fracture mode with a cup-cone shape. The fracture surface is dominated by a uniform distribution of bigger aluminium (flyer plate) shatter, confirming its larger flow before

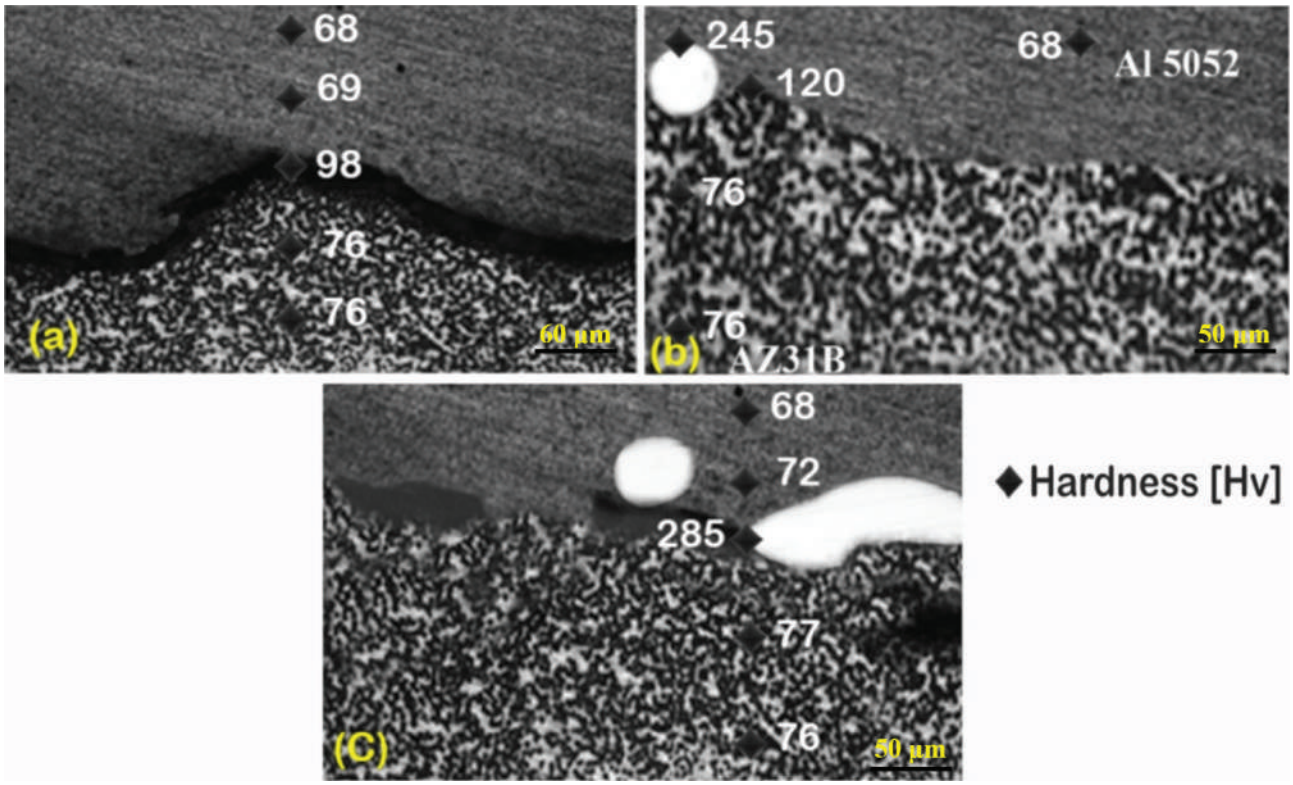


Figure 8. Hardness variation across the interface (a) Al 5052-AZ 31B (b) Al 5052-SS WM-AZ 31B (c) Al 5052-SS WM-SiC-AZ 31B .

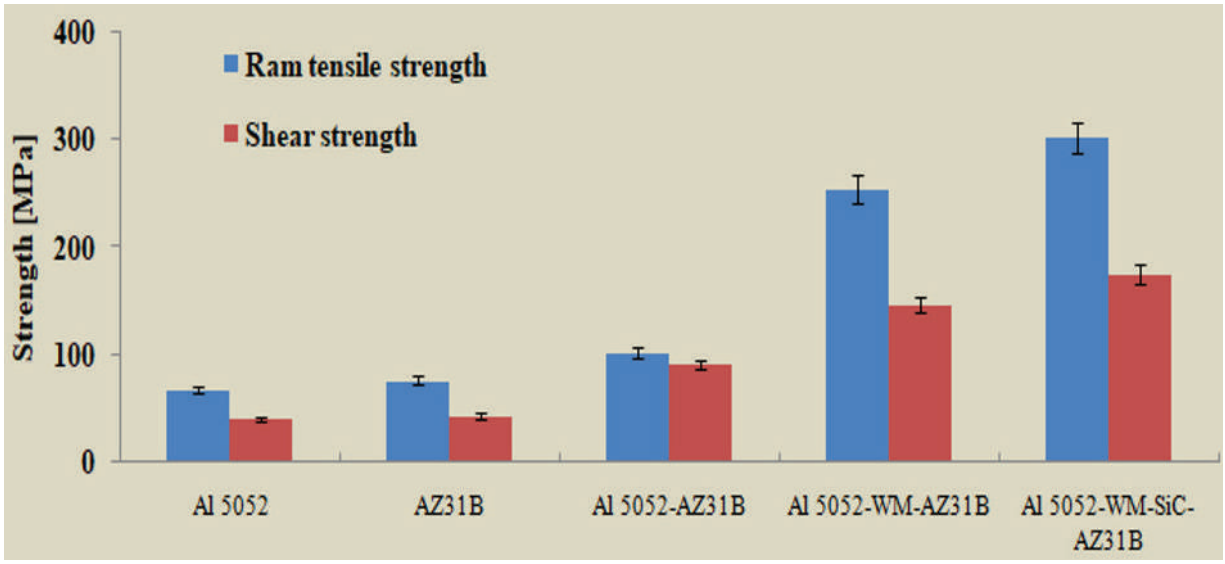


Figure 9. Ram tensile and shear strengths of the base alloys and explosive clads.

fracture. The impression created by the pulling of wires is visible in the fracture surface of the wire-mesh reinforced clad (Fig. 11b). Also, the fracture surface exhibits the evidence for a ductile mode of fracture. No significant defects are seen on the fractured surface. The fracture image of the Al 5052-WM-SiC-AZ31B explosive clad (Fig. 11c) is free from cleavage or intergranular fracture characteristics of the brittle fracture, as stated by Kumar et al [34]. Likewise, the evidence of wire-mesh and SiC sheared surfaces (Fig. 11d) with fibrous networks along with dimples is seen on

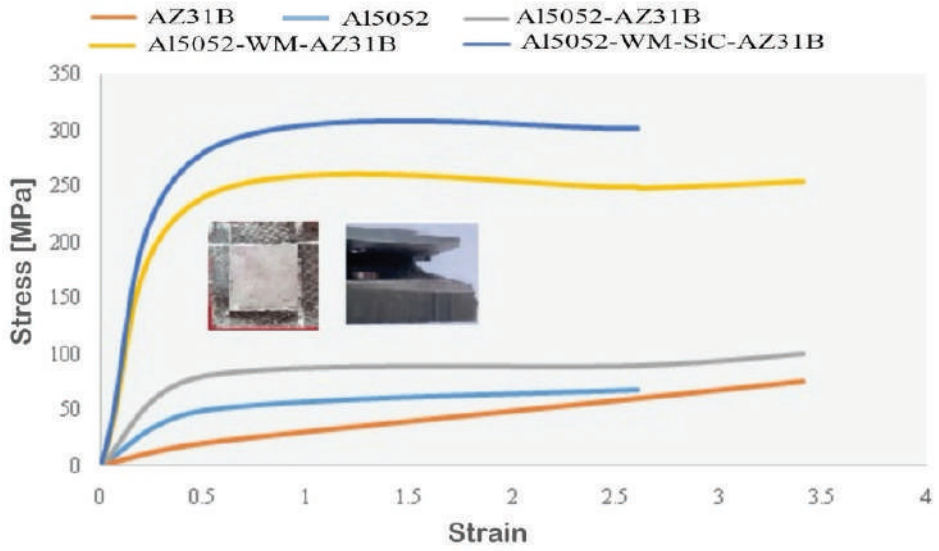


Figure 10. Stress-strain curve.

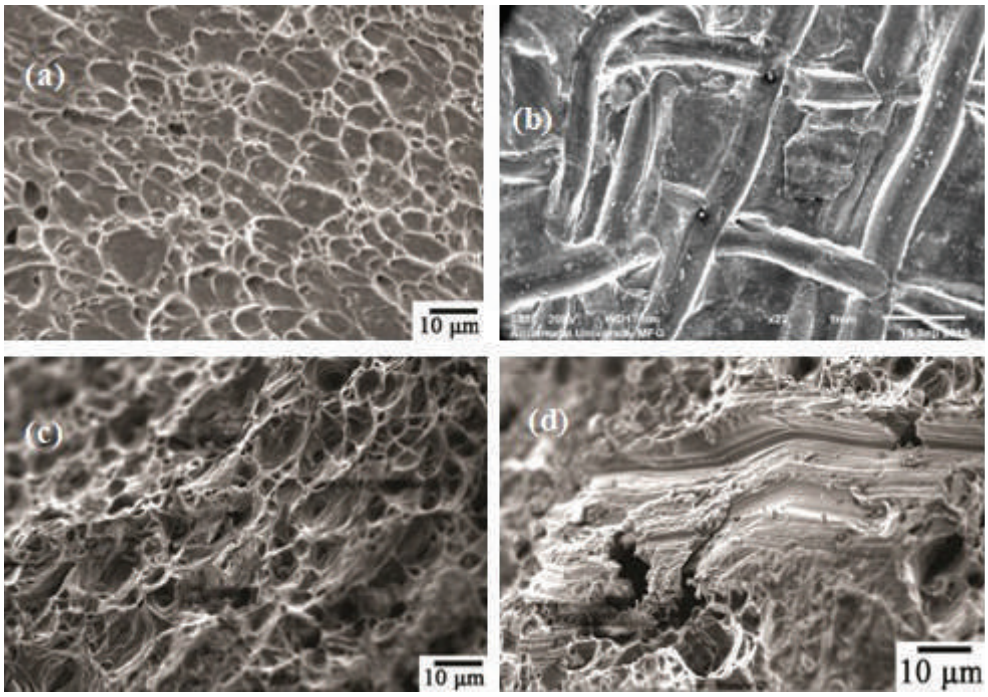


Figure 11. (a-c) Ram tensile interface fracture (a) Al 5052-AZ31B (b) with wire-mesh (c) with wire-mesh and Sic (d) Shear fracture surface of wire-mesh and SiC.

the shear surface obtained from the dissimilar explosive clad.

Therefore, we conclude that the industry offers significant potential for the application of SiC and wire-mesh reinforced Al/Mg explosive clad due to its ability to create strong, lightweight, and corrosion-resistant materials. The scalability of explosive cladding hinges on optimizing the process parameters to attain larger plates, enabling mass production. The long-term benefits such as reduced material waste, improved performance, and durability make it attractive. Explosive cladding of Al/Mg is suitable for aerospace, automotive, and marine industries where light weight coupled with high-performance materials are inevitable.

CONCLUSION

The salient findings of the novel study on the usage of reinforcements in explosive cladding of aluminium 5052-magnesium AZ31B explosive cladding are summarized here. The use of reinforcements in explosive cladding of weaker aluminium and magnesium alloys reduce the intermetallic formation and improve the ram tensile and shear strengths. The friction between the aluminium and magnesium is improved by the insertion of wire-mesh due to its potholed nature. Subsequently, the wire-mesh penetrates inside the mating alloys to create a strong bond. The silicon carbide particles form a band between dissimilar alloys to avoid the formation of reaction compounds, resulting in improved ram tensile (302 MPa) and shear (175 MPa) strengths. It is recommended to employ reinforcements in aluminium-magnesium explosive cladding.

NOMENCLATURE

ΔKE	Kinetic energy available (MJ/m^2)
Al	Aluminium
C	Carbon
$C_2H_2O_4$	Oxalic acid
C_f	Compressive wave velocity (m/s)
CH_3COOH	Acetic acid
Cr	Chromium
Cu	Copper
E	Young's modulus (N/m^2)
EDS	Energy Dispersive Spectroscope
Fe	Iron
H_v	Vickers hardness (N/m^2)
m_b	Mass of the base plate per unit area
m_f	Mass of the flyer plate per unit area
Mg	Magnesium
Mn	Manganese
Mo	Molybdenum
NaOH	Sodium hydroxide
Ni	Nickel
R	Loading ratio (mass of explosive /mass of flyer plate)
S	Sulfur
SD	Standoff distance (mm)
SEM	Scanning Electron Microscope
Si	Silicon
SiC	Silicon carbide particle
t	Flyer plate thickness
V_c	Collision point velocity(m/s)
V_d	Detonation velocity of the explosive
V_p	Velocity of the flyer plate (m/s)
WM	Wire-mesh
XRD	X-ray diffraction
Zn	Zinc
β	Dynamic bend angle (degree)
ν	Poisson's ratio
ρ	Density (kg/m^3)

AUTHORSHIP CONTRIBUTIONS

Authors equally contributed to this work.

DATA AVAILABILITY STATEMENT

The authors confirm that the data that supports the findings of this study are available within the article. Raw data that support the finding of this study are available from the corresponding author, upon reasonable request.

CONFLICT OF INTEREST

The author declared no potential conflicts of interest with respect to the research, authorship, and/or publication of this article.

ETHICS

There are no ethical issues with the publication of this manuscript.

STATEMENT ON THE USE OF ARTIFICIAL INTELLIGENCE

Artificial intelligence was not used in the preparation of the article.

REFERENCES

[1] Kumar P, Ghosh SK, Saravanan S, Barma JD. Experimental and simulation studies on explosive welding of AZ31B-Al 5052 alloys. Int J Adv Manuf Technol 2023;127:2387–2399. [CrossRef]

[2] Jin Q, Tian G, Li J, Zhao Y, Yan H. The study on corrosion resistance of superhydrophobic magnesium hydroxide coating on AZ31B magnesium alloy. Colloids Surf A Physicochem Eng Asp 2019;577:8–16. [CrossRef]

[3] Sairam YNV, Cherukuri TS, Kurra HP. A short review on magnesium alloys in multiple domains. Sigma J Eng Nat Sci 2023;41:1062–1069.

[4] Liu L, Ren D, Liu F. A review of dissimilar welding techniques for magnesium alloys to aluminum alloys. Materials 2014;7:3735–3757. [CrossRef]

[5] Saravanan S, Gajalakshmi K. Soft computing approaches for comparative prediction of ram tensile and shear strength in aluminium–stainless steel explosive cladding. Arch Civil Mech Eng 2022;22:1–16. [CrossRef]

[6] Wang HY, Liu LM, Jia ZY. The influence of adhesive on the Al alloy in laser weld bonding Mg–Al process. J Mater Sci 2011;46:5534–5540. [CrossRef]

[7] Meng Y, Lu Y, Li Z, Zhao S, Gao M. Effects of beam oscillation on interface layer and mechanical properties of laser-arc hybrid lap welded Al/Mg dissimilar metals. Intermetallics 2021;133:107175. [CrossRef]

[8] Kumar S, Wu C. Eliminating intermetallic compounds via Ni interlayer during friction stir welding of dissimilar Mg/Al alloys. J Mater Res Technol 2021;15:4353–4369. [CrossRef]
[9] Varmazyar J, Khodaei M. Diffusion bonding of aluminum–magnesium using cold rolled copper interlayer. J Alloys Compd 2019;773:838–843. [CrossRef]
[10] Zhu C, Xu S, Gao W, Meng Y, Lin S, Dai L. Microstructure characteristics and mechanical properties of Al/Mg joints manufactured by magnetic pulse welding. J Magnes Alloy 2023;11:2366–2375. [CrossRef]
[11] Jian H, Wang Y, Yang X, Xiao K. Microstructure and fatigue crack growth behavior in welding joint of Al–Mg alloy. Eng Fail Anal 2021;120:105034. [CrossRef]
[12] Liang Z, Qin G, Ma H, Yang F, Ao Z. The constitutional liquation at the interface of Al/Mg friction welding joints. Sci Technol Weld Join 2017;22:363–372. [CrossRef]
[13] Acarer M, Demir B, Dikici B, Salur E. Microstructure, mechanical properties, and corrosion resistance of an explosively welded Mg–Al composite. J Magnes Alloy 2022;10:1086–1095. [CrossRef]
[14] Chen P, Feng J, Zhou Q, An E, Li J, Yuan Y, Ou S. Investigation on the explosive welding of 1100 aluminum alloy and AZ31 magnesium alloy. J Mater Eng Perform 2016;25:2635–2641. [CrossRef]
[15] Ghaderi SH, Mori A, Hokamoto K. Analysis of explosively welded aluminum–AZ31 magnesium alloy joints. Mater Trans 2008;49:1142–1147. [CrossRef]
[16] Paul H, Petrzak P, Chulist R, Maj Ł, Mania I, Prażmowski M. Effect of impact loading and heat treatment on microstructure and properties of multi-layered AZ31/AA1050 plates fabricated by single-shot explosive welding. Mater Des 2022;214:110411. [CrossRef]
[17] Zeng XY, Wang YX, Li XQ, Li XJ, Zhao TJ. Effect of inert gas-shielding on the interface and mechanical properties of Mg/Al explosive welding composite plate. J Manuf Process 2019;45:166–175. [CrossRef]
[18] Feng J, Chen P, Zhou Q, Dai K, An E, Yuan Y. Numerical simulation of explosive welding using Smoothed Particle Hydrodynamics method. Int J Multiphysics 2017;11:315–326. [CrossRef]
[19] Su Z, Masaki M, Nishida M, Kawase M, Hokamoto K, Inao D. Characteristics of ejecta resulting from hypervelocity impact on Al/Mg explosive welding clad materials. Int J Impact Eng 2024;186:104869. [CrossRef]
[20] Grignon F, Benson D, Vecchio KS, Meyers MA. Explosive welding of aluminum to aluminum: analysis, computations and experiments. Int J Impact Eng 2004;30:1333–1351. [CrossRef]
[21] Chen X, Inao D, Tanaka S, Mori A, Li X, Hokamoto K. Explosive welding of Al alloys and high strength duplex stainless steel by controlling energetic conditions. J Manuf Process 2020;58:1318–1333. [CrossRef]
[22] Saravanan S, Raghukandan K. Microstructure, strength and welding window of aluminum alloy–stainless steel explosive cladding with different interlayers. T Nonferr Metal Soc 2022;32:91–103. [CrossRef]
[23] Elango E, Saravanan S, Raghukandan K. Experimental and numerical studies on aluminum–stainless steel explosive cladding. J Cent South Univ 2020;27:1742–1753. [CrossRef]
[24] Satyanarayan, Tanaka S, Mori A, Hokamoto K. Welding of Sn and Cu plates using controlled underwater shock wave. J Mater Process Technol 2017;245:300–308. [CrossRef]
[25] Somasundaram S, Krishnamurthy R, Kazuyuki H. Effect of process parameters on microstructural and mechanical properties of Ti–SS 304L explosive cladding. J Cent South Univ 2017;24:1245–1251. [CrossRef]
[26] Gülenç B, Kaya Y, Durgutlu A, Gülenç İT, Yıldırım MS, Kahraman N. Production of wire reinforced composite materials through explosive welding. Arch Civil Mech Eng 2016;16:1–8. [CrossRef]
[27] Robin LG, Raghukandan K, Saravanan S. Studies on wire-mesh and silicon carbide particle reinforcements in explosive cladding of Al 1100–Al 5052 sheets. J Manuf Process 2020;56:887–897. [CrossRef]
[28] Kumar P, Ghosh SK, Saravanan S, Barma JD, Meitei RK. Effects of reinforcements in Al 5052 and AZ31B explosively weld composites. Arch Civil Mech Eng 2024;24:1–16. [CrossRef]
[29] Saravanan S, Raghukandan K. Effect of silicon carbide and wire-mesh reinforcements in dissimilar grade aluminium explosive clad composites. Def Technol 2020;16:1160–1166. [CrossRef]
[30] Inao D, Mori A, Tanaka S, Hokamoto K. Explosive welding of thin aluminum plate onto magnesium alloy plate using a gelatin layer as a pressure-transmitting medium. Metals 2020;10:106. [CrossRef]
[31] Chen X, Inao D, Tanaka S, Li X, Bataev IA, Hokamoto K. Comparison of explosive welding of pure titanium/SUS 304 austenitic stainless steel and pure titanium/SUS 821L1 duplex stainless steel. T Nonferr Metal Soc 2021;31:2687–2702. [CrossRef]
[32] Athar MH, Tolaminejad B. Weldability window and the effect of interface morphology on the properties of Al/Cu/Al laminated composites fabricated by explosive welding. Mater Des 2015;86:516–525. [CrossRef]
[33] Saravanan S, Kumararaja K, Raghukandan K. Application of deep learning techniques to predict the mechanical strength of Al–Steel explosive clads. Metals 2023;13:373. [CrossRef]
[34] Kumar CWD, Saravanan S, Raghukandan K. Influence of grooved base plate on microstructure and mechanical strength of aluminum–stainless steel explosive cladding. T Indian I Metals 2019;72:3269–3276. [CrossRef]

Sigma Journal of Engineering and Natural Sciences
Web page info: https://sigma.yildiz.edu.tr
DOI: 10.14744/sigma.2025.1933

Research Article

Aczel alsina aggregation operators of (M,N,Q)-spherical hesitant fuzzy sets and their applications in multi-attribute decision-making

Şerif ÖZLÜ[1,*]

[1]*Nizip Vocational High School, Gaziantep University, Gaziantep, 27300, Türkiye*

ARTICLE INFO

Article history
Received: 26 March 2024
Revised: 15 July 2024
Accepted: 21 September 2024

Keywords:
Aczel Alsina Operators; Decision Making; Hesitant Fuzzy Sets; (M,N,Q)- Spherical

ABSTRACT

In this paper, we first present the concept of (m,n,q)-spherical hesitant fuzzy set by combining (m,n,q)-spherical fuzzy set and hesitant fuzzy set. In here, (m,n,q)-spherical hesitant fuzzy set has several advantages according to novel clusters because of including three different parameters. This model produces effective solutions to deal with vagueness and complex data. The framework of (m,n,q)-spherical hesitant fuzzy set is a generalization of hesitant fuzzy set, intuitionistic hesitant fuzzy set, picture hesitant fuzzy set and t- spherical hesitant fuzzy set having a gorgeous potential of overcoming with uncertain and vagueness events. The concepts defined above have different problems within themselves. Let's consider the t- spherical hesitant fuzzy set for different values of t, which is the most inclusive structure compared to other sets. Since the value t is the same for all degrees, in some cases the decision maker may have to change the value assigned by his opinion. However, for (m,n,q)- spherical hesitant fuzzy set, this situation can be solved with the least margin of error by changing any of the m, n, q values. The (m,n,q)-spherical hesitant fuzzy set is defined as the degrees of truth, indeterminacy, and falsity and sum of mth, nth and qth powers of maximum values in degrees with condition less than or equal 1 such as m, n and q are natural numbers. This concept provides a lot of advantages as three different parameters, carrying more information because of hesitant fuzzy set, hosting to several clusters in its own structure, being soft concept. In addition to, we develop the the basic operational laws like addition, power, product, scalar multiplication. Moreover, we introduce new operotors by utilizing t norm and t conorm of Aczel Alsina by adding a new parameter. The added parameter further increases the flexibility, thus increasing the comparability of the obtained results. The presented operators as following; (m,n,q)- Spherical hesitant fuzzy Aczel Alsina weighted averaging operator, (m,n,q)- Spherical hesitant fuzzy Aczel Alsina ordered weighted averaging operator, (m,n,q)- Spherical hesitant fuzzy Aczel Alsina hybrid weighted averaging operator and (m,n,q)- Spherical hesitant fuzzy Aczel Alsina weighted geometric operator, (m,n,q)- Spherical hesitant fuzzy Aczel Alsina ordered weighted geometric operator, (m,n,q)- Spherical hesitant fuzzy Aczel Alsina hybrid weighted geometric operator. On the basis of these presented operators, a algorithm is introduced to aid multi-criteria decision making problems. A example is introduced to depict the practicality and validity of our defined procedures and comparative analysis is given with helping to t-spherical hesitant fuzzy set and, there is an agreement among results.

Cite this article as: Özlü Ş. Aczel alsina aggregation operators of (M,N,Q)-spherical hesitant fuzzy sets and their applications in multi-attribute decision-making. Sigma J Eng Nat Sci 2025;43(6):2094–2107.

***Corresponding author.**
*E-mail address: serif.ozlu@hotmail.com

This paper was recommended for publication in revised form by Editor-in-Chief Ahmet Selim Dalkilic

Published by Yıldız Technical University Press, İstanbul, Turkey
© Author. This is an open access article under the CC BY-NC license (http://creativecommons.org/licenses/by-nc/4.0/).

INTRODUCTION

Multiple criteria decision making (MCDM) is an important study issue in many fields. Therefore, this subject has been integrated with more disciplines as business, engineering, psychology, social sciences and medical sciences. Owing to vagueness, many problems have appeared in the decision making environment. To overcome with these troubles, Zadeh [1] produced to concept of fuzzy sets (FS) in 1965. Then, when the FS fails to meet some difficulties, intuitionistic fuzzy set (IFS) [2] was defined by Atanassov such as sum of truth and falsity degree is in [0,1] as mathematically $0 \leq \mu + \nu \leq 1$, μ and ν are truth and falsity degree, respectively. To date, IFS has been extended owing to some limitations of IFS like $\langle 0.4,0.8 \rangle$ and $0.4 + 0.8 > 1$ and Yager [3] defined to Pythagorean FS (PyFS) such that $0 \leq \mu^2 + \nu^2 \leq 1$ where μ and ν are truth and falsity degree, respectively but when PyFS is insufficient to meet the needs, q-rung orthopair FS (q-ROPFS) [4] was constructed such as $0 \leq \mu^q + \nu^q \leq 1$ where μ and ν are truth and falsity degree, respectively for $q \geq 1$. The rise of the information age, the development of relations among interdisciplinary has led to the emergence of new cluster structures. Picture fuzzy set (PFS) [5] was introduced by Cuong and defined by three degrees such as truth, indeterminacy and falsity degree mathematically $0 \leq \mu + \eta + \nu \leq 1$, μ, η and ν are truth, indeterminacy and falsity degree, respectively. The t-spherical fuzzy set (t-SFS) and spherical fuzzy set (SFS) were defined by Mahmood [6, 7] such as $0 \leq \mu^t + \eta^t + \nu^t \leq 1$ and $0 \leq \mu^2 + \eta^2 + \nu^2 \leq 1$, respectively and also μ, η and ν are truth, indeterminacy and falsity degree, respectively for $t \geq 1$. Also, this subject has been worked by a lot of authors as following; Quek et al. [8] worked Multi-attribute multi-perception decision- making based on generalized t-spherical fuzzy weighted aggregation operators on neutrosophic sets; Garg and coauthors [9] gave to t-spherical fuzzy power aggregation operators and some applications; Ullah et al. [10] mentioned from correlation coefficient; Wu and others [11] defined to divergence measures of t-spherical fuzzy set.

Aczel and Alsina [12] proposed AA- TN and AA- TCN with condition having a parameter $p \in [0, \infty)$ in 1982. AA- TN and AA- TCN structures have been surveyed by several authors owing to variableness parameters. The different forms of AA- TN have been given in Generator of Parametric T-Norms [13]. Senapati and coauthors [14, 15] developed AA- aggregation operators under intuitionistic and interval valued intuitionistic fuzzy environment and tested over multiple attribute decision making. Moreover, Senepati [16] has carried a new level to AA family by combining AA aggregation operators and picture fuzzy sets. Then, Hussain and et al [17] proposed to Aczel-Alsina Aggregation Operators on t-SFS information and gave an application and Hussain and others [18] developed Novel Aczel-Alsina Operators for PyFs with application in Multi-Attribute Decision Making.

The above concepts are successfully utilized to obtain the most accuracy result but the authors can meet with some special situations as to be appointed several possible membership values about an subject. Accordingly, hesitant fuzzy set (HFS) [19, 20] can effectively overcome with these fuzzy cases. In later time, more papers have been proposed by combining HFS and a lot of concepts. For example; Beg and Rashid [21] defined intuitionistic hesitant fuzzy set (IHFS) in 2014 such that $\{\langle \mu_j(x), \nu_k(x) \rangle : j = 1,2, \ldots, \kappa; k = 1,2, \ldots, \zeta\}$ where $0 \leq \mu^+ + \nu^+ \leq 1$ for μ^+, ν^+ are the biggest truth, falsity values. Then, hesitant pythagorean fuzzy set (HPyFS) by combining PyFS and HFS has been proposed by Garg [22] such that $\{\langle \mu_j(x), \nu_k(x) \rangle : j = 1,2, \ldots, \kappa; k = 1,2, \ldots, \zeta\}$ where $0 \leq \mu^2 + \nu^2 \leq 1$ for μ_+, ν_+ are the biggest truth, falsity values. Moreover, Liu, Peng and Liu [23] offered q-rung orthopair hesitant fuzzy sets that defined as $\{\langle \mu_j(x), \nu_k(x) \rangle : j = 1,2, \ldots, \kappa; k = 1,2, \ldots, \zeta\}$ where $0 \leq \mu_+^2 + \nu_+^2 \leq 1$ for μ_+, ν_+ are the biggest truth, falsity values for $q \geq 1$. Wang and Li [24] defined to picture hesitant fuzzy set (PHFS) such that μ_+, ν_+ are the biggest truth, falsity values for $q \geq 1$. Wang and Li [24] defined to picture hesitant fuzzy set (PHFS) such that $\{\langle \mu j(x), \eta i(x), \nu k(x) \rangle : j = 1,2, \ldots, \kappa; i = 1,2, \ldots \vartheta; k = 1,2, \ldots, \zeta\}$ where $0 \leq \mu^+ + \eta^+ + \nu^+ \leq 1$ for μ, η and ν are truth, indeterminacy and falsity degree, respectively and Ashraf [25] introduced to T-Spherical Hesitant Fuzzy Set and defined as $\{\langle \mu_j(x), \eta_i(x), \nu_k(x) \rangle : j = 1,2, \ldots, \kappa; i = 1,2, \ldots \vartheta; k = 1,2, \ldots, \zeta\}$ where $0 \leq \mu_+^t + \eta_+^t + \nu_+^t \leq 1$ for μ, η and ν are truth, indeterminacy and falsity degree for $t \geq 1$, respectively.

Then, owing to the drawbacks of the above studies, the r,s,t- SFS structure was introduced by Ali and Naeem [26]. Then, some works have been made over r,s,t- SFS like Ali [27] has defined some applications based on aggregation operators over this concept and karaaslan and karamaz [28] introduced interval r,s,t- SFS and tested some applications see ([29], [30], [31], [32]) The r,s,t- SFS is another expansion of PFS for modelling the problems in which decision-makers have non-similar opinions about an alternative in wanted environment such that $< \mu, \eta, \nu >$ where $0 \leq \mu^r + \eta^s + \nu^t \leq 1$ for $r, s, t \in Z$. To explain the basic idea of back round of the r, s, t- SFS, we determine an example: an decision maker discusses the membership grade of an alternative such that $< 0.9, 0.9, 0.3 >$. This example is not defined with Picture fuzzy set, spherical fuzzy set or t-spherical fuzzy set for some values of t such that $0.9^3 + 0.9^3 + 0.3^3 > 1$ for t=3. If we define for t-SHFS, what needs to be done here is either the value t should be increased or the decision makers should change their views. The r,s,t- SFS solves without error margin for r=3, s=5, t=3. The benefits of r,s,t- SFS can be indicated as following;

1. The usage of three different variables improves the flexibility from the point of view of experts.
2. The (m,n,q)- SFS has much more comprehensive concept owing to containing many clusters. Therefore, changing the parameters will reveal us different clusters.

3. The (m,n,q)- SFS has comparative analysis in its own for some different values of m,n,q. When the above defined concepts are surveyed, it is open that many of them have different problems for example; alternatives in some clusters are determined by a decision maker, while some of them do not have neutral degree. In order to delete such irritabilities addressed IFS, q-ROFS or PyFS, we introduce a new cluster called as (m,n,q)- Spherical Hesitant Fuzzy Set. This structure is revealed by combining (m,n,q)- SFS and hesitant fuzzy set. The main motivations of this construction are as follows:
4. The t-spherical hesitant set (t-SHFS) which enables the emergence of the (m,n,q)- SHFS, is inadequate in many cases. In order to get rational results in MCDM, margin of error must be reduced. The structure of t-SHFS includes several values in membership, neutral and non- membership degrees and tth power of maximum values in membership, neutral and non- membership degrees should belong in [0,1] but this definition has some problems. For example, let define t-SHFS such that <{0.3,0.6},{0.5},{0.2,0.9}> for t=2 and tth power of maximum values that $0.6^2 + 0.5^2 + 0.9^2 > 1$. In here, there are two cases; either the decision makers' ideas should be changed, or the value of the natural number t should be increased. Two cases have different handicaps such that error margin will increase if opinion of decision makers is changed or, obtained results will change if natural number t is increased. This problem can be eliminated with (m,n,q)- SHFS. The error can be resolved with minimal damage If the above example is thought for r=2, s=2 and t=3.
5. The IFS, q-ROFS, PyFS, PFS, SFS, r,s,t-SFS and also generalizations of hesitant fuzzy set are special statements of (m,n,q)- SHFS. For example, in (m,n,q)- SHFS environment, if m=n=q, (m,n,q)- SHFS is converted to t-SHFS, if m=n=q=1, r,s,t-SHFS is converted to PHFS or if neutral degree is eliminated, this concept is swapped with IHFS, q-ROHFS or PyHFS, etc.. In Figure 1, we see that r,s,t-SHFS almost includes several generalizations of HFS. If the number of elements are induced in set and r,s,t are combined with different natural numbers, it is open that r,s,t-SHFS is converted to novel clusters. From the above discussions, it is clear that (m,n,q)- SHFS is more flexible, inclusive, superior according to a lot of sets. In here symbol "l" indicates number of elements into degrees.

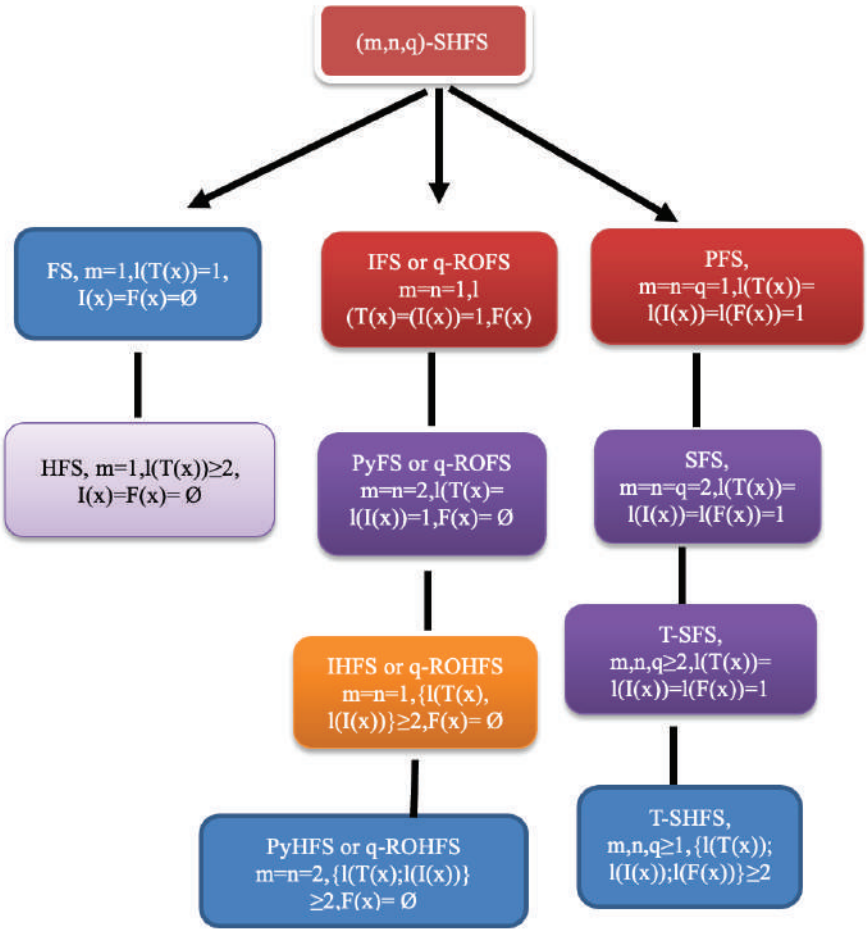


Figure 1. The characteristic comparisons of (m,n,q)- SHFS with different concepts.

Table 1. The list of abbreviations

The full spelling of names	Abbreviations
(m,n,q)-spherical hesitant fuzzy set	(m,n,q)-SHFS
(m,n,q)-spherical fuzzy set	(m,n,q)-SFS
Intuitionistic hesitant fuzzy set	IHFS
Picture hesitant fuzzy set	PHFS
t- spherical hesitant fuzzy set	T-SHFS
(m,n,q)- Spherical hesitant fuzzy Aczel Alsina weighted averaging operator	(m,n,q)-SHFAAWA
(m,n,q)- Spherical hesitant fuzzy Aczel Alsina ordered weighted averaging operator	(m,n,q)-SHFAAOWA
(m,n,q)- Spherical hesitant fuzzy Aczel Alsina weighted geometric operator	(m,n,q)-SHFAAWG
(m,n,q)- Spherical hesitant fuzzy Aczel Alsina ordered weighted geometric operator	(m,n,q)-SHFAAOWG
(m,n,q)- Spherical hesitant fuzzy Aczel Alsina hybrid weighted geometric operator	(m,n,q)-SHFAAHWG
Fuzzy sets	FS
Intuitionistic fuzzy set	IFS
Pythagorean fuzzy set	PyFS
q-rung orthopair FS	q-ROPFS
Picture fuzzy set	PFS
t-spherical fuzzy set	t-SFS
The spherical fuzzy set	SFS
Aczel Alsina- t Norm	AA- TN
Aczel Alsina- t Conorm	AA- TN
Hesitant fuzzy set	HFS
Picture hesitant fuzzy set	PHFS
T- Spherical Hesitant fuzzy Weighted Averaging operator	T-SHFWA
T- Spherical Hesitant fuzzy Weighted Geometric operator	T-SHFWG

Therefore, the contributions of this manuscript are offered as following;

- Firstly, we reveal a new cluster concept called as (m,n,q)-SHFS which generalized version all of the sets in Figure 1;
- We present equations of six different aggregation operators by combining Aczel Alsina operators which (m,n,q)-SHFAAWA, (m,n,q)-SHFAAOWA, (m,n,q)-SHFAAHWA and (m,n,q)-SHFAAWG, (m,n,q)-SHFAAOWG, (m,n,q)-SHFAAHWG;
- We develop a algorithm based on (m,n,q)-SHFAAWA and (m,n,q)-SHFAAWG;
- A example is solved for two operators and we present two tables called as Table 3 and Table 4. These tables indicate that A_4 alternative is the best alternative for all of values of λ out $\lambda = 2$; (3,5,7) and $\lambda = 5$; (9,4,2) for two operators. For all remaining cases, the best alternative is determined similarly. It should be noted is that the best alternative probabilistically is seen as A_4. A_2 and A_1 may be determined as the best alternative with a very low probability. Although the (m,n,q)-SHFAAWG and (m,n,q)-SHFAAWA are two different operators, the results are almost agreement. This statement indicates that the proposed operators are reality, effective, flexible and have more advantages because of including four different valuables. It should be noted that as if the number of variables increases, the flexibility of the set will increase.
- Lastly, a inclusive comparative analysis and geometrical interpretations are proposed to put forward the advantages of the offered operators.

The remainder of paper is organized as follow; section 2 includes basic definition and theorems about fuzzy set, hesitant fuzzy set, (m,n,q)-SFS, Aczel Alsina operators so on, in section 3, (m,n,q)-SHFS concept is defined and aggregation operators are to given, in section 4, a decision making method and an illustrative example are proposed to indicate effective and practically of aggregation operators and set, and results are compared in their own, in section 5, we offer a comparative analysis by using T-SHFS.

PRELIMINARY

In this section, we recall some basic notions of hesitant fuzzy sets, t-spherical fuzzy sets and Aczel Alsina t- norm and Aczel Alsina t- conorm.

Definition 2.1 *[7] Let X be a non-empty set. A T- spherical fuzzy set is defined over X as following;*

$T = \{(S(x), I(x), F(x)): 0 \le S^t(x) + I^t(x) + F^t(x) \le 1 for t \in Z\}$.

Definition 2.2 *[25] Let X be a non-empty set. A (m,n,q)-spherical fuzzy set (shortly (m,n,q)-SFS) is defined over X as following;*

$$T = \{(S(x), I(x), F(x)): 0 \le S^m(x) + I^n(x) + F^q(x) \le 1 for x \in X\}.$$

In here, $S: X \to [0,1]$, $I: X \to [0,1]$ and $F: X \to [0,1]$ and define membership, neutral and non- membership grades and m, n, q are some natural numbers.

Aczel-Alsina t-norm (TN) and t-conorm (TCN) were proposed by Aczel and Alsina in 1982 as follow.

Definition 2.3 *[12] Aczel- Alsina TN is defined as follow;*

$$T_{\Re}^{\lambda}(a,b) = \begin{cases} T_D(a,b), & if \lambda = 0 \\ min(a,b), & if \lambda = \infty \\ e^{-((-ln(a))^{\lambda} + (-ln(b))^{\lambda}))^{\frac{1}{\lambda}}} & \\ otherwise & \end{cases}$$

and

Aczel- Alsina TCN is defined as follow;

$$T_{\Re}^{\lambda}(a,b) = \begin{cases} T_D(a,b), & if \lambda = 0 \\ min(a,b), & if \lambda = \infty \\ 1 - e^{-((-ln(1-a))^{\lambda} + (-ln(1-b))^{\lambda}))^{\frac{1}{\lambda}}} & \\ otherwise & \end{cases}$$

where $\lambda \in [0, \infty)$.

ACZEL ALSINA AGGREGATION OPERATORS OF (m,n,q)-SPHERICAL HESITANT FUZZY SET

The concept of (m,n,q)-spherical fuzzy set ((m,n,q)-SFS) was defined by Ali and Naeem [25] in 2023. In this section, the concept of (m.n,q)-spherical fuzzy set is extended to (m,n,q)-spherical hesitant fuzzy set (shortly (m,n,q)-SHFS).

Definition 2.4 *Let X be a reference set. A (m,n,q)-spherical hesitant fuzzy set S is defined as follows:*

$$S = \{(x, T_S(x), I_S(x), F_S(x)): x \in X\}$$

where $T_S(x) = \{t_S(x): x \in X\}$, $I_S(x) = \{h_S(x): x \in X\}$ and $F_S(x) = \{f_S(x): x \in X\}$ are hesitant fuzzy sets. T_S, I_S and F_S depict truth-hesitant membership degree, neutral hesitant membership degree and falsity- hesitant membership degree of the element, respectively and with the condition $0 \le (T_S^+)^m + (I_S^+)^n + (F_S^+)^q \le 1$, in here T_S^+, I_S^+ and F_S^+ are maximum elements and also refusal degree is defined $\sqrt[z]{1 - T_S(x) - I_S(x) - F_S(x)}$ where z is the least common multiple of m,n and q. $\tilde{n}$ represents an element of (m,n,q)-SHFS and $S_E(X)$ denotes the set of all (m,n,q)-SHFSs on X. Also, all $x \in X$, completed certainty is $s = \{(x, \{1\}, \{0\}, \{0\})\}$ and also, completed uncertainty is defined $s = \{(x, \{0\}, \{0\}, \{1\})\}$. Furthermore, since a (m,n,q)-SHFS is characterized by truth-hesitant membership degree, neutral hesitant membership degree and falsity- hesitant membership degree, lengths of these sets may be different. So we denote the lengths of these sets corresponding to $x \in X$ with $l_x^{\bullet}$, l_x° and l_x° respectively.

Definition 2.5 *Let $A_\rho = \{x,(\{t_{A_{j\rho}}\}, \{h_{A_{k\rho}}\}, \{f_{A_{r\rho}}\}): x \in X\}$ be (m,n,q)-SHFS over X for $j = (1,2,...,l_x^{\bullet})$, $k = (1,2,...,l_x^{\circ})$ and $r = (1,2,...,l_x^{\circ})$. The basic operations of (m,n,q)-SHFS are defined for $\lambda \ge 1$ as follows:*

$$A_1 \oplus A_2 = \bigcup_{\substack{t_{A_1} \in t_{A_{j_1}} \ t_{A_2} \in t_{A_{j_2}} \\ h_{A_1} \in h_{A_{k_1}}, h_{A_2} \in h_{A_{k_2}} \\ f_{A_1} \in f_{A_{r_1}} \ f_{A_2} \in f_{A_{r_2}}}} \left\{ \begin{matrix} \sqrt[m]{1 - e^{-(\sum_{\rho=1}^{2} (-\ln(1-(t_{A_\rho})^m))^{\lambda})^{\frac{1}{\lambda}}}}, \\ \sqrt[n]{e^{-(\sum_{\rho=1}^{2} (-\ln(h_{A_\rho}^n))^{\lambda})^{\frac{1}{\lambda}}}}, \\ \sqrt[q]{e^{-(\sum_{\rho=1}^{2} (-\ln(f_{A_\rho}^q))^{\lambda})^{\frac{1}{\lambda}}}} \end{matrix} \right\} \quad (1)$$

$$A_1 \otimes A_2 = \bigcup_{\substack{t_{A_1} \in t_{A_{j_1}} \ t_{A_2} \in t_{A_{j_2}} \\ h_{A_1} \in h_{A_{k_1}}, h_{A_2} \in h_{A_{k_2}} \\ f_{A_1} \in f_{A_{r_1}} \ f_{A_2} \in f_{A_{r_2}}}} \left\{ \begin{matrix} \sqrt[m]{e^{-(\sum_{\rho=1}^{2} (-\ln(t_{A_\rho}^m))^{\lambda})^{\frac{1}{\lambda}}}}, \\ \sqrt[n]{1 - e^{-(\sum_{\rho=1}^{2} (-\ln(1-(h_{A_\rho})^n))^{\lambda})^{\frac{1}{\lambda}}}}, \\ \sqrt[q]{1 - e^{-(\sum_{\rho=1}^{2} (-\ln(1-(f_{A_\rho})^q))^{\lambda})^{\frac{1}{\lambda}}}} \end{matrix} \right\} \quad (2)$$

$$\eta A_1 = \bigcup_{\substack{t_{A_1} \in t_{A_{j_1}} \\ h_{A_1} \in h_{A_{k_1}} \\ f_{A_1} \in f_{A_{r_1}}}} \left\{ \begin{matrix} \sqrt[m]{1 - e^{-(\eta(-\ln(1-(t_{A_1})^m))^{\lambda})^{\frac{1}{\lambda}}}}, \\ \sqrt[n]{e^{-(\eta(-\ln(h_{A_1}^n))^{\lambda})^{\frac{1}{\lambda}}}}, \\ \sqrt[q]{e^{-(\eta(-\ln(f_{A_1}^q))^{\lambda})^{\frac{1}{\lambda}}}} \end{matrix} \right\} \quad (3)$$

$$A_1^{\eta} = \bigcup_{\substack{t_{A_1} \in t_{A_{j_1}} \\ h_{A_1} \in h_{A_{k_1}} \\ f_{A_1} \in f_{A_{r_1}}}} \left\{ \begin{matrix} \sqrt[m]{e^{-(\eta(-\ln(t_{A_\rho}^m))^{\lambda})^{\frac{1}{\lambda}}}}, \\ \sqrt[n]{1 - e^{-(\eta(-\ln(1-(h_{A_\rho})^n))^{\lambda})^{\frac{1}{\lambda}}}}, \\ \sqrt[q]{1 - e^{-(\eta(-\ln(1-(f_{A_\rho})^q))^{\lambda})^{\frac{1}{\lambda}}}} \end{matrix} \right\} \quad (4)$$

Definition 2.6 *Let determine a (m,n,q)-SHFS that $A_\rho = \{x,(\{t_{A_{j\rho}}\}, \{h_{A_{k\rho}}\}, \{f_{A_{r\rho}}\}): x \in X\}$ where $j = (1,2,...,l_x^{\bullet})$, $k = (1,2,...,l_x^{\circ})$ and $r = (1,2,...,l_x^{\circ})$. Then score function and accuracy function of (m,n,q)-SHFS are defined as following;*

$$s(A_\rho) = \frac{1 + \frac{1}{l_{x^{\bullet}}^m} (\sum_{t_{A_j} \in t_{A_{j_\rho}}} t_{A_j})^m - \frac{1}{l_{x^{\circ}}^n} (\sum_{h_{A_k} \in h_{A_{k_\rho}}} h_{A_k})^n - \frac{1}{l_{x^{\circ}}^q} (\sum_{f_{A_r} \in f_{A_{r_\rho}}} f_{A_r})^q}{2}$$

and accuracy function

$$\breve{A}(A_\rho) = \frac{1 + \frac{1}{l_{x^{\bullet}}^m} (\sum_{t_{A_j} \in t_{A_{j_\rho}}} t_{A_j})^m + \frac{1}{l_{x^{\circ}}^n} (\sum_{h_{A_k} \in h_{A_{k_\rho}}} h_{A_k})^n + \frac{1}{l_{x^{\circ}}^q} (\sum_{f_{A_r} \in f_{A_{r_\rho}}} f_{A_r})^q}{2}$$

Definition 2.7 *Let determine a (m,n,q)-SHFS that $A_\rho = \{x,(\{t_{A_{j\rho}}\}, \{h_{A_{k\rho}}\}, \{f_{A_{r\rho}}\}): x \in X\}$ where $j = (1,2,...,l_x^{\bullet})$, $k = (1,2,...,l_x^{\circ})$ and $r = (1,2,...,l_x^{\circ})$ for $w \in [0,1]$ and $\sum_{\rho=1}^{\varrho} w_\rho = 1$;*

1. $(m, n, q) - SHFAAWA: \Phi^{\varrho} \to \Phi$ is a mapping called as (m,n,q)-Spherical Hesitant Fuzzy Aczel Alsina Weighted

Averaging operator and $w_\rho \in [0,1]$ and $\sum_{\rho=1}^{\varrho} w_\rho = 1$ is defined as below;

$$(m,n,q)-SHFAAWA(A_1,A_2,\ldots,A_\varrho)$$

$$=\bigcup_{\substack{t_{A_1}\in t_{A_{j_1}},t_{A_2}\in t_{A_{j_2}},\ldots,t_{A_\varrho}\in t_{A_{j_\varrho}}\\ h_{A_1}\in h_{A_{k_1}},h_{A_2}\in h_{A_{k_2}},\ldots,h_{A_\varrho}\in h_{A_{k_\varrho}}\\ f_{A_1}\in f_{A_{r_1}},f_{A_2}\in f_{A_{r_2}},\ldots,f_{A_\varrho}\in f_{A_{r_\varrho}}}}\left\{\begin{matrix}\sqrt[m]{1-e^{-(\sum_{\rho=1}^{\varrho}w_\rho(-\ln(1-(t_{A_\rho})^m))^\lambda)^{\frac{1}{\lambda}}}},\\ \sqrt[n]{e^{-(\sum_{\rho=1}^{\varrho}w_\rho(-\ln(h_{A_\rho}^n))^\lambda)^{\frac{1}{\lambda}}}},\\ \sqrt[q]{e^{-(\sum_{\rho=1}^{\varrho}w_\rho(-\ln(f_{A_\rho}^q))^\lambda)^{\frac{1}{\lambda}}}}\end{matrix}\right\}$$

2. $(m, n, q) - SHFAAOWA$: $\Phi^\varrho \to \Phi$ is a mapping called as (m,n,q)-Spherical Hesitant Fuzzy Aczel Alsina Ordered Weighted Averaging operator and $w_\rho \in [0,1]$ and $\sum_{\rho=1}^{\varrho} w_\rho = 1$ is defined as below;

$$(m,n,q)-SHFAAOWA(A_1,A_2,\ldots,A_\varrho)$$

$$=\bigcup_{\substack{t_{A_{\sigma(1)}}\in t_{A_{j_{\sigma(1)}}},t_{A_{\sigma(2)}}\in t_{A_{j_{\sigma(2)}}},\ldots,t_{A_{\sigma(\varrho)}}\in t_{A_{j_{\sigma(\varrho)}}}\\ h_{A_{\sigma(1)}}\in h_{A_{k_{\sigma(1)}}},h_{A_2}\in h_{A_{k_{\sigma(2)}}},\ldots,h_{A_{\sigma(\varrho)}}\in h_{A_{k_\varrho}}\\ f_{A_1}\in f_{A_{r_1}},f_{A_{\sigma(2)}}\in f_{A_{r_{\sigma(2)}}},\ldots,f_{A_{\sigma(\varrho)}}\in f_{A_{r_{\sigma(\varrho)}}}}}\left\{\begin{matrix}\sqrt[m]{1-e^{-(\sum_{\rho=1}^{\varrho}w_\rho(-\ln(1-(t_{A_{\sigma(\rho)}})^m))^\lambda)^{\frac{1}{\lambda}}}},\\ \sqrt[n]{e^{-(\sum_{\rho=1}^{\varrho}w_\rho(-\ln(h_{A_{\sigma(\rho)}}^n))^\lambda)^{\frac{1}{\lambda}}}},\\ \sqrt[q]{e^{-(\sum_{\rho=1}^{\varrho}w_\rho(-\ln(f_{A_{\sigma(\rho)}}^q))^\lambda)^{\frac{1}{\lambda}}}}\end{matrix}\right\}$$

where $(\sigma(1), \sigma(2), \ldots, \sigma(\varrho))$ are the permutation of $(\rho = 1,2,\ldots,\varrho)$, including $A_{\sigma(\varrho-1)} \geq A_{\sigma(\varrho)}$.

3. $(m, n, q) - SHFAAHWA$: $\Phi^\varrho \to \Phi$ is a mapping called as (m,n,q)-Spherical Hesitant Fuzzy Aczel Alsina Hybrid Weighted Averaging operator and $w_\rho \in [0,1]$ and $\sum_{\rho=1}^{\varrho} w_\rho = 1$ is defined as below;

$$(m,n,q)-SHFAAHWA(A_1,A_2,\ldots,A_\varrho)$$

$$=\bigcup_{\substack{t_{A_{\sigma(1)}}\in \dot{t}_{A_{j_{\sigma(1)}}},t_{A_{\sigma(2)}}\in \dot{t}_{A_{j_{\sigma(2)}}},\ldots,t_{A_{\sigma(\varrho)}}\in \dot{t}_{A_{j_{\sigma(\varrho)}}}\\ h_{A_{\sigma(1)}}\in \dot{h}_{A_{k_{\sigma(1)}}},h_{A_2}\in \dot{h}_{A_{k_{\sigma(2)}}},\ldots,h_{A_{\sigma(\varrho)}}\in \dot{h}_{A_{k_\varrho}}\\ f_{A_1}\in \dot{f}_{A_{r_1}},f_{A_{\sigma(2)}}\in \dot{f}_{A_{r_{\sigma(2)}}},\ldots,f_{A_{\sigma(\varrho)}}\in \dot{f}_{A_{r_{\sigma(\varrho)}}}}}\left\{\begin{matrix}\sqrt[m]{1-e^{-(\sum_{\rho=1}^{\varrho}w_\rho(-\ln(1-(t_{A_{\sigma(\rho)}})^m))^\lambda)^{\frac{1}{\lambda}}}},\\ \sqrt[n]{e^{-(\sum_{\rho=1}^{\varrho}w_\rho(-\ln(h_{A_{\sigma(\rho)}}^n))^\lambda)^{\frac{1}{\lambda}}}},\\ \sqrt[q]{e^{-(\sum_{\rho=1}^{\varrho}w_\rho(-\ln(f_{A_{\sigma(\rho)}}^q))^\lambda)^{\frac{1}{\lambda}}}}\end{matrix}\right\}$$

where, $\dot{A}_\rho = \kappa\varpi_\rho A_\rho$ and κ is the very important balancing coefficient for $A_{\sigma(\varrho-1)} \geq A_{\sigma(\varrho)}$ and $\varpi_\rho = (1,2,\ldots,\varrho)$ is an associated vector.

Characteristic of (m,n,q)- Spherical hesitant fuzzy Aczel Alsina weighted averaging operator

Theorem 2.8 *Let determine collection of (m,n,q)-SHFSs that* $A_\rho = \{x,(\{t_{A_{j\rho}}\}, \{h_{A_{k\rho}}\}, \{f_{A_{r\rho}}\}): x \in X\}$ *where* $j = (1,2,\ldots,l_x^\cdot)$, $k = (1,2,\ldots,l_x^*)$ *and* $r = (1,2,\ldots,l_x^*)$ *for* $w_\rho \in [0,1]$ *and* $\sum_{\rho=1}^{\varrho} w_\rho = 1$. *Then their Aczel Alsina aggregated value by using (m,n,q)-SHFAAHWA is a (m,n,q)-SHFE and*

$$(m,n,q)-SHFAAWA(A_1,A_2,\ldots,A_\varrho)$$

$$=\cup_{\substack{t_{A_1}\in t_{A_{j_1}},t_{A_2}\in t_{A_{j_2}},\ldots,t_{A_\varrho}\in t_{A_{j_\varrho}}\\ h_{A_1}\in h_{A_{k_1}},h_{A_2}\in h_{A_{k_2}},\ldots,h_{A_\varrho}\in h_{A_{k_\varrho}}\\ f_{A_1}\in f_{A_{r_1}},f_{A_2}\in f_{A_{r_2}},\ldots,f_{A_\varrho}\in f_{A_{r_\varrho}}}}\left\{\begin{matrix}\sqrt[m]{1-e^{-(\sum_{\rho=1}^{\varrho}w_\rho(-\ln(1-(t_{A_\rho})^m))^\lambda)^{\frac{1}{\lambda}}}},\\ \sqrt[n]{e^{-(\sum_{\rho=1}^{\varrho}w_\rho(-\ln(h_{A_\rho}^n))^\lambda)^{\frac{1}{\lambda}}}},\\ \sqrt[q]{e^{-(\sum_{\rho=1}^{\varrho}w_\rho(-\ln(f_{A_\rho}^q))^\lambda)^{\frac{1}{\lambda}}}}\end{matrix}\right\}$$

Proof. Let use mathematical induction on ϱ and look for $\varrho = 1,2$;

$$w_1A_1=\bigcup_{t_{A_1}\in t_{A_{j_1}},h_{A_1}\in h_{A_{k_1}},f_{A_1}\in f_{A_{r_1}}}\left\{\begin{matrix}\sqrt[m]{1-e^{-(w_1(-\ln(1-(t_{A_1})^m))^\lambda)^{\frac{1}{\lambda}}}},\\ \sqrt[n]{e^{-(w_1(-\ln(h_{A_1}^n))^\lambda)^{\frac{1}{\lambda}}}},\\ \sqrt[q]{e^{-(w_1(-\ln(f_{A_1}^q))^\lambda)^{\frac{1}{\lambda}}}}\end{matrix}\right\}$$

and

$$w_2A_2=\bigcup_{t_{A_2}\in t_{A_{j_2}},h_{A_2}\in h_{A_{k_2}},f_{A_2}\in f_{A_{r_2}}}\left\{\begin{matrix}\sqrt[m]{1-e^{-(w_2(-\ln(1-(t_{A_2})^m))^\lambda)^{\frac{1}{\lambda}}}},\\ \sqrt[n]{e^{-(w_2(-\ln(h_{A_2}^n))^\lambda)^{\frac{1}{\lambda}}}},\\ \sqrt[q]{e^{-(w_2(-\ln(f_{A_2}^q))^\lambda)^{\frac{1}{\lambda}}}}\end{matrix}\right\}$$

from here

$$w_1A_1\oplus w_2A_2=\cup_{\substack{t_{A_1}\in t_{A_{j_1}}\ t_{A_2}\in t_{A_{j_2}}\\ h_{A_1}\in h_{A_{k_1}},h_{A_2}\in h_{A_{k_2}}\\ f_{A_1}\in f_{A_{r_1}}\ f_{A_2}\in f_{A_{r_2}}}}\left\{\begin{matrix}\sqrt[m]{1-e^{-(\sum_{\rho=1}^{2}w_\rho(-\ln(1-(t_{A_\rho})^m))^\lambda)^{\frac{1}{\lambda}}}},\\ \sqrt[n]{e^{-(\sum_{\rho=1}^{2}w_\rho(-\ln(h_{A_\rho}^n))^\lambda)^{\frac{1}{\lambda}}}},\\ \sqrt[q]{e^{-(\sum_{\rho=1}^{2}w_\rho(-\ln(f_{A_\rho}^q))^\lambda)^{\frac{1}{\lambda}}}}\end{matrix}\right\}.$$

Then, from here for $\varrho = \nu$, (m,n,q)-SHFAAWA holds as follow;

$$\bigcup_{\substack{t_{A_1}\in t_{A_{j_1}},t_{A_2}\in t_{A_{j_2}},\ldots,t_{A_\nu}\in t_{A_{j_\nu}}\\ h_{A_1}\in h_{A_{k_1}},h_{A_2}\in h_{A_{k_2}},\ldots,h_{A_\nu}\in h_{A_{k_\nu}}\\ f_{A_1}\in f_{A_{r_1}},f_{A_2}\in f_{A_{r_2}},\ldots,f_{A_\nu}\in f_{A_{r_\nu}}}}\left\{\begin{matrix}\sqrt[m]{1-e^{-(\sum_{\rho=1}^{\nu}w_\rho(-\ln(1-(t_{A_\rho})^m))^\lambda)^{\frac{1}{\lambda}}}},\\ \sqrt[n]{e^{-(\sum_{\rho=1}^{\nu}w_\rho(-\ln(h_{A_\rho}^n))^\lambda)^{\frac{1}{\lambda}}}},\\ \sqrt[q]{e^{-(\sum_{\rho=1}^{\nu}w_\rho(-\ln(f_{A_\rho}^q))^\lambda)^{\frac{1}{\lambda}}}}\end{matrix}\right\}$$

and for $\varrho = \nu + 1$;

$$\bigcup_{\substack{t_{A_1}\in t_{A_{j_1}},t_{A_2}\in t_{A_{j_2}},\ldots,t_{A_\nu}\in t_{A_{j_\nu}}\\ h_{A_1}\in h_{A_{k_1}},h_{A_2}\in h_{A_{k_2}},\ldots,h_{A_\nu}\in h_{A_{k_\nu}}\\ f_{A_1}\in f_{A_{r_1}},f_{A_2}\in f_{A_{r_2}},\ldots,f_{A_\nu}\in f_{A_{r_\nu}}}}\left\{\begin{matrix}\sqrt[m]{1-e^{-(\sum_{\rho=1}^{\nu}w_\rho(-\ln(1-(t_{A_\rho})^m))^\lambda)^{\frac{1}{\lambda}}}},\\ \sqrt[n]{e^{-(\sum_{\rho=1}^{\nu}w_\rho(-\ln(h_{A_\rho}^n))^\lambda)^{\frac{1}{\lambda}}}},\\ \sqrt[q]{e^{-(\sum_{\rho=1}^{\nu}w_\rho(-\ln(f_{A_\rho}^q))^\lambda)^{\frac{1}{\lambda}}}}\end{matrix}\right\}$$

$$\oplus\bigcup_{t_{A_{\nu+1}}\in t_{A_{j_{\nu+1}}},h_{A_{\nu+1}}\in h_{A_{j_{\nu+1}}},f_{A_{\nu+1}}\in f_{A_{j_{\nu+1}}}}\left\{\begin{matrix}\sqrt[m]{1-e^{-(w_{\nu+1}(-\ln(1-(t_{A_{\nu+1}})^m))^\lambda)^{\frac{1}{\lambda}}}},\\ \sqrt[n]{e^{-(w_{\nu+1}(-\ln(h_{A_{\nu+1}}^n))^\lambda)^{\frac{1}{\lambda}}}},\\ \sqrt[q]{e^{-(w_{\nu+1}(-\ln(f_{A_{\nu+1}}^q))^\lambda)^{\frac{1}{\lambda}}}}\end{matrix}\right\}$$

and thus

$$\bigcup_{\substack{t_{A_1}\in t_{A_{j_1}},t_{A_2}\in t_{A_{j_2}},\ldots,t_{A_{\nu+1}}\in t_{A_{j_{\nu+1}}}\\ h_{A_1}\in h_{A_{k_1}},h_{A_2}\in h_{A_{k_2}},\ldots,h_{A_{\nu+1}}\in h_{A_{k_{\nu+1}}}\\ f_{A_1}\in f_{A_{r_1}},f_{A_2}\in f_{A_{r_2}},\ldots,f_{A_{\nu+1}}\in f_{A_{r_{\nu+1}}}}}\left\{\begin{matrix}\sqrt[m]{1-e^{-(\sum_{\rho=1}^{\nu+1}w_\rho(-\ln(1-(t_{A_\rho})^m))^\lambda)^{\frac{1}{\lambda}}}},\\ \sqrt[n]{e^{-(\sum_{\rho=1}^{\nu+1}w_\rho(-\ln(h_{A_\rho}^n))^\lambda)^{\frac{1}{\lambda}}}},\\ \sqrt[q]{e^{-(\sum_{\rho=1}^{\nu+1}w_\rho(-\ln(f_{A_\rho}^q))^\lambda)^{\frac{1}{\lambda}}}}\end{matrix}\right\}$$

it holds for $\varrho = \nu + 1$ so provides for all ϱ.

Theorem 2.9 *(idempotency) Let determine collection of (m,n,q)-SHFSs that* $A_\rho = \{x,(\{t_{A_{j\rho}}\}, \{h_{A_{k\rho}}\}, \{f_{A_{r\rho}}\}): x \in X\}$ where $j = (1,2,\ldots,l_x^\cdot)$, $k = (1,2,\ldots,l_x^*)$ *and* $r = (1,2,\ldots,l_x^*)$ for $w_\rho \in [0,1]$ and $\sum_{\rho=1}^{\varrho} w_\rho = 1$. Let be $A_\rho = A$ for $(\rho = 1,2,\ldots,\varrho)$. Thus, $(m, n, q) - SHFAAWA(A, A, \ldots, A) = A$.

Proof. Firstly let write as following;

$$(m,n,q)-SHFAAWA(A_1,A_2,\dots,A_\varrho)$$

$$=\bigcup_{\substack{t_{A_1}\in t_{A_{j_1}},t_{A_2}\in t_{A_{j_2}},\dots,t_{A_\varrho}\in t_{A_{j_\varrho}}\\ h_{A_1}\in h_{A_{k_1}},h_{A_2}\in h_{A_{k_2}},\dots,h_{A_\varrho}\in h_{A_{k_\varrho}}\\ f_{A_1}\in f_{A_{r_1}},f_{A_2}\in f_{A_{r_2}},\dots,f_{A_\varrho}\in f_{A_{r_\varrho}}}}\left\{\begin{matrix}\sqrt[m]{1-e^{-(\sum_{\rho=1}^{\varrho}w_\rho(-\ln(1-(t_{A_\rho})^m))^\lambda)^{\frac{1}{\lambda}}}},\\ \sqrt[n]{e^{-(\sum_{\rho=1}^{\varrho}w_\rho(-\ln(h^n_{A_\rho}))^\lambda)^{\frac{1}{\lambda}}}},\\ \sqrt[q]{e^{-(\sum_{\rho=1}^{\varrho}w_\rho(-\ln(f^q_{A_\rho}))^\lambda)^{\frac{1}{\lambda}}}}\end{matrix}\right\}$$

since $\sum_{\rho=1}^{\varrho}w_\rho=1$;

$$=\bigcup_{\substack{t_{A_1}\in t_{A_{j_1}},t_{A_2}\in t_{A_{j_2}},\dots,t_{A_\varrho}\in t_{A_{j_\varrho}}\\ h_{A_1}\in h_{A_{k_1}},h_{A_2}\in h_{A_{k_2}},\dots,h_{A_\varrho}\in h_{A_{k_\varrho}}\\ f_{A_1}\in f_{A_{r_1}},f_{A_2}\in f_{A_{r_2}},\dots,f_{A_\varrho}\in f_{A_{r_\varrho}}}}\left\{\begin{matrix}\sqrt[m]{1-e^{-((-\ln(1-(t_{A_\rho})^m))^\lambda)^{\frac{1}{\lambda}}}},\\ \sqrt[n]{e^{-((-\ln(h^n_{A_\rho}))^\lambda)^{\frac{1}{\lambda}}}},\\ \sqrt[q]{e^{-((-\ln(f^q_{A_\rho}))^\lambda)^{\frac{1}{\lambda}}}}\end{matrix}\right\}$$

from here

$$=\left\{\sqrt[m]{1-e^{(\ln(1-(t_{A_\rho})^m))}},\sqrt[n]{e^{(\ln(h^n_{A_\rho}))}},\sqrt[q]{e^{(\ln(f^q_{A_\rho}))}}\right\}$$

for $e^{ln(x)}=x$;

$$=\left\{\sqrt[m]{1-(1-(t_{A_\rho})^m)},\sqrt[n]{(h^n_{A_\rho})},\sqrt[q]{(f^q_{A_\rho})}\right\}$$

and

$$=\left\{t_{A_\rho},\sqrt[n]{h^n_{A_\rho}},\sqrt[q]{f^q_{A_\rho}}\right\}.$$
$$=\{t_{A_\rho},h_{A_\rho},f_{A_\rho}\}.$$

Thus, $(m,n,q)-SHFAAWA(A_1,A_2,\dots,A_\varrho)=A$.

Theorem 2.10 *(monotonicity)*

Let define two (m,n,q)-SHFSs that $A_\rho=\{x,(\{t_{A_{j\rho}}\},\{h_{A_{k\rho}}\},\{f_{A_{r\rho}}\}):x\in X\}$ and $A^*_\rho=\{x,(\{t^*_{A_{j\rho}}\},\{h^*_{A_{k\rho}}\},\{f^*_{A_{r\rho}}\}):x\in X\}$ where $j=(1,2,\dots,l^\circ_x)$, $k=(1,2,\dots,l^\circ_x)$ *and* $r=(1,2,\dots,l^\circ_x)$.

If $A_\rho\le A^*_\rho(\rho=1,2,\dots,\varrho)$,

$(m,n,q)-SHFAAWA(A_1,A_2,\dots,A_\varrho)\le(m,n,q)-SHFAAWA(A^*,A^*,\dots,A^*)$.

Proof. If the following cases are surveyed for monotonicity;

- if $t_{A_\rho}\le t^*_{A_\rho}$ for $t_{A_{j_\rho}}\le t^*_{A_{j_\rho}}$;

$$\Leftrightarrow 1-(t_{A_\rho})^m\ge 1-(t^*_{A_\rho})^m$$
$$\Leftrightarrow -\ln(1-(t_{A_\rho})^m)\le -\ln(1-(t^*_{A_\rho})^m)$$
$$\Leftrightarrow \sum_{\rho=1}^{\varrho}w_\rho(-\ln(1-(t_{A_\rho})^m))^\lambda\le\sum_{\rho=1}^{\varrho}w_\rho(-\ln(1-(t_{A_\rho})^m))^\lambda$$
$$\Leftrightarrow -(\sum_{\rho=1}^{\varrho}w_\rho(-\ln(1-(t_{A_\rho})^m))^\lambda)^{\frac{1}{\lambda}}\ge-(\sum_{\rho=1}^{\varrho}w_\rho(-\ln(1-(t^*_{A_\rho})^m))^\lambda)^{\frac{1}{\lambda}}$$
$$\Leftrightarrow 1-e^{-(\sum_{\rho=1}^{\varrho}w_\rho(-\ln(1-(t_{A_\rho})^m))^\lambda)^{\frac{1}{\lambda}}}\le 1-e^{-(\sum_{\rho=1}^{\varrho}w_\rho(-\ln(1-(t^*_{A_\rho})^m))^\lambda)^{\frac{1}{\lambda}}}$$
$$\Leftrightarrow \sqrt[m]{1-e^{-(\sum_{\rho=1}^{\varrho}w_\rho(-\ln(1-(t_{A_\rho})^m))^\lambda)^{\frac{1}{\lambda}}}}\le\sqrt[m]{1-e^{-(\sum_{\rho=1}^{\varrho}w_\rho(-\ln(1-(t^*_{A_\rho})^m))^\lambda)^{\frac{1}{\lambda}}}}$$

- if $h_{A_\rho}\ge h^*_{A_\rho}$ for $h_{A_{j_\rho}}\ge h^*_{A_{j_\rho}}$;

$$\Leftrightarrow(-\ln(h^n_{A_\rho}))^\lambda\le(-\ln(h^{n^*}_{A_\rho}))^\lambda$$
$$\Leftrightarrow(\sum_{\rho=1}^{\varrho}w_\rho(-\ln(h^n_{A_\rho}))^\lambda)^{\frac{1}{\lambda}}\le\sum_{\rho=1}^{\varrho}w_\rho(-\ln(h^{n^*}_{A_\rho}))^\lambda)^{\frac{1}{\lambda}}$$
$$\Leftrightarrow e^{-(\sum_{\rho=1}^{\varrho}w_\rho(-\ln(h^n_{A_\rho}))^\lambda)^{\frac{1}{\lambda}}}\ge e^{-(\sum_{\rho=1}^{\varrho}w_\rho(-\ln(h^{n^*}_{A_\rho}))^\lambda)^{\frac{1}{\lambda}}}$$
$$\Leftrightarrow \sqrt[n]{e^{-(\sum_{\rho=1}^{\varrho}w_\rho(-\ln(h^n_{A_\rho}))^\lambda)^{\frac{1}{\lambda}}}}\ge\sqrt[n]{e^{-(\sum_{\rho=1}^{\varrho}w_\rho(-\ln(h^{n^*}_{A_\rho}))^\lambda)^{\frac{1}{\lambda}}}}$$

- if $f_{A_\rho}\ge f^*_{A_\rho}$ for $f_{A_{j_\rho}}\ge f^*_{A_{j_\rho}}$;

$$\Leftrightarrow(-\ln(f^q_{A_\rho}))^\lambda\le(-\ln(f^{q^*}_{A_\rho}))^\lambda$$
$$\Leftrightarrow(\sum_{\rho=1}^{\varrho}w_\rho(-\ln(f^q_{A_\rho}))^\lambda)^{\frac{1}{\lambda}}\le\sum_{\rho=1}^{\varrho}w_\rho(-\ln(f^{q^*}_{A_\rho}))^\lambda)^{\frac{1}{\lambda}}$$
$$\Leftrightarrow e^{-(\sum_{\rho=1}^{\varrho}w_\rho(-\ln(f^q_{A_\rho}))^\lambda)^{\frac{1}{\lambda}}}\ge e^{-(\sum_{\rho=1}^{\varrho}w_\rho(-\ln(f^{q^*}_{A_\rho}))^\lambda)^{\frac{1}{\lambda}}}$$
$$\Leftrightarrow \sqrt[n]{e^{-(\sum_{\rho=1}^{\varrho}w_\rho(-\ln(f^q_{A_\rho}))^\lambda)^{\frac{1}{\lambda}}}}\ge\sqrt[n]{e^{-(\sum_{\rho=1}^{\varrho}w_\rho(-\ln(f^{q^*}_{A_\rho}))^\lambda)^{\frac{1}{\lambda}}}}$$

Theorem 2.11 *(Boundedness) Let define collection of (m,n,q)-SHFSs that* $A_\rho=\{x,(\{t_{A_{j\rho}}\},\{h_{A_{k\rho}}\},\{f_{A_{r\rho}}\}):x\in X\}$ where $j=(1,2,\dots,l^\circ_x)$, $k=(1,2,\dots,l^\circ_x)$ *and* $r=(1,2,\dots,l^\circ_x)$ and A^+_ρ and A^-_ρ maximum and minimum elements for $\rho=1,2,\dots,\varrho$. Thus, $A^-_\rho\le(m,n,q)-SHFAAWA(A_1,A_2,\dots,A_\varrho)\le A^+_\rho$

Proof. We accept that $A^+_\rho=max\{A_\rho\}=\{(t^+_{A_{j\rho}},h^+_{A_{k\rho}},f^+_{A_{r\rho}})\}$ and $A^-_\rho=min\{A_\rho\}=\{(t^-_{A_{j\rho}},h^-_{A_{k\rho}},f^-_{A_{r\rho}})\}$ where $t^+_{A_{j\rho}}=max\{t_{A_{j\rho}}\}$, $h^+_{Ak_\rho}=min\{h_{Ak_\rho}\}$ and $f^+_{A_{r_\rho}}=min\{f_{A_{r_\rho}}\}$, and $t^-_{A_{j\rho}}=min\{t_{A_{j\rho}}\}$, $h^-_{Ak_\rho}=max\{h_{Ak_\rho}\}$ and $f^-_{A_{r_\rho}}=max\{f_{A_{r_\rho}}\}$. Thus,

$$\cup_{t^-_{A_1}\in t_{A_{j_1}},t^-_{A_2}\in t_{A_{j_2}},\dots,t^-_{A_\varrho}\in t_{A_{j_\varrho}}}\left\{\sqrt[m]{1-e^{-((-\ln(1-(t^-_{A_\rho})^m))^\lambda)^{\frac{1}{\lambda}}}}\right\}\le$$
$$\cup_{t_{A_1}\in t_{A_{j_1}},t_{A_2}\in t_{A_{j_2}},\dots,t_{A_\varrho}\in t_{A_{j_\varrho}}}\left\{\sqrt[m]{1-e^{-((-\ln(1-(t_{A_\rho})^m))^\lambda)^{\frac{1}{\lambda}}}}\right\}\le$$
$$\cup_{t^+_{A_1}\in t_{A_{j_1}},t^+_{A_2}\in t_{A_{j_2}},\dots,t^+_{A_\varrho}\in t_{A_{j_\varrho}}}\left\{\sqrt[m]{1-e^{-((-\ln(1-(t^+_{A_\rho})^m))^\lambda)^{\frac{1}{\lambda}}}}\right\}.$$

Similarly, the other parts can be surveyed and thus $A^-_\rho\le(m,n,q)-SHFAAWA(A_1,A_2,\dots,A_\varrho)\le A^+_\rho$

Definition 2.12 *Let determine a (m,n,q)-SHFS that* $A_\rho=\{x,(\{t_{A_{j\rho}}\},\{h_{A_{k\rho}}\},\{f_{A_{r\rho}}\}):x\in X\}$ *where* $j=(1,2,\dots,l^\circ_x)$, $k=(1,2,\dots,l^\circ_x)$ *and* $r=(1,2,\dots,l^\circ_x)$ *for* $w_\rho\in[0,1]$ *and* $\sum_{\rho=1}^{\varrho}w_\rho=1$;

1. $(m,n,q)-SHFAAWG$: $\Phi^\varrho\to\Phi$ is a mapping called as (m,n,q)-Spherical Hesitant Fuzzy Aczel Alsina Weighted Geometric operator and $w_\rho\in[0,1]$ and $\sum_{\rho=1}^{\varrho}w_\rho=1$ is defined as below;

$$(m,n,q)-SHFAAWG(A_1,A_2,\dots,A_\varrho)$$

$$=\cup_{\substack{t_{A_1}\in t_{A_{j_1}},t_{A_2}\in t_{A_{j_2}},\dots,t_{A_\varrho}\in t_{A_{j_\varrho}}\\ h_{A_1}\in h_{A_{k_1}},h_{A_2}\in h_{A_{k_2}},\dots,h_{A_\varrho}\in h_{A_{k_\varrho}}\\ f_{A_1}\in f_{A_{r_1}},f_{A_2}\in f_{A_{r_2}},\dots,f_{A_\varrho}\in f_{A_{r_\varrho}}}}\left\{\begin{matrix}\sqrt[m]{e^{-(\sum_{\rho=1}^{\varrho}w_\rho(-\ln(t^m_{A_\rho}))^\lambda)^{\frac{1}{\lambda}}}},\\ \sqrt[n]{1-e^{-(\sum_{\rho=1}^{\varrho}w_\rho(-\ln(1-(h_{A_\rho})^n))^\lambda)^{\frac{1}{\lambda}}}},\\ \sqrt[q]{1-e^{-(\sum_{\rho=1}^{\varrho}w_\rho(-\ln(1-(f_{A_\rho})^q))^\lambda)^{\frac{1}{\lambda}}}}\end{matrix}\right\}.$$

2. $(m,n,q)-SHFAAOWG$: $\Phi^\varrho\to\Phi$ is a mapping called as (m,n,q)-Spherical Hesitant Fuzzy Aczel Alsina Ordered Weighted Geometric operator and $w_\rho\in[0,1]$ and $\sum_{\rho=1}^{\varrho}w_\rho=1$ is defined as below;

$$(m,n,q)-SHFAAOWG(A_1,A_2,\ldots,A_\varrho)$$
$$=\bigcup_{\substack{t_{A_{\sigma(1)}}\in t_{A_{j_{\sigma(1)}}},t_{A_{\sigma(2)}}\in t_{A_{j_{\sigma(2)}}},\ldots,t_{A_{\sigma(\varrho)}}\in t_{A_{j_{\sigma(\varrho)}}}\\ h_{A_{\sigma(1)}}\in h_{A_{k_{\sigma(1)}}},h_{A_2}\in h_{A_{k_{\sigma(2)}}},\ldots,h_{A_{\sigma(\varrho)}}\in h_{A_{k_\varrho}}\\ f_{A_1}\in f_{A_{r_1}},f_{A_{\sigma(2)}}\in f_{A_{r_{\sigma(2)}}},\ldots,f_{A_{\sigma(\varrho)}}\in f_{A_{r_{\sigma(\varrho)}}}}}\left\{\begin{array}{l}\sqrt[m]{e^{-(\sum_{\rho=1}^{\varrho}w_\rho(-\ln(t^m_{A_{\sigma(\rho)}}))^\lambda)^{\frac{1}{\lambda}}}},\\ \sqrt[n]{1-e^{-(\sum_{\rho=1}^{\varrho}w_\rho(-\ln(1-(h^n_{A_{\sigma(\rho)}})))^\lambda)^{\frac{1}{\lambda}}}},\\ \sqrt[q]{1-e^{-(\sum_{\rho=1}^{\varrho}w_\rho(-\ln(1-(f^q_{A_{\sigma(\rho)}})))^\lambda)^{\frac{1}{\lambda}}}}\end{array}\right\}$$

where $(\sigma(1), \sigma(2), \ldots, \sigma(\varrho))$ are the permutation of $(\rho = 1,2,\ldots,\varrho)$, including $A_{\sigma(\varrho-1)} \geq A_{\sigma(\varrho)}$.

3. $(m, n, q) - SHFAAHWG$: $\Phi^\varrho \to \Phi$ is a mapping called as (m,n,q)-Spherical Hesitant Fuzzy Aczel Alsina Hybrid Weighted Geometric operator and $w_\rho \in [0,1]$ and $\sum_{\rho=1}^{\varrho} w_\rho = 1$ is defined as below;

$$(m,n,q)-SHFAAHWG(A_1,A_2,\ldots,A_\varrho)$$
$$=\bigcup_{\substack{t_{A_{\sigma(1)}}\in t_{A_{j_{\sigma(1)}}},t_{A_{\sigma(2)}}\in t_{A_{j_{\sigma(2)}}},\ldots,t_{A_{\sigma(\varrho)}}\in t_{A_{j_{\sigma(\varrho)}}}\\ h_{A_{\sigma(1)}}\in h_{A_{k_{\sigma(1)}}},h_{A_2}\in h_{A_{k_{\sigma(2)}}},\ldots,h_{A_{\sigma(\varrho)}}\in h_{A_{k_\varrho}}\\ f_{A_1}\in f_{A_{r_1}},f_{A_{\sigma(2)}}\in f_{A_{r_{\sigma(2)}}},\ldots,f_{A_{\sigma(\varrho)}}\in f_{A_{r_{\sigma(\varrho)}}}}}\left\{\begin{array}{l}\sqrt[m]{e^{-(\sum_{\rho=1}^{\varrho}w_\rho(-\ln(t^m_{A_{\sigma(\rho)}}))^\lambda)^{\frac{1}{\lambda}}}},\\ \sqrt[n]{1-e^{-(\sum_{\rho=1}^{\varrho}w_\rho(-\ln(1-(h^n_{A_{\sigma(\rho)}})))^\lambda)^{\frac{1}{\lambda}}}},\\ \sqrt[q]{1-e^{-(\sum_{\rho=1}^{\varrho}w_\rho(-\ln(1-(f^q_{A_{\sigma(\rho)}})))^\lambda)^{\frac{1}{\lambda}}}}\end{array}\right\}$$

where, $\dot{A}_\rho = \kappa\varpi_\rho A_\rho$ and κ is the very important balancing coefficient for $A_{\sigma(\varrho-1)} \geq A_{\sigma(\varrho)}$ and $\varpi_\rho = (1,2,\ldots,\varrho)$ is an associated vector.

Characteristic of (m,n,q)- Spherical hesitant fuzzy Aczel Alsina weighted geometric operator

Theorem 2.13 *Let determine collection of (m,n,q)-SHFSs that* $A_\rho = \{x,(\{t_{A_{j\rho}}\},\{h_{A_{k\rho}}\},\{f_{A_{r\rho}}\}): x \in X\}$ *where* $j = (1,2,\ldots,l^*_x)$, $k = (1,2,\ldots,l^\circ_x)$ *and* $r = (1,2,\ldots,l^\circ_x)$ *for* $w_\rho \in [0,1]$ *and* $\sum_{\rho=1}^{\varrho} w_\rho = 1$. *Then their Aczel Alsina aggregated value by using (m,n,q)-SHFAAHWG is a (m,n,q)-SHFE and*

$$(m,n,q)-SHFAAWG(A_1,A_2,\ldots,A_\varrho)$$
$$=\bigcup_{\substack{t_{A_1}\in t_{A_{j_1}},t_{A_2}\in t_{A_{j_2}},\ldots,t_{A_\varrho}\in t_{A_{j_\varrho}}\\ h_{A_1}\in h_{A_{k_1}},h_{A_2}\in h_{A_{k_2}},\ldots,h_{A_\varrho}\in h_{A_{k_\varrho}}\\ f_{A_1}\in f_{A_{r_1}},f_{A_2}\in f_{A_{r_2}},\ldots,f_{A_\varrho}\in f_{A_{r_\varrho}}}}\left\{\begin{array}{l}\sqrt[m]{e^{-(\sum_{\rho=1}^{\varrho}w_\rho(-\ln(t^m_{A_\rho}))^\lambda)^{\frac{1}{\lambda}}}},\\ \sqrt[n]{1-e^{-(\sum_{\rho=1}^{\varrho}w_\rho(-\ln(1-(h^n_{A_\rho})))^\lambda)^{\frac{1}{\lambda}}}},\\ \sqrt[q]{1-e^{-(\sum_{\rho=1}^{\varrho}w_\rho(-\ln(1-(f^q_{A_\rho})))^\lambda)^{\frac{1}{\lambda}}}}\end{array}\right\}$$

Proof. Let use mathematical induction on ϱ and look for $\varrho = 1,2$;

$$A_1^{w_1}=\bigcup_{t_{A_1}\in t_{A_{j_1}},h_{A_1}\in h_{A_{k_1}},f_{A_1}\in f_{A_{r_1}}}\left\{\begin{array}{l}\sqrt[m]{e^{-(w_1(-\ln(t^m_{A_1}))^\lambda)^{\frac{1}{\lambda}}}},\\ \sqrt[n]{1-e^{-(w_1(-\ln(1-(h^n_{A_1})))^\lambda)^{\frac{1}{\lambda}}}},\\ \sqrt[q]{1-e^{-(w_1(-\ln(1-(h^q_{A_1})))^\lambda)^{\frac{1}{\lambda}}}}\end{array}\right\}$$

and

$$A_2^{w_2}=\bigcup_{t_{A_2}\in t_{A_{j_2}},h_{A_2}\in h_{A_{k_2}},f_{A_2}\in f_{A_{r_2}}}\left\{\begin{array}{l}\sqrt[m]{e^{-(w_2(-\ln(t^m_{A_2}))^\lambda)^{\frac{1}{\lambda}}}},\\ \sqrt[n]{1-e^{-(w_2(-\ln(1-(h^n_{A_2})))^\lambda)^{\frac{1}{\lambda}}}},\\ \sqrt[q]{1-e^{-(w_2(-\ln(1-(h^q_{A_2})))^\lambda)^{\frac{1}{\lambda}}}}\end{array}\right\}$$

from here

$$A_1^{w_1}\otimes A_2^{w_2}=\bigcup_{\substack{t_{A_1}\in t_{A_{j_1}}\ t_{A_2}\in t_{A_{j_2}}\\ h_{A_1}\in h_{A_{k_1}},h_{A_2}\in h_{A_{k_2}}\\ f_{A_1}\in f_{A_{r_1}}\ f_{A_2}\in f_{A_{r_2}}}}\left\{\begin{array}{l}\sqrt[m]{e^{-(\sum_{\rho=1}^{2}w_\rho(-\ln(t^m_{A_\rho}))^\lambda)^{\frac{1}{\lambda}}}},\\ \sqrt[n]{1-e^{-(\sum_{\rho=1}^{2}w_\rho(-\ln(1-(h^n_{A_\rho})))^\lambda)^{\frac{1}{\lambda}}}},\\ \sqrt[q]{1-e^{-(\sum_{\rho=1}^{2}w_\rho(-\ln(1-(f^q_{A_\rho})))^\lambda)^{\frac{1}{\lambda}}}}\end{array}\right\}.$$

Then, from here for $\varrho = \nu$, (m,n,q)-SHFAAWA holds as follow;

$$\bigcup_{\substack{t_{A_1}\in t_{A_{j_1}},t_{A_2}\in t_{A_{j_2}},\ldots,t_{A_\nu}\in t_{A_{j_\nu}}\\ h_{A_1}\in h_{A_{k_1}},h_{A_2}\in h_{A_{k_2}},\ldots,h_{A_\nu}\in h_{A_{k_\nu}}\\ f_{A_1}\in f_{A_{r_1}},f_{A_2}\in f_{A_{r_2}},\ldots,f_{A_\nu}\in f_{A_{r_\nu}}}}\left\{\begin{array}{l}\sqrt[m]{e^{-(\sum_{\rho=1}^{\nu}w_\rho(-\ln(t^m_{A_\rho}))^\lambda)^{\frac{1}{\lambda}}}},\\ \sqrt[n]{1-e^{-(\sum_{\rho=1}^{\nu}w_\rho(-\ln(1-(h^n_{A_\rho})))^\lambda)^{\frac{1}{\lambda}}}},\\ \sqrt[q]{1-e^{-(\sum_{\rho=1}^{\nu}w_\rho(-\ln(1-(f^q_{A_\rho})))^\lambda)^{\frac{1}{\lambda}}}}\end{array}\right\}$$

and for $\varrho = \nu + 1$;

$$\bigcup_{\substack{t_{A_1}\in t_{A_{j_1}},t_{A_2}\in t_{A_{j_2}},\ldots,t_{A_\nu}\in t_{A_{j_\nu}}\\ h_{A_1}\in h_{A_{k_1}},h_{A_2}\in h_{A_{k_2}},\ldots,h_{A_\nu}\in h_{A_{k_\nu}}\\ f_{A_1}\in f_{A_{r_1}},f_{A_2}\in f_{A_{r_2}},\ldots,f_{A_\nu}\in f_{A_{r_\nu}}}}\left\{\begin{array}{l}\sqrt[m]{e^{-(\sum_{\rho=1}^{\nu}w_\rho(-\ln(t^m_{A_\rho}))^\lambda)^{\frac{1}{\lambda}}}},\\ \sqrt[n]{1-e^{-(\sum_{\rho=1}^{\nu}w_\rho(-\ln(1-(h_{A_\rho})^n))^\lambda)^{\frac{1}{\lambda}}}},\\ \sqrt[q]{1-e^{-(\sum_{\rho=1}^{\nu}w_\rho(-\ln(1-(f_{A_\rho})^q))^\lambda)^{\frac{1}{\lambda}}}}\end{array}\right\}$$
$$\otimes\bigcup_{t_{A_{\nu+1}}\in t_{A_{j_{\nu+1}}},h_{A_{\nu+1}}\in h_{A_{j_{\nu+1}}},f_{A_{\nu+1}}\in f_{A_{j_{\nu+1}}}}\left\{\begin{array}{l}\sqrt[m]{e^{-(w_{\nu+1}(-\ln(t^m_{A_{\nu+1}}))^\lambda)^{\frac{1}{\lambda}}}},\\ \sqrt[n]{1-e^{-(w_{\nu+1}(-\ln(1-(h^n_{A_{\nu+1}})^m))^\lambda)^{\frac{1}{\lambda}}}},\\ \sqrt[q]{1-e^{-(w_{\nu+1}(-\ln(1-(f^q_{A_{\nu+1}})^m))^\lambda)^{\frac{1}{\lambda}}}}\end{array}\right\}$$

and thus

$$\bigcup_{\substack{t_{A_1}\in t_{A_{j_1}},t_{A_2}\in t_{A_{j_2}},\ldots,t_{A_{\nu+1}}\in t_{A_{j_{\nu+1}}}\\ h_{A_1}\in h_{A_{k_1}},h_{A_2}\in h_{A_{k_2}},\ldots,h_{A_{\nu+1}}\in h_{A_{k_{\nu+1}}}\\ f_{A_1}\in f_{A_{r_1}},f_{A_2}\in f_{A_{r_2}},\ldots,f_{A_{\nu+1}}\in f_{A_{r_{\nu+1}}}}}\left\{\begin{array}{l}\sqrt[m]{e^{-(\sum_{\rho=1}^{\nu+1}w_\rho(-\ln(t^m_{A_\rho}))^\lambda)^{\frac{1}{\lambda}}}},\\ \sqrt[n]{1-e^{-(\sum_{\rho=1}^{\nu+1}w_\rho(-\ln(1-(h^n_{A_\rho})))^\lambda)^{\frac{1}{\lambda}}}},\\ \sqrt[q]{1-e^{-(\sum_{\rho=1}^{\nu+1}w_\rho(-\ln(1-(f^q_{A_\rho})))^\lambda)^{\frac{1}{\lambda}}}}\end{array}\right\}$$

it holds for $\varrho = \nu + 1$ so provides for all ϱ.

The proofs of idempotency, monotoncity and Boundedness can be proved as(m,n,q)-SHFAAWA

4. Algorithm for (m,n,q)-Spherical Hesitant Fuzzy Sets

In this section, we apply the presented (m,n,q)-SHFAAWA and (m,n,q)-SHFAAWG operators into an algorithm and test over a MCDM problem with π alternatives and ϱ criteria to indicate effective of averaging operators over (m,n,q)-SHFS. Let $\hat{A} = \{\hat{A}_1, \hat{A}_2, \ldots, \hat{A}_\pi\}$ be a set of alternatives, $C = \{C_1, C_2, \ldots, C_\varrho\}$ be a set of criterions and let $w_\rho = (w, w, \ldots, w)$ be a weight vector of criterions where $w > 0$, $\rho = 1,2,\ldots,\varrho$ and $\sum_{\rho=1}^{\varrho} w_\rho = 1$. Then, the following steps have been defined for algorithm.

1. Consist of Decision making matrix as $D = (d_{\theta\vartheta})_{\pi\times\varrho}$ for $\theta = 1,2,\ldots,\pi$ and $\vartheta = 1,2,\ldots,\varrho$,
2. Determine (m,n,q)-SHFEs by utilizing $d_\theta = (m, n, q) - SHFAAWA(d_{\theta1}, d_{\theta2}, \ldots, d_{\theta\varrho})$ and $d_\theta = (m, n, q) - SHFAAWG(d_{\theta1}, d_{\theta2}, \ldots, d_{\theta\varrho})$ for $\theta = 1,2,\ldots,\pi$,
3. Calculate score values of (m,n,q)-SHFEs,
4. Determine alternatives rankings in descending order.

An illustrative example

Let think a company, which wants to invest over different sectors in Turkey and thus executives of company determine four alternatives by evaluating under various criterions to find the most proper alternative to invest the money: (1) A_1 is a cyclic company; (2) A_2 is an aircraft company; (3) A_3 is a food company; (4) A_4 is an plastic production company. The investment company must decide according to the five criterions; (1) C_1 is the transportation; (2) C_2 is the labor; (3) C_3 is an environmental impact; (4) C_4 is proximity to raw material; (5) C_5 is experience and weight vector is presented as w = (0.3,0.3,0.2,0.1,0.1). The four alternatives are evaluated under the criterions by linguistic grades given in Table 1 provided by decision makers.

Step 1: Decision makers evaluate alternatives for each of criterions according to linguistic grade given in Table 1. Their evaluations are given in Table 1.

Step 2: Obtain aggregated values by utilizing $d_\theta = (m, n, q) - SHFAAWA(d_{\theta 1}, d_{\theta 2}, \ldots, d_{\theta \varrho})$ and $d_\theta = (m, n, q) - SHFAAWG(d\theta 1, d\theta 2, \ldots, d\theta\varrho)$ for θ = 1,2, . . . , π. Thus, results are as follow for (3,5,7), λ = 2 and (m,n,q)-SHFAAWA;

$$d_1 = \left\{\begin{array}{l}\{0.2714,0.1439,0.2709,0.1421,0.2738,0.1522\},\\ \{0.9965,0.9920,0.9951,0.9946,0.9978,0.9876,0.9924,0.9966\},\\ \{0.8035,0.9344,0.8831,0.8426,0.8884,0.9088,0.9309,0.9430,0.9459,\\ 0.9657,0.9586,0.9046\}\end{array}\right\}$$

$$d_2 = \left\{\begin{array}{l}\{0.2181,0.2271,0.11860.1443,0.2169,0.2259,0.1141,0.1414\},\\ \{0.9935,0.9916,0.9996,0.9992,0.9990,0.9995,0.9877,0.9916\},\\ \{0.9779,0.9836,0.9636,0.9732\}\end{array}\right\}$$

$$d_3 = \left\{\begin{array}{l}\{0.2423,0.2531,0.2345,0.2460,0.3998,0.2345\},\\ \{0.9999,0.9985,0.9980,0.9988,0.9985,0.9999,0.9999,0.9999\},\\ \{0.9945,0.9910,0.9874,0.9794,0.9662,0.9794\}\end{array}\right\}$$

$$d_4 = \left\{\begin{array}{l}\{0.4975,0.4995,0.3765,0.5047,0.3898,0.3933,0.3803,0.5066\},\\ \{0.99992,0.99995\},\\ \{0.9997,0.9999,0.99993,0.999930.99998,0.999996\}\end{array}\right\}$$

score values are found that $s(d_1) = -0.2376$, $s(d_2) = -0.4031$, $s(d_3) = -0.4320$ and $s(d_4) = -0.4559$. Thus, rankings are obtained that $A_1 > A_2 > A_3 > A_4$.

In here, we only give for (3,5,7), λ = 2 and score values are as follow for the other cases;

The results are as follow for (3,5,7), λ = 2 and (m,n,q)-SHFAAWG;

Table 2. Evaluations of alternatives made by decision makers

	C_1	C_2	C_3	C_4	C_5
A_1	{{0.30,0.10,0.40}, {0.30,0.40}, {0.70,0.60}}	{{0.40}, {0.50,0.40}, {0.70,0.40,0.50}}	{{0.70,0.40}, {0.30}, {0.70}}	{{0.50}, {0.90}, {0.50,0.30}}	{{0.50}, {0.30,0.50}, {0.70}}
A_2	{{0.20}, {0.50,0.20}, {0.40,0.50}}	{{0.60,0.30}, {0.30}, {0.60,0.50}}	{{0.40,0.50}, {0.40,0.70}, {0.40}}	{{0.50}, {0.40,0.60}, {0.40}}	{{0.40,0.30}, {0.50}, {0.60}}
A_3	{{0.30}, {0.10,0.30}, {0.30,0.40,0.50}}	{{0.40,0.50}, {0.40}, {0.40,0.50}}	{{0.50,0.40,0.80}, {0.30}, {0.50}}	{{0.60}, {0.30,0.40}, {0.50}}	{{0.70}, {0.40,0.30}, {0.40}}
A_4	{{0.50,0.60}, {0.20}, {0.30,0.20}}	{{0.80,0.40}, {0.20}, {0.30,0.20}}	{{0.30,0.50}, {0.50}, {0.30}}	{{0.80}, {0.40}, {0.20,0.10}}	{{0.80}, {0.30,0.20}, {0.30}}

Table 3. Ranking alternatives according to Score Values under (m,n,q)-SHFAAWA

(m,n,q);λ	A_1	A_2	A_3	A_4	Ranking Alternatives
(3,5,7);2	-0.2376	-0.4031	-0.4320	-0.4559	$A_1 > A_2 > A_3 > A_4$
(9,4,2);5	-0.0256	-0.0129	-0.4438	-0.4585	$A_2 > A_1 > A_3 > A_4$
(11,7,12);4	-0.4995	-0.4974	-0.4876	-0.4367	$A_4 > A_3 > A_2 > A_1$
(13,9,18);3	-0.4976	-0.4907	-0.4724	-0.4018	$A_4 > A_3 > A_2 > A_1$
(12,3,5);1	-0.3417	-0.3509	-0.3340	-0.2479	$A_4 > A_3 > A_1 > A_2$

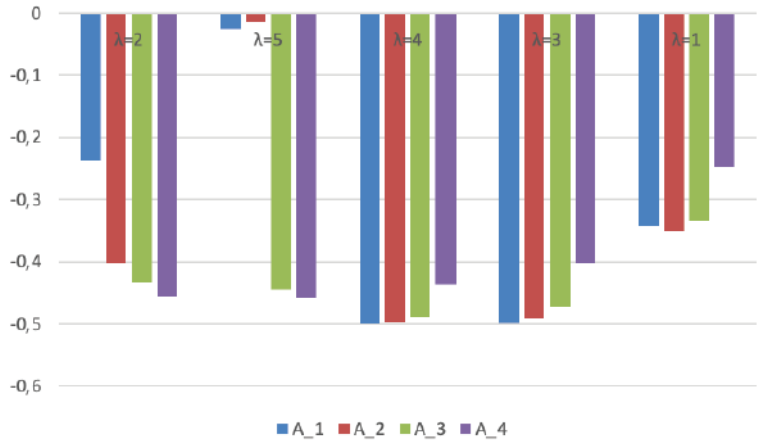


Figure 2. The graphical presentation of Table 3.

$$d_1 = \begin{Bmatrix} \{0.9902,0.9953,0.99995,0.999970.9795,0.9893\}, \\ \{0.4385,0.4394,0.4362,0.4399,0.4353,0.4407,0.4375,0.4367\}, \\ \{0.4943,0.3756,0.4242,0.3931,0.3801,0.3366,0.3782,0.3342, \\ 0.3308,0.3283,0.3737,0.3914\} \end{Bmatrix}$$

$$d_2 = \begin{Bmatrix} \{0.9960,0.9974,0.9996,0.9994,0.9985,0.9980,0.9997,0.9996\}, \\ \{0.1629,0.1917,0.1186,0.2654,0.2775,0.1638,0.2772,0.9916\}, \\ \{0.2355,0.1905,0.2469,0.2074\} \end{Bmatrix}$$

$$d_3 = \begin{Bmatrix} \{0.9871,0.9863,0.9939,0.9901,0.9798,0.9939\}, \\ \{0.9999,0.9985,0.9980,0.9988,0.9985,0.9999,0.0930,0.0995\}, \\ \{0.1540,0.1782,0.1613,0.1837,0.2017,0.1837\} \end{Bmatrix}$$

$$d_4 = \begin{Bmatrix} \{0.8106,0.8865,0.9852,0.9395,0.9800,0.9508,0.9639,0.8397\}, \\ \{0.1271,0.1264\}, \\ \{0.0698,0.0619,0.0619,0.06193,0.0512,0.0508\} \end{Bmatrix}$$

score values are found that $s(d_1) = 0.9800$, $s(d_2) = 0.9965$, $s(d_3) = 0.8447$ and $s(d_4) = 0.8887$. Thus, rankings are obtained that $A_2 > A_1 > A_4 > A_3$.

In here, we only give for (3,5,7), $\lambda = 2$ and score values are as follow for the other cases ;

Step 3: The score values have been given into Table 3 and Table 4,

Step 4: When the tables are surveyed, it is open that A_4 alternative is the best alternative for all of values of λ out $\lambda = 2$; (3,5,7) and $\lambda = 5$; (9,4,2) for two operators. For all remaining

Table 4. Ranking alternatives according to Score Values under (m,n,q)-SHFAAWG

(m,n,q);λ	A_1	A_2	A_3	A_4	Ranking Alternatives
(3,5,7);2	0.98	0.9965	0.8447	0.8887	$A_2 > A_1 > A_4 > A_3$
(9,4,2);5	0.8447	0.8887	0.9931	0.9999	$A_4 > A_3 > A_2 > A_1$
(11,7,12);4	0.989997	0.999998	0.999977	0.999998	$A_4 > A_3 > A_2 > A_1$
(13,9,18);3	0. 9883	0.99996	0.99999915	0.99999918	$A_4 > A_3 > A_2 > A_1$
(12,3,5);1	0.8106	0.9516	0.9779	0.9898	$A_4 > A_3 > A_1 > A_2$

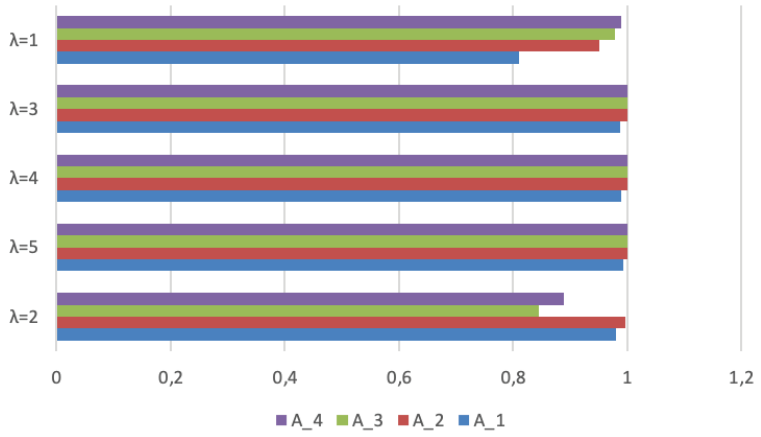


Figure 3. The graphical presentation of Table 4.

cases, the best alternative is determined similarly. It should be noted is that the best alternative probabilistically is seen as A_4. A_2 and A_1 may be determined as the best alternative with a very low probability. Although the (m,n,q)-SHFAAWG and (m,n,q)-SHFAAWA are two different operators, the results are almost agreement.. This statement indicates that the proposed operators are reality, effective, flexible and have more advantages because of including four different valuables. It should be noted that as if the number of variables increases, the flexibility of the set will increase.

COMPARATIVE ANALYSIS

In this section, the proposed SHFAAWG and SHFAAWA under (m,n,q)-SHFS environment are compared with some aggregation operators defined for the mobil telephones problem over T-SHFS [25]. If this example is solved with the proposed SHFAAWG and SHFAAWA, the results are as following; when the results are surveyed, there is agreement for λ = 1,3,4 under combinations of (m,n,q) of SHFAAWG and SHFAAWA, although there are some differences between the proposed rankings and ordering of Quran [30]. The basic reason that the proposed operators present four different variables, while Quran is using a parameter for calculations. It is open that the presented operators and cluster have more advantages in terms of flexible, hesitation degree, more reality results and for (m,n,q)-SHFAAWG;

Table 5. Ranking alternatives according to Score Values under (m,n,q)-SHFAAWA

(m,n,q);λ	A_1	A_2	A_3	A_4	Ranking Alternatives
(3,5,7);2	-0.0085	-0.2398	-0.4336	-0.3996	$A_1 > A_2 > A_4 > A_3$
(9,4,2);5	-0.0279	-0.0118	-0.4538	-0.4597	$A_2 > A_1 > A_3 > A_4$
(11,7,12);4	-0.5996	-0.4990	-0.4863	-0.4468	$A_4 > A_3 > A_2 > A_1$
(13,9,18);3	-0.59997	-0.4975	-0.4845	-0.4171	$A_4 > A_3 > A_2 > A_1$
(12,3,5);1	-0.3417	-0.3509	-0.3340	-0.2479	$A_4 > A_3 > A_1 > A_2$
T-SHFWA[25];q=3	0.2991	0.443	0.5798	0.737	$A_4 > A_3 > A_2 > A_1$

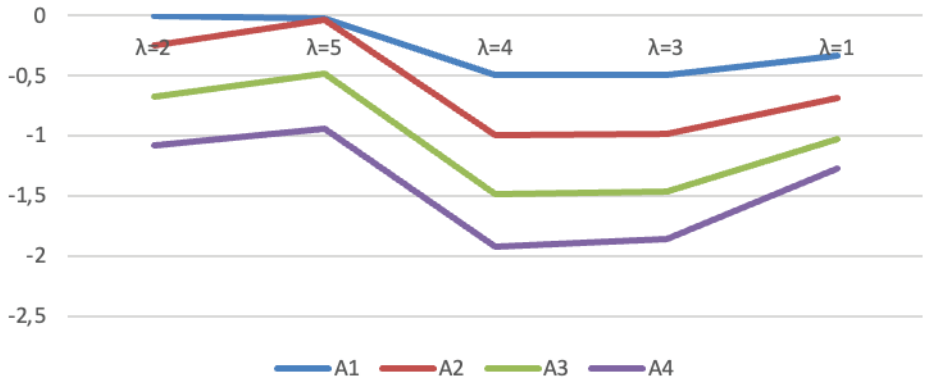


Figure 4. The graphical presentation of Table 5.

Table 6. Ranking alternatives according to Score Values under (m,n,q)-SHFAAWG

(m,n,q);λ	A_1	A_2	A_3	A_4	Ranking Alternatives
(3,5,7);2	0.9825	0.9889	0.7165	0.6680	$A_2 > A_1 > A_3 > A_4$
(9,4,2);5	0.9931	0.999991899	0.999991922	0.999991921	$A_3 > A_4 > A_2 > A_1$
(11,7,12);4	0.9899	0.99998	0.9999901	0.9999989	$A_4 > A_3 > A_2 > A_1$
(13,9,18);3	0.988397344	0.9999613	0.999991585	0.999991864	$A_4 > A_3 > A_2 > A_1$
(12,3,5);1	0.8106	0.9516	0.9779	0.9898	$A_4 > A_3 > A_1 > A_2$
TSHFWG[25];q=3	0.1669	0.377	0.518	0.703	$A_4 > A_3 > A_2 > A_1$

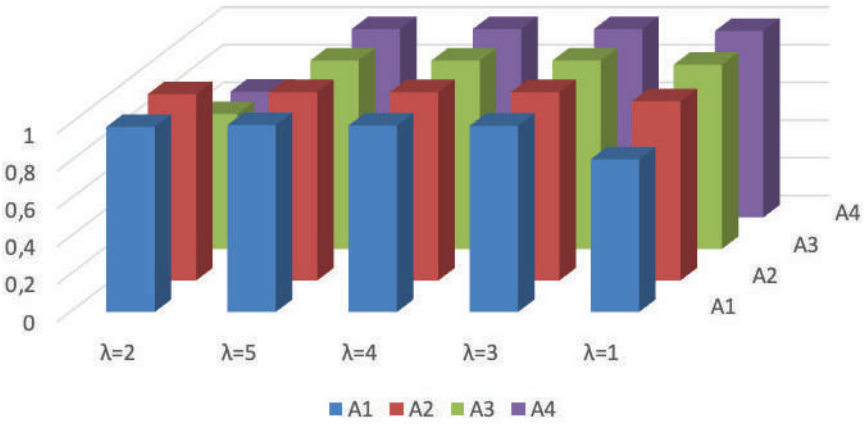


Figure 5. The graphical presentation of Table 6.

CONCLUSION

In this paper, the authors produce (m,n,q)- spherical hesitant fuzzy set by combining hesitant fuzzy set and (m,n,q)- spherical fuzzy set. The (m,n,q)- spherical hesitant fuzzy has a flexible structure than all existing concept as intuitionistic hesitant fuzzy set, t-spherical hesitant fuzzy sets, hesitant pythagorean fuzzy set, q- rang orthopair hesitant fuzzy set so on because of including three different parameters. The above defined concepts host several disadvantages owing to novel reasons as all of structures have same powers, not having some degrees, not carrying more information. These disadvantages have been the support point for the definition of this cluster. For example, let us define t-spherical hesitant fuzzy set being wider of above clusters as follow; $\langle\{0.9,0.7,0.8\},\{0.9,0.5\},\{0.3,0.4\}\rangle$ for $t = 3$ and with condition $0 \leq 0.9^3 + 0.9^3 + 0.4^3 \not\leq 1$ but it is clear that the condition is not provided as a result of the basic operations. In here, if t parameter is converted to different parameter only for truth degree, the problem is eliminated without error margin such as $0 \leq 0.9^7 + 0.9^3 + 0.4^3 \leq 1$. Therefore, (m,n,q)- spherical hesitant fuzzy set is a more flexible and more inclusive set.

Then, we define (m,n,q)- Spherical hesitant fuzzy Aczel Alsina weighted averaging operator, (m,n,q)- Spherical hesitant fuzzy Aczel Alsina ordered weighted averaging operator, (m,n,q)- Spherical hesitant fuzzy Aczel Alsina hybrid weighted averaging operator and (m,n,q)- Spherical hesitant fuzzy Aczel Alsina weighted geometric operator , (m,n,q)- Spherical hesitant fuzzy Aczel Alsina ordered weighted geometric operator, (m,n,q)- Spherical hesitant fuzzy Aczel Alsina hybrid weighted geometric operator. Thus, a new parameter is added and the obtained operators include four variables. Moreover, a new algorithm and an example are defined and compared one with the other. It is open that orderings have a big agreement when ranking of alternatives are surveyed. When the tables are surveyed, it is open that A_4 alternative is the best alternative for all of values of λ out $\lambda = 2$; (3,5,7) and $\lambda = 5$; (9,4,2) for two operators. For all remaining cases, the best alternative is determined similarly. It should be noted is that the best alternative probabilistically is seen as A_4. A_2 and A_1 may be determined as the best alternative with a very low probability. Although the (m,n,q)- Spherical hesitant fuzzy Aczel Alsina ordered weighted geometric operator, and (m,n,q)- Spherical hesitant fuzzy Aczel Alsina ordered weighted averaging operator, are two different operators, the results are almost agreement. This statement indicates that the proposed operators are reality, effective, flexible and have more advantages because of including four different valuables. It should be noted that as if the number of variables increases, the flexibility of the set will increase.

In future, we plan to present basic measures Hamming, Euclidean, Hausdorf, Generalized Dice measures, Hybrid measures, Vector measures, cross-entropy, aggregating operators based on (m,n,q)-spherical hesitant fuzzy set. Moreover, the measures and cluster can be carried to different dimensions by using the methods like TODIM ELECTRE etc.. In addition to, we work to justify whether this algorithm can be applied to large-scale data set.

DATA AVAILABILITY STATEMENT

The data sets generated during and/or analyzed during the current study are available from the corresponding author on reasonable request.

CONFLICT OF INTEREST

The authors declare that there is no conflict of interest regarding the publication of this paper.

ETHICS

This article does not contain any studies with human participants or animals performed by any of the authors.

STATEMENT ON THE USE OF ARTIFICIAL INTELLIGENCE

Artificial intelligence was not used in the preparation of the article.

REFERENCES

[1] Zadeh LA. Fuzzy sets. Inf Comput 1965;8:338–353. [CrossRef]

[2] Atanassov KT. Intuitionistic fuzzy sets. Fuzzy Sets Syst 1986;20:87–96. [CrossRef]

[3] Yager RR. Pythagorean membership grades in multicriteria decision making. IEEE Trans Fuzzy Syst 2014;22:958–965. [CrossRef]

[4] Yager RR. Generalized orthopair fuzzy sets. IEEE Trans Fuzzy Syst 2016;8:29–60.

[5] Cuong BC, Pham VH. Some fuzzy logic operators for picture fuzzy sets. In: Knowl Syst Eng (KSE), 8th Int Conf. IEEE; 2015. [CrossRef]

[6] Mahmood T, Ullah K, Khan Q, Jan N. An approach toward decision-making and medical diagnosis problems using the concept of spherical fuzzy sets. Neural Comput Appl 2019;31:7041–7053. [CrossRef]

[7] Ashraf S, Abdullah S, Mahmood T, Ghani F, Mahmood T. Spherical fuzzy sets and their applications in multi-attribute decision making problems. J Intell Fuzzy Syst 2019;36:2829–2844. [CrossRef]

[8] Quek SG, Selvachandran G, Munir M, Mahmood T, Ullah K, Son LH. Multi-attribute multi-perception decision-making based on generalized T-spherical fuzzy weighted aggregation operators on neutrosophic sets. Mathematics 2019;7:780. [CrossRef]

[9] Garg H, Ullah K, Mahmood T, Hassan N, Jan N. T-spherical fuzzy power aggregation operators and their applications in multi-attribute decision making. J Amb Intell Hum Comput 2021;12:9067–9080. [CrossRef]

[10] Ullah K, Garg H, Mahmood T, Jan N, Ali Z. Correlation coefficient for T-spherical fuzzy sets and their applications in clustering and multi-attribute decision making. Soft Comput 2020;24:1647–1659. [CrossRef]

[11] Wu MQ, Chen TY, Fan JP. Divergence measure of T-spherical fuzzy sets and its applications in pattern recognition. IEEE Access 2020;8:10208–10221. [CrossRef]

[12] Aczel J, Alsina C. Characterizations of some classes of quasilinear functions with applications to triangular norms and to synthesizing judgements. Aequat Math 1982;25:313–315. [CrossRef]

[13] Babu MS, Ahmed S. Function as the generator of parametric T-norms. Am J Appl Math 2017;5:114–118. [CrossRef]

[14] Senapati T, Chen G, Yager RR. Aczel-Alsina aggregation operators and their application to intuitionistic fuzzy multiple attribute decision making. Int J Intell Syst 2022;37:1529–1551. [CrossRef]

[15] Senapati T, Chen G, Mesiar R, Yager RR. Novel Aczel–Alsina operations-based interval-valued intuitionistic fuzzy aggregation operators and their applications in multiple attribute decision-making process. Int J Intell Syst 2022;37:22751. [CrossRef]

[16] Senapati T. Approaches to multi-attribute decision-making based on picture fuzzy Aczel–Alsina average aggregation operators. Comput Appl Math 2022;41:40. [CrossRef]

[17] Hussain A, Ullah K, Yang MS, Pamucar D. Aczel–Alsina aggregation operators on T-spherical fuzzy (TSF) information with application to TSF multi-attribute decision making. IEEE Access 2022;10:26011–26023. [CrossRef]

[18] Hussain A, Ullah K, Alshahrani MN, Yang MS, Pamucar D. Novel Aczel–Alsina operators for Pythagorean fuzzy sets with application in multi-attribute decision making. Symmetry 2022;14:940. [CrossRef]

[19] Torra V, Narukawa Y. On hesitant fuzzy sets and decision. In: 18th IEEE Int Conf Fuzzy Syst; 2009 Aug; Jeju Island, Korea. p. 1378–1382. [CrossRef]

[20] Torra V. Hesitant fuzzy sets. Int J Intell Syst 2010;25:529–539. [CrossRef]

[21] Beg I, Rashid T. Group decision making using intuitionistic hesitant fuzzy sets. Int J Fuzzy Log Intell Syst 2014;14:181–187. [CrossRef]

[22] Garg H. Hesitant Pythagorean fuzzy sets and their aggregation operators in multiple attribute decision-making. Int J Uncertain Quantif 2018;8:267–289. [CrossRef]

[23] Liu D, Peng D, Liu Z. The distance measures between q-Rung orthopair hesitant fuzzy sets and their application in multiple criteria decision making. Int J Intell Syst 2019;34:2104–2121. [CrossRef]

[24] Wang R, Li Y. Picture hesitant fuzzy set and its application to multiple criteria decision-making. Symmetry 2018;10:295. [CrossRef]

[25] Al-Quran A. A new multi attribute decision making method based on the T-spherical hesitant fuzzy sets. IEEE Access 2021;9:156200. [CrossRef]

[26] Ali J, Naeem M. r,s,t-spherical fuzzy VIKOR method and its application in multiple criteria group decision making. IEEE Access 2023;11:46454. [CrossRef]

[27] Ali J. Analysis and application of r,s,t-spherical fuzzy Aczel–Alsina aggregation operators in multiple criteria decision-making. Granul Comput 2024;9:17. [CrossRef]

[28] Karaaslan F, Karamaz F. Interval-valued (p,q,r)-spherical fuzzy sets and their applications in MCGDM and MCDM based on TOPSIS method and aggregation operators. Expert Syst Appl 2024;255:124575. [CrossRef]

[29] Işık G. A new method for conversion between Pythagorean fuzzy sets and intuitionistic fuzzy sets. Sigma J Eng Nat Sci 2022;40:188–195. [CrossRef]

[30] Kokoç M, Ersöz S. A comparison of the performance of entropy measures for interval-valued intuitionistic fuzzy sets. Sigma J Eng Nat Sci 2021;39:131–147. [CrossRef]

[31] Ayvaz B, Boltürk E, Kaçtıoğlu S. Supplier selection with TOPSIS method in fuzzy environment: an application in banking sector. Sigma J Eng Nat Sci 2015;33:351–362.

[32] Bali Ö, Tutun S, Pala A, Çörekçi C. A MCDM approach with fuzzy DEMATEL and fuzzy TOPSIS for 3PL provider selection. Sigma J Eng Nat Sci 2014;32:222–239.

Sigma J Eng Nat Sci, Vol. 43, No. 6, pp. 2108–2126, December, 2025

Sigma Journal of Engineering and Natural Sciences
Web page info: https://sigma.yildiz.edu.tr
DOI: 10.14744/sigma.2025.1907

Research Article

A model to protect disaster recovery centers from cyber threats with multi-layered network security architecture

Aykut YILMAZ[1,*], Ali GÜNEŞ[2]

[1]Department of Computer Engineering, Faculty of Engineering, Istanbul Aydin University, Istanbul, 34295,Türkiye
[2]Department of Software Development, Faculty of Applied Sciences, Istanbul Aydin University, Istanbul, 34295, Türkiye

ARTICLE INFO

Article history
Received: 14 May 2024
Revised: 02 July 2024
Accepted: 10 September 2024

Keywords:
Application Vulnerabilities; Cyber Security; Ddos And Botnet&Malware Attack; Disaster Recovery Center; Network Security

ABSTRACT

Services and applications open to the internet are the target of advanced cyber-attacks. Disaster Recovery Centers are one of the most important infrastructures where systems storing critical data operate with active backup mechanisms. As Disaster Recovery Centers systems are critical infrastructures for business continuity, cyber-attacks can cause valuable corporate and personal data to be seized by cyber attackers. This, in return, results in material and moral damages to institutions, individuals and states. An architecture has been developed to meet the security needs against cyber-attacks by utilizing new and emerging technological infrastructures on Disaster Recovery Centers (DRC). The flowchart and pseudocode structure of the architecture have been presented. Additionally, the scientific distinction lies in the success rates demonstrated by the architecture through the combined use of professional applications and framework systems. This architectural infrastructure has been simulated in the application environment and subjected to performance tests with accessible professional applications and real-world cyber-attack vectors. The novelty of this work is that it leverages all of the globally used and accessible EVE-NG, Nessus, OpenVAS, Kali, Parrot, Enterprise Attacker Tactics Techniques and Common Knowledge (MITRE ATT&CK), National Institute of Standards and Technology (NIST) v2 professional applications and framework systems, which are used and accessible worldwide, were used. A comprehensive application was carried out in a simulation environment with 99 different real-world systems, 14 virtual networks, 10 attack vectors, 10 internet protocols, and 150 different attack scenarios. The simulation was conducted in three phases: the first phase involved attacks aimed at partially or completely disrupting internet access, while the second and third phases involved attacks aimed at rendering the Application Service Servers (DMZ) and local network servers unavailable to the internet. As a result of attacks using various techniques on this network, attempts were made to damage target servers and devices. At the time of the attack, the network traffic between the attacker and the target device was examined using Wireshark and Forti Analyzer software. The developed Disaster Recovery Centers architecture ensured the protection of critical infrastructure and systems against cyber-attacks.

Cite this article as: Yılmaz A, Güneş A. A model to protect disaster recovery centers from cyber threats with multi-layered network security architecture. Sigma J Eng Nat Sci 2025;43(6):2108–2126.

***Corresponding author.**
*E-mail address: aykutyilmaz3@stu.aydin.edu.tr

This paper was recommended for publication in revised form by Editor-in-Chief Ahmet Selim Dalkilic

Published by Yıldız Technical University Press, İstanbul, Turkey
© Author. This is an open access article under the CC BY-NC license (http://creativecommons.org/licenses/by-nc/4.0/).

INTRODUCTION

The importance of protecting critical and valuable data has increased with the development of technology. Network security infrastructure and components have become critical due to the constant availability of data and the need to protect it. The value of data has led to an increase in cyber-attacks on critical systems where data is stored and protected.

Disaster Recovery Centers (DRC) consists of a combination of infrastructure systems built on critical systems. DRC systems are also vulnerable to cyber-attacks from the outside world because they work within their own cloud systems. Cyber-attacks target critical data and information held in DRC systems. Additionally, cyber criminals attempt to exploit vulnerabilities in DRC systems using a wide range of real-world or zero-day tactics and matrix exploitation methods.

DRC are of critical importance due to the sensitive data they contain. They are also among the infrastructure systems that are most intensely targeted by cyber-attacks. To ensure their effectiveness, DRCs must be designed and maintained with the utmost care and diligence.

Critical infrastructure systems in the DRC are at risk of cyber-attacks. These systems hold valuable data and connect sectors such as transportation, retail, communication, energy, water, and finance to internet networks [1]. To develop functional protection mechanisms for DRC infrastructure systems, Cyber Security and Network Security managers must be open to information sharing. These teams undertake the task of creating systems to detect and prevent cyber-attack vectors, prevent techniques and tactics that may come from internal or external space, whether targeted or untargeted [2].

Infrastructure systems serving the internet may be exposed to the threat of all kinds of cyber-attack vectors. While the current and modern security model to be applied in infrastructure systems prevents the structure from being vulnerable to attacks, the slightest mistake in architectural design will result in the collapse of the designed structure [3]. At this juncture, the main purpose of Cyber Security and Network Security is to ensure the highest level of protection for existing valuable and critical information. Information security encompasses valuable data belonging to individuals and consists of confidentiality, integrity, accessibility, and account authorization [4].

While the risk rate of vulnerability of DRC systems to cyber threats increases in proportion to the value of the data it contains, the DRC infrastructure consists of structures in which the data belonging to the center are used as active-active or active-passive [5]. The cyber world includes definitions that cover information system infrastructures and affect networks [6]. In addition, Cyber Security and Network Security units, infrastructure systems, information technology teams, institutions, states, private sector, and individuals are working to protect and maintain the cycle of valuable data [7]. The protection of data, which is the most fundamental task of security teams, also applies to DRC infrastructure systems. Failure to consider DRC systems as part of security can result in the snowball effect at the slightest vulnerability in the systems infecting the subcomponent systems and resulting in malicious individuals obtaining data [8]. Research has shown that cyber-attacks, tactics, techniques, and vector tools pose a significant threat to modern systems in a variety of ways. [9].

In critical infrastructure systems, emergency management, management of security policies, improvement of protection systems, dependency model of the data infrastructure, backup equipment and management system components should be easily accessible by critical system administrators in the event of an extraordinary situation [10]. DRC systems, which store critical and valuable information, are vulnerable to cyber-attack threats to the extent that they cannot fulfill their functions, allowing information security to be compromised and data to be stolen. When this situation occurs, the systems and infrastructures that interact with the valuable information obtained by individuals or groups that have malicious purposes, are seriously damaged and affected by the vulnerability [11].

Researchers have previously conducted similar studies [12]. The scientific articles written were mainly based on topics such as cyber security threats [13], various artificial intelligence software [14], MATLAB, Python supported machine learning modeling [15], history of cyber-attacks, blockchain technology, SCADA systems, IoT Technology [16-18].

The basic approaches of Cyber Security and Network Security include methods that aim to protect user computers, servers, mobile systems, electronic infrastructures, and prevent access and vulnerability methods, while ensuring that the data transferred between infrastructure systems is transmitted confidentially in whole [19,20]. The solution to structural security problems is the development of new and modern architectures for DRC systems [21]. Analysis of the impact of any vulnerability that may occur in critical infrastructures and risky anomaly operations on the systems is one of the important points for DRC components [22, 23].

Some of the studies in the literature used limited domain attack datasets such as CICDoS2017, CICDDoS2019, CICIoT2023, CIC-MalMem-2022, CICEV2023 and CICIoV2024. These datasets contain only attack vector data such as Distributed Denial of Service (DDoS), Brute Force, spoofing attack, IDS-DoS, Recon, Browser based attacks, Mirai, etc. within a limited and unchangeable area [24-27].

Akbaş discusses local networks and security modeling, network architectures, enterprise OPNET and Virtual private network (VPN-Virtual private network) as well as traditional network model architecture contents [28]. On the other hand, Kör proposes a real-time network security architecture to prevent Web Server and Domain Name System (DNS) attacks, using EKA and SPSS (Statistical Package for the Social Sciences) simulation

environment [29] and Büyükkılıç proposes a cyber security model for Small and Medium Enterprises (SME) systems. National Institute of Standards and Technology (NIST), Payment Card Industry Data Security Standard (PCI DSS), International Organization for Standardization (ISO), Control Objectives for Information and Related Technology (COBIT) standards are covered while addressing the basic cyber security practices required for SMEs to cope with cyber security threats [30]. Herrmann and Pridöhl studied cyber security and network security issues, Database Attacks (SQL Injection), DOS, Network Intrusion Detection System (NIDS) systems, Nessus and Metasploit attacks and vulnerability detection [31].

Çinar and Yildirim examined traditional modeling methods by drawing attention to network security and performance problems in large corporate structures and presented network management system architecture design. During modeling, the Open Systems Interconnection (OSI-Open Systems Interconnection) reference model, ISO standards and FCAPS model were used to determine the requirements for the cyber network security model [32]. AVCI, Cyber network, and security architecture developed on SCADA systems against cyber-attacks, is a study on smart natural gas systems. Analytic Hierarchy Process (AHP), Key Performance Indicators (KPI) determination processes were mentioned with the study on cyber-attacks, their effects, consequences, and protection methods [33].

Xiong et al. mapped cyber-attacks using the Enterprise Attacker Tactics Techniques and Common Knowledge (MITRE ATT&CK) matrix and examined the behavior and profile of the attacker from a technical perspective. With the use of matrix, prevention mechanisms for security vulnerabilities were also examined. They proposed a model and conducted test studies [34]. Frayssinet et al. proposes a methodology for cybersecurity management for government organizations. In the article, a cyber security method is proposed for government institutions using the NIST Cybersecurity Framework (CSF) [35]. Özarpa et al. studied cyber-attacks on autonomous vehicles and detection of attacks. They used ten different attack techniques in attack modeling and developed an architecture to prevent system vulnerabilities. They developed simulations on wireless networks and worked on reducing system vulnerabilities by closing direct access to the single processor of the system [36].

Güneş et al. conducted a study on cyber-attacks, attacks and methods on ports and port facilities and developed a model against cyber-attacks on SCADA infrastructures in port and container systems. While the model includes tactical mechanisms and protection methods against cyber-attacks, they simulated different scenarios. They utilized standards such as NIST, ISO 31000, ISO 27001 [37]. Kara et al. created a software tool to identify security vulnerabilities and detect cyber-attacks. They also simulated cyber-attacks [38]. Artificial networks, including Convolutional Neural Networks (CNN) and Recurrent Neural Networks (RNN), have been used in studies for anomaly detection. Attack scenarios were performed on the CSE-CIC-IDS2018 dataset, and the performance outputs of different artificial networks were compared [39].

There are different studies on artificial networks with ready-made data sets. These include machine learning algorithms such as Support Vector Machine (SVM), Naïve Bayes (NB), Artificial Neural Network (ANN), K-Nearest Neighbor (KNN-K-Nearest Neighbor) and Gated Recurrent Units (GRU) [40,41].

Numerous studies on the IoT ecosystem have focused on DDoS, malware, worms [42], data theft, trojans [43], rootkits, botnet infrastructures [44], backdoors, viruses, application vulnerabilities and communication protocols [45]. They conducted a study on IoT architecture targeted by various attack methods and compared the systems threatened by attacks on infrastructures and categorized the attacks [46,47]. Karaman et al. discuss diverse types of cyber-attacks, including Botnet, BruteForce-Web, BruteForce-XSS, FTP-BruteForce, BruteForceSSH, DDoS, Slowris, DoSattacks-GoldenEye, DoSattacks-Hulk, and DoSattacks-SlowHTTPTest. They used the CSE-CIC-IDS2018 dataset and artificial intelligence models to detect anomalies and analyze the damage caused by these attacks. The authors employed several machine learning methods, such as ANN, KNN, Naive Bayes, and SVM. They proposed a flowchart model to illustrate their findings. [48,49]. Erdem, developed a new firewall architecture different from traditional firewall models with Dynamic Intelligent Firewall Architect (DIFA). In accordance with this architecture, DIFA has developed and simulated a network security architecture that can manage itself and creates access rules by analyzing anomalies and malware through passing traffic data [50]. While there are numerous studies in literature, none have focused on modelling the architectural infrastructure of DRC. The aim of this study is to contribute to academic literature by addressing this gap.

MATERIALS AND METHODS

Malicious attacks and threats present a variety of risks, including those posed by malware, DDoS, botnets, code blocks, viruses, trojans, phishing attacks, and worms. [51]. Detecting and preventing these attacks in advance can be insured by systems with effective architectural design [52-55]. Cybercriminals have been attempting to exploit vulnerabilities in DRC systems with large scale and diverse attack vectors using real world zero-day tactics and matrix exploitation methods.

DRC critical systems vulnerabilities are large scale and operate by stealing valuable information, disrupting critical systems and services, and demanding ransom. Preventing cyber attackers is possible with a well-designed cyber network security architecture. Many advantages for safeguarding critical systems are offered by this study's design of the architecture model, which will be built using

next-generation architecture, layers, frameworks, and processes in accordance with the standard DRC modeling specified for the pertinent structures.

In this study, while developing the infrastructure architecture, frameworks such as EVE-NG simulator application, MITRE ATT&CK Enterprise, NIST were used. The simulation environment aims to create the functioning mechanism of living structures by processing scenarios in the real world.

While the attacks were conducted on an attacker profile sample in the internet environment, DDoS (Distributed Denial of Service), Zombie Computers (Botnet), Malware, browser service HTTP/HTTPS attacks, Application Vulnerabilities were implemented. The contribution of the multi layered and complex structure of the DRC architecture to the cyber network security factor has played an active role in preventing cyber threats, protection, and resistance against attacks.

Architectural Model Scenario and Roadmap

Traditional DRC systems are created to ensure business continuity, consisting of switches, routers, firewalls, server systems and data backup units with simple and limited features. Next-generation DRC architectures include more complex, flexible structures and generally have more features. It consists of switches with advanced features, routers, firewalls, threat detection and prevention systems, sandbox devices with malicious file and email scanning systems, data encryption and authentication systems, and load balancers systems. Next-generation network architectures are designed to be more flexible, secure, performance-driven and meet modern business needs such as digital transformation and cloud computing, such as large data centers and the Internet of Things (IoT). Infrastructure modeling enables the examination and construction of real-world simulations of critical systems using these structures. Infrastructure architectures that emerge through architectural maturity modeling protect systems against unforeseen attacks by analyzing vulnerabilities and weak points on critical systems.

In this study, cyber network and security DRC architectural model design was realized within the framework of confidentiality, integrity and accessibility concepts for critical infrastructure services where information and data flow take place. MITRE ATT&CK Enterprise and NIST v2 framework standards were used to design the architecture. MITRE ATT&CK Enterprise is a knowledge base and contains tactics, techniques and general knowledge that cyber attackers can use. The goal here is to help cybersecurity experts better understand the activities of attackers and create a matrix to develop defense strategies against these activities. [56,57]. The purpose of using NIST v2 in the study is to help in the management of the cyber risk map, prioritization, and measurement of improvements [58]. These framework standards have been reviewed, utilized and incorporated in the study. The framework is designed in accordance with the Multi-tier Model.

Definition of the Problem of DRC Infrastructure

DRC systems are the infrastructure containing the most critical data and components of a structure. These infrastructures are designed to ensure that the valuable data flowing in the live environment continues uninterrupted. As seen in literature review, architectural studies on DRC infrastructures in the academic field are quite insufficient. The studies that have been conducted are combined with various network topologies of insufficient maturity and reveal cyber network security models. In this study and to contribute to this academic gap, a cyber network security model has been developed for the DRC system and infrastructures architecture with scientific observation and perspective. The modern infrastructure architecture, which will be designed in accordance with the DRC infrastructure, will be developed in line with the data from the DRC system administrators, aiming to increase the maturity level of critical infrastructures, while reducing anomaly possibilities and risk map.

Architectural Simulation Scenario

To demonstrate the DRC architecture infrastructure, a real-world infrastructure, a simulation environment will be created. A fictitious multinational Company A is a retail center with more than 10,000 employees and 300 locations in and out of the country. The company generates annual revenues of $2 billion and allocates 2% ($40 million) of its revenues each year to the Infrastructure and Systems Department. The company wants to separate the traditional network infrastructure from the DRC infrastructure. The DRC architecture consists of specially designed, complex security systems against cyber-attacks. In this structure;

1. The connection line with three different Internet Service Providers (ISPs) has been redundantly established via Radio Link (RL) and Fiber Lines (MPLS). The inter-branch connection operates over Software-Defined Networks (SD-WAN). The infrastructure functions in an Active-Active configuration, providing real-time data synchronization. In the event of a failure at the data center located at the headquarters, it performs load balancing and takes over the traffic.
2. A DWDM (Dense Wavelength Division Multiplexing) redundant optical line will be used between the headquarters data center and the DRC. With this line, data will be synchronized instantaneously in a fast and secure manner. In this way, the traffic in between is encrypted.
3. The local DDoS protection system will redundantly block or accept unwanted accesses, ports, and services by filtering against requests from the outside world. Protection will be at layer 3,4,7 level.
4. Intrusion Prevention System & Intrusion Detection System (IPS&IDS) Firewall will protect the signature-based vulnerability and attack vectors in the legal

traffic passing through the DDoS device in the architecture with the most advanced signature database and will be capable of clearing zero-day anomaly attacks with artificial intelligence, machine learning and deep learning algorithms.

5. Packets that pass through the DDoS and IPS&IDS protection systems, which are built redundantly, will pass through the internet firewall and access the Application Layer Firewall (WAF-Web Application Firewall) for Web applications and use Load Balancing (LB-Load Balancer) and Global Server Load Balancing (GSLB-Global Server Load Balancing).
6. The DRC Fabric will be capable of distinguishing traffic from the Internet, Application Service Servers (DMZ), VPN or Campus environments. Traffic can be scanned in DMZ traffic and in the Sandbox product.
7. Incoming and outgoing traffic will pass through the Firewall installed in a redundant structure. The Firewall will create a socket to the address that the packet will try to access locally and send packets to the central router.
8. The central router will be built on a system that transfers data between layers 2 and 3 and at the same time achieves scalable 40GB/100GB port transfer speeds that are capable, flexible, and performant in accordance with the data center architecture. The data will pass through the central application architecture and protect the structure at layer 2 and 3 levels. Thus, it will establish an integrated structure in the architecture by providing integration with critical infrastructure systems.
9. Incoming traffic reaches the center through an IPsec tunnel using the SD-WAN architecture and secured with MPLS. The architecture can block local traffic between networks in the L2 and L3 layers. Certificate-based authentication systems prevent malicious network movement horizontally or vertically within the architecture.
10. In the subsections of the architecture, products that follow cyber-attack prevention tactics and mechanisms should be able to use advanced antivirus systems, classification products, attacker deception systems, network listening and anomaly detection software, vulnerability scanning and log reporting systems.

Similar simulations [59-62], [63-66] and scenario approaches are available in literature [67-70].

Architecture Model

To protect DRC systems from cyber-attack vectors, infrastructure design should be developed for the worst-case scenario. The architecture aims to prevent attacks from the internet environment at a high rate. To protect infrastructure systems from cyber-attacks and other forms of attack, it is designed in three phases.

In phase one of the DRC architecture depicted in Figure 1, the architecture is divided into different layers to separate the systems by design and to reduce the attack area to a micro level. Furthermore, the layering method allows different services to be provided and operated at the same time. Due to the structure of the three-layer architecture, traffic flow within the structure takes the form of a transfer to a lower layer and onward.

The architecture, internet and campus structure are designed to be redundant with three different internet providers. Cyber threats and possible access interruptions will continue to operate with high availability. DDOS devices prevent low-credibility access from the outside, while a wide variety of flood and port scanning operations used by attackers are blocked at the access layer. These devices

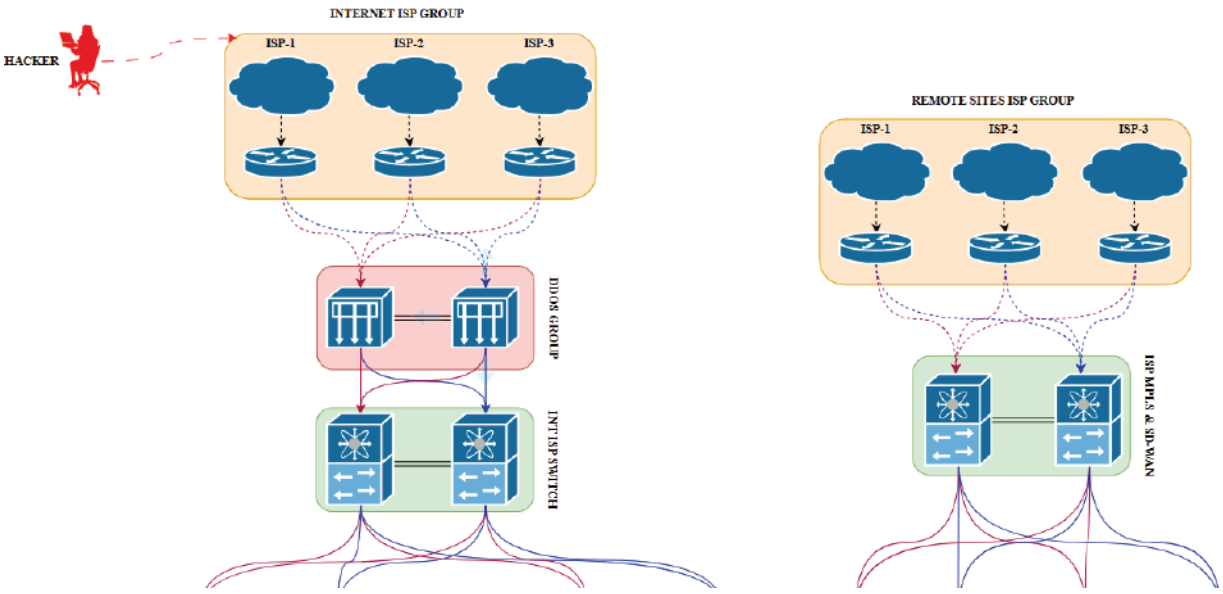


Figure 1. Tier-1 ISP, DDoS, SD-WAN MPLS architecture.

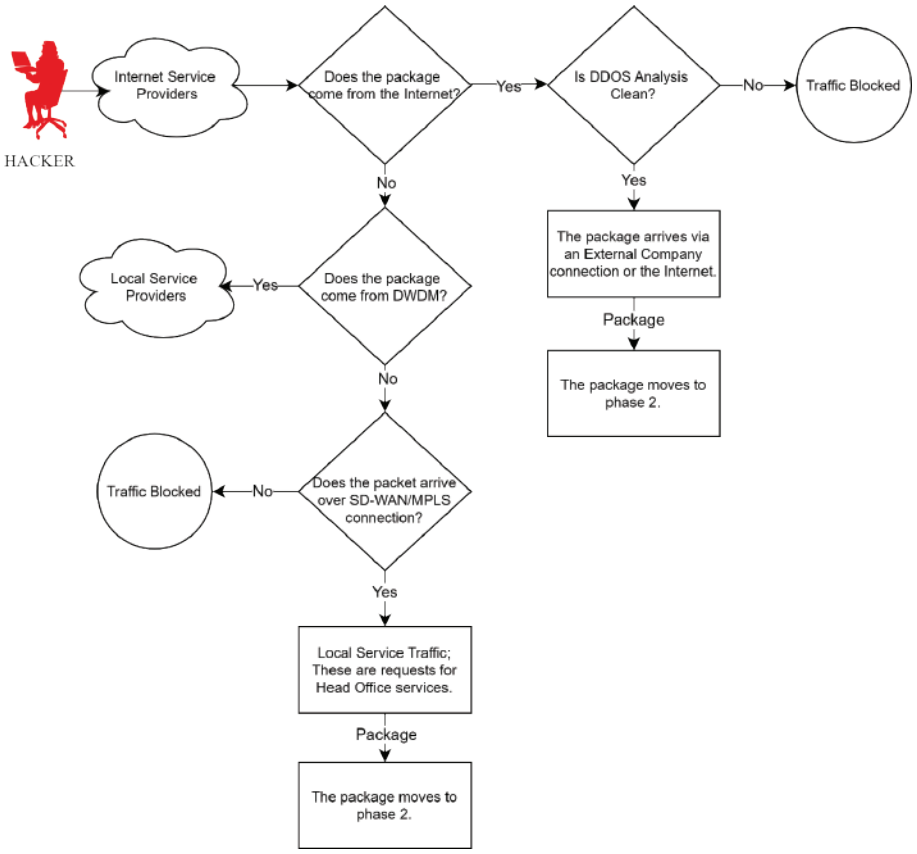


Figure 2. Tier-1 ISP, DDoS, SD-WAN MPLS flowchart.

will prevent BOTNET and DDOS attacks that may come from the volumetric and application layer or from different sources. Two DDOS and four internet provider equipment are located in the building with redundancy. As the campuses are part of the local network traffic, DDOS equipment is not located.

In the flowchart in Figure 2, it can be seen that, as a result of the inspection of the traffic over the internet, if it contains malicious packets, it is blocked, and if it is a clean packet, it is allowed to pass to the second stage. In the case of a local DWDM, SD-WAN, MPLS traffic, it is allowed to pass through the same query mechanisms.

```
Pseudocode Algorithm-1
1. Start;
2. Input: Malicious Data Traffic by the Attacker
3.   ISP1 Traffic
4.   ISP2 Traffic
5.   ISP3 Traffic
6.       If Packet Traffic is via the Internet?
7.             Answer > YES
8.                If Is DDoS Analysis Clean?
9.                   Answer > YES
10.                      go to Forward Package (Package comes via External Company connection or Internet)
11.                         go to Package moves to stage 2
12.                   If Answer > NO
13.                      Launch and Block DDoS Protection System
14.             Answer > NO
15.                If Traffic Is DWDN Fiber?
16.                   Answer > NO
17.                      If Does the If Package arrive via SD-WAN or MPLS connection?
18.                         go to Forward Package (Local Service Traffic; Requests for Headquarters services)
19.                            go to Package moves to stage 2
20. End
```

Figure 3. Tier-1 ISP, DDoS, SD-WAN MPLS pseudocode.

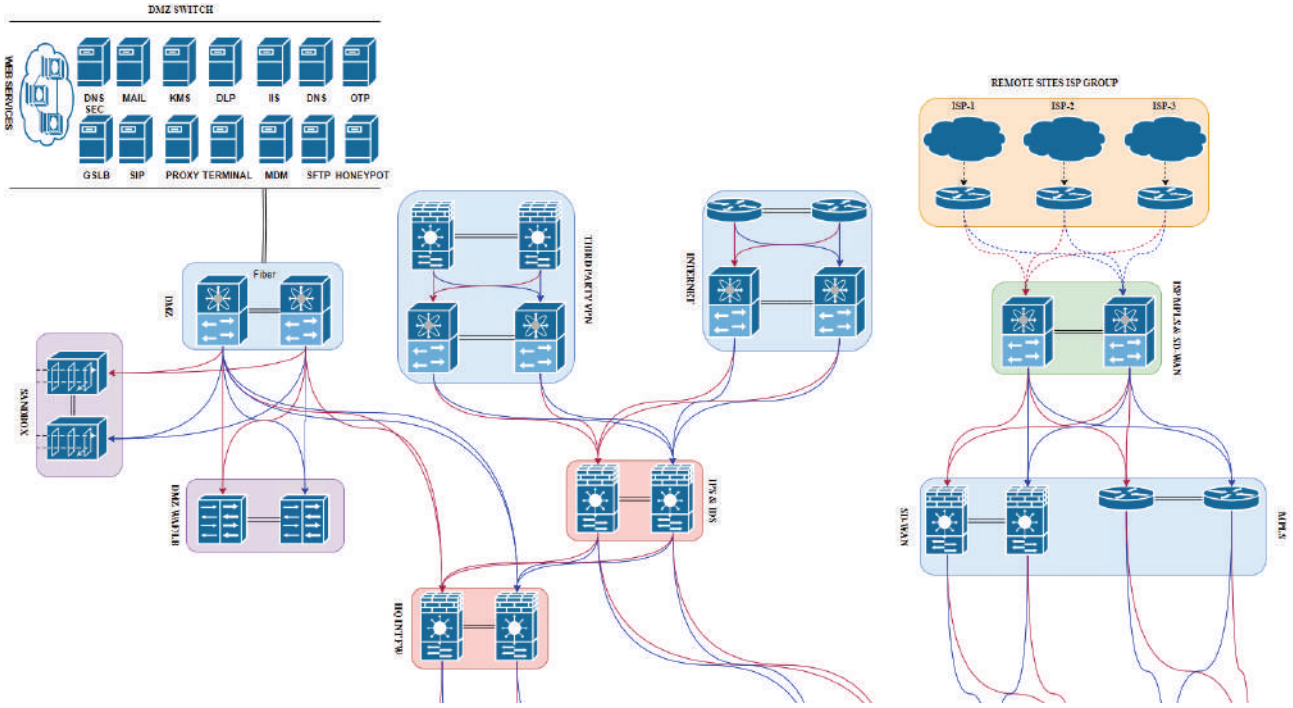


Figure 4. Tier-2 Internet, security systems, web services and remote site architecture.

Figure 3 shows the pseudocode structure of the first stage.

The traffic, which proceeds in accordance with the structure of the cyber network security architectural design with the second stage seen in Figure 4, is analyzed and controlled by passing through various control systems at each stage. By passing through the WAF/LB device, it is cleaned from any attack vectors that may be in HTTP or HTTPS traffic and the load is transferred to the upper layers in a balanced manner. If there is any attached file during data exchange through e-mail or file sharing systems, the Sandbox product scans it and the harmful file is blocked. Traffic coming from the internet and traffic from SD-WAN and MPLS campuses are separated and backed up in this layer.

While the rule sets in the architecture provide access to the traffic by macro and micro segmentation, IPS&IDS forces various malicious web traffic, potentially infected documents to pass through the controls on the systems and ensures that the traffic continues by cleaning and stopping possible threat vectors.

The architecture is based on four different structures: DMZ (Web Services), External Company VPN Lines, Internet Line and Campus area. The basic components of the architecture are designed by preserving the redundancy requirements of the active devices within the structure. In the second phase of the architecture, six fiber switches, two IPS&IDS firewalls, two internet firewalls, two remote site firewalls (SD-WAN firewall), four routers, two web application firewall (WAF), two sandboxes were configured. Redundancy and load distribution integrations between the devices were added to the design.

In the graph shown in Figure 5, detailed analysis of the incoming data packet continues to be performed. Due to the architecture layers, at each stage, it is checked whether the incoming traffic is a cyber-attack or a reliable traffic. At this stage, algorithms such as deep learning, artificial intelligence, machine learning used in systems can work. In Phase 2, each packet is scanned by DDoS, IPS&IDS, WAF/LB and firewall devices. Denial of service attacks attempted by cyber attackers are prevented by these protection walls. In the architecture, incoming traffic is evenly distributed to the subsystems through load balancing systems. SD-WAN and MPLS traffic, which are local traffic, can be transmitted as secure traffic with this infrastructure.

Figure 6 shows the pseudocode structure of stage 2.

The infrastructure equipment, which is the third stage of the architecture is shown in Figure 7. In the architecture, local network infrastructures rise on two different structures: local network infrastructure systems and service systems architecture zone. The basic components of the architecture were designed by preserving the redundancy requirements of the active devices within the structure. In the third phase of the architecture, twelve fiber switches, two wireless network controllers (WLC), two local firewalls, two remote site firewalls (SD-WAN firewalls), four routers and DWDM fiber, it is configured as tow web applications firewall (WAF) equipment. Redundancy and load distribution integration between the devices are shown in detail in the design.

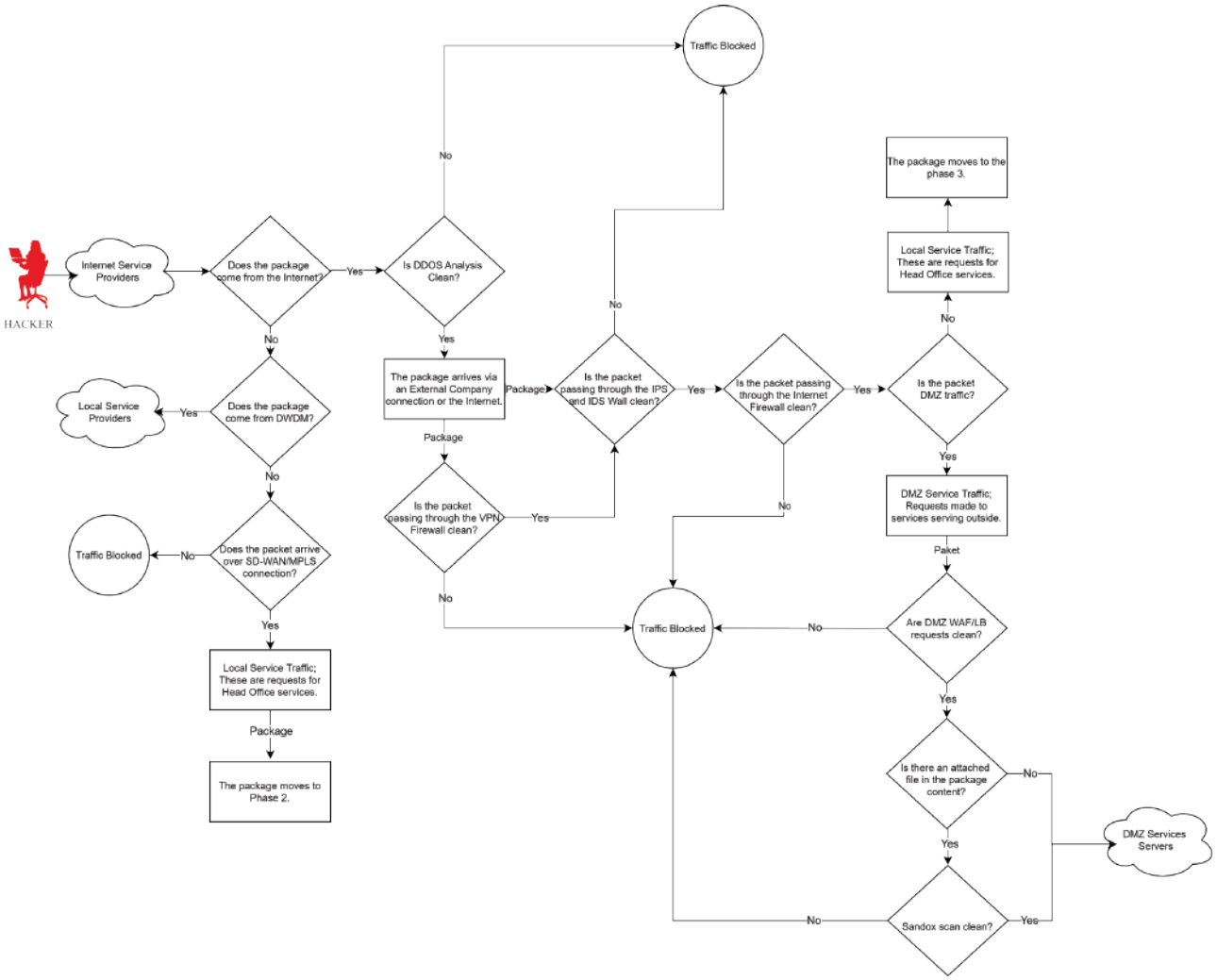


Figure 5. Tier-2 Internet, security systems, web services and remote site flowchart.

The local infrastructure, which is the last stage of the architecture, is shown in Figure 7. In the architecture, the packets that pass through different protection services until they access the local infrastructure are cleaned from DDoS, Botnet, Malware, Application vulnerability and other attacks until they reach the third stage.

The design of the DRC model architecture aims to avoid the slightest design weakness that may occur in the prevention of cyber threats. With the three-layer structure existing in the relevant architectural design, each layer has been developed as a redundant structure within itself. In architectural design, the level of breakdown between layers has been in micro and macro dimensions.

The flowchart in Figure 8 shows that the three-layer structure and the traffic circulating between the layers are in communication by passing through security transitions, devices that can be built with different algorithms and logic. Thus, the DRC architecture can ensure that the traffic generated by applying strict security rules in the transportation of critical data between layers is capable of ensuring that the traffic progresses within the desired security regulations.

Cyber Threats and Attack Vectors

With the DRC architecture developed in Figure 9, an important level of protection from cyber threats and attack vectors that may come from the internet environment is provided. Cyber threats are constantly researched academically and scientifically, and various methods are proposed to prevent attacks. The DRC architecture developed in Figure 9 is one of these architectural methods. Cyber threats and attacks, security gaps and risks, vulnerabilities and other pests, attempt to make systems inaccessible by using a variety of methods and techniques [71,72]. Some of the methods used by cyber attackers are viruses [73], worms [74], trojan horses [75], hackers [76], rootkits [77], spyware [78], ransomware [79], command injection [80], DDoS [81], software, firewall [82,83], TCP/IP, wireless [84], operating system, web servers and many other infrastructure vulnerabilities [85,86].

```
Pseudocode Algorithm-2
1.Start;
2. Input: Malicious Data Traffic by the Attacker
3.   ISP1 Traffic
4.   ISP2 Traffic
5.   ISP3 Traffic
6.      If Packet Traffic Is Via the Internet?
7.            Answer> YES
8.               If is DDoS Analysis Clean?
9.                  Answer > YES
10.                    go to Forward Package (Package comes via External Company connection or Internet)
11.                       If is IPS and IDS Analysis Clean?
12.                          Answer > YES
13.                             If is Internet Firewall Analysis Clean?
14.                             Answer > YES
15.                                   If Forward If Packet (Is the packet DMZ traffic?)
16.                                      If >YES (DMZ Service Traffic; Requests made to services serving outside.)
17.                                         If DMZ WAF/LB requests are clear?
18.                                            Answer > YES
19.                                               If is there any attached file in the package content?
20.                                                  Answer> YES
21.                                                     If Sandbox scan is clean?
22.                                                        Answer > YES
23.                                                           DMZ Services Servers
24.                                                        Answer > NO
25.                                                           Launch and Block Sandbox Protection System
26.                                                     Answer> NO
27.                                                           DMZ Services Servers
28.                                               Answer > NO
29.                                                  Launch and Block WAF/LB Protection System
30.                                            Answer > NO (Local Service Traffic; Requests for Headquarters services.)
31.                                               go to Package moves to stage 3
32.                                      Answer> NO
33.                                         Launch and Block Internet Firewall Protection System
34.                                   Answer> NO
35.                                      Launch and Block IPS and IDS Protection System
36.                    Answer> NO
37.                       Launch and Block DDoS Protection System
38.              Answer> NO
39.                 If Traffic Is DWDM Fiber?
40.                    Answer> YES
41.                       go to Package moves to stage 3
42.                    Answer> NO
43.                       If Does the Package arrive via SD-WAN or MPLS connection?
44                           go to Forward Package (Local Service Traffic; Requests for Head Office services)
45.                             go to Package moves to stage 3
46.
47.   End
```

Figure 6. Tier-2 Internet, security systems, web services and remote site pseudocode.

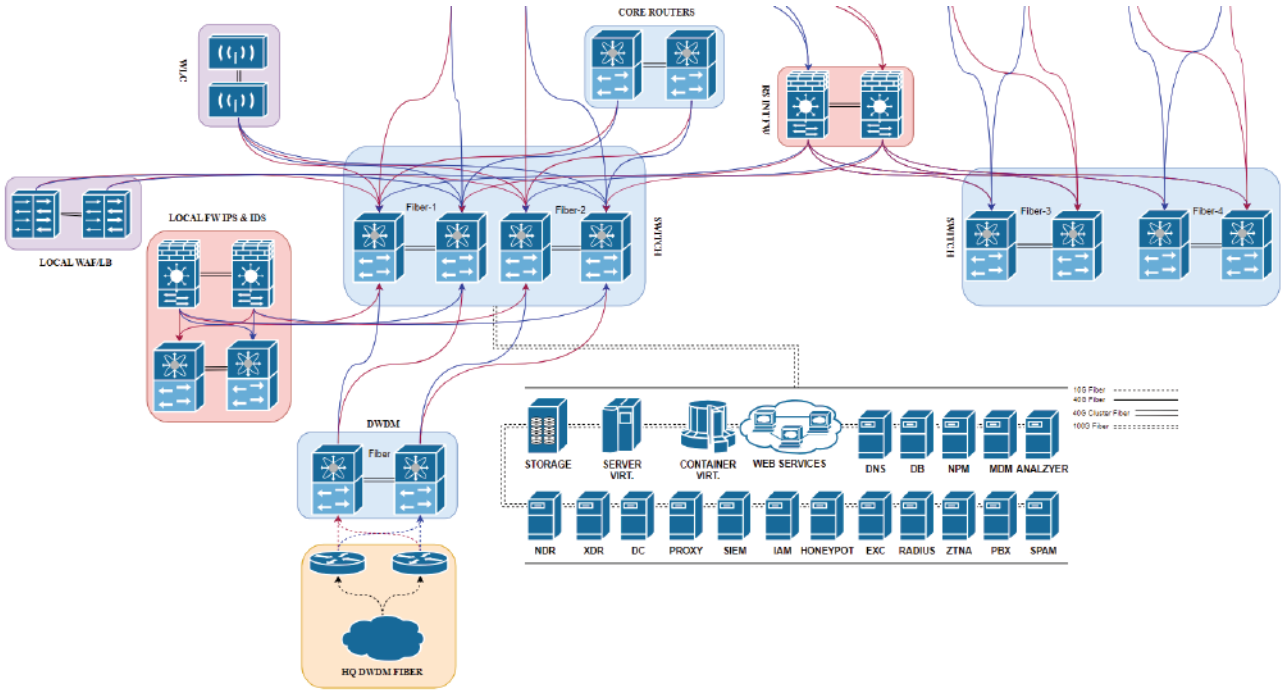


Figure 7. Tier-3 Local Infrastructure, services systems architecture.

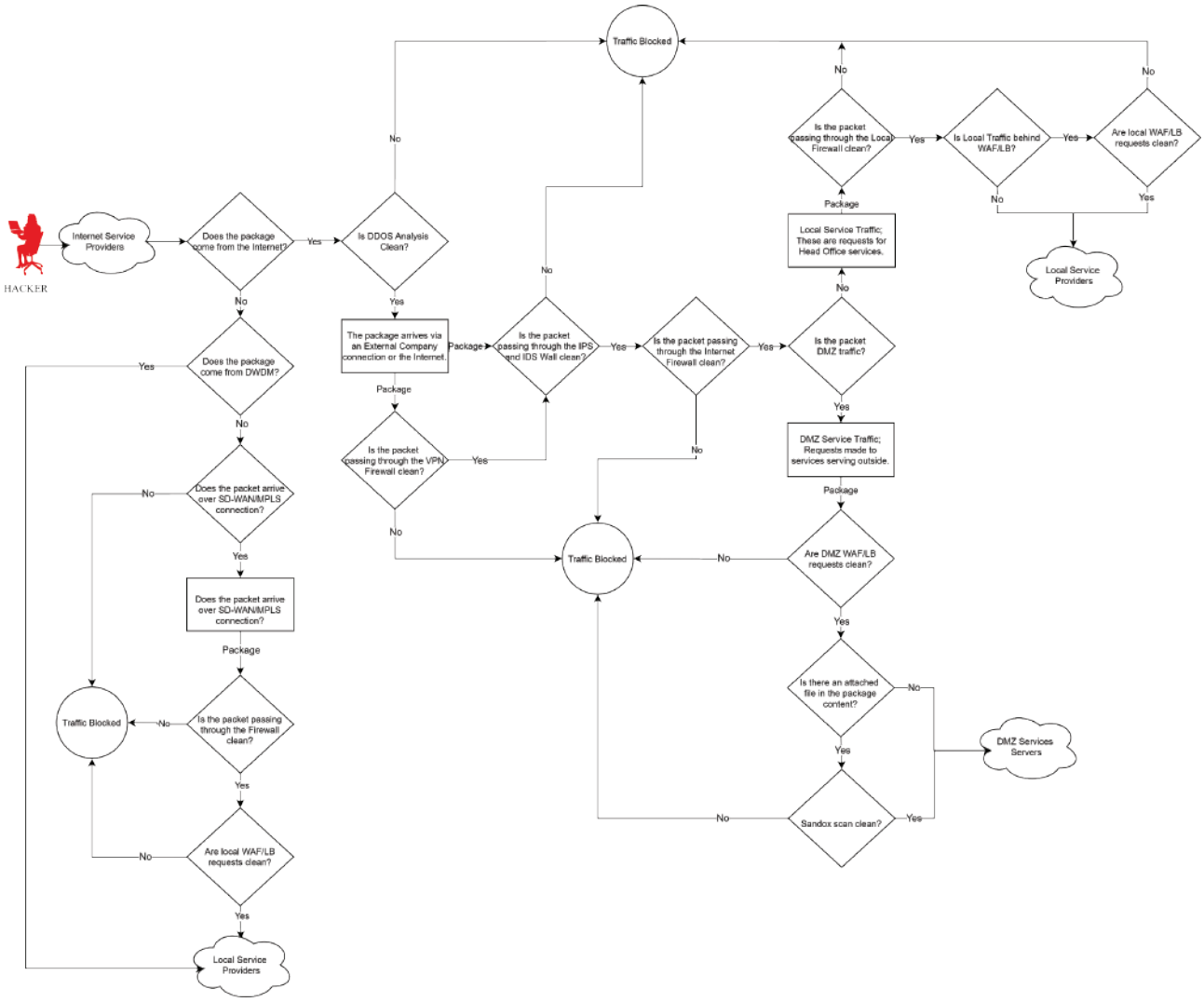


Figure 8. Tier-3 Local infrastructure, services systems flowchart.

MODEL TEST AND PERFORMANCE

The architectural model setup and roadmap, problem definition, simulation scenario, model architecture structure was developed with the cyber network and security architecture on the DRC infrastructure in Figure 9. Its infrastructure and component stages and detailed information of the developed architecture are given in Figures 1-9.

To prove the accuracy of the data obtained in the simulation environment, 150 different test operations were repeated in the simulation environment. For the simulation environment, open access, globally recognized professional infrastructure products were used. Simulation infrastructure and component systems can use algorithms and methods such as machine learning and artificial intelligence. The infrastructure components used in the simulation environment are given in Table 1.

A DRC infrastructure with a three-tier architecture was developed with the required systems. Cyber-attacks were

Table 1. DRC simulation software and hardware list

Pieces	Systems
1	Intel i7 12th Gen, 32GB RAM, 500GB M2 SSD
1	VMware® Workstation 17 Pro
1	EVE-NG 5.0.1 network and security simulator
1	Linux Kali, Parrot systems
1	OpenVas, Nessus10 attack simulators
1	Fortinet Analzyer 7.4.1
1	Wireshark 4.0.10
2	Fortinet Sandbox 4.4.4
2	Fortinet wireless controller 7.4.1
7	Internet service provider
14	VLAN
18	Fortinet Firewall,IPS&IDS, DDOS, WAF/LB 7.4.1
21	Windows server 2022 and Linux servers
28	Cisco Router, Switch L2&L3

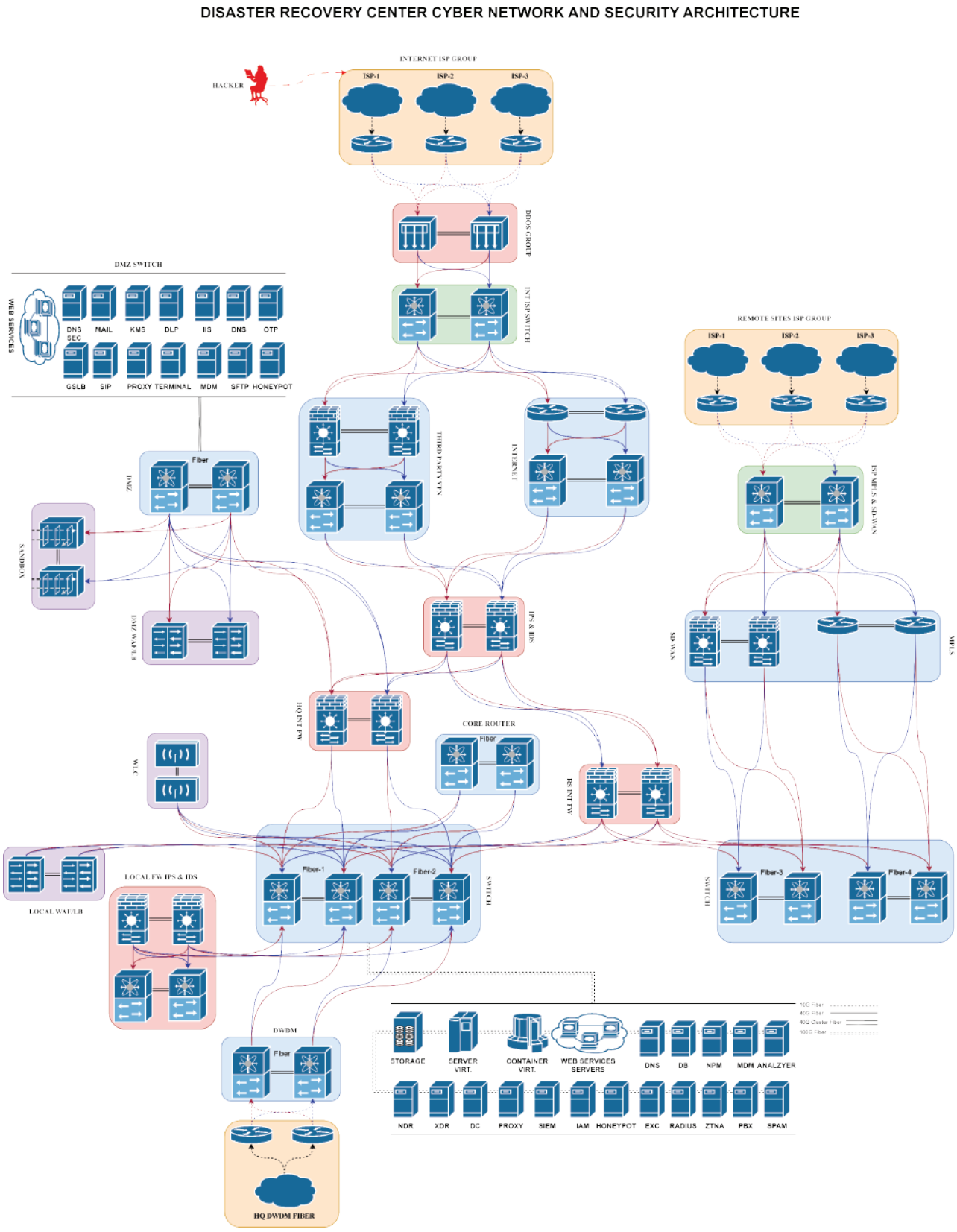


Figure 9. Disaster recovery center (DRC) cyberspace network security architecture.

made on the architecture and the effects of the system as a result of these attacks were observed with professional analysis software. The attacks generated by the attack simulators on the servers, software and hardware in the system infrastructure were designed and created to be similar to the attacks that can come from the internet environment.

In phase 1, the following results were obtained as a result of cyber-attacks on DDoS, SD-WAN and MPLS architecture with packets coming from the internet environment. During this phase, repetitive attacks were conducted, and random service servers that may be open to the internet within the infrastructure were selected and attacks were conducted to disable the service.

Table 2. DDoS, SD-WAN and MPLS attacks

Attack vector	Service	Number of attack	Protection %
tcp_syn_flood	http-https ssh-ftp-smb	101,938,66	99,99
udp_flood	dns-smb snmp-ntp	214,468,22	99,99
port_scanning	1-65535	995,941,89	99,99
land_attack	http-https icmp	221,040	99,99
smurf_attack	icmp	285,234,41	99,99
random_source attack	http-https	2,382,038,154	99,99
slowloris	http-https	31,680	99,99
rstfin_flood	ssh-https	1,546,702,37	99,99
syn_ack_flood	ssh-https	1,356,082,319	99,99
icmp_sweep	icmp	239,598,935	99,99
Total blocked attack numbers		3,977,719,408	

Table 3. Botnet& Malware attack vectors

Attack Vector	Malware	Victim	Source	Count	Total
“Gh0st.Rat	Botnet C&C	53	13	134	92.326
“Mirai.Botnet	Botnet C&C	8	33	52	13.728
“Xtreme.RAT	Botnet C&C	11	2	25	550
“Bladabindi	Botnet C&C	8	11	22	1.936
“JS/TiMove	Virus	1	2	27	54
“ASP/WebSh	Virus	1	2	18	36

Table 4. Application vulnerability attack vectors

Attack vector	Victim	Source	Count	Total
Zyxel.zhttpd.Webserver.Command	51	313	461	7,358,943
ThinkPHP.Controller.Parameter.RCE	4	85	150	51,000
Bash.Function.Definitions.RCE	8	6	282	14,100
Apache.Log4j.Error.Log.RCE	7	8	174	9,744
Remote.CMD.Shell	2	4	396	3,168
vBulletin.tabbedcontainer.Template	4	6	96	2,304
Citrix.Application.Delivery.Control	3	5	102	1,530
Netcore.Netis.Devices.Hardcoded	2	7	72	1,008
vBulletin.Routestring.widgetConfi	4	6	41	984
F5.BIG.IP.Traffic.Management.Us	2	4	97	776
MS.IE.XSS.Filter.Error.Handler	2	4	68	544
Ivanti.Avalanche.ImageFilePath	1	4	57	228
Oracle. WebLogic. Fusion. Middle	1	3	55	165

In Table 2, it is observed that with various attacks made with Hping3, LOIC, Hydra and Nmap applications, the infrastructure of the first stage security system, attack vectors are successfully blocked by 99.99% in the simulation environment. No interruption was observed in the internet services provided during the attack and the system continued to operate.

Similar architectural infrastructure tests were conducted in the second and third stages, and denial of service and application vulnerability attacks were made against security systems (IPS & IDS, firewall, WAF, Sandbox) and web services through which traffic from the internet passes.

For the purpose of denial of service for DRC architecture, attack simulation tools (Nessus, OpenVAS, Parrot) were used to simulate Botnet and Malware attacks from multiple sources simultaneously, and Table 3 shows the total number of attacks of Botnet & Malware attack vectors.

Vulnerability tests were conducted on many applications that run on the services and that may have a weak point in terms of vulnerability of infrastructure systems. As a result of the application vulnerability tests shown in Table 4, there are more than twenty application vulnerability attacks detected, out of which thirteen vulnerabilities are

Table 5. HTTP / HTTPS protocol attacks

Attack vector	Number of attack
SQL injection	9.661
XSS	8.763
Cross.Site.Scripting	8.537
HTTP.URI.SQL.Injection	2.577
TCP.Data.On.SYN	2.507
HTTP.Request.URI.Directory.Traversal	1.434
Nmap.Script.Scanner	1.349
Web.Server.Password.File.Access	1.062
Zyxel.zhttpd.Webserver.Command.Injection	461
Remote.CMD.Shell	396
Code Injection	305
Linux.Kernel.TCP.SACK.Panic.DoS	222
ZGrab.Scanner	204

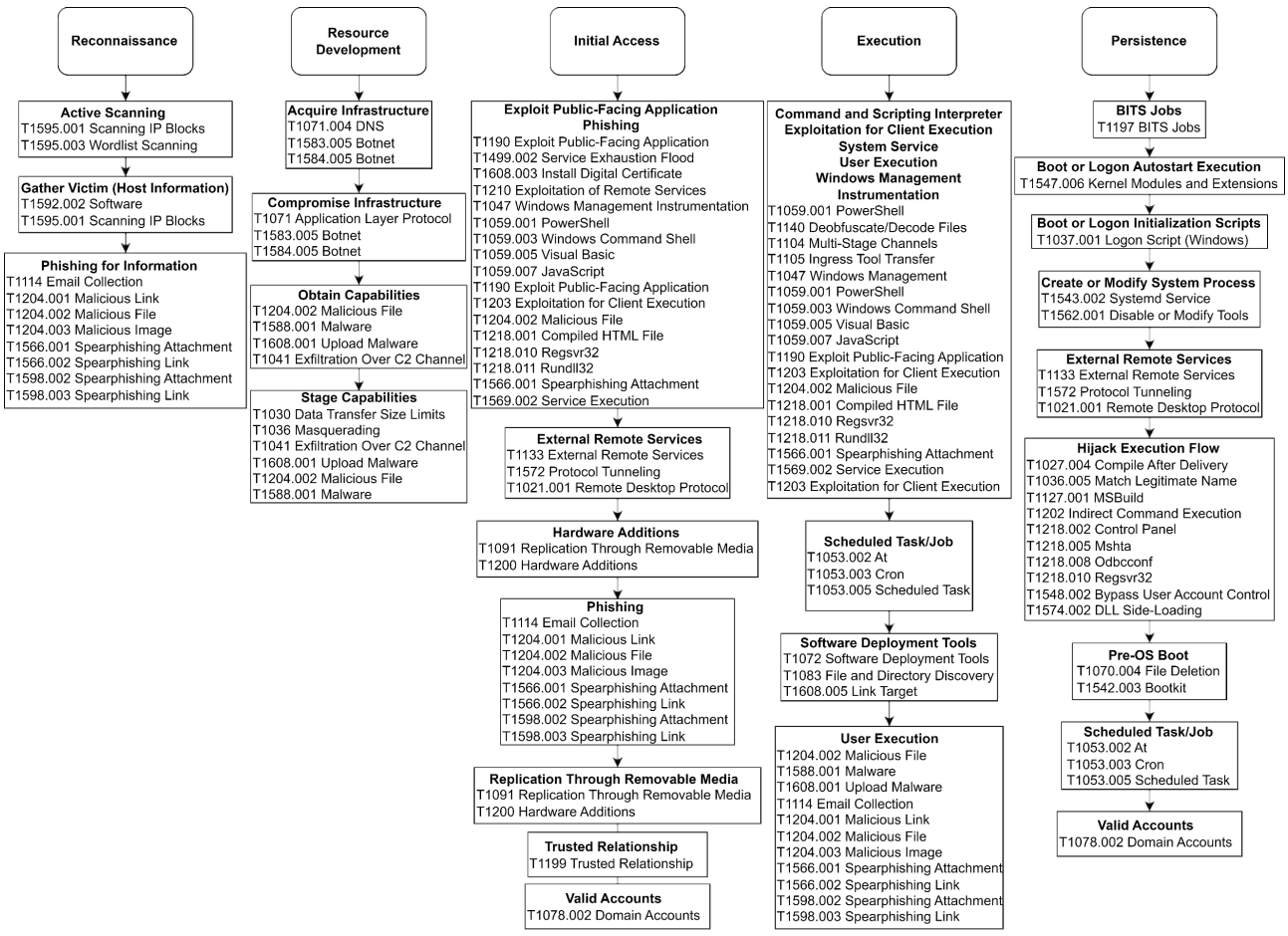


Figure 10. MITRE ATT&CK threat modeling and defense methodology map-1.

shown for illustration. The architectural infrastructure system can detect more than 29,462 application vulnerabilities with the signature database and countermeasures can be taken. Table 4 shows the most vulnerable application layer vulnerabilities of the systems in the attack area.

HTTP/HTTPS protocol attacks were performed using cyber-attack simulation tools (Nessus, OpenVAS, Parrot) in order to block services running in the DMZ infrastructure. While web services are invoked through HTTP/HTTPS protocols, these protocols have many security vulnerabilities due to their nature. The vulnerability attacks detected and blocked by the WAF system are shown in Table 5. It was observed that these attacks were blocked by the DRC architecture.

MITRE ATT&CK is used to classify cyber threat vectors, create attacker profiles and take precautions. This

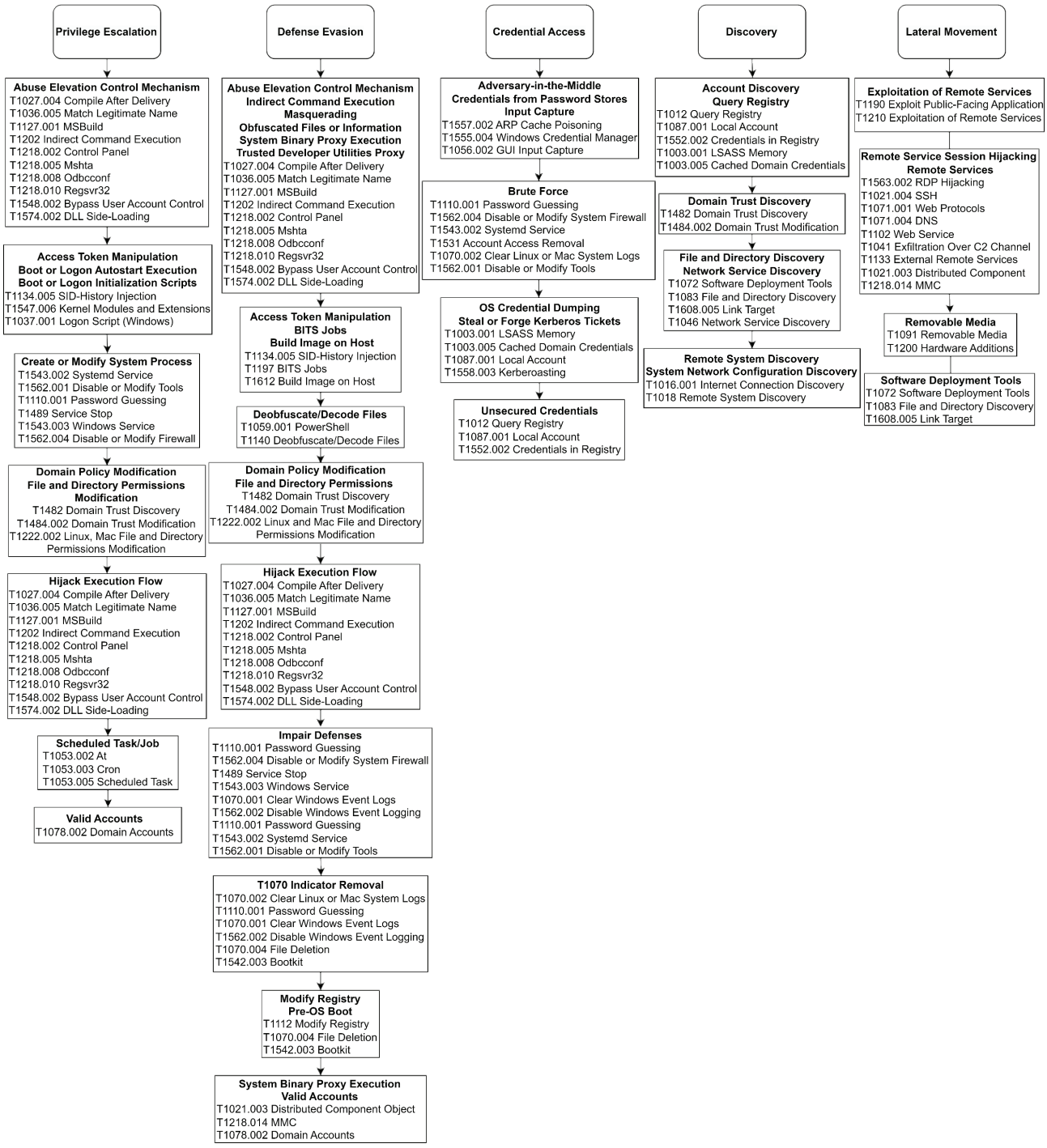


Figure 11. MITRE ATT&CK threat modeling and defense methodology map-2.

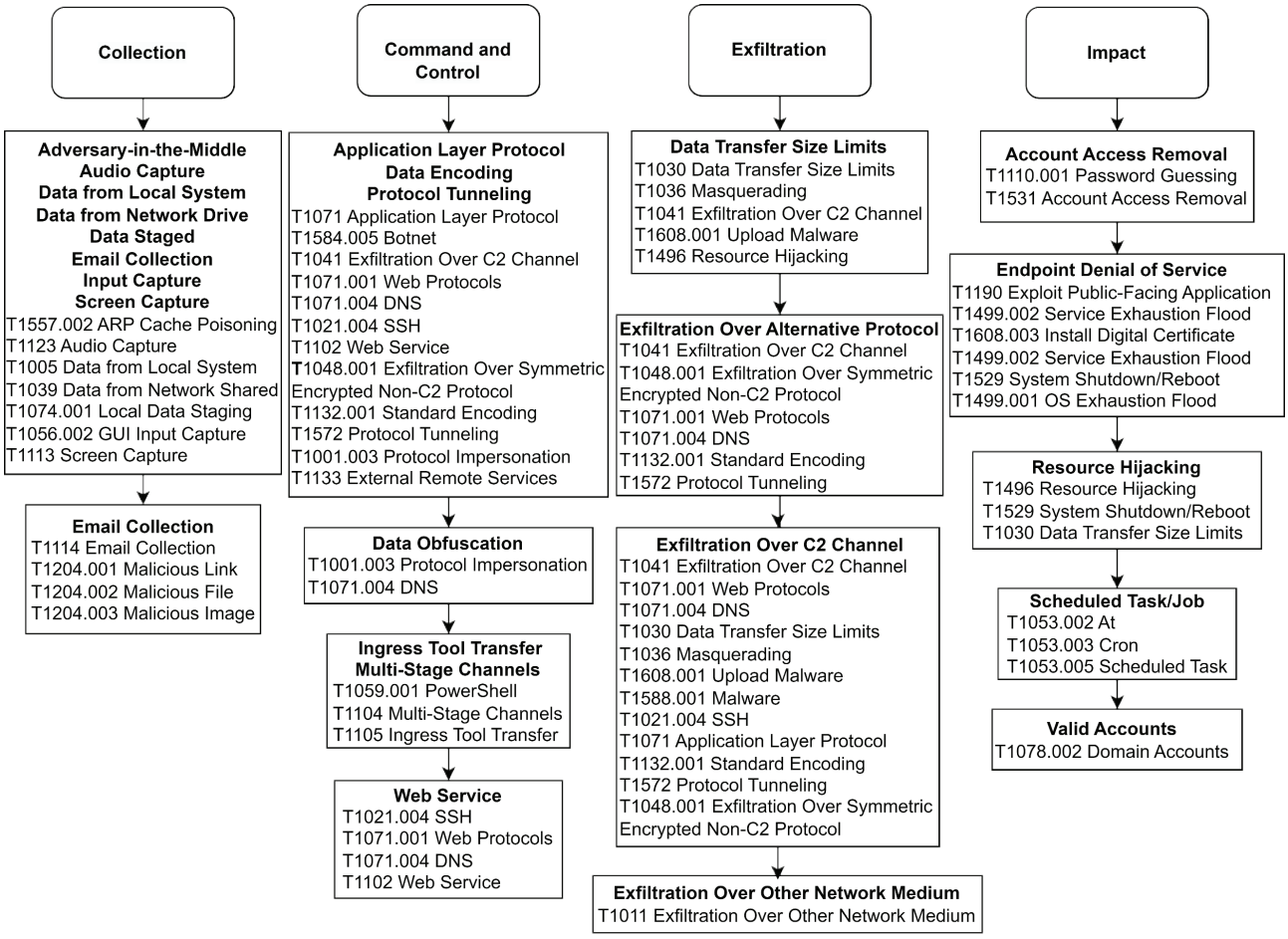


Figure 12. MITRE ATT&CK threat modeling and defense methodology map-3.

framework can be used to create an attack map of the attacker, which is used to gain a better understanding of the vulnerabilities of the system [87,88]. The maps in Figure 10 and Figure 11 help to understand the attacker's steps and improve cyber defense systems.

With the attack maps, future studies on cyber-attack protection and digital maturity will have a more scientific basis. As cyber-attacks continue to evolve and change, the need to systematically categorize the attacker profile and behavior map has led to the emergence of the MITRE ATT&CK and NIST v2 framework. When the results in Figure 12 are combined with the data obtained from Figure 10 and Figure 11, it is seen in the tests and performance evaluations conducted in the simulation environment that the architecture designed for the DRC infrastructure, which houses critical systems, has superior attack and threat prevention mechanisms.

CONCLUSION

Research and technological advancements have shown that cyber-attacks are increasing day by day. This increase underscores the critical need for robust cybersecurity measures to address the ever-evolving threats in the digital landscape. Academic studies in the field of cybersecurity and network security are making significant contributions, and these contributions are becoming more pronounced each year. The referenced studies highlight various types of threats that cyber attackers can deploy, and the findings obtained through studies on various available databases have added valuable insights to the literature.

The novelty of this study to the literature is the development of an architecture that leverages new and emerging technological infrastructures to address the security needs against cyber-attacks on DRC centers. The flowchart and pseudocode structure of this architecture have been detailed comprehensively. Additionally, the scientific novelty of this study lies in the successful integration of professional applications and frameworks such as EVE-NG, Nessus, OpenVAS, Kali, Parrot, MITRE ATT&CK Enterprise, and NIST v2. This integration has enabled the determination of the success limits of the architecture. The architectural infrastructure was simulated in the application environment, and real-world cyber-attack vectors were used to

conduct performance tests through accessible professional applications. This practical validation underscores the effectiveness and reliability of the architecture.

A significant challenge in cybersecurity are unknown zero-day attacks those that have not been previously identified and are not present in databases. These attacks remain a critical problem for existing infrastructure and systems. The developed architecture aims to provide effective protection against such attacks. In the first phase of the architecture, attacks were conducted on DDoS, SD-WAN, and MPLS systems using 10 different attack vectors and 10 different internet protocols. The behavior of these attacks was analyzed in detail using Wireshark packet analysis and Forti Analyzer software. The tests demonstrated that the protection layers could detect and block 99.99% of current and known attack vectors. The 0.01% error margin is anticipated to be due to the simulations conducted in a virtual environment.

In the second and third phases, attacks were conducted on DMZ web services and local network servers. These attacks, generated by attack simulators, were conducted using 57 different attack categories, 89.000 CVEs (Common Vulnerabilities and Exposures) and 219,000 different attack methods on IPS&IDS , layered firewalls, WAF structures, and sandbox products. The servers within the attack area did not exhibit any vulnerabilities, indicating the effectiveness of the developed architecture.

Global cybersecurity frameworks have facilitated the mapping of risks against the actions attackers may take to achieve their goals. Necessary improvements and plans have been implemented, and the ability to control and intervene in the accuracy of security measures has been enhanced, thereby preventing data loss. The real-time network traffic data obtained from the systems showed that malicious attacks designed to cause service interruptions failed. This finding confirms the success of the DRC architecture and infrastructure equipment.

The unique contribution of this research to science is the development of a cybersecurity architecture for DRC systems, an area not previously explored in such scope and detail by any academic author. The use of professional systems and advanced cyber-attack simulations has enabled the prevention of threats, and the data obtained has facilitated the development of a distinctive DRC architecture for distributed infrastructures that can be tiered. This model can be used by institutions and organizations to enhance the maturity level of their cybersecurity and network security, thus preventing potential economic losses.

Future recommendations for further development of this study include the integration of infrastructure systems such as Data Diodes (DataflowX), Secure Access Service Edge (SASE), and software and application-based data centers into the DRC infrastructure. These recommendations aim to further strengthen the current architecture and create a more effective defense mechanism against new cyber threats. Data diodes can minimize security vulnerabilities by making data flow unidirectional, preventing external access to critical systems. Secure Access Service Edge can play a crucial role in securing network access for users and devices, thereby preventing cyber-attacks. Software and application-based data centers can ensure the dynamic and flexible implementation of cybersecurity policies.

In conclusion, this study represents a significant advancement in the field of cybersecurity and network security. The developed DRC architecture has provided effective protection against various cyber-attacks, yielding findings that will inform future research in this field. As a valuable reference for both academic and professional communities, this study demonstrates the applicability of new technological developments and methodologies in cybersecurity. Consequently, it serves as an essential resource for researchers and experts working in the cybersecurity domain.

AUTHORSHIP CONTRIBUTIONS

Authors equally contributed to this work.

DATA AVAILABILITY STATEMENT

The authors confirm that the data that supports the findings of this study are available within the article. Raw data that support the finding of this study are available from the corresponding author, upon reasonable request.

CONFLICT OF INTEREST

The author declared no potential conflicts of interest with respect to the research, authorship, and/or publication of this article.

ETHICS

There are no ethical issues with the publication of this manuscript.

REFERENCES

[1] AFAD. 2014–2023 Critical Infrastructure Protection Roadmap Document. Ankara: Prime Ministry Disaster Emergency Management Presidency; 2014.

[2] Aslay F. Cyber attack methods and current situation analysis of Türkiye's cyber safety. Int J Multidiscip Stud Innov Technol 2017;1:24–28.

[3] Çölkesen TR. Network TCP/IP UNIX standard network information and internet backbone infrastructure. Istanbul: Papatya Yayıncılık; 2018.

[4] Baykara M, Daş R, Karadoğan İ. 1st International Symposium on Digital Forensics and Security (ISDFS'13); 2013; Elazığ, Türkiye.

[5] Svantesson D, Clarke R. A best practice model for e-consumer protection. Comput Law Secur Rev 2010;26:31–37. [CrossRef]

[6] Von Solms R, Van Niekerk J. From information security to cyber security. Comput Secur 2013;38:97–102. [CrossRef]

[7] Craigen D, Diakun-Thibault N, Purse R. Defining cyber security. Technol Innov Manag Rev 2014;4:13–21. [CrossRef]

[8] Wang W, Lu Z. Cyber security in the smart grid: survey and challenges. Comput Netw 2013;57:1344–1371. [CrossRef]

[9] Papp D, Ma Z, Buttyan L. Embedded systems security: threats, vulnerabilities, and attack taxonomy. In: 2015 IEEE 13th Annual Conf Privacy Secur Trust; 2015 Sep; Izmir, Türkiye. p. 145–152. [CrossRef]

[10] Luiijf E, Klaver M. Analysis and lessons identified on critical infrastructures and dependencies from an empirical data set. Int J Crit Infrastruct Prot 2021;35. [CrossRef]

[11] Setola R, De Porcellinis S, Sforna M. Critical infrastructure dependency assessment using the input–output inoperability model. Int J Crit Infrastruct Prot 2009;2:170–178. [CrossRef]

[12] Yaacoub JPA, Noura HN, Salman O, Chehab A. Robotics cyber security: vulnerabilities, attacks, countermeasures, and recommendations. Int J Inf Secur 2021;21:115–158. [CrossRef]

[13] Taylor PJ, Dargahi T, Dehghantanha A, Parizi RM, Choo KKR. A systematic literature review of blockchain cyber security. Digit Commun Netw 2020;6:147–156. [CrossRef]

[14] Kaur J, Ramkumar KR. The recent trends in cyber security: a review. J King Saud Univ Comput Inf Sci 2022;34:5766–5781. [CrossRef]

[15] Maglaras LA, Kim KH, Janicke H, Ferrag MA, Rallis S, Fragkou P, Maglaras A, Cruz TJ. Cyber security of critical infrastructures. ICT Express 2018;4:42–45. [CrossRef]

[16] Waseem M, Khan MA, Goudarzi A, Fahad S, Sajjad IA, Siano P. Incorporation of blockchain technology for different smart grid applications: architecture, prospects, and challenges. Energies 2023;16:820. [CrossRef]

[17] Khan MA, Saleh AM, Waseem M, Sajjad IA. Artificial intelligence enabled demand response: prospects and challenges in smart grid environment. IEEE Access 2022;11:1477–1505. [CrossRef]

[18] Dasgupta D, Akhtar Z, Sen S. Machine learning in cyber security: a comprehensive survey. J Def Model Simul 2020;19:57–106. [CrossRef]

[19] Cole E. Network security bible. Hoboken (NJ): John Wiley & Sons; 2011. p. 768.

[20] Aslan O, Yilmaz AA. A new malware classification framework based on deep learning algorithms. IEEE Access 2021;9:87936–87951. [CrossRef]

[21] Ouyang M, Hong L, Mao ZJ, Yu MH, Qi F. A methodological approach to analyze vulnerability of interdependent infrastructures. Simul Model Pract Theory 2009;17:817–828. [CrossRef]

[22] Wang S, Hong L, Ouyang M, Zhang J, Chen X. Vulnerability analysis of interdependent infrastructure systems under edge attack strategies. Saf Sci 2013;51:328–337. [CrossRef]

[23] Wang S, Hong L, Chen X. Vulnerability analysis of interdependent infrastructure systems: a methodological framework. Phys A 2012;391:3323–3335. [CrossRef]

[24] Yungaicela-Naula NM, Vargas-Rosales C, Perez-Diaz JA. SDN-based architecture for transport and application layer DDoS attack detection by using machine and deep learning. IEEE Access 2021;9:108495–108512. [CrossRef]

[25] Elubeyd H, Yiltas KD. Hybrid deep learning approach for automatic DoS/DDoS attacks detection in software-defined networks. Appl Sci 2023;13:3828. [CrossRef]

[26] Kim Y, Hakak S, Ghorbani A. DDoS attack dataset (CICEV2023) against EV authentication in charging infrastructure. In: 2023 20th Annual International Conference on Privacy, Security and Trust (PST); 2023. p. 1–9. [CrossRef]

[27] Carrier T, Victor P, Tekeoglu A, Lashkari HA. Detecting obfuscated malware using memory feature engineering. In: 8th International Conference on Information Systems Security and Privacy (ICISSP); 2022.

[28] Akbaş D. Modeling and analysis of an enterprise network and its security structures. TMMOB Elektrik Mühendisleri Odası Derg 2010. [CrossRef]

[29] Kör A. A dynamic solution model for cyber attacks. [Master's thesis]. Gazi University; 2015.

[30] Büyükkılıç M. Cybersecurity framework for small and medium size enterprises. [Master's thesis]. Bahçeşehir University Institute of Science; 2018.

[31] Herrmann D, Pridöhl H. Basic concepts and models of cybersecurity. In: The ethics of cybersecurity. Int Libr Ethics Law Technol 2020;21. Springer, Cham. [CrossRef]

[32] Çınar MS, Yıldırım A. Efficient management of an enterprise-wide area network with network management systems. NOHU J Eng Sci 2020;9:9–22.

[33] Avcı İ. Investigation of cyber security vulnerabilities and development of maturity model in smart natural gas networks. [PhD thesis]. Istanbul University; 2021.

[34] Xiong W, Legrand E, Aberg O, Lagerstorm R. Cyber security threat modeling based on the MITRE Enterprise ATT&CK matrix. Softw Syst Model 2021;21:157–177. [CrossRef]

[35] Frayssinet F, Esennarro M, Regalado FFJ, Reategui DM. Methodology based on the NIST cybersecurity framework as a proposal for cybersecurity management in government organizations. 3C TIC 2021;10:123–141. [CrossRef]

[36] Özarpa C, Avcı İ, Kara AS. Survey of cyber security risks and defense methods for autonomous vehicles. Eur J Sci Technol 2021;31:242–255.

[37] Güneş B, Kayışoğlu G, Bolat P. Cyber security risk assessment for seaports: a case study of a container port. Comput Secur 2021;103. [CrossRef]
[38] Kara Ş, Zengin A, Hizal S. Discrete event system identification based modeling and simulation of cyber attacks for the security of network systems. J Eng Sci Res 2022;5:186–202.
[39] Ruiz L, Chamon L, Ribeiro A. Graphon neural networks and the transferability of graph neural networks. Adv Neural Inf Process Syst 2020;33:1702–1712.
[40] Polat H, Polat O, Cetin A. Detecting DDoS attacks in software-defined networks through feature selection methods and machine learning models. Sustainability 2020;12:1035. [CrossRef]
[41] Assis MV, Carvalho LF, Lloret J, Proença ML Jr. A GRU deep learning system against attacks in software defined networks. J Netw Comput Appl 2021;177:102942. [CrossRef]
[42] De Donno M, Dragoni N, Giaretta A, Spognardi A. Analysis of DDoS-capable IoT malwares. In: 2017 Federated Conference on Computer Science and Information Systems (FedCSIS); 2017. p. 807–816. [CrossRef]
[43] Hallman R, Bryan J, Palavicini G, Divita J, Romero-Mariona J. Ioddos – the internet of distributed denial of service attacks. In: 2nd International Conference on Internet of Things, Big Data and Security; 2017. p. 47–58. [CrossRef]
[44] Specht S, Lee R. Taxonomies of distributed denial of service networks, attacks, tools and countermeasures. CEL2003-03, Princeton University, Princeton, NJ, USA; 2003.
[45] Vignau B, Khoury R, Hallé S. 10 years of IoT malware: a feature-based taxonomy. In: 2019 IEEE 19th International Conference on Software Quality, Reliability and Security Companion (QRS-C); 2019. p. 458–465. [CrossRef]
[46] Vignau B, Khoury R, Hallé S, Hamou-Lhadj A. The evolution of IoT malwares, from 2008 to 2019: survey, taxonomy, process simulator and perspectives. J Syst Archit 2021;116. [CrossRef]
[47] Bütün İ. Security implications of underlying network technologies on industrial internet of things. J Polytech 2022;25:223–229. [CrossRef]
[48] Karaman MS, Turan M, Aydin MA. Model application of anomaly based intrusion detection using artificial neural network. Eur J Sci Technol 2021;(Spec Issue):10–17.
[49] Çalkavur S, Guzeltepe M. Secure encryption from cyclic codes. Sigma J Eng Nat Sci 2022;40:380–389. [CrossRef]
[50] Erdem A, Kocaoğlu R. A new approach for network security: dynamic intelligent firewall architecture. J Fac Eng Archit Gazi Univ 2014;29:707–715. [CrossRef]
[51] Jang-Jaccard J, Nepal S. A survey of emerging threats in cybersecurity. J Comput Syst Sci 2014;80:973–993. [CrossRef]
[52] Or-Meir O, Nissim N, Elovici Y, Rokach L. Dynamic malware analysis in the modern era—a state of the art survey. ACM Comput Surv 2019;52:1–48. [CrossRef]
[53] Rabbani M, Wang YL, Khoshkangini R, Jelodar H, Zhao R, Hu P. A hybrid machine learning approach for malicious behaviour detection and recognition in cloud computing. J Netw Comput Appl 2020;151:102507. [CrossRef]
[54] Seo SH, Gupta A, Sallam AM, Bertino E, Yim K. Detecting mobile malware threats to homeland security through static analysis. J Netw Comput Appl 2014;38:43–53. [CrossRef]
[55] Utku A, Doğru İA. Permission based detection system for android malware. J Fac Eng Archit Gazi Univ 2017;32:1015–1024. [CrossRef]
[56] The MITRE Corporation. Enterprise Techniques. https://attack.mitre.org/techniques/enterprise/. Release date October 31, 2023. Accessed January 16, 2024.
[57] Bagui SS, Mink D, Bagui SC, Plain M, Hill J, Elam M. Using a graph engine to visualize the reconnaissance tactic of the MITRE ATT&CK framework from UWF-ZeekData22. Future Internet 2023;15:236. [CrossRef]
[58] National Institute of Standards and Technology (NIST). The NIST Cybersecurity Framework 2.0. https://nvlpubs.nist.gov/nistpubs/CSWP/NIST.CSWP.29.ipd.pdf. Release date August 8, 2023. Accessed on Jan 16, 2024.
[59] Aslan Ö, Aktuğ SS, Ozkan OM, Yilmaz AA, Akin E. A comprehensive review of cyber security vulnerabilities, threats, attacks, and solutions. Electronics 2023;12:1333. [CrossRef]
[60] Victor P, Lashkari AH, Lu R. IoT malware: an attribute-based taxonomy, detection mechanisms and challenges. Peer Peer Netw Appl 2023;16:1380–1431. [CrossRef]
[61] Tripathi D, Biswas A, Tripathi AK. An integrated approach of designing functionality with security for distributed cyber-physical systems. J Supercomput 2022;78:14813–14845. [CrossRef]
[62] Gaur A, Scotney B, Parr G, McClean S. Smart city architecture and its applications based on IoT. Procedia Comput Sci 2015;52:1089–1094. [CrossRef]
[63] GJ M, Kunte RS. A conceptual architecture design – building cyber security architecture for industrial control systems networks and for critical infrastructures. Int Res J Eng Technol 2024;6:1.
[64] Lu X, Dong R, Wang Q, Zhang L. Information security architecture design for cyber-physical integration system of air traffic management. Electronics 2023;12:1665. [CrossRef]

[65] Yousefnezhad N, Malhi A, Keyriläinen T, Främling K. A comprehensive security architecture for information management throughout the lifecycle of IoT products. Sensors 2023;23:3236. [CrossRef]
[66] Vijayakumaran C, Muthusenthil B, Manickavasagam B. A reliable next generation cyber security architecture for industrial internet of things environment. Int J Electr Comput Eng 2019;10:387–395. [CrossRef]
[67] Jalali R, El-Khatib K, McGregor C. Smart city architecture for community level services through the internet of things. In: 2015 18th International Conference on Intelligence in Next Generation Networks. IEEE; 2015. p. 108–113. [CrossRef]
[68] Jiang JR. An improved cyber-physical systems architecture for industry 4.0 smart factories. Adv Mech Eng 2018. [CrossRef]
[69] Lee J, Bagheri B, Kao HA. A cyber-physical systems architecture for industry 4.0-based manufacturing systems. Manuf Lett 2015;3:18–23. [CrossRef]
[70] Kırışoğlu S, Kara R, Özçelik İ. A new SNMP-based algorithm for network traffic balancing in virtual local area networks. J Fac Eng Archit Gazi Univ 2018;34:365–380. [CrossRef]
[71] Daş R, Bitikçi B. Analysis of different types of network attacks on the GNS3 platform. J Comput Inf Sci 2020;3:3. [CrossRef]
[72] Abomhara M, Koien MG. Cyber security and the internet of things: vulnerabilities, threats, intruders and attacks. J Cyber Secur 2015;4:65–88. [CrossRef]
[73] Jouini M, Rabai ABL, Aissa BA. Classification of security threats in information systems. Procedia Comput Sci 2014;32:489–496. [CrossRef]
[74] Khan I. An introduction to computer viruses: problems and solutions. Libr Hi Tech News 2012;29:8–12. [CrossRef]
[75] Rajesh B, Reddy YJ, Reddy BDK. A survey paper on malicious computer worms. Int J Adv Res Comput Sci Technol 2015;3:161–167.
[76] Jaiswal M. Computer viruses: principles of exertion, occurrence, and awareness. Int J Creat Res Thoughts 2017;5:648–651.
[77] Bickford J, Hare R, Baliga A, Ganapathy V, Iftode L. Rootkits on smartphones: attacks, implications, and opportunities. In: Proceedings of the Eleventh Workshop on Mobile Computing Systems & Applications; 2010 Feb 22–23; Annapolis, MD, USA. p. 49–54. [CrossRef]
[78] Javaheri D, Hosseinzadeh M, Rahmani AM. Detection and elimination of spyware and ransomware by intercepting kernel-level system routines. IEEE Access 2018;6:78321–78332. [CrossRef]
[79] Patil S, Jangra A, Bhale M, Raina A, Kulkarni P. Ethical hacking: the need for cyber security. In: 2017 IEEE International Conference on Power, Control, Signals and Instrumentation Engineering; 2017 Sep 21–22; Chennai, India. p. 1602–1606. [CrossRef]
[80] AlRimy BAS, Maarof MA, Shaid SZM. Ransomware threat success factors, taxonomy, and countermeasures: a survey and research directions. Comput Secur 2018;74:144–166. [CrossRef]
[81] CSO. DDoS attacks: definition, examples, and techniques. https://www.csoonline.com/article/571981/ddos-attacks-definition-examples-and-techniques.html. Release date January 31, 2022. Accessed January 16, 2024.
[82] Baysal K, Taşkın D. Blocking harmful images with a deep learning based next generation firewall. Sigma J Eng Nat Sci 2024;42:1133–1147. [CrossRef]
[83] Yılmaz A, Aslan Z. The impact of the COVID-19 pandemic on data usage rate in enterprise networks. J Anadolu Bil Vocat High Educ 2022;17:95–115. [CrossRef]
[84] Yılmaz A, Aslan Z. The role and future of 802.11ax technology in wireless network infrastructures: performance, security and innovation. J Anadolu Bil Vocat High Educ 2024;19:1–29. [CrossRef]
[85] Zolanvari M, Teixeira MA, Jain R. Effect of imbalanced datasets on security of industrial IoT using machine learning. In: 2018 IEEE International Conference on Intelligence and Security Informatics (ISI); 2018. p. 112–117. [CrossRef]
[86] Humayun M, Niazi M, Jhanjhi N, Alshayeb M, Mahmood S. Cyber security threats and vulnerabilities: a systematic mapping study. Arab J Sci Eng 2020;45:3171–3189. [CrossRef]
[87] Yamaguchi S, Leelaprute P. Hajime worm with lifespan and its mitigation evaluation against Mirai malware based on agent-oriented Petri net pn 2. In: 2019 IEEE International Conference on Consumer Electronics (ICCE); 2019. p. 1–4. [CrossRef]
[88] Shin Y, Kim K, Lee JJ, Lee K. Focusing on the weakest link: a similarity analysis on phishing campaigns based on the ATT&CK matrix. Secur Commun Netw 2022;2022. [CrossRef]

Sigma Journal of Engineering and Natural Sciences
Web page info: https://sigma.yildiz.edu.tr
DOI: 10.14744/sigma.2024.00154

Research Article

Heat generation from 32650 cylindrical cell battery pack at various load and speed conditions

Shashank GAWADE[1,2,*], Virendra BHOJWANI[2], Pradeep PATIL[1], M. ZUBAIRUDDIN[3]

[1]Jayawantrao Sawant College of Engineering, Pune, 411028, India
[2]MIT ADT University, Pune, 412201, India
[3]Aditya University, Surampalem, 533003, India

ARTICLE INFO

Article history
Received: 13 July 2024
Revised: 21 August 2024
Accepted: 25 October 2024

Keywords:
Electric Vehicles; Heat Generation; Joule's Heat; $LiFePO_4$

ABSTRACT

Electric vehicles are penetrating the transportation sector with a pace to reduce greenhouse gases and climate changes. Some limitations to penetrating in market are range, thermal performance, and battery cost. The performance of electric vehicles is majorly based on the quality and chemistry of the battery. The current study is on the Lithium Iron Phosphate battery pack of 48 V 42Ah with an ambient temperature. The current demand for electric vehicles varies with the speed under various loading conditions. Heating of the battery in real-time is one of the problems currently faced by automakers. The Joule's heat is the primary parameter for increasing the battery's temperature. Prediction of the heat generation in the battery was carried out with different mechanisms at constant charge/discharge rate, not with dynamic loading. The inefficient battery thermal management system may result in the thermal runaway, leading to fire catch incidents, hence estimation of the current withdrawal needs to be accurate. To predict heat generation, 1. Bernardi's equation used, but having limitation in predicting accurate heat prediction, 2. Ohmic/Joule's equation, the current must be known. Hence, experiments carried out to find the current withdrawal under different actual loading conditions. In this work, the temperature rise under various loading conditions is measured on the single-wheel vehicle model operated on a battery, at varying conditions of rolling resistance, load, speed, and test duration. Experiment results show a 7.6 & 6.7°C rise in battery temperature at 125 kg, 15km/hr speed for 75 min on concrete and tar roads, respectively. From the experimental result need of the battery thermal management system, heat dissipation rate can be efficiently designed.

Cite this article as: Gawade S, Bhojwani V, Patil P, Zubairuddin M. Heat generation from 32650 cylindrical cell battery pack at various load and speed conditions. Sigma J Eng Nat Sci 2025;43(6):2127–2139.

***Corresponding author.**
*E-mail address: ssgawade24@gmail.com

This paper was recommended for publication in revised form by Editor-in-Chief Ahmet Selim Dalkilic

Published by Yıldız Technical University Press, İstanbul, Turkey
© Author. This is an open access article under the CC BY-NC license (http://creativecommons.org/licenses/by-nc/4.0/).

INTRODUCTION

Conventional internal combustion engine (ICE) vehicles have limitations of harmful emissions, limited fossil fuel sources, and high transportation cost per kilometer. Conventional ICE vehicles are being replaced by electric vehicles (EVs) which use rechargeable batteries as a source of energy, a motor, and a controller. In the global market, the share of EVs in the automotive market has significantly increased in the last decade. Furthermore, extensive research in battery technology has remarkably decreased battery costs, resulting in a market share. Worldwide efforts are to improve the performance of EV batteries and the vehicle's performance. During the battery discharge, the cells used for battery construction generate a significant amount of heat, which causes a rise in the battery pack's temperature.

While the literature survey provides valuable insights into the heat generated in the cell at the laboratory level during constant current discharge, it also reveals a significant gap in our understanding. There are very few papers that delve into the current withdrawn from the battery at various speeds, under different payloads, and in different road conditions. These factors, such as rolling resistance, payload, and vehicle speed, can significantly vary the power demand at different intervals. This scarcity of literature underscores the urgency of further research in this area to ensure the optimal performance and safety of EV batteries under real-world conditions.

Lithium Iron Phosphate (LFP), Lithium Nickel-Cobalt-Aluminum Oxide (NCA), and Lithium-Nickel-Manganese-Cobalt-Oxide (NMC) batteries were experimentally tested at ambient temperature and under different operating currents, measuring cell voltage and surface temperature [1]. The elevated temperature affects the battery's performance, causing capacity fade, fire hazards, thermal runaway, etc [2]. Thermal runaway occurs when the cell's temperature is over the working temperature due to the heat-generating reactions within the cell, causing flammable gasses [3]. One impact of the cell's increase in temperature occurred on the battery's SoC estimation. SoC determines the present current density of the battery [4]. During the discharging of the cell, the heat evolved inside the cell, which causes the SEI layer to decompose, binder decomposition, enhance the rate of reaction, and decomposition of the electrolyte, which results in the gas buildup inside the cell [5].

A battery thermal management system was adopted to limit the temperature rise of the battery pack. Several thermal management techniques include air cooling systems, liquid cooling systems, phase change materials, composite phase change materials, etc. The selection of a suitable thermal management system depends on the heat generated in the battery pack. Hence, estimating the amount of heat generated in the battery pack is crucial in deciding the type of thermal management system. Researchers continuously develop battery thermal management systems (BTMS) by adopting different approaches. Few authors developed novel BTMS for Lithium-ion batteries (LIBs) employing air cooling strategies like symmetrical air-cooling, two-directional air-flow approach, air cooling coupled to water evaporation, and metal and non-metal foams [6-12]. Liquid excellent BTMS technique was studied extensively by various researchers [13], where coolants like water, Nanofluid, and water-ethylene glycol mixture, along with novel techniques/arrangements like micro-vascular composites, mini-channel aluminium tubes, circuitous channels, etc., were studied. In addition to this, researchers have investigated BTMS employing novel techniques using phase change materials (PCM), composite phase change materials (CPCM), and heat-pipe approach [11-18]. Hybrid cooling mechanism, where air and liquid cooling are adopted for efficient cooling [19]. Paraffin wax, along with Al_2O_3 Nanoparticles, shows enhancement in the charging and discharging process of the PCM [20]. Fly ash Nanofluid in the base of water-ethylene glycol (ratio 3:1) shows better heat dissipation over the simple water-ethylene glycol (ratio 3:1) as a coolant [3, 21]. Different authors used K-type thermocouples for thermal cycles during different processes [22-24]. The sources of heat generation in the LIB's are reversible heat generation and irreversible heat generation due to activation, concentration, and ohmic (electronic and ionic) polarizations – in with graphite/$LiFePO_4$ electrode materials [25]. One of the most used methods to measure the heat generated in the cell is the accelerating rate calorimeter (ARC), restricted to use under adiabatic conditions and for the high rate operating cells [26]. Allouhi et al. proposes the design of an electricity charging station for small-size electric vehicles powered by the same HRES. It help Moroccan authorities to have insight on the role that can play HRES systems to not only enhance the energy efficiency of supermarkets and lower their emissions but also how they can help in transitioning towards a clean and green mobility [27]. The lithium-ion batteries get affected due to the high temperature in view of safety and performance. Due to high temperatures side reactions occurred result to degradation of cell capacity and the fading of electrochemical performance [26]. Artificial intelligence and machine learning techniques show a promising future to predict the current withdrawal from the past data set [28].

In this work, an attempt is made to investigate the effect of the loading condition on the heat generated in the Lithium Iron Phosphate (LFP) cell. During real-time driving, the speed and payload on the vehicle vary which causes changes in the power demand and current demand from the battery. Currently, in the literature survey, the heat generated at the constant current output was discussed at different loading conditions. The experiment study gives the relationship of the current withdrawn from the battery with respect to the payload, rolling resistance, and speed of the vehicle. As the Joules heat, the major parameter to raise the temperature inside the battery solely depends on the withdrawn current. This study predicts the current withdrawal

and heat generated in the battery under different loading conditions. Depending on the battery's heat generated, the battery thermal management system's deployment can be easily selected. To evaluate the performance of the battery pack, a single wheel was tested using a test dynamometer at different load and speed conditions.

Heat Generation in the Cell

In the present study, lithium iron phosphate (LFP) type lithium-ion battery cells are investigated. The LFP cells use $LiFePO_4$ as a cathode material, while a form of carbon is an anode material. The lithium ions (Li^+) travel from the anode to the cathode through the electrolyte during the cell discharge and from the cathode to the anode during the cell charge. These ions get rapidly integrated into the cathode material once they reach the cathode. The charge and discharge reactions in the battery are presented in Eq.1 and 2, respectively [13].

Charge reactions:

$$FePO_4 + xLi^+ + xe^- = xLiFePO_4 + (1\text{-}x)\ FePO_4 \quad (1)$$

Discharge reactions:

$$LiFePO_4 - xLi^+ - xe^-\ xFePO_4 + (1\text{-}x)\ LiFePO_4 \quad (2)$$

The estimation of heat generation in the cell during the charge and discharge process is vital to deciding on the type of battery thermal management system for the battery pack. To estimate the heat generation within the battery cell, it is crucial to understand the mechanism of heat generation have mentioned various approaches for measuring the battery heat generation (1) through direct experimental tests, (2) by employing Bernardi's equations, and (3) by adopting electro-thermal coupling model. Predicting heat generation within the battery using the Bernardi equation is a highly effective, time-saving approach with equitable results [13].

In the LFP cell, heat generation is primarily due to polarization heat, heat released during chemical reactions, and Joule's heat. Of these, Joule's heat, which is related to Ampere^2 x Internal resistance, is the major contributor to heat generation in the cell. As the load and speed change, the power demand to cope with these conditions increases, leading to an increase in current and subsequently, the temperature of the cell.

The Bernardi equation is given below,

$$Qgen = I(U - V) - I\left[T - \frac{dU}{dT}\right] \quad (3)$$

where, Q_{gen} = the rate of heat generation (W), I = the cell current (A), U = the open circuit voltage (V), T = the temperature (K), and V = the cell terminal voltage (V). The first term of the equation quantifies the heat generation due to the polarization effects in the cell whereas the second term quantifies the entropic heat generation [29-32]. However, this equation does not consider the heat generation due to the phase change and mixing [33].

The term ∂U/ ∂T which is a derivative of OCV with respect to the temperature is termed as entropic coefficient of the cell.

Accurate estimation of heat generation is critical for EV batteries. Conventional means of heat estimation (i.e., Bernardi equation) work only for constant current discharge. However, fluctuating current conditions are the standard mode of operation for cells in EV applications. It is noted that Bernardi method is an indirect method of heat estimation based majorly on electrical parameters. It is also observed that the reversible part of Bernardi heat is negligible under drive cycle operation. Lithium-ion batteries can utilize various cathode chemistries, including LFP, LCO, and NMC. Each cathode chemistry has distinct advantages and disadvantages concerning specific capacity, energy/ power density, cost, and thermal stability [34].

EXPERIMENTAL SETUP AND PROCEDURE

For the experimental work, four parameters are considered with high priority, Speed of vehicle, Payload on vehicle, Time of drive, and the road surface itself. The coefficient of drag and road gradient were not considered for the study as the coefficient of drag is finalized by the vehicle manufacturer and is independent of the driver. Road gradient, in the urban area, the slope from underground to basement or elevation at the overhead bridge is present by maximum elevation is up to 500 meters, which covers in maximum of 2-3 minutes, so consideration of the same for the whole duration of time was exempted after expert comment.

The payload is an essential parameter of the vehicle. Here two two-wheeler vehicles were considered in the study. In a typical scenario average weight of a single person in India is 68 kg. Considering the vehicle running without a person, only the vehicle's weight plays a critical role. Hence, 80/2 kg was considered for lower-weight conditions. On the higher side, the average weight of the person is multiplied by 2.5 to consider variations in the weight. Furthermore, an additional 80 kg wt. of chassis was added to the calculation for deadweight and safety analysis for extreme variation in weight. All this counted to 250/2 kg as a higher side weight in the analysis.

As per the SAE J2452 standard, the rolling resistance for the tar road is 0.013, and for the concrete, it is 0.01. In urban areas, the roads are constructed with tar or concrete roads; hence, these conditions are implemented with the two Mild steel roads at the bottom of the Tire.

In the Indian context, the diversity in the weight and driving pattern of the driver gender was observed widely. The range of the vehicle majorly depends on the payload of the vehicle. As per observation, the male (age 30 onwards) drives smoothly with experience to gain high performance, whereas the female driving pattern differs from the male in which jerky motion is involved. After benchmarking with

MINITAB software, different payload combinations, time, and speed combinations were formulated with the surface response method.

Battery Pack

The battery pack of 48-volt 42 Ah is constructed with 32650 (32 mm diameter, 65 mm height of cell & Circular shape) lithium iron phosphate (LFP) cylindrical cell with nominal voltage 3.2 V and 6000 mAh capacity. The battery pack consists of 112 nos. in Two stacks, an upper and lower stack each containing 56 LFP cells. Technical specifications of the cells used for battery construction with battery are tabulated in Table 1. In each stack, the cells are arranged in eight series – seven parallel (8S7P) layout with an effective capacity of 42Ah and a nominal voltage of 24V. The upper and lower stacks are then connected in series to double the nominal voltage of the battery pack to 48V. The battery pack is used to operate an electric two-wheeler. The pictorial view of the battery pack is shown in Figure 1.

Table 1. Technical specifications of cell and battery pack

Parameter	Value	Battery pack
Nominal voltage	3.2 V	48 V
Cell capacity	6000 mAh	42 Ah
Diameter	32 mm	--
Height	65 mm	--
Mass	160 g	17.92 kg
Cut off voltage	2.8 V	--
Internal resistance	0.02 ohm	--



Figure 1. Battery pack

Experımental Setup

The objective of this work is to evaluate the temperature rise of the battery pack by measuring the battery cell's temperature during the vehicle's operation. The various operating conditions include rolling resistance, load, speed, and duration of operation. Rolling resistance of 0.01 and 0.013 are selected to simulate the tar and concrete road conditions [35]. With these rolling resistance values, tests were performed at different loads and speeds, as specified in Table 3. A chassis dynamometer test setup was developed to simulate the operating conditions with a single fixed roller. The laboratory setup is depicted in Figure 2. The wheel rolls over the single fixed roller (shaft) at various speeds through a chain and sprocket mechanism by a motor. The roller shaft is supported over the pillow bearing on the I-section base and is free to rotate. The wheel rotates over a shaft, which applies a rolling resistance to the wheel. The brushless DC motor controller takes power from the battery and supplies it to the motor as per the requirement. A 1 kΩ potentiometer communicates the power required to the controller based on the accelerator position. A 48V brushless DC motor with a maximum power of 1500 W and a maximum speed of 3000 rpm was used to drive the wheel assembly. The display on the front panel shows the battery voltage and the current. A miniature circuit breaker (MCB) protects the circuit from excessive current during overloading and short circuits.

The payload is an essential parameter of the vehicle. Here two two-wheeler vehicles were considered in the study. In a typical scenario average weight of a single person in India is 68 kg. Considering the vehicle running without a person, then only the weight of the vehicle plays a key role. Hence, 80/2 kg was considered for lower-weight conditions. On the higher side, the average weight of the person is multiplied by 2.5 to consider variations in the weight.

Furthermore, an additional 80 kg wt. of chassis was added to the calculation for deadweight and safety analysis for extreme variation in weight. All this counted to 250/2 kg as a higher side weight in the analysis. In the urban city as per the survey, 80-90% of the population drives a vehicle with 25 km/h speed due to the road, traffic, and signal control conditions, either on the tar road or concrete road.

Figure 2 shows the laboratory test setup with a 35 mm mild steel shaft under the tire to assess rolling resistance conditions. During each test, a data acquisition system records the voltage of the battery pack and the discharge current. To measure the cell's temperature, thermocouples were attached to the surfaces of the different cells in the upper and lower stacks. Type 'T' thermocouples with a temperature inaccuracy of ±0.75% were used to measure the cell's temperature. A multichannel data logger was used to record the temperature data at fixed intervals. The layout of the battery pack and the location of the thermocouples are depicted in Figure 3. The shaded cells show the location of the thermocouple.

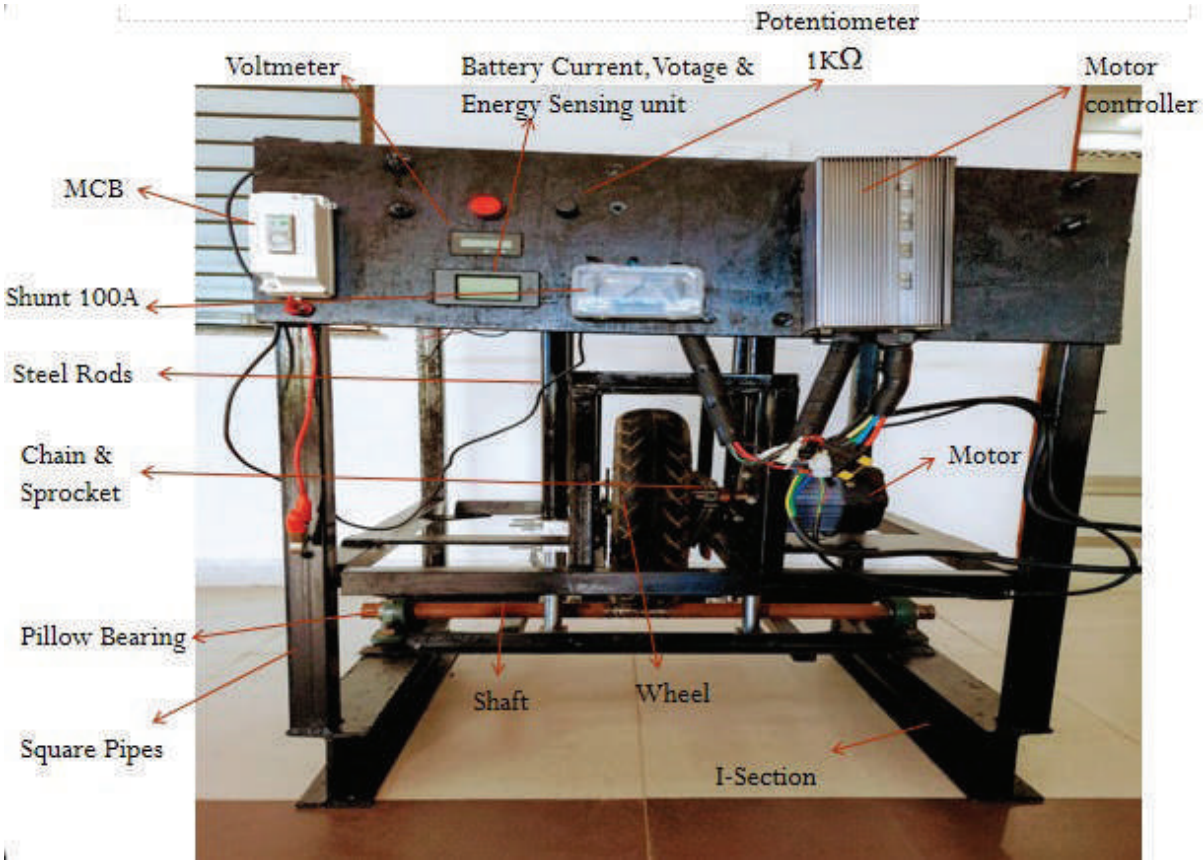


Figure 2. Test setup.

LA_1	LA_2	LA_3	LA_4	LA_5	LA_6	LA_7
LB_1	LB_2	LB_3	LB_4	LB_5	LB_6	LB_7
LC_1	LC_2	LC_3	LC_4	LC_5	LC_6	LC_7
LD_1	LD_2	LD_3	LD_4	LD_5	LD_6	LD_7
LE_1	LE_2	LE_3	LE_4	LE_5	LE_6	LE_7
LF_1	LF_2	LF_3	LF_4	LF_5	LF_6	LF_7
LG_1	LG_2	LG_3	LG_4	LG_5	LG_6	LG_7
LH_1	LH_2	LH_3	LH_4	LH_5	LH_6	LH_7

UA_1	UA_2	UA_3	UA_4	UA_5	UA_6	UA_7
UB_1	UB_2	UB_3	UB_4	UB_5	UB_6	UB_7
UC_1	UC_2	UC_3	UC_4	UC_5	UC_6	UC_7
UD_1	UD_2	UD_3	UD_4	UD_5	UD_6	UD_7
UE_1	UE_2	UE_3	UE_4	UE_5	UE_6	UE_7
UF_1	UF_2	UF_3	UF_4	UF_5	UF_6	UF_7
UG_1	UG_2	UG_3	UG_4	UG_5	UG_6	UG_7
UH_1	UH_2	UH_3	UH_4	UH_5	UH_6	UH_7

(a) Upper Stack (b) Lower Stack

Figure 3. Layout of battery pack and location of thermocouples.

Since each cell in the battery pack is subjected to the varying conditions of the convection, it is vital to measure the temperature of cells at various locations. To differentiate it, the cells in the battery pack are classified into regions as layer 1 (L1), layer 2 (L2), layer 3 (L3), and layer 4 (L4). Layer 1 includes the cell in the outermost region of the battery pack directly exposed to atmospheric air. Layer 2 includes the cells in the layer inside r 1, and layer 3 includes the cells inside r 4 in the core central part of the battery pack. Table 2 lists cells with thermocouples in each layer of the battery pack for the upper and lower stack.

Table 2. Thermocouples in different regions of battery pack

Region	Upper Stack	Lower Stack
L1	UA1, UA7, UH1, UH7	LA1, LA7, LH1, LH7
L2	UB2, UB6, UG2, UG6	LB2, LB6, LG2, LG6
L3	UC3, UC5, UF3, UF5	LC3, LC5, LF3, LF5
L4	UD4, UE4	LD4, LE4

RESULT AND DISCUSSION

Temperature Rise of Cell

The heat generated in the battery during the discharge is dissipated to the surrounding air by the convection mode of heat transfer. The heat transfer rate depends upon the ambient temperature heat transfer coefficient and is

Table 3. Test specifications

Sr. No.	Parameter	Lower value	Higher Value
1	Speed of vehicle (km/h)	05	25
2	Payload (kg)	80/2	{[(68x2.5) + 80] = 250}/2
3	Rolling resistance coefficient	0.01 for tar	0.013 for concrete
4	Time (minutes)	10	75

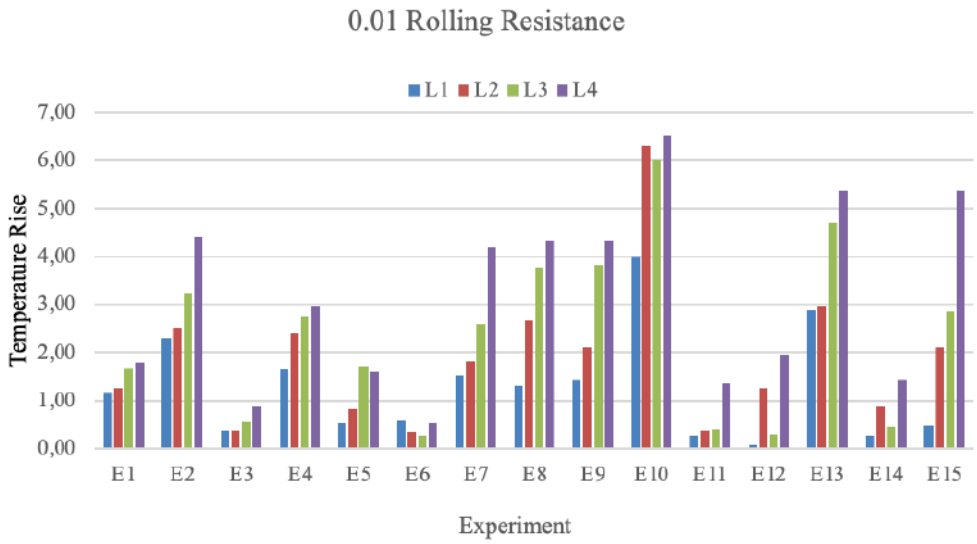
Table 4. Experimental value

Experiment No.	Designation	Rolling Resistance (RR)	Load (kg)	Speed (km/h)	Duration of Test (min)
1	E1	0.01	40	05	43
2	E2	0.01	82.5	05	75
3	E3	0.01	82.5	05	10
4	E4	0.01	125	05	43
5	E5	0.01	40	15	75
6	E6	0.01	40	15	10
7	E7	0.01	82.5	15	43
8	E8	0.01	82.5	15	43
9	E9	0.01	82.5	15	43
10	E10	0.01	125	15	75
11	E11	0.01	125	15	10
12	E12	0.01	40	25	43
13	E13	0.01	82.5	25	75
14	E14	0.01	82.5	25	10
15	E15	0.01	125	25	43
16	Y1	0.013	40	05	43
17	Y2	0.013	82.5	05	75
18	Y3	0.013	82.5	05	10
19	Y4	0.013	125	05	43
20	Y5	0.013	40	15	75
21	Y6	0.013	40	15	10
22	Y7	0.013	82.5	15	43
23	Y8	0.013	82.5	15	43
24	Y9	0.013	82.5	15	43
25	Y10	0.013	125	15	75
26	Y11	0.013	125	15	10
27	Y12	0.013	40	25	43
28	Y13	0.013	82.5	25	10
29	Y14	0.013	82.5	25	75
30	Y15	0.013	125	25	43

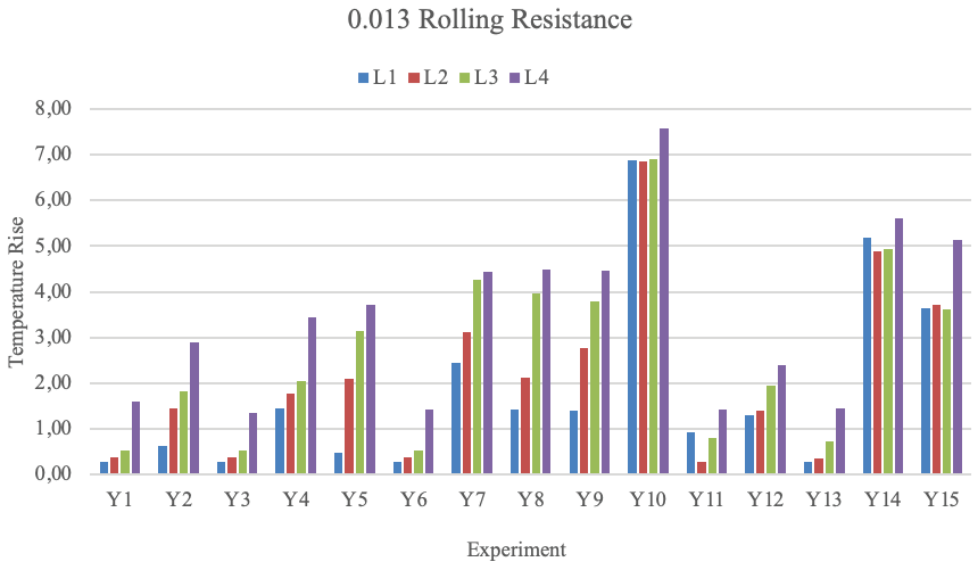
available for the convection. For the battery pack under investigation, the outer cells are exposed to the inner side of the battery pack. However, the cells at the inner locations are subjected to the heated trapped air in the battery pack. As a result, the heat transfer coefficient at the outer cell surface is more significant than that at the inner cells of the battery pack. Consequentially, it is evident that the inner cells are subjected to more extraordinary temperature rise than the outer cells of the battery pack. The average rise in temperature of cells in each region battery pack for all tests with rolling resistance of 0.01 and 0.013 are shown in Figure 4 a and b, respectively.

It is perceptible that the average rise in temperature of cells in the core region of the battery (L4) is more significant than all other layers, followed by regions L3, L2, and L1. The average temperature rise for the region L1 is lower than the other regions due to the higher convective coefficient. As ambient air enters the battery pack, it gets heated by heat generation in the cells, reducing the heat transfer rate from the cell to the air in the battery pack's central part. Because of this, the temperature rise in the L4 region of the battery is higher than in other regions.

The cells in the central part of the battery pack experience a lower heat dissipation rate, leading to a higher cell temperature than cells in other parts of the battery pack.



a) For Rolling Resistance 0.01



b) For Rolling Resistance 0.013

Figure 4. The average rise in temperature of cells in each region of the battery pack.

Table 4. Maximum temperature rise of the battery pack

Test	Maximum temperature rise	Test	Maximum temperature rise
E1	1.9	Y1	1.7
E2	4.5	Y2	3.1
E3	0.9	Y3	0.9
E4	3.3	Y4	3.5
E5	3.2	Y5	3.8
E6	1	Y6	1
E7	4.3	Y7	4.5
E8	4.5	Y8	4.7
E9	4.4	Y9	4.6
E10	6.7	Y10	7.6
E11	1.4	Y11	1.5
E12	2.1	Y12	2.4
E13	5.4	Y13	1.6
E14	1.5	Y14	5.7
E15	5.6	Y15	5.3

For all other cells, a portion of the heat generated by the cell is dissipated to the atmospheric air through the convection plus conduction mode of heat transfer. The cell surface temperature is crucial to measuring the entropic heat generation in the battery pack accurately. For this purpose, the maximum temperature rise of the cell is considered for each test. The maximum temperature rise of the battery pack for each test is detailed in Table 4.

Effect of Load on Maximum Temperature Rise

The experimental tests are conducted at varying loads, speeds, and test times. The effect of load on maximum temperature rise for various test conditions is exhibited in the graphical form in Figure 5. As the load increases from 40 to 125 kg, the temperature-increased behavior was observed at 05, 15 & 25 km/for 43, 75 & 43 minutes, respectively.

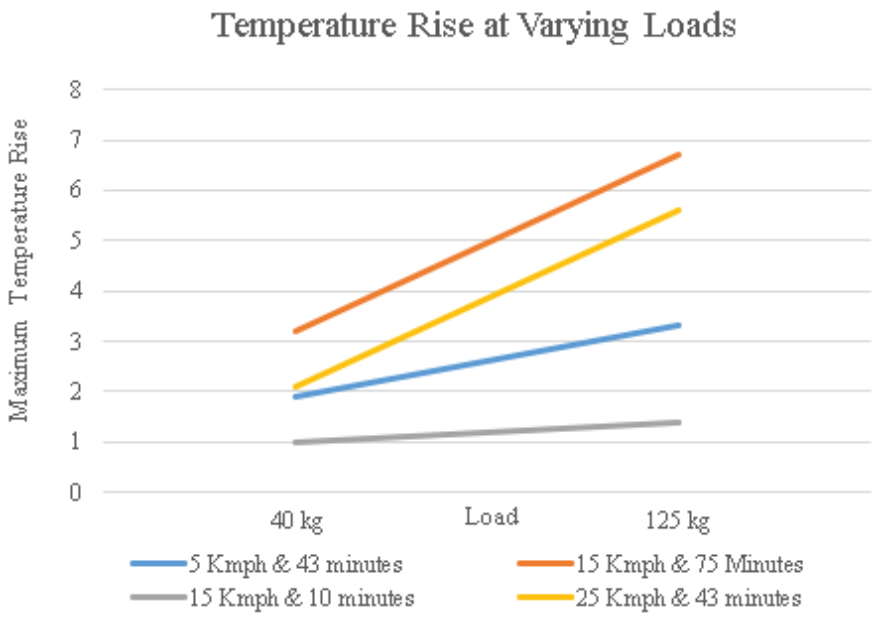


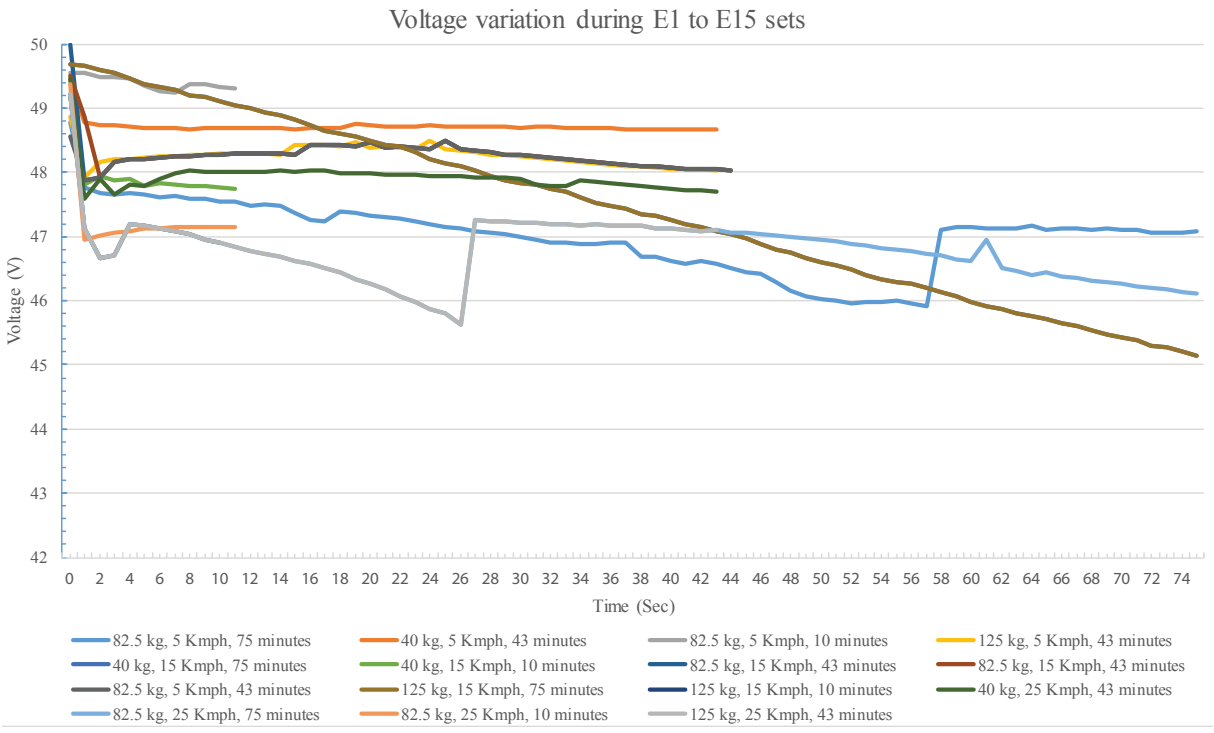
Figure 5. Temperature rise at varying loads.

Heat Generation Per Minute Under Dıfferent Loading Conditions

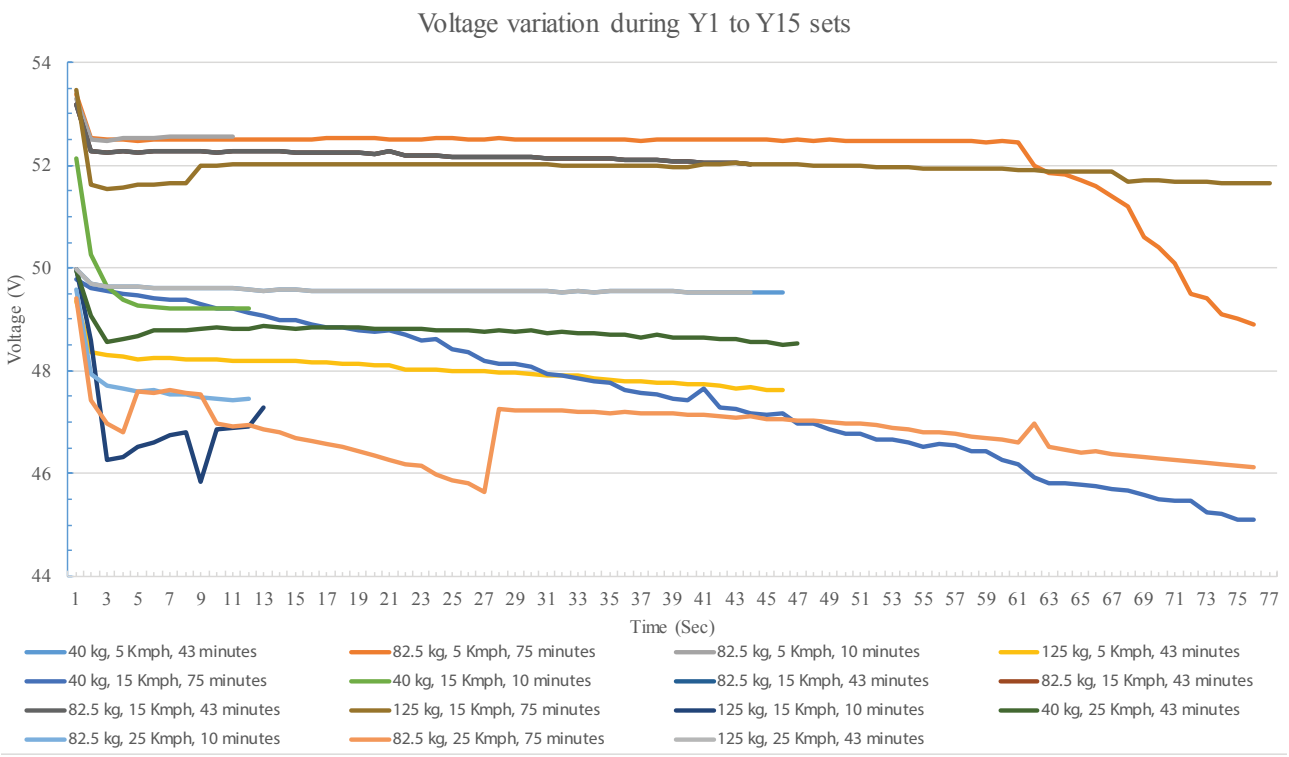
The voltage and current delivered by the battery pack and the cells' surface temperature were recorded during the test. The time-dependent current and voltage values are required to estimate the heat generation in the battery pack using the Bernardi theoretical model. The value of current and voltage values with time are shown in Figure 6 (a- ad). The rate of heat generation during each test is tabulated in Table 5.

Table 5. Temperature rise per minute for different tests

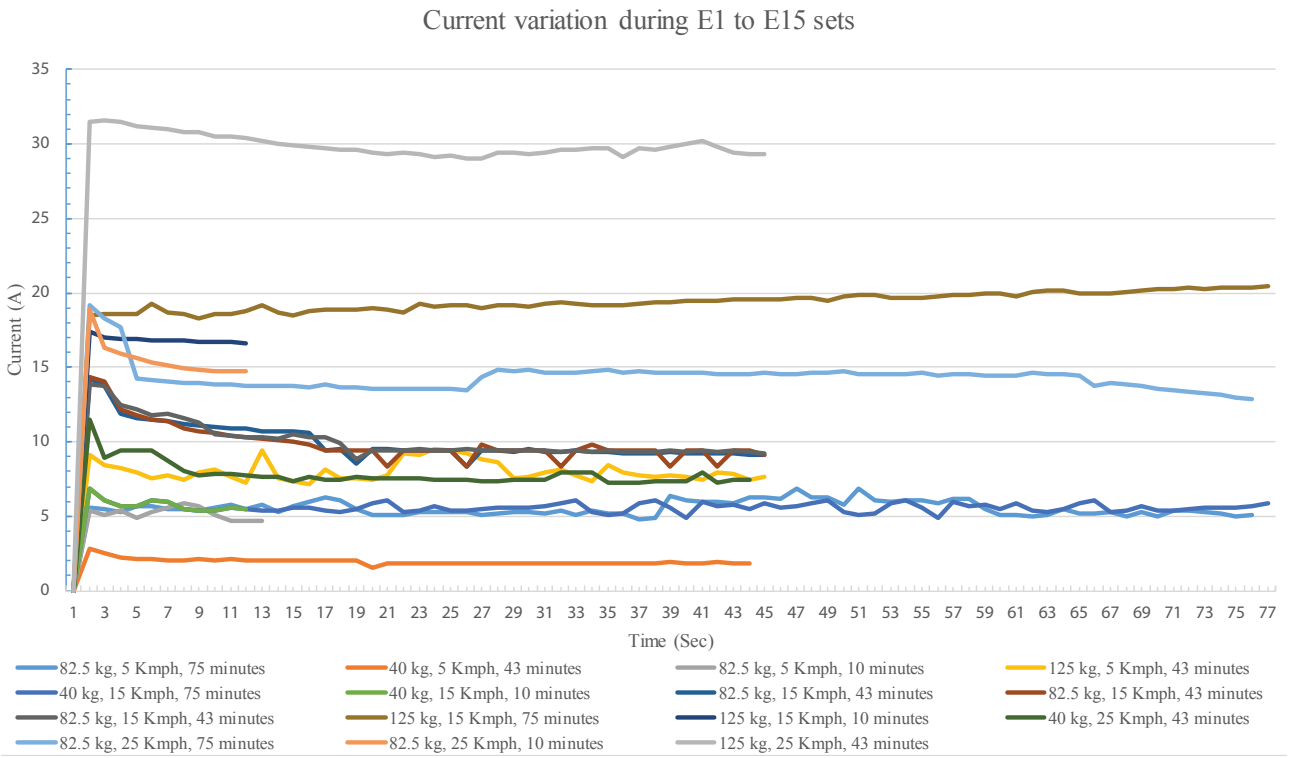
Test	Temperature rise per minute by exp. (°C)	Test	Temperature rise per minute by exp. (°C)
E1	0.67	Y1	0.78
E2	0.77	Y2	0.59
E3	0.18	Y3	0.30
E4	0.39	Y4	0.40
E5	0.60	Y5	0.80
E6	0.17	Y6	0.26
E7	0.41	Y7	0.56
E8	0.42	Y8	0.47
E9	0.41	Y9	0.41
E10	0.33	Y10	0.68
E11	0.07	Y11	0.16
E12	0.22	Y12	0.27
E13	0.28	Y13	0.08
E14	0.08	Y14	0.30
E15	0.20	Y15	0.15



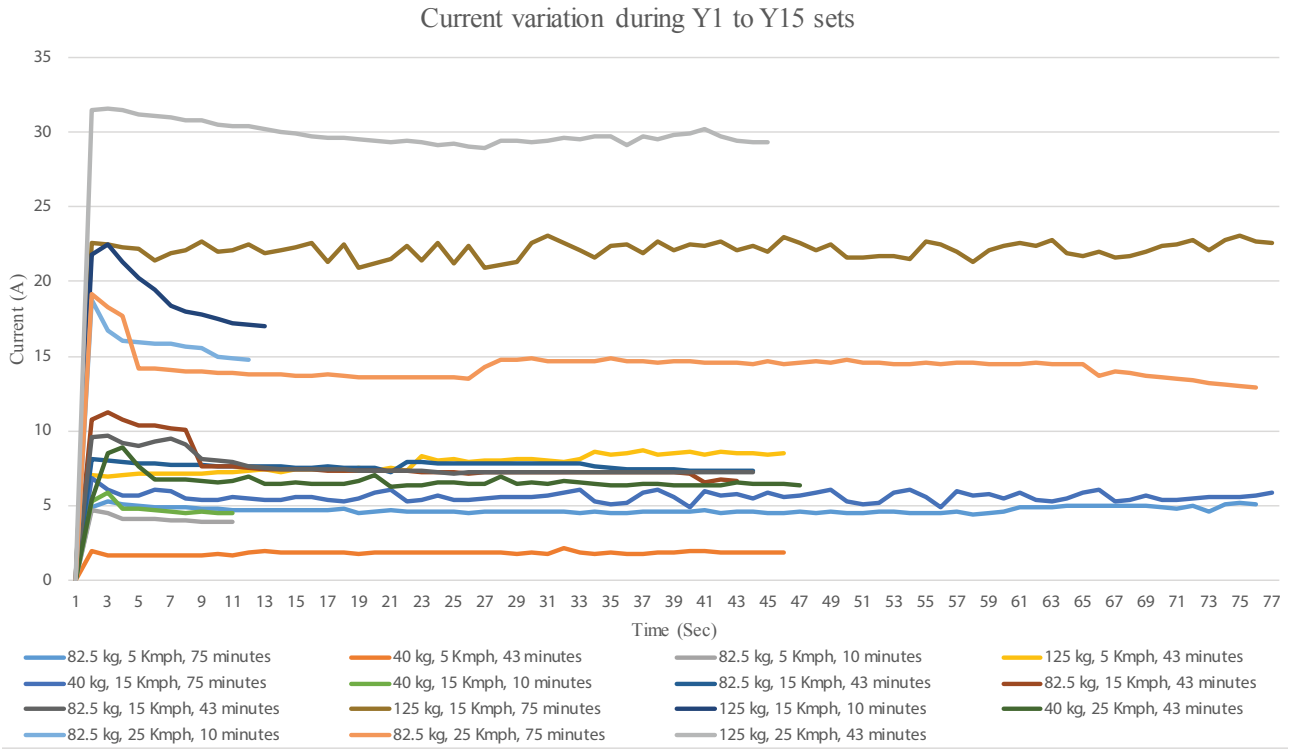
a) Voltage variation during E1 to E 15 sets.



b) Voltage variation during Y1 to Y 15 sets.



c) Current variation during E1 to E 15 sets.



d) Current variation during Y1 to Y 15 sets.

Figure 6. Effect on voltage and current at various load and speed

CONCLUSION

A single-wheel vehicle model was operated through a battery pack on a test dynamometer at varying rolling resistance, load, speed, and test duration conditions. The battery pack's voltage, current, and temperature were recorded during the test to investigate the temperature rise in the battery. It can be concluded that the temperature rise is within the permissible limit of the Lithium iron phosphate chemistry. So, natural heat dissipation from the cell's surface is sufficient to keep the cell in the working temperature range. The experiment study also discussed the relationship of the current withdrawn from the battery concerning the payload, rolling resistance, and speed of the vehicle. As the Joules heat, the major parameter to raise the temperature inside the battery solely depends on the withdrawn current. This study predicts the battery's current withdrawal and heat generated under different loading conditions. Depending on the battery's heat generated, the battery thermal management system's deployment can be easily selected. The following conclusions were drawn from the study.

- For rolling resistance of 0.01, for 125kg, 15 km/h & 75 min, the maximum absolute temperature recorded was 33.2°C with a temperature rise of 6.7°C in comparison to the ambient air at a temp 26.5°C. The maximum temperature of the battery pack is well below the safe operating temperature limits of the cell.
- For rolling resistance of 0.013, for 125kg, 15 km/h & duration of 75 min, the maximum absolute temperature recorded was 36.1°C with the temperature rise of 7.6°C in comparison to the ambient air at a temperature 28.5°C. The maximum temperature of the battery pack is well below the safe operating temperature limits of the cell.
- There is no need for a sophisticated active thermal management system to maintain the temperature of the battery pack.
- However, under extreme working conditions, if atmospheric temperature increased above 45°C, it would require a dedicated thermal management system.

AUTHORSHIP CONTRIBUTIONS

Authors equally contributed to this work.

DATA AVAILABILITY STATEMENT

The authors confirm that the data that supports the findings of this study are available within the article. Raw data that support the finding of this study are available from the corresponding author, upon reasonable request.

CONFLICT OF INTEREST

The author declared no potential conflicts of interest with respect to the research, authorship, and/or publication of this article.

ETHICS

There are no ethical issues with the publication of this manuscript.

STATEMENT ON THE USE OF ARTIFICIAL INTELLIGENCE

Artificial intelligence was not used in the preparation of the article.

REFERENCES

[1] Giammichele L, Colarossi D, D'Alessandro V, Falone M. Evaluation of the influence of lithium-ion battery composition on thermal power generation. Sustain Energy Fuels 2024;8:1566–1576. [CrossRef]

[2] Gümüşsu E, Ekici Ö, Köksal M. 3-D CFD modeling and experimental testing of thermal behavior of a Li-Ion battery. Appl Therm Eng 2017;120:484–495. [CrossRef]

[3] Feng X, Ouyang M, Liu X, Lu L, Xia Y, He X. Thermal runaway mechanism of lithium ion battery for electric vehicles: a review. Energy Storage Mater 2018;10:246–267. [CrossRef]

[4] Maurya M, Gawade S, Zope N. A study of different machine learning algorithms for state of charge estimation in lithium-ion battery pack. Energy Storage 2024;6:e658. [CrossRef]

[5] Keyser M, Kim GH, Neubauer J, Pesaran A, Santhanagopalan S, Smith K. Design and analysis of large lithium-ion battery systems. Artech; 2014.

[6] Huang Y, Mei P, Lu Y, Huang R, Yu X, Chena Z, et al. A novel approach for lithium-ion battery thermal management with streamline shape mini channel cooling plates. Appl Therm Eng 2019;157:113623. [CrossRef]

[7] Zhao Y, Zou B, Li C, Ding Y. Active cooling based battery thermal management using composite phase change materials. Energy Procedia 2019;158:4933–4940. [CrossRef]

[8] Jilte RD, Kumar R, Ahmadi MH, Chen L. Battery thermal management system employing phase change material with cell-to-cell air cooling. Appl Therm Eng 2019;161:114199. [CrossRef]

[9] Smith J, Singh R, Hinterberger M, Mochizuki M. Battery thermal management system for electric vehicle using heat pipes. Int J Therm Sci 2018;134:517–529. [CrossRef]

[10] Cao J, Ling Z, Fang X, Zhang Z. Delayed liquid cooling strategy with phase change material to achieve high temperature uniformity of Li-ion battery under high-rate discharge. J Power Sources 2020;450:227673. [CrossRef]

[11] Thorat P, Sanap S, Gawade S. A comparative study of thermo-physical properties of different nanofluids for effective heat transfer leading to Li-ion battery pack cooling. Energy Storage 2024;6:1–29. [CrossRef]

[12] Cracian A, Said U, Winardi S, Madhania S. The thermal characteristics of lithium-ferro-phosphate (LFP) battery pack. AIP Conf Proc 2024;020014. [CrossRef]

[13] Gonder J, Lustbader J, Pesaran A. Thermal management of batteries in advanced vehicles using PCM. Renew Energy 2008;2:134–147. [CrossRef]

[14] Saw LH, Ye Y, Yew MC, Chong WT, Yew MK, Ng TC. Computational fluid dynamics simulation on open cell aluminium foams for Li-ion battery cooling system. Appl Energy 2017;204:1489–1499. [CrossRef]

[15] Parsons KK, Mackin TJ. Design and simulation of passive thermal management system for lithium-ion battery packs on an unmanned ground vehicle. J Therm Sci Eng Appl 2017;9:1–9. [CrossRef]

[16] Qian X, Xuan D, Zhao X, Shi Z. Heat dissipation optimization of lithium-ion battery pack based on neural networks. Appl Therm Eng 2019;162:114289. [CrossRef]

[17] Fan R, Zhang C, Wang Y, Ji C, Meng Z, Xu L, et al. Numerical study on the effects of battery heating in cold climate. J Energy Storage 2019;26:100969. [CrossRef]

[18] Bai FF, Chen MB, Song WJ, Li Y, Feng ZP, Li Y. Thermal performance of pouch lithium-ion battery module cooled by phase change materials. Energy Proced 2019;158:3682–3689. [CrossRef]

[19] Jiang L, Zhou L, Li J, Zhang P, Zhou F, Liu Y. LFP battery pack combined heat dissipation strategy structural design. In: 7th Int Conf Energy Electr Power Eng (CEEPE); 2024. p. 1229–1233. [CrossRef]

[20] Kumar SK, Muniamuthu S, Mohan A, Amirthalingam P, Anbu Muthuraja M. Effect of charging and discharging process of PCM with paraffin and Al2O3 additive subjected to three point temperature locations. J Ecol Eng 2022;23:34–42. [CrossRef]

[21] Thorat P, Sanap S, Gawade S, Patil S. A simulation approach in analyzing performance of fly ash nanofluid for optimizing battery thermal management system used in EVs. Energy Storage 2024;6:e70005. [CrossRef]

[22] Zubairuddin M, Ravi Kumar R, Ali B. Thermomechanical analysis of laser welding of Grade 91 steel. Optik 2021;245:17510. [CrossRef]

[23] Pavan AR, Arivazhagan B, Zubairuddin M, Vasudevan M. Thermomechanical analysis of A-TIG and MP-TIG welding of 2.25Cr-1Mo steel considering phase transformation. J Mater Eng Perform 2019;28:4903–4917. [CrossRef]

[24] Zubairuddin M, Albert SK, Mahadevan S, Vasudevan M, Chaudhari V, Suri VK. Numerical simulation of multi-pass GTA welding of Grade 91 steel. J Manuf Process 2017;27:87–97. [CrossRef]

[25] Nazari A, Farhad S. Heat generation in lithium-ion batteries with different nominal capacities and chemistries. Appl Therm Eng 2017;125:1501–1517. [CrossRef]

[26] Shen W, Wang N, Zhang J, Wang F, Zhang G. Heat generation and degradation mechanism of lithium-ion batteries during high-temperature aging. ACS Omega 2022;7:44733–44742. [CrossRef]

[27] Allouhi A, Rehman S. Grid-connected hybrid renewable energy systems for supermarkets with electric vehicle charging platforms: optimization and sensitivity analyses. Energy Rep 2023;9:3305–3318. [CrossRef]

[28] Zayed ME, Kabeel AE, Shboul B, Ashraf WM, Ghazy M, Irshad K, et al. Performance augmentation and machine learning-based modeling of wavy corrugated solar air collector embedded with thermal energy storage. J Energy Storage 2023;74:109533. [CrossRef]

[29] Ismail NHF, Toha SF, Azubir NAM, Ishak NH, Hassan MK, Ibrahim BSK. Simplified heat generation model for lithium ion battery used in electric vehicle. IOP Conf Ser Mater Sci Eng 2013;53:1–6. [CrossRef]

[30] Kantharaj R, Marconnet AM. Heat generation thermal transport in lithium-ion batteries: a scale-bridging perspective. Nanoscale Microscale Thermophys Eng 2019;23:128–156. [CrossRef]

[31] Zhu S, Han J, Wang YN, Pn TS, Wei YM, Song WL, et al. In-situ heat generation measurement of the anode and cathode in a single-layer lithium ion battery cell. Int J Energy Res 2020;44:9141–9148. [CrossRef]

[32] Chen F, Yu X, Lacarrière B, Le Corre O. Cylindrical lithium-ion battery cells forecast. Energy Procedia 2017;142:4029–4036. [CrossRef]

[33] Lin C, Ren S. Comparative study on the heat generation behavior of lithium-ion batteries with different cathode materials using accelerating rate calorimetry. Energy Procedia 2017;142:3369–3374. [CrossRef]

[34] Chauhan VK, Bhattacharya J. Error estimation of Bernardi heat evaluation of Li-ion cells under drive cycle operation. Appl Therm Eng 2024;254:123870. [CrossRef]

[35] Neupane S, Alipanah M, Barnes D, Li X. Heat generation characteristics of LiFePO4 pouch cells with passive thermal management. Energies 2018;11:1243. [CrossRef]

Sigma Journal of Engineering and Natural Sciences
Web page info: https://sigma.yildiz.edu.tr
DOI: 10.14744/sigma.2024.00132

Research Article

Strategic load scheduling in smart home: Leveraging IOT and optimization algorithms for energy cost reduction

Ganesh SHIRSAT[1,*], Aniruddha MUKHERJEE[1], Ankit Kumar SHARMA[1]

[1]*University of Engineering & Management, Jaipur, Rajasthan, 303807, India*

ARTICLE INFO

Article history
Received: 24 July 2024
Revised: 11 September 2024
Accepted: 25 October 2024

Keywords:
Demand Response Programs; Energy Management; Internet-Of-Things; Peak to Average Ratio; Smart Devices; Smart Homes; Time Of Day (ToD) Tariff

ABSTRACT

The exponential growth of electrical energy demand can be attributed to the increase in population and urbanization. A strategic approach required to tackle this pressing issue involves the integration of Internet of Things (IoT) technologies and intelligent devices within households, a key initiative being undertaken by smart cities. India has implemented Time of Day (ToD) tariffs for electricity consumption, particularly targeting industrial sectors. Nevertheless, a notable observation is the limited utilization of Time of Day (ToD) tariffs within the residential electricity sector, signaling an area with potential for improvement. To enhance the efficiency of the electricity market through responsive measures, it is crucial to expand the implementation of Time of Day (ToD) tariffs to include the residential sector as well, thereby promoting a more effective and equitable system. The core focus of the research paper centers on the optimization of load scheduling in intelligent residences, with the objective of mitigating energy expenses and diminishing peak power demand, while upholding user comfort and operational efficiency at uncompromised levels. The research investigates the comparison of various algorithms like Ant Colony Optimization Algorithm (ACO), Whale Optimization Algorithm (WOA), Particle Swarm Optimization Algorithm (PSO), and Genetic Algorithm (GA) within the framework of cost reduction using ToD tariffs, with GA emerging as the most effective in achieving savings and decreasing peak-to-average ratio (PAR). This strategic approach not only benefits residential consumers in terms of cost savings but also proves advantageous for utility providers in managing resources effectively.

Cite this article as: Shirsat G, Mukherjee A, Sharma AK. Strategic load scheduling in smart home: Leveraging IOT and optimization algorithms for energy cost reduction. Sigma J Eng Nat Sci 2025;43(6):2140–2151.

INTRODUCTION

Smart homes and IoT-enabled appliances are gaining immense importance due to their ability to revolutionize daily living and energy efficiency. With the IoT within smart homes, it is possible to design smart home systems with advanced features for appliances control remotely [1]. Moreover, the smart homes are resulting with evolution of wearables and ambient devices for motion as well as health sensing and security, to build sustainable and

***Corresponding author.**
*E-mail address: ganeshshirsat1234@gamail.com

This paper was recommended for publication in revised form by Editor-in-Chief Ahmet Selim Dalkilic

Published by Yıldız Technical University Press, İstanbul, Turkey
© Author. This is an open access article under the CC BY-NC license (http://creativecommons.org/licenses/by-nc/4.0/).

smart living environment [2]. Appliance load monitoring in smart homes is also an important factor for attaining energy efficiency, and methods such as intrusive load monitoring (ILM) and non-intrusive load monitoring (NILM) have very good impact in controlling its power consumption [3]. Integrating IoT functionalities into Home Energy Management Systems (HEMS) can also increase energy savings in that it can supply customers with feedback information and support control over on of the main energy consumers like white goods in a home, showing also the growing relevance of smart home and IoT appliances in contemporary residential environments [4].

Energy management is confronted with significant challenges arising from the uncertainties associated with load consumption patterns and the sporadic nature of renewable energy generation, which adversely affects the management of active resources [5]. In order to mitigate these challenges, the implementation of efficient load scheduling is imperative, as it optimizes the utilization of renewable resources such as solar energy and energy storage systems, all while striving to minimize both costs and carbon emissions [6], [7]. Moreover, load scheduling plays an essential role within demand response initiatives, in which the deliberate redistribution of loads during intervals of diminished pricing can result in cost reductions for end-users, although it may also lead to rebound peaks and user discontent [7]. The application of sophisticated algorithms such as Enhanced Differential Evolution (EDE) and Genetic Algorithm (GA) facilitates the automation of responses to demand signals, thereby optimizing load schedules to achieve reductions in energy expenditures, carbon emissions, and peak-to-average ratios, whilst simultaneously enhancing user comfort [7]. Consequently, the efficacy of load scheduling is paramount for achieving an equilibrium between supply and demand, curtailing costs, and promoting sustainability within energy management frameworks.

The phenomenon of elevated energy expenditures and suboptimal energy utilization within smart homes is attributed to the escalating energy requirements and the deficiency of efficacious strategies for managing energy consumption during peak hours. Urban environments characterized as smart cities are profoundly dependent on the provision of efficient energy services, with Time-of-Use pricing emerging as an effective policy mechanism for reconciling electricity consumption patterns and alleviating strain on the electrical grid [8]. Scholars underscore the significance of scheduling energy usage during off-peak periods as a means to diminish energy costs, which necessitates meticulous profiling of appliances and the implementation of real-time monitoring systems for effective peak load management [9]. The proliferation of Internet of Things (IoT)-enabled smart homes is associated with an increase in energy consumption, thereby necessitating the development of optimization strategies aimed at enhancing both energy efficiency and user comfort [10] . Additionally, the convergence of Artificial Intelligence (AI) with IoT technologies promotes energy-efficient communication within smart homes, with novel algorithms and frameworks being devised to optimize Quality-of-Service during video streaming, consequently decreasing energy usage and enhancing performance metrics [11]. It is imperative to address these complexities through the deployment of cutting-edge technologies and optimization methodologies to mitigate the effects of rising energy costs and to enhance energy efficiency in smart residences.

The implementation of Time-of-Day (ToD) tariffs for the purpose of energy conservation presents numerous advantages, as substantiated by a variety of empirical research studies. ToD tariffs serve to incentivize consumers to realign their electricity consumption from peak demand periods to off-peak intervals, thereby mitigating peak load and fostering a more efficient utilization of energy resources. This behavioral modification not only contributes to energy conservation but also facilitates peak load shaving, which is essential for the preservation of grid stability and the diminishment of the necessity for costly grid expansions [12]. Moreover, the utilization of ToD tariffs has been empirically demonstrated to significantly lower power consumption while concurrently preserving benefits for both consumers and electricity providers, as evidenced by the application of genetic algorithms in the optimization of stepwise power tariffs [13]. In summary, the utilization of Time-of-Day (ToD) tariffs signifies a holistic approach designed to advance energy conservation, uphold grid reliability, and enhance economic efficiency, thereby rendering it as an exceptionally favorable framework for modern energy systems.

LITERATURE REVIEW

The practice of strategic load scheduling in smart homes equipped with IoT technology is imperative for curtailing energy costs and advancing energy management strategies. Several algorithms, notably the Whale Optimization Algorithm (WOA), Ant Colony Optimization Algorithm (ACO), Particle Swarm Optimization Algorithm (PSO), and Genetic Algorithm (GA), have been examined extensively for this purpose. Ant Colony Optimization (ACO) has been acknowledged as a proficient approach for enhancing energy management in smart residential contexts. By emulating the foraging behavior exhibited by ants, ACO algorithms are capable of efficiently scheduling domestic appliances to reduce energy expenses and peak demand [14]. ACO not only prioritizes cost reduction but also improves user comfort by ensuring that the scheduling of appliances is congruent with consumer requirements, thereby enhancing overall satisfaction [15]. ACO, renowned for its effectiveness in resolving combinatorial problems, has been adeptly employed in home energy management systems (HEMS) to enhance appliance scheduling while considering fluctuating pricing models and user comfort [16].

WOA, inspired by the social dynamics observed in cetacean populations, has demonstrated significant effectiveness in reducing energy expenditures and enhancing the peak-to-average ratio (PAR) through the optimal scheduling of domestic devices within sophisticated grid systems. PSO, recognized as a widely utilized heuristic optimization methodology, has found extensive application within home energy management systems (HEMS) to harmonize energy consumption and associated costs, capitalizing on its rapid convergence towards optimal solutions. Genetic Algorithms (GA), a prominent optimization methodology, has been rigorously applied in numerous research endeavors aimed at the creation of efficient Home Energy Management Systems (HEMS), specifically focusing on curtailing electricity expenditures and easing peak demand via the judicious scheduling of household devices [17]. These algorithms are customarily associated with advanced Internet of Things (IoT) technologies and real-time data analytics to bolster their operational efficacy. The fusion of GA with IoT-oriented controllers has revealed significant economic advantages and enhanced user gratification through the effective real-time optimization of load profiles [18].

In a similar vein, Particle Swarm Optimization (PSO) and Whale Optimization Algorithm (WOA) have been employed in tandem with predictive modeling to anticipate energy consumption patterns and enhance scheduling in accordance with user preferences and environmental variables [19]. The efficacy of these algorithms is corroborated through both simulations and empirical data, thereby demonstrating their capacity to facilitate significant reductions in energy costs while simultaneously ensuring user satisfaction [20, 21]. In summary, the predominant corpus of literature underscores the vital importance of these optimization methodologies in the evolution of smart home energy management, thus delineating the need for sustained research and development to proficiently tackle future challenges and uncertainties [22].

Problem Formulation

The regulation of energy within intelligent residential settings has achieved increased prominence due to rising energy costs and the necessity for sustainable approaches. This study is focused on two primary objectives: the reduction of costs and the improvement of efficiency in energy management. Through the utilization of time-of-day pricing structures and diverse optimization algorithms, this research endeavors to formulate strategies that mitigate energy expenses and optimize efficiency, all while maintaining the comfort of the inhabitants.

The primary objectives of this research are:

- To establish strategies centered on cutting energy expenditure in intelligent home systems.
- To analyze the use of time-of-day tariffs to boost energy efficiency in non-peak periods ultimately lowering electricity expenses.
- To evaluate the efficacy of various optimization algorithms specifically ACO, WOA, PSO, and GA in achieving these objectives.

This research assesses the application of diverse optimization algorithms for effective load scheduling, crucial for cost minimization and efficiency enhancement in smart homes while developing viable load scheduling methodologies.

SYSTEM MODEL

The utilization of metaheuristic algorithms within the Smart Home Energy Control (SHEC) system optimizes power consumption in smart devices by establishing efficient usage schedules. This integration aims to achieve cost reduction, decrease the Peak Average Ratio (PAR), and enhance user comfort (UC) through effective energy resource management. Through the proactive participation in demand response initiatives and the adjustment to fluctuating energy prices, the Smart Home Energy Controller (SHEC) system not only mitigates consumer energy

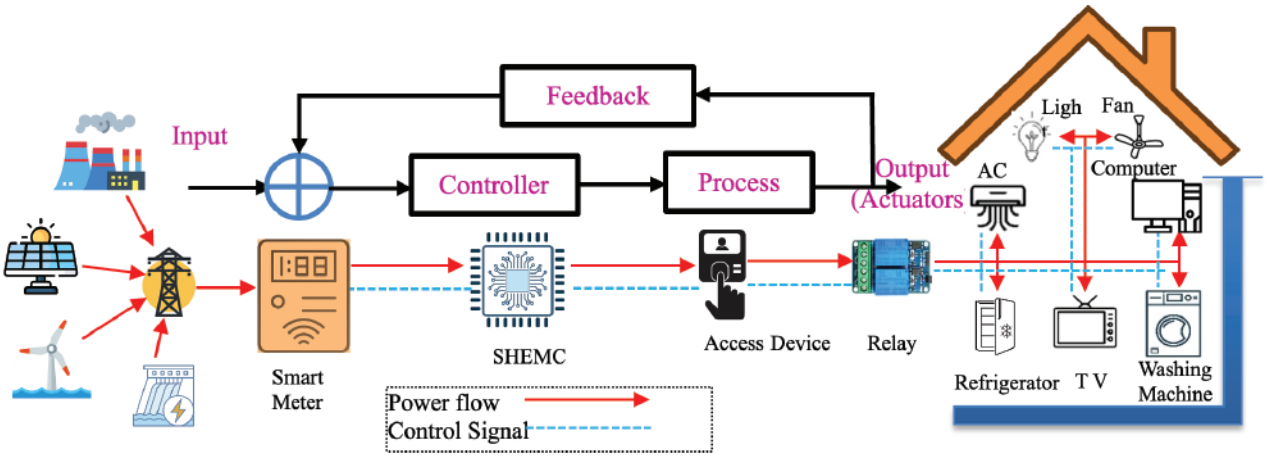


Figure 1. Workflow of Smart home energy management system.

expenditures but also enhances the overall efficiency and sustainability of Internet of Things (IoT)-integrated smart residences. Figure 1 delineates the proposed sequential workflow of the system, highlighting the procedural phases involved in the optimization of energy management.

Study Focus and Objectives

This study concentrates on optimizing energy management in a smart home environment using a set of ten commonly used appliances which are given in table 1. Each appliance is denoted by

n ϵ N = {1,2,3……10)

with energy management decisions made hourly across 24 time slots

s ϵ S = {0,1,2,3……23)

Energy Consumption and Cost Formulation

The total energy consumption of appliances within each time slot is calculated as:

$$AEC^S = \sum_{n=1}^{10} AEC_n \quad (1)$$

where AECn represents the energy consumption of appliance n.

The total energy consumption over 24 hours (AECT) is:

$$AEC_T = \sum_{n=1}^{24} AEC^S \quad (2)$$

Energy cost is determined by:

$$C = \sum_{s=1}^{24} (E_{rate} \times P_{rate}) \quad (3)$$

where E rate is the energy cost per hour and Prate is the power rating of connected appliances.

Optimization Objective

The objective function aims to minimize the total cost and reduce user discomfort due to waiting times $\omega_T = b - a$ before appliance operation.

It is formulated as:

$$min\Big(\sum_{s=1}^{24} [\, \omega_1 \times \sum_{n=1}^{10} (AEC_T \times E_{rate}) + (\omega_2 \times \omega_T) \,] \Big) \quad (4)$$

Here, ω1 and ω2 are weighting are weighting factors (either 0 or 1) balancing cost reduction and user comfort, with ω1+ω2=1.

Role of Smart Home Energy Controller (SHEC)

In residential environments integrated with the Internet of Things (IoT), the Smart Home Energy Controller (SHEC) plays a crucial role by responding to real-time demand signals and optimizing energy consumption with remarkable efficacy. It considers a multitude of factors, including price-driven demand response strategies, characteristics of appliances, operational timeframes, Time-of-Day (TOD) pricing structures, and the energy resources available from the grid to formulate optimal energy consumption schedules.

Pricing schemes

Many countries have implemented Time of Day (ToD) tariffs for electricity consumption, particularly targeting commercial and industrial sectors. In proposed ToD tariff three zone are considered based on load curve plotted by taking actual use of appliances from household consumer. These are Peak (6 to10 hrs. &18 to 22 hrs.), Valley (4 to 6 hrs.,10 to 12 hrs. & 16 to 18 hrs.) & Flat Zone (0 to 4 hrs., 12 to 16 hrs. & 22 to 23 hrs.). The primary goal of these tariffs is to encourage consumers to adjust their electricity usage to times of lower demand on the grid, ultimately aiding in load balancing. The increase in demand for electrical energy has grown significantly because of population growth and urban development. To address this issue, smart cities are utilizing Internet of Things (IoT) technology and smart devices within households.

In India, Maharashtra MSEDCL applies energy rates for consumer based on power consumption. The different energy rates are applied for different consumers based on Total energy Consumption (0-100,100-300,300-500,500

Table 1. Smart home Appliances and its rating

Sr. No	Appliances	Power Rating [Prate] (Watts)	Total Usage hrs. [Li]	Time Slots
1	Air Conditioner	1500	6	10–21
2	Computer	250	8	9–23
3	Electric kettle	1000	1	4–20
4	Coffee maker	1000	1	5–21
5	Water Dispenser	300	9	0-23
6	Oven	1000	2	4–21
7	Fan	500	5	0–23
8	Light	150	7	0–23
9	Washing Machine	1000	2	5-21
10	TV	100	6	0-23

onwards). Proposed ToD Method in which Energy rates are applied based on peak, Valley & flat zones of load curve.

In this study for Cost minimization of Smart Homes Two Methods were adopted

Case I: Cost minimization by saving the KW power consumption & using ToD tariff for power consumption

Case II: Cost minimization by only adopting ToD tariff for power consumption.

METHODOLOGY

In this study, we use two main approaches to optimize energy usage in smart homes: Single Interval Programming (SIP) and Multi-Interval Programming (MIP).These strategies are designated according to two distinct temporal phases in dispatch planning and pricing, referred to as predispatch and real-time [23]. SIP comes into play when we have set electricity prices ready to go for the whole day! The single interval program runs once each day to figure out the best schedule that fits user's preferences. Multi interval programming (MIP) works throughout each interval to find the ideal scheduling based on hourly real-time pricing conditions.

In particular circumstances, Single Interval Programming (SIP) is frequently preferred over Multi-Interval Programming (MIP) due to its various notable advantages. To begin with, SIP showcases computational clarity and heightened efficiency, targeting the optimization of energy usage during specific time intervals, which enables rapid calculations and on-the-fly adaptability. This characteristic renders SIP particularly suitable for prompt energy management decisions and scenarios necessitating swift modifications. Secondly, SIP necessitates a reduced volume of data in comparison to MIP, thereby rendering it advantageous in situations where extensive data across multiple intervals is either inaccessible or prohibitively expensive to obtain.

Numerous scholarly investigations have examined the challenge of optimal scheduling of domestic appliances via the utilization of diverse algorithms, including Genetic Algorithms (GA), Particle Swarm Optimization (PSO), Harmony Search Algorithm (HSA), Water Distribution Optimization (WDO), and Hybrid Genetic Harmony Search Algorithm (GHSA), among others [24-26].

In this paper a comparative performance of ACO, WOA, PSO and GA is given.

Ant Colony Optimization (ACO)

This research introduces an Ant Colony Optimization (ACO) strategy aimed at refining energy consumption schedules for residences within the framework of Time-of-Day (TOD) pricing. The Ant Colony Optimization (ACO) algorithm initiates its process with a collection of artificial ants, each of which constructs a potential energy consumption timetable by incrementally selecting hours for each appliance, informed by pheromone trails and heuristic information. The pheromone matrix experiences real-time updates based on the efficacy of the solutions generated, thus reflecting the attractiveness of each hour for the activation of appliances. This approach achieves a harmonious equilibrium between exploration (via stochastic selections influenced by pheromone concentration) and exploitation (by focusing on advantageous solutions identified throughout the algorithm's execution).

The technique incorporates various constraints within the optimization framework. These constraints include maintaining appliances within designated time frames and adhering to maximum usage limits. Furthermore, the objective function incorporates variable electricity pricing across different temporal intervals (peak, off-peak, and flat rates), aiming to discern schedules that minimize total expenditures while possibly considering idle periods for appliance usage. The optimization process is executed through numerous generations of ant solutions, employing mechanisms for pheromone evaporation and updates that promote convergence toward an optimal or near-optimal solution throughout successive iterations.

Whale Optimization Algorithm (WOA)

The Whale Optimization Algorithm (WOA) constitutes an advanced metaheuristic optimization approach that is predicated upon the social behaviors demonstrated by humpback whales, particularly highlighting their bubble-net feeding strategy. This algorithm is characterized by its proficiency in global search capabilities and its necessity for a limited quantity of control parameters, thus making it efficacious across a diverse array of optimization problems [27]. This investigation describes an optimization approach directed at the scheduling of electrical loads within a domestic setting, leveraging the WOA as a core methodology. The algorithm systematically improves the schedules via iterative processes, adeptly harmonizing the dual aims of exploration and exploitation to identify the optimal solution. Throughout this process, constraints are rigorously applied to guarantee that the schedules maintain their feasibility. The findings presented in this study provide robust support for the effectiveness and practicality of the aforementioned approach, particularly in relation to its capacity to facilitate substantial reductions in operational costs while simultaneously improving overall energy efficiency metrics, thereby further solidifying and amplifying the primary aim of demand-side management strategies as they pertain to the optimization of intelligent residential systems designed to enhance user experience and sustainability.

Particle Swarm Optimization (PSO)

The PSO algorithm is a technique for stochastic optimization based on population dynamics, draws inspiration from the collective behaviors observed in bird flocking and fish schooling [28]. PSO consists of particles representing potential solutions distributed randomly. Each particle's position and velocity are updated based on personal best and global best. The algorithm starts with initializing particles'

positions and velocities, followed by evaluating fitness function [29]. Particles adjust velocities and positions using a rule incorporating personal best and global best [30].

The proposed PSO framework initializes a swarm of particles, each representing a potential schedule. The evaluation of each particle's fitness is conducted according to the objective function, which takes into account the TOD rates and load constraints. The particles systematically revise their positional coordinates through a process informed by their individual prior experiences alongside the globally optimal solution identified by the swarm, influenced by cognitive and social factors. In order to ensure feasibility, additional constraints such as peak power limits and specified operational timeframes are enforced upon the scheduling framework of each particle. The algorithm efficiently converges towards an optimal or nearly optimal solution, thereby showcasing its proficiency in balancing cost minimization with adherence to constraints.

Genetic Algorithm (GA)

The Genetic Algorithm (GA) functions as an optimization methodology grounded in principles of natural selection and genetic theory, wherein essential elements facilitate the evolution of solutions to intricate challenges [31]. Entities within a population are representative potential solutions that are encoded in the form of chromosomes [32]. Parental entities are selected according to fitness levels and undergo crossover to generate novel offspring. The mutation mechanism enhances genetic diversity and expands the search parameter space, thereby reducing the likelihood of convergence to local optima. This repetitive sequence of selection, crossover, and mutation defines a singular generation, with the objective of advancing the quality of solutions through subsequent generations [31,33].

To enhance the effectiveness of optimizing residential electrical consumption while factoring in peak load management and time-of-use pricing, we have devised an innovative genetic algorithm (GA). Our methodology tackles the challenge by adaptively scheduling household appliances in alignment with variable electricity tariffs and temporal constraints. The algorithm is initialized utilizing pre-established appliance schedules and imposes limitations such as operational hours and maximum load thresholds. The objective function is designed to balance the reduction of electricity expenses with the comfort of consumers, wherein weighting coefficients are finely tuned to correspond to either overall consumption metrics or time-variable pricing rates. Implementing iterative processes of selection, crossover, and mutation, the genetic algorithm steadily optimizes schedules, consequently ensuring alignment with

Table 2. Comparison of Algorithms based on strength and weakness

Algorithm	Strength	Weakness
ACO	-Exhibits effectiveness in addressing combinatorial optimization challenges. -Demonstrates expertise in traversing extensive search landscapes. -Displays an aptitude for modification within shifting contextual paradigms.	-The incidence of premature convergence might ensue when pheromone trails reveal excessive potency. -The convergence speed is regularly recognized to be diminished when engaging with elaborate problems. -The process of parameter optimization can introduce considerable intricacies.
WOA	-Encourages rapid convergence without compromising the critical exploratory facets. -Mimics authentic behavioral patterns evident in the foraging methodologies of humpback whales.	- There exists a relative scarcity of research and a lack of established methodologies in comparison to alternative approaches. - The performance outcomes may fluctuate contingent upon the specific parameter configurations employed. - There may be difficulties encountered in highly multimodal landscapes.
PSO	-Rapid convergence, particularly in the context of unimodal optimization challenges - Straightforward execution and comprehensible interpretation - Effective in addressing dynamic optimization scenarios	-Challenges may arise when endeavoring to perform global exploration within complex landscapes. - The methodology is significantly sensitive to the configuration of parameters, which may profoundly influence performance indicators. - A proclivity for premature convergence may become apparent in certain circumstances.
GA	- Maintains diversity through genetic operations - Robust to different types of problems	- Convergence may be comparatively slower than that observed in Particle Swarm Optimization (PSO). - It necessitates meticulous calibration of population size, mutation rates, and crossover rates. -The degree of complexity related to implementation can vary greatly based on the specific genetic representation chosen.

peak power regulations and boosting overall efficiency in energy consumption. The empirical observations affirm the success of our methodology in diminishing electricity costs and enhancing consumption dynamics across a range of household environments.

A comparative examination of Ant Colony Optimization (ACO), Whale Optimization Algorithm (WOA), Particle Swarm Optimization (PSO), and Genetic Algorithm (GA) delineating their respective advantages and limitations is presented in Table 2 within the framework of optimization challenges. By comprehensively understanding their distinct attributes, one can more effectively evaluate their appropriateness for particular applications, especially in contexts where efficient energy management and load scheduling are of paramount importance.

Genetic Algorithms (GA) excel in intricate optimization tasks, especially with multimodal functions featuring several optimal solutions. Their maintenance of genetic diversity via crossover and mutation mitigates premature convergence, facilitating exploration of varied solution regions. Furthermore, GAs exhibit high adaptability, rendering them suitable for problems characterized by evolving environments or dynamic constraints, including scheduling and resource allocation.

RESULTS AND ANALYSIS

The focus of this study is the reduction of electricity expenses for residential consumers while ensuring user comfort. Simultaneously, the aim is to decrease the PAR ratio. In this study comparative results are obtained for both cases fixed charges as per current scenario & after applying the TOD tariff in Table 3 and Table 4. In this case, we have two cost rates first Based on MSEDCL power consumption (KW) slabs (i.e KW Slab) and second ToD tariff rates (i.e ToD rates). The initial energy consumption & Energy cost curve for a day is shown in Fig. 2.

In Proposed ToD Method in Energy rates are applied based on peak, Valley & flat zones of load curve. Initial Power consumption without appliances scheduling for KW

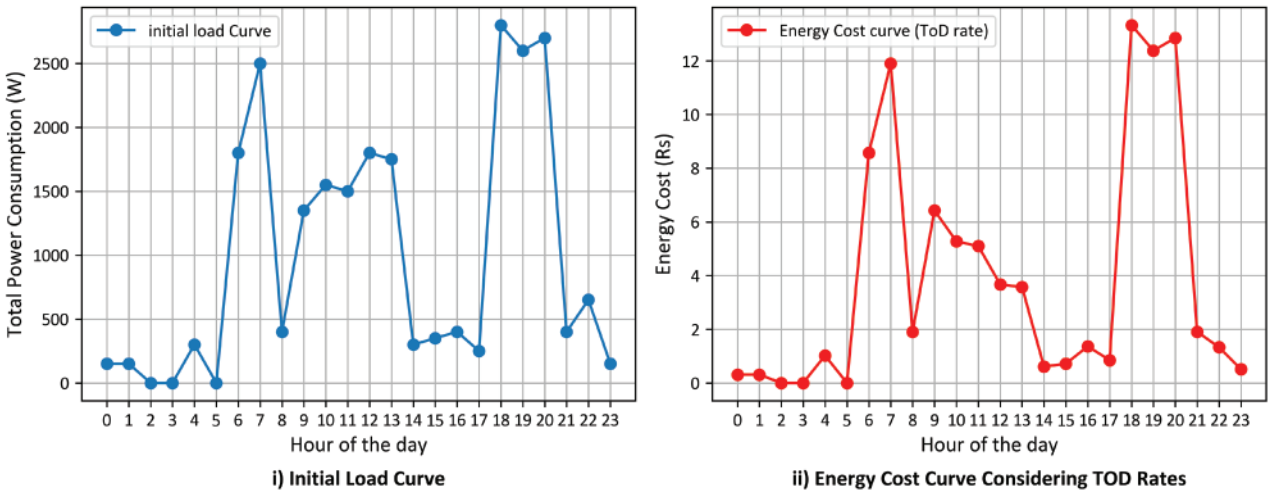


Figure 2. Energy Consumption and Cost Curve of smart home.

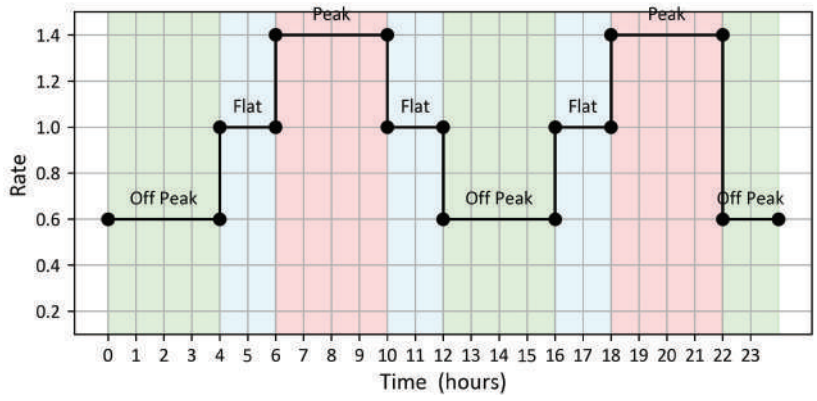


Figure 3. Consumer ToD tariff rates with respect to Slab rate.

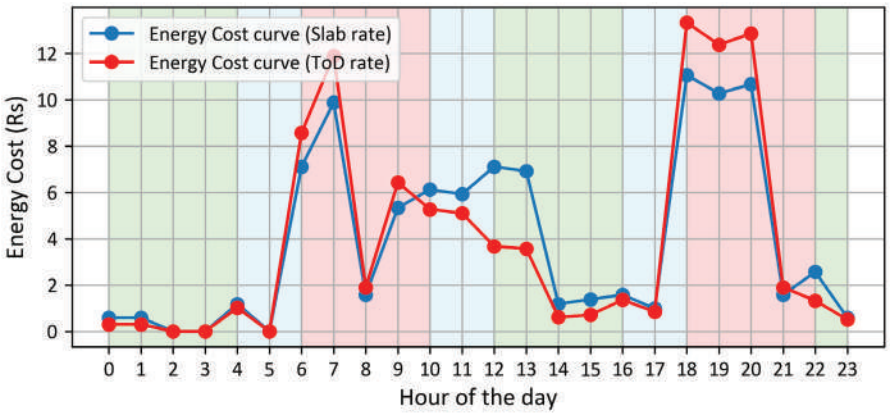


Figure 4. Comparison of Energy cost by Slab rate & ToD tariff.

Table 3. Comparative results for cost minimization by kw saving & ToD tariff saving

Algorithm	Pricing		Result	KW saving	Cost Saving	% KW saving	% Cost Saving	PAR Redu.	% PAR Redu.
ACO	KW Slab	Scheduled KW	20.72	3.13		13.12		0.19	6.73
		Scheduled Cost	193.76		35.24		15.39		
	ToD	Scheduled KW	20.78	3.07		12.87		0.17	6.02
		Scheduled Cost	183.97		40.1		17.9		
	Total Saving			3.07	45.03	12.87	19.66	0.17	6.02
WOA	KW Slab	Scheduled KW	12.99	10.86		45.53		-1.6	-57.8
		Scheduled Cost	106.84		122.2		53.34		
	ToD	Scheduled KW	13.22	10.63		44.57		-1.6	-54.96
		Scheduled Cost	108.9		115.2		51.4		
	Total Saving			10.63	120.1	44.57	52.45	-1.6	-54.96
PSO	KW Slab	Scheduled KW	15.07	8.78		36.81		-0.6	-19.5
		Scheduled Cost	130.22		98.78		43.14		
	ToD	Scheduled KW	14.91	8.94		37.48		-0.5	-18.09
		Scheduled Cost	121.32		102.8		45.86		
	Total Saving			8.94	107.7	37.48	47.02	-0.5	-18.09
GA	KW Slab	Scheduled KW	21.25	2.6		10.9		0.28	9.92
		Scheduled Cost	199.8		29.2		12.75		
	ToD	Scheduled KW	21.36	2.49		10.44		0.28	9.92
		Scheduled Cost	156.54		68.27		30.37		
	Total Saving			2.49	72.46	10.44	31.64	0.28	9.92

slab rate is 23.85 Kw (Unscheduled KW) and cost is 229 Rs (Unscheduled cost). Initial Power consumption without appliances scheduling for ToD rate is 23.85 Kw (Unscheduled KW) and cost is 224.07 Rs (Unscheduled cost). So cost saving by ToD tariff is 05 Rs (2%) which is also observed in Fig. 3. Initial PAR without scheduling is 2.82.

Computational Results for Case-I

The outcomes for case-I, where a flat rate tariff and Time of Day (ToD) tariff pricing are implemented are shown in Table 3. The table provides a comparative analysis of the electricity cost associated with the efficient scheduling of household appliances. This examination is conducted through SIP techniques employing in ACO, WOA, PSO, and GA algorithms. The load curve of Smart home before & after scheduling the appliances for each algorithm in case I is shown in Fig. 5, Fig. 6, Fig. 7 & Fig. 8. It is observed that some loads are not active for same day therefore there is saving in cost but due to this consumer comfort is disturbed because of unviability of specific load at important

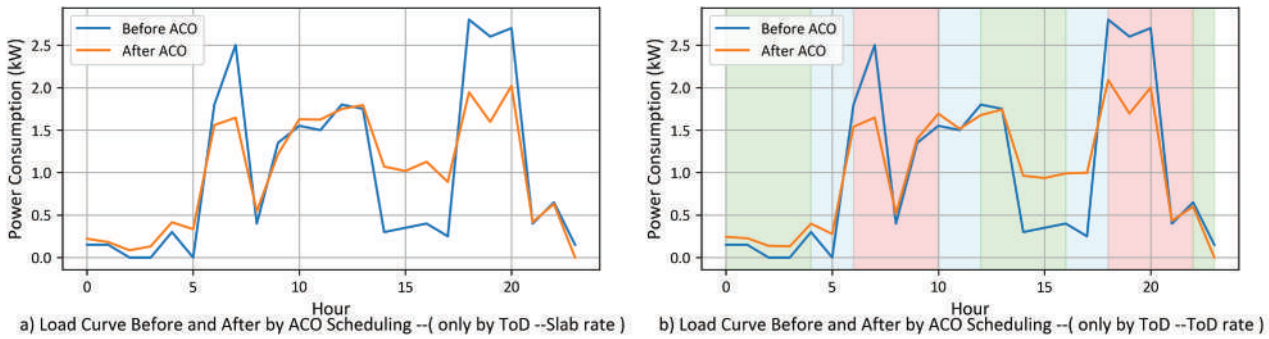


Figure 5. Load curve Before and After Scheduling load by ACO a) Slab rate b) ToD rate.

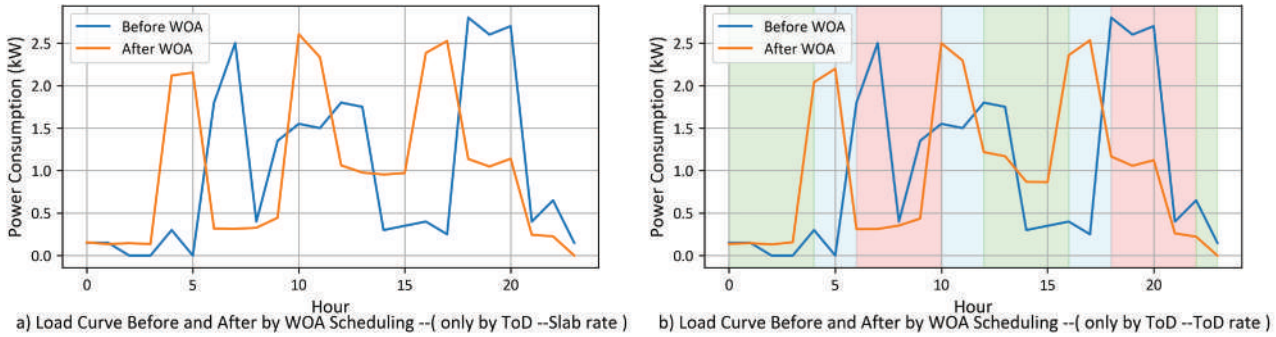


Figure 6. Load curve Before and After Scheduling load by WOA a) Slab rate b) ToD rate.

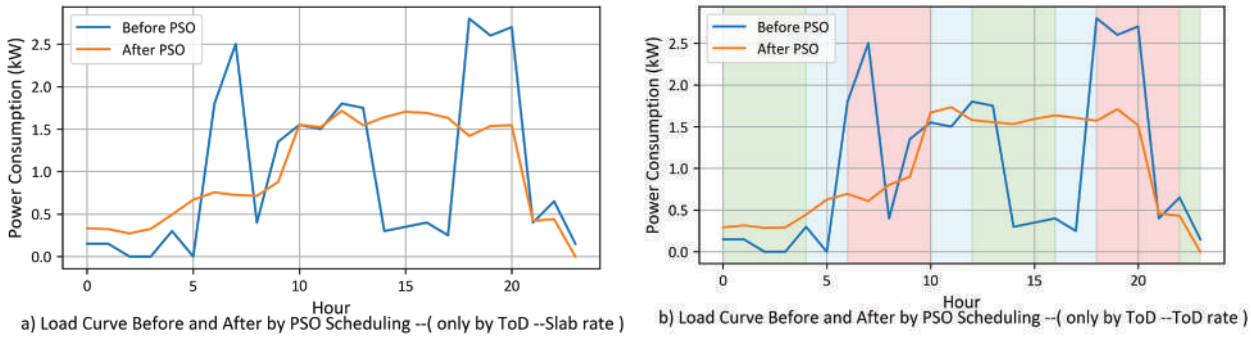


Figure 7. Load curve Before and After Scheduling load by PSO a) Slab rate b) ToD rate.

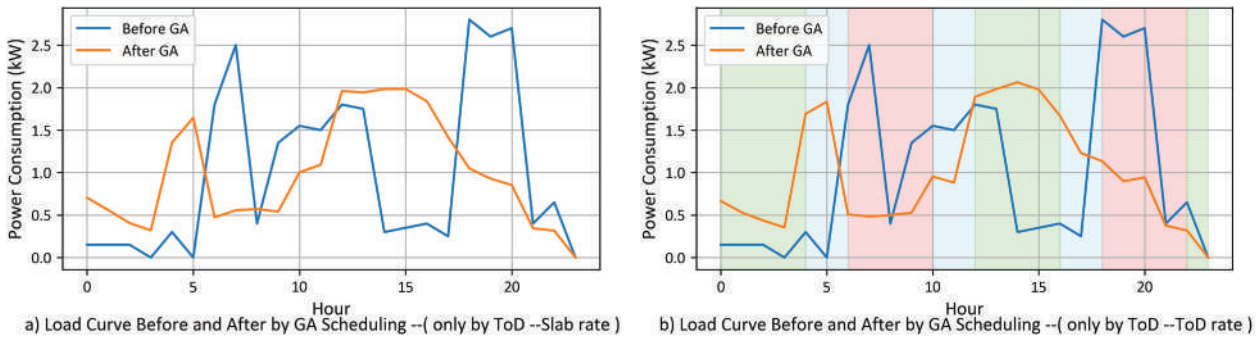


Figure 8. Load curve Before and After Scheduling load by GA a) Slab rate b) ToD rate.

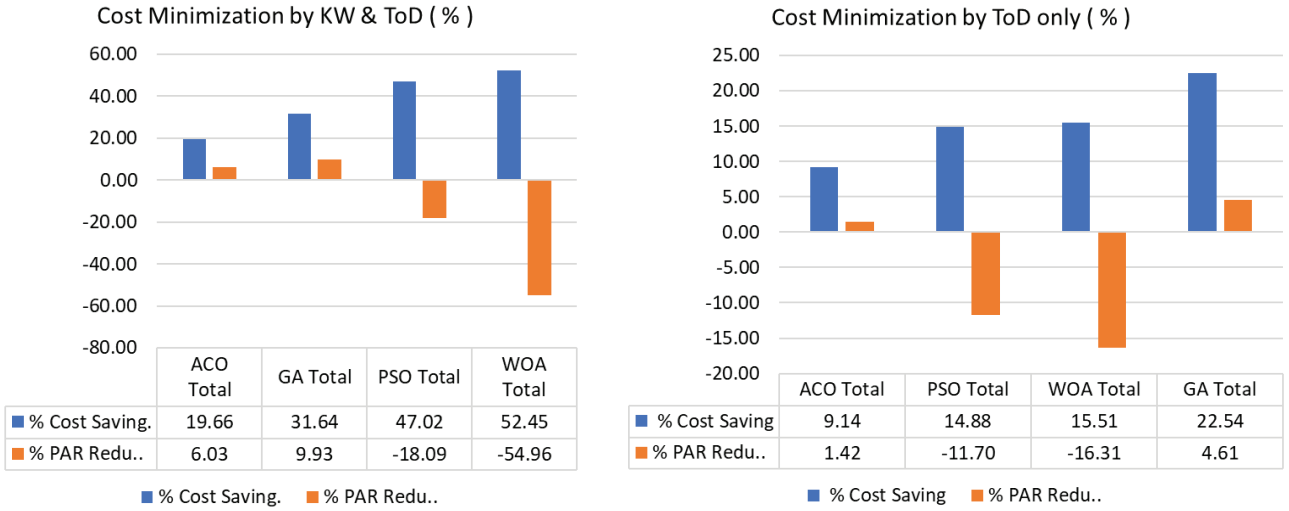
Table 4. Comparative results for cost minimization only by ToD tariff saving

Algorithm	Pricing		Result	KW saving	Cost Saving	% KW saving	% Cost Saving	PAR Redu	% PAR Redu.
ACO	KW Slab	Scheduled KW	23.85	0		0		0.05	1.77
		Scheduled Cost	229		0		0.00		
	ToD	Scheduled KW	23.85	0		0		0.04	1.42
		Scheduled Cost	208.06		16.01		7.15		
		Total Saving		0	20.94	0	9.14	0.04	1.42
WOA	KW Slab	Scheduled KW	23.85	0		0		-0.39	-13.83
		Scheduled Cost	229		0		0.00		
	ToD	Scheduled KW	23.85	0		0		-0.46	-16.31
		Scheduled Cost	193.48		30.59		13.65		
		Total Saving		0	35.52	0	15.51	-0.46	-16.31
PSO	KW Slab	Scheduled KW	23.85	0		0		-0.36	-12.77
		Scheduled Cost	229		0		0.00		
	ToD	Scheduled KW	23.85	0		0		-0.33	-11.70
		Scheduled Cost	194.93		29.14		13.00		
		Total Saving		0	34.07	0	14.88	-0.33	-11.70
GA	KW Slab	Scheduled KW	23.85	0		0		0.14	4.96
		Scheduled Cost	229		0		0.00		
	ToD	Scheduled KW	23.85	0		0		0.13	4.61
		Scheduled Cost	177.38		47.43		21.10		
		Total Saving		0	51.62	0	22.54	0.13	4.61

time. The percentage reduction in cost by optimal scheduling in case I with the help of all four algorithms comparison is shown in Fig. 9. (a) It is observed that ACO, WOA, PSO & GA algorithms minimized the electricity cost by 19.66%, 52.45, 47.02% and 31.52% respectively. In the same fig. PAR reduction is also shown for same as 6.03%, -54.96%, -18.09% and 9.93% respectively. Which shows that the optimal scheduling decreases cost but PAR reduction increases in some cases which is not good for the system. The best results are obtained by GA in consideration with cost saving and PAR reduction i.e 31.64% & 9.93%.

Simulation Results for Case-II

The load curve of Smart home before & after scheduling the appliances for each algorithm in case I is shown in Fig. 5, Fig. 6, Fig. 7 & Fig. 8. After load scheduling under slab rate



(a) Case I (b) Case II

Figure 8. Comparison of % cost saving & % PAR Reduction (a) case I (b) case II.

and ToD rate peak of load curve is minimized hence peak clipping is done. More amount of load is shifted in valley and flat tariff zone of ToD as compare to cost minimization by case I. In the case II cost minimization & PAR reduction by optimal scheduling of appliances in smart home with the help of ACO, WOA, PSO & GA algorithms is given in Table 4. The percentage reduction in cost by employing the algorithms are ACO (9.14%), WOA (15.51%), PSO (14.88%) & GA (22.54%). PAR reduction for the same are ACO (1.42%), WOA (-16.31%), PSO (-11.70%) & GA (4.61%) Which shows that cost saving is achieved in each case but reduction in PAR is not in every case. Total cost saving by scheduling the appliances by GA is 22.54% by shifting load in low ToD Tariff rate & PAR reduction is 4.61% which is greater than ACO, WOA & PSO.

If GA is employed for load scheduling under ToD tariff rate, without changing consumer power consumption (23.85 kW keeping Constant), cost saving in actual energy bill (22.54%). Also, the PAR reduced by 4.61% which is greater than KW slab rate this not happen in cost minimization by KW & ToD tariff.

CONCLUSION

In this study, the focus was on reducing electricity expenses for residential consumers while maintaining user comfort and decreasing the peak power demand to average demand ratio. Comparative results were obtained for fixed charges under the current scenario and after applying Time of Day (ToD) tariff. Different algorithms were used to optimize appliance scheduling and minimize costs. The results shows that ToD tariff led to cost savings of 2% compared to the current scenario.

The simulation results for case-I presented in this study demonstrate the effectiveness of employing like Ant Colony Optimization Algorithm (ACO), Whale Optimization Algorithm (WOA), Particle Swarm Optimization Algorithm (PSO), and Genetic Algorithm (GA) for optimal scheduling of appliances in a smart home under flat rate and ToD tariff pricing. The analysis of electricity pricing and adjustments to the load curve, conducted both prior to and subsequent to the implementation of scheduling, reveals significant decreases in expenditures; however, it is important to note that certain disruptions to consumer comfort may arise as a result of load unavailability during pivotal periods. Among the various algorithms scrutinized, the Genetic Algorithm (GA) emerges as the most effective in achieving a balanced interplay between cost reductions (31.64%) and reductions in the Peak-to-Average Ratio (PAR) (9.93%).

In the context of case-II, the findings reveal that load scheduling in accordance with Time-of-Day (ToD) tariff pricing facilitates peak clipping and promotes enhanced load distribution efficiency. The Genetic Algorithm (GA) once again surfaces as the preeminent algorithm, demonstrating noteworthy cost reductions (22.54%) and PAR decreases (4.61%) in comparison to the Ant Colony Optimization Algorithm (ACO), Whale Optimization Algorithm (WOA), and Particle Swarm Optimization Algorithm (PSO). In summary, the Genetic Algorithm (GA) substantiates its status as a viable option for the optimization of appliance scheduling within intelligent home environments, delivering significant advantages in terms of cost efficiency and reductions in PAR.

NOMENCLATURE

C_{p_f}	Specific heat, kJ / kg °C
AEC^s	Appliance Energy Consumption for slot, watt.
AEC_n	Nth Appliance Energy Consumption, watt.
AEC_T	Total Appliance Energy Consumption, watt.
C	Energy Cost, Rupees
E_{rate}	Energy Rate, Rupees
P_{rate}	Power rating, Watt
ω_T	Waiting Time, Sec.

REFERENCES

[1] Taghizad-Tavana K, Ghanbari-Ghalehjoughi M, Razzaghi-Asl N, Nojavan S, Alizadeh A. An overview of the architecture of home energy management system as microgrids, automation systems, communication protocols, security, and cyber challenges. Sustainability 2022;14:15938. [CrossRef]

[2] Shi Q, Yang Y, Sun Z, Lee C. Progress of advanced devices and Internet of Things systems as enabling technologies for smart homes and health care. ACS Mater Au 2022;2:394–435. [CrossRef]

[3] Franco P, Martinez JM, Kim YC, Ahmed MA. IoT based approach for load monitoring and activity recognition in smart homes. IEEE Access 2021;9:45325–45339. [CrossRef]

[4] Franco P, Martinez JM, Kim YC, Ahmed MA. A framework for IoT based appliance recognition in smart homes. IEEE Access 2021;9:133940–133960. [CrossRef]

[5] Albogamy FR, Khan SA, Hafeez G, Murawwat S, Khan S, Haider SI, et al. Real-time energy management and load scheduling with renewable energy integration in smart grid. Sustainability 2022;14:1792. [CrossRef]

[6] Rehman AU, Wadud Z, Elavarasan RM, Hafeez G, Khan I, Shafiq Z, et al. An optimal power usage scheduling in smart grid integrated with renewable energy sources for energy management. IEEE Access 2021;9:84619–84638. [CrossRef]

[7] Qais M, Loo KH, Hasanien HM, Alghuwainem S. Optimal comfortable load schedule for home energy management including photovoltaic and battery systems. Sustainability 2023;15:9193. [CrossRef]

[8] Nesmachnow S, Rossit DG, Toutouh J, Luna F. An explicit evolutionary approach for multiobjective energy consumption planning considering user preferences in smart homes. Int J Ind Eng Comput 2021;12:365–380. [CrossRef]

[9] Fakhar M, Yalcin E, Bilge A. IESR: Instant energy scheduling recommendations for cost saving in smart homes. IEEE Access 2022;10:52178–52195. [CrossRef]
[10] Shah A, Nasir H, Fayaz M, Lajis A, Ullah I, Shah A. Dynamic user preference parameters selection and energy consumption optimization for smart homes using deep extreme learning machine and bat algorithm. IEEE Access 2020;8:204744–204762. [CrossRef]
[11] Fensel A, Gómez Berbís JM. Energy efficiency in smart homes and smart grids. Energies 2021;14:2054. [CrossRef]
[12] Zhou B, Yang R, Li C, Cao Y, Wang Q, Liu J. Multiobjective model of time-of-use and stepwise power tariff for residential consumers in regulated power markets. IEEE Syst J 2018;12:2676–2687. [CrossRef]
[13] Li C, Tang S, Cao Y, Xu Y, Li Y, Li J, et al. A new stepwise power tariff model and its application for residential consumers in regulated electricity markets. IEEE Trans Power Syst 2013;28:300–308. [CrossRef]
[14] Isaac D, Kumar A. Optimal energy scheduling using ANT colony approach with consideration of consumers preferences in a residential smart home. Lect Notes Electr Eng 2024;1099:79–88. [CrossRef]
[15] Ramalingam SP, Shanmugam PK. A home energy management system with peak demand reduction using ant colony optimization and time of use pricing scheme. Lect Notes Electr Eng 2021:531–546. [CrossRef]
[16] Guezzaz A, Mahmood Z, Cheng B, Butt NA, Rehman GU, Zubair M, Badshah A, Aslam M. Efficient scheduling of home energy management controller (HEMC) using heuristic optimization techniques. Sustainability 2023;15:1378. [CrossRef]
[17] Shafqat W, Lee KT, Kim DH. A comprehensive predictive-learning framework for optimal scheduling and control of smart home appliances based on user and appliance classification. Sensors 2022;23:127. [CrossRef]
[18] Chatterjee A, Paul S, Ganguly B. Multi-objective energy management of a smart home in real time environment. IEEE Trans Ind Appl 2023;59:138–147. [CrossRef]
[19] Bahmanyar D, Razmjooy N, Mirjalili S. Multi-objective scheduling of IoT-enabled smart homes for energy management based on arithmetic optimization algorithm: A Node-RED and NodeMCU module-based technique. Knowl Based Syst 2022;247:108762. [CrossRef]
[20] Jin S, Choi J. Optimal load scheduling of home appliances considering operation conditions. Oresta 2022;5:2620–2747. [CrossRef]
[21] Salkuti R, El Makroum R, Khallaayoun A, Lghoul R, Mehta K, Zörner W. Home energy management system based on genetic algorithm for load scheduling: A case study based on real life consumption data. Energies 2023;16:2698. [CrossRef]
[22] Vanitha V, Vallimurugan E. A hybrid approach for optimal energy management system of Internet of Things enabled residential buildings in smart grid. Int J Energy Res 2022;46:12530–12548. [CrossRef]
[23] Goyal G, Verma S. Multi-interval programming based scheduling of appliances with user preferences and dynamic pricing in residential area. Sustain Energy Grids Netw 2021;27:100511. [CrossRef]
[24] Zhao Z, Lee WC, Shin Y, Song KB. An optimal power scheduling method for demand response in home energy management system. IEEE Trans Smart Grid 2013;4:1371–1378. [CrossRef]
[25] Mellouk L, Boulmalf M, Aaroud A, Zine-Dine K, Benhaddou D. Genetic algorithm to solve demand side management and economic dispatch problem. Procedia Comput Sci 2018;130:611–618. [CrossRef]
[26] Barbato A, Capone A. Optimization models and methods for demand-side management of residential users: A survey. Energies 2014;7:5787–5824. [CrossRef]
[27] Zhang J, Li H, Parizi MK. HWMWOA: A hybrid WMA-WOA algorithm with adaptive Cauchy mutation for global optimization and data classification. Int J Inf Technol Decis Mak 2023;22:1195–1252. [CrossRef]
[28] Vanneschi L, Silva S. Particle swarm optimization. Lect Notes Intell Syst 2023
[29] Konatowski S, Pawlowski P. PSO algorithm for UAV autonomous path planning with threat and energy cost optimization. Proc SPIE 2019;11014:30. [CrossRef]
[30] Ehteram M, Seifi A, Banadkooki FB. Structure of particle swarm optimization (PSO). Appl Mach Learn Agric Meteorol Sci 2023:23–32. [CrossRef]
[31] Sangari S, Devi. Crossover and mutation operations in GA-Genetic Algorithm. 2013.
[32] Shivan Othman P, Reber Ihsan R, Masoud Abdulhakeem R. The genetic algorithm (GA) in relation to natural evolution. Acad J Nawroz Univ 2022;11:243–250. [CrossRef]
[33] Windarto. An implementation of continuous genetic algorithm in parameter estimation of predator-prey model. AIP Conf Proc 2016;1718. [CrossRef]

Sigma Journal of Engineering and Natural Sciences
Web page info: https://sigma.yildiz.edu.tr
DOI: 10.14744/sigma.2025.01914

Research Article

Treatability of landfill leachate pre-treated with a two-stage biological treatment process to the level of receiving environment standards by using the fenton process

Uğur KURT[1], Ömer APAYDIN[1,*], Yaşar AVŞAR[1], Mustafa Talha GÖNÜLLÜ[1]

[1]*Department of Environmental Engineering, Faculty of Civil Engineering, Yildiz Technical University, Istanbul, 34522, Türkiye*

ARTICLE INFO

Article history
Received: 19 March 2025
Revised: 01 June 2025
Accepted: 02 September 2025

Keywords:
Biodegradability Rate; Fenton Process; Landfill Leachate Treatment; Organic Pollutant Removal

ABSTRACT

Although two-stage (Anaerobic+Aerobic) biological treatment methods are applied to the landfill leachate formed in Istanbul-Kömürcüoda Sanitary Landfill, discharge standard to the sewer cannot be achieved. Treatability with the classical Fenton process, which can provide the discharge standard to the sewer and is applicable, is the subject of this study. In this context, batch treatability studies were carried out with the Fenton process for both raw landfill leachate and pilot biological treatment plant effluent samples. The independent variables selected in this study are pH, Fe^{2+} and H_2O_2 doses. The dependent variables are organic pollutant removal (as chemical oxygen demand) and change in biodegradable organic matter content (as biological oxygen demand). In the study, treatability studies were primarily carried out with the Fenton process for the two-stage biological treatment plant effluent. When 50% theoretical H_2O_2 dose was applied, chemical oxygen demand removal efficiency was calculated as 74.8%. The biodegradability rate of the remaining organic pollution (as 25.2 of COD) was determined as 23%. However, the pollutant removal efficiencies obtained in the treatability studies conducted with the batch Fenton process for both raw leachate and anaerobic treatment plot plant effluent samples remained at low levels. In addition, optimum chemical doses for the two-stage biological treatment plant effluent within the scope of the Fenton process were determined as 0.5 kg $Fe(SO)_4.7H_2O/m^3$ and 5 L H_2O_2/m^3 wastewater. According to the results obtained in these studies; the organic pollution load removal efficiency can reach 97.4% (in terms of chemical oxygen demand) with the Fenton process applied to the pretreated water coming out of the two-stage biological treatment. As a result, with the Fenton process option where the procedure specified in this study will be applied, it will be possible to treat the landfill leachate at a level that will meet the sewer discharge standard in terms of organic pollutant parameters. It is thought that the treatment process proposed here can be used in the treatment of all industrial wastewaters with similar properties.

Cite this article as: Kurt U, Apaydın Ö, Avşar Y, Gönüllü MT. Treatability of landfill leachate pre-treated with a two-stage biological treatment process to the level of receiving environment standards by using the fenton process. Sigma J Eng Nat Sci 2025;43(6):2152–2163.

***Corresponding author.**
*E-mail address: apaydin@yildiz.edu.tr

This paper was recommended for publication in revised form by Editor-in-Chief Ahmet Selim Dalkilic

Published by Yıldız Technical University Press, İstanbul, Turkey
© Author. This is an open access article under the CC BY-NC license (http://creativecommons.org/licenses/by-nc/4.0/).

INTRODUCTION

In terms of waste hierarchy, sanitary landfill (SLF), also known as the final waste management option, is known as the traditional method that is needed regardless of which management option is applied. In addition to landfill gas, odor, and dust emissions, leachate is also formed in SLF facilities [1-3]. The leachate formed in SLF facilities contains a content that cannot be treated with traditional methods in terms of quantity and pollution intensity. Especially young landfill leachate contains quite complex, resistant, and dense pollutant types such as humus, ammonia nitrogen, heavy metals, inorganic salts, and organics [3-6]. Some factors affecting the amount and characteristics of leachate can be listed as the content of the stored solid waste (e.g. organic matter and moisture content), the depth of the landfill (assessment of groundwater and surface water exposure), the age of the stored waste (e.g. fresh domestic waste increases the leachate flow rate), top cover characteristics (permeability, slope, drainage status), operational conditions (e.g. compaction status of solid waste), climatic conditions (e.g. annual rainfall height, mm/year), hydrogeological conditions around the landfill and conditions in the landfill body [7]. The leachate flow rate likely to occur in SLF facilities is important in terms of planning treatment processes and varies from country to country and even from region to region in any country. In Denmark, leachate formation during operation is given as 350 mm/year, which is understood to be approximately 49% of the annual average rainfall height. In Sweden, the average leachate amounts formed by SLFs are 250-300 mm/year during the operation process, while this value is 10-40 mm/year for closed facilities with a clay top cover. The amount of leachate measured in SLFs in Istanbul, where leachate samples were taken within the scope of this article, varies between 730-1095 mm/year on average, and this value is approximately ten times the values estimated during the facility planning process [7]. Therefore, although literature information emphasizes that the amount of leachate likely to occur in SLFs will be 15-50% of the annual precipitation height, it is thought that it would be appropriate to take the average annual precipitation height in leachate estimates in Türkiye [7, 8]. SLF-related leachate must be treated at the level of the receiving environment standards. Otherwise, it is inevitable that irreversible negative situations will occur in the water, air, and soil environments around SLF [9-11]. In landfill leachate treatment, biological (anaerobic, aerobic, facultative), physical-chemical (chemical precipitation, chemical oxidation, flotation, air stripping, adsorption, coagulation-flocculation) and membrane (ultrafiltration, nanofiltration, reverse osmosis, membrane bioreactor) methods are generally used [12]. However, it is not possible to treat leachate at a level that will meet the receiving environment standards using traditional biological and chemical methods. Therefore, advanced oxidation methods must be used in SLF-related leachate treatment processes. Advanced oxidation methods can be evaluated within the scope of physicochemical treatment methods. One of the advanced oxidation methods is the Fenton reaction. The Fenton reaction plays an important role in converting organic pollutants into a range of products ranging from organic molecules to small inorganic molecules, thereby achieving complete degradation of pollutants and eliminating environmental pollution [13]. It is known that the Fenton reaction is successful in oxidizing many types of recalcitrant pollutants with its oxidation ability [14]. This success is due to the hydroxyl radicals (·OH) produced from H_2O_2 catalyzed by iron ions in acidic conditions and capable of removing recalcitrant organics in landfill leachate [15-19]. Transition metals (Fe, Cr, Mn) have catalytic effect ability resulting in faster oxidation reactions. In the presence of iron ions and relatively low pH values (pH: 3-4), H_2O_2 is converted to ·OH radicals. OH radical is the strongest oxidant except fluorine gas (F_2). In the treatability processes here, chemical oxygen demand (COD) and total organic carbon (TOC) were also taken into consideration as the two most important pollution indicators. Fenton reagents are effective on recalcitrant organic pollutants with the reaction mechanisms given in reactions from (1) to (9) [20-23].

$$Fe^{2+} + H_2O_2 \rightarrow Fe^{3+} + \cdot OH + OH^- \quad (1)$$

$$RH + \cdot OH \rightarrow H_2O + \cdot R \quad (2)$$

$$Fe^{3+} + H_2O_2 \rightarrow Fe^{2+} + HO_2 \cdot + H^- \quad (3)$$

$$Fe^{3+} + HO_2 \rightarrow Fe^{2+} + O_2 + H^- \quad (4)$$

$$\cdot OH + H_2O_2 \rightarrow H_2O + HO_2 \cdot \quad (5)$$

$$Fe^{2+} + HO_2 \cdot \rightarrow Fe^{3+} + HO_2 \cdot \quad (6)$$

$$\cdot OH + Fe^{2+} \rightarrow Fe^{3+} + OH^- \quad (7)$$

$$(COD/TOC) + H_2O_2(Fe^{2+}, Fe^{3+}) + H_2O_2 \rightarrow \text{Intermediate products} \quad (8)$$

$$H_2O_2(Fe^{2+}, Fe^{3+}) + \text{Intermediate products} \rightarrow CO_2 + H_2O + \text{Inorganic salts} \quad (9)$$

All these reactions (1-9) can occur simultaneously in the water environment. While reactions (1) and (2) are desired to reduce organic pollution through hydroxyl radical activity, reactions (3)-(7) are undesirable because they produce parameters that are non-oxidant or have weak oxidation potential. pH, temperature, alkalinity, and the presence of electron-charged anions negatively affect the Fenton oxidation efficiency by reducing the hydroxyl

radical. In order to increase the Fenton oxidation efficiency, pH optimization is required. The independent criteria for pH optimization, catalyst Fe(II) and oxidant H_2O_2 doses, should also be optimized. For some wastewaters and different leachate types, the optimum COD removal efficiencies obtained depending on the Fenton reactions and the independent criteria affecting the reactions are summarized in Table 1 [24-30].

The average values for the treatment performance of Fenton reagents on leachate types are given in Table 2 [32].

In this study, landfill leachate (LL) samples taken from Kömürcüoda Sanitary Landfill (SLF) facility, where approximately 10 tons per a day solid waste generated on the European side of Istanbul from 1994 to 2019 was regularly stored, were used. The treated water obtained as a result of the physical and biological treatment carried out in Kömürcüoda SLF can only meet the receiving environment standard by applying membrane processes. In membrane processes, there are problems of clogging and disposal of concentrate. Therefore, a lower-cost alternative treatment solution compared to membrane processes is the subject of this article by applying classical Fenton application before and after the physical and biological treatment in the SLF facility. In this study, it was planned to apply the classical Fenton process, one of the advanced oxidation methods, to the LL samples, which are well known to contain high-resistant organic matter. Here, controlled batch treatability studies were carried out to determine the levels of the main independent parameters (pH, H_2O_2, Fe^{2+}) that can reach the highest removal efficiencies for the main dependent criteria (COD and color removal efficiency). The main objective of this study is to analyze the treatability of both raw leachate samples and biological treatment plant effluent samples with the Fenton process. The treatability studies with the Fenton process were carried out separately for three different sample types: (1) raw landfill leachate from Kümürcüoda SLF, (2) pre-treated LL from anaerobic biological process effluent, and (3) pre-treated LL from anaerobic+aerobic biological process effluent available on Kümürcüoda SLF.

MATERIALS AND METHODS

In this study, the performance of Fenton Reactions, which are thought to provide an additional contribution to the insufficient biological treatment stages in landfill leachate treatment, was investigated. Raw leachate samples were obtained from Kömürcüoda SLF in Şile one of the districts on the Anatolian side of Istanbul. The wastewaters used in treatability studies, except for raw LL, were taken from the outlets of plot anaerobic and aerobic biological treatment reactors established for experimental purposes at Marmara University. The characterization of these samples is given in Table 3.

Table 1. Fenton's reaction reactant doses and COD removals for some wastewater types

Wastewater types	COD, mg/L	Fe(II), mg/L	H_2O_2, mg/L	COD removal, %	Fe(II)/COD, g/g	H_2O_2/COD, g/g	Ref.
[1]SS	1500	300	200	70	0.28	0.18	[18]
[2]SS	1100	900	900	63	1.30	1.30	[19]
[3]SS	1720	700	200	60	0.68	0.19	[20]
[4]AS	-	1500	1500	35	-	-	[21]
[5]SS	2000	200	1500	68	0.15	1.10	[22]
[6]AA	1190	100	1700	>95	0.09	1.50	[23]
[7]TE	250	200	200	78	1.03	1.03	[24]
[8]TE	590	-	310	86	-	0.53	[3]
[9]DWW	770	100	835	88	0.13	1.08	[31]

[1]Landfill leachate, upflow sequencing anaerobic reactor effluent; [2]Landfill leachate, Aerobic+ anaerobic reactor effluent; [3]Landfill leachate, aerobic reactor effluent; [4]Wastewater, upflow sequencing anaerobic reactor effluent; [5]Landfill leachate; [6]Aromatic amine production wastewater effluent; [7]Textile industry wastewater; [8]Textile industry wastewater, elektro-Fenton; [9]Domestic wastewater

Table 2. Fenton's reaction performance on landfill leachate types

Landfill leachate	H_2O_2/COD, g/g	H_2O_2/Fe(II), g/g	CODremoval, %	Reaction time, hour
Raw landfill leachate*	1.22 (n:10)	2.27 (n:12)	68.4 (n:19)	1.41 (n:14)
Pre-treated biologically	1.5 (n:11)	2.82 (n:12)	76.7 (n:16)	1.99 (n:16)

n: Runs numbers

Table 3. Characteristics of the landfill leachate used in the study

Sample types	Characteristics of landfill leachate used in the study				
	pH	COD, mg/L	BOD_5, mg/L	Total Fe, mg/L	Color, Pt-Co
Raw landfill leachate	6.5	17000	1400	85	460
Effluent from anaerobic process	6.7	6700	3800	59	410
Effluent from anaerobic +aerobic process	6.8	1750	620	21	142

In a study, it is emphasized that the independent criteria selected in experimental studies should be determined on a process basis [3]. In the study, the parameters that are widely used for the Fenton process and evaluated within the scope of the studies given in Table 1 were selected as independent process parameters. In this study, pH, H_2O_2 dose and Fe(II) dose were considered as independent criteria; and COD removal efficiency, color removal efficiency, turbidity removal efficiency and biodegradability rate were considered as dependent criteria.

Experimental studies were carried out in Ika-Werk brand jar test equipment. Five jars filled with 500 mL samples were used in each series of studies. Before the studies, the optimum pH was set as 3 for all sample types since it was reported in the literature that acidic pH conditions between 2 and 4 increase the oxidation performance of Fenton reactions [33, 34]. This data was also confirmed by the pH optimization study conducted within the scope of this study. Fe(II) was added to the leachate sample before H_2O_2 addition. H_2O_2 was added slowly to prevent possible foam formation. First, all samples were mixed at 300 rpm for one minute and then operated at 30 rpm for two hours. Considering the values given in Table 2 for both aged raw leachate and biologically treated wastewater, the reaction time was selected as two hours. The theoretical dose requirement of H_2O_2 for each sample was calculated from reactions (10) and (11) given below.

$$CH_4 + 2O_2 \cdot \rightarrow CO_2 + 2H_2O \quad (10)$$

$$CH_4 + 4H_2O_2 \rightarrow CO_2 + 6H_2O \quad (11)$$

According to reaction (10), 1000 mg O_2 can be taken as 1000 mg COD equivalent. In this case, H_2O_2/COD ratio can be calculated as 2.125 from reactions (10) and (11) (4*34/2*32= 2.125 g H_2O_2/g COD). According to this stoichiometric calculation, 2.125 mg H_2O_2 oxidant is required for each 1mg COD equivalent organic pollutant to be oxidized [31]. At the end of the reaction period, before COD, biological oxygen demand (BOD_5), color and turbidity measurements, H_2O_2 residue in the processed samples was removed. Removal of H_2O_2 residue was done by permanganometric method [35]. Residual H_2O_2 in the processed samples was removed by increasing the temperature of the processed sample to 70°C and pH to 10-11 before analysis. Then, the processed sample was left to settle for 40 minutes. COD, BOD_5, color and turbidity analyses were performed using samples taken from the upper clear phase of the sample after precipitation. The amount of Fe^{+2} remaining in the clear phase of the purified sample was determined to correct the COD value. The settled sludge volumes during and after the studies were also determined. $FeSO_4.7H_2O$ crystals were used as Fe^{+2} source and 30% H_2O_2 solution (d: 1.1 g/cm^3) was used as H_2O_2 source. pH adjustments were made with 1N H_2SO_4 and 1N NaOH. Remaining H_2O_2 determinations were made with 0.01 N $KMnO_4$ solutions. All reagents used were selected as Merck quality. pH was measured with Jenway 3040 Ion Analyzer. Color and turbidity were determined with Merck SQ 118 spectrophotometer. Total iron analysis was performed with UNICAM 929 AAS device. All analyses in the study were performed in accordance with standard methods [36]. All studies were performed in three repetitions and the arithmetic means obtained were evaluated in this study. All processes implemented in this study are given in detail as a flow chart in Figure 1.

RESULTS AND DISCUSSION

In this section, the results of the treatability studies conducted with the Fenton process are presented and discussed considering the existing literature. The mentioned evaluations were made separately within the scope of the treatability of anaerobic+aerobic treatment plant effluent, anaerobic treatment plant effluent and raw young landfill leachate as three different wastewater types. The pH optimization studies conducted for the anaerobic treatment plant effluent are shown in Figure 1 and Figure 2.

According to Figure 2, the highest COD removal efficiency was obtained as 73% at the pH 3. Optimum treatment efficiency by Fenton process for the anaerobic treated effluent sample was achieved at pH 3. This optimized pH was used as an independent criterion level in the studies conducted here. Literature data also confirms these pH levels [33-34].

Figure 3 shows that the treated wastewater after the Fenton process is 30% biodegradable. The highest biodegradability rate (0.33) is obtained at pH 3 as 33% (or 0.33). This shows that in addition to the direct COD removal

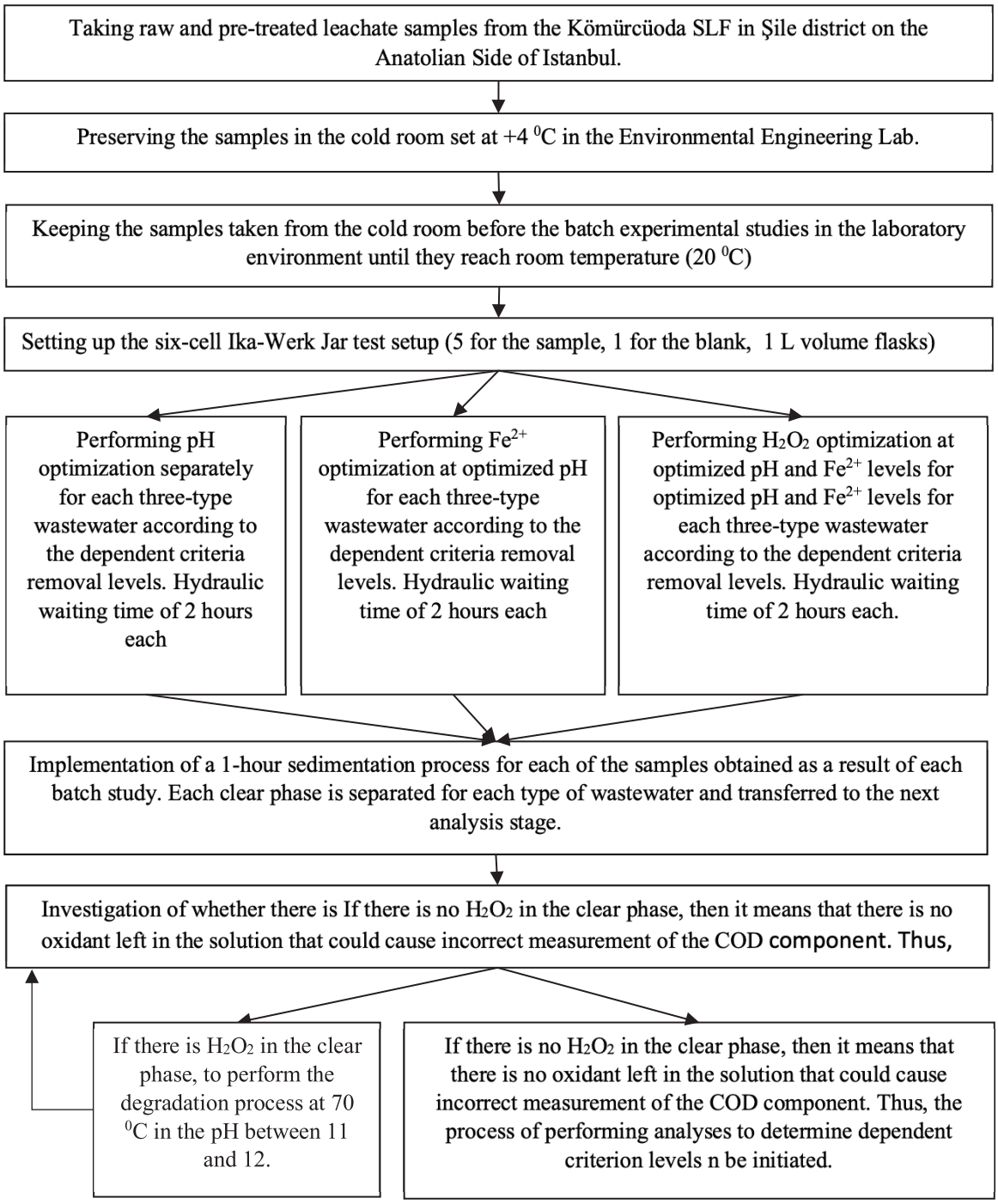


Figure 1. Flow diagram of the overall process for the current study.

effect of the Fenton process on the leachate, it also makes the remaining organic pollution partially biodegradable.

Results of Treatability Study Conducted with Fenton Process for Anaerobic+Aerobic Biologically Treated Landfill Leachate

The results of the treatability study conducted with anaerobic+aerobic biologically pretreated landfill leachate using Fenton process are given here. The results of the studies conducted to determine the optimum Fe^{2+} requirements are shown in Figure 4 (Working conditions; pH=3 and H_2O_2=2670 mg/L= 72 % of theoretical demand, COD= 1750 mg/L, reaction time:2 hour).

According to Figure 4, considering the consumed Fe^{2+} and the sludge volume to be produced, it would be appropriate to select the optimum value of 100 mg Fe^{2+}/L.

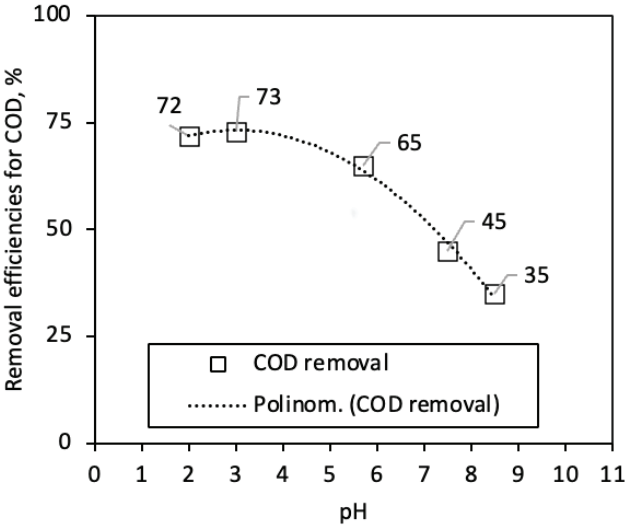


Figure 2. The results of pH optimization performed for COD removal in this study.

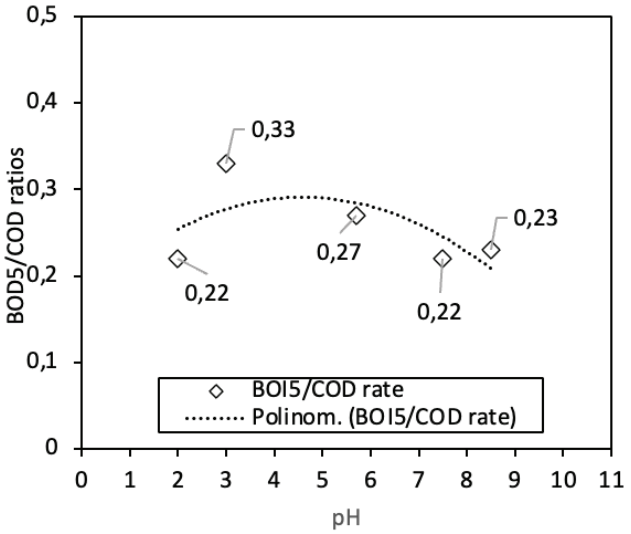


Figure 3. The results of pH optimization performed for BOD_5/COD ratios in this study.

Because, although there is a 3.9% increase in COD removal efficiency when a 200 mg Fe^{2+}/L dose is used, the amount of sludge that is likely to be formed may double. According to the results obtained from the studies, the removal efficiencies of COD, color and turbidity dependent variables were calculated as 76%, 99% and 99%, respectively. The final COD concentration decreased from 1750 mg/L to 440 mg/L. It was determined that 22.4% of the COD value (93 mg BOD_5/L) of the obtained treated landfill leachate (LL) was biodegradable. Optimum H_2O_2 doses, taking into account the previously determined optimum values of pH and Fe^{+2} the independent variables (pH: 3.0; Fe^{+2}: 100 mg/L) were given in Figure 5 for dependent parameters.

According to Figure 5, the optimum H_2O_2 dose is 1860 mg/L (50% of theoretical demand) and the optimum COD removal efficiency is 75%. The COD value of the treated sample with the Fenton process is 440 mg/L (Table 4). It is seen that this COD meets both the standards for sewer (<600 mg/L) and the standards for receiving environment standard [37]. In addition, it was understood in the analyzes that approximately 23% of the remaining COD is still biodegradable. Considering the 23% biodegradability level, the treated wastewater to be obtained after the Anaerobic + aerobic+ Fenton process can be biologically treated in large lagoons and the amount of organic matter can be further reduced. For the optimum Fe^{+2} dose (100 mg Fe^{+2}/L), the

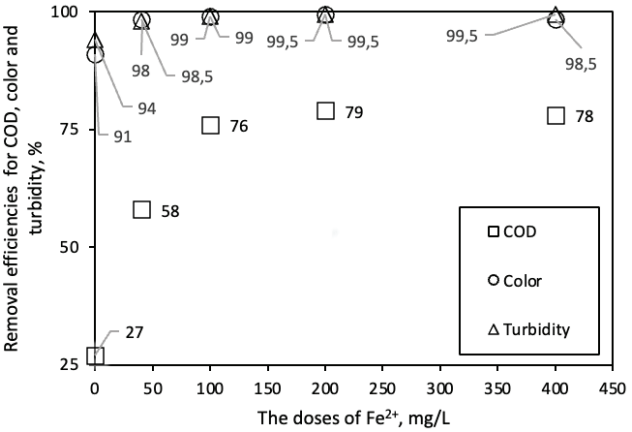


Figure 4. Studies to determine the optimum Fe^{2+} dose for the treated landfill leachate coming out of anaerobic+aerobic biological process.

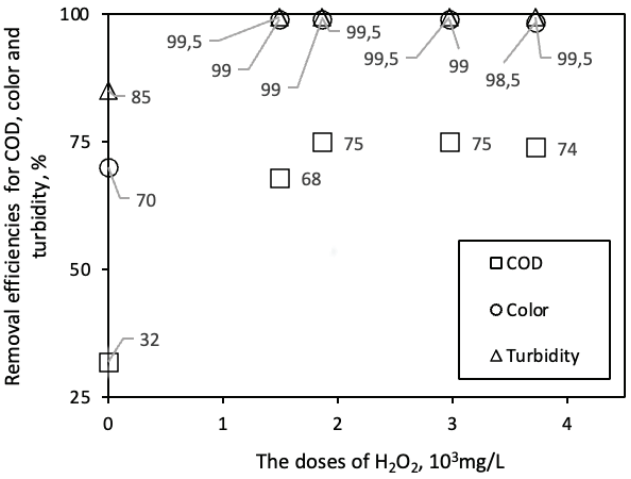


Figure 5. Studies to determine the optimum H_2O_2 dose for the treated landfill leachate coming out of anaerobic+aerobic biological process.

sludge volume obtained after 1 hour of sedimentation was obtained as 10% of the entire solution volume. In order to increase the COD removal efficiency, the following processes were specified for the clear phase obtained after the Anaerobic + aerobic + Fenton process + sedimentation:

-In order to get an idea about the additional removal possibilities of organic groups, 1000 mg/L of active carbon was added to the clear phase and mixed for 2 hours. The addition of active carbon provided an additional improvement in COD removal and the total treatment efficiency reached 83.5%. Therefore, as a result of the treatability studies, the final COD concentration could be reduced to 290 mg/L.

-The application of $KMnO_4$ at an amount of 1740 mg/L to the obtained clear phase for 2 hours was investigated. In this case, 85% COD removal and 260 mg/L final COD concentration were reached (reaction 12).

$$5CH_4 + 2\,4H^- + 8KMnO_4 \rightarrow 5CO_2 + 8Mn^{2+} + 22H_2O \quad (12)$$

Using equations 10 and 12, the $KMnO_4$/COD ratio can be calculated as 4 ($KMnO_4$/COD = 8*158/10*32 = 4 mg $KMnO_4$/mg COD). As can be seen; $KMnO_4$ and activated carbon applications give good results in increasing COD removal efficiency, but still, the treatment of young landfill leachate to the level that will meet the required receiving environment standard (condition: COD<500mg /L [37]) can be provided.

The results obtained in this section by applying Fenton process to anaerobic + aerobic biological process effluent is compared with Table 1 in terms of COD removal level (75%), and given below:

-A higher COD removal efficiency was achieved than the COD removal efficiency (70%) obtained by applying Fenton process to pre-treated landfill leachate taken from upflow sequencing batch anaerobic reactor effluent [20]. While the amount of iron consumed is less (100 mg Fe^{2+}/L< 300 mg Fe^{2+} /L), the oxidant dose is higher (1860 mg H_2O_2/ L>200 mg H_2O_2/L) than the specified study.

-A higher COD removal efficiency was achieved than the COD removal efficiency (63%) obtained by applying the Fenton process to pre-treated landfill leachate from the effluent of the aerobic + anaerobic reactor series [19]. While the amount of iron consumed is also less (100 mg Fe^{2+}/L<900 mg Fe^{2+}/L), the oxidant dose is higher (1860 mg H_2O_2/L>900 mg H_2O_2/L) than the specified study.

-A higher COD removal efficiency was achieved than the COD removal efficiency (60%) obtained by applying the Fenton process to the pretreated wastewater from the outlet of the aerobic biological reactor [20]. While the amount of iron consumed is also less (100 mg Fe^{2+} /L<900 mg Fe^{2+}/L), the oxidant dose is higher (1860 mg H_2O_2/ L>900 mg H_2O_2/L) than the specified study. As can be seen, when compared to previous leachate treatability studies, the optimized Fe^{2+} dose in this study is lower. On the contrary, the oxidant dose obtained in this study is higher than other studies. However, the COD removal efficiency was obtained as 7.14% and 25% higher than the other studies mentioned. It is thought that the most important reason for the higher COD removal in this study compared to other studies is the high optimum oxidant dose used.

From experimental studies, it is seen that the optimum Fe^{2+} dose applied to anaerobic + aerobically pretreated wastewater is 100 mg/L. While the increase in the Fe^{2+} doses used does not increase COD removal significantly, it is understood that the amount of sludge increases in proportion to the iron used. While the Fenton reaction decreases the fraction of biodegradable organic matter that is likely to occur, it increases the inorganic fraction as $Fe(OH)_3$. The inorganic fraction does not cause any toxicity. On the contrary, it is known that Fenton has detoxification properties [13].

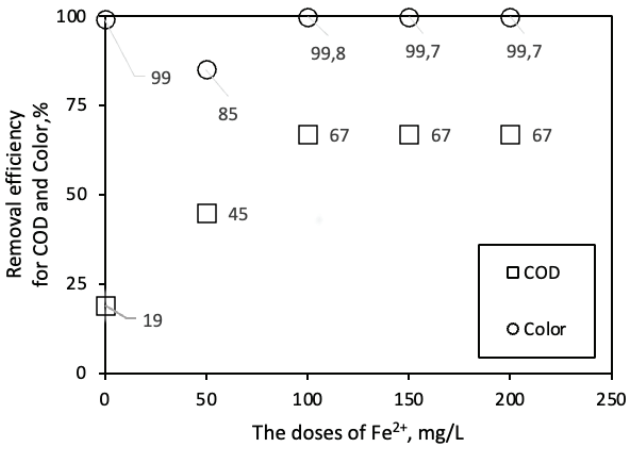


Figure 6. Studies to determine the optimum Fe^{+2} dose for the treated landfill leachate coming out of anaerobic biological process.

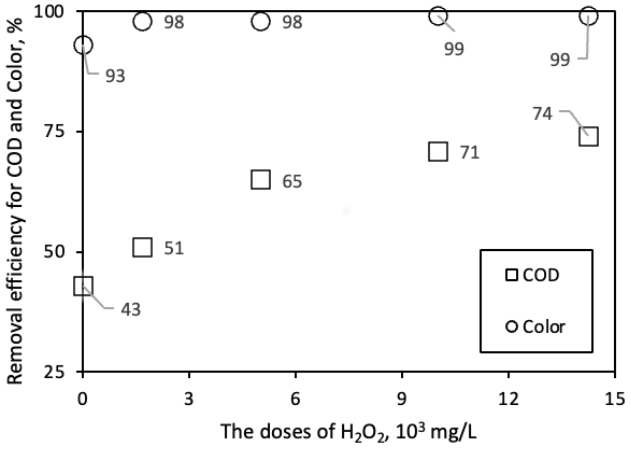


Figure 7. Studies to determine the optimum H_2O_2 dose for the treated landfill leachate coming out of anaerobic biological process.

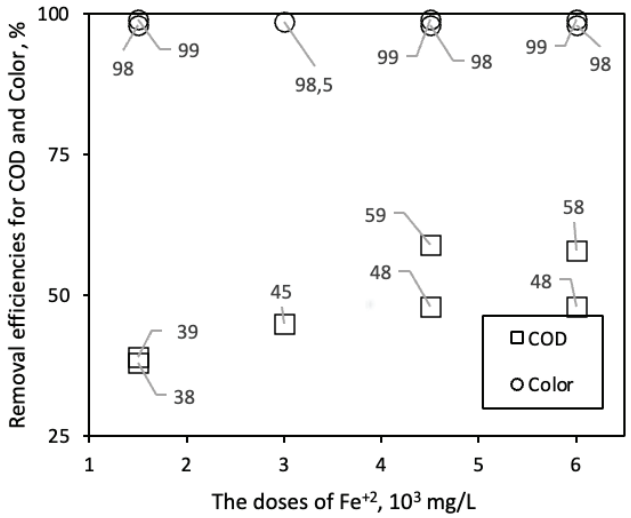


Figure 8. Studies to determine the optimum Fe^{+2} dose for the raw landfill leachate.

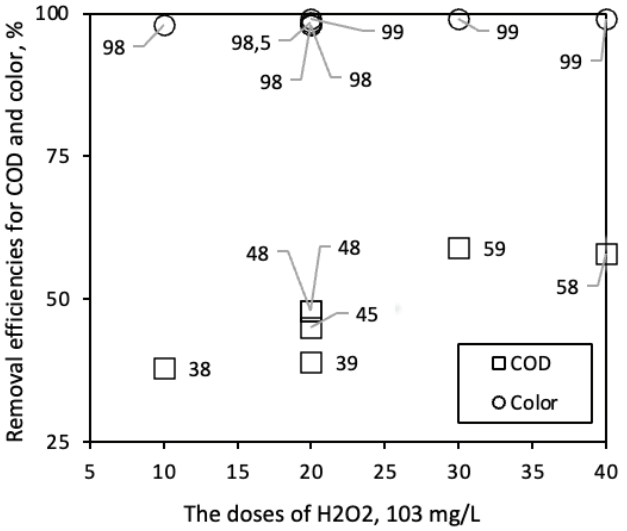


Figure 9. Studies to determine the optimum H_2O_2 dose for the raw landfill leachate.

Results of Treatability Study Conducted with Fenton Process for Anaerobic Biologically Pretreated Wastewater

In the studies conducted to determine the Fenton process efficiency for anaerobic treated leachate, optimum Fe^{2+} and H_2O_2 doses were determined and are given in Figure 6 and Figure 7, respectively.

For the special case of using optimum values of other independent variables (pH=3; 6660 mg H_2O_2/L= 47% of theoretical requirement; inlet COD= 6700 mg/L; reaction time: 2 hours), optimum Fe^{+2} dose was determined as 100 mg Fe^{+2} /L (Fig. 6). According to Figure 6, when 100 mg Fe^{+2}/L dose is applied to anaerobic treatment plant outlet samples, COD concentration in the clear phase after treatment decreases to 2190 mg/L (COD removal 67%). In addition, it is seen from Figure 6 that color removal efficiency is above 99% at the same Fe^{+2} dose.

For the special case where the optimum values of other independent variables are used (pH: 3, Fe^{+2}: 100 mg/L = 72% of the theoretical dose, inlet COD: 1750 mg/L, reaction time: 2 hours), the optimum H_2O_2 dose was determined as 5000 mg/L (Fig. 7).

As can be seen from Figure 7, when the H_2O_2 dose is 70% of the theoretical demand (10000 mg H_2O_2 /L), the COD removal efficiency is 71%. On the contrary, when the optimum dose, which is only 35% of the theoretical H_2O_2 dose, is applied, a COD removal efficiency of 65% is possible. As can be seen, in case of applying two times more H_2O_2, only a 9.23% increase in COD removal efficiency can be achieved. Therefore, the optimum H_2O_2 dose was accepted as 5000 mg/L in the section. In addition, in this study, biodegradability for the optimum H_2O_2 dose was approximately 50% (BOD_5: 1170 mg/L) and color removal efficiency was 99% (Fig. 7). In the determined optimum conditions, H_2O_2/COD (w/w), H_2O_2/Fe^{+2} (w/w) ratios were calculated as 0.75 and 50, respectively. At the end of the one hour settling period applied to all samples, the measured sludge volumes were obtained as 10% of all studies runs.

Results of Treatability Study for Raw Landfill Leachate Using Fenton Process

In the studies conducted to determine the Fenton process efficiency for raw landfill leachate, the optimum Fe^{+2} and H_2O_2 doses were determined and are given in Figure 8 and Figure 9, respectively.

As can be seen from Figure 8, when 20000 mg H_2O_2/L dose was applied to raw landfill leachate; COD removal efficiencies of 39%, 45%, 48% and 48% were obtained for 1500 mg Fe^{+2}/L, 3000 mg Fe^{+2}/L, 4500 mg Fe^{+2}/L and 6000 mg Fe^{+2}/L doses, respectively. Although the Fe^{+2}/L dose was increased by four times the initial dose (1500 mg/L H_2O_2/L, 6000 mg H_2O_2/L), only a 23.07% increase in COD removal could be obtained. On the other hand, when the same oxidant dose was applied (20 g H_2O_2/L), the COD removal efficiency was the same for both 4500 mg Fe^{+2}/L and 6000 mg Fe^{+2}/L doses (48%). Therefore, it is thought that 4500 mg Fe^{+2}/L can be accepted as the optimum Fe^{+2} dose. In the treatability studies conducted with the Fenton process for raw landfill leachate, no significant increase in COD removal was achieved by increasing the Fe^{+2} dose. It is understood that for doses higher than 6000 mg Fe^{+2}/L, no additional coagulation success will be provided in the removal of organics. From Figure 8, it is understood that the color removal efficiency is over 99% in all experimental studies conducted here. It was determined that the settled sludge volume in the experimental studies was at the level of 20% of the total sample volume.

As can be seen from Figure 9, when 15000 mg Fe^{+2}/L dose is applied to raw landfill leachate within the scope of Fenton process, 38% and 39% COD removal efficiency can

Table 4. Biodegradability results of raw landfill leachate and biologically pretreated landfill leachate before and after fenton process

Landfill leachate samples	Concentrations of pollutants before and after the application of the Fenton process			
	Before	After	Before	After
	COD, mg/L		BOD_5, mg/L	
Raw landfill leachate	17000	6850	14000	5950
Effluent from anaerobic process	6700	2380	3800	1170
Effluent from anaerobic+aerobic process	1750	440	620	101

be obtained for 10000 mg H_2O_2/L and 20000 mg H_2O_2/L oxidant doses, respectively. Despite doubling the oxidant dose, only a 2.63% increase in COD removal can be obtained. For the 4500 mg Fe^{+2}/L dose determined as optimum for Fe^{+2}, 48% and 59% COD removal efficiency can be obtained for 20000 mg H_2O_2/L and 30000 mg H_2O_2/L oxidant doses, respectively. Despite doubling the oxidant dose, only a 22.91% increase in COD removal efficiency can be obtained. According to Figure 9, when the oxidant dose is applied as 40000 mg H_2O_2/L, the COD removal efficiency decreases to 58% (for 6000 mg Fe^{+2}/L). Therefore, the optimum oxidant dose determined within the scope of the treatability of raw waste leachate, the properties of which are given in Table 3, by the Fenton process is 30000 mg H_2O_2/L. In other words, the optimum H_2O_2 dose was determined as 83% of the theoretical demand (For 17000 mg COD/L given in Table 3, theoretically 2.125*17000 mg H_2O_2 is required. The dose used here is 30000 mg H_2O_2/L, which is 83% of the theoretical dose). It is understood from Figure 9 that the color removal efficiency is above 98% in all experimental studies conducted here.

The effects of Fenton oxidation on biodegradability in raw and biologically pretreated landfill leachate samples are given in Table 4. Although the COD removal efficiency of the Fenton process seems to be higher in landfill leachate with low organic matter content (Anaerobic+aerobic pretreated effluent) compared to landfill leachate with high organic matter content (Raw young landfill leachate), the situation is exactly the opposite in terms of biodegradability. The BOD_5/COD ratios of the remaining COD load after Fenton application were calculated as 87% (5950/6850), 49% (1170/2380) and 23% (101/440) for raw landfill leachate, aerobic pretreatment effluent and anaerobic+aerobic pretreatment effluent samples, respectively. According to the obtained biodegradability results, it will be possible to meet the discharge criteria to the sewer with biological treatment following the Fenton process.

In this study, *firstly*; COD removal efficiencies obtained from the treatment of raw landfill leachate with Fenton process and anaerobic process were compared. COD removal efficiencies obtained from the treatment of raw waste leachate with Fenton process and anaerobic process were obtained as 59.7% and 60.6%, respectively. These results show that the same level of COD removal can be achieved with Fenton process and anaerobic biological processes. In BOD_5 removal, quite different removal levels were obtained (57.5% removal efficiency with Fenton process and 72.9% removal efficiency with anaerobic biological process). However, while the biodegradable level in the remaining organic matter load after Fenton process was 86.9%, this value could be only 56.7% as a result of anaerobic biological treatment. *Secondly*; COD removal efficiencies obtained from the treatment of anaerobically treated landfill leachate with Fenton process and aerobic biological process were compared. COD removal efficiencies obtained from the treatment of anaerobically treated waste leachate with the Fenton process and the treatment with the aerobic biological process were obtained as 64.5% and 73.9%, respectively. In BOD_5 removal, 69.2% and 83.7% levels were obtained for the Fenton process and the aerobic biological process. Although the BOD_5 removal efficiency was lower in the Fenton process than in the aerobic biological process, the situation is very different in terms of biodegradability levels. The remaining biodegradable organic matter levels after the treatment of anaerobically treated leachate with the Fenton process and the aerobic biological process were determined as 49.2% and 35.4%, respectively. In other words, it is understood that the amount of biodegradable organic matter remaining in the waste leachate treated with the Fenton process is 42.85% higher than in the aerobic biological process. *Thirdly*; After the application of the Fenton process to the two-stage biological treatment (Anaerobic + aerobic serial sequence) effluent sample, the basic pollutant removal and biodegradability levels were evaluated (Table 4 can be seen for the pollutant removal levels of each process). Two-stage biological treatment (anaerobic + aerobic) and anaerobic treatment and the application of a separate Fenton process after these processes can be evaluated in terms of non-biodegradable pollution. The remaining non-biodegradable pollution loads as a result of two-stage biological treatment and only anaerobic biological treatment were determined as 1130 mg/L (1750 mg/L -620 mg/L) and 1210 mg/L (2380 mg/L -1170 mg/L), respectively (Table 4). While the biodegradability levels of these non-biodegradable pollution loads were determined as 35.4% at the two-stage biological

treatment effluent, this value could be increased to approximately 50% with the help of the Fenton process in this study. Although the COD removal efficiency is 90% with two-stage biological treatment, the discharge criteria to the sewer cannot be met. As a solution, with the help of the Fenton process that will follow the two-stage biological treatment, the wastewater can be treated at a level that will provide the receiving environment standard for the sewer, as in this study. Because, with the Fenton process, an additional COD removal of 75% (COD decreases from 1750 g/L to 440 mg/L with the Fenton process) can be achieved and the total COD removal reaches 97% (COD decreases from 17 000 mg/L to 440 mg/L).

CONCLUSION

In this study, the Fenton process was applied as an advanced oxidation technique to young wastewater leachates that had undergone two-stage biological (first anaerobic then aerobic) and single-stage (only anaerobic) biological treatment processes. The most important independent criteria affecting the process, pH, Fe^{2+} and H_2O_2 doses, were optimized, and the reaction time was limited to 2 hours. It was determined that with Fenton process, both additional COD removal could be provided in pretreated waste leachate during biological treatment process and a significant part of the remaining organic pollutant load could be made biodegradable. Receiving environment; it refers to the near or distant environment such as lake, stream, coastal and sea waters, and groundwater where wastewater is discharged or indirectly mixed. It is known that it is very difficult to treat landfill leachate to a level that will meet the standards of the receiving environment with conventional treatment methods. In this study, this fact was brought to light once again as a result of treatability studies applied to young landfill leachate (five-year-old). As follows; although the young landfill leachate was treated with both anaerobic and anaerobic+aerobic biological methods, COD could only be reduced to three times the standards of the receiving environment (1750 mg/L>500 mg/L). Therefore, in this study, the Fenton process was applied separately to both anaerobic pretreated landfill leachate and anaerobic+aerobic pretreated landfill leachate. The remaining COD in the pretreated landfill leachate after anaerobic+aerobic treatment was measured as 1750 mg/L. In order to provide the receiving environment standard, the Fenton process was applied to the pretreated landfill leachate after anaerobic+aerobic treatment. Fenton process applications were carried out within the scope of the values of the independent criteria selected for the process optimized in this study (pH: 3, Fe^{2+}: 4500 mg/L, H_2O_2: 30000 mg/L). After the Fenton process, the COD value of the treated leachate can be reduced to the level of 440 mg/L (<500 mg/L). As a result, when the Fenton process is applied to the two-stage biological pretreatment effluent, compliance with the receiving environment standard in terms of COD can be achieved. With this study, it will be possible to overcome receiving environment limitation by using the Fenton process in the landfill leachate treatment processes planned to be carried out in the future. In addition, the biodegradable content of the pollutant forms remaining after treatment by Fenton process will also enable a sustainable landfill leachate treatment process. In the studies performed here with three different wastewater samples, the optimum chemical and oxidant doses required for the treated LL were also determined. When the Fenton studies performed on anaerobic+aerobic outlet were evaluated for optimum efficiency; the chemical substance and oxidant doses were calculated as 0.5 kg $Fe(SO)_4.7H_2O/m^3$ wastewater and 8 L $H_2O_2(30\%)/m^3$ wastewater. In anaerobic Fenton studies, the chemical substance and oxidant doses were calculated as 0.5 kg $Fe(SO)_4.7H_2O/m^3$ wastewater, 20 L $H_2O_2(30\%)$/m3 wastewater. In the Fenton process studies performed with raw wastewater, the chemical substance and oxidant doses were obtained as 22.5 kg $Fe(SO)_4.7H_2O/m^3$ wastewater, 100 L $H_2O_2(30\%)/m^3$ wastewater. From the obtained results, it is considered that the Fenton process is applicable only for anaerobic+aerobic effluent samples. Another chemical requirement in the Fenton process is to lower or raise the pH of the water to be treated. Because, the requirement to keep the pH between 3 and 4 in during process brings the cost of additional acid use to the agenda. Base addition may also be required after treatment. It is possible to use low pH industrial wastewater (e.g. metal industry) as an acid source in the treatment of wastewater with high pollution potential such as LL. In this case, it is important to control the heavy metal content of the wastewater planned to be treated. It is thought that detailed studies on the subject are needed for a sustainable wastewater treatment process. It is suggested that similar wastewaters, which cannot be sufficiently treated by conventional methods, should be treated with the classical Fenton process. According to the data obtained as a result of this study; it is clear that the classical Fenton process should be applied to the effluent, especially in facilities that cannot provide the receiving environment standard despite being biologically treated. Otherwise, membrane processes will need to be applied to provide the receiving environment standard, and this requires high costs due to the resulting concentrate and blockages in the system. It will be possible to increase the removal of organic pollutants by recycling the sluice output, whose biological treatability increases after the Fenton application, back to the biological processes. Detailed kinetic studies based on independent process parameters for similar wastewaters containing high organic pollution are considered as potential research areas based on the wastewater content.

ACKNOWLEDGEMENTS

The authors thank all everyone supported to them.

AUTHORSHIP CONTRIBUTIONS

Authors equally contributed to this work.

DATA AVAILABILITY STATEMENT

The authors confirm that the data that supports the findings of this study are available within the article. Raw data that support the finding of this study are available from the corresponding author, upon reasonable request.

CONFLICT OF INTEREST

The author declared no potential conflicts of interest with respect to the research, authorship, and/or publication of this article.

ETHICS

There are no ethical issues with the publication of this manuscript.

STATEMENT ON THE USE OF ARTIFICIAL INTELLIGENCE

Artificial intelligence was not used in the preparation of the article.

REFERENCES

[1] Zaman A, Ahsan T. Zero-waste: reconsidering waste management for the future. Routledge; 2020. [CrossRef]

[2] Apaydın Ö. Analysis of the special case of binary separation at source of municipal solid waste with the help of analytical hierarchy process in terms of environmental, economic, social and technical criteria. Pamukkale Univ Eng Sci J 2025;31:882–889. [Turkish] [CrossRef]

[3] Apaydın Ö. Deciding on the priority of process parameters using the analytical hierarchy process in electrochemical wastewater treatment and investigation of paint wastewater treatability. Desal Water Treat 2024;320:100587. [CrossRef]

[4] Kurtoglu-Akkaya G, Ayvaz-Cavdaroglu N, Bilgili MS. Aluminum accumulation in treatment using submerged membrane electro-bioreactor of young landfill leachate: statistical analysis. Environ Res Tech 2020;3:119–128. [CrossRef]

[5] Brown K, Ghoshdastidar AJ, Hanmore J, Frazee J, Tong AZ. Membrane bioreactor technology: a novel approach to the treatment of compost leachate. Waste Manag 2013;33:2188–2194. [CrossRef]

[6] He PJ, Xue JF, Shao LM, Li GJ, Lee DJ. Dissolved organic matter (DOM) in recycled leachate of bioreactor landfill. Water Res 2006;40:1465–1473. [CrossRef]

[7] Moravia WG, Amaral MC, Lange LC. Evaluation of landfill leachate treatment by advanced oxidative process by Fenton's reagent combined with membrane separation system. Waste Manag 2013;3:89–101. [CrossRef]

[8] Öztürk İ. Katı atık yönetimi ve AB uygulamaları. İSTAÇ AŞ: Teknik Kitaplar Serisi 2, İstanbul; 2010.

[9] Baştürk A. Katı atık depolama teknikleri ders notu. Yıldız Teknik Üniversitesi; İstanbul; 1998. Available at: https://bologna.yildiz.edu.tr/index.php?r=course/view&id=6581&aid=29&pid=0 Accessed on Nov 20, 2025.

[10] Idowu IA, Atherton W, Hashim K, Kot P, Alkhaddar R, Alo BI, et al. An analyses of the status of landfill classification systems in developing countries: Sub Saharan Africa landfill experiences. Waste Manag 2019;87:761–771. [CrossRef]

[11] Li HS, Zhou SQ, Sun YB, Feng P, Li JD. Advanced treatment of landfill leachate by a new combination process in a full-scale plant. J Hazard Mater 2009;172:408–415. [CrossRef]

[12] Li H, Zhou S, Sun Y, Lv J. Application of response surface methodology to the advanced treatment of biologically stabilized landfill leachate using Fenton's reagent. Waste Manag 2010;30:2122–2129. [CrossRef]

[13] Xiao J, Guo S, Wang D. An Fenton-like reaction: recent advances and new trends. Chem Eur J 2024;30:e202304337. [CrossRef]

[14] Tchobanoglous G, Burton FL, Stensel HD. Wastewater engineering: treatment and reuse. 4th ed. Boston: Metcalf & Eddy, Inc., McGraw-Hill; 2003.

[15] Gu Z, Chen W, Li Q, Zhang A. Treatment of semi-aerobic aged-refuse biofilter effluent from treating landfill leachate with the Fenton method. Process Saf Environ Prot 2020;133:32–40. [CrossRef]

[16] Iskander SM, Zeng T, Smiley E, Bolyard SC, Novak JT, He Z. Formation of disinfection byproducts during Fenton's oxidation of chloride-rich landfill leachate. J Hazard Mater 2020;382:21213. [CrossRef]

[17] Singh SK, Tang WZ, Tachiev G. Fenton treatment of landfill leachate under different COD loading factors. Waste Manag 2013;33:2116–2122. [CrossRef]

[18] Xu X, Zong S, Chen W, Liu D. Comparative study of bisphenol A degradation via heterogeneously catalyzed H2O2 and persulfate: reactivity, products, stability and mechanism. Chem Eng J 2019;369:470–479. [CrossRef]

[19] Zhang G, Qin L, Meng Q, Fan Z, Wu D. Aerobic SMBR/reverse osmosis system enhanced by Fenton oxidation for advanced treatment of old municipal landfill leachate. Bioresour Technol 2013;142:261–268. [CrossRef]

[20] Deng Y, Englehardt JD. Treatment of landfill leachate by the Fenton process. Water Res 2006;40:3683–3694. [CrossRef]

[21] Ghanbarzadeh LM, Sabour MR, Ghafari E, Amiri A. Energy consumption and relative efficiency improvement of photo-Fenton - optimization by RSM for landfill leachate treatment, a case study. Waste Manag 2018;79:58–70. [CrossRef]

[22] Wu Y, Zhou S, Zheng K, Ye X, Qin F. Mathematical model analysis of Fenton oxidation of landfill leachate. Waste Manag 2011;3:468–474. [CrossRef]

[23] Kurt U. Sızıntı sularının demir katalizli hidrojenperoksit oksidasyonu ile arıtılabilirliğinin araştırılması [master thesis]. Istanbul: Yıldız Technical University Graduate School of Natural and Applied Sciences; 2000. [Turkish]

[24] Lau IWC, Wang P, Fang HHP. Organic removal of anaerobically treated leachate by Fenton coagulation. J Environ Eng 2001;127:666. [CrossRef]

[25] Bae JH, Kim SK, Chang HS. Treatment of landfill leachates: ammonia removal via nitrification and denitrification and further COD reduction via Fenton's treatment followed by activated sludge. Water Sci Technol 1997;36:341–348. [CrossRef]

[26] Gau SH, Chang FS. Improved Fenton method to remove recalcitrant organics in landfill leachate. Water Sci Technol 1996;34:455–462. [CrossRef]

[27] Yo HC, Park MK, Kong MG, Lee ES, Cho SH. Treatment process train of landfill leachate. Proc 6th IAWQ Asia Pacific Reg Conf: Asian Waterqual '97; 1997:1709–1714.

[28] Kim YK, Huh IR. Enhancing biological treatability of landfill leachate by chemical oxidation. Environ Eng Sci 1997;14:73–79. [CrossRef]

[29] Casero I, Sicilia D, Rubio S, Perez-Bendito D. Chemical degradation of aromatic amines by Fenton's reagent. Water Res 1997;31:1985–1995. [CrossRef]

[30] Kang SF, Chang HM. Coagulation of textile secondary effluents with Fenton's reagent. Water Sci Technol 1997;36:215–222. [CrossRef]

[31] Kurt U. Fenton ve elektrokimyasal yöntemlerle evsel atıksuların arıtılabilirliğinin araştırılması [doctorial thesis]. Istanbul: Yıldız Technical University, Graduate School of Natural and Applied Sciences, Enivorenmental Enginering, ABD; 2007.

[32] Wu C, Chen W, Gu Z, Li Q. A review of the characteristics of Fenton and ozonation systems in landfill leachate treatment. Sci Total Environ 2021;762:143131. [CrossRef]

[33] Göde JN, Souza DH, Trevisan V, Skoronski E. Application of the Fenton and Fenton-like processes in the landfill leachate tertiary treatment. J Environ Chem Eng 2019;7:103352. [CrossRef]

[34] Babuponnusami A, Muthukumar K. A review on Fenton and improvements to the Fenton process for wastewater treatment. J Environ Chem Eng 2014;2557–2572.

[35] De Menezes MN, Kogawa AC, Salgado HRN. Status of hydrogen peroxide solution 10 V in commercialized samples. Pharmaceut Anal Acta 2017;8:1000567. [CrossRef]

[36] American Public Health Association, American Water Works Association, Water Environment Federation. Standard methods for the examination of water and wastewater. 19th ed. Washington: American Public Health Association; 1999.

[37] T.C. Mevzuat Bilgi Sistemi. Su Kirliliği Kontrolü Yönetmeliği. Available at: https://www.mevzuat.gov.tr/mevzuat?MevzuatNo=7221&MevzuatTur=7&MevzuatTertip=5 Accessed on Mar 18, 2025.

Sigma J Eng Nat Sci, Vol. 43, No. 6, pp. 2164–2173, December, 2025

Sigma Journal of Engineering and Natural Sciences
Web page info: https://sigma.yildiz.edu.tr
DOI: 10.14744/sigma.2025.1934

Research Article

Male lifestyle habits and in vitro fertilization outcomes: The effects of alcohol and smoking on sperm characteristics and pregnancy rates

Tamara AL-BARQ[1], Manal GHANNAM[2], Bilgen KAYMAKAMZADE[3,4], Evren HINCAL[2,3], Muhammad FARMAN[3,4,*]

[1]*Faculty of Medicine, Department of Medical Genetics, Near East University, Nicosia, 99138, Northern Cyprus, TRNC*
[2]*Faculty of Arts and Sciences, Department of Mathematics, Near East University, Nicosia, 99138, Northern Cyprus, TRNC*
[3]*Mathematical Research Center, Near East University, Nicosia, 99138, Northern Cyprus, TRNC*
[4]*Research Center of Applied Mathematics, Khazar University, Baku, AZ1096, Azerbaijan*

ARTICLE INFO

Article history
Received: 08 June 2024
Revised: 21 August 2024
Accepted: 06 November 2024

Keywords:
Alcohol Consumption; bHCG; Fertile Oocyte Donors; IVF; Semen Analysis; Smoking

ABSTRACT

A study of the effects of male smoking and alcohol consumption on the outcomes of the In Vitro Fertilization treatments involving young, fertile oocyte donors in Northern Cyprus. Data from 124 consecutive IVF cycles were analyzed retrospectively. Patient files and clinical records were used to collect information on male smoking and alcohol habits, semen analysis parameters, and IVF outcomes. SPSS software was one of the statistical techniques used to compare the results of several groups according to their alcohol and smoking habits. Statistical significance was set at a p-value of less than 0.05. The normal concentration of sperms, the morphology and motility rate were considerably less in the smokers and drinkers group than in the nonsmokers and non-drinkers group, by 14%, 8.1% and 15.2%, correspondingly. Furthermore, for males over 40, the drinking and smoking group has a considerably reduced proportion of normal sperm volume by 7% compared to the equivalent group for males under 40. This research shows that the act of smoking and the consumption of alcohol by males lessen the quality of sperm and have a negative influence on the outcomes of in vitro fertilization. The percentage of positive beta-human chorionic gonadotropin was about 21% lower in males who smoke and drink than those who abstain. These findings highlight the significance of providing counseling to males undergoing IVF regarding the potential adverse effects of these lifestyle habits on their fertility potential.

Cite this article as: Al-Barq T, Ghannam M, Kaymakamzade B, Hıncal E, Farman M. Male lifestyle habits and in vitro fertilization outcomes: The effects of alcohol and smoking on sperm characteristics and pregnancy rates. Sigma J Eng Nat Sci 2025;43(6):2164–2173.

***Corresponding author.**
*E-mail address: farmanlink@gmail.com

This paper was recommended for publication in revised form by Editor-in-Chief Ahmet Selim Dalkilic

Published by Yıldız Technical University Press, İstanbul, Turkey
© Author. This is an open access article under the CC BY-NC license (http://creativecommons.org/licenses/by-nc/4.0/).

INTRODUCTION

Infertility affects millions of couples worldwide. The inability to become pregnant after a year of sexual activity without the use of contraception is known as infertility. Numerous causes can lead to infertility, including aging in women, hormone imbalances, abnormalities in the uterus, and male issues such as low motility or sperm count [1]. A variety of medical procedures known as assisted reproductive technologies, or ART, are intended to help couples who fail to achieve pregnancy. The process of retrieving eggs from a woman's ovaries, fertilizing them with sperm in a controlled laboratory setting, and then transferring the resultant embryos to the woman's uterus is known as in vitro fertilization, or IVF. Intracytoplasmic sperm injection (ICSI) is a process that involves carefully inserting a single sperm into an egg which is frequently used when the male partner is infertile [2]. The complex process of sperm creation that takes place in the testes' seminiferous tubules is known as spermatogenesis. During childhood into the future, this amazing biological event continues unabated, guaranteeing a consistent supply of male gametes for possible fertilization. The process of spermatogenesis consists of several well phases that work together to produce good quality sperm cells. [3]. Egg development, or oogenesis, is an exceptional example of cellular biology that is carefully regulated inside the ovaries. Oogenesis starts during fetal development and progresses through a number of discrete phases, in contrast to spermatogenesis, which happens constantly all while a male's period of reproduction [4].

Even though assisted reproductive technologies have advanced significantly over the past 25 years, researchers are still attempting to identify additional variables that influence the outcome of IVF. This paper will show the effect of male smoking and drinking alcohol on the endpoints of IVF [5]. According to [6] smoking affects sperm negatively, in [7] found that smoking and alcohol impact the DNA of the sperm. Research has demonstrated the effects of smoking on a variety of biological levels such as sperm production [8], and analysis of the epidemiological literature, smoking cigarettes is linked to slight declines in motility [9]. Additionally, smoking is a major worldwide health threat that leads to a number of fatal diseases [10]. There is strong evidence that couples should be informed about the potential effects of smoking on the results of IVF treatments years in advance [11]. Few researches have examined how drinking alcohol affects a man's ability to conceive. Testicular shrinkage in men is linked to heavy alcohol consumption [12]. Male factors are considered to be responsible for thirty to fifty percent of cases of infertility. A few reasons for infertility or decreased fertility include endocrinopathies, age, congenital anatomical characteristics, gonadotoxic exposures, lifestyle choices, and dysfunctional testicles. A comprehensive medical history, a focused physical examination, and particular laboratory tests, including semen analysis, are all components of the male infertility screening procedure [13]. Ovarian insufficiency, diminished ovarian reserve, and male factor are the most frequent causes of infertility among the patients in this study.

All in vitro fertilization patients are ready to change their lifestyle. Therefore, it is important to ensure that people understand the healthy habits that can improve the chances of having an effective IVF cycle [14]. Therefore, the purpose of this research was to examine the effect of smoking and alcohol consumption for male on the outcomes of in vitro fertilization process using young, fertile oocyte donors in Northern Cyprus. The findings of this research should prove that lifestyle choices have an impact on the results of IVF. Figure 1 below illustrates our study's methodology and driving forces.

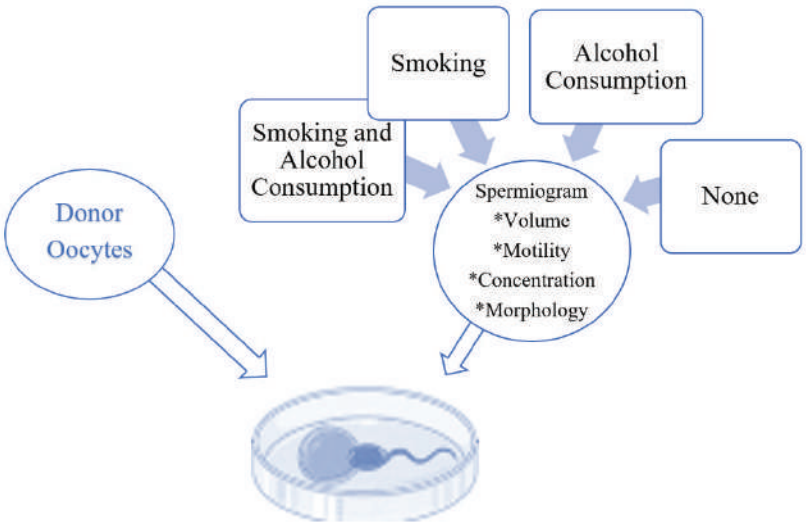


Figure 1. Alcohol and cigarette consumption by males versus the IVF results.

MATERIALS AND METHODS

Almost 124 consecutive IVF treatment cycles for young fertile oocyte donors between 2015 and 2023 at Near East University Hospital are included in this clinical data analysis. Patient files and clinical outcome records were the sources of the data. One type of embryo transfer cycle was examined in this study, which is IVF (in vitro fertilization–embryo transfer). Methods of treatment utilizing regular IVF, donor embryos, or donor sperm were excluded. Three classifications were used and tested to examine the effects of Alcohol and cigarette consumption, on the characteristics of human sperm and the outcomes of IVF.

To test the hypothesis When the standard deviation (σ) is unknown and n is less than 30, regarding the mean of the normal population, first, a small sample size n was assumed, where n represents the observations within the normally distributed population. Given that (r) is an unbiased estimate of σ and x is the sample mean [15].

$$H_0 : \mu = \mu_0 \; and \; H_1 : \mu \neq \mu_0 \; (two \; tailed)$$

After deciding the hypothesis and the Null hypothesis, a significance level (α) for the degree of freedom (D), should be determined by:

$$p\left(\underline{x} - t_{\frac{\alpha}{2}(D)} \frac{r}{\sqrt{n}}\right) = 1 - \alpha$$

Then the t-value can be calculated by using $t = \frac{\underline{x} - \mu_0}{\frac{r}{\sqrt{n}}}$

And the critical region was $|t| \geq t_{\frac{\alpha}{2}(D)}$

While, for two small samples taken from a normally distributed population, that have μ_1 and μ_2 as the mean of each sample and σ_1, σ_2 as the standard deviation for each, then, to calculate the standard error of the mean difference, let $\sigma_1 \neq \sigma_2$ and r_1 *and* r_2 be the sample estimations, then

$$r_{\underline{x}_1 - \underline{x}_2} = \sqrt{\frac{r_1^2}{n_1} + \frac{r_2^2}{n_2}}$$

The difference of the mean should have a certain value, so the hypothesis and null can be written as:

$$H_0: \mu_1 - \mu_2 = \Delta \; and \; H_1: \mu_1 - \mu_2 \neq \Delta \; (two \; tailed)$$

The significance level (α) for the degree of freedom (D), should be determined by:

$$p(\underline{x}_1 - \underline{x}_2 - t_{\frac{\alpha}{2}(D)} \sqrt{\frac{r_1^2}{n_1} + \frac{r_2^2}{n_2}} < \mu_1 - \mu_2 < \underline{x}_1 - \underline{x}_2 + t_{\frac{\alpha}{2}(D)} \sqrt{\frac{r_1^2}{n_1} + \frac{r_2^2}{n_2}}).$$

Then, the t-value can be calculated by:

$$t = \frac{\underline{x}_1 - \underline{x}_2 - \Delta}{\sqrt{\frac{r_1^2}{n_1} + \frac{r_2^2}{n_2}}}$$

And the critical region was $|t| \geq t_{\frac{\alpha}{2}(D)}$

A researcher's goal is frequently to determine whether the frequency of examples with a particular characteristic varies across levels of a factor or across combinations of levels of two or more factors. The chi-square test of goodness of fit is the proper test to use in these circumstances [16], given by:

$$x^2 = \sum \frac{(Observed \; value - Expected \; value)^2}{Expected \; value}, \text{ using } \alpha = 0.05$$

Drinking alcohol and smoking information for each male patient was checked from his medical records, which were normally created during the patient's initial visit to the clinic.

Table 1 displays the analysis of semen. designed by WHO according to [17], and table 2 represents the whole sample's clinical statistics taken from the IVF clinic in the Near East Hospital in Northern Cyprus.

Table 1. Normal limits of reference for semen analysis

Volume (*ml*)	>1.5
Concentration ($\times 10^6.ml^{-1}$)	> 39
pH	> 7.2
Motility (%)	> 32
Morphology (*Krufer*)	=> 4
Viscosity following liquefaction (*cm*)	< 2

Table 2. Clinical data gathered from Near East Hospital's IVF facility

Clinical Features	***The entire sample size (n = 124)***
BMI ($Kg.s^{-2}$), mean ±s.d. (*range*)	25.27 ± 4.01 (18.34-39.06)
Concentration of sperm ($\times 10^6.ml^{-1}$)	63.83 ± 52.21 (3-270)
Morphology of sperm (*Kruger*)	3.79 ± 3.27 (1-14)
Volume of sperm (*ml*)	3.09 ± 1.70 (0.30-10.60)
Motility of sperm %	42.87 ± 20.76 (0-90)
Age (*year*), mean ± s.d. (*range*)	42.2 ± 8.8 (22-67)

Table 3. Males' Drinking and smoking behaviors percentage in the sample

Lifestyle choices of men based on drinking and smoking	**The sample's Rate**
Alcohol status (%)	
abstainers	64.5%
Social Alcoholic	26.5%
Heavy drinkers	9%
Smoking and Alcohol status (%)	
Nonsmokers and abstainers	39.5%
At least one of the two habits	39.5%
Smokers and drinkers	21%
Smoking status (%)	
Nonsmokers	53.2%
Moderate smokers	15.3%
Heavy smokers	31.5%

BMI: body mass index; s.d.: standard deviation;

Data Analysis and Formulations

Almost 124 consecutive IVF treatment cycles for young fertile oocyte donors between 2015 and 2023 at Near East University Hospital are included in this clinical data analysis.

Table 3, displays the status of the research sample according to their life-style in drinking and smoking. Of the patients, 53.2%, 15.3%, and 31.5% were nonsmokers, moderate smokers, and heavy smokers. On the other hand, of the male population, 9%, 26.5%, and 64.5% were abstainers, social drinkers, and heavy drinkers, respectively. When it came to social behavior activities, the sample was divided into three groups, the first one consisted of 21% of the patients who were drinkers and smokers (+S/+D; group); the second group consisted of 39.5% were abstainers and nonsmokers (−S/−D; group); and the third one consisted from 39.5% of the patients that had at least one recreational behavior (−S/+D or +S/−D; group). As represented below in figure 2.

Patient files and clinical outcome records were the sources of the data considered in figures 3- 7 that designed data for the study. These are some selected variables and

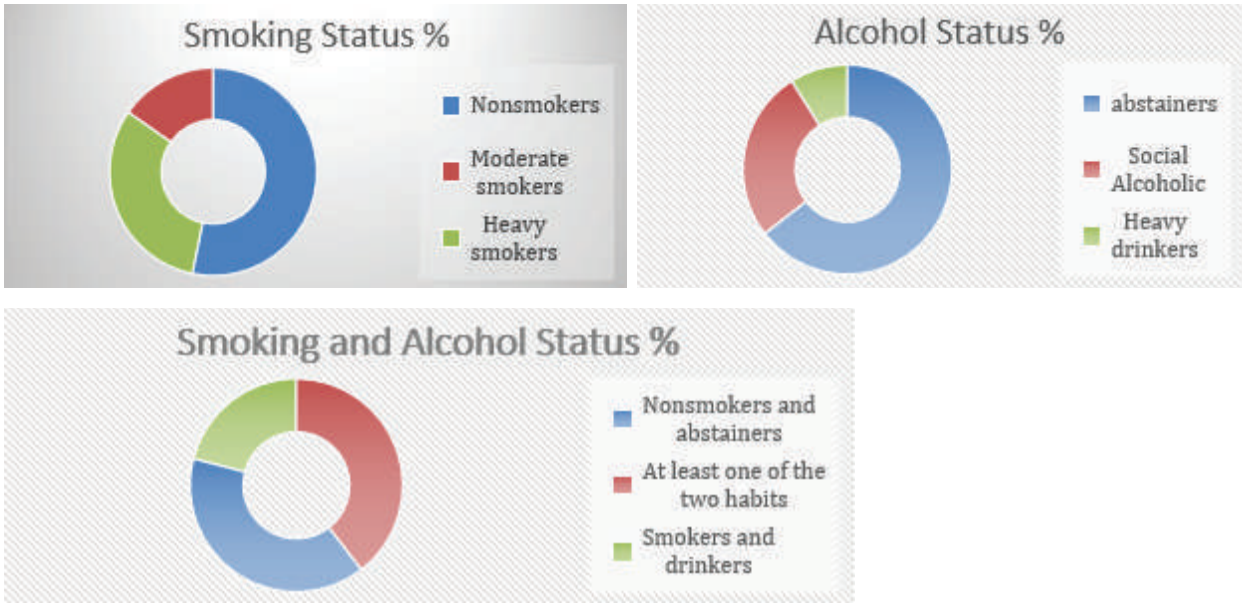


Figure 2. Males' drinking and smoking habits are the basis for the study's behavior patterns

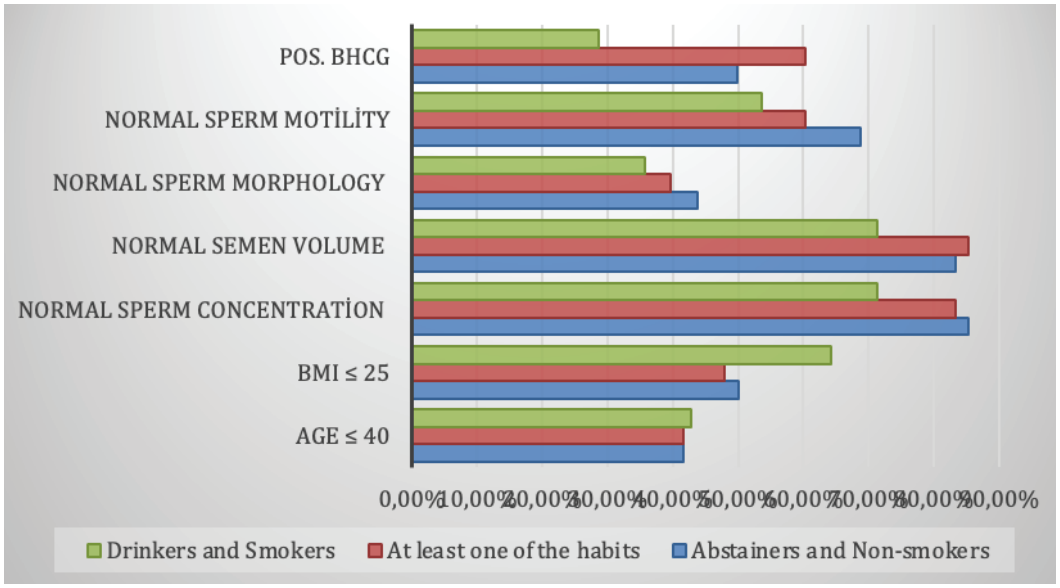


Figure 3. Characteristics of the sample based on male alcohol consumption and smoking.

permeates that are helpful in the analysis of the proposed problems with effective and novel techniques.

Figure 3 describes the male characteristics based on alcohol and cigarette consumption, the comparison was made after finding the percentage of the normal range of the males' age, BMI and each of the four Spermiogram values; the concentration, motility, volume, and morphology.

Figure 4, and Figure 5 describe the male characteristics for negative and positive bHCG respectively, versus the three groups, (+S/+D); (−S/−D); and (−S/+D or +S/−D).

Figure 6 and figure 7 show the effect of age associated with drinking and smoking, the only significant effect was in the volume of the sperm, which was lower for males older than 40 and had the two habits of drinking and smoking.

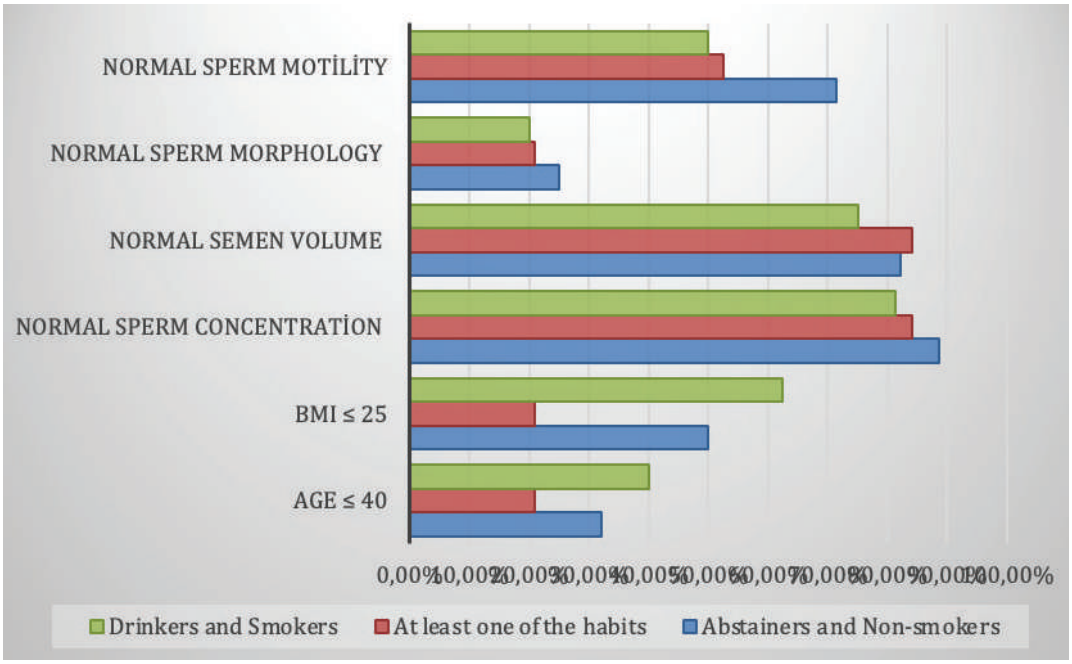


Figure 4. Characteristics of the sample based on the negative results of bHCG.

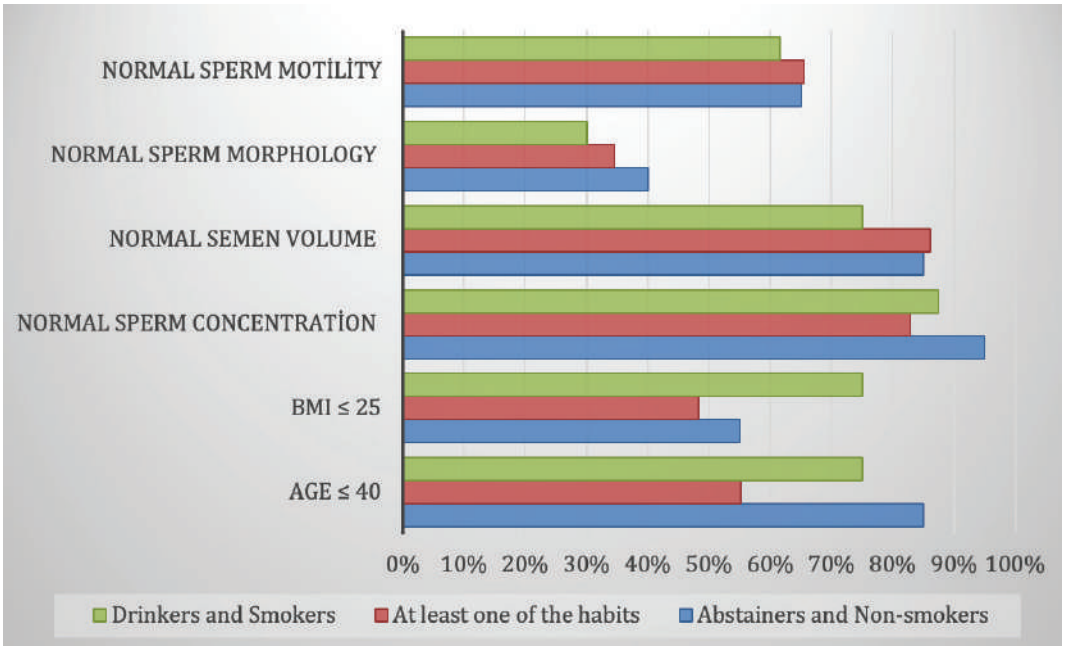


Figure 5. Characteristics of the sample based on positive results of bHCG.

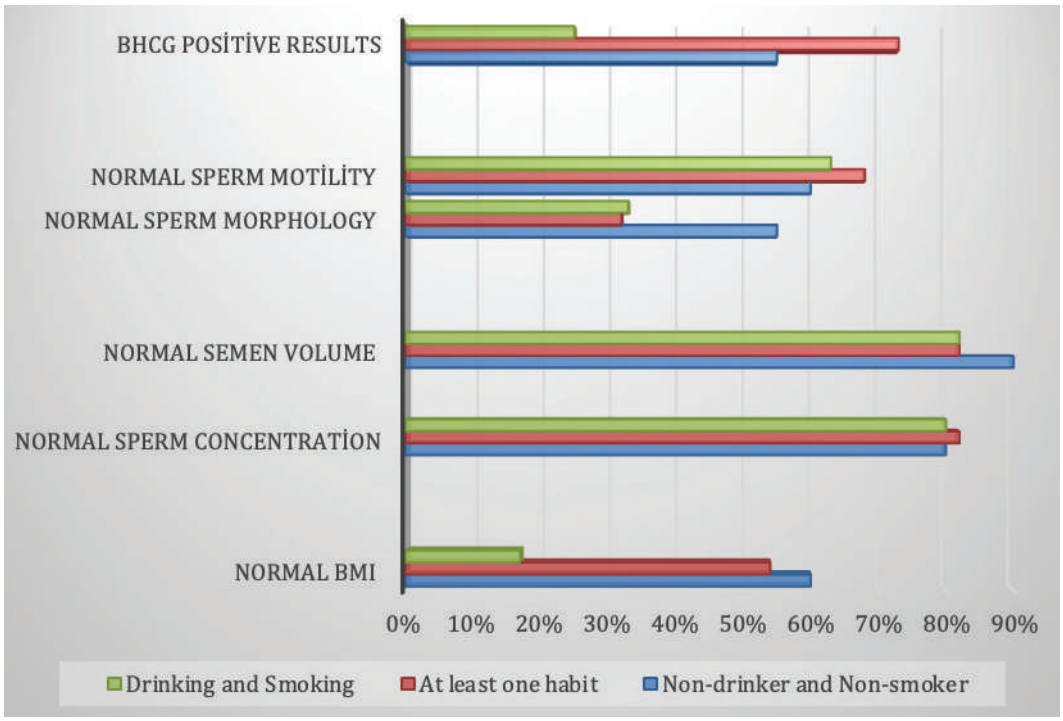


Figure 6. Characteristics of the sample based on the male age (≤40).

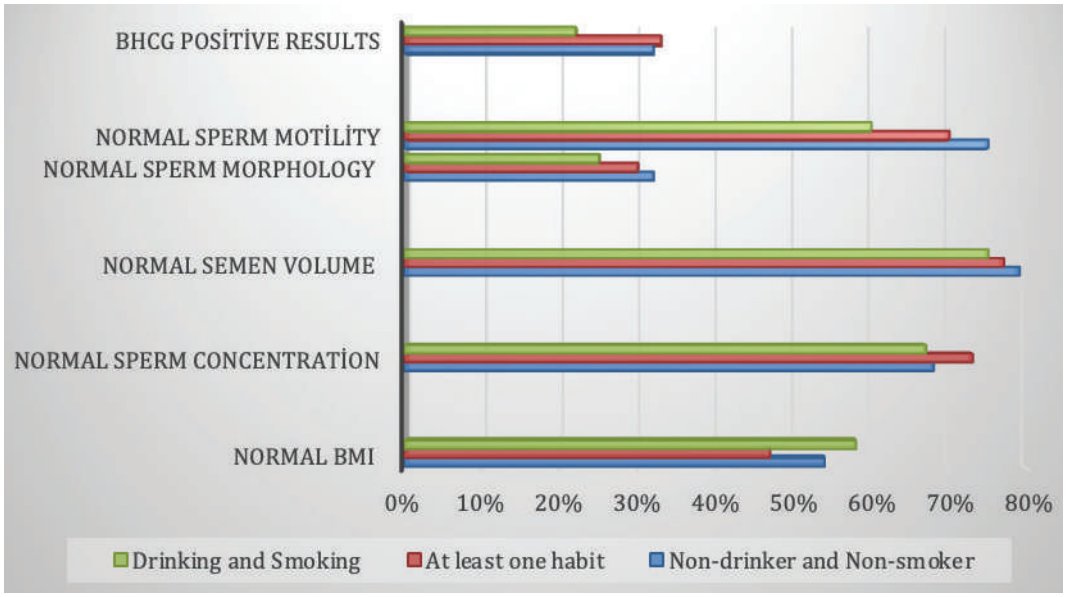


Figure 7. Characteristics of the sample based on the male age (> 40).

RESULTS AND DISCUSSION

The first classification of the data listed in table 4, demonstrates that, in comparison to the non-drinkers and non-smokers group (-D/-S) , the drinkers and smokers group (+D/+S) exhibited substantially decreased morphology , motility, and normal sperm concentration rates by 8.1%, 15.2%, and 14%, correspondingly. Table 4, also shows that there is a significant relation between alcohol and cigarette consumption, and the IVF bHCG positive results, it was 49.9% in non-drinkers and nonsmokers versus 28.6% for drinkers and smokers' group. However, the rates for age groups under 40 were not shown to have significantly correlated with drinking and smoking.

Table 5, describes the second classification of the data, which shows the effect of smoking and alcohol consumption

by males based on the IVF results in the sample. Comparing the percentages of the normal range, the table shows that the percentages of normal sperm concentration, motility, and morphology were significantly lower in the drinking and smoking group than in the nonsmokers and abstainers' group.

The third classification in Table 6, is based on dividing the sample into two groups according to age, less than 40 and more than 40, each group has three categories, (-D/-S; group), (-D/+S OR +D/-S;group), and the third one is (+D/+S;group). After testing each category in both groups, in this situation the percentage of normal sperm volume is significantly lower in the smoking and drinking group for males above 40 years old.

From the three classifications, it was found that cigarettes and alcohol consumption lower sperm concentration, motility, and morphology, while the sperm volume is affected for males above the age of 40, and if the sperm quality is affected that will reduce the possibility for a successful IVF result.

Numerous studies conducted in the last few years have shown the impact of alcohol use on reproductive outcomes like [18-20] and [21], while other research indicates a negative correlation between alcohol use and reproductive outcomes like [22,23] and [24]. Depending on the sample of the population used in this article, table 4 describes the male characteristics based on alcohol and cigarette consumption, the percentage of the normal range is the lowest in the situation of (+D/+S; group), but the results is significant for concentration, motility and morphology, while age and BMI did not show a significant difference. In table 5 , the sample was described by the male characteristics for negative and positive in comparison to the three groups, (+S/+D; group); (−S/−D, group); and (−S/+D or +S/−D; group), respectively, using bHCG. By contrasting the male spermiogram in the positive bHCG (-D/-S; group) with the negative bHCG (+D/+S; group), it was found that the normal percentage of the sperm concentration, motility and morphology, were significantly lower in (+D/+S; group).

According to [25], aging has a cumulatively detrimental effect on semen quality, while, Pasqualotto, et al., 2006 found that the only semen characteristic that seemed to decrease with cigarette consumption was semen volume, and in [26] found that semen volume and sperm motility in a convenience sample of healthy males from a non-clinical context dropped steadily between the ages of 22 and 80. For the

Table 4. Characteristics of the sample based on male Alcohol and cigarette consumption (n=124)

Clinical and Statistical Characteristics	*-D, -S*	*-D, +S or +D,-S*	p_1 *- value*	*+D, +S*	p_2 *- value*
Age ≤ 40	41.7%	41.7%	0.269	42.9%	0.709
Normal BMI	50%	47.9%	0.733	64.3%	0.857
Normal Sperm Concentration	85.4%	83.3%	0.500	71.4%	0.03
Normal Semen Volume	83.3%	85.4%	0.705	71.4%	0.414
Normal Sperm Morphology	43.8%	39.6%	0.850	35.7%	0.03
Normal Sperm Motility	68.8%	60.4%	0.096	53.6%	0.05
bHCG Positive Results	49.9%	60.4%	0.377	28.6%	0.047

BMI: body mass index, -D: abstainer, +D: Drinker, -S: Non-Smoker, +S: Smoker, -D, +S or +D,-S: at least one habit, If p<0.05 then, the data is assumed to be significant, p-values were calculated according to Chi-squared test or T-test, p_1 *- value*: testing -D,-S versus *-D, + S U +D, -S*, p_2 *- value*: testing *-D, -S* versus *+D, +S*.

Table 5. Characteristics of the sample based on the result of bHCG (n=124)

Classifications	Negative bHCG (n=64)			Positive bHCG (n=60)		
	-D, -S	*-D, +S or +D,-S*	*+D, +S*	*-D, -S*	*-D, +S or +D,-S*	*+D, +S*
Age ≤ 40	32.1%	21%	40%	85%	55.2%	75%
Normal BMI	50%	21%	62.5%	55%	48.3%	75%
Normal Sperm Concentration	88.6%*	84.2%	81.3%	95%*	82.8%	87.5%*
Normal Semen Volume	82.1%	84.2%	75%	85%	86.2%	75%
Normal Sperm Morphology	25%*	21%	20%	40%*	34.5%	30%*
Normal Sperm Motility	71.4%*	52.6%	50%	65%*	65.5%	61.5%*

BMI: Body mass index; -D: Abstainer; +D: Drinker; -S: Non-smoker; +S: Smoker; -D,+S or +D,-S: At least one habit; *p-value is statistically significant at the 0.05 level.

Table 6. Characteristics of the sample based on the male age

Attributes	Age ≤ 40 54			Age >40 70		
	-D, -S 37%	*-D, +S or +D,-S* 41%	*+D, +S* 22%	*-D, -S* 40%	*-D, +S or +D,-S* 43%	*+D, +S* 17%
Normal BMI	60%	54%	17%	54%	47%	58%
Normal Sperm Concentration	80%	82%	80%	68%	73%	67%
Normal Semen Volume	90%	82%	82%*	79%	77%	75%*
Normal Sperm Morphology	55%	32%	33%	32%	30%	25%
Normal Sperm Motility	60%	68%	63%	75%	70%	60%
bHCG Positive Results	55%	73%	25%	32%	33%	22%

BMI: Body mass index; -D: abstainer; +D: Drinker; -S: Non-Smoker; +S: Smoker; -D,+S or +D,-S; At least one habit; *p-value is statistically significant at the 0.05 level.

sample classification according to age in table 6, this study shows that the only significant effect of age associated with drinking and smoking was in the normal range of the sperm volume, which was lower for males older than 40 and had the two habits of drinking and smoking. In IVF research, mathematical modeling has emerged as a powerful tool that provides a framework for analyzing and understanding the complex interplay of factors that affect IVF outcomes. When clinical studies and laboratory tests' data are combined with mathematical models, the dynamics of in vitro fertilization (IVF) operations can be replicated [27] and modeling data relted to smoking effects also discussed in [28]. In vitro fertilization mathematical models frequently include statistics, differential equations, and optimization techniques as their basic building blocks. As scientific knowledge advances and new data is incorporated, these models are continuously updated and modified. They help researchers and practitioners make evidence-based decisions, which improves the effectiveness and success rates of IVF treatments while lowering risks and expenses. Several studies measuring the likelihood of follicle fertilization were conducted utilizing fuzzy matrix theory [29].

CONCLUSION

The aim of this study was to evaluate the influence of male smoking and alcohol consumption on the results of In Vitro Fertilization procedures that included young, fertile oocyte donors in Northern Cyprus, this contributes to the work's distinctiveness by illustrating how the daily routine of the male may impact the region's fertility results. The results of our research offer strong evidence that the lifestyle choices of men have a substantial impact on the quality of their sperm and the success rates of In Vitro Fertilization. The impact of a single drinking or smoking behavior on the outcomes of in vitro fertilization was not well supported by the data in this investigation. The analysis revealed that men who smoked and consumed alcohol had significantly lower percentages of normal sperm concentration, motility, and morphology compared to their non-smoking and non-drinking counterparts, while the normal sperm volume percentage was significantly lower when the age is greater than 40 in drinking and smoking group. A strong association was observed between these negative sperm parameters and reduced IVF success rates, as indicated by lower beta-human chorionic gonadotropin -positive results in the smoking and alcohol consumption group. These findings confirm the previous research results highlighting the detrimental effects of smoking and alcohol on male fertility. They emphasize the crucial role of counseling for male partners undergoing of In Vitro Fertilization treatments. If they were more educated about the potential negative consequences of these habits on their sperm health, they could possibly make more conscious decisions about this. In addition to that, our study adds valuable input to the evolving library of information on male lifestyle factors and their impact on of In Vitro Fertilization outcomes in specific populations. That would help healthcare professionals to provide tailored counseling and interventions to optimize fertility potential while improving the chances of successful of In Vitro Fertilization pregnancy.

Recommendation

In addition to considering other factors that may influence the outcome of fertilization, it is crucial to keep in mind that individuals respond differently to aging, drinking, and smoking. To gain a deeper understanding, more meticulously organized research is needed, ideally on a wider range of populations. Using a greater number of participants and ongoing evaluations by gathering information from several IVF clinics in Northern Cyprus will be the following stage in this paper's development. Furthermore, this research will be enhanced and demonstrate the substantial impact on clinical practices and public health by taking into account the differences in lifestyle, cultural customs, and healthcare-related behaviors.

ACKNOWLEDGMENTS

We would like to thank members of the Near East University Hospital Microbiology Laboratory and Mathematics Research Center.

AUTHORSHIP CONTRIBUTIONS

T,B.: Conceptualization, Methodology, Formal analysis, Writing-original draft, Writing review editing.

M.G.: Conceptualization, Methodology, Formal analysis, Software, Visualization, Writing an original draft,

B.K.: Formal analysis, Software, Visualization, Writing-review editing.

E.H.: Methodology, Formal analysis, Visualization, Methodology,

M.F: Methodology, Formal analysis, Software, Formatting, Writing review, editing.

Ethics approval and consent to participate

DATA AVAILABILITY STATEMENT

The authors confirm that the data that supports the findings of this study are available within the article. Raw

data that support the finding of this study are available from the corresponding author, upon reasonable request.

CONFLICT OF INTEREST

The author declared no potential conflicts of interest with respect to the research, authorship, and/or publication of this article.

ETHICS

The study was approved by the members of the Faculty of Medicine, Department of Medical Genetics, Near East University, Center of Excellent and Mathematics research center. All methods were carried out according to relevant guidelines and regulations.

STATEMENT ON THE USE OF ARTIFICIAL INTELLIGENCE

Artificial intelligence was not used in the preparation of the article.

REFERENCES

[1] Greil AL, Slauson-Blevins K, McQuillan J. The experience of infertility: a review of recent literature. Sociol Health Illn 2010;32:140–162. [CrossRef]

[2] Shen X, Xiao T, Han W, Ye H, Zhang Y, Huang G. The bibliometric analysis of studies on intracytoplasmic sperm injection from 2002 to 2021. Front Endocrinol 2023;14:1109623. [CrossRef]

[3] de Kretser DM, Loveland KL, Meinhardt A, Simorangkir D, Wreford N. Spermatogenesis. Hum Reprod 1998;13:1–8. [CrossRef]

[4] Gilbert SF. Developmental biology. 6th ed. Sunderland (MA): Sinauer Associates; 2000. Oogenesis. Available from: https://www.ncbi.nlm.nih.gov/books/NBK10008/.

[5] Klonoff-Cohen H. Female and male lifestyle habits and IVF: what is known and unknown. Hum Reprod Update 2005;11:180–204. [CrossRef]

[6] Zenzes MT. Smoking and reproduction: gene damage to human gametes and embryos. Hum Reprod Update 2000;6:122–131. [CrossRef]

[7] Rubes J, Lowe X, Moore D, Perreault S, Slott V, Evenson D, et al. Smoking cigarettes is associated with increased sperm disomy in teenage men. Fertil Steril 1998;70:715–723. [CrossRef]

[8] Wallach EE, Hughes EG, Brennan BG. Does cigarette smoking impair natural or assisted fecundity? Fertil Steril 1996;66:679–689. [CrossRef]

[9] Vine MF. Smoking and male reproduction: a review. Int J Androl 1996;19:323–337. [CrossRef]

[10] Günerhan H, Kaabar M, Celik E. Novel analytical and approximate-analytical methods for solving the nonlinear fractional smoking mathematical model. Sigma J Eng Nat Sci 2022;41:331–343.

[11] Klonoff-Cohen H, Natarajan L, Marrs R, Yee B. Effects of female and male smoking on success rates of IVF and gamete intra-Fallopian transfer. Hum Reprod 2001;16:1382–1390. [CrossRef]

[12] Hruska KS, Furth PA, Seifer DB, Sharara FI, Flaws JA. Environmental factors in infertility. Clin Obstet Gynecol 2000;43:821–829. [CrossRef]

[13] Eisenberg ML, Esteves SC, Lamb DJ, Hotaling JM, Giwercman A, Hwang K, et al. Male infertility. Nat Rev Dis Primers 2023;9:49. [CrossRef]

[14] Firns S, Cruzat VF, Keane KN, Joesbury KA, Lee AH, Newsholme P, et al. The effect of cigarette smoking, alcohol consumption and fruit and vegetable consumption on IVF outcomes: a review and presentation of original data. Reprod Biol Endocrinol 2015;13:1–13. [CrossRef]

[15] Farman M, Ahmad A, Akgül A, Saleem MU, Naeem M, Baleanu D. Epidemiological analysis of the coronavirus disease outbreak with random effects. Comput Mater Contin 2021;67:3215–3227. [CrossRef]

[16] Hall M, Richardson T. Basic statistics for comparing categorical data from 2 or more groups. Hosp Pediatr 2016;6:383–385. [CrossRef]

[17] Sunder M, Leslie SW. Semen analysis. In: StatPearls [Internet]. StatPearls Publishing; 2022.

[18] Rossi BV, Berry KF, Hornstein MD, Cramer DW, Ehrlich S, Missmer SA. Effect of alcohol consumption on in vitro fertilization. Obstet Gynecol 2011;117:136. [CrossRef]

[19] Sharma R, Biedenharn KR, Fedor JM, Agarwal A. Lifestyle factors and reproductive health: taking control of your fertility. Reprod Biol Endocrinol 2013;11:1–15. [CrossRef]

[20] Condorelli RA, Calogero AE, Vicari E, La Vignera S. Chronic consumption of alcohol and sperm parameters: our experience and the main evidences. Andrologia 2015;47:368–379. [CrossRef]

[21] Silva JV, Cruz D, Gomes M, Correia BR, Freitas MJ, Sousa L, et al. Study on the short-term effects of increased alcohol and cigarette consumption in healthy young men's seminal quality. Sci Rep 2017;7:45457. [CrossRef]

[22] De Jong AME, Menkveld R, Lens JW, Nienhuis SE, Rhemrev JPT. Effect of alcohol intake and cigarette smoking on sperm parameters and pregnancy. Andrologia 2014;46:112–117. [CrossRef]

[23] Karmon AE, Toth TL, Chiu YH, Gaskins AJ, Tanrikut C, Wright DL, et al. Male caffeine and alcohol intake in relation to semen parameters and in vitro fertilization outcomes among fertility patients. Andrology 2017;5:354–361. [CrossRef]

[24] Mínguez-Alarcón L, Chavarro JE, Gaskins AJ. Caffeine, alcohol, smoking, and reproductive outcomes among couples undergoing assisted reproductive technology treatments. Fertil Steril 2018;110:587–592. [CrossRef]

[25] Ramírez N, Estofán G, Tissera A, Molina R, Luque EM, Torres PJ, et al. Do aging, drinking, and having unhealthy weight have a synergistic impact on semen quality? J Assist Reprod Genet 2021;38:2985–2994. [CrossRef]

[26] Eskenazi B, Wyrobek AJ, Sloter E, Kidd SA, Moore L, Young S, et al. The association of age and semen quality in healthy men. Hum Reprod 2003;18:447–454. [CrossRef]

[27] Güvenir HA, Misirli G, Dilbaz S, Ozdegirmenci O, Demir B, Dilbaz B. Estimating the chance of success in IVF treatment using a ranking algorithm. Med Biol Eng Comput 2015;53:911–920. [CrossRef]

[28] Jan R, Yüzbaşı Ş, Attaullah A, Jawad M, Jan A. Fractional derivative analysis of asthma with the effect of environmental factors. Sigma J Eng Nat Sci 2024;42:177–188. [CrossRef]

[29] Raich VV, Gangele S, Verma N. Fuzzy matrix theory and infertility management – measures follicle fertilization possibility. Int J Fuzzy Math Arch 2016;11:79–84. [CrossRef]

Sigma Journal of Engineering and Natural Sciences
Web page info: https://sigma.yildiz.edu.tr
DOI: 10.14744/sigma.2024.00130

Research Article

Evaluation of health care systems using supervised and unsupervised machine learning approaches

Canan BULUT[1], Tuğba SÖNAL[2], Dilek KOLCA[3], Fatih TARLAK[4,*]

[1]Department of Medical Services and Techniques, Istanbul Kultur University, Istanbul, 34191, Türkiye
[2]Health Ministry of Turkey, Ataşehir District Health Directorate, Istanbul, 34100, Türkiye
[3]Department of Health Management, Istinye University, Istanbul, 34010, Türkiye
[4]Deparment of Bioengineering, Gebze Technical University, Gebze, 41400, Türkiye

ARTICLE INFO

Article history
Received: 07 June 2024
Revised: 21 August 2024
Accepted: 22 October 2024

Keywords:
Classification; Clustering; Health Indicators; Machine Learning

ABSTRACT

Both large- and small-scale health system evaluations are crucial. On a larger scale, it facilitates cross-national comparisons, monitors the advancement of global health objectives, aids in the formulation of public health policy, and ensures efficient use of resources. On a smaller scale, it helps countries figure out how well their health programs are working, see health trends, and find areas that need improvement. A health system is made up of a lot of different people and things, like organizations, institutions, resources, patients, and people who might become patients. All of these people and things work together to give health services to a group of people. This research gathered health indicators from 30 OECD (Organization for Economic Cooperation and Development) nations from 2006 to 2020 and evaluated them through both supervised and unsupervised machine learning methodologies. The findings, demonstrating high accuracy in machine learning methods (exceeding 93.3%), indicate that financial models alone are inadequate for evaluating healthcare systems. The complexity and multidimensional nature of these systems necessitate the inclusion of health indicators in the evaluation process. Even with enough money, people may not get the health outcomes they want if there aren't health policies that are based on the basic ideas of fairness, quality of service delivery, and efficiency that can be put into action. This study employs unsupervised machine learning techniques to analyze health indicators. This helps policymakers, researchers, and other people who are interested in healthcare systems learn more about their strengths and weaknesses. These insights can help policymakers make decisions, make it easier to compare medical systems in different countries, and help healthcare systems get better all the time.

Cite this article as: Bulut C, Sönal T, Kolca D, Tarlak F. Evaluation of health care systems using supervised and unsupervised machine learning approaches. Sigma J Eng Nat Sci 2025;43(6):2174–2185.

***Corresponding author.**
*E-mail address: ftarlak@gtu.edu.tr

This paper was recommended for publication in revised form by Editor-in-Chief Ahmet Selim Dalkilic

Published by Yıldız Technical University Press, İstanbul, Turkey
© Author. This is an open access article under the CC BY-NC license (http://creativecommons.org/licenses/by-nc/4.0/).

INTRODUCTION

Statistics is a basic tool that helps us draw meaningful conclusions from data, aids in scientific discoveries, helps us make good decisions, and gives us answers to many problems. Health statistics is a specialized subdiscipline that deals with analyzing, interpreting, and summarizing health data [1]. Health statistics are important for figuring out how healthy people and communities are, how common diseases are, how well health services work, and how health policies affect people. These numbers include a variety of quantitative tools used to study health problems, from big epidemiological studies to clinical trials.

When looking into complicated things like health statistics, comparisons and typologies can help you understand them better. Typologies facilitate the simplification of complex empirical realities, thereby enabling systematic analysis of similarities, variations, and the identification of patterns. Machine learning techniques are essential analytical instruments that enable the examination and interpretation of high-dimensional data [2, 3]. There are two main types of machine learning: supervised learning and unsupervised learning. When you use supervised machine learning, you train a model on labeled data that has known outcomes. When you use unsupervised machine learning, you find patterns and relationships in unlabeled data that don't have any known outcomes.

Supervised machine learning is a kind of learning in which the algorithm learns from labeled data, which means that the input data is matched with the right output labels. The goal of supervised learning is to teach the algorithm how to connect inputs to outputs so that it can make accurate predictions or classifications on data it hasn't seen before. In supervised machine learning, classification is a basic idea. It means using algorithms to put input instances into one of several pre-defined groups. Random Forest is a popular supervised machine learning algorithm that is well-known for being good at classification tasks [4].

On the other hand, unsupervised learning is a type of machine learning in which the algorithm looks for patterns, structures, or relationships in the data without any clear labeled output. It finds hidden patterns or structures in the data that is being input. Clustering algorithms are a type of unsupervised machine learning that puts similar data points into groups called clusters. These algorithms help find patterns or groups in a dataset without needing to set class labels ahead of time. K-Means clustering is a common unsupervised machine learning algorithm that divides a dataset into a certain number of groups. It works best when you already know how many clusters there are. K-Means puts each data point in the cluster that is closest to it and then keeps making these assignments better until the sum of the squared distances between data points and their centroids is as small as possible [5].

Standardized indicators are necessary to evaluate the health status of a particular population. These indicators, derived from health records and statistics of individuals and communities, are used to assess current conditions and make predictions about the future. Keeping accurate records and statistics is crucial to seeing things as they are and making wise choices.

Since its founding in 1948, the World Health Organization (WHO) has been a leader in creating health metrics and collecting and analyzing data that can be used to compare different countries [6]. In the 1960s, there was a push to work with other countries around the world and make health indicators and data more consistent. A lot of success has been made by the World Health Organization (WHO) in making rules and standards for gathering and analyzing health data that can be used to compare data from different countries. What are "health indicators"? They were made by the World Health Organization (WHO) and show many different parts of health. Some of these factors are the number of sick people, how well the health system is working, the things that affect health, and the trends in the health of the community. The purpose of these indicators is to help public health officials make choices and decide how to spend their money and time, and to allow people to compare countries. They help countries and international health groups track and rate the success of their health programs, identify health trends, and focus on areas that need work or improvement [7]. These factors are categorized by the World Health Organization (WHO) to help countries make fair decisions:

- **Health Status Indicators:** These show how healthy a person or society is overall by looking at things like the number of diseases, how easy it is to get medical care, and how long people generally live.
- **Risk Factors:** The World Health Organization (WHO) has created a number of signs and tools to help find, track, and protect public health when it comes to health-related risk factors. These things are very important for stopping the spread of diseases and making people healthier.
- **Service Coverage:** The World Health Organization (WHO) has created service coverage indicators to measure how easy it is to get healthcare services and how well they work. These indicators are used to keep an eye on health services and make them work better [7].

The list of health indicators is periodically updated to align with current health priorities. These indicators serve as a crucial tool in assessing the health status of populations, identifying disparities, and guiding evidence-based decision-making at local, national, and international levels. Recent advancements in the field of mathematical analysis have significantly contributed to the development of more accurate and efficient methods for approximating complex functions, which are highly beneficial for evaluating health systems [8-14]. While the literature includes some articles focused on evaluating healthcare systems [15-21], to the best of our knowledge, there are no published works that compare the evaluation performance of supervised and

unsupervised machine learning approaches in assessing healthcare indicators of countries. The aim of this study is to evaluate the health systems of 30 OECD countries based on 21 healthcare indicators from 2006 to 2020 using both supervised and unsupervised machine learning approaches.

MATERIAL AND METHODS

The work was done in three main separate steps: i) the healthcare indicators for OECD countries from 2006 to 2020 were gathered, ii) data processing (standardization) was done in Matlab 8.3.0.532 (R2014a) software (MathWorks Inc., Natick, MA, USA), and iii) the evaluation of health care systems was done employing machine learning methodology: the supervised classification and unsupervised clustering. The flowchart in Figure 1 outlines the main steps undertaken in this study. The following sections offer comprehensive explanations of each stage involved in the research process.

DATA COLLECTION

Traditionally, the classification of health systems in countries has often relied on economic-based structures in the literature. However, given the unique nature of healthcare services, which differ significantly from other types of services, a focus on fairness-oriented maximum accessibility becomes more crucial than merely ensuring equal distribution. Evaluations based on health indicators—the outputs of provided healthcare services—allow for more valuable and accurate predictions for future assessments. For this study, health status indicators, risk factors, and service coverage indicators from the years 2006 to 2020 for 30 OECD countries were utilized. Health indicator data were collected from the World Data Bank, Eurostat, and WHO databases. To ensure consistency and accuracy, the data were standardized before analysis. This step put all data on the same scale, usually through normalization or z-score standardization, so that differences in measurement units did not affect the results. The dataset covers indicators such as adolescent birth rate, total fertility rate, cancer incidence by type, tuberculosis incidence, cardiovascular death rate, rates of cancer, diabetes, or chronic respiratory diseases in people aged 30 to 70, maternal mortality, death rate from road traffic injuries, under-five mortality, infant mortality, life expectancy at birth, stillbirth rate, and neonatal mortality. The risk factor indicators included in the study are: tobacco use among persons aged 18+ years, total alcohol per capita (age 15+) consumption, prevalence of overweight and obesity in adults, proportion of the population using safely managed sanitation services, air pollution levels in cities, and prevalence of intimate partner violence. The service coverage indicators included were: the coverage rate of vaccination in the national program for vaccines such as diphtheria, tetanus, and pertussis, coverage rate of vaccination for measles, and tuberculosis case detection rate. All the indicators used, along with their codifications and explanations, are detailed in Table 1.

Machine Learning Classification and Evaluation

Machine learning classification trains models to classify data into preset classes. This procedure uses algorithms and statistics to learn patterns and relationships from labeled training data and to predict or label new data. This study classified OECD countries using financial models using decision tree regression (DTR) and support vector regression (SVR) (Fig. 2). Cross-validation tuned the DTR and SVR hyperparameters to optimize model performance. In this study it is selected DTR for its ability to handle complex, nonlinear interactions in the data, and SVR for its ability to handle high-dimensional data and reduce prediction error. These techniques have been successful in effectively

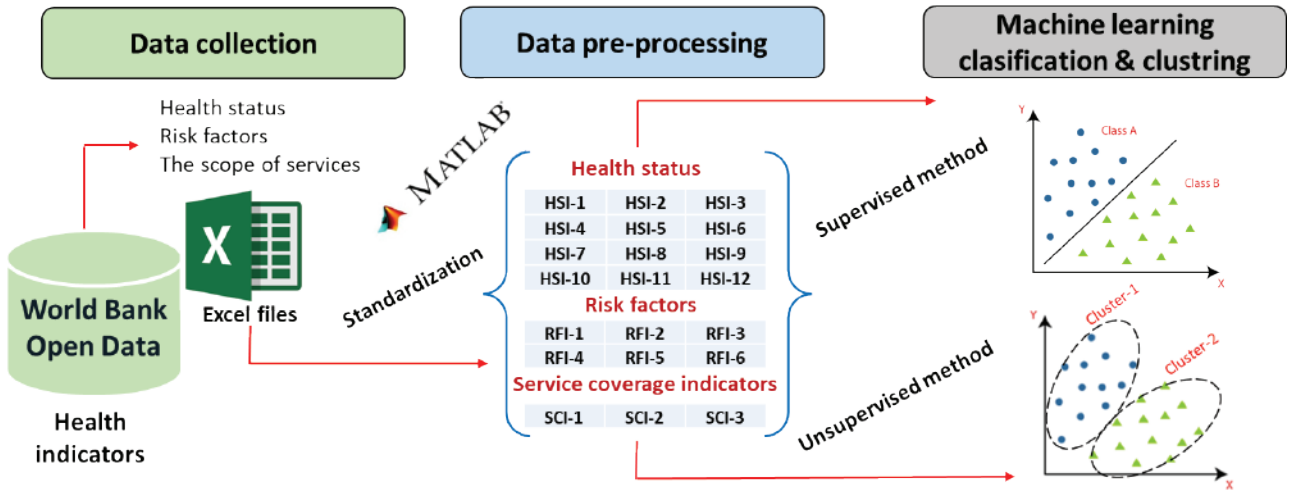


Figure 1. The flow chart outlining the main steps followed in the present study.

Table 1. The used health indicators with their explanations

Code	Health indicators	Explanation
HSI-1	Health status indicators	Adolescent birth rate
HSI-2		Total fertility rate
HSI-3		Cancer incidence rate, by type of cancer
HSI-4		Tuberculosis incidence rate
HSI-5		Rate of cardiovascular deaths, diseases, cancer, diabetes, or chronic respiratory diseases between the ages of 30 and 70
HSI-6		Maternal mortality rate
HSI-7		Death rate due to road traffic injuries
HSI-8		Under-five mortality rate
HSI-9		Infant mortality rate
HSI-10		Life expectancy at birth
HSI-11		Stillbirth rate
HSI-12		Neonatal mortality rate
RFI-1	Risk factors indicators	Tobacco use among persons aged 18+ years
RFI-2		Total alcohol per capita (age 15+) consumption
RFI-3		Overweight and obesity in adults' prevalence
RFI-4		Proportion of population using safely managed sanitation services
RFI-5		Air pollution levels in cities
RFI-6		Intimate partner violence prevalence
SCI-1	Service coverage indicators	Coverage rate of vaccination compared to vaccination for each vaccine (diphtheria, tetanus, pertussis) in the national program
SCI-2		Coverage rate of vaccination compared to vaccination for each vaccine (measles) in the national program
SCI-3		Tuberculosis case detection rate

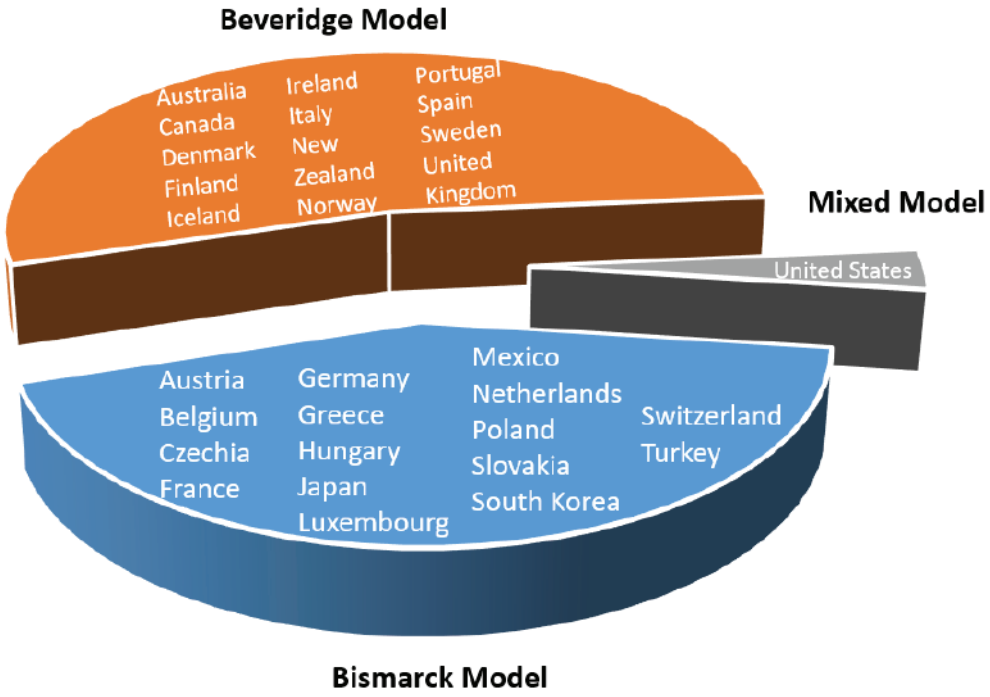


Figure 2. Classification of health care systems based on financial models.

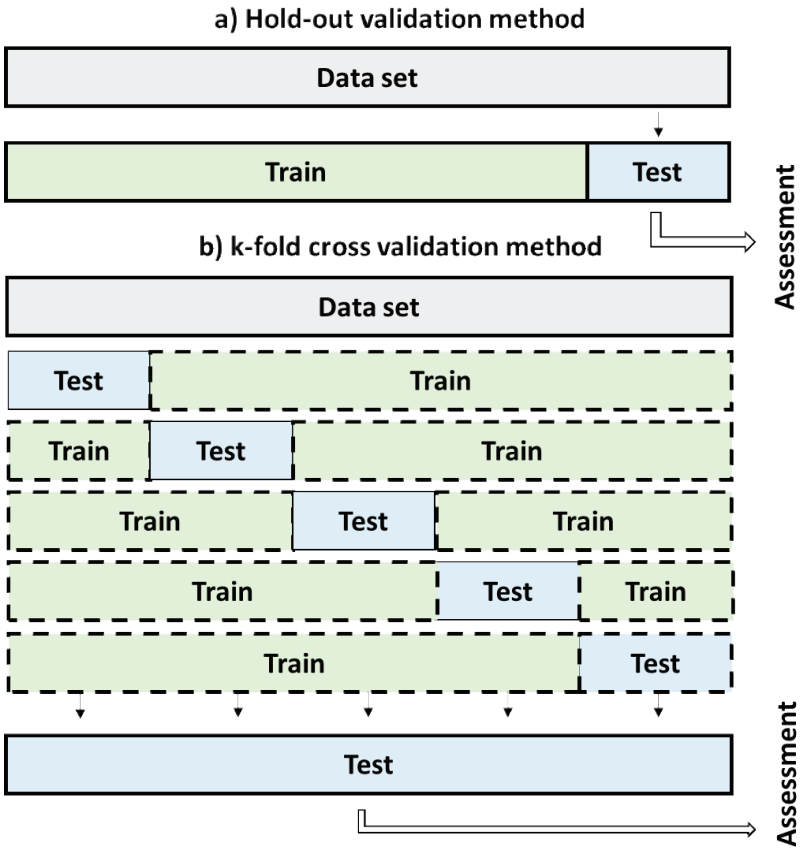


Figure 3. The schematic illustration of validation methods of a) hold-out validation and b) k-fold validation.

capturing the complex dynamics of financial data in healthcare systems.

Hold-out validation and k-fold cross-validation are two validation methods that are often used in machine learning. The dataset is split into two parts for hold-out validation: a training set and a test set [22–24]. The model is trained on the training set, and its performance is then evaluated on the test set. The dataset is split into k equal parts for k-fold cross-validation. One part is used for testing and the other parts are used for training in each iteration. To see how well the model works on the whole dataset, the results from all iterations are put together. Cross-validation is generally considered more unbiased, as it uses multiple partitions for testing, whereas hold-out validation can introduce bias due to random splitting. This study utilized a 10-fold cross-validation method, as illustrated in Figure 3.

By using a confusion matrix, which comprehensively divides the model's predictions into true positives, true negatives, false positives, and false negatives, the effectiveness of the proposed model on classification problems can be evaluated [18–20]. The confusion matrix facilitates the calculation of multiple performance metrics, such as sensitivity, recall, F1 score, and specificity, each providing insight into different aspects of the model's accuracy. Additionally, the average accuracy—which is determined by dividing the number of correctly categorized cases by the total number of examples—can be used to characterize the classifier's overall performance. This is represented mathematically by Equation (1) [25]:

$$Average\ accuracy = \frac{\left(\sum_{i=1}^{l} \frac{tp_i + tn_i}{tp_i + fn_i + fp_i + tn_i}\right)}{l} \quad (1)$$

where tp_i is the number true positive class, tn_i is the number true negative class, fp_i is the number false positive class, fn_i is the number false negative class, l is the number of evaluated classes.

RESULTS AND DISCUSSION

In this study, the burn images were trained using the deep learning algorithms GoogleNet, ResNet-50, and Inception-v3, which consist of 22, 50, and 48 layers, respectively, within the Matlab software environment. The training dataset comprised a total of 1294 burn images, broken down into 561 first-degree, 275 second-degree, and 458 third-degree burn images [26, 27].

For societies, resources are limited while needs are unlimited. The ability to meet maximum needs with these limited resources relies on accurate current situation analysis and future predictions. The situation is no different in healthcare services. Both the human resources capable of providing healthcare services and the medical equipment used in healthcare are constrained, and theories are generated to determine how to achieve maximum benefit, forming the foundation of healthcare systems [28].

The proper and logical interpretation of health indicators, which are tangible outputs of the healthcare systems used by countries, enhances the success of future healthcare policies by optimizing the use of limited resources allocated to healthcare services [29]. This allows for the optimal utilization of scarce resources. In this study, classification and interpretation are intended to be carried out based on health indica-tors from 2006 to 2020 for 30 OECD countries.

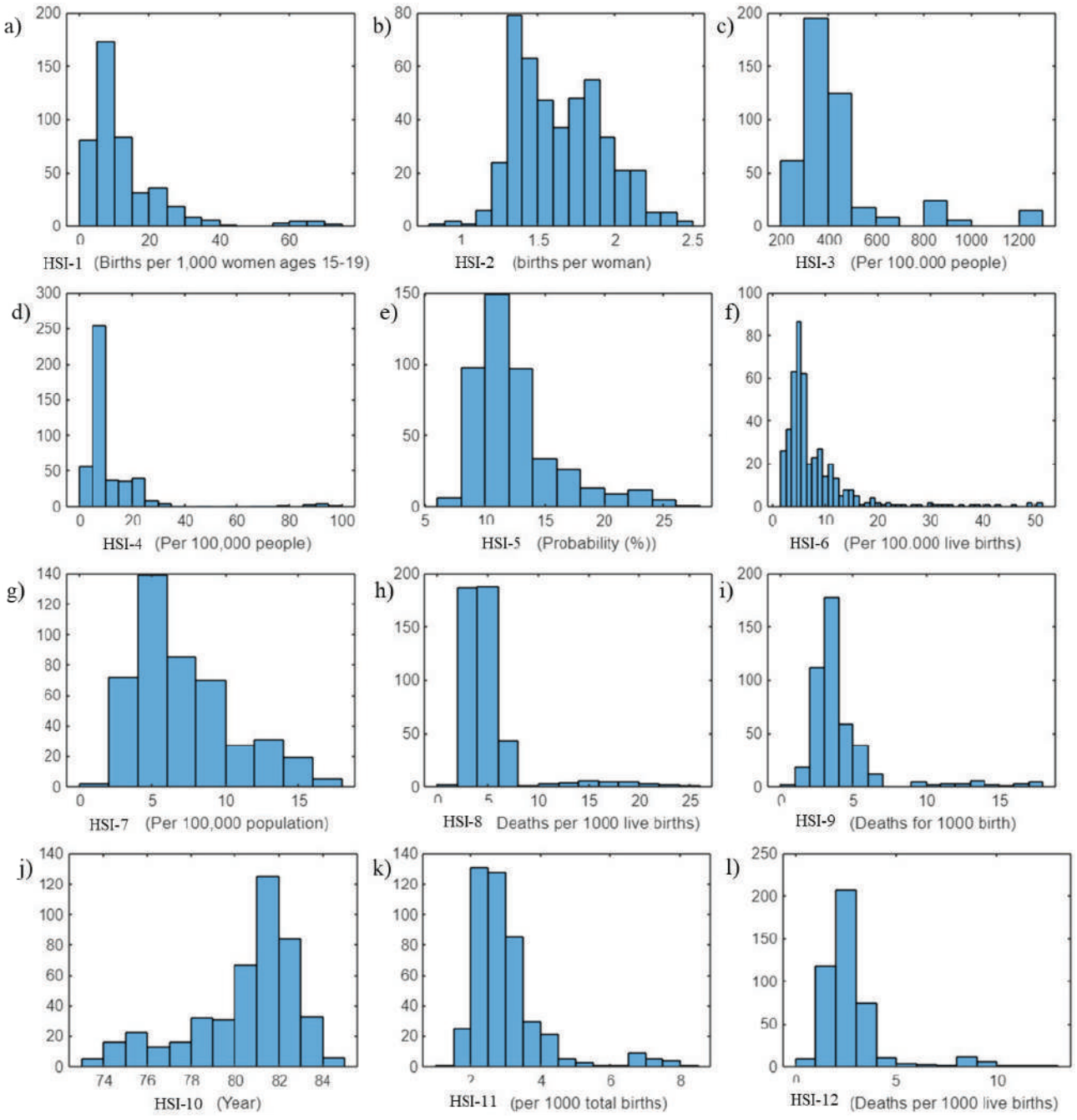


Figure 4. Histograms depicting the variables are shown for: a) HIS-1, b) HIS-2, c) HIS-3, d) HIS-4, e) HIS-5, f) HIS-6, g) HIS-7, h) HIS-8, j) HIS-9, j) HIS-10, k) HIS-11and l) HIS-12.

From the basic health indicators, statistics on birth (adolescent birth rate, total fertility rate), diseases (cancer incidence rate by type of cancer, tuberculosis incidence rate), causes of death (rate of cardiovascular deaths, deaths due to cancer, diabetes, or chronic respiratory diseases between the ages of 30 and 70, maternal mortality rate, death rate due to road traffic injuries), and age and gender-specific mortality (under-five mortality rate, infant mortality rate, life expectancy at birth, stillbirth rate, neonatal mortality rate) have been used as health status indicators (Fig. 4).

In the study, from the basic health indicators; non-communicable diseases (tobacco use among persons aged 18+ years, total alcohol per capita (age 15+) consumption, overweight and obesity in adults' prevalence), environmental risk factors (proportion of population using safely managed sanitation services, air pollution levels in cities), injuries (intimate partner violence prevalence) statistics were used as risk factor indicators (Fig. 5).

The study utilized basic health indicators, specifically focusing on vaccination coverage rates for each vaccine included in the national program, such as diphtheria, tetanus, pertussis, and measles. Additionally, the tuberculosis case detection rate was employed as a service coverage indicator, as illustrated in Figure 6.

Decision trees are adaptable and widely used categorization techniques. They work by iteratively splitting data into subsets based on the values of input features. These splits are determined by the algorithm's parameters to optimize information gain or Gini impurity. Decision trees are understandable and facilitate a simple depiction of the

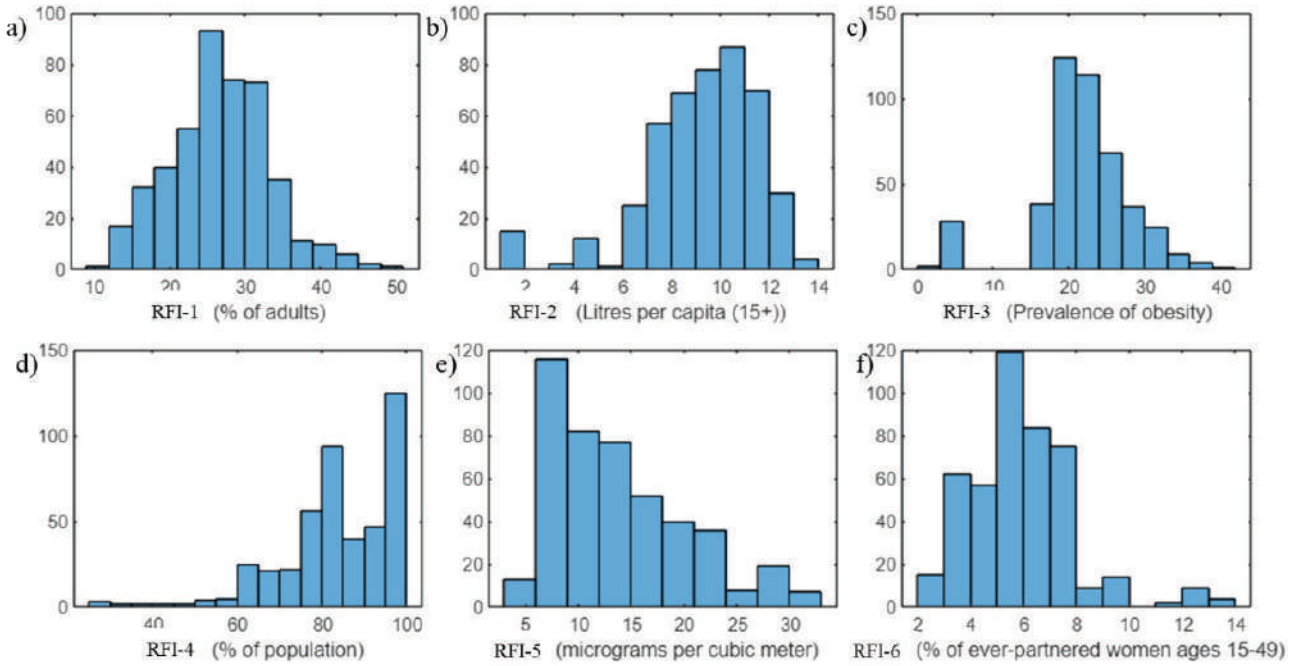


Figure 5. Histograms depicting the variables are shown for: a) RFI-1, b) RFI-2, c) RFI-3, d) RFI-4, e) RFI-5 and f) RFI-6.

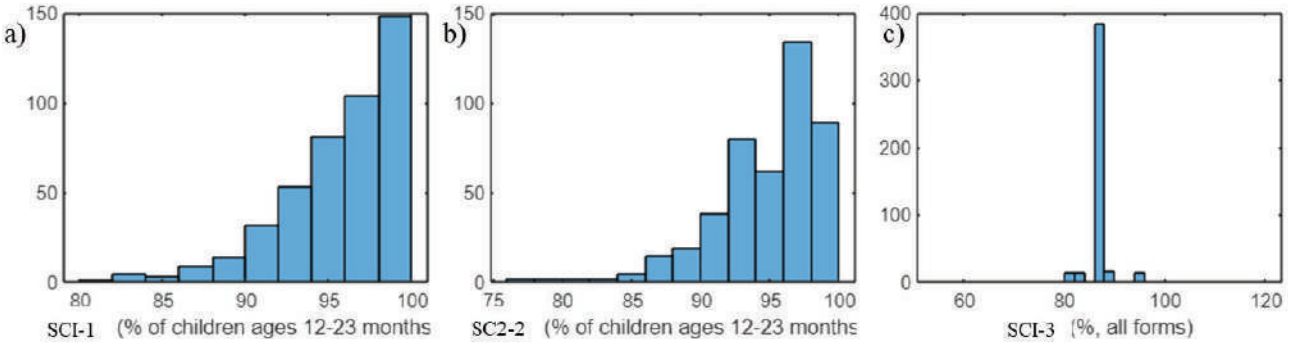


Figure 6. Histograms depicting the variables are shown for: a) SCI-1, b) SCI-2 and c) SCI-3.

decision-making process. Their ability to handle both qualitative and numerical data makes them suitable for many applications.

Support Vector Regression is an effective method used for classification and regression applications. It is highly effective for regression tasks that aim to predict continuous values. SVR aims to identify a hyperplane that best accommodates the data while reducing the margin of error. It determines the support vectors, which are the data points closest to the hyperplane. SVR uses a kernel function to map the data to a higher-dimensional space, enabling the identification of nonlinear correlations between variables.

Findings obtained from the supervised machine learning analysis results; when a classification is made based on health indicators, a similar result to the classification in the literature known as the beveridge, bismarck, and mixed model classification is obtained (Fig. 7). However, when the trends of countries under this classification are examined, changes in classifications are observed parallel to other developments in the OECD countries [30, 31].

As seen in Figure 7, the financial-based models (Beveridge, Bismarck, and mixed) used for classifying the healthcare systems of OECD countries can be simulated with an accuracy of 93.3% using the support vector machine algorithm and 96.7% using the decision tree algorithm. While these high accuracies highlight the importance of financial models in understanding and classifying healthcare systems, they are insufficient to capture the full complexity of these systems. Health systems are influenced by a wide range of stakeholders, including government agencies, private institutions, healthcare providers, and patients, and are characterized by services that cannot be delayed or replaced. Therefore, combining health indicator-based models with financial-based models provides a more comprehensive assessment. Health systems are multidimensional and shaped by economic, social, cultural, technological, and human factors. Financial models offer valuable insights into resource allocation and economic sustainability, but they fail to account for critical factors such as health outcomes, quality of care, equity, and patient satisfaction. Therefore, health policies and system designs must adopt a multidisciplinary approach that integrates financial analysis with public health, sociology, technology, and ethics to develop strategies that ensure health systems are economically sustainable and can provide high-quality, equitable, and accessible care to all.

While classifying countries' healthcare systems according to financing-based approaches might provide a high level of accuracy [32], to reveal the interconnections among these complex and multidimensional healthcare services,

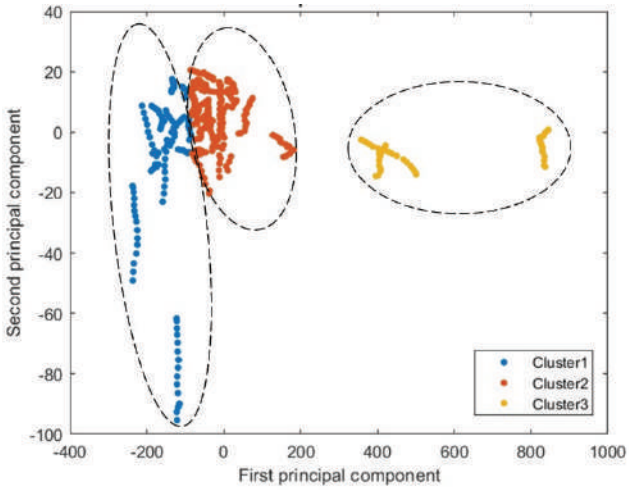


Figure 8. Cluster analysis of healthcare systems depending on the first two principal components using k-means clustering method.

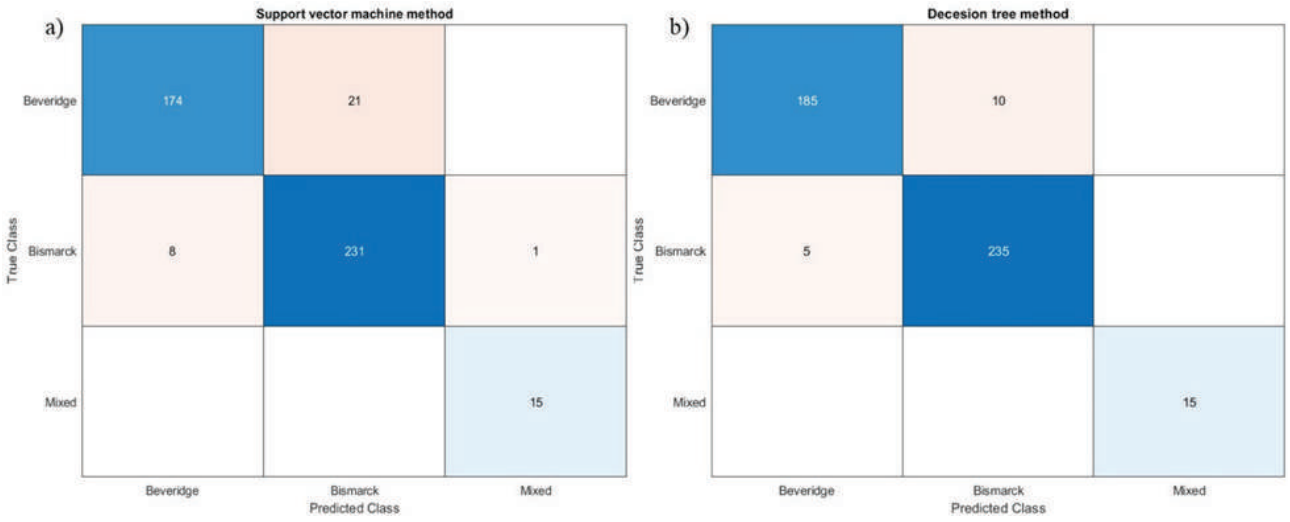


Figure 7. Classifying healthcare systems depending on a) support vector machine algorithm, b) decision tree algorithm.

the healthcare systems of OECD countries have been categorized into three clusters using the K-means method, an unsupervised machine learning technique, by utilizing the outputs of 21 key health indicators (Fig. 8).

Based on the unsupervised machine learning results observed in Figure 8, the representation of OECD countries divided into three clusters in the world map is presented with different colours for Cluster 1, Cluster 2, and Cluster 3. According to the results of cluster analysis, the world map displays that in Cluster 1; Austria, Japan, Mexico, Poland, Portugal, South Korea, Turkey, Spain, and Hungary countries are located; in Cluster 2; Belgium, Canada, Czechia, Denmark, Finland, France, Germany, Greece, Iceland, Ireland, Italy, Luxembourg, Netherlands, Norway, Slovakia, Sweden, Switzerland, and the United Kingdom countries are situated; and in Cluster 3, the United States, Australia, and New Zealand countries are included (Fig. 9).

The machine learning analysis indicates that the classification of OECD nations according to health metrics diverges from conventional classifications in the literature. Germany, traditionally linked to the Bismarck model, is included with the United Kingdom, recognized for the Beveridge model, in the classification based on health indicators (Group 2). The reclassification post-2013 can be ascribed to both nations embodying the social state paradigm, wherein healthcare services are funded through public resources such as taxes, indicating a transition towards a more universal healthcare model. Belgium has been classified with Group 2 countries since 2013, presumably because to its progressive healthcare policies that prioritize social fairness and extensive coverage. Slovakia demonstrates a notable reclassification in the post-2007 period, consistently aligning with Group 2 countries and demonstrating reforms focused on improving accessibility, quality, and equity in healthcare. These findings highlight the dynamic nature of healthcare systems, suggesting that traditional classifications may not adequately reflect the complexities and evolving characteristics of contemporary healthcare systems and require a more nuanced approach that integrates a variety of health indicators for a precise assessment.

The findings indicate that the United States, classified as a mixed model, also falls under Group 3 in the health indicators-based classification. New Zealand and Australia, categorized under the Beveridge model, are placed in Group 3, alongside the United States, based on a 15-year analysis of health indicators. Consequently, it can be asserted that evaluations based on health indicator outputs yield different outcomes than those derived from economic-based classifications in healthcare systems.

In the literature, among OECD countries; Czech Republic, Luxembourg, France, Greece, Netherlands, and Switzerland are classified under the Bismarck model group. However, in the obtained findings, when the 15-year health indicator data of these countries are evaluated, it can be seen that they are among the group 2 countries where Germany and the United Kingdom are located.

Among OECD countries, Spain and Hungary are classified under the Beveridge model when evaluating the healthcare system. However, in the analysis results of the data of both countries, it is possible to say that they are

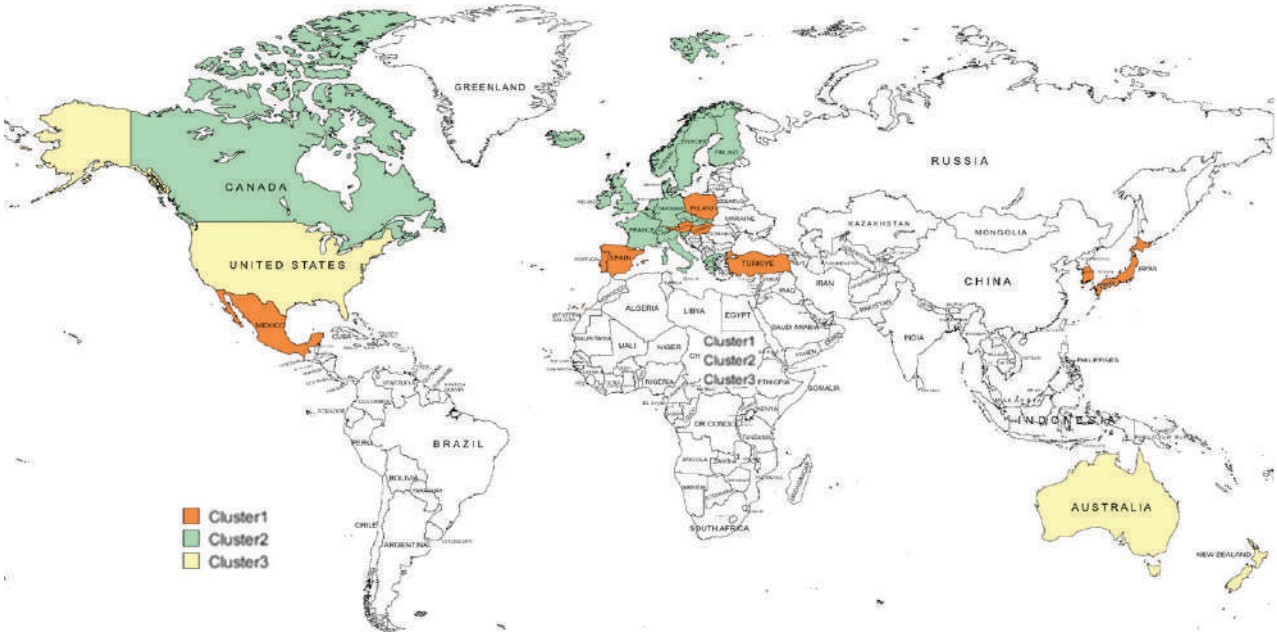


Figure 9. The illustration of OECD countries on world map depending on the cluster analysis of healthcare systems depending.

in the Group 1 category after 2016 when a health indicator-based classification is made.

This study highlights the importance of clustering healthcare systems as a mechanism for facilitating informed decision-making, policy formulation, and constructive dialogue among stakeholders. Utilizing machine learning methodologies renders the classification of healthcare systems more objective, data-driven, and adept at managing extensive datasets and intricate relationships characteristic of healthcare data. This study effectively used machine learning to classify the health indices of 30 OECD countries with high accuracy. This achievement demonstrates the significant potential of machine learning to provide valuable insights into the characteristics and effectiveness of health systems, thereby improving understanding of how other countries manage and deliver health care.

Health indicators are very important for both national and international levels because they provide critical information for assessing people's health status. Because health problems often create significant positive externalities and impact global public health, there is an urgent need for objective and accurate methodologies for classifying health systems. The primary goal of addressing global health challenges is to improve population health, which necessitates data-driven and objective methodologies for understanding and evaluating the effectiveness of health systems. Policymakers, researchers, and stakeholders can significantly benefit from these findings, as they establish a basis for continuous endeavors to optimize healthcare systems and, consequently, boost global health outcomes. Moreover, clustering according to health indicators can substantially aid in the development of health policy recommendations designed to improve community well-being and health [33-35]. This approach enables multiple essential processes: i) Objective Evaluation of Healthcare Systems: Clustering based on health indicators facilitates an impartial comparison of various healthcare systems, providing a greater insight into the performance of different countries regarding health outcomes and healthcare delivery. ii) Identifying Strengths and Weaknesses: By categorizing countries with similar health indicators, this approach facilitates a clearer distinction between the strengths and weaknesses inherent in each health system. This, in turn, facilitates the development of a more focused strategy to address areas requiring improvement. iii) Disseminating Effective Policy Strategies: When countries have similar health concerns and needs, clustering helps identify successful policy strategies. These practices can then be disseminated to other countries facing similar challenges, fostering a collaborative strategy to address common health concerns. iv) Identifying Best Practices: Analyzing the experiences of countries with similar health indicators facilitates the identification of best practices and can result in improved resource allocation and implementation methods among countries facing similar health challenges. v) Facilitating Collaboration: Clustering based on health indicators fosters collaboration and the sharing of experience among countries with similar health profiles. This collaboration may yield more cohesive and united strategies for addressing global health concerns. vi) Improved Health Policy Formulation and Execution: By elucidating the correlations between health indicators and healthcare system efficacy, clustering enhances the formulation and execution of health policies. This results in more informed decisions and more precisely focused actions that cater to the distinct needs of various populations.

Clustering based on health measures not only helps with objectively putting healthcare systems into groups and judging them, but it also plays a key role in making health policies that are more likely to improve people's health and well-being. The insights gained from this method could lead to positive changes in healthcare around the world. This makes it an essential tool for lawmakers, researchers, and other people who want to improve public health.

CONCLUSION

This study presents an innovative methodology employing a Deep Convolutional Neural Network (DCNN) model designed for the accurate detection and classification of skin burn severity using images sourced from medical atlases and textbooks. The model utilizes these images to identify key features, which are subsequently processed through a fully connected feedforward neural network. The purpose of this network is to categorize burns into three categories according to severity: first-degree, second-degree, and third-degree burns. The DCNN model described in this work is designed to significantly support medical professionals and healthcare providers by offering a swift and reliable approach for assessing the severity of skin burns, thereby facilitating prompt and appropriate treatment decisions. This DCNN-based model has applications extending beyond traditional clinical settings. This approach holds significant potential to enhance telemedicine, particularly in rural regions or underdeveloped nations where the scarcity of healthcare professionals is prevalent. This method is particularly advantageous in healthcare environments with limited resources, as it enables these facilities to determine burn severity more swiftly and precisely. This innovative technology employs deep learning to assess the severity of a burn. It will improve the treatment process by providing physicians with a method to quickly, fairly, and accurately assess burn severity. These assessment interfaces, which utilize deep learning techniques, can process comprehensive datasets to efficiently categorize burn injuries, thereby improving patient management. These digital platforms support healthcare professionals by providing access to educational resources and guidance. They also facilitate data collection and analysis for epidemiological research and enable remote consultations and assessments. This technology will significantly impact the management of burn injuries, a significant public health problem. It facilitates the prevention of burns and enhances the efficacy

of treatments, resulting in enhanced patient outcomes. Future extensions of this research may include the incorporation of authentic patient photographs to improve the model's ability to differentiate between superficial-partial and deep-partial thickness burns, as well as the development of algorithms to accurately estimate the Total Body Surface Area (TBSA%) affected. This enhancement would increase the clinical tool's utility in assessing and managing burn patients, thereby further advancing patient care and treatment strategies.

The outcomes of this study demonstrate that financial models alone are insufficient to fully explain the functioning of healthcare systems. This stems from the complexity of healthcare systems, which encompass numerous factors that influence their efficiency and outcomes. While financial models are essential for resource allocation, ensuring system sustainability, and assessing profitability, they do not comprehensively capture the complex dynamics of healthcare delivery, service quality, patient outcomes, social determinants of health, technological innovations, and cultural influences. It is challenging to compare healthcare with other industries due to its encompassing various domains such as ethics, technology, society, and culture. To better understand health systems, it's essential to examine them holistically, not just from a financial perspective. To achieve a comprehensive understanding, this approach must incorporate economic principles, as well as sociopolitical insights, cultural nuances, and technological advancements. This study highlights the importance of integrating health data with financial models to achieve a more detail understanding of health systems. This combination allows us to examine how factors such as resource allocation, service delivery, patient outcomes, and equity influence the overall quality, efficacy, and efficiency of healthcare services in a more comprehensive manner. For this approach to be effective, it is essential that both long-term financial sustainability and societal impacts are considered, and that individual health and well-being are not compromised by financial hardship. These findings suggest that policymakers and other stakeholders should adopt a multidisciplinary approach when formulating health policies. Value-based healthcare models and other strategies that consider health outcomes in financial decision-making can assist policymakers in promoting high-quality, patient-centered care. Real-time health data analytics can also facilitate informed decision-making grounded in factual information, thereby promoting more efficient resource utilization and reducing disparities in healthcare access and outcomes. In the future, additional research should emphasize the integration of concepts from diverse disciplines, such as economics, behavioral science, data science, and public health, to develop more effective models for evaluating healthcare systems. Additionally, exploring advanced technologies such as artificial intelligence and machine learning will enhance healthcare efficiency, facilitate trend prediction, and support policymakers in decision-making. These tools have important potential to increase the sensitivity and responsiveness of health systems, enabling more effective interventions. By advancing research in these areas, it can make sure that future health policies are more sustainable, equitable, and deliver high-quality services that meet the varying needs of diverse populations and improve overall health outcomes.

ACKNOWLEDGMENT

During the preparation of this work, the authors used Chatgpt to improve the writing and English of some sections. After using this tool/service, the authors reviewed and edited the content as needed, and they take full responsibility for the content of the publication

AUTHORSHIP CONTRIBUTIONS

Authors equally contributed to this work.

DATA AVAILABILITY STATEMENT

The authors confirm that the data that supports the findings of this study are available within the article. Raw data that support the finding of this study are available from the corresponding author, upon reasonable request.

CONFLICT OF INTEREST

The author declared no potential conflicts of interest with respect to the research, authorship, and/or publication of this article.

ETHICS

There are no ethical issues with the publication of this manuscript.

STATEMENT ON THE USE OF ARTIFICIAL INTELLIGENCE

During the preparation of this work, the authors used Chatgpt to improve the writing and English of some sections.

REFERENCES

[1] Ocaña-Riola R. The use of statistics in health sciences: situation analysis and perspective. Stat Biosci 2016;8:204–219. [CrossRef]

[2] Aldape-Pérez M, Alarcón-Paredes A, Yáñez-Márquez C, López-Yáñez I, Camacho-Nieto O. An associative memory approach to healthcare monitoring and decision making. Sensors 2018;18:2690. [CrossRef]

[3] Esteva A, Robicquet A, Ramsundar B, Kuleshov V, DePristo M, Chou K, et al. A guide to deep learning in healthcare. Nat Med 2019;25:24–29. [CrossRef]

[4] Jiang T, Gradus JL, Rosellini AJ. Supervised machine learning: a brief primer. Behav Ther 2020;51:675–687. [CrossRef]
[5] Eckhardt CM, Madjarova SJ, Williams RJ, Ollivier M, Karlsson J, Pareek A, et al. Unsupervised machine learning methods and emerging applications in healthcare. Knee Surg Sports Traumatol Arthrosc 2023;31:376–381. [CrossRef]
[6] Clift C. The role of the World Health Organization in the international system. Burns 2013;39:291–299. [CrossRef]
[7] World Health Organization. Health in sustainable development planning: the role of indicators. No. WHO/HDE/HID/02.11. World Health Organization; 2002.
[8] Wendt C. Mapping European healthcare systems: a comparative analysis of financing, service provision and access to healthcare. J Eur Soc Policy 2009;19:432–445. [CrossRef]
[9] Wendt C, Frisina L, Rothgang H. Healthcare system types: a conceptual framework for comparison. Soc Policy Adm 2009;43:70–90. [CrossRef]
[10] Freeman R, Frisina L. Health care systems and the problem of classification. J Compar Policy Anal 2010;12:163–178. [CrossRef]
[11] Ferreira PL, Tavares AI, Quintal C, Santana P. EU health systems classification: a new proposal from EURO-HEALTHY. BMC Health Serv Res 2018;18:1–11. [CrossRef]
[12] Lee S, Kim C. Estimation of association between healthcare system efficiency and policy factors for public health. Appl Sci 2018;8:2674. [CrossRef]
[13] Espinosa-González AB, Delaney BC, Marti J, Darzi A. The role of the state in financing and regulating primary care in Europe: a taxonomy. Health Policy 2021;125:168–176. [CrossRef]
[14] Klumpp M, Loske D, Bicciato S. COVID-19 health policy evaluation: integrating health and economic perspectives with a data envelopment analysis approach. Eur J Health Econ 2022;23:1263–1285. [CrossRef]
[15] Rajawat RS, Singh KK, Mishra VN. Approximation by modified Bernstein polynomials based on real parameters. Math Found Comput 2024;7:297–309. [CrossRef]
[16] Mishra VN, Rajawat RS, Sharma V. On generalized quantum Bernstein polynomials. Adv Pure Appl Algebr 2023;27:149–160. [CrossRef]
[17] Raiz M, Rajawat RS, Mishra VN. α-Schurer Durrmeyer operators and their approximation properties. Ann Univ Craiova Math Comput Sci Ser 2023;50:189–204. [CrossRef]
[18] Pandey S, Rajawat RS, Mishra VN. Approximation properties of modified Jain-Gamma operators preserving linear function. Palestine J Math 2023;12:169–182.
[19] Raiz M, Rajawat RS, Mishra LN, Mishra VN. Approximation on bivariate of Durrmeyer operators based on beta function. J Analysis 2023. [CrossRef]
[20] Bulut C, Sönal T, Kolca D, Tarlak F. Evaluation of COVID-19 mortality using machine learning regression methods based on health system indicators. Sigma J Eng Nat Sci 2024;42(6):1797–1805. [CrossRef]
[21] Bulut C, Kolca D, Tarlak F. Development of a software for detecting burn severity using convolutional neural network-based approach. Sigma J Eng Nat Sci 2024;43:598–606. [CrossRef]
[22] Anguita D, Ghio A, Ridella S, Sterpi D. K-Fold cross validation for error rate estimate in support vector machines. In: DMIN; 2009:291–297.
[23] Wong TT, Yang NY. Dependency analysis of accuracy estimates in k-fold cross validation. IEEE Trans Knowl Data Eng 2017;29:2417–2427. [CrossRef]
[24] Mengash HA, Mahmoud HH. Brain cancer tumor classification from motion-corrected MRI images using convolutional neural network. Comput Mater Continua 2021;68:1551–1563. [CrossRef]
[25] Sokolova M, Lapalme G. A systematic analysis of performance measures for classification tasks. Inf Process Manag 2009;45:427–437. [CrossRef]
[26] Deng X, Liu Q, Deng Y, Mahadevan S. An improved method to construct basic probability assignment based on the confusion matrix for classification problem. Inf Sci 2016;340:250–261. [CrossRef]
[27] De Diego IM, Redondo AR, Fernández RR, Navarro J, Moguerza JM. General performance score for classification problems. Appl Intell 2022;52:12049–12063. [CrossRef]
[28] Toth F. Classification of healthcare systems: Can we go further? Health Policy 2016;120:535–543. [CrossRef]
[29] Jacques O, Noël A. The politics of public health investments. Soc Sci Med 2022;309:115272. [CrossRef]
[30] Böhm K, Schmid A, Götze R, Landwehr C, Rothgang H. Five types of OECD healthcare systems: empirical results of a deductive classification. Health Policy 2013;113:258–269. [CrossRef]
[31] Ariaans M, Linden P, Wendt C. Worlds of long-term care: A typology of OECD countries. Health Policy 2021;125:609–617. [CrossRef]
[32] Benoît C. The regulatory path to healthcare systems' financialization. J Eur Soc Policy 2023;09589287231176776. [CrossRef]
[33] Bertin G, Carrino L, Pantalone M. Do standard classifications still represent European welfare typologies? Novel evidence from studies on health and social care. Soc Sci Med 2021;281:114086. [CrossRef]
[34] Capano G, Toth F. Health policy under the microscope: a micro policy design perspective. Front Public Health 2023;11:1180836. [CrossRef]
[35] De Carvalho G, Schmid A, Fischer J. Classifications of health care systems: Do existing typologies reflect the particularities of the Global South? Glob Soc Policy 2021;21:278–300. [CrossRef]

Sigma Journal of Engineering and Natural Sciences
Web page info: https://sigma.yildiz.edu.tr
DOI: 10.14744/sigma.2024.00130

Research Article

Evaluation of health care systems using supervised and unsupervised machine learning approaches

Canan BULUT[1], Tuğba SÖNAL[2], Dilek KOLCA[3], Fatih TARLAK[4,*]

[1]Department of Medical Services and Techniques, Istanbul Kultur University, Istanbul, 34191, Türkiye
[2]Health Ministry of Turkey, Ataşehir District Health Directorate, Istanbul, 34100, Türkiye
[3]Department of Health Management, Istinye University, Istanbul, 34010, Türkiye
[4]Deparment of Bioengineering, Gebze Technical University, Gebze, 41400, Türkiye

ARTICLE INFO

Article history
Received: 07 June 2024
Revised: 21 August 2024
Accepted: 22 October 2024

Keywords:
Classification; Clustering; Health Indicators; Machine Learning

ABSTRACT

Both large- and small-scale health system evaluations are crucial. On a larger scale, it facilitates cross-national comparisons, monitors the advancement of global health objectives, aids in the formulation of public health policy, and ensures efficient use of resources. On a smaller scale, it helps countries figure out how well their health programs are working, see health trends, and find areas that need improvement. A health system is made up of a lot of different people and things, like organizations, institutions, resources, patients, and people who might become patients. All of these people and things work together to give health services to a group of people. This research gathered health indicators from 30 OECD (Organization for Economic Cooperation and Development) nations from 2006 to 2020 and evaluated them through both supervised and unsupervised machine learning methodologies. The findings, demonstrating high accuracy in machine learning methods (exceeding 93.3%), indicate that financial models alone are inadequate for evaluating healthcare systems. The complexity and multidimensional nature of these systems necessitate the inclusion of health indicators in the evaluation process. Even with enough money, people may not get the health outcomes they want if there aren't health policies that are based on the basic ideas of fairness, quality of service delivery, and efficiency that can be put into action. This study employs unsupervised machine learning techniques to analyze health indicators. This helps policymakers, researchers, and other people who are interested in healthcare systems learn more about their strengths and weaknesses. These insights can help policymakers make decisions, make it easier to compare medical systems in different countries, and help healthcare systems get better all the time.

Cite this article as: Bulut C, Sönal T, Kolca D, Tarlak F. Evaluation of health care systems using supervised and unsupervised machine learning approaches. Sigma J Eng Nat Sci 2025;43(6):2174–2185.

***Corresponding author.**
*E-mail address: ftarlak@gtu.edu.tr

This paper was recommended for publication in revised form by Editor-in-Chief Ahmet Selim Dalkilic

Published by Yıldız Technical University Press, İstanbul, Turkey
© Author. This is an open access article under the CC BY-NC license (http://creativecommons.org/licenses/by-nc/4.0/).

INTRODUCTION

Statistics is a basic tool that helps us draw meaningful conclusions from data, aids in scientific discoveries, helps us make good decisions, and gives us answers to many problems. Health statistics is a specialized subdiscipline that deals with analyzing, interpreting, and summarizing health data [1]. Health statistics are important for figuring out how healthy people and communities are, how common diseases are, how well health services work, and how health policies affect people. These numbers include a variety of quantitative tools used to study health problems, from big epidemiological studies to clinical trials.

When looking into complicated things like health statistics, comparisons and typologies can help you understand them better. Typologies facilitate the simplification of complex empirical realities, thereby enabling systematic analysis of similarities, variations, and the identification of patterns. Machine learning techniques are essential analytical instruments that enable the examination and interpretation of high-dimensional data [2, 3]. There are two main types of machine learning: supervised learning and unsupervised learning. When you use supervised machine learning, you train a model on labeled data that has known outcomes. When you use unsupervised machine learning, you find patterns and relationships in unlabeled data that don't have any known outcomes.

Supervised machine learning is a kind of learning in which the algorithm learns from labeled data, which means that the input data is matched with the right output labels. The goal of supervised learning is to teach the algorithm how to connect inputs to outputs so that it can make accurate predictions or classifications on data it hasn't seen before. In supervised machine learning, classification is a basic idea. It means using algorithms to put input instances into one of several pre-defined groups. Random Forest is a popular supervised machine learning algorithm that is well-known for being good at classification tasks [4].

On the other hand, unsupervised learning is a type of machine learning in which the algorithm looks for patterns, structures, or relationships in the data without any clear labeled output. It finds hidden patterns or structures in the data that is being input. Clustering algorithms are a type of unsupervised machine learning that puts similar data points into groups called clusters. These algorithms help find patterns or groups in a dataset without needing to set class labels ahead of time. K-Means clustering is a common unsupervised machine learning algorithm that divides a dataset into a certain number of groups. It works best when you already know how many clusters there are. K-Means puts each data point in the cluster that is closest to it and then keeps making these assignments better until the sum of the squared distances between data points and their centroids is as small as possible [5].

Standardized indicators are necessary to evaluate the health status of a particular population. These indicators, derived from health records and statistics of individuals and communities, are used to assess current conditions and make predictions about the future. Keeping accurate records and statistics is crucial to seeing things as they are and making wise choices.

Since its founding in 1948, the World Health Organization (WHO) has been a leader in creating health metrics and collecting and analyzing data that can be used to compare different countries [6]. In the 1960s, there was a push to work with other countries around the world and make health indicators and data more consistent. A lot of success has been made by the World Health Organization (WHO) in making rules and standards for gathering and analyzing health data that can be used to compare data from different countries. What are "health indicators"? They were made by the World Health Organization (WHO) and show many different parts of health. Some of these factors are the number of sick people, how well the health system is working, the things that affect health, and the trends in the health of the community. The purpose of these indicators is to help public health officials make choices and decide how to spend their money and time, and to allow people to compare countries. They help countries and international health groups track and rate the success of their health programs, identify health trends, and focus on areas that need work or improvement [7]. These factors are categorized by the World Health Organization (WHO) to help countries make fair decisions:

- **Health Status Indicators:** These show how healthy a person or society is overall by looking at things like the number of diseases, how easy it is to get medical care, and how long people generally live.
- **Risk Factors:** The World Health Organization (WHO) has created a number of signs and tools to help find, track, and protect public health when it comes to health-related risk factors. These things are very important for stopping the spread of diseases and making people healthier.
- **Service Coverage:** The World Health Organization (WHO) has created service coverage indicators to measure how easy it is to get healthcare services and how well they work. These indicators are used to keep an eye on health services and make them work better [7].

The list of health indicators is periodically updated to align with current health priorities. These indicators serve as a crucial tool in assessing the health status of populations, identifying disparities, and guiding evidence-based decision-making at local, national, and international levels. Recent advancements in the field of mathematical analysis have significantly contributed to the development of more accurate and efficient methods for approximating complex functions, which are highly beneficial for evaluating health systems [8-14]. While the literature includes some articles focused on evaluating healthcare systems [15-21], to the best of our knowledge, there are no published works that compare the evaluation performance of supervised and

unsupervised machine learning approaches in assessing healthcare indicators of countries. The aim of this study is to evaluate the health systems of 30 OECD countries based on 21 healthcare indicators from 2006 to 2020 using both supervised and unsupervised machine learning approaches.

MATERIAL AND METHODS

The work was done in three main separate steps: i) the healthcare indicators for OECD countries from 2006 to 2020 were gathered, ii) data processing (standardization) was done in Matlab 8.3.0.532 (R2014a) software (MathWorks Inc., Natick, MA, USA), and iii) the evaluation of health care systems was done employing machine learning methodology: the supervised classification and unsupervised clustering. The flowchart in Figure 1 outlines the main steps undertaken in this study. The following sections offer comprehensive explanations of each stage involved in the research process.

DATA COLLECTION

Traditionally, the classification of health systems in countries has often relied on economic-based structures in the literature. However, given the unique nature of healthcare services, which differ significantly from other types of services, a focus on fairness-oriented maximum accessibility becomes more crucial than merely ensuring equal distribution. Evaluations based on health indicators—the outputs of provided healthcare services—allow for more valuable and accurate predictions for future assessments. For this study, health status indicators, risk factors, and service coverage indicators from the years 2006 to 2020 for 30 OECD countries were utilized. Health indicator data were collected from the World Data Bank, Eurostat, and WHO databases. To ensure consistency and accuracy, the data were standardized before analysis. This step put all data on the same scale, usually through normalization or z-score standardization, so that differences in measurement units did not affect the results. The dataset covers indicators such as adolescent birth rate, total fertility rate, cancer incidence by type, tuberculosis incidence, cardiovascular death rate, rates of cancer, diabetes, or chronic respiratory diseases in people aged 30 to 70, maternal mortality, death rate from road traffic injuries, under-five mortality, infant mortality, life expectancy at birth, stillbirth rate, and neonatal mortality. The risk factor indicators included in the study are: tobacco use among persons aged 18+ years, total alcohol per capita (age 15+) consumption, prevalence of overweight and obesity in adults, proportion of the population using safely managed sanitation services, air pollution levels in cities, and prevalence of intimate partner violence. The service coverage indicators included were: the coverage rate of vaccination in the national program for vaccines such as diphtheria, tetanus, and pertussis, coverage rate of vaccination for measles, and tuberculosis case detection rate. All the indicators used, along with their codifications and explanations, are detailed in Table 1.

Machine Learning Classification and Evaluation

Machine learning classification trains models to classify data into preset classes. This procedure uses algorithms and statistics to learn patterns and relationships from labeled training data and to predict or label new data. This study classified OECD countries using financial models using decision tree regression (DTR) and support vector regression (SVR) (Fig. 2). Cross-validation tuned the DTR and SVR hyperparameters to optimize model performance. In this study it is selected DTR for its ability to handle complex, nonlinear interactions in the data, and SVR for its ability to handle high-dimensional data and reduce prediction error. These techniques have been successful in effectively

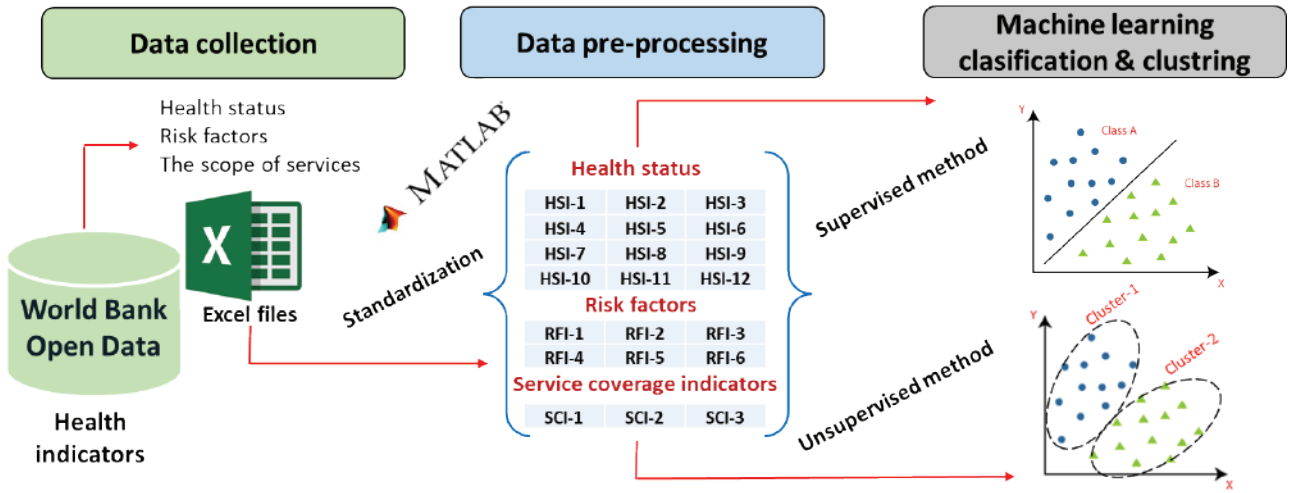


Figure 1. The flow chart outlining the main steps followed in the present study.

Table 1. The used health indicators with their explanations

Code	Health indicators	Explanation
HSI-1	Health status indicators	Adolescent birth rate
HSI-2		Total fertility rate
HSI-3		Cancer incidence rate, by type of cancer
HSI-4		Tuberculosis incidence rate
HSI-5		Rate of cardiovascular deaths, diseases, cancer, diabetes, or chronic respiratory diseases between the ages of 30 and 70
HSI-6		Maternal mortality rate
HSI-7		Death rate due to road traffic injuries
HSI-8		Under-five mortality rate
HSI-9		Infant mortality rate
HSI-10		Life expectancy at birth
HSI-11		Stillbirth rate
HSI-12		Neonatal mortality rate
RFI-1	Risk factors indicators	Tobacco use among persons aged 18+ years
RFI-2		Total alcohol per capita (age 15+) consumption
RFI-3		Overweight and obesity in adults' prevalence
RFI-4		Proportion of population using safely managed sanitation services
RFI-5		Air pollution levels in cities
RFI-6		Intimate partner violence prevalence
SCI-1	Service coverage indicators	Coverage rate of vaccination compared to vaccination for each vaccine (diphtheria, tetanus, pertussis) in the national program
SCI-2		Coverage rate of vaccination compared to vaccination for each vaccine (measles) in the national program
SCI-3		Tuberculosis case detection rate

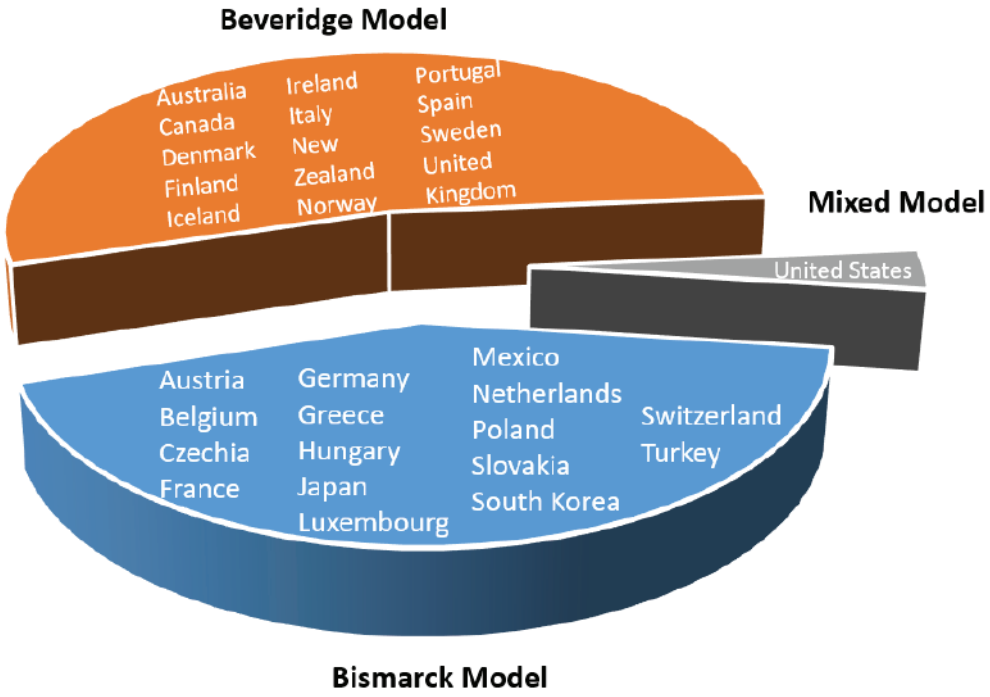


Figure 2. Classification of health care systems based on financial models.

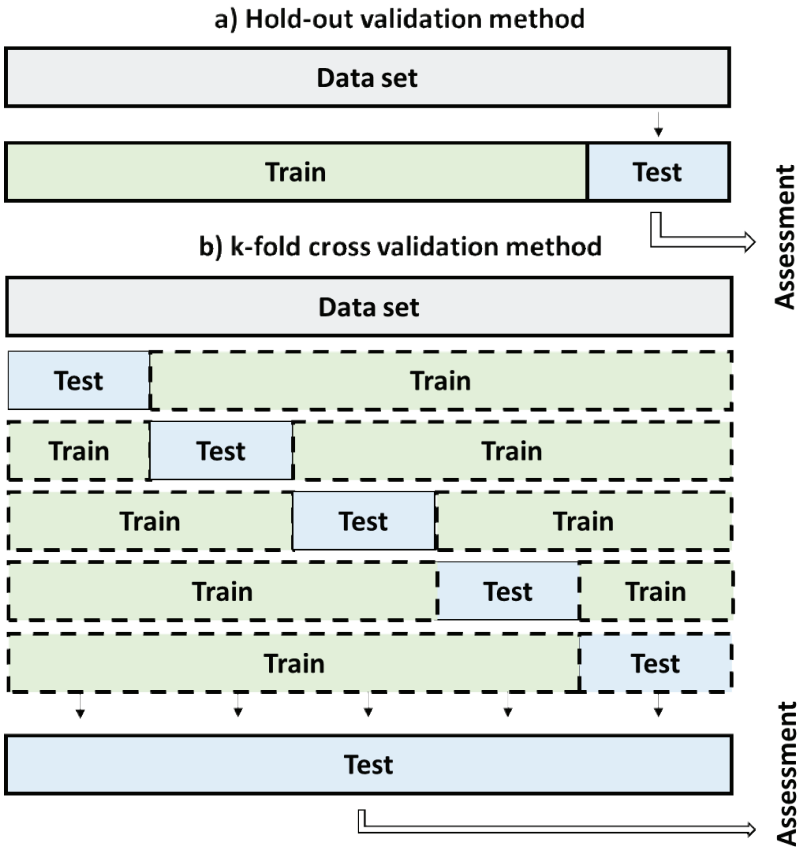


Figure 3. The schematic illustration of validation methods of a) hold-out validation and b) k-fold validation.

capturing the complex dynamics of financial data in healthcare systems.

Hold-out validation and k-fold cross-validation are two validation methods that are often used in machine learning. The dataset is split into two parts for hold-out validation: a training set and a test set [22–24]. The model is trained on the training set, and its performance is then evaluated on the test set. The dataset is split into k equal parts for k-fold cross-validation. One part is used for testing and the other parts are used for training in each iteration. To see how well the model works on the whole dataset, the results from all iterations are put together. Cross-validation is generally considered more unbiased, as it uses multiple partitions for testing, whereas hold-out validation can introduce bias due to random splitting. This study utilized a 10-fold cross-validation method, as illustrated in Figure 3.

By using a confusion matrix, which comprehensively divides the model's predictions into true positives, true negatives, false positives, and false negatives, the effectiveness of the proposed model on classification problems can be evaluated [18–20]. The confusion matrix facilitates the calculation of multiple performance metrics, such as sensitivity, recall, F1 score, and specificity, each providing insight into different aspects of the model's accuracy. Additionally, the average accuracy—which is determined by dividing the number of correctly categorized cases by the total number of examples—can be used to characterize the classifier's overall performance. This is represented mathematically by Equation (1) [25]:

$$Average\ accuracy = \frac{\left(\sum_{i=1}^{l} \frac{tp_i + tn_i}{tp_i + fn_i + fp_i + tn_i}\right)}{l} \quad (1)$$

where tp_i is the number true positive class, tn_i is the number true negative class, fp_i is the number false positive class, fn_i is the number false negative class, l is the number of evaluated classes.

RESULTS AND DISCUSSION

In this study, the burn images were trained using the deep learning algorithms GoogleNet, ResNet-50, and Inception-v3, which consist of 22, 50, and 48 layers, respectively, within the Matlab software environment. The training dataset comprised a total of 1294 burn images, broken down into 561 first-degree, 275 second-degree, and 458 third-degree burn images [26, 27].

For societies, resources are limited while needs are unlimited. The ability to meet maximum needs with these limited resources relies on accurate current situation analysis and future predictions. The situation is no different in healthcare services. Both the human resources capable of providing healthcare services and the medical equipment used in healthcare are constrained, and theories are generated to determine how to achieve maximum benefit, forming the foundation of healthcare systems [28].

The proper and logical interpretation of health indicators, which are tangible outputs of the healthcare systems used by countries, enhances the success of future healthcare policies by optimizing the use of limited resources allocated to healthcare services [29]. This allows for the optimal utilization of scarce resources. In this study, classification and interpretation are intended to be carried out based on health indica-tors from 2006 to 2020 for 30 OECD countries.

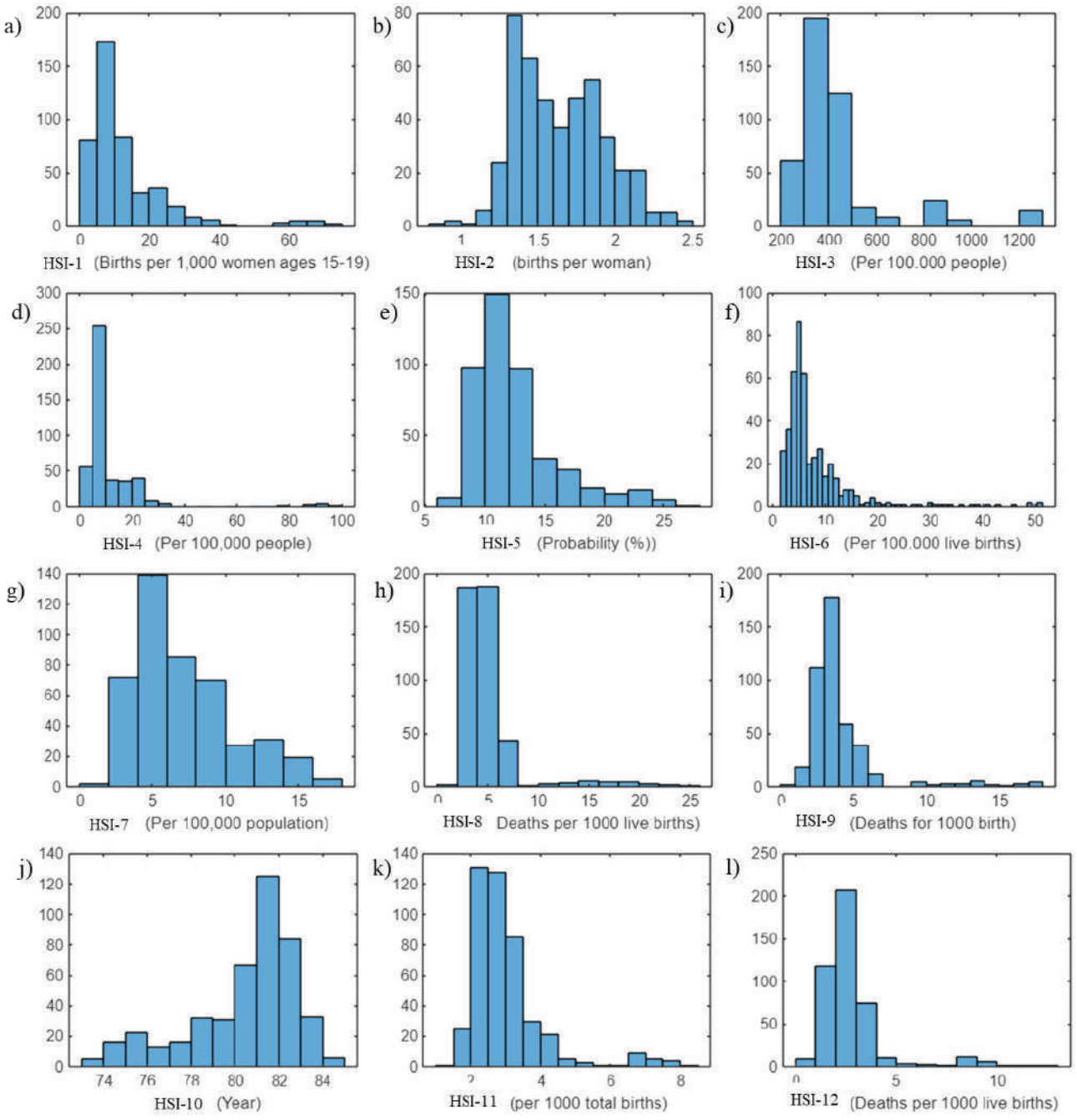


Figure 4. Histograms depicting the variables are shown for: a) HIS-1, b) HIS-2, c) HIS-3, d) HIS-4, e) HIS-5, f) HIS-6, g) HIS-7, h) HIS-8, j) HIS-9, j) HIS-10, k) HIS-11and l) HIS-12.

From the basic health indicators, statistics on birth (adolescent birth rate, total fertility rate), diseases (cancer incidence rate by type of cancer, tuberculosis incidence rate), causes of death (rate of cardiovascular deaths, deaths due to cancer, diabetes, or chronic respiratory diseases between the ages of 30 and 70, maternal mortality rate, death rate due to road traffic injuries), and age and gender-specific mortality (under-five mortality rate, infant mortality rate, life expectancy at birth, stillbirth rate, neonatal mortality rate) have been used as health status indicators (Fig. 4).

In the study, from the basic health indicators; non-communicable diseases (tobacco use among persons aged 18+ years, total alcohol per capita (age 15+) consumption, overweight and obesity in adults' prevalence), environmental risk factors (proportion of population using safely managed sanitation services, air pollution levels in cities), injuries (intimate partner violence prevalence) statistics were used as risk factor indicators (Fig. 5).

The study utilized basic health indicators, specifically focusing on vaccination coverage rates for each vaccine included in the national program, such as diphtheria, tetanus, pertussis, and measles. Additionally, the tuberculosis case detection rate was employed as a service coverage indicator, as illustrated in Figure 6.

Decision trees are adaptable and widely used categorization techniques. They work by iteratively splitting data into subsets based on the values of input features. These splits are determined by the algorithm's parameters to optimize information gain or Gini impurity. Decision trees are understandable and facilitate a simple depiction of the

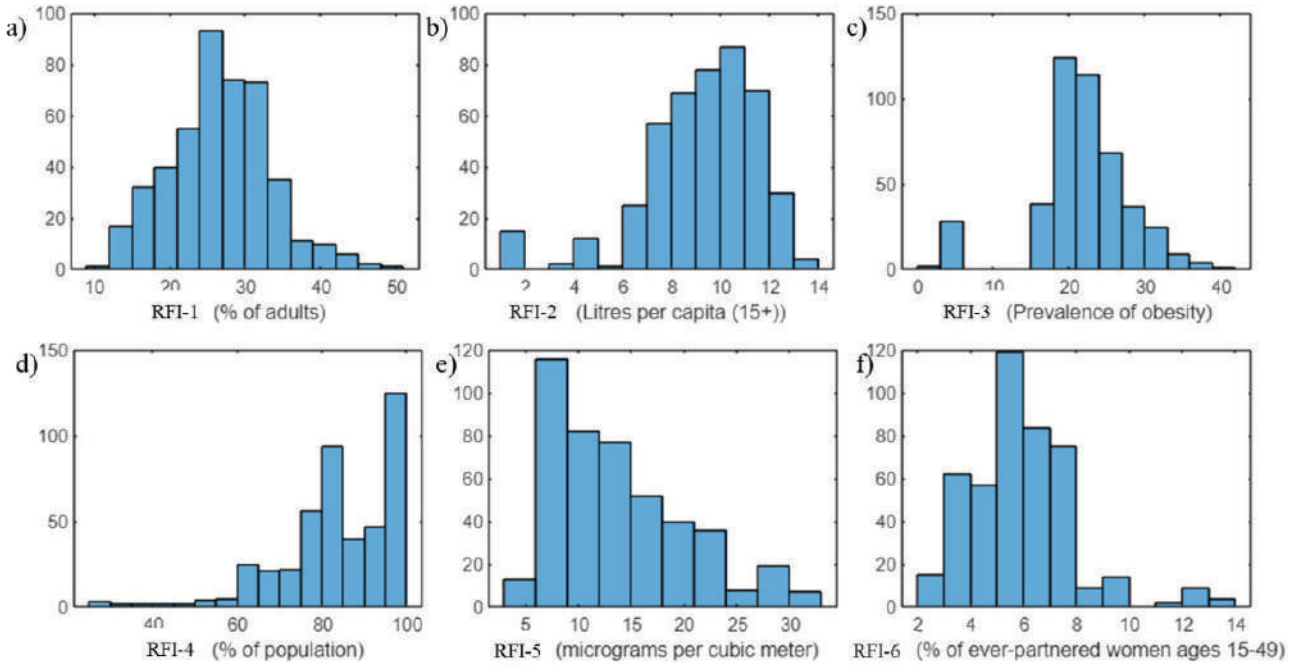


Figure 5. Histograms depicting the variables are shown for: a) RFI-1, b) RFI-2, c) RFI-3, d) RFI-4, e) RFI-5 and f) RFI-6.

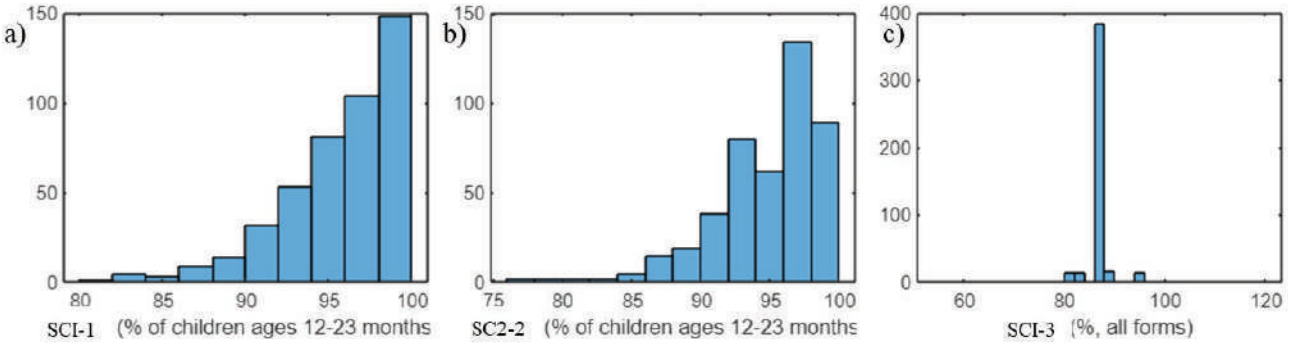


Figure 6. Histograms depicting the variables are shown for: a) SCI-1, b) SCI-2 and c) SCI-3.

decision-making process. Their ability to handle both qualitative and numerical data makes them suitable for many applications.

Support Vector Regression is an effective method used for classification and regression applications. It is highly effective for regression tasks that aim to predict continuous values. SVR aims to identify a hyperplane that best accommodates the data while reducing the margin of error. It determines the support vectors, which are the data points closest to the hyperplane. SVR uses a kernel function to map the data to a higher-dimensional space, enabling the identification of nonlinear correlations between variables.

Findings obtained from the supervised machine learning analysis results; when a classification is made based on health indicators, a similar result to the classification in the literature known as the beveridge, bismarck, and mixed model classification is obtained (Fig. 7). However, when the trends of countries under this classification are examined, changes in classifications are observed parallel to other developments in the OECD countries [30, 31].

As seen in Figure 7, the financial-based models (Beveridge, Bismarck, and mixed) used for classifying the healthcare systems of OECD countries can be simulated with an accuracy of 93.3% using the support vector machine algorithm and 96.7% using the decision tree algorithm. While these high accuracies highlight the importance of financial models in understanding and classifying healthcare systems, they are insufficient to capture the full complexity of these systems. Health systems are influenced by a wide range of stakeholders, including government agencies, private institutions, healthcare providers, and patients, and are characterized by services that cannot be delayed or replaced. Therefore, combining health indicator-based models with financial-based models provides a more comprehensive assessment. Health systems are multidimensional and shaped by economic, social, cultural, technological, and human factors. Financial models offer valuable insights into resource allocation and economic sustainability, but they fail to account for critical factors such as health outcomes, quality of care, equity, and patient satisfaction. Therefore, health policies and system designs must adopt a multidisciplinary approach that integrates financial analysis with public health, sociology, technology, and ethics to develop strategies that ensure health systems are economically sustainable and can provide high-quality, equitable, and accessible care to all.

While classifying countries' healthcare systems according to financing-based approaches might provide a high level of accuracy [32], to reveal the interconnections among these complex and multidimensional healthcare services,

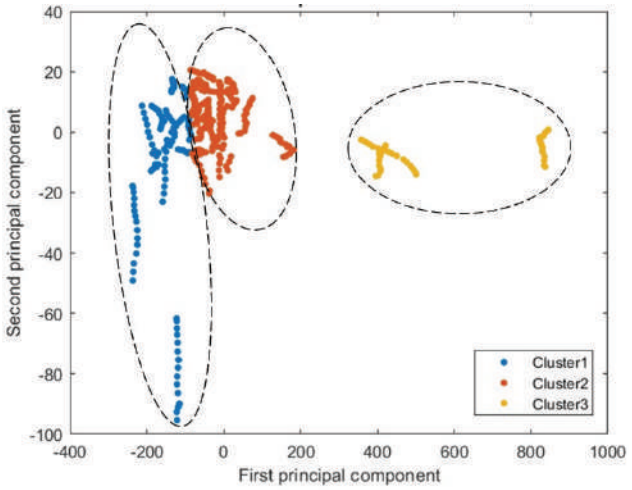


Figure 8. Cluster analysis of healthcare systems depending on the first two principal components using k-means clustering method.

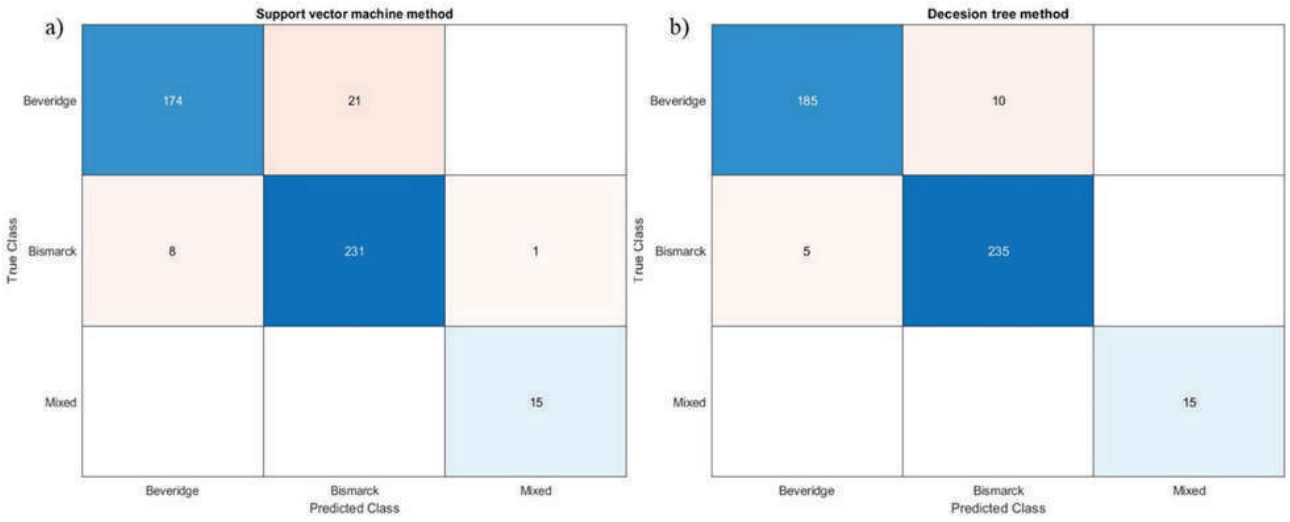


Figure 7. Classifying healthcare systems depending on a) support vector machine algorithm, b) decision tree algorithm.

the healthcare systems of OECD countries have been categorized into three clusters using the K-means method, an unsupervised machine learning technique, by utilizing the outputs of 21 key health indicators (Fig. 8).

Based on the unsupervised machine learning results observed in Figure 8, the representation of OECD countries divided into three clusters in the world map is presented with different colours for Cluster 1, Cluster 2, and Cluster 3. According to the results of cluster analysis, the world map displays that in Cluster 1; Austria, Japan, Mexico, Poland, Portugal, South Korea, Turkey, Spain, and Hungary countries are located; in Cluster 2; Belgium, Canada, Czechia, Denmark, Finland, France, Germany, Greece, Iceland, Ireland, Italy, Luxembourg, Netherlands, Norway, Slovakia, Sweden, Switzerland, and the United Kingdom countries are situated; and in Cluster 3, the United States, Australia, and New Zealand countries are included (Fig. 9).

The machine learning analysis indicates that the classification of OECD nations according to health metrics diverges from conventional classifications in the literature. Germany, traditionally linked to the Bismarck model, is included with the United Kingdom, recognized for the Beveridge model, in the classification based on health indicators (Group 2). The reclassification post-2013 can be ascribed to both nations embodying the social state paradigm, wherein healthcare services are funded through public resources such as taxes, indicating a transition towards a more universal healthcare model. Belgium has been classified with Group 2 countries since 2013, presumably because to its progressive healthcare policies that prioritize social fairness and extensive coverage. Slovakia demonstrates a notable reclassification in the post-2007 period, consistently aligning with Group 2 countries and demonstrating reforms focused on improving accessibility, quality, and equity in healthcare. These findings highlight the dynamic nature of healthcare systems, suggesting that traditional classifications may not adequately reflect the complexities and evolving characteristics of contemporary healthcare systems and require a more nuanced approach that integrates a variety of health indicators for a precise assessment.

The findings indicate that the United States, classified as a mixed model, also falls under Group 3 in the health indicators-based classification. New Zealand and Australia, categorized under the Beveridge model, are placed in Group 3, alongside the United States, based on a 15-year analysis of health indicators. Consequently, it can be asserted that evaluations based on health indicator outputs yield different outcomes than those derived from economic-based classifications in healthcare systems.

In the literature, among OECD countries; Czech Republic, Luxembourg, France, Greece, Netherlands, and Switzerland are classified under the Bismarck model group. However, in the obtained findings, when the 15-year health indicator data of these countries are evaluated, it can be seen that they are among the group 2 countries where Germany and the United Kingdom are located.

Among OECD countries, Spain and Hungary are classified under the Beveridge model when evaluating the healthcare system. However, in the analysis results of the data of both countries, it is possible to say that they are

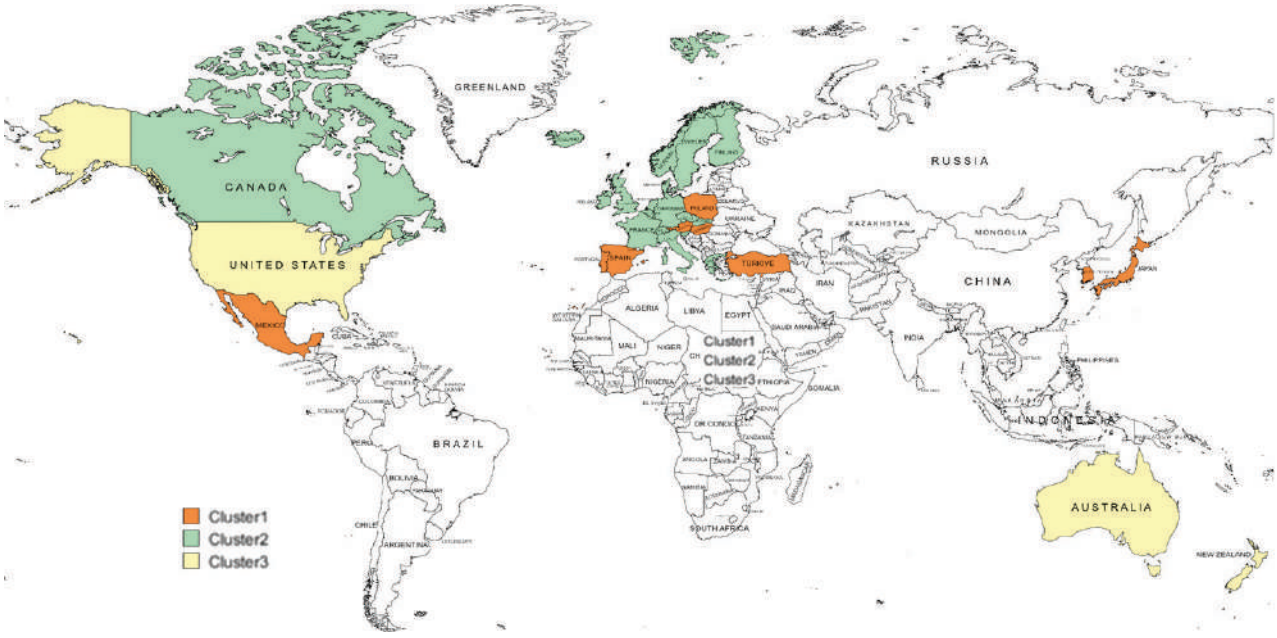


Figure 9. The illustration of OECD countries on world map depending on the cluster analysis of healthcare systems depending.

in the Group 1 category after 2016 when a health indicator-based classification is made.

This study highlights the importance of clustering healthcare systems as a mechanism for facilitating informed decision-making, policy formulation, and constructive dialogue among stakeholders. Utilizing machine learning methodologies renders the classification of healthcare systems more objective, data-driven, and adept at managing extensive datasets and intricate relationships characteristic of healthcare data. This study effectively used machine learning to classify the health indices of 30 OECD countries with high accuracy. This achievement demonstrates the significant potential of machine learning to provide valuable insights into the characteristics and effectiveness of health systems, thereby improving understanding of how other countries manage and deliver health care.

Health indicators are very important for both national and international levels because they provide critical information for assessing people's health status. Because health problems often create significant positive externalities and impact global public health, there is an urgent need for objective and accurate methodologies for classifying health systems. The primary goal of addressing global health challenges is to improve population health, which necessitates data-driven and objective methodologies for understanding and evaluating the effectiveness of health systems. Policymakers, researchers, and stakeholders can significantly benefit from these findings, as they establish a basis for continuous endeavors to optimize healthcare systems and, consequently, boost global health outcomes. Moreover, clustering according to health indicators can substantially aid in the development of health policy recommendations designed to improve community well-being and health [33-35]. This approach enables multiple essential processes: i) Objective Evaluation of Healthcare Systems: Clustering based on health indicators facilitates an impartial comparison of various healthcare systems, providing a greater insight into the performance of different countries regarding health outcomes and healthcare delivery. ii) Identifying Strengths and Weaknesses: By categorizing countries with similar health indicators, this approach facilitates a clearer distinction between the strengths and weaknesses inherent in each health system. This, in turn, facilitates the development of a more focused strategy to address areas requiring improvement. iii) Disseminating Effective Policy Strategies: When countries have similar health concerns and needs, clustering helps identify successful policy strategies. These practices can then be disseminated to other countries facing similar challenges, fostering a collaborative strategy to address common health concerns. iv) Identifying Best Practices: Analyzing the experiences of countries with similar health indicators facilitates the identification of best practices and can result in improved resource allocation and implementation methods among countries facing similar health challenges. v) Facilitating Collaboration: Clustering based on health indicators fosters collaboration and the sharing of experience among countries with similar health profiles. This collaboration may yield more cohesive and united strategies for addressing global health concerns. vi) Improved Health Policy Formulation and Execution: By elucidating the correlations between health indicators and healthcare system efficacy, clustering enhances the formulation and execution of health policies. This results in more informed decisions and more precisely focused actions that cater to the distinct needs of various populations.

Clustering based on health measures not only helps with objectively putting healthcare systems into groups and judging them, but it also plays a key role in making health policies that are more likely to improve people's health and well-being. The insights gained from this method could lead to positive changes in healthcare around the world. This makes it an essential tool for lawmakers, researchers, and other people who want to improve public health.

CONCLUSION

This study presents an innovative methodology employing a Deep Convolutional Neural Network (DCNN) model designed for the accurate detection and classification of skin burn severity using images sourced from medical atlases and textbooks. The model utilizes these images to identify key features, which are subsequently processed through a fully connected feedforward neural network. The purpose of this network is to categorize burns into three categories according to severity: first-degree, second-degree, and third-degree burns. The DCNN model described in this work is designed to significantly support medical professionals and healthcare providers by offering a swift and reliable approach for assessing the severity of skin burns, thereby facilitating prompt and appropriate treatment decisions. This DCNN-based model has applications extending beyond traditional clinical settings. This approach holds significant potential to enhance telemedicine, particularly in rural regions or underdeveloped nations where the scarcity of healthcare professionals is prevalent. This method is particularly advantageous in healthcare environments with limited resources, as it enables these facilities to determine burn severity more swiftly and precisely. This innovative technology employs deep learning to assess the severity of a burn. It will improve the treatment process by providing physicians with a method to quickly, fairly, and accurately assess burn severity. These assessment interfaces, which utilize deep learning techniques, can process comprehensive datasets to efficiently categorize burn injuries, thereby improving patient management. These digital platforms support healthcare professionals by providing access to educational resources and guidance. They also facilitate data collection and analysis for epidemiological research and enable remote consultations and assessments. This technology will significantly impact the management of burn injuries, a significant public health problem. It facilitates the prevention of burns and enhances the efficacy

of treatments, resulting in enhanced patient outcomes. Future extensions of this research may include the incorporation of authentic patient photographs to improve the model's ability to differentiate between superficial-partial and deep-partial thickness burns, as well as the development of algorithms to accurately estimate the Total Body Surface Area (TBSA%) affected. This enhancement would increase the clinical tool's utility in assessing and managing burn patients, thereby further advancing patient care and treatment strategies.

The outcomes of this study demonstrate that financial models alone are insufficient to fully explain the functioning of healthcare systems. This stems from the complexity of healthcare systems, which encompass numerous factors that influence their efficiency and outcomes. While financial models are essential for resource allocation, ensuring system sustainability, and assessing profitability, they do not comprehensively capture the complex dynamics of healthcare delivery, service quality, patient outcomes, social determinants of health, technological innovations, and cultural influences. It is challenging to compare healthcare with other industries due to its encompassing various domains such as ethics, technology, society, and culture. To better understand health systems, it's essential to examine them holistically, not just from a financial perspective. To achieve a comprehensive understanding, this approach must incorporate economic principles, as well as sociopolitical insights, cultural nuances, and technological advancements. This study highlights the importance of integrating health data with financial models to achieve a more detail understanding of health systems. This combination allows us to examine how factors such as resource allocation, service delivery, patient outcomes, and equity influence the overall quality, efficacy, and efficiency of healthcare services in a more comprehensive manner. For this approach to be effective, it is essential that both long-term financial sustainability and societal impacts are considered, and that individual health and well-being are not compromised by financial hardship. These findings suggest that policymakers and other stakeholders should adopt a multidisciplinary approach when formulating health policies. Value-based healthcare models and other strategies that consider health outcomes in financial decision-making can assist policymakers in promoting high-quality, patient-centered care. Real-time health data analytics can also facilitate informed decision-making grounded in factual information, thereby promoting more efficient resource utilization and reducing disparities in healthcare access and outcomes. In the future, additional research should emphasize the integration of concepts from diverse disciplines, such as economics, behavioral science, data science, and public health, to develop more effective models for evaluating healthcare systems. Additionally, exploring advanced technologies such as artificial intelligence and machine learning will enhance healthcare efficiency, facilitate trend prediction, and support policymakers in decision-making. These tools have important potential to increase the sensitivity and responsiveness of health systems, enabling more effective interventions. By advancing research in these areas, it can make sure that future health policies are more sustainable, equitable, and deliver high-quality services that meet the varying needs of diverse populations and improve overall health outcomes.

ACKNOWLEDGMENT

During the preparation of this work, the authors used Chatgpt to improve the writing and English of some sections. After using this tool/service, the authors reviewed and edited the content as needed, and they take full responsibility for the content of the publication

AUTHORSHIP CONTRIBUTIONS

Authors equally contributed to this work.

DATA AVAILABILITY STATEMENT

The authors confirm that the data that supports the findings of this study are available within the article. Raw data that support the finding of this study are available from the corresponding author, upon reasonable request.

CONFLICT OF INTEREST

The author declared no potential conflicts of interest with respect to the research, authorship, and/or publication of this article.

ETHICS

There are no ethical issues with the publication of this manuscript.

STATEMENT ON THE USE OF ARTIFICIAL INTELLIGENCE

During the preparation of this work, the authors used Chatgpt to improve the writing and English of some sections.

REFERENCES

[1] Ocaña-Riola R. The use of statistics in health sciences: situation analysis and perspective. Stat Biosci 2016;8:204–219. [CrossRef]

[2] Aldape-Pérez M, Alarcón-Paredes A, Yáñez-Márquez C, López-Yáñez I, Camacho-Nieto O. An associative memory approach to healthcare monitoring and decision making. Sensors 2018;18:2690. [CrossRef]

[3] Esteva A, Robicquet A, Ramsundar B, Kuleshov V, DePristo M, Chou K, et al. A guide to deep learning in healthcare. Nat Med 2019;25:24–29. [CrossRef]

[4] Jiang T, Gradus JL, Rosellini AJ. Supervised machine learning: a brief primer. Behav Ther 2020;51:675–687. [CrossRef]
[5] Eckhardt CM, Madjarova SJ, Williams RJ, Ollivier M, Karlsson J, Pareek A, et al. Unsupervised machine learning methods and emerging applications in healthcare. Knee Surg Sports Traumatol Arthrosc 2023;31:376–381. [CrossRef]
[6] Clift C. The role of the World Health Organization in the international system. Burns 2013;39:291–299. [CrossRef]
[7] World Health Organization. Health in sustainable development planning: the role of indicators. No. WHO/HDE/HID/02.11. World Health Organization; 2002.
[8] Wendt C. Mapping European healthcare systems: a comparative analysis of financing, service provision and access to healthcare. J Eur Soc Policy 2009;19:432–445. [CrossRef]
[9] Wendt C, Frisina L, Rothgang H. Healthcare system types: a conceptual framework for comparison. Soc Policy Adm 2009;43:70–90. [CrossRef]
[10] Freeman R, Frisina L. Health care systems and the problem of classification. J Compar Policy Anal 2010;12:163–178. [CrossRef]
[11] Ferreira PL, Tavares AI, Quintal C, Santana P. EU health systems classification: a new proposal from EURO-HEALTHY. BMC Health Serv Res 2018;18:1–11. [CrossRef]
[12] Lee S, Kim C. Estimation of association between healthcare system efficiency and policy factors for public health. Appl Sci 2018;8:2674. [CrossRef]
[13] Espinosa-González AB, Delaney BC, Marti J, Darzi A. The role of the state in financing and regulating primary care in Europe: a taxonomy. Health Policy 2021;125:168–176. [CrossRef]
[14] Klumpp M, Loske D, Bicciato S. COVID-19 health policy evaluation: integrating health and economic perspectives with a data envelopment analysis approach. Eur J Health Econ 2022;23:1263–1285. [CrossRef]
[15] Rajawat RS, Singh KK, Mishra VN. Approximation by modified Bernstein polynomials based on real parameters. Math Found Comput 2024;7:297–309. [CrossRef]
[16] Mishra VN, Rajawat RS, Sharma V. On generalized quantum Bernstein polynomials. Adv Pure Appl Algebr 2023;27:149–160. [CrossRef]
[17] Raiz M, Rajawat RS, Mishra VN. α-Schurer Durrmeyer operators and their approximation properties. Ann Univ Craiova Math Comput Sci Ser 2023;50:189–204. [CrossRef]
[18] Pandey S, Rajawat RS, Mishra VN. Approximation properties of modified Jain-Gamma operators preserving linear function. Palestine J Math 2023;12:169–182.
[19] Raiz M, Rajawat RS, Mishra LN, Mishra VN. Approximation on bivariate of Durrmeyer operators based on beta function. J Analysis 2023. [CrossRef]
[20] Bulut C, Sönal T, Kolca D, Tarlak F. Evaluation of COVID-19 mortality using machine learning regression methods based on health system indicators. Sigma J Eng Nat Sci 2024;42(6):1797–1805. [CrossRef]
[21] Bulut C, Kolca D, Tarlak F. Development of a software for detecting burn severity using convolutional neural network-based approach. Sigma J Eng Nat Sci 2024;43:598–606. [CrossRef]
[22] Anguita D, Ghio A, Ridella S, Sterpi D. K-Fold cross validation for error rate estimate in support vector machines. In: DMIN; 2009:291–297.
[23] Wong TT, Yang NY. Dependency analysis of accuracy estimates in k-fold cross validation. IEEE Trans Knowl Data Eng 2017;29:2417–2427. [CrossRef]
[24] Mengash HA, Mahmoud HH. Brain cancer tumor classification from motion-corrected MRI images using convolutional neural network. Comput Mater Continua 2021;68:1551–1563. [CrossRef]
[25] Sokolova M, Lapalme G. A systematic analysis of performance measures for classification tasks. Inf Process Manag 2009;45:427–437. [CrossRef]
[26] Deng X, Liu Q, Deng Y, Mahadevan S. An improved method to construct basic probability assignment based on the confusion matrix for classification problem. Inf Sci 2016;340:250–261. [CrossRef]
[27] De Diego IM, Redondo AR, Fernández RR, Navarro J, Moguerza JM. General performance score for classification problems. Appl Intell 2022;52:12049–12063. [CrossRef]
[28] Toth F. Classification of healthcare systems: Can we go further? Health Policy 2016;120:535–543. [CrossRef]
[29] Jacques O, Noël A. The politics of public health investments. Soc Sci Med 2022;309:115272. [CrossRef]
[30] Böhm K, Schmid A, Götze R, Landwehr C, Rothgang H. Five types of OECD healthcare systems: empirical results of a deductive classification. Health Policy 2013;113:258–269. [CrossRef]
[31] Ariaans M, Linden P, Wendt C. Worlds of long-term care: A typology of OECD countries. Health Policy 2021;125:609–617. [CrossRef]
[32] Benoît C. The regulatory path to healthcare systems' financialization. J Eur Soc Policy 2023;09589287231176776. [CrossRef]
[33] Bertin G, Carrino L, Pantalone M. Do standard classifications still represent European welfare typologies? Novel evidence from studies on health and social care. Soc Sci Med 2021;281:114086. [CrossRef]
[34] Capano G, Toth F. Health policy under the microscope: a micro policy design perspective. Front Public Health 2023;11:1180836. [CrossRef]
[35] De Carvalho G, Schmid A, Fischer J. Classifications of health care systems: Do existing typologies reflect the particularities of the Global South? Glob Soc Policy 2021;21:278–300. [CrossRef]

Sigma J Eng Nat Sci, Vol. 43, No. 6, pp. 2186–2197, December, 2025

Sigma Journal of Engineering and Natural Sciences
Web page info: https://sigma.yildiz.edu.tr
DOI: 10.14744/sigma.2025.1935

Research Article

Cosine Kumaraswamy family of distributions: Properties and applications to real-world datasets

Ibrahim ALI[1], Alhaji Modu ISA[1], Sule Omeiza BASHIRU[2,*], Arum Kingsley CHINEDU[3]

[1]*Department of Mathematics and Computer Science, Borno State University, Maiduguri, 602104, Nigeria*
[2]*Department of Mathematics and Statistics, Confluence University of Science and Technology, Osara, Kogi State, 2344, Nigeria*
[3]*Department of Statistics, University of Nigeria, Nsukka, 900001, Nigeria*

ARTICLE INFO

Article history
Received: 27 August 2024
Revised: 03 October 2024
Accepted: 31 October 2024

Keywords:
Cosine Family of Distributions, Order Statistics, Maximum Likelihood Estimation, Quantile Function, Lomax Distribution

ABSTRACT

This study presents the cosine Kumaraswamy family of distributions, a new family of probability distributions formed by combining the cosine and Kumaraswamy families. Several statistical properties of the family are derived, such as the quantile function, moments, moment-generating function, survival and hazard functions, and order statistics. The model parameters are estimated using the maximum likelihood method. A special case, called the cosine Kumaraswamy Lomax distribution, is discussed in detail, and its probability density and hazard functions are explored for different parameter values. To assess its usefulness, the cosine Kumaraswamy Lomax distribution is compared with other well-known models using three real datasets from the medical and engineering fields. The findings show that this distribution provides a better fit than the competing models, proving its flexibility and suitability for different types of data. Overall, the cosine Kumaraswamy family offers a useful addition to statistical modeling with strong practical applications.

Cite this article as: Ali I, Isa AM, Bashiru SO, Chinedu AK. Cosine Kumaraswamy family of distributions: Properties and applications to real-world datasets. Sigma J Eng Nat Sci 2025;43(6):2186–2197.

INTRODUCTION

The need for flexible probability distributions has become important in statistical research because they help describe different kinds of data more accurately and support reliable analysis in areas such as engineering, finance, and biological sciences. This interest has led to the creation of generalized families of distributions, known as generators, which extend traditional models by adding extra parameters. These added parameters allow the new distributions to handle complex data features like heavy tails and varying failure rates. The main goal of these developments is to create models that provide a better fit for various types of data. However, it is well known that no single distribution can describe all kinds of data, so researchers continue to design new probability distributions to meet this need.

In recent years, several new families of probability distributions have been developed to improve how data are modeled in different areas such as economics, engineering,

***Corresponding author.**
*E-mail address: bash0140@gmail.com

This paper was recommended for publication in revised form by Editor-in-Chief Ahmet Selim Dalkilic

Published by Yıldız Technical University Press, İstanbul, Turkey
© Author. This is an open access article under the CC BY-NC license (http://creativecommons.org/licenses/by-nc/4.0/).

biology, environmental studies, medicine, and finance. Well-known examples include the Kumaraswamy-G family [1], Weibull-G family [2], power Lindley-G family [3], weighted exponentiated-G family [4], sine Kumaraswamy-G family [5], sine Topp-Leone-G family [6], Topp-Leone odd exponential half logistic-G family [7], extended cosine generalized family [8], Sec-G family [9], logistic cotangent exponentiated generalized family [10], sine type II Topp-Leone family [11], cosine Topp-Leone family [12], secant Kumaraswamy family [13], and exponentiated cosine Topp-Leone family [14].

Building on this foundation, this study introduces a new family of probability distributions called the cosine Kumaraswamy family. It is formed by combining the Kumaraswamy and cosine families of distributions. This integration brings together the parameter-driven flexibility of the Kumaraswamy model with the trigonometric structure of the cosine model, resulting in a more versatile framework. The new family is better able to capture variations in skewness, kurtosis, and tail behavior than many existing models. The Lomax distribution emerges as a special case of this family and showed a better fit for some real datasets than the related submodels. The cosine Kumaraswamy family increases the applicability of classical distributions and serves as a flexible tool for modeling real-world data.

MATERIALS AND METHODS

The cumulative distribution function (cdf) and the probability density function (pdf) of the Kumaraswamy family of distributions (FOD) are expressed in equations (1) and (2) as follows:

$$R(x) = 1 - \left[1 - G(x)^{\theta}\right]^{\lambda} \tag{1}$$

$$r(x) = \lambda\theta g(x) G(x)^{\theta-1}\left[1 - G(x)^{\theta}\right]^{\lambda-1} \tag{2}$$

where $\lambda > 0$ and $\theta > 0$ are shape parameters, while $g(x)$ and $G(x)$ represent the pdf and cdf of a baseline distribution, respectively.

The cdf of the cosine FOD is given by:

$$F(x) = 1 - cos\left[\frac{\pi}{2}R(x)\right] \tag{3}$$

The corresponding pdf is:

$$f(x) = \frac{\pi}{2} r(x) sin\left[\frac{\pi}{2}R(x)\right] \tag{4}$$

By substituting equations (1) and (2) into equations (3) and (4), we get the cdf and pdf of the cosine Kumaraswamy (CK)-G FOD as follows:

$$F(x) = 1 - \cos\left\{\frac{\pi}{2}\left[1 - \left(1 - G(x)^{\theta}\right)^{\lambda}\right]\right\} \tag{5}$$

$$f(x)=\frac{\pi}{2}\lambda\theta g(x)G(x)^{\theta-1}\left[1-G(x)^{\theta}\right]^{\lambda-1}\sin\left\{\frac{\pi}{2}\left[1-\left(1-G(x)^{\theta}\right)^{\lambda}\right]\right\} \tag{6}$$

The survival function $S(x)$, hazard function $h(x)$, reverse hazard function $rh(x)$, and the cumulative hazard function $R(x)$ for the CK-G FOD are given in equations (7) to (10):

$$S(x) = cos\left\{\frac{\pi}{2}\left[1 - \left(1 - G(x)^{\theta}\right)^{\lambda}\right]\right\} \tag{7}$$

$$h(x)=\frac{\pi}{2}\lambda\theta g(x)G(x)^{\theta-1}\left[1-G(x)^{\theta}\right]^{\lambda-1}tan\left\{\frac{\pi}{2}\left[1-\left(1-G(x)^{\theta}\right)^{\lambda}\right]\right\} \tag{8}$$

$$rh(x)=\frac{\frac{\pi}{2}\lambda\theta g(x)G(x)^{\theta-1}\left[1-G(x)^{\theta}\right]^{\lambda-1}sin\left\{\frac{\pi}{2}\left[1-\left(1-G(x)^{\theta}\right)^{\lambda}\right]\right\}}{1-cos\left\{\frac{\pi}{2}\left[1-\left(1-G(x)^{\theta}\right)^{\lambda}\right]\right\}} \tag{9}$$

$$R(x) = -ln\left\{cos\left\{\frac{\pi}{2}\left[1 - \left(1 - G(x)^{\theta}\right)^{\lambda}\right]\right\}\right\} \tag{10}$$

Quantile Function

The quantile function of the CK-G FOD is given as:

$$\phi(u) = x = G^{-1}\left\{\left[1 - \left[1 - \frac{\cos^{-1}(1-u)}{\pi/2}\right]^{\frac{1}{\lambda}}\right]^{\frac{1}{\theta}}\right\} \tag{11}$$

Mixture Representation

The pdf and the cdf of the CK-G FOD can be expanded using power series expansion as follows:

Expanding the sine function in the pdf of the proposed family using a Taylor series gives:

$$sin\left\{\frac{\pi}{2}\left[1 - \left(1 - G(x)^{\theta}\right)^{\lambda}\right]\right\} = \sum_{i=1}^{\infty}\frac{(-1)^i}{(2i+1)!}\left(\frac{\pi}{2}\right)^{2i+1}\left[1 - \left(1 - G(x)^{\theta}\right)^{\lambda}\right]^{2i+1}$$

$$\left[1 - \left(1 - G(x)^{\theta}\right)^{\lambda}\right]^{2i+1} = \sum_{j=0}^{\infty}(-1)^j\binom{2i+1}{j}\left(1 - G(x)^{\theta}\right)^{\lambda j}$$

$$\left(1 - G(x)^{\theta}\right)^{\lambda j+\lambda-1} = \sum_{k=0}^{\infty}(-1)^k\binom{\lambda j+\lambda-1}{k}G(x)^{\theta k}$$

$$f(x) = \sum_{i,j,k=0}^{\infty}\frac{(-1)^{i+j+k}}{(2i+1)!}\frac{\pi^{2i+2}}{2^{2i+2}}\binom{2i+1}{j}\binom{\lambda j+\lambda-1}{k}\lambda\theta g(x)G(x)^{\theta k+\theta-1}$$

$$Let\ \Psi_{i,j,k} = \frac{(-1)^{i+j+k}}{(2i+1)!}\frac{\pi^{2i+2}}{2^{2i+2}}\binom{2i+1}{j}\binom{\lambda j+\lambda-1}{k}$$

Therefore,

$$f(x) = \sum_{i,j,k=0}^{\infty}\Psi_{i,j,k}\ \lambda\theta g(x)G(x)^{\theta(k+1)-1} \tag{12}$$

The cdf of the proposed family can also be expanded using power series expansion as follows:

$$cos\left\{\frac{\pi}{2}\left[1-\left(1-G(x)^{\theta}\right)^{\lambda}\right]\right\}=\sum_{l=0}^{\infty}\frac{(-1)^{l}}{(2l)!}\frac{\pi^{2l}}{2^{2l}}\left[1-\left(1-G(x)^{\theta}\right)^{\lambda}\right]^{2l}$$

$$\left[1-\left(1-G(x)^{\theta}\right)^{\lambda}\right]^{2l}=\sum_{n=0}^{\infty}(-1)^{n}\binom{2l}{n}\left(1-G(x)^{\theta}\right)^{\lambda n}$$

$$\left(1-G(x)^{\theta}\right)^{\lambda n}=\sum_{p=0}^{\infty}(-1)^{p}\binom{\lambda n}{p}G(x)^{\theta p}$$

$$F(x)=1-\sum_{l,n,p=0}^{\infty}\frac{(-1)^{l}}{(2l)!}\frac{\pi^{2l}}{2^{2l}}\binom{2l}{n}\binom{\lambda n}{p}G(x)^{\theta p}$$

$$\text{Let } \omega_{l,n,p}=\frac{(-1)^{l}}{(2l)!}\frac{\pi^{2l}}{2^{2l}}\binom{2l}{n}\binom{\lambda n}{p}$$

Therefore,

$$F(x)=1-\sum_{l,n,p=0}^{\infty}\omega_{l,n,p}\,G(x)^{\theta p} \tag{13}$$

Equations (12) and (13) represent the reduced forms of the new family.

MATHEMATICAL PROPERTIES

Moment

The moment of the CK-G FOD is derived as follows:

$$\mu_r'=E(x^r)=\int_{-\infty}^{\infty}x^r f(x)dx$$

$$\mu_r'=\sum_{i,j,k=0}^{\infty}\Psi_{i,j,k}\,\lambda\theta\int_0^{\infty}x^r\;g(x)G(x)^{\theta(k+1)-1}dx$$

$$\text{Let } \phi=\int_0^{\infty}x^r\,g(x)G(x)^{\theta(k+1)-1}dx \tag{14}$$

$$\mu_r'=\sum_{i,j,k=0}^{\infty}\lambda\theta\,\Psi_{i,j,k}\,\phi$$

Moment Generating Function (MGF)

The MGF of the CK-G FOD is given by:

$$M_x(x)=E(e^{tx})=\int_{-\infty}^{\infty}e^{tx}f(x)dx$$

$$M_x(x)=\sum_{i,j,k=0}^{\infty}\Psi_{i,j,k}\,\lambda\theta\int_0^{\infty}e^{tx}\;g(x)G(x)^{\theta(k+1)-1}dx$$

$$\text{Let } \rho=\int_0^{\infty}e^{tx}\;g(x)G(x)^{\theta(k+1)-1}dx \tag{15}$$

$$M_x(x)=\sum_{i,j,k=0}^{\infty}\lambda\theta\Psi_{i,j,k}\rho$$

Order Statistics

Let $x_1, x_2, ..., x_n$ be a random sample of size n with pdf f(x) and cdf F(x). The pdf of the order statistics is given by:

$$f_{n:m}(x)=\frac{f(x)}{B(n,m-n+1)}[F(x)]^{n-1}[1-F(x)]^{m-n}$$

For the CK-G FOD, the pdf of the order statistics is given by:

$$f_{n:m}(x)=\frac{\sum_{i,j,k=0}^{\infty}\Psi_{i,j,k}\;\lambda\theta g(x)G(x)^{\theta(k+1)-1}}{B(n,m-n+1)}\left[1-\sum_{i,p=0}^{\infty}\omega_{i,n,p}\,G(x)^{\theta p}\right]^{n-1}\left[\sum_{i,p=0}^{\infty}\omega_{i,n,p}G(x)^{\theta p}\right]^{m-n} \tag{16}$$

PARAMETER ESTIMATION

Maximum Likelihood Estimation

Let $x_1, x_2, ..., x_n$ be an observed random sample of size n from the CK-G family, then the likelihood function can be expressed as:

$$\ell=\prod_{i=1}^{n}\left[\frac{\pi}{2}\lambda\theta g(x)G(x)^{\theta-1}\left[1-G(x)^{\theta}\right]^{\lambda-1}sin\left\{\frac{\pi}{2}\left[1-\left(1-G(x)^{\theta}\right)^{\lambda}\right]\right\}\right]$$

Taking the natural logarithm, the log-likelihood function simplifies to

$$\begin{aligned}\log\ell=n\log\left(\frac{\pi}{2}\right)+n\log(\theta)\;+n\log(\lambda)+\sum_{i=1}^{n}\log g(x)\\+(\theta-1)\sum_{i=1}^{n}\log g(x)+(\lambda-1)\sum_{i=1}^{n}log\left[1-G(x)^{\theta}\right]\\+\sum_{i=1}^{n}\log sin\left\{\frac{\pi}{2}\left[1-\left(1-G(x)^{\theta}\right)^{\lambda}\right]\right\}\end{aligned} \tag{17}$$

Now, we determine the first-order conditions

$$\begin{aligned}\frac{\partial\ell}{\partial\theta}=&\frac{n}{\theta}+\sum_{i=1}^{n}\log G(x)+(\lambda-1)-\sum_{i=1}^{n}\frac{G(x)^{\theta}\log G(x)}{(1-G(x)^{\theta})}\\&-\sum_{i=1}^{n}\frac{\pi}{2}\lambda\left(1-G(x)^{\theta}\right)^{\lambda-1}\times G(x)^{\theta}\log G(x)\tan\left\{\frac{\pi}{2}\left[1-\left(1-G(x)^{\theta}\right)^{\lambda}\right]\right\}\end{aligned} \tag{18}$$

$$\begin{aligned}\frac{\partial\ell}{\partial\lambda}=&\frac{n}{\lambda}+\sum_{i=1}^{n}\log(1-G(x)^{\theta})\\&-\sum_{i=1}^{n}\frac{\pi}{2}\left(1-G(x)^{\theta}\right)^{\lambda}\log(1-G(x)^{\theta})\tan\left\{\frac{\pi}{2}\left[1-\left(1-G(x)^{\theta}\right)^{\lambda}\right]\right\}\end{aligned} \tag{19}$$

$$\begin{aligned}\frac{\partial\ell}{\partial\xi}=&\sum_{i=1}^{n}\frac{g'(x)}{g(x)}+(\theta-1)\sum_{i=1}^{n}\frac{g(x)}{G(x)}-\sum_{i=1}^{n}\frac{\theta g(x)G(x)^{\theta-1}}{(1-G(x)^{\theta})}\\&-\sum_{i=1}^{n}\frac{\pi}{2}\lambda\theta g(x)G(x)^{\theta-1}\left(1-G(x)^{\theta}\right)^{\lambda-1}\tan\left\{\frac{\pi}{2}\left[1-\left(1-G(x)^{\theta}\right)^{\lambda}\right]\right\}\end{aligned} \tag{20}$$

Since obtaining closed-form solutions for this system of equations is challenging, numerical solutions can be found using iterative methods.

SUB-MODEL

We introduce the Lomax distribution, as proposed by [15], as a specific case within the CK-G distribution family. The cdf and pdf of the Lomax distribution are provided in equations (21) and (22) below.

$$G(x) = 1 - \left(1 + \frac{x}{\beta}\right)^{-\alpha} \tag{21}$$

$$g(x) = \frac{\alpha}{\beta}\left(1 + \frac{x}{\beta}\right)^{-(\alpha+1)} \tag{22}$$

where, $\alpha > 0$ and $\beta > 0$ are the shape and scale parameters respectively

Cosine Kumaraswamy – Lomax (CKL) Distribution

By substituting equation (21) into equation (5), the cdf of the cosine Kumaraswamy Lomax (CKL) distribution is given by:

$$F(x) = 1 - cos\left\{\frac{\pi}{2}\left[1 - \left(1 - \left(1 - \left(1 + \frac{x}{\beta}\right)^{-\alpha}\right)^{\theta}\right)^{\lambda}\right]\right\} \tag{23}$$

And by substituting equations (21) and (22) into (6), we have the associated pdf given as:

$$f(x) = \frac{\pi}{2}\lambda\theta\left(\frac{\alpha}{\beta}\left(1 + \frac{x}{\beta}\right)^{-(\alpha+1)}\right)\left(1 - \left(1 + \frac{x}{\beta}\right)^{-\alpha}\right)^{\theta-1} \times\left[1 - \left(1 - \left(1 + \frac{x}{\beta}\right)^{-\alpha}\right)^{\theta}\right]^{\lambda-1} sin\left\{\frac{\pi}{2}\left[1 - \left(1 - \left(1 - \left(1 + \frac{x}{\beta}\right)^{-\alpha}\right)^{\theta}\right)^{\lambda}\right]\right\} \tag{24}$$

The pdf and cdf plots of the CKL distribution are shown in Figure 1.

Figure 1 illustrates that the CKL distribution's pdf is approximately symmetric, right-skewed, and unimodal. The cdf starts at zero and approaches one, confirming its validity as a probability distribution.

The functions $S(x)$, $h(x)$, $rh(x)$, $R(x)$ and the $\phi(u)$ of the CKL distribution are given in equations (25) to (29):

$$S(x) = cos\left\{\frac{\pi}{2}\left[1 - \left(1 - \left(1 - \left(1 + \frac{x}{\beta}\right)^{-\alpha}\right)^{\theta}\right)^{\lambda}\right]\right\} \tag{25}$$

$$h(x) = \theta\lambda\left[\frac{\alpha x}{\beta}\left(1 + \frac{x}{\beta}\right)^{-(\alpha+1)}\right]\left[1 - \left(1 + \frac{x}{\beta}\right)^{-\alpha}\right]^{\theta-1} \times\left[1 - \left(1 - \left(1 + \frac{x}{\beta}\right)^{-\alpha}\right)^{\theta}\right]^{\lambda-1} tan\left\{\frac{\pi}{2}\left[1 - \left(1 - \left(1 - \left(1 + \frac{x}{\beta}\right)^{-\alpha}\right)^{\theta}\right)^{\lambda}\right]\right\} \tag{26}$$

$$rh(x) = \frac{\theta\lambda\left[\frac{\alpha x}{\beta}\left(1 + \frac{x}{\beta}\right)^{-(\alpha+1)}\right]\left[1 - \left(1 + \frac{x}{\beta}\right)^{-\alpha}\right]^{\theta-1}\left[1 - \left(1 - \left(1 + \frac{x}{\beta}\right)^{-\alpha}\right)^{\theta}\right]^{\lambda-1} sin\left\{\frac{\pi}{2}\left[1 - \left(1 - \left(1 - \left(1 + \frac{x}{\beta}\right)^{-\alpha}\right)^{\theta}\right)^{\lambda}\right]\right\}}{1 - cos\left\{\frac{\pi}{2}\left[1 - \left(1 - \left(1 + \frac{x}{\beta}\right)^{-\alpha}\right)^{\theta}\right)^{\lambda}\right]\right\}} \tag{27}$$

$$R(x) = -ln\left[cos\left\{\frac{\pi}{2}\left[1 - \left(1 - \left(1 - \left(1 + \frac{x}{\beta}\right)^{-\alpha}\right)^{\theta}\right)^{\lambda}\right]\right\}\right] \tag{28}$$

$$\phi(u) = \beta\left\{1 - \left(1 - \left(1 - \left(1 - \frac{\cos^{-1}(1-u)}{\frac{\pi}{2}}\right)^{\frac{1}{\lambda}}\right)^{\frac{1}{\theta}}\right)^{-\frac{1}{\alpha}}\right\} \tag{29}$$

The survival and hazard function plots of the CKL distribution are shown in Figure 2.

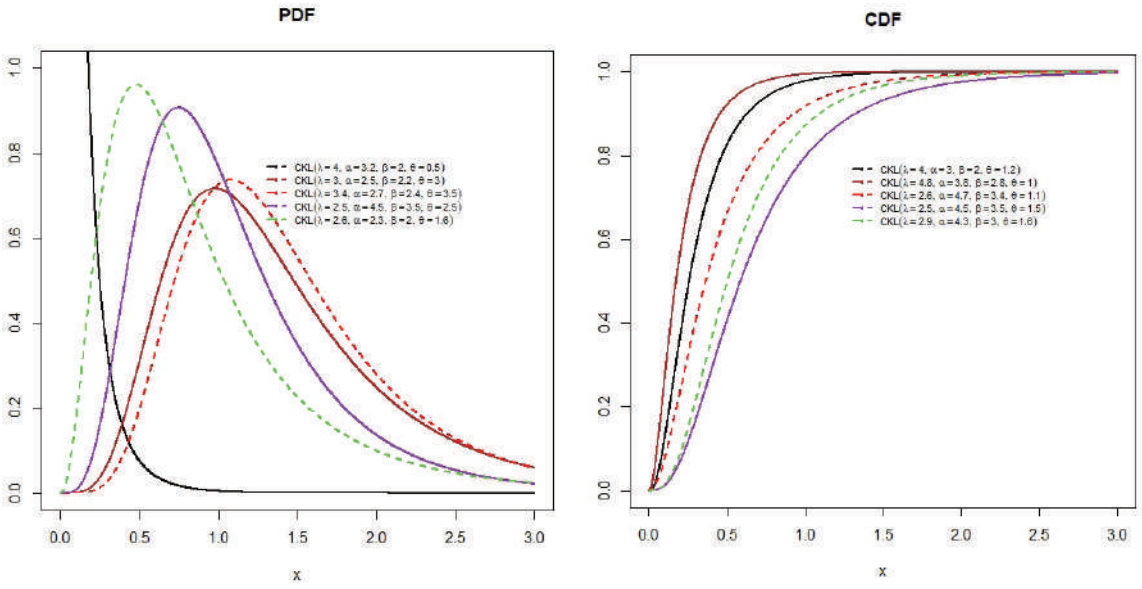


Figure 1. pdf and cdf plots of the CKL distribution.

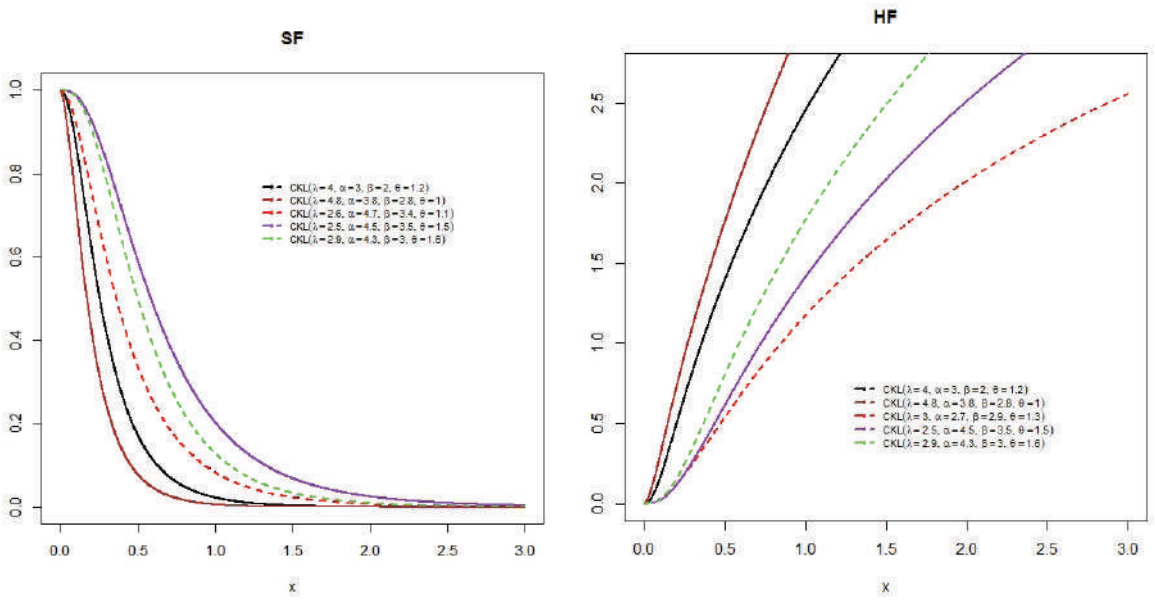


Figure 2. Survival function and Hazard function plots of the CKL distribution.

Figure 2 illustrates that the hazard function of the CKL distribution exhibits an increasing hazard rate, indicating that the risk of an event occurring rises over time. The survival function, on the other hand, decreases from 1 to 0, indicating a lower probability of survival with time.

APPLICATION

This section shows how useful the cosine Kumaraswamy Lomax (CKL) distribution is by applying it to three real datasets. The CKL model is compared with some well-known distributions, such as the Lomax (L) [16], Lehmann type II Lomax (LTIIL) [17], half-logistic Lomax (HLL) [18], and power Lomax (PL) [19] models. Model parameters are estimated using the maximum likelihood estimation (MLE) method. To compare the models, different goodness-of-fit criteria are used, such as the Akaike information criterion (I_A), Bayesian information criterion (I_B), corrected Akaike information criterion (I_{CA}), and Hannan–Quinn information criterion (I_{HQ}). The model with the smallest values of these measures gives the best fit to the data.

First Data

The first dataset, sourced from [20], consists of the number of million revolutions before failure recorded for 23 ball bearings during life tests. The data is as follows:

17.88, 28.92, 33.0, 41.52, 42.12, 45.6, 48.8, 51.84, 51.96, 54.12, 55.56, 67.8, 68.44, 68.88, 84.12, 93.12, 98.64, 105.12, 105.84, 105.84, 127.92, 128.04, 173.4.

Descriptive statistics for the first dataset are shown in Table 1, and the graphs are shown in Figure 3. The parameter estimates and goodness-of-fit results for the first dataset are shown in Table 2, with the estimated pdf, cdf, survival function, and P–P plots in Figure 4.

Table 1 shows the descriptive statistics for the first dataset, which indicate moderate positive skewness and a leptokurtic shape. These features are also shown in the plots in Figure 3. The kernel density plot supports the presence of positive skewness, while the TTT plot suggests an increasing failure rate. The box plot further shows that the dataset contains some outliers.

The goodness-of-fit measures in Table 2 indicate that our proposed CLK model outperforms the other distributions tested, as it has the lowest evaluation metric values. Figure 4 shows the fitted density, cdf, survival function (sf), and P–P plots of the CLK model for the dataset, indicating that the model fits the data very well.

Second Data

The second dataset, as discussed by [20], consists of failure times for 24 mechanical components. The observations are as follows:

Table 1. Descriptive statistics of the first data

Min	Mean	Median	Range	Skewness	Kurtosis	Max
17.88	73.85	67.80	155.52	0.7972	3.1410	173.4

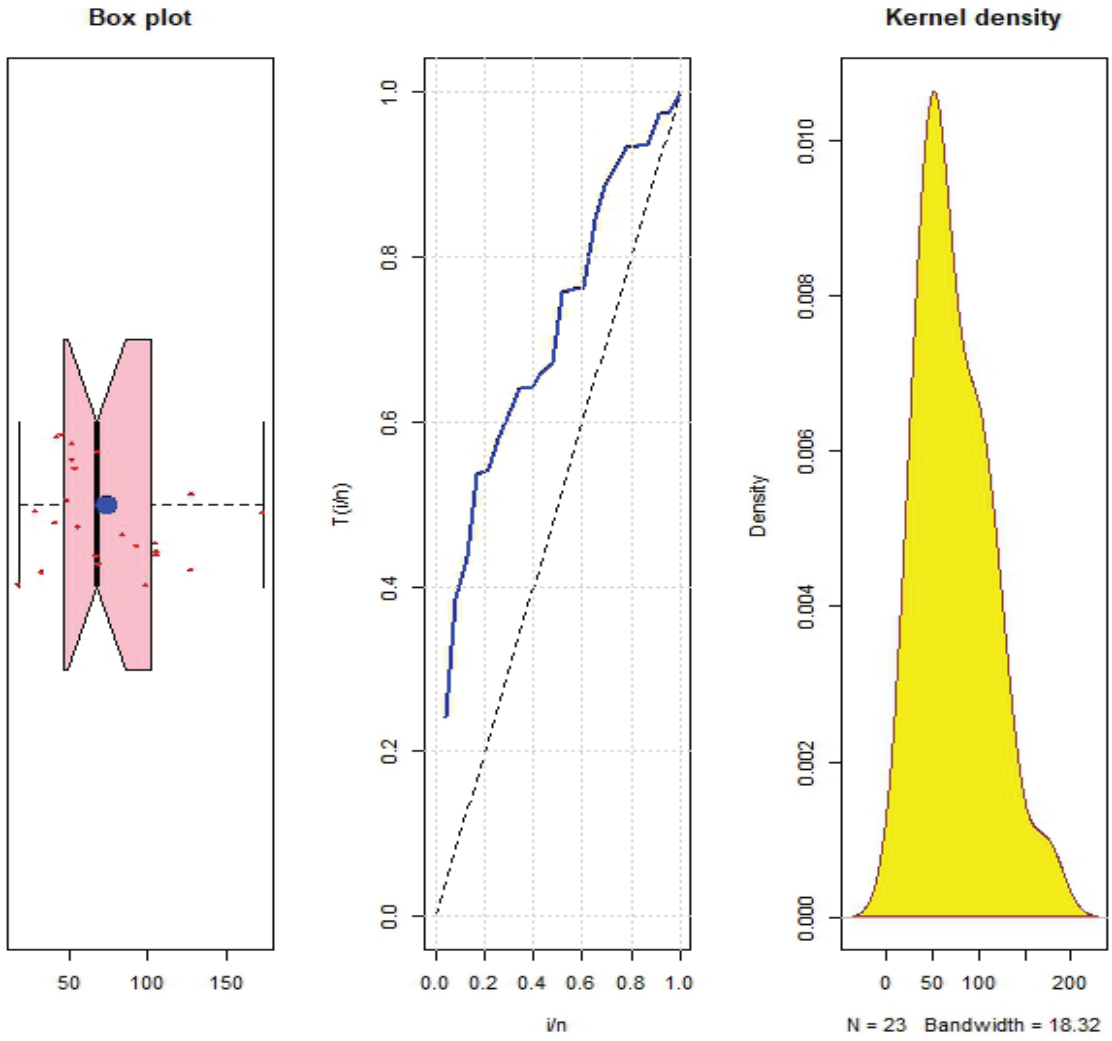


Figure 3. Visual representations of the first dataset.

Table 2. Goodness-of-fit measures for each distribution applied to the first dataset.

MODEL	MLE	-LL	I_A	I_B	I_{CA}	I_{HQ}
CKL	$\hat{\lambda} = 62.9734$ $\hat{\theta} = 268.109$ $\hat{\alpha} = 0.3772$ $\hat{\beta} = 0.00095$	113.9990	235.9980	240.5400	238.2202	237.1403
L	$\hat{\alpha} = 648816.1$ $\hat{\beta} = 47988211$	121.9459	247.8918	250.1628	248.4918	248.4629
LTIIL	$\hat{\gamma} = 0.0403$ $\hat{\alpha} = 13.5307$ $\hat{\lambda} = 12.6983$	136.9632	279.9263	283.3328	281.1895	280.783
HLL	$\hat{\alpha} = 1332.639$ $\hat{\beta} = 0.000015$	119.2122	242.4244	244.6954	243.0244	242.9956
PL	$\hat{\alpha} = 105.5535$ $\hat{\beta} = 0.55500$ $\hat{\lambda} = 800.9172$	134.881	275.762	279.1685	277.0251	276.6187

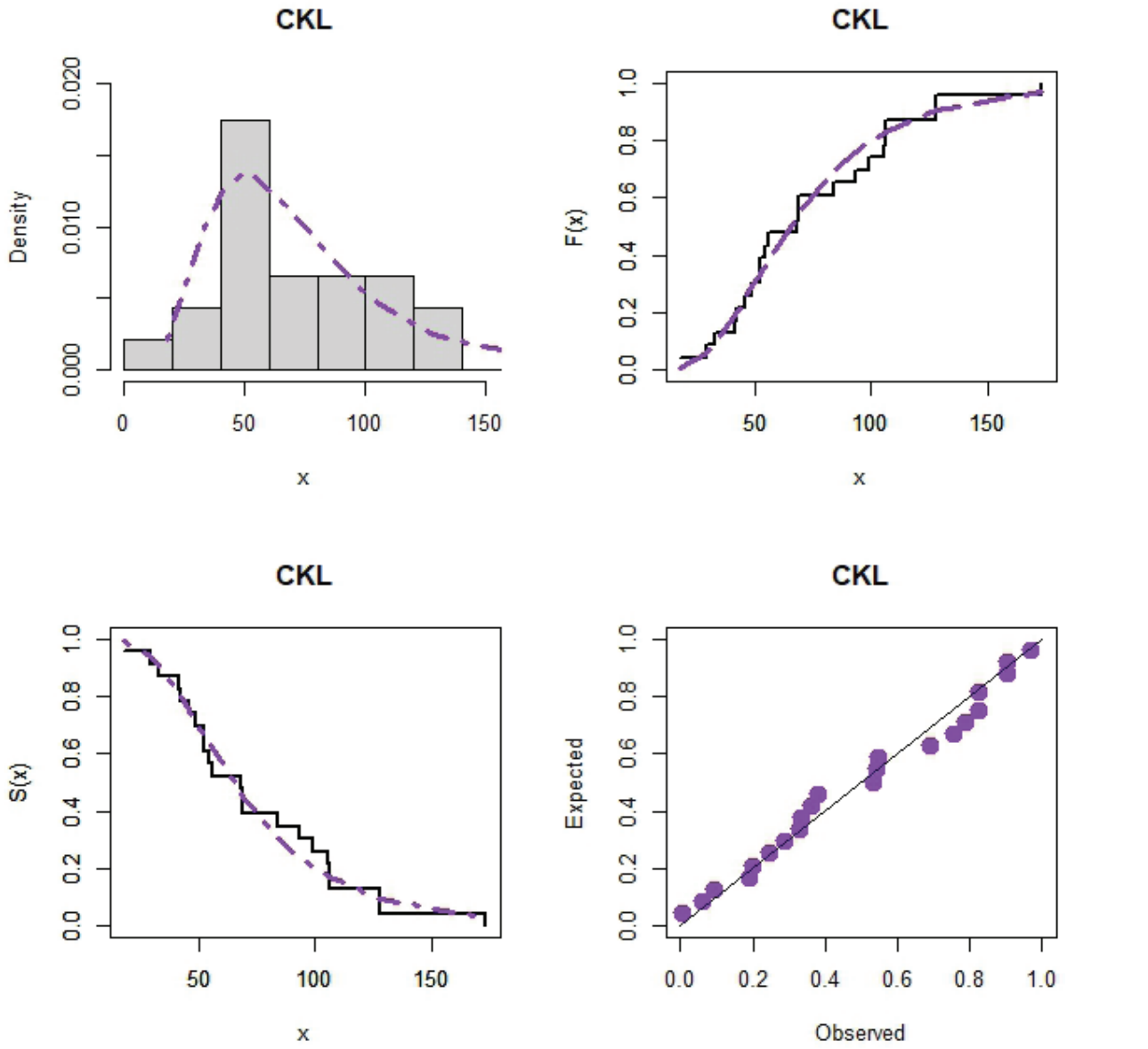


Figure 4. Fitted density, cdf, SF and PP plot of the CLK model to the first data.

30.94, 18.51, 16.62, 51.56, 22.85, 22.38, 19.08, 49.56, 17.12, 10.67, 25.43, 10.24, 27.47, 14.70, 14.10, 29.93, 27.98, 36.02, 19.40, 14.97, 22.57, 12.26, 18.14, 18.84

Descriptive statistics for the second dataset are shown in Table 3, and the graphs are shown in Figure 5. The parameter estimates and goodness-of-fit results for the second dataset are shown in Table 4, with the estimated pdf, cdf, survival functions, and P–P plots in Figure 6.

The descriptive statistics presented in Table 3 indicate that the dataset is highly positively skewed and leptokurtic. Figure 4 shows the presence of outliers in the box plot, while the TTT plot reveals an increasing failure rate. Additionally, the kernel density plot suggests that the dataset is right-skewed.

The goodness-of-fit measures in Table 4 indicate that our proposed CKL model outperforms the other distributions,

Table 3. Descriptive statistics of the second data

Min	Mean	Median	Range	Skewness	Kurtosis	Max
10.24	22.97	19.24	41.32	1.3454	4.3599	51.56

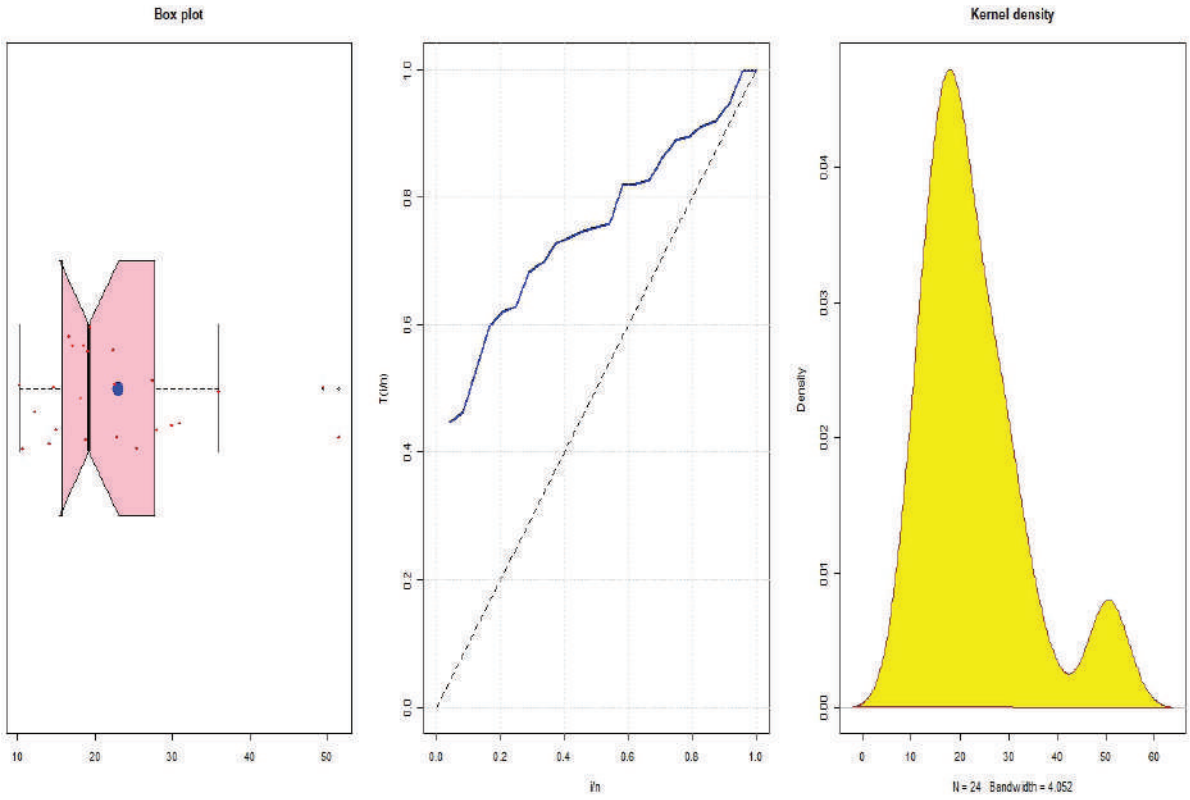


Figure 5. Visual representations of the second dataset.

Table 4. Goodness-of-fit measures for each distribution applied to the second dataset

MODEL	MLE	-LL	I_A	I_B	I_{CA}	I_{HQ}
CKL	$\hat{\lambda} = 0.221000$ $\hat{\theta} = 78.39050$ $\hat{\alpha} = 82262.37$ $\hat{\beta} = 179403.6$	85.5086	179.0174	183.7296	181.1226	180.2675
L	$\hat{\alpha} = 2061805$ $\hat{\beta} = 47372304$	99.2231	202.4463	204.8024	203.0177	203.0714
LTIIL	$\hat{\gamma} = 2.135900$ $\hat{\alpha} = 838177.7$ $\hat{\lambda} = 41118771$	99.2231	204.4463	207.9805	205.6463	205.3839
HLL	$\hat{\alpha} = 565.0091$ $\hat{\beta} = 0.00011$	95.9624	195.9249	198.281	196.4963	196.5499
PL	$\hat{\alpha} = 84.1146$ $\hat{\beta} = 1.29310$ $\hat{\alpha} = 4310.37$	94.9106	195.8214	199.3555	197.0214	196.7590

as evidenced by its lowest evaluation metric values. Figure 6 shows the fitted density, cdf, sf, and P–P plots of the CLK model for the dataset, indicating that the model fits the data very well.

Third Data

The third dataset, sourced from [21], includes the relief times (in minutes) for 20 patients treated with an analgesic.

"1.1, 1.4, 1.3, 1.7, 1.9, 1.8, 1.6, 2.2, 1.7, 2.7, 4.1, 1.8, 1.5, 1.2, 1.4, 3, 1.7, 2.3, 1.6, 2"

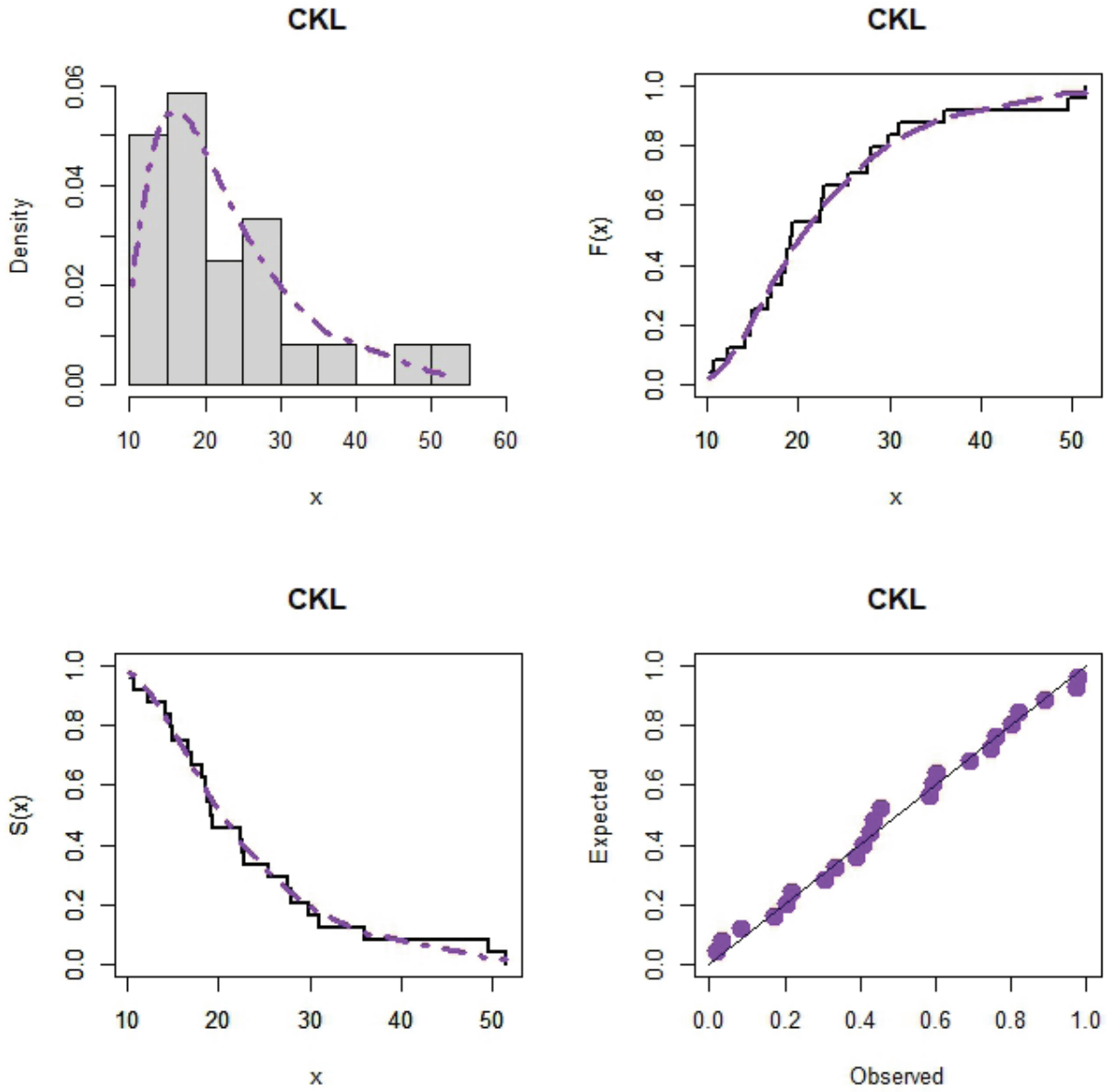


Figure 6. Fitted density, CDF, SF and PP plot of the CKL model to the second data.

Descriptive statistics for the third dataset are shown in Table 5, and the graphs are shown in Figure 7. The parameter estimates and goodness-of-fit results for the third dataset are shown in Table 6, with the estimated pdf, cdf, survival function, and P–P plots in Figure 8.

The descriptive statistics presented in Table 5 indicate that the dataset is highly positively skewed and leptokurtic. Figure 7 shows the presence of outliers in the box plot, while the TTT plot reveals an increasing failure rate. Additionally, the kernel density plot suggests that the dataset is right-skewed.

The goodness-of-fit results in Table 6 show that the proposed CKL model performs better than the other distributions, as it has the lowest values for the evaluation measures. Figure 8 shows the fitted density, cdf, sf, and P–P

Table 5. Descriptive statistics of the third data

Min	Mean	Median	Range	Skewness	Kurtosis	Max
1.1	1.9	1.7	3	1.7197	5.9241	4.1

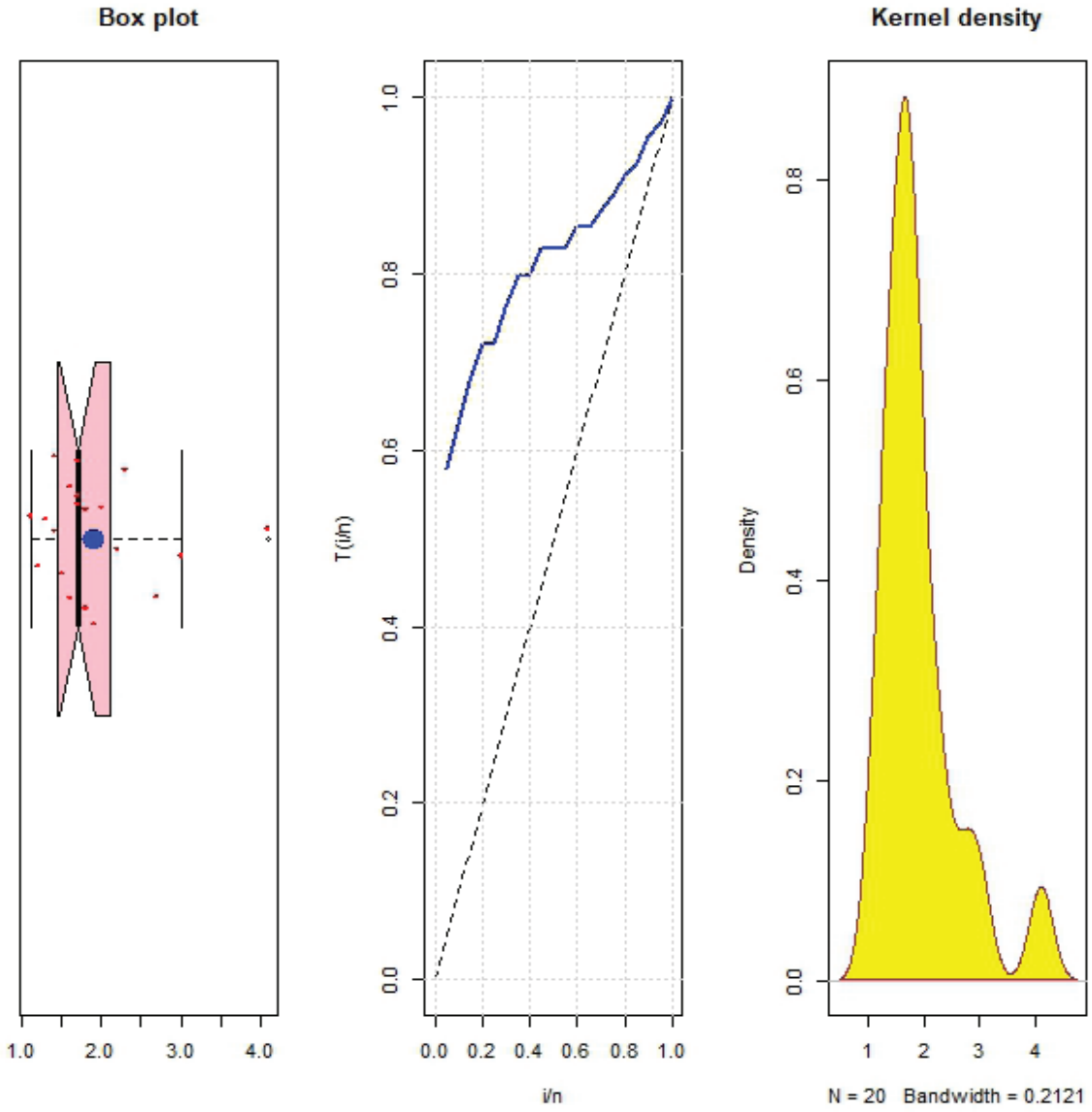


Figure 7. Visual representations of the third dataset.

Table 6. Goodness-of-fit measures for each distribution applied to the third dataset

MODEL	MLE	-LL	I_A	I_B	I_{CA}	I_{HQ}
CKL	$\hat{\lambda} = 5.79830$ $\hat{\theta} = 41.2967$ $\hat{\alpha} = 1.61060$ $\hat{\beta} = 0.28520$	15.9688	39.9376	43.9205	42.6043	40.7151
L	$\hat{\alpha} = 1929.1945$ $\hat{\beta} = 36673966$	32.83708	69.6742	71.6657	70.3800	70.0629
LTIIL	$\hat{\gamma} = 0.732000$ $\hat{\alpha} = 3357085$ $\hat{\lambda} = 4670060$	32.8371	71.6742	74.6614	73.1742	72.2573
HLL	$\hat{\alpha} = 3710.142$ $\hat{\beta} = 0.000200$	29.6508	63.3016	65.2931	64.0075	63.6904

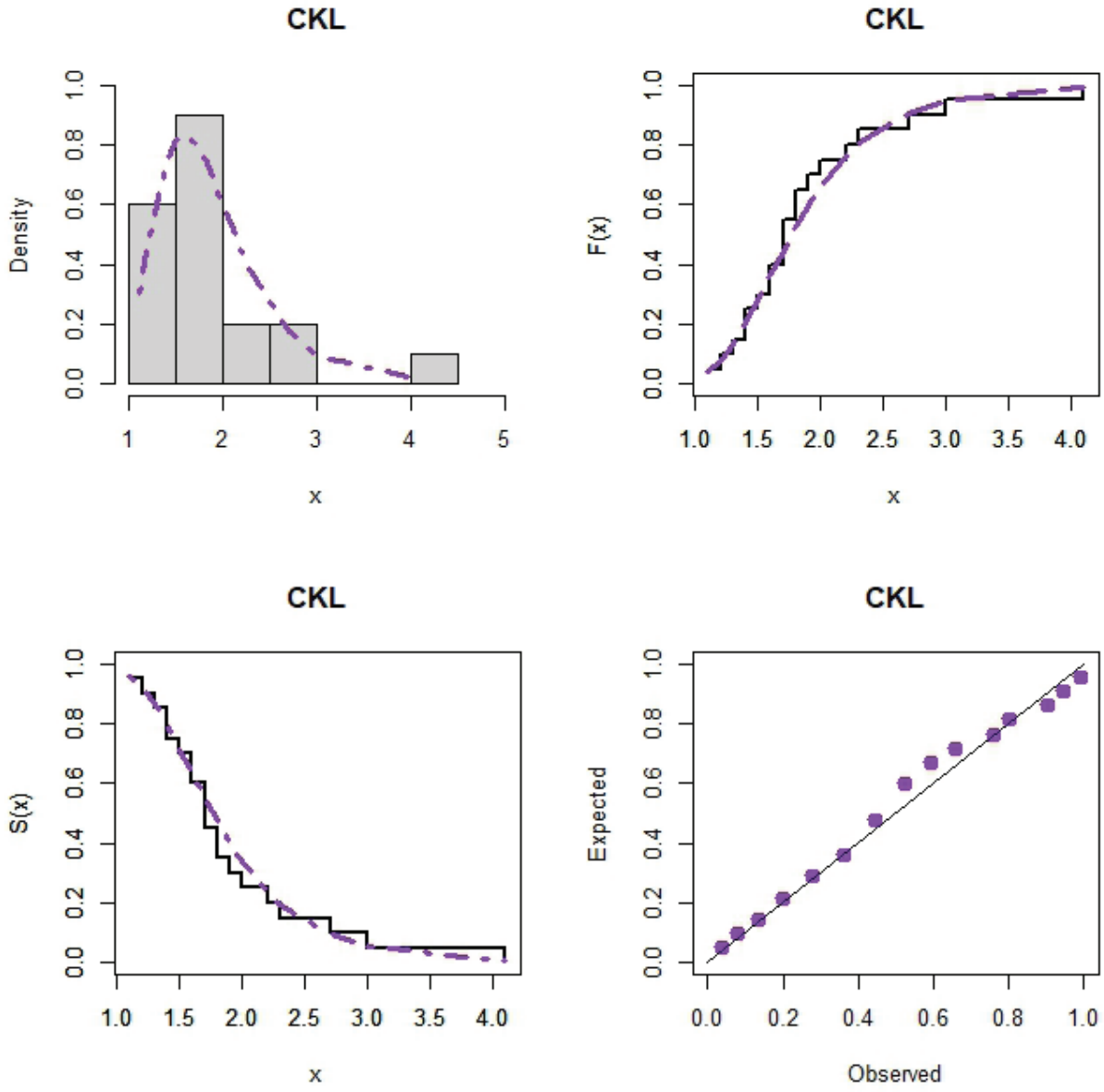


Figure 8. Fitted density, cdf, SF and PP plot of the CKL model to the third data.

plots of the CLK model for the dataset, indicating that the model fits the data very well.

RESULTS AND DISCUSSION

The cosine Kumaraswamy Lomax (CKL) distribution was applied to three real datasets from engineering and medical studies. The findings show that the CKL model is flexible and can handle different types of data. In all three cases, the CKL model performed better than the Lomax, Lehmann type II Lomax, half-logistic Lomax, and power Lomax models.

The lower I_A, I_B, I_{CA}, and I_{HQ} values show that the CKL model fits the data well. Results from the analysis of the two data indicate that the CKL model can be used in both engineering and medical studies. In engineering, it can be used to describe how long components last, helping improve maintenance and design. In medicine, it can be used to study relief times and support treatment choices.

CONCLUSION

This study introduced a new FOD called the cosine Kumaraswamy FOD, created by combining the Kumaraswamy and cosine families. The main properties of the family, such as the quantile function, moments, and order statistics, were derived.

A submodel of this family, the cosine Kumaraswamy Lomax (CKL) distribution, was proposed. Its performance was tested with three real datasets from engineering and medical fields and compared with other known models. The CKL model gave the best fit in all cases, showing that it can handle different types of data well.

The CKL distribution adds a useful tool to statistical modeling. Future work can build on this family to create new submodels with broader use and better performance in various areas.

REFERENCES

[1] Cordeiro GM, De Castro M. A new family of generalized distributions. J Stat Comput Simul 2011;81:883–898. [CrossRef]

[2] Bourguignon M, Silva RB, Cordeiro GM. The Weibull-G family of probability distributions. J Data Sci. 2014;12:53–68. [CrossRef]

[3] Hassan AS, Nassr SG. Power Lindley-G family of distributions. Ann Data Sci 2019;6:189–210. [CrossRef]

[4] Ahmad Z, Elgarhy M, Hamedani GG. The weighted exponentiated family of distributions: properties, applications and characterizations. J Iranian Stat Soc 2019;19:209–228. [CrossRef]

[5] Chesneau C, Jamal F. The sine Kumaraswamy-G family of distributions. J Math Ext 2020;15:1–26.

[6] Al-Babtain AA, Elbatal I, Chesneau C, Elgarhy M. Sine Topp-Leone-G family of distributions: theory and applications. Open Phys 2020;18:574–593. [CrossRef]

[7] Chipepa F, Oluyede B. The Topp-Leone odd exponential half logistic-G family of distributions: model, properties and applications. Pak J Stat 2021;37:253–277. [CrossRef]

[8] Mahmood Z, Jawa TM, Sayed-Ahmed N, Khalil EM, Muse AH, Tolba AH. An extended cosine generalized family of distributions for reliability modeling: characteristics and applications with simulation study. Math Prob Eng 2022;2022:3634698. [CrossRef]

[9] Souza L, de Oliveira WR, de Brito CCR, Chesneau C, Fernandes R, Ferreira TA. Sec-G class of distributions: properties and applications. Symmetry. 2022;14:299. [CrossRef]

[10] Tashkandy YA, Nagy M, Akbar M, Mahmood Z, Gemeay AM, Hossain MM, et al. The exponentiated cotangent generalized distributions: characteristics and applications to chemotherapy treatment data. IEEE Access 2023;11:35697–35709. [CrossRef]

[11] Isa AM, Doguwa SI, Alhaji BB, Dikko HG. Sine Type II Topp-Leone G family of probability distribution: mathematical properties and application. Arid Zone J Basic Appl Res 2023;2:124–138. [CrossRef]

[12] Nanga S, Nasiru S, Dioggban J. Cosine Topp-Leone family of distributions: properties and regression. Res Math 2023;10:2208935. [CrossRef]

[13] Nanga S, Sayibu SB, Angbing ID, Alhassan M, Benson AM, Abubakari AG, et al. Secant Kumaraswamy family of distributions: properties, regression model, and applications. Comput Math Methods 2024;2024:8925329. [CrossRef]

[14] Osi AA, Doguwa SI, Abubakar Y, Zakari Y, Abubakar U. Development of exponentiated cosine Topp-Leone generalized family of distributions and its applications to lifetime data. UMYU Scientifica 2024;3:157–167. [CrossRef]

[15] Souza L. New trigonometric classes of probabilistic distributions [master thesis]. State of Pernambuco, Brasil; 2015.

[16] Lomax KS. Business failures: another example of the analysis of failure data. J Am Stat Assoc 1954;49:847–852. [CrossRef]

[17] Isa AM, Kaigama A, Akeem AA, Sule OB. Lehman Type II Lomax distribution: properties and application to real data set. Commun Phys Sci 2023;9:63–72.

[18] Anwar M, Zahoor J. The half-logistic Lomax distribution for lifetime modeling. J Probab Stat 2018;2018:3152807. [CrossRef]

[19] Rady EHA, Hassanein WA, Elhaddad TA. The power Lomax distribution with an application to bladder cancer data. SpringerPlus 2016;5:1838. [CrossRef]

[20] Arshad MZ, Iqbal MZ, Al Mutairi A. A comprehensive review of datasets for statistical research in probability and quality control. J Math Comput Sci 2021;11:3663–3728.

[21] Bashiru SO. A study on the properties of a new exponentiated extended inverse exponential distribution with applications. Reliab Theory Appl 2023;3:59–72.

Sigma Journal of Engineering and Natural Sciences
Web page info: https://sigma.yildiz.edu.tr
DOI: 10.14744/sigma.2025.1936

Research Article

Enhancing battery safety and performance through advanced cooling solutions for electric vehicles

Madhavi NERKAR[1,*], Govind Rai GOYAL[1], Aniruddha MUKHERJEE[2], Bhanu Pratap SONI[3]

[1]University of Engineering and Management, Jaipur, Rajasthan, 303807, India
[2]Baba Farid College of Engineering and Technology, Bathinda, Punjab, 151001, India
[3]College of Engineering & Technical Vocational Education and Training, Fiji National University, Fiji, 15676, India

ARTICLE INFO

Article history
Received: 05 November 2024
Revised: 13 February 2025
Accepted: 27 March 2025

Keywords:
Air Cooling; Battery Temperature Performance; Battery State of Charge; Electric Vehicle

ABSTRACT

The increasing stipulation of electric vehicles underscores the critical requirement for effective thermal management in lithium-ion battery systems, particularly during high-rate charging. Overheating and Capacity Degradation remain a primary challenge, as it impact battery safety, lifespan, and performance. The study examines a thorough evaluation of cooling techniques to improve battery packs' thermal management under situations of fast discharge. A comprehensive analysis of heat generation and dissipation mechanisms within the battery cells has been conducted to identify critical factors influencing thermal performance in battery packs. This paper has been focused on battery pack temperature and state of charge analysis at different atmospheric conditions.

The air cooling technique is evaluated through simulation studies to determine the effectiveness of maintaining an optimal temperature range. The result demonstrates significant improvement in thermal regulation, exploring the benefits and limitations of the proposed cooling strategy. Simulation studies highlight the impact of air cooling on temperature control by using an auto-tune Propotional-Integral-Derivatives controller, revealing significant improvements in thermal stability, battery lifespan, and overall efficiency by 13.11%. In addition to improving battery performance and longevity. It has been evaluated on the OPAL-RT real-time simulator's test bench. The proposed strategy enhances the overall safety and efficiency of high-power battery systems. For the creation of efficient heat management techniques in the future of battery technologies, the study offers valuable suggestions.

Cite this article as: Nerkar M, Goyal GR, Mukherjee A, Soni BP. Enhancing battery safety and performance through advanced cooling solutions for electric vehicles. Sigma J Eng Nat Sci 2025;43(6):2198–2212.

***Corresponding author.**
*E-mail address: madhavi.nerka78@gmail.com

This paper was recommended for publication in revised form by Editor-in-Chief Ahmet Selim Dalkilic

Published by Yıldız Technical University Press, İstanbul, Turkey
© Author. This is an open access article under the CC BY-NC license (http://creativecommons.org/licenses/by-nc/4.0/).

INTRODUCTION

Numerous automobile manufacturers are introducing electric cars as a more advantageous and ecologically friendly option to internal combustion engine automobiles. Throughout the next few years, the number of EVs will increase rapidly [1]. Electric vehicles (EVs) are cutting-edge and difficult substitutes for conventional automobiles. They are advantageous to the environment since they have minimal running costs and may use renewable energy sources. The flourishing popularity of EVs has created problems with the management of load and effective charging infrastructure [2]. The most affordable energy storage technology for EVs at the moment is lithium-ion batteries because of their massive specific energy, high specific power, low self-discharge rate, high voltage, very long lifespan, and remarkable recyclability [3, 4]. However, Li-ion battery performance will be influenced by operation and even storage temperature [5]. Studies indicate that temperature is the key contributor to battery aging which has an adverse impact on internal resistance and capacity [6].

In battery thermal management (BTM), the most modern advances are being implemented to address the expected problems and ensure battery safety. By using a heat transfer intensification technique, the BTM technology improves battery safety by ensuring battery operation performance derived from mechanical, electrochemical, and the battery's thermo kinetic characteristics under both typical and unusual operating situations. It's also critical to maintain the proper operating temperature and avoid overheating for safe operation in optimal temperature range i.e. 15°C to 35°C.as shown in Figure.1. Thus, creating a BTM system that is dependable and safe is an important research objective [7]. This study is important because it examines innovative battery thermal management system (BTMS) techniques. They are necessary to increase lithium-ion battery's lifespan and performance in automobiles that are electrically driven. The research offers helpful recommendations for creating efficient temperature management systems in battery technologies of the future [8].

Several studies have been explained on creating an accurate thermal management system (TMS) that enhances the lifespan of battery. performance is one of the key components in the building of an electric car [9]. In practice, this issue may contain some restrictions which turn it into a constraint optimization problem. Their benefit, meanwhile, is that they can handle complicated problems far better than numerical ones, particularly in current situations with a huge number of input factors [10]. One of the issues that manufacturers are now dealing is real-time battery heating. The temperature rise in battery is the main influencing factor as a Joule's heat. Instead of using dynamic loading, various techniques were used to predict the heat generation in battery at a fixed charge/discharge rate [11]. One crucial ability that has been applied extensively to power battery cooling and preheating is the TMS of the battery at a suitable temperature. It will guarantee the power battery operates steadily and safely. Author provided a summary of status of research on the TMS for power batteries, thoroughly comparing four distinct cooling system types Phase-change materials, heat pipes, liquid cooling, air cooling, and two kinds of heating system internal and external heating heating [12]. Combining several cooling systems as shown in Figure 2 based on the benefits and drawbacks of various cooling methods is now the main growth route for Lithium-ion battery thermal management technology as given in Table 1. An appropriate cooling techniques may be chosen and combined to satisfy various thermal management user requirements [13].

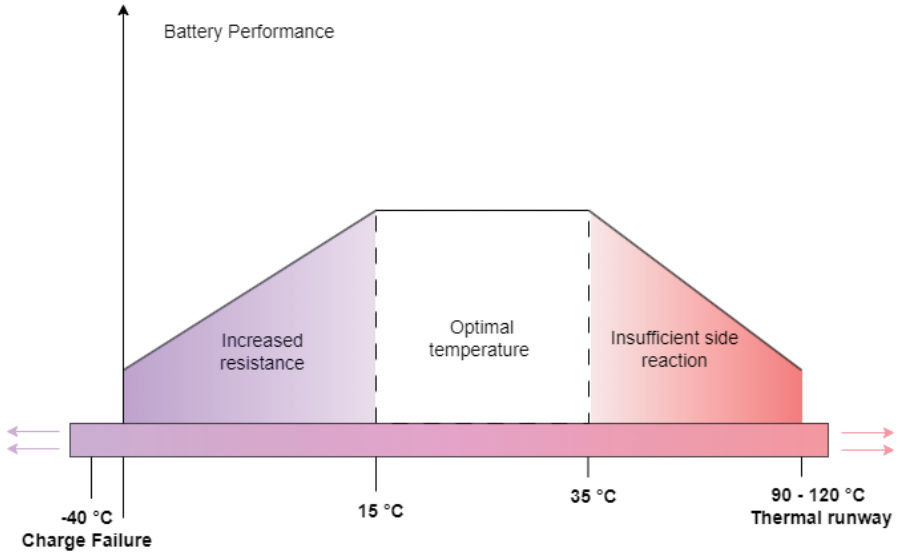


Figure 1. Temperature range of lithium-ion battery.

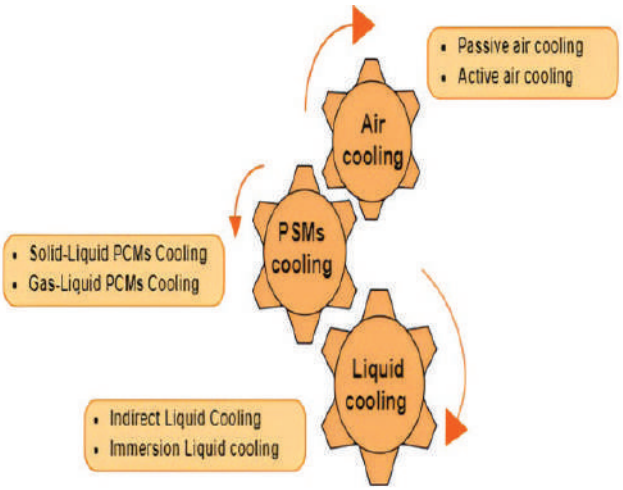


Figure 2. Different cooling technologies in BTMS.

The air cooling mechanism is generally employed to decrease the temperature of battery packs. The Air cooling (AC) mechanisms are lightweight, compact scale, low viscosity, low maintenance costs, minimal expenditure, and direct and safe medium access. The principle of AC may be divided into two types: active and passive [14]. An active cooling system differs from a passive one in that the former requires a powerful motor, such as a fan to circulate air as seen in Figure 3.

Effectual heat regulation of Li-ion batteries is necessary since at what temperature they determine their performance attributes and safe operation. A number of barriers prevent the widely used cooling techniques from achieving the intended heat regulation of balanced temperatures, powerful battery distribution, and a permitted maximum temperature [15]. Efforts are being made to find cutting-edge cooling techniques that might overcome the drawbacks of existing techniques and be used in battery thermal management systems of the future [16].

Given the layout constraints of automobile batteries in Figure 4, thermal management is crucial thus, a design approach for efficient cooling should be precisely chosen [17]. In the automobile sector, in particular, forced air cooling has been seen as an affordable alternative [18]. New battery pack concepts, creative cooling channel designs, and creative thermally conductive materials significantly increase air-cooling

Table 1. The evaluation of the benefits and drawbacks of various cooling systems

Types of cooling	Thermal Conductivity	Uniform Temperature	Cost	Structure	Compactness	Weight
Air cooling	Medium	Low	Low	Low	High	Low
Liquid cooling	High	Medium	Medium	Medium	Low	High
PCM cooling	Low	High	High	High	Low	High

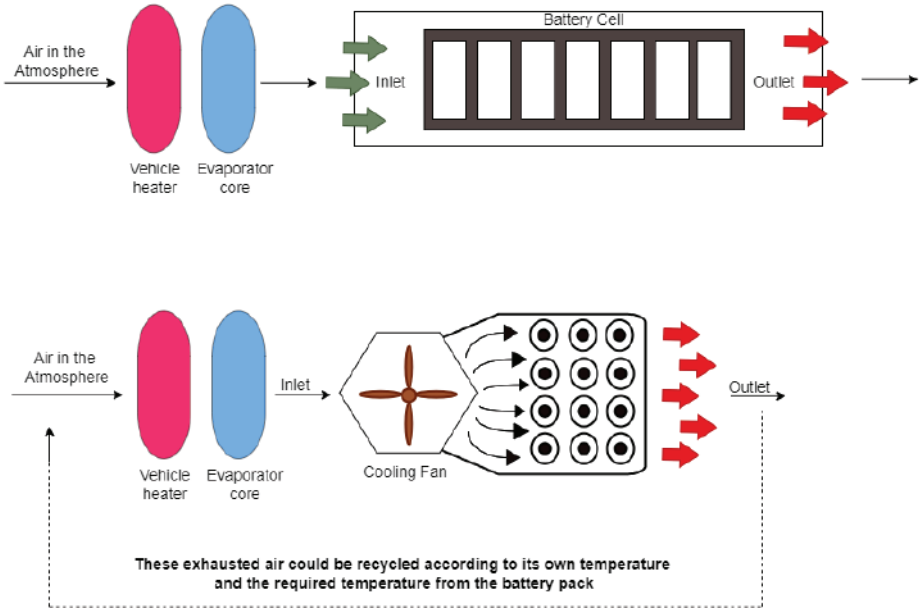


Figure 3. The air-cooling BTMS schematic design shows a) passive air cooling and b) active air cooling.

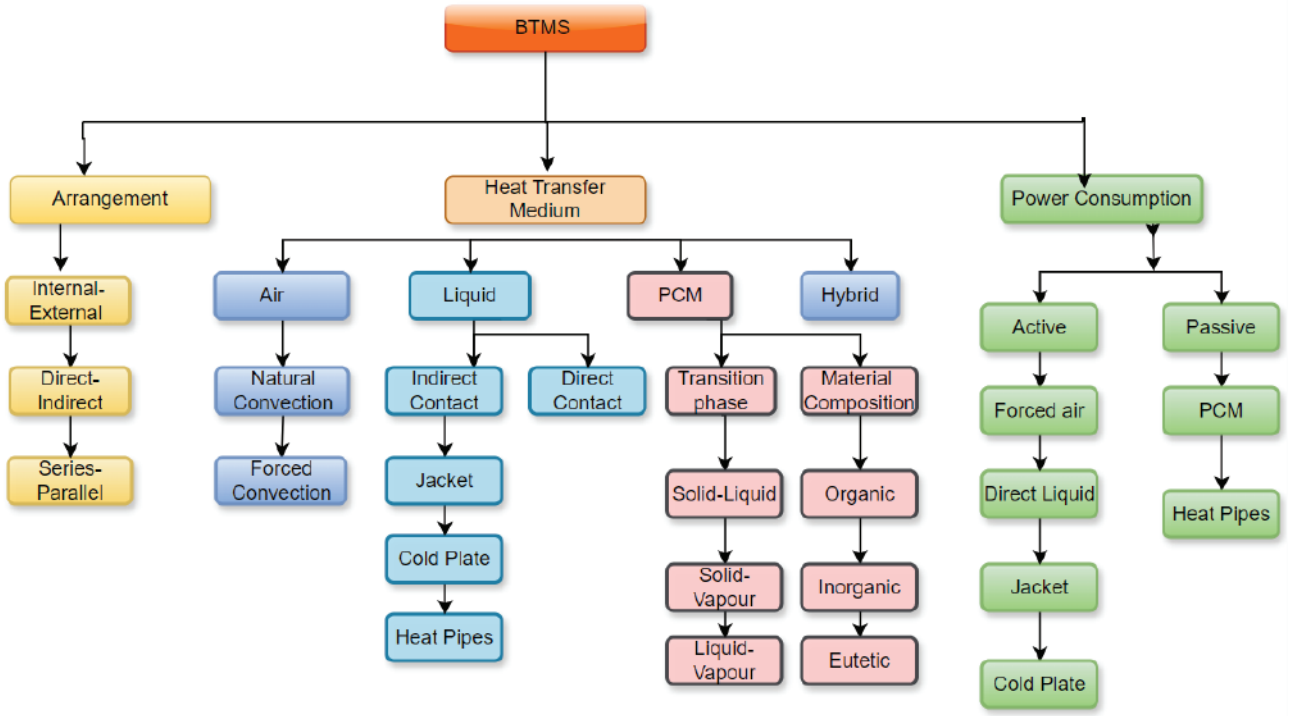


Figure 4. Classification of Li-ion battery thermal management techniques.

Table 2. Summery of cooling methods, key references and research gap

Cooling method	Research gap
Air Cooling Systems [14]	Limited suitability for high-capacity batteries.
Heat Pipe Systems [15]	Performance limitations under dynamic loads, manufacturing, and integration complexity.
Liquid Cooling Systems [16]	complex structure, larger energy consumption, heavier overall weight, liquid leakage,
Phase Change Materials (PCM)[17]	Low thermal conductivity, slow heat dissipation, integration challenges with active systems.
Hybrid Cooling Systems [21]	Increased design complexity, higher production cost, and scalability issues for large EV fleets.
Direct Refrigerant Cooling [22]	High initial cost, complex system architecture, refrigerant safety, and environmental impact concerns.

efficiency, according to rigorous testing and sophisticated computational numerical models [19]. The heat production phenomenon of Lithium-ion batteries through the charge and discharge treatments is a reason for an increase in temperature is observed surrounding Lithium batteries. One of the main types of BTMS which are utilized to increase the safety and efficiency of electric power trains, is examined in this paper. To improve different BTMS design objectives, this study specifically examines It describes air-cooled BTMS methods (design parameter optimization (both passive and active)) and techniques (using algorithms or iteration) [20].

RESEARCH MOTIVATION

Existing BMS systems frequently use static or semi-static prototypes, which are insufficient to manage the complexity of actual battery consumption, where situations vary owing to shifting operating requirements, environmental factors, and battery aging processes. This system's limited ability to adapt dynamically to new inputs of data as well as modify its execution plan serves as a strong indicator of this problem. Maintaining battery cycle life and reducing safety risks requires efficient temperature management [21]. Battery heat regulation and a classification of lithium-ion battery heat regulation methodologies, as seen in Figure 4, are essential to preserving the battery temperature within a safe range [22]. As a result, there is a significant gap in using predictive analytics, which might stop issues before they start and decrease the risks of aging as well as battery failure [23]. To prevent thermal runaway initiation, an evolution of effective battery heat regulation technologies is required. These reactions raise the internal battery temperature

sharply, which destabilizes and deteriorates the internal structures of the battery and ultimately results in battery failure [24]. An essential component of electric cars is the safety performance of lithium-ion batteries, which directly affects driving distance as well as safety. A battery thermal management system (BTMS) is crucial [25]. Techniques to control the temperature in cylindrical packs of lithium-ion batteries with a focus on optimizing efficiency, safety, and life. Primary concerns for the EV system manufacturer are the battery safety issues. Maintaining the ideal temperature is one of the most significant scientific problems. It has restricted the overall use of batteries [26].

Our work has addressed the direct air-cooling technology for temperature reduction in battery packs which significantly increases system efficiency. The BMS keeps an eye on vital indicators like voltage, current and internal ambient temperature when the device is being charged. The discharged cycle is a crucial part of maintaining these batteries. Historically, assessing these batteries' charge and discharge properties has involved laborious laboratory procedures requiring oscilloscope readings. Advanced cooling solutions are essential in EVs to improve battery safety, performance and longevity. By efficiently managing battery temperatures, these systems prevent overheating, reduce degradation, and ensure stable performance.

They play a pivotal role in preventing thermal runaway supporting fast charging by dissipating heat during rapid charging sessions, and enhancing the driving range. In autonomous vehicles, predictive thermal management boosts operational reliability, while commercial and industrial EVs benefit from robust cooling systems that handle prolonged use and heavy loads. A simulation model of the BMS has been created to overcome inefficiency and expedite the testing procedure. The curves showing different charge percentages and discharge rates at various ambient temperatures will be produced using the suggested model. Furthermore, by using the current simulation framework, further investigation into how temperature and state of charge SoC affect battery performance will be possible thanks to this model.

Table 2 shows the summary of cooling methods with references and research gaps observed. The contributions of the research paper are:

1. As per the author's knowledge from a literature survey, very few researchers have focused on battery pack tempremature analysis at different atmospheric conditions.
2. An applicability and proposed design method to investigate an improved performance of battery pack.
3. Comparison of performance via simulation studies and experimental tests conducted on the OPEL-RT 4510 simulator.

These main achievements of the study are the development of an extensive modelling framework that accurately depicts the complicated nonlinearities of Lithium-ion batteries as well as the proof that it is effective enough in enhancing energy management mechanisms. The remaining part of the study is covered in the second chapter, which also covers the mathematical formulation for the SoC formula and generic battery model. The methodology of the research is covered in the third chapter and outcomes and analysis are covered in chapter four. The fifth chapter holds a conclusion for the same.

PROBLEM FORMULATION

An electrical equivalent circuit representation of Lithium-ion cells created using the MATLAB/Simulink environment is presented in this article [27]. It is discovered that the battery temperature is primarily influenced by three factors: heat production, thermal diffusion and heat conduction [28].

Charge Model

The process of adding electrical charge to a rechargeable cell or battery is known as battery charging. There are a number of different charging techniques, including burp charging, float charging, trickle charge current-voltage-current (IUI) charging, random charging, pulsed charging, taper charging, and constant current and constant voltage. The charge model is represented in Eq. (1).

These equations are used in the model for Lithium-ion batteries.

Charge Model ($I^* < 0$)

$$f_{22}(It, I*I) = V_0 - K.\frac{Q}{It+0.1.Q}.I* - K.\ \frac{Q}{Q-It}.It + A'.\exp(-B'.It) \quad (1)$$

The ambient temperature as well as the battery pack unbalanced charge is caused by frequent charging and discharging. When an EV is in traction, this unbalancing charge is unable to supply the necessary power requirement and may possibly result in an explosion or fire [29]. However, the battery pack needs to be protected from any hazardous conditions by safety and protection requirements.

Discharge Model

During battery discharge, the positive ions of lithium from the cathode go in the direction of the anode, reducing the stored charge. The whole charge and discharge sustain time is taken into account with the required safe period since cell and pack voltages strongly depend on charging and discharging current rates [30]. The meanings of the symbols used in equations 1 and 2 in all mathematical expressions are shown in Table 3.

The discharge model is shown as

Discharge Model ($I^* > 0$)

$$f_{12}(It, I*I) = V_0 - K.\frac{Q}{Q-It}.I* - K.\ \frac{Q}{Q-It}.It + A'.\exp(-B'.It) \quad (2)$$

Table 3. Lithium-ion batteries charging and discharging Model parameters.

Nomenclature:	
V_0	Constant voltage (V)
exp (s)	Exponential zone dynamics (V)
K	Polarization constant (Ah−1) or Polarization resistance(Ohms)
I*	Dynamics of low frequency current (A)
I	current in the battery (A)
It	Extracted capacity (Ah)
Q	Maximum battery capacity (Ah)
A'	Exponential voltage (V)
B'	Exponential capacity (Ah)-1

SoC Estimation Using Coulomb Counting Method

Generally speaking, the SoC of the battery is determined by dividing its nominal capacity Q (n) by its current capacity Q (t). The nominal capacity, or maximum charge that the battery can withstand, is defined by the manufacturer.

SoC is represented as

$$SoC(t) = \frac{Q(t)}{Q_{(n)}} \quad (3)$$

High charging as well as discharging efficiency Lithium-ion batteries SoC estimation may be completed quickly using the coulomb counting method. According to an investigation of the charging and discharging properties, the coulomb counting method is a practical and precise How to calculate lithium-ion batterie's state of charge (SoC) [31]. Only in cases of forced convection with constant physical characteristics is Newton's law applicable. Several heat transmission theories are highlighted, along with their close relationships. The link between temperature differential and surface heat flow as a drivable force may also be used to categorize heat transfer events [32].

Battery capacity equation

The aim of battery is to maintain its temperature in order to capacity varies when the temperature deviates from reference temperature T_{ref}. In order to preserve capacity, BTMS increase their life. Within an acceptable range. While lower temperatures might temporarily impair capacity, higher temperatures may accelerate deterioration rate

$$Q(T) = Q_{nominal} * [1 - \alpha * (T - T_{ref})] \quad (4)$$

Where,

Q (T) - The temperature-dependent capacity of the battery.

$Q_{nominal}$ - The nominal capacity at a reference temperature Tref

α - Constant, α > 0

T - The battery's temperature-dependent efficiency.

T_{ref} - The reference temperature where the nominal capacity $Q_{nominal}$ is measured.

Battery efficiency equation

Temperature dependent efficiency of a battery is represented by

$$\eta(T) = \eta_{ref} * [1 - \beta * (T - T_{ref})] \quad (5)$$

Where,

η (T) - The temperature-dependent efficiency of the battery

η_{ref} - The reference efficiency at temperature Tref.

B - A constant that reflects how sensitive the efficiency is to temperature changes.

T and T_{ref} - As previously defined

Efficiency decreases when the battery temperature diverges from the optimal range.

State of charge (SoC) equation

$$SoC(T) = SoC_{initial} - \int \frac{I(t)}{d(t)} Q(T) * \eta(T) \quad (6)$$

Where,

SoC (T) - The state of charge at temperature T.

$SoC_{initial}$ - The initial state of charge.

I (t) - Current flowing over time.

Q (T) ×η (T) - The temperature-dependent capacity adjusted for efficiency.

In this instance, the discharge with varied discharging currents is always accurate, and the Coulomb counting method is helpful for measuring the battery's state of charge [33].

MATERIALS AND METHODS

Battery Configuration Development

MATLAB and Simulink were used to create a 3S4P (three series, four parallel) Lithium-ion battery stack model for the battery architecture. To get a minimal voltage of 11.1 V (3 x 3.7 V) and a total load of 10.4 Ah (4 x 2.6 Ah), this arrangement was used and specification of Lithium-ion battery are included in the Table 4. The model applied established electrochemical principles and battery dynamics using custom scripts and Simulink blocks to accurately represent battery activity. The framework as given in Figure 5 include modules for cell modelling, 3S4P cell connections, and the deployment of a BMS interface so we can monitor as well as control. To check out the performance of the battery pack under real-life conditions, it was made to simulate dynamic load situations, which represent the inconsistent urging frequently seen in renewable energy applications [23].

Table 4. Specifications of lithium- ion battery [34] [drawn by the author]

Normal capacity	2.6 Ah
Minimum capacity	2.5 Ah
Nominal voltage	3.7 V
Charging voltage	4.2 V
Discharge cut-off voltage	3.0 V
Internal resistance	0.014231 ohm
Standard charge current	0.52 A
Max. charge current	2.6 A
Max. discharge current	5.2 A

The following presumptions underlie the battery model that is implemented in MATLAB/Simulink [28]

1. The model's specifications, which are presumed to remain constant during the charging process, are defined by the discharge characteristics.
2. Self-discharge effects are excluded, and the battery is presumed to be memory-effect-free.
3. The battery is presumed to be memory-effect-free, self-discharge effects are excluded.
4. Internal resistance is viewed as constant during both charging and discharging cycles, staying unaffected by changes in current amplitude.
5. Temperature is incorporated into the model since it affects the system's overall behavior.
6. Even though vibration impacts might affect the model's performance, they are not taken into account.

Performance Evaluation

To assess the Lithium-ion battery model performance under various operating situations, a number of simulations were run. To replicate discharge cycles at constant loads throughout a variety of atmospheric temperatures (-20, -10, 0°C, 27°C, 30°C, 35°C, 50°C and 60°C), a simulation prototype was set up. Throughout these simulations, temperature and state of charge were tracked using the proper sensor blocks to document changes over time. To evaluate the battery stack's overall performance an effect of varying ambient temperatures on SoC distribution was examined.

Implementation of Air Cooling Method

This method describes the precise procedures for putting in place a cutting-edge cooling system for EV battery packs. In certain situations, air cooling systems may be less effective than liquid cooling; yet, they have benefits, including being lighter, simpler, and requiring less maintenance. For some EV designs, these features can make air cooling a viable option, especially where weight and space are concerns to be taken into account [35]. Maintaining optimal battery temperatures requires effective cooling technology, as shown in Figure 6. The flow chart for the suggested model shows the compleate cooling system design process.

Temperature Control and Optimization

To control fan operation based on battery cell temperature, a MATLAB control method was created. The Simulink model was included with temperature criteria for fan activation and deactivation. SoC and temperature were tracked as a function of time and load conditions in simulations

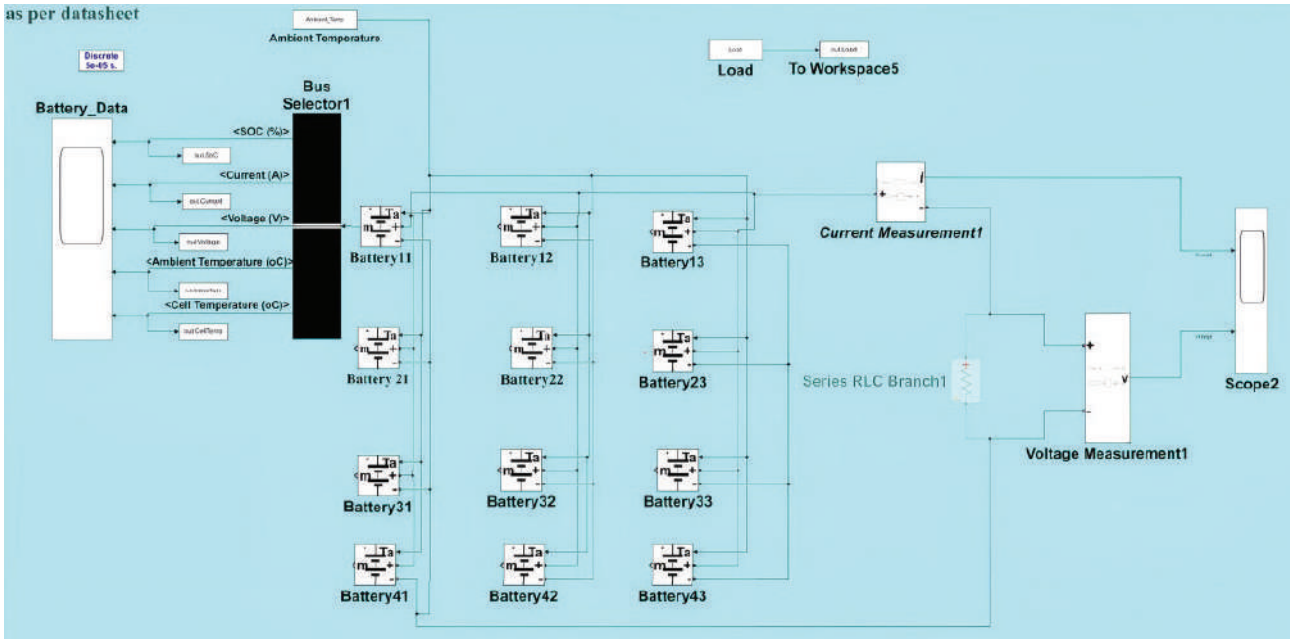


Figure 5. Simulation model 3S4P prototype battery pack.

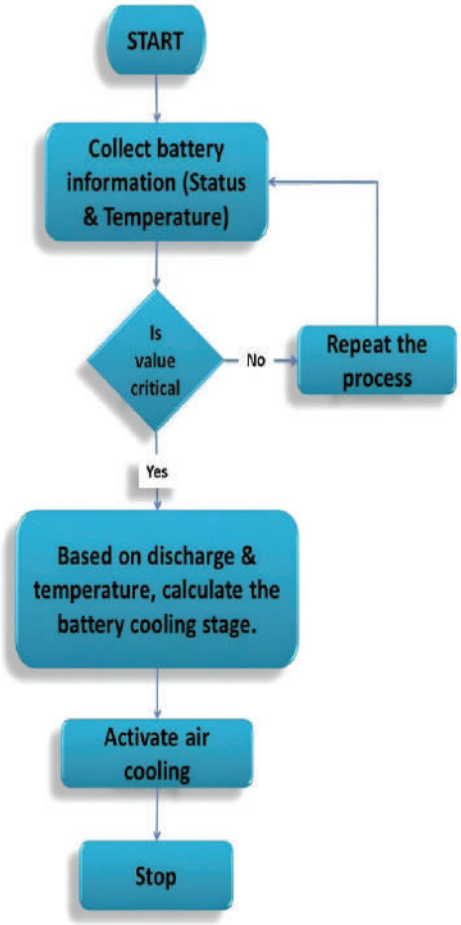


Figure 6. Battery pack without cooling mechanism.

that compared battery performance with and in absence of the cooling device as depicted in Figure 7.

PID Controllers

One of the best ways to guarantee adequate cooling and preserve device dependability is through Propotional -derivative –integral (PID)-based designs. In order to maintain the heat sink's uniform surface temperature, it turns on the cooling fan and controls its speed [36]. The PID control is well known for being a simple and efficient technique for temperature control applications as shown in Figure 8. According to statistics, the kind of control is used by more than 97% of industrial controllers [37]. This paper describes the method of creating a PID controller using MATLAB as an alternative to manually programming a micro-controller to regulate the desired temperature [38]. The time needed for controller design is greatly decreased by using this technique.

Throughout the simulation, voltage, current, SoC, and temperature data were gathered and examined using MATLAB's data logging features. Trends and connections between the distribution of SoC, temperature fluctuations, and the effectiveness of the cooling method were found using the statistical analysis tools in MATLAB.

RESULTS AND DISCUSSION

The modelling of battery pack performance for varying ambient temperatures over an hour is the primary objective of this section. The C-rate is a metric used in battery systems, especially electric cars that quantifies how quickly

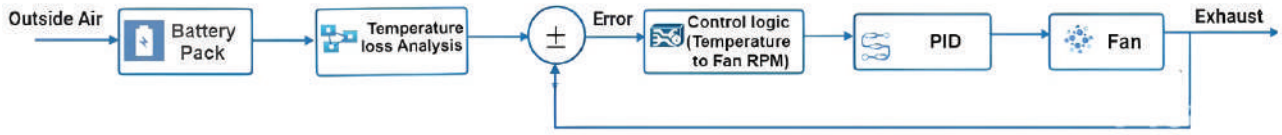


Figure 7. Battery pack with air cooling mechanism.

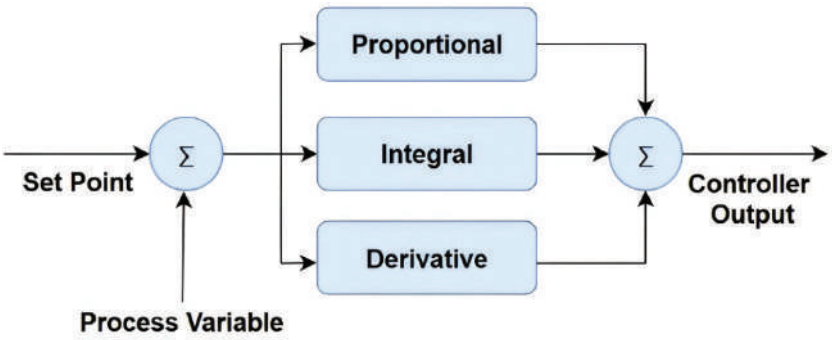


Figure 8. PID controller.

a battery charges or discharges in relation to its capacity. It impacts the relationship between voltage and ampere-hours (Ah). At low C-rates, the voltage drops slowly and the battery delivers nearly full capacity. At medium C-rates (1C), the voltage declines faster but still provides most of its capacity. At high C-rates, voltage drops sharply and the battery delivers less capacity due to inefficiencies and heat build-up. In this work, the model runs at a 0.2 °C rate, as at low °C rates, the voltage drops slowly so that temperature and SoC analysis will be fine.

Overall, the battery temperature gradually aligns with the ambient temperature of 30 C, impacting SoC, current, and voltage behaviour over time as shown in Figure 9. Similar relationships for current, voltage, and SoC can be generated at various ambient temperatures. The current initially remains high in both scenarios due to cooling demands in hot conditions and heating demands in cold conditions before gradually decreasing as the battery stabilizes. The voltage drops more quickly in high temperatures due to increased internal resistance, while in cold conditions, it remains stable initially but declines sharply at low SoC levels.

SoC and Temperature of Battery Pack Without Air Cooling

The primary interaction in this case is the temperature differential between the battery and atmospheric air. This type of evaluation is crucial because battery performance is significantly affected by temperature variations. Here is

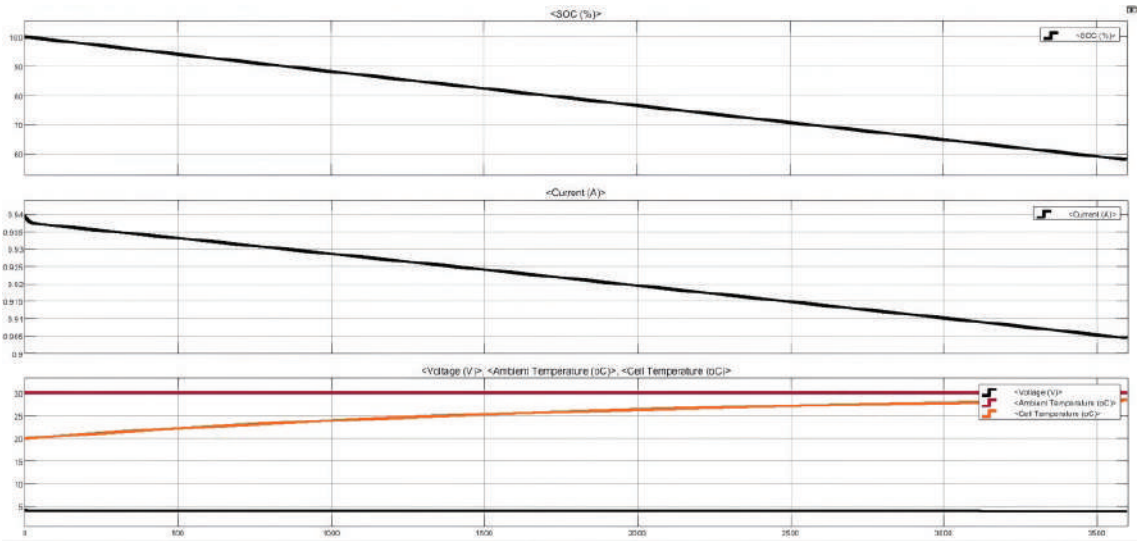
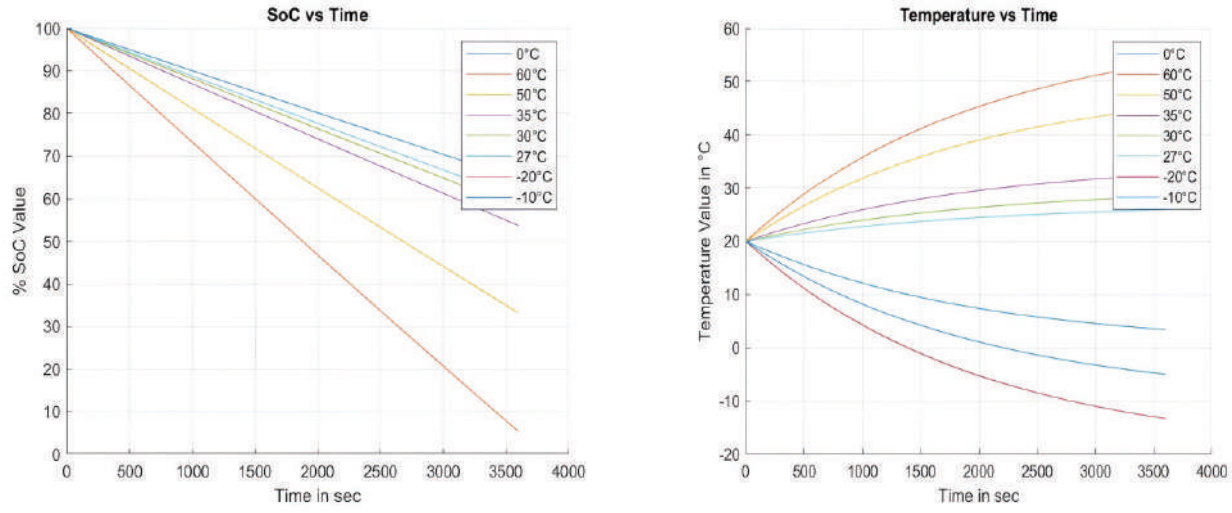
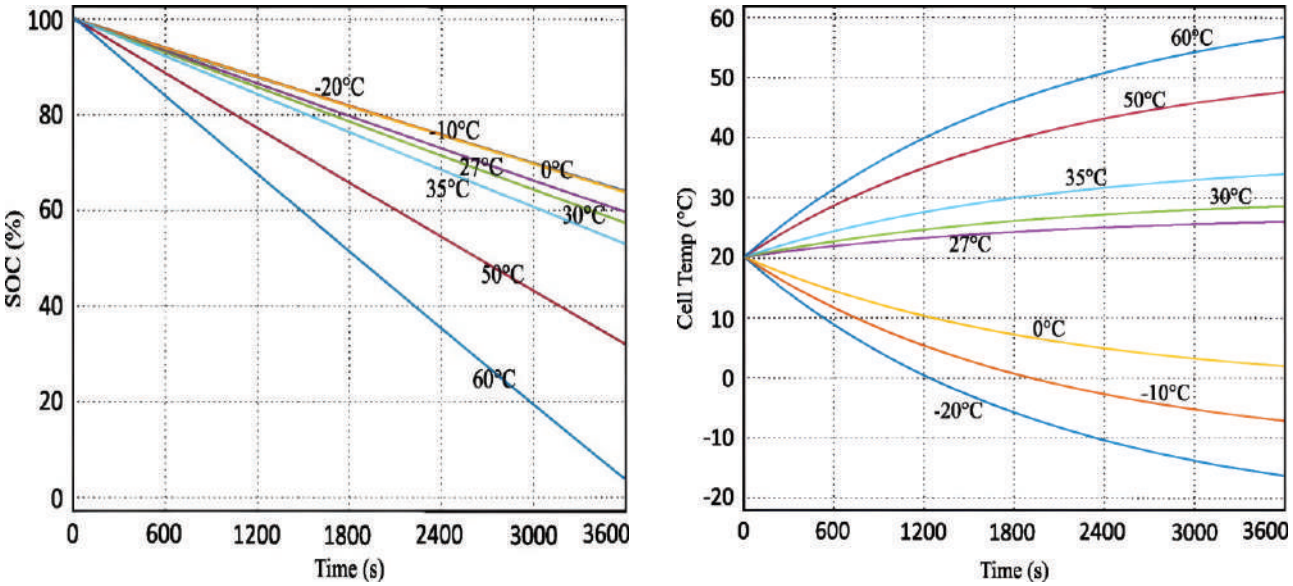


Figure 9. Voltage, current and SoC characteristics EV battery pack at ambient Temperature 30 °C.



(a) (b)

Figure 10. Simulated SoC and temperature at different atmospheric temperatures of battery pack.



(a) (b)

Figure 11. Real time SoC and Temperature at different Atmospheric Temperatures of battery pack.

a summary of the expected observations from Figure 10. based on common trends.

The SoC is a dynamic metric that varies significantly with changes in ambient temperature because of the battery's composition of chemicals and how the temperature management mechanism works. In high temperatures, faster SoC depletion occurs due to increased energy consumption and inefficiencies, while in low temperatures, the SoC may appear stable but is accompanied by a reduction in usable capacity and charging efficiency. The battery temperature tends to align with the ambient temperature over time. This is a natural process because the BTMS works to balance internal temperature changes with the external environment.

Real-Time Validation

The proposed model of the battery pack shown in Figure 5 is authenticated in the OPAL-RT 4510 real-time digital simulator (RTS). It allows moreover, accurate parallel evaluations in real-time, and the results are quite similar to the real system outcomes [39]. As depicted in Figure 12,

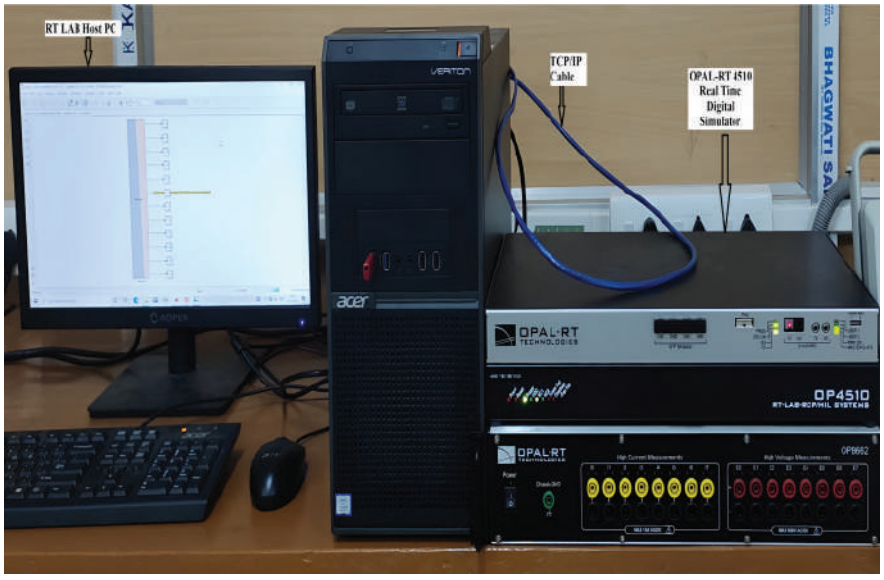


Figure 12. Real-time digital simulation platform installed in the lab.

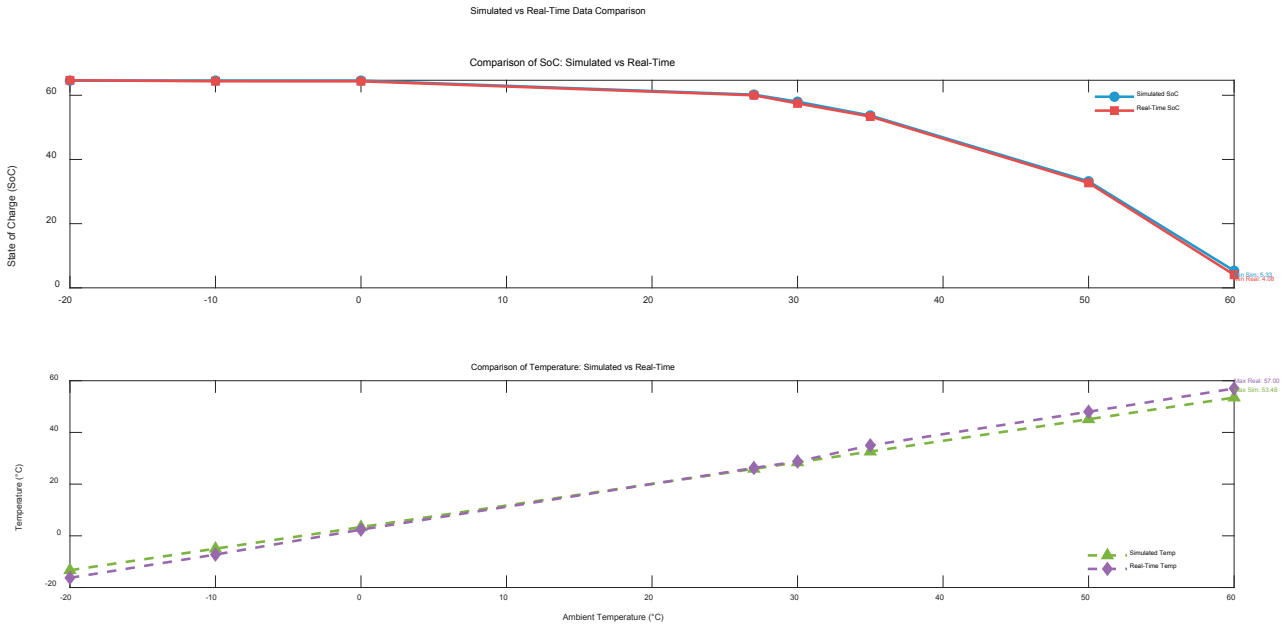


Figure 13. Comparative analysis of SoC and temperature

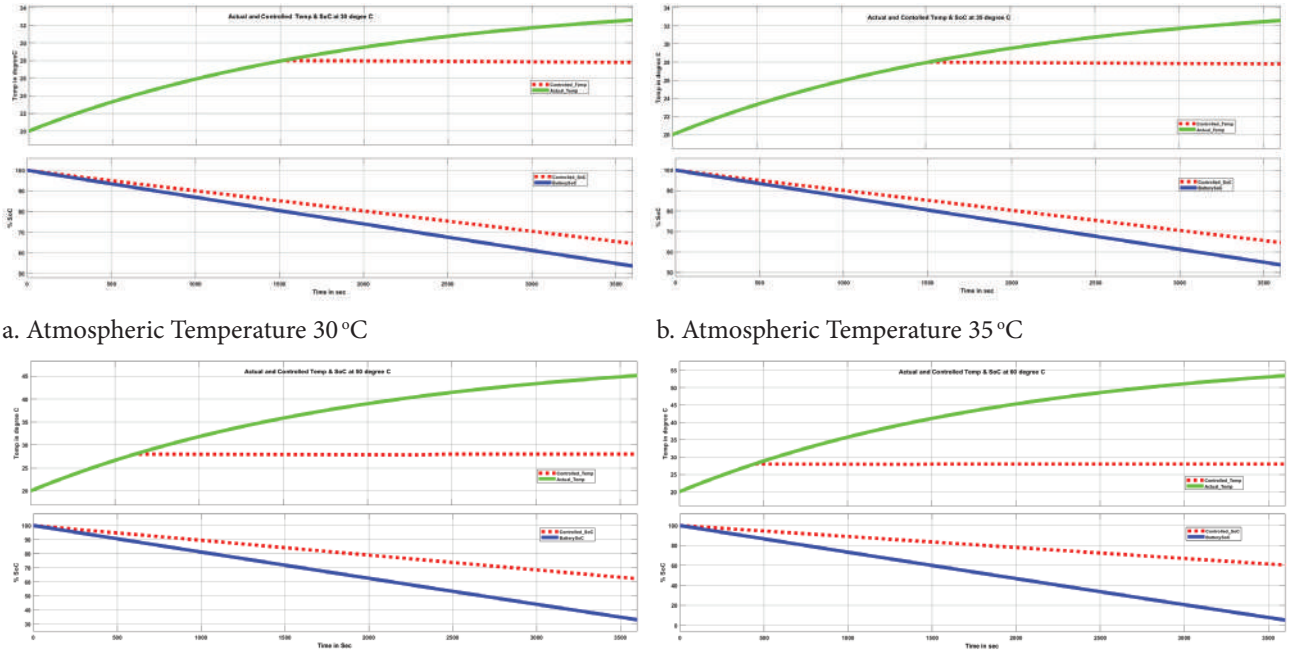
the laboratory setup with OPAL-RT arrangements comprises of MATLAB-enabled host PC with RT-LAB connections. Results from simulations and actual applications agreed. The performance of a system is successfully validated [40-41]. An interlink connecting the host PC and RTS is established by a TCP/IP cable. RT-LAB, which is already integrated with MATLAB, is used to immediately improve the proposed control strategy on a Simulink/MATLAB platform. The simulated result of SoC and Temperature of the 3S4P battery pack is validated in OPAL-RT as shown in Figure 11. The MATLAB simulations offer an idealized baseline for initial design while OPAL-RT provides real-world validation by accounting for factors such as temperature effects, dynamic behaviour and degradation.

In OPAL-RT, SoC might be lower due to inefficiencies, higher power demands, energy losses, and temperature might rise more than predicted especially under high load conditions due to thermal effects that are often simplified or not fully captured in MATLAB simulations. These discrepancies as given in Figure 13 emphasize the importance of refining the MATLAB model to account for real-world factors such as thermal dynamics and battery aging to achieve a more accurate prediction for the behaviour of the system, leading to more reliable performance validation.

SoC and Temperature of Battery Pack With Air Cooling

Air cooling helps keep the battery cooler, improving charging efficiency and SoC, and extending battery life while preventing overheating. Without cooling, higher temperatures can reduce performance and degrade the battery faster. The cooling system's ability to manage temperature spikes during rapid discharge has been assessed by analyzing profiles over time at various temperature levels. Figure 14. compare battery temperature and SoC with and without air cooling for ambient temperature 30°C and more than 30°C as the set point is 28°C Without cooling (green colour), the battery overheats quickly, rising above the controller's set temperature due to inefficient heat dissipation. With air cooling (black colour), the battery temperature is better controlled, staying closer to the set point. The SoC behaviour without cooling (black colour), SoC drops more rapidly due to overheating and reduced efficiency. With air cooling (green colour), SoC depletes more slowly as the battery operates more efficiently at lower temperatures, improving overall performance and range.

An auto-tune PID controller continuously adjusts its parameters based on system feedback to optimize performance. The 30°C is the ambient temperature from Table 5, PID controller has very significant role in regulating battery's temperature by controlling the cooling system. As the temperature exceeds target of 28°C, PID controller turns the fan on and adjusts its speed dynamically to maintain the battery temperature close to the set point ensuring optimal battery performance and longevity. The air cooling mechanism is activated in response to a noticeable rise in battery temperature, which would otherwise increase significantly beyond the threshold if left uncontrolled. Once the cooling system is engaged, the temperature is regulated effectively preventing the battery from overheating.



a. Atmospheric Temperature 30 °C

b. Atmospheric Temperature 35 °C

c. Atmospheric Temperature 50 °C

d. Atmospheric Temperature 60 °C

Figure 14. Battery calefaction and SOC with and without air cooling.

Table 5. SoC and Temperature analysis for with and without controller

Ambient temp °C	Simulated value		Real time value		Controlled SoC	Controlled tempeature	Improved efficiency
	SoC	Tempe-rature	SoC	Temperature			
	100	**20**	**100**	**20**	**100**	**20**	
-20	64.562	-13.3118	64.68	-16.25	64.562	-13.3118	0%
-10	64.5619	-4.9648	64.37	-7.25	64.5619	-4.9648	0%
0	64.5618	3.3822	64.36	2.40	64.5618	3.3822	0%
27	60.1962	25.9194	60.00	26.25	60.1962	25.9194	0%
30	58	28.4237	57.46	28.75	65.3258	27.95	7.86%
35	53.7	32.6	53.38	35	64.5813	27.79	11.20%
50	33.2	45.1	32..7	48	62.2096	28	29.50%
60	5.326	53.4768	4.08	57	60.3696	28	56.28%

When comparing real-time values with controlled values of performance at 27°C, when the cooling might not have been required or as successful, these gains are significant. The greater improvement shown at 30 °C can be ascribed to the data being recorded at precisely timed intervals when temperature regulation is more important. The benefits of air cooling at higher temperatures are reflected in the SoC and efficiency improvements. The air cooling assist the battery in retaining maximum performance by lowering thermal stress, enhancing energy retention and lowering power losses from overheating. This demonstrates how crucial active cooling systems are to preserving battery life and increasing its operating range particularly in hot weather.

After stabilizing the temperature, an improvement in SoC of about is observed in Figure 15, indicating that the battery is able to retain more charge when operating at a controlled temperature. Additionally, the efficiency of the battery improves by approximately 7.86% for 30°C, meaning that the battery delivers energy more effectively when air cooling is applied.

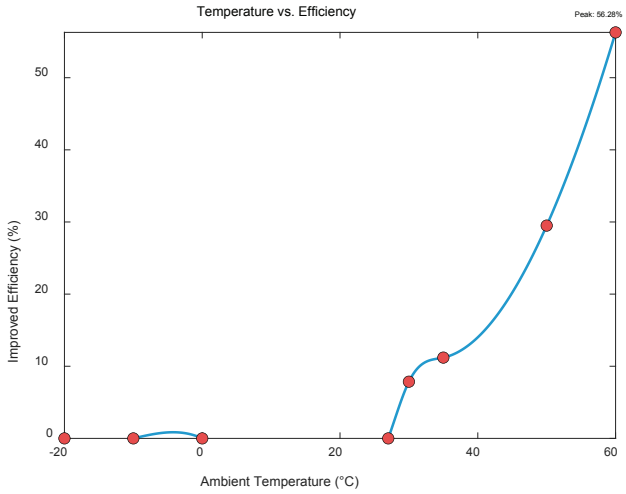


Figure 15. Improvement of efficiency due to PID controller.

CONCLUSION

The prime benefaction of this research is the incorporation of sophisticated computational models into Battery Thermal Management System frameworks, which shows how they may be used practically to enhance Electric Vehicle battery performance. The battery differential temperature has been measured and analyzed at different ambient temperatures via on OPAL-RT platform. A rapid simulator was deployed to operate both the suggested and conventional network designs, and a comparative analysis of simulation and real-time experimental results gives crucial information on how well the cooling mechanism maintains optimal temperature levels within the battery pack. The simulation studies highlight the impact of air cooling on temperature control, When reveals to the significant improvements in thermal stability and battery lifespan. The overall efficiency has been improved to 13.11%. Results show that the performance and safety of lithium-ion batteries in practical applications may be remarkably enhanced by the application of strong Battery Thermal Management System frameworks. When an economical direct air conditioning method is used for Electric-vehicles, the stability of a system increases.

For battery management systems, using an auto-tuner Proportional-Integral-Derivatives (PID) controller has several advantages, especially when it comes to temperature control and State of Charge stability. In comparison systems without auto-tuners, are more vulnerable to inefficiencies and quicker deterioration. It guarantees more efficient energy utilization, lowers battery wear, and prolongs battery life. Controlling the heat produced during charging and discharging helps to maintain safe and dependable battery performance by minimizing thermal degradations. In the future AI and Smart Thermal Management for the enhancement of battery performance, in which AI-driven cooling optimizes thermal regulation grounded on driving patterns while smart detectors cover and adapt battery temperature in real-time, may be studied.

AUTHORSHIP CONTRIBUTIONS

Authors equally contributed to this work.

DATA AVAILABILITY STATEMENT

The authors confirm that the data that supports the findings of this study are available within the article. Raw data that support the finding of this study are available from the corresponding author, upon reasonable request.

CONFLICT OF INTEREST

The author declared no potential conflicts of interest with respect to the research, authorship, and/or publication of this article.

ETHICS

There are no ethical issues with the publication of this manuscript.

STATEMENT ON THE USE OF ARTIFICIAL INTELLIGENCE

Artificial intelligence was not used in the preparation of the article.

REFERENCES

[1] Nerkar M, Mukherjee A, Soni BP. A review on optimization scheduling methods of charging and discharging of EV. AIP Conf Proc 2022;2452:040002. [CrossRef]

[2] Nerkar M, Mukherjee A, Soni BP, Soni A. GA optimized algorithms for scheduling the load of household appliances to charge electric vehicles. In: Int Conf Intell Comput Tech Smart Energy Syst. Singapore: Springer Nature Singapore; 2023. p. 91–101. [CrossRef]

[3] Aneke M, Wang M. Energy storage technologies and real life applications–a state of the art review. Appl Energy 2016;179:350–377. [CrossRef]

[4] Bukhari SMAS, Maqsood J, Baig MQ, Ashraf S, Khan TA. Comparison of characteristics--lead acid, nickel based, lead crystal and lithium based batteries. In: 2015 17th UKSim-AMSS Int Conf Model Simul UKSim. IEEE; 2015. p. 444–450. [CrossRef]

[5] Naik I, Nandgaonkar M. Review of the approaches and modeling methodology for lithium-ion battery thermal management systems in electric vehicles. In: Adv Mater Mech Eng Singapore: Springer Singapore; 2021. p. 75–109. [CrossRef]

[6] Spitthoff L, Shearing PR, Burheim OS. Temperature, ageing and thermal management of lithium-ion batteries. Energies 2021;14:1248. [CrossRef]
[7] Olabi AG, Maghrabie HM, Adhari OHK, Sayed ET, Yousef BA, Salameh T, et al. Battery thermal management systems: Recent progress and challenges. Int J Thermofluids 2022;15:100171. [CrossRef]
[8] Yue QL, He CX, Wu MC, Zhao TS. Advances in thermal management systems for next-generation power batteries. Int J Heat Mass Transf 2021;181:121853. [CrossRef]
[9] Buidin TIC, Mariasiu F. Battery thermal management systems: Current status and design approach of cooling technologies. Energies 2021;14:4879. [CrossRef]
[10] Khamehchi E, Mahdiani MR. Gas allocation optimization methods in artificial gas lift. New York: Springer Int Publishing; 2017. [CrossRef]
[11] Gawade S, Bhojwani V, Patil P, Zubairuddin M. Heat generation from 32650 cylindrical cell battery pack at various load and speed conditions. Sigma J Eng Nat Sci 2024. Preprint. doi: 10.14744/sigma.2024.00154 [CrossRef]
[12] Wang X, Liu S, Zhang Y, Lv S, Ni H, Deng Y, et al. A review of the power battery thermal management system with different cooling, heating and coupling system. Energies 2022;15:1963. [CrossRef]
[13] Fu P, Zhao L, Wang X, Sun J, Xin Z. A review of cooling technologies in lithium-ion power battery thermal management systems for new energy vehicles. Processes 2023;11:3450. [CrossRef]
[14] Zhao G, Wang X, Negnevitsky M, Zhang H. A review of air-cooling battery thermal management systems for electric and hybrid electric vehicles. J Power Sources 2021;501:230001. [CrossRef]
[15] Zhao R, Zhang S, Liu J, Gu J. A review of thermal performance improving methods of lithium ion battery: Electrode modification and thermal management system. J Power Sources 2015;299:557. [CrossRef]
[16] Garud KS, Tai LD, Hwang SG, Nguyen NH, Lee MY. A review of advanced cooling strategies for battery thermal management systems in electric vehicles. Symmetry 2023;15:1322. [CrossRef]
[17] Kannan C, Vignesh R, Karthick C, Ashok B. Critical review towards thermal management systems of lithium-ion batteries in electric vehicle with its electronic control unit and assessment tools. Proc Inst Mech Eng Part D J Automob Eng 2021;235:1783–1807. [CrossRef]
[18] Park H. A design of air flow configuration for cooling lithium ion battery in hybrid electric vehicles. J Power Sources 2013;239:30–36. [CrossRef]
[19] Zhao G, Wang X, Negnevitsky M, Zhang H. A review of air-cooling battery thermal management systems for electric and hybrid electric vehicles. J Power Sources 2021;501:230001. [CrossRef]
[20] Akinlabi AH, Solyali D. Configuration, design, and optimization of air-cooled battery thermal management system for electric vehicles: A review. Renew Sustain Energy Rev 2020;125:109815. [CrossRef]
[21] Ahmadian-Elmi M, Zhao P. Review of thermal management strategies for cylindrical lithium-ion battery packs. Batteries 2024;10:50. [CrossRef]
[22] Rao GAP, Kumar SS. A review of integrated battery thermal management systems for lithium-ion batteries of electric vehicles. ePrime Adv Electr Eng Electron Energy 2024;8:100526. [CrossRef]
[23] Tapaskar RP, Revankar PP, Ganachari SV. Advancements in battery management systems for electric vehicles: A MATLAB-based simulation of 4S3P lithium-ion battery packs. World Electr Veh J 2024;15:222. [CrossRef]
[24] Shahid S, Agelin-Chaab M. A review of thermal runaway prevention and mitigation strategies for lithium-ion batteries. Energy Convers Manag X 2022;16:100310. [CrossRef]
[25] Zhang W, Zhang J, Zhang G, Hu Y, Shao D, Jiang L, et al. A novel leak-proof thermal conduction slot battery thermal management system coupled with phase change materials and liquid-cooling strategies. Energies 2024;17:939. [CrossRef]
[26] Amosedinakaran S, Kannan R, Kannan S, Ramkumar A, Suresh S, Bhuvanesh A. Performance analysis for battery stability improvement using direct air cooling mechanism for electric vehicles. ePrime Adv Electr Eng Electron Energy 2024;8:100585. [CrossRef]
[27] Kim J, Kowal J. Development of a matlab/simulink model for monitoring cell state-of-health and state-of-charge via impedance of lithium-ion battery cells. Batteries 2022;8:8. [CrossRef]
[28] Omariba ZB, Jared OK. Modelling and simulation of lithium-ion battery with temperature effects using MATLAB/Simulink. Int J Res Adv Eng Technol 2019;5:67–76.
[29] Rahman M, Rashid MM, Rahman A, Khan S. Resonant-boost LC converter base charge balancing system for electric vehicle. ARPN J Eng Appl Sci 2016;11:362–367.
[30] Wang S, Fernandez C, Chen M, Wang L, Su J. A novel safety anticipation estimation method for the aerial lithium-ion battery pack based on the real-time detection and filtering. J Clean Prod 2018;185:187–197. [CrossRef]
[31] Ng KS, Moo CS, Chen YP, Hsieh YC. Enhanced coulomb counting method for estimating state-of-charge and state-of-health of lithium-ion batteries. Appl Energy 2009;86:1506–1511. [CrossRef]
[32] Cheng KC, Fujii T. Heat in history Isaac Newton and heat transfer. Heat Transf Eng 1998;19:9–21. [CrossRef]
[33] Zine B, Bia H, Benmouna A, Becherif M, Iqbal M. Experimentally validated coulomb counting method for battery state-of-charge estimation under variable current profiles. Energies 2022;15:8172. [CrossRef]

[34] EEMB. Battery model: LIR18650 2600mAh, manufacturer. Lithium-ion Battery Data Sheet. EEMB Co. Ltd. Available at: https://www.ineltro.ch/media/downloads/SAAItem/45/45958/36e3e7f3-2049-4adb-a2a7-79c654d92915.pdf Accessed on Nov 10, 2025.

[35] Raj KG, Srinivas TN, Jeswanth MG, Sundaram NM. A smart and efficient cooling system design for high-performance electric vehicle battery packs. In: IOP Conf Ser Earth Environ Sci 2024;1375:012030. [CrossRef]

[36] Sundara Mahalingam V, Kumaraguruparan G. Simulation of temperature controlled fan using MATLAB. J Emerg Technol Innov Res 2018;5:932–936.

[37] Åström KJ, Hägglund T. Revisiting the Ziegler–Nichols step response method for PID control. J Process Control 2004;14:635–650. [CrossRef]

[38] Nakamori S. Arduino-based PID control of temperature in closed space by pulse width modulation of AC voltage. Int J Comput Syst Eng 2021;21:49-56. [CrossRef]

[39] Sharma S, Verma V, Behera RK. Real-time implementations of shunt active power filter with reduced sensors. IEEE Trans Ind Appl 2019;56:1850–1861. [CrossRef]

[40] Bahadır A, Aydoğdu Ö. Modelling of a brushless dc motor driven electric vehicle and its PID-fuzzy control with dSPACE. Sigma J Eng Nat Sci 2023;41:156–177. [CrossRef]

[41] Ranjan A, Behera MK, Saikia LC. An advance control of grid integrated wind turbine driven DFIG-battery system with grid power shaping under gust wind variation. IETE J Res 2023;70:3030–3051. [CrossRef]

Sigma Journal of Engineering and Natural Sciences
Web page info: https://sigma.yildiz.edu.tr
DOI: 10.14744/sigma.2025.1937

Research Article

Static and dynamic slope stability analyses based on finite elements method: The example of Birecik Slopes

Ferit TAYLAN[1], Ali SARIIŞIK[1], Mustafa ULUKAVAK[2], Songül CAN[1,*]

[1]*Department of Civil Engineering, Harran University, Şanlıurfa, 63510, Türkiye*
[2]*Department of Map Engineering, Harran University, Şanlıurfa, 63510, Türkiye*

ARTICLE INFO

Article history
Received: 02 March 2024
Revised: 12 June 2024
Accepted: 17 October 2024

Keywords:
Dynamic Analysis; Factor of Safety; Finite Elements Method (FEM); Plaxis 2d; Slope Stability

ABSTRACT

This study examines slope stability along a critical section of the Birecik coastal road in Şanlıurfa province, Turkey, known for its challenging terrain characterized by frequent segregations, low soil strength, and steep slopes near the Euphrates River. The research focused on assessing landslide risks and proposing mitigation measures to ensure safety for pedestrians and vehicles. Because the coastal road is heavily used and is stuck between the slopes and the Euphrates River. Initially, unmanned aerial vehicle (UAV) flights were used to create a three-dimensional model of the slope. On-site observations identified a critical section and a critical two-dimensional section obtained on the three-dimensional model using ArcGis10. Given the presence of nearby structures at the tip of the slope, ten adjacent structures were simulated using static and dynamic analyses to assess their impact on stability under potential future urban development scenarios. Stability analyses were conducted without structures initially and then with simulated structural loads applied as linear loads at the sloping tip and specific distances behind it. For dynamic analyses, Sivrice Earthquake (24.01.2020) parameters were used. For analysis, Plaxis two dimensional was used, and the strength reduction method was used based on the finite element method (FEM). This study revealed factors of safety, shear forces, and displacements, and the static and dynamic analysis results were compared. Results showed that horizontal displacements increased under earthquake conditions with minimal changes in safety factors. However, the slope is unsafe with a minimum factor of safety of 1.199 for static and 1.190 for dynamic analysis by affecting structural load at the tip of the slope. Also, results showed that for this model, the main reason that causes slope failure is structural load. For this study, the most remarkable result is that the dynamic shear stresses are lower than static shear stresses, while the dynamic displacements are higher than static displacements. The results show that plain strain or two-dimensional analyses are unreliable.

Cite this article as: Taylan F, Sarıışık A, Ulukavak M, Can S. Static and dynamic slope stability analyses based on finite elements method: The example of Birecik Slopes. Sigma J Eng Nat Sci 2025;43(6):2213–2233.

***Corresponding author.**
*E-mail address: songul_537@hotmail.com

This paper was recommended for publication in revised form by Editor-in-Chief Ahmet Selim Dalkilic

Published by Yıldız Technical University Press, İstanbul, Turkey
© Author. This is an open access article under the CC BY-NC license (http://creativecommons.org/licenses/by-nc/4.0/).

INTRODUCTION

Slope stability is a subject that geotechnical engineering has been dealing with for a long time and is still an area that is approached with interest in both application and research by engineers and researchers interested in geotechnical engineering [1]. In addition, it is one of the most frequently encountered issues that force engineers working in geotechnical engineering to find solutions [2]. After the collapse events that occur due to the deterioration of the balance of the slopes, losses can be as significant as those caused by other natural disasters, especially earthquakes [3].

Slope stability is generally defined as the ratio of the forces that resist the effects that try to slip the layers to the forces that try to slip them. It is usually accepted as the weak part of the slope resting on a discontinuity [4]. The leading cause of slip on slopes is the forces of gravity. In addition, shear stresses of the slope may increase because of additional loads on the slopes, making the slope inclination steeper and causing the destruction of the toe, which prevents the slope from slipping, as a result of natural and artificial factors. Artificial and natural quakes (explosions, earthquakes, construction excavations, and other constructions, etc.) can reduce the friction (Ø) and cohesion (c) between the particles forming the soil. Also, the water pressure in the voids results from the partial or complete filling of the cavities in the soil layers with water. It increases the water content, especially in cohesive soils, causing a decrease in the shear strength of the soil. In slopes, the increases in shear forces and the water content, especially in cohesive soils, cause a reduction in the shear strength of the soil. In slopes, because of the increases of shear stresses in the soil layers forming the slope or the decreases of the shear strength of the soil, the balance of the slopes can be disturbed, and collapse occurs [5].

Earthquakes are the most significant and essential natural dynamic factor that threatens the long-term stability of slopes [6]. Although slopes maintain their stability under natural processes and external effects, it is unknown whether the slope has reached its shear strength. Slopes thought to be stable may lose their stability after sudden earthquakes that cause additional significant stresses on the soil [7]. Horizontal forces caused by earthquakes can cause instabilities such as rock falls and rotational and translational slope failures, especially on slopes with very steep inclinations. For this reason, considering the earthquake effect in the slope designs or analyses is vital for healthy slope designs and analyses and to prevent loss of lives and properties that may occur due to slope collapses [8].

There are many methods used within the scope of slope equilibrium analyses, finite element method (FEM), finite difference method, and probabilistic slope stability analyses. the most commonly used methods are limit equilibrium analyses and finite element method (FEM). In general, Limit Equilibrium Analyses Methods are used for static slope stability analyses, while dynamic slope stability analyses can be performed in addition to static slope stability analyses with finite element method (FEM).

In the limit equilibrium method, assumptions are made about the collapsing mass's motion behavior, the collapse surface's location and shape, and the forces acting on the collapsing mass [3]. In addition, in these methods, the stress-strain relationship is not considered, and the slope deformations cannot be obtained in Limit Equilibrium Analyses since it is assumed that the soil block on the possible failure surface moves as a whole [3,9]. Besides that, no failure surface is considered in Finite Element Method (FEM), and models with complex and irregular geometry can be analyzed accurately. In addition, values such as stresses, deformations, and pore pressures can be calculated in slope stability analyses made with the Finite Element Method (FEM) [10].

One of the methods used in dynamic slope stability analyses is pseudo-static analyses. In this method, dynamic slope stability analyses are performed by converting the horizontal and vertical accelerations of the earthquake into horizontal and vertical inertia forces and applying these forces to the center of collapsed mass on the possible slip surface [9]. In the analyses in question, the horizontal acceleration of the earthquake is assumed to be large enough to cause the slope to collapse, and this acceleration acts on the sliding mass as a horizontal static force[11]. This method is more accessible because the calculations continue after the earthquake accelerations are converted into inertial forces, similar to the static limit equilibrium analyses. However, representing the complex earthquake motion only with vertical and horizontal forces is the most significant disadvantage of this method. Therefore, it is not accepted as a healthy analysis method [9].

In pseudo-static analyses, the factor of safety of the slope against collapse is calculated, but the deformations in the slope cannot be obtained. However, due to earthquake forces, the displacements on the slope are considered when determining whether a slope is safe after an earthquake. Therefore, analyses that give displacements in seismic slope stability analyses are healthier and preferred [9]. That's why, in this study, dynamic analyses were performed on a numerical two-dimensional slope model by finite element method (FEM).

In recent years, many studies have been conducted on slope stability. For this purpose, factor of safety, displacement, and shear stresses occurring in slopes have been revealed by analyzing various conditions and models. In addition, various precautionary suggestions have been presented for slope safety as a result of the research. Static and dynamic analyses were carried out with plaxis 2D and 3D in wet and dry environments [12-14].

In the analysis performed on the three-dimensional dynamic slope model created within the scope of a project carried out in Three Gorges Reservoir, the slope was investigated in the rainless-earthquake, rainy-earthquake conditions. The results showed that porosity has a greater

effect on the safety factor in rainfall conditions compared to the permeability coefficient and saturation. It was determined that the safety factor corresponding to the vertical downward seismic effect is smaller than the safety factor corresponding to the vertical upward seismic effect. [15].

Finite element and limit equilibrium analyzes were carried out under static and dynamic loading for dry and wet conditions on 3 critical slopes determined on the Gerese-Belta route in Southern Ethiopia. It was observed that the safety coefficients obtained from the Slide 2D program using the limit equilibrium analysis were higher than the safety coefficient values obtained from the finite element based Phase 2D program. As a result of this study, the Bench method used in limit equilibrium analysis was determined as an economical method that can be used to alleviate soil slopes and was recommended for use [16].

Micke Didit et al. [17] investigated the effect of the structural loads applied to the tip slope on slope stability using the finite difference method. For this purpose, a three-dimensional slope model was created, and analyses were performed. As a result of the analyses, it was revealed that the shear stresses on the slope increased as the structural load was applied closer to the slope tip. It was also understood that the safety factor value increased as the structural load was moved away from the sloping tip.

Dejian Li et al. [18] investigated the effect of large-diameter cast-in-situ piles on slope stability under impact load. Safety factors were calculated using the strength reduction method under the effect of static load and assuming the impact pile construction vibration at the toe of the slope as dynamic load. Here, the relationship between the reduction factor and the parameters of the slope shear strength and the displacements between two points at the toe of the slope was established. As a result, it was found that the safety factor obtained from the analysis under dynamic effect was lower than the safety factor obtained in static analysis.

Onyango et al. [19] conducted analyses to investigate the stability of a slope constructed on a specific section of the Qinglong-Xingyi Highway and to devise an appropriate stabilization method. For this purpose, a 2-dimensional slope model was created using the ANSYS program using the finite element method. After the analyses, it was understood that the slope was sensitive to external effects and that measures should be taken against slope failure. It was decided that piles placed in rock soil were the most appropriate measures to prevent slope failure. After the analyses by modeling the piles, it was understood that the slope failure surface disappeared, and the displacements decreased.

In this study, static and dynamic analyses were performed. Static analyses were used to examine the safety of the coastal road, which is heavily used, to understand the current situation of the slope. Understanding whether it is close to collapse is important without any dynamic effects because it can give important data before collapse so that there is enough time to take measures. The coastal road heavily used by vehicle and pedestrian traffic has to be investigated whether the slope in question would collapse after an earthquake that occurred suddenly and without any known time. Slides that are assumed to be safe in static conditions can fail after earthquakes, which causes additional forces and horizontal displacements. This reality makes it necessary to examine them under the dynamic effects of earthquakes. For that, dynamic analyses were performed to see the effects of earthquakes on slope stability. In this study, slope stability analyses were carried out in a pilot area of Birecik Coastal Road. To perform analyses, the slope model should first be generated. A Unmanned Aerial Vehicle drone was used to do that. By Unmanned Aerial Vehicle flights, point cloud of the field was genereated. Using the cloud point data of the field, the three dimensional model of the slopes was generated using ArcGis10.8. Then, the critical section of slopes was determined by observations made in the field. And again the critical section of slopes was generated using ArcGis10.8 for two dimensional stability analyses. It is converted to dxf format to upload to the Plaxis program. Then, the critical section of the slope was uploaded to Plaxis. Also, it was understood that a slope failure occurred in the area in 2019, and there were buildings at the tip of the slope when the failure occurred. The failure point that occurred in 2019 is near our examined point. For the possibility of construction of new buildings in the examined area in the future, ten adjacent buildings were modeled at the top of the slope, and their weight was calculated and implemented as a line load. The line load was affected at the top of the slope with different distances from the tip of the slope. In this scope, the static and dynamic analyses were performed, and Finite Element Method (FEM) was used. Sivrice earthquake data were used for dynamic analyses, which occurred in 2020. While performing static and dynamic stability analyses, the strength reduction (Phi-C reduction) technique was applied, the factors of safety were calculated for both cases, and the displacements and shear stresses were also revealed. Finally, the slope stability analyses were examined by comparing the dynamic and static analysis results. This study showed that dynamic shear stresses are lower than static shear stresses, while dynamic displacements are higher than static displacements. These results revealed that plain strain or two-dimensional analysis is inaccurate.

This study conducted static and dynamic slope stability analyses in a pilot region of steep and high slopes on the Birecik Halfeti coastal road, consisting of fragmented, fractured, cracked, and low-strength sandy-clay limestone. First, a two-dimensional critical section was obtained from the three-dimensional terrain model created by the studies in the area under investigation. While choosing the critical section, the slope's height, the discontinuities' condition, and the slope's inclination were considered. In the geological survey report, in which the soil parameters are provided, it has been understood that there is no groundwater and no flowing surface water in the slopes that are the subject of the investigation. Also, observations made in the field show no flowing surface water. In light of these data, two-dimensional analyses were carried out, and the

factors of slope safety, displacements, and shear stresses on the slope were calculated.

Usage of Plaxis Software

Plaxis software is a program based on FEM developed to perform stability analyses, stress deformation analyses, consolidation, structure-soil interaction, bearing capacity, and groundwater flow analyses within the scope of various applications in the field of geotechnical engineering [8]. While performing analyses with Plaxis software, analyses are performed in two-dimensional models under axisymmetric or plane strain and three-dimensional conditions. It uses triangular elements with 6 or 15 nodes to describe strains in two-dimensional analyses [20, 21]. The use of 15-node triangular elements provides a 4th-order interpolation for calculating numerical unions and displacements involving 12 stress points; the use of 6-node triangular elements gives a 2nd-order interpolation for calculating numerical unions and displacements involving 3 stress points (Fig. 1) [22].

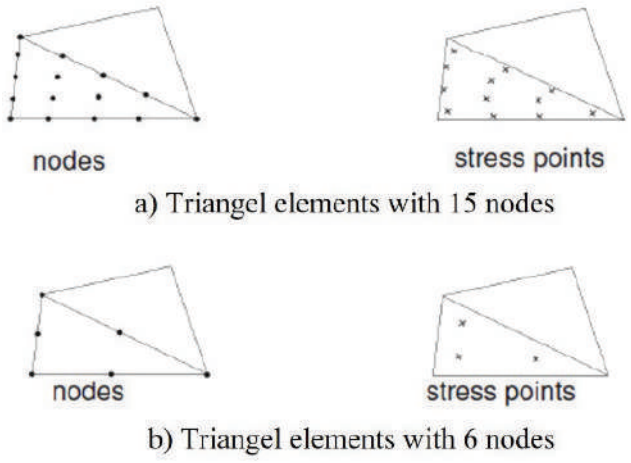


Figure 1. 15 and 6 nodes triangle elements [22] [created by author].

Mohr Coloumb and Hardening Soil Failure Criteria are used in slope stability analyses with Plaxis software. The Hardening Soil Failure Criteria is more suitable for excavation slopes, while the Mohr Coloumb failure criterion is more suitable for the analyses of existing slopes. In the analyses made according to the Mohr Coloumb Failure Criteria, it is generally accepted that the soil exhibits an elastic behavior until the failure occurs, and the soil behaves plastically after the collapse [23]. In addition, the most used methods in the calculation of the factor of safety in FEM are Strength Reduction Method and Gravity Increasing Method [24]. In the strength reduction method, the shear strength parameters (c and Ø) of the soil are gradually reduced until collapse occurs, and the factor of safety for slope is calculated with the help of stress-displacement analyses. It gives more effective results in the analyses of existing slopes [24]. In this study, the strength reduction (Phi-C) method was used to calculate the factor of safety within the scope of static and dynamic slope stability analyses.

MATERIALS AND METHODS

Generating of Slope Model

To perform slope stability analyses, a numerical model slope section is needed. For this reason, aerial photographs of the region were taken by unmanned aerial vehicle (UAV) flights over the study area. The study used an Octo V3 model UAV belonging to TurkUAV company and a Sony RX100 MII camera with a 20.2 Megapixel resolution CMOS sensor. The platform, which has a control distance of 1500 meters, has a flight time of 22 minutes (Fig. 2) [25].

First of all, a flight plan was created. The flight plan was created with 4 transverse routes, longitudinal flights on these routes, and autonomous flights from a fixed height of 80 meters, such that aerial photographs were taken with 80% longitudinal and 70% transverse overlap. To ensure the spatial relationship of the images obtained from aerial photographs with the physical earth, 10 ground control points were marked



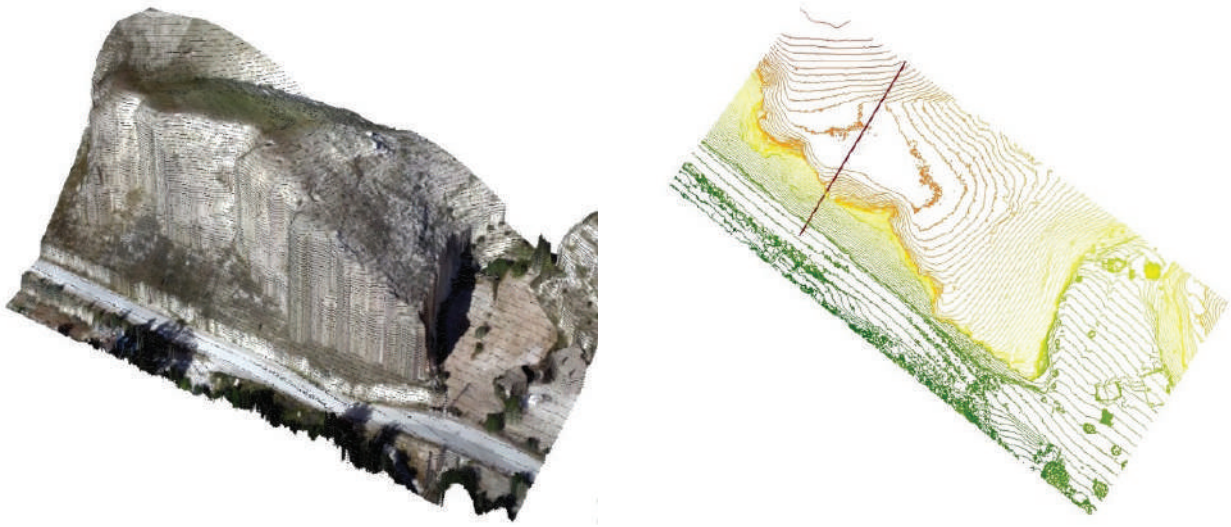
Figure 2. The digital camera system and UAV used in flight.

on the ground in the study area using the CORS-enabled GNSS system, and coordinate information was obtained.

Aerial photographs of the area were taken along the route in the flight plan. Then, 222 aerial photographs suitable for model creation were evaluated. The software Pix4D, which is a part of Harran University and produces point clouds from aerial photographs, was used to evaluate the aerial photographs. As a result of the evaluation of the photographs, point cloud data consisting of 206767 points was obtained. Since the acquired point cloud data is in the WGS84 system, it was converted to the UTM 3-degree projection defined in the ITRF-96 coordinate system using ground control points (Fig. 3). The three-dimensional numerical model of the area is also obtained in this coordinate system [24]. The position accuracy of the model created for the study area is ±1.27 cm, and this accuracy has been tested with ground control points. The three-dimensional model of the study area with contours, the digital elevation model with contour curves, and the critical section were created using the ArcGis10.8 version and are shown in Figure 4. Finally, after the observations made in the field, the essential section line of the slope, considered

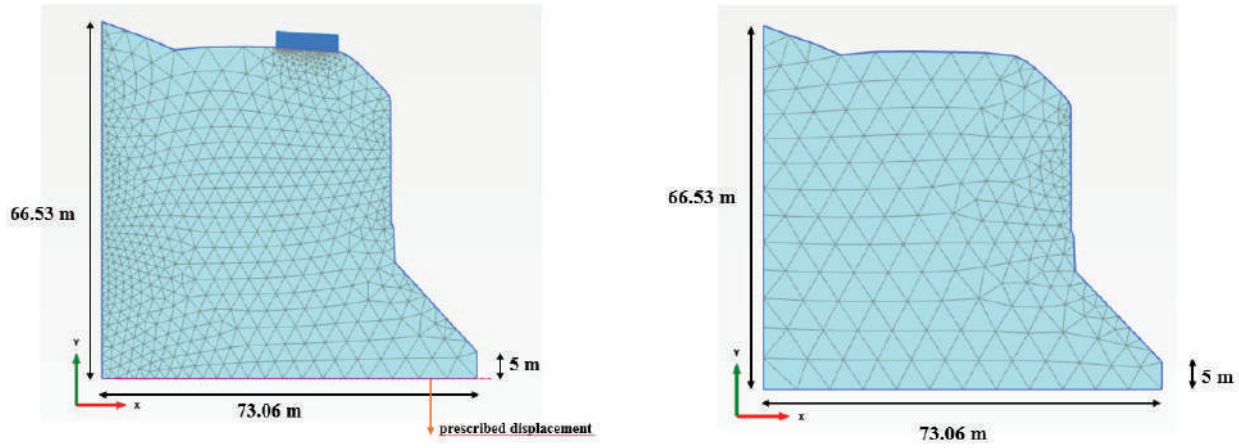


Figure 3. UAV flight in the field to create the slope model.



(a) (b)

Figure 4. Slope models obtained by field study, a) contoured three-dimensional model of the study area, b) contoured digital elevation model and critical section line of the study area



(a) (b)

Figure 5. (a) 2d critical slope model inserted into plaxis software, (b) for dynamic and static analyses with the initial location of the line load.

risky according to the slope height, inclination, and current discontinuities, as shown in Figure 4-b, was produced using the ArcGis10.8 program. The critical section obtained was transferred to Plaxis software, as shown in Figure 5.

The Building Properties Used in Analyses

For two-dimensional analyses, it is thought that there are 10 adjacent buildings with 4-story concrete structures, and all building's properties are the same. The Building was modeled as 4 floors, 3 m floor height, 12 m width, and 12 m length. The foundation is modeled as 12 m in width, 120 m in length, and 0.5 m in thickness. The building and the foundation weights are calculated. While calculating the floor weight, the mass of the building participating in the earthquake was taken as a basis, and the live load and dead load values given in Turkish Code 498 (TS498) [26] and the mass participation ratio presented in Turkish Seismic Code 2018 (TSC2018) were used. Finally, using these parameters, a line load was calculated as 766.17 kN/m/m, which was applied to the top of the slope through 12 m.

Stability Analyses

The soil structure of the slope consists of a single layer, and the highest point of the slope is 66.53 m, and its width is 73.06 m. Two-dimensional slope stability analyses were performed in Plain Strain conditions and using triangular elements with 15 nodes. Soil material was modeled according to Mohr-Coulomb, and long-term drained analyses were performed for static and dynamic analyses. First, analyses were carried out to determine the absence of structure loads on the slope. Then, the analyses were carried out by placing a line load through 12 m on top of the slope. The soil parameters used in the analyses are given in Table 1. Since there is no groundwater and surface water, the groundwater level wasn't specified in the model.

Static Slope Stability Analyses

Static analyses were first performed without the line load on the slope. It was carried out in two stages: Deformations and factor of safety (FS). Then, the line load was applied on the top of the slope as 766,17 kN/m/m (very high for a four-story structure) through 12 m at the tip of the slope, 5 m, 10 m, and 15 m backward from the tip of the slope, and analyses were carried out. Analyses were carried out in two stages, if the load is on the slope: Loading and FS. In the Loading phase, the loads were activated, and plastic analysis was performed. In the FS phase, the factor of safety was calculated, and Phi-C reduction (safety) analysis was performed. Since the slope was not completely horizontal, the Gravity Loading calculation was made in the initial phase. In addition, in the static stability analyses, the slope model was meshed with medium coarseness, passed to the calculation stages, and the analyses were completed.

Table 1. Soil parameters used in analyses [27] [created by author]

Natural Per Unit Weight (γ_n) (kN/m^3)	Modulus of Elasticity (Mpa)	Poisson Ratio	Cohesion (c) kN/m^2	Internal Friction Angle (Ø)
18.10	78.56	0.30	275	32.5

Dynamic Slope Stability Analyses

Rayleigh damping is needed both to resist Rayleigh waves and to obtain more realistic results in the analyses made with plain strain models in which the earthquake situation is examined. For soils, damping usually occurs due to improved plasticity, viscous properties, and friction (Lanzo and Vucetic, 1999). In Plaxis software, damping is expressed in terms of Rayleigh damping, which is proportional to the stiffness and mass of the model [28].

$$C = \alpha M + \beta K \quad (1)$$

In this equation, C is the damping, K is the stiffness, M is the mass, and α (alpha) and β (beta) are the Rayleigh coefficients. The coefficient α (alpha) expresses the contribution of the mass during damping. Lower frequencies are damped as the value of α (alpha) increases. The coefficient β (beta) expresses the contribution of stiffness during damping. As the β (beta) increases, it dampens more significant frequencies.

At the point of calculating the periods of the soil, if the soil layer consists of a single layer, the soil's natural period can be calculated using equation 2 [29]. In equation 2, H represents the thickness of the soil layer, and V is shear wave velocity. For the calculation of α and β, firstly, two frequencies were calculated for soil, and equation 2 was used. Then frequencies were converted to frequency of vibrations, and for calculation of α and β, % 5 damping ratio was used, and they are calculated as Rayleigh α (alpha)= 0.62874, Rayleigh β (beta)= 0.00347. These coefficient values were used in analyses.

At the point of calculating the periods of the soil, if the soil layer consists of a single layer, the soil's natural period can be calculated using equation 2 [29]. In equation 2, H represents the thickness of the soil layer, and V is shear wave velocity. For the calculation of α and β, firstly, two frequencies were calculated for soil, and equation 2 was used. Then frequencies were converted to frequency of vibrations, and for calculation of α and β, % 5 damping ratio was used, and they are calculated as Rayleigh α (alpha)= 0.62874, Rayleigh β (beta)= 0.00347. These coefficient values were used in analyses.

$$T_g = \frac{4H}{V} \quad (2)$$

$$\alpha + \beta * \omega_i^2 = 2 * \omega_i * \xi_i \quad (3)$$

Dynamic analyses were first carried out to assess the slope's absence of line load. Then, as in the static analyses, the line load was applied 766,17 kN/m/m through 12 m at the tip of the slope, 5 m, 10 m, and 15 m backward from the tip, and analyses were carried out. Dynamic analysis was carried out in three stages: Earthquake, Deformations, and FS (factor of safety) for the absence of structure load. In the Earthquake phase, the Sivrice earthquake was affected, and dynamic analysis was performed. In the Deformations phase, the limits of deformations were determined, and plastic analysis was performed, and in the FS phase, the Phi-C reduction (Safety) analysis was performed.

In case the Line Load is applied on top of the slope, dynamic analyses were solved in four stages. In the first loading phase, loads were activated, and plastic analysis was carried out. In the second phase, the Earthquake phase, the Sivrice earthquake was applied, and dynamic analysis was carried out. The third stage was made as Deformations and plastic analysis were carried out, the fourth stage was the FS stage, the factor of safety calculation was made, and Phi-C reduction (Safety) analysis was performed.

In the dynamic analyses, Line Displacement was defined at the bottom of the slope, and Ux=0.01m was entered, Displacement X: prescribed, Displacement Y: Fixed was set, and in this stage, acceleration time parameters of Sivrice earthquake were loaded into the program as the table. The highest ground acceleration value of the Sivrice earthquake transferred to the program is 292.8 cm/s2, and the earthquake's time interval was 30 seconds (Fig. 6).

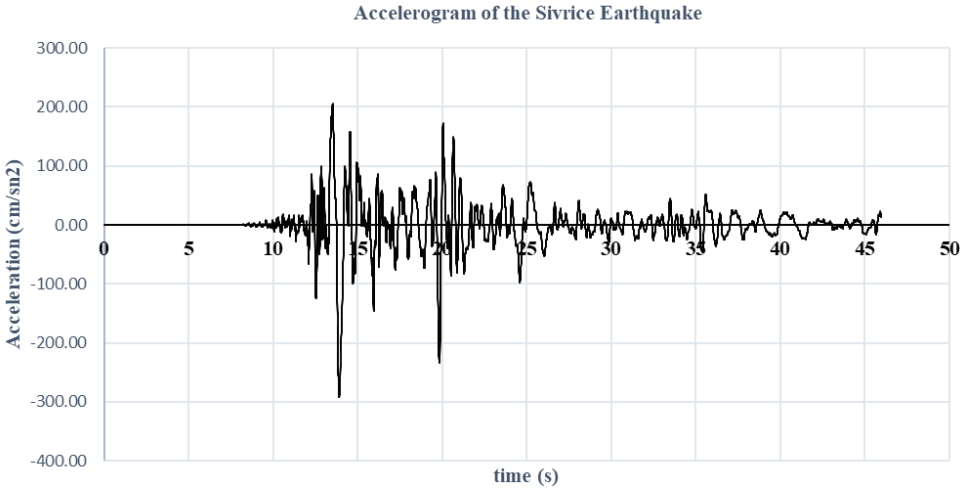


Figure 6. The accelogram of the Sivrice earthquake [30] [open access by AFAD].

Xmin: Viscous, Xmax: None, Ymin: Viscous, Ymax: None were determined to absorb the stress increases caused by the dynamic earthquake effect. If this is not done, the stress increases will be reflected in the soil body [30]. In addition, medium mesh coarseness was used for the slope model in dynamic stability analyses, the calculation phases were started, and the analyses were completed.

RESULTS AND DISCUSSION

Static Analyses Results

According to the results of the static analyses, the safety factor was found to be the highest for the absence of line load on top of the slope, and the safety factor was calculated as 1.695. In addition, the case with the lowest factor of safety in static analyses, that is, the riskiest case, is that the line load is at the tip of the slope. If the line load is applied at the tip of the slope, the slope's safety factor against collapse was calculated as 1.199, as it is seen in Table 2 that the factors of safety increase as the line load moves away from the tip of the slope.

In static analyses, the largest horizontal displacement value occurs when the line load is applied at the tip of the slope, and the total displacement value is calculated as 0.2645 m. Also, according to the results of the static analyses, it is seen in Figure 7 that the displacements increase significantly when the line load is placed at the tip of the slope compared to the case in which no load on a slope, and the displacements decrease with the line load moving away from the tip of the slope. In the absence of the load, the displacements occur as 0.0047 m and in a small area of the vertical surface of the slope.

The largest horizontal displacements occur on the vertical surface of the slope and around the load. It is also seen in Figure 8 that the horizontal displacements on the vertical surface of the slope decrease as the load moves away from the tip of the slope by changing its color from red to yellow.

According to the results of static analyses, there is an increase in the maximum shear stress values when the line load is applied to the slope. It is seen in Figure 9 that as the line load moves away from the tip of the slope, there is a slight decrease in the maximum shear stress values compared to the situation when the load is at the tip of the slope. As the load moves away from the tip of the slope, maximum shear stresses decrease.

Table 2. Factors of safety obtained by static slope stability analyses

The position of the line load and factors of safety					
Position of the load	**No load**	**At the tip of slope**	**5 m back from tip of slope**	**10 m back from tip of slope.**	**15 m back from tip of slope**
Factor of safety (FS)	1.695	1.199	1.280	1.355	1.437

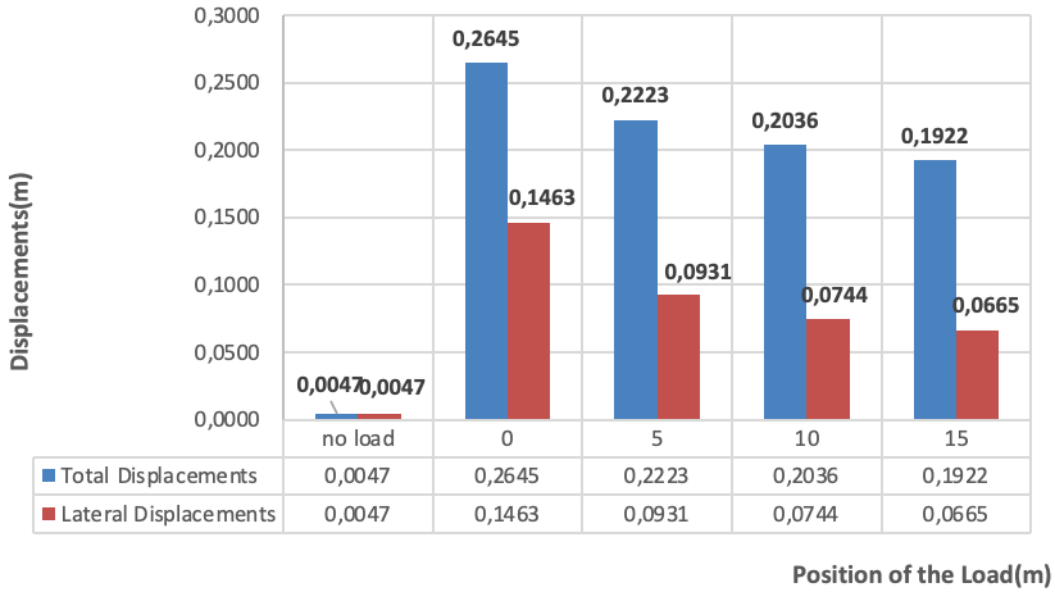
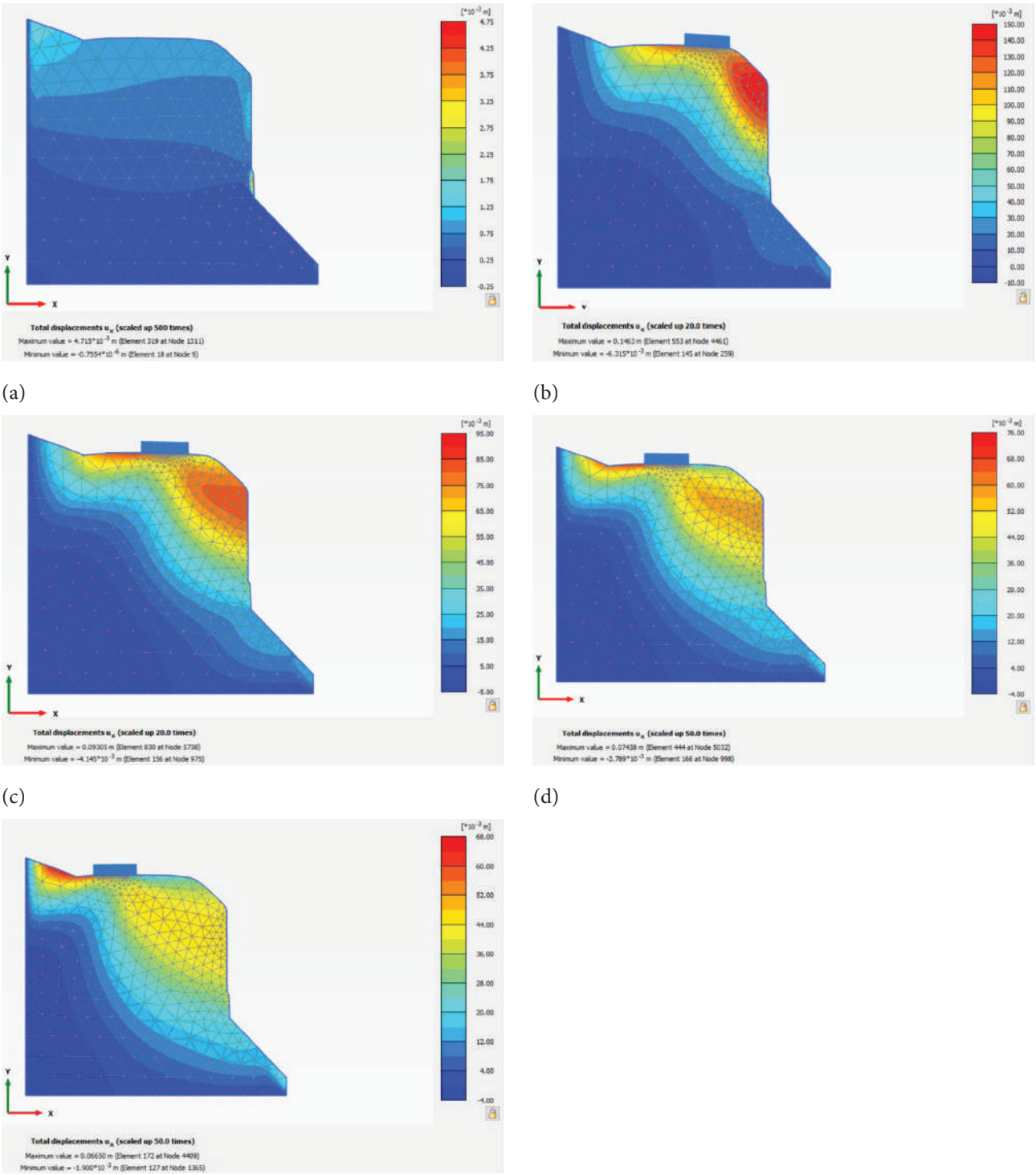


Figure 7. Total and horizontal displacements (m).

It is seen in Figure 10 that the most significant shear stresses occur at the base of the slope and at the intersection of the vertical surface of the slope and the inclined surface.

It can be seen in Figure 11 that a potential slip surface occurs surface when no load is on the slope. However, the fractures occur in the intersections of vertical and inclined



(a)

(b)

(c)

(d)

(e)

Figure 8. The locations of largest horizontal displacements occurred as a result of static analyses: a) no load on the slope, b) line load at the tip of the slope, c) line load 5 m behind the tip of the slope, d) line load 10 m behind the tip of the slope, e) line load 15 m behind the tip of the slope.

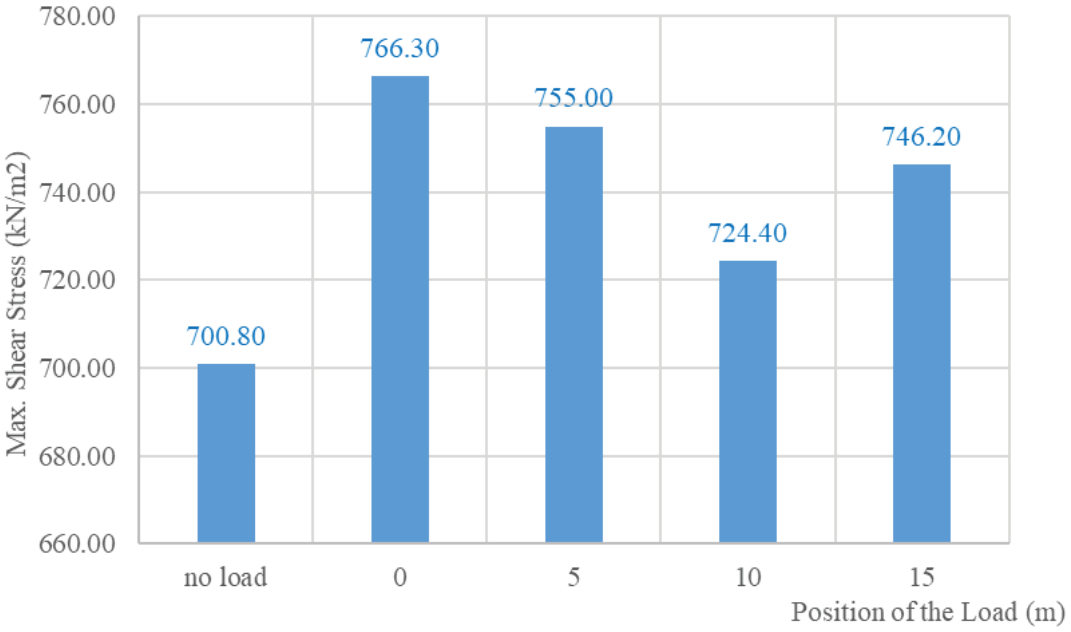


Figure 9. The maximum shear stresses occurred in the slope due to static analyses.

surfaces. Also, the possible slip surface becomes very evident when the load is placed at the sloping tip, and the potential slip surface almost disappears when the load is 5 m away from the sloping tip. The potential slip surface is formed again when the load is 10 m away from the tip of the slope but not as prominent as when the load is at the tip of the slope. And if the load is 15 m away from the tip of the slope, the potential slip surface almost completely disappears.

In high-load situations, the safety factor increases as the excavation length increases. This is most likely due to model-specific reasons. The reason why larger models (16 – 32 m) provide a slightly higher safety factor is probably a result of element distribution [31]. PLAXIS automatically creates a finer mesh around the surface charge area and may have made more minor elements on this region in the large model than in the small model. A thinner mesh will reduce the safety factor. More extended excavation will not reduce the safety factor when the surface load is high enough.

Dynamic Analyses Results

The factors of safety (FS) obtained from dynamic analyses are given in Table 3. As shown in Table 3, there is a severe decrease in safety factors with the effect of the load on the tip of the slope. It is also seen that the factors of safety increase as the load moves away from the tip of the slope. According to the results of the dynamic analyses, as expected, the safest case with the highest safety factor of the slope occurs when there is no load on top of the slope. Also, the most negative situation with the most minor safety factor in dynamic analyses is that the load was placed on the tip of the slope.

The displacements obtained in dynamic analyses are given in Figure 12. It can be seen that the total displacements in the slope decrease when the load is applied at the tip of the slope, and when the load is moved away from the tip of the slope, the displacements increase. Also, it can be seen that horizontal displacements have constantly increased. Horizontal displacements under dynamic loading were found to be 0.203, 0.246, 0.257, 0.289, and 0.418 for unloaded and 0.5, 10, and 15 m loading conditions, respectively. Total displacements under dynamic loading were found to be 0.333, 0.253, 0.266, 0.323, and 0.419 for unloaded and 0.5, 10, and 15 m loading conditions, respectively (Fig. 12).

In dynamic analyses, in every case, it can be seen that the largest displacements occur at the toe of the slope and in a small area of the vertical surface where the vertical surface intersects with the inclined surface, which starts with the toe of the slope. Also, it can be seen in Figure 13 that while the load is moving away from the tip of the slope, the displacement effect is decreased by changing the color red to turquoise.

As is seen in Figure 14, as a result of dynamic analysis, there is an increase in the maximum shear stress values by applying the load on top of the slope. A slight decrease in the maximum shear stress values occurs as the load is 10 m away from the tip of the slope. Shear stress takes its maximum value when the load is 15 m away from the tip of the slope, as shown in Figure 14. Under dynamic loads, the maximum shear stress was calculated as 671.70 kN/m2, 686.70 kN/m2, 700.20 kN/m2, 683 kN/m2, 1022 kN/m2 for unloaded and 0, 5, 10 and 15 m loaded cases (Fig. 14). Also, it can be seen in

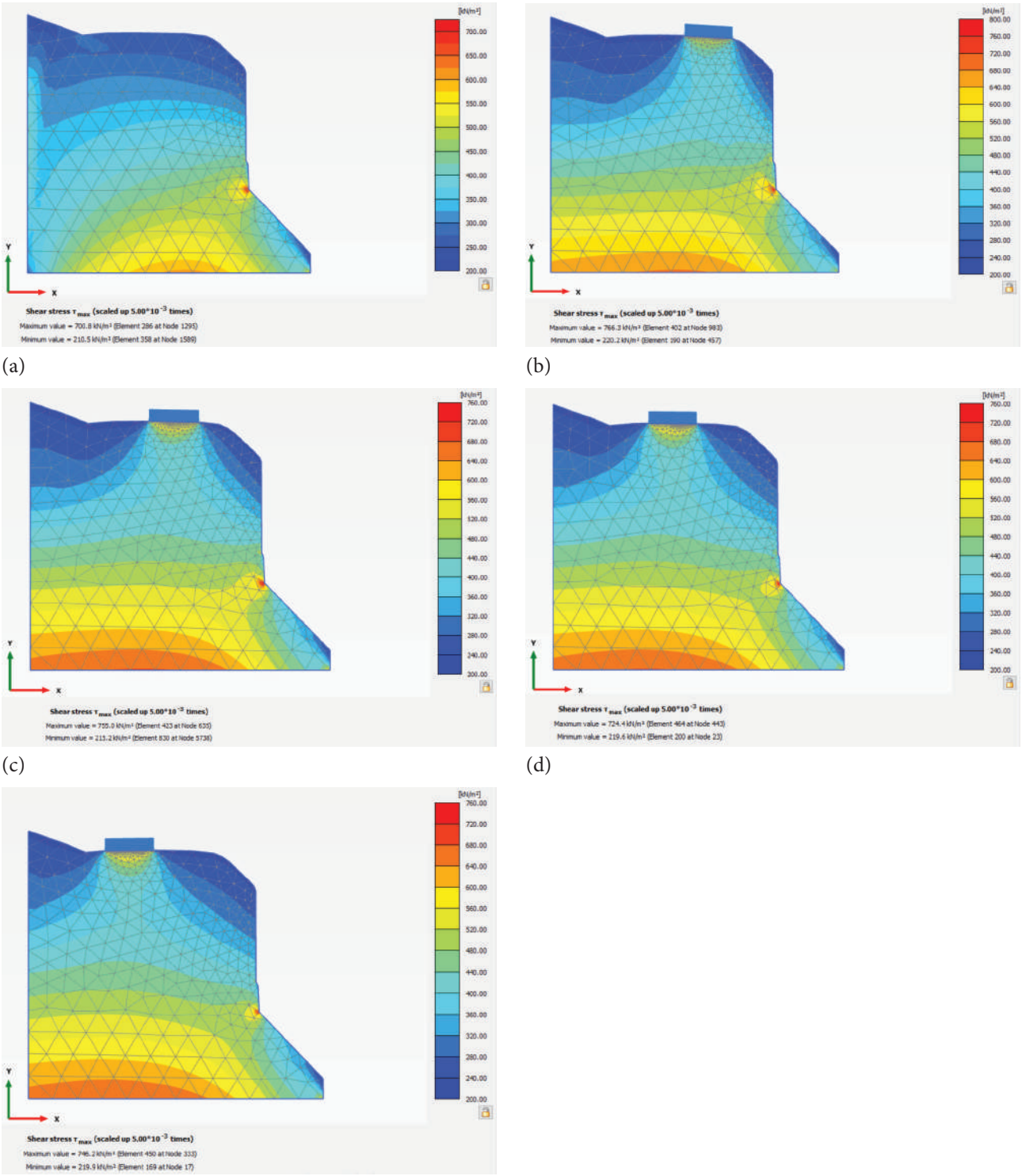


Figure 10. The locations of max. Shear stresses occurred in the slope as a result of static analyses: a) no load on the slope, b) line load at the tip of the slope, c) line load 5 m behind the tip of the slope, d) line load 10 m behind the tip of the slope, e) line load 15 m behind the tip of the slope.

Figure 15 that maximum shear occurs at the bottom of the slope and the intersection of the vertical surface and inclined surface. It is seen in Figure 10 that the most significant shear stresses occur at the base of the slope and at the intersection of the vertical surface of the slope and the inclined surface.

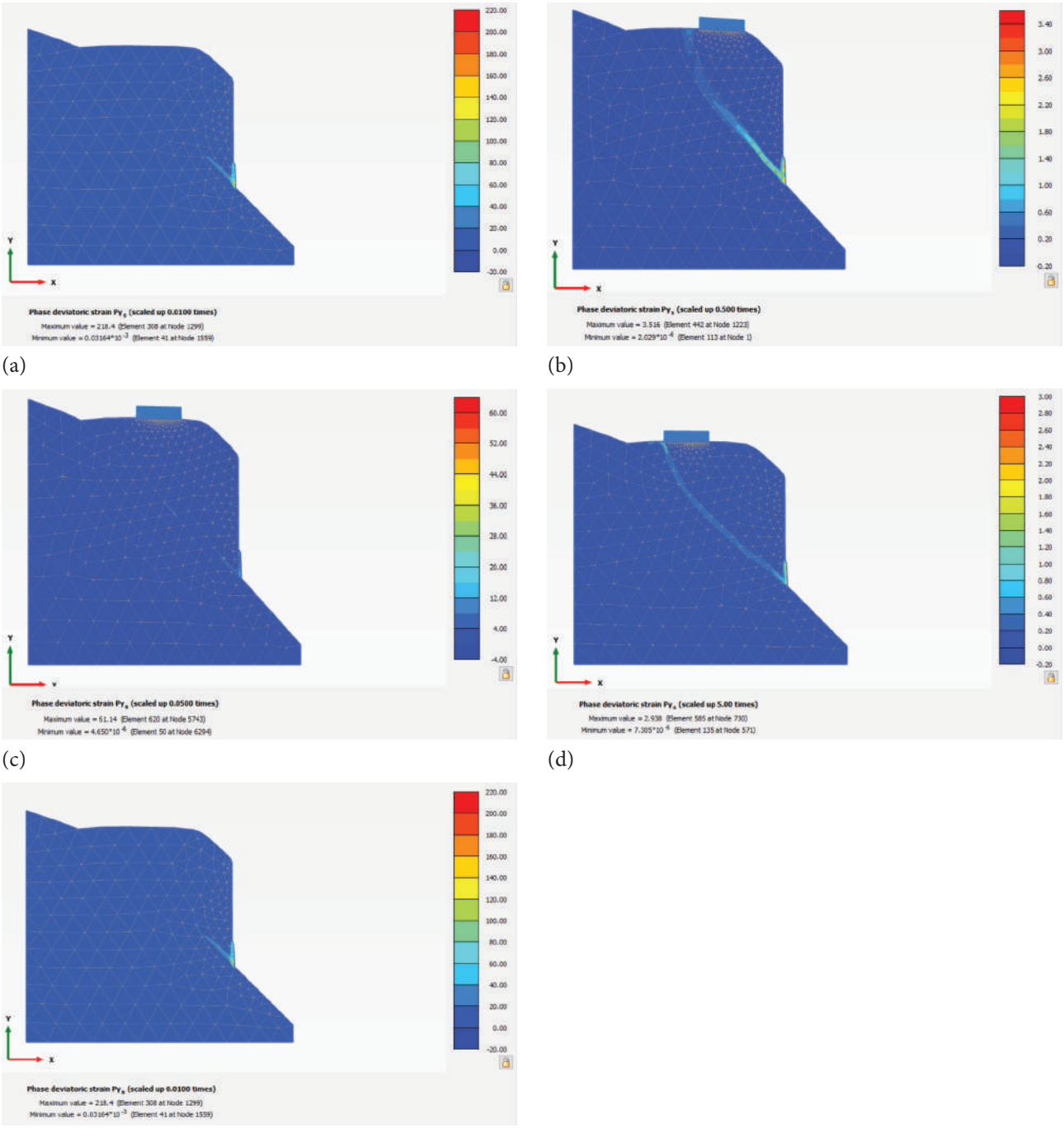


Figure 11. Fracture mechanism that occurred in the slope as a result of static analyses; a) no load on the slope, b) line load at tip of the slope, c) line load 5 m behind the tip of the slope, d) line load 10 m behind the tip of the slope, e) line load 15 m behind the tip of the slope.

Table 3. Results of dynamic analyses

The position of the line load and factors of safety					
Position of the load	**No load**	**At the tip of the slope**	**5 m back from the tip of the slope**	**10 m back from the tip of the slope**	**15 m back from the tip of the slope**
Factor of safety (FS)	1.664	1.190	1.296	1.351	1.442

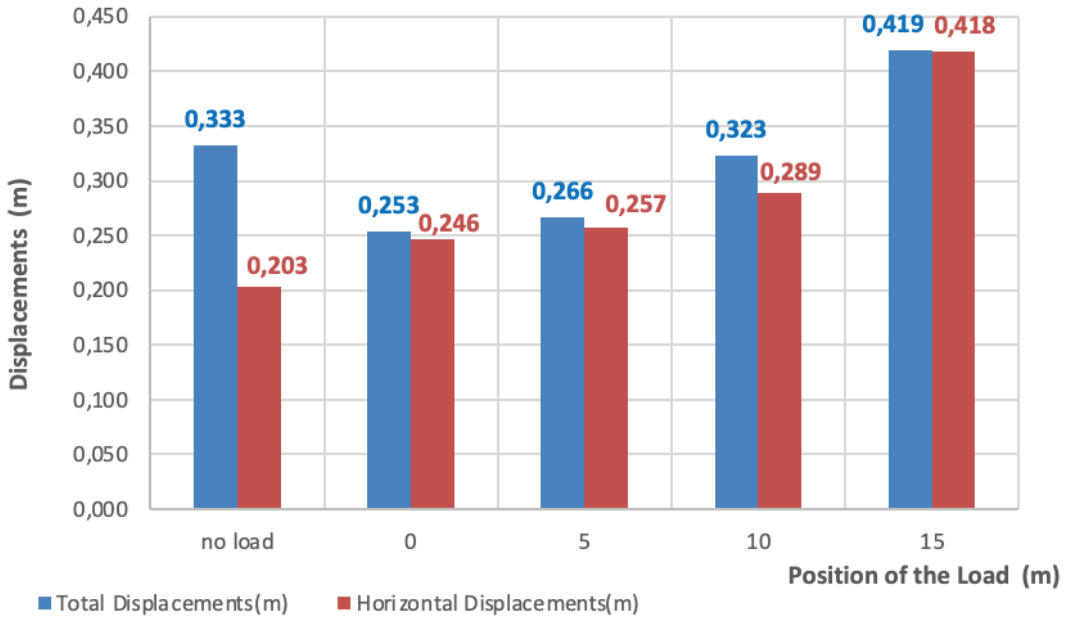


Figure 12. Displacements occurred in the slope due to dynamic analyses.

Evaluations of Results

Factor of safety (FS)

There is a maximum difference of 29.262 % between the safety factor calculated in static analyses, and this difference is at most 28.571% in dynamic analyses. In the static and dynamic analyses, Table 4 shows that applying the load on top of the slope affects the safety of the slope. Safety factors increase when the load moves away from the tip of the slope. Also, the position of the load 5 m and more away from the tip of the slope does not have any impact on the factor of safety for static and dynamic analysis in terms of destabilizing the slope. FS>1 indicates a stable slope [32, 33]. According to Christian, if FS is greater than 1, the slope is stable, but if FS is less than 1, the slope is unstable. According to the study conducted by Le Ta Meko et al. (2023), the factor of safety is gradually decreasing [34]. A significant strain has occurred here, and this strain's contours define the sliding surface. According to the study by Shah et al. (2021), as the slope decreases, the factor of safety decreases [35]. In this study, the slope is stable under all conditions. In their study conducted in 2023 by Kassa and Meten [36], FS values decrease under static and dynamic loading conditions, and the slope is not stable. According to the modeling results, the factor safety increases for the slope angle decreases (Kale et al. [37]). According to the results of the analysis, a decrease in slope height tends to increase the safety factor [38-40]. In this study, the factor of safety gradually increases under static and dynamic loads. In this respect, this study is compatible with the studies done by Kassa et al., Kale et al., Anbalagan, Raghuvanshi et al. (2014), and Shiferaw [36-40].

Theoretically, all slopes with a factor of safety greater than one are safe. However, many design standards recommend using a FoS greater than one. This is because, over time, the slope becomes unstable due to rain, earthquakes, or erosion. In this case, the slope's safety factor decreases temporarily or permanently. Over time, the factor of safety becomes less than one, and the slope collapses or landslides may occur. It is seen in Table 4 that the safety factors obtained in dynamic analyses are less than for cases where there is no load and the load is at the tip of the slope compared to the static analyses. In the other cases, it can be seen that the safety factors are nearly equal to or higher than those obtained in static analyses. As a result of the static analysis, the factor of safety was calculated as 1.695, 1.199, 1.280, 1.355, 1.437 for no-load and 0.5, 10.15 m loading conditions, respectively. Under dynamic loading conditions, it was found to be 1.664, 1.190, 1.296, 1.351, 1.442 in unloaded and 0, 5, 10, 15 m loading conditions, respectively.

If the static analysis is taken as a reference, which is the case that there is no load on the slope, the factor of safety obtained from the most critical case, which is the load on the slope tip in dynamic analysis, decreases by 29.794 %.

If no structure is on top of the slope for long-term stability, the minimum safety factor must be 1.20 based on effective stress according to Turkish Code 8853. And if there is a structure on the slope, the factor of safety should be at least 1.20 in case of earthquake and 1.80 based on total stress according to TS8853 [41]. It is understood that the slope under investigation is unsafe in cases where the load is on top of the slope for static and dynamic analysis. For the other four cases, it is safe against collapse, according to TS8853 [41].

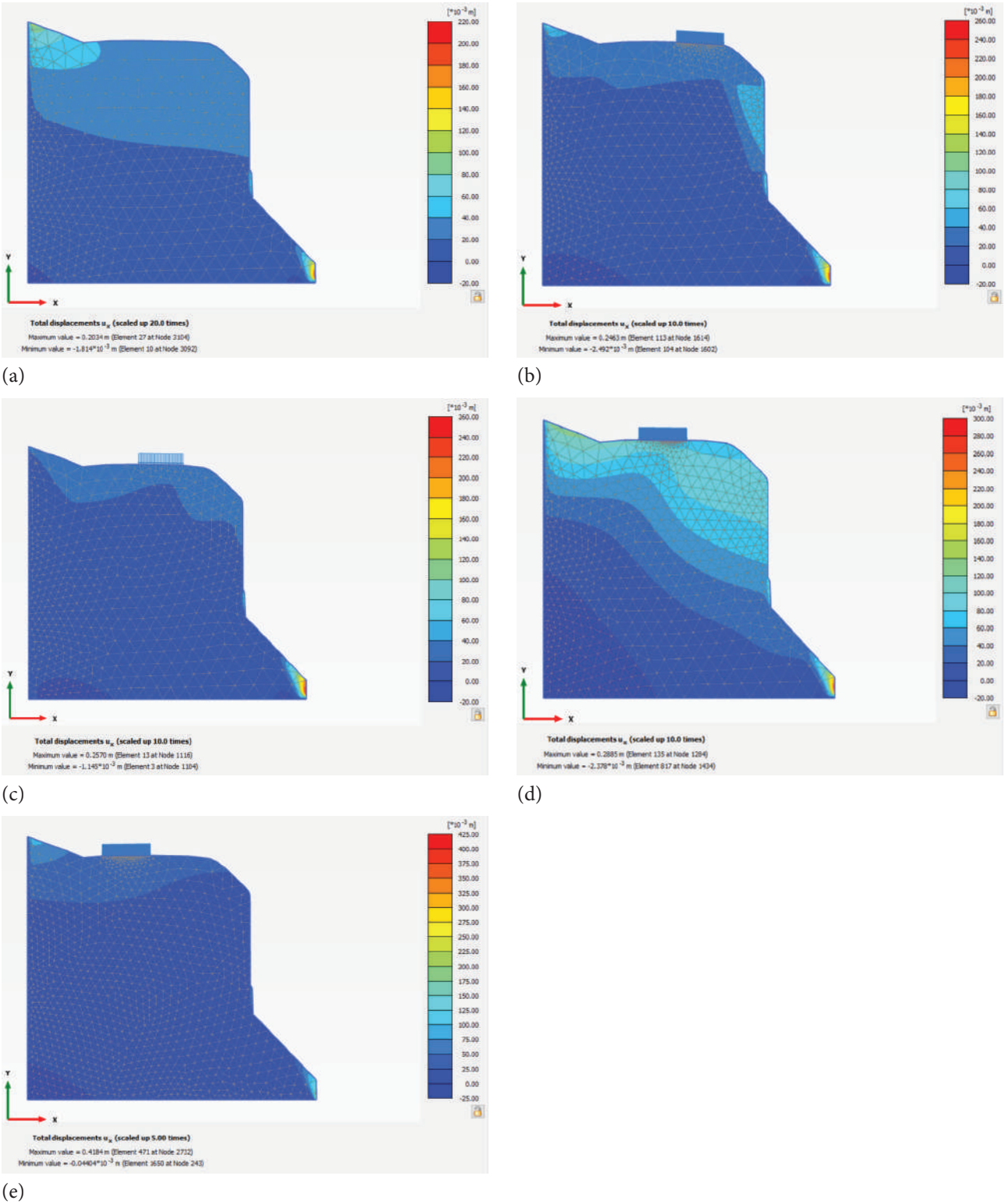


Figure 13. The locations of horizontal displacements that occured in the slope as a result of the dynamic analyses: a) no load on the slope, b) the load is at the tip of the slope, c) the load is 5m behind the tip of the slope, d) the load is 10m behind the tip of the slope, e) the load is 15m behind the tip of the slope.

Also, the minimum factor of safety for slope stability is accepted to be at least 1.0 for Eurocode7 and BS. That's why it can be stated that the slope under investigation is safe, according to Eurocode7 and BS [42]. Also, it can be understood from dynamic analyses that in terms of displacements, the slope under investigation is unsafe against

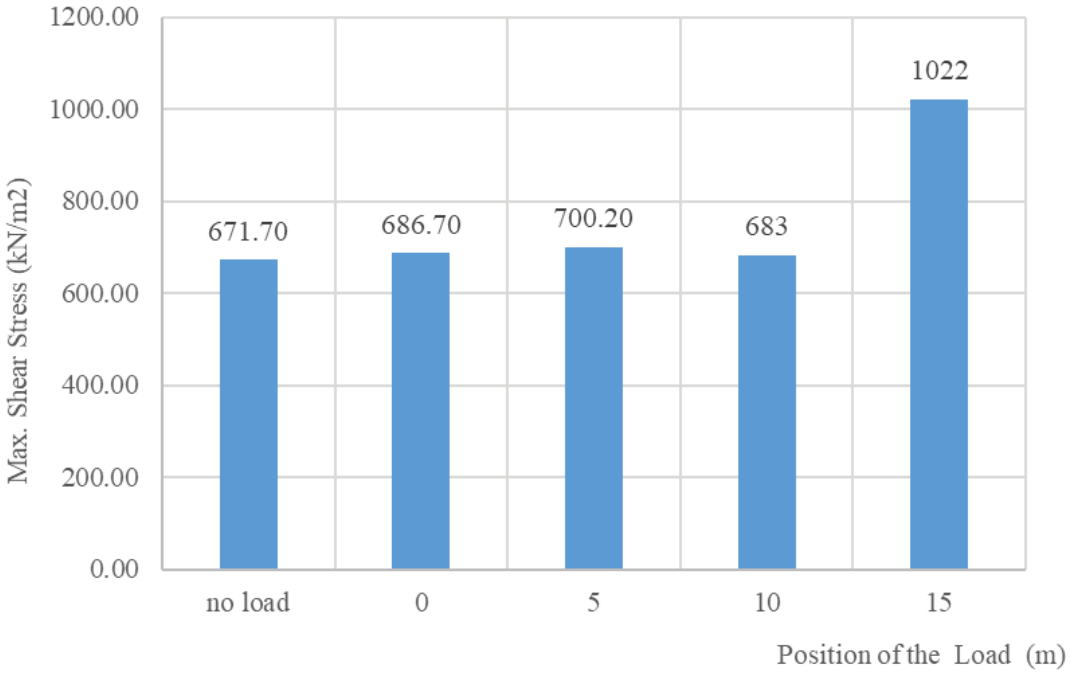


Figure 14. The maximum shear stresses occurred in the slope due to dynamic analyses.

collapse. Although the calculated factors of safety generally indicate that the slope is safe according to Eurocode7, BS, and TC8853, the soil strength forming the slope is very low, the soil layer is very cracked and fractured, the discontinuities are many, and their directions are variable and since these features cannot be fully modeled in Plaxis software the slopes can be evaluated as risky.

As seen in Figures 7 and 9, when shear stresses are increased by placing the load on top of the slope, the horizontal displacements increase, and when shear stresses decrease, the horizontal displacements decrease. The horizontal displacement is reduced while shear stress is raised only for the caseload 15 m away from the tip of the slope. This is because the slope soil's backward becomes more rigid compared to the tip of the slope, and shear stress can be absorbed. Figures 11 and 14 show horizontal displacements increase by applying earthquake effects in dynamic analysis.

Largest Horizontal Displacements (Ux)

Permanent damage from earthquakes causes permanent deformations. A moderate input to the base displacement causes large deformations in the changes. Calculations are made with undrained effects and zero dilatation angles. Suction develops in water during earthquakes, and large values can work for fine-grained, homogeneous soils. However, cavitation occurs in cracks in clay and coarse soils. A FEM-based software, PLAXIS (2D), is used in the numerical analysis. The slope is divided into small elements, and a stress-strain relationship is defined for each case. Mesh refinement and some elements strongly affect the calculated FoS (Fig. 13, 15). As seen in Figure 13, the maximum total displacement in the unloaded condition was calculated as 0.2034 m. When the loading condition was examined for 0, 5, 10, and 15 m, it was seen that the total displacements increased, and the maximum movements were concentrated in the region where the loading condition was present (Figs. 13a-13e).

In static analyses, minimal horizontal displacements occur when no load is on the slope. The largest horizontal displacements are increased significantly by placing the load at the tip of the slope. The largest horizontal displacements decrease as the structure moves away from the tip of the slope. The fact that the largest horizontal displacements in the static analyses occur when the load is at the tip of the slope is due to the increases in stresses in the slope soil by the line load. It is also seen in Figure 16 that as the load moves away from the tip of the slope, the largest horizontal displacements decrease regularly in static analyses. As a result of the static analysis (Fig. 16), horizontal displacements were calculated as 0.0047 m, 0.1463 m, 0.0931 m, 0.0744 m, and 0.0665 m for unloaded and 0, 5, 10, and 15 m loading conditions, respectively. As a result of dynamic analysis, horizontal displacements were calculated as 0.203 m, 0.246 m, 0.257 m, 0.289 m, and 0.418 m for unloaded and 0, 5, 10, and 15 m loading conditions, respectively (Fig. 16).

When the earthquake is applied to the slope, the largest horizontal displacements increase significantly compared to the static analysis results. It is seen in Figure 16 that as

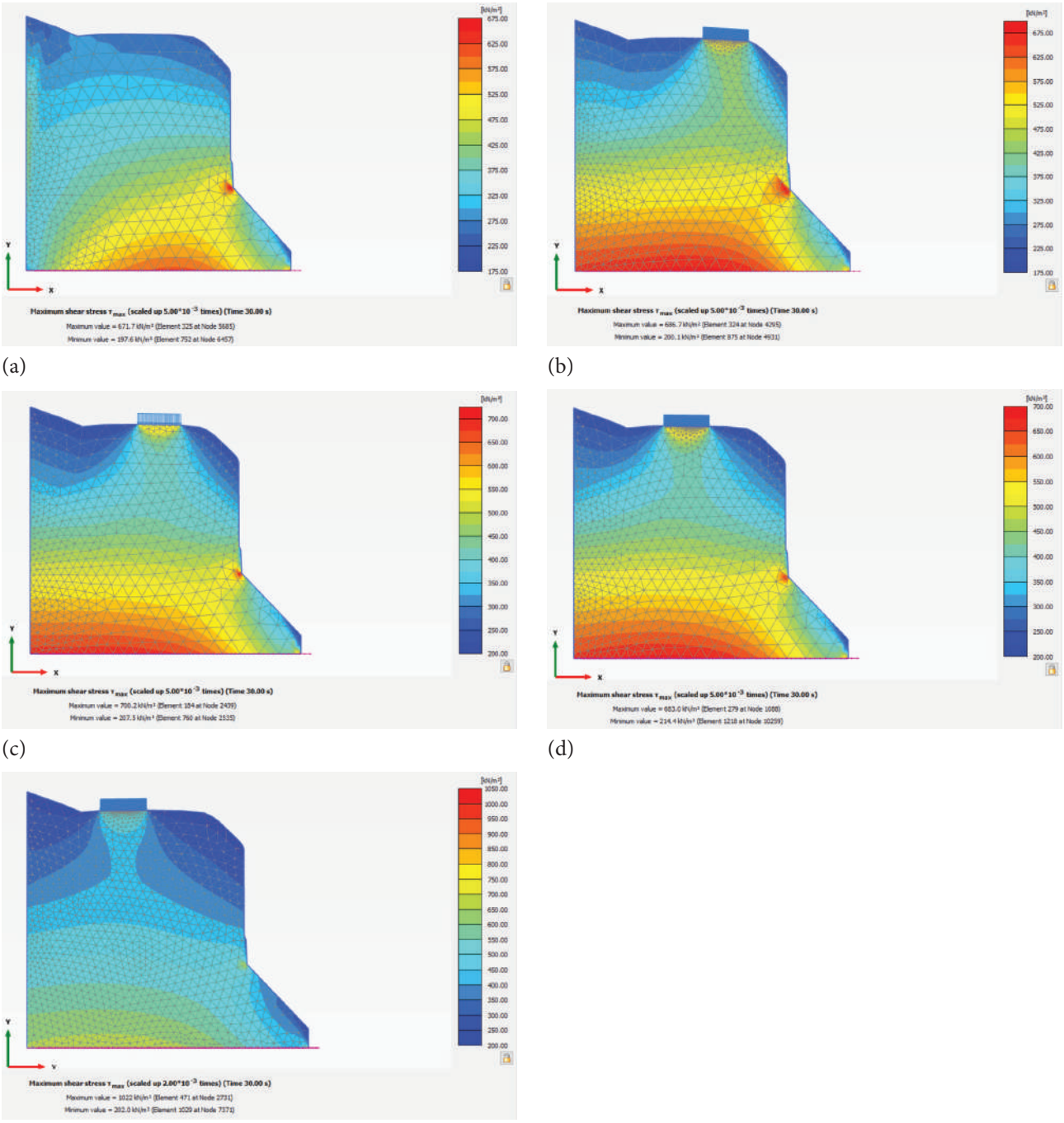


Figure 15. The locations of max. Shear stresses occurred in the slope result of dynamic analyses: a) no load on the slope, b) line load at the tip of the slope, c) line load 5 m behind the tip of the slope, d) line load 10 m behind the tip of the slope, e) line load 15 m behind the tip of the slope.

the load moves away from the tip of the slope, the largest horizontal displacements continually increase. In the literature, it is accepted that the limit of displacements for slope should be between 50 and 100 mm [7]. Because of that, it can be concluded that according to the analysis results regarding displacements, the slope under investigation is unsafe. The Nguyen et al. study determined that horizontal displacements decreased under dynamic loads [41]. According to the survey by Shiferaw et al., total displacements increase under static and dynamic load conditions [14]. This is attributed to the fact that actual measurements do not confirm the calculated results. Horizontal displacement results were supported by the study by Shiferaw et al. [14]. In addition, the increase in displacement (Fig. 13) will

Table 4. Factors of safety obtained from the result of static analyses and dynamic analyses and the differences between them (%)

	Static analyses		Dynamic analyses			
Position of the load (m)	**Factor of safety (FS)**	**Difference (%)**	**Factor of safety (FS)**	**Difference (%)**	**Differences between the factors of safety (%)**	**Decrease in the most critical case(%)**
no load	**1.695**		**1.664**		1.830	**29.794**
0	**1.199**	**29.262**	**1.190**	28.486	0.751	
5	1.280	24.484	1.296	22.120	-1.250	
10	1.355	20.060	1.351	18.810	0.295	
15	1.437	15.221	1.442	13.341	-0.348	

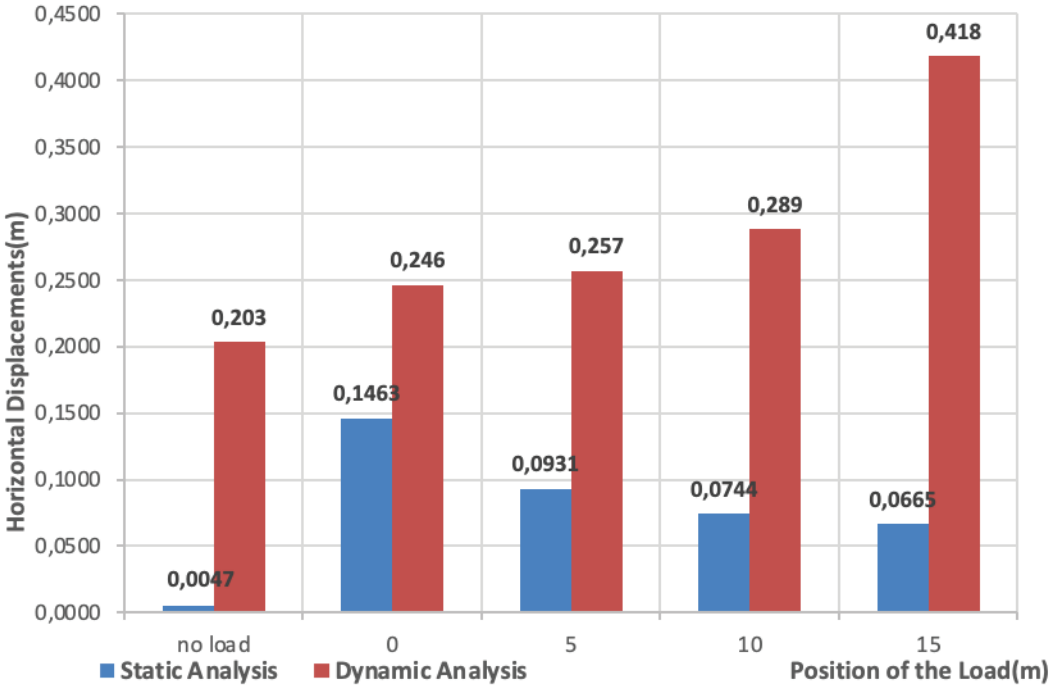


Figure 16. Horizontal Displacements obtained by dynamic and static analyses

cause damage to wastewater and drinking water infrastructure systems, and water leaks to the sloping ground due to these damages. In this case, it will cause sliding surfaces to become more apparent or new sliding surfaces to form, and as a result, collapses will occur.

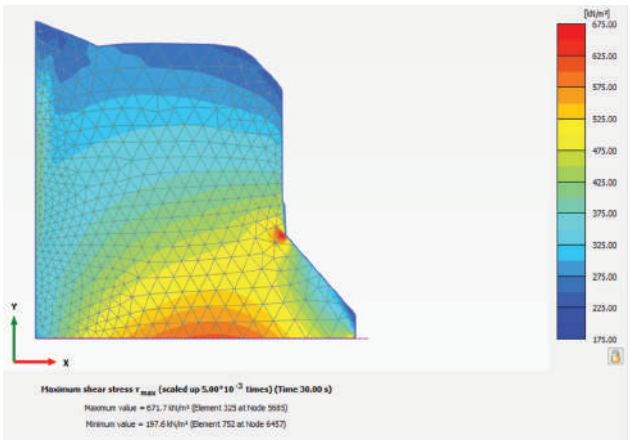
Maximum Shear Stresses (τ max)

Figure 9 shows that a higher maximum shear stress is generally obtained in static analyses. The maximum shear stresses occured in dynamic analyses are higher only when the load is 15 m away from the tip of the slope. This is because the slope height increases from the tip of the slope to the backward, that is, towards the infinite part of the slope. In addition, the maximum shear stresses in dynamic analyses are smaller than the maximum shear stresses obtained in static analyses because the shear stresses are damped with the increase in displacements due to the dynamic earthquake effect. It is observed that the maximum shear stress increases compared to the unloaded case due to the increase in total displacements. The stresses are concentrated from the load region to the lower part of the soil (Fig. 14,15).

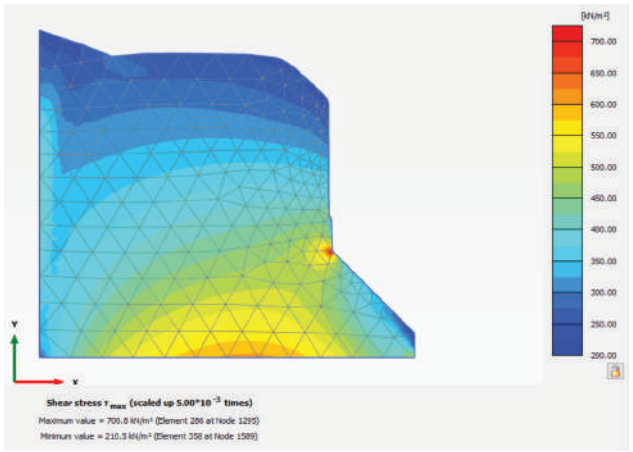
In static and dynamic analyses, it is seen that the maximum shear stresses occur at the base of the slope and the intersection of the vertical surface and the inclined surface of the slope. In the field, it has been observed that there are



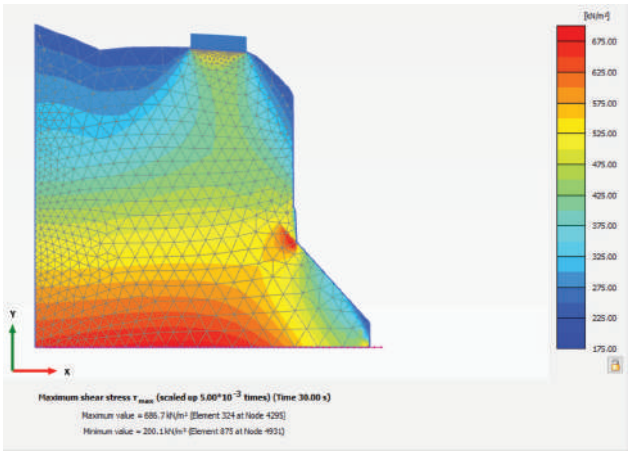
(a)



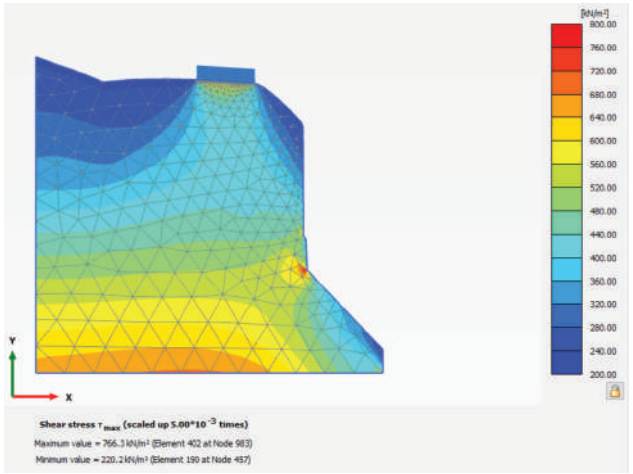
(b)



(c)



(d)



(e)

Figure 17. As result of the analyses, the locations of the maximum shear stresses occurred in the slope and the crushing-cover slips observed in the field; a) crushing-cover slips observed in the field, b) static analyses: the structure is not on the slope, c) dynamic analyses: the structure is not on the slope, d) static analyses: the structure is at the tip of the slope, e) dynamic analyses: the structure is at the tip of the slope.

crushes and cover throws at the point where the inclined surface starts with the toe of the slope and the starting of the vertical surface of the slope. In this sense, it is understood that the results of the analyses are consistent with the observations made in the field. The maximum shear stress places that occur in the slope are shown in Figure 17. The geometry

of the slope is one of the significant essential parameters which affect its stability [44]. The slope geometry can be altered by decreasing the slope angle and height and removing material from the landslide point in the study area [38-40]. Slope angle and height affect slope stability, as adding these parameters increases shear stress while reducing shear strength on the implicit failure surface [43]. According to the study conducted by Rawat and Mohanty (2021), it was observed that shear stresses increased towards the ends of the slope [46]. Hamouma et al. (2020) reported that shear stresses increase when moving from a smooth surface to a rough surface [47]. Shear stress results are consistent with the study by Rawat and Mohanty and Hamouma [46,47].

CONCLUSION

This study investigates the slope stability in a pilot area along the Birecik Halfeti coastal road. Both static and dynamic analyses were conducted using Finite Element Method (FEM) and Plaxis V20 software. The analyses considered various scenarios with and without external loads applied to different distances on the slope. The findings revealed that plain strain (two-dimensional) analysis is accurate, and they are summarized below.

1. It is understood that the main factor that reduces safety for static and dynamic analyses is the load to be applied at the top of the slope. A dynamic earthquake has a minimal effect on safety.
2. The factor of safety decreases by dynamic effect 1.695 to 1.664 (%1.830) with no load, which is consistent with the result of the study conducted by Dejian Li et al. (2023).
3. As a result of the static and dynamic analyses, the most significant shear stresses occurred in the intersection of the vertical surface and inclined surface, starting with the toe and bottom of the slope. These results are consistent with the crushing and capping in the intersection of the vertical surface and inclined surface observed in the field.
4. It is expected that higher shear stresses will occur for dynamic analyses than static analyses. However, shear stresses obtained from dynamic analyses are lower than those obtained from static analyses, while the displacements in dynamic analyses are higher than those in static analyses. It can be stated that this is a fault of plain strain or two-dimensional analyses.
5. According to the factor of safety obtained in dynamic and static analyses, it is understood that the slope is unsafe just in case the load is at the tip of the slope. The other four cases are safe, according to TS8853. However, according to Eurocode7 and BS, the slope is safe for all cases.
6. According to the study conducted by Micke Didit et al. (2022), the displacement in static analysis decreases when the load moves away from the tip of the slope, and the results are consistent with our study.
7. The increases in displacements due to dynamic effects will also affect the safety of the polygon points of the region's high and medium voltage lines and close to the slope tips. In this case, these lines and polygon points must be moved further away to a safer distance.
8. Additionally, more reliable results will be obtained by supporting 2D analyses with 3D analyses and investigating slope safety by modeling the discontinuities and separations in 2D and 3D models.
9. The most suitable stabilization methods for this slope are considered to ensure the safety of the coastal road by laying it on a slope with 45 degrees and beveling, removing the parts where segregations are intense, and then covering it with a steel wire mesh.
10. In the scenario of opening the region to possible construction in the future and constructing structures at the tip of the slope, it was understood that the slope was unsafe when the structure load was applied at the tip of the slope. In this case, as an alternative suggestion for risk mitigation, it is recommended as a priority measure not to allow constructions at a safe distance from the tip of the slope in the long term. However, if construction cannot be prevented, it will eliminate the possibility of reducing the slope's inclination and beveling it. Under this condition, building pile retaining walls that will stop the movement in the slope becomes necessary. However, the slope height is too high, and in some places, it restricts the construction of retaining walls; in this case, it becomes necessary to prevent the leakage of surface water or water from construction and infrastructure systems to the sloping ground. Also, it becomes necessary to establish a slope monitoring mechanism that will allow constant monitoring of the slope movements and formation of new possible sliding surfaces in the slope and to take instant measures according to the data to be obtained
11. The region in question receives the most precipitation during winter, while summers are dry and hot. This situation contributes to the continuous and repeated occurrence of dissociations in the limestone that forms the slope. With global climate change, the sudden and sometimes excessive occurrence of precipitation contrary to the characteristics of the region and the increase of summer temperatures above the regional average and their duration will contribute to the intensification of the expansion-contraction cycle, further increase of existing discontinuities and separations in the slope and the occurrence of slope failures on a larger scale in this region. Considering this fact, taking more extensive measures to prevent partial ruptures on the slope surface and total failures will be necessary. For this purpose, it would be healthy to build pile retaining walls to prevent displacements and possibly sliding surfaces. As a result, existing separations can be removed using machinery or special explosives, and the surface should be covered with wire mesh to prevent small pieces from separating and falling from the surface due to seasonal effects.

This study was carried out to investigate the safety of the heavily used road sandwiched between the coastal road and the slopes. An actual application was included using an unmanned aerial vehicle. Slides that are assumed to be safe in static conditions can fail after earthquakes, which causes additional forces and horizontal displacements. This reality makes it necessary to examine them under the dynamic effects of earthquakes. For that, dynamic analyses were performed to see the impact of earthquakes on slope stability.

ACKNOWLEDGEMENTS

I want to express my gratitude to Dynamic Engineering which facilitated the acquisition of soil parameters in this study, to GIS expert and mapping technician İbrahim Halil İRCAN who provided the opportunity and contribution to the use of the ArcGis10.8 program, to Mustafa ULUKAVAK who is Assoc. Prof. Dr. at Harran University who contributed to the creation of the 3D numerical models of the slopes for this study, and my supervisor, Prof. Dr. Ali SARIIŞIK, who is a professor at Harran University, whose experience I benefited from.

AUTHORSHIP CONTRIBUTIONS

"Taylan" Study conception and design, Acquisition of data, Analysis and interpretation of data, Drafting of manuscript, Critical revision

"Ulukavak" Acquisition of data, Critical revision, Drafting of manuscript

"Sarıışık" Critical revision, Drafting of the manuscript

"Can" Critical revision, Drafting of manuscript, Analysis, and interpretation of data.

DATA AVAILABILITY STATEMENT

The authors confirm that the data that supports the findings of this study are available within the article. Raw data that support the finding of this study are available from the corresponding author, upon reasonable request.

CONFLICT OF INTEREST

The author declared no potential conflicts of interest with respect to the research, authorship, and/or publication of this article.

ETHICS

There are no ethical issues with the publication of this manuscript.

STATEMENT ON THE USE OF ARTIFICIAL INTELLIGENCE

Artificial intelligence was not used in the preparation of the article.

REFERENCES

[1] Griffiths DV, Marquez RM. Three-dimensional slope stability analysis by elasto-plastic finite elements. Geotechnique 2007;57:537–546. [CrossRef]

[2] Tekin A. Slope stability analyses with finite elements and limit equilibrium methods. Istanbul: Istanbul University, Institute of Science and Technology; 2011.

[3] Taşkıran T, Yavuz VS, Keskin MS. Investigation of slope stability with two and three dimensional models. Dicle Univ Fac Eng J Eng 2015;6:1–8.

[4] Alizadeh NM. Determination of the critical slip surface in slope stability analysis. Gazimağusa: Eastern Mediterranean University; 2013.

[5] Köse H, Kahraman B. Rock mechanics. 5th ed. İzmir: Dokuz Eylül University Faculty of Engineering Publications; 2014.

[6] Ulusay R. Landslides and irregularities in engineering slopes: Types, effects and mitigation of damages. Ankara; 2007.

[7] Konuk Ç. Slope stability analysis and investigation of earthquake effects on slopes. Istanbul: Istanbul Technical University, Institute of Science and Technology; 2005.

[8] Duncan WC, Chris M. Rock slope engineering. Boca Raton: CRC Press; 2004.

[9] Kramer SL. Geotechnical earthquake engineering. Ankara: Gazi Publishing House; 2003. [CrossRef]

[10] Duncan JM. State of the art: Limit equilibrium and finite-element analysis of slopes. J Geotech Eng 1996;122:577–596. [CrossRef]

[11] Coduto DP. Geotechnical engineering: Principles and practices. Upper Saddle River: Pearson; 1999.

[12] Alzabeebee S. Calibration of a finite element model to predict the dynamic response of a railway track bed subjected to low- and high-speed moving train loads. Transp Infrastruct Geotech 2023;10:504–520. [CrossRef]

[13] Meko L, Chemeda YC, Meko B. Road cut slope stability analysis for static and dynamic (pseudo-static analysis) loading conditions. Open Geosci 2023;15:20220561. [CrossRef]

[14] Shiferaw HM, Teshager GM, Hailu SA, Shiferaw TM. Numerical modelling of traffic-induced dynamic loading on a two-story residential building. Beni-Suef Univ J Basic Appl Sci 2023;12:106. [CrossRef]

[15] Wang J, Wang Z, Sun G, Luo H. Analysis of three-dimensional slope stability combined with rainfall and earthquake. Nat Hazards Earth Syst Sci 2024;24:1741–1756. [CrossRef]

[16] Gebreyohannes D, Getahun E, Jothimani M. Slope stability assessment in the seismically and landslide-prone road segment of Gerese to Belta, Rift Valley, Ethiopia. PLoS One 2024;19:e0296807. [CrossRef]

[17] Didit M, Zhang X, Zhu W. Slope stability considering the top building load. Open J Civ Eng 2022;12:123017.
[18] Li D, Zhang J, Lian Y, Tang W. Dynamic stability analysis for slope under the impact load of large diameter punched cast-in-place pile. Int J Geosynth Ground Eng 2023;9:29. [CrossRef]
[19] Onyango JA, Zhang C. Numerical analysis of slope stability by strength reduction in finite elements using ANSYS: A case study of Qinglong–Xingyi Expressway contract section T1 (K11+790–K11+875). Environ Earth Sci Res J 2019;6:89–96. [CrossRef]
[20] Plaxis Connect Edition V20. General information. Delft: Delft University of Technology & BV; 2019. p. 4.
[21] Toma MA. Earthquake response analysis of pile supported structures: Correspondence of Plaxis 2D with Eurocode 8. Trondheim: NTNU; 2017.
[22] Plaxis 2D reference manual. Delft: Plaxis; 2018.
[23] Albataineh N. Slope stability analyses using 2D and 3D methods. Akron: University of Akron; 2006.
[24] Shlash A. Comparative study of slope stability by geotechnical software programs. Nicosia: Near East University, Graduate School of Applied Sciences; 2020.
[25] Yunus K, Şenol Hİ, Memduhoğlu A, Şeyma A, Ulukavak M, Polat N. UAV use in volume calculations: The example of Osmanbey campus. Turk J Photogramm 2019;1:7–10.
[26] TSE. TS-498. Ankara: Türk Standartları Enstitüsü; 1998.
[27] Dynamica Engineering. Şanlıurfa province Birecik district rockfall analyses, slope stability analyses and geotechnical reports, and preparation of application projects service procurement. Şanlıurfa; 2019.
[28] Plaxis version 8 dynamics manual.
[29] Sawada S. A simplified equation to approximate natural period of layered ground on the elastic bedrock for seismic design of structures. In: Proceedings of the 13th World Conference on Earthquake Engineering. Canada; 2004.
[30] Disaster and Emergency Management Authority. Available at: https://tadas.afad.gov.tr/waveform-detail/50813 Accessed on Nov 24, 2025.
[31] Lindberg N. Three-dimensional effects in slope stability for shallow excavations: Analyses with the finite element program PLAXIS (master thesis). Lindberg, Niclas: Luleå University of Technology; 2020.
[32] Christian JT. Geotechnical engineering reliability: How well do we know what we are doing. J Geotech Geoenviron Eng 2004;130:985–1003. [CrossRef]
[33] Shariati M, Fereidooni D. Rock slope stability evaluation using kinematic and kinetic methods along the Kamyaran–Marivan road, west of Iran. J Mt Sci 2021;18:779–793. [CrossRef]
[34] Meko L, Chemeda YC, Meko B. Road cut slope stability analysis for static and dynamic (pseudo-static analysis) loading conditions. Open Geosci 2023;15:20220561. [CrossRef]
[35] Shah SRA, Kumar A, Ali TH, Hakro MR, Zardari MA. Numerical modelling of soil-nail and secant pile in Plaxis 2D: A case study of tomb of Jam Nizam-Al-Din Samoo, Makkli Thatta. Civ Environ Eng 2021;17:706–717. [CrossRef]
[36] Kassa M, Meten M. Slope stability analysis using kinematic, limit equilibrium, and finite element models at Dessie town, northern Ethiopia. Arab J Geosci 2023;16:675. [CrossRef]
[37] Kale RY, Khan I, Kharbade A, Sakle C. An analytical study on slope stability of a highway embankment. 2021;8:5.
[38] Anbalagan R. Landslide hazard evaluation and zonation mapping in mountainous terrain. Eng Geol 1992;32:269–277. [CrossRef]
[39] Raghuvanshi TK, Ibrahim J, Ayalew D. Slope stability susceptibility evaluation parameter (SSEP) rating scheme—an approach for landslide hazard zonation. J Afr Earth Sci 2014;99:595–612. [CrossRef]
[40] Shiferaw HM. Study on the influence of slope height and angle on the factor of safety and shape of failure of slopes based on strength reduction method of analysis. Beni-Suef Univ J Basic Appl Sci 2021;10:31. [CrossRef]
[41] TS 8853. Yamaç ve şevlerin dengesi ve hesap metotları–zeminde. Ankara: Türk Standartları Enstitüsü; 1991.
[42] British Standard. Eurocode 7: Geotechnical design. 2004.
[43] Nguyen AD, Nguyen VT, Kim YS. Finite element analysis on dynamic behavior of sheet pile quay wall dredged and improved seaside subsoil using cement deep mixing. Int J Geo-Eng 2023;14:9. [CrossRef]
[44] Büyükkağnıcı CZ, Işık NS. Limit equilibrium methods in slope stability analysis: Comparison of success rates calculated with Eurocode 7 and BS 8006 standards. TUBAV J Sci 2019;12:18–29.
[45] Popescu M. A suggested method for reporting landslide remedial measures. International Union of Geological Sciences Working Group on Landslides; 2001. [CrossRef]
[46] Rawat P, Mohanty S. 1D and 2D dynamic site response of landfill site through numerical analysis. In: Local site effects and ground failures: Select proceedings of 7th ICRAGEE 2020. Singapore: Springer; 2021. p. 91–103. [CrossRef]
[47] Hamouma D, Messameh A, Tallah N. Finite element analysis of soil–pile interface under cyclic loading. Int J Civ Eng Technol 2020;11:49–57. [CrossRef]

Sigma Journal of Engineering and Natural Sciences
Web page info: https://sigma.yildiz.edu.tr
DOI: 10.14744/sigma.2025.1938

Research Article

Simulation of engine oil driven second grade ternary hybrid nanofluid flow subject to thomson and troian slip velocity addressing the thermo-convection effect

Tusar Kanti DAS[1,*], Mintu SAUD[1], Nayanto HAJONG[1], Bidyut KALITA[1]

[1]*Department of Mathematics, Dudhnoi College, Dudhnoi, Assam, 783124, India*

ARTICLE INFO

Article history
Received: 12 June 2024
Revised: 03 August 2024
Accepted: 06 November 2024

Keywords:
Critical Shear Rate; Exponential Heat Source; Second-Grade Ternary Hybrid Nanofluid; Suction Effect; Thermo-Convection Effect; Thomson; Troian Slip Velocity

ABSTRACT

The furnished article primely focuses on the second-grade ternary hybrid flow and thermal characteristics triggered by vertical stretching sheets, featured with buoyant and thermo-convection effect subjects to Thomson and Troian velocity slip at the boundary. The ternary hybrid Nanofluid is composed of engine oil blended with three distinct nanocomposites: Ag, Cu, and graphene. Furthermore, the thermal boundary layer equation addresses the nonlinear exponential heat source and the thermo-convection effect. The aforementioned assumption leads to a schematic model framed with coupled partial differential equations revamped into an array of coupled ordinary differential equations via some relevant similarity variable, which are numerically solved by the bvp4c method. The novel contribution embraces the impact of Thomson and troian slip velocity, thermo-convection parameter, and exponential power law index alongside the second-grade fluid factor and suction parameter over the flow and thermal trajectory outline. It is noteworthy that the augmented variation in Thomson and Troian slip velocity and suction parameters diminished the flow pattern, but the opposite trend is noted with the escalating parameters such as second-grade fluid factor and critical shear rate. Moreover, the thermal diffusion profile appears in an elevated pattern with increased Thomson and Troian slip velocity, exponential heat source, and power law index. Beyond these, the heat transfer rate in the vicinity of the wall promptly rises with the augmentation in the Second-grade fluid parameter, critical Shear rate, thermos convection parameter, suction parameter, and power law index. Researchers can build on these findings to explore new material combinations and refine theoretical fluid dynamics and thermal management models.

Cite this article as: Das TK, Saud M, Hajong N, Kalita B. Simulation of engine oil driven second grade ternary hybrid nanofluid flow subject to thomson and troian slip velocity addressing the thermo-convection effect. Sigma J Eng Nat Sci 2025;43(6):2234–2247.

***Corresponding author.**
*E-mail address: tusarkantidas1995@gmail.com, dastusar95@dudhnoicollege.ac.in

This paper was recommended for publication in revised form by Editor-in-Chief Ahmet Selim Dalkilic

Published by Yıldız Technical University Press, İstanbul, Turkey
© Author. This is an open access article under the CC BY-NC license (http://creativecommons.org/licenses/by-nc/4.0/).

INTRODUCTION

Hybrid Nanofluid and its Application

Hybrid nanofluids stand as innovative pioneers in fluid dynamics as they are engineered by integrating various nanoparticulate species into the foundational composition of fluids. Additionally, after numerous studies conducted to determine the performance of these alternative fluids, they display enhanced thermal conductivity and heat preservation capabilities within various industrial sectors. The performance differences and improvements emanate from the interaction of the different types of nanoparticles, leading to a boosted thermal conductivity and optimal performance in heat transfer. The stability of these kinds of fluids can be acquired by escalating the individual dispersion of nanoparticulate, fending off the particle agglomeration. Furthermore, the better aspect ratio and the synergistic impacts of nanocomposite contribute to their comprehensive performance. Also, the boosted heat conductivity of nano-fluidics conveyed tangible convenience such as prompt energy control efficacy, brushing up the performance and structure, and optimizing expenses and costs. This makes them advantageous for supplication where efficient thermal dissipation and heat management are censorious, such as refrigeration structures for microchip technology, locomotive appliances, and heat exchangers. Ongoing research and development in this area aim to optimize Hybrid nanofluids› properties further to address specific needs in various industries, including energy production, electronics, and manufacturing.

Literature Review

Roy and Pop [1] inspected a second-grade hybrid nanofluid›s flow and heat conduction feature over a stretching sheet. Second-grade fluids demonstrate non-Newtonian behavior, distinguished by a nonlinear alliance between stress and strain rate. Hybrid nanofluids are a blending of unadventurous base fluids and nanoparticles, known for their improved thermal conductivity alongside heat conduction properties. By inquiring about advanced scientific mathematical flow modeling to assess the dynamics and the innovative mechanisms of heat transmission in processes that involve advanced engineering industrial utilization, such as cooling mechanisms and heat management over electronic devices, Nadeem et al. [2] conducted a computational breakdown of a second-grade fuzzy hybrid nanofluid flow across a stretching/shrinking surface.This inquiry has recourse to numerical simulation to characterize flow and thermal allocation, laying out visions for augmenting the transfer of thermal energy processes in implementation, for instance, solar collectors› thermal power storage systems. Jawad et al. [3] probed into the features of radiative second-grade hybrid nanofluid flow subjected to Lorentz force. By exploring the reciprocation between radiation, nanoscale particulates, and non-Newtonian flow features, the investigation grants consideration to phenomena pertinent to magnetic fluid actuators and drug-targeting structures. Roy and Ghosh [4] explored magneto-dynamic (MHD) free convection about second-grade hybrid Nanofluid across an adjustable thermos-flux surface. The concurrent study inquires how discrepancy in thermo-flux significantly exerts an impact on the heat transfer mechanism that involves convection, offering intuitions into designing coherent cooling devices, geothermal power extraction, and elevating thermal comfort in assembling and molding environments. Sakthi et al. [5] scrutinized the entropy generation of second-grade hybrid Nanofluid around a diverging passage, emphasizing the hyperthermia therapeutic facet that involves hauling up the temperature of intended tissues to persuade therapeutic effects, such as cancer treatment. Improvement of heat transfer efficiency in various engineering and biomedical applications. Zulqarnai et al. [6] examined the effect of entropy generation on exponentially permeable stretching/shrinking surfaces in second-order fuzzy hybrid nanofluids. Understanding and minimizing entropy generation is important to optimize the design and operation of thermal systems, energy conversion devices, and environmental management systems. Hosseinzadeh et al. [7] Investigated the second-order viscoelastic non-Newtonian nanofluid flow over a curved stretching surface in the appearance of MHD. Both viscous and elastic features which are present in viscoelastic fluid often found in biological fluids and polymer solutions. This reasearch explored the impact of magnetic flow behavior, providing perception into controlling fluid dynamics in abundant applications, such as medication administration, polymer manufacturing, and biomedical devices. Shah et al. [8] presented an alternative evaluation of the Cattaneo-Christov framework applied to magnetohydrodynamic second-grade nanofluid motion, incorporating with Soret and Dufour effects. The Cattaneo–Christov model extends Fourier›s law to account for finite thermal wave propagation velocities, while the Soret and Dufour effects expound mass and thermal diffusion in fluid flow, respectively. The study of heat and mass transport in magnetically influenced nanofluid systems, relevant to processes like energy conversion and material fabrication, necessitates an assessment of Soret and Dufour influences in MHD nanofluid motion. Abbas et al.[9] performed a numerical investigation of chemically reactive second-order nanofluid flow past an exponentially curved stretching surface. Chemical reactions within a fluid can significantly change its flow and heat transfer properties. The research provides intuition into the optimization of chemical processes such as nanoparticle synthesis, catalytic reactions, and biochemical engineering applications. Zaman et al. [10] computationally scrutinized an unsteady second-order bio-magnetic micropolar blood-based nanofluid flow with moving gyro taxis microorganisms. The research looked at the complex issues of biofluids, microbes, magnetic fields and nanocrystals. Understanding such phenomena is key in biomedical applications, such as biodegradation of compounds

and drug transport also in which regard to environment microbes in action within living systems. Gangadhar et al. [11] examined the effects of anomalous heat absorption and Arrhenius energy on the MHD flow of a generalized second order fluid over a nonlinear stretching surface, in the light of Cattaneo-Christov thermal absorption theory and thermal radiation. Arrhenius energy describes the temperature dependence of reaction rates in chemical kinetics, while anomalous thermal absorption delineates the uneven absorption of energy in a liquid. This research enhances comprehending of thermal transfer processes in intricate fluid flows relevant to environmental engineering, industrial processes and material synthesis. Farooq et al. [12] performed a computational study on convective thermal transfer in second-order MHD nanofluid flow across a stretching surface through a porous medium. In various engineering applications such as thermal exchangers, filtration and underground fluid flow, porous media are crucial. Understanding the interface between fields, nanofluids, and porous structures is important for optimizing thermal transfer and fluid flow in porous media-based systems. Rath and Nayak [13] investigated the higher-order MHD movement of a nanofluid over a deformable plate, considering the influences of activation energy along with thermophoresis and Brownian motion phenomena. A thin viscous effects in which a substance is held to a solid surface is what we term slip flow. Thermophoresis, Activation energy, and brownian motion play a vital role in particle transport and thermal transfer in nanofluidic flows in which we see also to include issues related to nanoparticle synthesis, nanofluidic heat exchangers, and microfluidic systems. Naveed Khan et al. [14] observed chemically reactive elements in the boundary layer flow of a second order nanofluid over an exponentially stretching surface. Stagnant point flows which are placed in a variety of engineering applications including heat transfer, combustion, and aerodynamics.In these flows comprehending chemical reactions is critical for optimising processes such as jet flow control in propulsion systems, combustion, and chemical vapor deposition.

Recent advancements in the study of second-grade hybrid nanofluids and fluid dynamics have been highlighted through numerous investigations focusing on the intricate behavior of diverse nanofluids under different conditions. Kezzar et al. [15] explored the impact of slip velocity and temperature jump on entropy generation in second-grade hybrid nanofluids within Jeffery-Hamel flow, shedding light on innovative approaches to heat management and fluid efficiency in complex flows. Reza-E-Rabbi et al. [16] performed a computational investigation to examine how radiative heat transfer influences nonlinear second-grade nanofluids in the presence of Arrhenius activation energy and sinusoidal magnetic forces, thereby advancing the understanding of complex nanofluid behaviors.Additionally, Haq and Ali [17] examined fractional hybrid nanofluids subjected to transverse magnetic fields, highlighting key aspects of Newtonian thermal behavior and the role of magnetic effects in governing heat transport. Finally,The MHD flow of second-grade fluids including shedding light on the combined effects of magnetic fields, thermal convection, nanoparticles with gyrotactic microorganisms across a heated convective sheet, and biological microbes on fluid behavior was investigated by Ahmed et al. [18]. These studies enhance our understanding of magnetic influences and thermal phenomena in complex fluid systems and nanofluid dynamics.

According to recent research on nanofluids emphasize their especial flow and thermal properties, importantly impacting thermal transfer processes across abundant applications. AKAJE et al. [19] investigate the heat and mass transfer dynamics in Casson nanofluids influenced by variable inclined magnetic fields, emphasizing how such conditions can optimize thermal performance. However, Li et al. [20] analyzed the behavior of ternary nanofluids over a stretching sheet, taking into account the velocity slip effects. El Hattab et al. [21] examined magnetohydrodynamic (MHD) natural convection within a square cavity utilizing carbon nanotube–water nanofluids, demonstrating how fin con y urations contribute to enhanced thermal dissipation. The investigation by Nath et al. [22] focused on MHD Casson hybrid nanofluid flow across porous cylindrical boundaries, revealing the complex interplay between structural hierarchy and magnetic influences [23-26]. In addition to the aforementioned research, some other explorer [27-29] put forward there handy contribution in the context of nanofluid.

The Novel Features and Applications of the Prescribed Model

This scientific survey emphasize that no prior research has presented a pioneering model that intricately combines an exponentially varying thermal source, the effects of thermo-convection and buoyancy on fluid flow across a stretching surface. A ternary hybrid nanofluid composed of silver (Ag), copper (Cu), and graphene which is known for exceptional heat properties are the main character of this model. This model examine synergetic effects of these three different nanoparticles by interacting them and supplying how they combine to impact thermal transfer and fluid dynamics. A large enhancement in displaying realistic fluid behavior is introduced by consideration of Thomson and Trion slip conditions at the boundary surface especially at the microscale where slip phenomena have a significant affect on performance. As per the author's concern, no prior investigation has been carried out combining this effect over the considered geometry. To computationally solve the designed problem, the bvp4c approach will be employed.

Furthermore, the present model has several applications that primely include enhanced thermal management. In high-tech applications such as thermal exchangers, electronic devices and high-performance cooling systems the model's detailed analysis can be directly applied to enhance heat management systems. Superior thermal dissipation

and energy efficiency can be obtained by improving the hybrid nanofluid composition. However, The perception from this model can help in the enhancement of manufacturing processes like polymer processing and thin-film deposition which involves in stretching surface. Stretching surfaces and hibrid nanofluids cobined to improve the process efficiency and product quality.

Infact, buoyancy effects models and the thermo-convection are essential for designing cooling systems in automotive and aerospace applications. Reliability and efficiency of aerospace and engines components are increased depending on enhanced cooling performance. The model›s exploration of exponentially varying heat sources provides valuable guidance for optimizing heat transfer and energy conversion processes for renewable energy technologies like solar thermal collectors.

The primary purpose of this investigation are:

- What insightful examination of thermal diffusion across stretching surface can be procured from the numerical simulation of second-grade ternary hybrid nanofluid?
- To discuss the consequences of suction velocity on the Nusselt number.
- How promptly does the thermo-convection factor affect the flow trajectory and thermal transmission?
- How does the Thomson and Troian slip velocity create an impact on the flow behavior and the characteristics of thermal transmission?
- Moreover, in what manner does the exponential heat source influence the simultaneous flow configuration within the framework of thermal transport?

In essence, this study analyzes the behavior of a ternary second-grade hybrid nanofluid in relation to heat dispersion over a stretching interface. Furthermore, the work examined the impact of suction velocity on the Nusselt number, examines the thermoconvection parameter's role in dictating both thermal distribution and flow dynamics, scrutinizes the influence of Thomson and Troian slip phenomena on thermal transport and momentum, and evaluates the modifications initiated by an exponential thermal source to the flow pattern and overall thermal transfer behavior.

MATHEMATICAL FORMULATION

The Crosser-Hamilton model (Abbas et al.[23]) based, A two-dimensional steady and incompressible second-grade ternary hybrid nanofluid flow is taken into account via a vertical stretching sheet. *Ag, Cu* and *Graphene* are the three nanocomposites used in the composition of ternary hybrid Nanofluid. The total volume fraction is kept below 15%. The high flexibility and resistance of graphene, the greater thermal conductivity of Cu, and the higher electric conductivity of Ag are the reasons behind the use of these nanoparticles in industrial and engineering applications that involve the heat transfer phenomena. The following are the underlying assumptions:

- The prescribed flow is assumed to be generated by the stretching surface.
- The velocity in the vicinity of the wall is prescribed as $u_w = bx$ as depicted in Figure 1.
- Furthermore, Thomson and Troian slip velocity is considered.
- An exponential heat source is considered, where n, indicates the power law index.
- The thermo-convection effect reflected by the term γ is also preferred in the concurrent model. Here, $\gamma = \frac{\partial T_\infty}{\partial y} + \frac{g}{c_p}$ is the vertical thermal convection parameter, which can

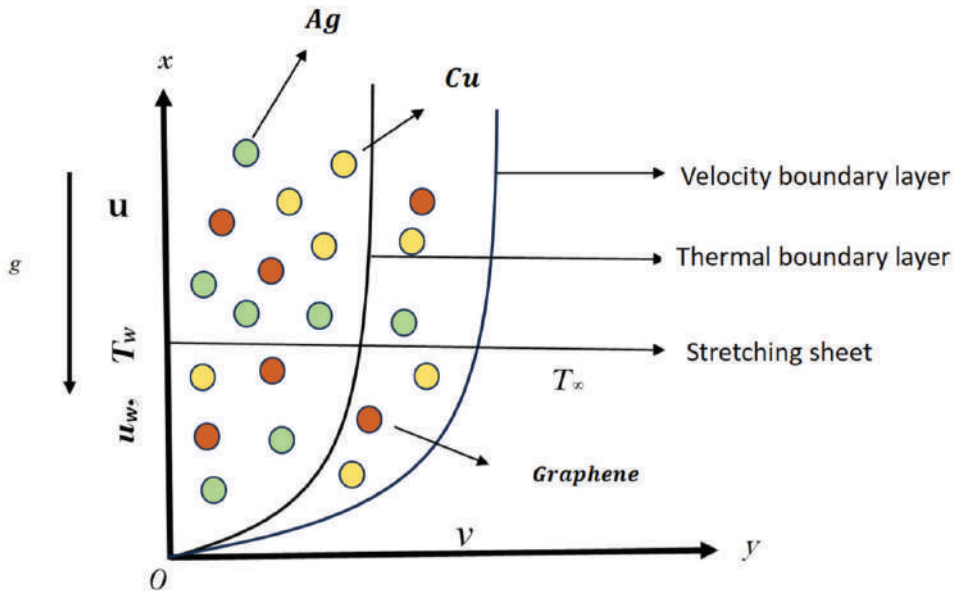


Figure 1. Physical flow diagram of the proposed model.

also be termed as a stratification parameter. Here, the term $\frac{g}{C_p}$, that indicates the rate of reversible work settled by the prescribed fluid is presumed to be negligible; thus, the role of the term $\frac{\partial T_\infty}{\partial y}$ is decisive.

- The Nanofluid chosen for the ongoing problem is composed of *Ag, Cu,* and graphene nanoparticles dispersed in ethylene glycol.
- The temperature at the vicinity of the surface, T_w is assumed to be greater than the ambient temperature, T_∞.

By addressing the aforementioned assumption, the mathematical model turns out to be the following form of governing equations. (Shah et al. [8], Li et. al. [20], Deka and Paul [24])

$$\frac{\partial u}{\partial x} + \frac{\partial v}{\partial y} = 0 \tag{1}$$

$$u\frac{\partial u}{\partial x} + v\frac{\partial u}{\partial y} = \frac{\mu_{THnf}}{\rho_{THnf}}\frac{\delta^2 u}{\delta y^2} + \frac{2\alpha_1}{\rho THnf}\frac{\delta u}{\delta y}\frac{\partial^2 u}{\partial x \partial y} - g\beta_T\,(T - T_\infty) \tag{2}$$

$$u\frac{\partial T}{\partial x} + v\frac{\partial T}{\partial y} = \frac{K_{THnf}}{(\rho C_p)_{THnf}}\frac{\partial^2 T}{\partial y^2} + \frac{Q}{(\rho C_p)_{THnf}}(T - T_\infty).e^{-ny}\sqrt{\frac{b}{v_f}} - \gamma u \tag{3}$$

The Boundary Constraints are (Li et. al.[20])

$$u = u_w + u_1\frac{\partial u}{\partial y}\frac{1}{\sqrt{1-u_2\frac{\partial u}{\partial y}}},\ v = v_w,\ T = T_w \ \ at\ y = 0 \tag{4}$$

$$u \to 0, T \to T_\infty\ at\ y \to \infty \tag{5}$$

The similarity transformation variables that are employed in the concurrent problem are:

$$\eta = \sqrt{\frac{b}{v_f}}y,\ u = bxf'(\eta),\ v = \sqrt{v_f b}\,f(\eta), \theta(\eta) = \frac{T - T_\infty}{T_w - T_\infty} \tag{6}$$

By implementing the aforementioned similarity transformation variable, equations (2)-(3), subject to the boundary constraints (4) and (5), can be revamped into the following array coupled equations.

$$\begin{aligned} &-f'(\eta)^2 + f(\eta).f''(\eta) + \frac{\mu_{Thnf}}{\mu_f}.\frac{\rho_f}{\rho_{Thnf}}.f''(\eta) \\ &+ \frac{\rho_f}{\rho_{Thnf}}.2K.f''(\eta)^2 + \frac{(\beta_T)_{Thnf}}{(\beta_T)_f}.G_r.\theta(\eta) = 0 \end{aligned} \tag{7}$$

$$\begin{aligned} &f(\eta).\theta'(\eta) + \frac{K_{Thnf}}{K_f}.\frac{(\rho C_p)_f}{\rho(C_p)_{Thnf}}.\frac{1}{P_r}.\theta''(\eta) \\ &+ \frac{(\rho C_p)_f}{\rho(C_p)_{Thnf}}.Se^{-n\eta}.\theta(\eta) - \gamma_3 f'(\eta) = 0 \end{aligned} \tag{8}$$

The revamped boundary constraints are (Li et. al.[20])

$$f(0) = S_*,\ f'(0) = 1 + \gamma_1\frac{f''(0)}{\sqrt{1-\gamma_2 f''(0)}},\ \theta(0) = 1 \tag{9}$$

$$f'(\infty) \to 0, \quad \theta(\infty) \to 0 \tag{10}$$

Here,

$$K = \frac{\alpha_1 b}{\rho_f v_f},\ G_r = \frac{\beta_T(T_w - T_\infty)}{b^2 x},\ S = \frac{Q}{b(\rho C_p)_f},$$

$$\gamma_3 = \frac{\gamma x}{T_w - T_\infty},\ \gamma_1 = u_1 b\sqrt{\frac{b}{v_f}},\ \gamma_2 = u_2^* ab\sqrt{\frac{b}{v_f}},\ u_2(x) = \frac{a}{x}u_2^*$$

The authors are also curious to assess the consequences of the dimensionless physical parameters on the rate of stress proximate to the surface (Skin friction coefficient) and the rate of thermal transmission (Nusselt Number) near the surface.

$$Skin\ Friction\ Coefficient = Cf_x\sqrt{Re_x} = \frac{\mu_{Thnf}}{\mu_f}f''(0)$$

$$Nusselt\ Number = \frac{Nu_x}{\sqrt{Re_x}} = -\frac{K_{Thnf}}{K_f}\theta'(0)$$

Elucidation of Physical Variables Pertinent to Prevailing Ternary Hybrid Nanofluid (Abbas et. al.[23])

Density

$$\rho_{Nf} = (1 - \phi_{S1})\rho_f + \phi_{S1}\rho_{S1}$$
$$\rho_{Hnf} = (1 - \phi_{S2})\rho_{Nf} + \phi_{S2}\rho_{S2}$$
$$\rho_{Thnf} = (1 - \phi_{S3})\rho_{Hnf} + \phi_{S3}\rho_{S3}$$

Dynamic viscosity

$$\mu_{Thnf} = \mu_f(1 - \phi_{S1})^{-\frac{5}{2}}(1 - \phi_{s2})^{-\frac{5}{2}}(1 - \phi_{s3})^{-\frac{5}{2}}$$

Thermal conductivity

$$k_{Nf} = k_f\left\{\frac{k_{S1} + (m-1)k_f - (m-1)\phi_{S1}(k_f - k_{S1})}{k_{S1} + (m-1)k_f + \phi_{S1}(k_f - k_{S1})}\right\}$$
$$k_{Hnf} = k_{Nf}\left\{\frac{k_{S2} + (m-1)k_{Nf} - (m-1)\phi_{S2}(k_{Nf} - k_{S2})}{k_{S2} + (m-1)k_{Nf} + \phi_{S2}(k_{Nf} - k_{S2})}\right\}$$
$$k_{Thnf} = k_{Hnf}\left\{\frac{k_{S3} + (m-1)k_{Hnf} - (m-1)\phi_{S3}(k_{Hnf} - k_{S3})}{k_{S3} + (m-1)k_{Hnf} + \phi_{S3}(k_{Hnf} - k_{S3})}\right\}$$

Specific heat capacity

$$(\rho C_p)_{Nf} = (1 - \phi_{S1})(\rho C_p)_f + \phi_{S1}(\rho C_p)_{S1}$$
$$(\rho C_p)_{Hnf} = (1 - \phi_{S2})(\rho C_p)_{Nf} + \phi_{S2}(\rho C_p)_{S2}$$
$$(\rho C_p)_{Thnf} = (1 - \phi_{S3})(\rho C_p)_{Hnf} + \phi_{S3}(\rho C_p)_{S3}$$

Table 1. Thermo-physical characteristics of engine oil and the three different nanocomposites

Physical attribution	Engine oil	Ag	Graphene	Cu
$\rho\ (kgm^{-3})$	863	10500	2250	8933
$K\ (Wm^{-1}K^{-1})$	0.1404	429	2500	401
$\Sigma\ (sm^{-1})$	2.09×10^{-12}	6.3×10^7	1×10^7	59.6×10^6
$C_p\ (Jkg^{-1}K^{-1})$	2048	235	2100	385

MATERIALS AND METHODS

Initially, the non-dimensional higher-order ODEs reformulated into an equivalent first-order boundary value problem, incorporating the associated boundary conditions. Numerical solutions for the dimensionless ordinary differential equations are calculated using the widely used MATLAB bvp4c solver in conjunction with the shooting technique. The bvp4c solver exhibits exceptional proficiency in managing boundary value problems, delivering precise outcomes even for complex or unstable systems due to its refined mesh adaptation process. This function enhances computational efficiency by minimizing processing effort and maximizing the overall performance of numerical computation. In order to utilize the bvp4c solver effectively, an initial guess conforming to its spatial constraints is required. The bvp4c solver, with a convergence threshold set at 10^{-4}, proves to be the most suitable method for estimating the numerical solutions of such intricate non-dimensional ODEs, outperforming other techniques in terms of accuracy. The validation of the employed methodology is demonstrated in Table 2.

RESULT AND DISCUSSION

The furnished second grade ternary hybrid nanofluid flow under investigation is generated by a transverse stretching surface subject to Thomson and Troian slip velocity. Furthermore, the thermo-convection effect alongside the exponential heat source is incorporated into the thermal boundary layer equation to enhance the thermal gradient over the flow geometry. The entire set of coupled equations that represent the physical flow geometry is based on the Cross-Hamilton nanofluid model [23]. As the addition of silver, copper and graphene nanocomposite to the second-grade fluid escalates the thermo-physical characteristic of second grade fluid, that is why the whole study is analyzed with second grade ternary hybrid nanofluid.Table 1 reflects the thermo-physical characteristics of engine oil and the three different nanocomposites, and Table 2 delineates the infallibility of the current investigation, which is an analogy to the finding of Devi and Devi [25] and Wang [26]. The graphical representation of the velocity and thermal distribution curve for the variation in different non-dimensional factors are sketched keeping fixed, $S = 0.1$, $K = 0.10$, $\gamma_1 = 0.1$, $\gamma_2 = 0.1$, $\gamma_3 = 0.1$, $S_* = 0.1$, $n = 2$.

Table 2. Resemblance of -θ'(0) with the results procured by Devi and Devi [25] and Wang [26] [created by author]

Pr	Devi and Devi[25]	Wang[26]	Present study with $S, \gamma_3 = 0$
2.0	0.91135	0.9114	0.9114
7.0	1.89540	1.8954	1.8954
20.0	3.35390	3.3539	3.3539

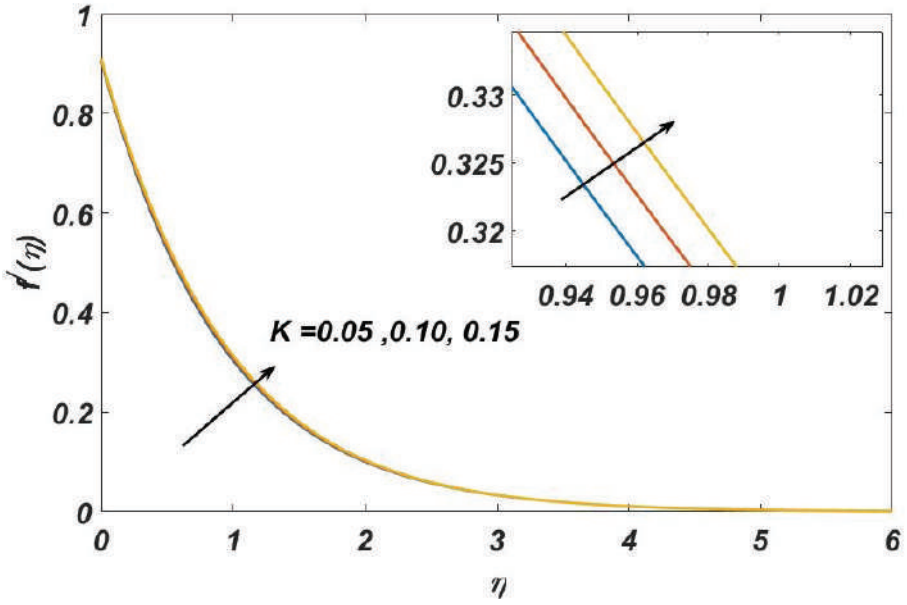


Figure 2. Impact of K on velocity distribution profile.

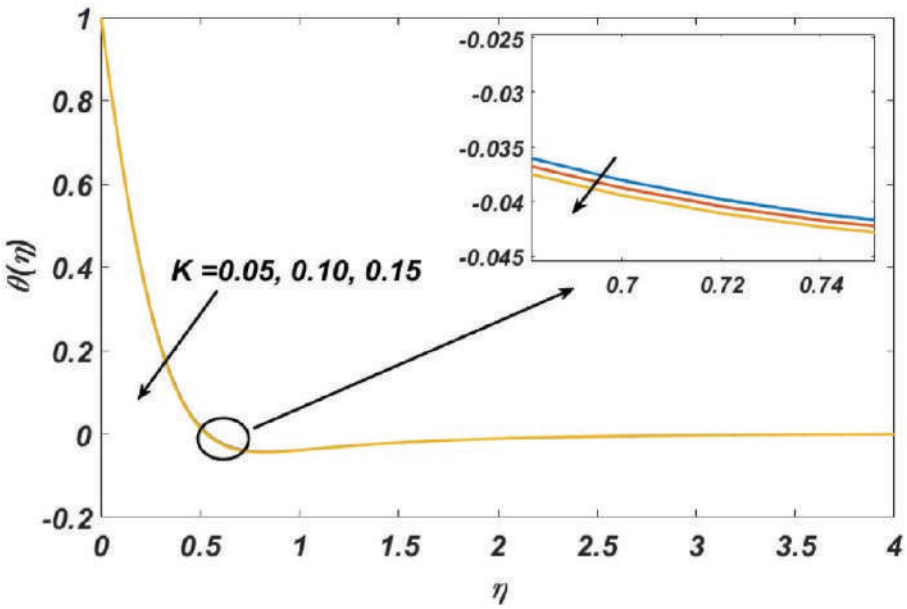


Figure 3. Impact of K on Thermal distribution profile.

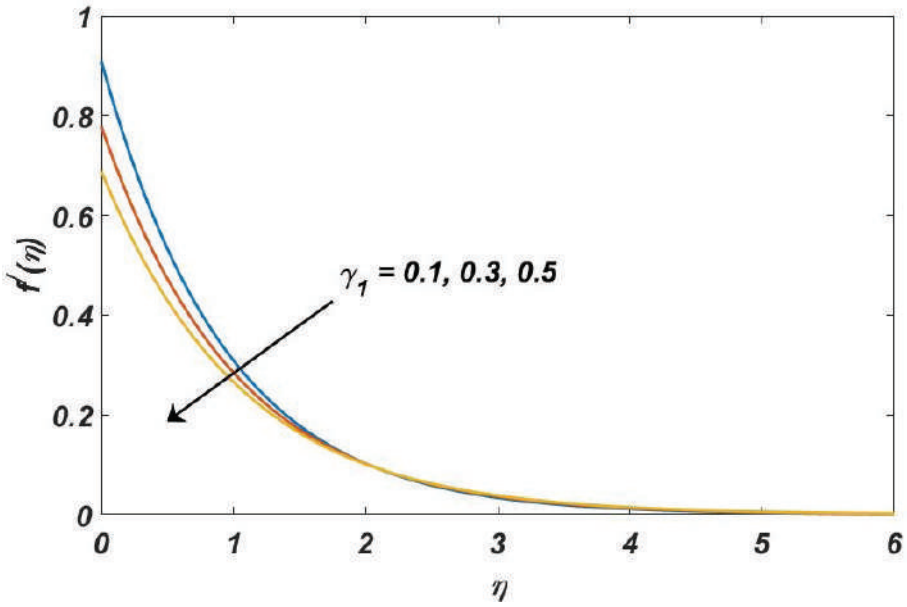


Figure 4. Impact of γ_1 on Velocity distribution profile.

In Figure 2 and Figure 3, the impact of the second-grade fluid factor on velocity and thermal distribution profile are portrayed. It has been observed that with the elevation in the numeric value of the second-grade fluid parameter, the flow profile looked to be an upsurge, while the thermal distribution profile exhibits a revert trajectory. Shah et al.[8] have obtained similar results over stretchable riga sheets for the velocity profile, opposite to the result proclaimed by Hosseinzadeh et. al. [7]. However, the impacts of the second-grade fluid parameter over the thermal profile have not been discussed by Shah et al. [8] and Hosseinzadeh et. al. [7]. Furthermore, as shown in Table 3, the reduction in the rate of tangential stress and the rate of thermal transmission at the vicinity of the stretch surface is perceived with the incremented values of the second-grade fluid parameter, K. The augmentation in K leads to the increment in elasticity, which in turn upsurges the fluid flow at the vicinity of the surface, as the fluid can stretch and flow more easily. Conversely, the increased elasticity efficiently limits the thermal transmission or energy exchange.

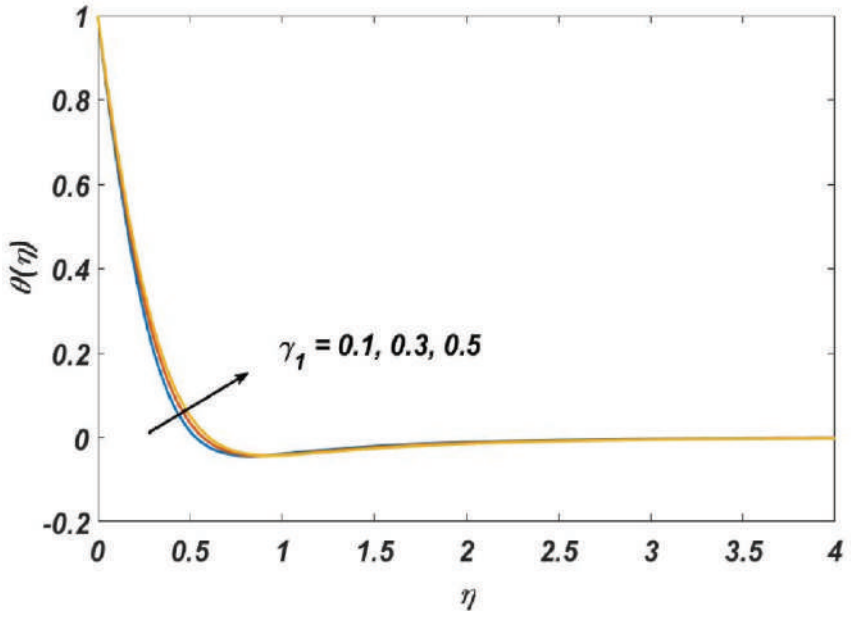


Figure 5. Impact of γ_1 on Thermal distribution profile.

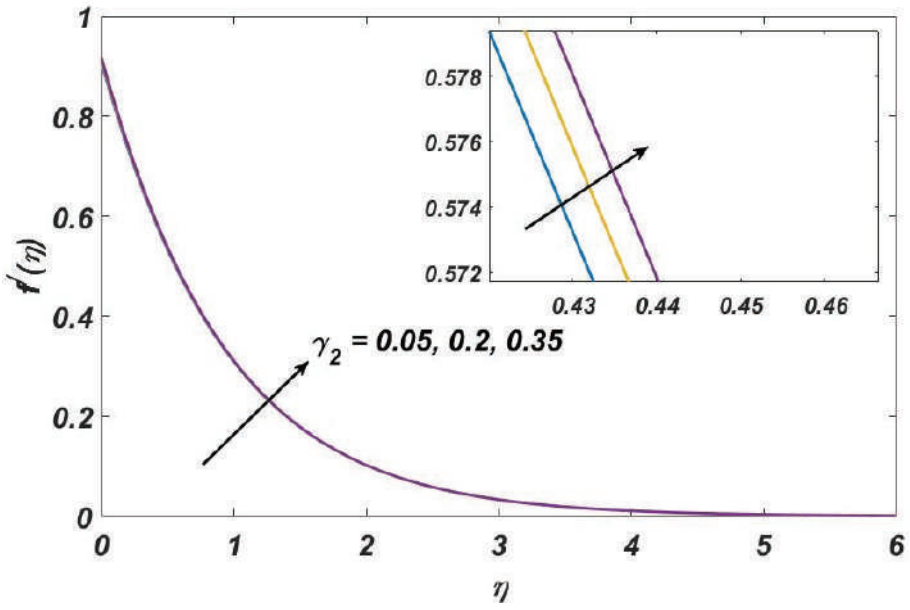


Figure 6. Impact of γ_2 on Velocity distribution profile.

The designated model is featured in a way where the boundary undergoes the consequences of Thomson slip velocity, which is depicted in Figure 4 and Figure 5. As shown in Figure 4, the velocity profile of second grade ternary hybrid Nanofluid promptly dropped with the numeric escalation of Thomson slip velocity, γ_1. Whereas the thermal distribution curve significantly arises for the numeric elevation of the slip factor γ_1 as shown in Figure 5. These results occur due to the fact that greater slip at the vicinity of the boundary reduces frictional drag. The reduced interaction with the boundary allows less momentum transfer, leading to a drop in velocity. Conversely, the thermal distribution increases because the reduced frictional drag indicates less energy is lost to resistance, allowing more energy to be retained in the fluid. The opposite pattern is noted in both velocity and thermal distribution profiles for rising factor γ_2 as shown in Figure 6 and Figure 7. When critical shear rate, γ_2 is uplifted, then the velocity curve appears to manifest an upward trend, whereas the thermal profile falls in a downward pattern. Over Newtonian fluid, similar results

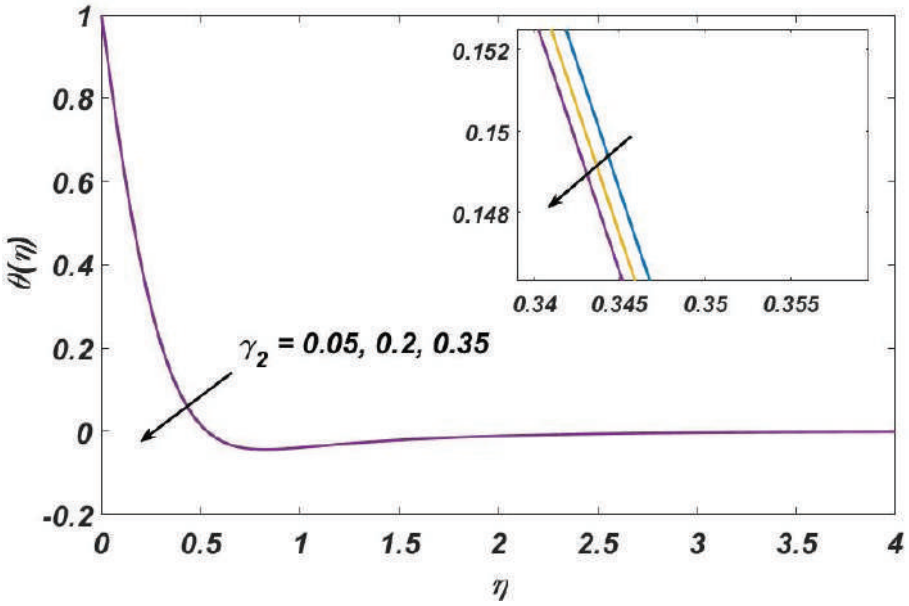


Figure 7. Impact of γ_2 on Thermal distribution profile.

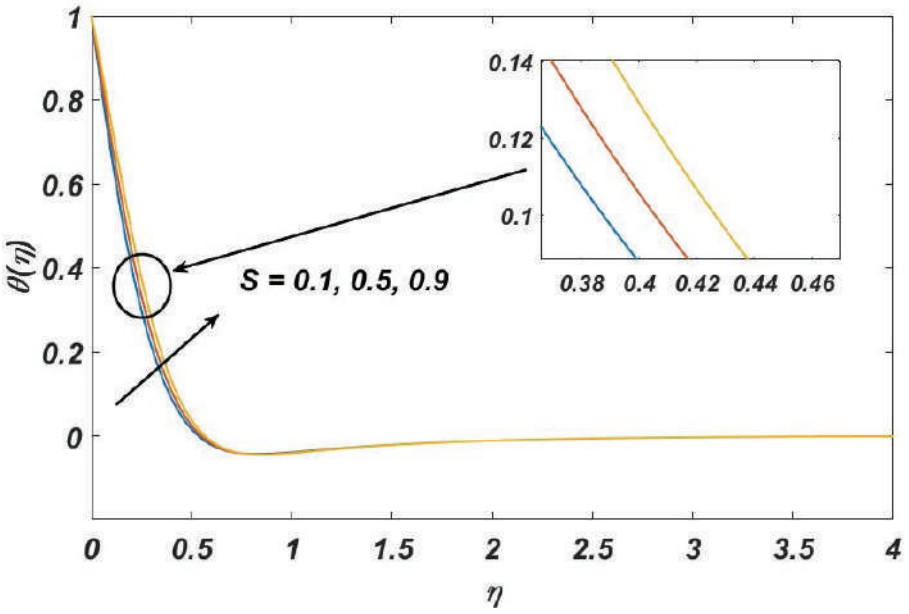


Figure 8. Impact of S on thermal distribution profile.

are obtained by Li et. al.[20] for the slip and critical shear factor.

Figure 8 and Figure 9 demonstrate the influences of exponential heat source, S and power law index, n over the thermal profile. The heat distribution profile looked to be upraised for both exponential heat source, S and power law index n, as shown in Figure 8 and Figure 9. It is because, with a greater thermal source factor and power law index (which intensify the heat source significantly), the nano-composites sop up that amount of thermal energy, which allows an extensive amount of diffusion of heat throughout the system. For non-exponential i.e. linear heat source, a similar pattern in the thermal profile is proclaimed by Li et al. [20] considering Newtonian hybrid nanofluid.

In Figure 10, 11, 12, the impacts of the thermo-convection parameter, γ_3 and suction velocity, S_* are portrayed respectively. Figure 10 illustrates a significant increase in the heat profile as the values of γ_3, indicative of thermo-convection or stratification, are raised. This enhancement is linked to the increased thermal gradients

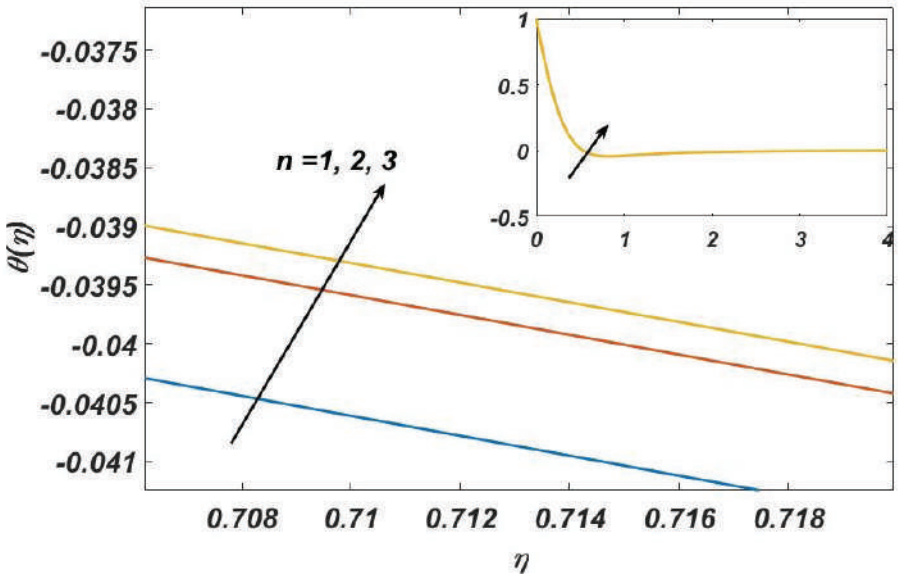


Figure 9. Impact of n on thermal distribution profile.

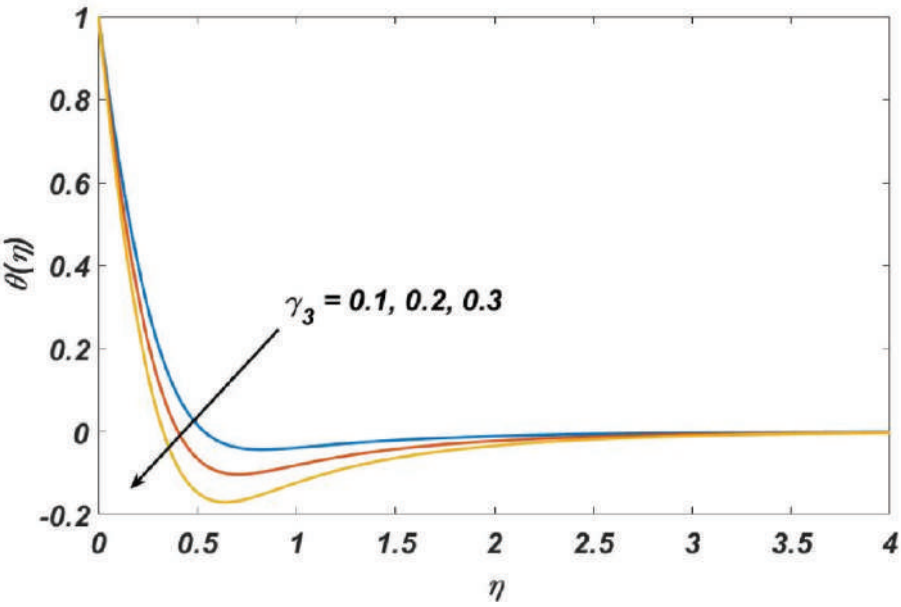


Figure 10. Impact of γ_3 on thermal distribution profile.

observed within the boundary layer of the second-grade ternary hybrid nanofluids. With a rise in the parameter value, the temperature difference between adjacent layers becomes more pronounced, promoting stronger and more effective interaction among the nanocomposite elements. Such intensified interaction enhances thermal convection, ensuring a more uniform spread of heat across the system. The increase in thermal diffusion arises from the intensified motion and interaction of the nanoparticles, which together enhance the overall efficiency of heat transmission. Consequently, the observed rise in temperature dispersion indicates higher thermal sensitivity and diffusion potential within the fluid, resulting from increased parameter magnitudes. Deka and Paul [24], found this result for unsteady Newtonian fluid past an infinite moving vertical cylinder.

Again, as portrayed in Figure 11, it has been significantly noted that the velocity profile shows a downward trajectory with a lofted suction velocity. The reason behind the downward trajectory of the velocity profile is the lower pressure created by the alofted suction velocity. Also, the increased suction velocity factor leads to a drop in the thermal distribution profile at the vicinity of the surface, and

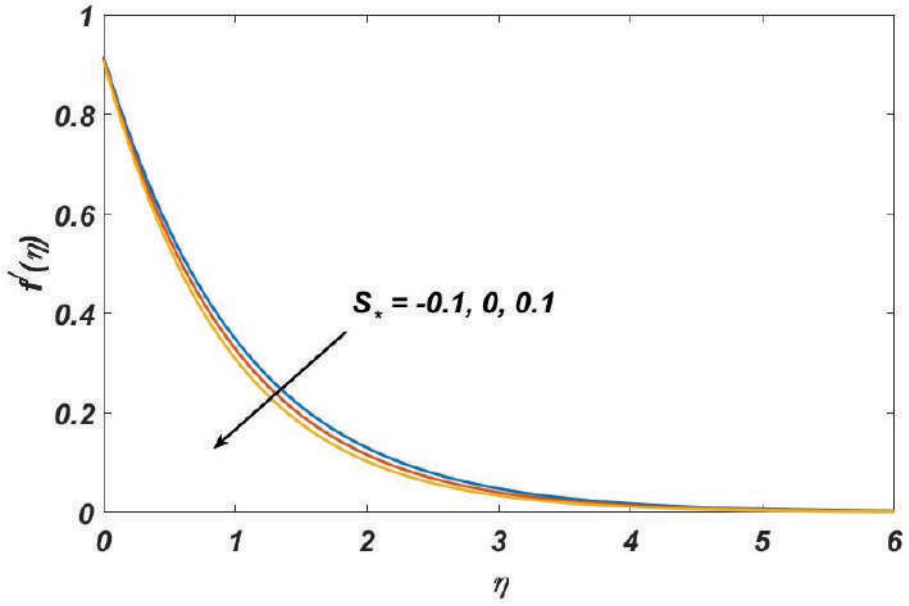


Figure 11. Impact of S_* on velocity distribution profile.

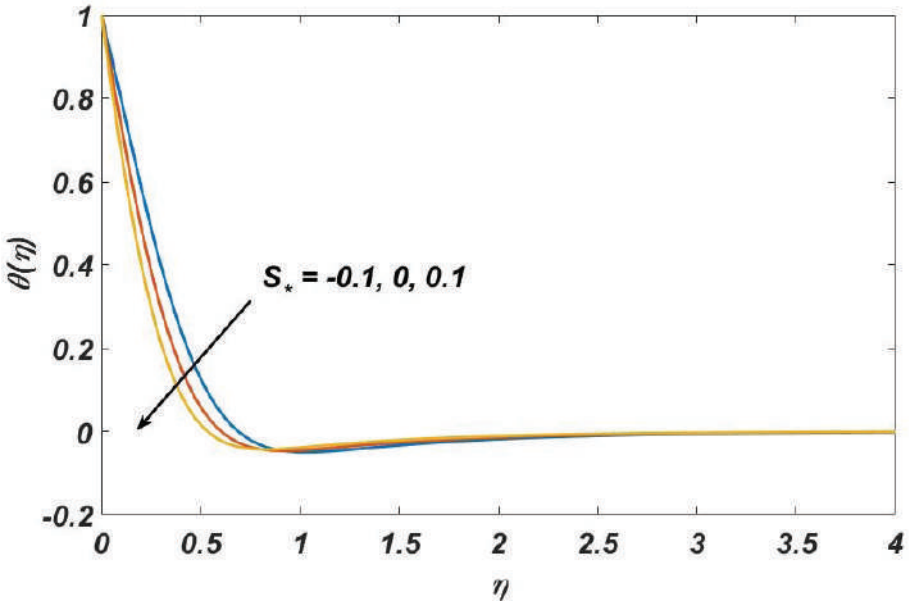


Figure 12. Impact of S_* on thermal distribution profile.

it is more significant due to thermal stratification or thermos-convection impact, as shown in Figure 12.

The impact of γ_1, γ_2, γ_3, K, S, S_* over the skin friction coefficient and Nusselt number are demonstrated in Table 3. It has been observed that the augmented value of the second grade fluid factor appears to decline the rate of shear stress proximate to the vertical surface. As K rises from 0.05 to 0.15, the reduced percentage in the rate of tangential stress at the vicinity is about 4.08%. This decline mainly results from the rise in viscosity linked to greater K values, which suppresses the fluid's reaction to shear stresses. Conversely, the Nusselt number shows an increase of about 0.52% as K changes from 0.05 to 0.15. This rise in the Nusselt number signifies improved convective heat exchange, resulting from changes in flow dynamics that facilitate a more uniform spread of thermal energy within the boundary layer. A similar pattern is also noted in the skin friction coefficient for the Thomson velocity slip parameter, γ_1, but the opposite is the pattern for critical shear rate, γ_2. Simultaneously, the Nusselt number shows a decline pattern in numeric with

Table 3. Demonstration of physical value of shear stress rate at vicinity, skin friction coefficient and thermo-efficiency rate at vicinity (Nusselt number) with varying dimensional parameter

S	K	γ_1	γ_2	γ_3	S^*	n	Skin friction coefficient	Nusselt number
0.1	0.10	0.1	0.1	0.1	0.1	2	-1.2048	4.6992
0.5							-1.2047	3.9555
0.9							-1.2047	3.1172
0.1	0.05	0.1	0.1	0.1	0.1	2	-1.2293	4.6867
	0.10						-1.2048	4.6992
	0.15						-1.1811	4.7115
0.1	0.10	0.1	0.1	0.1	0.1	2	-1.2048	4.6992
		0.3					-0.9653	4.4092
		0.5					-0.8094	4.1945
0.1	0.10	0.1	0.05	0.1	0.1	2	-0.9560	4.6954
			0.2				-1.2111	4.7064
			0.35				-1.2194	4.7158
0.1	0.10	0.1	0.1	0.1	0.1	2	-1.2048	4.6992
				0.2			-1.2048	5.4047
				0.3			-1.2048	6.1102
0.1	0.10	0.1	0.1	0.1	-0.1	2	-1.0922	2.5949
					0		-1.1471	3.5835
					0.1		-1.2048	4.6992
0.1	0.10	0.1	0.1	0.1	0.1	1	-1.2048	4.6839
						2	-1.2048	4.6992
						3	-1.2048	4.7146

rising values of S, γ_1. Moreover, it is noteworthy to mention that the heat transmission rate at the vicinity exhibits a prompt elevation in terms of values with the amplified second grade fluid factor (K), critical shear rate (γ_2), Thermo-convection parameter (γ_3), Suction parameter (S_*), Power law index (n).

CONCLUSION

The proposed model deals with the investigation of second grade ternary hybrid nanofluid flow subject to Thomson and Troian slip velocity featured by thermo-convection effect via stretching sheet. Graphene nanoparticles are used along with Ag and Cu due to their flexibility, high resistance, and high thermal conductivity. The following noteworthy discoveries have been made from the aforementioned investigation.

- The Velocity distribution profile raises for the higher value of the second-grade fluid parameter and critical shear rate. Higher second-grade fluid parameter typically corresponds to greater non-Newtonian effects, which can enhance velocity gradients in the boundary layer. Similarly, a greater critical shear rate implies that the fluid can sustain larger shear stresses without significant changes in flow characteristics.
- The velocity distribution profile also diminishes for higher values of Thomson and troian slip velocity and Suction parameter. Increased slip velocity at the boundary reduces the no-slip condition, allowing the fluid to slip more freely and thereby reducing the velocity gradients near the boundary. Also, increased suction draws fluid away from the surface, which diminishes the velocity distribution near the surface.
- The skin friction coefficient is boosted with a critical shear rate and suction parameter, while the skin friction coefficient dropped for higher values of non-dimensional heat source parameter, second-grade fluid parameter and Thomson and Troian slip velocity.
- The thermal distribution profile upsurges for bigger Thomson and Troian slip velocity, non-dimensional heat source parameter and power law index but reduces with a rise of second grade fluid parameter, critical shear rate, thermo-convection parameter and suction parameter. A higher Thomson and Troin slip velocity enhances thermal convection by reducing thermal boundary layers. Increased heat source represents a greater heat generation rate within the system, thus elevating the temperature distribution. An increased second-grade fluid coefficient suggests more dominant non-Newtonian characteristics, which may reduce the rate of heat transfer. Increased

critical shear rate signifies that the fluid's response to shear stresses is more constrained, affecting the thermal profile. A stronger thermo-convective effects that may alter heat transfer dynamics, and the increased suction suction velocity extracts heat from the surface, leading to lower thermal profiles.

- The Nusselt number augmented with elevated values of second grade fluid parameter, critical shear rate, thermo-convection parameter, suction parameter and power law index, conversely diminished with increasing values of non-dimensional heat source parameter and Thomson and Troian slip velocity.

The proposed framework holds broad potential in the field of advanced heat management, especially in improving cooling performance for electronic components, thermal exchangers, and other high-efficiency systems. Additionally, it delivers meaningful understanding for refining production techniques across sectors such as polymer fabrication and thin-film coating. Additionally, the model›s analysis of thermo-convection, buoyancy effects, and exponentially varying heat sources is crucial for improving cooling performance in aerospace and automotive systems and optimizing renewable energy technologies such as solar thermal collectors.

We can further extend this investigation to diverse geometrical configurations such as conical disks, rotating disks or spheres, concentric cylindrical channels, etc., considering the same or other constraints and factors, as it can broaden the applicability of the findings. This research provides a solid foundation for continued exploration of nanofluid dynamics and thermal transport processes. Researchers can build on the aforementioned findings to explore new material combinations and refine theoretical models in fluid dynamics and thermal management.

NOMENCLATURE

u_w	The surface velocity at vicinity (m/s)
u, v	Velocity along horizontal and vertical direction respectively (m/s)
g	Gravitational acceleration (m/s^2)
Q,S	Dimensionless ($JK^{-1}\ m^{-3}\ s^{-1}$) and non-dimensionless heat source factor
n	Power Law Index
v_w	Suction velocity (m/s)
K	Second grade fluid parameter
b	Rate of stretching (s^{-1})
T_w	Temperature at the vicinity of the wall (K)
T_∞	Temperature at the ambient (K)
$S_\star$	Suction parameter
Pr	Prandtl number
Gr	Grashof number
$(C_p)_f$, $(C_p)_{Nf}$	Specific heat capacity of base fluid (Engine Oil), Nanofluid ($J\ Kg^{-1}\ K^{-1}$)
$(C_p)_{Hnf}$, $(C_p)_{Thnf}$	Specific heat capacity of hybrid Nanofluid, Ternary hybrid Nanofluid ($J\ Kg^{-1}\ K^{-1}$)

Greek symbols

α_1	Second grade material constant
β_T	Thermal expansion coefficient (K^{-1})
γ_1	Thomson and Troian slip velocity
γ_2	Critical Shear rate
γ_3	Dimensionless Thermo-convection parameter
ρ_f	The density of the base fluid (Engine Oil) (kgm^{-3})
ρ_{Nf}	The density of the Nanofluid (kgm^{-3})
ρ_{Hnf}	Density of the Hybrid Nanofluid (kgm^{-3})
ρ_{Thnf}	The density of the Ternary Hybrid Nanofluid (kgm^{-3})

Subscripts

S1, S2, S3	Ag, Cu and Graphene nanoparticles
f	Base fluid (Engine Oil)
Nf	Nanofluid
Hnf	Hybrid Nanofluid
Thnf	Ternary Hybrid Nanofluid

AUTHORSHIP CONTRIBUTIONS

Authors equally contributed to this work.

DATA AVAILABILITY STATEMENT

The authors confirm that the data that supports the findings of this study are available within the article.

CONFLICTS OF INTEREST

The authors declare no conflict of interest.

FUNDING

Not Applicable

REFERENCES

[1] Roy NC, Pop I. Flow and heat transfer of a second-grade hybrid nanofluid over a permeable stretching/shrinking sheet. Eur Phys J Plus 2020;135:768. [CrossRef]

[2] Nadeem M, Siddique I, Awrejcewicz J, Bilal M. Numerical analysis of a second-grade fuzzy hybrid nanofluid flow and heat transfer over a permeable stretching/shrinking sheet. Sci Rep 2022;12:1631. [CrossRef]

[3] Jawad M, Saeed A, Tassaddiq A, Khan A, Gul T, Kumam P, Shah Z. Insight into the dynamics of second grade hybrid radiative nanofluid flow within the boundary layer subject to Lorentz force. Sci Rep 2021;11:4894. [CrossRef]

[4] Roy NC, Ghosh A. Magnetohydrodynamic natural convection of second-grade hybrid nanofluid on variable heat flux surface. AIP Adv 2022;12: 035243. [CrossRef]

[5] Sakthi I, Das R, Reddy PBA. Entropy generation on MHD flow of second-grade hybrid nanofluid flow over a converging/diverging channel: An application in hyperthermia therapeutic aspects. Eur Phys J Spec Top 2023:;233:1233–1249. [CrossRef]
[6] Zulqarnain RM, Nadeem M, Siddique I, Mansha A, Ghallab AS, Samar M. Impacts of entropy generation in second-grade fuzzy hybrid nanofluids on exponentially permeable stretching/shrinking surface. Sci Rep 2023;13:22132. [CrossRef]
[7] Hosseinzadeh K, Mardani MR, Paikar M, Hasibi A, Tavangar T, Nimafar M, Shafii MB. Investigation of second grade viscoelastic non-Newtonian nanofluid flow on the curve stretching surface in presence of MHD. Results Eng 2023;17:100838. [CrossRef]
[8] Shah F, Hayat T, Momani S. Non-similar analysis of the Cattaneo–Christov model in MHD second-grade nanofluid flow with Soret and Dufour effects. Alex Eng J 2023;70:25–35. [CrossRef]
[9] Abbas N, Ali M, Shatanawi W. Chemical reactive second-grade nanofluid flow past an exponential curved stretching surface: Numerically. Int J Mod Phys B 2023;38:2450026. [CrossRef]
[10] Zaman T, Shah Z, Rooman M, Khan W, Garalleh HA. Computation analysis of unsteady second grade biomagnetic micropolar blood-based nanofluid flow with motile gyrotactic microorganisms. Int J Model Simul 2024:1–18. [CrossRef]
[11] Gangadhar K, Sujana Sree T, Thumma T. Impact of Arrhenius energy and irregular heat absorption on generalized second-grade fluid MHD flow over nonlinear elongating surface with thermal radiation and Cattaneo–Christov heat flux theory. Mod Phys Lett B 2024;38:2450077. [CrossRef]
[12] Farooq U, Irfan M, Khalid S, Jan A, Hussain M. Computational convection analysis of second-grade MHD nanofluid flow through porous medium across a stretching surface. Z Angew Math Mech 2024:e202300401. [CrossRef]
[13] Rath C, Nayak A. MHD second-grade nanofluid slip flow over a stretching sheet subject to activation energy, thermophoresis, and Brownian effects. Phys Scr 2024;99:035228. [CrossRef]
[14] Khan MN, Khan AA, Alqahtani MA, Wang Z, Hejazi HA, AzZo'bi EA. Chemically reactive aspects of stagnation-point boundary layer flow of second-grade nanofluid over an exponentially stretching surface. Numer Heat Transf B Fundam 2025;86:1622–1638.
[15] Kezzar M, Talbi N, Dinarvand S, Das S, Sari MR, Nasr S, Akhlaghi Mozaffar A. Velocity slip and temperature jump effects on entropy generation of MHD second-grade hybrid nanofluid in Jeffery–Hamel flow. Int J Numer Methods Heat Fluid Flow 2024;34:3637–3658. [CrossRef]
[16] Reza-E-Rabbi S, Ali MY, Ahmmed SF. Nonlinear radiative second-grade nanofluid with sinusoidal magnetic force and Arrhenius activation energy: A computational exploration. Alex Eng J 2024;104:66–84. [CrossRef]
[17] Haq SU, Ali F. Analysis of Newtonian heating in fractional hybrid nanofluid with the influence of transverse magnetic field. Int J Heat Fluid Flow 2024;106:109293. [CrossRef]
[18] Ahmed MF, Yasmin H, Ali F, Raizah Z, Lone SA, Saeed A. MHD flow of second-grade fluid containing nanoparticles having gyrotactic microorganisms across heated convective sheet. Z Angew Math Mech 2024;104:e202300950. [CrossRef]
[19] Akaje TW, Olajuwon BI, Musiliu Tayo RAJI. Computational analysis of the heat and mass transfer in a Casson nanofluid with a variable inclined magnetic field. Sigma 2023;41:512–523. [CrossRef]
[20] Li S, Puneeth V, Saeed AM, Singhal A, Al-Yarimi FA, Khan MI, et al. Analysis of the Thomson and Troian velocity slip for the flow of ternary nanofluid past a stretching sheet. Sci Rep 2023;13:2340. [CrossRef]
[21] El Hattab M, Boumhaout M, Oukach S. MHD natural convection in a square enclosure using carbon nanotube–water nanofluid with two isothermal fins. Sigma J Eng Nat Sci 2024;42:1075–1087. [CrossRef]
[22] Nath JM, Paul A, Das TK. Heat transfer characteristics of magnetohydrodynamic Casson stratified hybrid nanofluid flow past a porous stretching cylinder. J Therm Eng 2021;10:1137–1148. [CrossRef]
[23] Abbas M, Khan N, Hashmi MS, Alotaibi H, Khan HA, Rezapour S, et al. Importance of thermophoretic particles deposition in ternary hybrid nanofluid with local thermal non-equilibrium conditions: Hamilton–Crosser and Yamada–Ota models. Case Stud Therm Eng 2024;56:104229. [CrossRef]
[24] Deka RK, Paul A. Convectively driven flow past an infinite moving vertical cylinder with thermal and mass stratification. Pramana 2013;81:641–665. [CrossRef]
[25] Devi SU, Devi SA. Heat transfer enhancement of Cu–Al_2O_3/water hybrid nanofluid flow over a stretching sheet. J Niger Math Soc 2017;36:419–433.
[26] Wang CY. Free convection on a vertical stretching surface. Z Angew Math Mech 1989;69:418–420. [CrossRef]
[27] Zulqarnain RM, Nadeem M, Siddique I, Samar M, Khan I, Mohamed A. Numerical study of second-grade fuzzy hybrid nanofluid flow over the exponentially permeable stretching/shrinking surface. Front Phys 2023;11:1301453. [CrossRef]
[28] Siddique I, Khan Y, Nadeem M, Awrejcewicz J, Bilal M. Significance of heat transfer for second-grade fuzzy hybrid nanofluid flow over a stretching/shrinking Riga wedge. AIMS Math 2023;8:295–316. [CrossRef]
[29] Ali Q, Riaz S, Memon IQ, Chandio IA, Amir M, Sarris IE, Abro KA. Investigation of magnetized convection for second-grade nanofluids via Prabhakar differentiation. Nonlinear Eng 2023;12:20220286. [CrossRef]

Sigma J Eng Nat Sci, Vol. 43, No. 6, pp. 2248–2262, December, 2025

Sigma Journal of Engineering and Natural Sciences
Web page info: https://sigma.yildiz.edu.tr
DOI: 10.14744/sigma.2025.1939

Research Article

Experimental and microstructural investigation of geopolymer concrete

Swapnil D. KURHADE[1,2,*], Subhash V. PATANKAR[1]

[1]*Department of Civil Engineering, Sanjivani College of Engineering, Kopargaon, 423601, India*
[2]*Department of Civil Engineering, Pimpri Chinchwad College of Engineering, Pune, 411044, India*

ARTICLE INFO

Article history
Received: 20 June 2024
Revised: 14 August 2024
Accepted: 22 October 2024

Keywords:
GPC (Geopolymer concrete); Ordinary Portland Cement; Rapid Chloride Penetration Test (RCPT); Water-to-Binder Ratio, X-ray Diffraction (XRD)

ABSTRACT

Ordinary Portland cement is the main binding agent in ordinary concrete and contributes to about 5 to 7 percent of all carbon dioxide emitted in the world. Also, the dumping of fly ash as a dangerous waste by thermal plants cause serious environmental problems. Geopolymer concrete has become a sustainable building block, using industrial byproducts, and has a promising future as an alternative of concrete. Several parameters were considered in order to determine the performance of Geopolymer concrete with some of them being water-to-binder ratio and the region of sand distribution under constant parameters to maximize the compressive strength. Geopolymer Concrete specimens were subjected to durability tests including rapid chloride penetration test, and acid resistance test. Also, microstructural studies were carried out through the X-ray diffraction. This analysis also gave analytical information regarding the phase and elemental structure of the geopolymer concrete as well as the elements of cesium, sulfur, nitrogen, carbon and cobalt. The findings can be added to the comprehensive interpretation of the material properties and performance of geopolymer concrete that can be used as an environmentally-friendly substitute in the construction industry. This paper has been rigorously researched on the phase composition of Geopolymer concrete material by X-ray diffraction test and the durability aspect by rapid chloride penetration test by use of 3-cells Rapid Chloride Penetration Test apparatus and comparison of experimental results with the conventional concrete.

Cite this article as: Kurhade SD, Patankar SV. Experimental and microstructural investigation of geopolymer concrete. Sigma J Eng Nat Sci 2025;43(6):2248–2262.

INTRODUCTION

According to the survey results, fly ash production is almost 780 million tons each year on the world-wide level [1]. The utilization rates however show that only some half of this entire size, which is estimated as being between 17 and 20 percent, is in fact utilized. India annually produces over 220 million tons of fly ash [2]. Geopolymer concrete (GPC) presents numerous environmental advantages [3]. GPC has the potential to save CO_2 emissions by up to 80% when compared to concrete made with regular Portland cement [4]. Approximately 70% of India's electricity generation relies on coal, resulting in significant fly ash production, which is often disposed of in landfills and ash ponds [5]. However, when combined with proper chemicals, the fly

*Corresponding author.
*E-mail address: skurhade2@gmail.com, swapnil.kurhade@pccoepune.org

This paper was recommended for publication in revised form by Editor-in-Chief Ahmet Selim Dalkilic

Published by Yıldız Technical University Press, İstanbul, Turkey
© Author. This is an open access article under the CC BY-NC license (http://creativecommons.org/licenses/by-nc/4.0/).

ash that can be used as a substitute of Portland cement in composite to create geopolymer concrete [6]. The manufacturing of cement contributes to almost 8% of the world's CO_2 emissions [7]. The ratios of alkaline accelerator to industrial waste fly ash and Na_2SiO_3/NaOH are essential to obtaining the necessary compressive strength of GPC [8]. The greatest degree of compression was identified by examining several ratios of these components; the highest values were obtained when the amount of alkaline activator to industrial waste fly ash ratio was among 0.5 and 0.30 [9]. Fine aggregate meeting grading zone-I specifications exhibits greater flow compared to zone-II, III, and IV, attributed to its inclusion of coarser sand particles. The grading of fine aggregate and water quantity have minimal effects on compressive strength in GPC with a consistent W-to-B ratio of 0.35 [10]. Larger coarse aggregates correspond to decreased compressive strength in GPC, likely due to increased micro cracks [11]. This suggests that changes in pore structure resulting from coarse aggregate size variations significantly influence strength development [12]. The duration and temperature of curing greatly influence the strength of hardened GPC. Remarkably, curing at room temperature results in substantial strength enhancements compared to curing at elevated temperatures [13]. Fly ash-based GPC represents a concrete variant which utilizes fly ash, a residue from coal combustion, as a primary constituent in lieu of traditional Portland cement. This eco-friendly alternative has garnered attention for its potential in curbing carbon emissions linked with cement production and for its capacity to repurpose industrial waste materials. The process of the formation of a geopolymer binder, which will hold the aggregates together, is largely dependent on the chemical reaction between fly ash and an activating solution, in the production of FGC (Fly ash Based geopolymer concrete). This is normally a solution made of alkali metal hydroxides or silicates which are used to catalyze the geopolymerization process.

Type F fly ash, which is rich in calcium and alumina and silica is widely used in the manufacture of FGC (Fly ash Based Geopolymer concrete). Combined with a silica fume activating solution, which consists of well dispersed particles of amorphous silica, FGC shows the possibility of achieving very high early compressive strength [14]. Experimental findings of geopolymer concrete mix between grade M20 to M40, using the proposed mix design method, show that the mixes have satisfactory workability and compressive strength [15]. Particularly, M30 grade is chosen to be cast with Type F fly ash being favored over Type C because it is more effective [16]. Grade P100 fly ash among the possibilities is selected between P10-100. The ideal conditions of curing the fly ash based mixes include high temperatures of above 30 °C to a maximum of 50 °C of at least 24 hours long [17]. A mix design approach to engineered dune sand concrete (DSC) based on close packing and mortar film thickness theories reached 50 MPa compressive and excellent workability, and both the results of performance and the variations in performance were associated with the difference in mortar film thickness. The DSC was characterized by the weak cement intensity and good eco-efficiency that indicates the success of the method in the balancing of mechanical, environmental, and economic forces [18]. One study examined self-compacting fiber-reinforced mortars (SCFs) with recycled brick powder (RBP) and two classes of cement and discovered that RBP enhances the durability and polypropylene fibers enhance the durability and strength. Flexural and compressive strength, porosity, and water absorbency of 32 SCFRM mixes were experimented upon [19]. One study evaluated the influence of different ratios of EPDMGR (ethylene propylene diene monomer granulated rubber) and test zones on the mechanical and durability characteristics of self-compacting concrete/mortars and that the ability to enhance flexural strength (up to 5% EPDMGR) was associated with the height of the porosity, whereas the compressive strength varied based on the location. The statistical analysis depicted that the independent variables affected properties, i.e., properties in dependence of EPDMGR ratio and element zone [20]. The authors assessed the effects of using 2-4 wt% silica fume (micro-silica and nano-silica) in place of white-Portland cement on the compressive and flexural strengths, and freeze-thaw resistance of the self-compacting mortars, discovering that these were improved. Nano silica significantly decreased the micro-cracks and pore size which increased the strength and durability due to its greater pozzolanic activity [21]. The research addresses the application of the waste tire aggregate (WTA), as an alternative to sand and cement in self-compacting concrete in an effort to achieve sustainability and resource savings. Findings suggest that concrete WTA does not lose its proper performance in terms of the different mechanical and durability tests, which can justify the use in civil engineering [22]. Evaluation of glass sand use in place of micro aggregates in micro-concrete with the contents of binders between 570 and 658 kg/m 3 is the subject of the study. Findings reveal that glass sand can be used to improve mechanical properties and durability, which in this case will justify its use in structural repair [23]. The paper investigates the effects of adding binder content to self-compacting concrete (SCC) on their fresh and hardened characteristics and found out that an increase in binder content enhances compressive strength whereas it also affects shrinkage and creep. It lays stress on the need to do more research on these effects [24]. The article discusses sustainable building through the use of pulverized fuel ash (FA) to produce lightweight aggregates and self-compacting concrete with a demonstration that FA can be used to form the environmentally-friendly material, which has the proper strength to serve as the structural material. The research mentions the opportunity of FA to minimize the environmental impact of construction [25]. The experiment compared fly ash/slag geopolymer concrete that incorporated different proportions of recycles of coarse aggregate (RCA) and it results that the highest proportion of 20% combined with 0.3 per cent of steel fiber, the results are an environmentally friendly type of concrete that had enough mechanical strength. Nevertheless, an increase in the

level of RCA leads to a significant decrease in compressive, tensile, and flexural strength [26]. The fly ash (by product of coal power plants) generates cenospheres which add value to the concrete by making it stronger, less dense and more absorptive. Such properties render it useful in the development of lightweight composite materials [27]. Researchers are looking into using eco-friendly construction material such as sticky rice pulp, Samanea Saman pods, human hair as a way of improving the properties of concrete and minimizing environmental impact on the environment. These natural resources have the potential of providing sustainable cost effective building solutions [28]. This paper explores the impact of Nano Silica (n-SiO_2) and Nano Zinc Oxide (n-ZnO) in concrete and it is established that n- SiO_2 with 0.75 percent replacement is very instrumental in enhancing both compressive and tensile strength. Nano Silica is also better in durability with n-ZnO giving moderate benefits with n-SiO2 being better according to Ultrasonic Pulse Velocity (UPV) tests [29]. This paper examines the usage of copper slag and fly ash as a substitute of sand and cement in concrete and the best mixture of fly ash and copper slag is 5 percent fly ash and 20 percent copper slag which has better strength and durability. Also, incorporation of 5 percent nano silica and 5 percent micro silica also increases flexural strength [30]. The paper examines the application of cenospheres in place of cement in concrete revealing that the density decreased by up to 4.80 per cent and that compressive, flexural, and tensile strength increased with the inclusion of calcium lactate. Maximal changes in mechanical properties are obtained at replacement of cenosphere at 10 percent [31]. The article investigates the application of organic additives such as jaggery and sticky rice pulp in concrete to improve quality without increasing the amount of cement and CO_2 emissions and therefore provides a more ecological alternative to chemical additives. Such additives will not have adverse environmental impacts as they can enhance concrete properties [32]. The type of microstructural properties of geopolymer concrete examined in this paper through an XRD (X-ray diffraction) test is an advanced technique. XRD enables the researcher to study the crystalline arrangement of the material, and to determine the existing phases which gives technical evidence of its composition and probable performance possibilities.

MATERIALS AND METHODS

The materials that were used to make geopolymer concrete specimens of fly ash comprise of low-calcium fly ash as a binding binding substance, aggregates, alkaline solutions, water, and mixtures of them. In this study, low-calcium fly ash, with a particle fineness measured through the Blane apparatus as shown in Figure 1a, was purchased from the Thermal Power Plant located in the village of Eklahare Nashik in Maharashtra. The fly ash had a P100 of 638 m^2/kg, as demonstrated in Figure 1b. A successful mixture of geopolymer concrete was accomplished using low-calcium fly ash, with silicon and aluminum oxides comprising around 80% of the total material and maintaining a Si-to-Al ratio of roughly 2. The iron oxide content typically varies from 10% to 20% by weight, while the calcium oxide content is under 5% by weight. The loss on ignition, an indicator of the carbon content, reveals a minimal concentration of approximately 2% in the fly ash.

The Nashik laboratory analyzed the particle size of the fly ash using Blane's apparatus through an air permeability

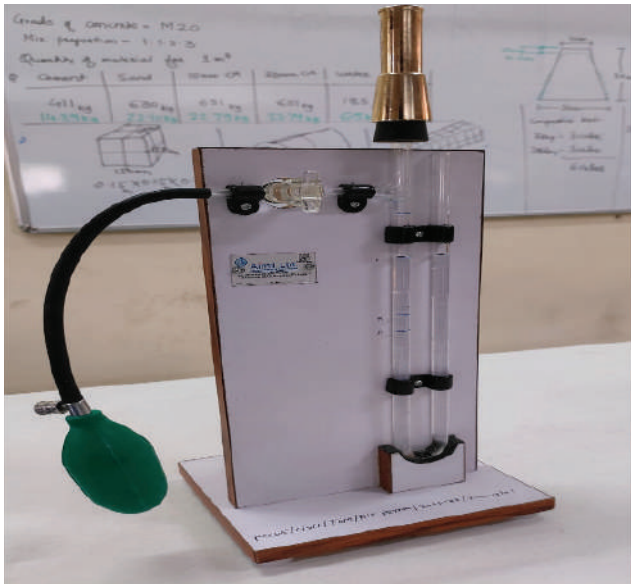


Figure 1a. Blaine's apparatus.

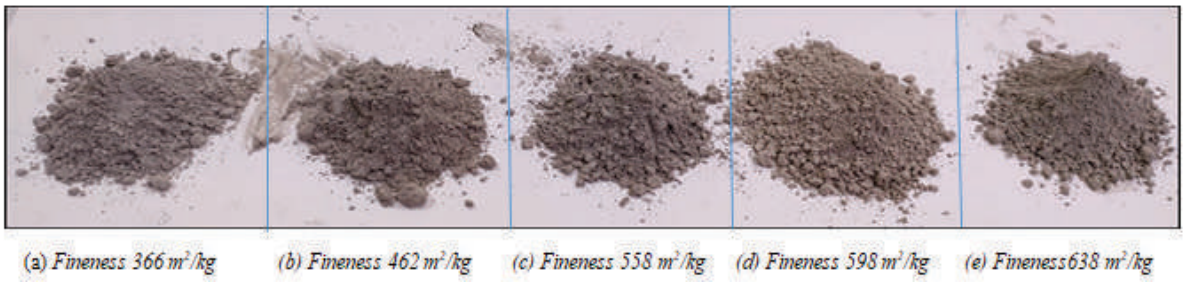


Figure 1b. Fly ash sample.

Table 1. Fly ash (chemical properties)

Sr. No.	1	2	3	4		5	6
Chemical Composition %	**$SiO_2 + Fe_2O_3 + Al_2O_3$**	**SiO_2**	**MgO**	**SO_3**	**Na_2O**	**Loss of ignition**	**Total chloride**
Sample-I	92.44	60	2	0.9	0.58	1.1	0.03
Sample-II	92.8	59.6	2	0.9	0.57	1.09	0.033
Sample-III	91	59	2	0.9	0.65	0.94	0.027
Sample-IV	93.19	58.7	1.9	0.9	0.49	1.3	0.027
Sample-V	93.42	58.3	1.7	0.7	0.56	0.8	0.024
Specifications as per IS 3812:1981	70	35	5	3	1.5	5	0.05

Table 2. Fly ash (physical properties)

Sr. No.	1	2	3	4	5	6
Physical properties of FA	**Fly ash Color**	**Residue retained on 45µm%**	**Specific surface area (Blaine), m2/kg**	**Specific gravity**	**Moisture content %**	**Autoclave expansion %**
Sample I	Light grey	15.38	366	2.25	0.25	0.029
Sample-II	Light grey	9.8	462	2.25	0.31	0.029
Sample-III	Light grey	6.72	558	2.25	0.34	0.028
Sample-IV	Grayish White	5.14	598	2.3	0.28	0.024
Sample-V	Grayish White	0	638	2.3	0.27	0.024
Specifications as per IS 3812:1981	---	34 (maximum)	320 (minimum)	---	2 (maximum)	0.8

test. The residue on the 45µm IS sieve was 0% for a sample fineness of 638 m^2/kg fly ash as shown in Figure 1b. The chemical and physical properties of fly ash are mentioned in table number 1 and table number 2 respectively. Coarse aggregates with maximum sizes of 20 mm and 12.5 mm were crushed and tested in accordance with IS: 383-1970[33]. Fine aggregates were divided into ZoneI, ZoneII, ZoneIII, and ZoneIV as shown in Table 3 along with its properties, each with corresponding fineness moduli. Crushed sand, with a fineness modulus of 3.2 and a specific gravity of 2.72, was primarily used as the fine aggregate. The fine aggregate was utilized in a dry state after sieving to a size smaller than 4.75 mm. various tests on specific gravity, water absorption, moisture content, and fineness modulus were conducted on both coarse and fine aggregates. Total 72 numbers of cubes were casted for different mix design to test on 7 days, 14 days and 28 days as shown in Figure 1c. Also M30 grade of concrete is while designing the mix design of geopolymer concrete.



Figure 1c. Ambient temperature curing system (36 cubes).

Table 3. Properties: Details of fine aggregate

Properties	Coarse aggregates	Fine aggregates			
		ZoneI	ZoneII	ZoneIII	ZoneIV
Specific Gravity	2.81	2.68	2.72	2.63	2.59
% Water absorption	0.45%	0.7%	1.5%	2.1 %	2.3%
% Moisture content	0.15%	0.79%	0.66%	0.50 %	0.43
Fineness Modulus	7.02	3.2	3	2.7	2.3

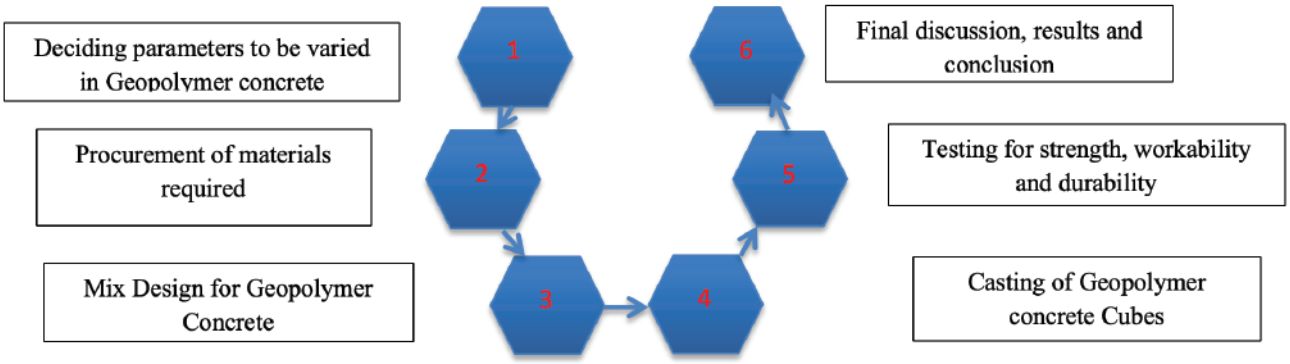


Figure 2. Methodology of experimentation.

In geopolymer concrete, agents like NaOH and Na_2SiO_3 are utilized as activators. It's advisable to mix these alkaline solutions at least 30 minutes before use. Moreover, a superplasticizer can be added to enhance workability.

The experiment comprised establishing the water-to-binder ratio and sand zone parameters by casting cubes. Following parameter fixation, durability assessments were carried out, including the Rapid Chloride Penetration Test (RCPT) and acid attack evaluation. Subsequently, an experimental inquiry employing X-ray Diffraction (XRD) analysis which is conducted to thoroughly examine the properties of GPC. This comprehensive study encompasses the mix design, durability assessment, and microstructural investigation of GPC (Fig. 2).

The ratio of water to binder was systematically changed over a range with the increments of 0.3, 0.35, 0.4, 0.45 and 0.5. It was seen that a ratio of 0.3 gave satisfactory compressive strength to geopolymer concrete specimens. The increased strength was however accompanied by reduced workability therefore making the mixture less malleable and harder to work with. On the other hand, when the ratio was 0.5, the geopolymer concrete had an increased workability, which meant that it could be manipulated easily when the concrete was placed, but this was achieved at the expense of compressive strength. After weighing between these aspects, the best choice was 0.35 which gave a balance between sufficient compressive strength and workability of geopolymer concrete mix, as it appears in Table 4. Table 5

Table 4. Mix design chart for adjusting the fly ash to alkaline ratios

Fineness of fly ash (m^2./kg)	W-to-GPC ratio (kg/m^3)	Na_2Sio_3 solution (kg/m^3)	Coarse aggregate (kg/m^3)	Fly ash quantity (kg/m^3)	Sand (kg/m^3)	Extra water (kg/m^3)	NaOH (kg/m^3)	Total water (kg/m^3)
638.00	0.30	67.50	1340.39	450.00	690.51	34.10	67.50	108.35
	0.35	52.50	1323.04		681.56	50.40	52.50	108.35
	0.40	61.25	1284.86		661.90	40.74	61.25	108.35
	0.45	70.00	1246.68		642.23	31.08	70.00	108.35
	0.50	78.75	1208.51		622.57	21.43	78.75	108.35

Table 5. Mix design: For ZoneI, ZoneII, ZoneIII, ZoneIV

Fly ash fineness	Coarse aggregate	Fineness aggrgate zones	Extra water in Ltrs.	Fly ash quantity	NaOH	Total water in Ltrs.	Na_2SiO_3	Sand
638.00	1312.93	ZoneI	22.61	450.00	78.75	109.23	78.75	706.96
	1353.92	ZoneII	21.73		78.75	108.35	78.75	666.86
	1374.58	ZoneIII	21.07		78.75	107.69	78.75	646.86
	1394.94	ZoneIV	20.85		78.75	107.47	78.75	626.71

All dimensions are in kg/m^3, except fly ash fineness is in m^2/kg.

also lists also mix design of various zones of natural sand by maintaining fineness and quantity of fly ash constant.

In the cube casting process, it was done on fine aggregates of Zones I, II, III and IV, where the aim was to establish the best type of fine aggregate in order to maximize the compressive strength of geopolymer concrete (GPC). It was performed by first combining all solid ingredients before gradually adding sodium hydroxide (NaOH) and sodium silicate (Na_2SiO_3) solutions. By adding water and the solutions of NaOH and Na_2SiO_3 to the dry mixture, the liquid phase of the mixture was obtained. Further four minutes thickening was then done to obtain homogenization of the mixture of geopolymers. The freshly blended fly ash-based GPC was of a greyish color and its workability was determined by the slump cone test according to the provision of IS: 1199-1959 [34]. Different proportions of mixing were cast which took into consideration the different ratios of fly ash-alkaline solution and the incorporation of fine aggregates of different zones. After casting, specimens were initially left to cure in an oven at 90 °C at 24 hours. The cubes were then demolded and allowed to cure under ambient room temperature (around 29 °C) 7, 14 and 28 days after the heat curing process. The curing process provided an opportunity to assess mechanical properties of the geopolymer concrete subjected to various curing time and an effect of aggregate zones.

RESULTS AND DISCUSSION

Effect of Water-to-Binder Ratio on Workability

As part of experimental investigations, the influence of altering ratios of water to geopolymer binder on the flexibility and compressive power of Geopolymer Concrete (GPC) has been investigated. This ratio is a percentage of the total water over the geopolymer binder, which is the fly ash, sodium silicate and sodium hydroxide solutions. Total water contains both intrinsic water in the mixture and any other water added to the mixture. Five ratios were researched namely 0.50, 0.45, 0.40, 0.35 and 0.30 and keeping a constant concentration of geopolymer binder at 450 Kg/m^3. Conventionally, when the water to cement ratio of a typical cement concrete is lowered, the compressive strength decreases. Nevertheless, in GPC, flexibility has been observed to be enhanced through reduction in the ratio of water to geopolymer binder.

It has been observed that as the ratio between water and geopolymer binder increases keeping all other factors constant, fluidity increases. Particularly, flow is built up in small steps. When the ratio attains 0.50, the slurry has the characteristics of flowing like self-compacting concrete. Further examination at ratios of 0.35 and 0.30 indicates that the mixture creeps over a long period of time yet it remains coherent and viscous. However, when the ratio is increased to 0.30, the mixture becomes sturdier to mix because of increased viscosity. Under ratios of 0.35, the details of its influence on compressive strength and malleability surface are provided. Although a lower water to geopolymer binder ratio of less than 0.35 might theoretically increase compressive strength, it might equally decrease malleability making the mixture harder to manipulate and place. Therefore, it is inevitable that construction intentions need to achieve a balance between the optimal compressive strength and sufficient malleability. More importantly, a careful mixing and correct curing are essential at lower water to geopolymer binder ratios to realize the potential of geopolymerization and attain the required properties of strength. Moreover, the characteristics peculiar to fly ash, sodium silicate, and sodium hydroxide solution in the geopolymer binder could also contribute to the reaction to changes in the water-to-geopolymer binder ratio.

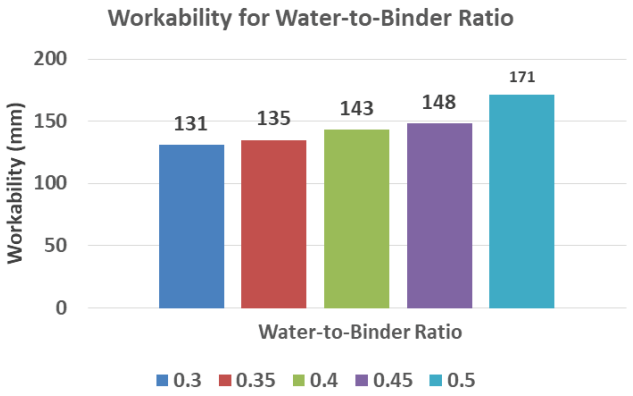


Figure 3. Effect of water-to-binder ratio on workability.

More research is justified to look into the implications of even lesser water-to-geopolymer binder ratios. The increase in the ratio of water to binder predisposes increased malleability to geopolymer concrete. The additional water provides additional lubrication between particles, which makes the mixture more liquid and easier to place just like traditional concrete. A progressive increase in the ratio of water to binder between 0.30 and 0.50 has shifted the malleability significantly; this can be indicated by the change of 131 mm into 171 mm (Fig. 3).

Effect of Water-to-Binder Ratio on Compressive Strength

The study involved the exploration of the effects of changing the water to binder ratio of geopolymer, all other experimental parameters remaining unchanged, on compressive potency of the geopolymer concrete. Results reveal a pattern that can be observed: the higher the ratio of water to geopolymer binder, the lower the compressive strength of geopolymer concrete. This is a function of the trend followed by the traditional cement concrete whereby the typical increase in water content normally results in a decrease in compressive strength. It implies that compressive strength of geopolymer concrete is inversely proportional to water to geopolymer binder ratio. This finding underscores the significant effect of water on the viscosity of the mixture, which is most probably, due to the role of water in reducing the viscosity. Figure 4 elaborates on compressive strength on 7th, 14th, and 28th days, which unveils different results of different curing treatment procedures. In fact, with geopolymer concrete (GPC), the correlation between the water-to-binder (W/B) ratio and compressive strength is usually inverse, like the ordinary Portland cement concrete. The compressive strength of geopolymer concrete is normally reduced with an increase in the W/B ratio. The reason is that, the higher the W/B ratio, the more porous the structures and the less dense the matrix is, hence lowering the strength. It is worth noting that the compressive strength is highest at a water to binder ratio of 0.30. However, it is crucial to admit that water-to-geopolymer binder ratio of 0.30 provides a more compact mixture, which makes it more difficult to handle. In order to strike a balance between the mechanical strength and workability, water-to-geopolymer binder (W/B) ratio of 0.35 is offered. This ratio is supposed to enable sufficient workability at the mix and pouring stage and a dense microstructure, which is necessary in maximizing the compressive strength and the durability of the geopolymer concrete. The images used explain the correlation between the ratio of water and binder and the compressive strength of geopolymer concrete. Although the compressive strength of the water-to-binder ratio of 0.30 is the highest according to the data, the paste manueverability is limited by its high viscosity. On the other hand, a water to binder ratio of 0.5 provides superior plasticity but low compressive strength. Considering all these the ratio of water and geopolymer binder is selected as 0.35 in order to have a balance between the malleability and compressive strength.

It is evident that the strength of geopolymer concrete is highly affected by the water to binder ratio. Increase in water to binder ratio can result in reduction in compressive strength. Excessive water content in the amalgam may end up in a porous overall concrete structure, and this is very harmful to the entire strength of the binding matrix. A higher W/B ratio might contribute to a weaker Interfacial Transition Zone (ITZ) between the aggregate particles and the geopolymer binder. This circumstance can lead to reduced bond strength and consequently, diminished compressive strength. The compressive strength diminishes as the water-to-binder ratio escalates. Specifically, at a higher W/B ratio of 0.50, the compressive strength is lower (36.45 MPa) in contrast to the mix with a W/B ratio of 0.30 (46.64 MPa) (Fig. 4).

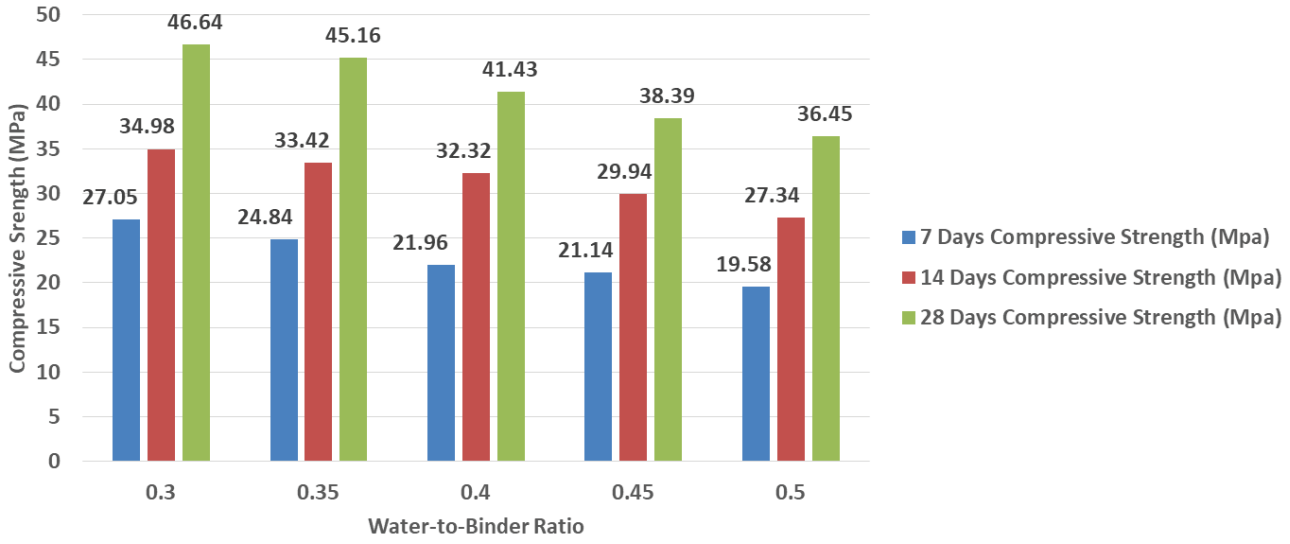


Figure 4. Effect of water to binder ratio on compressive strength of GPC.

Water-to-Geopolymer Binder Ratio vs Compressive Strength Mathematical Model

Step 1: Define Variables

x: Water-to-binder ratio (independent variable)

y: Compressive strength at different ages (dependent variable)

The compressive strengths for 7 days, 14 days, and 28 days can each be modeled as a function of the water-to-binder ratio.

Step 2: Observed Data Points

For 7 days (blue):

W/B = 0.30, y = 27.05 MPa

W/B = 0.35, y = 24.84 MPa

W/B = 0.40, y = 21.96 MPa

W/B = 0.45, y = 21.14 MPa

W/B = 0.50, y = 19.58 MPa

For 14 days (red):

W/B = 0.30, y = 34.98 MPa

W/B = 0.35, y = 33.42 MPa

W/B = 0.40, y = 32.32 MPa

W/B = 0.45, y = 29.94 MPa

W/B = 0.50, y = 27.34 MPa

For 28 days (green):

W/B = 0.30, y = 46.64 MPa

W/B = 0.35, y = 45.16 MPa

W/B = 0.40, y = 41.43 MPa

W/B = 0.45, y = 38.39 MPa

W/B = 0.50, y = 36.45 MPa

Step 3: Select a Regression Model

Given the nonlinear nature of the data that can be fitted a polynomial regression (typically quadratic or cubic) to each set of compressive strengths. The model can be represented as:

$y=ax^2+bx+c$

Where x is the water-to-binder ratio and y is the compressive strength.

Step 4: Perform Regression

Now calculate the coefficients a, b and c for each curve (7, 14, and 28 days) by fitting a quadratic regression to the data.

Here are the quadratic models for compressive strength as a function of the water-to-binder (W/B) ratio for 7, 14, and 28 days:

7 Days Compressive Strength:

$y_7=52.706x^2-114.08x+96.0$

14 Days Compressive Strength:

$y_{14}=31.728x^2+39.28x-96.0$

28 Days Compressive Strength:

$y_{28}=62.315x^2-49.043x-6.571$

Where:

x is the water-to-binder ratio and y is the compressive strength in MPa

These models represent the relationship between the water-to-binder ratio and compressive strength for each curing age. One can use these equations to predict the compressive strength for different W/B ratios within the tested range (0.30 to 0.50)

Effect of Zoning of Fine Aggregates on Workability

The water content and fine aggregate zoning are pivotal parameters influencing the workability of geopolymer concrete. According to the slump analysis, it can be stated that fine sand classified within the grading zone IV has a better workability than others. As a result, the relationship between water content and fine sand zoning in the grading zone IV, in particular, gains top priority in achieving workable geopolymer concrete formulations. It is worth noting that the sand that belongs to zone I will have coarser properties compared to those of sands in the other zones, i.e. zone II, III, and IV. This roughness equates to a lower surface area of zone I sand compared to those of its counterparts. As a rule the smaller particles require greater quantities of water to lubricate effectively. Comparing the performance of fine aggregates obtained in zone I and II (180 mm) to the performance of fine aggregates obtained in zone III and IV (161 mm) as indicated in Figure 5, the former has a better performance because it has relatively reduced surface area. The effect of fine aggregate grading on compressive strength after 28 days of curing is illustrated on the visual representation and presented in the form of the provided figure. It is noteworthy that geopolymer concrete samples that pertain to the grading zone I, II, III and IV reflect subtle differences in compressive strength. Interestingly, though the ratio of water to geopolymer binder is held constant at 0.35, the water content and fine aggregate grading cause minimal effects on compressive strength of geopolymer concrete. It is however notable that concrete composition that incorporate sand of grading zone II exhibit greater compressive strength as compared to sand obtained elsewhere.

Effect of Zoning of Fine Aggregates on Compressive Strength of Geopolymer Concrete

The effects of the various fine aggregate grading zones on the 28-day compressive strength of geopolymer concrete

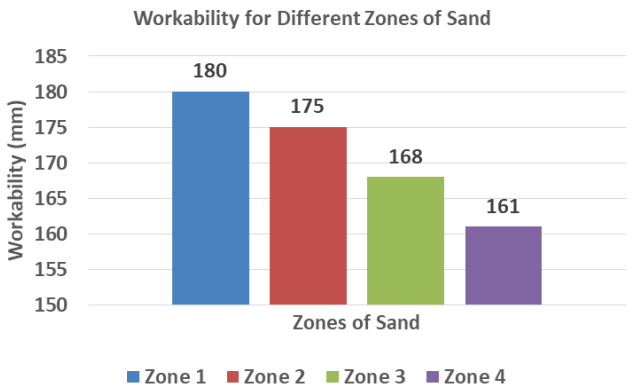


Figure 5. Effect of zoning of fine aggregates on workability.

indicate that varying grading zones may have effects on the strength of concrete. In most cases, geopolymer concrete prepared using fine aggregates obtained in different regions can exhibit different compressive strengths. As an example, concrete made using the fine aggregates of grading zone II may have a better compressive strength compared to concrete made using aggregates of other grading zones. This signifies that, choice of fine aggregate grading zones exudes much influence on the final strength properties of geopolymer concrete after a 28-day curing period. The findings reveal the presence of a regular pattern: the compressive strength is more apt to increase in accordance with the grading area of the fine aggregate. Amazingly, the highest compressive strength of 38.37 Mpa is on zone 4 in relation to the other zones.

Geopolymer Concrete (GPC) compressive strength with a standard water to binder (W/B) ratio of 0.35 is quite variable depending on grading properties of natural sand used as well as the specific dosage of water used. The sand within the grading zone IV exhibits superior compressive strength when compared to the one within zone I. This observation reveals the critical position of sand grading in dictating the strength of concrete. In addition, the amount of water in GPC is critical in the density. High water level usually results in low concrete density hence compressive strength is affected. The compressive strength of 38.37 Mpa, in this case, indicates that the GPC mix using sand in Zone IV has attained a greater level of strength compared to that which makes use of sand in Zone I as illustrated in Figure 6. The results indicate the complexity of interactions among the sand grading, water content, and the resulting compressive strength of GPC formulations.

Rapid Chlorine Penetration Test (RCPT)

Rapid Chloride Permeability Test (RCPT) is a fast method of determining the level of resistance of concrete to the entry of chloride ions. Using the technique, rapid data on the permeability of concrete to chlorides are generated, the lower the electrical conductivity, the lower the permeability and the greater resistance to chloride ingress, which implies enhanced durability. The effectiveness of the RCPT makes it to be typically used in the development of specifications and quality control. The RCPT equipment is usually made up of digital LED displays which give the voltages around the concrete specimen being studied. The test system is comprised of two diffusion chambers in which solutions of sodium hydroxide (NaOH) and sodium chloride (NaCl) are made with each solution having a concentration of 0.3 M. Concrete specimens are cast in molds with a diameter of 100 mm and a thickness of 50 mm with a constant water-binder ratio of 0.35 in the mix preparation. In the NaCl solution, 30 grams (or 3% by weight) of sodium chloride is dissolved in 1 liter of distilled water and the mixture is thoroughly stirreded to be fully dissolved. The solution is applied in the RCPT test following proper preparation. The RCPT apparatus measures the current flowing through the geopolymer concrete specimen every half hour whilst keeping the voltage constant to 59V. The table 6 shows the results of experimental data at different time periods, which develops the relation between current readings and change of temperature at various time periods, which lasts 360 minutes. Below is a little description of the crucial elements of the table 6: Time (min): This is the time in minutes elapsed throughout the experiment, and it starts at 0 and continues up to 360 minutes. C1, C2, C3 (mA): The columns are current measurements of three different cells which were

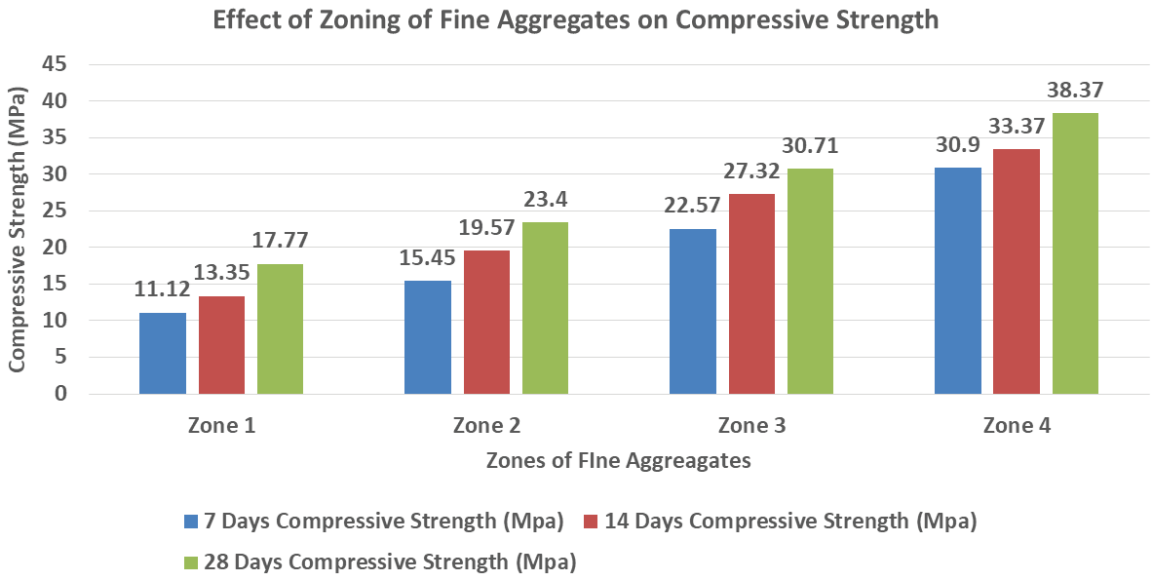


Figure 6. Effect of zoning of fine aggregates on compressive strength.

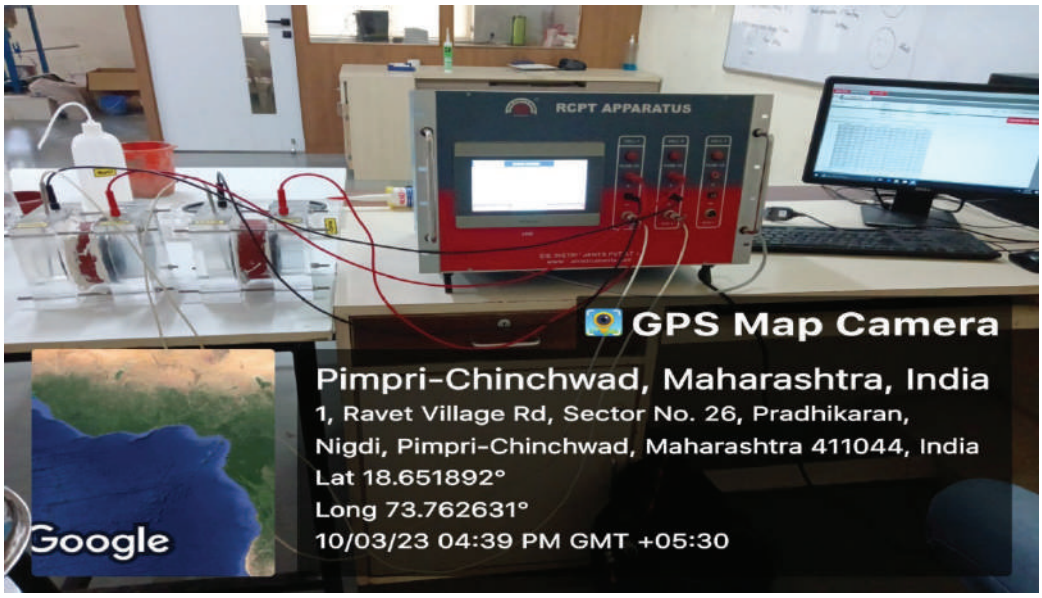


Figure 7. 3-cells RCPT apparatus.

Table 6. RCPT test readings

V	Time (min)	C1 (mA)	C2 (mA)	C3 (mA)	Temp1 °C	Temp 2 °C	Temp3 °C
59	30	79.5	76.3	79.5	86.3	83.9	76.1
59	60	89	89.4	86.2	54.6	44.4	49.3
59	90	110.3	125.2	112.5	79.3	59.5	67.8
59	120	130.4	140.4	132.9	91.8	84.3	78.7
59	150	132.8	159.9	152	101	98.7	100.6
59	180	189.1	189.9	193.4	100.6	96.8	100.4
59	210	226.3	196.4	202.4	99.6	95.2	96.6
59	240	240.9	228.9	216.2	93.5	94.5	98.5
59	270	256.6	240.9	240.1	88.4	93.1	100.2
59	300	289.8	269.6	249.4	97.6	92.6	98.3
59	330	299.2	289.5	264.4	86.3	91.8	98
59	360	309.5	316.7	310.3	85.0	90	97.5

recorded in each time interval as in Figure 7 (C1, C2, and C3) as in mill amperes (mA). Temp1, Temp2, Temp3 (°C): These are columns that show temperature values of three sensors at each time point, which were recorded in degrees Celsius (°C). Readings made are then used to determine the current through each cell after every 30 minutes. One of the popular techniques used to assess the ability of geopolymer concrete to resist chloride penetration is the analysis of its behavior depending on the current passed through the cell. This rigorous testing procedure assists in determining the concrete durability in chloride-rich environments like coastal areas or any other area that uses deicing salts, and thus helps to make decisions pertaining to materials and construction procedures and protective measures to counter the long-term structural integrity.

The chloride ion penetration is one of the crucial signatures of the maintenance of GPC since the construction of the concrete structure may be corroded and degraded by excessive chloride penetration. Based on the mean of the 03 cell samples of 3796.56 coulombs, it is evident that the average penetration of the chloride ion moderate into the Geopolymer sample was noted. The moderate chloride ion penetration indicates that the geopolymer sample exhibits a degree of resistance to chloride penetration but is not totally non-permeable.

X-Ray Diffraction Test (XRD)

X-ray diffraction (XRD) is an important method to analyze geopolymer concrete (GPC) both quantitatively and qualitatively. In this test, powder was taken out of the tested cubes. When dealing with the samples, it is imperative to make sure that they are not moist or that they are finely powdered. The powdered sample is put on a plate and inserted to the XRD machine where it is analyzed. The use of x-rays due to the high energy and short wavelength as compared to visible light is preferable in analyzing the crystal plane distance in crystalline materials. The results obtained from the XRD test are typically presented as a graph plotting intensity against the angle of refraction (2θ) as shown in Digure 8.

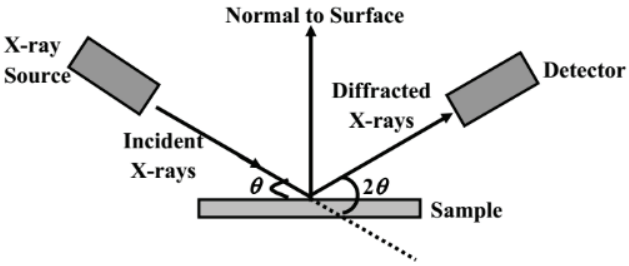


Figure 8. Schematic diagram of XRD setup.

Intensity indicates the chemical composition at specific points within the sample, while the angle of refraction represents the angle at which X-rays diffract from the sample after interaction. This graph shown in Figure 9 provides valuable information about the crystalline structure and composition of the geopolymer concrete sample.

Peak location is the maximum intensity around the hypothetical Bragg angle, and peak intensity is the magnitude of this maxima. Position of diffraction peaks is affected by variations in crystal structure. As a result, two substances with distinct crystal structures will yield various sets of XRD scan are observed.

Following the smooth graph obtained from the XRD test, the XRD patterns for GPC were displayed in Fig. 10. The primary crystalline phase identified was quartz as silicon dioxide, calcite as calcium carbonate. Sulphate phases such as mirabilite and arcanite were also detected. Portlandite in the form of calcium hydroxide at 2 thetas equal to 26.780 was present in the GPC sample. The existence of portlandite phase indicates the hardened state of the GPC which contributes to the solidification of the geopolymer concrete. Calcium hydroxide ($Ca(OH)_2$) can react with the aluminosilicate precursors in the geopolymer

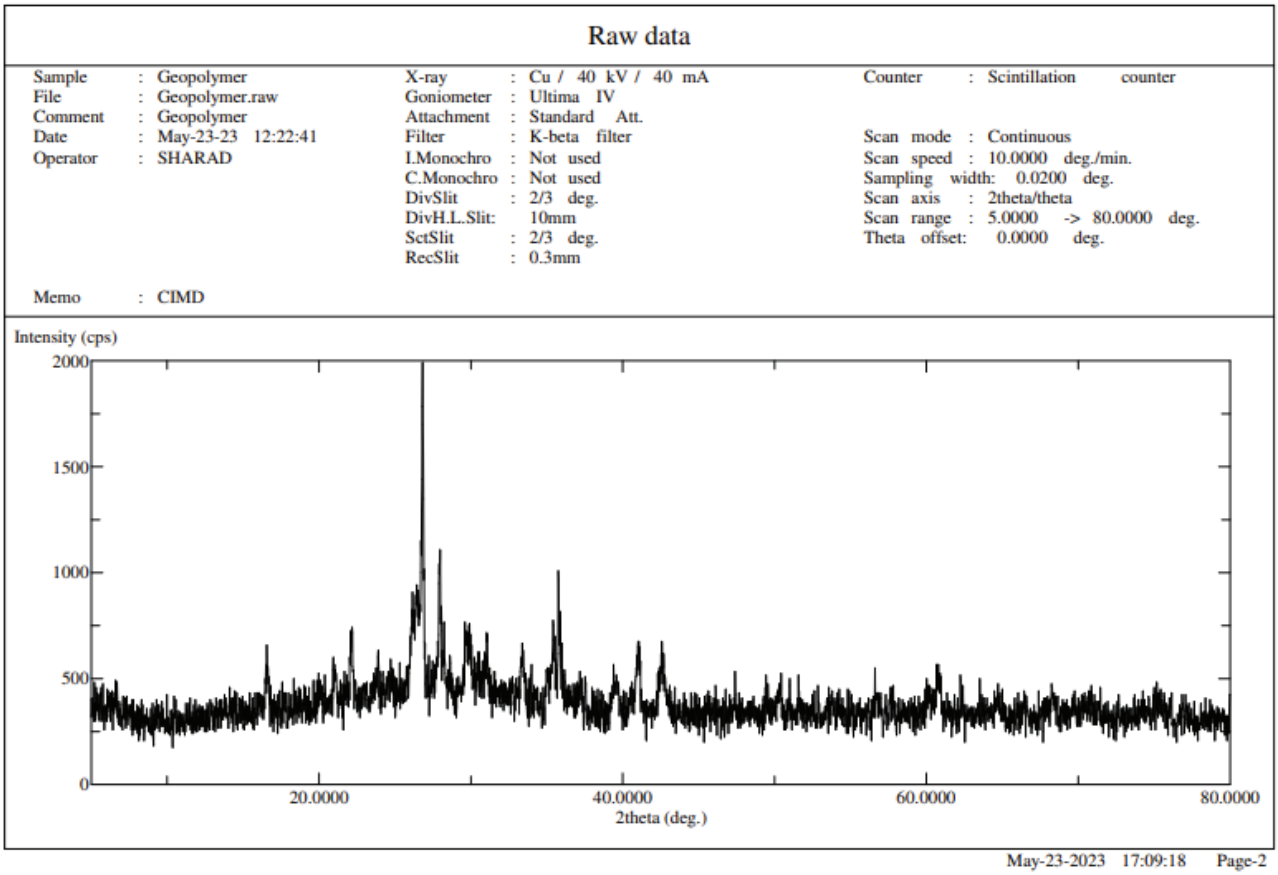
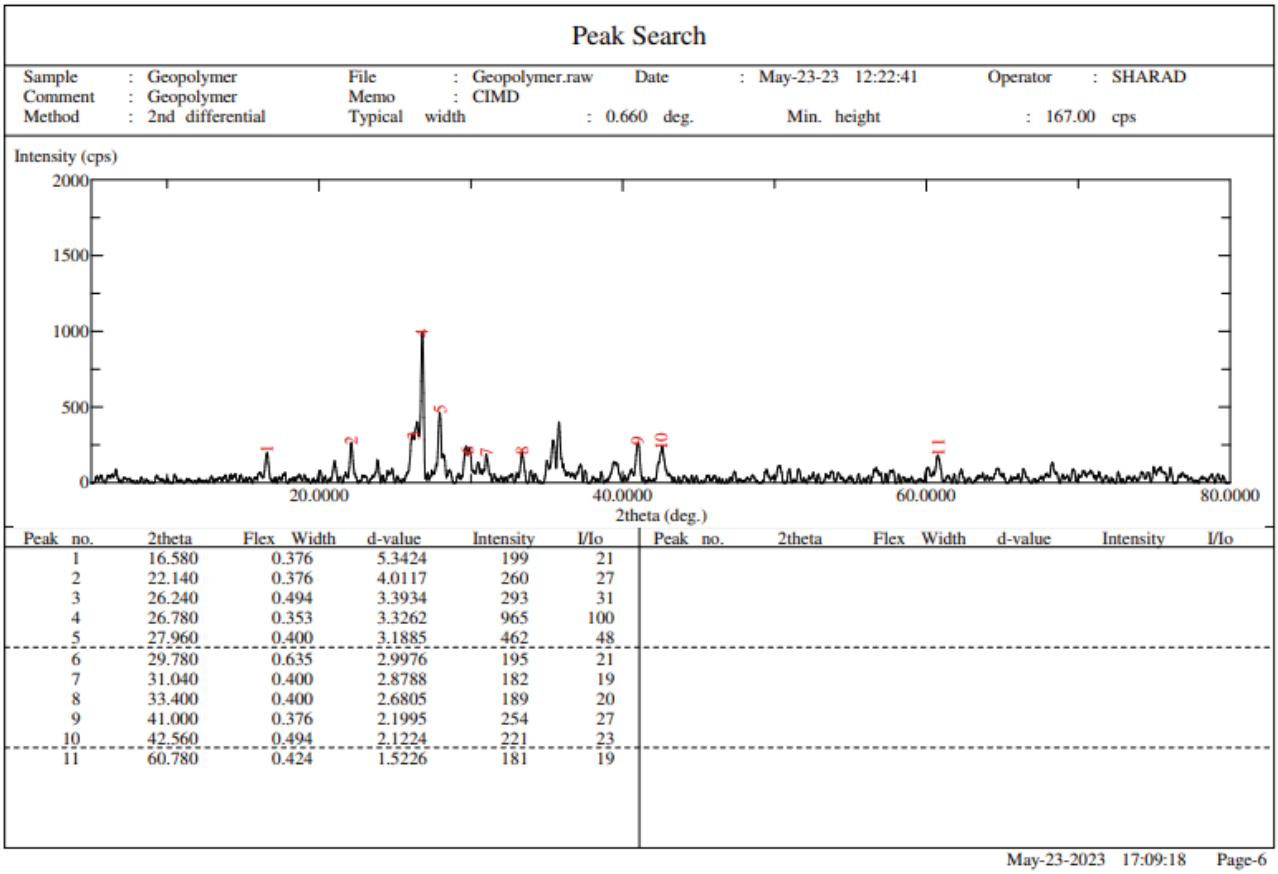


Figure 9. XRD test analysis of raw data.



Peak no.	2theta	Flex	Width	d-value	Intensity	I/Io
1	16.580		0.376	5.3424	199	21
2	22.140		0.376	4.0117	260	27
3	26.240		0.494	3.3934	293	31
4	26.780		0.353	3.3262	965	100
5	27.960		0.400	3.1885	462	48
6	29.780		0.635	2.9976	195	21
7	31.040		0.400	2.8788	182	19
8	33.400		0.400	2.6805	189	20
9	41.000		0.376	2.1995	254	27
10	42.560		0.494	2.1224	221	23
11	60.780		0.424	1.5226	181	19

Figure 10. XRD test analysis of smoothing data.

matrix, leading to additional pozzolanic reactions. This can potentially enhance the strength and durability of the geopolymer concrete by forming additional calcium silicate hydrate (C-S-H) gel, which contributes to the overall matrix.

Co (NCS) 4Cs3 is a compound that is a combination of many elements such as Cesium, Sulphur, Nitrogen, Carbon, and Cobalt, all of which are found in a different amount. The highest quantity of Cesium (Cs) in the compound as indicated by the pie chart in Figure 11 is 49.4 percent whereas the lowest quantity amounts to Carbon (C) at 8.4 percent as indicated by the table below the pie chart.

The geopolymer concrete is prepared as a result of the polymerization of aluminosilicate materials under the influence of an alkaline activator. The cesium ions (Cs +) may react with this process in a number of ways: Cesium is involved in the chemical reaction of the geopolymerization process, which may change the way the three dimensional aluminosilicate network is formed. This has the potential of reinforcing the matrix according to the integration of cesium into the structure. Cesium can influence the development of N-A-S-H (sodium aluminosilicate hydrate) or C-A-S-H (calcium aluminosilicate hydrate) gels which is highly important in determining the mechanical strength of geopolymers. Geopolymer concrete can have sulfur in different forms, either as sulfates (e.g., gypsum - $CaSO_4 2H_2O$) or sulfides. The geopolymerization process involves the participation of these sulfur compounds in chemical reactions. The existence of the sulfur can influence the stability and formation of the N-A-S-H (sodium aluminosilicate hydrate) or C-A-S-H (calcium aluminosilicate hydrate) gels which are important in the strength of geopolymers. Nitrogen in the geopolymer concrete is capable of affecting

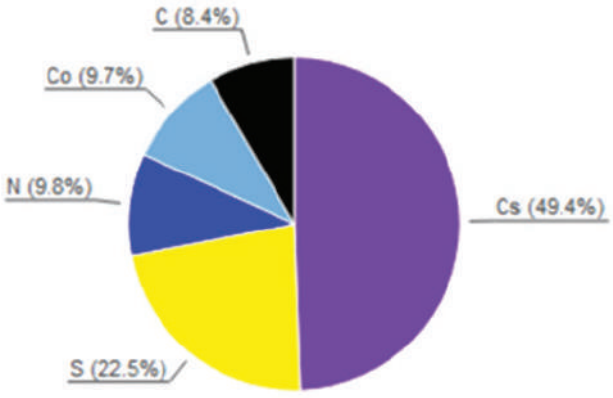


Figure 11. Phase composition.

the properties such as strength of the concrete, its durability and stability with regard to chemical stability. Nitrogen may be added to the geopolymer concrete in many different ways including nitrates, nitrites, ammonia, and other forms of nitrogenous compounds. These compounds are capable of influencing the alkalinity and chemistry as a whole of the geopolymer matrix. Nitrates (NO 3 -) and nitrites (NO 2 -) are oxidizers and may be involved in the reaction which may affect the setting and the hardening of geopolymer concrete. Carbon content of geopolymer concrete can affect its mechanical characteristics especially compressive, tensile, and flexural strengths to a significant extent. The consequences are very conducive to the type and quantity of carbon added, and its dispersion in the matrix. The carbon fibers tend to increase the mechanical properties and durability through reinforcement of material whereas carbon blacks and carbonates may alter porosity and density, which may influence strength and durability. Cobalt contains cobalt in geopolymer concrete may have various implications on the mechanical characteristics of the concrete because of the chemical and physical properties associated with cobalt. The effect is both positive and negative based on the form, concentration and distribution of cobalt in the geopolymer matrix. Cobalt ions (Co 2 +) are able to enter the geopolymer gel structure (N-A-S-H or C-A-S-H), which may alter the network connectivity and density. The introduction of cobalt compounds is also known to increase compressive strength by controlling the addition and refine the gel network and microstructure. Increased loading and density of the matrix decreases porosity and increases load-bearing capacity.

Cobalt, sulfur, nitrogen, carbon, and cesium Co(NCS) 4 Cs 3 compound, which can affect the characteristics of geopolymer concrete, interact during the process of geopolymerization. It is possible to have cesium altering the aluminosilicate network and this may enhance the matrix. The presence of sulfur, nitrogen and carbon can influence the development of the important gels (N-A-S-H or C-A-S-H), which influences the mechanical strength and the durability. The gel network can be modified using cobalt to improve the microstructure and compressive strength of the geopolymer.

CONCLUSION

- Parameters that were varied included; the alkaline activator to fly ash ratio and the various areas of sand in order to learn their effects on the strength of geopolymer concrete. A ratio of 0.35 for the alkaline activator to fly ash was found to provide good strength. Increasing the solution/fly ash ratio enhances workability, with a ratio of 0.50 considered more practical.
- In the case of a solution/fly ash ratio of 0.35, the fine aggregate grading and water content influence compressive strength. Zone 4 sand exhibits better conformity compared to Zone 1.
- From the Rapid Chloride Penetration Test test, average value of the 03 cells as 3796.56 coulombs, it is clearly indicated that the moderate chloride ion penetration into the Geopolymer sample if compare with the conventional concrete, Geopolymer concrete is more durable than the conventional concrete.
- Microstructural analysis using the X-ray Diffraction shows the phase constitution and the element constitution of geopolymer concrete, which consists of Cesium, Sulphur, Nitrogen, Carbon, and Cobalt. The above findings can be utilized to understand the performance and composition of geopolymer concrete. Also the existence of portlandite phase indicates the hardened state of the GPC which contributes to the solidification of the geopolymer concrete [34].
- Geopolymer concrete often has a higher degree of amorphous or poorly crystalline phases, which contributes to its superior resistance to chemical attacks like sulfate or chloride penetration. Normal concrete, with its crystalline calcium silicate hydrates (C-S-H), is more vulnerable to such degradation.
- The aluminosilicate framework in geopolymer concrete, observed in X-ray diffraction, typically provides better resistance to high temperatures compared to normal concrete, which can break down at elevated temperatures.

ACKNOWLEDGEMENTS

This experimental work were carried out in Testing of Materials Lab from both the colleges i.e. (Sanjivani College of Engineering, Kopargaon and Pimpri Chinchwad College of Engineering, Pune).The authors would like to thank for this support.

AUTHORSHIP CONTRIBUTIONS

Authors equally contributed to this work.

DATA AVAILABILITY STATEMENT

The authors confirm that the data that supports the findings of this study are available within the article. Raw data that support the finding of this study are available from the corresponding author, upon reasonable request.

CONFLICT OF INTEREST

The author declared no potential conflicts of interest with respect to the research, authorship, and/or publication of this article.

ETHICS

There are no ethical issues with the publication of this manuscript.

STATEMENT ON THE USE OF ARTIFICIAL INTELLIGENCE

Artificial intelligence was not used in the preparation of the article.

REFERENCES

[1] Al Bakri Abdullah MM, Kamarudin H, Ismail KN, Bnhussain M, Zarina Y, Rafiza AR. Correlation between Na_2SiO_3/NaOH ratio and fly ash/alkaline activator ratio to the strength of geopolymer. Adv Mater Res 2011;341–342:189–193. [CrossRef]

[2] Aleem A, Sundararajan V. Chemical formulation of geopolymer concrete with M-sand. Int J Res Civ Eng Archit Des 2013;1:54–60.

[3] Assi LN, Deaver E, ElBatanouny MK, Ziehl P. Investigation of early compressive strength of fly ash-based geopolymer concrete. Constr Build Mater 2016;112:807–815. [CrossRef]

[4] Bagchi SS, Ghule SV, Jadhav RT. Fly ash fineness - comparing residue on 45 micron sieve with Blaine's surface area. Indian Concr J 2012;86:39–42.

[5] Ghambhir ML. Concrete technology (theory and practice). 055; 2009.

[6] Fazli H, Yan D, Zhang Y, Zeng Q. Effect of size of coarse aggregate on mechanical properties of metakaolin-based geopolymer concrete and ordinary concrete. Materials (Basel) 2021;14:3316. [CrossRef]

[7] Guades EJ. Experimental investigation of the compressive and tensile strengths of geopolymer mortar: the effect of sand/fly ash (S/FA) ratio. Constr Build Mater 2016;127:484–493. [CrossRef]

[8] Hassan A, Arif M, Shariq M. Use of geopolymer concrete for a cleaner and sustainable environment – a review of mechanical properties and microstructure. J Clean Prod 2019;223:704–728. [CrossRef]

[9] IS 456. Plain concrete and reinforced. Bur Indian Stand 2000;4:1–114.

[10] IS 1343:2012. Prestressed concrete-code of practice. Bur Indian Stand Manak Bhavan, New Delhi 110002; 2012:55.

[11] Patankar SV, Ghugal YM, Jamkar SS. Effect of concentration of sodium hydroxide and degree of heat curing on fly ash-based geopolymer mortar. Indian J Mater Sci 2014;2014:1–6. [CrossRef]

[12] Karthik S, Mohan KSR. A Taguchi approach for optimizing design mixture of geopolymer concrete incorporating fly ash, ground granulated blast furnace slag and silica fume. Crystals 2021;11:1279. [CrossRef]

[13] Ahmed HU, Mohammed AA, Rafiq S, Mohammed AS, Mosavi A, Sor NH, et al. Compressive strength of sustainable geopolymer concrete composites: a state-of-the-art review. Sustainability 2021;13:13502. [CrossRef]

[14] Le TA, Nguyen TN, Nguyen KT. Experimental, numerical, and theoretical studies of bond behavior of reinforced fly ash-based geopolymer concrete. Appl Sci 2022;12:7812. [CrossRef]

[15] Zheng C, Wang J, Liu H, GangaRao H, Liang R. Characteristics and microstructures of the GFRP waste powder/GGBS-based geopolymer paste and concrete. Rev Adv Mater Sci 2022;61:117–137. [CrossRef]

[16] Kurhade SD, Patankar SV. Effect of water-to-binder (W/B) ratio and various zones of river sand on properties of geopolymer concrete. Mater Today Proc 2023;7:162. [CrossRef]

[17] Rahmati M, Toufigh V. Evaluation of geopolymer concrete at high temperatures: an experimental study using machine learning. J Clean Prod 2022;372:133608. [CrossRef]

[18] Xing G, Luo X, Miao P, Qiao L, Yu X, Qin Y. Proposed mix design method for dune sand concrete using close packing model and mortar film thickness theory. J Mater Civ Eng 2023;35:1017–1030. [CrossRef]

[19] Etli S. Effect of recycled brick powder on the properties of self-compacting fiber reinforced mortars produced with different cement types. Front Struct Civ Eng 2024;18:743–759. [CrossRef]

[20] Akgül M, Etli S. Investigation of the variation of mechanical and durability properties of elements manufactured with rubber substituted SCMs with element height. Constr Build Mater 2024;428:136300. [CrossRef]

[21] Etli S, Yılmaz T, Hansu O. Effect of white-Portland cement containing micro and nano silica on the mechanical and freeze-thaw properties of self-compacting mortars. Eng Sci Technol an Int J 2024;50:101614. [CrossRef]

[22] Etli S. Evaluation of the effect of silica fume on the fresh, mechanical and durability properties of self-compacting concrete produced by using waste rubber as fine aggregate. J Clean Prod 2023;384:135590. [CrossRef]

[23] Lakusic S, Ed. Effect of glass sand used as aggregate on micro-concrete properties. J Croat Assoc Civ Eng 2023;75:39–51. [CrossRef]

[24] Bhirud YL. Effects of cementitious ingredients on long term properties of self-compacting concrete. Sigma J Eng Nat Sci 2024;1067–1074. [CrossRef]

[25] Altayawi OAZ. Using of thermal power plant fly ash to produce semi-lightweight aggregate and concrete. Sigma J Eng Nat Sci – Sigma Mühendislik ve Fen Bilim Derg 2024;4142-48. [CrossRef]

[26] Lakew AM, Al-Mashhadani MM, Canpolat O. Strength and abrasion performance of recycled aggregate based geopolymer concrete. Sigma J Eng Nat Sci 2021;40:155-161. [CrossRef]

[27] Zanjad N, Pawar S, Nayak C. Use of fly ash cenosphere in the construction industry: a review. Mater Today Proc 2022;62:2185–2190. [CrossRef]

[28] Bengal SN, Pammar LS, Nayak CB. Engineering application of organic materials with concrete: a review. Mater Today Proc 2022;56:581–586. [CrossRef]

[29] Nayak CB, Taware PP, Jagadale UT, Jadhav NA, Morkhade SG. Effect of SiO_2 and ZnO nano-composites on mechanical and chemical properties of modified concrete. Iran J Sci Technol Trans Civ Eng 2022;46:1237–1247. [CrossRef]

[30] Patil L, Nayak CB, Jagadale UT, Patil L, Nayak CB, Jagadale UT. Effect of copper slag and fly ash and nano material to strengthen the properties of concrete. J Emerg Technol Innov Res 2022;9:831–838.

[31] Zanjad N. Experimental study on different properties of cenosphere based concrete using calcium lactate. Sigma J Eng Nat Sci 2023;42:1786–1796. [CrossRef]

[32] Bengal SN, Ghodmare S, Nayak CB, Tomar A. Organic admixtures as additive: an initiative to reduce carbon dioxide emission due to concrete. Macromol Symp 2024;413:1–11. [CrossRef]

[33] IS 2386 (part III). Method of test for aggregate for concrete. Part III- Specific gravity, density, voids, absorption and bulking. Indian Stand 1963; (Reaffirmed 2002).

[34] Lal D, Chatterjee A, Dwivedi A. Investigation of properties of cement mortar incorporating pond ash – an environmental sustainable material. Constr Build Mater 2019;209:20–31. [CrossRef]

Sigma Journal of Engineering and Natural Sciences
Web page info: https://sigma.yildiz.edu.tr
DOI: 10.14744/sigma.2025.1940

Research Article

Double-sided bandpass frequency selective surface design for C band WLAN radome applications

Burak Can KIŞLA[1], Bilge ŞENEL[1,*]

[1]*Department of Electrical and Electronics Engineering, Süleyman Demirel University, Isparta, 32260, Türkiye*

ARTICLE INFO

Article history
Received: 13 August 2024
Revised: 29 September 2024
Accepted: 02 November 2024

Keywords:
Aerospace; Antennas; C Band Applications; Electromagnetics, Frequency Selective Surfaces (FSS); Radomes

ABSTRACT

Frequency Selective Surfaces (FSSs) are crucial for controlling the transmission and reflection of specific electromagnetic wave frequencies. FSSs play a critical role in various technologies, including wireless communication and radar systems, by targeting specific regions of the electromagnetic spectrum to improve system performance. Integrating FSS on a radome can transmit the wave within the passband while scattering the wave outside the passband. Radomes provide protection for antenna systems from environmental conditions while permitting the transmission of electromagnetic waves. The objective of this study is design, fabrication, and measurement of a 5 GHz bandpass double-sided FSS intended for integration within a radome structure. In the study, aperture, and patch-type FSS structures that provide bandpass filter characteristics were used. The design comprises two distinct shapes, with the front surface patch and the rear shape resulting from the excavation of the copper plate. FR-4 (ε_r = 4.4) and t = 1.66 mm) is used as substrate. For simulations, CST Microwave Studio was employed. After unit cell design and analysis in CST, optimization and sensitivity analysis were performed to meet requirements. Then FSS was fabricated, and transmission loss measurement was performed. According to simulation results -33 dB S_{11} and -0.58 dB $S_{21}$was obtained for optimum aperture and patch sizes. The simulation and measurement results of transmission loss are very close to each other. Therefore, the developed FSS is recommended for use in wireless communication technologies within the 5GHz band.

Cite this article as: Kışla BC, Şenel B. Double-sided bandpass frequency selective surface design for C band WLAN radome applications. Sigma J Eng Nat Sci 2025;43(6):2263–2271.

INTRODUCTION

Frequency selective surfaces (FSSs) are a rapidly growing research area in electromagnetic engineering. These surfaces essentially enable wave control by allowing electromagnetic waves to transmission, reflect, or absorb only certain frequencies. FSSs block electromagnetic waves in certain frequency bands while allowing others to pass. They are versatile elements that can be used in many areas such as advanced antenna systems, stealth technologies, radar cross-section reduction, and spectrum control [1].

FSSs are spatial electromagnetic filters. They could be operating as either band-stop or bandpass filters depending on the application area. These structures play a critical

***Corresponding author.**
*E-mail address: bilgeturkel@sdu.edu.tr

This paper was recommended for publication in revised form by Editor-in-Chief Ahmet Selim Dalkilic

Published by Yıldız Technical University Press, İstanbul, Turkey
© Author. This is an open access article under the CC BY-NC license (http://creativecommons.org/licenses/by-nc/4.0/).

role in radar systems used for target detection and tracking, SAR radars, jamming technologies, signal quality enhancement in MRI devices, and signal filtering in wireless communication systems. Mainly, manipulating and processing electromagnetic waves with FSSs play a vital role in a wide range of applications as mentioned earlier [2-3]. However, FSSs widespread use, especially in military systems, emerged in the mid-1960s, the first known patent in this field was belong to Marconi and Franklin in 1919 [1]. This study aims to design, fabrication, and measurement of a 5 GHz bandpass double-sided FSS intended for integration within a radome structure. The designed FSS is for WLAN applications.

The smallest structural element in FSSs, known as the unit cell, is fundamental to their design and function [4–6]. FSSs consist of various patches and apertures arranged in a periodic pattern. When electromagnetic waves interact with these structures, they exhibit band-pass and band-stop characteristics. The patches and apertures placed on the dielectric create capacitive and inductive effects, which determine the filter's characteristics. [1]. Radomes are dome-like structures used to protect antennas and other sensitive electronic equipment. They are widely used in radar systems. Their primary function is to protect antennas and electronic equipment from adverse weather conditions and other environmental disturbances. Importantly, radomes are engineered to minimize interference with electromagnetic wave performance, thus preserving the functionality and efficiency of the enclosed antenna systems [7]. FSSs and radomes are individually very important elements for military and civilian mobile communication systems. Combining these two structures and designing radomes as FSS will increase mobility especially for air platforms. Because lightness is very important especially for Unmanned Aerial Vehicles (UAVs). The innovative part of our work is that the FSS we designed in this study could be used as a radome on flat air platforms.

The square slotted FSS structure and the gridded square loop FSS structure are widely used in various applications due to their frequency transmission characteristics. However, when analyzing the transmission response of these structures with respect to frequency, a sharp drop is not observed when transitioning to frequencies outside the transmission band. To create a more sharply selective FSS structure for frequencies outside the transmission band, it would be advantageous to implement FSSs on both sides of the dielectric substrate [8], [9]. Because of this reason we have chosen double-sided FSS structure.

Furthermore, FSSs provide significant benefits in antenna design by aiding in directing and focusing the antenna's performance on specific frequency ranges. They can block signals from undesired frequency bands, thereby reducing noise, and can be employed to control the reflection and scattering of electromagnetic waves, effectively expanding the frequency band [10]. In the 4-7 GHz range, Wu and colleagues introduced wideband gridded square FSSs for electromagnetic waves, achieving a stopband using a two-tiered FSS configuration [11]. Additionally, Braz and Campos investigated a simple structure based on fractal geometry [12]. They examined a broad-frequency-tunable FSS in the range of 3.5 GHz to 5.8 GHz for electromagnetic shielding applications [13-16].

There are studies where FSS based filters are used as bandpass filters in 5G applications. Studies targeting wireless communication applications in the 5 GHz band, such as WLAN (Wireless Local Area Network) and WiMAX (Worldwide Interoperability for Microwave Access), are crucial in the context of using FSS as bandpass filters [17]. In Duan's study, a minimum FSS insertion loss of 0.58 dB was observed within the 7.6 to 13.5 GHz range for radomes [18]. Sheng designed a miniaturized conformal wideband FSS for X-band (@ 8.7 GHz resonance frequency) with stable transmission performance [19]. These studies aim to increase the performance of wireless communication technologies and use the electromagnetic spectrum more efficiently. In this study, we are also aimed to design and manufacture a double-sided FSS at 5 GHz for WLAN applications. FSS is manufactured on FR-4 which is cheap and easy to find.

FSS based bandpass filters can isolate or direct the frequencies of wireless communication systems like WLAN and WiMAX in the 5 GHz region [20]. This can assist in reducing interference and collisions between networks. Especially in urban areas or for dense wireless networks, FSSs are indispensable for better connection quality and data transmission rates. Such studies may encompass various factors, including FSS design, material selection, radome geometry, and electromagnetic simulations. Consequently, FSS-based bandpass filters emerge as a significant element in advancing and improving wireless communication technologies. The combination of bandpass filters, which are essential elements for wireless communication systems, and radomes used to protect antennas on aerial platforms, into a single structure increases the importance of our work in terms of mobility and compactness.

The manuscript organization is as follows: FSS design procedure explained elaborately in Section II. Also design process of our work is presented in this section. Investigation of design parameters according to dimensions of patches and apertures is presented in Section III. Production of our FSS and measurement procedure is explained in Section IV. While results and discussions are explained in Section V, the manuscript is concluded with Section VI.

Frequency Selective Surfaces (FSS) Design

In the introduction, it was mentioned that FSS acquire their electromagnetic wave filtering characteristics based on specific patches and apertures. Generally, information about patches and apertures is provided in Figure 1.

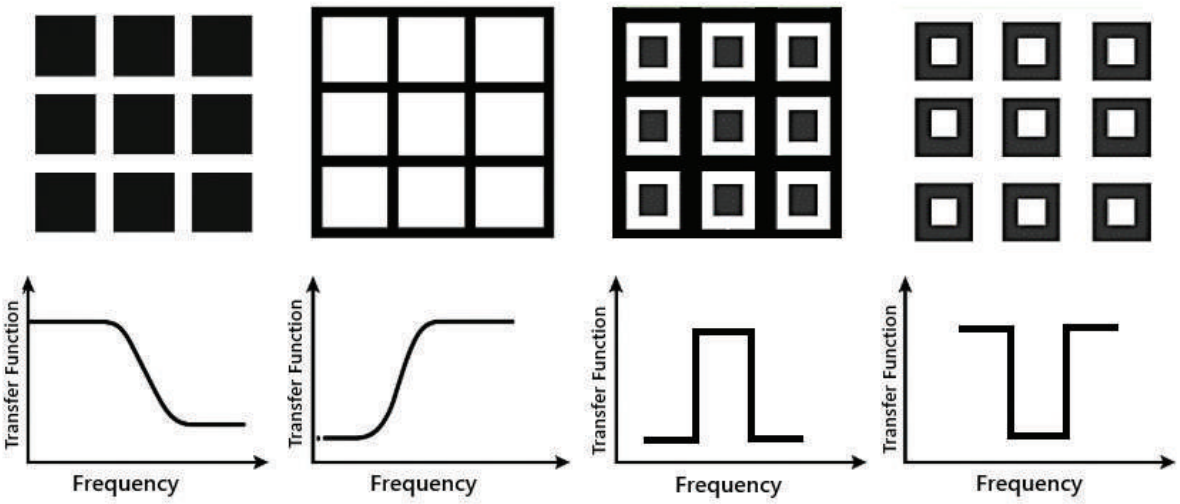


Figure 1. FSS types.

In Figure 1, the FSS filter characteristics are presented in the following order: low-pass filter, high-pass filter, band-pass filter, bandstop filter.

Maxwell's equations and the corresponding boundary conditions for electromagnetic boundary value problems support a variety of different field configurations or solutions. These distinct field configurations are often referred to as "modes." The most known modes are transverse electromagnetic (TEM), transverse electric (TE), and transverse magnetic (TM) modes. In TEM mode, both the electric and magnetic field components are perpendicular to the direction of propagation. TE is characterized by electric field components are perpendicular to the direction of propagation, while TM has magnetic field components are perpendicular to the direction of wave propagation. In this study, the simulation has been performed using TE and TM modes.

When examining patch-type FSSs, The current induced by the electromagnetic wave incident on the conductive patch geometry scatters in accordance with the Equation 1. J_s is the induced surface current density on conductive patches. A is the magnetic vector potential resulting from the radiation of the induced current. Equation 1 can be used to calculate the magnetic vector potential created by the current at any point in the medium in which the FSS is located, for cases where the current induced in the conductive patch is known [22].

$$\nabla^2 \mathrm{A} + \omega^2 \mu\varepsilon \mathrm{A} = -\mu \mathrm{J}_s \tag{1}$$

The electric field inside a conductive patch is null. Due to boundary conditions, the tangential components of the electric field are continuous, hence indicating that the tangential component of the electric field on the conductive patch is also zero. The magnitude of the electric field strength (E_s) of the scattered wave is provided according to Equation 2 below:

$$\mathrm{E}_s = -\mathrm{j}\omega\mu\mathrm{A} + 1/\mathrm{j}\omega\epsilon\, \nabla.(\nabla.\mathrm{A}) \tag{2}$$

The duality theorem will be utilized in solving the equations. The solution involves using boundary conditions, ensuring the tangential components of the magnetic field intensity are continuous within the apertures. The current density is expressed as follows according to Equation 3 [22].

$$J(x,y) = \sum\sum J_{mn} e^{j.\left(k_{xg}+\frac{2\pi.m}{a}\right).x + j.\left(k_{yg}+\frac{2\pi.n}{b.\sin(\Omega)}-\frac{2\pi.m}{a}.\cot(\Omega)\right).y} \tag{3}$$

The "Equivalent Circuit Model" in FSSs is a simple and analytical calculation technique. This model emerged through the work of Marcuvitz in modeling periodic grids, with the initial analysis being provided by Anderson [21], [22]. These models are widely employed today due to their assistance in explaining the behavior of FSSs.

In FSS design, the choice of the conductive surface has a direct impact on the equivalent circuit model's resistance, leading to variations in the characteristic structure of the FSS. The resonant frequencies of the structure vary depending on the polarization of the incident wave, and the angle of wave incidence also affects the resonance frequency. The structure's resonance frequency is largely dependent on the dielectric substrate because the dielectric constant provides insights into the material's response to electromagnetic waves.

For simulations, CST Microwave Studio was employed. The design comprises two distinct shapes, with the front surface patch and the rear shape resulting from the excavation of the copper plate. The dielectric plate used has a dielectric constant of 4.4 (ε_r = 4.4) and a loss tangent ($tan\delta$ = 0.02) of 0.02, and it is made of FR-4 material with a thickness of 1.6 mm (t = 1.6).

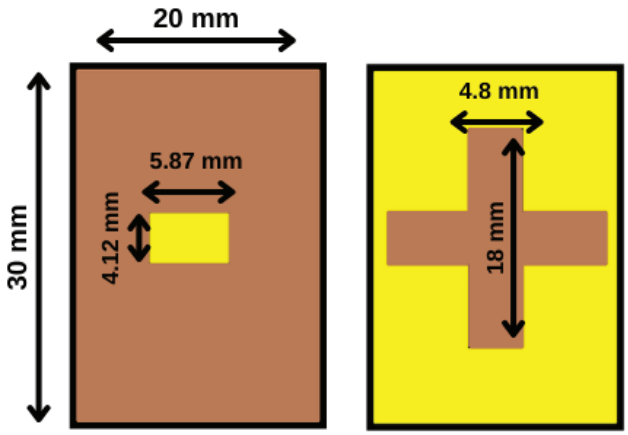


Figure 2. The dimensions of front and back surfaces of the proposed double sided FSS.

The dimensions of the proposed double-sided FSS are shown in Figure 2. The dimensions of the patch and apertures are critically important in forming the equivalent circuit model and influencing the behavior of electromagnetic waves. This design has been created through an optimization process, which also includes sensitivity analysis. Further details on this topic will be provided in the upcoming section.

The simulation was conducted in the frequency domain. Two ports were established for unit cell analysis in the z-direction, providing the S-parameters. Reflection and transmission coefficients provide insights into the manipulation of electromagnetic waves. In FSSs, the filter's requirements are determined based on these parameters. The aim of this article is for the proposed FSS to exhibit bandpass characteristics at 5 GHz.

Periodic arrays of conductive patches or apertures placed on a dielectric medium exhibit reflection and transmission properties that vary with frequency. Achieving a reflection coefficient (S_{11}) below -10 dB is a targeted parameter. In the proposed FSS in this study, this value is approximately -32.72 dB as shown in Figure 3.

The transmission coefficient is expected to be close to 0 dB to achieve a bandpass filter characteristic. This parameter provides information about electromagnetic wave manipulation like S_{11}. Improvement in transmission characteristics

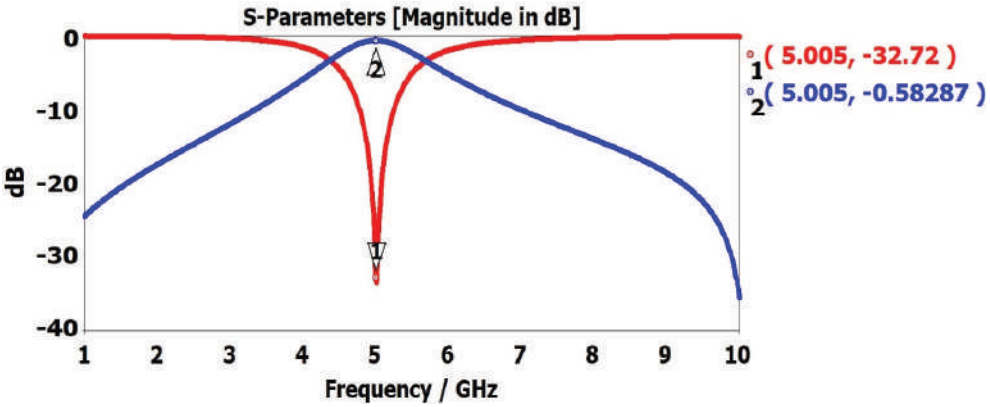


Figure 3. Reflection and transmission coefficient of proposed FSS.

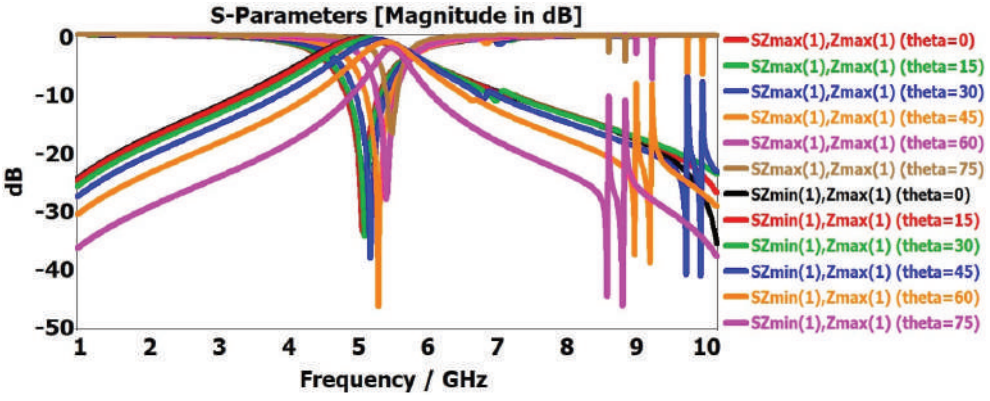


Figure 4. Variation of reflection and transmission coefficient according to the θ.

can be achieved by altering the dielectric substrate. In this article, an approximately -0.58 dB transmission coefficient has been obtained, as also shown in Figure 3.

In this study, the parameter theta (θ), which represents the wave incidence angle, has been included in the simulations. Figures 4 depicts the variation of S_{11} and transmission coefficients with respect to the electromagnetic wave's angle of incidence. According to the Figure 4 if θ increases center frequency (f_c) shifts towards right on the x-axis. Also, S_{11} and transmission coefficients of FSS degrades at 5GHz.

INVESTIGATION OF THE DESIGN PARAMETERS

The dimensions of the patches and apertures have been increased and decreased leading to obtaining an optimal result and subsequently addressing sensitivity. Firstly, the other side was always kept stationary. The increase and decrease in the aperture portion have been made by 10% and patches portion have been made by 20%. Transmission coefficients have been shared for this section. Frequency shift has been observed in the simulation environment, indicating that the FSS is tunable.

This section provides a detailed explanation of the optimization work and sensitivity analysis conducted for the proposed FSS. As a result, it has been revealed that there may be frequency shifts for this

FSS depending on the patch and aperture sizes. If patch and aperture sizes decrease, f_c shifts towards left on the x-axis and if patch and aperture sizes increase, f_c shifts towards right on the x-axis as seen in Figure 5 and 6. We get the best results for dimensions as seen in Figure 2 at center frequency of 5 GHz.

PCB Fabrication and Measurement of Designed FSS

FSS fabrication and measurement require considerable attention due to factors such as geometric precision, material selection and correct alignment. The challenges of FSS design and measurement extend to the optimization process, which requires fine-tuning to meet specific frequency and angle requirements. Despite these complex processes, what makes FSS technology valuable is its ability to

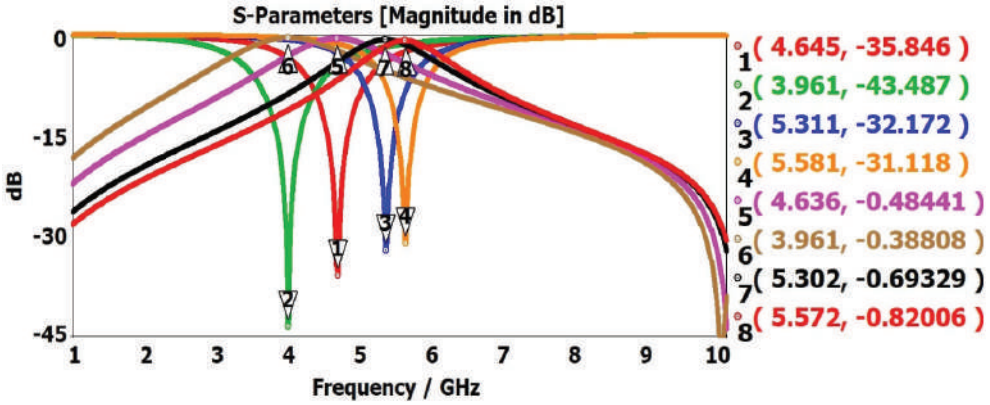


Figure 5. Change in reflection and transmission coefficient with 20% patch sizes increase and decrease.

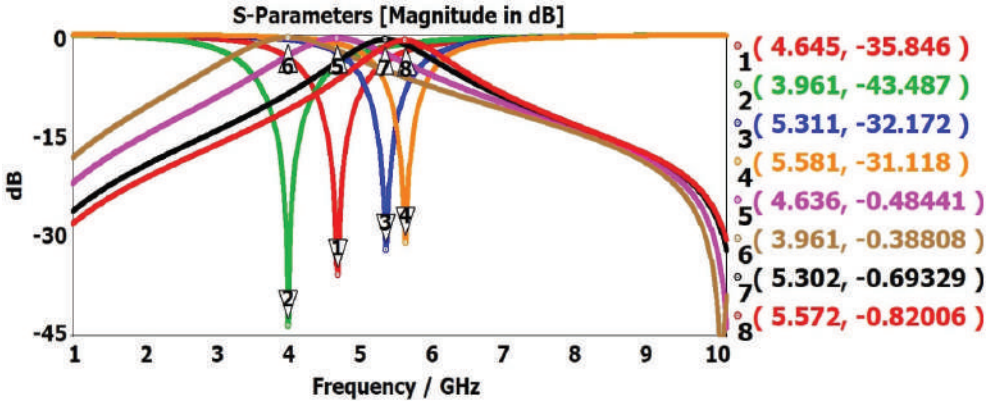


Figure 6. Change in reflection and transmission coefficient with 10% aperture sizes increase and decrease.

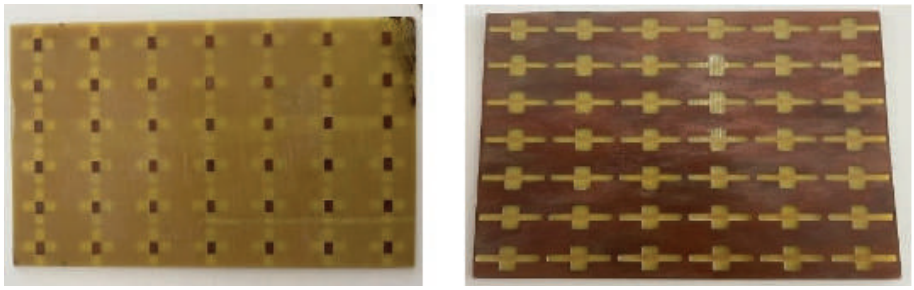


Figure 7. Front and back surface of produced double-sided FSS.

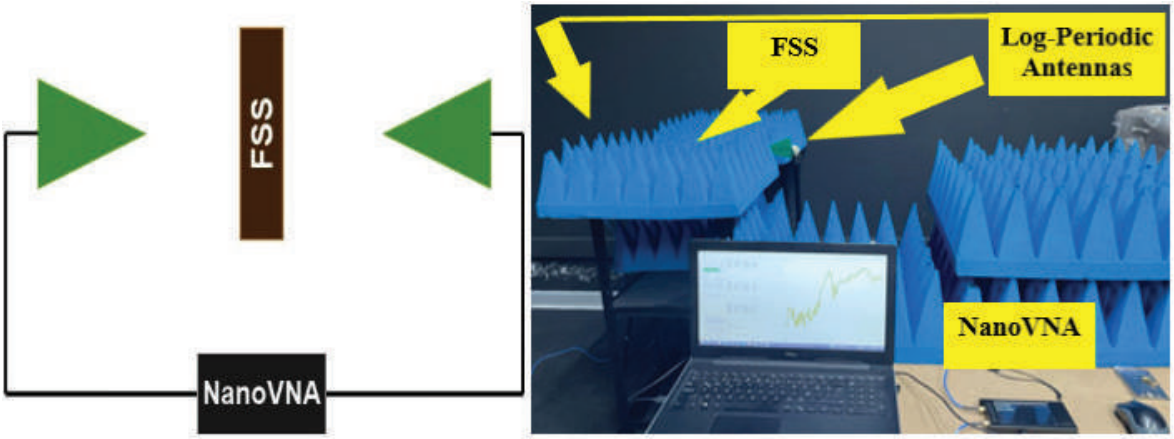


Figure 8. Free Space Measurement Setup Schematic and Setup.

configure electromagnetic wave behavior in a desired way. Although free-space measurements are challenging, they help us understand how FSSs work, allowing us to improve their performance and use them in more areas. Although all mentioned complexity the FSSs have the potential radical transformations in electromagnetic engineering and determine the direction of future technological innovations. The proposed FSS is manufactured with Computer Numerical Control (CNC), ensuring precision and consistency in production. CNC technology plays a crucial role in achieving the intricate geometries required for FSS structures [23]. First, the unit cell design of the FSS was developed, and then it was expanded across the plate for manufacturing. Once obtained in plate form, the production was carried out through milling using CNC technology. The produced sample is shown in Figure 7.

The free-space method, as elaborated in this article, has far-reaching implications in the study and development of FSS materials [28]. The rigorous measurement and characterization facilitated by the free-space method foster innovation and progress in these areas, underscoring the collaborative efforts of engineers and academicians in advancing the frontiers of electromagnetic design.

A superficial mechanism was preferred for measurement. The reason for this is that there are studies in the literature that make measurements in this way [29]. The "*D*" length of the antenna is 10 cm. Here, the far field calculation was made as 33 cm according to the far field formula for 5 GHz. For measurements, antennas are adjusted to the far-field distance (33 cm), and Vector Network Analyzer (VNA) calibration is performed. Given the significance of cables and antennas, potential issues in this regard are carefully considered. First, measurements are taken in free space, and then measurements with the sample are carried out, with the difference between them providing the desired measurement result. A NanoVNA 6.3 GHz version previously used in the literature for a broadband complex permittivity measurement was used in the measurement [30]. Figure 8 shows the Free Space Measurement setup and schematic.

In Figure 9, the blue-colored data represents the measurement results, while the red-colored data represents the simulation results.

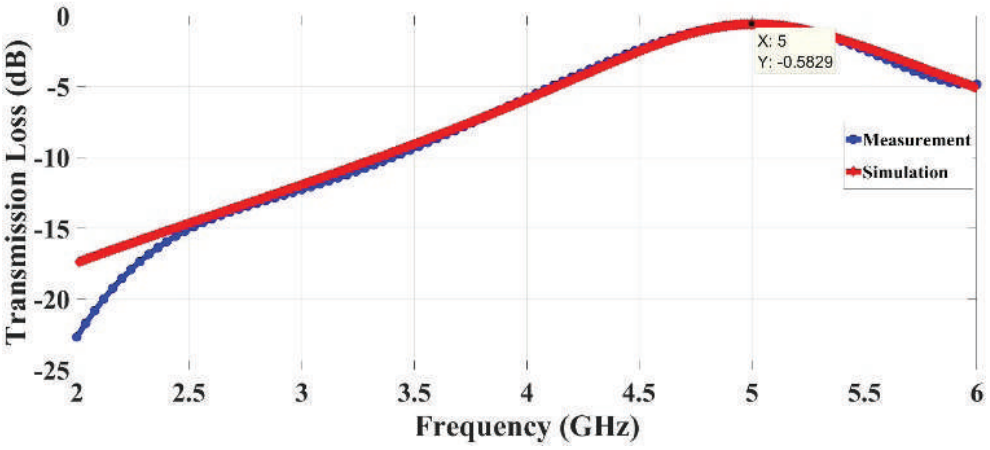


Figure 9. Measurement and simulation results up to 6 GHz.

RESULTS AND DISCUSSION

As mentioned earlier, in this study, low-cost, lightweight a bandpass double-sided FSY is designed for wireless communication systems. It is very important that wireless communication systems, especially those designed for unmanned aerial vehicles, are designed to be cost-effective and lightweight [31]. In CST Studio Suite software, a bandpass frequency selective surface design was created using the frequency domain in the appropriate frequency range. Apertures and patches type were chosen from the literature when creating the unit cell model. Then, a simulation was performed by creating double sides. The reason for choosing the resulting structure is ease of production. For the design, the length values of the patch and aperture were examined parametrically. The simulation was repeated for each length and width value and the best value for electromagnetic transmission was selected as the design. When the literature was examined, it was observed that frequency domain was used for such material designs. The design and optimization process of the proposed FSS in this study is summarized in the flowchart as shown in Figure 10.

We compare our study with the existing literature in Table 1. First, a bandpass FSS designed for WLAN and WiMAX was examined [17]. Second, an FSS antenna radome system was proposed for airborne and ground applications in the X-band [24], where analytical analysis, simulation, and production processes are described. The transmission coefficient for 9.4 GHz to 16 GHz was reported to be between 0.1-0.3 dB. Third, a new metamaterial element with properties across different frequency ranges was presented for radome applications [25]. Fourth, a dual-band sandwich radome was proposed for airborne applications [26]. Lastly, the electromagnetic performance analysis of a radome based on a novel graded dielectric inhomogeneous wall structure was presented [27]. According to Table 1 and the literature, the double-sided FSS proposed in this study is in line with current research and can be effectively used in radome applications.

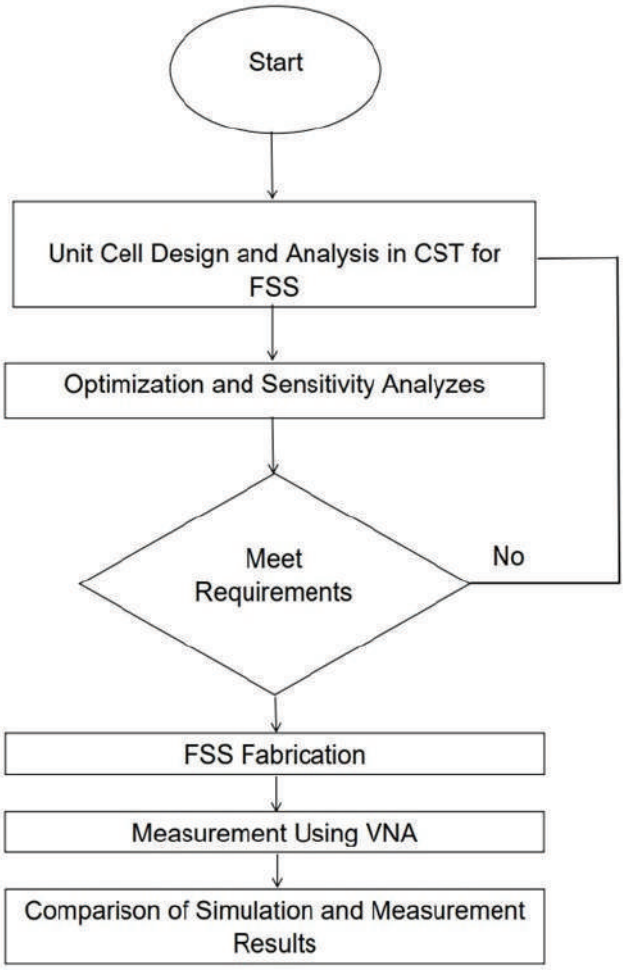


Figure 10. FSS design flowchart.

Table 1. Frequency selective surfaces comparison table

Ref.	Frequency	Transmission Coefficient
[17]	5 GHz	0.22 dB
[24]	9.4-16 GHz	0.1-0.3 dB
[25]	8.5-10.3 GHz	0.3-0.6 dB
[26]	1.5–1.6 6.49–6.7 GHz	1.6 dB
[27]	10 GHz	0.5-0.62 dB
This Work	5 GHz	0.58 dB

The integration of FSS within radome structures represents a significant advancement in antenna engineering. Our study offers an advantage for radome applications due to its double-sided structure, which provides a tunable feature thanks to its patches and apertures. This design is aimed to be a reference for future studies in the literature and to provide a practical solution in industrial applications. Double-sided FSSs provide several advantages in radome applications. The double-sided design interacts with electromagnetic waves on both sides, improving the efficiency of the radome and providing strong electromagnetic shielding. This configuration improves signal accuracy and system reliability by reducing signal loss like traditional radomes. These advanced designs offer a counterpoise between electromagnetic performance and structural integrity, particularly in aerospace-defense applications, and represent a significant step forward in antenna technology.

The double-sided FSS structure significantly increases the mechanical robustness of the radome. Precise control of electromagnetic interference in antenna systems increases the reliability and stability of communication systems. For this reason, the double-sided frequency selective surface proposed in the study is highly recommended for WLAN and WiMAX applications.

In conclusion, this article presents the simulation, fabrication, and measurement of the proposed FSS, specifically designed for the 5 GHz band within the C-band. Various studies utilizing different patch and aperture designs were examined in Table 1, and their advantages and disadvantages were carefully considered during the development of the FSS radome design. The rationale for focusing on the 5 GHz range is its relevance to applications such as Wi-Fi and WiMAX. This study follows the existing literature, offering a valuable contribution to antenna and radome engineers.

CONCLUSION

In this study, the design, analysis, and transmission measurement of a double-sided bandpass FSS were conducted. Based on frequency domain simulations and parametric analyses, the structure that demonstrated the optimal transmission characteristic (-0.58 dB) was selected as the final design. The selected patches and apertures were integrated into the design due to their frequent use in the literature, with an aim to introduce novelty through this integrated approach. Another objective was to achieve ease of fabrication with these shapes. Measurements were carried out using the free-space measurement method, confirming the performance of the working design. The primary goal of this design is to offer a rapidly applicable and adaptable solution for radome and antenna researchers in the academic field. From an industrial perspective, this study is expected to make a significant contribution, particularly given the growing importance of UAVs. In UAVs, weight management is a critical challenge; by embedding this structure into the body of the UAV instead of incorporating a portable wireless communication filter, gains in both weight and payload efficiency can be achieved. This study aims to provide insights and guidance for researchers in both academia and industry. In our future FSY studies, bandpass form patch and aperture type FSYs will be designed with different substrate materials. Conformal FSY designs and printed circuits with the unit cell model in this study will be performed.

AUTHORSHIP CONTRIBUTIONS

Authors equally contributed to this work.

DATA AVAILABILITY STATEMENT

The authors confirm that the data that supports the findings of this study are available within the article. Raw data that support the finding of this study are available from the corresponding author, upon reasonable request.

CONFLICT OF INTEREST

The author declared no potential conflicts of interest with respect to the research, authorship, and/or publication of this article.

ETHICS

There are no ethical issues with the publication of this manuscript.

STATEMENT ON THE USE OF ARTIFICIAL INTELLIGENCE

Artificial intelligence was not used in the preparation of the article.

REFERENCES

[1] Munk BA. Frequency selective surfaces: theory and design. New York: John Wiley & Sons; 2000. [CrossRef]

[2] Shavit R. Radome electromagnetic theory and design. Hoboken: Wiley; 2018. [CrossRef]

[3] Wang J, Feng D, Xu L, Zhang R, Hu W. Synthetic aperture radar target feature modulation using active frequency selective surface. IEEE Sens J 2018;19:2113–2125. [CrossRef]

[4] Bayatpur F, Sarabandi K. Design and analysis of a tunable miniaturized-element frequency-selective surface without bias network. IEEE Trans Antennas Propag 2010;58:1214–1219. [CrossRef]
[5] Imran AI, Elwi TA. A cylindrical wideband slotted patch antenna loaded with frequency selective surface for MRI applications. Eng Sci Technol Int J 2017;20:990–996. [CrossRef]
[6] Wu TK. Improved bandpass FSS for wireless communications. In: 2014 USNC-URSI Radio Science Meeting (Joint with AP-S Symposium). IEEE; 2014. p. 153. [CrossRef]
[7] Kozakoff DJ. Analysis of radome-enclosed antennas. Norwood: Artech House; 2010.
[8] Ferreira D, Caldeirinha RF, Cuinas I, Fernandes TR. Square loop and slot frequency selective surfaces study for equivalent circuit model optimization. IEEE Trans Antennas Propag 2015;63:3947–3955. [CrossRef]
[9] Lee CK, Langley RJ. Equivalent-circuit models for frequency-selective surfaces at oblique angles of incidence. IEE Proc H Microw Antennas Propag 1985;132:395–399. [CrossRef]
[10] Qiu H, Rahman SU, Ullah H. A compact SWB monopole antenna and FSS. Int J Adv Netw Appl 2023;14:5658–5665. [CrossRef]
[11] Chatterjee A, Parui SK. A dual layer frequency selective surface reflector for wideband applications. Radioengineering 2016;25:67–72. [CrossRef]
[12] Braz EC, Campos AL. Dual/wide band multifractal frequency selective surface for applications in S- and X-band. Microw Opt Technol Lett 2014;56:2217–2222. [CrossRef]
[13] Sivasamy R, Moorthy B, Kanagasabai M, Samsingh VR, Alsath MGN. A wideband frequency tunable FSS for electromagnetic shielding applications. IEEE Trans Electromagn Compat 2018;60:280–283. [CrossRef]
[14] Majidzadeh M, Ghobadi C, Nourinia J. Quadruple filtering mechanism through an effective sketch of reconfigurable frequency selective surface. IET Microw Antennas Propag 2016;10:1605–1612. [CrossRef]
[15] Majidzadeh M, Ghobadi C, Nourinia J. Novel single layer reconfigurable frequency selective surface with UWB and multiband modes of operation. AEU Int J Electron Commun 2016;70:151–161. [CrossRef]
[16] Majidzadeh M, Ghobadi C, Nourinia J. A reconfigurable frequency-selective surface for dual-mode multiband filtering applications. Int J Electron 2017;104:369–381. [CrossRef]
[17] Tariq M, Zahid MN. Design and performance analysis of band pass filter using frequency selective surface for 5G communication. Proc Eng Technol Innov 2023;23:15–22. [CrossRef]
[18] Duan K, Chen K, Jiang T, Zhao J, Feng Y. Ultrawideband frequency selective radome utilizing 2.5-D lossy layers. IEEE Antennas Wirel Propag Lett 2023;22:2427–2431. [CrossRef]
[19] Sheng X, Wang H, Liu N, Wang K. A conformal miniaturized bandpass frequency selective surface with stable frequency response for radome applications. IEEE Trans Antennas Propag 2024;72:2423–2433. [CrossRef]
[20] Majidzadeh M. 2.4/5.8 GHz WLAN filtering in secure electromagnetic applications: a single layer frequency selective surface. Smart Sci 2017;5:199–205. [CrossRef]
[21] Marcuvitz N. Waveguide handbook. London: Institution of Engineering and Technology; 1986. [CrossRef]
[22] Doken B. Design for the structural surface material at which reflection and transmission characteristics can be controlled [dissertation]. Istanbul: Istanbul Technical University; 2017.
[23] Wang Q, Tang XZ, Zhou D, Du Z, Huang X. A dual-layer radar absorbing material with fully embedded square-holes frequency selective surface. IEEE Antennas Wirel Propag Lett 2017;16:3200–3203. [CrossRef]
[24] Tahseen HU, Yang L, Zhou X. Design of FSS-antenna-radome system for airborne and ground applications. IET Commun 2021;15:1691–1699. [CrossRef]
[25] Narayan S, Gulati G, Sangeetha B, Nair RU. Novel metamaterial-element-based FSS for airborne radome applications. IEEE Trans Antennas Propag 2018;66:4695–4707. [CrossRef]
[26] Zhou L, Pei Y, Fang D. Dual-band A-sandwich radome design for airborne applications. IEEE Antennas Wirel Propag Lett 2016;15:218–221. [CrossRef]
[27] Yazeen PM, Vinisha CV, Vandana S, Suprava M, Nair RU. Electromagnetic performance analysis of graded dielectric inhomogeneous streamlined airborne radome. IEEE Trans Antennas Propag 2017;65:2718–2723. [CrossRef]
[28] Idrees M, Buzdar S, Khalid S, Khalid MA. A miniaturized polarization-independent frequency selective surface with stepped profile for shielding applications. Appl Comput Electromagn Soc J 2016;31:531–536.
[29] Khajevandi A, Oraizi H. Utilizing interdigital and supershape geometries for the design of frequency selective surfaces with high angular and polarization stabilities. Sci Rep 2022;12:7054. [CrossRef]
[30] González-Teruel JD, Jones SB, Robinson DA, Giménez-Gallego J, Zornoza R, Torres-Sánchez R. Measurement of the broadband complex permittivity of soils in the frequency domain with a low-cost vector network analyzer and an open-ended coaxial probe. Comput Electron Agric 2022;195:106847. [CrossRef]
[31] Belen A, Tetık E, Başak H. 3D printed stacked antenna for WLAN drone communication. Sigma J Eng Nat Sci 2023;42:656–664. [CrossRef]

Sigma Journal of Engineering and Natural Sciences
Web page info: https://sigma.yildiz.edu.tr
DOI: 10.14744/sigma.2025.1941

Research Article

Comparative study of fermatean fuzzy soft sets with normalized distances and its application in diagnose infectious diseases

Saika SHEWALI[1], Borah Manash JYOTI[2], Mahanta Dimpal JYOTI[1,*]

[1]*Department of Mathematics, The Assam Kaziranga University, Assam, 785006, India*
[2]*Department of Mathematics, Bahona College, Assam, 785101, India*

ARTICLE INFO

Article history
Received: 19 June 2024
Revised: 08 August 2024
Accepted: 06 November 2024

Keywords:
Chikungunya; Fermatean Fuzzy Soft Set, Medical Diagnosis; Normalized Distances

ABSTRACT

The employment of Fermatean fuzzy soft sets with normalized distances in the perspective of diagnosis in medical treatment are observed in this research. The effectiveness of normalized distances—such as Fermatean, Hamming, and Euclidean measures—in handling the inherent uncertainty in medical data is evaluated. Through a comparative analysis, we assess their performance in medical diagnosis tasks, aiming to demonstrate how these methods can enhance the accuracy and reliability of diagnostic systems. The goal of the research is to shed light on how Fermatean fuzzy soft sets with normalized distances might enhance the precision and dependability of medical diagnostic systems. This illustrative example of Chikungunya highlights the benefits of combining normalized distances into Fermatean fuzzy soft set frameworks, contributing to advancements in medical decision support systems.

Cite this article as: Shewali S, Jyoti BM, Jyoti MD. Comparative study of fermatean fuzzy soft sets with normalized distances and its application in diagnose infectious diseases. Sigma J Eng Nat Sci 2025;43(6):2272–2278.

INTRODUCTION

An essential concept for decision-making issues is uncertainty. Because of inconsistencies and unreliable data, individuals making decisions are frequently finding it challenging to provide their evaluation of an object in clear values. Theory of fuzzy sets (FS), in his groundbreaking work, in 1965 Zadeh [1] proposed a membership function that is a powerful instrument for resolving issues with imprecision, vagueness, and uncertainty. The function's value fell between 0 and 1. Though there was no membership function—that is, only acceptances—in real life, FS theory resolved a great deal of practical issues. In real life, rejection is precisely as important as acceptance. After providing clarification on the issue, Atanassov [2] in 1986 proposed the intuitionistic fuzzy set (IFS) theory, which uses the membership and non-membership functions, the sum of the membership and non-membership grades, which equals 1. This criterion also limits the resolution of inaccurate, ambiguous, and vague problems.

In 2013 Yager [3] has offered Pythagorean fuzzy sets (PFS) as a solution to this problem. Because PFS uses the criterion that the sum of the squares of the membership and non-membership grades must be equal to or less than one, it is more extensive than IFS. PFs is also a particular case

*Corresponding author.
*E-mail address: dimpaljmahanta@gmail.com

This paper was recommended for publication in revised form by Editor-in-Chief Ahmet Selim Dalkilic

Published by Yıldız Technical University Press, İstanbul, Turkey
© Author. This is an open access article under the CC BY-NC license (http://creativecommons.org/licenses/by-nc/4.0/).

of Neutrosophic Set initiated by Smrandache [4] in 2019.In the literature there are many studies on FS, IFS and PFS theories [5-10]. These theories have restrictions in spite of all potential solutions. Limitations include things like not taking the parameterization tool into consideration and how to set the membership function in each specific object. These restrictions make it more difficult for decision-makers to reach the right conclusion throughout the analysis.

A solution to the stated limitations was found when Molodtsov [11] in 1999 presented a novel technique called Soft Set, in which the preferences for each alternative were expressed in separate parameters. According to Molodtsov, there is a lot of room for application of soft set theory in different mathematical fields. Soft set theory is expanding quickly in all directions and finding applications in many mathematical fields. [12,13]. Maji et al. [14], [15,16] defined fuzzy soft sets u (FSS) and intuitionistic fuzzy soft sets (IFSS) in 2001 and 2004 respectively and assessed their various properties. Peng et al. [17] defined the Pythagorean fuzzy soft set (PFSS) in 2015 by fusing PFS and IFSS. In [18] and [19] the key components of PFSS were investigated and applied to a variety of domains, including medical diagnosis and team selection for business investment issues with stocks, etc.

Senapati and Yager [20]implemented the Fermatean fuzzy set in 2020, wherein the membership and non-membership degrees satisfy the condition $0 \leq m_H^3 + n_G^3 \leq 1$. This was a novel concept introduced in the literature that produced superior results in defining uncertainties when compared to the intuitionistic fuzzy set and Pythagorean fuzzy set. In cases where IFS and PFS are unable to support data containing uncertainty, FFS provides decision makers with additional flexibility. By extending the spatial scope of membership and non-membership, the FFS enhances its abilities to describe uncertain information when compared to IFS and PFS.Various FFS attributes, including score and accuracy, are provided by Senapati and Yager [20]. The TOPSIS method, which is often used to handle MCDM problems, has been used to tackle the FFS problem. Furthermore, according to Senapati and Yager, the TOPSIS approach—which is commonly used to address MCDM problems—was used to conduct the FFS. The TOPSIS method, which is commonly used in MCDM issues, has also been applied to FFS, as mentioned by Senapati and Yager [20].

Senapati and Yager [21] carried out this work by delving into a number of new operations, such as the division, subtraction, and Fermatean arithmetic mean operations on FFSs. They also employed the Fermatean fuzzy weighted product model to address MCDM problems. Senapati and Yager [21]in 2019 have defined novel aggregation operators that are a component of the FFS and have examined the attributes that go along with them.

Kirisci [22] introduced the concept of Fermatean fuzzy soft sets (FFSS) along with an entropy measure derived from it. Shahzadi and Akram [23] present a decision support method based on the FFSS notion to increase the efficacy of anti-virus masks.

Whether two sets are sharp, fuzzy, or vague, comparing them is the primary issue in real-world situations. The relevant tools for comparing the similarity of two sets are matching function-based similarity measures and distance measures. Measures of similarity and distance indicate how similar and different something is from another. First, fuzzy set similarity measures were introduced by Wang in 1997 [24]. Researchers have proposed a variety of similarity measures for fuzzy sets, including interval-valued fuzzy sets, intuitionistic fuzzy sets. In 2008 Majumdar and Samanta [25] defined similarity measure for soft set and in 2011 [26] for fuzzy soft sets. Later on it has been extended to IFSS [27], IVFSS [28], PFSS [29]. Among the various structures discussed so far, FFSS [30] being the most generalized one.

As the Fermatean fuzzy soft set is a great tool for handling more than PFSS and IFSS, it is also important to determine the distance similarity. Machine learning, pattern recognition, and distributed memory problems can all be resolved with the help of distance measures. The two most widely used distance measurements are Euclidean and Hamming distances. This article discusses new distance measures based on FFSSs that are employed to quantify uncertain information. These include normalized Euclidean distance, normalized Hamming distance, Fermatean distance, and cosine distance. A comprehensive theoretical background of these distance measures along with a decision-making algorithm has been provided. Examples of validated techniques for medical decision making are offered.

Preliminaries

Here are essential definitions that lay the groundwork for the upcoming discussion.

Soft set

Let $\mathcal{E}$ represents a collection of parameters and let $\mathcal{U}$ denote the universal set. Defined as a pair $(\mathcal{A}, \mathcal{E})$, a soft set (SS) is characterized over $\mathcal{U}$, where $\mathcal{A}$ is a function $\mathcal{A} : \mathcal{E} \rightarrow P_{SS}(\mathcal{U})$ In essence, the SS can be described as a parameterized assortment of subsets of the set $\mathcal{U}$ [18].

Fuzzy soft set

A pair $(\mathcal{A}, \mathcal{E})$ is denoted as a fuzzy soft set over the universal set $\mathcal{U}$ provided that the mapping $\mathcal{A} : \mathcal{E} \rightarrow f(\mathcal{U})$ represents a correspondence from $\mathcal{A}$ to the collection of all fuzzy sets in $\mathcal{U}$, where $f(\mathcal{U})$ denotes the set encompassing all fuzzy subsets of $\mathcal{U}$. [18]

Intuitionistic fuzzy soft set

The notation $If(\mathcal{U})$ is used to represent the intuitionistic fuzzy power set of $\mathcal{U}$, where $\mathcal{A} \subset \mathcal{E}$ An ordered pair $(\mathcal{F}, \mathcal{A})$ is defined as an intuitionistic fuzzy soft set over $\mathcal{U}$ if the function $\mathcal{A} : \mathcal{E} \rightarrow If(\mathcal{U})$ holds [18].

Pythagorean fuzzy soft set

The Pythagorean fuzzy soft set is defined as a pair $(\mathcal{A}, \mathcal{E})$ where $\mathcal{A} : \mathcal{E} \rightarrow P_{PFS}(\mathcal{U})$ represents the collection of Pythagorean fuzzy subsets of $\mathcal{U}$. Within the context of

Pythagorean fuzzy soft sets, it holds that $\mathcal{T}_{\mathcal{P}}^2(a) + \mathcal{I}_{\mathcal{P}}^2(a) \leq 1$ and in cases where $\mathcal{T}_{\mathcal{P}}(a) + \mathcal{I}_{\mathcal{P}}(a) \leq 1$, Pythagorean fuzzy soft sets transition into intuitionistic fuzzy soft sets.[18]

Fermatean fuzzy set

The Fermatean fuzzy set (FS) denoted by $\mathcal{F}$ in the universal set $\mathcal{U}$ can be described as a structured entity defined as $\mathcal{F} = \{< a, \mathcal{T}_{\mathcal{F}(a)} + \mathcal{I}_{\mathcal{F}(a)} >: a \in \mathcal{U}\}$, where the functions $\mathcal{T}_{\mathcal{F}}: \mathcal{U} \to [0,1]$ and $\mathcal{I}_{\mathcal{F}}: \mathcal{U} \to [0,1]$ and adhere to the constraint $0 \leq \mathcal{T}_{\mathcal{F}(a)}^3 + \mathcal{I}_{\mathcal{F}(a)}^3 \leq 1$ [18].

Fermarean fuzzy soft set

Let $\mathcal{U}$ be a set, $\mathcal{E}$ be the set of parameter. $P_{FS}(\mathcal{U})$ the whole of all FSs on $\mathcal{U}$. Let $\mathcal{A} \subset \mathcal{E}$ A pair $(\mathcal{F}, \mathcal{A})$ is called Fermarean fuzzy soft set (FFSS) over $\mathcal{U}$ where $\mathcal{F} : \mathcal{A} \to P_{FS}(\mathcal{U})$. A FSS on $\mathcal{U}$ is a family of parameters formed by some Fermatean fuzzy sub sets on $\mathcal{U}$. For any parameter $\mathcal{E} \in \mathcal{A}$. $\mathcal{F}(\mathcal{E})$ is a FFSS associate with $\mathcal{E}$ of $\mathcal{U}$, then it is called Fermatean fuzzy value set of parameter $\mathcal{E}$. $\mathcal{F}(\mathcal{E})$ can be written as $\mathcal{F}(\mathcal{E}) = \{< a, \mathcal{T}_{\mathcal{F}(\mathcal{E})}(a) + \mathcal{I}_{\mathcal{F}(\mathcal{E})}(a) >: a \in \mathcal{U}\}$

Where $\mathcal{T}_{\mathcal{F}(\mathcal{E})}(a)$ and $\mathcal{I}_{\mathcal{F}(\mathcal{E})}(a)$ are membership and nonmembership functions respectively. The conditions $0 \leq \mathcal{T}_{\mathcal{F}(\mathcal{E})}^3(a) + \mathcal{I}_{\mathcal{F}(\mathcal{E})}^3(a) \leq 1$ holds [18].

Measure of Similarity Based on Distance for Fermatean Fuzzy Soft Sets

The definitions of hamming, Euclidean, Fermatean, and cosine distances between two Fermatean fuzzy soft sets are given in this section. Based on these distances, similarity measures are suggested. Chikungunya is an infectious viral disease that is transmitted to humans through the bites of infected mosquitoes. It manifests with symptoms including fever, joint pain, muscle pain, headache, fatigue, and rash. We construct a Fermatean fuzzy soft set utilizing the observed symptoms. By defining a distance function, we can assess whether a patient is afflicted with chikungunya or not. In this situation, we employ typical Chikungunya patent information to compute the dissimilarity between two typical patents. If the calculated distance approaches zero, the patent is classified as positive for chikungunya. Conversely, if the distance exceeds 0.5, it suggests that the patients may be affected by other conditions.

Definition Let $\mathcal{U} = \{u_1, u_2, u_3 \ldots u_n\}$ be an initial inverse and $\mathcal{E} = \{e_1, e_2, e_3, \ldots, e_m\}$ be the set of parameters. Let $FFS(\mathcal{U})$ denotes the set of all Fermatean fuzzy subsets of $\mathcal{U}$. Also let $(\mathcal{A}, \mathcal{E})$ and $(\mathcal{B}, \mathcal{E})$ be two FFSSs over $\mathcal{U}$, where $\mathcal{A}$ and $\mathcal{B}$ are mappings given by $\mathcal{A}, \mathcal{B}: \to FFS(\mathcal{U})$. Define the following distances between $(\mathcal{A}, \mathcal{E})$ and $(\mathcal{B}, \mathcal{E})$ as follows:

Hamming Distance:

$$HD\{(\mathcal{A},\mathcal{E}),(\mathcal{B},\mathcal{E})\} = \sum_{i=1}^{n}\sum_{j=1}^{m}\left\{\left|\mathcal{T}^3_{\mathcal{A}(e_j)}(x_i) - \mathcal{T}^3_{\mathcal{B}(e_j)}(x_i)\right| + \left|\mathcal{F}^3_{\mathcal{A}(e_j)}(x_i) - \mathcal{F}^3_{\mathcal{B}(e_j)}(x_i)\right|\right\} \quad (1)$$

Normalized Hamming Distance:

$$NHD\{(\mathcal{A},\mathcal{E}),(\mathcal{B},\mathcal{E})\} = \frac{1}{2mn}\sum_{i=1}^{n}\sum_{j=1}^{m}\left\{\left|\mathcal{T}^3_{\mathcal{A}(e_j)}(x_i) - \mathcal{T}^3_{\mathcal{B}(e_j)}(x_i)\right| + \left|\mathcal{F}^3_{\mathcal{A}(e_j)}(x_i) - \mathcal{F}^3_{\mathcal{B}(e_j)}(x_i)\right|\right\} \quad (2)$$

Euclidean Distance:

$$ED\{(\mathcal{A},\mathcal{E}),(\mathcal{B},\mathcal{E})\} = \sqrt{\sum_{i=1}^{n}\sum_{j=1}^{m}|\mathcal{T}^3_{\mathcal{A}(e_j)}(x_i) - \mathcal{T}^3_{\mathcal{B}(e_j)}(x_i)|^2 + |\mathcal{F}^3_{\mathcal{A}(e_j)}(x_i) - \mathcal{F}^3_{\mathcal{B}(e_j)}(x_i)|^2} \quad (3)$$

Normalized Euclidean Distance:

$$NED\{(\mathcal{A},\mathcal{E}),(\mathcal{B},\mathcal{E})\} = \frac{1}{2mn}\sqrt{\sum_{i=1}^{n}\sum_{j=1}^{m}|\mathcal{T}^3_{\mathcal{A}(e_j)}(x_i) - \mathcal{T}^3_{\mathcal{B}(e_j)}(x_i)|^2 + |\mathcal{F}^3_{\mathcal{A}(e_j)}(x_i) - \mathcal{F}^3_{\mathcal{B}(e_j)}(x_i)|^2} \quad (4)$$

Fermatean Distance:

$$FD\{(\mathcal{A},\mathcal{E}),(\mathcal{B},\mathcal{E})\} = \left\{\sum_{i=1}^{n}\sum_{j=1}^{m}|\mathcal{T}^3_{\mathcal{A}(e_j)}(x_i) - \mathcal{T}^3_{\mathcal{B}(e_j)}(x_i)|^2, \sum_{i=1}^{n}\sum_{j=1}^{m}|\mathcal{F}^3_{\mathcal{A}(e_j)}(x_i) - \mathcal{F}^3_{\mathcal{B}(e_j)}(x_i)|^2\right\} \quad (5)$$

Normalized Fermatean Distance:

$$NFD\{(\mathcal{A},\mathcal{E}),(\mathcal{B},\mathcal{E})\} = \left\{\sum_{i=1}^{n}\sum_{j=1}^{m}\frac{1}{mn}|\mathcal{T}^3_{\mathcal{A}(e_j)}(x_i) - \mathcal{T}^3_{\mathcal{B}(e_j)}(x_i)|^2, \frac{1}{mn}\sum_{i=1}^{n}\sum_{j=1}^{m}|\mathcal{F}^3_{\mathcal{A}(e_j)}(x_i) - \mathcal{F}^3_{\mathcal{B}(e_j)}(x_i)|^2\right\} \quad (6)$$

$$= \{\mathcal{T}^-(x_i), \mathcal{F}^-(x_i)\}$$

$$< \mathcal{T}, \mathcal{F} > = \frac{\mathcal{T}^-(x_i)}{\mathcal{T}^-(x_i) + \mathcal{F}^-(x_i)}, \frac{\mathcal{F}^-(x_i)}{\mathcal{T}^-(x_i) + \mathcal{F}^-(x_i)}$$

Cosine Distance:

$$CD\{(\mathcal{A},\mathcal{E}),(\mathcal{B},\mathcal{E})\} = 1 - \text{cosine similatity} \quad (7)$$

Where Cosine similarity

$$= \frac{1}{mn}\sum_{i=1}^{n}\sum_{j=1}^{m}\frac{\mathcal{T}^3_{\mathcal{A}(e_j)}(x_i)\mathcal{T}^3_{\mathcal{B}(e_j)} + \mathcal{F}^3_{\mathcal{A}(e_j)}(x_i)\mathcal{F}^3_{\mathcal{B}(e_j)}}{\sqrt{\mathcal{T}^6_{\mathcal{A}(e_j)}(x_i) + \mathcal{F}^6_{\mathcal{A}(e_j)}(x_i)}\sqrt{\mathcal{T}^6_{\mathcal{A}(e_j)} + (x_i)\mathcal{F}^6_{\mathcal{B}(e_j)}(x_i)}}$$

We have established three distance functions to gauge the dissimilarity between two patients with chikungunya. If the calculated distances fall below 0.5, we conclude both have a similar condition; otherwise, if distances exceed 0.5, their conditions may differ. For Fermatean distance, when $\mathcal{T} > \mathcal{F}$, the decision favors the true membership value.

Application on Chikungunya

We develop a decision-making approach utilizing the similarity measure of two Fermatean fuzzy soft sets. This measure is instrumental in assessing the likelihood of an individual with specific symptoms being ill. We employ

various distance measures such as Normalized Hamming Distance, Normalized Euclidean Distance, and cosine distance for this estimation process. Determining whether someone has chikungunya involves creating Fermatean fuzzy soft sets for both the disease and the individual's symptoms. By assessing the similarity measure between these sets, if it's below 0.5, it indicates a likelihood of the individual having chikungunya. Conversely, a similarity measure equal to or greater than 0.5 suggests the person is unlikely to have the disease.

Proposed approach

1. A Fermatean fuzzy soft set is formulated to represent disease characteristics across the universal set $\mathcal{U}$, leveraging insights from medical experts.
2. A Fermatean fuzzy soft set is established across the universe $\mathcal{U}$ in the context of a patient application.
3. To assess the dissimilarity between a Fermatean fuzzy soft set for disease and a Fermatean fuzzy soft set for patients, compute the Hamming Distance, Euclidean Distance, Cosine Distance, and Fermatean Distance.
4. Determine similarity measure between them.
5. Assess the outcome by applying similarity measures.

The flowchart of the proposed approach is given in the following Figure 1.

Example 1 Here, we present an illustration of a decision-making approach within a Fermatean fuzzy soft set context employing a similarity measure.

We choose an exemplary case, such as a patient afflicted with Chikungunya. By comparing the similarity between suspected patients and this ideal case, doctors can swiftly diagnose the disease. This approach facilitates expedited medical decision-making and fosters a supportive environment for patient care.

Let us consider a patient who was suffering from Chikungunya. Using Chikungunya patient data we will decide for a set of new patients, $\mathcal{P}_1$, $\mathcal{P}_2$, $\mathcal{P}_3$ and universal set $\mathcal{U} = \{x_1, x_2, x_3\}$ and $\mathcal{E} = \{e_1, e_2, e_3, e_4\}$ be the set of parameters. Consider $(\mathcal{A}, \mathcal{E})$, $(\mathcal{A}, \mathcal{P}_1)$, $(\mathcal{A}, \mathcal{P}_2)$, $(\mathcal{A}, \mathcal{P}_3)$ are four Farmatean fuzzy soft sets over $\mathcal{U}$ Here $\mathcal{A}$ is known person. We have to calculate the distance of $\mathcal{P}_i$ from $\mathcal{A}$ Tabular represention of $(\mathcal{A}, \mathcal{E})$, $(\mathcal{P}_1, \mathcal{E})$, $(\mathcal{P}_2, \mathcal{E})$ and $(\mathcal{P}_3, \mathcal{E})$ are presented in the Table 1, Table 2, Table 3 and Table 4 respectively.

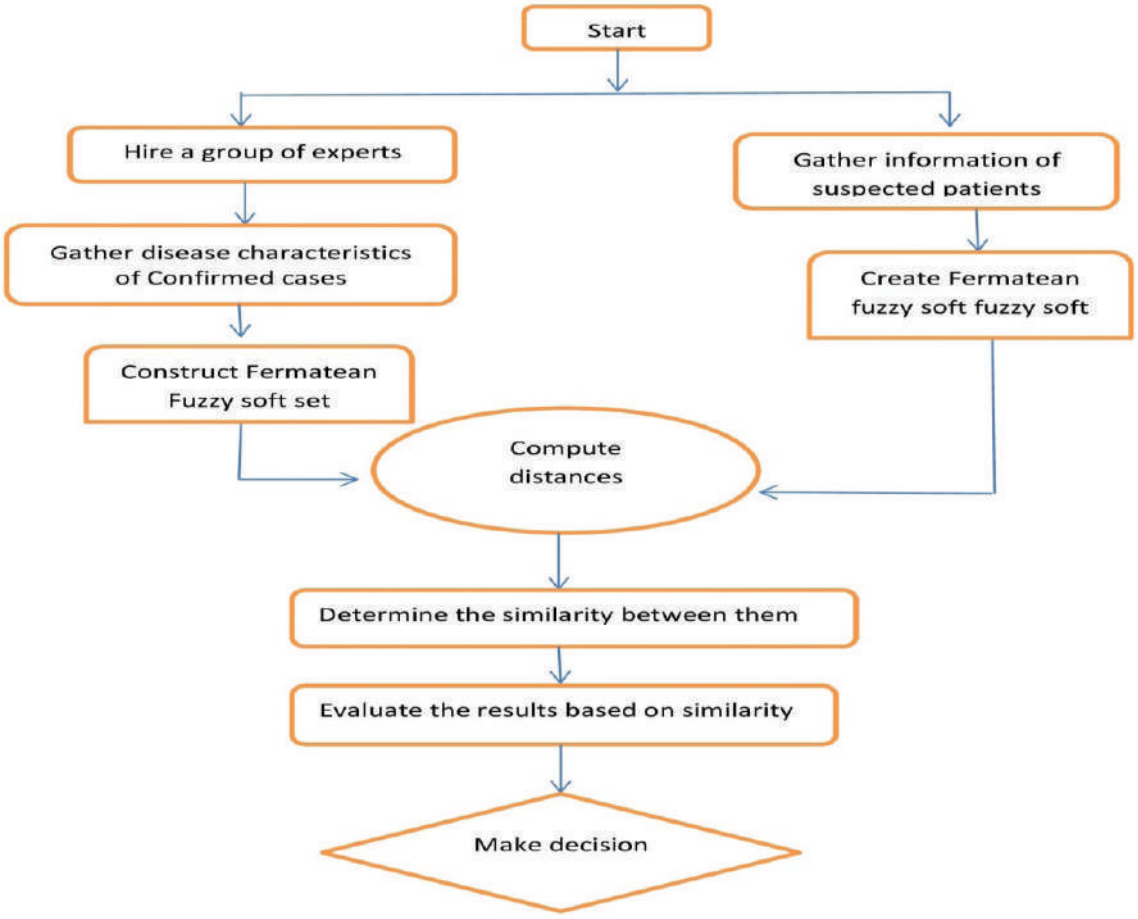


Figure 1. Flow chart of proposed approach

Table 1. Tabular representation of set $(\mathcal{A}, \mathcal{E})$

$(\mathcal{A}, \mathcal{E})$	Fever (e_1)	Headache (e_2)	Join pain (e_3)	Rash (e_4)
x_1	(1, 0)	(1, 0)	(1, 0)	(1, 0)
x_2	(1, 0)	(1, 0)	(1, 0)	(1, 0)
x_3	(1, 0)	(1, 0)	(1, 0)	(1, 0)

Table 2. Tabular representation of set $(\mathcal{P}_1, \mathcal{E})$

$(\mathcal{P}_1, \mathcal{E})$	Fever (e_1)	Headache (e_2)	Join pain (e_3)	Rash (e_4)
x_1	(0.7, 0.5)	(0.6, 0.4)	(0.8, 0.6)	(0.4, 0.2)
x_2	(0.6, 0.6)	(0.5, 0.5)	(0.7, 0.7)	(0.3, 0.3)
x_3	(0.8, 0.4)	(0.7, 0.3)	(0.9, 0.5)	(0.5, 0.1)

NHD = 0.408, *NED* = 0.107, *CD* = 0.121, *NFD* = (0.86,0.137), *NFD* = (0.86,0.137)

Table 3. Tabular representation of set $(\mathcal{P}_2, \mathcal{E})$

$(\mathcal{P}_2, \mathcal{E})$	Fever (e_1)	Headache (e_2)	Join pain (e_3)	Rash (e_4)
x_1	(0.8, 0.6)	(0.7, 0.5)	(0.6, 0.4)	(0.5, 0.3)
x_2	(0.8, 0.7)	(0.7, 0.6)	(0.6, 0.5)	(0.5, 0.4)
x_3	(0.9, 0.5)	(0.8, 0.4)	(0.7, 0.3)	(0.6, 0.2)

NHD = 0.383, *NED* = 0.100, *CD* = 0.074, *NFD* = (0.846,0.153)

Table 4. Tabular representation of set $(\mathcal{P}_3, \mathcal{E})$

$(\mathcal{P}_3, \mathcal{E})$	Fever (e_1)	Headache (e_2)	Join pain (e_3)	Rash (e_4)
x_1	(0.9, 0.6)	(0.8, 0.5)	(0.7, 0.4)	(0.6, 0.3)
x_2	(0.8, 0.7)	(0.7, 0.6)	(0.6, 0.5)	(0.5, 0.4)
x_3	(0.8, 0.6)	(0.7, 0.5)	(0.6, 0.4)	(0.5, 0.3)

NHD = 0.396, *NED* = 0.100, *CD* = 0.085, *NFD* = (0.821,0.178)

Calculation of Normalized Hamming Distances

By (2) Normalized Hamming Distances between $\mathcal{A}$ and $\mathcal{P}_1, \mathcal{P}_2, \mathcal{P}_3$ are as

$$NHD(\mathcal{A}, \mathcal{P}_1) = 0.408, NHD(\mathcal{A}, \mathcal{P}_2) = 0.383, NHD(\mathcal{A}, \mathcal{P}_3) = 0.396$$

According to equation (2) the decision by the above distance the patients $\mathcal{P}_1, \mathcal{P}_2, \mathcal{P}_3$ are Chikungunia positive.

Calculation of Normalized Euclidean Distances

By (4) Normalized Euclidean Distances between $\mathcal{A}$ and $\mathcal{P}_1, \mathcal{P}_2, \mathcal{P}_3$ are as

$$NED(\mathcal{A}, \mathcal{P}_1) = 0.107, NED(\mathcal{A}, \mathcal{P}_2) = 0.100, NED(\mathcal{A}, \mathcal{P}_3) = 0.100$$

According to equation (4) the decision by the above distance the patients $\mathcal{P}_1, \mathcal{P}_2, \mathcal{P}_3$ are Chikungunia positive.

Calculation of Cosine Distances

By (7) Cosine Distances between $\mathcal{A}$ and $\mathcal{P}_1$, P_2, P_3 are as

$$NED(\mathcal{A}, \mathcal{P}_1) = 0.121, NED(\mathcal{A}, \mathcal{P}_2) = 00.074, NED(\mathcal{A}, \mathcal{P}_3) = 0.085$$

According to equation (7) the decision by the above distance the patients $\mathcal{P}_1, \mathcal{P}_2, \mathcal{P}_3$ are Chikungunia positive.

Calculation of Normalized Fermatean Distances

By (6) Normalized Fermatean Distances between $\mathcal{A}$ and $\mathcal{P}_1, \mathcal{P}_2, \mathcal{P}_3$ are as

$$NFD(\mathcal{A}, \mathcal{P}_1) = (0.86,0.137), NFD(\mathcal{A}, \mathcal{P}_2) = (0.846,0.153),$$
$$NFD(\mathcal{A}, \mathcal{P}_3) = (0.821,0.178)$$

According to equation (6) the decision by the above distance the patients $\mathcal{P}_1, \mathcal{P}_2, \mathcal{P}_3$ are Chikungunia positive.

After the calculation of Normalized Hamming Distances, Normalized Euclidean Distances, Cosine Distances and Normalized Fermatean Distances we find that the patients $\mathcal{P}_1, \mathcal{P}_2, \mathcal{P}_3$ are all Chikungunia positive.

RESULTS AND DISCUSSION

This research focuses on using Fermatean fuzzy soft sets, along with several normalized distance methods, to help diagnose infectious diseases, especially chikungunya. The study looks at different distance measures—such as Fermatean, Hamming, and Euclidean—to find out which one works best for diagnosing diseases, especially when the data isn't completely clear or consistent. Compared with earlier fuzzy set models like intuitionistic and Pythagorean sets, the Fermatean fuzzy approach gives researchers and doctors more flexibility in making judgments that reflect real situations. New distance function can effectively group patients based on their symptoms, improving how diagnoses are made is one of the key outcome of this study. Specifically, a distance close to zero suggests a positive chikungunya diagnosis, while a distance greater than 0.5 indicates alternative conditions. After determination of Normalized Hamming Distances, Normalized Euclidean Distances, Cosine Distances and Normalized Fermatean Distances we find that the patients $\mathcal{P}_1, \mathcal{P}_2, \mathcal{P}_3$ are all Chikungunia positive. When normalized distance measures are applied within the Fermatean fuzzy soft set (FFS) framework, medical diagnosis systems tend to become more accurate and dependable, according to the study's comparison. The results also show that including FFS in medical decision-making tools could help improve how infectious diseases are identified. These findings support the view that pairing Fermatean fuzzy soft sets with the right distance methods can help doctors and researchers make better decisions in uncertain medical conditions, while also giving space for more work to be done in this area.

CONCLUSION

When different distance measures were applied within the FFSS framework, the study found noticeable improvements in how precisely and consistently diagnoses were made. This combination not only raised the level of accuracy but also made the medical diagnostic process more dependable overall. In short, integrating these distance measures helped the system perform better and increased confidence in its diagnostic results.The case of Chikungunya illustrated how this approach can be used effectively in real healthcare situations, showing its practical value.

The results indicate that FFSS could be a useful tool in medical decision-support systems, particularly when the available data is uncertain or incomplete. This opens up space for more research into how FFSS can be applied to other medical areas and decision-making problems. Overall, the work shows that combining Fermatean fuzzy soft sets with normalized distance measures can make diagnostic processes more efficient and help improve patient outcomes.

AUTHORSHIP CONTRIBUTIONS

Authors equally contributed to this work.

DATA AVAILABILITY STATEMENT

The authors confirm that the data that supports the findings of this study are available within the article. Raw data that support the finding of this study are available from the corresponding author, upon reasonable request.

CONFLICT OF INTEREST

The author declared no potential conflicts of interest with respect to the research, authorship, and/or publication of this article.

ETHICS

There are no ethical issues with the publication of this manuscript.

STATEMENT ON THE USE OF ARTIFICIAL INTELLIGENCE

Artificial intelligence was not used in the preparation of the article.

REFERENCES

[1] Zadeh LA. Fuzzy sets. Inf Comput 1965;8:338–353. [CrossRef]

[2] Atanassov KT. Intuitionistic fuzzy sets. Heidelberg: Physica-Verlag; 1999. [CrossRef]

[3] Yager RR. Pythagorean membership grades in multicriteria decision making. IEEE Trans Fuzzy Syst 2013;22:958–965. [CrossRef]

[4] Smarandache F. Neutrosophic set is a generalization of intuitionistic fuzzy set, inconsistent intuitionistic fuzzy set, pythagorean fuzzy set, spherical fuzzy set, and q-rung orthopair fuzzy set, while neutrosophication is a generalization of regret theory, grey system theory, and three-ways decision revisited. J New Theory 2019;29:1–31. [CrossRef]

[5] Das R, Mukherjee A, Tripathy BC. Application of neutrosophic similarity measures in covid-19. Ann Data Sci 2022;9:55–70. [CrossRef]

[6] Garg H. A new generalized pythagorean fuzzy information aggregation using einstein operations and its application to decision making. Int J Intell Syst 2016;31:886–920. [CrossRef]
[7] Garg H. A novel correlation coefficients between pythagorean fuzzy sets and its applications to decision-making processes. Int J Intell Syst 2016;31:1234–1252. [CrossRef]
[8] Garg H. Some series of intuitionistic fuzzy interactive averaging aggregation operators. SpringerPlus 2016;5:999. [CrossRef]
[9] Peng XD, Yang Y. Multiple attribute group decision making methods based on pythagorean fuzzy linguistic set. Comput Eng Appl 2016;52:50–54.
[10] Peng X, Selvachandran G. Pythagorean fuzzy set: state of the art and future directions. Artif Intell Rev 2019;52:1873–1927. [CrossRef]
[11] Molodtsov D. Soft set theory—first results. Comput Math Appl 1999;37:19–31. [CrossRef]
[12] Herawan T, Deris MM. A soft set approach for association rules mining. Knowl Based Syst 2011;24:186–195. [CrossRef]
[13] Xiao Z, Gong K, Zou Y. A combined forecasting approach based on fuzzy soft sets. J Comput Appl Math 2009;228:326–333. [CrossRef]
[14] Maji PK, Biswas R, Roy AR. Fuzzy soft sets. J Fuzzy Math 2001;9:589–602.
[15] Maji PK, Roy AR, Biswas R. Intuitionistic fuzzy soft sets. J Fuzzy Math 2001;9:677–692.
[16] Maji PK, Roy AR, Biswas R. On intuitionistic fuzzy soft sets. J Fuzzy Math 2004;12:669–684.
[17] Peng X, Yang Y, Song J, Jiang Y. Pythagorean fuzzy soft set and its application. Comput Eng 2015;41:224–229.
[18] Athira TM, John SJ, Garg H. Entropy and distance measures of pythagorean fuzzy soft sets and their applications. J Intell Fuzzy Syst 2019;37:4071–4084. [CrossRef]
[19] Athira TM, John SJ, Garg H. A novel entropy measure of pythagorean fuzzy soft sets. AIMS Math 2020;5:1050–1061. [CrossRef]
[20] Senapati T, Yager RR. Fermatean fuzzy sets. J Ambient Intell Human Comput 2020;11:663–674. [CrossRef]
[21] Senapati T, Yager RR. Fermatean fuzzy weighted averaging geometric operators and its application in multi-criteria decision-making methods. Eng Appl Artif Intell 2019;85:112–121. [CrossRef]
[22] Kirisci M. New entropy and distance measures for fermatean fuzzy soft sets with medical decision-making and pattern recognition applications. Research Square. Preprint. 2022. doi: 10.21203/rs.3.rs-1796355/v1 [CrossRef]
[23] Shahzadi G, Akram M. Group decision-making for the selection of an antivirus mask under fermatean fuzzy soft information. J Intell Fuzzy Syst 2021;40:1401–1416. [CrossRef]
[24] Wang WJ. New similarity measures on fuzzy sets and on elements. Fuzzy Sets Syst 1997;85:305–309. [CrossRef]
[25] Majumdar P, Samanta SK. Similarity measure of soft sets. New Math Nat Comput 2008;4:1–12. [CrossRef]
[26] Majumdar P, Samanta SK. On similarity measures of fuzzy soft sets. Int J Adv Soft Comput Appl 2011;3:1–8.
[27] Çağman N, Deli I. Similarity measures of intuitionistic fuzzy soft sets and their decision making. arXiv 2013;1301.0456.
[28] Sonia PT, Gupta P. Innovative similarity distance and entropy measures for interval-valued fuzzy soft set. J Intell Fuzzy Syst 2022;43:3067–3086. [CrossRef]
[29] Athira TM, John SJ, Garg H. Similarity measures of pythagorean fuzzy soft sets and clustering analysis. Soft Comput 2023;27:3007–3022. [CrossRef]
[30] Kirisci M. Measures of distance and entropy based on the fermatean fuzzy-type soft sets approach. Univ J Math Appl 2023;7:12–29. [CrossRef]

Sigma Journal of Engineering and Natural Sciences
Web page info: https://sigma.yildiz.edu.tr
DOI: 10.14744/sigma.2025.00027

Research Article

Centralized controller-based on optimal power flow (OPF) algorithm for power management in microgrid systems

Abumuslim KHUJAEV[1,*], Abbas UĞURENVER[1]

[1]*Institute of Graduate Studies, Department of Electrical and Electronic Engineering, Istanbul Aydın University, Istanbul, 3472945, Türkiye*

ARTICLE INFO

Article history
Received: 06 July 2024
Revised: 21 August 2024
Accepted: 22 October 2024

Keywords:
Centralized Controller; Renewable Energy; Microgrid System; Optimal Power Flow; Power Management; Solar PV

ABSTRACT

The advent of renewable energy sources and their power management in microgrid (MG) systems have seen significant changes recently. Efficient and reliable power management is one of the key strategies in developing microgrid systems. This paper studies and analyzes the microgrid system with an optimal power flow (OPF) algorithm-based power management method. The proposed OPF will work as a centralized controller, enhance the switching between energy sources, dynamic loads, batteries and main grid to ensure efficient, reliable and sustainable power management and enhanced performance for the microgrid system. Microgrids are technologically advanced systems that are incorporated with different types of energy sources which connect and disconnect the sources with the main grid based on the system condition. In other hand, microgrids with uncontrollable energy sources and loads can have variation in power flow. The rapid changes in the system will lead to poor power quality. The system contains a solar PV, a battery energy storage system (BESS), an electric vehicle (EV), main grid and dynamic loads. optimal power flow receives inputs from microgrid system and target output to optimize stability, reliability and efficiency in power quality. Simulations were carried out based on MATLAB/Simulink and the OPF used as a centralized controller and the results obtained enhanced the power quality of microgrid systems. The system was analyzed in three different scenarios, in normal condition, abnormal condition of solar PV and abnormal condition of batteries. Hence, the proposed OPF enhanced the power quality, optimized performance of switching between energy sources and main grid.

Cite this article as: Khujaev A, Uğurenver A. Centralized controller-based on optimal power flow (OPF) algorithm for power management in microgrid systems. Sigma J Eng Nat Sci 2025;43(6):2279–2293.

INTRODUCTION

In today's rapidly growing world, the production of electricity increased significantly due to industrialization, population growth, and high demand for electrical power for electric appliances. Electricity is generated from a range of energy sources, such as coal, natural gas, and renewable energy sources <] analyzed a multi-level inverter based

*Corresponding author.
*E-mail address: abumuslimkhujaev@stu.aydin.edu.tr

This paper was recommended for publication in revised form by Editor-in-Chief Ahmet Selim Dalkilic

Published by Yıldız Technical University Press, İstanbul, Turkey
© Author. This is an open access article under the CC BY-NC license (http://creativecommons.org/licenses/by-nc/4.0/).

three-phase system during dynamic load condition. The controller is developed to supply real power even with the variation happened in voltage and current. The proposed method promised enhanced performance at DC voltage level. Moreover, theoretical model was evaluated with real time data. A DC-DC boost buck converter is a crucial component of the power system which has a MOSFET switch, traditional buck converter, capacitors and inductors. Author in [30] proposed a technique that is more reliable than the conventional converter. The proposed method had better result in terms of switching frequency and dynamic load. Another article used bidirectional buck-boost converter to improve dc voltage for the grid system [31]. This is done by minimizing the inductor current and inductor current ripple. The experimental results showed better results than the conventional type of buck boost converter. Hence, the controller was not used in an AC/DC microgrid system.

Author in [32] presented an optimal power flow (OPF) controller used in hybrid microgrids. The author claimed that the plugging and un-plugging of appliances can penetrate the flow of power in the system. Especially during islanded mode, the appliances require fast response to overcome the variation in voltage and current of the loads. Therefore, the MG system require steady state stability by employing OPF to operate efficiently. The proposed technique is used in an AC/DC system to maximize its control strategy and overcome economic challenges in the future. Another author has examined the issues and challenges encountered by power systems over the past decade [33]. The author used grey wolf optimization technique to have robust control over microgrid system. The system included diesel, engine solar PV, and battery systems. The proposed method offers an improved dispatching technique for loads and sources, ensuring an economical power supply while minimizing reliance on the main grid. MATLAB/Simulink is used to validate results. However, the author did not study the OPF algorithm in real time to see if it can improve the performance of the microgrid system. A non-linear controller for renewable energy sources were studied in a DC microgrid systems. Author claimed that the conventional PI controller used in MG systems was short in providing robust control and stable power distribution in the system [34]. Moreover, interconnection damping assessment-passivity based controller (IDA-PBC) is employed to regulate the DC-link of the system. The proposed controller was tested in three different conditions and experimental results were presented. Hence, the controller was not used in AC/DC microgrids.

Summary

The following Table 1 presents the comparison of different controllers used in microgrid system.

For the basis of the following paper, the optimal power flow algorithm-based power management strategy, performance of an AC/DC hybrid microgrid, renewable energy source, and energy storage system were studied. The study was conducted accordingly, and I present my acknowledgement to authors who contributed to developing hybrid microgrid systems. Referring to the above studies there were several controlling techniques to enhance power flow and managing microgrid systems. Many articles used controllers and converters to improve performance of the power system. Moreover, switching techniques between grid-connected and islanded modes were seen in some of the studies. An article studied the AC/DC microgrid system powered by DC power sources [37]. However, the author did not implement real-time values to show correctness of the controller in real-time scenarios. Overall, the summary of the research focused on developing controllers to maintain optimal power flow in microgrid systems. However, several challenges in AC/DC microgrid systems remain unaddressed by the authors cited in the literature review. The AC/DC hybrid microgrid system requires renewable energy sources and backup batteries to support the grid during periods of low solar PV irradiance. It also needs the capability to switch between grid-connected and islanded modes and a centralized controller to always manage the switching. The issues must be addressed, and proper component selection is essential. An optimal power flow algorithm-based power management is required to achieve enhanced power flow in microgrids. In this paper the research is going to achieve the following items. This paper aims to achieve the following objectives.

1. Creating an AC/DC microgrid system.
2. Identifying sources and loads for the system.
3. Identifying values for the loads and sources.
4. Connecting a three-phase circuit breaker between main grid and microgrid system.
5. Analyzing the performance of the system with existing components.
6. Integrating Three-phase stand-alone inverter control design with PI controller to generate PWM signal for the switch.
7. Integrating bidirectional converters in DC sources to boost voltage regulation to a desired voltage level.
8. Integrating a centralized controller to control and provide optimal power flow to the hybrid microgrid system.
9. Analyze the effect of OPF centralized controller in three conditions such as normal condition, solar irradiance abnormal condition and batteries abnormal condition.

Microgrid System

Microgrids normally consist of loads, solar PV, battery energy storage system, electric vehicle, main grid, and they are designed to work in grid connected and islanded modes [38]. The solar PV incorporates DC-DC boost converter to boost the voltage level to a desired voltage level [39]. One of the main characteristic of MG is that they can support the MG by balancing the loads with renewable energy sources, they will be connected to the grid when the sources are not able to deliver enough power. Furthermore, when the MG is connected to the main grid it is called grid connected

Table 1. Comparison of different controllers

Ref	Controller	Disturbance	Electrical Network	Remark
[24]	GA/AC OPF Algorithm	Operational challenges of the microgrids	AC/DC microgrid	Capable of catching variation to provide enhanced power flow
[26]	Hybrid power-sharing control	Low-frequency power oscillations and dynamic load behavior	DC microgrid	Damping low-frequency oscillation
[28]	UCS	Switching challenges in islanded mode	Distributed generation (DG) network	Improved performance in grid-connected/islanded modes with no need for switching
[21]	Buck-boost converter	Voltage balancing and losses	6S1P battery pack	Showed high balancing efficiency
[35]	MPPT incorporates with a TLBC	Output voltage distortion, inductor current ripple and switching losses	PV system	Optimal power extraction from solar PV system
[31]	Bidirectional buck-boost converter	Inductor current ripple	B3CFIDC	Robust control over dc-dc voltage and current distribution
[34]	A non-linear control structure	Power losses	DC microgrid	Super-capacitor voltage regulation
[30]	DC-DC buck-boost converter	Uncertainties in microgrid systems	DC system	Better conversion ability compared to conventional controllers
[23]	Multi-stage PD(1+PI) controller	Voltage and load variation	Buck converter system	Showed better result than other buck converters
[29]	MLI	Unstable real power across the DC-link components	AC/DC microgrid system	Higher efficiency than the other types of controllers
[18]	VSC	Voltage variation during islanded mode	AC/DC microgrid system	The controller was able to provide desired voltage level even when the sources have changes
[32]	OPF	variation in load/source values when the system changes from one mode to another mode	38-bus AC/DC hybrid microgrids	more effective in hybridizing AC distribution systems
[20]	SLC	Fluctuation during dynamic load behavior	AC/DC hybrid microgrids	Maximizes efficiency for a solar PV and BESS
[19]	FCS-MPC	Uncertainties due to the loads and sources	AC/DC microgrid	Better voltage regulation in grid-connected and islanded modes
[36]	SUDC	Synchronization issues in power distribution	SUDC	The controller is capable of voltage regulation in bot grid-connected and islanded mode
[27]	DWT	IGBT switch breakdown failure	Equivalent boost converter circuit with MPPT	Enhanced performance in Microgrid system

mode, but when it is disconnected from the main grid it is called islanded mode and it connect/disconnect with a switch [40]. The reason to keep MG disconnected from the main grid is because of the disturbances, fault, and poor power quality and voltage/current fluctuation in the main grid. In islanded mode the MG enables enhanced power quality, reduces power losses, and improved system efficiency [41]. There are AC, DC and hybrid MG (AC/DC) MG systems. Depending on the requirements of the sources used, and types of loads one need to choose what type of MG is suitable for their design. For only DC components a DC MG is suitable to include, for AC loads and AC sources one should use AC MG system. However, when having the mixture of DC and AC energy sources and loads one should use hybrid MG system [42]. A hybrid MG contains one DC bus and one AC bus, and all the AC/DC sources and loads are connected through AC/DC buses depending on their configuration. The benefits of using hybrid MG is that it minimizes the use of too many converters and buses and it ensures cost effective design [43].

A MG normally incorporates energy sources, loads and energy storage systems. For a typical MG systems energy sources are located close to the residents. Solar PV, BESS, EV are examples of the distributed energy resources (DER) s [44, 45]. Therefore, DER located close to the users will help the system to lower the amount of power losses. The power generation by only solar PV system is unpredictable. Therefore, it is essential to include ESS systems to ensure

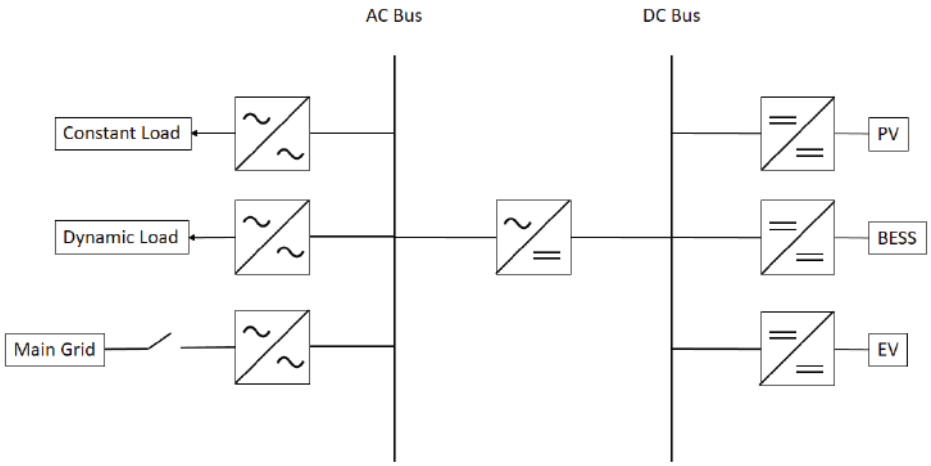


Figure 1. The hybrid microgrid model.

Table 2. The nominal values for the AC and DC buses, frequency and nominal voltage for the MG

Item	Nominal value
$freq_n$	50 Hz
AC V_n	400 V
DC V_n	400 V
R_{grid}	1.8
L_{grid}	4 μH

reliability in the MG [46]. In case of high-power generation by the solar PV the ESS systems allows charging and discharge when the power generation is low or the electricity tariffs are high. There are many types of ESS to store energy and one of the common used batteries are lithium-ion batteries. The MG includes a dynamic load and a constant load. Figure 1 shows the type of MG system used in this paper. The actual design of the MG system is shown in Appendix 1.

The MG model was built and tested in MATLAB/Simulink and some nominal values presented in Table 2.

The solar PV is used as an energy source that supply power to MG. The solar PV array delivers maximum power point of 218.871 W. The power generation by a solar panel is highly dependent on solar irradiance (SI), the normal level for a solar PV is 1000 W/m^2. In this paper the temperature is neglected. The formula for solar PV is given in equation 1. To increase the total power generated from solar PV, it is necessary to expand the number of solar panels to the desired amount, as illustrated in equation 2 [47, 48].

$$P_{module} = \frac{Solar\ Irradiance\ (\frac{W}{m^2})}{1000\ (W)} \times Maximum\ Power\ (W) \quad (1)$$

$$Total\ P_{pv} = Parallel\ strings \times Series - connected\ modules\ per\ string \times P_{module} \quad (2)$$

The nominal value for solar PV is shown in Table 3.

Table 3. Specifications of solar PV panel

Item	Value
P_{module}	218.871
Parallel strings	6
Series-connected modules per string	15

The battery storage system includes a lithium-ion battery and the specifications for the battery are given in Table 4.

Table 4. Specifications of BESS battery

Item	Value
Nominal voltage (V)	120
Rated Capacity (Ah)	180
Initial state-of-charge (%)	50
Battery response time (s)	0.1

The EV source includes a lithium-ion battery and the specifications are given in Table 5.

Table 5. Specifications of EV source

Item	Value
Nominal voltage (V)	120
Rated Capacity (Ah)	180
Initial state-of-charge (%)	50
Battery response time (s)	0.1

The constant load and dynamic load values are mentioned in Table 6. The dynamic loads fluctuated based on the demand changes throughout the day.

Table 6. Specifications of the constant load and dynamic load.

Item	Value
Constant load (W)	8000
Dynamic load (W)	5000~10000

Optimal Power Flow

The MG power management works based on OPF model and the OPF works as a centralized controller to enhance the efficiency and reliability of the MG system. The centralized controller receives information from MG, process it and gives reference current to EV and connect/disconnects the switch in MG system. The OPF model is used to reduce excess power losses and costs for the system. There many types of OPF can be used to calculate the output and process it in the MG. However, to measure the values throughout the day, dynamic load changes, dynamic solar irradiance and other components makes the analysis quiet challenging. Therefore, this paper analyzes the MG system in MATLAB/Simulink with linear programming codes to enhance the performance of the system. The inputs and the outputs for the centralized controller based on OPF is shown in Figure 2. The simulation run for 2.4 seconds as the system takes long time to run if the simulation time increases. 2.4 seconds considered as 24 hour or a day.

Flow chart chart of the optimal power flow algorithm

The paper's OPF is built to minimize the power losses and always keep THE MG at its maximal stable condition. Initially the working condition of MG is examined and then the predictions and OPF values are studied. The OPF and prediction values from time t were sampled then prediction values t+Δt , were predicted. The values that were sampled were solar irradiance PV, loads, BESS and state of charge of electric vehicle. The optimized value for the output includes grid switch and reference current for the EV. The flow chart of the centralized controller for microgrid power management is presented in Figure 3.

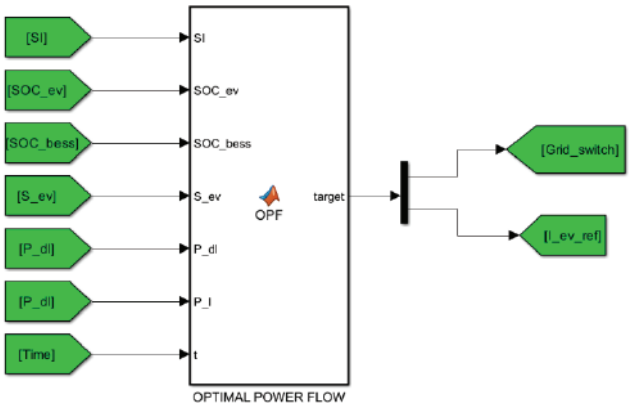


Figure 2. Centralized controller based on OPF algorithm.

Microgrid components and their function

The following Table 7 shows how the system works to process in OPF algorithm and maintain its efficient performance.

The OPF function in isnladed mode

The aim of the OPF is to minimize the power difference between the power generated and load demand. The total power generated from energy sources were summed and the loads were summed at every hours. The total load power then was subtracted from total source power to show the minimum result to keep the Microgrid in islanded mode. In islanded mode, the net power indicates that the generated power is greater than the load demand. The formulas are presented in equation 3, equation 4, and equation 5. The BESS power, and EV power are dependent on SOC charge percentage. If state of charge is zero both the batteries cannot deliver any power to the microgrid system.

$$P_G = P_{pv} + (P_{bess} \times SOC_{bess}) + (P_{ev} \times SOC_{ev}) \quad (3)$$

$$P_L = P_{dl} + P_{cl+}P_{losses} \quad (4)$$

$$P_{net} = P_G - P_L \quad (5)$$

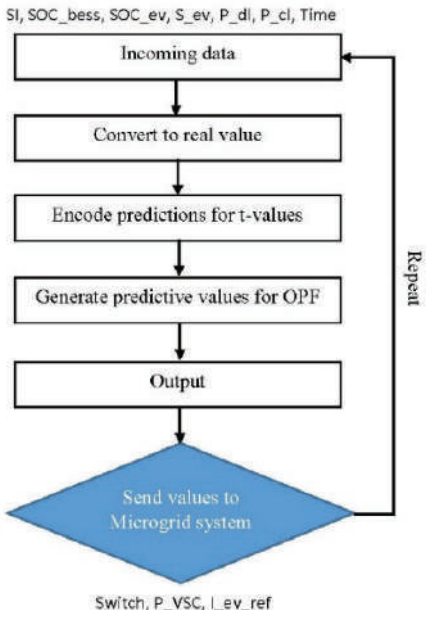


Figure 3. The flow chart of the centralized controller for microgrid power management.

Table 7. Shows the working principles of the MG components

Grid Switch	It is only closed and ensures the MG to supply itself from PV, BESS and EV sources as much as it can. It is only closed when the power generated by the PV, BESS and EV cannot supply enough power is lower than the loads power in the MG. Therefore, the disturbances are neglected in the OPF.
Solar PV	The solar PV generates power based on solar irradiance throughout the day. It does not supply power to the MG when the switch is in grid connected mode. Moreover, the temperature is not considered is this paper.
BESS	The BESS can charge from PV panel and it does not supply any power when the MG is in grid connected mode.
EV	The EV battery connect/disconnect from the MG. In grid connected mode it does not supply any power to the MG.
Constant Load	It is constant.
Dynamic Load	The dynamic load fluctuates during the day.

Table 8. State of charge for BESS and EV batteries

Item	Value
SOC_{BESS} (min)	1%
SOC_{BESS} (max)	99%
SOC_{EV} (min)	1%
SOC_{EV} (max)	99%

The limitations for the state of charge for BESS battery, EV battery, and maximum power for BESS battery, and EV battery are presented in equation 6-9. The system must not cross this limits. The maximum power for both the BESS battery, and EV batteries are 9kW. The maximum state of charge of BESS battery and the minimum state of charge for BESS battery is presented in Table 15. The maximum state of charge of EV battery and the minimum state of charge for EV battery is also presented in Table 8.

$$SOC_{BESS}\,(\min) \le SOC_{BESS} \le SOC_{BESS}\,(\max) \quad (6)$$

$$SOC_{EV}\,(\min) \le SOC_{EV} \le SOC_{EV}\,(\max) \quad (7)$$

$$-P_{BESS}\,(\min) \le P_{BESS} \le P_{BESS}\,(\max) \quad (8)$$

$$-P_{EV}\,(\min) \le P_{EV} \le P_{EV}\,(\max) \quad (9)$$

The output control values are presented as in formula 10.

$$Target\ (Output) = Switch, P_{VSC}, I_EV_REF \quad (10)$$

The OPF function in grid connected mode

In grid connected mode, the microgrid does not take power from DC bus sources. As in islanded mode, the measurements will be differentiated, and the results will dictate which parameters need to be controlled in the output. The system is grid-connected when the generated power from the DC bus is less than the load demand.

The formulas are presented in equation 11, equation 12, and equation 13. Moreover, when the system is grid connected, the BESS battery charge itself from solar PV panel power generation. The EV battery do not discharge when it is disconnected from the system nor it charges. It only works by receiving reference current from the OPF controller.

$$P_G = P_{pv} \quad (11)$$

$$P_L = P_{dl} + P_{cl+}P_{losses} \quad (12)$$

$$P_{net} = P_G - P_L \quad (13)$$

The system limitations are presented in equation 14-17. The system must not cross this limits to remain at grid connected mode.

$$SOC_{BESS}\,(\min) \le SOC_{BESS} \le SOC_{BESS}\,(\max) \quad (14)$$

$$SOC_{EV}\,(\min) \le SOC_{EV} \le SOC_{EV}\,(\max) \quad (15)$$

$$-P_{BESS}\,(\min) \le P_{BESS} \le P_{BESS}\,(\max) \quad (16)$$

$$-P_{EV}\,(\min) \le P_{EV} \le P_{EV}\,(\max) \quad (17)$$

Predictions of time varying components

Microgrid system is simulated based on time varying data. Thus, it is necessary to make predictions to make the system to work more effectively, provide the most accurate result for the outputs of the OPF controller. The dynamic values of the system are state of charge for BESS and EV batteries, solar irradiance, dynamic load and EV switch. The values received from these components need to give prediction for better performance and to be stimulated in timely basis.

The predicted results then will be processed to give output for the grid switch, reference power for the voltage source converter, and reference current for the EV battery. The input i(t) values are presented in equation 18.

$$i(t) = [SI(t)\ SOC_{BESS}(t)\ SOC_{EV}(t)\ P_{dl}(t)\ S_{EV}(t)] \quad (18)$$

The predicted values are presented in equation 19.

$$i(t+\Delta t) = [SI(t+\Delta t)\ SOC_{BESS}(t+\Delta t)\ SOC_{EV}(t+\Delta t)\ P_{dl}(t+\Delta t)\ S_{EV}(t+\Delta t)] \quad (19)$$

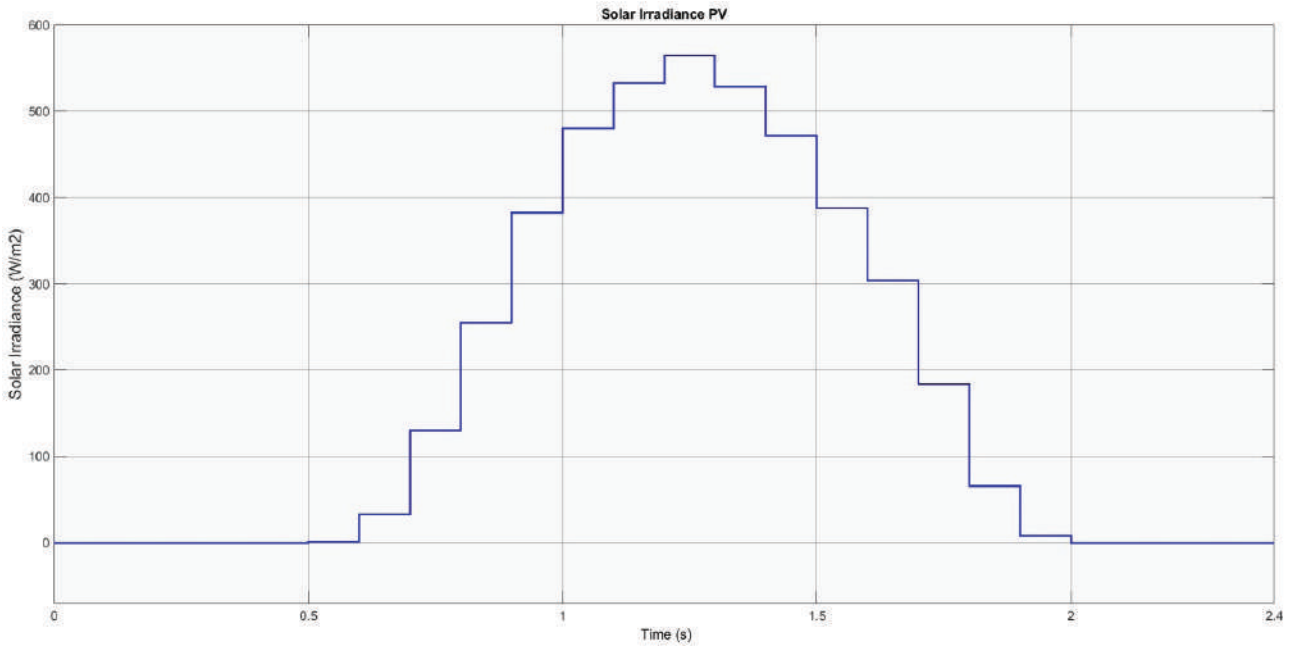


Figure 4. Shows the solar irradiance of the PV panel throughout the day.

Each predicted values are processed based on their characteristics and power performances.

The BESS battery discharges when the switch is islanded and charges from the solar PV during the grid connected mode. The EV system also performs as BESS battery, but the EV is assumed to be disconnected from 8 morning to 16 evening and from 18 evening to 20 evening.

The grid switch is either to be connected or disconnected is determined by the net power in the MG. If the generated power exceeds the load power, the MG can sustain itself, but it will supply power from main grid if the generated power is less than load power. The formula is shown in equation 20.

$$P_{net} = P_{gen} - P_l \tag{20}$$

Initially, it is verified whether the PV can supply energy to the loads. If the power from the PV is insufficient, the batteries must discharge to meet the load demand. When in grid-connected mode, the batteries are charged by the solar PV. The net power determines if the system operates in islanded mode (OPF) or grid-connected mode. In grid-connected mode, changes in the grid switch and reference current EV can be observed.

RESULTS AND DISCUSSION

The simulations and analysis of the MG system and OPF as a centralized controller were conducted in MATLAB/Simulink and the results were presented in this section of the paper. The outputs from the OPF are the reference values for grid switch, power to the voltage source converter and reference current for EV system and they were analyzed in all conditions. Later, the results of grid power, total solar PV power, BESS power, EV power and the loads power were presented in this paper. Finally, the voltage at the DC bus, voltage of the grid system and the current from the voltage source converter were presented.

The results were obtained based on three conditions as mentioned below.

- Normal Condition
- Abnormal solar irradiance PV, where the sun disappears, and the irradiance drops to zero.
- A condition where both battery energy storage system and electric vehicle experience zero charge.

The results in each condition then were discussed at the end of this section.

Normal condition

The simulation results show the performance of the OPF as a centralized controller in normal condition. The grid switch goes to grid connected mode twice throughout the day, the power to the voltage source converter follows the switching mode and the reference current changes a lot during the day as shown in Figure 5. The grid is islanded at (switch=1) and grid-connected at (switch=0).

The results for the power of the MG units are presented in Figure 6. The grid power activates twice when the MG is grid-connected, the PV power increases when the solar irradiance increases. The power results of dynamic load, constant load, BESS battery and EV batteries are also presented during normal condition.

The results for voltage of the grid system, the current from the voltage source converter, and the voltage at the

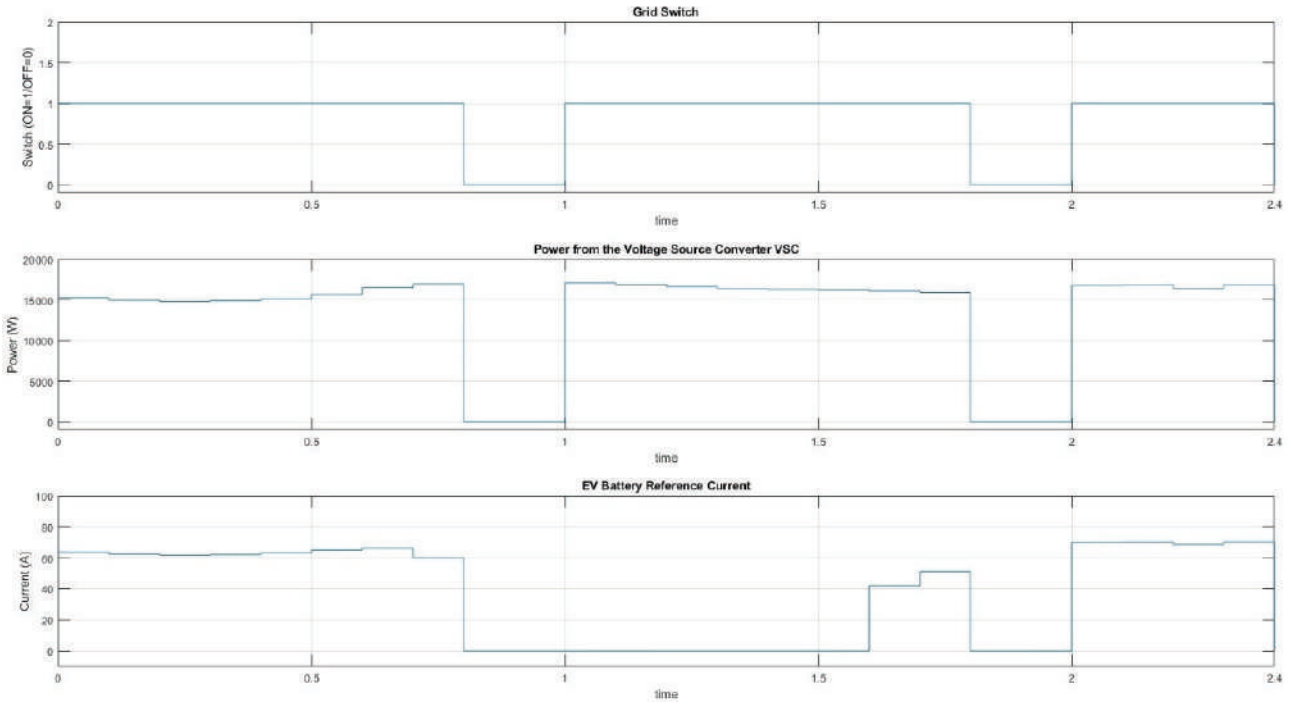


Figure 5. Shows the grid switch, power from the VSC, and the EV battery reference current in normal condition.

DC bus are presented in Figure 7. After changes occur in switching modes the voltages experience voltage surge and it stabilizes shortly. The fluctuations occurred at 0.8s, 1s, 18s and at 2s. The DC bus and voltage at the grid side were able to maintain 400 V at all time.

Solar irradiance abnormal condition

Here, the results are presented in solar irradiance PV abnormal condition, where the sun follows irradiance output until 1.2 seconds and then goes to zero. In this case, MG system will experience changes in switching. The sudden change in solar irradiance changes the performance of the grid switching mode. Here, the grid switch experience islanded mode three times and followed by the power from the VSC. The EV battery reference current changes many times throughout the day. The grid is islanded at (switch=1) and grid-connected at (switch=0). The results are presented in Figure 8.

The power results of the grid, solar PV, dynamic load, constant load, BESS battery and the EV battery are presented in Figure 9.

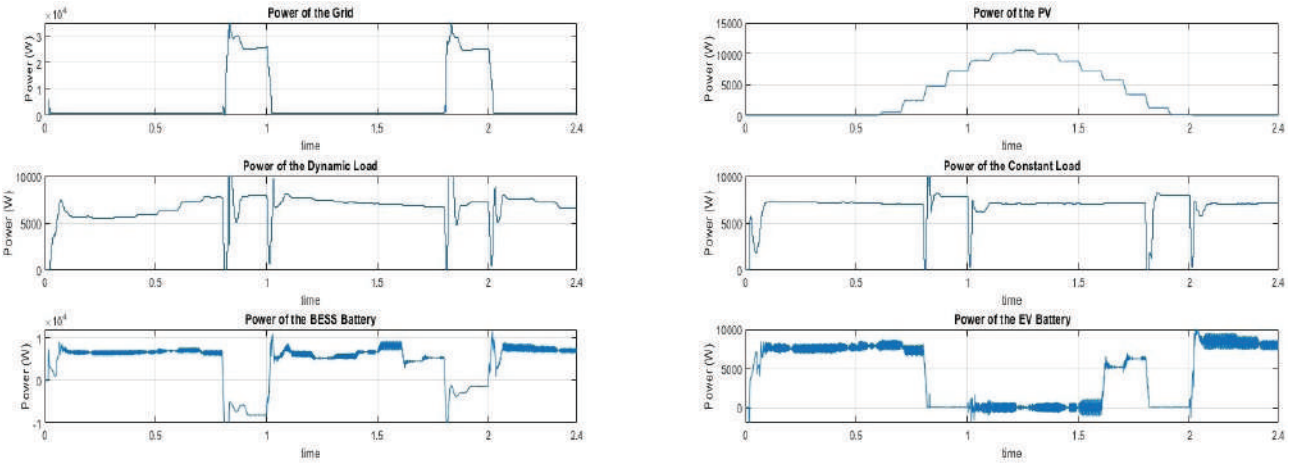


Figure 6. Shows the power results for OPF during normal condition.

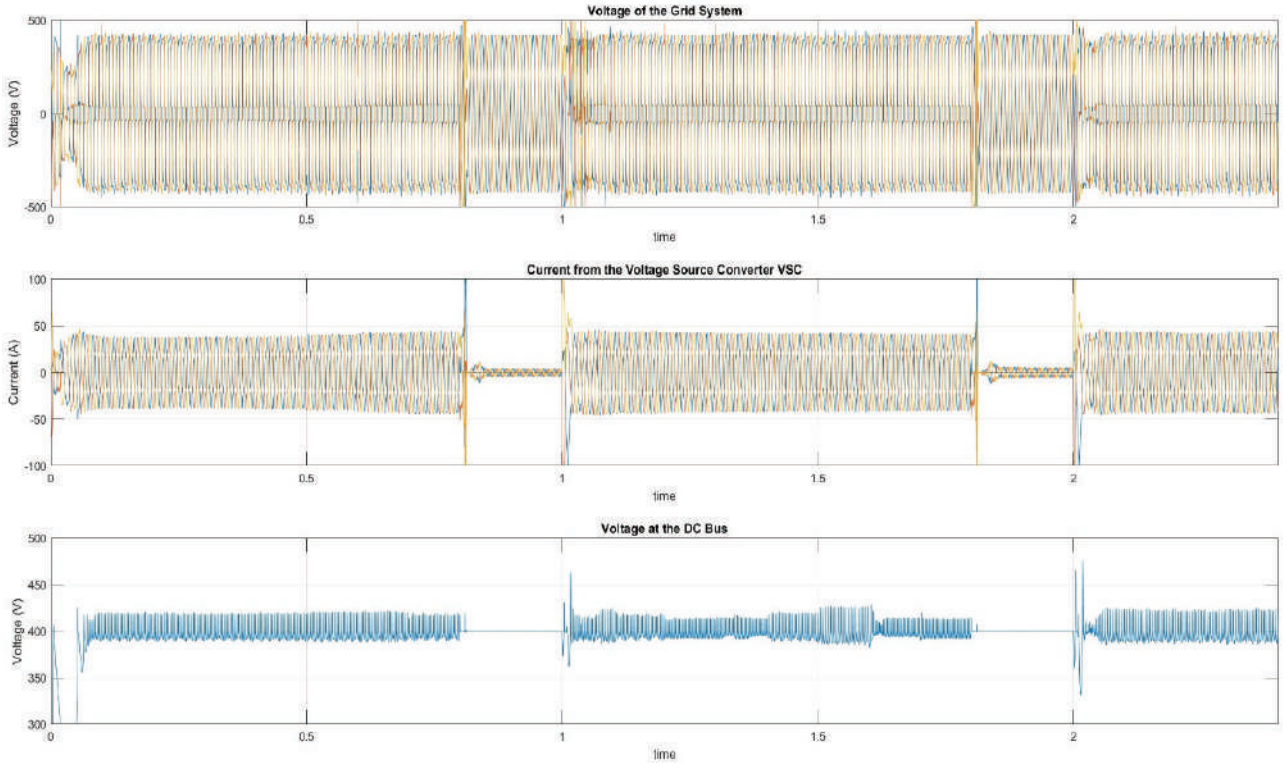


Figure 7. Voltage at the grid system, current at VSC, voltage at the DC bus for OPF in normal condition.

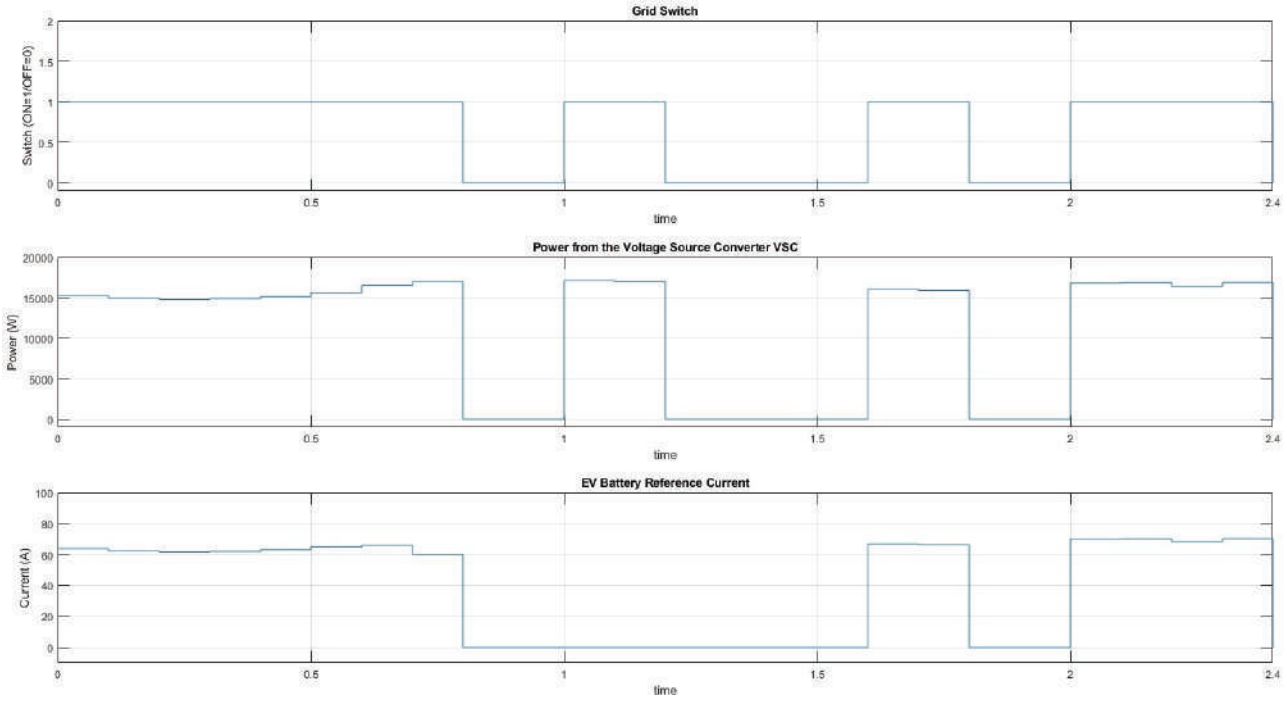


Figure 8. Shows the grid switch, power from the VSC, and the EV battery reference current in solar irradiance abnormal condition.

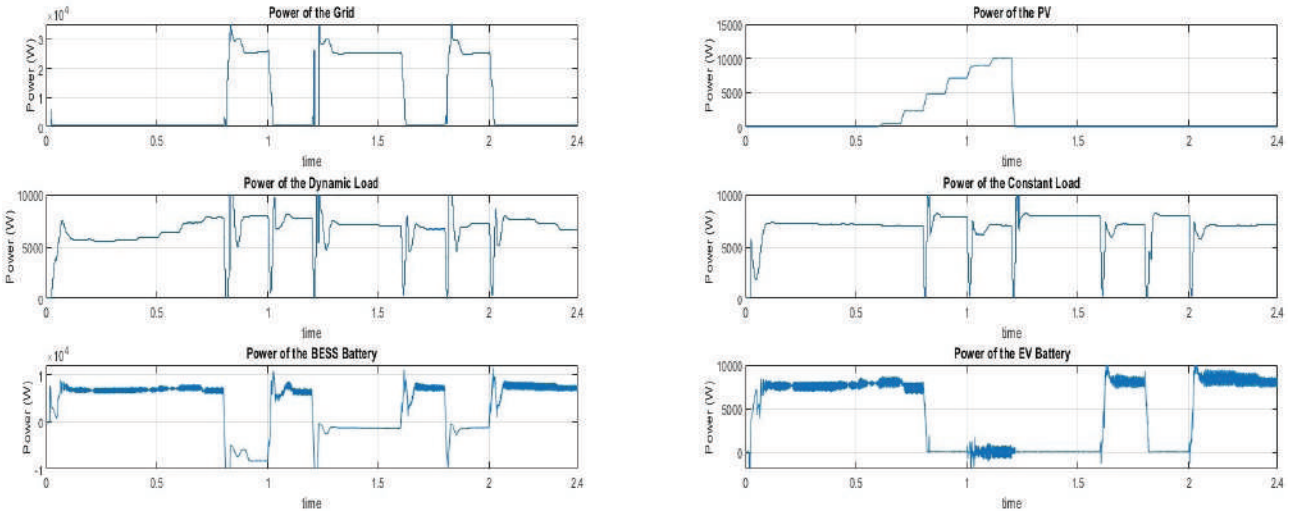


Figure 9. Shows the power results for OPF during solar irradiance abnormal condition.

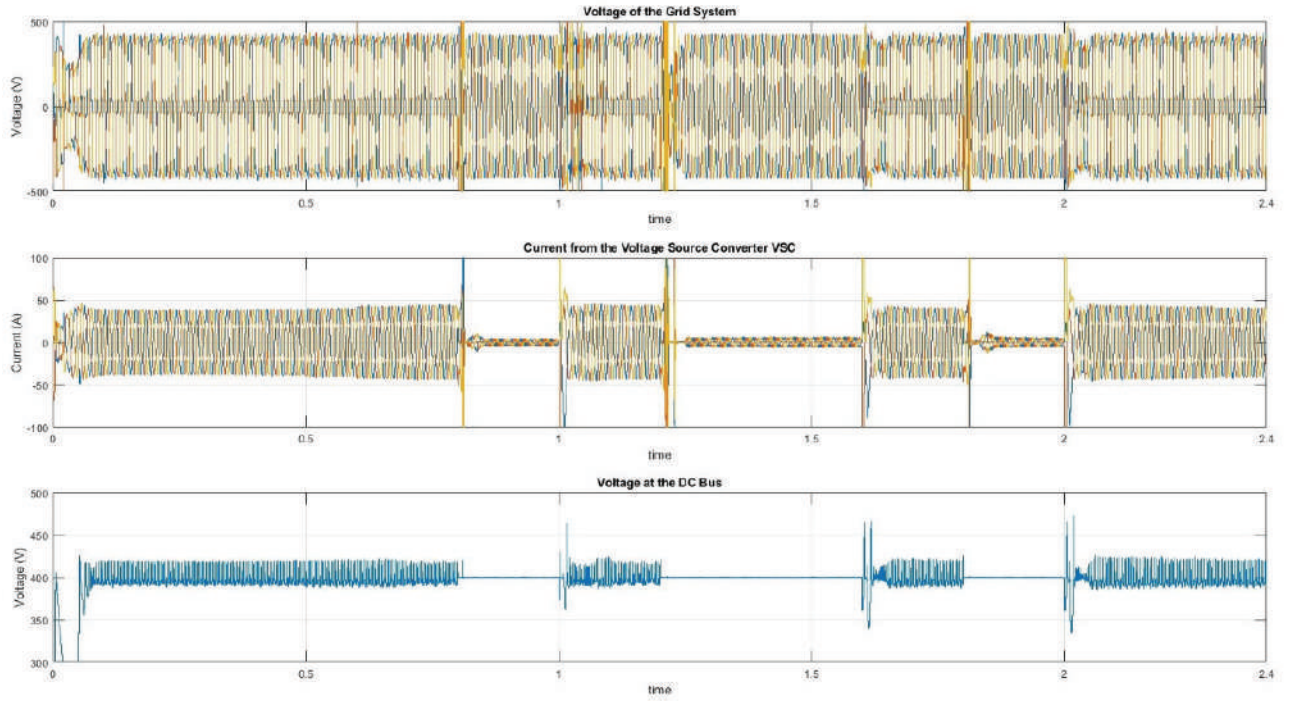


Figure 10. Voltage at the grid system, current at VSC, voltage at the DC bus for OPF in solar irradiance abnormal condition.

The results for voltage of the grid system, voltage at the DC bus, and current for the VSC are presented in Figure 10.

c. The State of Charge (SOC) for both the Battery Energy Storage System (BESS) and Electric Vehicle (EV) at 0% condition

The results for grid switch, power from the VSC, and the EV battery reference current are presented in Figure 11. At sate of zero charge for BESS and EV the MG system fully supported by the main grid power supply. The grid switch remains at grid-connected mode (switch=0).

The MG purpose is to balance power quality, overcome limitations, reduce power losses and enhance cost efficiency of a system. The OPF controller used as a power management strategy to effectively control the power flow of the system.

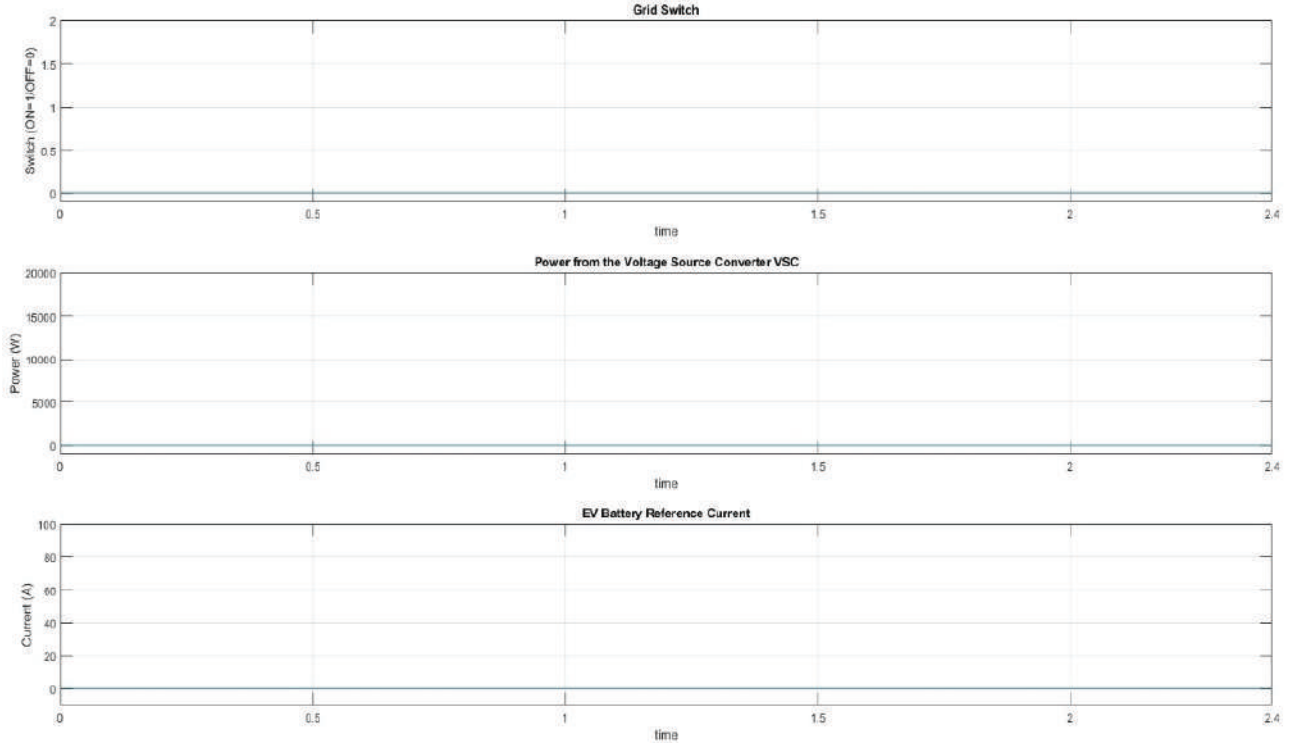


Figure 11. Shows the grid switch, power from the VSC, and the EV battery reference current in the EV, and BESS battery SOC 0% condition.

However, there are some ripples occurred when the switching modes changed from 0 to 1 or 1 to 0. These fluctuations need to be kept at minimum so the system can have much better performance both before and after switching modes. There are some works need to be done for future work. For future studies, the limitations such as fluctuations occurring immediately after switching modes, as observed in the results need to be reduced, and the system can be analyzed in a microgrid system with a higher capacity to better understand the effect of the controller. Moreover, the number of power sources such as wind power, and other renewable energy sources can be added to the system. Hence, the proposed project can be realized in real project and the comparison between simulation and prototype will be verified and will be discussed further.

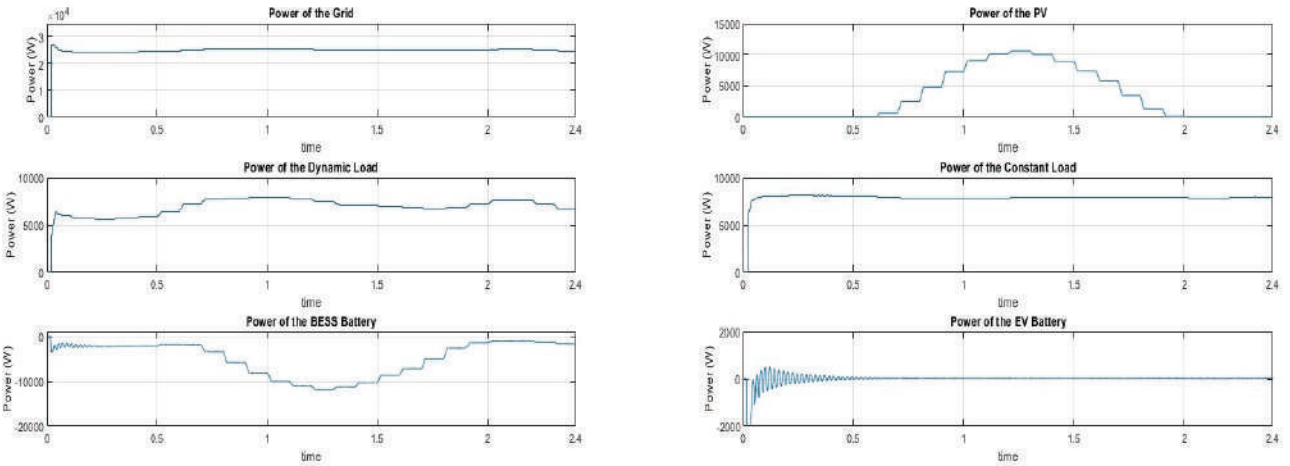


Figure 12. Shows the power results for OPF during EV and BESS battery SOC 0% condition.

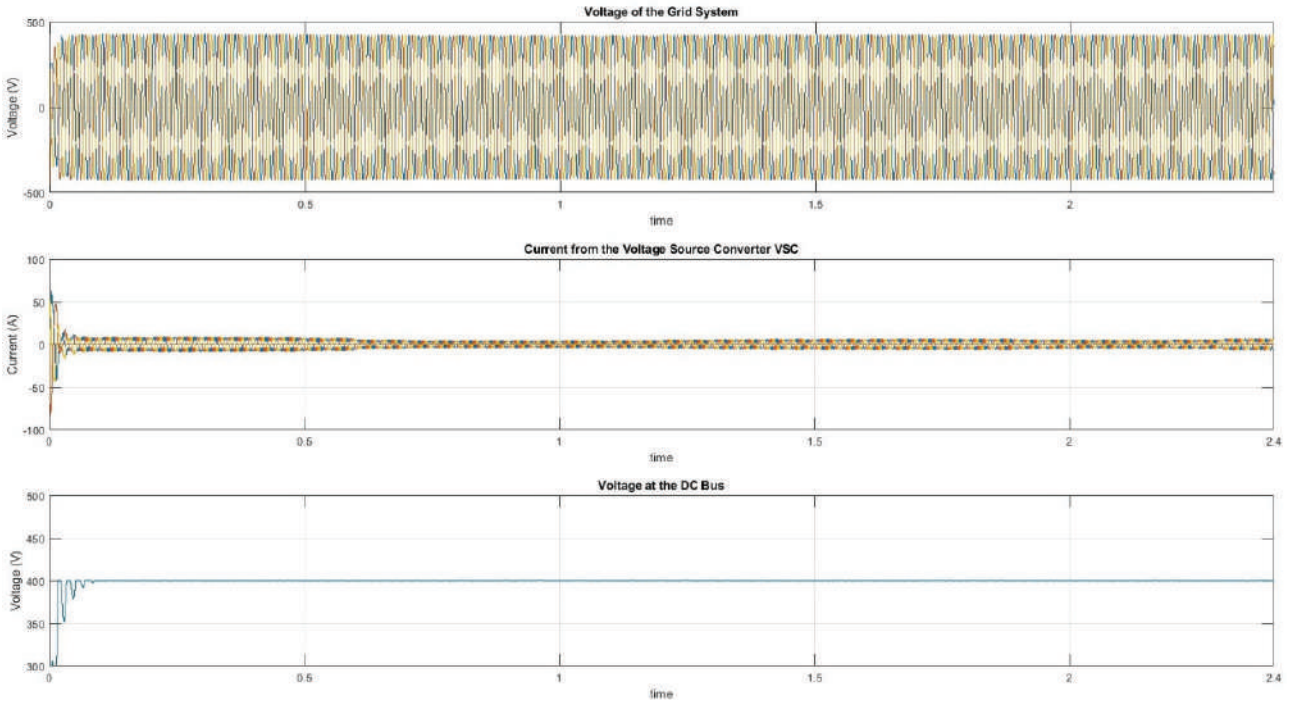


Figure 13. Voltage at the grid system, current at VSC, voltage at the DC bus for OPF in EV and BESS battery SOC 0% condition.

CONCLUSION

As the world rapidly advances, the use of renewable energy sources is also on the rise. To ensure efficient and reliable power distribution in Microgrid systems, power management strategies must be enhanced. The energy sources can experience disturbances, faults and fluctuations in parameters that's why the controllers are required to balance these disturbances. More research has been conducted to minimize instability in Microgrid system. Some researchers used PI controllers to improve the performance of the Microgrid system. However, this paper incorporated optimum power flow used as a centralized controller to control the switching mode between renewable energy source and main grid power. The Microgrid (MG) consists of dynamic load, constant load, solar PV, Battery Energy Storage system (BESS) and electrical vehicle battery, and a grid. The optimum power flow (OPF) is used to provide safe and economic operation of Power Systems. Some Real-life cases such as the uncertainty of load demand and the changing in Irradiance level which affect the microgrids efficiency have been taken into the account. The inputs of the OPF received information from Microgrid and processed them with an algorithm and presented output results for grid switch, reference power for voltage source converter and reference current for the EV battery. The results showed that the OPF can control the switching modes when the power supply from sources is lower than loads. After switching occurred there were ripples in the voltages, this is because of the sudden change in grid switch. For future work it is necessary to improve the system for better performance and minimize the fluctuations in voltage at the grid and voltages at the DC bus.

The analysis and simulations indicate that the OPF based power management strategy can be implemented in a hybrid Microgrid system to enhance power flow, power supply efficiency and reliability of the system.

AUTHORSHIP CONTRIBUTIONS

Authors equally contributed to this work.

DATA AVAILABILITY STATEMENT

The authors confirm that the data that supports the findings of this study are available within the article. Raw data that support the finding of this study are available from the corresponding author, upon reasonable request.

CONFLICT OF INTEREST

The author declared no potential conflicts of interest with respect to the research, authorship, and/or publication of this article.

ETHICS

There are no ethical issues with the publication of this manuscript.

STATEMENT ON THE USE OF ARTIFICIAL INTELLIGENCE

Artificial intelligence was not used in the preparation of the article.

REFERENCES

[1] Bragatto T, Carere F, Gatta FM, Geri A, Maccioni M, Simbolotti G. Electrical energy production from coal: Technical and economic performances during the last twenty years. In: 2022 IEEE International Conference on Environment and Electrical Engineering and 2022 IEEE Industrial and Commercial Power Systems Europe (EEEIC / I&CPS Europe). Prague, Czech Republic: IEEE; 2022. p. 1–6. [CrossRef]

[2] Belge AT, Mishra S, Alegavi S. A review on alternative energy sources. In: 2022 5th International Conference on Advances in Science and Technology (ICAST). Mumbai, India: IEEE; 2022. p. 558–563. [CrossRef]

[3] Lebsir A, Benamimour T. Renewable energies in the twenty-first century: A global-view. In: 2023 Second International Conference on Energy Transition and Security (ICETS). Adrar, Algeria: IEEE; 2023. p. 1–6. [CrossRef]

[4] Wang Z, Jiang T, Liu G, Hu J, Lu S. Study on optimization of consumption and delivery scheme of high-proportion renewable energy grid in zero-carbon park based on cuckoo search. In: 2023 2nd International Conference on Clean Energy Storage and Power Engineering (CESPE). Xi'an, China: IEEE; 2023. p. 207–211. [CrossRef]

[5] Swain A, Dash SS, Bastia S, Bagarty DP, Behera S. Source side control analysis of an AC microgrid fed with hybrid renewable distributed energy sources. In: 2020 3rd International Conference on Energy, Power and Environment: Towards Clean Energy Technologies. Shillong, India: IEEE; 2021. p. 1–5. [CrossRef]

[6] Habibnia S, Mahdavi MS, Gharehpetian GB, Ahmadiahangar R, Rosin A, Vinnikov D. A new master-slave based centralized control method for an AC microgrid with multiple distributed energy resources. In: 2022 IEEE 13th International Symposium on Power Electronics for Distributed Generation Systems (PEDG). Kiel, Germany: IEEE; 2022. p. 1–6. [CrossRef]

[7] Pattnayak SK, Choudhury S, Nayak N, Bagarty DP, Biswabandhya M. Maximum power tracking & harmonic reduction on grid PV system using chaotic gravitational search algorithm based MPPT controller. In: 2020 International Conference on Computational Intelligence for Smart Power System and Sustainable Energy (CISPSSE). Keonjhar, India: IEEE; 2020. p. 1–6. [CrossRef]

[8] Xiao W. Photovoltaic power system: Modelling, design and control. Hoboken, NJ: John Wiley & Sons; 2017. [CrossRef]

[9] Baranzelli C, Lavalle C, Sgobbi A, Aurambot J, Trombetti J, Jacobs J, et al. Regional patterns of energy production and consumption factors in Europe: Exploratory project EREBILAND: European regional energy balance and innovation landscape. LU Regional patterns of energy production and consumption factors in Europ: Publications Office; 2016. Available at: https://data.europa.eu/doi/10.2788/357099 Accessed on Nov 25, 2025.

[10] Yılmaz A, Alkan A. Investigation of power system transient disturbances in frequency and time-frequency domains. SIGMA 2014;32:154–162.

[11] Brandao DI, Ferreira WM, Alonso AMS, Tedeschi E, Marafao FP. Optimal multiobjective control of low-voltage AC microgrids: Power flow regulation and compensation of reactive power and unbalance. IEEE Trans Smart Grid 2020;11:1239–1252. [CrossRef]

[12] Ekinci S. Power system stabilizer design for multi-machine power system using bat search algorithm. SIGMA 2015;33:627–633.

[13] Pourbabak H, Alsafasfeh Q, Su W. A distributed consensus-based algorithm for optimal power flow in DC distribution grids. IEEE Trans Power Syst 2020;35:3506–3515. [CrossRef]

[14] Hu J, Ma H. Distributed real-time optimal power flow strategy for DC microgrid under stochastic communication networks. J Mod Power Syst Clean Energy 2023;11:1585–1595. [CrossRef]

[15] Eajal AA, Yazdavar AH, El-Saadany EF, Salama MMA. Optimizing the droop characteristics of AC/DC hybrid microgrids for precise power sharing. IEEE Syst J 2021;15:560–569. [CrossRef]

[16] Mahouti P, Belen MA, Pa H, Güne F. Design of a high efficiency power amplifier for wireless and radar applications. 2015.

[17] Kabak M, Taşkınöz G. Determination of the installation sites of wind power plants with spatial analysis. A model proposal. Sigma J Eng Nat Sci 2020;38:441–457.

[18] Yasseen H, Csatár J. Power management strategy of AC/DC hybrid microgrids based on integrating battery SoC conditions to state logic control algorithm. In: 2024 12th International Conference on Smart Grid (icSmartGrid). Setubal, Portugal: IEEE; 2024. p. 727–731. [CrossRef]

[19] Al-Ammar EA, Habib HUR, Waqar A, Wang S, Rahman MM, Ahmed A. Predictive direct power control of voltage source converters in microgrids during reconfiguration. In: 2020 Advances in Science and Engineering Technology International Conferences (ASET). Dubai, UAE: IEEE; 2020. p. 1–6. [CrossRef]

[20] Singh S, Narayanan V, Singh B, Panigrahi BK. Multiple voltage source converters based microgrid

with solar photovoltaic array and battery storage. e-Prime Adv Electr Eng Electron Energy 2024;7:100408. [CrossRef]

[21] Ganesan S, Nagarajan AP. An efficient buck-boost converter for fast active balancing of lithium-ion battery packs in electric vehicle applications. Comput Electr Eng 2024;118:109429. [CrossRef]

[22] Abdel-Moneim MG, Hamad MS, Abdel-Khalik AS, Hamdy RR, Hamdan E, Ahmed S. Analysis and control of split-source current-type inverter for grid-connected applications. Alex Eng J 2024;96:268–278. [CrossRef]

[23] Shayeghi H, Rahnama A, Takorabet N, Thounthong P, Bizon N. Designing a multi-stage PD(1+PI) controller for DC–DC buck converter. Energy Rep 2022;8:765–773. [CrossRef]

[24] Rousis AO, Konstantelos I, Strbac G. A planning model for a hybrid AC–DC microgrid using a novel GA/AC OPF algorithm. IEEE Trans Power Syst 2020;35:227–237. [CrossRef]

[25] Khan MN, Schulz NN. An optimal neighborhood energy sharing scheme applied to islanded DC microgrids for cooperative rural electrification. IEEE Access 2023;11:116956–116966. [CrossRef]

[26] Derbas AA, Kheradmandi M, Hamzeh M, Hatziargyriou ND. A hybrid power sharing control to enhance the small signal stability in DC microgrids. IEEE Trans Smart Grid 2022;13:1826–1837. [CrossRef]

[27] Ghosh SS, Chattopadhyay S, Das A, Medikondu NR, Almawgani AHM, Alhawari ARH, et al. Wavelet-based rapid identification of IGBT switch breakdown in voltage source converter. Microelectron Reliab 2024;152:115283. [CrossRef]

[28] Liu J, Liu J, Zhao Y. A unified control strategy for three-phase inverter in distributed generation. IEEE Trans Power Electron 2014;29:1176–1191. [CrossRef]

[29] Kumar N, Saha TK, Dey J. Multilevel inverter (MLI)-based stand-alone photovoltaic system: Modeling, analysis, and control. IEEE Syst J 2020;14:909–915. [CrossRef]

[30] Soheli SN, Sarowar G, Hoque MA, Hasan MS. Design and analysis of a DC–DC buck boost converter to achieve high efficiency and low voltage gain by using buck boost topology into buck topology. In: 2018 International Conference on Advancement in Electrical and Electronic Engineering (ICAEEE). Gazipur, Bangladesh: IEEE; 2018. p. 1–4. [CrossRef]

[31] Wu F, Fan S, Li X, Luo S. Bidirectional buck–boost current-fed isolated DC–DC converter and its modulation. IEEE Trans Power Electron 2020;35:5506–5516. [CrossRef]

[32] Eajal AA, El-Saadany EF, Ponnambalam K. Optimal power flow for converter-dominated AC/DC hybrid microgrids. In: 2017 IEEE International Conference on Industrial Technology (ICIT). Toronto, Canada: IEEE; 2017. p. 603–608. [CrossRef]

[33] Aljribi SFA. Optimal power flow for hybrid AC–DC microgrid. International Renewable and Sustainable Energy Conference (IRSEC), 2022.

[34] Ravada BR, Tummuru NR. Control of a supercapacitor-battery-PV based stand-alone DC-microgrid. IEEE Trans Energy Convers 2020;35:1268–1277. [CrossRef]

[35] Chellakhi A, El Beid S, Abouelmahjoub Y, Mchaouar Y. An efficient implementation of three-level boost converter with capacitor voltage balancing for an advanced MPPT approach in PV systems. e-Prime Adv Electr Eng Electron Energy 2024;9:100688. [CrossRef]

[36] Zhong QC, Ming WL, Zeng Y. Self-synchronized universal droop controller. IEEE Access 2016;4:7145–7153. [CrossRef]

[37] Wang Y, Liu Y, Bian J, Ji R. DC voltage control strategy research in multi-terminal HVDC system based on optimal AC/DC power flow. In: 2016 IEEE PES Asia-Pacific Power and Energy Engineering Conference (APPEEC). Xi'an, China: IEEE; 2016. p. 1948–1952. [CrossRef]

[38] Hamidieh M, Ghassemi M. Microgrids and resilience: A review. IEEE Access 2022;10:106059–106080. [CrossRef]

[39] Pathan J. Model predictive control of DC–DC buck converter and its comparison with PID controller.

[40] Nabatirad M, Razzaghi R, Bahrani B. Decentralized energy management and voltage regulation in islanded DC microgrids. IEEE Syst J 2022;16:5835–5844. [CrossRef]

[41] Ortmeyer T, Daryanian B, Datka P, Freeman L, Burns C. Design and benefit cost analysis of the Potsdam microgrid. In: 2022 IEEE Power & Energy Society General Meeting (PESGM). Denver, USA: IEEE; 2022. p. 1–5. [CrossRef]

[42] Liu T, Lai Y, Xue A, Yin Y, Chen Y, Yin X. Research and application of AC&DC hybrid power grid stability control technology. In: 2023 8th Asia Conference on Power and Electrical Engineering (ACPEE). Tianjin, China: IEEE; 2023. p. 2445–2449. [CrossRef]

[43] Peng S, Xie N, Wang C. A self-adaptive power flow analysis methodology for AC/DC hybrid system. IEEE Trans Power Deliv 2023;38:2261–2273. [CrossRef]

[44] Fleischhacker A, Corinaldesi C, Lettner G, Auer H, Botterud A. Stabilizing energy communities through energy pricing or PV expansion. IEEE Trans Smart Grid 2022;13:728–737. [CrossRef]

[45] Saif A, Khadem SK, Conlon MF, Norton B. Impact of distributed energy resources in smart homes and community-based electricity market. IEEE Trans Ind Appl 2023;59:59–69. [CrossRef]

[46] Shehzad M, Jamal N, Muqeet HA, Mirsaeidi S, Muttaqi KM. Cost effective analysis of stationary and mobile energy storage systems in prosumer

microgrid considering system reliability and real-time pricing scheme. In: 2023 IEEE International Conference on Energy Technologies for Future Grids (ETFG). Wollongong, Australia: IEEE; 2023. p. 1–5. [CrossRef]

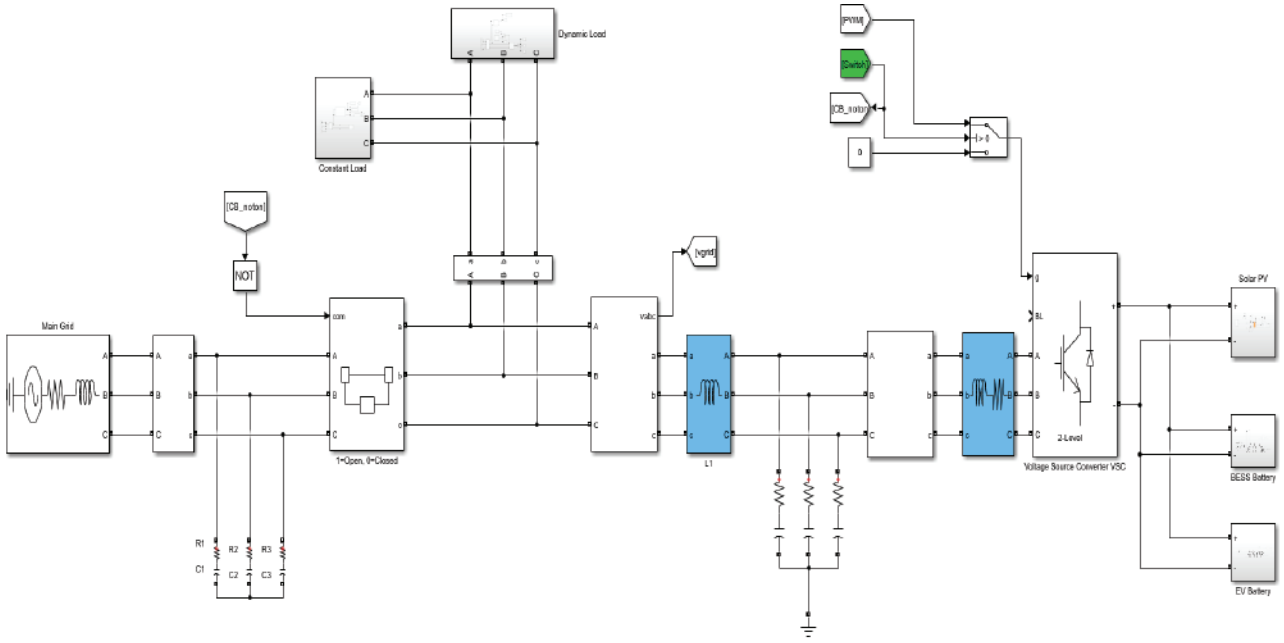
[47] Statnett. Rep data from the power system industry, 2021. Available at: https://www.statnett.no/en/for-stakeholders-in-the-power-industry/data-from-the-power-system/ Accessed on Feb 07, 2024.

[48] EU Science Hub. European Commission, Photovoltaic Geographical Information System (PVGIS) data 2023. Available at: https://joint-research-centre.ec.europa.eu/photovoltaic-geographical-information-system-pvgis_en Accessed on Feb 07, 2024.

APPENDICES

APPENDIX 1

The hybrid MG system with necessary components are given in Appendix 1.



Appendix 1. Shows the complete model of the hybrid MG system used in this paper.